COPY

ISEC'99

JUNE 21 - 25, 1999
CLAREMONT RESORT
BERKELEY, CA USA

7TH INTERNATIONAL SUPERCONDUCTIVE ELECTRONICS CONFERENCE

EXTENDED ABSTRACTS

DISTRIBUTION STATEMENT A
Approved for Public Release
Distribution Unlimited

CO-SPONSORS:

IEEE Superconductivity Council

Jet Propulsion Laboratory

NASA Glenn Research Center at Lewis Field, Cleveland, OH

NIST, Boulder

Office of Naval Research

Northrop Grumman Corporation

Papers have been reproduced as submitted by the authors.
Inclusion of a paper in these abstracts is in no way intended to restrict its publication anywhere else.

DTIC QUALITY INSPECTED 4

19990909 051

REPORT DOCUMENTATION PAGE

Form Approved
OMB No. 0704-0188

Public reporting burden for this collection of information is estimated to average 1 hour per response, including the time for reviewing instructions, searching data sources, gathering and maintaining the data needed, and completing and reviewing the collection of information. Send comments regarding this burden estimate or any other aspect of this collection of information, including suggestions for reducing this burden to Washington Headquarters Service, Directorate for Information Operations and Reports, 1215 Jefferson Davis Highway, Suite 1204, Arlington, VA 22202-4302, and to the Office of Management and Budget, Paperwork Reduction Project (0704-0188) Washington, DC 20503.
PLEASE DO NOT RETURN YOUR FORM TO THE ABOVE ADDRESS.

1. REPORT DATE *(DD-MM-YYYY)*	2. REPORT DATE	3. DATES COVERED *(From - To)*
June 21, 1999	Special	NA

4. TITLE AND SUBTITLE
7th International Superconductive Electronics Conference Extended Abstracts

5a. CONTRACT NUMBER
NA

5b. GRANT NUMBER
N00014-99-1-0939

5c. PROGRAM ELEMENT NUMBER
NA

6. AUTHOR(S)
Not Applicable

Ted Van Duzer, Symposium Manager

5d. PROJECT NUMBER
NA

5e. TASK NUMBER
NA

5f. WORK UNIT NUMBER
NA

7. PERFORMING ORGANIZATION NAME(S) AND ADDRESS(ES)
International Superconductive Electronics Conference
June 21-25, 1999 Berkeley, CA USA

8. PERFORMING ORGANIZATION REPORT NUMBER
NA

9. SPONSORING/MONITORING AGENCY NAME(S) AND ADDRESS(ES)
Office of Naval Research
ONR 251: Kasey E. Howard
Ballston Centre Tower ONe
800 North Quincy St Arlington, VA 22217-5660

10. SPONSOR/MONITOR'S ACRONYM(S)
ONR

11. SPONSORING/MONITORING AGENCY REPORT NUMBER
PR#-99PR07227-00

12. DISTRIBUTION AVAILABILITY STATEMENT
No limitations

13. SUPPLEMENTARY NOTES
none

14. ABSTRACT
Publication of extended abstracts as submitted for oral and poster presentation at the 7th International Superconductive Electronics Conference held June 21 - 25, 1999 in Berkeley, CA USA.

15. SUBJECT TERMS
Superconductive Electronics

16. SECURITY CLASSIFICATION OF:			17. LIMITATION OF ABSTRACT	18. NUMBER OF PAGES	19a. NAME OF RESPONSIBLE PERSON
a. REPORT	b. ABSTRACT	c. THIS PAGE			Ted Van Duzer
none	none	none	UU	603	19b. TELEPONE NUMBER *(Include area code)* 510/642-3306

Leadership of ISEC'99

Conference Chairman

Ted Van Duzer

Program Committee

Stephen R. Whiteley, Chairman

John Clarke	William R. McGrath
Oleg Mukhanov	Ron Ono
Randy Simon	Richard Withers

International Advisory Committee

USA

John Clarke	Oleg Mukhanov
Martin Nisenoff	Ron Ono
John X. Przybysz	John W. Spargo

Europe

Denis Crete	Gordon Donaldson
Sergio Pagano	Horst Rogalla
Oleg Snigirev	Dag Winkler

Asia

Hisao Hayakawa	Takeshi Kobayashi
Jong-chul Park	Akira Shoji
Shuichi Tahara	Pei Heng Wu

Preceding Page Blank

PREFACE

Welcome to the biennial International Superconductive Electronics Conference, ISEC'99, which was first held in Tokyo in 1991 and subsequently again in Tokyo, and then in Glasgow, Scotland, Boulder, Colorado, USA, Nagoya, Japan, and Berlin, Germany.

In the main part of this year's Conference, the oral papers are all presented in plenary sessions. There are two poster sessions in each of which the authors are present for a two-hour period and the posters are available for a full day. For the first time, a set of topical workshops is appended to the three days of oral and poster sessions. The aim of the workshops is to focus attention in small groups on the status of the various subjects and to reach consensus on the directions that research should take. The day of workshops will be summarized in a wrap-up session at the end of the day.

The book of Extended Abstracts is intended to provide a coherent record of the research presented at the Conference. The papers are not peer-reviewed nor is this book copyrighted, so the papers may be published elsewhere. Some of the papers, or extended versions of them, will be published in a special issue of *Superconductor Science and Technology*. The results of the workshop discussions will appear on the Conference web site, www.isec99.org, which will be maintained for one month after the Conference.

I would like to thank everyone who has participated in the planning and formation of the Conference. The committee membership is listed on the following page. The International Advisory Committee was very helpful in deciding on several key structural aspects of the Conference. Mark Jeffrey's effort in setting up and maintaining the web site is greatly appreciated. We thank the several students from UC Berkeley who are voluntarily helping with the registration. The Program Committee devoted considerable talent and extensive time and effort in paper selection, organization and finding session chairs. We appreciate also the willingness of their companies and laboratories in making their involvement possible. Very special thanks is owed to Stephen Whiteley, the Program Committee Chairman, who devoted uncountable hours to bring together the abstracts and extended abstracts and to form the program. It also has been a pleasure to work with Paula Pair and Virginia Schultz of Centennial Conferences, who have handled to logistics of this Conference.

Special appreciation goes to the several organizations listed on the cover, which have provided essential financial support for the conference. I would like to thank those who facilitated the support.

T. Van Duzer, Chairman, ISEC'99

1999 International Superconductive Electronics Conference

PROGRAM SUMMARY

Monday, June 21

4:00 PM – 7:00 PM	**Registration**
5:00 PM – 7:00 PM	**Reception**
7:00 PM – 9:00 PM	**Poster Session I Installation**

Tuesday, June 22

8:20 AM – 10:00 AM	**Opening Remarks and Oral Session** – General Plenary
10:00 AM – 10:15 AM	**Coffee Break**
10:15 AM – 12:15 PM	**Oral Session** – Analog/Digital and Digital/Analog Conversion
12:15 PM – 1:15 PM	**Lunch**
1:15 PM – 3:15 PM	**Oral Session** – Digital Circuits
3:15 PM – 3:30 PM	**Coffee Break**
3:30 PM – 5:45 PM	**Oral Session** – Analog Filters and Subsystems
7:30 PM – 9:30 PM	**Poster Session I**

Wednesday, June 23

8:30 AM – 10:15 AM	**Oral Session** - HTS Josephson Junctions
10:15 AM – 10:30 AM	**Coffee Break**
10:30 AM – 12:15 PM	**Oral Session** – Materials and Fabrication
	Free Afternoon
12:15 PM – 2:00 PM	**Poster Session I Removal**
5:00 PM – 6:00 PM	**Poster Session II Installation**
7:30 PM – 9:30 PM	**Poster Session II**

Thursday, June 24

8:30 AM – 10:00 AM	**Oral Session** – Mixers and Detectors
10:00 AM – 10:15 AM	**Coffee Break**
10:15 AM – 12:15 PM	**Oral Session** – SQUIDs I
12:15 PM – 1:15 PM	**Lunch**
1:15 PM – 3:15 PM	**Oral Session** – SQUIDs II
3:15 PM – 3:30 PM	**Coffee Break**
3:30 PM – 5:15 PM	**Oral Session** – Analog Instruments and Novel Coolers
5:15 PM – 6:00 PM	**Poster Session II Removal**
	CONFERENCE ENDS

ISEC'99 Workshops

Friday, June 25

8:00 AM – 8:30 AM	**Continental Breakfast**
8:30 AM – 11:30 AM	**Workshops**
11:30 AM – 12:30 PM	**Lunch**
12:30 PM – 3:15 PM	**Workshops**
3:15 PM – 3:30 PM	**Coffee Break**
3:30 PM – 5:00 PM	**Joint Session – Wrap-up**
	WORKSHOPS END

TECHNICAL PROGRAM

Opening Remarks 8:20 - 8:30

Ted Van Duzer, University of California, Berkeley

Oral Session 1, Tuesday Morning 8:30 - 10:00
General Plenary

Chair: Hisao Hayakawa

Or1.1 8:30 (Invited) Superconducting digital technology
Shuichi Tahara, Hideaki Numata, Shinichi Yorozu, Yoshihito Hashimoto, and Shuichi Nagawasa
Fundamental Research Laboratories, NEC Corp., Tsukuba

Or1.2 9:00 (Invited) SQUIDs: Present and future
John Clarke
Department of Physics, UC Berkeley

Or1.3 9:30 (Invited) HTS technology for wireless communications
Randy Simon
Conductus

BREAK 10-10:15

Oral Session 2, Tuesday Morning 10:15 - 12:15
Analog/Digital and Digital/Analog Conversion

Co-Chairs: John Spargo and Mark Jeffery

Or2.1 10:15 Progress in high resolution ADC
O. Mukhanov, D. Brock, A. Kirichenko, W. Li, S. V. Rylov, J. M. Vogt, V. K. Semenov, T. Fillipov*, and Yu. A. Polyakov**
*HYPRES, *SUNY, Stony Brook*

Or2.2 10:30 Superconducting bandpass delta-sigma modulator
J. F. Bulzacchelli, H.-S. Lee, J. A. Misewich, and M. B. Ketchen**
*MIT, *IBM Watson Laboratory*

Or2.3 10:45 Demonstration of Josephson sigma-delta analog-to-digital converters
D. L. Miller, J. X. Przybysz, A. H. Worsham, E. J. Dean, M. G. Forrester, and B. D. Hunt
Northrup Grumman STC

Or2.4 11:00 Comparison of superconductor analog-to-digital converters (theory)
V. K. Semenov
SUNY, Stony Brook

Or2.5 11:15 All-digital measurement of the energy sensitivity of a superconductive comparator
D. A. Feld, K. K. Berggren, J. P. Sage, A. Siddiqui, and T. Weir
MIT Lincoln Laboratory

Or2.6 11:30 Analog demonstration of a high-temperature superconducting sigma-delta modulator with 27 GHz sampling
M. G. Forrester, B. D. Hunt, D. L. Miller, J. Talvacchio, and R. M. Young
Northrup Grumman STC

Or2.7 11:45 A high-temperature superconducting delta-sigma modulator based on a multilayer technology with bicrystal Josephson junctions
B. Ruck, Y. Chong, R. Dittmann, A. Engelhart, E. Sodtke, and M. Siegel*
*GmbH Jülich, *Seoul National Laboratory*

Or2.8 12:00 Integrated microwave circuits for digital-to-analog converter on high-temperature Josephson junction arrays
A. M. Klushin, C. Weber, M. Siegel, S. I. Borovitskii, R. K. Starodubrovskii*, K. Yu. Platov**, M. Yu. Kuprianov**, and R. Semerad****
*GmbH Jülich, *KVARZ, Nizhny Novgorod,*
Moscow State University,Technischen Universität München*

LUNCH 12:15-1:15

Oral Session 3, Tuesday Afternoon 1:15 - 3:15
Digital Circuits

Co-Chairs: Shuichi Tahara and John Przybysz

Or3.1 1:15 Advanced base station based on superconductive devices and software-defined radio technology
A. Fujimaki, H. Hayakawa , M. Katayama, and A. Ogawa
Nagoya University

Or3.2 1:30 RSFQ subsystem for petaflops-scale computing: "cool-0"
P. Bunyk, M. Dorojevets, K. K. Likharev, P. Litskevitch, L. Wittie, and D. Zinoviev
SUNY Stony Brook

Or3.3 1:45 Component development for a 16 Gb/s digital superconducting ring data bus
M. Jeffery, N. Yoshikawa, J. Koshiyama*, L. Zheng, and T. Van Duzer*
*UC Berkeley, *Yokohama National University*

Or3.4 2:00 10 Kelvin operation of a high speed digital crossbar switch
A. M. Spooner, M. Leung, R. D. Sandell, L. R. Eaton, and J. W. Spargo*
**Sierra Monolithics, TRW*

Or3.5 2:15 A baseband demonstration of a spread spectrum modem using SFQ technology
*E. J. Dean, P. D. Dresselhaus, J. X. Przybysz, A. H. Worhsam, and S. V. Polonsky**
*Northrup Grumman, *RSFQ Consulting, Inc.*

Or3.6 2:30 Simulations of ultra-high-speed high temperature superconductor digital circuits combining process variations and thermal noise
M. Jeffery, L. Zheng, S. R. Whiteley, and T. Van Duzer
UC Berkeley

Or3.7 2:45 Production of Gold codes for a spread spectrum modem using SFQ technology
*P. D. Dresselhaus, E. J. Dean, J. X. Przybysz, A. H. Worsham, and S. V. Polonsky**
*Northrup Grumman STC, *RSFQ Consulting, Inc.*

Or3.8 3:00 Synchronous 5-10 Gb/s digital superconducting amplifier circuits fabricated with a horseshoe architecture
*W. J. Perold and M. Jeffery**
*University of Stellenbosch, South Africa, *UC Berkeley*

BREAK 3:15 - 3:30

Oral Session 4, Tuesday Afternoon 3:30 - 5:45
Analog Filters and Subsystems

Co-Chairs: Randy Simon and Martin Nisenoff

Or4.1 3:30 (Invited) Can low-cost, high-reliability cryocoolers be a reality?
M. Nisenoff
Naval Research Laboratory

Or4.2 4:00 A superconducting RF three-pole filter in HF range
E. Gao, S. Sahba, H. Xu, and Q. Y. Ma
Columbia University

Or4.3 4:15 Design and fabrication of narrow-band compact configuration hairpin filters
S. Ohshima, T. Tomiyama, T. Kinpara, M. Kusunoki, and M. Mukaida
Yamagata University

Or4.4 4:30 High-frequency modes in lumped-element superconducting filters
S. Berkowitz, J.-F. Liang, and V. Borzenets
Conductus

Or4.5 4:45 Predicting nonlinear effects in superconducting microwave transmission lines from mutual inductance measaurements
*J. C. Booth, L. R. Vale, R. H. Ono, and J. H. Claassen**
*NIST, Boulder, *Naval Research Laboratory*

Or4.6 5:00 Comparison of microwave and mutual inductance measurements of the inductive nonlinearity of HTS thin films
J. H. Claassen, J. C. Booth, J. A. Beall, L. R.Vale, D. A. Rudman, and R. H. Ono*
*NIST, Boulder, *Naval Research Laboratory*

Or4.7 5:15 Two-dimensional resonators for local oscillators
K-C Huang, A. Jenkins, and D. Dew-Hughes
University of Oxford

Or4.8 5:30 Phase locking of 270-440 GHz Josephson flux flow oscillators
J. Mygind, V. P. Koshelets, S. V. Shitov*, L. V. Filippenko*, V. L.Vaks**, A. M. Baryshev***, W. Luinge***, and N. Whyborn****
*Technical University of Denmark, Lyngby, *Institute of Radio Engineering and Electronics, Moscow, **Institute for Physics of Microstructure, Nizhny Novgorod, ***SRON-Groningen*

POSTER SESSION I 7:30 - 9:30

Group 1 - Digital

PI-1.1 Measurements of an HTS four stage shift register circuit
J. H. Park, Y. H. Kim, J. H. Kang, T. S. Hahn, C. H. Kim, K. R. Jung*, J. M. Lee, and S. S. Choi*
*Korea Institute of Science and Technology, University of Inchon**

PI-1.2 Low-jitter on-chip clock for RSFQ circuit applications
*Y. Zhang and D. Gupta**
*Conductus, Inc., *HYPRES*

PI-1.3 Monte Carlo simulation of trap type single hole memory cell using layered structure of high-T_c superconductor
Q.Y. Cai, J. F. Jiang, and M. X. Tong
Shanghai Jiao Tong University

PI-1.4 Design and experimentation of BSFQ logic devices
T. Hosoki, H. Kodaka, M. Kitagawa, and Y. Okabe
RCAST, Univ. of Tokyo

PI-1.5 Time characteristics of a Josephson balanced comparator
*T. Filippov and M. Znosko**
*SUNY Stony Brook,NY, *Moscow State University*

PI-1.6 A new approach of optimization procedure for superconducting integrated circuits
K. Saitoh, Y. Soutome, Y. Tarutani, and K. Takagi
Advanced Research Laboratory, HITACHI

PI-1.7 A cell-based design approach for RSFQ circuits using binary decision diagram
N. Yoshikawa and J. Koshiyama
Yokohama National University

PI-1.8 Long Josephson junctions merged into the RSFQ environment
V. K. Kaplunenko and Y. Zhang
Conductus

PI-1.9 All-NbN integrated circuits based on NbN/AlN/NbN tunnel junctions
H. Terai and Z. Wang
Communication Research Laboratory, Japan

PI-1.10 High-speed and medium-speed testing of the RSFQ muiltiplexer and demultiplexer
L. Zheng, S. Whiteley, X. Meng, and T. Van Duzer
UC Berkeley

PI-1.11 High speed operation of RSFQ circuits up to 30 GHz
F. Furuta, Y. Suzuki, H. Hasegawa, E. Oya, A. Fujimaki, and H. Hayakawa
Nagoya University

PI-1.12 Phase-locked operation of RSFQ ring oscillators
C. A. Mancini and M. F. Bocko
University of Rochester

PI-1.13 Operating margins for a superconducting voltage waveform synthesizer
S. P. Benz, C. A. Hamilton, and C. J. Burroughs
NIST, Boulder

PI-1.14 An asynchronous SFQ-pulse arbiter for high performance digital applications
S. Yorozu, D. Zinoviev, and S. Tahara*
*NEC, Ibaraki, *SUNY at Stony Brook, NY*

PI-1.15 Design of a 10 GHz high-voltage driver operating with SFQ inputs
N. Harada, A. Yoshida, and N. Yokoyama
Fujitsu Ltd., Atsugi

PI-1.16 A single flux quantum cryogenic random access memory
A. F Kirichenko , O. A. Mukhanov, and D. K. Brock
HYPRES

PI-1.17 Analysis model of floating gate type memory cell consist of superconductor single electron transistor
J. F. Jiang, Q. Y. Cai, and M. X. Tong
Shanghai Jiao Tong University

PI-1.18 Microwave coupling of SINIS junctions in a programmable Josephson voltage standard
*R. Behr, H. Schulze, F. Müller, J. Kohlmann, J. Niemeyer, and I. Y. Krasnopolin**
Physikalisch-Technische Bundesanstalt, Braunschweig,
**Russian Research Institute for Metrological Service, Moscow*

Group 2 - SQUIDs

PI-2.1 Transport and noise properties of high T_c bicrystal junctions
K. Enpuku, T. Minotani, F. Shiraishi, and S. Ohta
Kyushu University

PI-2.2 High-T_c ramp-edge junctions and dc SQUIDs with a Ga-doped YBCO barrier
*I-H Song, E-H Lee, S-Y Yoon, and G. Park**
*Samsung Advanced Institute of Technology, Korea, *Sogang University, Korea*

PI-2.3 High-T_c SQUIDs on bicrystal substrate with low permittivity
M. Matsuda, S. Ono, K. Kato, K. Yokosawa, H. Oyama***, *and S. Kuriki***
*Muroran Institute of Technology, Japan, *Central Research Laboratory, Hitachi Ltd, **Hokkaido University*

PI-2.4 Peculiarities of RF SQUID response in finite magnetic fields
*E. Il'ichev, V. Schultze, R. P. J. IJsselsteijn, R. Stolz, V. Zakosarenko, H. E. Hoenig, H.-G. Meyer, and M. Siegel**
*Institute for Physical High Technology, Jena, Germany, *Forschungszentrum Jülich*

PI-2.5 Low-frequency noise and linearity of $YBa_2Cu_3O_7$ SQUID magnetometers in static magnetic fields
S. Krey, H.-J. Barthelmess, and M. Schilling
Universität Hamburg

PI-2.6 Low frequency flux noise in $YBa_2Cu_3O_x$ dc SQUIDs cooled in static magnetic fields
M. Sager, P. R. E. Petersen***, T. Holst, Y. Q. Shen, and J. Bindslev Hansen**
*NKT Research Center, Brøndby, Denmark, *Technical University of Denmark, **Rigshospitalet, Copenhagen*

PI-2.7 Direct coupled YBCO dc SQUID magnetometers
*P. R. E. Petersen***, Y. Q. Shen, M. Sager *, T. Holst, B. H. Larsen, and J. Bindslev Hansen**
NKT Research Center, Brøndby, Denmark,
**Technical University of Denmark, **Rigshospitalet, Copenhagen*

PI-2.8 Multipurpose LTS SQUID sensors
R. Stolz, L. Fritzsch, and H.-G. Meyer
Institute for Physical High Technology, Jena, Germany

PI-2.9 Field sensitivity limitation due to pick-up coil resonances
H. Seppä and M. Kiviranta
VTT Automation, Measurement Technology, Espoo, Finland

PI-2.10 Comparison of dc SQUID readout methods based on positive feedback
M. Kiviranta and H. Seppä
VTT Automation, Measurement Technology, Espoo, Finland

PI-2.11 Optimisation of a YBCO dc SQUID amplifier
D. L. Tilbrook, C. P. Foley, W. V. Waller, and Y. M. Wilson
CSIRO Telecommunications & Industrial Physics, Lindfield, Australia

PI-2.12 Optimisation of the SQUID read-out circuit for cryogenic particle detector
S. V. Uchaikin
Max-Planck Institut für Physik, München, Joint Institute for Nuclear Research, Dubna

PI-2.13 High-T_c SQUID microscope with sample chamber
S. Tanaka, O. Yamazaki, R. Shimizu, and Y. Saito
Toyohashi University of Technology

PI-2.14 Study into the feasibility of SQUID sensors for use in geophysical exploration
G. Macmillian, P. de Groot, Y. Zhuravlev, and D. Rassi**
*Southampton University, *University of Wales Swansea*

PI-2.15 Characterization of a dc-SQUID based accelerometer circuit for a superconducting gravity gradiometer
R. Scharnweber and J. M. Lumley
Oxford Instruments

PI-2.16 NDE system based on HTS SQUID array
M. Espy, R. H. Kraus, Jr., A. Matlashov,L. Atencio, and R. Cantor
Los Alamos National Laboratory

PI-2.17 HTS dc SQUID arrays fabricated on bicrystal substrates
*R. Cantor, M. A. Espy, A. Matlashov, R. H. Kraus, Jr., *
Y. Fan, Y. Gim, and Q. X. Jia
Los Alamos National Laboratory

Group 3 - Analog

PI-3.1 Microstrip coupled SNS Josephson junctions on p-type InAs
K. Biedermann, T. Matsuyama, and U. Merkt
Universität Hamburg

PI-3.2 Measurements of the dielectric properties of strontium titanate at sub-millimeter wavelengths using Josephson junction driven oscillators
P. F. McBrien, W. E. Booij, F. Kahlmann, M. G. Blamire, E. J. Tarte, E. J. Romans, and C. M. Pergrum**
*University of Cambridge, *Strathclyde University*

PI-3.3 Study of the magnetic tuning effect in HTS coplanar resonators
T. Nurgaliev, S. Miteva, A. Jenkins, and D. Dew-Hughes**
*Institute of Electronics BAS, Sofia Bulgaria, *University of Oxford*

PI-3.4 Experimental observation and simulation of unusual microwave response for the superconducting microstrip resonator at small DC magnetic field
C. K. Ong, X. S. Rao, and B. B. Jin
National University of Singapore

PI-3.5 Superconductor-semiconductor-superconductor (S/N/S) interferometers with phase sensitive conductance at V = 0 and V = Δ/e
J. Kutchinsky, R. Taboryski, J. Bindslev Hansen, M. Wildt, C. B. Sørensen*, and P. E. Lindelof**
*Technical University of Denmark, *University of Copenhagen*

PI-3.6 Extremely underdamped Josephson junctions for macroscopic quantum experiments
B. Ruggiero, E. Esposito, C. Granata, M. Russo, and P. Silvestrini
Istituto di Cibernetica del CNR, Arco Felice, Italy

PI-3.7 Third harmonics generation from Y-Ba-Cu-O bicrystal Josephson junctions in coplanar waveguides
H. Shimakage, J. C. Booth, L. R. Vale, and R. H. Ono
NIST, Boulder

PI-3.8 Microwave properties of tunable $TE_{01\delta}$ mode sapphire-loaded cavity resonators with $YBa_2Cu_3O_{7-\delta}$ endplates
S. Y. Lee, H. J. Kwon, J. H. Lee, W. I. Yang, J. K. Kim, W. H. Lee, and J. Hur
Konkuk University, Seoul, Korea

PI-3.9 Preparation of all oxide ferromagnetic/ferroelectric/superconducting hetero-structures for advanced microwave applications
S. Hontsu, H. Nishikawa, H. Nakai, J. Ishii, M. Nakamori, A. Fujimaki**, Y. Noguchi, , H. Tabata***, and T. Kawai****
*Kinki University, *Kumano Technical College, **Nagoya University, ***Osaka University*

Group 4 - Detectors and Mixers

PI-4.1 Development of transition-edge microbolometers for space applications
A. Luukanen, H. Sipilä, K. Kinnunen, A. Manninen*, A. Nuottajärvi*, J. Pekola*, S. Pöyhönen*, I. Suni**, and J. Salmi***
*Metorex International, Espoo, Finland, *University of Jyväskylä, Finland, **VTT Automation, Finland, VTT Electronics, Finland,*

PI-4.2 Molybdenum-gold proximity bilayers as transition edge sensors for microcalorimeters and bolometers
*T. C. Chen*****, F. M. Finkbeiner***, A. Bier***, B. DiCamillo*****, *University of Maryland, **NASA/Goodard Space Flight Center, ***Global Science & Technology Inc.*

PI-4.3 Nonequilibrium kinetic inductive response of Y-Ba-Cu-O photodetectors
*C. Williams, R. Adam, R. Sobolewski, and O. Harnack**
University of Rochester, NY
** Forschungszentrum Jülich, Germany*

PI-4.4 Optimization of 115 GHz wave-guide mixer based on HTS Josephson junction
O. Harnack, M. Darula, J. Scherbel, J-K. Heinsohn, M. Siegel, D. Diehl, and P. Zimmermann**
Forschungszentrum Jülich, Germany,
**Radiometer Physics GmbH, Meckenheim, Germany*

PI-4.5 Sub-micron long HTS hot-electron mixers
O. Harnack, B. S. Karasik, W. R. McGrath, A. W. Kleinsasser, and J. B. Barner
Jet Propulsion Laboratory

PI-4.6 A nanoscale YBCO mixer optically coupled with a bow tie antenna
F. Rönnung, S. Cherednichenko, D. Winkler, and G. Gol'tsman,*
*Chalmers University of Technology, *Moscow State Pedagogical University*

PI-4.7 Large area $YBa_2Cu_3O_{7-x}$ bolometers on Si substrates
L. R. Vale, R. H. Ono, D. G. McDonald, and R. J. Phelan**
*NIST, Boulder, *Boulder Metric, Inc.*

PI-4.8 Characterization of planar log-periodic antennas at low temperatures using HTS Josephson junctions
*J. Chen ******, E. Kobayashi*, K. Nakajima***, T. Yamashita***, and J. Zmuidzinas****
**Tohoku University, **CREST, Japan Science and Technology Corporation, ***California Institute of Technology*

PI-4.9 Mesoscopic SNS mixers using negative resistance at low voltage
T. Matsui and H. Ohta
Communications Research Laboratory, Japan

PI-4.10 Heterodyne type response in SIS direct detector
A. Karpov, J. Blondel, P. Dmitriev, and V. Koshelets**
Institut de Radioastronomie Millimétrique, St. Martin d'Hères, France,
**Institute of Radio Electronics and Engineering, Moscow*

Group 5 - Junctions and Fabrication

PI-5.1 Fabrication and properties of Nb/AlOx/Nb self-shunted Josephson junctions with high critical current densities
V. Patel, S. K. Tolpygo, W. Chen, and J. E. Lukens
State University of New York at Stony Brook

PI-5.2 Enhancement of the dc supercurrent in double-barrier Nb/Al-AlOx-Al-AlOx/Nb junctions
*I. P. Nevirkovets *** and J. B. Ketterson**
**Northwestern University*
***National Academy of Sciences of the Ukraine*

PI-5.3 Submicron Nb/Al-AlOx/Nb tunnel junctions with high critical current densities
X. Meng , A. Bhat, L. Zheng, A. Wong, and T. Van Duzer
University of California ,Berkeley

PI-5.4 SINIS fabrication process for realizing integrated circuits in RSFQ impulse logic
D. Balashov, M. I. Khabipov, F.-Im. Buchholz, W. Kessel, and J. Niemeyer
Physikalisch-Technische Bundesanstalt, Braunschweig

PI-5.5 Electrical characteristics of NbN Josephson junctions with Nb/AlOx/Nb multilayered barriers
T. Iwai, Y. Ninomiya, T. Aoyama, R. Oke, H. Akaike, A. Fujimaki, and H. Hayakawa
Nagoya University

PI-5.6 Characteristics of NbN/AlN/NbN tunnel junctions operating at 10 K
Z. Wang, H. Terai, A. Kawakami, and Y. Uzawa
Communications Research Laboratory, Japan

P1-5.7 Fabrication of Josephson superconductor-normal metal-superconductor series arrays using a focused ion beam
R. W. Moseley, A. J. Bennett, W. E. Booij, E. J. Tarte, and M. G. Blamire
University of Cambridge

PI-5.8 Transport properties of Nb/InAs(2DEG)/Nb Josephson field-effect transistors
A. Richter, M. Koch, T. Matsuyama, and U. Merkt
Universität Hamburg

PI-5.9 Improvement of uniformity of NbCN/MgO/NbCN Josephson junctions for large scale circuit application
H. Yamamori and A. Shoji
Electrotechnical Laboratory, Japan

PI-5.10 SNS and SIS Josephson junctions with dimensions down to the sub-μm region prepared by a unified technology
L. Fritzsch, H. Elsner, M. Schubert, and H.-G. Meyer
Institute for Physical High Technology, Jena, Germany

PI-5.11 Nondestructive imaging of the microwave properties of superconducting thin film devices and substrates with a scanning microwave near-field microscope
Y. J. Feng, L. Liu, Q. G. Liu, L. X. You, L. Kang, and P. H. Wu
Nanjing University

PI-5.12 Material science and surface impedance Z(T,f,H) of Nb and YBCO and their quantitative modeling by the leakage current of weak links
Jürgen Halbritter
Forschungszentrum Karlsruhe

PI-5.13 Effect of the CeO_2 buffer layer thickness on the microwave properties of YBCO thin films
K. D. Develos, M. Kusunoki, M. Mukaida, and S. Ohshima
Yamagata University

PI-5.14 A new epitaxial $BaSnO_3$ buffer layer for $YBa_2Cu_3O_{7-\delta}$ thin films on MgO substrates
M. Mukaida, Y. Takano, K. Chiba, T. Moriya, M. Kusunoki, and S. Ohshima
Yamagata University

PI-5.15 Microscopic model for double-barrier SIS'IS Josephson junctions
*A. Brinkman, A. A. Golubov, H. Rogalla, and M. Yu. Kupriyanov**
*University of Twente, *Moscow State University*

PI-5.16 Investigation of SFQ integrated circuits using Nb fabrication technology
H. Numata, M. Tanaka, Y. Kitagawa, and S. Tahara
NEC, Tsukuba

PI-5.17 Superconductor-semiconductor-superconductor junctions using NbN
T. Akazaki, H. Yamaguchi, J. Nita, and H. Takayanagi
NTT Basic Research Labs

PI-5.18 Full-scale integration of superconductor electronics for petaflops computing
L. A. Abelson, Q. P. Herr, G. L. Kerber, M. Leung, and T. S. Tighe
TRW

PI-5.19 Study of correlation between the microstructure and phase inhomogeneities of Y-Ba-Cu-O epitaxial films and their dc and microwave properties
*A. K. Vorobiev, Y. N. Drozdov, S. A. Gusev, V. L. Mironov, N. V. Vostokov, E. B. Kluenkov, S. V. Gaponov, and V. V. Talanov**
Institute for Physics of Microstructures RAS, Nizhny Novgorod
**University of Maryland*

Oral Session 5, Wednesday Morning 8:30 - 10:15
HTS Josephson Junctions

Co-Chairs: Horst Rogalla and Gustavo Alvarez

Or5.1 8:30 Use of C-axis microbridge junctions for HTS single flux quantum circuits
P. J. Hirst, J. S. Satchell, I. L. Atkin, M. J. Wooliscroft, and R. G. Humphreys
DERA, Malvern, UK

Or5.2 8:45 On the characteristic voltage of highly oxygenated YBCO grain boundary junctions
*J. P. Sydow, M. Berninger, R. A. Buhrman, and B. H. Moeckly**
*Cornell Univeristy, *Conductus*

Or5.3 9:00 Resonant tunneling and tunnel anomalies in YBCO-junctions
J. Halbritter
Forschungszentrum Karlsruhe, Germany

Or5.4 9:15 Homoepitaxial $YBa_2Cu_3O_{7-x}$ SNS junctions with N-layers of Fe-doped YBCO and $Pr_{1+x}Ba_{2-x}Cu_3O_y$
T. Usagawa, J. Wen, T. Utagawa, S. Koyama, and K. Tanabe
Superconductivity Research Laboratory, ISTEC

Or5.5 9:30 Fabrication of natural-barrier ramp-edge Josephson junctions
M. Horibe, Y. Inagaki, G. Matsuda, N. Hayashi, K. Kawai, M. Maruyama, A. Fujimaki, and H. Hayakawa
Nagoya University

Or5.6 9:45 3-D intrinsic Josephson junctions using c-axis thin films and single crystals
S-J Kim, Yu. I. Latyshev,and T. Yamashita
Tohoku University and CREST, Japan Science and Technology Corp. (JST)

Or5.7 10:00 Optimum characteristics of high temperature Josephson junctions for "lumped" array applications
R. H. Ono and S. P. Benz
NIST, Boulder

BREAK 10:15 - 10:30

Oral Session 6, Wednesday Morning 10:30 - 12:15
Materials and Fabrication

Co-Chairs: Sam Benz and Jiro Yoshida

Or6.1 10:30 Effects of process parameters on the fabrication of edge-type YBCO Josephson junctions by interface treatments
J.-K. Heinsohn, R. Hadfield, and R. Dittmann
Forschungszentrum Jülich GmbH

Or6.2 10:45 Effect of deposition conditions and annealing process on crystallinity and superconducting properties of high-T_c multilayers
Y. Li, T. Utagawa, and K. Tanabe
SRL, ISTEC, Tokyo

Or6.3 11:00 Source optimization for magnetron sputter-deposition of NbTiN tuning elements for SIS Thz detectors
N. N. Iosad, B. D. Jackson, F. Ferro, J. R. Gao, S. N. Polyakov***, P. N. Dmitriev****, and T. M. Klapwijk***
*University of Groningen, The Netherlands, *Space Research Organization of The Netherlands, **Delft University of Technology, ***Moscow State Univeristy, ****Institute of Radioelectronics, Moscow*

Or6.4 11:15 Nb-based single-electron devices fabricated with a planarized process
W. Chen, D. J. Flees, J. R. Friedman, V. Patel, J. Mannik, and J. E. Lukens
State University of New York at Stony Brook

Or6.5 11:30 Spin injection properties of $YBa_2Cu_3O_y$ films
K. Lee, W. Wang, I. Iguchi, B. Friedman, T. Ishibashi**, and K. Sato***
*Tokyo Institute of Technology and CREST, Japan Science and Technology Corporation, *Sam Houston State University, Huntsville, Texas and the Electrotechnical Laboratory, **Tokyo Institute of Agriculture and Technology*

Or6.6 11:45 Hybrid ferromagnet-Nb switch for superconducting nonvolatile memory
T. W. Clinton, P. R. Broussard, and M. Johnson
Naval Research Laboratory, Washington, DC

Or6.7 12:00 Thin film tunable dielectrics for HTS RF applications
B. H. Moeckly and Y. M. Zhang
Conductus

FREE AFTERNOON

POSTER SESSION II, Wednesday evening 7:30-9:30

Group 1 - Digital

PII-1.1 Superconducting flip-chip bonding with a μm-scale gap
M. Aoyagi, H. Nakagawa, H. Sato, T. Taino, and H. Akoh*
*Electrotechnical Laboratory, Japan, *Kyushu University*

PII-1.2 Design of an RSFQ Banyan switching node for petaflops computing
D. Zinoviev
SUNY at Stony Brook, NY

PII-1.3 Digital-to-analog converter based on digital processing of SFQ pulses (progress report)
V. K. Semenov and Yu. A. Polyakov
SUNY at Stony Brook, NY

PII-1.4 Experiments and simulations of picosecond pulse switching and turn-on delay time in Y-Ba-Cu-O Josephson junctions
R. Adam, C. Williams, R. Sobolewski, O. Harnack, and M. Darula**
*University of Rochester, NY, * Research Center Jülich, Germany*

PII-1.5 Clock-frequency and temperature margins of a high-temperature superconductor delay-line memory
W. Hattori and S. Tahara
NEC, Tsukuba

PII-1.6 Characteristic analysis of single electron transistor made by double unit cell of $YBa_2Cu_3O_7$
J. Guo, J. F. Jiang, and Qi.Yu. Cai
Shanghai Jiao Tong University

PII-1.7 Reduction of power consumption of RSFQ circuits by inductance-load-biasing
N. Yoshikawa and Y. Kato
Yokohama National University

PII-1.8 Optimization of RSFQ circuits based on Monte Carlo yield analysis
N. Yoshikawa and K. Yoneyama
Yokohama National University

PII-1.9 Inductance calculation of 3D superconducting loop with ground plane
C. K. Teh, M. Kitagawa, and Y. Okabe
RCAST, Univ. of Tokyo

PII-1.10 Behavior of vortex in Josephson junction network and its application on logic circuit
K. Hohkawa and K. Koh
Kanagawa Institute of Technology

PII-1.11 Can superconductivity become a viable electronic technology?
M. Nisenoff
Nisenoff Associates, North Bethesda, MD

PII-1.12 A superconductive high-resolution time-to-digital converter
O. A. Mukhanov and A. F. Kirichenko
HYPRES

PII-1.13 Multiple bit rate clock recovery circuit: theory
V. K. Kaplunenko
Conductus

PII-1.14 A feasibility study on a high-end digital communication system based on SFQ technology
S. Yorozu and S. Tahara
NEC, Tsukuba

PII-1.15 Towards a 16 kilobit sub-nanosecond Josephson memory
Q. P Herr and L. Eaton
TRW

PII-1.16 Design of a 16-Kbit superconducting latching/SFQ hybrid RAM
S. Nagasawa, H. Hasegawa, T. Hashimoto, H. Suzuki, K. Miyahara, and Y. Enomoto
Superconductivity Research Laboratory, ISTEC

Group 2 - SQUIDs

PII-2.1 LTS gradiometers based on superconducting imaging surface design
A. N. Matlashov, R. H. Kraus, Jr., and M. A. Espy
Los Alamos National Laboratory

PII-2.2 First phantom and human evoked response measurements for a whole-head superconducting imaging surface MEG system
R. H. Kraus, Jr., A. N. Matlachov, M. A. Espy, R. Cantor, P. Ruminer, and L. Atencio
Los Alamos National Laboratory

PII-2.3 Experimental investigation of high temperature superconducting imaging surface gradiometry
M. A. Espy, A. N. Matlashov, and Robert H. Krauss, Jr.
Los Alamos National Laboratory

PII-2.4 Planar single layer HTSC-SQUID gradiometers with high balance
L. Dörrer, S. Wunderlich, F. Schmidl, and P. Seidel
Friedrich-Schiller-Universität Jena, Germany

PII-2.5 Characteristics of the planar second-order high-T_c SQUID gradiometer
S. G. Lee, Y. Hwang, J. T. Kim, and Y. K. Park**
Korea University, Jochiwan,
**Korea Research Institute of Standards and Science*

PII-2.6 Low T_c magnetometer used for active shielding in the frequency regime DC-500 Hz in biomagnetic measurements
*D. Platzek and H. Nowak**
University Hospital Jena, Germany
**JENASENSORIK, Jena, Germany*

PII-2.7 Noise characteristics of double relaxation oscillation superconducting quantum interference devices with reference junction
Y-H. Lee, H. Kwon, J-M. Kim, Y-K. Park, and J-C. Park
Korea Research Institute of Standards and Science

PII-2.8 Design and construction of an HTS dc SQUID electronic gradiometer NDE system
J. Y. Kim, S. G. Hahn, J. H. Kang, E. H. Lee, I. H. Song*, J. H. Gohng**
University of Inchon, Korea,
**Samsung Advanced Institute of Technology , Korea*

PII-2.9 Optimization of field homogeneity in Helmholtz-like coils for measuring the balance of planar gradiometers
M. A. Nordahn, T. Holst, and Y. Q. Shen*
*NKT Research Center, Denmark, *Technical University of Denmark and Rigshospitalet, Copenhagen*

PII-2.10 Comparison of calibration methods for SQUID gradiometers
P. H. Ornelas, A. C. Bruno, and C. H. Barbosa
Pontificia Universidade Católica do Rio de Janeiro

PII-2.11 Two-dimensional spatial frequency response of SQUID planar gradiometers
E. Andrade Lima, A. C. Bruno, and J. Szczupak
Pontificia Universidade Católica do Rio de Janeiro

PII-2.12 LTS SQUID gradiometer system for *in vivo* magnetorelaxometry
L. Warzemann, J. Schambach, P. Weber, W. Weitschies, and R. Kötitz**
Friedrich-Schiller-Universität Jena, Germany,
**Institut für Diagnostikforschung GmbH Berlin*

PII-2.13 Magnetic nanoparticle relaxation measured by a low T_c SQUID system
A. Haller, S. Hartwig, H. Matz, J. Lange, Th. Rheinländer, R. Kötitz, W. Weitschies, and L. Trahms
PTB-Berlin and Institut für Diagnostikforschung GmbH Berlin

PII-2.14 A cryocooled helmet-shaped MEG measurement system
K. Sata, T. Yoshida, S. Fujimoto, S. Miyahara, and Y. M. Kang
Daikin Industries, Ltd., Japan

PII-2.15 Magnetocardiographic application of directly-coupled high T_c dc SQUID magnetometer with bicrystal junctions of high junction resistance
H. Kwon, I-S. Kim, Y-H. Lee, J-M. Kim, Y-K. Park, and J-C. Park
Korea Research Institute of Standards and Science

PII-2-16 Simulation of a SQUID Transformer with moats
*G. Benz, W. Jutzi , and D. Drung**
*University of Karlsruhe, *PTB Berlin*

Group 3 - Analog

PII-3.1 Experimental observation of subharmonic gap structures in long Josephson junctions
*M. A. Nordahn, M. H. Manscher, J. Mygind, and L. V. Filippenko**
Technical University of Denmark,
**Institute of Radio Engineering and Electronics RAS, Moscow*

PII-3.2 Forward and backward wave in Cherenkov flux-flow oscillators
A. M. Baryshev, A. V. Yulin, V. V. Kurin*, V. P. Koshelets**, P. N. Dmitriev**, and L. V. Filippenko***
Groningen Space Res. Org. and Materials Science Center, The Netherlands,
**Institute for Physics of Microstructures, RAS, Nizhny Novgorod*
***Institute of Radio Engineering and Electronics RAS, Moscow*

PII-3.3 Numerical simulations of the current gain of fluxonic Josephson transistors
S. Weiss, J. Schuler, T. Bauch, D. Koelle, and R. Gross
Unviersität zu Köln, Germany

PII-3.4 Plasma nature of superconductor transition
N. P. Netesova
M. V. Lomonosov Moscow State University

PII-3.5 Dynamic properties of asymmetric discrete vortex-flow transistors
B. A. Davidson, V.Granata, E. Sarnelli, and S. Pagano
Istituto di Cibernetica-CNR, Arco Felice (NA), Italy

PII-3.6 States in the structure of two rings
I. N. Zhilyaev and S. G. Boronin
Institute of Microelectronics Technology, Russian Academy of Science, Moscow Region

PII-3.7 Analysis of propagation power dependence of attenuation of superconducting stripline using TDGL equation
S. Yoshimori, A. Kobayashi, and M. Kawamura
Takushoku University, Tokyo

PII-3.8 Phase-locked Josephson junction arrays with distributed coupling circuits
V. K. Kornev, A. V. Arzumanov, and N. A. Shcherbakov
Moscow State University

PII-3.9 Design and preparation of single chip HTS coplanar waveguide bandpass filters
H. Kanaya, T. Nakamura, K. Sashiyama, K. Yoshida, T. Uchiyama, H. Shimakage*, and Z. Wang**
*Kyushu University, *KARC Communications Research Laboratory, Japan*

PII-3.10 Evaluation of high-power Stirling cryocoolers for communications applications
V. Borzenets, J. Ramsden, and R. W. Simon
Conductus, Inc.

PII-3.11 Fabrication and characterization of electrically tunable high-T_c superconducting resonators incorporating barium strontium titanate as tuning material
*E-H. Lee, J. Sok, S-J. Park, J-S. Lee, I-H. Song, J. Kwak, K-R. Jung, J-Y. Kim, S-Y. Yoon and D-Y. Jeon**
*Samsung Advanced Institute of Technology, Korea, *KAIST, Korea*

Group 4 - Detectors and Mixers

PII-4.1 Normal metal hot-electron microbolometer with on-chip protection by tunnel junctions
D. Chouvaev, L. Kuzmin , and M. Tarasov
Chalmers University of Technology, Sweden

PII-4.2 NbN hot electron bolometric mixers at frequuencies between 0.7 and 3.1 THz
P. Yagoubov, M. Kroug, H. Merkel, E. Kollberg, J. Schubert, H.-W. Hübers**
Chalmers University of Technology,
**DLR Institute of Space Sensor Technology, Berlin*

PII-4.3 NbN phonon-cooled hot-electron bolometers prepared on MgO substrates
S. Miki, N. Kaya,Y. Uzawa, A. Kawakami*, and Z. Wang**
Kobe University,
**Kansai Adv. Res. Ctr, Communications Research Laboratory, Japan*

PII-4.4 Low noise single sideband SIS mixers for MM and submillimeter radioastronomy
A. Karpov, J. Blondel, M. Voss, D. Billon-Pierron, P Pasturel, and K. H. Gundlach
Institut de Radioastronomie Millimetrique

PII-4.5 Characteristics of superconducting tunnel junction with a microstrip coil for X-ray detectors
H. Nakagawa, M. Aoyagi, H. Akoh, T. Taino, K. Maehata*, K. Ishibashi*, H. Satoh**, T. Ikeda**, T. Oku**, C. Otani**, W. Ootani**, H. Kato**, K. Kawai**, H. Miyasaka**, H. M. Shimizu**, H. Takizawa**, and H. Watanabe***
*Electrotechnical Laborataory(ETL) Japan, *Kyusyu University, Fukuoka Japan **The Institute of Physical and Chemical Research (RIKEN), Japan*

PII-4.6 Characteristics of Nb/Al/AlOx/Al/Nb superconducting tunnel junction with a Al_2O_3 buffer layer for X-ray detectors
H. M. Shimizu, T. Ikeda, H. Kato, K. Kawai, H. Miyasaka, T. Oku, W. Ootani, C. Otani, H. Sato, Y. Takizawa, H. Watanabe, H. Nakagawa, M. Aoyagi*, and H. Akoh**
*The Institute of Physical and Chemical Research(RIKEN) Japan, *Electrotechnical Laboratory (ETL) Japan*

PII-4.7 RF responses of double-junction SQUID models
Y. Mizugaki, J. Chen, K. Nakajima, and T.Yamashita
Tohoku University and CREST, Japan Science and Technology Corp.

PII-4.8 Detection of emitted radiation spectra from a quasiparticle-injected high T_c $YBa_2Cu_3O_{7-y}$ superconductor
E. Kume, H. Takahashi, and I. Iguchi
Tokyo Institute of Technology and CREST, Japan Science and Technology Corp.

Group 5 - Junctions and Fabrication

PII-5.1 Coplanar transmission lines with meandering center conductors in Y-BaCu-O/Au bilayers
C. Weber, R. Ono, J. C. Booth, L. Vale , S. Benz, A. M. Klushin, H. Kohlstedt*, and R. Semerad***
*NIST, Boulder, *Forschungszentrum Jülich, Germany, **Technischen Universität München, Germany*

PII-5.2 Fabrication of YBCO/CeO_2/YBCO crossover and via structures for digital circuit and integrated SQUID applications
A. Tsukamoto, T. Fukazawa, Y. Soutome, Y. Tarutani, and K. Takagi
Hitachi, Ltd. Advanced Research Laboratory

PII-5.3 Inferring $YBa_2Cu_3O_{7-x}$ grain boundary T_c microstructure from critical current temperature dependence
J. A. Luine, A. M. Klushin, and V. Z. Kresin***
*TRW, *Forschungszentrum Jülich, Germany , **Lawrence Berkeley Laboratory*

PII-5.4 Flux-flow resonant current steps in intrinsic Josephson junctions on $Bi_2Sr_2CaCu_2O_8$ single crystal
*H. B. Wang***, T. Tachiki*, Y. Aruga*, Y. Mizugaki***, J. Chen***, K. Nakajima***, T. Yamashita***, and P. H. Wu*****
**Tohoku University, **CREST, Japan Science & Technology Cooperation ***University of Nanjing*

PII-5.5 $YBa_2Cu_3O_{7-x}$ Josephson junctions and dc SQUIDs based on 45° a-axis tilt and twist grain boundaries: atomically clean interfaces for applications
*F. Tafuri***, F. Carillo*, F. Lombardi*, F. Miletto Granozio*, U. Scotti di Uccio*, G. Testa***, E. Sarnelli***, K. Verbist****, and G. Van Tendeloo*****
**Università di Napoli "Frederico II", **Seconda Università di Napoli, Istituto di ***Cibernetica del CNR, Arco Felice, Italy, ****University of Antwerp,Belgium*

PII-5.6 Tunneling characteristics of Nd-Ba-Cu-O/Pr-Ba-Cu-O/Nd-Ba-Cu-O planar and ramp-edge junctions
G. A. Alvarez, M. Sato, T. Utagawa, T. Morishita, Y. Enomoto , K. Tanabe , K. Toma, U. Kawabe**
International Superconductivity Technology Center
**Chiba Institute of Technology*

PII-5.7 Nature of interface engineered high-T_c Josephson junctions
S. S. Tinchev
Bulgarian Academy of Sciences

PII-5.8 Intrinsic Josephson effects in submicrometer Bi2212 mesas fabricated by using focussed ion beam etching
D. Winkler, N. Mros, A. Yurgens, and V. Krasnov, E. J. Tarte, D. T. Foord*, W. E. Booij*, and M. G. Blamire**
*Chalmers University of Technology and Göteborg University, Sweden, *University of Cambridge*

PII-5.9 Fabrication of trilayer junctions using YBCO surface treatment
M. Maruyama, T. Furutani, K. Yoshida, M. Horibe, A. Fujimaki, and H. Hayakawa
Nagoya University

PII-5.10 Fabrication of ramp-type junctions using a two angle ion beam etching process
U. Schoop, M. Schonecke, S. Schymon, T. Bauch, A. Marx, B. Wiedenhorst, L. Alff, and R. Gross
Universität zu Köln, Germany

PII-5.11 Proposal of new PLD "Eclipse-Aurora Method" and its application to NiO/YBCO Josephson junction formation suitable for low noise SQUID
T. Kobayashi, M. Tachiki, and C. Cai
Osaka University

PII-5.12 Fabrication and transport properties of asymmetric high-T_c d-wave $YBa_2Cu_3O_{7-x}$ Josephson junctions
H. Arie, K. Yasuda, H. Kobayashi, and I.Iguchi
Tokyo Institute of Technology

PII-5.13 Fabrication of c-axis oriented YBaCuO trilayer junctions
H. Akoh, H. Sato, A. Kaneko, and K. Hohkawa**
*Electrtechnical Laboratory, Japan, *Kanagawa Institute of Technolgy, Japan*

PII-5.14 Fabrication of $HgBa_2CaCu_2O_y$ grain boundary junctions using cation exchange method
Y. Yu, S. L. Yan, L. Fang, Y. Y. Xie, J. Z. Wu, S. Han, H. Shimakage, and Z. Wang**
*University of Kansas, USA, *Communications Research Laboratory, Japan*

PII-5.15 Effect of mode of deposition on high-I_cR_n YBCO ramp junctions using $PrBa_2Cu_{3-x}Ga_xO_7$ barriers
J. M. Murduck, R. Hu, and C. L. Pettiette-Hall
TRW

PII-5.16 In-situ monitoring of the growth of oxide thin films at high oxygen pressure
J. Klein, C. Höfener, L.Alff, and R. Gross

PII-5.17 Effects of sputtered SiO_2 passivation layers on YBCO microbridges and step-edge junctions
J. Du, K. E. Leslie, C. P. Foley, G. L. Harding, B. Sankrithyan, and D. L. Tilbrook
CSIRO Telecommunications & Industrial Physics, Australia

PII-5.18 Superconducting NbN films grown using pulsed laser deposition for potential application in internally shunted Josephson junctions
A. Bhat, X. Meng, A. Wong, and T. Van Duzer
UC Berkeley

Oral Session 7, Thursday Morning 8:30 - 10:00
Mixers and Detectors

Co-Chairs: Dag Winkler and Boris Karasik

Or7.1 8:30 (Invited) Superconducting transition-edge sensor microcalorimeters for x-ray microanalysis
J. M. Martinis, D. A. Wollman , G. C. Hilton , K. D. Irwin, N. F. Bergren, and D. A. Rudman
NIST, Boulder

Or7.2 9:00 A hot-electron direct detector for radioastronomy
*B. S. Karasik, W. R. McGrath, H. G. LeDuc, and M. E. Gershenson**
*Jet Propulsion Laboratory, *Rutgers University*

Or7.3 9:15 Noise temperature of a NbN hot-electron bolometric mixer at frequencies from 0.7 to 5.2 THz
J. Schubert, A. Semenov, G. Gol'tsman*, H.-W. Hübers, G. Schwaab**, B. Voronov*, and E. Gershenzon**
DLR Institute of Space Sensor Technology, Berlin,
**State Pedagogical University, Moscow,*
***Ruhr University Bochum, Germany*

Or7.4. 9:30 Cryogenic performance of semiconducting Y-Ba-Cu-O for infrared detection
M. Almasri, D. P. Butler, Z. Celik-Butler, R. Adam, and R. Sobolewski**
*Southern Methodist University, Texas, *University of Rochester, NY*

Or7.5. 9:45 Infrared hot-electron NbN superconducting photodetectors for imaging applications
K. S. Il'in, A. A. Verevkin*, G. N. Gol'tsman***, and R. Sobolewski***
**Moscow State Pedagogical University, **University of Rochester, NY*

BREAK 10:00 - 10:15

Oral Session 8, Thursday Morning 10:15 - 12:15
SQUIDs I

Co-Chairs: Dieter Koelle and Colin Pergrum

Or8.1 10:15 (Invited) Radio frequency amplifier based on a niobium dc SQUID with microstrip input coupling
M. Mück, M.-O. André, J. Clarke, C. Hagmann, J. Gail**, and C. Heiden***
*University of California, Berkeley, *Lawrence Livermore National Laboratory, **Justus-Liebig-Universität Gießen, Germany*

Or8.2 10:45 A radiofrequency SQUID amplifier with a microstrip input coil: simulations and experiment
M. A. Tarasov , A. S. Kalabukhov, O. V. Snigirev, S. I. Krasnosvobodtsev*, and E. S. Stepantsov**
**Russian Academy of Sciences, Moscow, Moscow State University,*

Or8.3 11:00 A new family of low-T_c multiloop SQUIDS
D. Drung, S. Knappe, C. Aßmann, M. Peters, K. Wenzel, and Th. Schurig
Physikalisch-Technische Bundesanstalt, Berlin

Or8.4 11:15 Direct read out flux locked loop circuit with automatic tuning of bias current and bias flux for high T_c SQUID
T. Hirano, T. Nagaishi, and H. Itozaki
Sumitomo Electric Industries, Ltd., Japan

Or8.5 11:30 High-frequency characterization of dc SQUID series array amplifiers incorporating intracoil damping
P. A. Neil, R. G. Benson, D. A. Burns, A. M. Corey, C. S. Flynn, and M. Huber
University of Colorado at Denver

Or8.6 11:45 Shapiro-step SQUIDs— theory and experiments
*B. Chesca***, S. Weiss***, K. Barthel*, D. Koelle****, A. I. Braginski*, and R. Gross**
**Forschungzentrum Jülich, Germany*
***Universität Augsburg, Germany*
****Universität zu Köln*

Or8.7 12:00 64-Channel whole-head SQUID system in a superconducting magnetic shield
H. Ohta[1,2], M. Aono[2], T. Matsui[1], Y. Uchikawa[3], K. Kobayashi[3], K. Tanabe[3], S. Takeuchi[3], K. Narasaki[4], S. Tsunematsu[4], Y. Koyabu[4], Y. Kamekawa[4], K. Nakayama[5], T. Shimizu[5], Koike[6], K. Hoshino[6], H. Kotaka[6], E. Sudoh[6], H. Takahara[6], Y. Yoshida[8], K. Shinada[7], M. Takahata[7], Y. Yamada[7], and K. Kamijo[9]
[1]Communications Research Laboratory, [2]The Institute of Physical and Chemical Research(RIKEN), [3]Tokyo Denki University, [4]Sumitomo Heavy Industry, [5]Nihonkeiki Corp., [6]Mitsui Mining & Smelting, [7]Shimadzu Corporation. [8]National Research Institute of Metals, [9]NEC Tsukuba

LUNCH 12:15 - 1:15

Oral Session 9, Thursday Afternoon 1:15 - 3:15
SQUIDs II

Co-Chairs: Robin Cantor and Keiji Enpuku

Or9.1 1:15 (Invited) Low-frequency noise in YBCO dc SQUIDs and vortex imaging by low-temperature scanning electron microscopy
D. Koelle, R. Gross, S. Keil, R. Straub*, M. Fischer*, M. Peschka*, R. P. Huebener*, K. Barthel***
*Universität zu Köln, *Universitat Tübingen,*
***Forschungszentrum Jülich, Germany*

Or9.2 1:45 Improved direct-coupled high-T_c SQUID magnetometers for operation in magnetically unshielded environment
F. Ludwig, D. Drung, S. Bechstein, J. Beyer, and Th. Schurig
Physikalisch-Technische Bundesanstalt, Berlin

Or9.3 2:00 A HTS gradiometer for unshielded operation from moving platforms
M. N. Keene, N. J. Exon, T. Horton, R. G. Humphreys, and J. S. Satchell
DERA, Malvern, UK

Or9.4 2:15 A high T_c superconducting magnetic gradiometer for mobile operation
T. R. Clem, D. J. Overway, J. W. Purpura, G. I. Allen, J. T. Bono, R. H. Koch, J. R. Rozen*, and G. A. Keefe**
Coastal Systems Station, Panama City, USA,
**IBM T.J. Watson Research Center, NY*

Or9.5 2:30 Long baseline HTS flipchip gradiometer
K. A. Kouznetsov, J. Borgmann, R. McDermott, J. Clarke, R. H. Koch, C. Soble**, and V. Matijasevic***
University of California, Berkeley
**IBM Thomas J. Watson Research Center, NY, **Conductus*

Or9.6 2:45 High temperature single layer SQUID gradiometers with long baseline and parasitic effective area compensation
C. M. Pegrum, A. Eulenburg, E. J. Romans, C. Carr, A. J. Millar, and G. B. Donaldson
University of Strathclyde, Glasgow

Or9.7 3:00 Different applications of high-T_c SQUID sensors
P. Seidel, F. Schmidl, S. Wunderlich, L. Dörrer, R. Weidl, T. Vogt, and S. Linzen
Friedrich-Schiller-Universität Jena, Germany

BREAK 3:15 - 3:30

Oral Session 10, Thursday Afternoon 3:30 - 5:15
Analog Instruments and Novel Coolers

Co-Chairs: Stuart Berkowitz and Andre Wong

Or10.1 3:30 (Invited) Low-field NMR and MRI of room temperature samples detected with a high-T_c SQUID
R. McDermott , K. Schlenga, J. Clarke, R. E. de Souza, A. Wong-Foy, and A. Pines
UC Berkeley and Lawrence Berkeley National Laboratory

Or10.2 4:00 RF Measurements of high-temperature superconducting resonators at 25 T
W. Brey, R. Withers, C. Soble, and V. Soghomonian
Conductus

Or10.3 4:15 Scanning evanescent microwave probe (SEMP)
X.-D. Xiang
Lawrence Berkeley National Laboratory

Or10.4 4:30 Chip cooling by normal metal-insulator-superconductor Peltier effect
*J. P. Pekola, A. J. Manninen, M. M. Leivo, K. Arutyunov, J. K. Suoknuuti, T. I. Suppula, and B. Collaudin**
University of Jyväskylä, Finland
**ESTEC, The Netherlands*

Or10.5 4:45 Cooling by S_1IS_2 tunnel junctions
A. J. Manninen, J. K. Suoknuuti, M. M. Leivo, and J. P. Pekola
University of Jyväskylä, Finland

SQUID Workshop, Friday

Chair: John Clarke

SQUID W-1 Cryogenic calorimeter based on superconducting phase transition thermometer with thermal feedback and SQUID read out circuit for it
O. Meier, F. Pröbst*, W. Seidel*, M. Sisti*, and S. V. Uchaikin****
**Max Planck Institüt für Physik, Munich*
***Joint Institute for Nuclear Research, Dubna*

SQUID W-2 A HTS dc SQUID system for geomagnetic prospection
*A. Chwala, R. Stolz, J. Ramos, V. Schultze, H.-G. Meyer, and D. Kretzschmar**
*Institute for Physical High Technology, *Technical University Berlin*

SQUID W-3 High T_c SQUID microscope head for room temperature sample
T. Nagaishi and H. Itozaki
Itami Research laboratories, Sumitomo

Oral Session 1

General Plenary

Superconducting Digital Technology

Shuichi Tahara, Hideaki Numata, Shinichi Yorozu, Yoshihito Hashimoto, Shuichi Nagawasa

Fundamental Research Laboratories, NEC Corporation, 34 Miyukigaoka, Tsukuba, Ibaraki 305-8501, Japan

Abstract – In this paper, we describe our superconducting digital technology. Superconducting devices have intrinsically superior characteristics than those of semiconductor devices. And also, Nb/AlOx/Nb junctions have ideal current-voltage characteristics for digital applications. These reasons are why superconducting devices using Nb/AlOx/Nb junctions have are being actively developed. Presently, we can fabricate more than twenty thousand junctions on one chip. Using the niobium technology, a superconducting 4-kbit RAM has been already successfully developed. We have demonstrated the operation of a network system with a superconducting chip. Some problems, such as difficulty in high-speed testing, disturbance from trapped magnetic flux and so on, have been overcome by some excellent techniques, such as a clock-driven testing method, moat structures and so on. The developed technologies must become the basic keys for the development of the digital application with a single flux quantum device, which is a promising component for ultra-high speed systems in the twenty first century.

I. Introduction

Superconductive devices, with their high intrinsic switching speed and low power dissipation, are promising circuit elements for future ultrahigh performance computer and communication applications. A system clock using a superconductive device can operate at speed up to more than ten GHz, which is impossible to achieve with semiconductor devices. In addition, the power dissipation of superconductive LSI chips is 2 to 3 orders of magnitude smaller than that of semiconductor LSI chips. Due to their low power dissipation characteristics, many superconductive chips have densely packed into a small space. As a result, media delay decreases. Therefore, the total performance can be drastically improved by superconductive LSIs, in comparison with using semiconductor LSIs.

In order to install superconducting devices into the systems, competitors, such as semiconductor devices, must be overcome. It is, however, impossible to replace all of semiconductor devices with superconducting devices, considering the remarkable progress of silicon LSI technologies. Therefore, it is more important then ever for superconducting devices to consider appropriate goals for development. As the system will be more complex, the defference between peak and average performance of the system will be estimated to be larger. Superconducting devices must be possible to close average performance up to peak performance due to their characteristics of short latency. In future systems, several technologies such as semiconductors, superconductors, optical devices, and so on should coexist. Thus, this system will be a hybrid system. We have developed superconducting digital technology in accordance with the above.

In this paper, we review our developed superconducting digital technologies based on an Nb/AlOx/Nb junction technology. First, we describe fabrication technology. We developed a fabrication process with 2-layer interconnections, which is called a standard process. And also, advanced fabrication technology has been developed using a planarization technique. Using the fabrication technology, we developed a 4-kbit random access memory chip as an example of superconducting integrated circuits. Second, we show some key technologies that have been developed in order to overcome problems such as difficulty of high-clock-frequency testing and disturbance from trapped magnetic flux, which are peculiar to superconducting devices. Third, we describe the superconducting network system, which is the first superconducting digital demonstration system including interfaces between a superconducting chip and semiconductor equipment. Finally, we discuss the strategy for developing superconducting digital devices.

II. Fabrication technologies

Figure 1 shows a schematic cross-section of the superconducting devices [1]. This structure consists of Nb/AlOx/Nb junctions, two Nb interconnections (wirings), an Nb ground plane, SiO_2 insulators and Mo resistors. The Nb, Al, SiO_2 and Mo films were deposited by magnetron sputtering. Etching masks were formed by i-line (365 nm) stepper lithography. The deposited films were patterned by reactive ion etching (RIE). The insulators between wirings were formed using a bias-sputtering technique, to obtain good step coverage. The minimum line and space width was 1.5μm, and sheet resistance was 1.2Ω. The minimum junction area was 2 x 2 μm^2. Excellent uniformity and

Manuscript reported April 28. A part of this work was performed under the management of FED as a part of the MITI R&D of Program (Superconducting Electron Devices Project) supported by NEDO.

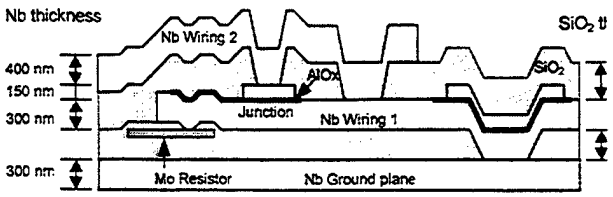

Fig. 1 Schematic cross-section of the superconducting devices. This fabrication process is called "NEC standard process".

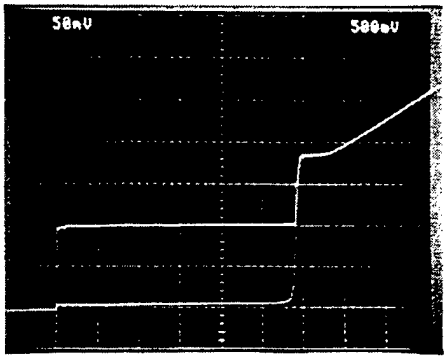

Fig. 2 I-V characteristics of 1000 serially connected Josephson junctions (2 x 2 □m^2). Vertical axis (I) : 0.05mA/div. Horizontal axis (V) : 0.5V/div. Standard deviation of critical current is 0.9%.

controllability of the junction critical current were achieved using the following Josephson junction technology. The standard deviation of the critical current scattering for 100 serially connected 2 μm junctions was as small as 0.9% as shown in Fig. 2. We called the above fabrication process NEC standard process.

Planarization is a key technology in fabricating higher-density superconducting circuits. A planarized structure is required in order to achieve reliable insulation for vertical integration. It also makes it possible to form electrical contacts on small junctions in a self-aligned fashion by exposing junction electrode surfaces. We have mainly focused on fabricating circuits with reliable insulation and we have developed mechanical polishing planarization (MPP) with neutral slurry [2]. A PRESI E312 polisher was used for MPP. Although an alkaline slurry is usually used in chemical mecanical polishing (CMP) for semiconductors, we used a neutral slurry of Fujimi 4101. The reasons are that the step height of a Josephson device is rather low, and the insulator thickness needs to be accurate for the proper operation of circuits. It is difficult to control the insulator thickness when the polishing rate is too high. Therefore, chemical enhancement is not required.

The polishing rate for sputtered SiO_2 was 81 nm/min with an excellent run-to-run variation of ±2%. The thickness uniformity after polishing is important for the correct operation of the Josephson circuits. The SiO_2 thickness after the MPP process was measured optically at every 3-mm step in a 3-inch wafer and its uniformity was below ±6%. No size dependence of planarity was observed when the underlying line width was below 20 μm. Excellent reproducibility and uniformity of the polishing characteristics were obtained. Figure 3 shows the cross-secctional SEM photograph of the memory cell. The difference between the fabricated thickness and designed one is below 10% and it is within a designed margin for correct operation.

We have developed 4-kbit RAM by using the above standard process. The RAM chip has been fabricated by NEC standard process. In the RAM, we used vortex transitional memory cells which has a capability for the high-speed memory operation because it activated by several signals without a timing sequence, and because a single flux quantum is stored in the cell. Approximately 21000 Josephson junctions are included in this RAM, which has a circuit size of 4.5mm x 4.5mm. Approximately 99.8% of the bits operated. A minimum access time of 380 ps was obtained for a memory cell in the memory plane with the power dissipation was calculated as 9.5 mW.

III. Key issues - Clock-Driven On-Chip Testing and Glond-plane Moats –

Superconducting circuits are capable of operating at clock frequencies over ten GHz. As far as using conventional external equipment, multiple reflection between the test equipment and the test chip because of impedance mismatching may cause unexpected errors in the operation of

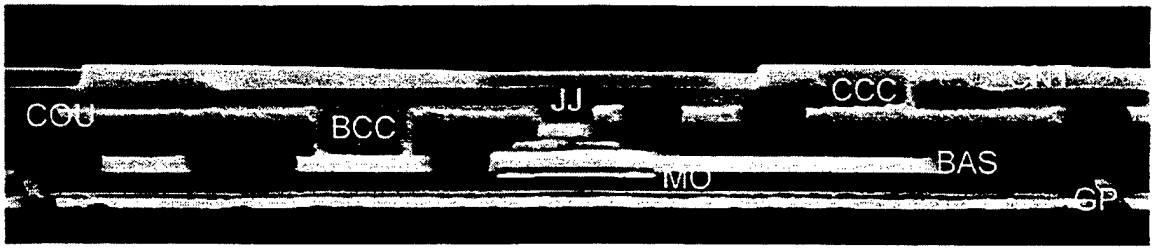

Fig. 3 Cross-sectional SEM photograph of 22 μm × 22 μm vortex transitional memory cell planarized using MPP. GP is a ground plane, and BAS, COU, and CNT, respectively, are base, counter, and top wiring layers. JJ means junction and MO means a Mo resistor. BCC and CCC are contact holes. MPP was used to planarize two insulators; one was between BAS and COU and the other was between COU and CNT.

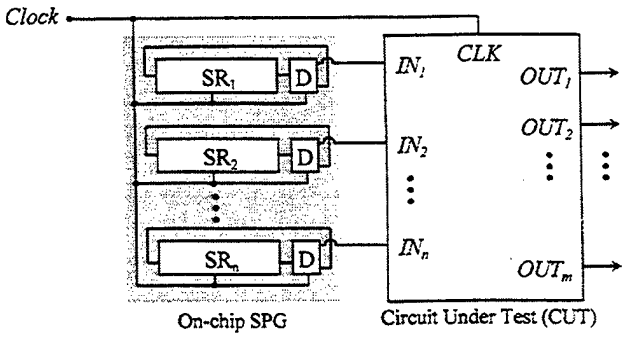

Fig.4 Schematic diagram of clock-driven on-chip testing circuit. SR denotes a shift register, D denotes a D-flip-flop

the test chip. Therefore, to carry out high-speed testing of superconducting logic circuits, the on-chip testing method is a promising. Several kinds of on-chip testing methods have been proposed and demonstrated [4]-[6]. We also propose an on-chip testing method with an on-chip signal-pattern generator (SPG) driven by a clock signal for high-speed testing of latching logic circuits [7]. We call our method "Clock-Driven On-chip Testing".

Figure 4 shows the schematic diagram of the clock-driven on-chip testing circuit. Although the SPG can be designed in various forms, the most convenient way for latching-type superconductor circuits is using a feedback shift register, that is conventionally called the Johnson counter. In a Johnson counter, the output of the last-stage D-flip-flop is fed back to the first-stage one. The SPG consists of only D flip-flops and requires no external control signal, so the design and operation are very simple. And also, the SPG can be constructed on the same chip as the circuit under testing, so the crosstalk or reflection of the high-speed test-signals can be greatly reduced. This SPG is faster than any pipelined logic circuit, so the SPG should not limit the maximum clock frequency of the testing for the pipelined latching logic circuits. These features make it easy to obtain high-speed operation of the circuit under testing up to the maximum clock-frequencies.

We describe another intrinsic problem on operating superconducting circuits, that is, disturbance from trapped magnetic flux. The operating yield of the superconducting circuits depends strongly on trapped magnetic flux caused by the external magnetic field. To relax such strict low-field requirements, groundplane moats have been incorporated into superconducting devices [8,9]. A moat is a square hole or a narrow rectangular gap in the groundplane. We have designed several moat shapes and arrangements, and evaluate their effect by analyzing the I-V characteristics of 1000 serially connected SQUIDs [10]. A SQUID test circuit consists of 1000 serially connected 2-junction SQUIDs which are arranged in a matrix of 50-rows x 20-columns. The 2-junction SQUIDs are used to increase magnetic field sensitivity. The critical current of a junction is designed to be 0.1 mA. Several moat shapes and arrangements were formed in the groundplanes under the SQUID test circuits.

We designed 1 μm wide narrow rectangular moats and 1 x 1 μm square moats, surrounding each 2-junction SQUID. The surrounded area is 40 x 80 μm. Several kinds of arrangements having different spacing between the moats are designed, and tested. The measurements were carried out with an external magnetic field of several milli-Gauss. Figure 5(a) shows an example of an I-V characteristic of a SQUID test circuit having narrow rectangular moats. There is no influence of the trapped magnetic flux, because the external magnetic field within the surrounded area of 40 x 80 μm is kept to less than one flux quantum Φ_0 in this measurement. For comparison, the I-V characteristics for a groundplane with no moats is shown in Fig. 5(b). Here, the influence of the trapped magnetic flux is considerable.

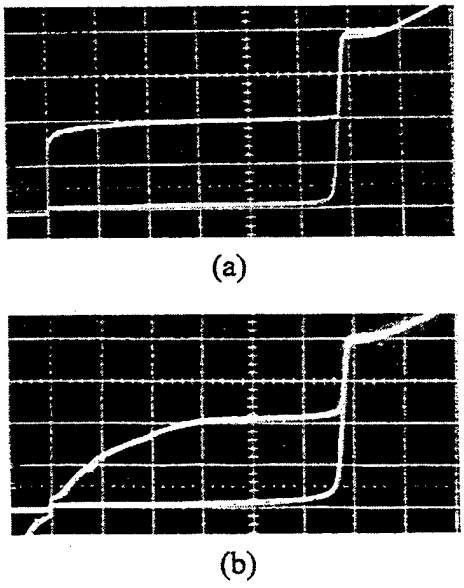

Fig. 5 I-V characteristics of 1000 serially connected SQUID gates (a)with moat structures (b) without moat structures. Vertical axis (I) : 0.05mA/div. Horizontal axis (V) : 0.5V/div. Standard deviation of critical current is 0.9%.

IV. System demonstration - Superconducting Network –

In order to develop an application using novel devices such as superconductors, it is important to demonstrate a system operation using such novel devices. Because there must be a lot of issues to be solved for system integration. In the case of superconducting devices, interface concerning frequency and voltage level between superconductors and semiconductors should be developed for system integration. However, so far there have been very few system-level demonstrations of such digital systems using superconducting devices [11-13].

We have reported on the first complete system-level demonstration a superconducting digital communication system prototype, which we feel a milestone for our superconducting technology [14]. Our concept of this prototype is minimum size complete system, and it can be made using currently available technologies. Our system is focused on parallel processor communication using superconducting devices [15]. In the high-performance

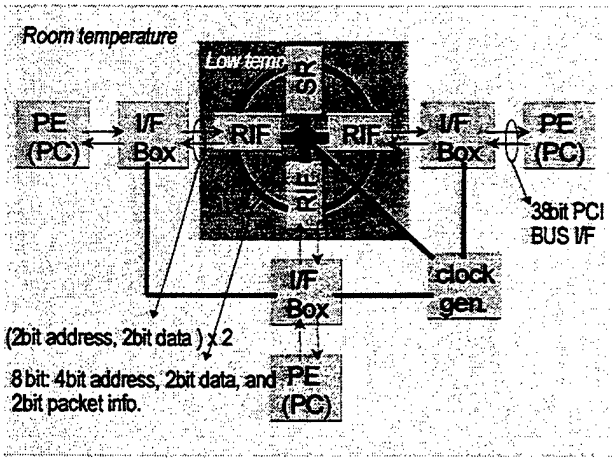

Fig. 6 Block diagram of the demonstration system.

computing environment, one of the keys for their high-performance operation is data switching technology between processors. It becomes very important that the throughput of the switching network should be increased and its turn-around-time should be decreased in the multi-processor system. As the superconducting devices can be packed in the smaller area compared with the case using the semiconductor devices, the superconducting network is expected increase the performance of the multi-processor system.

Our prototype has three nodes, which is the minimum needed to communicate with each other with checking to decode node address. Figure 6 shows a block diagram of our system. The system consists of three-node conventional PCs as processing elements (PE), three interface boxes (I/F Box), and a superconducting network chip. We used on superconducting-chip pipelined-ring network architecture, which is a modified version of a typical bus architecture . Ring architecture is distributed and scales linearly up to its performance limits. The ring node connects only to its neighbors, reducing the interconnection cost. This allows a ring to easily expand in the domain of multiple chips and modules. The point-to-point links of a ring are easier to drive at high speed. Also, a dual counter-rotating ring increase the fault tolerance of networks. Such ring architecture properties are especially advantages when using superconducting device which has of fabrication limitations.

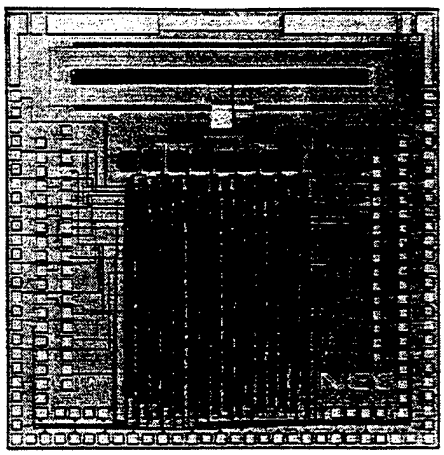

Fig.7 Photograph of the fabricated network chip.

The network chip (Fig. 7) consists of three ring interface circuits (RIFs), a slot repeater circuit (SR), and superconducting microstrip line wiring between these circuits. Each RIF has an address. The functions of the RIF circuits are mainly to decode packet addresses and routing, and to arrange the blocking of data between incoming data from the processor and network. The function of the SR circuit is to redefine (change the validity of) slots.

Figure 8 is a photograph of successful system operation. We confirmed the successful system operation by making one node to transfer image data to other node. The interface box consists of parallel serial converters, serial parallel converters, a FIFO output buffer, and a level conversion circuit. The network system operates successfully at approximately 100 MHz. The clock frequency is restricted by the speed of the interface ICs, not by that of the superconductive chip. As we also confirmed the 2 GHz operation of the switching chip, we can estimate the total throughput of the system can be increased to more than 10 Gbps.

V. Discussions

We have developed superconducting digital technologies. And also, we have demonstrated capability of superconducting devices for digital applications. However, the time is not still ripe to put superconducting digital devices to practical use. What should we do next step ? First, we have to develop more advanced fabrication technology in which we can fabricate at least 100,000 Josephson junctions per chip. Large scale integration is one of the most significant technologies for digital application. We may need a much higher grade fabrication line which is capable of fabricating at least 1 million Josephson junctions per chip with a high yield in the future. Second, we have to develop the design technologies. These days, a CMOS CPU can operate at more than 1 GHz. So, single flux quantum devices which are expected to operate at more than ten GHz are more attractive than latching devices. In that case, design technologies including architecture and chip-level layout will be very important. Third, packaging technologies will need to be developed. A high-speed and high-density MCM with solder bonding will be required for chip-to-chip communication. The interface between the 4.2 K components and the room-temperature components also needs to be improved.

As well, we have to continue to demonstrate the high-level performance of superconducting devices from a chip-level to a system-level. The features of superconducting devices are high-speed, low-power dissipation, and high-sensitivity. The demonstration should clearly show these advantages over semiconductors. High-end routers and front-end processors including AD converters and processors for wide-band communication, engines for image processing and so on, may be good targets for the next generation.

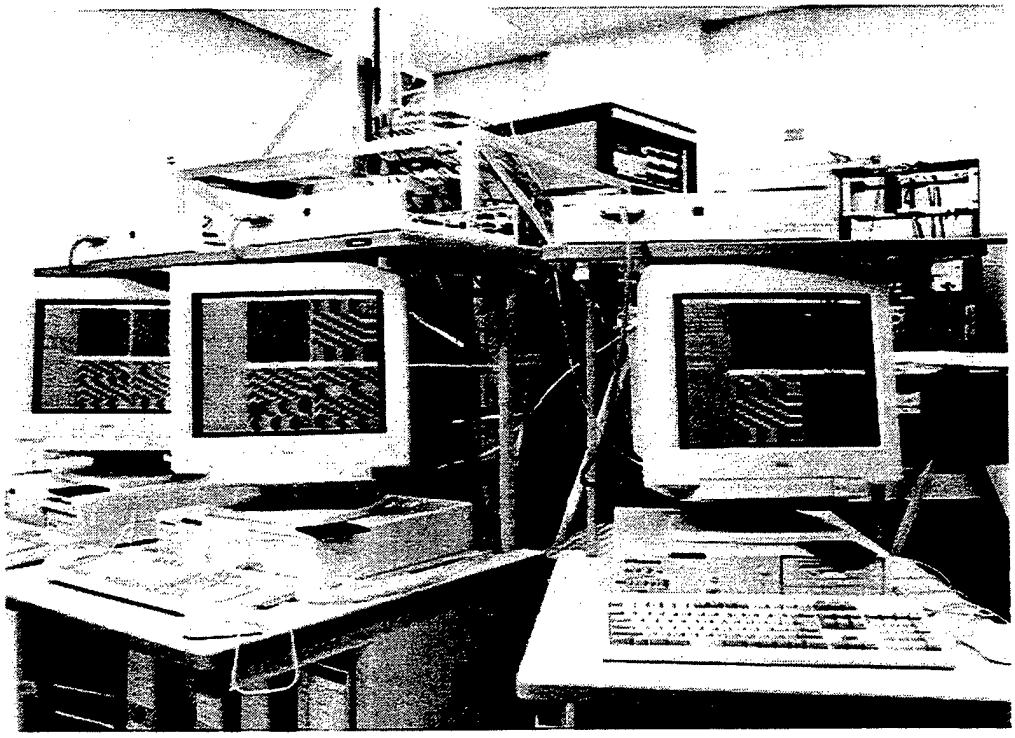

Fig. 8 Photograph of system operating experiment.

VI. Conclusion

We reviewed our developed superconducting digital technologies using Nb/AlOx/Nb Josephson junctions. We have developed a highly reliable and controllable fabrication process. Using this fabrication process, we developed integrated circuits such as 4-kbit RAM and a network chip. The clock-driven on-chip testing method and appropriate moat structures were developed in order to eliminate several problems such as difficulty in high-speed testing, disturbance from trapped magnetic flux. The network system included interface technologies was successfully demonstrated even though it was on a small scale.

Acknowledgments

The authors would like to thank Dr. J. Sone for his continuous encouragement during this work, and Ms. M. Tanaka and Mr. Y. Kitagawa for their assistance in the fabrication.

References

[1] S. Nagasawa, Y. Hashimoto, H. Numata and S. Tahara, IEEE Trans. Appl. Supercond., 5, pp. 2447-2452, 1995.

[2] H. Numata, S. Nagasawa, M. Tanaka and S. Tahara, Applied Superconductivity Conference, EEB-01, 1998.

[3] S. Nagasawa, S. Tahara, H. Numata, and S. Tsuchida, IEEE Trans. Appl. Supercond., 4, pp. 19-24, 1994.

[4] A. Kirichenko, O. Mukhanov and A. Ryzhikh, IEEE Trans. Appl. Supercond., 7, pp. 3438-3441, 1997.

[5] J. Z. Deng, N. Yoshikawa , S. Whiteley and T. Van Duzer, IEEE Trans. Appl. Supercond., 7, pp. 3634-3637, 1997.

[6] Q. Herr, K. Gaj, A. Herr, N. Vukovic, A. Mancini, M. Bocko and M. Feldman M, IEEE Trans. Appl. Supercond., 7, pp. 2975-2978, 1997.

[7] Y. Hashimoto, S. Yorozu, H. Numata and S. Tahara, Applied Superconductivity Conference, EDE-06, 1998.

[8] S. Bermon and T. Gheewala, IEEE Trans. Mag., 19, pp. 1160-1164, 1983.

[9] M. Jeffery and Van Duzer T, Appl. Phys. Lett., 67, 99. 1769-1771, 1995.

[10] S. Nagasawa, H. Numata, C. Kato and S. Tahara, Extended Abstracts of 5th International Superconductive Electronics Conference, pp. 192-194, 1995.

[11] N. Dubash, V. Borzenets, Y. Zhang, V. Kaplunenko, J. Spargo, A. Smith and T. Van Duzer, Extended Abstracts of 6th International Superconductive Electronics Conference , pp. 31-33, 1997.

[12] A. Worsham, A. Miklich, D. Miller, J. Kang, J. Przybysz, IEEE Trans. Appl. Supercond., 7, pp. 2476-2479, 1997.

[13] M. Hosoya, W. Hioe, S. Kominami, H. Nagaishi and T. Nishino, IEEE Trans. Appl. Supercond., 6, pp. 172-177, 1996.

[14] S. Yorozu, Y. Hashimoto, H. Numata, S. Nagasawa and S. Tahara, Applied Superconductivity Conference, EBB-01, 1998.

[15] S. Tahara, S. Yorozu, H. Matsuoka, IEEE Trans. Appl. Supercond., 7, pp. 3164-3167, 1995.

HTS Technology for Wireless Communications

Randy W. Simon
Conductus, Inc., Sunnyvale, California 94086

Abstract— As the 1990s draw to a close, product development based on HTS electronic technology is increasingly targeted at communications applications for both commercial and government customers. The small companies founded to commercialize HTS electronics are almost exclusively focused on this work. The current applications of HTS technology in communications systems are based upon the performance characteristics of superconducting microwave filters as well as the enhancements to semiconductor pre-amplifiers afforded by cryogenic operation. The dynamic expansion of the commercial wireless industry is providing a variety of opportunities for the use of HTS technology. In this paper, we examine the current state of this new industry and its future prospects.

I. Introduction

Following many years of wide-ranging exploration of application opportunities, the HTS electronics industry in its second decade of existence has identified wireless communications as the area with the greatest potential. In particular, the use of HTS preselect filters in receiver front ends in both commercial base stations and in specialized government installations has become the predominant near-term application for the technology.

The underlying superconductive technology supporting these applications has been well enough in hand for several years to support intense product development. As a result, the most significant engineering efforts have been in the areas of cryogenic packaging, cryocooler integration and overall product design rather than in the filter technology itself. Despite this trend, there continues to be significant work on HTS filter technology and its ability to address increasingly demanding applications continues to grow.

Recent years have seen increasing interactions between the HTS industry and the potential user community for HTS filter products. As a result, products are being designed in response to real industry trends and specific customer needs. The initial application for the products has been to enhance coverage of wireless base stations. This represents a market opportunity of modest size but is viewed by the industry to be the precursor to greater opportunities in applications where the technology can provide interference rejection, capacity improvements and other significant benefits in the wireless infrastructure. The performance of HTS filter technology has been well documented in a wide variety of real-world installations for a number of years. The biggest challenge faced by the HTS industry is no longer its ability to provide high-performance products but rather to establish a viable economic model supporting the wide-scale deployment of the technology that is widely accepted by the wireless industry.

In the government marketplace, performance considerations tend to play a greater role versus economic considerations and HTS technology is beginning to find acceptance in a variety of applications where highly sensitive receivers are required. The overall market potential is smaller than the commercial market but continuing successful field deployments suggest that this market will be a viable one.

Manuscript received May 17, 1999

II. Filter Technology

The intrinsic low-loss characteristics of superconductors allow for the fabrication of microwave resonators with quality factors far in excess of what can be realized by conventional technologies. As a result, multipole filters with minimal insertion losses can be obtained. Two approaches to using superconductors for this purpose have been applied to products for communications systems. One uses thick-film technology in conjunction with cavity resonators and the other uses thin-film technology in conjunction with microstrip filter designs. Both approaches can be used to create filters that can outperform conventional designs.

Generally speaking, the combination of increasing losses along with design and fabrication complexity has limited conventional filter designs for communications systems to eight or, in some cases, eleven poles. In fairness, specific application requirements in the commercial wireless industry has not been a force driving the development of higher-order filters to date. On the other hand, evolving trends in the wireless infrastructure are creating needs for more selective filters and superconductive designs offer strong advantages in this regard.

Superconductive microstrip technology in particular provides the capability of realizing microwave filters with large numbers of poles in very compact packages. HTS filters with sixteen and nineteen poles have been fabricated on 2-inch wafers and delivered as part of communications systems. Thick-film approaches require considerably larger cavity structures, but nevertheless have led to commercially-

available filters for cellular base stations with as many as 24 poles. Both approaches are capable of providing low-loss filters with very high numbers of poles if applications require them.

HTS microwave filter design technology has been advancing for a number of years and is gaining a fair measure of maturity in terms of design tools, simulation techniques and available topologies. The need for narrow-band filters, specialized filters and the desirability of very compact designs in the thin-film arena has led to a series of advances including the use of quasi-elliptic functions, designs with asymmetric filter response, constant-delay designs and others. Recent work has added the ability to introduce multiple transmission zeros in HTS filter responses.

HTS filter subsystems built to date have incorporated a variety of high-performance filters. Both commercial and government systems have utilized narrow-band filters with fractional bandwidths well under 1%. Other filters have demonstrated extraordinary amounts of out-of-band rejection at frequencies very close to the pass band edge. Specialized filters for digital applications have demonstrated pass band ripple of only a couple of tenths of a dB. Customers continue to ask for increasingly demanding filters and HTS technology is proving itself to be up to the task.

Supporting the work in HTS filter design has been steady improvements in materials for use in microwave filters. YBCO is used in both thick-film and thin-film filter designs. Thallium-based cuprates with higher critical temperatures are also employed in thin-film designs. In the early days of HTS thin-film filters, for example, unloaded Q values between 10,000 and 20,000 at cellular frequencies were about the best that could be routinely obtained. Today, quality factors of 50,000 or even 100,000 can be achieved. Along with the quality improvements in HTS films are increased production capabilities. Industry-wide, thousands of HTS wafers are routinely produced by several sources, including the small companies in the business.

III. System Design

HTS technology for the commercial wireless industry has for the most part been delivered in the form of receiver front-end subsystems designed to be retrofitted into existing cellular base stations. Products offered by at least four different companies have incorporated HTS filters, cryogenically-cooled low-noise preamplifiers and integrated cryocoolers.

A. *Configurations and Protocols*

For commercial base stations, current HTS products are configured either as "omni systems" which contain two channels of filters and amplifiers or "sectorized systems" which contain 6 channels of filters and amplifiers. Systems have been built for a number of different frequency bands. The most prevalent to date has been the AMPS cellular band centered near 850 MHz. The first HTS products to address this market utilized bandpass filters tailored for one or the other of the two cellular operators licensed in each geographical region of the United States and other countries using the same spectrum. Later product offerings addressed the interleaving of spectral allocation between the two operators that results in what is known as the "A-B problem" in the industry. In order to combat interference from the other carrier, filter sets for the B carriers incorporate notch filters and filter sets for the A comprise two separate bandpass filters including one very narrow bandpass.

HTS filters have also been designed for the PCS spectrum in the United States (centered around 1.9 GHz), for the GSM spectrum in Europe and for a number of other bands in use around the world. Since the HTS products are front-end subsystems used between the base station antenna and the radio receivers in the base station, the products are relatively independent of the protocols or modulation schemes in use at the station. The three dominant digital transmission modulation formats in use for cellular and PCS networks are known as Time Division Multiple Access ("TDMA"), Code Division Multiple Access ("CDMA") and Global System for Mobile Communication ("GSM"). Existing analog cellular networks are increasingly in the process of upgrading to digital formats. Apart from specific performance requirements driven by unique problems encountered by the various formats, the same HTS filter subsystems are applicable to all of them.

In conjunction with HTS filter technology, there is also cryocooled low-noise amplifiers (LNA) technology, which is typically based on discrete GaAs HEMT technology used on specially-made miniature printed circuits. Such circuits are tailored for operation at cryogenic temperature and are designed to be mounted on the cold packages that house the HTS filters. Noise figures for the cryogenic LNAs are typically no more than a few tenths of a dB or even less, depending upon the frequency of operation. Generally speaking, systems have at least one cryocooled LNA for each filter in the product.

HTS subsystems products exist for both indoor and outdoor deployment with housings appropriate to each. A variety of product features are available including bypass systems that switch in conventional filters in the event of a

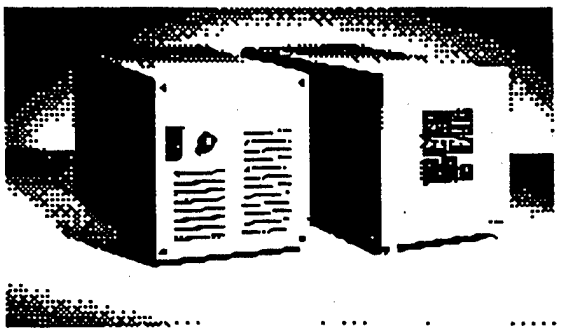

Figure 1 – A Conductus ClearSite® filter subsystem. The unit on the left is the Gifford-McMahon cryocooler compressor, the unit on the right is the filter unit and system controller. The two fit in a standard 19-inch rack.

failure of the cryogenic system, remote monitoring capability, variable gain setting and multiple configuration capability. The products increasingly offer benefits to system operators beyond the specific technical advantages of HTS technology.

With respect to government applications, there have been systems of varying levels of complexity ranging from simple filter-amplifier pairs to ten-channel systems with intelligent switching and variable gain at each output stage. Systems have already been built for at least a dozen different frequency bands of interest to various government agencies. For this diverse set of applications, there are many more frequencies of interest than are in use in the commercial wireless bands.

B. Cryocoolers

HTS filter systems are generally built using the two most readily available cryogenic refrigerators in the temperature range of interest: Gifford-McMahon and Stirling. Each approach has its virtues and its drawbacks.

Gifford-McMahon coolers are used by several of the HTS system vendors in commercial systems because of their ample cooling power and their record for reliability. These coolers are essentially the same as the refrigeration engines in cryopumps that have been used for decades in semiconductor manufacturing equipment. They have been engineered over time for ruggedness and reliability for use in an environment where downtime is prohibitively expensive. Mean-time-before-failure (MTBF) for some designs can be as much as 100,000 to 150,000 hours (17 years.) As a result, these coolers are very desirable for commercial installations where the reliability of an unproven new technology represents a critical barrier to overcome in establishing the market.

The drawbacks of Gifford-McMahon coolers are primarily that they are fairly heavy, draw a fair amount of electrical power and are sensitive to orientation (inverting the unit can cause lubrication oil contamination of the system.)

Stirling coolers are widely used in military applications where their relatively small size and light weight are important considerations. Government applications for HTS technology often involve the need for relative portability and light weight. Systems may need to be transported in arbitrary orientations. They may also need to be operated under circumstances in which the noise of the operating cooler can be obtrusive. Under these conditions, Stirling coolers are the favored approach.

The drawbacks to Stirling coolers are primarily their limited cooling capacity and their limited operating lifetime. Tactical Stirling coolers developed for military applications have MTBFs of 2,500-5,000 hours. More recent Stirling designs promise lifetimes of 15,000-20,000 hours (up to 2 years), but there is little field data to support these claims at this point. As a result, the use of Stirling coolers in the commercial arena represents more of a challenge to HTS vendors who need to convince customers of their products' reliability.

Other cooler approaches continue to attract the interest of HTS system manufacturers -- pulse tube coolers are one example – but the availability of a steady supply of manufactured units is an essential requirement for any cooler type. A second -- and by no means lesser -- requirement for coolers is that their cost be acceptably low. At the current stage of the industry's development, the cryocooler represents by far the largest single cost element in HTS filter subsystems and remains the primary challenge in the establishment of a viable long-term business model for commercial products. Products for the government can incorporate the costs associated with coolers with less difficulty than in the intensively competitive commercial arena. The difficulty facing the industry is that even optimistic estimates for the size of the market for HTS filter products do not necessarily provide a need for large enough cooler volumes to drive their costs to ideal levels. The existence of additional markets for such coolers beyond HTS filter systems would be a significant positive force in the industry.

IV. The Market Opportunity

The essential attraction of the wireless communications market is its sheer size. The market for wireless communications services, which includes cellular, personal communications services (PCS) and wireless local loop (WLL) services, has grown enormously during the past decade. This rapid growth has been driven by decreasing prices for wireless handsets, a more favorable regulatory environment, increasing competition among service providers and a greater availability of services and RF spectrum. A number of developing countries are installing wireless telephone networks as an alternative to installing, expanding or upgrading traditional wireline networks. Given all these trends, industry analysts estimate that the number of wireless subscribers worldwide will grow from 200 million in 1997 to 700 million in 2002. This implies a compound annual growth rate of 37%. This extraordinary growth in wireless communications has required, and will continue to require, substantial investment by service providers in infrastructure equipment. Industry analysts estimate that annual spending by wireless service providers on infrastructure equipment was approximately $32 billion in 1997 and will rise to approximately $93 billion in 2002.

HTS electronics companies have been developing products for the wireless market since the early 1990s with the first real installations beginning after the middle of the decade. HTS filter systems have now been deployed in several hundred base stations throughout the United States and their use is accelerating. The key hurdles that the technology faces are market acceptance of a new and unknown technology, accumulation of sufficient data demonstrating the performance benefits of the technology, and demonstration of the economic viability of the approach. HTS filter subsystems are considerably more expensive to deploy than their conventional counterparts because of the addition of refrigeration components as well as the current low-volume cost structure of the industry. As a result, the industry has devoted considerable efforts to accumulating data that demonstrates that the initial expenses associated with installing HTS wireless equipment are paid back, in many cases quite rapidly, by the economic benefits provided by the equipment.

V. APPLICATIONS

A. Commercial Wireless Networks

The initial application for HTS filter subsystems has been the use of the systems in rural base stations to increase the range of the stations and improve coverage within the cells. Rural cellular networks in the United States were largely installed during the era of bulky portable cellular phones that could transmit up to 3 W of RF power. In recent years, the overwhelming ascendance of low-power (0.6 W) pocket phones has created a significant uplink deficit in these networks. The coverage footprint of rural cells with the low-power phones was too small and filled with holes.

The immediate benefit provided by HTS filter subsystems in this environment is to lower the receiver noise floor of the cell site and thereby enhance its sensitivity. The noise figure of conventional base station front ends can be anywhere from 2 dB to as much as 5-6 dB. The noise figure of HTS front ends is typically well below 1 dB (often as low as 0.5 dB.) This sensitivity enhancement can be readily characterized by SINAD (signal-intensity-noise and distortion) measurements in the cell's coverage area. Even a 1 dB reduction in noise floor improves SINAD by 3 dB in the critical fade margin or hand-off region where the base station's capabilities are marginal. As a result, call clarity is enhanced, fewer calls are dropped and hand-offs to adjacent cells are successfully completed.

In field trials with wireless operators by all the HTS system vendors, there are well-documented significant increases in base station coverage, reductions in dropped call rates, improvements in in-building coverage, enhancements in voice quality and increases in billable minutes. In one specific trial, a customer originally planned to install an additional cell site at significant cost in order to solve a serious coverage problem, but installing HTS filter subsystems in the adjacent cells enabled the operator to avoid this expense. Deployment of the units provided dramatic increases in network performance and immediately eliminated the coverage gap. Tests with low-power portable phones demonstrated clear voice quality and no dropped calls while traveling through the former dead zone. Costs for a new cell site can range in the hundreds of thousands of dollars.

Another benefit of the combination of HTS filter technology and cryocooled low-noise amplifiers in coverage-limited environments is the ability to safely increase system gains without risking amplifier saturation. With appropriate system adjustments, the system-level increases in uplink budget can greatly exceed what is gained specifically by the improvement in preamplifier noise figure. As a result, many field trials of the technology are demonstrating range improvements beyond what is predicted from amplifier noise figure calculations alone and the performance benefits to the operators become quite substantial. Tests at many cell sites around the country of systems from multiple vendors have demonstrated increases in billable minutes of 30-50% over extended periods of time. Because of such results, interest in the technology by cellular operating companies has been growing steadily.

The market for HTS filter subsystems for coverage enhancement has been estimated to include as much as 25% of existing cellular base stations, of which there are currently approximately 30,000 in the United States. Some cellular operators have already indicated their intention to use the technology in such a percentage of their networks. Whether the actual market penetration can approach these levels remains to be seen. Competing technologies and complex economic issues remain as obstacles to the widespread deployment of HTS technology for this purpose. But if the technology is deployed for coverage enhancement in thousands of base stations in the United States (and undoubtedly like numbers abroad), this alone would create a market for HTS filter subsystems well into the tens of millions of dollars per year.

Predictions for a much larger market for HTS filter subsystems are predicated upon the use of the technology to combat growing problems of interference in wireless communications systems. Radio interference to communication systems can arise from many different sources, and cause operational problems via many different mechanisms. Such interference can be broadly classified as co-channel, near-channel or far-channel, referring to the cases where the interfering signal originates on the same, nearby or far-off frequencies as the "victim" communication service. In the latter two cases, interference generally results from deficiencies in the interferer's transmitter or the victim's receiver (and, rarely, characteristics of nearby structures which re-radiate the energy). The rapid growth of wireless networks with new systems and protocols coming on line all the time ensures that even communication links that are interference-free today are likely to encounter problems tomorrow, impacting capacity, coverage and ultimately, revenue.

HTS filter systems do not offer a solution to problems associated with co-channel interference. However, adjacent-band interference is a prime target for high-performance filters. Adjacent-band interference can occur when strong signals from one service on an adjoining band are inadequately filtered by receiver preselect filters of the service in question. These signals enter the receiver RF front end and produce intermodulation products that fall into the wanted passband.

In cellular systems, the adjacent bands allocated to the two service providers in each area represent potential sources for interference. The power management features of the cellular system lead to what is called the "near-far" problem in which mobiles served by a distant base station of one carrier interfere with a nearby base station of the second carrier.

The proliferation of wireless services has multiplied the number of potential interference sources. For example, specialized mobile radio (SMR) and airphone services operate in bands adjacent to standard cellular frequencies. The PCS infrastructure in the United States will include up to six different carriers in adjacent frequency bands.

The various competing digital protocols create unique mechanisms for interference. For example, in paired frequency allocations, nearby TDMA mobile station transmitters are likely to cause interference to CDMA receiver base stations, because the TDMA mobiles employ relatively

powerful transmissions (in short timeslots) whereas, by comparison, the CDMA mobile transmissions operate at minimum possible power. The situation is worsened if the TDMA service operates in an unpaired band where the same frequency is used by mobiles and base stations, since then both are candidate interferers to the CDMA service.

There are models that indicate that the use of HTS front ends in CDMA systems can increase the uplink capacity of the system or alternatively expand coverage. This occurs because of the lowering of the system noise floor which allows for more channels in the spread-spectrum format and diminishes the "cell breathing" phenomenon.

Conventional wisdom holds that interference is a phenomenon that is significant only in dense urban and suburban cell sites. For these reasons, rural base stations often have very minimal filtering in their front ends, preferring to maximize sensitivity by avoiding filter losses. Recent field tests have shown that even rural cell sites are often subject to considerable amounts of interference at surprisingly high signal levels. This may account for some of the qualitative enhancements to cellular service seen in rural field trials of HTS filter systems.

Generally speaking, however, since urban and suburban cell sites comprise roughly 70% of the infrastructure and account for even a higher percentage of call traffic, it is clear that applications that pertain to those sites are needed for the HTS filter industry to really take off. Industry trends point in the direction of increasing sources and quantities of interference. It remains for HTS technology to demonstrate its value in combating interference and improving the performance of urban and suburban base stations. The industry is working hard to accomplish this task over the next few years. Projections indicate that the number of wireless base stations worldwide will grow to the hundreds of thousands over the next five years. If HTS technology finds a home in even a small percentage of them, there will be a significant business established.

B. Government Applications

A broad range of government agencies, particularly in the defense, intelligence and law enforcement areas, have specialized needs for high-performance communications systems. Customers in these areas often have requirements to receive very weak radio signals from a variety of sources. As a result, they constitute a market for very high-performance receivers.

The HTS companies have been providing receiver subsystems for government customers for several years. These systems utilize the same basic building blocks as the commercial front-end products but are packaged to meet the specific needs of the government customers. Deployments of these systems have demonstrated greatly enhanced performance over the conventional technology that they replace and in some cases provide customers with capabilities that never existed before.

The market potential for these systems is smaller than what is available in the commercial world but, on the other hand, the number of different applications is much greater. There are innumerable communications systems in the military and other government agencies and many have demanding performance needs and deal with common wireless system problems such as range limitations and interference. As the government gains confidence in the use of HTS technology, it is likely that it will be deployed in a growing number of applications.

VI. FUTURE CONSIDERATIONS

The first generation of wireless systems used analog technology. We are now in the midst of the second generation of wireless systems that employ a variety of digital air interface standards. Telecommunications industry participants are currently considering a variety of standards for third-generation wireless networks. The industry increasingly appears to be headed towards the standardization of a single, converged CDMA-based third generation standard that accommodates equally the existing dominant network standards in use today (including TDMA and GSM, which are both time domain modulation schemes.). The goal of third-generation wireless (3G) is to offer high burst rate packet communications in addition to high-quality voice and medium data rate services.

Spectral allocations for 3G wireless systems comprise 230MHz in the bands 1885-2025MHz and 2110-2200MHz. At the present time, portions of these same bands are being used for deployment of second-generation wireless systems. Furthermore, there are likely to be multiple standards used for different services particularly in order to enable handover to existing cellular systems. Differing standards may well be allocated to adjoining bands so that 3G standards must be able to co-exist with non-3G systems . It is also expected that frequency allocations to operators will consist of one or more 5MHz blocks within the spectrum. All of these factors strongly suggest that various forms of adjacent band inference will manifest themselves to a significant degree in 3G systems.

The driving goal of 3G wireless is to be able to handle data communications as well as voice. At present, wireless data applications are dominated by relatively undemanding services such as electronic mail and fax services, Short Message Services (SMS) and 9.6 kbit/s GSM data. As succeeding generations of wireless services come on line, new applications such as smart messaging, file transfer, videophony, wireless imaging, remote healthcare and others will become increasingly important and place higher demands upon the infrastructure.

There are a growing number of industry experts who believe that interference problems will be severe in 3G systems and that extremely high-performance filter technology will be needed to combat the problem. Some analyses indicate that even today's best HTS filters will be insufficient to deal with some predicted interference mechanisms and that greatly improved HTS filters will be needed. Such circumstances present both a challenge and an opportunity for the industry.

The longer-term goal for the HTS electronics industry is to become sufficiently well-established in the communications infrastructure to be able to begin to introduce other kinds of products beyond front-end filter

subsystems. There already has been activity in filters for the transmit side of base stations and there may be more opportunities in this area as time goes on. Beyond that, there are other elements in the base station that may benefit from HTS and cryoelectronic technology. And there are other elements of communications systems that may also provide attractive opportunities. Future trends in the industry such as software radio technology provide examples.

At present, some twelve years after the discovery of high-temperature superconductivity, there is now a very young industry based on HTS materials that is producing real products for real market needs. It is too early to judge whether the technology will find a large and successful business within the telecommunications industry but the progress is encouraging and the opportunities remain plentiful.

ACKNOWLEDGMENT

The author would like to acknowledge the assistance of his colleagues at Conductus for providing industry information, test data and applications expertise.

Oral Session 2

Analog/Digital and Digital/Analog Conversion

Progress in the Development of a Superconductive High-Resolution ADC

O. A. Mukhanov, D. K. Brock, A. F. Kirichenko, W. Li, S. V. Rylov†, and J. M. Vogt
HYPRES, Inc., 175 Clearbrook Road, Elmsford, NY 10523, USA

V. K. Semenov, T. V. Filippov, Yu. A. Polyakov
Department of Physics, SUNY, Stony Brook, NY 11794, USA

Abstract—This paper is a progress report on the development of a high-resolution analog-to-digital converter (ADC) which uses a phase modulation/demodulation architecture. Presented are an analysis of the performance limitations, proposed design improvements, and recent test results. Test results for new versions of room temperature VXI-based interface and processing modules are also described.

I. Introduction

Recently, we reported the first full implementation and high-speed performance evaluation of our high-resolution superconductive ADC, which uses a phase modulation-demodulation technique [1]. This initial demonstrated ADC performance was competitive with the best reported semiconductor ADCs to date. However, the performance was considerably lower than projected. In order to identify reasons for this discrepancy and ways to improve the ADC, we have conducted further tests and performed a systematic ADC design analysis and revision.

II. ADC System

We have expanded our superconductive ADC concept to include a cryogenic/room-temperature interface (Fig. 1) with semiconductor post-processing to facilitate additional selectable decimation filtering to achieve dynamic programmability of ADC resolution and bandwidth. This hybrid scheme allows us to reduce the complexity (i.e. junction count) of the superconductive ADC chip while enhancing the overall ADC performance and versatility.

III. ADC Front-End Design Analysis

The most critical part of the ADC system is the ADC front-end (Fig. 2). This block consists of a clock generator (ac/SFQ Converter) producing an SFQ (single flux quantum) clock from an external sinewave and a modulator/ demodulator performing an analog-to-digital conversion using a phase (time-delay) modulation technique. The modulator/demodulator comprises a reference phase generator (RPG), a quantizer, and a race arbiter (or synchronizer).

A. Reference Phase Generator

The accuracy of the ADC cannot exceed the accuracy of the reference phase, which is modulated by the measured signal. In previous papers [1-3] the RPG had not been discussed; it was presented simply as an ideal source of dc voltage exactly corresponding to one half of the clock frequency. In accordance with the fundamental Josephson relationship between voltage and phase, the RPG produces a linearly growing phase.

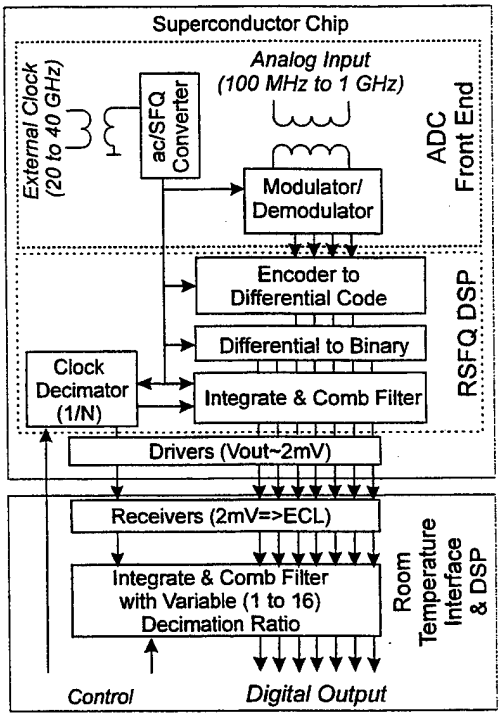

Fig. 1. Block diagram of the new-generation ADC system combining a superconductive ADC chip with room-temperature post-processing.

A basic element of the RPG is a delay line, which is implemented using a Josephson Transmission Line (JTL) with an additional output tap (Fig. 3). These elements are connected sequentially, while the taps are connected with the generator output **R** via equal inductances $L1,...Lm$ (Fig. 2). This produces packets with a fixed number (m) of voltage pulses per packet, or an m-step staircase of the phase as shown in Fig. 4.

Each SFQ pulse passing through the delay lines produces 2π phase steps on the taps. The output of RPG (point **R** in Fig. 2a) produces a staircase-shaped phase φ_R with smaller step sizes to make the height of all m steps equal to 2π. The growth of φ_R leads to a growth in current I_q. However, each time I_q exceeds the critical current I_C of junction J1 (Fig. 2), the current drops down to its initial value I_C-ΔI (Fig. 4b).

Manuscript received May 7, 1999.
This work was supported in part by the Office of Naval Research under contract No. N00014-99-C-0128.
†Now with IBM Watson Research Center, Yorktown Heights, NY.

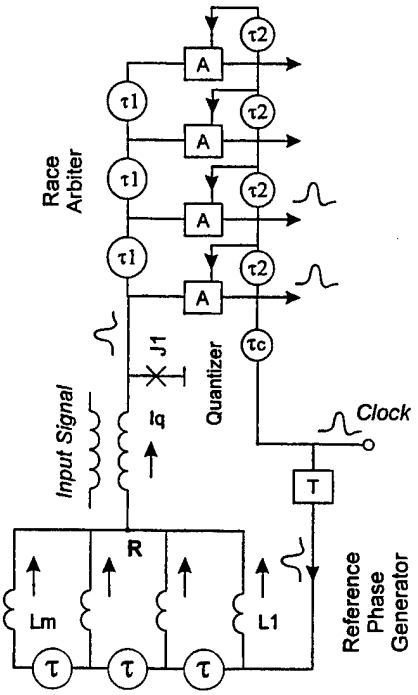

Fig. 2. General structure of the ADC front-end.

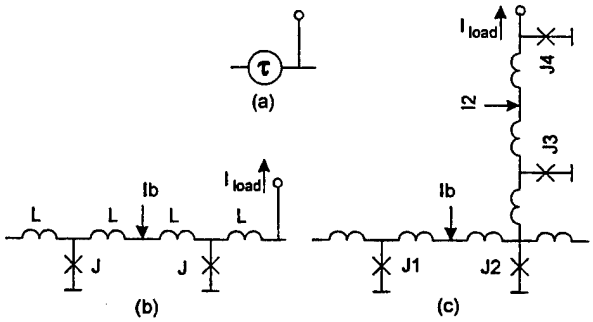

Fig. 3. Delay line for SFQ pulses: (a) notation; (b) the simplest implementation using a section of JTL; (c) an advanced implementation with reduced influence of load current I_{load} on propagation delay.

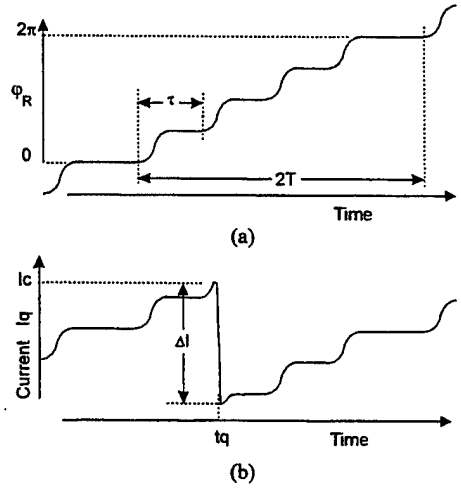

Fig. 4. Operation of the Reference Phase Generator (RPG): (a) RPG produces multi-step staircases of phase; (b) however switching of junction J1 keeps current Iq (c) within margins ΔI.

B. Modulation/Demodulation

The input signal (current) modulates current Iq and, as a result, shifts switching time t_q (Fig. 4b). This time shift (or delay) can be detected in a race arbiter by using a set of similar delay lines and clocked comparators (arbiters) **A** (see top of Fig. 2). The delay in these lines ($\tau 1$) is slightly higher than in the generator to compensate for the clock skew $\tau 2$ between arbiters: $\tau 1=\tau+\tau 2$. For proper operation of the ADC, the delay τc is adjusted to provide that the lower half of the arbiters generate SFQ pulses "1" in the absence of an input signal.

C. ADC Performance Factors

The modulation/demodulation ADC described above has a particularly unique feature—the digitization of a dc signal is insensitive to variations of the clock frequency. Indeed, a variation of the clock period does not change the local (within a clock period) moments of the switching of junctions in the RPG and quantizer; however, the circuit is sensitive to other factors, which can influence circuit timing (delays) and affect the ADC performance.

Factor 1: Individual circuit delays depend on their corresponding bias currents Ib (Fig. 3b). This effect can be used to increase performance by manual delay adjustment, but can also reduce the operating margins due to the introduction of external noise in the bias current. The sensitivity to such deviations could be reduced if all circuitry were fed with a single power line. Currently, we are using many independent power lines to afford the greatest insight during testing.

Factor 2: These delays also depend on load currents I_{load} (Fig. 3). This effect is more difficult to eliminate than Factor 1, because these currents depend on the input signal itself. In particular, the delays are decreased after each switching event of junction J1. This effect can be alleviated if the load current is not allowed to flow via the main delay line, but rather is buffered using additional junctions (J3 and J4 in Fig. 3c).

Factor 3: Circuit delays also depend on the time intervals between successive propagating SFQ pulses. This effect is especially important for the delay lines in the race arbiter block, where the time intervals between subsequent SFQ pulses are modulated by the measured signal.

These key factors limit the ADC performance. Factor 1 is responsible for extra time jitter and thus reduces the ADC signal-to-noise ratio (SNR), while Factors 2 and 3 produce nonlinear distortions and therefore reduce the ADC's Spur Free Dynamic Range (SFDR). Substantial modifications of the ADC front-end design addressing all of these factors are in progress. To verify some of our conclusions, we have made several initial design modifications of the ADC chip reported in [1]. In particular, we have streamlined and simplified the clock and signal paths to the race arbiter. These changes were intended to address Factor 3 as described above.

IV. Test Results

We have tested and evaluated the performance of several modified 14-bit ADC designs with 2-channel race arbiters and 1:64 on-chip decimating ratios. The ADC evaluation test setup was identical to that described in [1]. In order to compare the new ADC performance to our previous test results [1], we ran the ADC chip at the same 11.2 GHz clock and output sampling rate of 175 MS/s (1:64) as was described in [1]. Fig. 5 shows a typical measured FFT spectrum yielding the Effective Number of Bits (ENOB), signal to noise and distortion ratio (SINAD), and SFDR. We tested the ADCs using 10 MHz and 50 MHz sinewaves. For the 10 MHz test, we performed additional post-process filtering in software to remove high-frequency components and effectively reduce the output sampling rate to Nyquist (22 MHz). For the 50 MHz test, no additional filtering was done.

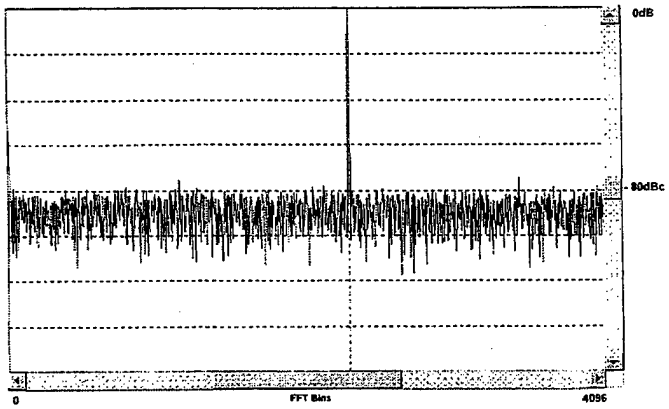

Fig. 5. Measurement of the ADC performance at 175 MS/s (11.2 GHz clock frequency with 1:64 decimation ratio) using an 8K-point FFT spectrum. For 50 MHz input sinewave: ENOB = 8.9 bits, SINAD = 55.3 dB, SFDR = -74.3 dBc (12.3 SFDR bits).

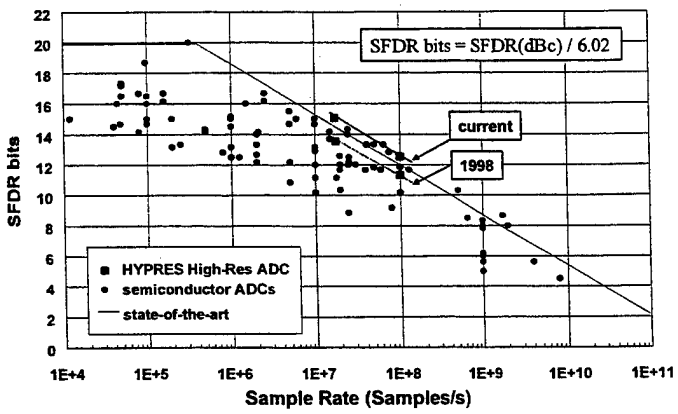

Fig. 6. SFDR bits vs. Sampling rate plot of the ADC performance with our 1998 and current results superimposed. The state-of-the-art semiconductor ADC data are courtesy of B. Walden [4]. The superconductive ADC data are for 14-bit, 2-channel ADC chips operating with an 11.2 GHz clock.

The new results show virtually the same ENOB (SINAD) performance as before: for 10 MHz sinewaves, the measured ENOB of the modified ADC chip achieved the same 12.0 bits at 22 MS/s as the previous ADC design. However, the SFDR performance improved noticeably: -89.7 dBc compared to -80.6 dBc previously. In the case of 50 MHz sinewaves, we observed a similar trend. The ENOB for the 50 MHz tests remained virtually the same (increasing from 8.8 to 8.9 bits) while the SFDR improved from -68.6 dBc to -74.3 dBc. These results are consistent with our theoretical conclusions described in section III.C (Factor 3).

The revised ADC design demonstrates stable operation up to a 12.0 GHz clock rate; however, the measured SFDR at this clock rate was somewhat lower (by about 9 dB) than that at 11.2 GHz. At a 12.8 GHz clock rate, the amount of digital errors (glitches) became too high to conduct further ADC performance evaluation.

Fig. 6 shows an ADC performance plot (SFDR bits vs. Sample Rate) for state-of-the-art semiconductor ADCs as compiled by B. Walden [4]. Our previous [1] and current ADC data are superimposed for comparison. As a direct result of our ADC design modifications, our recent SFDR results now surpass the best reported semiconductor ADC performance to date.

V. Room Temperature Interface and DSP

As shown in Fig. 1, the new generation room-temperature section of our ADC system consists of receiver modules to amplify and convert the ADC chip outputs to ECL levels and a DSP (digital signal processor) module to provide additional decimation filtering with a user-programmable oversampling ratio. The 200 MHz receivers were implemented using a VXI environment to improve shielding, grounding, and power supply, compared to our previous interface implementation using regular VME-bus [1].

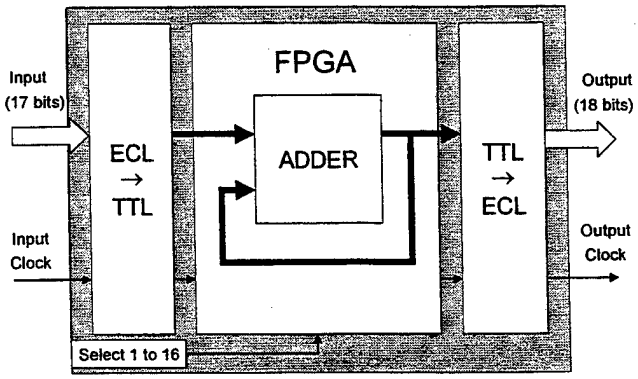

Fig. 7. Block diagram of the DSP module - an integrate and comb filter with a variable 1 to 16 oversampling ratio.

The DSP module performs an integrate and comb filter function, with user-selectable oversampling ratio. It is implemented using a C-size VXI module and has a 17-bit differential ECL data input, an 18-bit differential ECL data output, as well as a clock input and a clock output. Every time a clock signal is received, the data present at the input are added to the content of an accumulator. After a pre-selected number of samples have been added, the output of the module is updated with the sum of these numbers, an

output clock signal is generated, and the accumulator is cleared. The number of samples to be combined is selected via a front panel switch in the range 1-16.

Fig. 7 shows a block diagram of the DSP module. The accumulator and the output clock generator are implemented in a Xilinx XC4003E Field Programmable Gate Array (FPGA). Since the FPGA uses TTL signal levels, the inputs and outputs of the module are level shifted in ECL → TTL and TTL → ECL converters. The current version of the DSP module can operate at an input clock frequency of 80 MS/s limited by the FPGA speed. The next version of the DSP module is being designed to operate at up to 400 MS/s.

Table I shows a summary of the testing of the room-temperature interface including the DSP module at f = 80 MS/s using a 14-bit ADC chip with 1:64 decimation ratio. In order to meet the 80 MS/s limitation, we had to restrict the operation of the ADC chip to a 5.12 GHz clock frequency (64 x 80 MHz). The results obtained show correct operation of the DSP module at different oversampling ratios N: the DSP module produced an ENOB gain corresponding to the expected gain of $\log_2(f/2NBW)^{1/2}$, where BW is the signal bandwidth.

Fig. 8 shows a photo of the VXI-based system comprising a clock receiver module, four 4-bit data receiver modules, and the oversampling DSP module. The receiver modules contain additional features such as monitoring outputs of the ADC chip using a regular oscilloscope, etc. A new set interface of modules, which are currently under development, will operate up to 2 GS/s.

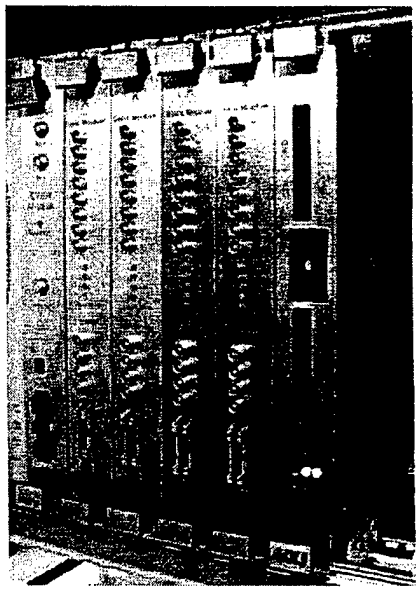

Fig. 8. Room temperature VXI receiver and DSP boards. From left to right: clock receiver, four data receivers, and DSP module.

TABLE I

ROOM-TEMPERATURE OVERSAMPLING MODULE

(test results with an ADC chip operating at 80 MS/s, 5.12 GHz internal clock, and 5 MHz input sinewave)

oversampling ratio of the module N	1	2	3	4
average ENOBs	6.21	6.68	6.94	7.15
gain (experiment)	0.00	0.47	0.73	0.94
gain (theory)	0.00	0.50	0.79	1.00
increm. gain (experiment)	0.00	0.47	0.26	0.21
increm. gain (theory)	0.00	0.50	0.29	0.21
error (10 measurements)	0.03	0.08	0.03	0.03

VI. Conclusions

We have identified a number of factors that can limit the performance of our high-resolution ADCs based on the phase modulation/demodulation architecture. The key issues can be attributed to the certain design facets affecting the timing of the front-end section of the ADC system. Our initial, relatively minor, design modifications addressing some of these issues allowed us to improve the ADC linearity. For the first time, the measurement results demonstrated SFDR performance exceeding the best reported semiconductor ADCs. With further design modifications, we expect to exceed the performance of state-of-the-art semiconductor ADCs substantially.

Acknowledgment

The authors would like to thank D. Gaidarenko for advice on ADC chip testing and the HYPRES fabrication team for producing the ADC chips.

References

[1] S. V. Rylov, D. K. Brock, D. V. Gaidarenko, A. F. Kirichenko, J. M. Vogt, and V. K. Semenov, "High resolution ADC using phase modulation-demodulation architecture," *IEEE Trans. Applied Supercond.*, vol. 9, 1999. (in press).

[2] S. V. Rylov and R. P. Robertazzi, "Superconducting high-resolution A/D converter based on phase modulation and multi-channel timing arbitration," *IEEE Trans. on Appl. Supercond.*, vol. 5, pp. 2260-2263, June 1995.

[3] S. V. Rylov, L. A. Bunz, D. V. Gaidarenko, M. A. Fisher, R. P. Robertazzi, and O. A. Mukhanov, "High resolution ADC system," *IEEE Trans. Appl. Supercond.*, vol. 7, pp. 2649-2652, Jun. 1997.

[4] Bob Walden, HRL Laboratories, walden@hrl.com.

Superconducting Bandpass Delta-Sigma Modulator

John F. Bulzacchelli and Hae-Seung Lee
Department of Electrical Engineering and Computer Science, Massachusetts Institute of Technology, Cambridge, MA 02139

James A. Misewich and Mark B. Ketchen
IBM Research Division, T.J. Watson Research Center, Yorktown Heights, NY 10598

Abstract—**Bandpass delta-sigma modulators digitize narrowband signals with high dynamic range and linearity. The required sampling rate is only a few times higher than the center frequency of the input. This paper presents a superconducting bandpass delta-sigma modulator for direct analog-to-digital conversion of RF signals in the GHz range. The input signal is capacitively coupled to one end of a microstrip transmission line, and a single flux quantum (SFQ) balanced comparator quantizes the current flowing out of the other end. Quantization noise is suppressed at the quarter-wave resonance of the transmission line (about 2 GHz in our design). Circuit performance at a 20 GHz sampling rate has been studied with several long JSIM simulations. Full-scale (FS) input sensitivity is 20 mV (rms), and in-band noise is -53 dBFS and -57 dBFS over bandwidths of 39 MHz and 19.5 MHz, respectively. In-band intermodulation distortion is better than -69 dBFS.**

I. Introduction

In a radio receiver, analog-to-digital (A/D) conversion of signals at RF or high IF frequencies greatly simplifies the analog circuitry, improves flexibility and testability, and allows the reception of multiple communication standards through software reprogramming [1], [2]. Realizing these benefits requires an A/D converter capable of digitizing GHz signals with a large dynamic range (above 10 bits). Traditionally, flash A/D converters have been used to digitize signals above 1 GHz, but their resolution and linearity (typically, below 8 bits) are inadequate for radio applications. Semiconductor bandpass delta-sigma ($\Delta\Sigma$) modulators digitize IF signals with high dynamic range and linearity, and recently a bandpass $\Delta\Sigma$ modulator with a 1 GHz input frequency has been demonstrated in SiGe technology [2]. Even in advanced semiconductor technologies like SiGe, however, the difficulty of generating fast, precise pulses in the feedback path of the $\Delta\Sigma$ modulator loop limits the sampling rate to a few GHz (e.g., 4 GHz for the modulator reported in [2]). In this paper, we present a superconducting bandpass $\Delta\Sigma$ modulator based on single flux quantum (SFQ) circuits. The center frequency of the input signal is just above 2 GHz, and the sampling rate is 20 GHz. Such a high sampling rate improves the performance of the modulator by allowing a higher oversampling ratio for a given bandwidth. The low loss of a superconducting microstrip resonator ensures proper noise-shaping with both large and small inputs – a feature often lacking in modulators with lower-Q resonators [2]. The circuit will be presented after a brief review of bandpass $\Delta\Sigma$ modulators.

Manuscript received April 30, 1999.
J. F. Bulzacchelli gratefully acknowledges the support of an IBM Cooperative Fellowship.

II. Bandpass Delta-Sigma Modulators

A low-pass $\Delta\Sigma$ modulator can be transformed into a bandpass $\Delta\Sigma$ modulator by replacing the forward path integrator with a resonator, as shown in Fig. 1. In a low-pass $\Delta\Sigma$ modulator, the integrator transfer function is maximum at dc, and the large loop gain suppresses quantization noise at low frequencies. In a bandpass $\Delta\Sigma$ modulator, the resonator transfer function is maximum at the resonant frequency (F_0), and the large loop gain suppresses quantization noise at frequencies near F_0. For a modulator using a single resonator, the signal-to-noise ratio (SNR) can be expressed (in power) as [1]

$$\mathrm{SNR} = K\left(\frac{F_s}{2\Delta F}\right)^3, \qquad (1)$$

where F_s is the sampling rate, ΔF is the signal bandwidth, and K is a multiplicative constant typically less than 1. As in the case of a first-order low-pass $\Delta\Sigma$ modulator, SNR improves by 9 dB for each doubling of the oversampling ratio, which is defined to be $F_s/2\Delta F$. Since the SNR is independent of F_0, the center frequency of the input can be a substantial fraction (e.g., 1/4) of the sampling rate.

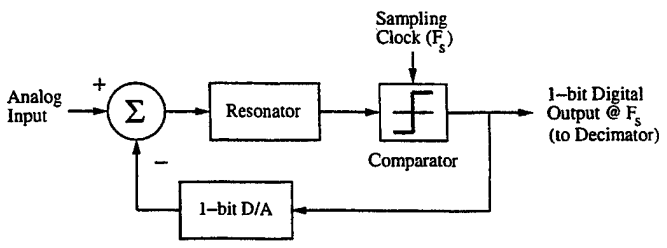

Fig. 1. Basic bandpass delta-sigma modulator.

III. Superconducting Circuit Design

The schematic of the superconducting bandpass $\Delta\Sigma$ modulator is presented in Fig. 2. (To avoid clutter, the Josephson transmission line (JTL) amplifiers for the sampling pulse are represented as lines with arrows.) An analog input with source resistance R_s is capacitively coupled to one end of a superconducting microstrip transmission line. A high loaded Q (> 5000) for the microstrip resonator is obtained by keeping capacitor C_c small. The current flowing out of the right end of the microstrip line is quantized by a standard SFQ timed comparator [3] comprising Josephson junctions J_1 and J_2. If the current is above threshold, the sampling pulse switches junction J_2, generating an SFQ pulse on the output of the modulator. Otherwise, the sampling pulse switches junction J_1, and no output pulse is generated. Each SFQ output pulse represents a binary "1", and its absence represents a binary "0" [3]. The SFQ voltage pulses across J_2 also inject current back into the microstrip line, implicitly providing a "feedback" signal to the resonator (cf. Fig. 1). At frequencies at which the microstrip resonator shunts junction J_2 with a very low impedance, the current injected back into the resonator is magnified, and the quantization noise is suppressed. One such frequency corresponds to the quarter-wave resonance of the microstrip line. Since the impedance of capacitor C_c is much higher than Z_0, the left end of the microstrip line is effectively terminated in an open circuit, which at quarter-wave resonance is reflected as a short circuit shunting J_2. As shown in the simulations discussed below, the quantization noise is also minimized at other frequencies, corresponding to higher-order modes on the microstrip line.

Other circuit details shown in Fig. 2 enhance modulator performance. Voltage source V_{bias} ($\approx \Phi_0 F_s/2$) biases the SFQ comparator to produce about half "1"s and half "0"s. (Φ_0 is the magnetic flux quantum.) At very high frequencies, inductor L_{res} isolates the SFQ comparator from the low impedance (1 Ω) microstrip line so that the switching speed of junction J_2 is not degraded. The addition of series inductor L_{res} does alter the resonant frequencies; as an example, the quarter-wave resonance is reduced from 2.5 GHz to just below 2.1 GHz for the component values given in Fig. 2. Current source I_0 improves the comparator's dynamics near metastability by limiting the total phase drop across J_1 and J_2.

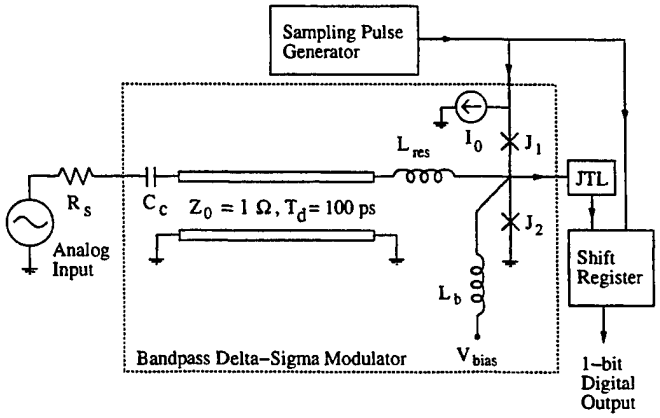

Fig. 2. Superconducting bandpass delta-sigma modulator loaded by JTL and shift register. The circuit parameters are: R_s=50 Ω, C_c=0.11 pF, L_{res}=20 pH, L_b=100 pH, I_{c1}=I_{c2}=270 μA, and I_0=380 μA.

IV. Simulated Results

The entire circuit depicted in Fig. 2 has been simulated with JSIM, which included the stochastic extension reported in [4] for modeling thermal noise. Standard JTL and shift register circuits [3] provided a realistic load for the SFQ comparator in the modulator. Circuit operating temperature was 4.2 K, and I_cR_n products were 300 μV, typical for shunted ($\beta_c = 1$) 1 kA/cm^2 Nb junctions. To decrease the noise contribution from the room-temperature (300 K) source resistor, a 6 dB resistive attenuator (at 4.2 K) was placed between resistor R_s and capacitor C_c in the simulated circuit. In all the simulations, voltage source V_{bias} biased the SFQ comparator to produce 51.2% "1"s, avoiding idle tone problems [1] sometimes observed at exactly half of full-scale (FS).

Fig. 3 plots the output spectra of the modulator at a 20 GHz sampling rate with (a) no input and (b) a large input (-0.76 dBFS) at 2.13 GHz. The minimum in the noise power at 2.05 GHz corresponds to quarter-wave resonance. Under both input conditions, proper noise-shaping is observed, and in-band noise is -53 dBFS and

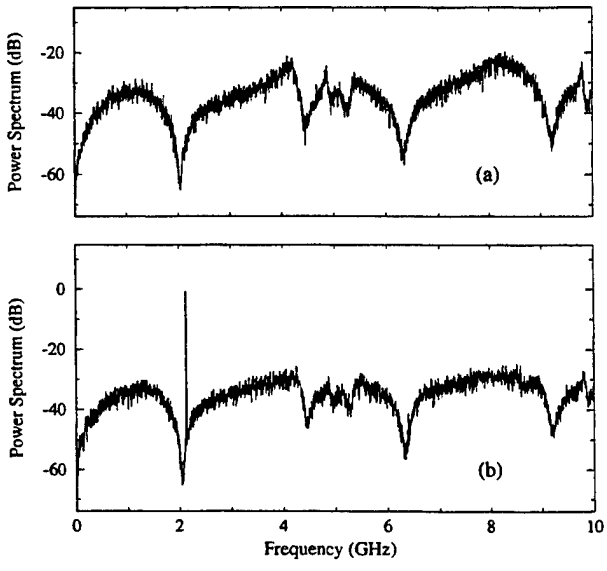

Fig. 3. Simulated output spectra of superconducting bandpass modulator sampling at 20 GHz with (a) no input and (b) a large input (-0.76 dBFS) at 2.13 GHz. In both cases, in-band noise is -53 dBFS and -57 dBFS over bandwidths of 39 MHz and 19.5 MHz, respectively. The output code lengths were 32768.

-57 dBFS over bandwidths of 39 MHz and 19.5 MHz (centered at 2.05 GHz), respectively. There are also noise power minima at other frequencies. Near dc, inductor L_b shunts junction J_2 with a low impedance, and quantization noise is minimized – an effect utilized in superconducting low-pass $\Delta\Sigma$ modulators [5]. The other minima correspond to higher-order modes on the microstrip line, including some above 10 GHz which appear in the digital domain as "aliased" modes. To prevent these aliased modes from interfering with the desired noise-shaping, the sampling rate and microstrip resonances have been chosen so that no aliased modes fall near 2 GHz.

In-band intermodulation (IM) distortion exhibits a frequency dependence similar to that of quantization noise: minimum at 2.05 GHz and highest at the band edges. Fig. 4 shows the results of a worst-case IM distortion test for a signal bandwidth of 39 MHz. Both input amplitudes were -6.8 dBFS, and the input frequencies were selected so that the upper third-order and fifth-order IM distortion products fell at 2.031 and 2.07 GHz, respectively. The distortion product at 2.031 GHz is clearly visible and is -69.3 dBFS (roughly, 11-bit linearity); the distortion product at 2.07 GHz is buried beneath the noise floor (-83 dBFS). A larger (-55.0 dBFS) distortion product at 1.875 GHz is also seen; since this product is below the band of interest, it can be removed with digital filtering.

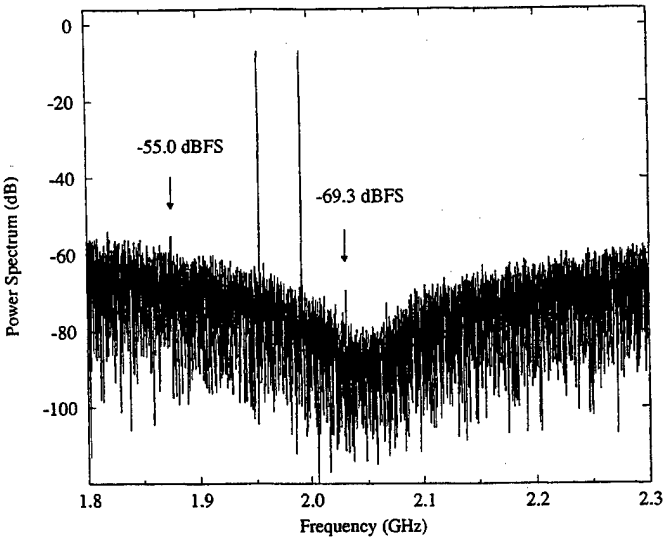

Fig. 4. Two-tone intermodulation distortion test of superconducting bandpass modulator sampling at 20 GHz. In the JSIM simulation, the input frequencies were 1.953 and 1.992 GHz, and both input amplitudes were -6.8 dBFS. The output code length was 491520.

V. Discussion

Even with the 6 dB resistive attenuator included in the simulated circuit, a full-scale input is only 20 mV (rms). Removal of the resistive attenuator would increase sensitivity by a factor of 2, at the cost of a small increase in in-band thermal noise. Such high sensitivity simplifies the design of the RF preamplifier, as only modest (< 20 dB) gain is needed in front of the A/D converter. Still higher sensitivity could be obtained by increasing capacitor C_c, but the effect on loaded Q would have to be studied.

As illustrated in Fig. 4, the noise power spectrum does not go to zero at 2.05 GHz but levels out at a nonzero value. For this reason, narrowing the bandwidth from 39 MHz to 19.5 MHz reduced in-band noise by only 4 dB, instead of the 9 dB predicted by (1). The excess noise at 2.05 GHz is not due to thermal noise but to delay modulation effects in the SFQ comparator. For input currents just slightly above threshold, the delay before an SFQ pulse is generated across junction J_2 is larger than usual. Such variations in comparator delay are known to degrade SNR in $\Delta\Sigma$ modulators [6]. To check this explanation, the delay modulation was made negligibly small by setting junction capacitance to 0 and increasing I_cR_n to 4.7 mV. With a sampling rate of 20 GHz and no input, in-band noise was then -61 dBFS and -70 dBFS over bandwidths of 39 MHz and 19.5 MHz, respectively – in accordance with (1). While an I_cR_n product of 4.7 mV is impossible for Nb, similar performance could be obtained with more realistic parameters (e.g., $I_cR_n = 1$ mV). Since SNR is limited more by circuit dynamics than by thermal noise, the bandpass modulator is also suitable for implementation in high-T_c technology. Currently, a bandpass modulator test chip is being fabricated at HYPRES, Inc. [7].

Acknowledgment

We would like to thank S. Rylov, O. Mukhanov, V. Semenov, T. Tewksbury, A. Karanicolas, and J. Lloyd for valuable advice and discussions.

References

[1] S. Jantzi, R. Schreier, and M. Snelgrove, "The design of bandpass $\Delta\Sigma$ ADCs," in *Delta-Sigma Data Converters: Theory, Design, and Simulation*, S. R. Norsworthy, R. Schreier, and G. C. Temes, Eds. Piscataway, NJ: IEEE Press, 1997, ch. 9, pp. 282–308.

[2] W. Gao, J. A. Cherry, and W. M. Snelgrove, "A 4 GHz fourth-order SiGe HBT band pass $\Delta\Sigma$ modulator," in *1998 Symp. VLSI Circuits Dig. Tech. Papers*, Honolulu, June 1998, pp. 174–175.

[3] K. K. Likharev and V. K. Semenov, "RSFQ logic/memory family: a new Josephson-junction technology for sub-terahertz-clock-frequency digital systems," *IEEE Trans. Appl. Superconduct.*, vol. 1, pp. 3-28, March 1991.

[4] J. Satchell, "Stochastic simulation of SFQ logic," *IEEE Trans. Appl. Superconduct.*, vol. 7, pp. 3315-3318, June 1997.

[5] J. X. Przybysz, D. L. Miller, E. H. Naviasky, and J. H. Kang, "Josephson sigma-delta modulator for high dynamic range A/D conversion," *IEEE Trans. Appl. Superconduct.*, vol. 3, pp. 2732-2735, March 1993.

[6] J. A. Cherry, W. M. Snelgrove, and P. Schvan, "Signal-dependent timing jitter in continuous-time $\Sigma\Delta$ modulators," *Electron. Lett.*, vol. 33, pp. 1118-1119, June 1997.

[7] HYPRES niobium process flow and design rules are available from HYPRES, Inc., 175 Clearbrook Rd., Elmsford, NY 10523.

DEMONSTRATION OF JOSEPHSON SIGMA-DELTA ANALOG-TO-DIGITAL CONVERTERS

D. L. Miller, J. X. Przybysz, A. H. Worsham, E. J. Dean, M. G. Forrester, and B. D. Hunt
Northrop Grumman Science and Technology Center, 1350 Beulah Rd., Pittsburgh, PA 15235

Abstract—The sigma-delta architecture is the method of choice for designers and manufacturers of analog-to-digital converters (ADCs) for high dynamic range applications. This architecture uses oversampling and precise feedback to generate a shaped spectral distribution of the quantization noise. Subsequent digital filtering suppresses out-of-band quantization noise, yielding a large signal to in-band noise ratio. A unique advantage of superconducting electronics is the availability of the flux quantum to provide quantum mechanically accurate feedback at GHz rates. Josephson digital technology extends sigma-delta ADCs from MHz sampling rates to GHz sampling rates, from kHz signal bandwidths to MHz signal bandwidths, with comparable or better dynamic range when compared to semiconductor implementations. This paper presents circuits for Josephson sigma-delta ADCs, including single-loop and double-loop modulators, and circuits for quantized feedback. Experimental results are reported.

I. INTRODUCTION

Analog-to-Digital Converters (ADCs) are used in many applications, from audio recording to radar systems, to take advantage of powerful and robust digital signal processing and digital data storage capabilities. In audio applications, the demand for fidelity has driven the market to ever higher dynamic range ADCs, and the speed of semiconductor logic coupled with the simplicity of the Sigma-Delta (Σ–Δ) architecture [1] have made this the method of choice in this frequency range.

Superconductivity offers the potential to extend the bandwidth of high dynamic range Σ–Δ ADCs to MHz bandwidths while maintaining or extending the dynamic range. Single Flux Quantum (SFQ) logic offers a unique technology for the implementation of Σ–Δ ADCs. Multi-GHz operation of digital circuits has been demonstrated by many groups[2-3], and the availability of the flux quantum provides quantum mechanical stability in the feedback.

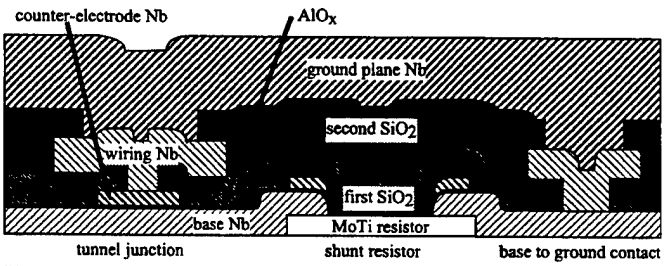

Fig. 1. The Northrop Grumman Nb process has been developed for high yield and flexible design. An eight level process is used to make high quality Nb/AlOx/Nb trilayers. The eighth level (TiAu) is not shown.

Manuscript received April 30, 1999.
This work was supported in part by U.S. Office of Naval Research under contract no N0001495C0195.

II. FABRICATION

The Northrop Grumman Low Temperature Superconductor (LTS) process consists of eight levels as shown in Fig. 1. Six of these levels are metallic, and two are insulating. In-situ ion-beam cleaning or back sputtering precedes all metal depositions. A more complete description of the process is given in [4]. Circuits reported here were operated at 4.2 K.

III. SUPERCONDUCTING CIRCUITS FOR SIGMA-DELTA ADCS

A. Single-Loop Sigma-Delta Modulators

The key component of a sigma-delta ADC is the modulator, which performs the integration, sampling, and feedback functions. A simple first order modulator[5,6] consists of an inductor in series with an SFQ decision circuit. Such a modulator has been operated at sampling frequencies up to 45 GHz, albeit without storage or filtering of the digital output [5].

A more complex single-loop modulator, Fig. 2, with inductive input and complementary feedback has been suggested by the work of Lin et al.[7]. We have designed and fabricated such a modulator using the fabrication process of [4].

Our modulator differs from the circuit of [7] in that the quantizing inductor has been reduced to 40 pH. This provides a quantization interval of 52 μA, large compared to thermal noise from the junction shunting resistors. Additionally, we used damping resistors to reduce microwave oscillations in the quantizing inductor.

A block diagram of the modulator test is shown in Fig. 3. Clock signals were provided by an HP pulse-pattern generator for 225 MHz tests or an HP frequency synthesizer for 2 GHz tests. Additional clock signals were derived from the master to drive the sampling clock, the superconducting output amplifier, and the digital data collection board. After on-chip

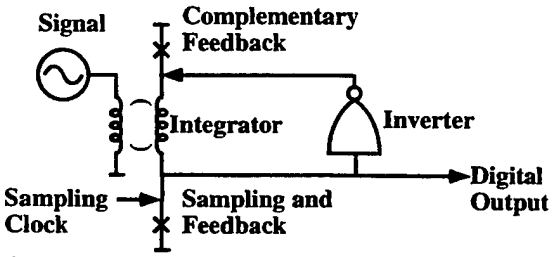

Fig. 2. A complementary feedback single-loop Σ–Δ modulator has demonstrated noise shaping of over 130 dB.

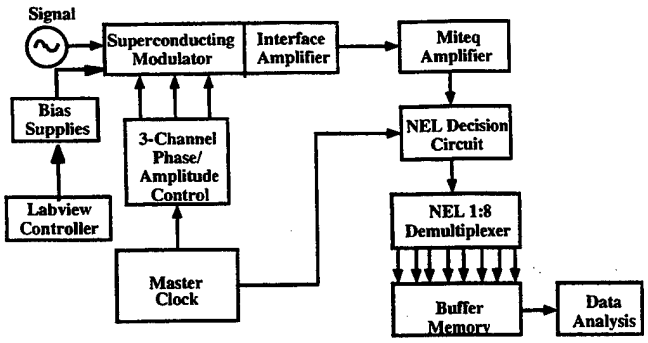

Fig. 3. Flow diagram for data collection from the Σ–Δ modulator.

amplification[8], the digital output of the modulator was further amplified with a standard commercial amplifier. A decision circuit, also constructed from commercial parts, reestablished the bit pattern at ECL levels and the data was dumultiplexed 1:8 for collection by a buffer memory, where it was stored for off-line analysis.

Fig. 5(a) shows the experimental result with a sampling rate of 225 MHz with a signal frequency of 200 kHz. For this figure, 2^{20} consecutive data were collected from the buffer memory and converted to the frequency domain by a fast Fourier Transform (FFT) algorithm. The resulting spectral distribution clearly shows the quantization noise shaping typical of single-loop modulators, and SNR of 76 dB. Fig. 5(b) shows a measurement taken with a sampling rate of 2 GHz and a signal frequency of 5.01 MHz. Again the data show typical noise shaping over the entire sampling bandwidth. SNR for this measurement was 52 dB (10 MHz signal bandwidth). For each of these measurements the signal was ~20 dB below the theoretical maximum.

B. Second Order Modulators

The advantages of the Σ–Δ approach are realized in higher order modulators. As a rule of thumb, a second order

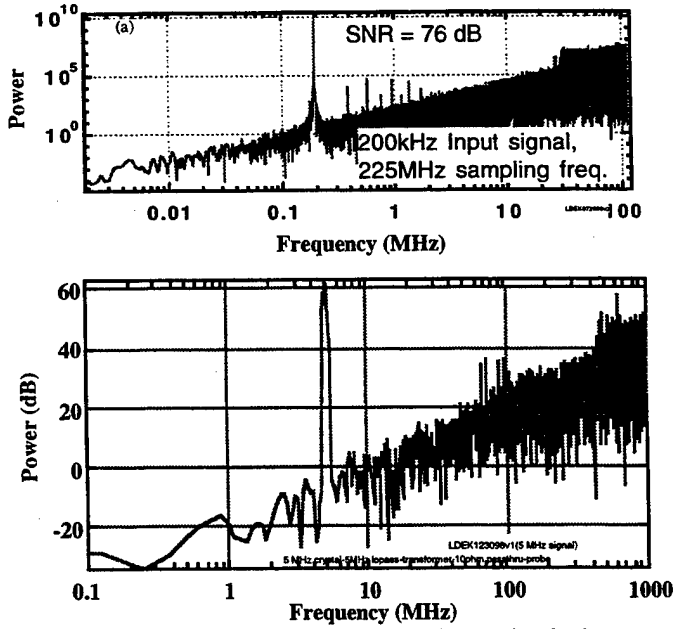

Fig. 4. The Fourier transform of single-loop data shows noise shaping over 19 octaves of frequency.

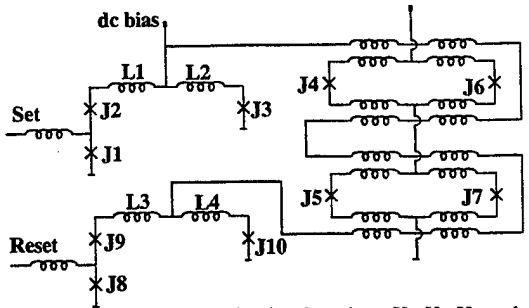

Figure 5. An M=2 Φ_0 feedback circuit. Junctions J2, J3, J9, and J10 are latching junctions. All other junctions are shunted. A set pulse latches J2 and J3, diverting the dc bias through the control inductor and causing junctions J4 and J5 to pulse. A reset pulse latches J9 and J10, resetting the control current and pulsing J6 and J7.

modulator can be expected to provide 1 extra bit of resolution per octave of oversampling when compared to a single-loop modulator. A concept for a second order superconductive modulator[9] is shown in Fig. 6. In this modulator, a signal current is applied to a resistor, providing a signal voltage to the inductor, L1. The L1 current is then the time integral of the signal voltage. The second loop consists of another resistor-inductor pair, with the first loop current acting as the second loop signal. The current in L2 is sampled by SFQ clock pulses supplied to a decision circuit. For L2 currents below threshold, the clock pulse is buffered and a "0" is output. For currents above threshold, the sampling junction pulses, outputting a "1" and feeding back Φ_0=2.07 mV•ps to the integrating inductor. This feedback is quantum mechanically precise, independent of circuit biases, and provides a major advantage of superconductive circuits with respect to semiconductor implementations which rely on consistency in a large number of electrons for precision in feedback.

The first loop feedback, $M\Phi_0$ in Fig. 6, is triggered by a "1" from the sampling junction and provides M flux quanta of feedback. Gain (M) is used in this circuit to achieve optimal noise shaping.

A feedback amplifier circuit with a gain of 2 is shown in Fig. 5. This amplifier uses series connected dc SQUIDs driven by a control line. Current in the control line is controlled with SFQ pulses through a pair of dc-biased latches.

The feedback amplifier of Fig. 5 has been extended to a gain of 4 and was fabricated in our Nb technology for evaluation. Voltage mode test results of the feedback circuit are shown in Fig. 10. For this test, an overbiased junction was used as a clock and drove a t-flip-flop. The flip-flop outputs were used to drive the set and reset latches, respectively. Thus the feedback circuit was driven at half the circuit clock frequency. Operation of the circuit was verified by applying the Josephson voltage-to-frequency realtion, V = f•483 MHz, to the SQUID stack and the clock junction. With correct operation, that is a gain of 4, the voltages should have a ratio of 2., Fig. 6 shows that the feedback operated at more than 5 GHz.

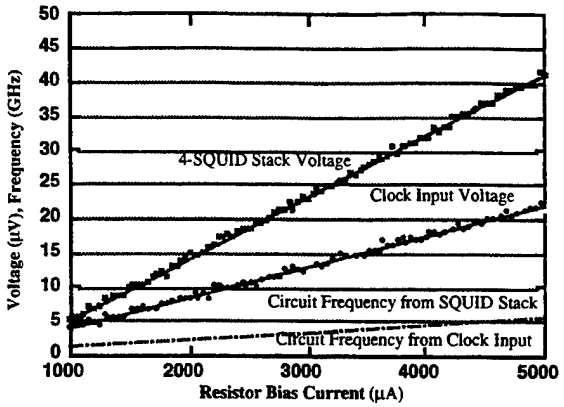

Fig. 6. Average voltage response of M=4 Φ_0 circuit. Converted to frequency, the input and output signals agree to the accuracy of the data.

A second order modulator using this feedback technique with M=4 was also fabricated and tested. For this test, the circuit was clocked at 180 MHz, and the output displayed on an HP spectrum analyzer. Fig. 7 shows the spectrum analyzer data along with the results of two MATLAB simulations. The results have been offset by for display purposes. The two upper curves show results with no feedback to the first integrator, i.e. single-loop operation. The lower curves show double-loop behavior with a feedback gain of 4. In double-loop operation, the noise in the signal band is suppressed by ~12 dB. This is the expected improvement from a feedback gain of 4.

C. High Temperature Superconductor Modulator

Recent progress in the fabrication of High Temperature Superconductor (HTS) Josephson junctions has permitted the demonstration of modest circuits in these materials. We have designed and fabricated a single-loop Σ–Δ modulator, using a deposited barrier HTS junction process [10] which includes a ground plane for the control of inductances. A complete description and test results of this modulator are reported in a companion paper [11].

IV. CONCLUSION

Sigma-delta ADCs offer dynamic range advantages over other architectures through oversampling and noise shaping. We have designed, fabricated and tested both single- and double-loop SFQ-based Σ–Δ modulators. Single-loop modulators have been exercised at 2 GHz clock rates and have shown a dynamic range of 52 dB for 10 MHz signal bandwidth. Double-loop modulators have demonstrated characteristic Σ–Δ noise shaping, with performance consistent with the feedback gain. This work forms the basis for ADCs whose dynamic range significantly exceeds that of existing semiconductor devices for rf signals.

ACKNOWLEDGMENT

The authors would like to thank Steve Whiteley, Andy Pershall, Gene Kolnowski, and Stan Pieseski for helpful discussions.

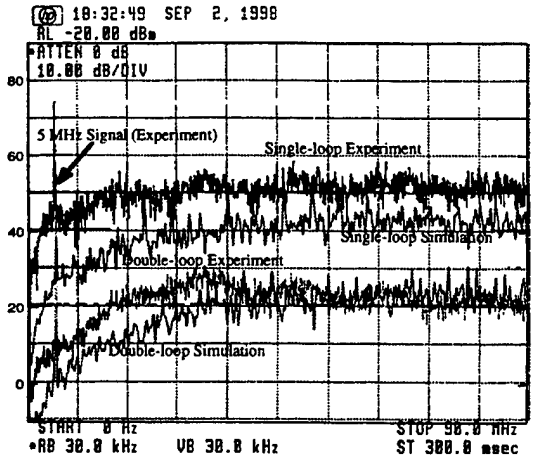

Figure 7. Simulated and measured output of a two-loop modulator with M=4. Upper curves show operation with first loop feedback (i.e. single-loop operation). Lower curves show double-loop operation. Curves are offset for clarity.

REFERENCES

[1] J. C. Candy and G. C. Temes, *Oversampling A/D Converters,* (New York, IEEE Press, 1992).

[2] Q. P. Herr and M. J. Feldman, "Error Rate of RSFQ Circuits: Theory," *IEEE Trans. on Apl. Supercond.*, vol 7, pp2661-2664, June 1995.

[3] A. H. Worsham, A. H. Miklich, D. L Miller, and J. X. Przybysz, "Single Flux Quantum Circuits for 2.5 Gbps Data Switching," *IEEE Trans. on Apl. Supercond.*, vol 7, pp2476-2479, June 1995.

[4] D.L. Miller, J.X. Przybysz, A.H. Worsham, and E.J. Dean, "Flux Quantum Sigma-Delta Analog-to-Digital Converters for re Signals," *IEEE Trans on Apl. Supercond,* to be published.

[5] D. L. Miller, J. X. Przybysz, D. L. Meier, Joonhee Kang, and A. H. Worsham, "Characterization of a Superconductive Sigma-Delta Analog to Digital Converter," *IEEE Trans. on Apl. Supercond.*, **5**, 2453-2456, June 1995.

[6] J. X. Przybysz, D. L. Miller, E. H. Naviasky, and J. H. Kang, "Josephson sigma-delta modulator for high dynamic range A/D conversion," *IEEE Trans. on Apl. Supercond.*, **3**, 2732 -2735, March 1993.

[7] C. Lin, S. V. Polonsky, D. F. Schneider, V. K. Semenov, P. N. Shevchenko, and K. K. Likharev, "Development of sensitive SFQ-counting A/D converter," *Extended Abstracts of 4th ISEC*, pp. 90-91, Boulder, CO.

[8] J. X. Przybysz, J. H. Kang, D. L. Miller, S. S. Martinet, and A. H. Worsham, "Interface circuits for input and output of Gigabit per second data," *Extended Abstracts of 5th ISEC*, pp. 304-306, Sept. 1995.

[9] J. X. Przybysz, D. L. Miller, and E. H. Naviasky, "Two-Loop Modulator for Sigma-Delta Analog to Digital Converter," *IEEE Trans. on Apl. Supercond.*, **5**, 2248-2251, June 1995.

[10] B. D. Hunt, M. G. Forrester, J. Talvacchio, R. M. Young, and J. D. McCambridge, "High-Tc SNS Edge Junctions with Integrated YBa2Cu3Ox Groundplanes", *IEEE Trans. Appl. Supercond.*, 7, 2936 (1997).

[11] M. G. Forrester, B. D. Hunt, D. L. Miller, J. Talvacchio, and R. M. Young, "Analog Demonstration of a High Temperature Superconducting Sigma-Delta Modulator with 27 GHz Sampling", *this conference.*

Comparison of Superconductor Analog-to-Digital Converters (Theory)

Vasili K. Semenov
SUNY, Stony Brook, NY 11794-3800, USA

Abstract—All high-accuracy ADCs developed with our participation demonstrate a significant discrepancy between experimentally measured and expected performances. We have found that this discrepancy is caused by oversimplified theoretical analysis, which in particular underestimates the nonlinear properties of Josephson junctions affected by SFQ pulses. The new theory shows that the previous performance projections for modulator/demodulator ADC could be saved by simple design revisions. It helps us to suggest the novel multi-comparator structure for delta ADC, which, we think, could demonstrate even better performance. This structure could be favorable for both low and high Tc superconductor electronics.

I. Introduction

Superconductor Analog-to-Digital Converters (ADCs) have been under investigation for many years. However, till now the major task was to illustrate feasibility rather than to commercialize superconductor digital electronics. We believe the task is completed at this conference: the current revision of a high-resolution superconductor ADC fabricated and tested at HYPRES, Inc. at 175 MHz Nyquist rate has the better Spur Free Dynamic Range (SFDR) than any semiconductor ADC [1].

However we have found a significant discrepancy between measured and expected performance (the reached performance is lower). This inconsistency stimulated a drastic revision of priorities in design optimization as well as some basic postulates. This report presents a draft of our revised approach to the design of high-accuracy superconductor ADCs.

2. Underestimated Difficulties

The uncertainty of sampling time (aperture time τ_a) is one of the most fundamental parameters describing performance of an ADC (see, for example, Ref. 1). For example, 14-bit accuracy at 200 MHz sampling rate corresponds to τ_a below 0.5 ps. We found that almost any analog component of superconductor ADCs containing Josephson junctions contributes to this uncertainty. Indeed, let us consider a uniform Josephson Transmission Line (JTL) (Fig. 1) that is used to transfer SFQ pulses between functional devices

Manuscript received May 15, 1999.
This work was supported in part by the NAVY and directly by HYPRES, Inc. and Ericsson AB.

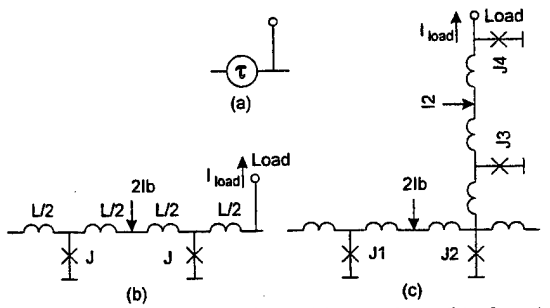

Fig. 1. Delay line for SFQ pulses: (a) notation; (b) the simplest implementation using a section of JTL; (c) an advanced implementation with reduced influence of load current I_{load} on propagation delay [2].

A. Influence of an External Noise

It is well known that the propagation delay of a JTL τ depends on its bias current *Ib*. Figure 2 (solid line) shows this dependence for our "standard" line (inductance $\beta_l = 2\pi I_c L/\Phi_0$ and capacitance β_c=1. This property is

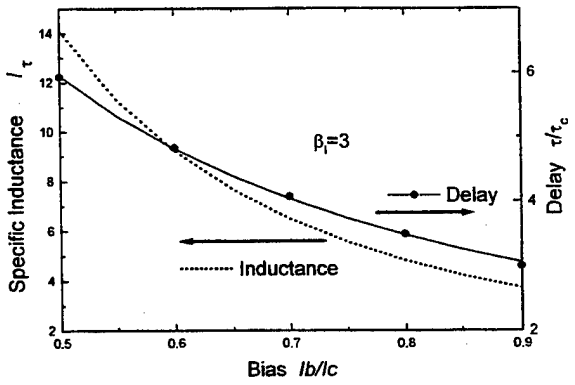

Fig. 2. Dependences of propagation delay (solid line) and effective inductance (dotted line) of JTL on bias current Ib.

very convenient for delay adjustments. Unfortunately it provides an undesirable conversion of an external noise into a delay jitter. It is interesting to note that at a given current noise the value of the jitter does not depend on a JTL length. Indeed, the larger number of Josephson junctions *k* in the JTL leads to a proportionally smaller specific current noise per junction, however the total jitter is accumulated from those reduced inputs of all *k* junctions. As an example, our standard JTL (Ic=0.25mA, Ib=0.7Ic) has current sensitivity about 30ps/mA, e.g. variation of the bias current on 17μA leads to 0.5ps delay variation.

The sensitivity to deviation of bias current can be drastically reduced if the voltage of the power line is

stabilized by unshunted junctions [3]. But it can be done only for the very few bias voltages multiple to the gap voltage of the Josephson junctions (~2.6 mV for niobium technology)!

B. Influence of an Analog Signal

A. Delay depends on load current: High-resolution superconductor ADCs can use similar JTLs either to generate a reference signal [1], or to compensate a digitized signal [3]. These JTLs should provide an essentially variable load current (depending on the digitized signal), which, in contract with noise, cannot be eliminated. Let us to show that the influence of the load current on the JTL's dynamics can be described in terms of a nonlinear inductance.

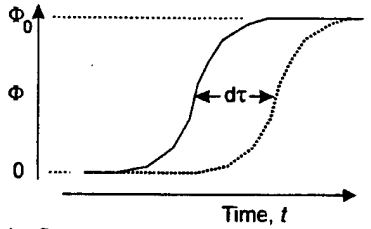

Fig. 3. Magnetic flux passes through a Josephson junction with delay dependent on the applied current *Ib*: solid line - larger current, dotted line - smaller current. Derivative of the average flux on the current defines a new kind of inductance, which is not related with a geometry of the circuit.

Indeed, the variation of the delay means the variation of magnetic flux (Fig. 3). The inductance L could be defined as the first derivative of the magnetic flux over current:

$$L = \langle d\Phi / dI \rangle = (f \cdot \tau_c)(\Phi_0 / I_c) \cdot l_\tau, \qquad (1a)$$

where f is the frequency of SFQ pulses while l_τ is a dimensionless factor:

$$l_\tau = d(\tau / \tau_c) / d(I_b / I_c) \qquad (1b)$$

shown for our standard parameters in Fig.1 by the dot line.

This inductance (about 0.5 pH for typical parameters: $f \cdot \tau_c$=0.067, Ic=0.25 mA, Ib/Ic=0.7) is about half of the Josephson inductance associated with critical current of a Josephson junction $L_J=\Phi_0/I_c$. However, it is more nonlinear (see, for example, dot line in Fig. 2), and therefore it hurts the ADC linearity. Note, that the influence of the inductance cannot be drastically attenuated by using a multi-tab string of sequentially connected JTL (see, Fig. 2 in Ref. 2) because the described mechanism defines an append to the delay, so the delay is accumulated from appends produced by all junctions. Fortunately, in the more complex circuit (Fig. 1c) the delay line is isolated from load current I_{Load} by junction J3, J4, and, as a result, the current cannot affect the propagation delay.

B. Delay depends on frequency: Figure 4 shows that the propagation delay also depends on the frequency of SFQ pulses. This dependence is relatively low at nominal bias (the line with open squares), but it becomes much more essential if the bias current is low (line with open circles). This effect dramatically restricts the margins for an adjustment of the delay by the bias current.

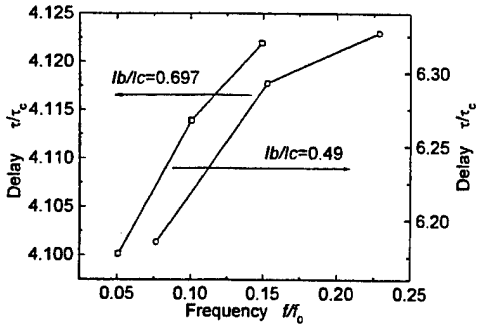

Fig. 4. Dependence of propagation delay on frequency of SFQ pulses for nominal (open squares) and lower (open circles) bias currents.

3. New Opportunities

A. Interleaving:

It has been shown that the resolution of an ADC can be limited by the dependence of propagation delay on frequency of SFQ pulses. This difficulty can be avoided by interleaving of several identical ADCs. Figure 5 illustrates this very common maneuver for a system consisting of 2 identical ADCs.

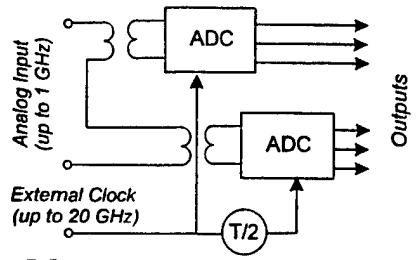

Fig. 5. Two ADCs operate in the interleave mode: each of them samples with period T, but the clock pulses of the second ADC are shifted on one half of the clock period. It allows to get twofold higher effective sampling frequency, while all components operate at the same (lower) clock frequency.

B. Delta ADC with Multiple Comparators.

The most unpleasant mistake with our old design of delta ADC [4] is a hidden integration of two functions in one device. This device is the clocked comparator [5,6], which besides comparison also withdraws magnetic fluxes or operates as Digital-to-Analog Converter (DAC). Figure 6 shows the novel delta ADC with comparators completely separated from DAC. It contains only one new component: a "nondestructive" comparator. Such a comparator can be derived, for example, from a conventional clocked comparator [5, 6] by replacing its lower junction with a 2-junction interferometer and using magnetic rather than direct coupling with analog signal (Fig. 7). Now several comparators (two in Fig. 6) can sample the same signal in the interleave mode. Simple RSFQ cells (D cell and Inverter)

convert sampling results into a complementary (or dual road) presentation. The outputs of the cells control corresponding phase generators with floating grounds (Fig. 7). The phase generators controlled by the other comparator are connected in series and also operate in the interleave mode. Here is a list of advantages of the novel ADC.

- Effective sampling frequency is larger than clock frequency, so one can expect better performance.
- The Feedback loop is highly symmetrical, so the nonlinear effects described above are dramatically compensated.
- The optimization criteria for comparators and phase generators are separated: the comparator are optimized for the current sensitivity, while phase generators are optimized for linearity (or for independence of load current).

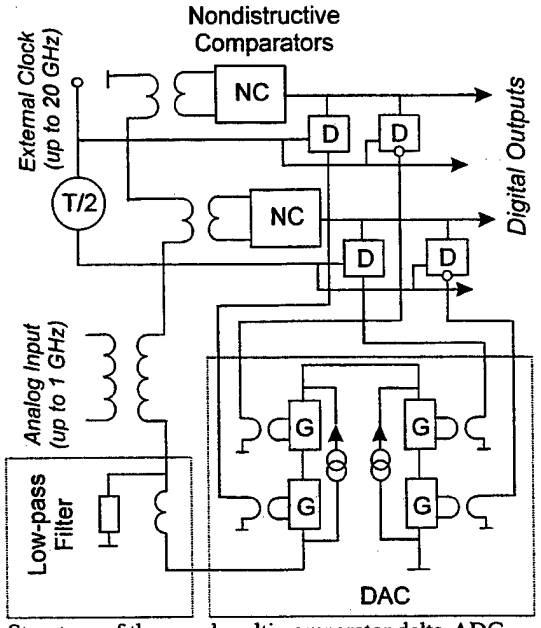

Fig. 6. Structure of the vovel multi-comparator delta-ADC

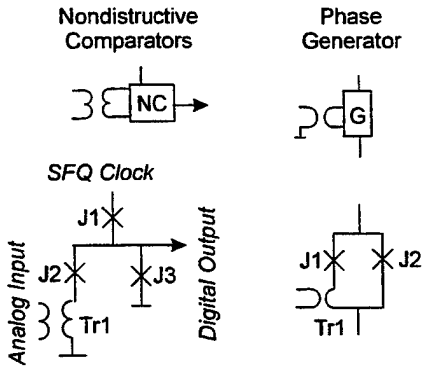

Fig. 7. Notations and equivalent circuits of 2 basic components of the ADC

IV. Discussion

We found that a "low-frequency" dynamic of circuits with overdamped Josephson junctions affected by SFQ pulses still contains white spots. In particular, such circuits can behave as very nonlinear inductances, which are capable of dramatically reducing the ADC performance.

The negative impact of these novel inductances has different postfaces on modulation/demodulation and delta ADCs. We think we know how to reduce this impact into the developed modulation/demodulation ADC without significant changes of its structure (Fig. 1 in Ref. 2).

The new effects created more damages in the earlier suggested delta ADCs [4]. However, the suggested here novel structure for delta ADC looks now even more attractive than modulation/demodulation ADC. In particular, it allows two basic quantity (clock and sampling frequencies) to be unbound. This means that the sampling frequency can approach 100 GHz even for the standard 1kA/cm2 HYPRES's fabrication technology. Moreover, the new ADC is very simple and transfers digital data via the larger number of output channels. This is functionally equivalent to a single-quantizer ADC with multiplexer. Such multiplexing is vitally important for people who believe in very simple superconductor ADCs based on high-Tc materials, which must to use semiconductor postprocessing with the highest possible sampling rate.

As a final conclusion we would like to state is that we are now even more confident with our near and long term prospects for the superconductor ADCs (Fig. 6 in Ref. 2)

Acknowledgement

We would like to thank D. Zinoviev for assistance with numerical calculations (Fig. 2), T. Filippov, A. Kirichenko, O. Mukhanov, S. Rylov, and E. Wikborg for helpful notices during numerous discussions, D. Durand, K. Likharev, J. Przybysz, E. Track, and T. VanDuzer for sharing their experience in the field of superconductor electronics. I would also like to thank S. Lutterbie for great editorial help

References

[1] *Delta-Sigma Data Converters*, S. R. Norsworthy, R. Schreier, and G. C. Temes, Eds. , New York, IEEE Press, 1997.

[2] O. A. Mukhanov *et al.*, "Progress in the Development of a Superconductive High-Resolution ADC", *This Conference.*

[3] "Josephson Computer Technology: An IBM Research Project," IBM J. Res. Develop., vol. 24, Mar. 1980.

[4] V.Semenov, "Implementation of Oversampling Analog-to-Digital Converter Based on RSFQ Logic," Ext. Abstract of ISEC'97, vol.1, pp. 41-43, 1997.

[5] V.K. Semenov, T.V. Filippov, Yu. A. Polyakov, and K.K. Likharev, SFQ Balanced Comparators at Finite Sampling Rate, *IEEE Trans. on Appl. Supercond* , vol. 7, pp. 3617-21, June 1997.

[6] T. Filippov and M. Znosko, "Time Characteristics of a Josephson Balanced Comparator," *This conference.*

All-Digital Measurement of the Energy Sensitivity of a Superconductive Comparator

David A. Feld, Karl K. Berggren, Jay P. Sage, Aleem Siddiqui, and Terry Weir
Lincoln Laboratory, Massachusetts Institute of Technology, Lexington MA 02420-9108, USA

Abstract—We have performed all-digital sensitivity measurements of low-T_c superconductive quantum-flux-parametron (QFP) comparators. Previously, Ko and Lee [1] proposed that the sensitivity of QFP comparators could approach h (Planck's constant) when biased at the center of the gray zone and clocked at 100's of GHz, thus rivaling the sensitivity of SQUIDs [2]. S_ε is a measure of the signal energy that can be resolved by a comparator. A device with a smaller S_ε can resolve smaller signal energy in a given length of time. In previous work we operated a quantum-flux-parametron (QFP) comparator at 40 MHz clock rate and measured its sensitivity to be ~1500 h [3]. In that work we compared Ko and Lee's energy-sensitivity theory based on the measurement slope of the gray zone with a direct measurement of S_ε in which the signal-to-noise ratio is measured when a small input sinewave is applied. Good agreement was found between the two measurements. In this earlier work, the signal-to-noise measurements were made by using an analog spectrum analyzer to measure the comparator's output. At higher clock frequencies, the comparator becomes more sensitive, and we require an all-digital analysis to avoid distortions of the low-level, wide-band, analog output voltage. In this work we digitally processed the output bits to determine both the slope of the gray zone and to measure S_ε directly. A 4 MHz input sinewave was phase locked to the comparator clock operating at 128 MHz. The digital outputs were amplified and read into an HP 16500C digital waveform analyzer which stores the values of 64k sequential output bits. A 64k-point FFT was performed. The noise floor was flat in all 64k frequency bins except in the two frequency bins corresponding to the input sinewave. The sensitivity is found to be as small as 800 h.

I. INTRODUCTION

Comparators, such as the quantum flux parametron (QFP), are critical elements in the front ends of high-resolution analog-to-digital (A/D) converters, timing discriminators, and other analog circuits. See [1] for details of the operation of the QFP. One important figure of merit for a comparator is its energy sensitivity S_ε. S_ε is the product of the minimum energy that can be detected during a measurement time, ΔT, and ΔT. If two comparators are operated for the same period of time, then the comparator with the smaller S_ε is capable of detecting a smaller potential energy oscillation in its input. That comparator is said to have "better energy sensitivity". Much work has been applied to measuring the energy sensitivity of SQUIDs in which the input and output are both analog signals [2]. It has been shown that Planck's constant h (6.6×10^{-34} J s) is an approximate lower bound on S_ε because Heisenberg's uncertainty principle may not be violated.

There has, however, been little work in measuring S_ε and comparing it to theory in superconductive comparators. This is important as comparator clock rates are pushed into the GHz range. Figure 1 shows the block diagram of an experiment used to measure S_ε for a quantum flux parametron (QFP) comparator. In the experiment of Fig. 1, the sensitivity is measured by determining the minimum amplitude sinewave that can be detected by the QFP when data from it are collected for a specified period of time. In previous work we showed how spectral analysis of the digital output could be used to determine the sensitivity [3]. In that work the digital output of the QFP was treated as an

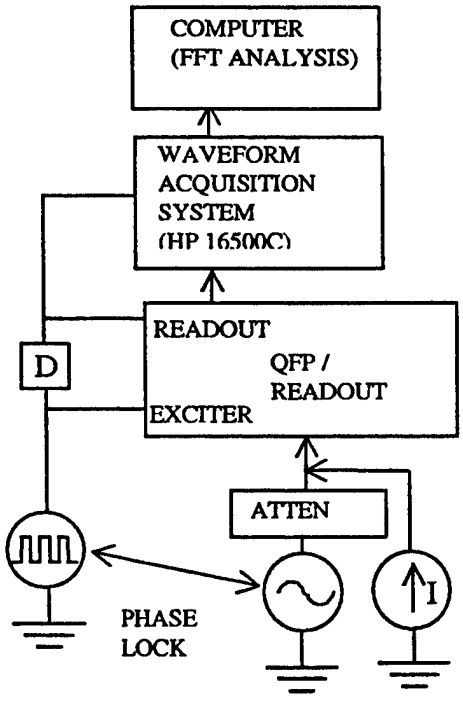

Fig. 1 QFP sensitivity experiment is shown for QFP biased in center of "gray" zone. Clock source is phase-locked to lower-frequency sinewave source. QFP receives its analog input from attenuated sinewave source. QFP is activated by square-wave clock source. Readout is activated by delayed clock source. Digital output from the QFP comparator is amplified and stored by a digital waveform analyzer (HP-16500). The result can be FFT analyzed by computer.

Manuscript received May 15, 1999. The Department of Defense under Air Force contract F19628-95-C-0002 supported this work. Opinions, interpretations, conclusions and recommendations are those of the author and are not necessarily endorsed by the United States Air Force.

analog signal and an analog spectrum analyzer was used to measure the power spectrum of the output. In this work the digital output is treated as a digital signal – for each clock cycle, the outputs are sampled and stored in semiconductor memory (HP 16500C). The data are subsequently transferred to a computer for digital processing. The digital acquisition technique is important for three reasons: (1) analog noise is not introduced into the output waveform, (2) a high-resolution frequency analysis can be performed over a bandwidth equal to half the clocking frequency (3) a variety of statistical analyses can be easily computed.

II. Experimental Overview

Here is how the experiment shown in Fig. 1 is conducted. A squarewave clock supplies the necessary current into the exciter input to actuate the QFP. When the QFP is actuated, a large positive or negative current is delivered into the QFP's output inductor. If the QFP's internal noise sources could be excluded then the direction of this output current would bepositive if the injected input current is positive and would be negative if the input current is negative. Thermal noise from the QFP's damping resistors is a random source of additive current noise to the input and creates a region where for a given external input, there is a probability that the QFP will generate a particular outcome at its output. This region is known as the gray zone.

Aside from actuating the QFP, the clock is used to convert the direction of current in the output inductor into a voltage (no voltage) that can be read out to room temperature electronics. To achieve this the clock is delayed by about one quarter of a cycle to drive the readout circuit. The readout circuit is a SQUID that is coupled to the QFP output inductor. When the clock current rises, the SQUID enters the voltage-state (a digital "1") provided that the output current is flowing in the direction required to suppress the SQUID threshold current. A room temperature amplifier is used to amplify the SQUID output voltage, so that an HP-16500C digital waveform analyzer can threshold the amplified data and store the digital value of the QFP for each clock cycle. The waveform analyzer can store up to 64k samples in a sequential format. After 64k samples are acquired, the data are read from the acquisition system into a computer for analysis.

A dc input current is adjusted to operate the QFP where it is most sensitive – this is known as threshold operation [4]. At this value of input current, the output delivers an equal number of digital "1's" and "0's" due to the influence of internal thermal noise. Hence the QFP is operated in the center of its thermally induced transition region or "gray zone". A tiny current, typically a few 100's of nA, is also injected into the QFP to perform sensitivity measurements.

III. Sensitivity Theory

In [3] we give the derivation for two ways to compute the energy sensitivity as expressed by (1) and (2) below:

$$S_\varepsilon = \Delta E \Delta T = \left[\frac{L(I_{3dB})^2}{2}\right]\left[\frac{1}{\Delta B}\right] \quad (1)$$

$$S_\varepsilon = \Delta E \Delta T = \frac{2P_0(1-P_0)L}{\left(\frac{dP}{dI}\right)^2 f_B} \quad (2)$$

(1) is used to compute the energy sensitivity by determining the minimum detectable input sinewave. (2) is used to compute the energy sensitivity based on the slope of the gray zone. The two methods should give identical results. Here, L is the differential input inductance of the QFP, I_{3dB} is the rms amplitude of the minimum detectable sinewave, ΔB is the frequency resolution of the experiment that is the reciprocal of the time duration of the experiment. P_0 is the probability that the QFP's output is a "1". f_B is the frequency at which the QFP is clocked. dP/dI is the slope of the gray zone at the P_0 operating point.

IV. Results

A 4 MHz input sinewave was applied to the input of the comparator. The amplitude of the applied sinewave was

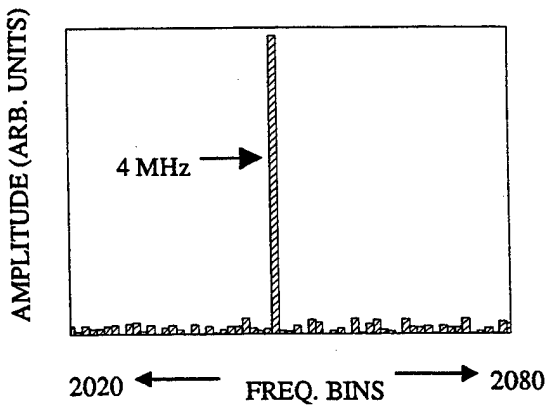

Fig.2 Digitally acquired power spectrum showing power in the digital output stream of a QFP comparator operated at 128 MHz when a small 4 MHz input sinewave is applied at its input. Sixty of the 64k frequency bins are shown. By measuring the signal power in the output and by comparing it to the noise floor we conclude that the comparator has a sensitivity of ~800h at this operating frequency.

measured to be 341 nA rms. The comparator clock was operated at 128 MHz, 64k digital samples were acquired, and the digital data were read into a computer where a 64k-point FFT was performed. Fig. 2 shows a plot of the magnitude of 60 bins from the output of the FFT. The length of the experiment was 0.5 mS which is the time it takes to acquire 64k samples. ΔB is the binwidth of the FFT which is 1/(0.5 ms) = 2 kHz. Exactly 2000 cycles of the 4 MHz sinewave occur while the 64k digital samples are acquired since the clock and sinewave source are phase locked. Figure 2 shows the output of the FFT of the waveform. The floor is flat for all frequency bins excluding the dc and 4MHz bins as expected. Because the clock and data are phase locked and since there are an integral number of clock cycles for the duration of the experiment, there is no evidence of splatter or non-flat terms near the 4 MHz tone. The amplitude of the minimum detectable sinewave, I_{3dB}, was computed to be 24 nA by realizing from Fig. 2 that a 4 MHz input sinewave with a 24 nA amplitude would have been detectable at 3dB above the noise floor.

Next, dP/dI was computed by "sweeping out" the QFP gray zone shown in Fig. 3. The gray zone was measured by applying a dc current to the QFP input, clocking the QFP at 128 MHz, acquiring 64k binary samples, and transferring that data to the computer, where the number of "1's" obtained was totaled. A fraction was computed from the sum total of "1's out of the 64k samples acquired. Figure 3 is a plot of this fraction as a function of the dc input current. Once the gray zone was acquired, it was then fit to an integrated Gaussian with sigma and mean as parameters. An excellent fit was obtained as shown in Fig. 3. The slope of the integrated Gaussian, dp/dI for $P_0 = 0.5$, the chosen operating point, was computed from sigma ($\sigma = 2.5$ μA). L

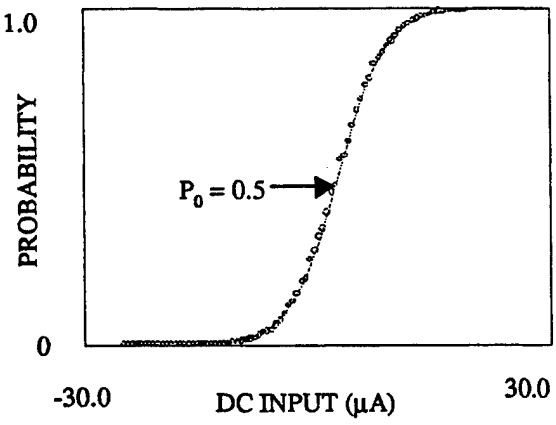

Fig.3 shows digitally acquired "Gray zone" plot and a two-parameter integrated Gaussian fit with mean and variance as parameters. The slope at the point $P_0 = 0.5$ was extracted from this plot for use in computing the energy sensitivity.

was estimated to be about 4 pH. The results for the two expressions for energy sensitivity were computed using (1) and (2) and both were found to be in reasonably good agreement and gave an energy sensitivity of ~800 h (Planck's constant).

V. Conclusion

We have developed an all-digital technique for measuring the energy sensitivity of QFP comparators. This was done by two methods that are in good agreement. This will be a useful technique as clock rates are increased into the GHz range, where the sensitivity is expected to approach 10's of h. The technique is extendable to other types of superconductive and semiconductor comparators.

Acknowledgment

The authors would like to acknowledge the MIT Lincoln fabrication team for fabricating the QFP devices.

References

[1] H. Ko, and G. Lee, "Noise analysis of the quantum flux parametron," *IEEE Trans. Appl. Supercond.*, vol. 2, pp. 156-164, September 1992.

[2] D. Van Harlingen, R. Koch, and J. Clarke, "Superconducting Quantum Interference Device with Very Low Magnetic Flux Noise Energy,"*Appl. Phys. Lett.*, 41(2), 15 July, 1982.

[3] D. Feld, J. Sage, K. Berggren, and A. Siddiqui, "Measurement of the Energy Sensitivity of a Superconductive Comparator," *IEEE Trans. Appl. Supercond.*,accepted for publication, June 1999.

[4] D.Feld, and J.P. Sage, "Uniformity Limits in Arrays of Analog Sense Circuits," *Proceedings of the International Superconductive Electronics Conference (ISEC), Extended abstracts,* Berlin, Germany, Vol 2, pp. 293- 5, June 1997.

Analog Demonstration of a High Temperature Superconducting Sigma-Delta Modulator with 27 GHz Sampling

M. G. Forrester, B. D. Hunt, D. L. Miller, J. Talvacchio, and R. M. Young
Northrop Grumman Science and Technology Center, Pittsburgh, PA 15235-5098

Abstract — **We have successfully fabricated and tested a high temperature superconducting (HTS) sigma-delta modulator for analog-to-digital conversion. This is the first demonstration of a GHz sampling A-to-D in HTS. The fifteen-junction Single Flux Quantum (SFQ) circuit, fabricated using an epitaxial multilayer HTS process with YBCO/Co-YBCO/YBCO edge junctions, was internally clocked at 27 GHz and used to convert a 5.01 MHz signal. The modulator demonstrated a spur-free dynamic range of more than 75 dB. Two-tone measurements with 5.01 MHz and 5.51 MHz signals demonstrated third order intermodulation products to be lower than –59 dBc. Demonstration of a functional HTS modulator represents a significant milestone in the development of high dynamic range ADCs suitable for such applications as surveillance radar.**

I. Introduction

The Sigma Delta (Σ–Δ) architecture is the preferred approach to high dynamic range A-to-D converters [1]. This oversampling approach is used in audio applications where signals at kHz frequencies are sampled at MHz by a Σ–Δ modulator, and the resulting bit stream digitally filtered, to provide resolution of 18–20 bits. Superconducting digital logic working at GHz clock speeds can potentially be applied to the conversion of 10-20 MHz signals. Realization of such a circuit in HTS technology will allow this performance while using a relatively compact, reliable, cryocooler, suitable for airborne and space applications. Towards this end we have fabricated a simple HTS Σ–Δ single-loop modulator, with fifteen YBCO/Co-YBCO/YBCO edge junctions, in an epitaxial multilayer process utilizing three YBCO layers, two epitaxial insulators, and integrated Au resistors. We have measured its performance at 35K by inputting a 5.01 MHz signal, and sending the output bit stream into a spectrum analyzer to measure the relative amplitude of the unwanted harmonics which determine the spur-free dynamic range (SFDR). With 27 GHz sampling rate we measured a SFDR of > 75 dB, comparable to our previous demonstration of an LTS modulator [2]. Two-tone tests showed third-order intermodulation products to be < –59 dBc, instrument limited.

II. Circuit Design

The schematic of the modulator circuit is shown in Fig. 1. In this modulator, the critical junctions are Jb and Js, which perform threshold detection on the current in Li, and, to a lesser extent, J1, which balances the sampler when both Jb and Js pulse in response to a clock input. Both the clock and the output were isolated from the sampling junction by Josephson transmission line for stability. Operation of the modulator is described in [2].

The circuit was simulated using WRSPICE, and layout inductances, including junction parasitics, were extracted for comparison with design values. The fabrication process permits junctions at any angle. This design used four cartesian orientations. Low value resistors, fabricated with interdigitated terminals, were designed using measured contact resistances.

III. Circuit Fabrication

To fabricate the circuit we employed a multilayer process similar to that reported previously [3,4], with the addition of

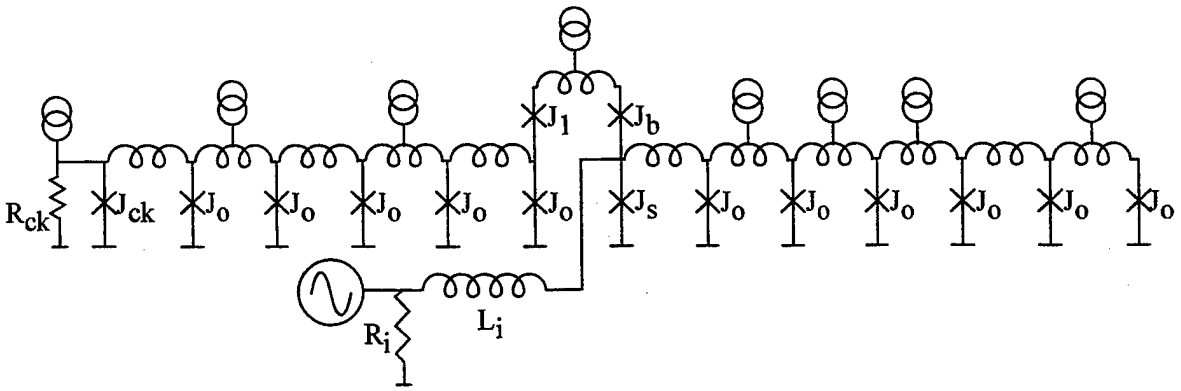

Fig. 1 Schematic diagram of the designed HTS Σ–Δ modulator. Designed junction critical currents are 320 μA, except J1 and Jb, which are 250 μA. Li = 20pH, Ri = 10 mΩ and Rck = 0.2Ω.

Manuscript received April 30, 1999.
This work was supported in part by ONR Contract N00014-96-C-0007 and AFOSR Contract F49620-98-2-0234.

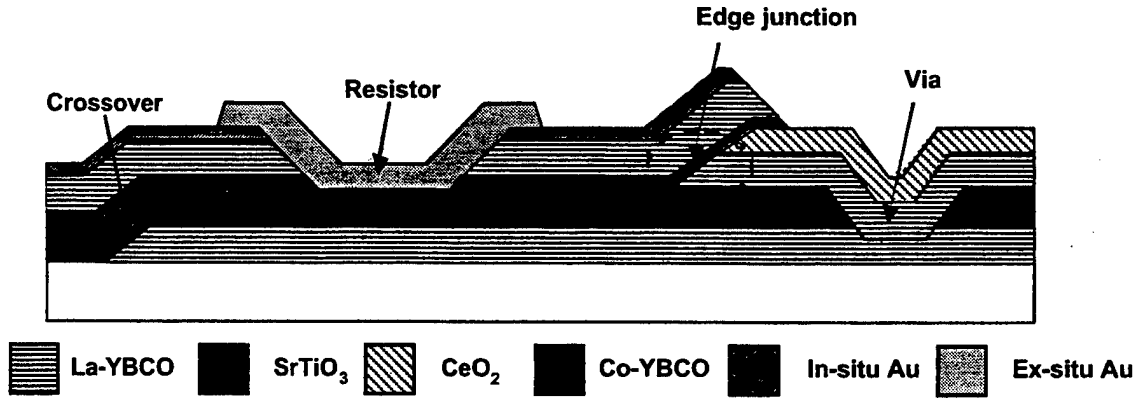

Fig. 2 — Schematic cross-sectional view of the HTS multilayer circuit process, illustrating key process components.

an ex-situ gold layer to form resistors. The process, whose schematic cross-section is shown in Fig. 2, used Pulsed Laser Deposition (PLD) for both YBCO and insulating $SrTiO_3$ and CeO_2 layers, with the exception of the groundplane. For this first YBCO layer we used coevaporated YBCO on a $NdGaO_3$ substrate [5] because of its low RMS roughness (typically 1.0 nm, compared to 1.5 to 2.0 for PLD YBCO). This smoothness, which is obtained somewhat at the expense of superconducting properties such as T_c and penetration depth, is found to improve targeting of the desired junction critical current (I_c) and resistance (R_n). All layers were patterned using a reflowed photoresist process (to produce tapered resist sidewalls) and angled ion milling with either pure Ar or 20% O_2 in Ar, depending on the layer and desired edge angle.

An outline of the process sequence is as follows: as-delivered coevaporated films of 225 nm thickness were patterned and etched, then cleaned using an rf oxygen plasma followed by an Ar/O_2 ion mill (our "standard clean"). Approximately 200 nm of $SrTiO_3$ (STO) was deposited by PLD, and vias patterned by ion milling through the STO and part way into the groundplane. After another standard clean the base electrode bilayer of 200 nm $YBa_{1.95}La_{0.05}Cu_3O_x$ (La-YBCO) and 50 nm CeO_2 was deposited, patterned, and cleaned. After a wet etch in 0.3% Br in methanol a 10 nm N-layer of $YBa_2Cu_{2.80}Co_{0.20}O_x$ and 200 nm La-YBCO counterelectrode were deposited by PLD, followed in-situ by 100 nm of sputtered Au. The Au-coated counterelectrode was patterned by ion milling. Finally a gold resistor layer was defined by lifting-off 200 nm of Au, with a Ti adhesion layer. Contact between the resistors and the La-YBCO counterelectrode was always through the in-situ Au.

IV. Process Characterization

Candidate chips for circuit testing were selected by characterizing test areas within the circuit chip. This ensured that, for example, critical currents were close to the design values, and spreads were sufficiently good to give a high probability of a working circuit on that chip. These test areas included:

- 19 individual junctions of sizes representative of the circuit (3.2 and 2.5 μm wide)
- Direct-injection SQUIDs to measure the inductance per square of microstrip lines
- Series-arrays of base-electrode-to-groundplane vias
- Series-arrays of counterelectrode-groundplane and base-electrode-groundplane crossovers
- Resistors in the 10 mΩ and 0.1 Ω ranges.

The desired critical current density of 100 μA/μm (5×10^4 A/cm^2 for 0.2 μm thick base electrodes) was obtained in the temperature range of 35 to 40 K. Thus circuits were tested in that temperature range. Junction IV curves were RSJ-like but with a few μA of hysteresis. Typical junction R_nA products were 1.4 Ω-μm^2, yielding $R_n \approx 2.1$ Ω for a 3.2 μm wide junction. We have found that junctions significantly above 1 Ω tend to have wider critical current spreads than desired — typically 20-30% one-sigma, which is inferior to our best values of 10-12%. Such wide spreads are not a major problem for this modulator since it has only one critical junction pair.

Measured microstrip inductances were 0.8 pH/sq and 1.2 pH/sq for base-electrode-over-groundplane and counterelectrode-over-groundplane, respectively. Since the latter configuration dominates the circuit the agreement with the design value of 1.5 pH/sq (which had anticipated higher temperature operation) was sufficient.

Critical currents of vias and crossovers were of order several-mA for temperatures below about 65 K, and thus did not limit the application of the desired biases of hundreds of μA.

The Au-YBCO contact resistivity was measured to be about 5×10^{-8} Ω-cm^2. This value is high enough that the nominal 10 mΩ input resistor is dominated by contact resistance rather than the resistance of the ex-situ Au layer.

V. Circuit Measurements

The measurements performed on this HTS circuit are essentially the same as previously reported for a Nb-based Σ–Δ modulator [2], except for those which required a latching amplifier, which was readily fabricated in Nb technology but not in HTS. A stable 5.01 MHz oscillator was used as a signal source. The output of this oscillator was low pass filtered to insure that harmonics present in the signal were below –90 dBc. Signal amplitude was controlled with a key-switched resistive attenuator. The clock frequency was controlled at 27 GHz by a dc current applied to the 0.2 Ω clock resistor, R_{ck}, in parallel with the clock junction, and was measured by using the Josephson voltage to frequency relation: $f=V/\Phi_0$. A dc offset current, applied to the signal input of the modulator, insured a positive voltage at the integrator.

A Hewlett-Packard 72109A spectrum analyzer was used to display the spectral output of the modulator. The output signal was measured at 5.01 MHz and at 10.02 MHz using 10 Hz resolution bandwidth for maximum sensitivity. The results of this measurement are shown in Fig. 3. The upper curve shows the reproduction of the input signal at 5.01 MHz. The lower curves, centered at 10.02 MHz, show the response at the first harmonic, with and without an input signal. Down to the noise floor of the spectrum analyzer there is no evidence of a harmonic. The small observed structure, independent of the presence of an input signal, is thought to be due to external interference. By mis-adjusting the circuit biases it was easy to bring the 10.02 MHz harmonic well into range. Biases were optimized to bring the harmonic below the noise floor.

Further evidence of the modulator linearity was obtained by measurement of third order intermodulation products. Signal sources at f_1 = 5.01 MHz and f_2 = 5.51 MHz were combined with a power combiner. Six dB of attenuation of each port of the power combiner isolated the signal sources from each other. Signal levels were adjusted to yield output

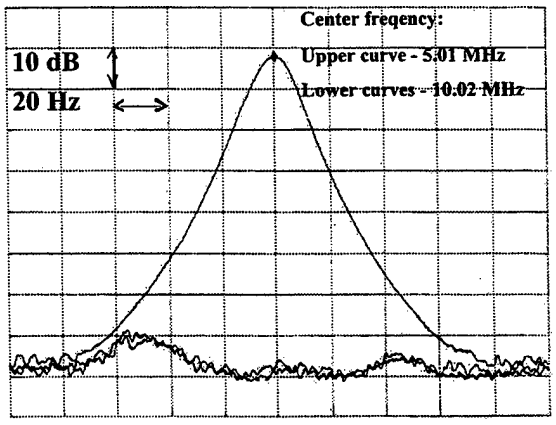

Fig. 3 — Spectral response of the HTS Σ–Δ modulator. The upper curve, centered at 5.01 MHz, is the output at the signal frequency. The lower curves, centered at 10.02 MHz, show the absence of harmonic response from the modulator above the noise floor of the spectrum analyzer.

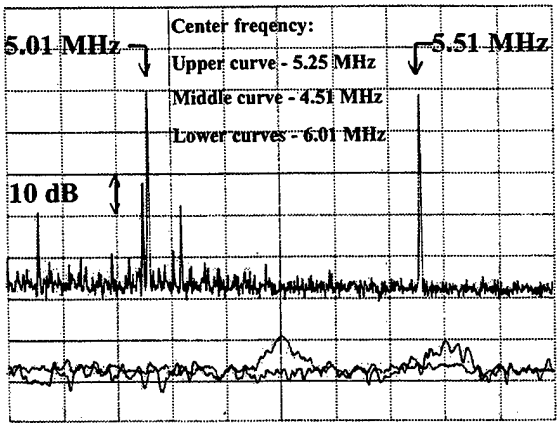

Fig. 4 — Third order intermod test of the HTS modulator. The upper curve shows the two input signals at 5.01 and 5.51 MHz, with 100 kHz/division scale and 1 kHz resolution bandwidth. The middle (lower) curve, centered at 4.51 MHz (6.01 MHz) was measured at 10 Hz resolution bandwidth and expanded to a scale of 10 Hz/division to increase sensitivity. The small responses in the lower curves are within the distortion spec of the spectrum analyzer.

peaks 6 dB lower than the signal of Fig. 3, as measured by the spectrum analyzer. Note that this represents the same peak-to-peak voltage swing as in the previous measurement. The output was measured at 6.01 MHz ($2f_2$-f_1) and 4.51 MHz ($2f_1$-f_2). In the latter case, an intermodulation product was visible at a level of approximately –59 dBc.

V. Conclusions

We have demonstrated, for the first time, an HTS Σ–Δ modulator, fabricated with an extendible multilayer process. The circuit was operated at 27 GHz clock frequency, and demonstrated a spur-free dynamic range of > 75 dB, and third order intermodulation products less than –59 dBc. Extension of the circuit to higher frequencies, and the use of a more-complex double-loop modulator architecture, will take full advantage of the high speed and quantum accuracy of superconducting digital circuits, and should result in ADCs with 18-20 bits of SFDR on a 20 MHz signal bandwidth.

References

[1] J. C. Candy and G. C. Temes, "Oversampling A/D Converters," IEEE Press, 1992.

[2] D. L. Miller, J. X. Przybysz, D. L. Meier, J. H. Kang, and A. H. Worsham, "Characterization of a Superconductive Sigma-Delta Analog to Digital Converter," IEEE Trans. on Applied Superconductivity 5(2), 2453 (1995).

[3] B. D. Hunt, M. G. Forrester, J. Talvacchio, J. D. McCambridge, and R. M. Young, "High-Tc Superconductor/Normal-Metal/Super-conductor Edge Junctions and SQUIDs with Integrated Groundplanes," Appl. Phys. Lett. 68, 3805 (1996)

[4] J. Talvacchio, M. G. Forrester, B. D. Hunt, J. D. McCambridge, R. M. Young, X. F. zhang, and D. J. Miller, "Materials Basis for a Six-Level Epitaxial HTS Digital Circuit Process," IEEE Trans. Appl. Supercond., Vol. 7, No. 2, 2051 (1997).

[5] Theva Dünnschichttechnik GmbH, Hauptstr. 1b, D-85386 Dietersheim, Germany

A High-Temperature Superconducting Delta-Sigma Modulator based on a Multilayer Technology with Bicrystal Josephson Junctions

Bernhard Ruck, Yonuk Chong*, Regina Dittmann, Achim Engelhardt, Erik Sodtke and Michael Siegel
Institut für Schicht- und Ionentechnik (ISI), Forschungszentrum Jülich GmbH, 52425 Jülich, Germany

Abstract—We have designed, fabricated and successfully tested a first-order delta-sigma modulator using a High-Temperature Superconducting (HTS) multilayer technology with bicrystal Josephson junctions. The circuit has been fabricated on a $SrTiO_3$ bicrystal substrate. The $YBa_2Cu_3O_7/SrTiO_3/YBa_2Cu_3O_7$ trilayer was fabricated by laser deposition. The bottom layer served as a superconducting groundplane. The Josephson junctions were formed at the bicrystal line in the upper layer. The integrator resistance has been made from a Pd/Au thin film. The circuit consists of a dc/SFQ converter, a Josephson transmission line, a comparator, a L/R integrator and an output stage. The correct operation of the modulator has been tested using dc measurements. The linearity of the modulator was studied by measuring the harmonic distortions of a 19.5 kHz sine wave input signal. From the recorded spectrum, a minimum resolution of at least 5 bit can be estimated. This accuracy was limited by the noise of the preamplifier. The correct operation of the current feedback loop was demonstrated by cutting the feedback inductance.

I. Introduction

The principle of delta-sigma modulation [1] is commonly used for high-resolution analog to digital converters (ADC) with a bandwidth up to audio frequencies. The use of the rapid single flux quantum logic (RSFQ) [2] would allow one to increase the frequency range up to the MHz regime without loosing accuracy in voltage resolution. Delta-sigma ADC's have been designed, fabricated and tested in Low-Temperature Superconductor (LTS) RSFQ technology [3, 4].

The block diagram of a first-order delta-sigma modulator is shown in Fig. 1. An input signal of the bandwidth f_0 is integrated and the result is sampled by a clocked comparator with the frequency f_s. The digitized signal is subtracted from the input signal in a feedback loop. This type of feedback causes the averaged output of the comparator to be exactly the input signal. The ratio between the sampling frequency and the Nyquist frequency of the signal is the oversampling ratio OSR = $f_s / (2f_0)$. The deviation of the quantized output of the comparator from the analog input signal can be described as noise and is named quantization noise. The simulated

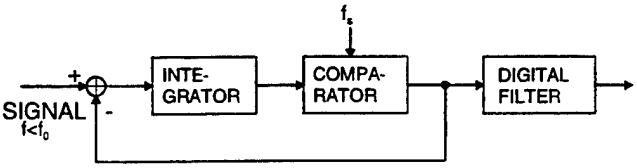

Fig. 1. Block diagram of a first-order delta-sigma modulator with a digital filter.

amplitude spectrum of the output of a first-order delta-sigma is shown in Fig. 2. The quantization noise is shifted to higher frequencies. It is obvious that the signal-to-noise ratio can be improved tremendously by filtering the frequencies above the signal bandwidth f_0. As calculated in [1], the resolution can be improved by 1.5 bit with doubling the OSR for a first order delta sigma modulator. Simple oversampling without feedback increases the resolution only by 0.5 bit.

II. Experimantal Results

A. Circuit Design

The implementation of a first-order delta-sigma modulator in LTS RSFQ technology was proposed in [3]. The equivalent scheme of the circuit is given in Fig. 3. The integrator is realized by the parallel connection of the resistor R1 and the inductance L21. The L/R time constant has to be considerably larger than the clock period. A signal current at the input causes a voltage drop across R1. This voltage is integrated as

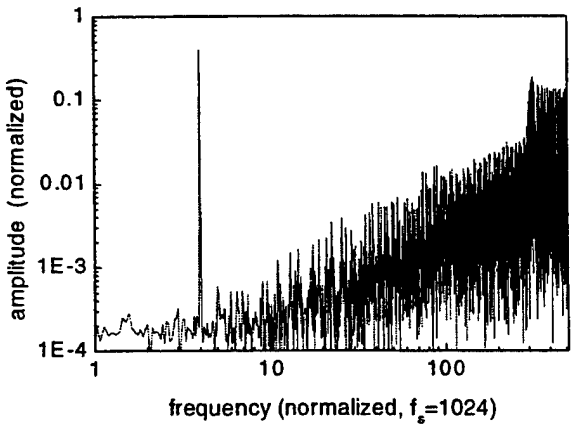

Fig. 2. Fourier transformation of the output signal of a first-order delta-sigma modulator for a sine wave input signal of the normalized frequency equal 4.

Manuscript received April 30, 1999.
* On leave from Superconductivity Lab., Department of Physics, Seoul National University, Seoul 151-742, Korea.
This work was supported in part by Deutsche Forschungsgemeinschaft, Nr. Si704/1-1.

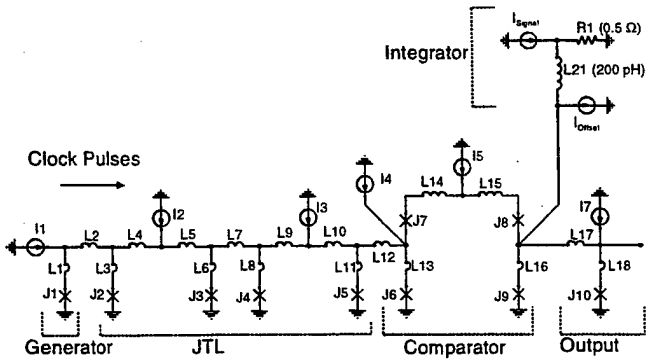

Fig. 3. Equivalent scheme of a first order delta sigma modulator in RSFQ technology.

a current by the inductance L21. The current signal is now evaluated by a comparator, which is formed by the two Josephson junctions (J8 and J9) in series. If a single flux quantum (SFQ) clock pulse from the clock generator J1 is applied at the upper junction either the upper or the lower junction is switching. If the current through L21 is larger than zero the lower junction switches, i. e. reproduces the SFQ pulse which appears at the output representing a logical '1'. At the same time a flux quantum Φ_0 is stored in the loop R1-L21-L16-J9. The current through L is now reduced by Φ_0/L21, realizing a feedback with quantum mechanical accuracy.

B. Preparation

A photo of the circuit is shown in Fig. 4. The different layers for the circuit were deposited on a $SrTiO_3$ bicrystal substrate with an asymmetric 24° grain boundary. The inductances of the circuit are reduced by a partial superconducting groundplane. The high value of inductance L21 for the integrator is realized by a large square loop without groundplane. The resistance R1 is made from a Pd/Au thin film which is contacted to the YBCO by larger gold pads.

C. Measurements

In order to generate the clock pulses, the Josephson junction J1 is biased above the critical current. An additional Josephson transmission line (JTL) is necessary to decouple the comparator from the generator J1.

The dc characteristics of the circuit were measured at a temperature of 34 K as shown in Fig. 5. The bias for the clock generator J1 was kept constant. Only the signal current was varied, while the voltages across J8 and J9 were measured. For low signal currents, J8 always switches with the clock pulses, while for high signals currents always J9 switches. This is indicated by the equal values for the average voltages. In an intermediate region both junctions can switch. There the circuit works as a modulator. The slope of the voltage across J8 is given by the resistance of R1.

In order to identify harmonic distortions which could limit the linearity of the modulator, a pure sine wave signal (19.5 kHz) was applied to the input of the circuit. No harmonics in a frequency span of 100 kHz could be observed as shown in Fig 6. The signal at frequencies between (30 – 36) kHz and (90 – 95) kHz are caused by disturbances of the computer and not by harmonics of the input signal. The accuracy of the measurement was limited by the amplifier noise. From the recorded spectrum, a resolution of 5 bit as a worst-case calculation can be estimated. The actual resolution is likely to be much higher. However, the exact estimation of the resolution and of the quantization noise would require a direct recording of the high frequency digital output. This feature

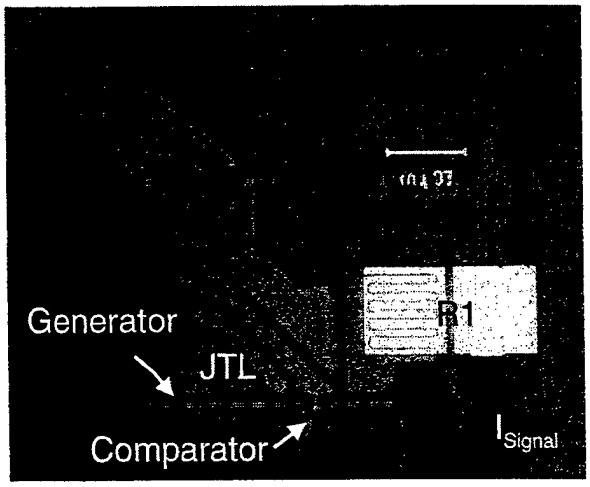

Fig. 4. Photo of the fabricated multilayer circuit. The bicrystal line is indicated by a dashed line.

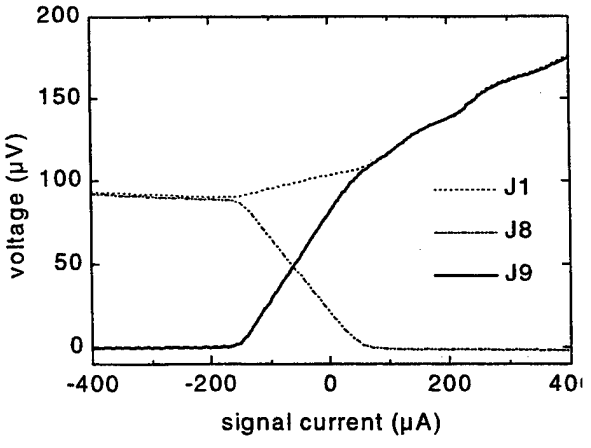

Fig. 5. dc characteristics of the investigated circuit at T=34K.

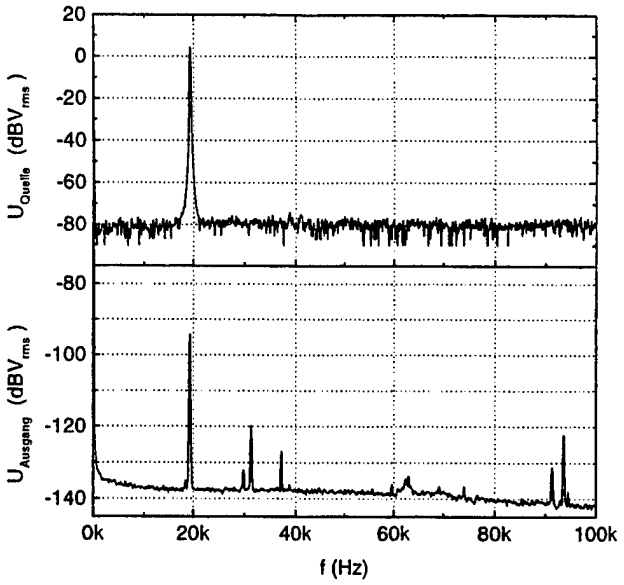

Fig. 6. Frequency spectrum of the sinusoidal input current (upper curve) and spectrum of the output voltage of the Sigma-delta modulator.

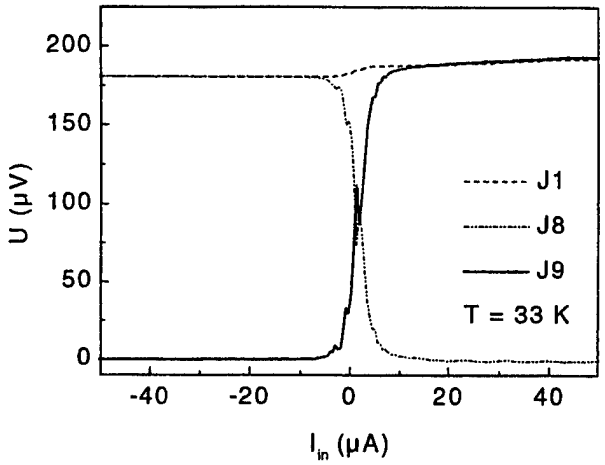

Fig. 7. Experimental dependence of the output voltage vs. signal current of the balanced comparator measured with the cutted feedback loop at a temperature of 33 K.

would raise the complexity of the circuit and was not included in our first experiments.

In order to test the effect of the feedback the inductance L21 has been cut off. Repeating the measurement analogous to the one shown in Fig. 5, we were able to characterize the operation of the comparator directly. Fig. 7 shows that the intermediate region has been reduced to about 12 μA and the slope was much steeper. This value is comparable or even better than previously measured values for a comparator circuit realized in a planar technology [5]. Therefore it can be concluded that the enlarged intermediate region of the delta-sigma modulator is controlled by the feedback loop and that the comparator itself works correctly.

IV. SUMMARY

The basic function of a delta-sigma modulator in a HTS multilayer technology has been verified experimentally. A complete characterization of the performance of the modulator would require a direct access to the digital output. Due to the low output voltages and the high operation frequency this was not possible with the present measurement setup.

From spectrum measurements up to 100 kHz, a worst case resolution of 5 bit could be estimated. The actual resolution is likely to be much higher.

For advanced measurements, the development of a high-speed interface from the HTS RSFQ circuit to semiconductor logic is necessary. To exploit the high-speed properties of the modulator for a high sampling frequency f_s, a serial-to-parallel converter is also necessary to reduce the clock speed of the digital filter. If the digital filter is driven at lower speed, this part can be implemented in CMOS technology, which is more suitable for VLSI at the current state of the art.

ACKNOWLEDGMENT

The authors would like to thanks V.K. Semenov for helpful discussions.

REFERENCES

[1] J. C. Candy and G. C. Temes, "Oversampling methods for A/D and D/A conversion", IEEE Press, (1992) 1

[2] K. K. Likharev and V. K. Semenov, „RSFQ logic/memory family: a new Josephson-junction technology for sub-Terahertz-clock-frequency digital systems", IEEE Trans. Appl. Supercond. **1** (1991) 3

[3] D. L. Miller, J. X. Przybysz, E. H. Naviasky and J. H. Kang, "Josephson Sigma-delta modulator for high dynamic range A/D conversion", IEEE Trans. Appl. Supercond. **3** (1993) 2732

[4] D.L. Miller, J.X. Przybysz, A.H. Worsham and E.J. Dean, Flux Quantum Sigma-delta Converters for rf Signals", IEEE Trans. Appl. Supercond., in press *[Applied Supercond. Conf., Palm Springs, Sept. 15 - Sept. 19, 1998, USA]*

[5] B. Oelze, B. Ruck, M. Roth, R. Dömel, M. Siegel, A.Yu. Kidiyarova-Shevchenko, T.V. Filippov, M.Yu. Kupriyanov, G. Hildebrandt, H. Töpfer, F.H. Uhlmann, W. Prusseit, „Rapid single flux quantum balanced comparator based on high-T_c bicrystal Josephson junctions", Appl. Phys. Lett. **68**, 2732 (1996)

Integrated Microwave Circuits for Digital-to-Analog Converters based on High-Temperature Superconductor Josephson Junction Arrays

Alexander M. Klushin*, Clemens Weber, Michael Siegel
Forschungszentrum Jülich GmbH, Institut für Schicht und Ionentechnik, Jülich, Germany

Solomon I. Borovitskii, Ruslan K. Starodubrovskii
Institute of Electronic Measurements "KVARZ", Nizhny Novgorod, Russia

Konstantin Yu. Platov, Mikhail Yu. Kupriyanov
Institute of Nuclear Physics Moscow State University, Moscow, Russia

Robert Semerad
Physikalische Fakultät der Technischen Universität München, Garching, Germany

Abstract—A digital-to-analog converter (DAC) based on series arrays of high-temperature (HTS) Josephson junctions can work properly when the microwave bias current distribution in large arrays is uniform. Unfortunately, the considerable microwave attenuation per overdamped junction with normal resistances $R_N \approx 0.1\ \Omega$ results in a strong total attenuation of the microwave signal in traditional layout. Also, the meander geometry of the array, necessary when using bicrystal junctions, disturbs the uniformity of the rf current, especially in the millimeter waveband. To overcome these drawbacks we coupled the meander array inductively to a parallel transmission line. The mechanism of microwave coupling in which both external and mutual frequency locking takes place was studied numerically. A circuit with a coplanar waveguide feed line was fabricated and successfully tested at an operating frequency of 30 GHz. A microstrip line with a small attenuation for pumping of HTS junction arrays at frequencies up to 120 GHz was demonstrated.

I. Introduction

Recently a new concept of a digital-to-analog converter (DAC) based on series arrays of high-temperature (HTS) Josephson junctions with nonhysteretic current-voltage characteristic (IVC) was suggested [1]. The DAC can work properly when the ac bias current distribution in large arrays is uniform. HTS Josephson junctions demonstrated characteristic voltage 200-300 μV at liquid nitrogen temperatures and are very attractive for using DAC at the millimeter wave band microwaves bias current. It can operate at the same microwave frequencies as conventional Josephson voltage standard systems based on niobium tunnel junction arrays. Unfortunately, the considerable microwave attenuation per overdamped junction results in a strong total attenuation of the microwave signal. Also currently available substrate materials, suitable for fabrication of HTS junction arrays, exhibit too large relative dielectric permittivity $\varepsilon > 10$ and dielectric losses $\tan\delta > 10^{-3}$, when applying at frequencies about 100 GHz. Additionally, the meander geometry of the array, necessary when using bicrystal junctions, disturbs the uniformity of the microwave current, especially in the millimeter waveband. To overcome these drawbacks we have suggested coupling the meander array inductively to a parallel transmission line [2]. In this paper we will discuss in detail the mechanism of microwave coupling in which both external and mutual frequency locking takes place. The microwave properties of a microstrip feed line on a thin substrate were studied.

Manuscript submitted on May 12, 1999.
This work was supported by German BMBF.
*on leave of the Institute of Electronic measurements KVARZ, Nizhny Novgorod, Russia.

II. Concept of the Integrated Microwave Circuit

The discussed microwave circuit consists of two basic parts: the Josephson junction array and the microwave transmission line (Fig. 1). In our experiments we have used arrays made by meandering Au-$YBa_2Cu_3O_7$ bilayer strips across the grain-boundary in yttria-stabilized-zirconia (YSZ) bicrystal substrates [2]. For dc current the junctions are connected in series. For ac-current the array consists of loops connected in parallel. Each loop includes two Josephson junctions, inductance L and two capacitors C (Fig. 1). This design supports both the mutual phases locking of the junctions in neighboring loops and the inductive coupling to the transmission line.

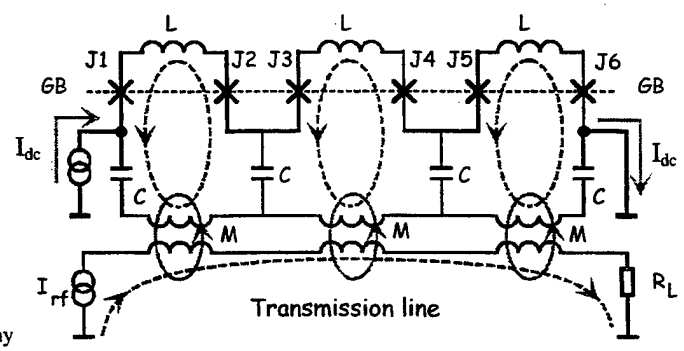

Fig. 1. Simplified scheme of the integrated microwave circuit.

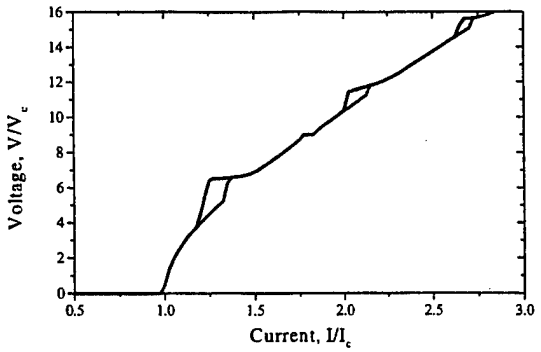

Fig. 2. Current-voltage characteristic for a six-junction array with $Z_L/Z_C = 2$ under influence of an external ac-current source at f=1.5 f_c, I_c = 1 mA, V_c = 100 μV.

A standard microstrip line (MSL), a coplanar waveguide (CPW) or a slot line can be used as feed lines. This provides feeding of microwave power to each two-junction loop and induces rf bias current in it. The resistive matching load R_L is important for obtaining an uniform rf distribution. It prevents reflections that would create a standing-wave pattern in the array. The decay of the driving rf amplitude along the loop line, which appears due to the dissipation of the microwave power in the stripline, can be easily compensated by an appropriate variation of mutual inductances M by geometrical changes in the design.

The concept developed allows us to choose the substrate materials for the junction array and the transmission line independently, and thus to design circuits with parameters close to the optimum values.

III. Design Simulation and Fabrication of the Microwave Circuits

Two different types of circuits have been designed and fabricated. They were optimized for drive frequencies in the interval from 20 GHz to 40 GHz and from 70 GHz to 120 GHz respectively. CPW and MSL were used as feed lines in low and high frequency designs respectively. Optimal parameters for the circuit design had been found previously by simulating device operation.

A. Simulations

It follows from Fig.1 that the character of the Josephson junction microwave connection depends on the relation between inductive Z_L and capacitive Z_C impedances at the working frequency. This is supposed to be a factor 1.5 - 2 larger than the characteristic frequency f_c of the individual junctions. At $Z_L << Z_C$ all the junctions in the structure are connected in series and their mutual synchronization is very difficult to achieve. However, at $Z_L >> Z_C$ the loops with the junctions are connected in parallel, which leads to the desired effects. The results of numerical simulations by means of the PSCAN program [4] confirm this simple analysis. The simulated circuit consisted of a six-junction array. A 5% spread of the critical currents and normal junction resistance was taken into account. In this case the stability of a given in-phase solution can be proved. It was shown that for $Z_L/Z_C = 0.2$ no phase locking would occur. The current voltage characteristics of three junctions in the array in the case $Z_L/Z_C = 2$ are shown in Fig.2. The resonance frequencies of the two feedback loops can be seen clearly. The first peculiarity near the frequency f=1.15 f_c, corresponds to the resonance frequency of the large feedback loop (all three inductances L and two capacitances C, see Fig. 1) and the second peculiarity corresponds to the frequency f = 2.0 f_c of the small feedback loop.

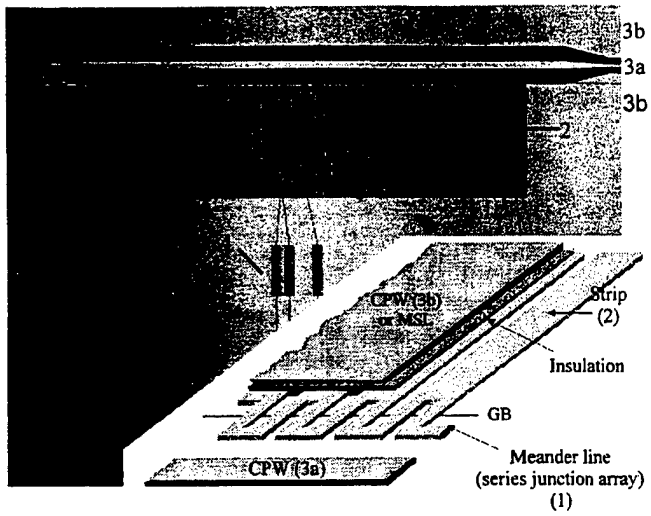

Fig. 3: Schematic layout of the new microwave circuit. The CPW is partly lifted to show the insulation layer and the microstrips below. Background: top view photograph.

Applying microwave irradiation at a frequency 1.5 f_c leads to the formation of the current step. We can further enlarge the current step height by increasing the amplitude of the external frequency source. The calculation confirms that at the same time the regions of mutual coherence are destroyed by competition from an external locking mechanism.

B. Circuit with CPW feed line

Fig. 3 shows the layout of the integrated microwave circuit with CPW feed line (3) [2]. The meander line (1) runs along the grain boundary, representing the series array of shunted bicrystal Josephson junctions, 256 in total. One side of each meander loop is connected to the strip line (2) with the area 0.025 mm^2. The 1 μm thick SiO_2 film was deposited on the top of the strips to provide the isolation between the superconductor and the outer conductor (3b) of the CPW (3). The central (3a) and outer (3b) conductors of CPW were fabricated from 0.7 μm thick Au films.

The values of inductive and capacitive impedances estimated from the layout geometry ($Z_L/Z_C \approx 1,5$) were close to the parameters, which had been used in the simulation. Under external irradiation in the frequency range of 30 GHz the first current step was demonstrated on 8 different segments of the array, containing 2, 2, 4, 8, 16, 32, 64, 128 junctions [2].

Nevertheless even at these relatively low rf-frequencies, the main contribution to the attenuation in the CPW is determined

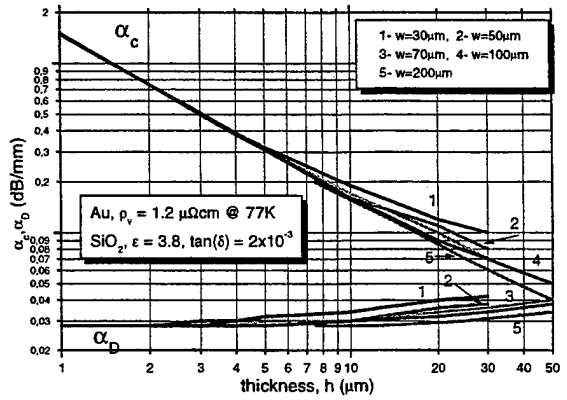

Fig. 4. Dependencies MSL conductor α_c and dielectric α_D losses on dielectric thickness.

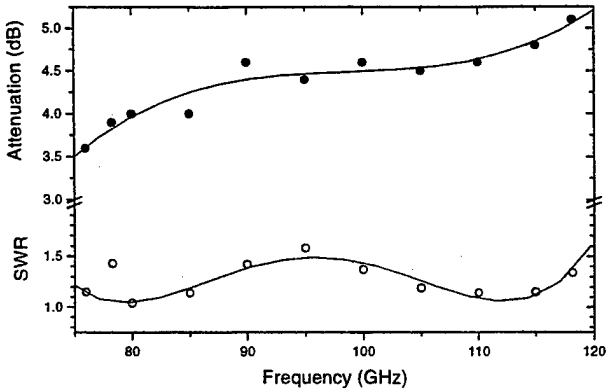

Fig. 5. Attenuation (filled circle) and SWR (unfilled circle) for 8 mm length MSL with two fineline taper antennas. Lines are drown to guide the eye.

by the dielectric loss tan δ in the YSZ substrates. From the measured attenuation at a temperature of 78 K [2], it can be shown that tan δ increase in the frequency range from 10 GHz to 40 GHz as $\tan\delta \approx 1.05\cdot10^{-3} f\,(\mathrm{GHz}) - 2\cdot10^{-2}$. Extrapolating this dependence to f = 100 GHz we get $\tan\delta \approx 8.5\cdot10^{-2}$, which leads to considerable attenuation ~ 3 dB/mm. It is for this reason that in our high frequency version of the circuit we focus on the MSL feed line.

C. MSL feed line

We supposed that this MSL should be fabricated on a flip chip and would consist of thin gold films deposited on both sides of a thin dielectric substrate. Fig. 4 shows the attenuation at a frequency of 75 GHz due to losses in the conductor (Au) and dielectric (SiO_2) as a function of dielectric thickness for varying microstrip width *w*. It is clearly seen that at a thickness larger than 20 μm the losses in the conductor are greatly suppressed, while the dielectric losses remain small.

For the experimental testing a special circuit, consisting of MSL with two finline taper antennas [5] connected by microstrip line with two bends, was fabricated. Mica with a dielectric permittivity of 6 - 6.5 and the thickness of 25 μm was used as a substrate. The width and length of the central strip was 0.13 mm and 8 mm respectively. The wave impedance of the MSL was equal to 16 Ω.

The measured values of the MSL attenuation and the standing wave ratio (SWR) are shown in Fig. 5 as a function of microwave frequency from 75 GHz to 120 GHz. The data demonstrated good matching between a WR-10 waveguide and the microstrip via the two finline taper antennas. The SWR does not exceed 1.6 throughout the whole frequency band. Full attenuation at the frequencies from 70 GHz to 90 GHz, typical for the classical voltage standard, does not exceed 4.5 dB. Taking into account that the main contribution to the attenuation comes from the two finline taper antennas, we can conclude that the real attenuation in the line is of the order of 0.1 dB/mm. This value is close to that of the design requirement.

IV. SUMMARY

The new method proposed here for coupling external microwave irradiation with the Josephson junction array offers a solution to one of the main problems of the DAC device. Namely, we can combine the advantage of larger junction characteristic frequencies (provided by their resistance ~0.1 Ω) and simultaneously get rid of the large rf losses, which occurred in the case of traditional layout solutions. Correspondence between measurements at a frequency of 30 GHz and the results of simulation confirm the validity of the developed approach. The fabricated flip chip MSL, with low attenuation in a wide frequency band, provides an opportunity for a further increase of the irradiation frequency of HTS Josephson junction arrays for DAC.

ACKNOWLEDGMENT

We thank A. I. Braginski and A. Lauer for support and stimulating discussions.

REFERENCES

[1] A. M. Klushin, S. I. Borovitskii, C. Weber, E. Sodtke, R. Semerad, W. Prusseit, V. D. Gelikonova, and H. Kohlstedt, "Programmable voltage standards based on HTS Josephson junction arrays", *Proc. Applied Superconductivity,* Proceedings of (EUCAS'97), H. Rogalla, D. H. A. Blank Eds., vol. 1, pp.587-590, 1997.

[2] A. M. Klushin, C. Weber, H. Kohlstedt, R. K. Starodubrovskii, A. Lauer, I. Wolff, and R. Semerad, "New Microwave Circuits for Programmable Voltage Standards using High-Temperature Josephson Junction Arrays", *IEEE Trans. Appl. Supercond.*, in press.

[4] S. V. Polonsky, V. K. Semenov, and P. N. Shevchenko, "PSCAN: personal superconductor circuit analyzer", *Supercond. Sci. Technol.*, vol. 4, pp. 667-670, 1991.

[5] F. Müller, R. Pöpel, J. Kohlmann, J. Niemeyer, W. Meyer, T. Weimann, L. Grimm, F.-W. Dünschede, P. Gutmann, "Optimized 1 V and 10 V Josephson series arrays", *IEEE Trans. Instrum. Meas*, vol. 46, pp.229-232, 1997.

Oral Session 3

Digital Circuits

Advanced Base-Station Based on Superconductive Devices and Software-Defined Radio Technology

Akira Fujimaki and Hisao Hayakawa
Department of Quantum Engineering, Nagoya University, Nagoya 464-8603 Japan

Masaaki Katayama and Akira Ogawa
Department of Information Electronics, Nagoya University, Nagoya 464-8603 Japan

Abstract—This paper outlines the idea of the Intelligent Super Base-Station (ISB) which is an advanced cellular base-station. The ISB is based on the software radio techniques. We present three different architectures with which the ISB is constructed. For each architecture, the superconducting devices are essential for the ISB system because of the high-speed nature and high sensitivity nature of superconducting analog-to-digital converters based on the single flux quantum logic. We also present the scenario of the development of the ISB using LTS and HTS junction technology.

I. Introduction

In the mobile communication systems represented by a cellular phone system, new radio standards and advanced services are proposed one after another, then come to the market in a short time. This situation will continue till the multimedia communication systems are established well. When a new service starts, a new function should be added in all of the base-stations existing over the whole area at the same time. Thus, a highly flexible base-station is required strongly to cope with such a rapid change in the mobile communication systems.

Furthermore, the base-stations including antennas, receivers, and transmitters have to be constructed newly, if a new standard is introduced. This construction is time-consuming and entails much cost.

Considering the situation mentioned above, we have studied on next-generation cellular base-stations from the point of view of the wireless communication systems and of the superconducting devices two years before. Then, we have proposed an advanced base-station referred to as "Intelligent Super Base-Station (ISB)" [1,2]. The ISB is based on the software radio [3,4] and smart antenna technology. The modulation and demodulation are performed in the digital domain, so that high flexibility can be realized. The ISB not only has the capability to reconfigure transceiver systems to both legacy services and new advanced services by downloading appropriate software, but also has the flexible wireless band width on demand. Furthermore, the ISB has the capability to unify current or future base-stations for the different standards.

Superconducting devices including analog components and high-speed digital circuits are essential for realizing the ISB system. In this article, we report the several architectures of the ISB and benefits in each architecture. We also describe the scenario of the development based on LTS and HTS junction technology.

Manuscript received May 1, 1999.

This work is supported in part by Project for Rising Researchers from Graduate School of Engineering, Nagoya University (FY1997) and by the Hibi Research Grant (FY1998).

II. Outline Of Intelligent Super Base-Station

Figure 1 shows the block diagram of the receiver in the goal of the ISB system. The transmitter is constructed with the almost reverse system.

The ISB system must cover wider band width up to 1.4GHz in Japan, because the frequency of the present or future mobile communication ranges from 800MHz of the cellular phones to 2.2GHz of IMT2000. However, it is not realistic to cover such a wide band in a single receiver from a point of view of the signal-to-noise ratio. In addition, a semiconductor linear low-noise amplifier (LNA) with 1.4GHz-band-width placed before an analog-to-digital converter (ADC) is very difficult to obtain. Thus, we split the band by means of a filter

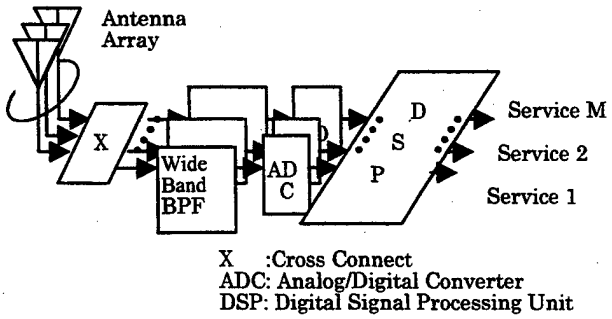

Fig. 1 Block Diagram of the Intelligent Super Base-Station (Receiver). Bandpass Filters and ADCs are made of superconductors.

bank into several subbands, though an increase in the hardware of the system is unavoidable. Of course, the subband is desired to have the bandwidth as wide as possible. The similar idea has been proposed by Arnott *et al.*[5] In each subband, the RF signal from the air is independently amplified, digitized, and down-converted to the base-band. The digital bit stream of each output of ADC is sent to a semiconductor digital signal processor where the channel selection and demodulation are performed digitally.

III. Architectures And Benefits

We discuss the three different architectures with which the receiver chain from RF to base-band is formed for each subband. The first architecture shown in Fig. 2 (a) is referred to as "the digital baseband radio". The second one indicated in Fig. 2 (b) and the third one in Fig. 2 (c) are also referred to as "the digital IF radio" and "the digital RF radio", respectively. All of the architectures are based on the software radio receiver technique and superconducting devices, thus have the high flexibility for the change of systems' features such as the modulation scheme, allocated frequency band.

The common benefits of using superconducting devices to all of the architectures are as follows. The biggest advantage will be brought by the employment of the superconductor ADC. As is well-known, the ADCs based on the oversampling technique and single-flux-quantum (SFQ) logic gates have high potential for dynamic range (80-100dB) and input band width (50-100MHz) [6-9] compared to those of semiconductor ADCs. According to Woerner [10], the ADC used in the ISB system should have the dynamic range of about 100dB corresponding to the effective number of bits of 16 in order to obtain the output carrier-to-noise ratio (CNR) of 10dB. This calculation has been done under the input CNR of 10dB and carrier-to-interference ratio of -80dB. On the other hand, the input band width of at least several tens of MHz is needed, which corresponds to the typical band width of a given standard at present. Taking a slow developing speed of 1.5-bit/8-years for any given semiconductor ADC into account [11], the SFQ-based ADCs are suitable for the ISB system. Recently, a similar idea of applying the SFQ-based ADCs to the front-end of a software radio receiver has been proposed independently by the group of SUNY at Stony Brook and Ericsson [12].

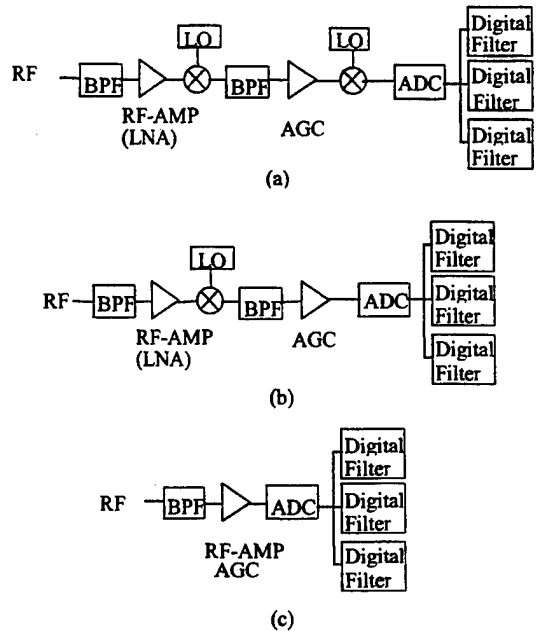

Fig. 2 Architectures of the receiver chain from RF to the baseband for each subband. (a) Digital baseband radio, (b) Digital IF radio, and (c) Digital RF radio.

Another advantage of SFQ-based ADCs is high sensitivity. The minimum power of input signals required to drive SFQ circuits is less than 1μW, while that of high-speed semiconductor ADCs is around 1mW. The nature of high sensitivity brings the reduction in the gain of LNA by 30dB. Usually, the product of the gain and bandwidth is considered constant for a given amplifier. Thus, the reduction in the gain enhances the band width covered by the LNA, widening the frequency band for each subband.

In addition to the SFQ-based ADCs, analog bandpass filters made of superconducting films are required for the ISB system [5]. The low loss nature enables us to make the thin-film filters with higher selectivity and lower insertion loss, which are required to reduce the width of guard bands between adjacent subbands and to eliminate aliases generating in the AD conversion. For the reasons described above, we can conclude that the superconducting technology including improved noise figure of a given LNA operating at low temperatures is essential for the ISB.

There are several benefits peculiar to each architecture shown in Fig. 2 other than the above. In the digital baseband radio, the front-end from antenna to down-converter is composed of all analog devices. The advantages of this architecture come from the traditional system, that is, the availability of the proven system architectures, low-cost RF and IF analog component, and readily available computer design tools. On the other hand, the disadvantages are imperfections of the analog devices such as nonlinearity, temperature-sensitive nature, frequency-dependent noise, etc. In particular, the poor phase performance often causes a fatal increase in the bit error rate (BER) of the system.

Such disadvantages are alleviated in the digital IF radio and almost lost in the digital RF radio. BER will be reduced due to the exactly linear phase performance of digital filters especially in the digital RF radio. In addition, the volume of the hardware is highly reduced. Thus, the digital RF architecture should be applied to the final goal of the ISB system.

The bandpass sampling technique is usually adopted to

convert the frequency band down to the baseband. However, there is no guide to design a bandpass sigma-delta modulator, which is the front-end of the most typical oversampling ADC. In contrast, lowpass sigma-delta modulators have been studied a lot so far. Taking this situation into account, the most realistic or easily achievable architecture is thought to be the digital IF radio with a lowpass sigma-delta modulator. The lowpass modulator can cover the IF band in stead of a bandpass modulator if the frequency of the IF band is set close to DC. Exact band selection is performed in the digital filter.

IV. Scenario Of Development

We have already tackled the development of the superconducting component of the ISB. We have examined the lowpass and bandpass sigma-delta modulators by means of the numerical calculations with JSIM and FFT program. The present subject is how to realize a second- or higher order modulator to enhance the dynamic range together with broader band width.

The digital decimation filters are needed for the oversampling ADCs. We have started to develop these filters and fabricated their elements such as a shift register. The chip was produced in the NEC standard process [13,14] based on the advanced Nb/AlOx/Nb Josephson integration technology through Special Coordination Funds for promoting Science and Technology Agency of the Japanese Government. The shift register operates correctly up to 30GHz [15], and a shift register with taps has also been demonstrated at a low frequency. Now, we are designing a digital lowpass filter. We plan to develop ADCs with the lowpass modulators in a couple of years as the first step, then move to the bandpass modulators.

As described before, the semiconductor ADCs cannot compete in sensitivity with the superconductor ADCs. Thus, a superconducting sigma-delta modulator alone is thought to be meaningful even if the advantages are lost in the band width or dynamic range. In this case, the decimation is performed by semiconductor DSPs. When we take this architecture, the HTS junction technology will be available because the modulator including an interface circuit can be constructed with a few hundreds of junctions. This is our target of the development of HTS junction technology.

V. Conclusion

We outlined an idea of the ISB, which is based on the software radio techniques. The superconducting devices including analog bandpass filters are essential for the ISB system. In particular, the SFQ-based ADCs are potentially superior to the semiconductor ADCs in dynamic range, band width, sensitivity, which bring us the benefits unachivable with semiconductor technology. We set ADCs as a target of LTS and HTS LSI application.

References

[1] A. Fujimaki, M. Katayama, and H. Akaike, Report of Project for Rising Reserchers, "Application of superconductive technologies to advanced wireless communication systems," *edited by Graduate School of Engineering, NagoyaUniv.* August 1998. (in Japanese)

[2] A. Fujimaki, and M. Katayama, "Toward the Intelligent Super Base-Station with software defined radio techniques and superconductive devices," *Technical report of IEICE*, CAS-98, pp. 85-92, March 1999. (in Japanese)

[3] J. Mitola, "The software radio architecture," *IEEE Commun. Mag.*, vol.33, pp. 26-38, May 1995.

[4] J. Mitola, "Technical challenges in the globalization of software radio," *IEEE Commun. Mag.*, pp. 84-89, Feb. 1999.

[5] R. Arnott, S. Ponnekanti, C. Tailor, and H. Chaloupka, "Advanced Base Station Technology," *IEEE Commun Mag.*, vol. 36, pp. 96-102, Feb. 1998.

[6] V. K. Semenov, Y. A. Polyakov, and T. A. Filippov, "Analog-to-digital converters with on-chip digital low-pass filters," ECB-03, *1998 Applied Superconductivity Conf.*, Palm Desert, CA., Sept. 1998.

[7] S. V. Rylov, D. K. Brock, D. V. Gaidarenko, A. F. Kirichenko, J. M. Vogt, and V. K. Semenov, "High resolution ADC using phase modulation-demodulation architecture," ECB-01, *1998 Applied Superconductivity Conf.*, Palm Desert, CA., Sept. 1998.

[8] A. H. Worsham, D. L. Miller, P. D. Dresselhaus, and J. X. Przybysz, "Superconducting modulators for high dynamic range delta-sigma analog-to-digital converters," EDE-01, *1998 Applied Superconductivity Conf.*, Palm Desert, CA., Sept. 1998.

[9] D. L. Miller, J. X. Przybysz, and A. H. Worsham, "Flux quantum sigma-delta analog-to-digital converters for rf signals," EOD-01, *1998 Applied Superconductivity Conf.*, Palm Desert, CA., Sept. 1998.

[10] B. D. Woerner, "Analog-to-digital interface in multimode radio receivers," *PIMRC'98*, Boston, MA., Sept. 1998.

[11] R. H. Walden, "Performance trends for analog-to-digital converters," *IEEE Commun. Mag.*, pp. 96-101, Feb. 1999.

[12] E. B. Wikborg, V. K. Semenov, and K. K. Likharev, "RSFQ Front-end for a software radio receiver," EKB-02, *1998 Applied Superconductivity Conf.*, Palm Desert, CA., Sept. 1998.

[13] H. Numata, S. Nagasawa, and S. Tahara, "Fabrication process for submicron Josephson junctions," *Extended Abstracts of 1993 Int'l Superconductive Electronics Conf.*, pp. 280-281, Boulder, CO., Sept. 1993.

[14] S. Nagasawa, Y Hashimoto, H. Numata, and S. Tahara, "A 380ps, 9.5mW Josephson 4-Kbit RAM operated at a high bit yield," *IEEE Trans. Appl. Supercond.*, vol. 5, pp. 2447-2452, June 1995.

[15] F. Furuta, Y. Suzuki, H. Hasegawa, E. Oya, A. Fujimaki, and H. Hayakawa, "High speed operation of RSFQ circuits up to 30GHz," *Extended Abstracts of 1999 Int'l Superconductive Electronics Conf.*, in this volume, Berkeley, CA., June 1999.

RSFQ Subsystem for Petaflops-Scale Computing: "COOL-0"

Paul Bunyk*, Mikhail Dorojevets+, Konstantin Likharev*, Peter Litskevitch*,
Larry Wittie†, and Dmitry Y. Zinoviev*
*Physics and Astronomy Department, Departments of †Computer Science and +Electrical and Computer Engineering
SUNY, Stony Brook, NY 11794, USA

***Abstract*— The goal of the Hybrid Technology MultiThreading (HTMT) project is to develop a multithreaded computer architecture that would utilize novel electronic and optoelectronic technologies to achieve petaflops-scale performance. The RSFQ subsystem consists of processors (SPELLs), cryoelectronic memory, and switching interprocessor network (CNET). Our estimations show that a future 0.8 μm niobium-trilayer RSFQ technology should make it possible to implement SPELLs operating with average clock frequency of 100 GHz. The total bandwidth of CNET would be 0.7 PB/sec, with end-to-end latency of only 17 ns. The physical size of the subsystem (excluding cryogenic equipment) would be only 0.5 m^3, and power dissipated in helium would be as low as 250 W. We have successfully fabricated and tested several key functional blocks of the subsystem, including the critical path of an integer adder.**

I. Introduction

The development of digital superconductor technology is dominated presently by RSFQ logic [1] because of its two unique features: very high speed and extremely low power consumption. Though the necessity of deep refrigeration of RSFQ circuits does not allow this technology to compete with CMOS for most digital applications, in high-performance computer systems, the refrigeration costs would be a negligible component of the total cost.

To achieve a peak performance of 1 petaflops using CMOS technology which will be available in the next decade, one would need 50 to 100 thousand chips, with a total power consumption of ~10 MW. The management of power of such proportions would take a sizeable building, and even this discouraging estimate stems from a very optimistic assumption of 70 nm fabrication technology. Moreover, the significant (300 ns-scale) latency of interprocessor communication in a system of such a physical size makes the system prone to stalling for communication-intensive programs.

Manuscript received May 1, 1999.
The HTMT project and the work described in this paper are supported by DARPA, NSA, and NASA, and in part by NSF grant No. ECS-9700313.

The HTMT concept [2] assumes a hierarchical organization of the petaflops computing system (Fig. 1) with multiple levels of distributed memory: holographic data storage (HRAM), semiconductor SRAM and DRAM, and cryomemory (CRAM), as well as three types of processors: SRAM- and DRAM-based processors-in-memory (PIMs), and RSFQ superconductor processing elements (SPELLs) operating at liquid helium temperature.

A powerful method of hiding memory access latency (which can be as high as 1000 processor cycles) is multithreading. This technique reduces the processor idle time by overlapping the execution of separate tasks called threads. Multithreading and context prefetching have been accepted as the key techniques of latency tolerance in the HTMT program execution model [2] and COOL-I instruction set architecture [3]. PIMs find ready threads, allocate the context of a ready thread in CRAM, and initiate its execution in a SPELL. When a SPELL finishes the execution of a thread, an SRAM PIM fetches the results from CRAM into SRAM. All of these multilevel activities can be performed in parallel.

II. RSFQ Technology Assumptions

Niobium-trilayer RSFQ technology with minimum Josephson junction size of 0.8 μm and critical current density of 20 kA/cm^2 has been accepted as the target technology for our first design (called "COOL-0" [5]). So far the most complex RSFQ integrated circuits have been built using a commercially available 3.5 μm fabrication technology, allowing a maximum clock frequency of about 30 GHz. The scaling shows that VLSI circuits implemented with 0.8 μm RSFQ technology should have an on-chip clock rate from 60 to 120 GHz, with power dissipation of 100 nW per logic gate.

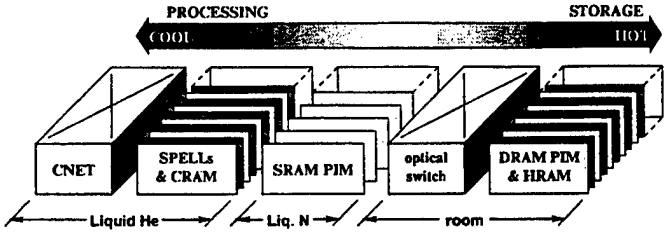

Fig. 1. HTMT computer concept.

Not only the 0.8 μm technology is sufficient to reach petaflops performance in a system of a reasonable size, but the patterning equipment for such design rules is presently very inexpensive. As a result, a pilot line for the 0.8 μm fabrication technology may be available on a very short time scale (3 to 4 years from now), with an estimated investment of about $30M.

III. SPELL Organization

In order to organize the instruction streams so that all functional units can operate in parallel, each SPELL has 16 multi-stream units (MSU). Each MSU executes all integer, control, and floating-point compare operations within one thread, using a 64-bit integer functional unit and eight 32-bit branch units sharing a 32-bit address adder, all operating with ~15 ps cycle. Each SPELL has 5 floating-point units (FPUs). The MSUs can communicate with the floating-point functional units and CRAM via an intra-processor network (PNET) at a speed of 30 Gbps per wire. This speed is limited solely by the inductance of chip-to-MCM pins. The processor-memory interface works at the same speed.

The SPELL instruction pipeline consists of the MSU data path, PNET, CRAM and FPUs. Except for the Memory Access/FP Execute macrostage, only instructions belonging to different strands can be simultaneously processed within each macrostage.

Each MSU includes a unified set of 64 general-purpose registers shared by all strands, and a number of miscellaneous registers. Hardware reserved exclusively for each strand includes a program counter, an instruction register with strand control logic, 4 condition registers, and a reservation station.

All types of dependencies among instructions are enforced by distributed scoreboard-like logic that sets/clears a Wait bit associated with each register. When an instruction is issued, its destination register is marked as "not ready" by setting its Wait bit to 1. When the result is written into the register, its Wait bit is cleared.

A. Integer Adder Critical Path

We have designed and experimentally verified at low and high frequency the critical path of our 64-bit integer adder [4] which is an important and representative building block of the HTMT computer.

The critical path consists of a chain of uniform stages and a feedback microstip line (Fig. 2). Each stage has an inverter INV, two splitters S and two mergers M in the data path and a splitter in the clock path. Stages are connected using Josephson transmission lines. Since this is just a one-bit critical path of a complete adder, one input/output of each merger/splitter is not used.

A 64-bit integer adder needs 6 stages to compute all carry propagate and generate signals and 4 more to compute the initial propagate/generate bits and the final sum, the total of 10 stages.

All inverters are clocked using counterflow clock generated by an overbiased Josephson junction. We can inject an SFQ pulse into the first stage using a dc/SFQ converter, measure the average voltage in the return path V_{out}, and remove the pulse from the ring by turning off dc current feeding the microstrip line receiver.

If we inject an SFQ pulse into the first inverter, the pulse starts propagating along the chain and eventually apperas in the output, returns to the first inverter via the feedback path and keeps circulating until an error occures. In this state we observe non-zero voltage V_{out} which is proportional to the pulse circulation frequency. We can inject more data pulses to see respective voltage steps.

The inverter chain has been fabricated using 3.5μm niobium-trilayer technology available from HYPRES, Inc. The dc bias margins of th circuit were ±26%. The clock frequency in the HF experiment was $\sim 10\,GHz$. Experimental estimations of the bit error rate (BER) are shown in Fig. 2. The BER can be as low as 10^{-19} in the best operating point. Theoretically, the circuit should also work at double frequency (with more than one SFQ pulse propagating within one stage) but no BER measurements for this case were performed yet.

IV. CNET

The CNET is a self-routing, multi-stage packet switching cryo-network enabling any SPELL to access local memory buffers belonging to other SPELLs. The most beneficial designs of the CNET that provide the best performance are self-routing networks using minimal 2×2 crosspoint switches [6]: banyan networks and meshes. The major difference between these two classes of networks is that in a banyan network there exists a unique path from any input to any output, while in a mesh multiple paths connect each input to each output. To ensure network liveness and avoid packet loss due to congestion, CNET features limited internal FIFO buffering and a flow control mechanism based on backpressure.

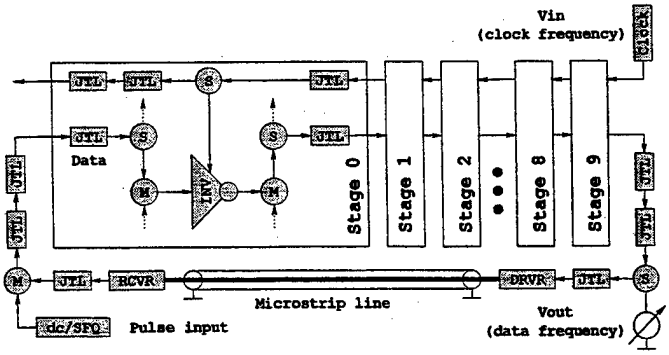

Fig. 2. 64-bit integer adder critical path: high-frequency bit error rate (BER) experiment

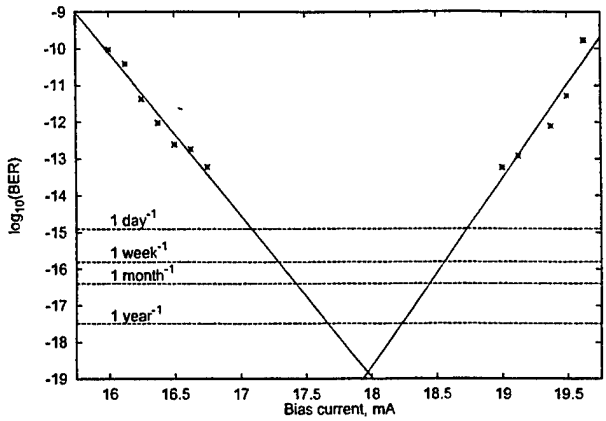

Fig. 3. BER in the critical path

Remarkably, the designs of both the 12×2048 banyan network and the 6×4^6 mesh considered for the implementation of CNET have the same number of switching nodes (24,576), despite of their very different structure. The banyan system has smaller one-way trip latencies than the mesh (17.2 ns vs 22.1 ns). However, it uses more FIFO buffers per node (76 vs 61). Both networks can deliver about 0.7 PB/s in random accesses. The implementation of CNET would require from 1.9 to 2.3 billions of Josephson junctions.

The similarity of major characteristics of the considered networks makes it difficult to choose one good solution out of two. The choice must be based on secondary parameters (e.g., delay variation) which have to be studied in more detail.

V. Physical Structure and Parameters

Each processor can be implemented as a set of seven 2 cm×2 cm chips, including two double-cluster MSU chips, one chip housing 6 FPUs, processor-memory interface, and PNET, and four CRAM chips. The chips should be flip-chip mounted on a 20 cm×20 cm cryo multi-chip module (CMCM), 8 processing modules per CMCM. Physically, CMCM is just a silicon wafer fabricated using the same niobium-based process, but without Josephson junctions. The absence of Josephson junctions on CMCM gives the hope that they may be fabricated from 30-cm silicon wafers with appreciable yield. All 512 CMCMs of a petaflops computer will be mounted vertically around an octagonal prism [7]. The interior of this cylinder will be occupied by 160 printed circuit boards with 5-layer wiring.

The RSFQ circuits on each CMCM would dissipate ~0.5 W power. Even with the current conservative assumption of copper wires, the overall power load at 4 K is about 1 kW. For this power level, the efficiency of existing helium recondensers results in room-temperature power of approximately 0.3 MW. A side view of the hypothetical supercomputer is shown in Fig. 4.

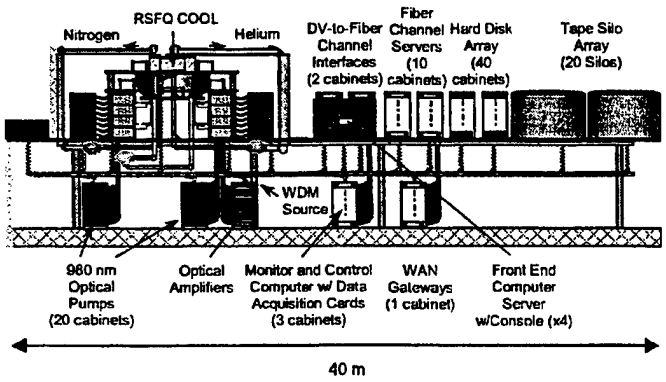

Fig. 4. HTMT system side view (courtesy of L. Bergman)

VI. Conclusions

Our preliminary design (COOL-0) has revealed no obvious stumbling blocks on the way toward a compact RSFQ subsystem with very low power consumption, capable of sustaining near-petaflops performance. Our next plan is to develop a much more detailed subsystem design (COOL-I) based on deep-submicron Josephson junction technology and better matched with COOL-I instruction set architecture [3].

Acknowledgment

Useful discussions with Lynn Abelson, Guang Gao, Burton Smith, Thomas Sterling, and other members of the HTMT collaboration are gratefully acknowledged. High-speed adder experiment would not be possible without valuable help by Yuri Polyakov.

References

[1] K. Likharev and V. Semenov, "RSFQ logic/memory family: a new Josephson junction technology for sub-teraherz clock frequency digital systems," *IEEE Trans. on Appl. Supercond.*, vol. 1, pp. 3–28, Mar. 1991.

[2] G. Gao, K. K. Likharev, P. C. Messina, and T. L. Sterling, "Hybrid technology multithreaded architecture," in *Proc. Frontiers'96*, (Annapolis, MD), pp. 98–105, Feb. 1996.

[3] M. Dorojevets, "The COOL-I ISA handbook: Version 1.00," Technical Report 11, SUNY at Stony Brook, RSFQ System Group, Jan. 1999.

[4] P. Bunyk and P. Litskevitch, "Case study in RSFQ design: Fast pipelined 32-bit adder," *IEEE Trans. on Appl. Supercond.*, June 1999. In press.

[5] M. Dorojevets, P. Bunyk, D. Zinoviev, and K. Likharev, ""COOL-0": Design of an RSFQ subsystem for petaflops computing," *IEEE Trans. on Appl. Supercond.*, June 1999. In press.

[6] D. Zinoviev, "Design of an RSFQ banyan switching node for petaflops computing." Presented at ISEC'99, Berkeley, CA, June 1999.

[7] L. Abelson, Q. Herr, G. Kerber, M. Leung, and T. Tighe, "Manufacturability of superconductor electronics for a petaflops-scale computer," *IEEE Trans. on Appl. Supercond.*, June 1999. In press.

Component Development for a 16 Gb/s Digital Superconducting Ring Data Bus

M. Jeffery, N. Yoshikawa*, J. Koshiyama*, L. Zheng, and T. Van Duzer
Department of Electrical Engineering and Computer Sciences, University of California, Berkeley CA 94720-1770,
*Division of Electrical and Computer Engineering, Yokohama National University, Tokiwadai 156, Hodogaya-ku, Yokohama 240, Japan

Abstract --**We are working on a fundamental study of the issues involved in constructing an ultra-high-speed superconducting Rapid Single Flux Quantum (RSFQ) ring data bus, and toward demonstrating the key circuit components. The bus consists of a data-driven self-timed RSFQ data ring. Data packets are input to the ring and passed along the bus to decoder circuits, which interpret the address and remove the message from the bus if appropriate. The ring is therefore analogous to a railroad with data trains, or packets, switched between processors. We have simulated and designed the basic ring circuit, with simple input and output decoder circuits. We have also designed, fabricated, and tested MUX and DEMUX circuits which are the key circuit components for data input and output from the ultra-high speed data ring.**

I. Introduction

We are working to develop advanced architectures and key circuit components using digital superconducting technologies. These circuits are candidates for ultra-high-speed applications of the future. Specifically, we are developing an ultra-high-speed ring data bus based upon superconducting Rapid Single Flux Quantum (RSFQ) logic [1]. One application of the RSFQ data ring is for computer architectures of the future that will require data transfer rates between processors greater than a terrabit per second (1 Tb/s = 10^{12} b/s) [2].

RSFQ circuits are superconducting, and the logical information is encoded on picosecond voltage pulses with quantized area. The advantage of the technology is that the power dissipation is approximately 10,000 less than room temperature electronics, and the maximum speed can be as high as several hundered gigahertz. However, there are several fundamental issues that should be resolved in order to realize ultra-high speed RSFQ circuits. The main issue is clock distribution and timing of the ultra-high speed circuits. We have proposed a method to overcome the timing problem, called data-driven self-timing [3]. In this scheme the circuit is broken into modules and the clock for each module is obtained from dual rail inputs of data and inverse data.

Figure 1a shows a schematic diagram of the prototype ring data bus system. The circuit consists of an RSFQ ring fabricated onto four chips that are re-flow solder bump bonded to a superconducting multi-chip-module (MCM). Data packets are input and output from the ring by bus decoder and MUX/DEMUX circuits. With a 2-bit wide 32 Gb/s data ring a 64 Gb/s data transfer rate can be obtained.

Manuscript received April 30, 1999.
This work was supported in part by TRW Space and Electronics and a matching California MICRO grant 97-189 and 98-159

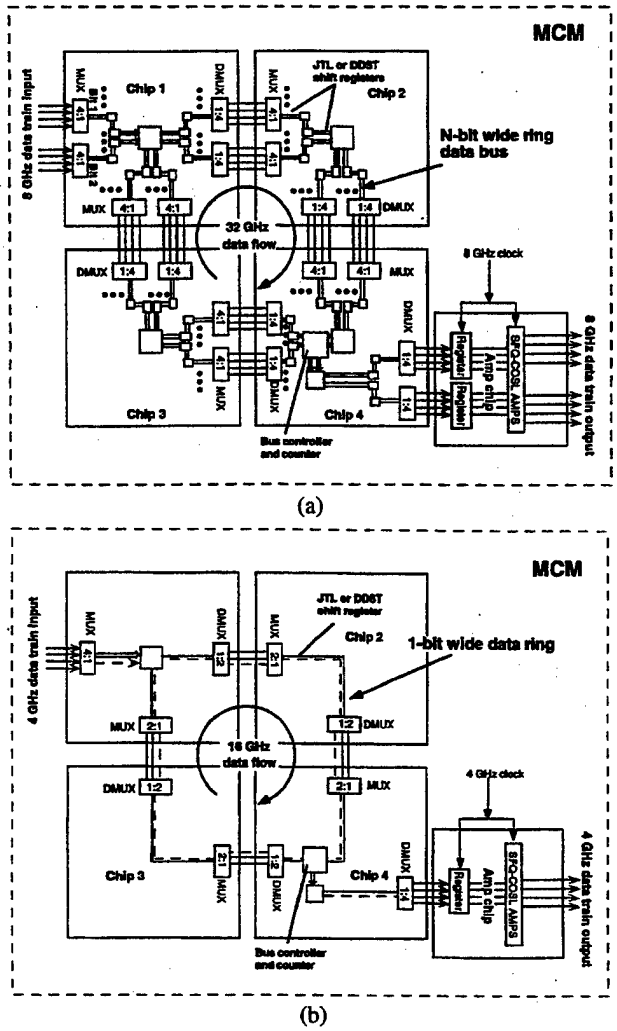

FIG. 1 (a) The 2-bit wide 64 Gb/s data-bus architecture with a single input and output decoder. (b) A simplified 1-bit wide 16 Gb/s architecture. The key components are the data ring, input and output decoders, MUX and DEMUX, and off-chip amplifier circuits.

Ultra-high-speed transfer of picosecond voltage pulses between chips on the MCM is difficult due to the inductance of the solder bumps. The RSFQ data pulse is significantly attenuated when it is transferred between chips. Therefore, the RSFQ data must be reduced to lower speed for transfer between chips on an MCM. For the circuit in Fig. 1a, the reduction of speed at the chip-to-MCM interface is accomplished with 1:4 DEMUX circuit. The high data rate is restored at the MCM-to-chip interface with a 4:1 MUX.

In the present work we are focusing on component development for the simplified 16 Gb/s system in Fig. 1b. At 16 Gb/s the data transfer rate can be 8 Gb/s between chips on the MCM and hence 2-bit MUX and DEMUX circuits are

required. We have focused our effort on developing the basic ring architecture in Fig. 1b at 16 Gb/s, MUX and DEMUX circuits, and output digital amplifier circuits. These components are necessary building blocks for a future ring demonstration.

II. Simulations and Optimization

Effort has focused on designing the MUX/DEMUX circuits used at the interface of the data ring [4,5], see Fig. 1. We use a modular architecture so that large DEMUX circuits can be constructed from smaller 2-bit components. As an example, a 1:8 DEMUX is constructed from seven 1:2 DEMUX sub-circuits [4]. Fig. 2 is a simulation of the 8:1 MUX RSFQ circuit with a 20 Gb/s output data stream.

Related research at UC Berkeley has been applied to the design and demonstration of output digital amplifier circuits which will act as an interface with room temperature electronics [6]. Amplifiers have been designed, simulated, and fabricated using the high critical current fabrication process developed in our laboratory [7]. These amplifiers have been successfully tested at 10 Gb/s [6].

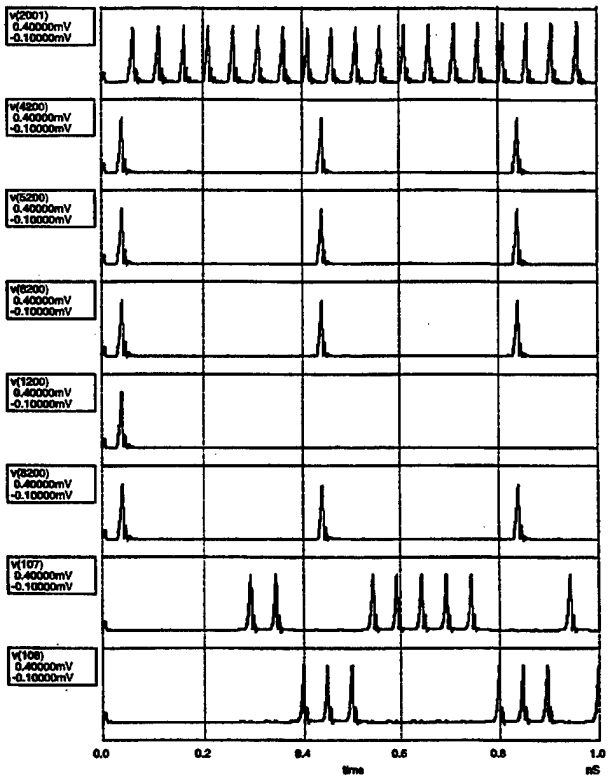

FIG. 2. 20 GHz SPICE simulation of the 8:1 MUX circuit. A picosecond data pulses in a clock period corresponds to a logical "1", and no pulse corresponds to a logical zero. The top trace is the internal clock, and the traces 2-6 are the inputs at 2.5 Gb/s. The last 2 traces are the multiplexed output 110001111100010 at 20 Gb/s, and its inverse. These output data are generated by combining the traces 2-6 in Fig. 2 sequentially at the 8-bit MUX inputs with bits 3-5 set to zero.

We have also designed and simulated simplified ring architectures and bus decoder circuits [1]. Figure 3 shows a SPICE simulation of a basic data ring assuming that the ring is fabricated on a single chip. The simulation demonstrates RSFQ data flow at 16 Gb/s. In the simulation, the period of data transfer around the ring is 1 ns. We have also designed and simulated bus decoder circuits.

For all of these circuits, we have focused our effort on optimizing the design so that the circuits can operate at ultra-high-speed. Specifically, we have implemented Monte Carlo simulations to calculate theoretical yield including measured fabrication process spreads. We have also calculated the effect of timing delays that result from parameter spreads. For all circuits, the theoretical yield and the dc bias margins have been maximized for high-speed operation by many computer simulations.

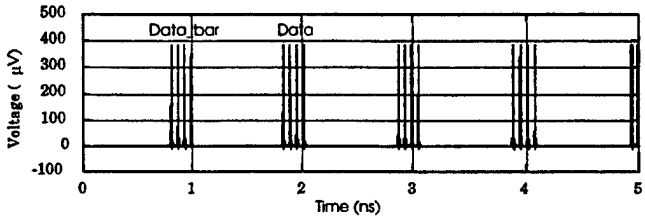

FIG. 3. SPICE simulation of a 4-bit RSFQ packet propagating around the data ring at 16 Gb/s. The period of rotation of the data packet around the ring is 1 ns.

III. Circuit Layouts

We have laid-out and fabricated the basic ring circuit and the MUX/DEMUX circuits. Figure 4a shows the 1:2 DEMUX circuit, and Fig. 4b shows the basic data ring fabricated on a single chip with the bus decoder circuit. We fabricated the circuits using the HYPRES commercial fabrication process, and the MUX/DEMUX were also fabricated using the process developed in our laboratory. The dimensions of the DEMUX circuit in Fig. 4a is 1.6 mm x 0.7 mm, and the complete data railroad in Fig. 4b is fabricated on a single 5 mm x 5 mm chip.

In Fig. 4a the DEMUX is laid-out for on-chip high-speed testing. In this scheme, we use shift registers at the input and outputs of the circuit under test. The shift registers are loaded with data at low-speed, and then a high-speed on-chip RSFQ clock generator is used to push the data through the circuit under test. Since the 1:2 DEMUX is data-driven self-timed, the data generate their own high-speed clock within the circuit. Finally, the output data are collected in shift registers and read out at low-speed to check the circuit functionality.

The data railroad consists of a 100-element dual rail JTL ring with 4-bit data and data inverse generators in the top right corner in Fig. 4b. Data input to the ring circulate in the counter-clockwise direction. A 4-bit shift register on the left side of the ring is intended to remove skew between the data and their inverse. The output decoder circuit is shown in the center of Fig. 4b.

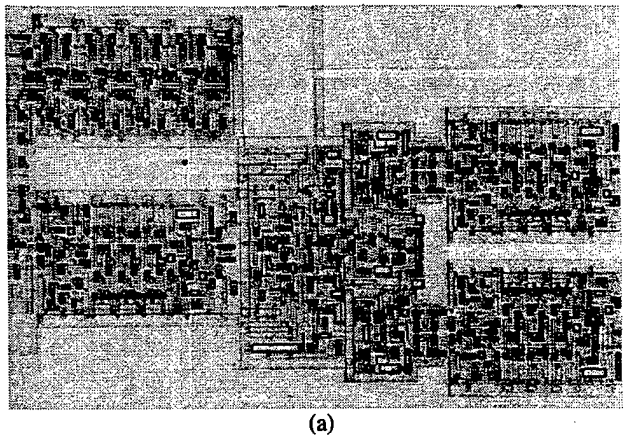

(a)

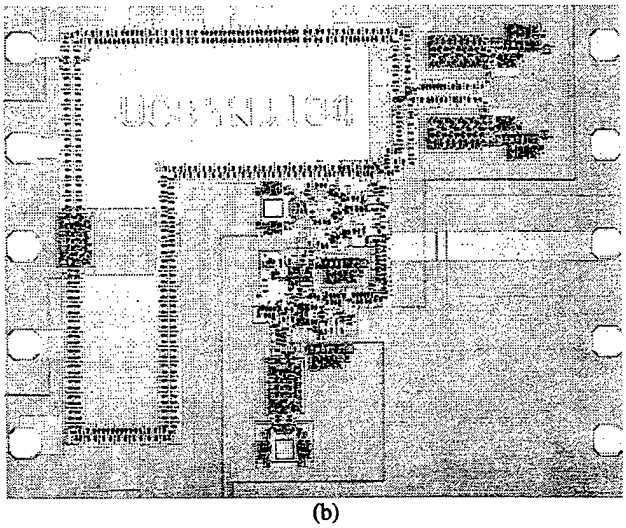

(b)

FIG. 4. (a) Micrographs of DSST 2-bit DEMUX with on chip testing and (b) Fabricated 16 Gb/s data ring with an output decoder circuit.

IV. Test Results

Figure 5 shows experimental test data of the 1:2 DEMUX Fig. 4a operating at ultra-high speed. The experimental DEMUX data in Fig. 5 is for an internal 18.5 Gb/s clock and low speed shift register inputs and outputs shown in Fig. 4a. At low speed, the circuit was operational with experimental dc bias margins of (+/-15%), and at high speed the bias margins are significantly reduced.

In Fig. 5 the rising and falling edges correspond to SFQ pulses. The top trace is the input data pattern (1010 1011 1110 0000 0000 0000). The second trace is the initial signal to the 18.5 GHz on-chip clock generator. The third and bottom traces are the complementary output data patterns. Correct operation is observed with (11 11 00 11 00 00) in the first DEMUX output and (11 11 11 11 10 01) in the second output.

The basic ring in Fig. 4b has been tested and, unfortunately, was not operational. We believe there were problems with large fabrication process variations and the circuit layout lacked adequate moats, or holes in the ground plane to trap stray magnetic flux. We have made a new layout to correct these problems and fabrication is in progress.

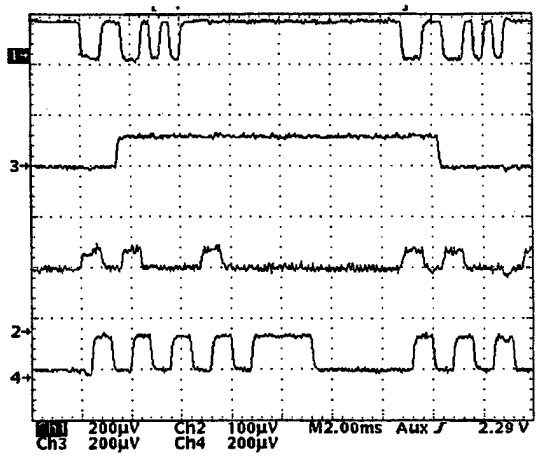

FIG. 5 Low speed input and output for an 18.5 GHz high-speed on-chip test of the 2-bit DEMUX circuit in Fig. 4a.

V. Summary and Future Work

We have designed the basic components of an ultra-high-speed RSFQ ring data bus. The circuit components consisting of the basic ring, output decoder, MUX/DEMUX, and output amplifier have been simulated and optimized. Our simulations include Monte Carlo process variations so that the circuits have a high probability of working at ultra-high speed.

We have laid out and fabricated the component circuits and the MUX/DEMUX has been successfully tested at low speed. The DEMUX circuit has also been demonstrated at 18.5 Gb/s using on-chip testing. We are presently working to demonstrate the complete data ring and all of the components at higher speeds.

References

[1] M. Jeffery, L. Zheng, N. Yoshikawa, J. Koshiyama and T. Van Duzer, "Single-Flux-Quantum Railroads: Component Development for a 64 Gb/s Digital Superconducting Ring Data Bus," presented at the *1998 Applied Superconductivity Conference*, Palm Desert CA.

[2] S. Yorozu *et al.*, "Full Operation of Three-Node Pipeline-Ring Switching Chip for Superconducting Network System," presented at the 1998 Applied Superconductivity Conference, Palm Desert CA. To appear in *IEEE Trans. Appl. Supercond.*

[3] Z. Deng, N. Yoshikawa, S. Whiteley and T. Van Duzer, "Data-driven Self-Timed RSFQ Digital integrated Circuit and System," *IEEE Trans. Appl. Supercond.*, vol. 7, No. 2, pp. 363-3637, June 1997.

[4] L. Zheng *et al.*, "RSFQ Multiplexer and Demultiplexer," presented at the 1998 Applied Superconductivity Conference, Palm Desert CA. To appear in *IEEE Trans. Appl. Supercond.*

[5] N. Yoshikawa, Z. Deng, S. R. Whiteley and T. Van Duzer, "Simulation and 18 Gb/s Testing of a Data-Driven Self-Timed RSFQ Demultiplexer," presented at the 1998 Applied Superconductivity Conference, Palm Springs CA. To appear in *IEEE Trans. Appl. Supercond.*

[6] A. Bhat, X. Meng, S. Whiteley, M. Jeffery, and T. Van Duzer, "A 10 GHz Digital Amplifier in an Ultra-Small-Spread High-J_c Nb/Al-Al$_x$/Nb Integrated Circuit Process," presented at the 1998 Applied Superconductivity Conference, Palm Desert CA. To appear in *IEEE Trans. Appl. Supercond.*

[7] X. Meng, A. Bhat, and T. Van Duzer, "Very low critical current spreads in Nb/AlOx/Nb integrated circuits using low temperature and low stress ECR PECVD silicon oxide films," presented at the 1998 Applied Superconductivity Conference, Palm Desert CA. To appear in *IEEE Trans. Appl. Supercond.*

10 Kelvin Operation of a High Speed Digital Crossbar Switch

A. Spooner
Sierra Monolithics, Inc., 103 W. Torrance Blvd., Ste. 102, Redondo Beach, CA 90277

M. Leung, R.D. Sandell, L.R. Eaton, J.W. Spargo
TRW Space & Electronics Group, One Space Park, Redondo Beach, CA, 90278

Abstract—A critical component for high bandwidth communications links is a digital switch. Applications of digital switches can range from acting as programmable interconnections on a multi-chip board to sophisticated self-routing of packets in an Asynchronous-Transfer Mode (ATM) network. Superconductivity offers desirable features such as high input/output bandwidth, high channel count, scalability, low latency and low interchannel skew.

We report here on a 16 X 16 crossbar switch circuit fabricated in TRW's NbN integrated circuit process. The crossbar matrix is based on a previously reported crossbar switch fabricated in Nb and operated with low bit error rate up to 3 Gb/s [1]. In the circuit reported here, the header decode function for packet routing was replaced with an architecture functionally similar to many commercially available semiconductor chips. This design uses 8 parallel addressing bits to select 1 of 256 crosspoints for each of 16 input ports and 16 output ports. Once selected, the crosspoint requires no power to remain selected, and the input to output path remains available until released. An arbitrary number of crosspoints on the input row can be selected for multicasting operation. An additional difference from the previously reported switch is on-chip amplifiers for the outputs, providing a complete single chip switch.

After fabrication, the chip was flip-chip packaged for test in a variable temperature dewar, and tested at 10 Kelvin. We will report 1 Gb/s data throughput in broadcast mode at 10 Kelvin, as well as discuss the decoder design.

I. Introduction

A digital data switch, operating at 10 K, raises intriguing possibilities for cryo-cooler based packaging, broadening the available insertion markets and improving customer acceptance. Such a packaged switch, accompanied by additional circuitry such as a fast memory, would advance the state of the art for ground based and space based digital communication. We have constructed and tested a 16 x 16 crossbar switch in NbN. The addressing architecture follows that of switches of a common industry standard, furthering customer acceptance by being "plug and play." Additionally, the switch chip contains latching output amplifiers, simplifying the packaging needs by condensing the circuitry onto a single chip.

Superconducting switch designs are typified by low power operation (including the cooling power to maintain cryogenic temperatures) and low channel-to-channel skew. The low power consumption allows high density layout without regard to thermal issues common in semiconductor layout, reducing the skew to time-of-flight differences between signal paths, which is controlled by the cell size. Tighter lithography rules will lead to further reduction in skew, in contrast to semiconductor limits imposed by transistor heating. In the current layout, the worst case channel-to-channel skew for a 16 X 16 crossbar switch is a path length difference of ~3.5 mm, or a time of flight difference of about 25 ps, much less than a bit length. Low skew implies much simpler clock recovery requirements at the output of the switch, further simplifying use. Alternatively, a clock signal can be broadcast with low skew, if a free channel was available.

Once the switch is configured, a crosspoint consumes only a few microWatts in transmitting data. The power required to set up a single crosspoint is similarly in the few microWatts range.

The components of the switch fabric and latching amplifier are similar to a previously reported 3 Gb/s Nb switch [1], however, the address decoding architecture differs. The previously reported switch contained the address in a header on the data, due to constraints imposed on the total system power. The switch reported here has address lines separate from the data lines, and the addressing uses 8 parallel bits to select 1 of the 256 crosspoints. This architecture matches (at least in function, if not in implementation) a common commercial architecture.

II. Architectural Trades

The goal of this design was to emulate the functionality as closely as possible commercial, semiconductor digital crosspoint switches. Commercially available switches use high speed GaAs technology to perform the 16 X 16 crosspoint switch function, and are targeted for Asynchronous Transfer Mode (ATM) switching applications. Although conceptually different (the semiconductor switch uses a MUX at the output) than our pure crossbar design, the two are operationally identical. The switch control is provided by two 4-bit words; one word specifies an input channel and the other specifies the output channel. Addresses are sequentially loaded until the switch is configured. An important feature of

Manuscript received April 30, 1999. This work was supported in part by NASA contract No. NAS3-26960

this architecture is that data passing through a non-changing crosspoint remains undisturbed.

In order to exactly emulate the conceptual design of the semiconductor switch, the circuit would have required 2750 MVTL gates. However, with the development of a crosspoint cell that does not require continuous power to remain closed, the total gate count can be reduced. An added advantage of making all the switches self latching, is that each switch can now be controlled using an X-Y addressing technique. This technique only requires 16 column and 16 row drivers, reducing the total logic device count from 2750 gates to 516 gates. The current design uses 228 MVTL gates, 256 crosspoints, and 32 latching amplifiers.

The basic Crosspoint Switch has 16 input channels and 16 output channels. The input and output channels form a square switching matrix in which any output channel can be supplied from any input channel. This switching architecture is capable of unrestricted point-to-point, multi-cast and broadcast operation, which means that any input can be routed to any number of outputs at the same time.

The switching configuration is setup via an 8 bit parallel control bus. The 4 MSBs are used to select any one of the 16 output channels and the 4 LSBs identify the input channel that is to be routed to that specific output channel. Upon application of the LOAD signal, any input channel previously connected to the selected output channel is disconnected, and the newly selected input channel is connected. The LOAD signal is normally only one MVTL (Modified Variable Threshold Logic) clock period in duration. While the LOAD signal is held true, the information passing through the single selected output channel is invalid, but the data passing through all of the other output channels is completely uninterrupted. Upon removal of the LOAD signal the 8 bit control bus can be reconfigured to update any other output channel. In this way all the output channels can be reconfigured, one at a time, and in any sequence.

III. Circuit Design and Block Diagram

A. Crosspoint Design

The crosspoint cell has been described previously. The cell was translated to our NbN process, altering the design to accommodate the larger specific inductance in NbN films, over Nb films.

B. Decoder Design

The address decoder design uses MVTL logic gates. The row decoder and the column decoder generates the two signals needed to select a crosspoint (select and clamp, respectively). The only functional deviation of this design from that of the semiconductor switch control is that each output is updated individually rather than altogether in a single clock cycle. As a design requirement, the validity of the information passing through any non-changing output channels remains undisturbed, as in the semiconductor device. The integrity of this final control logic circuit design has been confirmed using the DesignWorks™ Logic Simulator.

C. Latching Amplifiers

The switch uses a number of buffer stages, both internally and on the output of the switch. We use current step-up Josephson junctions internally to boost the current drive from the MVTL decoders to the select and clamp lines. A latching stack of 4 Josephson junctions in series boosts the output voltage to several millivolts, so that the interface to the user requires only simple, commercial amplifiers. The figure below shows the schematic of the amplifiers.

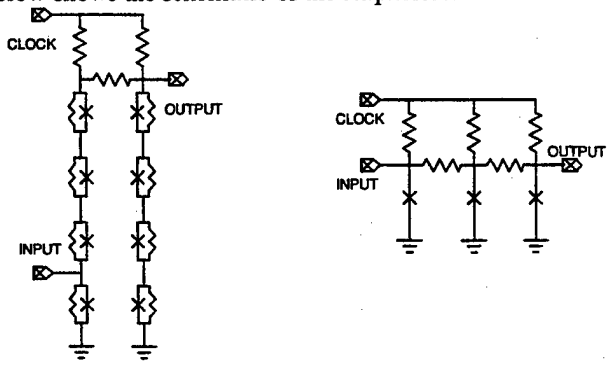

Figure 1: The Josephson stack amplifier (left) buffers the output of the switch and delivers several millivolts to a semiconductor preamplifier. The current gain amplifier (right) boosts the input current by using sequentially larger Ic junctions. Both amplifiers use latching junctions.

D. System Block Diagram

The system block diagram is shown below in Figure 2. The current design does not have contention detection or contention resolution.

Also not addressed in this current work are packaging issues; the thermal, mechanical, and electrical design that adequately preserves signal integrity while simultaneously allowing operation within a reasonable power budget.

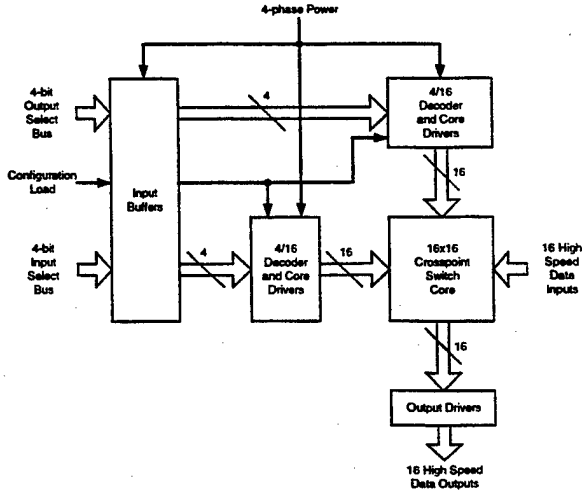

Figure 2: System block diagram, showing I/Os.

IV. Chip Layout and Fabrication

To support cryocooler operation of the switch, the circuit was constructed in TRW's NbN foundry process, generally characterized by its critical current density of 1000 A/cm^2 at 10 K. The switch fabric, decoders, and output buffers occupy a 1 cm^2 chip, but could easily be compressed into a smaller area. The chip is shown in Figure 3.

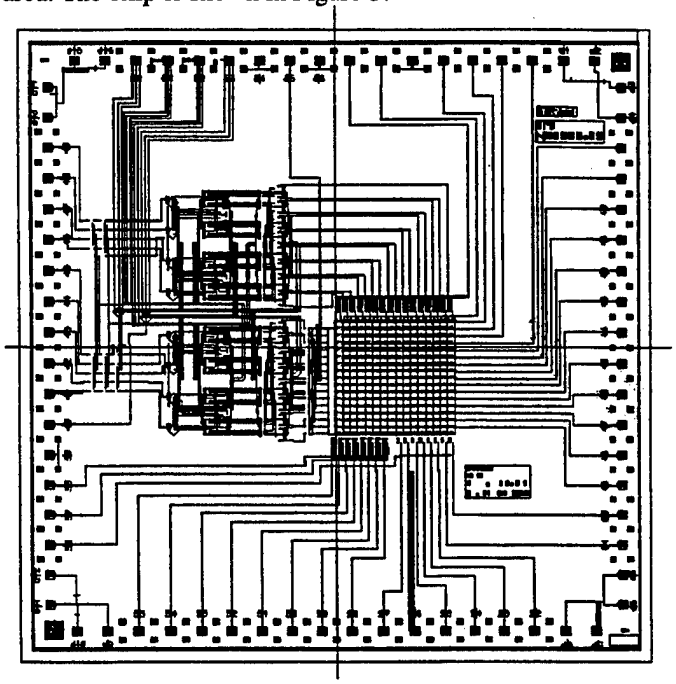

Figure 3: The 16 X 16 crossbar switch chip. The switch fabric occupies the square area near the center of the chip. The MVTL decoder circuit with the parallel inputs is on the left side. Care is taken to control the impedance of the transmission lines carrying the four-phase clock. The output transmission lines are at the bottom of the chip.

V. Crosspoint Performance

Switch operation can be verified in broadcast mode, and does not require the addressing circuit. Broadcast mode data at 8 Mb/s and 1 Gb/s are shown below in Figure 4.

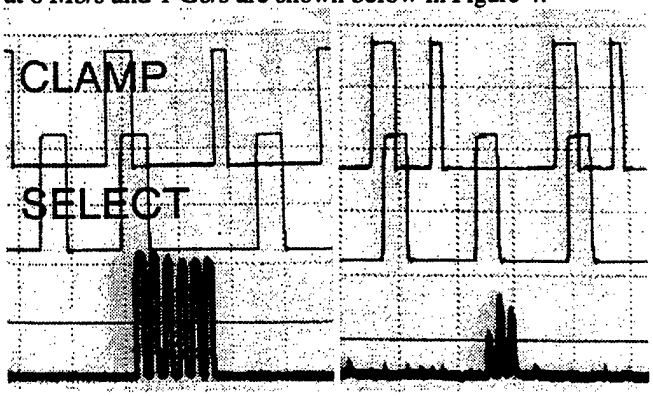

Figure 4: Crosspoint operation at 8 Mb/s (left) and 1 Gb/s (right). The data at 8 Mb/s demonstrates the timing arrangement between clamp (top trace), select (middle trace), and data throughput (bottom trace). Neither addressing signal alone is able to close the crosspoint. When both signals are simultaneous, the crosspoint closes and transmits data (bottom trace on both). When CLAMP is high again, the crosspoint is reset and returned to the open state. Note that the crosspoint continues transmitting data when both clamp and select are low, thus demonstrating that the crosspoint can be maintained with zero power. N. B. The data at 1 Gb/s is delayed (because of varying cable lengths) from the addressing signals, but is correct operation; the addressing signals are different for the two data rates shown. The vertical scale in both oscillograms is 5 mV/div.

The latching output amplifier gives an output of ~10 mV at low data rates. There is clear evidence of bandwidth limiting at 1 Gb/s, as indicated by the reduced amplitude and the shape of the data envelope. This suggests that the crosspoint has a somewhat slow rise/fall time in comparison to that of the output amplifier. Further improvements in data rate will occur with finer lithography and higher junction critical current density. For example, the Nb version, with twice the critical current density, and smaller design features, operated to at least 3 Gb/s

VI. Summary and Future Prospects

Data throughput of an ultra-low power, low skew, multicasting digital switch has been demonstrated. The technology used is a NbN 10 K superconducting IC process, which is more easily amenable to system integration with a cryocooler, than a Nb 4.5 K process. Superconducting switches are envisioned to be an enabling component for high bandwidth digital communications, particularly for massively parallel processing applications.

Higher data rates can be achieved with a NbN IC process that features higher critical current density, for lower capacitive time constants.

Further work is required before a useful system can be presented to a prospective user. The thermal, electrical, and mechanical construction needs careful attention to limit the power dissipation and preserve the signal integrity. For example, high bandwidth cables with limited thermal conductivity are necessary for such a system. Driver and amplifier circuits will need to be developed in order to interface to the user. Finally, methods to deal with contention will need to be incorporated.

Acknowledgment

The work here would not have been possible without the support of the TRW Josephson foundry team.

References

[1] R. D. Sandell, J. W. Spargo, M. Leung, S. R. Whiteley, "High data rate switch with amplifier chip," unpublished.

A Baseband Demonstration of a Spread Spectrum Modem Using SFQ Technology

Eric J. Dean, Paul D. Dresselhaus, John X. Przybysz, and A. Hodge Worsham
Northrop Grumman Science and Technology Center, 1350 Beulah Rd., Pittsburgh, PA 15235

Stas V. Polonsky
RSFQ Consulting Inc., Stony Brook, NY USA

***Abstract*—We have successfully constructed a baseband demonstration of a spread spectrum modem using SFQ technology. A baseband demonstration consists of modulating (encoding) data with a spreading code, transmitting the coded data to a receiver and demodulating (decoding) the data using a copy of the original spreading code. The transmitted data were created with a 2 GHz, 4-bit SFQ code generator creating a 15 bit spreading code and modulating a ~130 MHz data source. This data was output through a 10X superconducting latch and fed through 50 Ω coaxial cables to a SFQ receiver chip in a separate dewar. No amplification of the AC signal between the dewars was needed, however, a slight DC bias was added to the output signal in order to provide sufficient flux bias to the input SQUID on the receiver. The receiver chip consists of an identical SFQ code generator to that in the transmitter and a data demodulation gate. Modulating the received data with the code generator produced a replica of the data signal in RZ form.**

I. Introduction

High bandwidth spread spectrum communications provides a demonstration of the strengths offered by SFQ technology [1]. The speed of operation of SFQ technology is superior to that offered in silicon technologies. This speed advantage is at a premium when faced with problems that are not easily parallelizable. The spread spectrum modulator/demodulator (MODEM) that we are developing highlights the need for a fast nonparallelized technology; correlation functions in the receiver will have to be done within a few clock cycles.

A major part of a spread spectrum modem consists of the baseband construction. This consists of taking a data pattern, modulating it with a predetermined code and transmitting the modulated (encoded) data to the outside world. This encoded data is received at a separate location and the modulation is removed, thus recovering the original data pattern. In this work, the data are modulated and demodulated by bit patterns produced by a 4-bit pseudorandom binary sequence (PRBS) generator, which produces a 15-bit code. This requires a PRBS generator with a clock rate much greater (2 GHz) than the data rate (~130 MHz). Each data bit is encoded with a sequence of 15 code bits through an exclusive or (XOR) operation. These encoded data are then transmitted to a receiving station on a separate chip in a separate dewar. The receiver chip contains its own identical PRBS code generator.

Manuscript submitted April 26, 1999.

This work was supported by contract F19628-94-C-0097, funded by BMDO/IST and technically managed by Air Force Research Lab, Hanscom.

Data is recovered by demodulating the received code with the code produced on-chip, with manual synchronization of the two codes.

This paper will discuss the data modulation, transmission and demodulation aspects. The aspects of code generation are discussed in more detail in [2].

II. Circuit Design

The transmitter and receiver circuits are almost identical. They each consist of code generators operating at a 2 GHz clock rate that produce two possible 4-bit pseudorandom codes; an XOR cell to modulate the data signal with the code, and I/O circuitry.

The transmit circuit is shown in Figure 1. The code generator can produce two different 15-bit codes, depending on the feedback configuration. Feeding back the output of stages 3 and 4 produced the time forward code, while feeding back the output of stages 1 and 4 produced the time reversed code. The code was enabled or disabled by the "RESET" line. When enabled, the code generator fed out the 15 bit code indefinitely; when disabled, the code generator fed out all 0's. The data source controls a current controlled switch, which either permits or prevents the passage of SFQ clock pulses (thus replicating the NRZ data signal in an RZ form) to one of the data inputs of the XOR gate. The XOR gate modulates the data signal with the code. Details of the operation of the current controlled switch may be found in [2]. The output of the modem XOR gate is fed to a 10X latching amplifier [3].

The receiver circuit is shown in Figure 2. It has an input SQUID that receives the RZ data from the transmitter and converts it into SFQ data. The receiver has a code generator identical to the one in the transmitter. The receiver code was then XORed with the data from the input SQUID. The

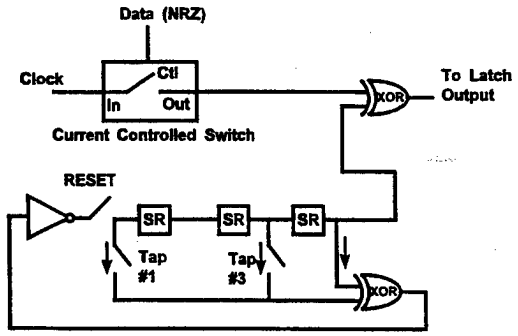

Figure 1: Block diagram for the modem transmitter. The code generator, modulator XOR and the current controlled switch all share a common clock.

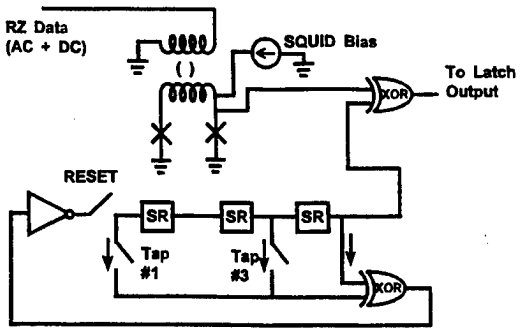

Figure 2: Block diagram for the modem receiver. The code generator and XOR share a common clock.

output of the XOR, which is an RZ representation of the original data pattern, is then sent to a latching output amplifier.

III. Testing Setup

A. MHz/GHz Circuitry

The experimental setup is shown in Figure 3. Experimental details not specific to this experiment may be found in Ref. [4]. It consists of a transmit chip containing a code generator and a data modulator in one dewar and a receiver chip consisting of an identical code generator and a data demodulator in another dewar. Both the transmitter and receiver chips receive RF power from the same HP83624 RF frequency synthesizer fed through a phase shifter/splitter box. This allows for independent amplitude and phase control for the output latches for each circuit and for the clock. The two circuits share the same clock signal.

The 10 MHz reference signal on the frequency synthesizer provided a common trigger for three HP8082A pulse generators and for a Tektronix 11801A digital sampling scope. While all of the pulse generators received the identical trigger signal, the pulse parameters (signal

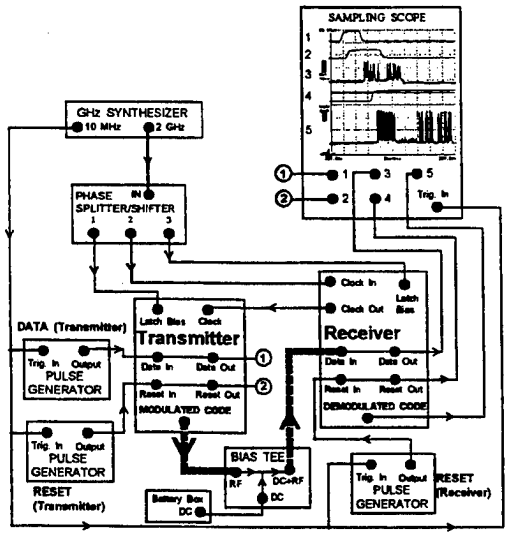

Figure 3: Block diagram for the baseband demonstration. The heavy dotted line is the line for transferring encoded data.

amplitude, DC offset, pulse width and pulse delay from trigger signal) could all be adjusted independently. The pulse generators provided a "RESET" signal for the transmitter, a "DATA" signal for the transmitter and a "RESET" signal for the receiver. The three pulse generator signals, plus the output signals for the transmitter and receiver circuits were all fed into the sampling scope. For both the transmitter and receiver chips, the SFQ modulated/demodulated data were amplified by a superconducting 10X output latch for transmission outside of the dewar. The latching amplifier outputs and the clock lines were AC coupled (~10 MHz cutoff frequency) to eliminate the presence of low frequency ground loops [3].

IV. Results

A. Transmitter Data Modulation

The transmitter is responsible for the top three scope traces in Figures 4 and 5. The top trace represents a data signal. A high level indicates a data "1" while a low signal indicates a data "0". The width of the data "1" is one period of the code generator. The second trace represents the "RESET" signal enabling (high) and disabling (low) the code generator. The "RESET" signal allows the code generator to produce two complete periods of code before being disabled. The output of the code generator is shown as the third trace. Both the forward (Figure 4) and time reversed (Figure 5) codes were produced by altering the feedback configuration in the transmitter code generator.

B. Data Transmission, Reception and Demodulation

The modulated code was sent through the 10X latching amplifier producing 2GHz, RZ data with roughly an 8 mV AC level. Ideally this signal would be sent through only 50 Ω cables to the receiver circuit where it would be sensed by the input SQUID on the receiver. The receiver SQUID has its own separate bias line to adjust its sensitivity to incoming signals. However when testing the SQUID with a separate data source, we found that the SQUID would not sense any AC coupled signals with less than a 20mV peak-to-peak level regardless of the bias current setting. This prompted us to add the bias tee to the circuit. The bias tee provides a bit of additional flux bias to the input SQUID, causing it to trigger at smaller AC levels. We typically added 200 μA of DC bias. The DC bias through the bias tee can be reduced (but not eliminated) to roughly 50 μA by increasing the on chip DC bias of the SQUID, however, increasing the DC bias of the SQUID too much will send it into the voltage state. The latching output of the transmitter dewar was left AC coupled for noise considerations.

Providing the proper DC bias to the input SQUID on the receiver led to the proper operation of the demodulator. The fourth trace in Figures 4 and 5 shows the "RESET" line enabling the code generator on the receiver chip. This code generator produced the identical code (either forward or time reversed) as the code generator on the transmit chip. The XOR gate in the modulation portion of the receiver chip removed the modulation impressed on the data in the transmit

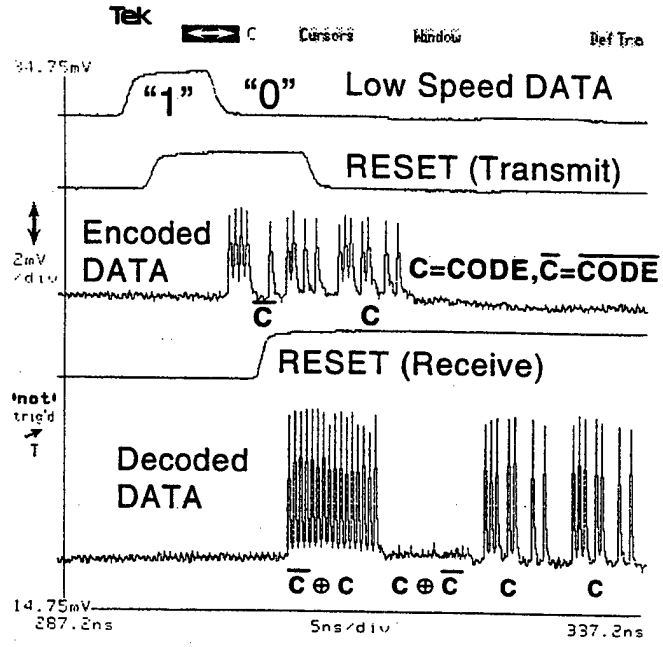

Figure 4: Data modulation and demodulation at 2 GHz with a 15 bit time forward code. Traces from top represent Data (to transmitter), Reset (to transmitter), Modulated data (from transmitter), Reset (to receiver) and demodulated data (from receiver). The ⊕ symbol represents the XOR operation. The relative timing of the scope traces should be disregarded due to cable delays.

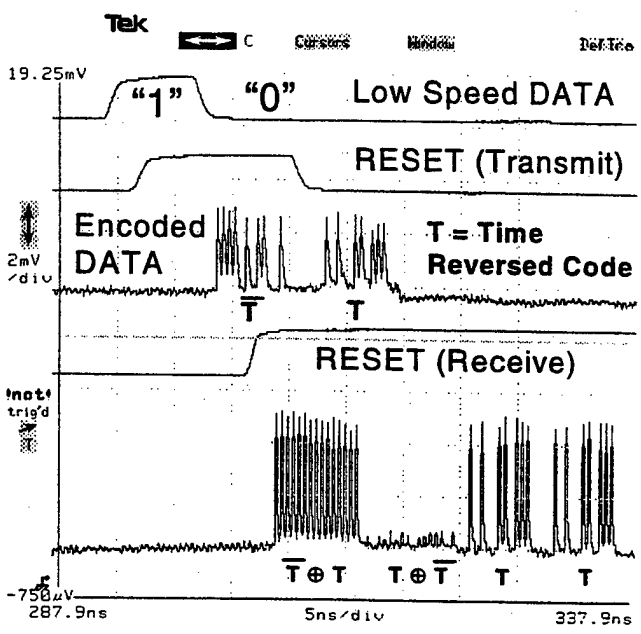

Figure 5: Data modulation and demodulation at 2 GHz with a 15 bit time reversed code. Traces from top represent Data (to transmitter), Reset (to transmitter), Modulated data (from transmitter), Reset (to receiver) and demodulated data (from receiver). The ⊕ symbol represents the XOR operation. The relative timing of the scope traces should be disregarded due to cable delays.

C. *Margins*

We do not expect the margins of this circuit to be significantly worse than that of a single code generator/modulator. The only two "connected" points between the two circuits are the clock line and the data line containing the modulated data. The AC margins on the DC/SFQ converter used for the clock permit as much as ±5 dB variance in the clock amplitude while still operating properly. The line carrying the encoded data has four different bias variables (AC latch bias on transmitter, DC latch bias on transmitter, flux bias to the bias tee and DC bias to the input SQUID on the receiver); these bias levels may be adjusted to ensure reliable data transfer while providing little or no perturbation to the remainder of their respective circuits.

V. Conclusions

We have demonstrated a baseband construction of a spread spectrum communications system. It provides for data modulation with a PRBS code, transmission to a separate receiving station over 50 Ω cables, and demodulation of the signal to provide a replica of the original data signal. This method shows an advance over previous dewar-to-dewar data transfer methods using MVTL logic [5]. The absence of an AC drive for the receiver input SQUID removes one additional place where synchronization of the incoming code must be performed; the additional DC flux bias that we added, while inconvenient, entails no additional synchronization issues.

The components tested here represent additional pieces necessary for a spread spectrum communications system. They will fulfill a need, not currently met by semiconductor systems, for a high speed, multiple user communications link.

Acknowledgment

The authors would like to thank Dr. D.L. Miller for technical assistance, S.J. Pieseski for fabrication expertise, Dr. Dallas Hayes and Mr. John Turtle of the Air Force Research Laboratory for program guidance.

References

[1] K. Likharev and V. Semenov, "RSFQ logic/memory family: a new josephson junction technology for sub-terahertz clock frequency digital systems," IEEE Trans. on Appl. Supercond., vol. 1, pp. 3-28, 1991.

[2] P.D. Dresselhaus, E.J. Dean, J.X. Przybysz, and S.V. Polonsky, "Modulation and Demodulation of 2 GHz Pseudo Random Binary Sequence Using SFQ Digital Circuits," IEEE Trans. on Applied Superconductivity 9(2), (1999).

[3] J. X. Przybysz, D. L. Miller, S. S. Martinet, J. H. Kang, A. H. Worsham and M. L. Farich, "Interface circuits for chip-to-chip data transfer at GHz rates," *IEEE Trans. Appl. Supercond.*, vol. 7, No. 2, June 1997, pp. 2657-2660.

[4] E. J. Dean, P. D. Dresselhaus, J. X. Przybysz, A. H. Miklich, A. H. Worsham, and S. V. Polonsky, "Bit Error Rate Measurements for GHz Code Generator Circuits," IEEE Trans. on Applied Superconductivity 9(2), (1999).

[5] J. X. Przybysz, J. D. McCambridge, and P. D. Dresselhaus, "Dewar-to-Dewar Data Transfer at 2 Gigabits per Second," IEEE Trans. on Applied Superconductivity 9(2), (1999).

Simulations of Ultra-High-Speed High Temperature Superconductor Digital Circuits Combining Process Variations and Thermal Noise

M. Jeffery, L. Zheng , S. R. Whiteley, and T. Van Duzer
Department of Electrical Engineering and Computer Sciences, The University of California, Berkeley CA 94720-1770

Abstract- **We previously modified the WRspice commercial circuit simulator to include Monte Carlo yield analysis and thermal noise fluctuations. Using the simulator we quantitatively compared the effect of process variations on theoretical yield for two T flip-flop circuits, one by TRW including parasitic inductances and an idealized circuit from Conductus with no parasitic inductance. These results demonstrated quantitatively the effect of parasitic inductance on the theoretical yield of the circuits at ultra-high speed. We also calculated bit error rates due to thermal noise for these circuits assuming no process variations. In the present work, we combine the Monte Carlo and thermal noise simulations to quantify the effect of process variations on the bit error rates of the circuit. We also present theoretical yield results for an HTS cascaded T flip-flop circuit consisting of 38 junctions and operating at ultra-high-speed.**

I. Introduction

The main challenges for demonstrating complex rapid single flux quantum (RSFQ) high temperature superconductor (HTS) circuits are process variations of the Josephson junctions, and parasitic inductance. We previously examined the effect of process variations and parasitic inductance on theoretical yield of an HTS T flip-flop [1]. We also combined thermal noise into the WRspice commercial circuit simulator and calculated circuit bit error rates [1]. In the present work, as an additional test of the thermal noise simulator, we calculate the gray zone and bit error rate of an RSFQ comparator. We combine process variations and thermal noise in an ideal T flip-flop in order to calculate the effect of process variations on bit error rate (BER) at different temperatures.

Furthermore, we simulate larger HTS circuits, with 30 or more Josephson junctions, in order to quantify the effect of process variations on theoretical yield for larger circuits. As a test circuit, we have simulated the cascaded T flip-flop counter including Monte Carlo process variations and calculated the theoretical yield of the circuit. We assume the present state-of-the-art HTS process variations, and an ideal HTS process, in the simulations.

In the following section we calculate the gray zone and BER of an RSFQ comparator. These results are compared to previous experimental results of LTS and HTS comparators, and are found to be in excellent agreement. We combine Monto Carlo analysis and thermal noise in Sec. 3, and calculate thermal noise errors of an ideal T flip-flop. In Sec. 4 we give simulation results for the Monte Carlo yield of the cascaded T flip-flop counter including parasitic inductance. A summary and conclusion are given in the final section.

Manuscript received April 30, 1999.
This work was supported by ONR grant # FDN00014-98-1-0084

II. Test of the Thermal Noise Simulator: RSFQ Comparator Grey Zone and BER Calculation

We previously added thermal noise into the WRspice commercial Josephson circuit simulator [1,2]. As a first test of the simulator we calculated the thermal noise rounding of a Josephson I-V curve, and obtained excellent agreement with Ambegaokar and Halperin analytic result [1]. However, some questions remained as to the validity of the simulation results in comparison with other BER measurements on RSFQ comparators.

We have therefore simulated the basic RSFQ comparator shown schematically in Fig. 1a. The comparator consists of two Josephson junctions. When a current bias is injected between the junctions, an RSFQ pulse from the input Josephson transmission line (JTL) will appear at the output JTL if the bias is above the threshold of the comparator. However, if thermal noise is present in the circuit, there is a finite probability that the comparator will misfire. We have simulated the circuit in Fig. 1a, including thermal noise from the Josephson junction normal resistance, and with the experimental parameters given by Fillipov and co-workers in [3].

Figure 1b shows the gray zone, or firing probability, of the comparator Fig. 1a calculated using WRspice at 4.2 K and with

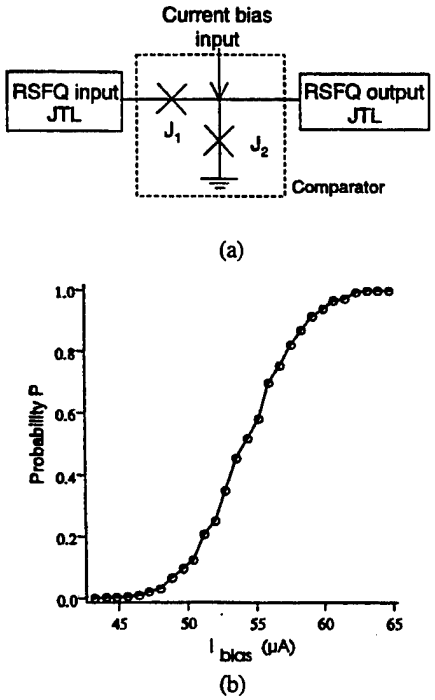

FIG. 1. (a) A schematic diagram of an RSFQ comparator. JTLs are used to feed RSFQ pulses to and from the comparator. (b) The comparator gray zone calculated at 4.2 K using the parameters in Ref. [3].

a 10 GHz RSFQ input. The random thermal fluctuations are equally plus and minus, therefore at the threshold of the comparator there is a 0.5 probability that the comparator will either fire or not fire. As the bias is increased above the comparator threshold, the probability of the comparator misfiring decreases. Note that there are *no fitting parameters* in the simulation results in Fig. 1b, and that this theoretical result is in excellent agreement with the experimental result of Fillipov and co-workers [3].

We have also simulated the circuit in Fig. 1a at 40 K for HTS parameters similar to those used in the BER measurements by Ruck and co-workers in Jülich [4]. Unfortunately, the exact fabricated parameters in the Jülich experiment were not known, and hence we have assumed critical currents of 375 μA and I_cR_n equal to 100 μV. The calculated BER of this HTS comparator at 40 K is shown in Fig. 2.

With our simulator it is difficult to calculate bit error rates less than 10^{-5}, since this requires simulations with more than 10^5 clock cycles per data point. However, the results in Fig. 2 show that above the threshold of the comparator the BER decreases approximately exponentially as predicted by analytic theory [3]. If we extrapolate the results in Fig. 2 to a bias equal to half the critical current of the Josephson junction, then the corresponding BER is 10^{-12}. This result compares well to the Jülich experiment which reported a BER of 10^{-11} at 40 K with an optimal bias [4].

Intuitively, the low BER is understood by looking at the circuit Fig. 1a. When the input dc bias is a significant fraction of the J_2 critical current and given an RSFQ input, the probability of thermal noise erroneously switching the junction J_1 becomes very small. For general digital circuits, it is not always the case that the input bias will be far above the threshold of the comparator. Hence, the Jülich result, which is an important demonstration of the possibility of low BER in HTS circuits, may not be applicable to general circuits.

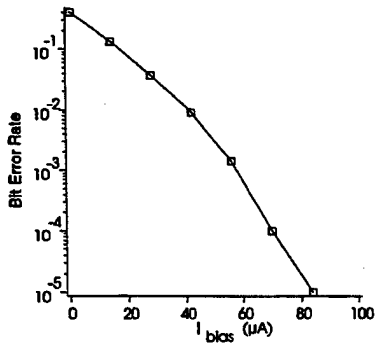

FIG. 2 HTS Comparator bit error rate calculated as a function of bias current at 40 K. The error rate drops approximately exponentially as the bias is increased above the threshold of the comparator.

III. Combined Monte Carlo and Thermal Noise Simulations

We have extended our previous work [1] to combine both process variations and thermal noise in the simulations. Satchel has previously included thermal noise in Monte Carlo optimization of RSFQ circuits [5]. In the present work, we calculate the effect of process variations and thermal noise for the simplified T flip-flop circuit given in Ref. [1]. Figure 3 shows 100 GHz simulation data for the T flip-flop including process variations and thermal noise.

We are in the process of calculating the BER of the ideal T flop-flop with Monte Carlo process variations and noise. For all simulations we assume the present HTS state-of-the-art process variations given in Table 1. These simulation results will be presented at the ISEC'99 conference.

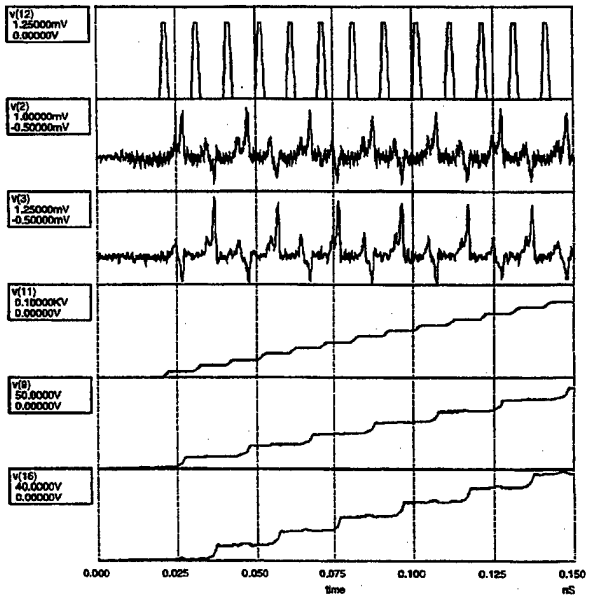

(a)

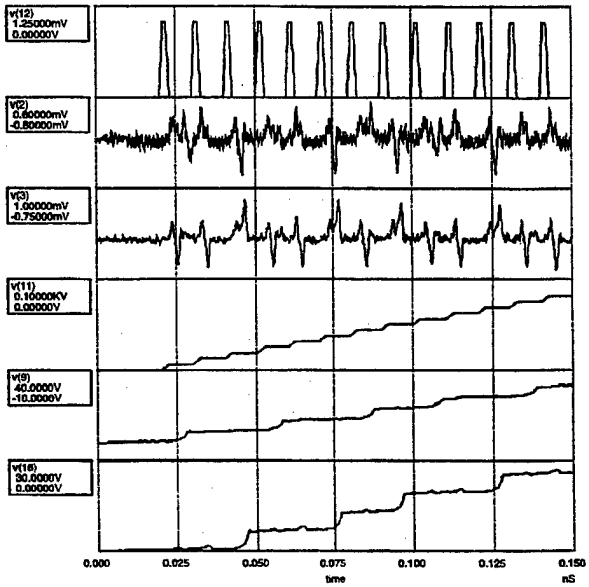

(b)

FIG. 3 (a) 100 GHz T flip-flop simulation at 40 K with state-of-the-art HTS Monte Carlo process variations given in Table 1. No errors are detected in the simulation interval (a). The top trace is the input and the 2nd and 3rd traces are the divided-by-two outputs. The last three traces are 2π phase jumps of the input JTL and the two output Josephson junctions, respectively. (b) The same simulation, but with different random Monte Carlo parameters. In (b) there are thermal noise errors observed at the output, and hence the 2π phase jumps do not match (a).

IV. Monte Carlo Simulations of a Cascaded Toggle Flip-Flop Counter

In order to further quantify the effect of process variations, we have calculated the theoretical yield, with no thermal noise, for the cascaded T flip-flop counter Fig. 5a. This circuit consists of 38 Josephson junctions, includes parasitic inductance, and assumes an I_cR_n of 500 μV. The T flip-flop component circuit was designed by TRW and demonstrated at 40 K and low-speed [6]. The theoretical yield results for the counter in Fig. 5a with the two different sets of process variations of Table 1 are given in Fig. 5b.

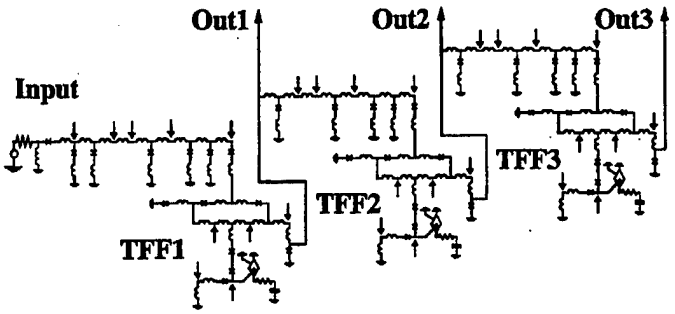

(a)

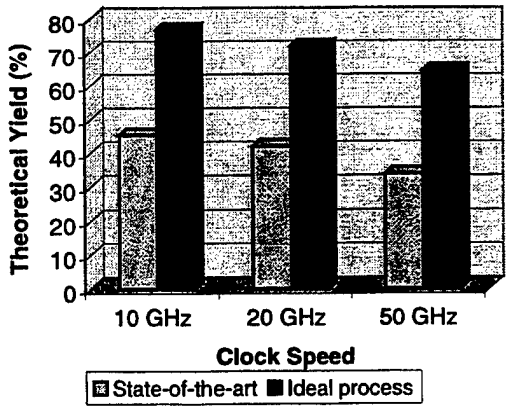

(b)

FIG. 5. (a) Cascaded T flip-flop counter and (b) Monte Carlo yield results for the process variations given in Table 1.

With 10 GHz clocks the yields are 46% and 77% given present state-of-the-art and an ideal process, respectively. These yields decrease by approximately 12% as the input clock speed is increased to 50 GHz. Hence, similar to the small component circuit analyzed previously [1], the process variations and clock speed have a significant effect on the theoretical yield of large HTS circuits.

TABLE I
1σ PROCESS SPREADS USED IN MONTE CARLO SIMULATIONS

Process Variations*	I_c	R_n	L
Ideal	5%	2.5%	5%
Present HTS state-of-the-art	10%	5%	15%

*Local variations. Global variations are zero for I_c and R_n, 15% 1σ for L

V. Summary and Conclusion

We have used Monte Carlo and thermal noise simulations to analyze HTS circuits. As an additional test of the thermal noise simulator, we have calculated the gray zone and BER of an RSFQ comparator. Our results are in excellent agreement with previous experiments.

We have incorporated thermal noise and Monte Carlo process variations into the WRspice commercial Josephson circuit simulator. We have simulated an ideal T flip-flop operating at 100 GHz including simultaneously both process variations and thermal noise. Depending upon the random parameters chosen, bit errors are clearly observed at 40 K. We are in the process of calculating the BER of this circuit including both process variations and thermal noise.

Finally, we have implemented Monte Carlo simulations of larger cascaded T flip–flop counters, neglecting thermal noise. The yield is 34% with the present state-of-the-art process variations, parasitic inductance, and a 50 GHz input clock. The yield increases to 65% with an ideal HTS process. As expected, improving the existing fabrication technology will significantly increase the possibility of realizing complex HTS circuits at ultra-high-speed.

Acknowledgement

We gratefully acknowledge Bernhard Ruck for providing information regarding the Jülich HTS BER experiment. We would also like to thank Quentin Herr and Adrian Sun at TRW, and Martin Forrester at Northrop Grumman, for useful discussions.

References

[1] M. Jeffery, P. Xie, S. R. Whiteley, and T. Van Duzer, "Monte Carlo and Thermal Noise Analysis of Ultra-High-Speed High Temperature Superconductor Digital Circuits" Presented at the 1998 Applied Superconductivity Conference, Palm Desert CA, to appear in *IEEE Trans. Appl. Superconduct.*

[2] For more information on WRspice contact S. Whiteley, Email: stevew@srware.com, Phone: (408) 735-8973, FAX: (408) 245-4033.

[3] T. Fillipov, Y. Polyakov, V. Semenov, and K. Likharev, "Signal Resolution of RSFQ Comparators," *IEEE Trans Appl. Superconduct.*, vol. 7, pp. 2240-2243, June 1995.

[4] B. Ruck, B. Oelze, R. Dittmann, A. Engelhardt, and others, "Measurement of the Dynamic Error Rate of a High Temperature Superconductor Rapid Single Flux Quantum Comparator," Appl. Phys. Lett., Vol. 72 No. 18, pp. 2328-2331, 1998.

[5] J. Satchell, "Limitations on HTS SFQ Logic," Presented at the 1998 Applied Superconductivity Conference, Palm Desert CA, to appear in *IEEE Trans. Appl. Superconduct.*

[6] A. G. Sun, D.J. Durand, J.M. Murduck, S.V. Rylov, M.G. Forrester, B.D. Hunt, "HTS SFQ T-flip flop with directly coupled readout," Presented at the 1998 Applied Superconductivity Conference, Palm Desert CA, to appear in *IEEE Trans. Appl. Superconduct.*

Production of Gold Codes for a Spread Spectrum Modem Using SFQ Technology

Paul D. Dresselhaus, Eric J. Dean, John X. Przybysz, and A. Hodge Worsham
Northrop Grumman Science and Technology Center, 1350 Beulah Rd., Pittsburgh, PA 15235

Stas V. Polonsky
RSFQ Consulting Inc., Stony Brook, NY USA

Abstract—**We have designed, fabricated (in Nb-AlOx-Nb) and tested a Gold code generator using SFQ technology, a necessary component for a spread spectrum communications system with capacity for a significant number of users. Having over 500 Josephson junctions, this design represents a significant advance in the integration of JJ technology to perform more complex tasks. Two six-bit code generators (each producing 63 bit codes) were modulo-2 added with an SFQ XOR gate to produce the Gold code. Different Gold codes were created by varying the relative timing of the "Reset" signals sent to the two code generators.**

I. Introduction

Spread spectrum communications has been the method of choice for engineers designing 21st century wireless communications systems. In the spread spectrum communications system using code division multiple access (CDMA), multiple users are distinguished by their own code sequence encoding their data stream [1]. The encoding could consist of a high speed code pattern created by a pseudorandom binary sequence (PRBS) generator.

To keep different users from interfering with each other, each user is assigned their own unique code. For processing concerns, it is desired to use as long a code sequence as possible. However, for an n-bit PRBS generator, there are only n possible code sequences of maximal length.

This problem of a small number of code sequences is circumvented if we use two PRBS generators to create what are called Gold codes. Gold codes consist of two PRBS codes modulo-2 added with one another. The Gold code created then depends on (1) the two individual PRBS sequences (the sequences must not be time delayed replicas of one another) and (2) the time delay between the "start" of the two sequences. Using this scheme 2^n-1 possible Gold codes of length 2^n-1 may be created, with auto- and cross-correlation properties almost as good as individual PRBS sequences.

We have constructed a Gold code generator in Nb/AlOx/Nb using SFQ technology. This generator uses two hard wired six bit code generators with different feedback patterns to produce two different PRBS sequences which are then XOR'ed to produce a Gold code sequence. We may vary the timing between the start of the two PRBS sequences to produce different Gold code sequences. The Gold codes are analyzed in real time to determine the offset between the two PRBS sequences.

This paper will discuss Gold code generation. The details of code generation and data modulation may be found in more detail in Ref. [2].

Manuscript submitted April 26, 1999.

This work was supported by contract F19628-94-C-0097, funded by BMDO/IST and technically managed by Air Force Research Lab, Hanscom.

II. Circuit Design

The block diagram for the Gold code generator is shown in Figure 1. It consists of two six bit code generators and one XOR gate to combine the two codes. The code generators consist of a series of cascaded shift registers, one or more XOR gates and an inverter. Feeding back the output from different shift register stages produces different code patterns. The code patterns of interest are those of maximal length (= 63 for a six-stage shift register). There are six possible maximal length codes, half of which are time reversed. The feedback configuration for each code generator was hard wired to save space and pin count; four bit code generators have previously been designed with variable feedback configurations [2].

Each code generator has its own "Reset" line that enables or disables the operation of the code generator. The output of each code generator is sent to an XOR to produce the Gold code; each PRBS code generator output is also sent to its own 1X latching output for monitoring. The output of the Gold code XOR is sent to a latching 10X amplifier [3].

Both code generators and the Gold code XOR share a common clock. The individual code generators have timing concerns that dictate the clock distribution mechanism; details of these concerns for four bit code generators may be found in [2]. A more general discussion of clock distribution in cascaded shift register systems may be found in [4]. The

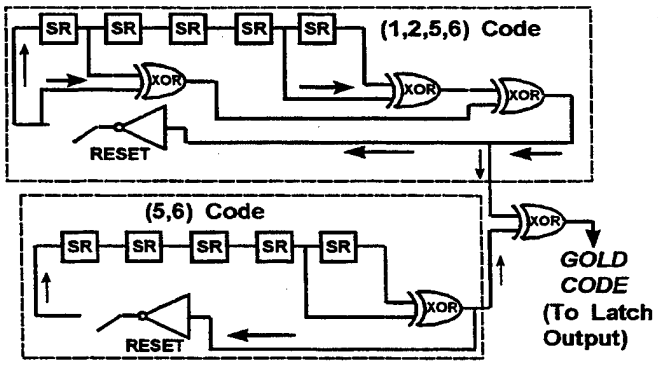

Figure 1: Block diagram for the Gold code generator. All of the cells share a common clock.

clock first releases the data in the last shift register stage in each code generator, next clocks the remainder of each code generator in parallel, and finally clocks the XOR for the Gold code. The chip layout is shown in Figure 2.

This Gold code design does not contain any circuitry to modulate data with the Gold code, however, modulation of data depends only on the operation of one XOR gate which is independent of the code generator circuit. Our success in modulating data with four- and six-bit code sequences in the past [2] suggests that the extra effort required to modulate data with a Gold code is minimal.

III. Testing Setup

The Gold code generator, consisting of two code generators XOR'ed together, is contained entirely on chip. All GHz signals come from a HP83624 RF frequency synthesizer fed through a phase shifter/splitter box. Both code generators share a common clock line. The output latches for the two code generators and the Gold code generator all share a common latch drive, however, each latching output contains its own DC tweak line, permitting slight optimization of each latch output. The HP frequency synthesizer also produced a 10 MHz reference signal used to trigger two HP8082A pulse generators and for a Tektronix 11801A digital sampling scope. With the exception of the trigger signal, the two pulse generators could operate independently of one another. The pulse generators provided "Reset" signals for the two code generators. The 1X latching outputs for the two individual code generators and the 10X latching output for the gold code generator were AC coupled (~10 MHz cutoff frequency) to the sampling scope. The circuit received DC biases from Tektronix VX4730 D/A boards contained in a Tektronix VX1410 mainframe. The D/A boards, A/D boards and the sampling scope were controlled by software written in LabView [5]. More details of our measurement techniques may be found in Ref. [6]. All measurements were performed in an unshielded environment.

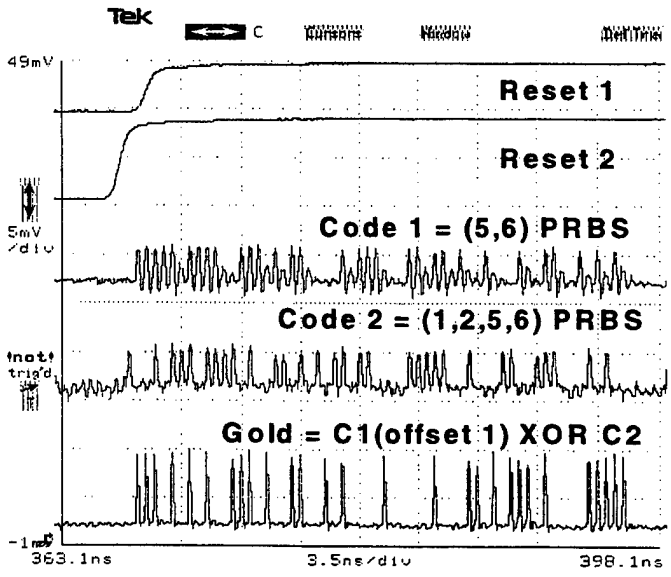

Figure 3: 63 bit Gold code generation at 2 GHz. Traces from top represent Reset (code generator #1), Reset (code generator #2), code (from code generator #1), code (from code generator #2) and the Gold code output..

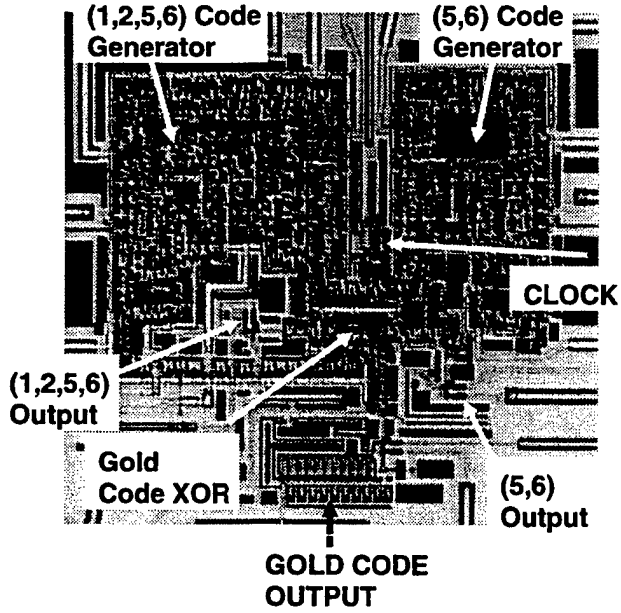

Figure 2: Gold code generator layout fabricated using the 1100 A/cm^2 Northrop Grumman Niobium process.

IV. Results

The results will be described in separate segments with the assistance of Figures 3 and 4.

A. *Individial PRBS Code Generation*

The individual code generators were set up in configurations feeding back either bits 5 and 6 (code generator #1) or bits 1, 2, 5, and 6 (code generator #2). The two individual code generators could be investigated independently of the other.

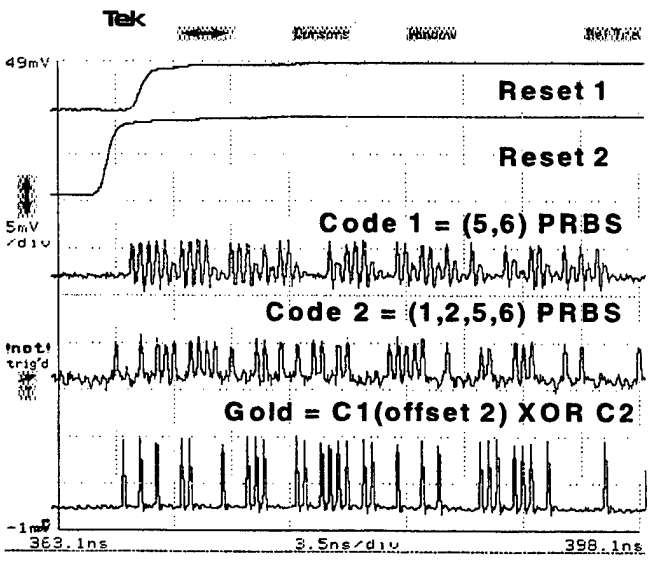

Figure 4: 63 bit Gold code generation at 2 GHz. The trace descriptions are the same as in Figure 5. The reset pulse for code generator #2 has been shifted one clock cycle earlier, allowing the production of a completely different Gold code.

B. Gold Code Generation

The Gold code output depends on the output of each code generator and the offset (in clock cycles) between them. This may be written as

$$GOLD[N] = CODE_1(N + N') \oplus CODE_2(N),$$

Where N (or N + N') represent bits in each code and ⊕ is the modulo 2 addition accomplished digitally by an XOR gate. N varies from 0 to the code length (63 for a six-bit code generator).

The outputs for each code generator and the output for the Gold code generator are shown in Figures 3 and 4. Each reset pulse enables its own code generator. One sees that by varying the timing between the individual code generators by a single clock cycle generates a completely different Gold code.

We have developed a method to check the correctness of the Gold code output using software written in LabView. The software enabled the computer to acquire a scope trace (as a series of (x,y) values), convert it to a digital form (a 1 or 0 output for every clock cycle), using the techniques developed previously to monitor the bit error rates of our PRBS code generators [6]. The software, given two six-bit code generator tap sequences, calculated these six-bit codes and then calculated all possible Gold codes by varying the timing between the individual codes and performing the modulo 2 addition. This software then determined whether the code from the scope trace matched a computer generated Gold code, and if so, what the timing difference between the two individual code generators (in clock cycles) was. A screen shot of the software front panel is shown in Figure 5.

We found that when running at 2 GHz the Gold code XOR was clocked one clock cycle later than the two code output stages of the individual code generators. The reason for this clock cycle delay is that the clock pulse must run through roughly 50 stages of Josephson Transmission line (JTL) looping around code generator #2 in order to reach the Gold code XOR, with an associated delay of roughly 500 psec. This clock cycle delay will not have any adverse effect on either of the code generators.

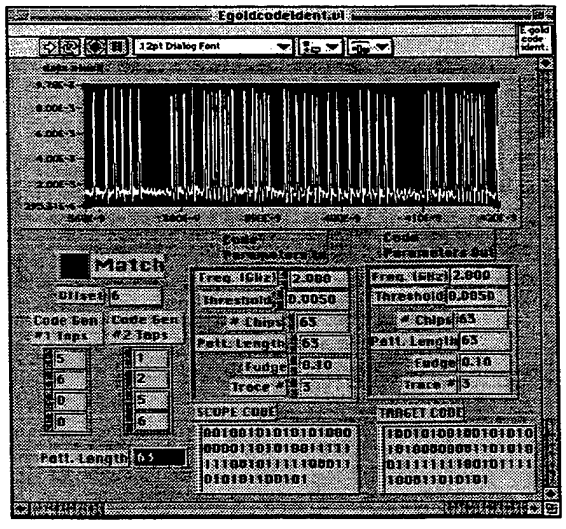

Figure 5: Front panel screen shot of the LabView software used to identify Gold codes created by our circuit.

C. Margins

Despite the fact that we now have two code generators operating as opposed to one, the margins for the individual bias lines were as good as for a single code generator. We expected that since there were only two major "connection" points for the two circuits - at the DC/SFQ clock generation and at the XOR Gold code generation. Both the DC/SFQ converter and the XOR gate have traditionally had very large margins. Individual bias margins ranged from ±18% to ±61%; the global bias margin was ±9%.

V. Conclusions

The construction of Gold codes is a significant accomplishment. This greatly increases the number of users that may be placed on a communications link independently. The simple creation of Gold codes from a mixing of two PRBS codes allows for a modular system design using previously developed code generator circuits. The individual code generator circuits, optimized through multiple design cycles, enable the production of a Gold code generator as robust as the individual units.

This circuit also represents an advance in terms of circuit design size. By optimizing small subcircuits, larger circuits may be constructed with minimal concerns about fabrication yield.

Acknowledgment

The authors would like to thank Dr. D.L. Miller for technical assistance, S.J. Pieseski for fabrication expertise, Dr. Dallas Hayes and Mr. John Turtle of the Air Force Research Laboratory for program guidance.

References

[1] Robert C. Dixon, *Spread Spectrum Systems*, 2nd ed., Wiley, 1984.

[2] P.D. Dresselhaus, E.J. Dean, J.X. Przybysz, and S.V. Polonsky, "Modulation and Demodulation of 2 GHz Pseudo Random Binary Sequence Using SFQ Digital Circuits," IEEE Trans. on Applied Superconductivity 9(2), (1999).

[3] J. X. Przybysz, D. L. Miller, S. S. Martinet, J. Kang, A. H. Worsham, and M. L. Farich, "Interface Circuits for Chip-to-Chip Data Transfer at GHz Rates," IEEE Trans. on Applied Superconductivity 7(2), pp. 2657-2660, (1997).

[4] C. A. Mancini, N. Vukovic, A. M. Herr, K. Gaj, M. F. Bocko and M. J. Feldman, "RSFQ Circular Shift Registers," IEEE Trans. on Applied Superconductivity 7(2), pp. 2832-2835 (1997).

[5] LabView is a trademark of National Instruments, 6504 Bridge Point Parkway, Austin, TX 78730-5039.

[6] E. J. Dean, P. D. Dresselhaus, J. X. Przybysz, A. H. Miklich, A. H. Worsham, and S. V. Polonsky, "Bit Error Rate Measurements for GHz Code Generator Circuits," IEEE Trans. on Applied Superconductivity 9(2), (1999).

Synchronous 5-10 Gb/s digital superconducting amplifier circuits fabricated with a horseshoe architecture

Willem J. Perold
Department of Electrical and Electronic Engineering, University of Stellenbosch, Stellenbosch, South Africa

Mark Jeffery
Department of Electrical Engineering and Computer Sciences, University of California, Berkeley CA 94720-1770

Abstract— At clock speeds beyond 5 GHz the direct, non-averaged, detection of superconducting circuit outputs is difficult. We have previously demonstrated synchronous digital amplifier circuits based upon stacked Complementary Output Switching Logic (COSL) gates. Various stacks were designed with outputs ranging from 3 mV to 6 mV, and the circuit designs were optimized for 5 - 10 GHz operation using a Monte Carlo method. The circuits were fabricated by HYPRES using a 2.5 kA/cm^{2}process, and were tested successfully at 5-10 GHz. However, the measured bit error rate was not acceptable for general applications. Subsequent analysis revealed that parasitic inductances in the layout, which were not included in the original Monte Carlo simulations, significantly reduce the theoretical yield of the circuit. This contributed to an increased bit error rate at ultra-high speed. We have therefore redesigned the amplifier layout using a novel horseshoe architecture. The horseshoe geometry minimizes the parasitic inductances and simulations show that the revised circuit should have a very high theoretical yield with 10 GHz clocks. Fabrication of the new circuit is in progress using the HYPRES 2.5 kA/cm^2 foundry, and we will present test results in the range of 1 GHz to 10 GHz.

I. Introduction

Typical output voltages of superconducting logic circuits range from about 0.1 mV to approximately 2.5 mV. We have previously demonstrated that Complementary Output Switching Logic (COSL) voltage-state gates are capable of delivering 2.5 mV into 50 Ω at frequencies ranging from 5-18 GHz [1], [2], [3] with a very low bit error rate (BER) ($<10^{-11}$ at 2 GHz).

At frequencies in excess of 5 GHz it is very difficult to interface such small voltages to external electronics and either on-chip or off-chip amplification is required to make non-averaged measurements a possibility. Off-chip amplifiers can be quite expensive and, due to the large bandwidth, also rather noisy. An on-chip amplifier thus seems to be an attractive solution, but difficult to implement, especially at high speed.

The first attempt at on-chip amplification was the Suzuki stack [4]. A Suzuki stack is very sensitive to variations in the critical current of the Josephson junctions. This can lead to a substantial reduction in the output voltage. Another serious drawback of the Suzuki stack is the inability to switch off at high frequencies when the clock goes negative. This is due to the relatively high shunt capacitances of the Josephson junctions when standard critical current density (J_c) fabrication processes (1 kA/cm^2 or 2.5 kA/cm^2) are used. Therefore, with a conventional 1 or 2.5 kA/cm^2 J_c process, with moderate parameter variations [5], the Suzuki stack is not a viable proposition for on-chip amplification at greater than 2 GHz.

However, amplifier circuits similar to the Suzuki stack have been fabricated with a high J_c (10 kA/cm^2) ultra-small-spread process developed at UC Berkeley [6]. In this case, the stack was demonstrated successfully at 10 GHz with a 4.5 mV output, and had a bit error rate less than 10^{-11} at 5 GHz [7]. The disadvantage of these high J_c circuits is that they require a multi chip module (MCM) in order to interface them with larger digital superconducting circuits fabricated using a conventional process.

In the present work we examine a new design for an on-chip amplifier. This circuit was designed to be robust to process variations, and able to operate at ultra-high-speed fabricated with a conventional 1 or 2.5 kA/cm^2 process. Two amplifier configurations based on stacked two-junction SQUID's have been proposed previously [8]. Unfortunately, after fabrication and testing, these circuits were found to have an unacceptably high bit error rate. In the present work the relative merits of the different configurations will be briefly discussed, and a novel horseshoe layout architecture will be presented that should solve most of the problems experienced with the initial layouts. The horseshoe architecture minimizes the parasitic inductances in the circuit. An advantage of the proposed amplifier circuit is that it can be integrated on the same chip with other high density digital circuits without using an MCM.

II. COSL stack with a single driver

A schematic circuit diagram of the amplifier configuration is shown in Fig. 1. The amplifier is similar to a stack of COSL gates, but a single one-junction SQUID is used to drive the four two-junction SQUID's. The inductance of the one-junction SQUID is therefore split in parallel to the control lines of each of the two-junction SQUID's. The nominal output voltage at 10 GHz was determined by simulations to be 5 mV. Intuitively, when the one-junction SQUID is switched, the currents in the one-junction SQUID inductances suppress the two-junction SQUID switching points equally. When Clock 2 is applied, the entire two-junction SQUID stack is easily switched.

The circuits were designed and fabricated using the HYPRES 2.5 kA/cm^2 process [9]. Monte Carlo yield anal-

Manuscript received April 30, 1999.

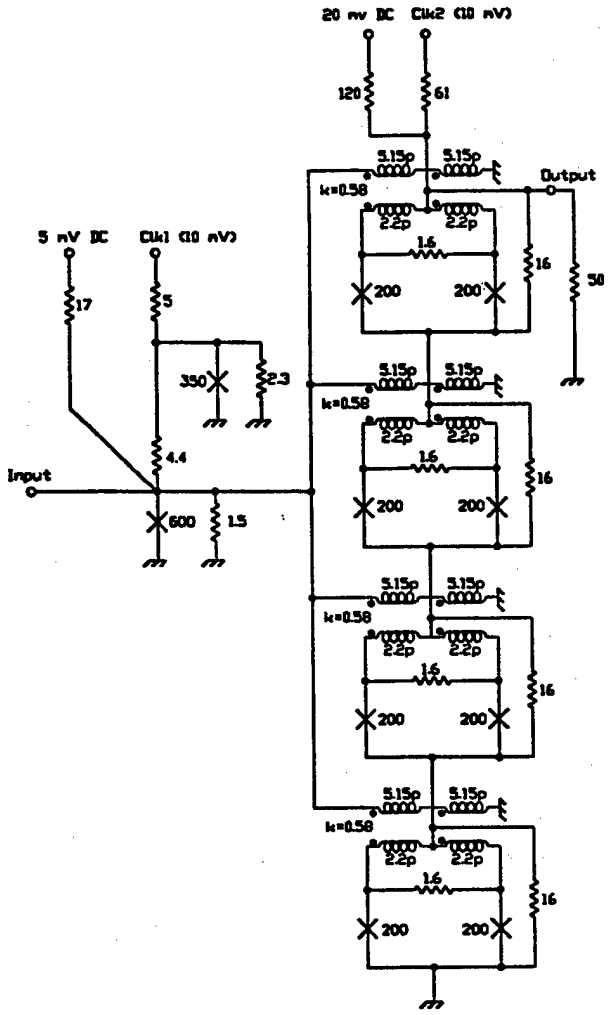

Fig. 1. Circuit diagram of a 4 SQUID stack amplifier with a single one-junction SQUID driver.

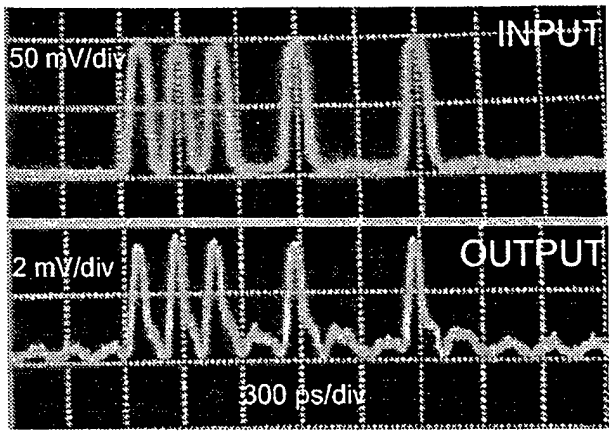

Fig. 2. Measured response of 4 SQUID stack amplifier to a pseudo-random bit sequence input at a clock frequency of 5 GHz. The measured data is averaged.

yses [5] were implemented at a clock frequency of 10 GHz, for 50 Monte Carlo cycles. The 3σ global variations on Josephson junction critical current density, resistance and inductance were taken as 10%, 15% and 15% respectively. The local 3σ variations on Josephson junction area, resistance and inductance were taken as 10%. The non-trimmed yield was calculated as 94%. With input trimming [10] the yield improved to 100%. These simulations neglect parasitic inductance of the one-junction SQUID lines connecting to the two-junction SQUID's.

The one-junction SQUID driver was laid out to ensure that each inductance branch, feeding the two-junction SQUID's in the stack, had the same inductance. However, it was suspected that the parasitic inductance in the inductance branches of the one-junction SQUID driver might cause a problem. Hence, an additional layout was fabricated which attempted to minimize the parasitic inductances.

In Fig. 2 the averaged measured performance of the stack amplifier is shown at a frequency of 5 GHz. The relatively large input voltage is sent through a resistive 50 Ω to 5 Ω matching network. When the probe attenuation is taken into account the output voltage is larger than 4 mV. Unfortunately, bit errors were clearly seen in the unaveraged output data, and the overall BER of the circuit was not acceptable for general applications.

As described in the following section, we resimulated the circuits, including the parasitic inductance, and found that the parasitic inductance indeed had a marked influence on the performance. We believe that the performance of the stack configuration can be substantially improved when an optimum layout is used, where parasitic inductances are kept to an absolute minimum.

III. Layout Considerations

The two original amplifier layout approaches are shown in Fig. 3. In the layout Fig. 3(a) the one-junction SQUID inductances form a tree and the parasitic inductances are equal. The parasitic inductances are estimated from SLINE [11] to be 4.1 pF. The second layout Fig. 3(b) was a first attempt to minimize the parasitic inductances. However, in this layout the parasitic inductances are not equal. The top and bottom parasitic parts are estimated as 1.9 pF, and the two inner portions as 0.64 pF.

In order to include the effect of non-optimum layout procedures on circuit yield, the parasitic inductances were modeled as lumped elements in the Monte Carlo analyses. The yield of the 4 SQUID stack with a single driver was determined for the two cases (Fig. 3), both for the 2.5 kA/cm^2 process. The respective untrimmed yields for 50 Monte Carlo cycles at a frequency of 10 GHz were 34% and 66%. With input trim the yields were calculated as 34% and 78% respectively. The drastic increase in yield when the parasitic inductance of the driver circuit is reduced, clearly demonstrates the importance of minimizing parasitic inductance.

In order to optimize the layout of the 4 SQUID stack with a single driver, we completely revised the layout with

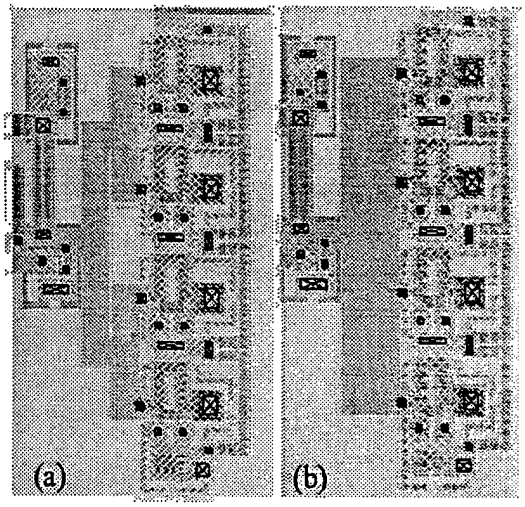

Fig. 3. Two different layout approaches for the inductive portion of the driver circuit. On the left (a) the inductances are made equal, and on the right (b) attempts were made to minimize the total parasitic inductances. Only portions of the respective layouts are shown.

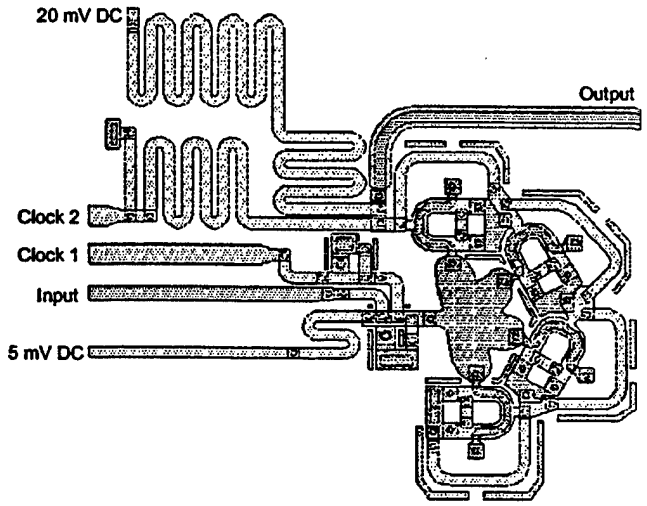

Fig. 4. Optimized horseshoe architecture of 4 SQUID stack amplifier. The output feeds an off-chip 50 Ω load resistor. Rounded structures are used to minimize local electromagnetic field concentrations.

the goal of minimizing the parasitic inductance. The parasitic inductances were minimized by folding the stacked two-junction SQUID's in a horseshoe pattern, as shown in Fig. 4. This novel design ensures equal parasitic inductance in each of the four inductive branches. The parasitic inductance in each branch was calculated by SLINE as approximately 0.7 pF, which gives a noticeable improvement when compared to the values for the previous layouts. The rounded Josephson junctions and resistor structures are noticeable.

The untrimmed yield of the new layout, including the parasitic inductances, was calculated as 92% for 50 Monte Carlo cycles. The yield increased to 98% with input trim. This is a vast improvement in yield when compared to the other layouts. The curved resistors and transmission lines in the layout have the additional advantage of minimizing the electromagnetic field concentrations. Test results of this new amplifier layout will be reported at the ISEC99 conference.

IV. Summary

We demonstrated how parasitic layout inductances can adversely affect the measured performance of superconducting stack-amplifier circuits. Parasitic layout components, which were not part of the original circuit design, can lead to unacceptable bit error rates in real applications. We have proposed a novel horseshoe amplifier structure to minimize the parasitic inductances in our stacked COSL output amplifier. This optimized layout has excellent theoretical yield and demonstrates the importance of good layout procedures when operating in the microwave regime.

References

[1] M. Jeffery, W.J. Perold, and T. Van Duzer, "Superconducting complementary output switching logic operating at 5-10 Gb/s", *Appl. Phys. Letters*, vol. 69, pp. 2746-2748, 1996.

[2] M. Jeffery, W.J. Perold, and T. Van Duzer, "Experimental Demonstration of Complementary Output Switching Logic Approaching 10 Gb/s Clock Frequencies", *IEEE Trans. on Appl. Superconductivity*, vol. 7, pp. 2665-2668, 1997.

[3] M. Jeffery, W.J. Perold, and T. Van Duzer, "Superconducting complementary output switching logic circuits operating at 18 GHz", unpublished.

[4] H. Suzuki, A. Inoue, T. Imamura, and S. Hasuo, "A Josephson driver to interface Josephson junctions to semiconductor transistors", *Dig. Tech. Papers*, Int. Electron Devices Meeting, pp. 290-293, 1988.

[5] M. Jeffery, W.J. Perold, Z. Wang, and T. Van Duzer, "Monte Carlo optimization of superconducting Complementary Output Switching Logic circuits", *IEEE Trans. on Appl. Superconductivity*, vol. 8, pp. 104-119, 1998.

[6] X. Meng, A. Bhat, and T. Van Duzer, "Very low critical current spreads in Nb/AlOx/Nb integrated circuits using low temperature and low stress ECR PECVD silicon oxide films", *IEEE Applied Superconductivity Conference*, Palm Desert, California, 13-18 September 1998.

[7] A. Bhat, X. Meng, S. Whiteley, M. Jeffery, and T. Van Duzer, "A 10 GHz digital amplifier in an ultra-small-spread high-J_c Nb/Al-Alx/Nb integrated circuit process" *IEEE Applied Superconductivity Conference*, Palm Desert, California, 13-18 September 1998.

[8] W.J. Perold, M. Jeffery, and T. Van Duzer, "Synchronous Superconducting Amplifier Circuits for 5 - 10 GHz Applications", *IEEE Applied Superconductivity Conference*, Palm Desert, California, 13-18 September 1998.

[9] HYPRES, 175 Clearbrook Road, Elmsford, New York, 10523. Phone: (914) 592-1190. Design rules are available via the HYPRES home page at http://www.hypres.com.

[10] W.J. Perold, M. Jeffery, Z. Wang, and T. Van Duzer, "Complementary Output Switching Logic - A new superconducting voltage-state logic family" *IEEE Trans. on Appl. Superconductivity*, vol. 6, pp. 125-131, 1996.

[11] Whiteley Research Inc., 456 Flora Vista Avenue, Sunnyvale, CA 94086. Homepage: http://www.srware.com

Oral Session 4

Analog Filters and Subsystems

Can Low-Cost, High-Reliability Cryocoolers be a Reality?

M. Nisenoff
Nisenoff Associates
5605 Whitney Mill Way, Suite 302
North Bethesda MD 20852-3141 USA
- 1 – (301) 984 - 0833: - 1 – (301) 984 - 3325 FAX: m.nisenoff@ieee.org

Abstract - Now, and in the foreseeable future, superconductivity will be a cryogenic technology. Accordingly, to bring superconducting electronic technology to the market place, the superconducting technologist must consider the *entire* system, that is, the superconducting and associated conventional components (if they are also operated at cryogenic temperatures), the cryogenic enclosure as well as the cryogenic refrigeration system. The development of cryogenic refrigerators ("cryocooler") has, to date, be driven by the needs of the infrared (IR) detector and the cryogenic vacuum pump communities. Much progress has been made in the past two decades on improving efficiency, increasing lifetime and, in some cases, lowering cost. A general overview of the status of cryocoolers, available on the open markets and under development, will be presented along with data on what has been achieved on efficiency, reliability and how the cost of these cryocoolers might be reduced. General trends on efficiency, input power, mass, volume and cost of cryocoolers will be presented. With sufficient market pull, cryocoolers can become available in a configuration that will enable the technologist to integrate these cryocoolers with the cryogenically cooled electronic components such that the cryogenic aspects of the *total* system will be ***transparent and invisible to the end user.***

I. INTRODUCTION

During the past thirty years, there has been considerable excitement in the scientific world about the very unique properties of the superconducting state and on the very exciting electronic applications that might be realized from the use of this technology. For example, SQUID magnetic sensors have found many potential applications in medical diagnostics, Non-Destructive Evaluation (NDE), geophysical exploration, etc. The concept of a very high performance superconducting digital computer had been explored in both the USA and Japan. After the discovery of high temperature superconductivity, there was an explosion of interest as these materials could be operated at temperatures near the boiling point of liquid nitrogen at atmospheric pressure. Many of the applications previously explored using low temperature superconducting materials were re-explored using the high temperature materials and many new and exciting applications have been proposed.

Despite the fact that High Temperature Superconductivity (HTS) materials could be operated at much higher temperatures than Low Temperature Superconductivity (LTS) materials, superconducting electronics remains a cryogenic phenomenon. Most the demonstrations of superconducting applications, either LTS or, later, HTS, used liquid cryogens to provide the required refrigeration. In the laboratory, liquid cryogens may be acceptable but in most deployments outside the research laboratory, the logistics of providing a supply of liquid cryogen is considered to be a very serious barrier to the introduction of superconducting electronics into the commercial market place. In order to insure that superconducting electronics can be successfully introduced into the commercial marketplace closed cycle, mechanical cryogenic refrigeration systems ("cryocooler") must be integrated with the superconducting components to make a complete package in which the cryogenic nature of the equipment is ***invisible to the user***. The use of cryogenics and superconductivity in electronic applications must be "transparent" to the user if the superconductive equipment is to penetrate into the commercial marketplace. The objective of this manuscript is to present the basic concepts of mechanical cryogenic refrigeration systems, and to present data on the electrical input power and mass of cryocoolers operating in the 60-80 K temperature range and, finally, to present the trends in the characteristics of cryocoolers as a function of operating temperature and cooling capacity.

Manuscript received on 5 May 1999.
Work done while author was at the Naval Research Laboratory, Washington DC 20375-5347 USA

II. CRYOGENIC REFRIGERATION PERFORMANCE.

In this manuscript, we will deals only with the most general concept of a cryogenic refrigeration system and only stress technological trends. For more detailed discussions of the various thermodynamic cycles and their implementation in cryogenic refrigerators, the reader is refereed to a number of text books and the proceedings of technological conferences on cryogenic refrigeration.

In the most general terms, a closed cycle mechanical cryogenic refrigerator ("cryocooler") can be treated as a machine that extracts an amount of heat Q_L from some low temperature station, T_L and reject an amount of heat Q_H, at some higher temperature T_H while an quantity of work W is consumed in moving the heat from the cold to the hot temperature station. As can be found in any elementary thermodynamics textbook, the efficiency for this process, known as the Carnot Efficiency, can be written as $(T_H-T_L)/T_L$. This assumes that all processes performed during the thermodynamic cycle are done in a reversible manner. Since all real machines have irreversibility losses, a real machine will have an efficiency inferior to that predicted by the Carnot Relationship.

In the case of a real cryocooler with a given cooling capacity, the efficiency that can be realized is dependent on many factors, such as operating (cold) temperature, friction between moving components, electrical losses in motor windings, etc.

(1) If the characteristics of cryooolers are examined, it can be seen that the efficiency for a given cooling capacity will vary with the operating (cold) temperature. For example, a 1 Watt cryocooler with operating (cold) temperature near 77 K will have an efficiency near 7 percent of Carnot, while, for a 1 Watt cryocooler operating near 4 K, an efficiency near 2 percent of Carnot is typical.
(2) The efficiency of cryocoolers varies with overall cooling capacity. For cryocoolers with very large cooling capacities (greater than 1,000 Watts), efficiencies approaching 30 percent of Carnot independent of operating temperature can be achieved while for cryocoolers operating near 77 K with cooling capacities of 1 Watt, have efficiencies near 7 percent but only 2 percent of Carnot Efficiency for 4 K cryocoolers.
(3) If the characteristics of cryocoolers operating at a given temperature are examined, the electrical input power does not vary proportionally with cooling capacity as one would expect from the Carnot Relationship but increase as the cooling capacity to the 0.8 power.

In the open literature and based on manufacturer's brochures, one can prepare a plot for cryocoolers operating in the 60-80 K temperature range. In Figure 1, data for a large number of such cryocoolers is plotted as electrical input power (left hand vertical axis) and mass (right hand vertical axis) as a function of cooling capacity of the cryocooler. The cooling capacities ranged from 0.15 Watts to 350 Watts. The line of slope one (represented by dots) represents the electrical input power as a function of cooling capacity IF the efficiency is independent of lift and has a value of 30 percent Carnot, the value commonly found for very large cryocoolers. The data points (square dots) for electrical input power is above the 30 percent Casrnot line for low cooling capacities and approaches the 30 percent line at high cooling capacities. This indicates that the actual efficiency of cryocoolers is near 30 percent of Carnot for large cooling capacity decreasing as the lift decreases. (See item (2) immediately above.) The slope of the line through the data points (downward pointing triangles) representing the mass of the cryocooler are also shown with a trend line (short dashes) drawn through the triangles. The trend lines for both the electrical input power as a function of cooling capacity and the mass as function of cooling capacity both can be represented by power laws with slope of 0.8. (See item (3) immediately above.) Power law dependences with slope 0.8 are frequently observed when cryocooler data is plotted. There is no known scientific rationale for such a power dependence.

If one combines the above trends with information obtained from the open literature and from manufacturer's brochures, one can prepare a plot (see Figure 2) showing the trends that the input power and mass of cryogenic refrigerators as a function of operating temperature for several values of cooling capacity. The shaded areas on the curve for 1Watt cooling capacity indicates the spread of input power data for 77 K (determined from Figure 1), 35 K, 20 K 10 K and 4 K cryooolers that have been built. The curves for cooling capacities other than the 1 Watt have been scaled from the 1Watt curve according to an experimentally deduced trend that the electrical input power and mass for cryocoolers operating at a given temperature, varies approximately as the 0.8 power of the cooling capacity, (See Item (3)immediately above and Figure 1.)

The plot of the type shown in Figure 2 should be very helpful to superconducting technologists. If a technologist would like to estimate values for the electrical input power and mass of a cryoooler operating at a given temperature and with a given cooling capacity, this plot can provide this information. Selecting a given operating temperature (from the bottom (horizontal) scale) and then moving vertically upward to the appropriate load line curves, the coordinate of this point taken from the left hand vertical scale is the approximate electrical input power

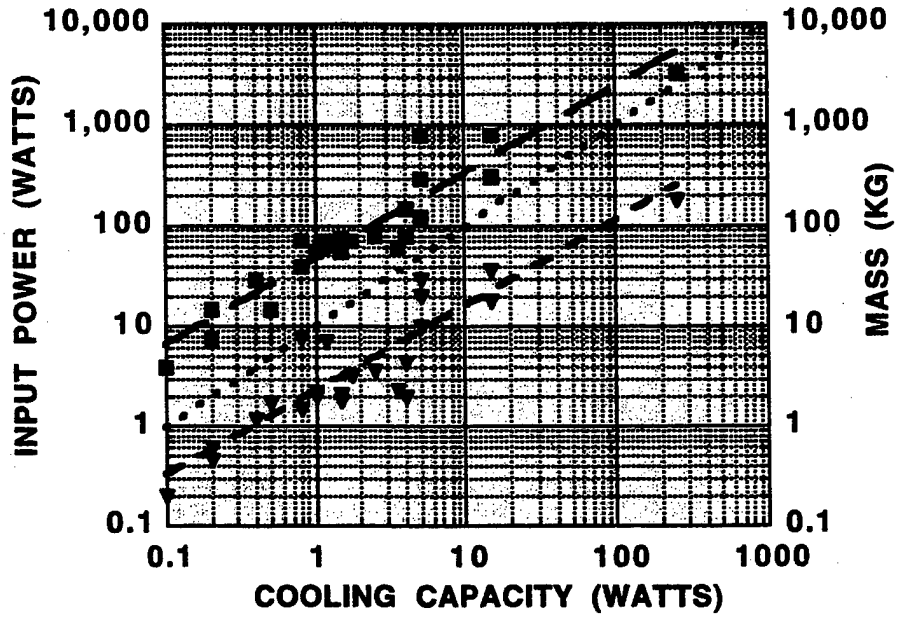

Figure 1. Plot of electrical input power (square symbols) and mass (downward pointing triangles) for a number of commercially available cryocoolers with design point operating temperature between 60 K and 80 K. The dotted line with slope 1 on log-log plot represents efficiency as function of cooling capacity for cryocoolers having efficiencies of 30 percent of Carnot, independent of cooling capacity

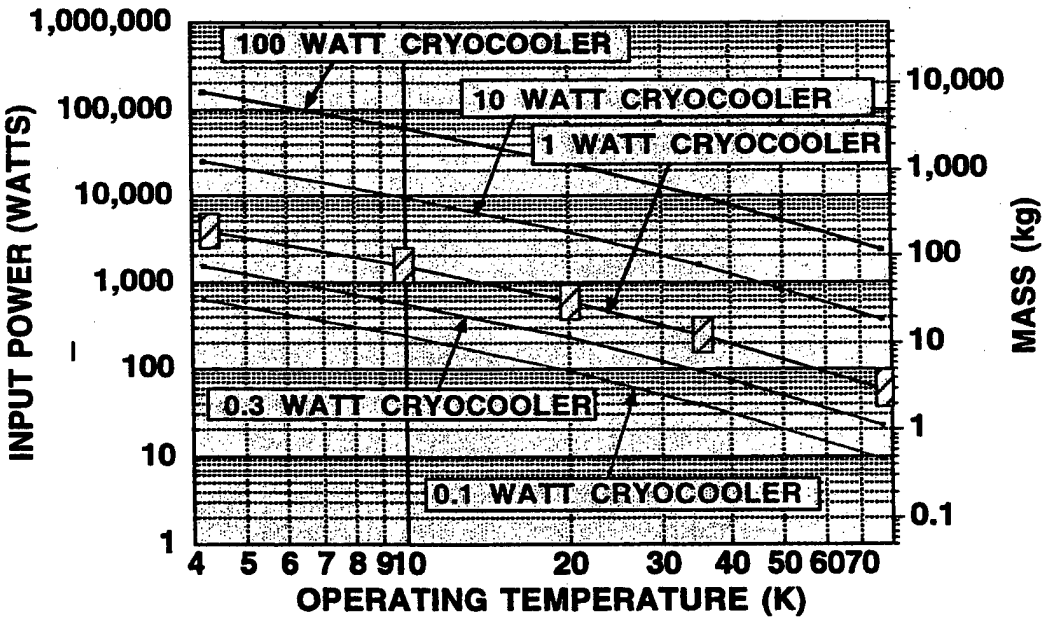

Figure 2. Plot of the electrical input power and mass of cryocooler operating at various cold temperatures and cooling capacities. The shaded areas on the 1 Watt cooling capacity curve shows the spread in values of electrical input power for cryocooler operating at the indicated temperature. The 1Watt curve is based on data from available cryocooler while the curves for other cooling capacities are scaled from the 1Watt curve using trends determined from cryocooler data.

while the coordinate of the point read from the right hand vertical scale indicates the approximate mass of a nominal cryocooler with the specified cooling capacity and operating temperature.

Figure 2 can also provide insight on how the characteristics of cryogenic refrigerators vary with the operating temperature and with the heat load. If an operating point on one of the cooling capacity curves has been specified, one can estimate the increase in electrical input power (and associated mass) if the operating temperature were to be lowered or estimate the decrease in input power and mass if the operating temperature were raised. Similarly, at a given operating point, one can estimate the increase in electrical input power (and associated increase in mass) as the required cooling capacity is raised, possibly, due to poor thermal design of the package containing the superconducting components and how the input power and mass of the cryocooler could be decreased with a more efficient thermal design of the package.

III. CRYOCOOLER RELIABILITY

Another crucial aspect of systems in which cryocooalers are integrated with superconductive electronic components is the ***reliability of the cryocooler.*** Although cryocoolers are quite complex mechanical systems, there are a number of examples of comparably complex mechanical systems that have achieved remarkable operating lifetime. For example, most household refrigerators operate reliably for more than 20 years, while, VCR video players, that have very close tolerances, can function reliably for times much longer than five years. Hence, there is an excellent chance that similar level of reliability or operating lifetime may be achieved for cryogenic refrigerators. ***The secret to long operating lifetime for household refrigerators and VCR's has been large scale production*** where expensive non-recurring expenses required for manufacturing and aligning the critical components in these systems can be amortized over a large number of units and thus reduce unit price. Hence, large cumulative production of cryocoolers should also promote drastically increased operating lifetimes.

IV. OST OF CRYOCOOLERS

Another concern frequently raised about the use of cryogenic refrigeration systems with superconducting electronic applications is the relatively high cost of typical cryocoolers, which, when purchased in single or small quantities. The cost of a small 77 K cryocooler maybe approximately 5,000 US$ while a large capacity (about 10 Watt) 77 K cooler or a 1 Watt cryocooler operating near 4 K may cost between 30,000 US$ and 40,000 US$. In the area of industrial engineering, there is a quantity known as the "Learning Curve" which is a measure of the reduction in manufacturing cost with increased cumulative production of the particular item. For items such as automobiles and (small) electrical machinery, the Learning Curve has a value of about 80 percent; that is, as the cumulative quantity of the item is doubled, the cost will be reduced to 80 percent of the previous cost. The value of Learning Curves for a given product depends very crucially on the complexity of the item and many other factors but tends to range between about 75 percent to 85 percent. It is possible to make prediction on the possible cost of cryocoolers made in large quantity by assuming that the value of the Learning Curve will be about 80 percent, and that the cost of a "typical" cryocooler in small quantity production will cost about 20,000 US$. Under these assumption, the cost of a "typical" cryocooler would decrease from 20,000 US$ per unit in small quantity production to about 3,000 US$ per unit for production of 1,000 units per year and below 1,000 US$ per unit for production of 100,000 units per year! ***Hence, the reality of low cost, high reliability cryogenic refrigerators depends crucially on the quantity of cryogenic refrigerators manufactured, the large the quantity manufactured, the lower the price and the more reliable the cryocooler.***

CONCLUSION

In this paper, we have briefly reviewed the current status of cryogenic refrigerators ("cryocoolers") and have presented several trend charts illustrating the variation of electrical input power and mass of cryocoolers as a function of operating temperature for several values of cooling capacity. It was also demonstrated that the cost of cryocoolers would decrease and the operating lifetime increase with increasing cumulative quantity of cryocoolers manufactured. These tendencies would be consistent with experience in the manufacturing of other systems, such as household refrigerators, VCR video players, induction motors and computer memory cells. Thus the issue of low cost, high reliability cryogenic refrigeration systems ("cryocooler") is an example of the paradox of "which came first, the chicken or the egg". ***If superconducting electronic technology is to be a commercial success, the cryogenics must be "transparent" to the user, which means the cryoooler must be low cost and be highly reliable.*** However, to have low cost, highly reliable cryooolers available for use with superconducting electronic systems, the cryocooler must be manufactured in large quantity!! It is the responsibility of the superconducting electronic community to formulate an approach that will resolve this paradox.

A Superconducting RF Three-pole Filter in HF Range

Erzhen Gao, Shapur Sahba [+], Hui Xu, Q. Y. Ma
Electrical Engineering, Columbia University, New York, NY 10027
[+] Also with U.S. Army, HQ-CECOM, Ft. Monmouth, NJ 07703

Abstract — A new RF 3-pole filter operating at high frequency (HF, 3-30 MHz) was designed and fabricated. The filter is of small size and has a high Q-value than conventional copper filter. The key for the 3-pole filter design is the utilization of three identical high temperature superconducting (HTS) distorted spiral resonators. The three spirals are patterned and fabricated on a two-inch HTS wafer. Each spiral contains 25 turns with homogenous separation between adjacent turns. The distances between three spirals were designed so they were mutually coupled and a low insertion loss (0.7 dB) was obtained. Three poles were found at about 18 MHz with insertion of about -0.7 dB and reflection about -15 dB. The flexibility of the new filter design provides us with easy ways to improve our design.

I. Introduction

Devices fabricated on HTS thin films have been investigated since the discovery of HTS materials [1]-[2]. Most of them are microstrip or cavity structures in the frequency range of GHz used in microwave communication partly because of the size limitation of the HTS film [3]-[4]. The major advantage of using HTS materials to make filters is their promise of high Q-value due to low electrical loss. However, it is impossible to design a filter using conventional quarter-wavelength parallel-coupled approach with a frequency in the range of MHz on a HTS substrate because its size is usually limit to 2~3 inches. One way to realize the low frequency filter on limited wafer size is the lumped-element approach [5]. Several structures of resonators have been developed for magnetic-resonance imaging receiver coil at a frequency as low as few MHz with high Q (>10^4) [6], [7]. Self-resonant spiral resonators have been used to build a three-port RF filter [8]. However, the insertion loss was high.

A new self-resonant spiral resonator at 18 MHz was designed. Based on this resonator design, a three-pole filter was designed, fabricated, and tested. The insertion of this filter is –0.7 dB, compared with the previous design of about –2 dB [8].

Manuscript received April 30, 1999

This project was sponsored by the Naval Research Laboratory (NRL), Washington, D.C., under the contract #N00014-96-1-G017.

II. Three-Pole HTS Filter

The basic element used in our filter design is a spiral resonator which is patterned and fabricated on a two-inch wafer with an HTS thin film (300 nm YBCO on LAO substrate with 0.508 mm of thickness). The spiral contains 25 turns with homogenous separation between adjacent turns, as shown in Fig. 1.

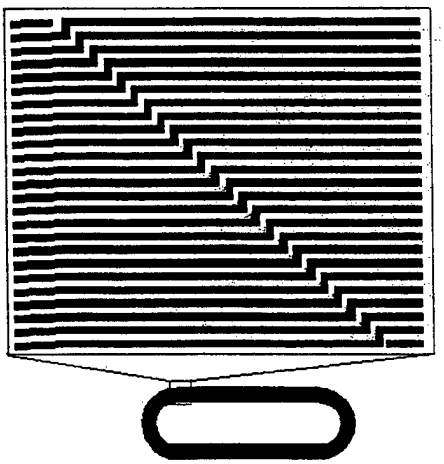

Fig. 1. A 25-turn spiral resonator at 18 MHz was designed as the basic element used in a three-pole filter. It was fabricated on a wafer with a high-temperature superconducting thin film.

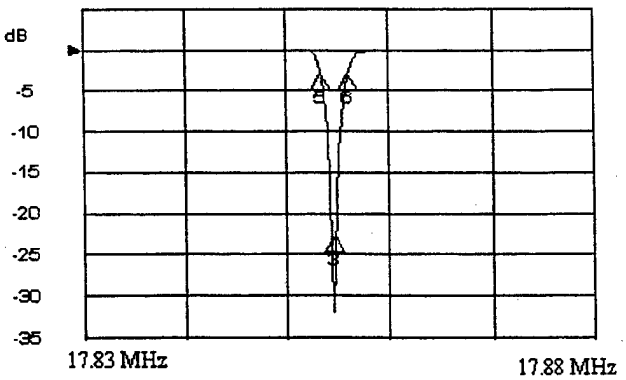

Fig. 2. Measurement the reflection of a 25-turn spiral resonator at 18 MHz.

A spiral resonator was tested at 77 K with a copper coupling loop. The reflection of this spiral resonator is shown in Fig. 2. The resonant frequency is 17.855 MHz and unloaded Q-value is over 13,000.

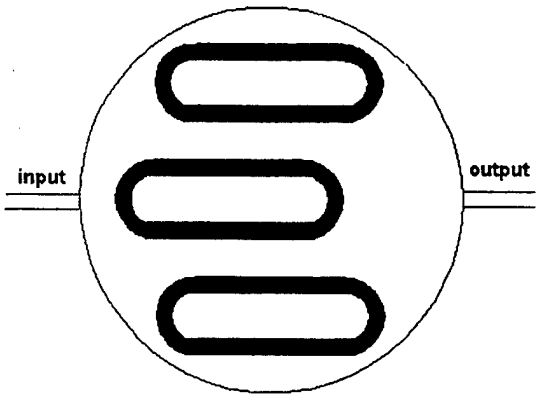

Fig. 3. A three-pole filter make of three resonators and two coupling loops, in which each resonator contains a 25-turn spiral.

A three-pole filter consists of three identical spiral resonators placed side by side on a 2-inch HTS film, as shown in Fig. 3. It was tested at 77 K. Three peaks were found around 18 MHz with a low insertion about –0.7 dB as shown in Fig. 4. The results of these three filters are summarized in Table 1.

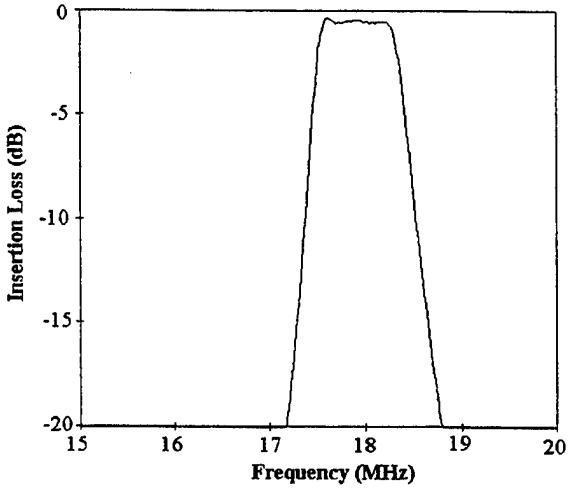

Fig. 4. Return loss (S_{11}) and insertion loss (S_{12}) of an HTS three-port filter.

TABLE 1. SUMMARY OF THREE DIFFERENT 3-POLE FILTERS

	Peak #1		Peak #2		Peak #3	
	S_{11}	S_{21}	S_{11}	S_{21}	S_{11}	S_{21}
f(MHz)	17.63		17.93		18.18	
loss(dB)	-18.36	-0.38	-19.34	-0.44	-21.21	-0.56

III. MODELING AND SIMULATION

The self-resonant spiral resonator was simulated using an equivalent circuit with lumped elements as shown in Fig. 5. In the circuit, V represents source, R_1=50 Ohm, the input resistance; R_2 the loss resistance of the spiral, C_2 the effective inter-turn capacitance, L_1 the inductance of the pick up loop, and L_2 the effective inductance of the spiral. The inductance were calculated by

$$L_2 = 0.03937\frac{a^2n^2}{8a+11w} \qquad (1)$$
$$L_1 = \frac{1}{n^2}L_2$$

where L are in nanohenry, a is an radius of a circular spiral, w the width of the spiral, and n the number of turns of a spiral, as shown in Fig 5. The effective radius of our noncircular spiral was calculated by

$$a = \sqrt{\frac{\text{aear of a spiral}}{\pi}} \qquad (2)$$

The coupling between L_1 and L_2 was described by a mutual inductance, M_{12}. As an approximation, M_{12} was calculated by

$$M_{12} = knL_1 \qquad (3)$$

where nL_1 is the mutural inductance when L_1 is placed on the top of L_2 and k is a matching coefficient between L_1 and L_2. The circuit can be analysed by

$$R_1I_1 + j\omega L_1I_1 + j\omega M_{12}I_2 = V$$
$$j\omega M_{12}I_1 + j\omega L_2I_2 + \frac{1}{j\omega C_2}I_2 + R_2I_2 = 0 \qquad (4)$$

where $\omega=2\pi f$ is angular frequency and $j=\sqrt{-1}$. The circuit was simulated and the reflection as a function of frequency and matching coeficient is shown in Fig. 6

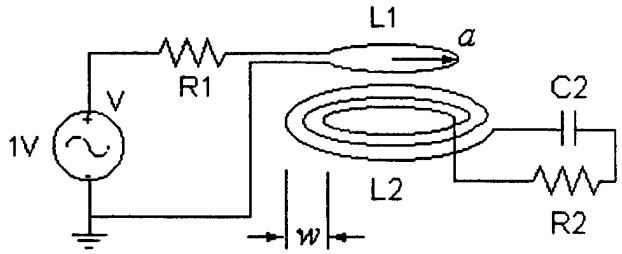

Fig. 5. Model of the self-resonant spiral resonator

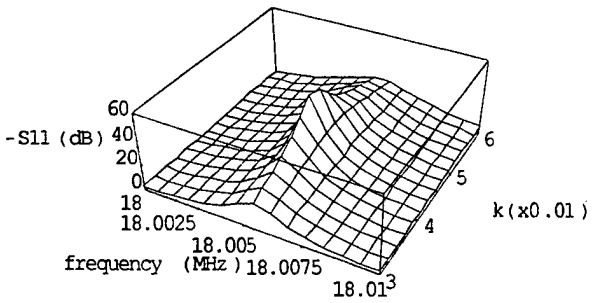

Fig. 6. The reflection of a self-resonant spiral resonator as a function of frequency and matching coefficient, k, between the pick-up loop and the resonator.

Simular to the self-resonant spiral resonator, a three-pole filter was simulated by a circuit model that is shown in Fig. 7 and the results of reflection and insertion are shown in Fig. 8 and Fig. 9.

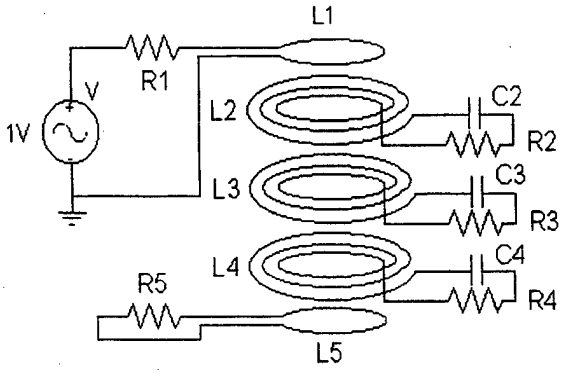

Fig. 7. A model of three-pole spiral filter.

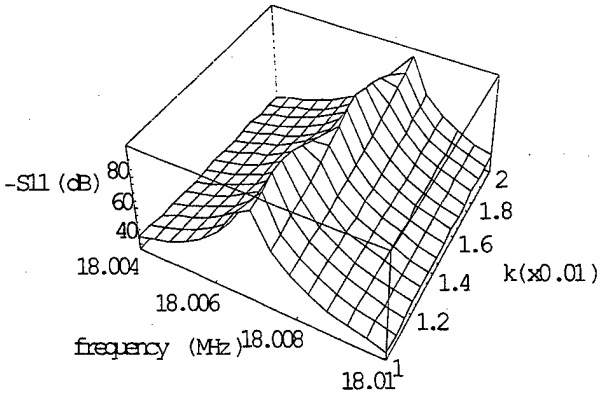

Fig. 8. The reflection of a three-pole spiral filter as a function of frequency and matching coefficient, k, between the coils and pick-up loops.

ACKNOWLEDGMENT

The authors would like to thank Jim DeMarco and Hybrid-Tek, Inc. for their assistance in packaging the devices.

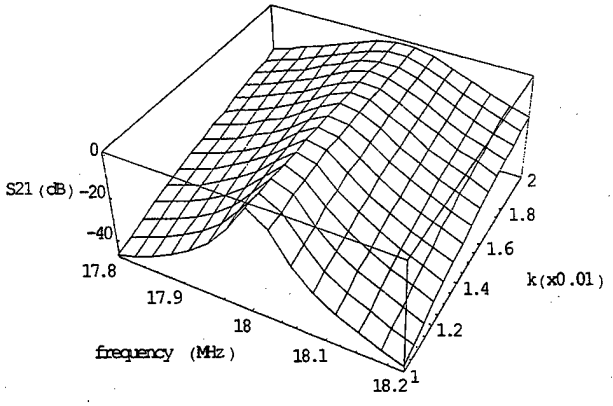

Fig. 9. The insertion of a three-pole spiral filter as a function of frequency and matching coefficient, k, between the coils and pick-up loops.

REFERENCES

[1] M. Rolfes, "Superconductors: the wireless industry comes of age," *Superconductor Industry*, pp. 24-30, Winter 1995.

[2] N. Newman and W. G. Lyons, "High-temperature superconducting Microwave devices: fundamental issues in materials, physics, and engineering," *J. Superconduct.* Vol. 6, no. 3, pp. 119-58, 1993

[3] R. R. Mansour and Andre Zybura, "Superconducting millimeter-wave E-plane Filters," *IEEE Trans. Microwave Theory Tech.*, vol. 39, no. 9, pp. 1488-92, Sept. 1991.

[4] G.-C. Liang, D. Zhang, C.-F. Shih, M. E. Johansson, and R. S. Withers, "High-power high-temperature superconducting microstrip filter for cellular base-station applications," *IEEE Trans. Appl. Superconduct.*, vol. 5, no. 2, pp. 2652-55, June 1995.

[5] D. Zhang, G.-C. Liang, C.-F. Shih, R. S. Withers, M. E. Johansson, and A. D. Cruz, "Compact forward-coupled superconducting microstrip filters for cellular communication," *IEEE Trans. Appl. Superconduct.*, vol. 5, no. 2, pp. 2656-9, June 1995.

[6] R. S. withers, G.-C. Liang, B. F. Cole, and M. Johansson, "Thin-film HTS probe coils for magnetic-resonance imaging," *IEEE Trans. Appl. Superconduct.*, vol. 3, no. 1, pp. 2450-3, March 1993.

[7] J. R. Miller, Ph.D. Dissertation, May of 1998, Columbia University, New York, NY10027.

[8] Erzhen Gao, Shapur Sahba, Hui Xu, Q.Y. Ma "A Superconducting RF Resonator in HF Range and its Multi-pole Filter Applications" to be published in IEEE Trans. App. Supercon. June 1999.

Design and Fabrication of Narrow-band Compact Configuration Hairpin Filters

S. Ohshima, T.Tomiyama, T. Kimpara, M. Kusunoki and M.Mukaida
Department of Electrical and Information Engineering, Yamagata University, Yonezawa 992-8510 Japan

Abstract—In order to reduce the size of a filter we have investigated a cross-coupled filter which is one of the elliptic filters. We designed a four-resonator cross-coupled bandpass filter with a resonance frequency, fr, 5GHz, band width, 4% and 1 %, and ripple 0.01dB by computer simulator. It was found by simulation that skirt property and attenuation value at out of band of the cross-coupled filter were superior to that of conventional half-wave length hairpin filters. We fabricated the superconducting four-resonator cross-coupled filer and measured the filter properties. The skirt property and bandwidth quite agreed with simulated values. We found that elliptic filters are superior to Chebyshev filters to reduce size.

I. Introduction

Superconducting bandpass filters are expected to be small insertion loss, sharp skirt property, low pass band ripple and high attenuation at out of band [1-3]. We need many resonators in the filter to realize such properties, however, the size of filters is restricted, because it is yet very difficult to fabricate large size high-temperature superconducting films (HTS films). So, we must examine to reduce the size of filters. Enokihara et al reported the miniaturized hairpin filters [4]. They could fabricate four-element hairpin bandpass filter with fr 1.5 GHz using 12 x 12 mm² YBCO film on LaAlO3 substrate using approximately 1/10 wave length hairpin resonator. On the other hand, It is well known that elliptic function filters with small number of resonators can exhibit sharp skirt property [5]. So, we are investigating the cross-coupled filter which is one of elliptic filters [6]. We show the simulation and experimental results of 5 GHz HTS cross-coupled filter in this paper. The comparison of filter properties between a cross-coupled filter and a Chebyshev hairpin filter is also discussed.

II. Design and Simulation

Fig. 1 shows the calculated performance of a lowpass filter calculated by Chebyshev and elliptic functions. In this calculation, we use following specifications; number of resonator =4, ripple magnitude = 0.12 dB. It is found that the elliptic filter show sharp stopband response compared with that of Chebyshev filter. Fig. 2 shows the configuration of four-resonator cross-coupled and conventional hairpin filters (Chebyshev filter). We designed the configuration of both filters by an electromagnetic analysis simulator, Sonnet EM. It is very important to decide the value of c an d to get good response. The value of c and d were determined by the coupling parameter which could be calculated by Sonnet EM.

Manuscript received April 30, 1999. This work was supported in part by the Grant-in-Aid for Scientific Research on Priority Areas of the Ministry of Education, Science, Sports and Culture.

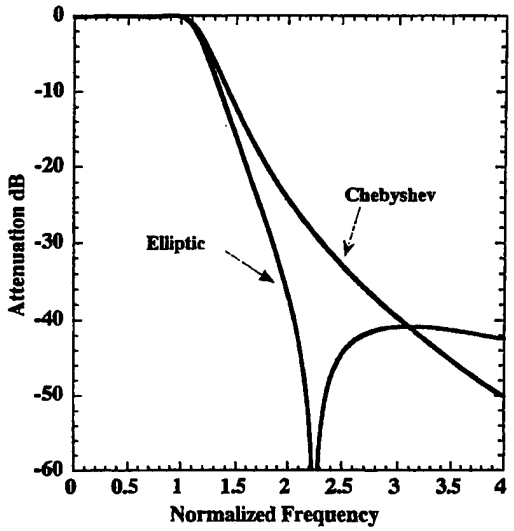

Fig. 1 Calculated insertion-loss response of Chebyshev and elliptic lowpass filters of 4-resonator and passband ripple of 0.12 dB.

TABLE I
The size of hairpin and cross-coupled filters.

	hairpinfilter	cross-coupler filter	
resonance frequency	5GHz	5GHz	
band width	4%	4%	1%
Size of filter (mm)			
w	0.350	0.350	0.350
W	9.250	12.250	12.500
L	5.955	4.150	6.000
a	5.775	5.775	5.525
b	0.950	0.950	1.500
c1	0.825	0.850	1.600
c2	1.000	—	—
d1	—	0.250	1.450
d2	—	0.700	1.200

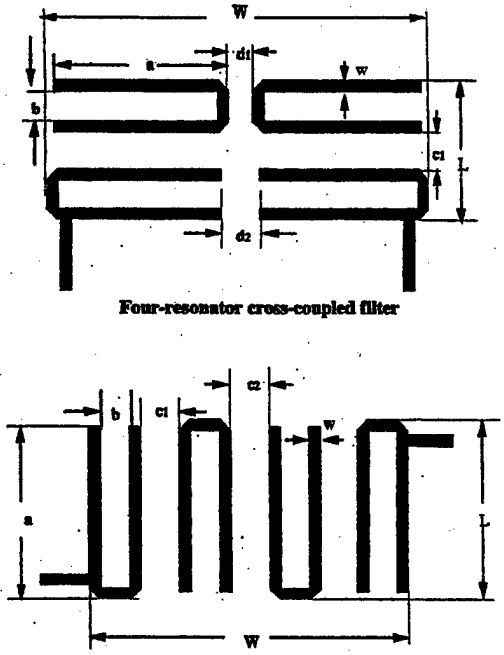

Fig.2 The configuration of four-resonator cross-coupled and conventional hairpin filters.

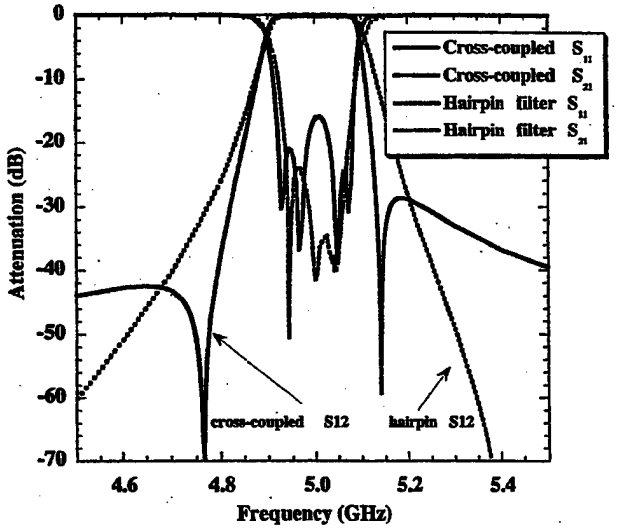

Fig.3 The simulation value of S11 and S12 of cross-couple and hairpin filters calculated by an electromagnetic simulator.

The decided values are shown in table 1. As shown in this table, the size of a hairpin filter is slightly larger than a cross-coupled filter. It is also clarified that as decreasing the bandwidth of filter the size increases.

Fig.3 shows the simulation results of S11 and S21 of four-resonator cross-coupled and hairpin filters. S11 and S12 indicate return loss and insertion loss, respectively. As shown in this figure, the S12 curve of a cross-coupled filter is quite sharp and sharper than that of a hairpin filter. The sharpness of skirt property of a four-resonator cross-coupled filter approximately corresponds to that of eight-resonator hairpin filter.

Fig.4 shows the S11 and S12 of a cross-coupled filter with 1% and 4% bandwidth. The configuration of both filter is the same shown in table 1. It is found that the bandwidth and skirt property of each filter quite agree with that of specifications.

III. Experimental Results

Fig. 5 shows the experimental and simulation results of a four-resonator cross-coupled filter with 4% bandwidth. The filter was made by YBCO thin films on MgO substrate. The Tc and thickness of YBCO film were approximately 87 K and 600 nm, respectively. The ground plane was also YBCO film. The experimental result of attenuation response quite agreed with that of simulated results, however, the return loss of experimental was slightly different. The insertion loss and bandwidth of YBCO cross-coupled filter at 77 K was about -0.29 dB and 4%, respectively.

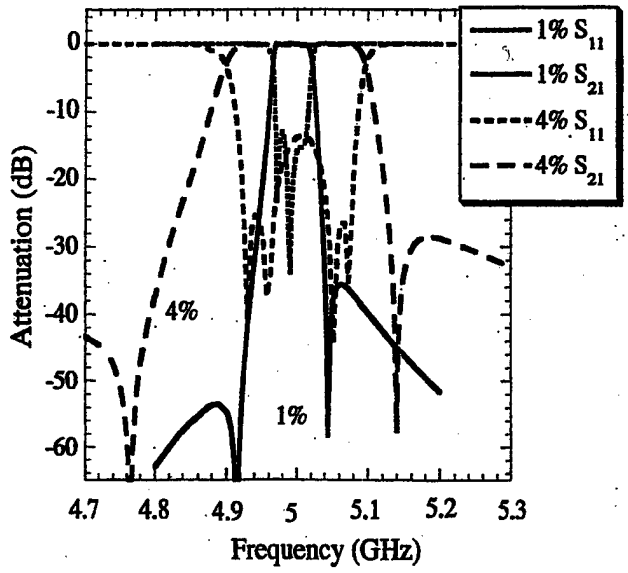

Fig.4 The simulation results of S11 and S21 of cross-coupled filters with 4% and 1% bandwidth calculated by an electromagnetic simulator.

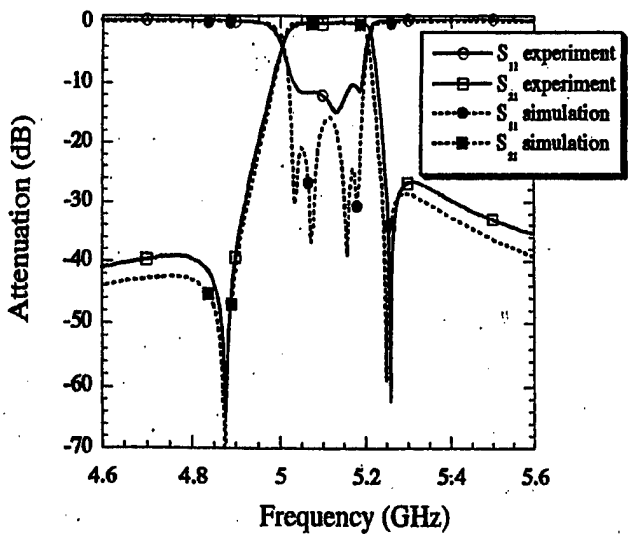

Fig.5 The simulation and experimental results of the four-resonator cross-coupled filters. The superconducting filter is made by YBCO thin films on MgO substrate.

IV. Conclusions

The compact configuration filter was investigated. We designed and determined the configuration of a four-resonator conventional hairpin and cross-coupled filters with resonance frequency 5 GHz and bandwidth 4%, 1% and ripple 0.01dB. The insertion response of cross-coupled filter was superior to that of a conventional hairpin filter. We fabricated the four-resonator cross-coupled filter using YBCO films. The filter response quite agreed with that of simulated result. The insertion loss was less than 0.3 dB at 77 K. The sharpness of skirt property of a four-resonator cross-coupled filter approximately corresponds to that of a eight-resonator conventional hairpin filter. It was found that the elliptic filter is superior to the Chevyshev filter to reduce the size.

References

[1] W.G.Lyons, R.R.Bonetti, A.E.Williams, P.M.Mankiewich, M.L.Omalley and J.M.Mamm. IEEE. Tran. Mag. vol 27, 253-2539, 1991.
[2] T.Tomiyama, D. Okai, M.Kusunoki and S. Ohshima, Advances in Superconductivity X (Springer-Verlag, Tokyo 1998) 1157-1160
[3] G.L.Matthai and G.L.Hey-Shipton, IEEE. Trans. MTT, vol.41 2345-2352 1997.
[4] I.Bohl and P.Bhartia Microwave Solid State Circuit Design (A Wiley-International Publication, New York 1988) section 6
[5] A. Enokihara and K/ Setsune, J. Superconductivity, vol. 10, 49-51, 1997.
[6] J.S. Hong and M.J.Lancaster, IEEE. Trans. MTT. vol 46, 45-49 1998.

High-Frequency Modes in Lumped-Element Superconducting Filters

S. Berkowitz, J-F Liang and V. Borzenets

Conductus, Inc., 969 West Maude Ave., Sunnyvale, CA 94086
phone: 408-523 9439 fax: 408-523 9999 email: sjb@conductus.com

The use of capacitively-loaded inductors to realize lumped-element superconducting filters leads to unwanted high-frequency modes. For example, filters for the cellular spectrum near 900 MHz show higher-frequency modes in the range from 3 GHz to 15 GHz. Experimental measurements and simulations of these modes will be shown. Implementations of low-pass filtering in diplexed filters will be discussed as a method of eliminating this problem.

Predicting Nonlinear Effects in Superconducting Microwave Transmission Lines from Mutual Inductance Measurements

James C. Booth, L. R. Vale, R. H. Ono
National Institute of Standards and Technology, Boulder, CO 80303

J. H. Claassen
Naval Research Laboratory, Washington, DC 20375-5343

Abstract—We demonstrate the use of a new experimental technique based on mutual inductance measurements to quantitatively predict nonlinear effects in microwave devices fabricated from high temperature superconductor (HTS) materials. The mutual inductance measurements yield the current dependence of the penetration depth $\lambda(J)$ in unpatterned HTS thin films. This information is used to calculate third-harmonic generation in coplanar waveguide (CPW) transmission lines and compares very well with actual measurements of CPW transmission lines of variable dimensions fabricated from $YBa_2Cu_3O_{7-\delta}$ thin film samples. The mutual inductance measurements should prove extremely valuable as a screening technique for microwave applications of HTS materials that require very low nonlinear response.

I. Introduction

Microwave circuits fabricated from high temperature superconductor (HTS) materials often suffer from detrimental nonlinear effects, such as intermodulation distortion [1],[2] and harmonic generation [3]. The practical result of this nonlinear response is the creation of unpredictable interference signals within the frequency band of interest for many microwave applications. These nonlinear effects can seriously compromise the utility of microwave devices fabricated from HTS materials. What is urgently needed is an experimental technique that can be used to predict the nonlinear response of HTS microwave devices based on the starting material, prior to device fabrication.

In order to study the nonlinear response of HTS devices, we have developed a model nonlinear system, consisting of coplanar waveguide (CPW) transmission lines fabricated from $YBa_2Cu_3O_{7-\delta}$ (YBCO) thin films grown by pulsed-laser deposition. The nonlinear response of transmission lines of different geometries is determined from measurements of the generated third-harmonic signal as a function of incident power. This model nonlinear system allows us to perform detailed characterization measurements after every step in the device fabrication process, from film growth through device patterning and nonlinear evaluation. We have used this model nonlinear system to determine the relative importance of different processing variables, such as film deposition conditions [4], patterning methods, and device geometry [5], in minimizing nonlinear response. As a result of our investigation, we have identified a low frequency mutual inductance measurement for use as a screening technique for evaluating the nonlinear response of HTS materials prior to device fabrication [6]. We demonstrate how these mutual inductance measurements can be used to predict the nonlinear response of patterned devices of variable geometries at microwave frequencies.

Manuscript received April 30, 1999.
Contribution of the U.S. Government, not subject to U.S. copyright.
This work supported in part by the Office of Naval Research.
The contribution of J.C.B. was supported in part by a NIST/National Research Council postdoctoral research associateship.

II. Mutual Inductance Measurements

We grow superconducting YBCO thin films by pulsed-laser deposition on $LaAlO_3$ substrates up to 15 mm x 15 mm. Before patterning the thin film samples into coplanar waveguide devices, we perform a number of characterization measurements to help determine the film quality. Sapphire dielectric resonator measurements yield the surface resistance, which at 76 K is typically in the range 250 to 300 $\mu\Omega$ when scaled to 10 GHz. We also use mutual inductance measurements to determine the transition temperature (typically 90-91 K) and the critical current density (typically 3-3.5 x 10^6 A/cm^2 at 76 K).

In addition to these characterization measurements, we exploit a new technique based on mutual inductance measurements to determine the dc current dependence of the penetration depth $\lambda(J)$ [6]. Such measurements are motivated by recent theoretical work that shows that a current-dependent penetration depth can lead to nonlinear effects in microwave devices [7]. These calculations assume a quadratic dependence of $\lambda(J)$ in order to calculate the third-order nonlinear products, but until now there has not been any direct experimental confirmation of this form for $\lambda(J)$. Figure 1 shows the results of the mutual inductance measurements of $\lambda(J)$ for a 50 nm YBCO thin film at 76 K. These measurements show that the dependence of λ on dc current density is indeed quadratic, at least up to current densities approaching the critical current density J_c (which is determined from mutual inductance measurements to be approximately

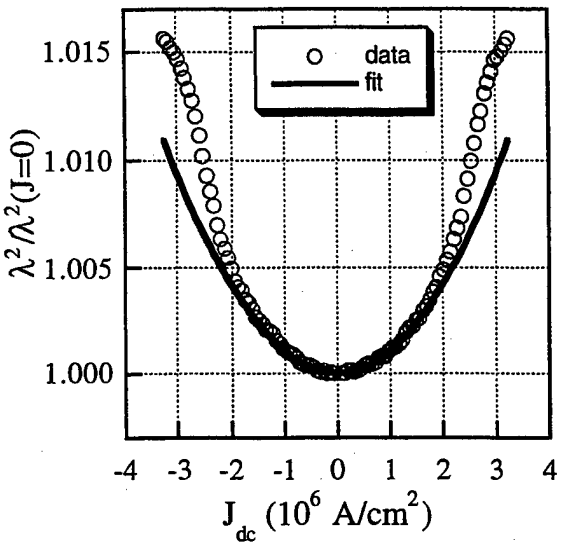

Fig.1. Current dependence of the penetration depth for a 50 nm YBCO film at 77 K, obtained using a 10 kHz mutual inductance technique.

3.4 x 10^6A/cm^2 for this sample). We fit the data in the low-current region of Fig. 1 to the form

$$\lambda^2(T,J) = \lambda^2(T)\left[1+\left(\frac{J}{J_0(T)}\right)^2\right] \qquad (1)$$

and obtain J_0 = 3.1 x 10^7 A/cm^2 at 77 K. Similar measurements on a thicker film (400 nm) grown by pulsed-laser deposition under slightly different growth conditions yield a similar value of J_0 = 3.5 x 10^7 A/cm^2 at 77 K. These results are significant because, if this $\lambda(J)$ response is the dominant source of nonlinear effects, the theoretical analysis of Dahm et al. [7],[8] can be used to calculate the third-order nonlinear products of a wide range of different devices fabricated from these materials. These measurements also yield the value of the penetration depth for zero applied current density $\lambda(J=0)$, which is important for calculating both the linear and nonlinear response of microwave devices.

III. TRANSMISSION LINE MODEL

We use these results for $\lambda(J)$ to calculated the nonlinear (current-dependent) inductance per unit length $L(I) = L_0 + L'\cdot I^2$ present in planar structures, following Dahm [7]. We have generalized the analysis of Dahm to calculate the third-harmonic signal generated by a short length of HTS transmission line at microwave frequencies, instead of calculating the intermodulation products in a resonant structure. The details of the calculation of the third-harmonic signal as a function of incident power (P_{inc}) are presented elsewhere [5]; we quote here just the result for the third-harmonic signal P_3:

$$10\log_{10}(P_3) = -2\cdot IP_3 + 3*10\log_{10}(P_{inc}) \; . \qquad (2)$$

If we plot the measured power in the third-harmonic as a function of incident power on a log-log scale, (2) predicts that the P_3 data will have a slope of 3 with an intercept point $-2IP_3$. The quantity IP_3 is called the third-order intercept. It corresponds to the point where a line of slope 3 fit through P_3 would intercept a line of slope 1 fit through the fundamental; see Fig. 2 for an example [9]. The third-order intercept at frequency ω for a transmission line of length ℓ, center linewidth w, thickness t, and characteristic impedance Z_0 is given by the following expression (in dBm) [5]:

$$IP_3 = 10\log_{10}\left(\frac{2J_0^2(T)}{\mu_0\omega\lambda^2(T)}\frac{w^2t^2Z_0^2}{\Gamma\ell}\right) + 30 \qquad (3)$$

Γ is a geometrical factor that depends on the current distribution, and is given by [5]

$$\Gamma = \frac{w^2t^2\int J^4\,dS}{\left(\int J\,dS\right)^4} \; . \qquad (4)$$

The third-harmonic response calculated from (2) and (3) is strictly valid for transmission lines that have a length ℓ that is smaller than the effective wavelength so that the lumped-element approach used in [5],[7] is valid. We have calculated the effect of connecting together a series of such small elements to create a transmission line of arbitrary length L. As long as the third-harmonic signal remains much smaller than the fundamental ($P_3 << P_1$), the third-harmonic signal for the individual elements all add in phase, and the result (3) is valid for any transmission line length [10].

Figure 2 shows an example of the measured third-harmonic signal at 76 K as a function of incident power for a CPW transmission line fabricated from a 400 nm YBCO thin film. The CPW transmission line has a center conductor linewidth of 105 μm and a length of 6.54 mm, and has a nominal characteristic impedance of 50 Ω. The solid lines in Fig. 2 are fits of slope 1 and 3 to the fundamental and third-harmonic data, respectively. We compare the values for IP_3 extracted experimentally using (2) with the values for IP_3 calculated from (3) using inductively determined values for J_0 and λ, along with the transmission line's dimensions. For this CPW device, using J_0 = 3.5 x 10^7 A/cm^2 and λ = 312 nm (Γ is calculated to be 3.03 x 10^{11} m^{-2}), we calculate IP_3 = 82.7 dBm. This value compares extremely well with the experimentally determined value of IP_3 = 82.7 dBm, particularly considering that (3) uses only experimentally determined quantities (no adjustable parameters) to calculate IP_3.

The inset of Fig. 2 shows the saturation of P_3 observed as the incident power becomes high. At the point where P_3 begins to deviate noticeably from the "slope 3" behavior

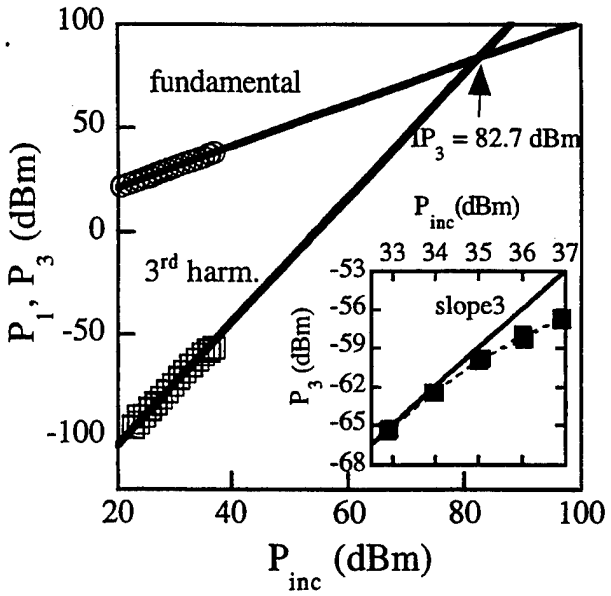

Fig. 2. Measured third-harmonic signal vs. incident power for a 105 μm wide, 6.54 mm long CPW transmission line. The device was fabricated from a 400 nm YBCO thin film. The solid line through the fundamental (P_1) data is a fit to a line of slope 1 and the solid line through the third-harmonic (P_3) data is a fit to a line of slope 3. The inset shows the deviation from slope 3 that occurs for high incident powers.

($P_{inc} \approx 35$ dBm), we estimate the peak rf current density to be 3.65×10^6 A/cm^2 (the average rf current density for this power is 8.5×10^5 A/cm^2). This deviation from "slope 3" behavior occurs because the shape of $\lambda(J)$ is no longer quadratic for such large peak current densities (see Fig. 1). In this case, more terms are needed in the expansion of $\lambda(J)$ in (1), and the third-harmonic vs. incident power data will in general no longer obey the slope 3 behavior, which results from a purely quadratic form for $\lambda(J)$.

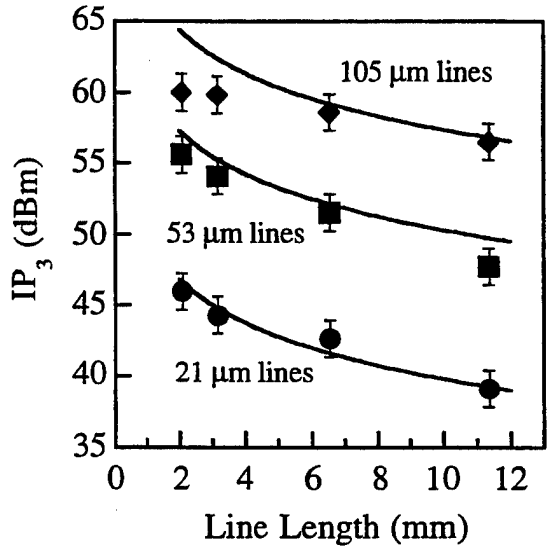

Fig. 3. Third-order intercepts vs. line length for an HTS transmission line with a 5 GHz fundamental signal. The center conductor linewidths are 21 μm, 53 μm, and 105 μm. The solid lines are calculated from (3), with $\lambda(77\text{ K}) = 354$ nm and $J_0(77\text{ K}) = 3.1 \times 10^7$ A/cm^2. The error bars represent the standard deviation of IP_3 determination across the chip.

IV. Third-Harmonic Response for Different Geometries

To confirm that the third-harmonic response predicted by (2) and (3) is generally valid, we determine the third-order intercept point IP_3 at 76 K for a number of different transmission line geometries, as shown in Fig. 3. These data are for 11 different CPW transmission lines fabricated from a single 50 nm YBCO thin film, with different linewidths and lengths. As this thin film sample was grown under nominally identical deposition conditions to the sample of Fig. 1, we expect the inductively measured values of $J_0(77\text{ K}) = 3.1 \times 10^7$ A/cm^2 and $\lambda(77\text{ K}) = 354$ nm to accurately describe the resulting third-harmonic generation of all devices on this chip. This is precisely what is observed in Fig. 3, which shows as solid lines the prediction of (3), *based solely on the inductively measured values of λ and J_0 and the transmission line dimensions.* These data illustrate the power of the inductive results for predicting the nonlinear response of microwave devices of arbitrary geometry.

V. Conclusions

We have developed a new screening technique for predicting the nonlinear response of microwave devices fabricated from HTS materials. The technique uses low-frequency (10 kHz) mutual inductance measurements of unpatterned superconducting films to determine the current dependence of the penetration depth $\lambda(J)$ [6]. These mutual inductance measurements predict third-harmonic generation in CPW devices of different geometries patterned from YBCO thin films. This technique provides a valuable method for determining the nonlinear response of HTS microwave devices prior to circuit fabrication.

V. References

[1] Z. Ma, E. de Obaldia, G. Hampel, P. Polakos, P. Mankiewich, B. Batlogg, W. Prusseit, H. Kinder, A. Anderson, D.E. Oates, R. Ono, and J. Beall, IEEE Trans. Appl. Supercond. 7, 1911 (1997).
[2] B.A. Willemsen, T. Dahm, and D.J. Scalapino, Appl. Phys. Lett. 71, 3898 (1997).
[3] C. Wilker, Z.-Y. Shen, P. Pang, W.L. Holstein, and D.W. Face, IEEE Trans. Appl. Supercond. 5, 1665 (1995).
[4] James C. Booth,et al., "Simultaneous optimization of the linear and nonlinear microwave response of YBCO films and devices," IEEE Trans. Appl. Supercond., in press.
[5] James C. Booth, J.A. Beall, D.A. Rudman, L.R. Vale, and R.H. Ono, "Geometry dependence of nonlinear effects in high temperature superconducting transmission lines at microwave frequencies," J. Appl. Phys., in press.
[6] J. H. Claassen, James C. Booth, J.A. Beall, D.A. Rudman, L.R. Vale, and R.H. Ono, "Nonlinear inductive response of high temperature superconducting films measured by the mutual inductance technique," Appl. Phys. Lett., in press. See also J.H. Claassen et al., "Comparison of Microwave and Mutual Inductance Measurements of the Inductive Nonlinearity of HTS Thin Films," these proceedings.
[7] T. Dahm and D.J. Scalapino, J. Appl. Phys. 81, 2002 (1997).
[8] R.B. Hammond, E.R. Soars, B.A. Willemsen, T. Dahm, D.J. Scalapino, and J.R. Schrieffer, J. Appl. Phys. 84, 5662 (1998).
[9] Note that this particular specification of the intercept point is arbitrary; any intercept point is sufficient to describe the data if the slope is fixed.
[10] James C. Booth, J.A. Beall, L.R. Vale, and R.H. Ono, "Distributed nonlinear effects in planar transmission lines," 53rd Automated RF Technologies Group (ARFTG) Digest, in press.

Comparison of Microwave and Mutual Inductance Measurements of the Inductive Nonlinearity of HTS Thin Films

J. H. Claassen
Naval Research Laboratory, Washington, DC, 20375-5343

James C. Booth, J. A. Beall, L. R. Vale, D. A. Rudman, L. R. Vale, and R. H. Ono
National Institute of Standards and Technology, Boulder CO 80303

Abstract—A quadratic dependence of penetration depth on supercurrent density may be observed both by an inductive measurement on unpatterned films or by a microwave measurement of third harmonic generation in coplanar waveguide. Results for the two methods are compared for a series of YBCO films. We find good agreement between the two measurements.

I. Introduction

One important contribution to nonlinearity in superconducting circuits is the current dependence of the penetration depth λ. This is predicted by BCS theory to have the form

$$\lambda^2(T,J)=\lambda^2(T,0)[1+(J/J_o)^2], \quad (1)$$

where J is the current density. The parameter J_o sets the current scale for which nonlinear effects become important. Calculations of J_o as a function of temperature have been presented for the case of a BCS superconductor [1].

Fits to third harmonic generation in coplanar waveguide made with YBCO films show that (1) can account for the data over a range of guide dimensions and length [2]. On the other hand, measurements of intermodulation distortion in microstrip resonators made from TBCCO films [3] could be better fit to a dependence

$$\lambda^2(T,J)=\lambda^2(T,0)[1+|J/J_o|]. \quad (2)$$

In the microwave measurements rf currents are concentrated near patterned edges of the HTS films, where secondary effects such as flux entry, degraded superconducting properties, etc, could be important. It would be valuable to be able to independently measure the $\lambda(J)$ dependence of films prior to their being patterned and incorporated in a microwave circuit. We show here that a well-known mutual inductance technique used to measure the penetration depth in unpatterned films [4] can be extended to obtain a measure of the current dependence of λ. Preliminary comparisons of companion films to those used in third harmonic generation studies show good agreement between the inferred J_o values.

Manuscript received April 30, 1999
The portion of this work performed at the National Institute of Standards and Technology was supported in part by the Office of Naval Research.

II. Measurement Method

To make our inductive measurement, we combine a small ac current (typically 10 kHz) with a dc current component in a drive coil. The ac voltage across a secondary coil is detected with a lock-in amplifier. The two coils are positioned on opposite sides of the film on a common axis. It is shown in [4] that the best results are obtained if the coils are small compared to the film extent and are as thin as possible in the axial direction--that is, have the shape of a washer.

The ac coupling between the coils is purely inductive except very close to the transition temperature. With knowledge of the coil parameters and film thickness, the measured mutual inductance may be used to infer the penetration depth of the superconductor [4].

The dc current in the drive coil induces a screening supercurrent in the superconducting film. The radial dependence J(r) of the screening current in the film may be calculated with good accuracy by assuming that it completely screens magnetic fields from the reverse side [5]. (Actually some field "leaks" through the film and indeed this is the basis for the measurement of λ. However, in practical cases this represents a small correction to J(r).) Fig. 1 shows a calculation of J(r) for the coil used in our experiment, assuming the coil is pressed against the film side of the sample. It can be seen that J is peaked with a maximum near the mean radius of the coil windings and dropping off fairly rapidly with increasing r.

If λ depends on J, application of a dc current to the drive coil results in a sample whose penetration depth is not homogeneous. If the variations in λ across the film are small, it can be shown that the mutual inductance measurement yields a weighted average of $\lambda(r)$. It is plausible that the strongest weighting is just where the screening current has its maximum. In what follows, we assume that the measured penetration depth corresponds to the maximum screening current J. There is of course some error in this approximation, and we do not claim that one has a precision $\lambda(J)$ measurement by this technique. However it surely will yield numerical values of adequate accuracy for purposes of selection and comparison, as well as establishing the form of the $\lambda(J)$ relationship.

III. Heating Effects

In order to induce film currents large enough to significantly effect λ, a rather large dc coil current is frequently needed. The power dissipated in the coil causes the film to heat up, and since λ depends on temperature this gives

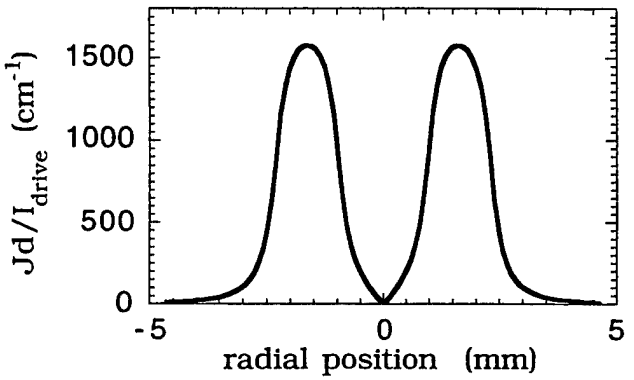

Fig. 1 The calculated radial dependence of the screening sheet current Jd (d is the film thickness) in the superconducting film normalized to the dc drive current in the coil used in our experiment.

a spurious effect unrelated to the $\lambda(J)$ dependence of interest. Heating effects turn out to be significant only in the thickest HTS films of interest. (The coil current required to generate a given current density in the film is proportional to the film thickness, cf. Fig. 1). We can nevertheless make measurements with our existing mutual inductance setup provided two conditions are met: (a) $\lambda(J)$ must have the quadratic form of (1), and (b) the film must have strong pinning. We first cool the film through its transition with a current I_{trap} in the drive coil. It can be shown [6] that if pinning is strong, the current density in the film is subsequently proportional to $(I_{coil}-I_{trap})$. We then fit our data to

$$\Delta\lambda = AI_{coil}^2 + B(I_{coil}-I_{trap})^2, \quad (3)$$

where the coefficient A is related to the heating effect and we can obtain J_o from the coefficient B [6].

A better solution to the heating problem is currently being investigated. A modified drive coil is used, consisting of two interspersed windings. The film current density will then be proportional to the sum of the dc currents in the two windings while the power dissipation is proportional to the sum of their squares. It is possible to keep the latter constant (ensuring a constant film temperature) while varying the former, thus sweeping the film current density at a constant temperature

IV. Mutual Inductance Results

Fig. 2 gives representative results for three samples measured by the inductive method. Two of them are YBCO films of thicknesses 50 and 450 nm. These were cooled with an appropriate trapping current, as discussed above. The data shown is the residual after subtracting away the fitted heating term in (3), thus is the intrinsic contribution due to film current J. The heating term for the 450 nm film was ~4 times greater than the effect of current, while in the case of the 50 nm film it was relatively unimportant and could have been ignored with little error. In both cases the dependence on current is quadratic as in (1), with similar values of J_o.

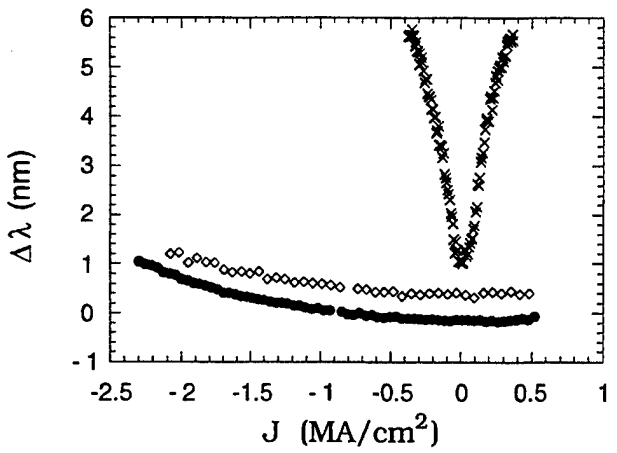

Fig. 2. The change of penetration depth λ as a function of film current density J for various samples referenced in Table 1: solid circles: 11301-2; diamonds, L397-169; crosses: 5264-3. In the first two cases measurements were taken with a trapped film current; the fitted heating contribution to the raw data has been removed. In the last case the estimated heating effect is negligible and there was no trapped current. The data are offset vertically for clarity.

The third sample shown in Fig. 1 was a commercially obtained 650 nm TBCCO film specified as having a low microwave surface resistance. In this case the effect of film current is much larger than that due to heating, and no correction has been made in the data. Clearly the dependence is not quadratic, and perhaps (2) would be a better fit.

Table 1 shows the fitted values for J_o for all the samples that have been measured inductively to date. Also given are other film parameters at 78 K: the penetration depth and the inductively measured critical current density [5]. Clearly there is a correlation between all these measures of film quality.

TABLE I

Summary of results on various samples. Thickness and penetration depth are given in nm, and current densities in MA/cm^2. J_c values were measured inductively by the technique of Ref. [5]. The rf values of J_o were obtained from companion samples patterned into coplanar waveguide, and are an average over results from a variety of lengths and waveguide dimensions. The "dc" values were found by the inductive method described here.

sample #	material	substrate	thickness	λ	J_c	$(J_o)_{dc}$	$(J_o)_{rf}$
L397-169	YBCO	LAO	50	360	3.4	31	28
L397-414	YBCO	LAO	400	315	2.9	35	27
L397-441	YBCO	LAO	400	390	2.2	19	18
11301-2	YBCO	LAO	450	345	2.3	28	NA
11209-1	YBCO	AlO	350	460	1.1	5	NA
5264-3	TBCCO	LAO	650	385	0.8	NA[a]	NA

[a]The $\lambda(J)$ characteristic, shown in Fig. 1, could not be fit to a quadratic dependence.

V. Comparison with Microwave Measurements

Some of the samples listed in Table 1 had companions deposited under identical conditions that were made into coplanar waveguides. Assuming the third harmonic generation in these guides is due entirely to a nonlinear penetration depth of the form (1), it is possible to deduce a value of the coefficient J_0 [2]. Table 1 shows that there is rather good correlation between the rf and inductive determinations, for films covering a range of thickness and preparation conditions. Note that the maximum J_0 measured at 78 K, $\sim 3 \times 10^7$ A/cm^2, is a factor 2 to 4 smaller than the BCS prediction [1], depending on whether an s-wave or d-wave symmetry of the order parameter is assumed.

VI. Conclusions

In the case of the best YBCO films it appears that the $\lambda(J)$ dependence is quadratic and there is good agreement between microwave and inductive measurements. Since the latter is done on unpatterned films, it may prove useful in vetting films prior to subsequent processing into circuits. For the one TBCCO film we measured, the $\lambda(J)$ dependence is clearly not quadratic. We have also observed a non-quadratic response in some poorer quality YBCO films. As the observed nonlinearity of even the best films measured is substantially larger than the prediction of the BCS model, there is the possibility of improved film performance with optimized deposition procedures.

References

[1] T. Dahm and D. J. Scalapino, "Theory of microwave intermodulation in a high-T_c superconducting microstrip resonator", *Appl. Phys. Lett*, vol. 69, pp. 4248-4250, December 1996.

[2] James C. Booth, J. A. Beall, D. A. Rudman, L. R. Vale, and R. H. Ono, "Geometry dependence of nonlinearities in high temperature superconducting transmission lines at microwave frequencies", in press.

[3] Balam A. Willemsen, K. E. Kihlstrom, and T. Dahm, "Unusual power dependence of two-tone intermodulation in high-T_c superconducting microwave resonators", *Appl. Phys. Lett*, vol. 74, pp. 753-755, February 1999.

[4] J. H. Claassen, M. L. Wilson, J. M. Beyers, and S. Adrian, "Optimizing the two-coil mutual inductance measurement of the superconducting penetration depth in thin films", *J. Appl. Phys*, vol. 82, pp. 3028-3034, September 1997.

[5] J. H. Claassen, M. E. Reeves, and R. J. Soulen, Jr., "A contactless method for measurement of the critical current density and critical temperature of superconducting films", *Rev. Sci. Intstrum*, vol. 62, pp. 996-1004, April 1991.

[6] J. H. Claassen, James C. Booth, J. A. Beall, D. A. Rudman, L. R. Vale, and R. H. Ono, "Nonlinear inductive response of high temperature superconducting films measured by the mutual inductance technique", *Appl. Phys. Lett*, in press.

Two-dimensional resonators for local oscillators

Kao-cheng Huang, Alan Jenkins and David Dew-Hughes
Department of Engineering Science, University of Oxford, UK

Abstract— The expedited globalization of satellite technology has brought about a rapid boost in satellite competition, and increased utilization of wireless communications remote data devices. In space communications receivers, there is an expanding demand for higher performance from local oscillators. The determining conditions are high Q values, high circulating power and low amplifier noise figures. In spite of their low insertion loss, conventional one-dimensional high temperature superconducting (HTS) resonator-feedback oscillators suffer from high peak current densities inside the resonator, and thus have a limited power handling characteristics. To achieve higher power oscillators, it is possible to introduce two-dimensional microstrip resonator to balance the internal current distribution. To this end, 3 GHz two-dimensional resonators have been fabricated from TBCCO 2212 thin films deposited by RF sputtering onto 2 cm square $LaAlO_3$ substrates. This paper demonstrates the frequency stabilizer role and the frequency response of two-dimensional resonator. The considerable improvement for the performance of resonator-feedback oscillators constructed using such HTS resonators will also be presented.

I. Introduction

The rapid global build-out of wireless communications of networks concurs with progress in high-volume fabrication methods for passive electronic components using thin-film superconductors. The commercial opportunity lies in receiver front-end products that combine spectral selectivity with extremely low-noise performance, which improves the uplink\downlink imbalance in wireless networks.

Oscillators are widely used in communication systems such as radio (cellular radio), general mobile radio, paging receivers, microwave links and satellite assisted communication and navigation systems. Modern portable radios must equip high performance while operating from a small and portable power supply. The oscillator must therefore supply low-noise performance with minimum power loss.

Maximization of Q value of resonators and minimization of phase noise are critical for local oscillators. These performance improvements is realized by incorporating high-temperature superconductor RF resonators. Many researchers have described the one-dimensional resonator-based oscillator.[1][2] However, it appears that none have taken into account the fact that two-dimensional resonators have higher Q-value and higher power handling characteristics. We have therefore designed and tested two microstrip resonators for application in a local oscillator.

Manuscript received April 30, 1999.
This work was supported in part by the Swire Groups and EPSRC.

II. TBCCO Material

High temperature superconductors for microwave applications are fabricated in the form of thin films on a low loss dielectric substrate. The film are deposited on lanthanum aluminate, which has a dielectric loss tangent of $1 * 10^{-5}$ and a relative dielectric constant of 24 at 10 GHz and room temperature. The sizes of the substrate currently in use are 2 cm square, with a thickness of 0.5 mm. The film fabrication process includes a two-step process in which a Tl-free precursor film is grown at room temperature by RF sputter deposited from a Ba:Ca:Cu composition 2:1:2 oxide target. This is followed by a post-deposition anneal with Tl-2212 powder in a closed crucible. The annealing temperature affects phase purity, surface impedance and the critical temperature. Figure 1 shows the quality of the films which is measured by the unloaded Q factor of end wall replacement technique.[3] These TBCCO films have a microwave surface resistance of 203 μΩ at 10 GHz and 77K. These films exhibit a unique combination of microwave properties - high temperature operation, low surface resistance and low power dependence.

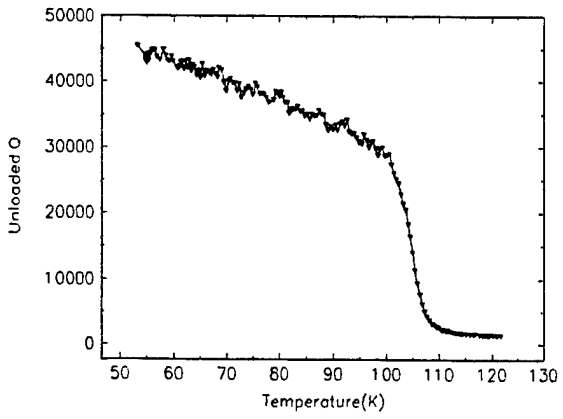

Fig.1 Unloaded Q measured by full end wall replacement method.

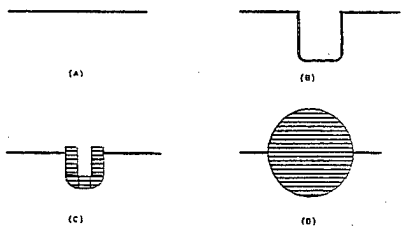

Fig.2 (A)-(C) Structure variations of two dimensional hairpin resonators. (A) Conventional half-wavelength edge-coupled line resonator. (B) miniaturized one-dimensional hairpin resonator. (C) two-dimensional hairpin resonator. (D) disk resonator.

III. RESONATORS

Some structures of microstrip resonators are demonstrated in Fig. 2. Resonators A and B are one dimensional resonators whereas resonators C and D are two dimensional resonators. The resonant condition of resonators A and B is that their length is an integer value of half wavelength and the resonant conditions of resonators C and D is the total length of the circumference equals an integer number of wavelength. Resonator A is a conventional edge-coupled resonator. The fundamental mode occurs at half wavelength. Resonator B is introduced to reduce the size of resonator A. These resonators have maximum current density at the edges of the microstrip line for their fundamental mode. Therefore, this mode will suffer from edge effects such as radiation loss and power dependence resulted from edge damage when compared to other modes. In addition, resonator A at L-band is too large to realize in superconductor. Resonator B takes less space than resonator A which extents the applicable frequency range for the available superconductor film. Assume the hairpin resonator consists of a parallel coupled line and a straight line, the resonance characteristics can be analyzed by the following equation:[4]

$$(Z_{pe}Z_{po}\cot\theta_{pe}\cot\theta_{po} - Z_s^2)\sin\theta_s + Z_s(Z_{pe}\cot\theta_{pe} + Z_{po}\cot\theta_{po})\cos\theta_s - Z_s(Z_{po}\cot\theta_{pe} - Z_{po}\cot\theta_{pe}) = 0$$

Where

Zs characteristic impedance of the single line.
Zpe, Zpo even mode and odd mode impedance of the parallel coupled lines,
θs electrical length of the single line,
θpe, θpo even and odd mode electrical length of the parallel coupled line.

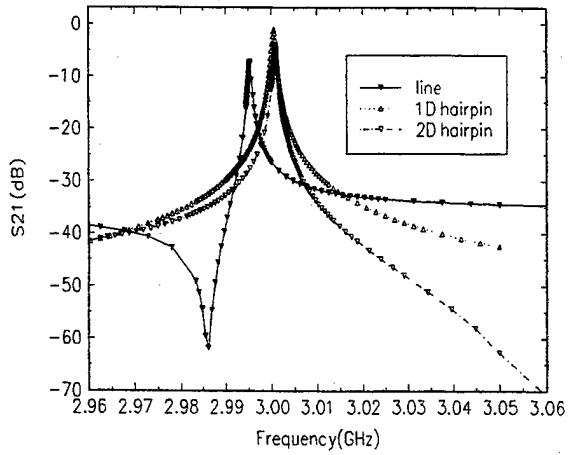

Fig.3 Simulated frequency response of three different resonators.

Because the width of previous two resonators are relatively narrow and high current density causes lower Q value and lower power handling ability, a two dimensional hairpin resonator is newly developed and shown in Fig.2(C). Resonator C has bigger width but shorter length than resonator B.(Width B = 0.15 mm, C = 1.6 mm; Length B = 13.24 mm, C = 12.39 mm). So the resonator C has similar perimeter to B but a larger area which reduces the current density on the film. Besides, from the definition of unloaded Q

$$Q_u = \omega\frac{E}{P}$$

Where E: time averaged stored energy in the resonator,
P: energy loss per second.

resonator C has more space to store energy than resonator B. Therefore, unlike resonators A and B, resonator C has higher Q and power handling ability. This can be used to design highly selective filter and low phase noise oscillators.

Figure 2(D) shows a disk resonator reported by A. Jenkins[5]. Its fundamental mode is TM11. Although TM01 mode can get rid of the edge effects and its Q is six times of TM11's, it takes two times more space than TM11 mode. Before larger size of superconductor film become available, TM01 mode can only be operated at C-band and above. So TM11 mode of disk resonator is applied at this oscillator even though it is shared by two orthogonal modes.[6] Any slight defects on the disk will result in lower Q by reason of coupling between these two modes.

The resonator C has less end radiation loss than resonator A and B because there seems a single full wavelength around the two dimensional hairpin resonator. Due to the asymmetric configuration, the resonator C (1) does not have mode degeneration problems as does the resonator D, (2) does not have current peak on outer side of the hairpin resonator line for fundamental mode (which is odd mode), and (3) can go to lower frequency than does the resonator D.

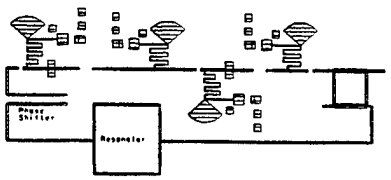

Fig.4 The layout of oscillator.

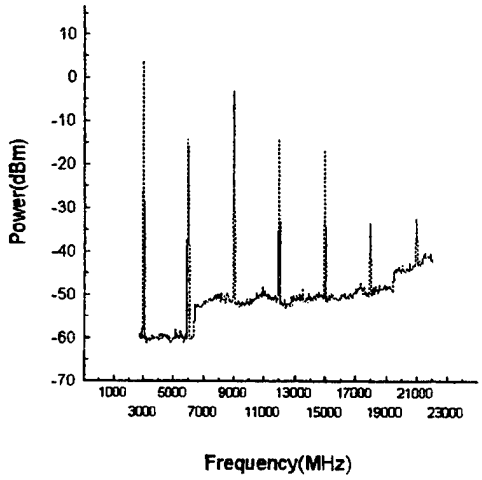

Fig. 5 The frequency response of oscillator.

Figure 3 shows the 3 GHz resonance of a edge-coupled line resonator, one dimensional and two dimensional hairpin resonators respectively which is modeled by HP EEsof. From Fig.3, the unloaded Q of two-dimensional superconducting hairpin resonator is 4460.52 while that of the edge coupled resonator is 4140.63 at 3GHz, 77K.

IV. Oscillators

The oscillator circuit was assembled with two-stage low noise amplifier, branch-line coupler, phase shifter and copper resonator.

The active component is two-stage amplifier operating in frequency band 2.5 to 3.5 GHz with a gain about 20 dB. The active device used in the amplifier is HP GaAs 10135 with a 1 mm gate length and a gate width of 83 μm. The signal from the amplifier is divided by a branch-line coupler with equal power splits. One port of coupler supplies the output signal while the other port feeds the signal back to a weak coupled resonator. The signal from the resonator is then fed back to the input of the amplifier through the microstrip phase shifter. To achieve the oscillation condition, the phase shift around the feedback loop should be an integer multiple of 2π radians at the oscillation frequency. This condition can be met by mechanical change of length of microstrip line. The microstrip layout of the oscillator is shown in Fig.4.

The amplifier is operated with the devices biased at Vg1 + Vg2=-0.4V, Vd1+Vd2=1.6V, Id1+Id2=30 mA. which are the optimum dc bias conditions to reach low noise without serious signal distortion. The achieved gain of the amplifier is greater than the insertion loss of the resonator. Figure 5 shows that the oscillator has strong harmonic oscillations which go up to 21 GHz. Figure 6 demonstrates the spectrum of the oscillator close to carrier noise performance at 77K. The output frequency is 2.989 GHz.

V. Conclusion

Two dimensioal hairpin resonator is compared with three different resonators. A hybrid oscillator, integrating a two stage GaAs FET amplifier fabricated on RT/Duroid substrate and two-dimensional microstrip resonator is successfully designed, fabricated and measured.

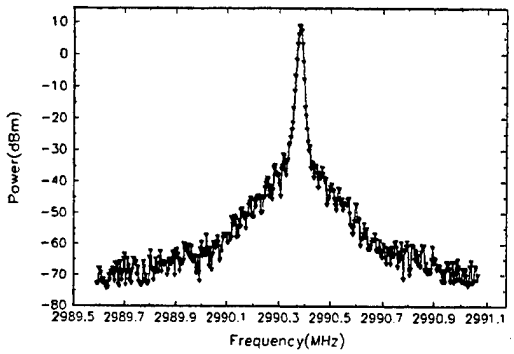

Fig6. The frequency response of oscillator with two dimensional hairpin resonator.

References

[1] R. Kojouharov, *et al*, "High thermal stability microwave oscillator based on HTSC resonator," *Proceedings of the 1996 IEEE International Frequency Control Symposium*, pp. 761-771, 1996.

[2] A. P. S. Khanna, *et al*, "A superconducting resonator stabilized low phase noise oscillator," *Microwave Journal*, vol. 34, pp. 127-129, February 1991.

[3] C. L. Bohn, "Radio frequency surface resistance of large-area Bi-Sr-Ca-Cu-O thick films on Ag plates, "*Appl. Phys. Lett.*, vol. 55, pp 304-306,1989

[4] M. Sagawa, *et al*, "Miniaturized Hairpin Resonator Filters and Their Application to Receiver Front End MIC's," *IEEE MTT*, vol. 37, pp. 1991-1997, December 1989.

[5] A. Jenkins, *et al*, "Microstrip disk resonators for filters fabricated from TBCCO thin films, ," *IEEE Trans. Applied Superconductivity*, vol. 17, pp. 2793-2796, June 1997.

[6] Zhi-Yuan Shen, *High Temperature Superconducting Microwave Circuits*, 1st ed., Artech House, 1994.

Phase Locking of 270-440 GHz Josephson Flux Flow Oscillators

Jesper Mygind
Department of Physics, Technical University of Denmark, B309, DK-2800 Lyngby, Denmark

Valery P. Koshelets, Sergey V. Shitov, Lyudmila V. Filippenko, Vladimir L. Vaks*
Institute of Radio Engineering and Electronics, RAS, Mokhovaya 11, 103907 Moscow, Russia
*Institute for Physics of Microstructure, RAS, GSP-105, 603600 Nizhny Novgorod, Russia

Andrey M. Baryshev, Willem Luinge, Nick Whyborn
SRON-Groningen, P.O. Box 800, 9700 AV Groningen, the Netherlands

Abstract—External phase locking of a Josephson Flux Flow Oscillator (FFO) to a 10 MHz reference oscillator is demonstrated experimentally in the frequency range 270 - 440 GHz. A linewidth as low as 1 Hz (as determined by the resolution bandwidth of the spectrum analyzer) has been measured. This linewidth is far below the fundamental level given by shot and thermal noise of the free-running tunnel junction. The combination of narrow linewidth, wide band tunability, and low noise is important for spectral radio astronomy applications.

I. Introduction

The FFO [1] is a long Josephson junction in which an applied dc magnetic field and a bias current drive a unidirectional flow of fluxons. The velocity and density of the fluxons and thus the power and frequency of the emitted mm-wave signal may be easily tuned by either of the two external parameters. It has been demonstrated that the FFO is very useable as local oscillator integrated with a SIS-mixer in a single-chip sub-mm wave receiver [2]. Receiver noise temperatures below 100 K (DSB) have been achieved at 500 GHz [3], and the antenna beam, approx. f/10 with sidelobes < -17dB, enables a good coupling of the integrated receiver to the real telescope. The frequency resolution of the receiver is very important for spectral radio-astronomy applications. It is determined by the instant linewidth as well as the long-time stability of the local oscillator. Together this should be better than 1 PPM of the center frequency. Recently a reliable technique for linewidth measurements has been developed [4] and a free-running FFO linewidth of only few hundred kHz was measured [4,5].

At voltages above a certain boundary voltage, V_b, the FFO linewidth increases and the IV-curve (IVC) of the FFO is modified [5]. Both indicate that the internal damping abruptly increases above $V_b \approx 950\ \mu V \approx 1/3$ of the superconductor gap voltage, V_g, for Nb-AlO_x-Nb tunnel junctions. A simple model was introduced [5] based on Josephson radiation self-coupling (JSC) [6]. It explains both the increased linewidth and the experimental IVCs. Since we bias with an ideal current source only the positive slope of a structure in the IVC can be traced out. A sharp resonance therefor looks like a nearly constant-voltage step. An external dc current in an overlying control line generates the magnetic field applied to the junction.

For low normalized damping $\alpha l < 1$ the most prominent step structure is the discrete and nearly equidistant Fiske steps (FSs). The shunt damping parameter is α and $l = L/\lambda_J$ is the junction length normalized to the Josephson penetration length, λ_J. The FSs originate in the resonant junction cavity modes, and so the voltage of a given FS is nearly independent of the magnetic field. The stability of the FSs and thus their apparent magnitude, however, varies strongly with the magnetic field due to the nonlinear interactions in the long junction [7]. At higher damping the FSs gradually overlap and the structure transforms into a single curve, the Eck step, the voltage of which depends linearly on the magnetic field. Somewhat misleading the low-voltage side of the Eck peak is called the flux flow step (FFS). In our samples for $V > 950\ \mu V \approx V_g/3$ the damping exceeds the critical limit $\alpha l \geq \pi$ and a smooth FFS appears.

The JSC caused by the quasiparticle absorption of the internal *ac* Josephson radiation (Photon Assisted Tunneling, PAT) results in "bumps" in the IVC at $V_{JSC} = V_g/(2p + 1)$ with $p = 0, 1, 2,..$ which gives $V_{JSC} = V_g/3$ for $p = 1$. The effect of JSC explains the strongly increased damping [5] and thus the smear-out and vanishing of the FSs for $V \geq V_g/3$.

A numerical model of the flux flow in the FFO that takes into account all known noise sources (both internal and external) has been developed [8] and used for a comprehensive study of the linewidth, Δf, of the FFO. Δf has been calculated including thermal noise in the bias resistors as well as external low frequency interference from the current bias and control line circuitry. Fluctuations in the external bias parameters are accounted for by the dynamic resistance $R_d^I = dV_{FFO}/dI^B$ (bias current tuning) and the differential tuning resistance of the control line $R_d^{CL} = dV_{FFO}/dI^{CL}$. Only the low frequency components of the noise current density $S_i(f)$ need to be included in this calculation. The cut-off frequency is determined in a self-consistent way [9]. The superposition of shot and thermal (white) noise of a tunnel junction mainly determines Δf especially at large values of R_d ($\Delta f \propto R_d^2$).

Manuscript received April 30, 1999.
The work was supported in parts by the Russian SSP "Superconductivity", the Danish Research Academy, the Danish Natural Science Foundation, the Netherlandse Organisatie voor Wetenshappelijk Onderzoek (NWO) grant, ESA TRP contract 11/653/95/NL/PB/SC, and INTAS contract 97-1712.

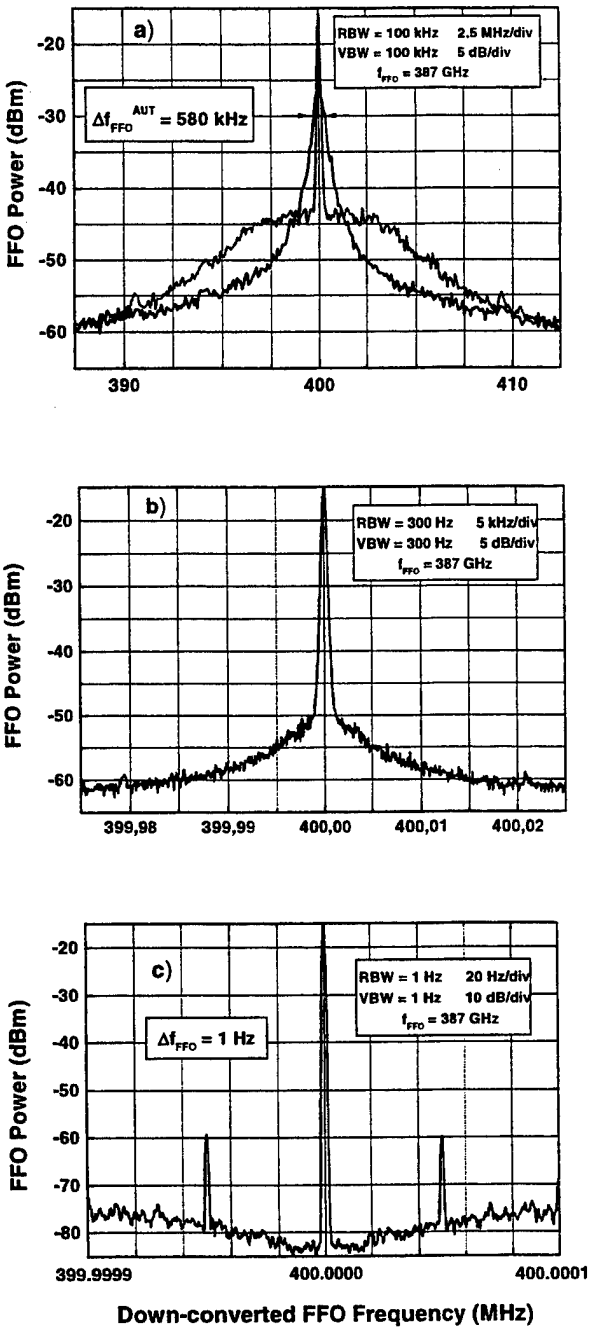

Fig. 1. Emitted radiation from the FFO (f = 387 GHz) down converted to a 400 MHz IF frequency. The power spectra recorded at different frequency spans and resolution bandwidths (RBW) clearly show the phase locking.

In the case of an external interference both R_d^I and R_d^{CL} "convert" the low frequency external noise current, I_{lf},to frequency fluctuations following the same relations: $\Delta f \propto R_d * I_{lf}$. Experimentally, for small R_d the external interference determines the FFO linewidth. The R_d^{CL} value is very low (about 5 mΩ) when biased on FS and increases considerably between steps. For $V > V_b$ in the "pure" flux-flow regime $R_d^{CL} \approx 0.1\ \Omega$ and remain almost independent of voltage. The noise caused by an external interference via R_d^{CL} ($I_{lf} \approx 0.1\ \mu A$) becomes dominant for $R_d < 10\ m\Omega$ in the resonant regime ($V < V_b$) and at $R_d < 0.1\Omega$ in the "viscous" flux-flow regime ($V > V_b$) with the present FFO design.

According to [9] the radiation linewidth may be reduced by altering the differential resistance and by changing the spectral noise density at low frequencies, $f < \Delta f$. This can be done by resistively shunting the junction at low frequencies and/or suppressing the current fluctuation by an external phase locking (PLL) system with a bandwidth large than Δf. In this paper a significant reduction of the FFO linewidth relative to the intrinsic FFO linewidth (determined by the wide band thermal fluctuations) is demonstrated by using an external electronic phase locked loop (PLL).

II. EXPERIMENTAL RESULTS AND DISCUSSION

The details of the circuit design and set-up are published elsewhere [4,5]. In the frequency range up to 600 GHz the FFO linewidth is measured by a new experimental technique [4], where the submm-wave signal coming from the FFO is mixed in the SIS mixer with the n-th harmonic of the external reference synthesizer frequency f_{SYN} (≈10 GHz, n ≈60). A high-pass microstrip filter with a cut-off frequency of about 200 GHz prevents the external reference signal (as well as its harmonics) from reaching the FFO. The intermediate frequency (IF) signal, $f_{IF} = \pm (f_{FFO} - n\ f_{SYN})$, is amplified in a cooled amplifier ($T_n \approx 20$ K, gain 27 dB). After additional room temperature amplification the ≈400 MHz IF signal enters the PLL system. In this unit the signal frequency is divided by four and (in a Frequency-Phase Discriminator) compared with a 100 MHz reference signal phase locked to the 10 GHz reference synthesizer. Via the Loop Bandwidth Regulator (maximum bandwidth about 10 MHz) an output signal proportional to the phase difference is returned to the FFO through a miniature coaxial cable and a cold 50 Ω resistor mounted on the bias plate. The same coaxial cable entering the cryostat is used for both the 10 GHz synthesizer signal and the PLL control output. Two couplers with microstrip filter are used to combine and split these signals.

In order to perform accurate linewidth measurement, the IF spectra have to be averaged with a sufficiently small video bandwidth. In the measurement of the autonomous FFO linewidth, Δf_{AUT}, we used the PLL system with a relatively low loop gain and narrow bandwidth setting (< 10 kHz) for *frequency locking* of the FFO to the 10 GHz synthesizer. As seen in Fig. 1a the shape of the measured linewidth is unchanged, but the average frequency is stabilized (frequency locking,).

It was experimentally found [8] that the PLL system can considerably narrow the FFO linewidth if Δf_{AUT} is initially lower (at the 3 dB level) than the PLL regulation bandwidth, B_{PLL}. In the opposite case where $\Delta f_{AUT} > B_{PLL}$ only frequency locking without a noticeable linewidth change is achieved. For Δf_{AUT} smaller than B_{PLL} (2.5 MHz < Δf_{AUT} < 10 MHz)

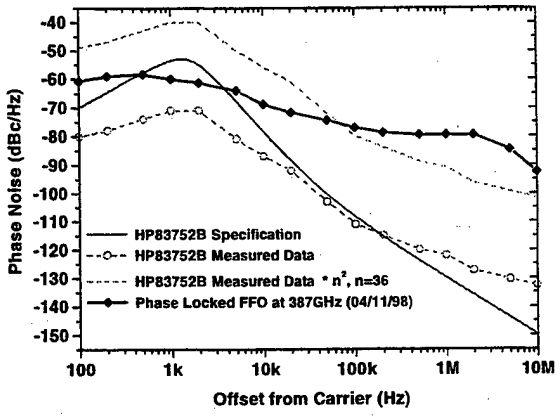

Fig. 2. Phase noise of the FFO phase locked at 387 GHz compared to data for the HP synthesizer.

there is an increase of the FFO power at the central frequency while the FFO linewidth is reduced [8]. By further decreasing Δf_{AUT} below 2 MHz (measurements were done at different values of R_d^I and R_d^{CL}) a sharp peak appears at the central frequency. Real phase locking takes place for $\Delta f_{AUT} <$ 2.5 MHz. Fig. 1 shows IF power spectra of the phase locked FFO measured at f_{FFO} = 387 GHz for different settings of the spectrum analyzer. A FFO linewidth as low as 1 Hz is presented in Fig. 1c. Actually this value is determined by the minimum resolution bandwidth of the spectrum analyzer.

It should be noted that a vertical step ($R_d^I = 0$) appears in the FFO IVC with the FFO locked. The position of this step is insensitive to small changes in the control line current, and accordingly also $R_d^{CL} = 0$. A hold-in range of the FFO bias voltage as large as 1.5 μV has been experimentally measured. This corresponds to a PLL regulation band of about 750 MHz. The pull-in limit which depends on the position of the operation point on the FS was approximately equal to the hold-in range. An additional 100 MHz reference signal can be applied from a second synthesizer phased locked to the first one. In this case the position of the PLL step could be tuned precisely by incrementing the reference signal in the frequency range 90 - 110 MHz in steps of 0.1 Hz (minimum increment of the synthesizer). This corresponds to voltage accuracy of $2*10^{-16}$ V.

The phase noise of the phase locked FFO is plotted in Fig. 2 (data from Fig. 1) as function of the offset from the carrier. The specification and measured data for the HP83752B synthesizer are shown in Fig. 2 for comparison. Actually the FFO was locked to the 36-th harmonic of the synthesizer at this measurements, but the phase noise of the FFO is measured relatively to the synthesizer and is not limited by the synthesizer noise multiplied to n^2 = 1296 (inside the PLL bandwidth).

Based on the above technique for phase locking of the FFO an all-superconducting Phase Locked Integrated Receiver has been proposed [8]. In this concept two separate SIS mixers are placed on the receiver chip and connected to the same FFO. One SIS mixer serves as the heterodyne detector of the receiver while the other is used for phase locking of the FFO. A simple prototype Integrated Receiver for the frequency range 400-450 GHz with PLL system is presently being tested for practical radio astronomy. The fully integrated astronomical receiver is under construction.

ACKNOWLEDGMENT

The authors thank Th. de Graauw, H. Golstein, M. Samuelsen, and H. van de Stadt for and fruitful discussions, and H. Smit and D. Van Nguyen for help in the experiments.

REFERENCES

[1] T. Nagatsuma, K. Enpuku, F. Irie, and K. Yoshida, "Flux-Flow type Josephson oscillator for millimeter and submillimeter wave region", *J. Appl. Phys.* vol. 54, pp. 3302-3309, 1983; see also Pt. II, *J. Appl. Phys.* vol. 56, pp. 3284, 1984; Pt. III, *J. Appl. Phys.* vol. 58, pp. 441, 1985; Pt. IV, *J. Appl. Phys.* vol. 63, pp. 1130, 1988.

[2] V.P. Koshelets, S.V. Shitov, L.V. Filippenko, A.M. Baryshev, W. Luinge, H. Golstein, H. van de Stadt, J.-R. Gao, T. de Graauw, "An Integrated 500 GHz Receiver with Superconducting Local Oscillator", *IEEE Trans. on Appl. Supercond.*, vol. 7, pp. 3589-92, 1997.

[3] S.V. Shitov, A.B. Ermakov, L.V. Filippenko, V.P. Koshelets, A.B. Baryshev, W. Luinge, Jian-Rong Gao, "Superconducting Chip Receiver for Imaging Applications". ASC-98, EMA-09, *IEEE Trans. on Appl. Supercond.* 1999, in press.

[4] V.P. Koshelets, S.V. Shitov, A.V. Shchukin, L.V. Filippenko, and J. Mygind, "Linewidth of submillimeter wave flux-flow oscillators," *Appl. Phys. Lett.*, vol. 69, pp. 699-701, July 1996.

[5] V.P. Koshelets, S.V. Shitov, A.V. Shchukin, L.V. Filippenko, J. Mygind and A.V. Ustinov, "Self-pumping effects and radiation linewidth of FFO," *Phys. Rev. B*, vol. 56, pp. 5572-77, Sept. 1997.

[6] L.-E. Hasselberg, M.T. Levinsen, M.R. Samuelsen, "Theories of subharmonic gap structures in superconducting junctions," *Phys. Rev. B*, vol. 9, pp. 3757-3765, 1974.

[7] M. Cirillo, N. Grønbech-Jensen, M.R. Samuelsen, M. Salerno, and R.V. Rinati "Fiske Modes and Eck Step in long Josephson junctions: Theory and experiment" *Phys. Rev B*, vol. 58, pp. 12377-83, 1998.

[8] V.P. Koshelets, S.V. Shitov, A.V. Shchukin, L.V. Filippenko, P.N. Dmitriev, V.L. Vaks, J. Mygind, A.B. Baryshev, W. Luinge, H. Golstein, "Flux Flow Oscillators for Sub-mm Wave Integrated Receivers". ASC-98, EQB-04, *IEEE Trans. on Appl. Supercond.* 1999, in press.

[9] K.K. Likharev *Dynamics of Josephson Junctions and Circuits*, Gordon and Breach 1986.

POSTER SESSION I

Group 1 - Digital

Measurements of an HTS Four Stage Shift Register Circuit

J. H. Park, Y. H. Kim, J. H. Kang*, T. S. Hahn , C. H. Kim, K. R. Jung*, J. M. Lee, and S. S. Choi

Korea Institute of Science and Technology, Seoul 136-791, Korea

*University of Inchon, Inchon 402-749, Korea

Abstract—**We fabricated a four stage shift register using YBCO bicrystal junctions and tested their operations by a computer-controlled digital measurement set-up. Laser ablated YBCO films were used in this work and they had a clean surface. Data shifts from a stage to the next stage were controlled by current pulse injected to the bias lines located between the stages. To measure the correct operation of the circuit we placed a read SQUID next to each side of the shift register. Read SQUIDs were inductively coupled to the nearby shift register stages. A probe equipped with high speed coax lines were used in this experiment and the interference between the read SQUIDs was the major obstacle in testing the multi-stage shift register circuit.**

Low-Jitter on-Chip Clock for RSFQ Circuit Applications

Yongming Zhang [a)] and Deepnarayan Gupta [b)]
a) Conductus, Inc., 969 West Maude Ave., Sunnyvale, CA 94086
b) HYPRES, 175 Clearbrook Rd., Elmsford, NY 10523

Abstract—The ultra narrow linewidth of a long Josephson junction (LJJ) oscillator offers low timing jitter as a clock source. In this abstract, we will discuss the improvement of an LJJ clock by using an annular geometry. We demonstrate the integration of an annular LJJ with a clock decimator which consists of a serial chain of toggle-flip-flops (TFFs). Each TFF divides its input frequency by a factor of 2. We have also developed a clock frequency selector. The clock selector circuit can choose either the master clock f_m or one of its sub-harmonics ($f_m/2^m$, m=1 to n), based on the select inputs. The generation of a set of clocks will enable us to integrate the on-chip LJJ clock with a flash analog-to-digital converter.

I. INTRODUCTION

The need for generation and distribution of a stable, low-jitter, on-chip, clock is well known in the superconducting electronics community. The RSFQ technology is based on the presence or absence of a *fluxon* (a quantum of magnetic flux, $\Phi_0=h/2e$ =2.07 mV.ps) in a circuit with respect to a clock. Almost all RSFQ circuits are clocked. The timing of the clock pulse, also in the form of a fluxon, is very important. Currently, high-performance RSFQ circuits, such as a digitizer employing a wide bandwidth ADC [1-2], derive the fluxon clock from an external signal generator. There are two problems with this approach: 1) the external clock source is expensive and adds to the system complexity, and 2) at high frequency, external clock jitter affects the circuit performance. The first problem is of immediate concern for commercialization of digitizer instruments with 10-20 GHz bandwidth. The second problem is expected to impede the development of higher performance superconducting technology in the future.

It is well known that a very stable, high-frequency oscillator can be made using the propagation of sine-Gordon solitons in a nonlinear system - the long Josephson junction (LJJ). The long junction has some unique features that are unattainable by overdamped RSFQ circuits, such as a very narrow radiation linewidth. For an LJJ working in the resonant soliton mode, a linewidth less than 40 kHz is obtainable at 12 GHz [3]. Fluxons generated at one junction end can provide very narrow clock pulses for RSFQ circuits. We has demonstrated both experimentally [3] and numerically [4] that the RSFQ pulses generated by an LJJ can be successfully launched into RSFQ circuits. It shows that a LJJ-based soliton oscillator providing adequate power for clocking SFQ circuits.

Manuscript received April 30, 1999.
This work was supported in part by the National Science Foundation under Grant No. DMI-9861554.

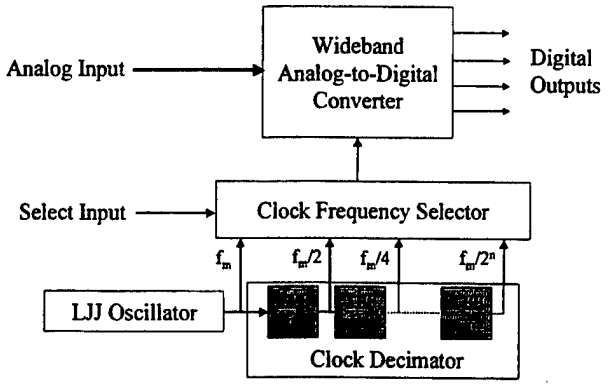

Fig. 1 A proposed flash ADC with integrated LJJ clock.

Currently, we are developing a low-jitter on-chip clock for ADC circuit applications. A block diagram of the wideband ADC with on-chip clock is shown in Fig.1. The LJJ oscillator acts as the master clock source. The clock frequency is decimated using a chain of toggle-flip-flops (TFFs). The clock selector chooses either the master clock (f_m) or one of its sub-harmonics, based on the select inputs, and supplies the stream of SFQ clock pulses to the ADC. In this paper, we demonstrate for the first time the integration of an annular long junction oscillator with SFQ circuits, some unique features by using an annular junction instead of a linear one-dimensional LJJ are discussed. We also show the test results for a clock frequency selector circuit

II. ANNULAR LONG JUNCTION COUPLED TO SFQ ELEMENTS

A long Josephson junction can be formed not only by a linear one-dimensional geometry, but also by an annular or ring-shaped geometry [5-6]. An annular LJJ not only eliminates boundary effects, but also, due to flux quantization, makes it possible to trap a single soliton. The trapped solitons can move under an infinitely small bias current, and therefore eliminates the supercurrent.

Fig. 2 shows the circuit that integrates an underdamped annular LJJ with RSFQ circuits. The circuit is very similar to the previous circuit [3] except the long junction is now in an annular geometry. The long junction is terminated with a Josephson transmission line (JTL) at one point. Another end of the JTL is connected to a chain of an eight-stage TFFs. All Josephson junction in the RSFQ cells are resistively shunted. A superconducting control line is designed above the LJJ to apply a dc current I_{CL} in the control-line and create a magnetic field in the long junction.

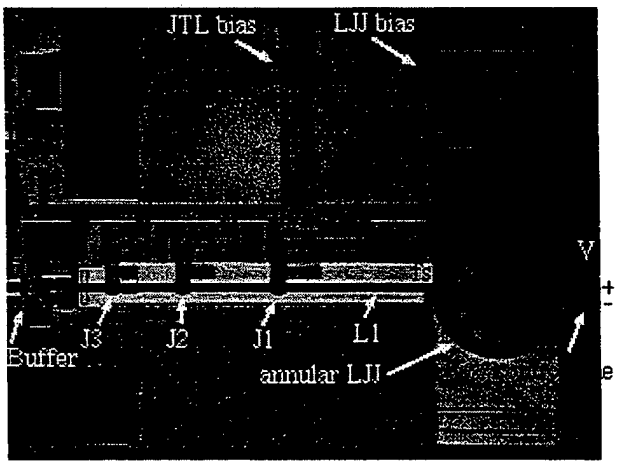

Fig. 2 An optical micrograph of a fabricated annular long junction that is coupled to the SFQ circuit. The length of the junction is 230 μm, and the width is 5 μm. The circuit was fabricated using HYPRES 1kA/cm^2 Nb/AlOx/Nb junction fabrication process.

DC characterization of this integrated long junction shows similar behavior as an isolated annular LJJ. It shows a series of evenly spaced voltage steps, each step corresponding to a discrete number of solitons and antisolitons circulating around the junction. These steps correspond to resonant soliton modes. The step voltage is related to the soliton propagation velocity u by [6]

$$V_n = (nu/l)\Phi_0, \qquad (1)$$

Where n is the total number of solitons and antisolitons and l is the junction length (circumference) of the junction. For the annular junction, n satisfies the relation $n=n_0+2i$, where $i=0,1,2,\ldots$, and n_0 is the number of solitons initially trapped. With no trapped soliton ($n_0=0$), the even series of voltage steps is observed and the supercurrent reaches its maximum (7.0mA) when there is no applied field ($I_{CL}=0$). With one trapped soliton $n_0=1$, however, the odd series of the voltage steps is observed, see Fig.3 for step $n=1,3,5$. The odd series is associated with a very small (0.8mA) supercurrent.

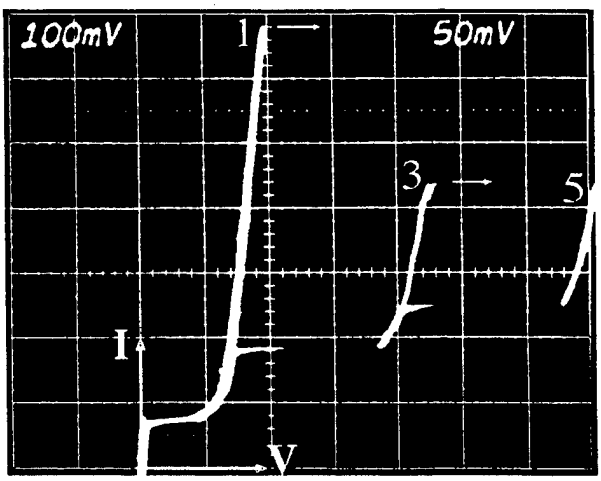

Fig. 3 Current vs voltage for various numbers of solitons at 4.2K There is one trapped soliton. The number next to each curve is the total number of the solitons and antisolitons moving to produce that curve.

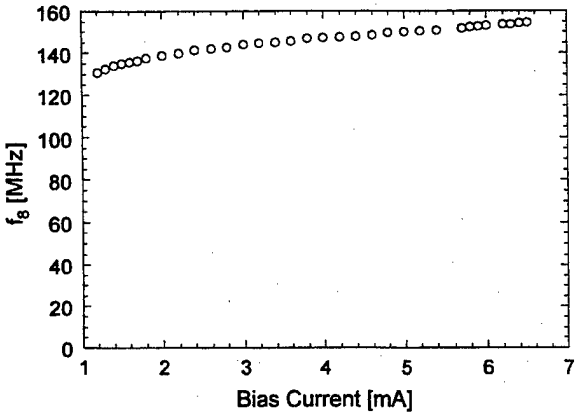

Fig. 4 Resonance frequency at the 8th TFF output fg vs bias current of the annular long junction biased on the n=1 step (I_{CL}= 9mA).

For the applications as an on-chip clock, an annular LJJ with one trapped soliton seems as the preferred choice. The small supercurrent makes the long junction oscillator much easy to bias. We noticed that the first resonant mode (n=1) in Fig. 3 has a bias range from 1 to 7 mA while for a linear LJJ the bias range is from 3.5 to 5.5mA [2]. Also, for a linear LJJ, our measurement shows that it is difficult to 1) bias on the first soliton step due to a large supercurrent, 2)keep bias on the resonant step for a long time before it switches to the supercurrent or the normal states. Both problems disappear for the annular LJJ with one trapped soliton.

The even series was obtained by careful cooling through the transition temperature with zero bias current, to ensure that flux was not trapped in the film or the junction. To trap one soliton in the annular junction, two methods have been used in the experiment. In the first method, we leave a suitable bias current present while cooling. Since it is hard to determine the bias current, the process is difficult to control. In the second method, we first cool the circuit to 4.2K without any bias, producing even series of soliton modes. We then apply an external magnetic field using a control current (I_{CL}). The supercurrent I_C suddenly drops from a constant value (7.2mA) to a minimum (about 0.8mA for the sample shown in Fig.2) when the I_{CL} reaches a certain level (9mA). At this field, one soliton (2π-kink) is trapped in the junction, the even series disappears and the odd series appears simultaneously. The second method is very reproducible and Fig. 3 was obtained via this method.

When we bias the LJJ on the soliton steps, we observed a digital output at the 8th TFF output. It indicates the fluxons in an annular LJJ can be successfully launched into a Josephson transmission line and coupled to RSFQ TFFs. With a microwave spectrum analyzer, we measured the radiation frequency accurately from the TFF output. Fig. 4 shows the radiation frequency at the 8th FF output when the LJJ is biased on the first step shown in Fig.3. Since each TFF divides the frequency by 2, we can calculate the oscillation frequency inside the LJJ as $f_S = f_8 \times 2^8$. An RSFQ pulse is generated in the first JTL junction J1when the soliton in the LJJ passes the interface point. For a bias current of 6mA, f_8 =152.96MHz, corresponding to f_S=39.16GHz, in good agreement with the first step voltage shown in Fig. 3.

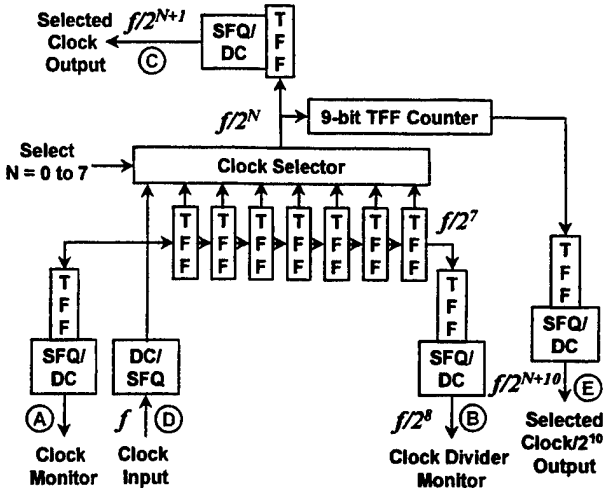

Fig.5 The clock frequency selector circuit.

III. CLOCK FREQUENCY SELECTOR

The performance of an ADC circuit is usually characterized over a wide range of sampling clock frequencies [1]. In order to incorporate an LJJ on-chip clock into the ADC circuit, a clock-frequency selector circuit was also developed. The clock selector circuit facilitates the circuit characterization as well as improves testability. The clock frequency is decimated using a chain of TFFs. The clock selector chooses either the master clock (f_m) or one of its binary sub-harmonics, based on the select inputs. We have implemented a version of this circuit where 8 different clock frequencies ($f/2^N$, N= 0,1,2,..,7) can be generated and selected (Fig. 5). We added a 9-bit TFF counter to decimate the selected clock frequency down by a factor of 2^9 to be able to monitor the outputs (E) on a low bandwidth oscilloscope. Fig. 6 shows selected clock outputs for N = 2, 5, and 7. The clock selector circuit also operates over a wide range of input clock frequencies. Fig. 7 shows the selected clock outputs at different master clock frequencies.

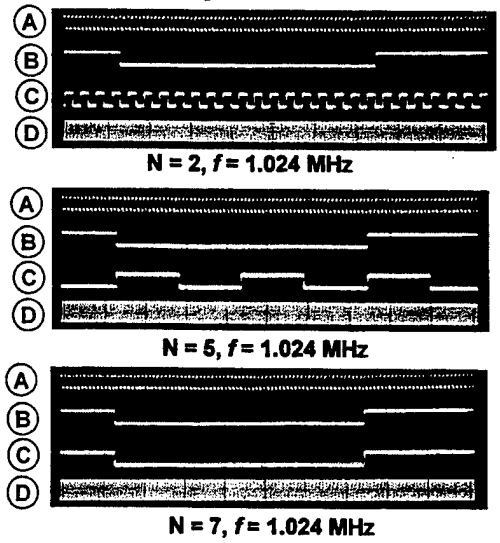

Fig. 6 Four different selected clock outputs ("C" with a frequency of $f/2^{N+1}$) for N = 2, 5 and 7 are shown.

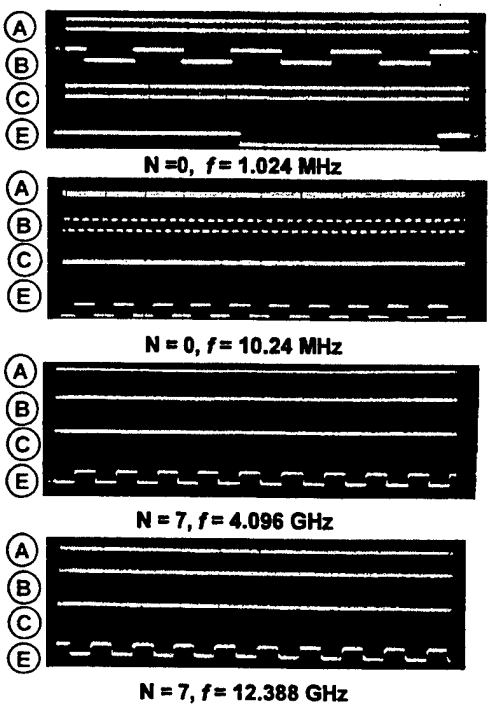

Fig. 7 The selected clock outputs at different master clock frequencies.

IV. CONCLUSIONS

In conclusion, our experiments confirm that an underdamped annular long junction can be used as a stable on-chip master clock for ADC circuits. Measurements from the LJJ/RSFQ hybrid circuit show clear resonant steps in the I-V curves. With one trapped soliton, the annular junction has a very *wide stable bias range* on the first soliton resonant step that has oscillation frequencies around 40GHz. A 2π phase leap at the LJJ/JTL interface creates one RSFQ pulse during each oscillator period for the single soliton mode. We also developed a clock frequency selector circuit that operates over a wide input clock frequency range.

ACKNOWLEDGMENT

Stimulating discussions with Seva Kaplunenko, Alex Kirichenko, and Steve Kaplan are acknowledged.

REFERENCES

[1] P. Bradley, "A 6-bit Hosephson flash A/D Converter with GHz input bandwidth", *IEEE Trans. on Appl. Superconduct.*, vol. 3, no. 1, 1993.

[2] S.B. Kaplan, P. Bradley, D.K. Brock, D.V. Gaiderenko, D. Gupta et al, "A superconductive flash digitizer with on-chip memory," to appear in *IEEE Trans. on Appl. Supercond.*, June 1999.

[3] Y. M. Zhang, V. Borzenets, V. K. Kaplunenko, and N. B. Dubash, "Underdamped long Josephson junction coupled to overdamped single-flux-quantum circuits," *Appl. Phys. Lett.*, vol. 71, pp. 1863-1865, Sept. 1997.

[4] Yongming Zhang, "Modeling of a long Josephson junction coupled to SFQ elements", to appear in *IEEE Trans. Appl. Superconduct.*, June 1999.

[5] A. Davidson, B. Dueholm, B. Kryger and N.F. Pedersen, "Experimental investigation of trapped sine-Gordon solitons", *Phys. Rev. Lett.*, vol.55, pp.2059-2062, November 1985.

[6] A. Davidson, B. Dueholm, and N.F. Pedersen, "Experiments on soliton motion in annular Josephson junctions", *J. Appl. Phys.*, vol.60, pp.1447-1454, August 1986.

Design and Experimentation of BSFQ Logic Devices

T. Hosoki, H. Kodaka, M. Kitagawa and Y. Okabe
Research Center for Advanced Science and Technology, University of Tokyo
4-6-1 Komaba, Meguro-ku, Tokyo 153-8904, JAPAN

Abstract—The rapid single flux quantum (RSFQ) logic needs synchronous pulses for each gate, so the clock-wiring problem is more seriously when designing larger scale circuits with this logic. So we have proposed a new SFQ logic which follows Boolean algebra perfectly by using set and reset pulses. With this logic, the level information of current input is transmitted with these pulses generated by level-to-pulse converters, and each gate calculates logic using its phase level made by these pulses. Therefore, our logic needs no clock in each gate. We named this logic "Boolean SFQ (BSFQ) logic." In this conference, we report design and experimentation of AND gate with inverting input based on BSFQ logic. The Experimental results of OR and XOR gate are also reported.

I. INTRODUCTION

The primary logic for single flux quantum circuits is the rapid single flux quantum (RSFQ) logic that has been proposed by Likharev group [1]. Many approaches have been made with this logic, and it is not too much to say that RSFQ supports today's superconductive electronics. Recently T flip-flop operating at 370 gigahertz and fundamental logic gates operating at several tens gigahertz were reported. But this is pulse logic which recognize "1" state when an SFQ pulse comes and "0" state when no pulses come at a certain time. Therefore each fundamental logic gate needs synchronous pulses and has 1 clock delay. Several studies have been proposed such as DDST [2] and dual rail logic for asynchronous circuits [3] to improve this logic, but the problem that each gate needs clock timing is remained.

So we have proposed a new SFQ logic which follows Boolean algebra perfectly by using set and reset pulses [4]. We named this logic "Boolean SFQ (BSFQ) logic. This logic is a level logic like CMOS and needs not clock for each gate. Clock is required for each block of combination circuit when sequential circuits are made up, but the number of clock wires is much less than RSFQ logic and the delay is 1 clock for each block of the combination circuit.

Manuscript received April 30, 1999.
The part of this work was performed through Special Coordination Funds for promoting Science and Technology of the Science and Technology Agency of the Japanese Government.

II. BSFQ LOGIC

A. Level to pulse converter

This was called "DC-to-SFQ converter" before, but the old name often led to confusion with RSFQ DC-to-SFQ converter and the operation seems to be difficult to understand by the name. Therefore we renamed to above-mentioned.

This circuit converts the level information of input current I_{in} to SFQ pulses. If I_{in} changes its state from low to high, the phase level of inductance L_1 increases, and a pair of SFQs is generated under L_2 and L_4. An SFQ on the side of L_2 is only transmitted to set JTL because Ic_2 is smaller than Ic_3, and another SFQ remains trapped at the converter. Then when I_{in} returns its state to low, J_1 is broken and the left SFQ is also transmitted to reset JTL, and the converter returns to initial state.

B. AND, OR gates

AND and OR gates have same circuit structure and only parameters of the elements are different. Each gate is divided into two parts:—pulse-to-level converting part (left side from J_0 in Fig. 1), and level-to-pulse converting part. When input current is set to high, that is, set pulse comes to a gate, the phase level of L_1 increases because the SFQ is trapped the loop which contains J_0 and L_1. Then the level-to-pulse converting part generates a pair of SFQs. If both of inputs are set to high, the phase of L_1 increases twofold. Phase threshold of L_1, which the set pulse is transmitted on, is set to 2 steps at AND gate and 1steps at OR gate. Adjusting inductance and biases sets these thresholds. Trapped SFQ is coupled with another SFQ, which transmitted from reset JTL and disappears.

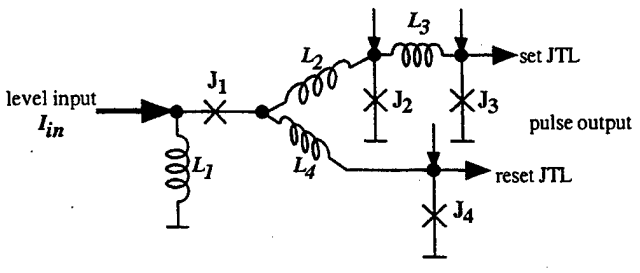

Fig. 1: Level to pulse converter

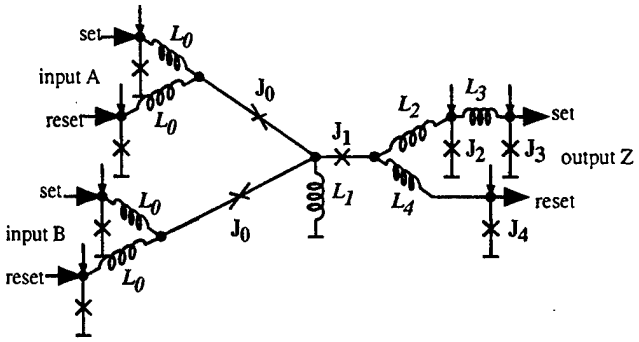

Fig. 2: 2-input AND, OR gate

C. Inverter

BSFQ circuit is a dual rail logic. An inverter with a dual rail logic is generally obtained only by crossing lines, but fundamental gates with present BSFQ logic use same inductance L_0 to both of set and reset input terminals, so that it is not able to distinguish set and reset line. Therefore an inverter with BSFQ logic is obtained by putting an SFQ in relevant reset input terminal at initial state.

D. XOR Gate

It is well known that XOR gate can be made from combination of above-mentioned gates, but the number of junctions is several times larger than other gates. So we propose another type of XOR gate. This uses level-to-pulse converter and RSFQ confluence buffer. If either input becomes high, an SFQ is trapped the loop which contains J_0 and L_1, and set pulse is output. Then when the input becomes low or another input becomes high, the trapped SFQ is coupled with subsequent SFQ and disappears.

III. Design and Experimentation

We designed AND with input-invert terminal, OR, and XOR circuits. Each circuit has two level-to-pulse converters and a pulse-to-level converter because all of these circuits are 2-input 1-output circuits.

The chip was fabricated using their standard Nb/AlOx/Nb process by NEC Corporation [5].

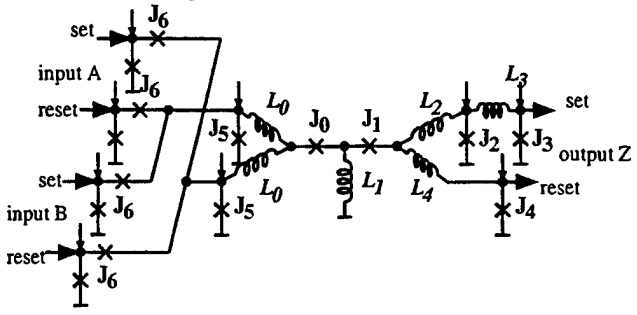

Fig. 3: XOR gate

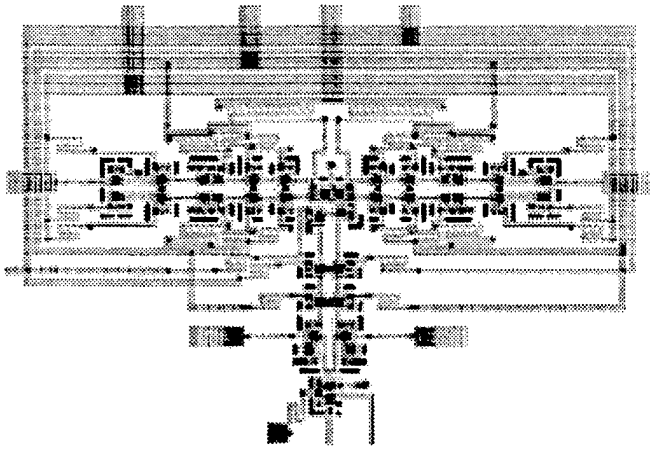

Fig. 4: Layout of an OR circuit

IV. Results

Fig. 5 and Fig. 6 are as the results of the same AND circuit. The invert-input terminals are connected to the confluence buffers with RSFQ DC to SFQ converters. If a terminal is set to high at initial state, the input whose reset JTL has the connection to the confluence buffer is inverted. Both of input-invert terminals were set to high at initial state in Fig. 6. Therefore, both of inputs were inverted and this circuit operated as (NOT A) AND (NOT B), that is, A NOR B.

Fig. 7 and Fig. 8 show the results of OR and XOR gate, respectively. Output voltage changes to high for a short time when both of inputs change from high to low. (Fig. 7) The reason for this is probably that either input signal delays in measurement system, and the gate seems to operate correctly.

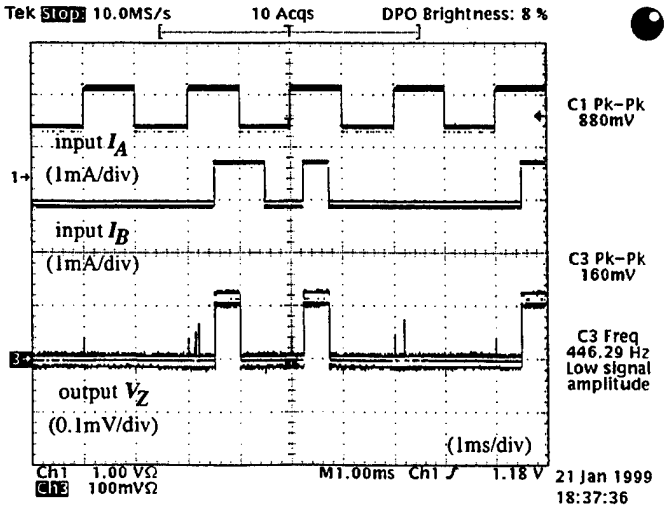

Fig. 5: AND gate without invert-input biases

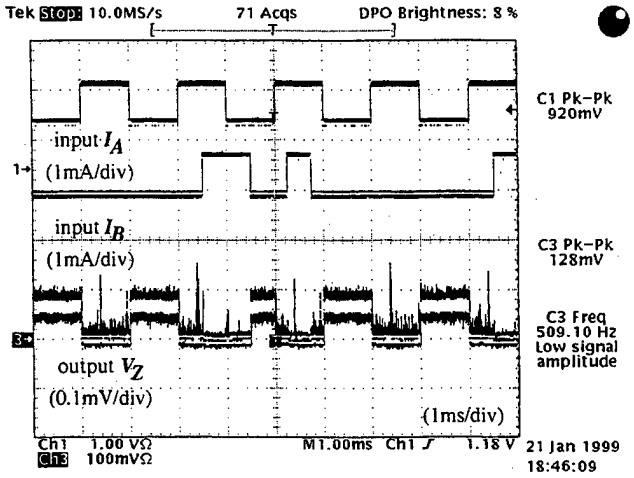

Fig. 6: AND gate with invert-input biases (equals to NOR gate)

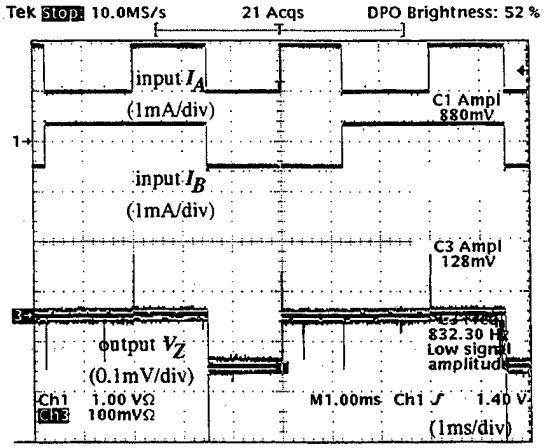

Fig. 7: OR gate

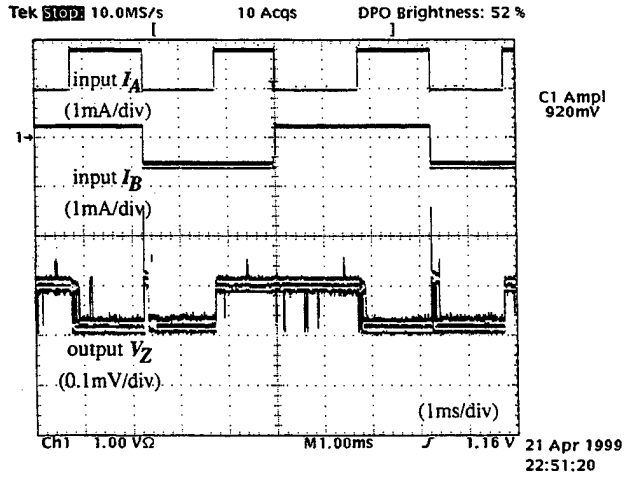

Fig. 8: XOR gate

V. Discussion

Fundamental logic gates with BSFQ operated correctly. But if an error is occurred somewhere from unexpected flux trapping in the circuits, these gates are not able to recover themselves with present logic, and we must make circuits temperature higher than critical temperature or use some forcible measures. So it is much difficult to correct the operation of complicated circuit when even an error occurs. We have designed and tested some combination circuits such as full adder and decoder, but have not get the results with proper outputs yet.

We are now designing improved BSFQ logic gates to solve this problem. The improved gates are able to correct the operation themselves, and inverter can simply obtained by crossing lines like other dual rail logics.

VI. Conclusion

We have designed and gotten the experimental results with correct operation of fundamental BSFQ logic gates, that is, AND, OR, inverter, and XOR. So we will make more study for designing the improved BSFQ logic gate, many input/output combination circuits and sequential circuits.

References

[1] K. K. Likharev and V. K. Seminov, "RSFQ logic/memory family: A new Josephson-junction technology for sub-terahertz-clock frequency digital systems," *IEEE Tans. Appl. Superconduct.*, vol. 1, pp. 1-28, March 1991.

[2] Z. J. Deng, N. Yoshikawa, S. R. Whiteley, and T. Van Duzer, "Data-driven self-timed RSFQ digital integrated circuit and system," *IEEE Trans. Appl. Superconduct.* Vol. 7, pp. 3634-3637, June 1997.

[3] M. Maezawa, I. Kurosawa, M. Aoyagi, H. Nakagawa, Y. Kameda, and T. Nanya, "Rapid single-flux-quantum dual-rail logic for asynchronous circuits," *IEEE Trans. Appl. Superconduct.*, vol. 7, pp. 2705-2708, June 1997.

[4] H. Kodaka, T. Hosoki, M. Kitagawa, and Y. Okabe, "SFQ data processing with Set/Reset information," *IEEE Transaction on Applied Superconductivity.*, in press.

[5] S. Nagasawa, Y. Hashimoto, H. Numata, and S. Tahara, "A 280 ps, 9.5 mW Josephson 4-Kbit RAM Operated at a High Bit Yield", *IEEE Trans. Appl. Superconduct.*, vol. 5, pp. 2447-2452, 1995

Time Characteristics of a Josephson Balanced Comparator

Timur Filippov
SUNY at Stony Brook, NY 11794-3800, USA

Maxim Znosko
Moscow State University, Moscow 119899, RUSSIA

Abstract—We consider the time characteristics of a balanced comparator formed by two Josephson junctions connected in series. Such a decision-making junction pair is an essential component of all RSFQ cells. The analysis is performed within the framework of a simple time-dependent oscillator model. Turn-on delay and uncertainty (jitter) of comparator switching times are analyzed taking into account the influence of thermal fluctuations and the finite time duration of clock pulse. Restrictions on speed performance of RSFQ cells caused by both times are considered. Some practical recommendations on the clock frequency increase are also discussed.

I. Introduction

The noise immunity of RSFQ circuitry has been under intensive theoretical and experimental consideration for the last several years. The main efforts were focused on analysis of two major components of these circuits: a current-switched Josephson junction and a phase-driven comparator. Both time and current statistics of switching events have been studied in the case of a single junction [1], [2]. A simple theory to describe the current statistics of the comparator has been developed and tested experimentally [3], [4]. In [5] the first attempt to analyze time statistics (switching time or turn-on delay and switching time jitter) was performed for a strongly overdamped Josephson junctions (McCumber-Stewart parameter β_c=0) and instant change of external signals. Because these conditions are not satisfied in practical RSFQ circuits, our goal was to extend the theoretical analysis of the balanced comparator.

II. Model

The balanced comparator (Fig.1) consists of two Josephson junctions J_{c1} and J_{c2}, with close values of the critical current I_c. The junctions are connected in series as seen by the clock pulse but in parallel for the signal current I_x to be measured. If an SFQ pulse arrives at the clock input, it causes a 2π-leap of the Josephson phase across either J_{c1} or J_{c2}, depending on whether I_x is lower or higher than a threshold current I_t (in the case of similar junctions I_t=0).

Manuscript received April 30, 1999.
This work was supported in part by ONR Grant # N000149810082, directly by HYPRES, ERICSSON and Russian Program on "Advanced Problems of Condensed Matter Physics".

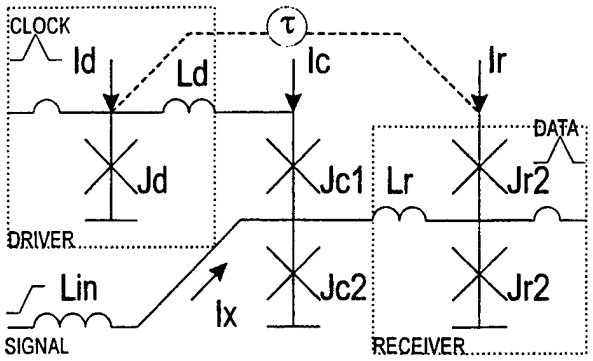

Fig.1 Equivalent circuit of the balanced comparator and its environment.

We will consider the comparator within the framework of the time-dependent oscillator model [6], [7] and accept the phase drop $\phi_0=\varphi_1+\varphi_2$ across two junctions to be a fixed function of time: $\cos[\phi_0(t)/2] = 2\exp(-\kappa t) - 1$. The parameter κ characterizes the speed of driving waveform and its value depends on the comparator driver. (The procedure to extract the parameter κ is described in [3].)

The phase difference $x = \varphi_2 - \varphi_1$ behaves like a Gaussian packet with the mean coordinate $\langle x(t)\rangle$ and deviation $\sigma^2(t)$. The exact expressions for $\langle x(t)\rangle$ and $\sigma^2(t)$ can be found in [7]. The switching of the lower junction J_{c2} caused by arrival of a clock pulse can be described in terms of the transition probability P from the initial state located at $\langle x(t_0)\rangle$ to the interval $[A,\infty)$:

$$P = \frac{1}{(4\pi\sigma^2)^{1/2}} \int_A^\infty \exp\left(-\frac{(x-\langle x\rangle)^2}{4\sigma^2}\right) dx \,. \qquad (1)$$

As usual (see, e.g., [2]) we can introduce the density probability

$$\rho(t) = \frac{\frac{\partial P}{\partial t}}{P(\infty)-P(0)}, \qquad (2)$$

which satisfies the normalization condition, and write the expressions for turn-on delay (n = 1) and switching time jitter (n = 2) as follows:

$$\langle t^n \rangle = \frac{\int_0^\infty t^n \frac{\partial P}{\partial t} dt}{P(\infty)-P(0)} = \frac{\int_{y_1}^{y_2} t^n(y) e^{-y^2} dy}{\sqrt{\pi}[P(\infty)-P(0)]}, \qquad (3)$$

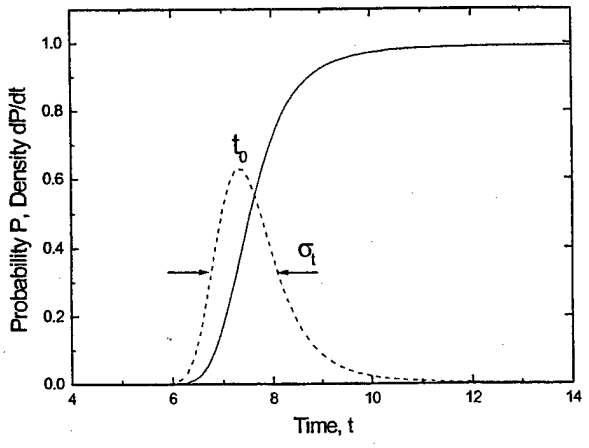

Fig.2 The time dependencies of transition probability (solid line) and the probability density (dashed line) for β_c=1, κ/ω_c=0.3 and $I_x/2I_c$=0.04 .

where $y = \dfrac{\langle x(t)\rangle - A}{2\sigma(t)}, y_1 = y(0), y_2 = y(\infty).$

Expanding $t^n(y)$ in series near $y = 0$, we get

$$\langle t\rangle = t_0, \quad \langle x(t_0)\rangle = A, \tag{4}$$

$$\sigma_t = \langle t^2 - \langle t\rangle^2\rangle^{1/2} = \frac{\sqrt{2}\sigma}{d\langle x(t_0)\rangle/dt}. \tag{5}$$

The turn-on delay t_0 corresponds to the moment of time when the mean coordinate <x> reaches the boundary A; the switching time jitter σ_t is the time required for a Gaussian packet to cross the boundary A at rate $d\langle x\rangle/dt$.

III. Main results

The typical dependencies of the transition probability (1) and probability density (2) on time are shown in Fig.2. Time

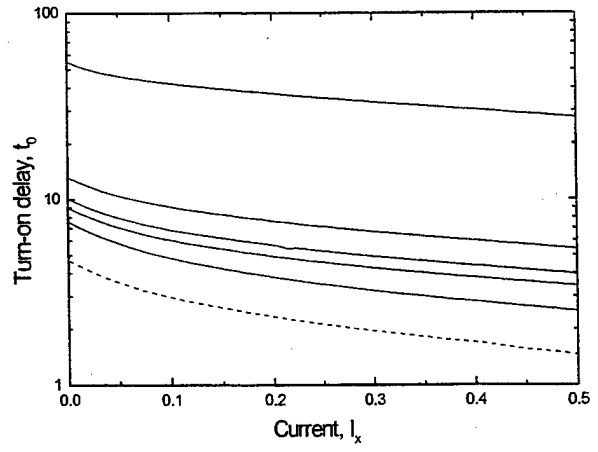

Fig.3 Turn-on delay versus I_x for different switching rates κ / ω_c = 0.01, 0.1, 0.2, 0.3, 1 (from top to bottom) and β_c = 1, $\gamma = 10^{-3}$. Current is measured in the units of $2I_c$. $\gamma = I_T/I_c$, where the $I_T = 2\pi\ k_B T/\Phi_0$. Dashed line: κ/ω_c=1, β_c=0.01

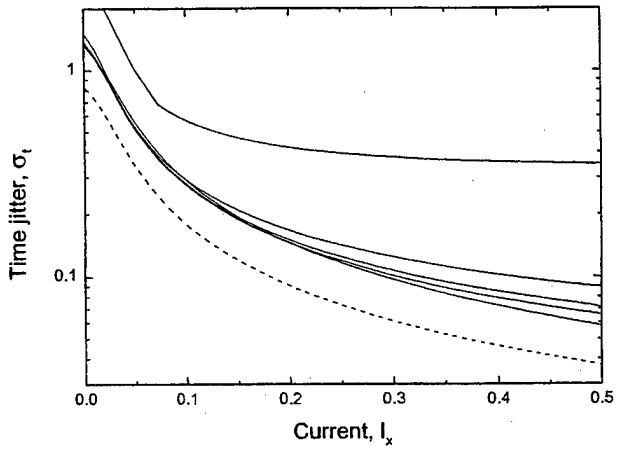

Fig.4 Time jitter versus I_x for different κ switching rates κ/ω_c = 0.01, 0.1, 0.2, 0.3, 1 (from top to bottom) and β_c = 1, $\gamma = 10^{-3}$. Current is measured in the units of $2I_c$. Dashed line: κ/ω_c=1, β_c = 0.01 .

is measured in units of $\omega_c^{-1} = \Phi_0/2\pi I_c R$. Results of numerical calculations for turn-on delay and switching time jitter are presented in Fig.3 and Fig.4 respectively.

The two main conclusions can be done. First, the both time characteristics depend on input current I_x and grow for small I_x. This means that cells loaded by small input current restrict the maximum clock frequency ($f_{max} < 1/t_0$) and introduce a large time uncertainty in the position of output pulses. Second, turn-on delay and time jitter are higher for smaller dimensionless κ. So it is better to use "sharp" clock pulses to decrease t_0 and σ_t. This situation is opposite to the gray zone ΔI_x of the comparator (Fig.5), which requires "soft" clock pulses for its reduction.

Note that the time characteristics have been calculated for $A=\pi/2+1/2$ [2]. To check the quasi-independence on the boundary A, we have calculated turn-on delay and switching time jitter for different values of the boundary A. Results are

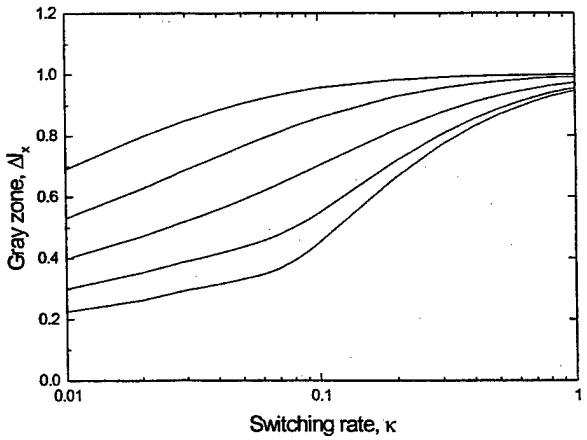

Fig.5 Gray zone versus switching rate κ/ω_c for different β_c=0.01,0.1,1,10,100 (from top to bottom). The gray zone is measured in the units of $(2\pi I_c I_T)^{1/2}$.

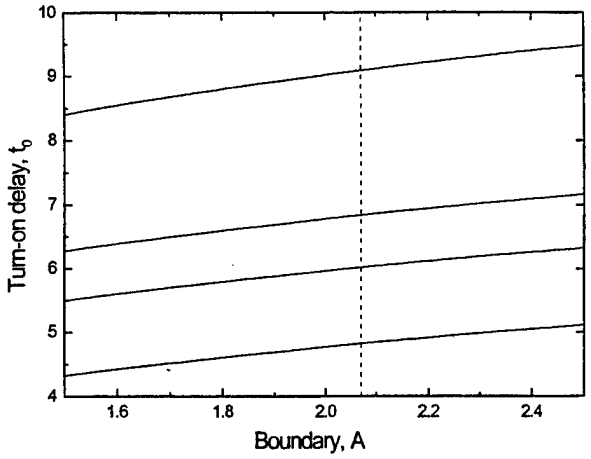

Fig.6 Turn-on delay versus A for different switching rates κ/ω_c=0.1,0.2,0.3,1 (from top to bottom) and β_c = 1, $\gamma = 10^{-3}$. Dashed line corresponds to $A=\pi/2+1/2$.

presented in Fig.6 for turn-on delay. One can see the dependence on A is not too strong (such a quasi-independence on A is valid also for time jitter).

IV. Discussion

Parameter κ is determined by the comparator driver and can be varied in the broad range [4]. Its typical dimensionless value is about 0.1 for a "standard" RSFQ driver. The use of "soft" clock pulses (smaller κ), as shown in [4], reduces the gray zone of a comparator and the probability of decision errors (we use the classification of errors given in [5]). But simultaneously it increases the probability of timing errors and therefore reduces the maximum clock frequency. Because both kinds of errors should be minimized the recommendation [4] to reduce κ by using "soft" driving pulses which are spread as much as possible over the available time interval between the neighboring pulses is not valid.

For dimensionless $\kappa = 0.1$ and input current $I_x/I_c = 0.7$ the switching time jitter is about 0.1 or 0.1ps for the standard 1-kA/cm^2 technology of HYPRES, Inc [8]. This is small enough for one particular cell, but for N cells connected in series the resulting time jitter grows as $N^{1/2}$ [5], [9] and becomes critical for long timing loops. (That is why a designer should avoid long clock lines or optimize them at least comparing data and clock loops.) One segment of a Josephson transmission line can be considered as a comparator in which the upper junction is replaced by nonlinear inductance and a similar analysis can be applied also to JTL.

The dashed lines in Fig.3 and Fig.4 correspond to the particular case considered in [5]: an overdamped Josephson junction (β_c=0.01) and instant change of driving waveform ($\kappa/\omega_c = 1$). One can see that they approximately represent the most practical case (β_c=1, κ/ω_c=0.1). This means that the approach developed in [5] can be used to make tentative estimates of timing errors.

In a logical SFQ cell (e.g., T-flip-flop which is formed by two comparators) the input current I_x is determined by the intrinsic flux state of the cell. So it is the designer's responsibility to make it large enough to reduce switching uncertainty and corresponding timing errors. Note that the increase of I_x comparative to the gray zone ΔI_x also decreases the probability of decision errors. The upper limit of current to be measured is restricted by so-called storage errors [5].

In the case of SFQ analog-to-digital converters, current I_x is an analog waveform to be quantized. The particular quantizer described in [10] includes a digital/analog feedback and the effective signal current I_x is held close to threshold current I_t: $|I_x-I_t|=\Phi_0/L_{in}\cong\Delta I_x$ (Fig.1). The corresponding time uncertainty of output SFQ pulses is unacceptably large (~10ps) and can break the operation of the whole device. To eliminate this effect a special circuit (Receiver in Fig.1) should be implemented. This is an additional comparator connected via relatively small inductance L_r. In this case the input current for the second comparator is larger than its gray zone and appropriately delayed (τ in Fig.1) clock pulse switches the second comparator with small time uncertainty. However this scheme requires additional efforts to minimize the interplay of two comparators. But a simple estimation shows that such a quantizer will operate at frequency up to 40GHz.

Acknowledgment

We would like to thank V.Semenov and K.Likharev for numerous stimulating discussions.

References

[1] K.Likharev, *Dynamics of Josephson Junctions and Circuits*. New York: Gordon & Breach, 1986.

[2] A.Pankratov, "On certain time characteristics of dynamical systems driven by noise," *Phys. Lett.*, vol. A234, pp. 329-335, 1997.

[3] T.Filippov, V.Semenov and K.Likharev, "Signal resolution of RSFQ comparators," *IEEE Trans. Applied Superconductivity*, vol.5, pp.2240-2243, June 1995

[4] V Semenov, T.Filippov, Y.Polyakov and K.Likharev, "SFQ balanced comparators at a finite sampling rate," *IEEE Trans. Applied Superconductivity*, vol.7, pp. 3617-3621, June 1997

[5] A.Rylyakov and K.Likharev, "Pulse jitter and timing errors in RSFQ circuits," *IEEE Trans. Applied Superconductivity*, in press.

[6] T.Filippov, "Quantum dissipation properties of a Josephson balance comparator," *JETP Lett*, vol. 61, pp. 858-864, May 1995

[7] T.Filippov, "The quantum dissipative properties of a Josephson balance comparator," *Russian Microelectronics*, vol. 25, pp. 250-256, 1996

[8] *HYPRES Designs Rules*, available from HYPRES, Inc., 175 Clearbrook Rd., Elmsford, NY 10523, phone 914-592-1190.

[9] P.Bunyk and P.Litskevich, "Case study in RSFQ design: Fast pipelined 32-bit adder," *IEEE Trans. Applied Superconductivity*, in press.

[10] J.Lin, V.Semenov and K.Likharev, "Design of SFQ-counting analog-to-digital converter," *IEEE Trans. Applied Superconductivity*, vol 5, pp. 2252-2259, June 1995.

A New Approach of Optimization Procedure for Superconducting Integrated Circuits

K. Saitoh, Y. Soutome, Y. Tarutani and K. Takagi
Advanced Research Laboratory, HITACHI Ltd. 1-280 Higashi-Koigakubo Kokubunji-shi Tokyo, 185-8601 Japan

Abstract — We have developed and tested a new circuit simulation procedure for superconducting integrated circuits which can be used to optimize circuit parameters. This method reveals a stable operation region in the circuit parameter space in connection with the global bias margin by means of a contour plot of the global bias margin versus the circuit parameters. An optimal set of parameters with margins larger than these of the initial values has been found in the stable region.

I. INTRODUCTION

Ultra-high-speed operation (up to 100 GHz) and low power consumption (μW/gate) have been expected for superconducting devices and circuits. Use of a single-flux-quantum (SFQ) digital bit is the most effective way to realize such performance [1].

Generally speaking, the non-linearity of Josephson junction characteristics and the transient properties of SFQ propagation adversely circuit operation, making it difficult to obtain a circuit with a large operation margin. Therefore, effective simulation procedures that enable optimization of circuit parameters to increase the operation margin are needed. Methodological study in this field is also important to develop more practical superconducting circuits. Recently, the Monte Carlo method has been applied to the optimization procedure and has proven useful [2], [3]. However, to determine the optimal parameter set, Monte Carlo sampling and circuit simulations must be repeated many times which requires a huge calculation time. Thus, a simple and useful simulation procedure for optimization is desired.

In this paper, we have developed and tested such a circuit-simulation procedure for superconducting integrated circuits. Circuit simulations and margin calculations were performed for four modeled processes and circuit operation regions were revealed based on analysis of the resultant margins. We will show that this analysis can be used to find out an optimal set of parameters with a small number of sample circuits.

Manuscript received April 30, 1999.
This work was supported by New Energy and Industrial Technology Development Organization (NEDO) through International Superconductivity Technology Center (ISTEC).

II. METHOD

As mentioned, the sampling of circuit parameters based on a modeled process spreads plays an important role in the Monte Carlo method. Locating centers-of-gravity in the circuit parameter space is usually the goal of the algorithm used in the optimization procedure. However, it is questionable whether this method provides a unique optimal parameter set in the case of larger process spreads (parameter variation).

On the other hand, margin calculation is also useful for finding the optimal parameter set. With this method the calculations give numerically rigorous results for both circuit parameters and bias margin at the same time. The disadvantage of this method is that the number of circuit elements is limited because the calculation time increases exponentially with an increasing number of circuit elements to be optimized.

Here, we propose a circuit simulation procedure that includes features of both the Monte Carlo and margin calculation methods in that it includes parameter sampling and rigorous margin calculations. The procedure is summarized as follows. First, sample circuits are prepared by randomly generating some circuit parameters based on parameter variations in the modeled process. Circuit simulations are then performed and logic functionality checked. The circuit parameters and bias margin are obtained for the sample circuits that show the correct logic function. Finally, contour plot analysis is done to obtain a stable operation region within a parameter space. We assumed four model processes and fifty sample-circuit programs were prepared for each model.

To test this method, we used a basic rapid-single-flux-quantum (RSFQ) SET-RESET flip-flop (SRFF) circuit. A schematic circuit diagram is shown in Fig.1.

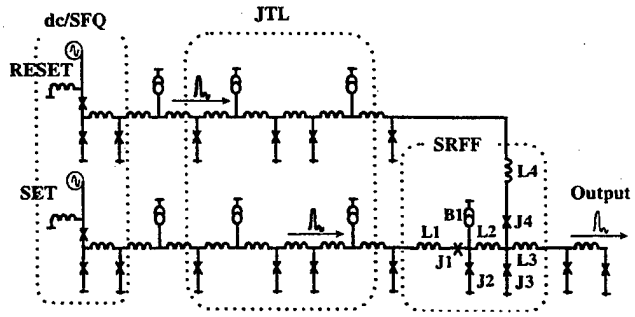

Fig.1 Schematic diagram of the test circuit. (RSFQ SET-RESET flip-flop gate)

TABLE I

PARAMETER VARIATIONS (1σ) USED IN MARGIN CALCULATIONS

Process	J_c	R_n	L
LTS (Ideal)	5%	2.5%	5%
HTS1 (State of art)	10%	5%	15%
HTS2 (Medium)	15%	10%	10%
HTS3 (Large)	25%	15%	20%

The circuit consists of dc/SFQ converters, Josephson transmission lines (JTL), and an SRFF logic gate. Margins were obtained for the circuit elements of the SRFF gate, namely the Josephson junctions J1 to J4, inductors L1 to L4, and the gate bias of B1. Circuit simulations and margin calculations were performed using the WinS circuit simulator [4].

The parameter variations we used are summarized in Table I. These variations were modeled by Jeffery et al. in their study of Monte Carlo analysis [3].

III. Results and Discussion

A. *Yield and bias margin*

First, we investigated the process variation dependence of the sampling yield.

1) LTS: In this case, correct operation was obtained for all sample circuits. The bias margin decreased only slightly (a decrease of a few percent was observed in three sample circuits) .
2) HTS1: Correct operation was again obtained in all sample circuits. However, the bias margin range decreased in 19 sample circuits.
3) HTS2: Incorrect operation occurred in one sample circuit and the bias margin range decreased in 25 sample circuits.
4) HTS3: Incorrect operation was observed in nine sample circuits, and the bias margin range decreased in 28 sample circuits.

The yield clearly fell as the parameter variation increased. Using the data from our calculation of the bias margin and circuit elements, we carried out further analyses to find a stable operation region and an optimal set of parameters.

B. *Stable Operation Region*

With our method, a stable operation region can be found in the parameter space based on the bias margin range. A contour plot of the bias margin for selected circuit elements is used for this analysis. Results for each parameter variation are depicted in Fig. 2. The inductive parameter ($\beta_L = 2\pi LI_c/\Phi_0$), which is important for designing RSFQ circuits, is also depicted. Circuit elements of junction J2 and inductor L2 were selected for the contour plot since these parameters determine β_L of an SRFF gate.

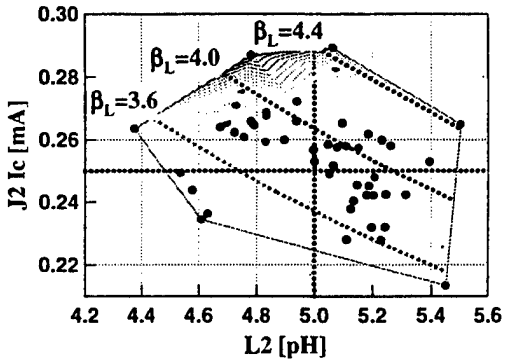

(a)

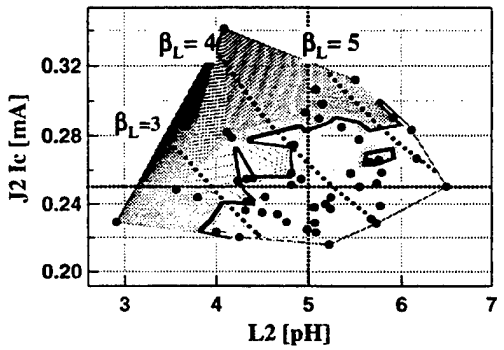

(b)

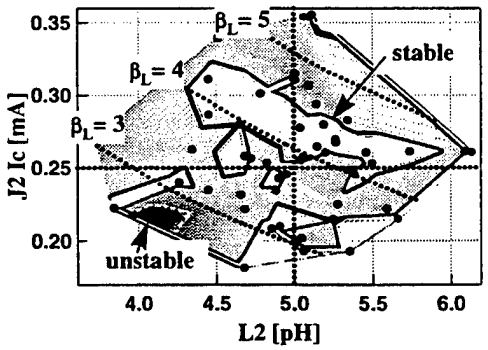

(c)

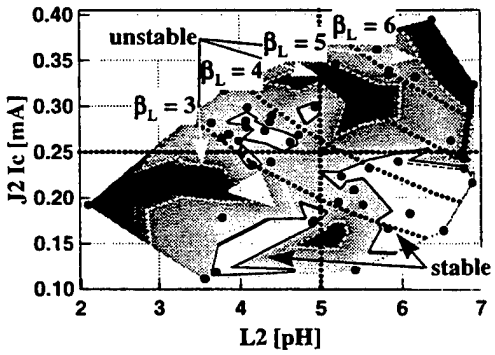

(d)

Fig. 2. Contour plots of the bias margin for the distribution of the critical current (J2) and inductor (L2).
(a) LTS, (b) HTS1, (c) HTS2, (d) HTS3

In Fig. 2, a light (dark) region indicates a higher (lower) margin range. In this analysis, we defined a region having a margin range of more than 50% as stable and one with a range of less than 20% as unstable. The thin solid line (dotted line) indicates the stable (unstable) region. Features of these contour plots are summarized as follows.

(i) LTS: In this case, a stable operation region including the initial parameter set was clearly formed.

(ii) HTS-1: A stable operation region could be found in the parameter space with a smaller critical current of J2 and a larger inductance of L2. Another notable feature is a dimple, i.e. a small region in which the margin range slightly decreased, that was found in the stable region.

(iii) HTS-2: The structure of the contour plot changed dramatically in this case: the stable region was smaller and localized. As well as the localized stable region, there is another stable region around the edge of the sampling boundary. This stable region also exists in the region mentioned in case (ii).

(iv) HTS-3: The shrinking and localizing tendency of the stable regions was apparently enhanced. At the same time, a larger unstable region appeared near the stable regions. This coexistence of stable and unstable region is a special feature revealed by our method. The stable region can be found in the parameter space with a lower critical current and a higher inductance; we will call this region the robust stable region.

The results of this analysis suggests how the stable region is broken down by increased parameter variation. The complicated structure in the worst case (Fig. 4(d)) indicates that it will be very difficult to find an optimal set of parameters when there is large process variation. From another point of view, the robust stable region might contain an optimal parameter set. This point will be discussed in detail below.

C. Optimal set of parameters

In our method, the margins of selected circuit elements are calculated in every run. Thus, it is easy to find a parameter set that has a larger margin. A typical comparison is summarized in Table II. The optimal set of parameters in Table II were found in the robust stable region of the worst case (HTS-3). Circuit elements with bold (italic) characters indicate that the margin range was enhanced (reduced). Though the margin ranges of J3 and J4 were reduced, the parameters in the optimal set are obviously more robust than the initial set. In particular, the enhancement for the gate bias condition (B1) would be promising for stable operation, which provides a useful indicator for experimental investigation.

Therefore, we believe our method is useful for optimizing the design of superconducting integrated circuits. Testing on other circuits such as a T-flip-flop gate, including global parameter variation, and experimental verification of the method are our future objectives.

TABLE II

COMPARISON OF PARAMETER VALUES AND MARGINS

Element	Initial (margin)	Optimal (margin)
J1	**0.25 mA (-33.4%, 90%)**	**0.29 mA (-40.1%, 90%)**
J2	**0.25 mA (-90%, 40.1%)**	**0.24 mA (-90%, 66.1%)**
J3	*0.25 mA (-90%, 53.4%)*	*0.24 mA (-90%, 45.4%)*
J4	*0.20 mA (-60.5%, 69.3%)*	*0.19 mA (-47.5%, 54.8%)*
L1	3.6 pH (-90%, 90%)	3.6 pH (-90%, 90%)
L2	**5.0 pH (-38.0%, 90%)**	**6 pH (-38.0%, 90%)**
L3	3.6 pH (-90%, 90%)	3.3 pH (-90%, 90%)
L4	2.6 pH (-90%, 90%)	3.3 pH (-90%, 90%)
B1	**0.18 mA (-56.3%, 90%)**	**0.18 mA (-88.2%, 90%)**

IV. CONCLUSION

We have developed and tested a new circuit simulation procedure. Even though our sampling number was small (50 sampling circuits for each model process), the parameter variation dependence of the bias margin revealed a robust stable region in the parameter space. Based on this analysis, an optimal set of parameters was found in the stable region. We believe that this method is a promising tool for circuit parameter optimization and will help lead to a useful design method for superconducting integrated circuits.

ACKNOWLEDGMENT

K.S sincerely thanks Prof. N. Yoshikawa, Dr. M. Jeffery, Prof. T. van Duzer and Dr. S. Kaplunenko for their stimulating discussion.

REFERENCES

[1] K. K. Likharev and V. K. Semenov, "RSFQ Logic/Memory Family: A New Josephson-Junction Technology for Sub-Terahertz-Clock-Frequency Digital Systems," *IEEE Trans. Appl. Supercond.*, vol. 1, No.1, pp. 3-28, March 1991.

[2] T. Harnisch, J. Kunert, H. Toepfer and H. F. Uhlmann, "Design centering methods for yield optimization of cryoelectronic circuits", *IEEE Trans. Appl. Supercond.*, vol. 7, No. 2, pp. 3434-3437, June 1997.

[3] M. Jeffery, P. Y. Xie, S. R. Whitely and T. van Duzer, "Monte Carlo and Thermal Noise Analysis of Ultra-High-Speed High Temperature Superconducting Digital Circuits", to appear in *IEEE. Trans. Appl. Supercond.*, (ASC'98).

[4] S. Kaplunenko, http://www home.pacbell.net/kapl

A Cell-Based Design Approach for RSFQ Circuits using Binary Decision Diagram

Nobuyuki Yoshikawa and Junichi Koshiyama
Divsion of Electrical and Computer Engineering, Yokohama National University
Tokiwadai 79-5, Hodogaya-ku, Yokohama 240-8501, Japan

Abstract— We will propose a cell-based design approach for RSFQ circuits based on a binary decision diagram (BDD). The BDD is a way to represent a logical function using a directed graph which consists of binary switches having one input and two outputs. Since complex logic circuits can be implemented in the form of regular arrays of the BDD binary switches, we can use a cell-based layout methodology for the design of the RSFQ circuits. In this study, we implemented the BDD binary switches by a D_2 flip-flop. Inthe BDD design approach we use a cell library which contains a binary switch, pulse splitters, confluence buffers and JTLs. All cell layouts in the library have identical widths and heights, so that any logic function can be laid-out by simple connection of the library cells. As a case study, we implemented a 1-bit RSFQ half adder and a 3-bit encoder for a flash AD converter.

I. Introduction

Rapid single flux quantum (RSFQ) digital circuits have been developed extensively because of their potentially high performance with clock frequency beyond hundreds of gigahertz and extremely low power consumption [1]. However, since the RSFQ logic circuits need a lot of Josephson transmission lines (JTL) for the connection of gates and the distribution of clock signals, the design of the RSFQ logic circuits is very complicated and time consuming.

We have proposed a new design approach for the RSFQ logic circuits based on a binary decision diagram (BDD) [2]. The BDD [3], [4] is a way to represent a logical function using a directed graph which consists of binary switches having one input (root) and two outputs (branches). These BDD binary switches have binary internal states, which switch a messenger entering from the root into one of two branches depending on their internal state. It has been proven that any combinational logic function can be represented by the BDD and it becomes very simple in some cases compared with the function represented by conventional Boolean logic elements, such as inverter, AND and OR. We have shown that the BDD is effectively implemented by the RSFQ circuits by replacing the binary switches with D_2 flip-flops [5] and the messenger with an SFQ.

The BDD RSFQ circuits have following advantages: (i) Any combinational logic function can be implemented in the form of regular arrays of the BDD binary switches, i.e. D_2 flip-flops. (ii) The circuits are dual rail logic [6], [7], therefore distribution of clock signals is not required. (iii) Modularity of the circuits is very high. All these features are fit to using a cell-based design methodology.

Manuscript received April 30, 1999.

In this paper, we will propose a cell-based design approach on the BDD RSFQ circuits. We have made a cell library which contains a BDD binary switch and several basic cells for routing. All cells in the library have identical width and length, so that any logic function can be laid-out by simple connection of the basic cells. As a case study, we implemented a 1-bit RSFQ half adder and a 3-bit encoder for a flash AD converter.

II. BDD RSFQ Logic Circuits

Figure 1 is an example of the representation of the logic function $f = x_1x_2 + x_2x_3 + x_1x_3$ by the BDD. When one traces from the top of the graph, if the state of the binary switch x_1 is "1" one will move to the switch x_2 along a right arrow, or if "0" move along a left arrow. Continuing this procedure, one will reach the end of the graph labeled by "0" or "1". This value is a solution of the logic function. In order to realize the RSFQ logic circuits using the BDD, we have employed a D_2 flip-flop as the BDD binary switche as shown in Fig. 2 [2]. In this case, the root and the two branches of the BDD binary switch correspond to a "Clock" and complementary outputs "Out" and "$\overline{\text{Out}}$" of the D_2 flip-flop, respectively. The internal state of the switch is set by an input of an SFQ pulse into complementary input, "Data" and "$\overline{\text{Data}}$". The input of an SFQ pulse into "Data" ("$\overline{\text{Data}}$") changes the state of the flip-flop into the "1" ("0") state, regardless of the previous state. When an SFQ pulse is applied to the "Clock", an SFQ is outputted at "Out" or "$\overline{\text{Out}}$" depending on the state of the flip-flop, e.g. "Out" for the "1" state.

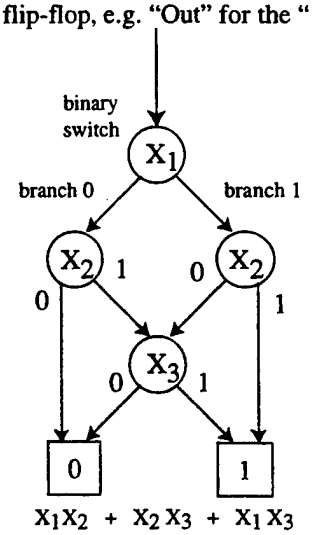

Fig. 1 The binary decision diagram (BDD). The figure shows an example of the logical function $X_1X_2 + X_2X_3 + X_1X_3$

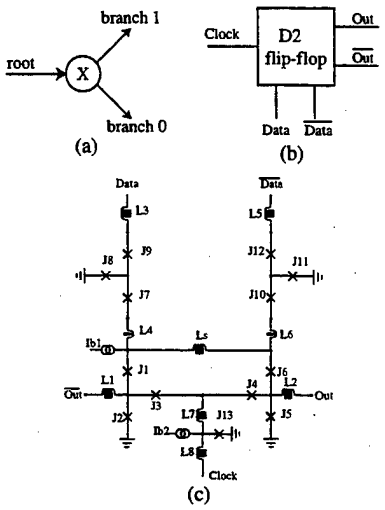

Fig. 2 Implementation of a BDD binary switch by a D_2 flip-flop. (a) A BDD binary switch. (b) Its implementation using a D_2 flip-flop. (c) A circuit diagram of the D_2 flip-flop.

III. Cell Based Design Methodology for BDD RSFQ Circuits

In order to implement the BDD RSFQ circuits effectively and to reduce the design time, we propose a cell-based design approach. Figure 3 shows an example of a cell library for BDD RSFQ circuits, which consists of JTLs, confluence buffers, pulse splitters, JTL crosses and a D_2 flip-flop. All cells have identical heights and widths (120 μm x 120 μm in this case assuming a standard HYPRES Nb process), except that the D_2 flip-flop is twice the size of the other cells because of its high complexity. All the positions of input and output terminals in each cell are at the same positions each other so that connection between terminals is always satisfied. Supply lines are distributed horizontally and shared between cells in the same row. Corresponding to directions of the signal flow, we prepared seven kinds of JTL cells, five confluence buffers, five pulse splitters and two JTL crosses. We also prepared three sets of JTL cells which include two to four Josephson junctions to adjust the signal delay at the JTL cells.

IV. A Case Study

To illustrate the efficiency of the cell-based design approach in designing the BDD RSFQ circuits, we have designed two kinds of logic circuits.

A. Design of a 1-bit Half Adder

Figure 4 shows an example of the cell-based design of a 1-bit half adder. (A, $\overline{A}$) and (B, $\overline{B}$) are the adder input, and (C_O, $\overline{C_O}$) and (S, $\overline{S}$) are the carry output and the sum output, respectively. The circuit is composed of two D_2 flip-flops, three pulse splitters and three confluence buffers. SPICE simulations (Fig. 4 b) shows that the propagation delay of the carry is 160 ps and the global dc-bias margin is -30% ~ +38% at 10 Gb/s assuming the Nb Josephson process with critical current density of 1 kA/cm^2. These values are equal to those of our previously custom-designed circuit [2]. The total dimension of the circuit is 600 μm x 720 μm (see Fig. 4 c), which is almost equal to that of our previous design.

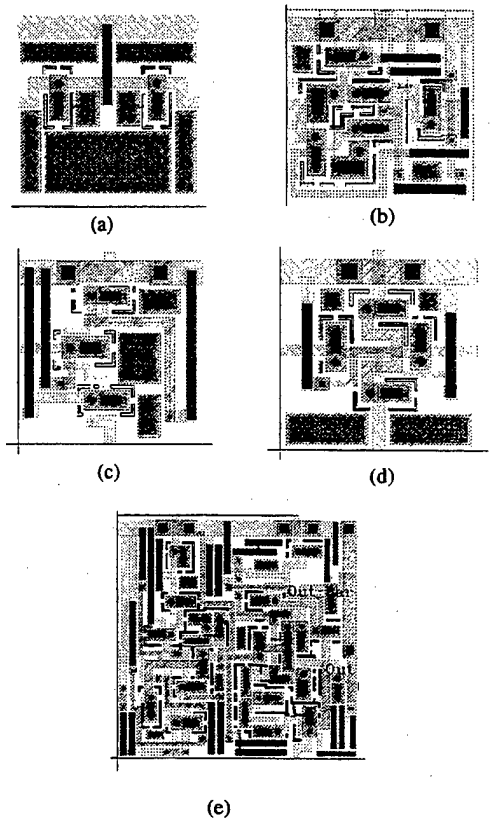

Fig.3 Example of a cell library for BDD SRFQ circuits. (a)A 2-junction JTL (b) A confluence buffer. (c) A pulse splitter . (d) A JTL cross (e) A binary switch.

B. Design of a 3-bit Encoder

Figure 5 shows an example of a 3-bit encoder for a flash AD converter [8], [9]. (A, $\overline{A}$), (B, $\overline{B}$), (C, $\overline{C}$), (D, $\overline{D}$), (E, $\overline{E}$), (F, $\overline{F}$), and (G, $\overline{G}$) are thermometer code inputs from comparators, and (x0, $\overline{x0}$), (x1, $\overline{x1}$) and (x2, $\overline{x2}$) are binary code outputs. The circuit is composed of eight D_2 flip-flops. Note that the circuit using the conventional logic gates needs two EXOR gates, four OR gates, five AND gates and two inverters [9]. SPICE simulations (Fig. 5 b) show that the latency is 300ps and the global dc-bias margin is -28% ~ +38% at 10 Gb/s conversion rate. The performance is better than that of voltage state logic such as MVTL [9]. The total dimension of the circuit is 960 μm x 2160 μm (see Fig. 5 c).

IV. Conclusion

We have proposed a cell-based design approach using the BDD for the design of RSFQ circuits. It was shown that the designing effort was dramatically reduced by using a BDD cell library composed of a limited set of library cells without reducing the integration density and performance. It should be pointed out that the BDD cell-based design approach is compatible with the design automation becauseof its high modularity of the library elements.

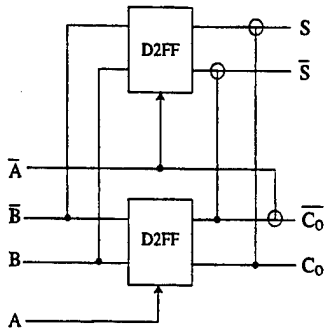

(a)

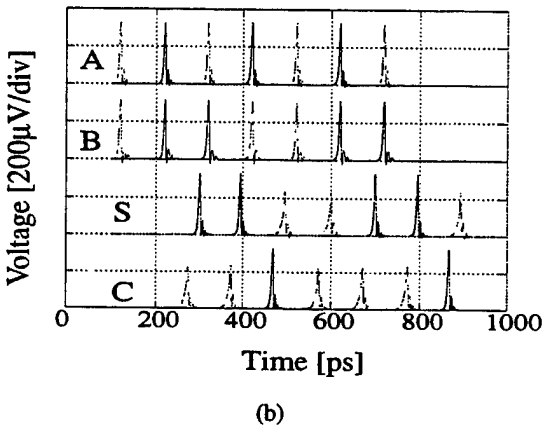

(b)

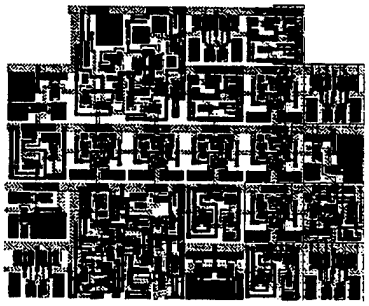

(c)

Fig. 4 Implementation of a 1-bit RSFQ half adder. (a) A ciruit diagram. (b) Simulation results. (c) Mask layout.

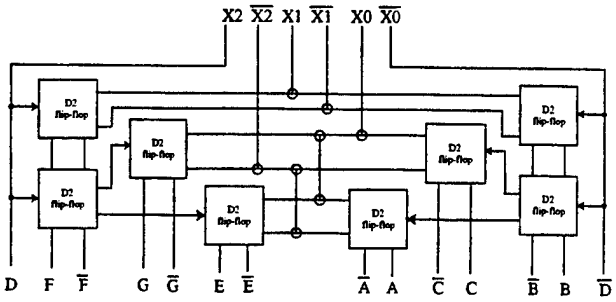

(a)

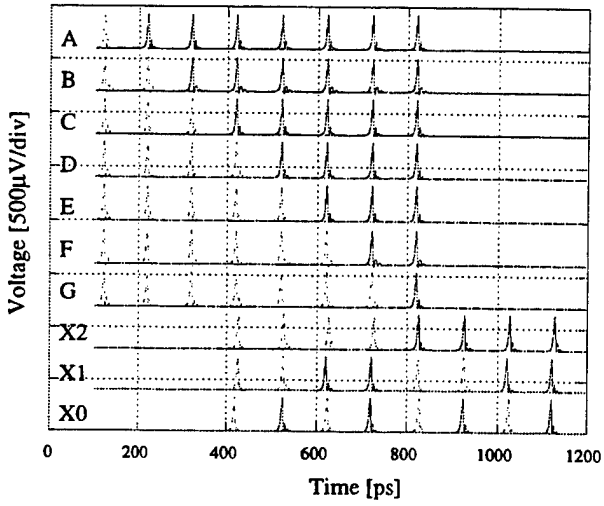

(b)

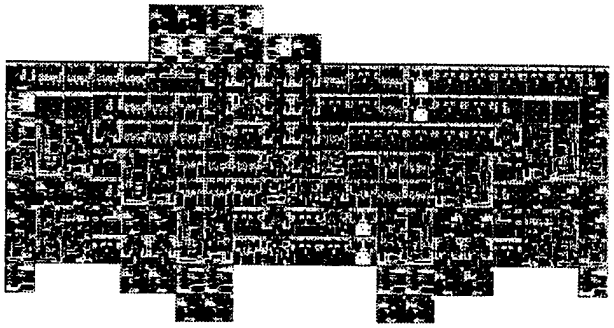

(c)

Fig.5 Implementation of a 3-bit encoder for a flash AD converter. (a)A circuit diagram. (b)Simulation results. (c) Mask layout.

REFERENCES

[1] K. K. Likharev and V. K. Semenov, "RSFQ logic/memory family:A new Josephson-junction technology for sub-terahertz-clock frequency digi tal systems," IEEE Trans. Appl. Superconductivity,vol. 1,pp. 1-28,March, 1991.

[2] N. Yoshikawa, H. Tago and K. Yoneyama, "A new approach for RSFQ logic circuits based on the binary decision diagram", presented at the 1998 Applied Superconductivity Conference, Palm Springs CA. To appear in IEEE Trans. Appl. Superconductivity.

[3] S. B. Akers, "Binary decision diagrams", IEEE Trans. Comput., vol. C-27, pp. 509-516, 1978.

[4] R. E. Bryant "Graph-based algorithms for Boolean function manipulation," IEEE Trans. Comput., vol. C-35, pp. 677-691, 1986.

[5] N. Yoshikawa, Z. J. Deng, S. R. Whiteley and T. Van Duzer, "Design and testing of data-driven self-timed RSFQ demultiplexer", Extended Abstract of ISEC'97, Berlin, Germany, June, pp. 353-355, 1997.

[6] Z. J. Deng, N. Yoshikawa, S. R. Whiteley and T. Van Duzer, "Data-driven self-timed RSFQ digital integrated circuit and system," IEEE Trans. on Applied Superconductivity, Vol. 7, pp.3634-3637, June, 1997.

[7] M. Maezawa, I. Kurosawa, M. Aoyagi, H. Nakagawa, Y. Kameda and T. Nanya, "Rapid single-flux-quantum dual-rail logic for asynchronous circuits," IEEE Trans. Appl. Superconductivity, vol. 7, pp. 3634-3637, June, 1997.

[8] E. S. Fang, D. Hebert and T. Van Duzer, "A Multi-gigahertz Josephson flash A/D converter with a pipelined encoder using large-dynamic-range current-latch comparators", IEEE Trans. Magn., 27, pp. 2891-2894, March 1991.

[9] M. Jeffry, W. Perold, W. Wang and T. Van Duzer, "Monte Carlo optimization of superconducting complementary output switching logic circuits", IEEE Trans. Appl. Superconductivity, vol. 8, pp.104-119, September 1998.

Long Josephson Junctions Merged into the RSFQ Environment

Vsevolod Kaplunenko, Yongming Zhang
Conductus, Inc., 969 West Maude Ave., Sunnyvale, CA 94086

Abstract—The long Josephson junction (LJJ) is added to the superconducting circuit simulator "WinS", which was initially designed for rapid single flux quantum (RSFQ) logic and simple superconducting analog devices. LJJ is described in terms of normalized parameters, which are widely used. LJJ is also available for the circuit optimization. Graphic user interface enables an easy implementation of the LJJ into the RSFQ circuit and provides different monitors to see LJJs internal state (i.e., phase or voltage distribution.) As an example, the simple RSFQ circuit, which sends a number of fluxons to LJJ in order to excite different zero-field steps, was simulated and optimized.

I. Introduction

The success in connecting a long Josephson junction (LJJ) to the rapid single flux quantum (RSFQ) circuits [1] encourages us to add LJJ into the superconducting circuit simulator "WinS" [2]. LJJ is implemented as a compound element. This is the subcircuit with the predefined (fixed) structure. There are two other examples of the predefined elements: Josephson transmission line (JTL) and passive transmission line (PTL). The common feature of the compound elements is that they can be flattened in a separate window to see their internal structure but any modifications made in that window can not be addressed back to the compound element. The flattened circuit can be used to form a new subcircuit instead. The main advantage of the compound element is an automatic structure regeneration upon any parameter change. The change of LJJ length, for instance, automatically causes change in number of used lumped elements.

LJJ is described in terms of normalized parameters, which are common used. Extra visualization tools are also added to "WinS" in order to monitor dynamics of the LJJ. They show the instantaneous voltage and phase distribution along the junction as a function of time as well as the tracks of fluxon position within the LJJ. LJJ parameters can be used for the circuit parameter optimization and for the voltage-current characteristic calculation. Section II describes an example of the combination of an RSFQ circuit with LJJ. For this example the RSFQ cell is designed to send specified number of fluxons into the LJJ. This is needed in order to excite different zero-magnetic field resonances in LJJ. The discussion of interface between heavily shunted RSFQ cells and an unshunted LJJ is presented in section III, and section IV is a conclusion.

Manuscript received April 30, 1999.

II. RSFQ to Long Josephson Junction Fluxon Sender

Recently long Josephson junction has been suggested as a precise clock source for RSFQ analog-to-digital converters [3]. The internal LJJ soliton resonance modes (so-called zero-field steps [4]) are used for that purpose. The frequency of such resonance depends on the number of fluxons propagating in LJJ. Typically, it is possible to set this number to be between one and five by varying magnetic field and bias current. This procedure can not be easily automated that is why we have suggested a simple RSFQ circuit shown in Fig.1. The circuit is designed to send specified number of fluxons into the LJJ.

DC-to-SFQ converter (dc_sfq in Fig. 1) transforms input current pulses into fluxons and send them to the six junctions Josephson transmission line (JTL). The junctions J_1-J_4 form the interface between the RSFQ circuit and LJJ. The interface consists of two buffer stages (J_1-J_2 and J_3-J_4,) which prevent fluxon propagation back from LJJ to the circuit input. When fluxons (within LJJ) approaches the LJJ end, it is reflected back as anti-fluxon (see also Fig. 3 discussion.) This sends simultaneously two fluxons (or 4π phase leap) back to the RSFQ circuit. The speed of a single RSFQ buffer stage is not high enough to resolve these two fluxons and escape them through junction J_4. This is a reason of adding the second buffer stage. The whole interface is not a "pure" digital RSFQ circuit, because both buffers have to treat signal simultaneously. Fig. 2 shows the quantum mechanical phase difference at points marked in Fig. 1 by P_1-P_4 monitors. This phase is a time integral of the instantaneous voltage, and it is used because 2π leap of the phase enables us to detect the fluxon, which passes the monitor connection points. Fig. 2

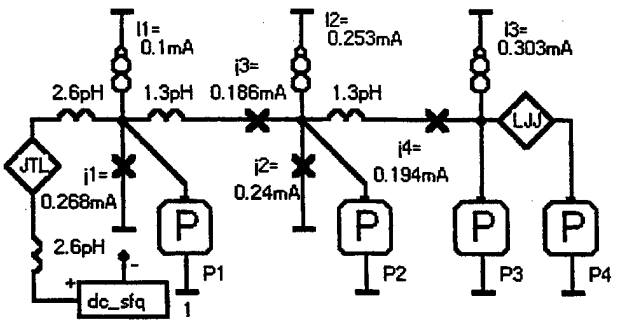

Fig1. Equivalent circuit of the simulated cell. dc_sfq is an DC-to-SFQ converter, JTL- six junctions Josephson transmission line, which has the following parameters: critical current of the junction is 0.24 mA, its bias is 0.17mA, the interconnecting inductors are 2.6pH. LJJ-long Josephson junction with α=0.2, β=0, γ=0.5, length=30, λ_j=10μ, linear critical current density J_{cl}=0.035mA/μ.

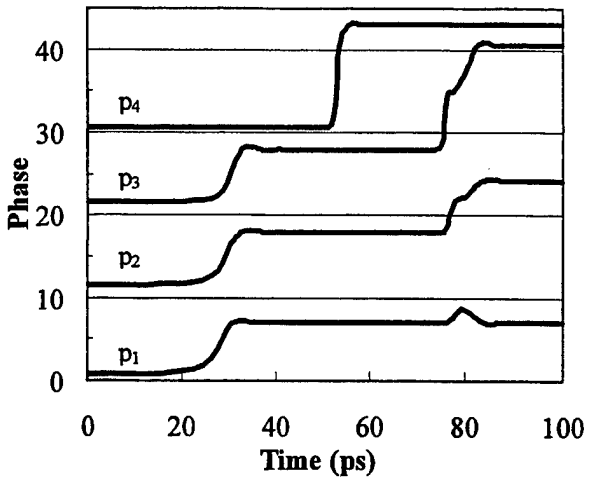

Fig2. The time dependencies of the quantum mechanical phase calculated at the connection point of the monitors P_1-P_4 in Fig. 1. Curves are shifted for clarity.

shows the fluxon generated by DC-to-SFQ converter, which proceeds to the LJJ. This is reflected by a first 2π leap in curves p_1-p_3 (Fig. 2). Then fluxon reflects from other end of the LJJ (4π jump in p_4) and comes back. At this moment it relatively fast switches junction J_4 (steep jump in p_3), and then junction J_3 switches slowly. The latter sends fluxon back to the LJJ. This process also can be seen in Fig.3, which shows the fluxon position within the LJJ as a function of time.

TABLE I
PARAMETER MARGINS FOR CIRCUIT'S ELEMENTS IN FIG. 1

	I_1	I_2	I_3	J_1	J_2	J_3	J_4	α	Υ	J_{cl}
-%	90	51	50	49	55	90	64	21	30	41
+%	90	48	48	85	51	58	48	37	32	38

Fluxon is perfectly reflected from the right side of the junction. Then it leaves LJJ at the left side and came back after the time period required for J_3 to switch. Thus junction J_3 sends fluxon back to LJJ. Despite such a complex behavior the very good margins were obtained for this circuit as Table I shows. The first three parameters in the table are the bias currents I_1-I_3, J_1-J_4 are the critical currents of the corresponding junctions in Fig.1, and α-LJJ losses, γ-LJJ bias, J_{cl}-LJJ linear critical current density.

III. RSFQ to LJJ Interface

The interaction of LJJ with the RSFQ interface circuit can be understood from the energy conservation point of view. The energy, which is required to switch single junction, is

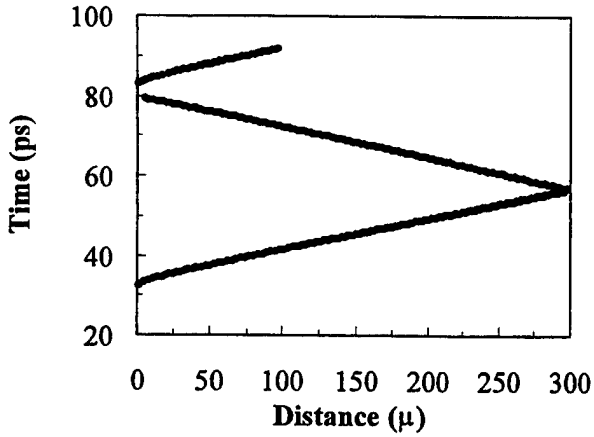

Fig. 3 Fluxon position in long Josephson junction as a function of time. The junction length is 300μ

$E_{sj}=\Phi_0 I_c/\pi$, where Φ_0 - flux quantum, and I_c - critical current of the junction. The energy of the fluxon in LJJ can be estimated as $E_{ljj}=2\lambda_j J_{cl}\Phi_0/\pi$ [4]. The effective critical current $2\lambda_j J_{cl}$ =0.7mA of the LJJ is higher than the sum of critical currents of junctions J_2, J_3 and J_4 (0.62mA from Fig. 1), which should be switched. Thus the energy of fluxon in LJJ is enough to switch all three mentioned junctions. In Table I the lower margin for LJJ critical current is about 40%. This means that even lower energy of the fluxon in LJJ is needed to have it reflected from the interface cell. This is because one of the junctions J_2 or J_3 switches first and pickup extra energy from the bias source I_2.

IV. Conclusion

We have developed the simulation tool, which enables us to study different interfaces between long Josephson junctions and RSFQ logic circuits. The first example of such an interface is developed and optimized for a circuit, which sends fluxons from RSFQ cells into LJJ.

References

[1] Y.M. Zhang, V. Borzenets, V.K. Kaplunenko, and N.B. Dubash "Underdamped long Josephson junction coupled to overdamped single-flux-queantum circuits", Appl. Phys. Lett. Vol. 71, 1863 1997.

[2] V.K Kaplunenko, "Interactive Simulator for Superconducting Electronics" http://home.pacbell.net/kapl (unpublished)

[3] Y. M. Zhang, and D. Gupta "Low-jitter on-chip clock for RSFQ circuit applications," #148 at this conference.

[4] K. K. Likharev, "Dynamics of Josephson Junction and Circuits," Philadelphia: Gordon and Breach Science Publisher, 1991

All-NbN Integrated Circuits Based on NbN/AlN/NbN Tunnel Junctions

Hirotaka Terai and Zeng Wang
Kansai Advanced Research Center, Communications Research Laboratory, Ministry of Posts and Telecommunications, 588-2 Iwaoka, Iwaoka-cho, Nishi-ku, Kobe 651-2401, Japan

Abstract— We report on progress in all-NbN integrated circuit technologies that are based on NbN/AlN/NbN tunnel junctions fabricated on Si substrates. For single flux quantum (SFQ) circuit applications, overdumped junctions were constituted by inserting the 12-nm-thick Cu resistive layers parallel to the NbN/AlN/NbN tunnel. The specific capacitance of the junction and the sheet inductance of the NbN stripline were estimated to be 56 fF/μm² and 1.2 pH in a dc-SQUID measurement. We designed and fabricated circuits consisting of dc/SFQ converters, Josephson transmission lines, and T flip-flop based SFQ/dc converters. The circuit was operated with a bias margin of more than ±15% at 4.2 K.

I. Introduction

Superconducting single flux quantum (SFQ) digital electronics offers the possibility of ultra high speed logic at extremely low power [1]. The SFQ circuits have been developed with the Nb integrated circuit technology based on high-quality $Nb/AlO_x/Nb$ tunnel junctions, but the low operating temperature (4.2 K) requires a liquid helium cooling or high cost closed-cycle refrigerators. An approach on 10 K superconductor integrated circuits is expected to reduce the cooling cost by using high-T_c materials such as NbN, Nb_3Ge, and $YBa_2Cu_3O_{7-x}$, *et. al.* [2]. These high-T_c materials, however, are well known to have a short superconducting coherence length ξ and a long penetration depth λ, which make it difficult to fabricate tunnel junctions and constitute circuits. NbN is the best choice for 10 K large scale superconducting integrated circuits at the present time. Several groups have reported on the NbN integrated circuit technology based on NbN/MgO/NbN tunnel junctions [3][4], but there have not been any reports on the operation of all-NbN SFQ circuits.

We have recently developed high quality NbN thin films and high current density NbN/AlN/NbN tunnel junctions fabricated on single-crystal MgO substrates [5][6]. The NbN/AlN/NbN tunnel junction had a low barrier height compared with that of the NbN/MgO/NbN junction. This low barrier height is useful for fabricating high-J_c tunnel junctions and it is also helpful for reducing the junction capacitance [7]. The non-uniformity of the critical current was estimated to be less than ±4.5% for 400 NbN/AlN/NbN junction arrays fabricated on Si wafer [8]. In this paper, we report on the fabrication of the all-NbN SFQ circuits and discuss the operating properties.

Manuscript received April 30, 1999. This work was supported in part by the Hyogo Science and Technology Association.

II. Fabrication Process

Fabrication of integrated circuit follows a seven mask step process. The cross-sectional view of an integrated circuit is illustrated in Fig. 1. The deposition condition of NbN films was described in detail elsewhere [7]. All of the NbN layers were patterned by reactive ion etch (RIE). SiO evaporation films were employed for isolation and planarization.

The fabrication process started with the deposition of the 400-nm-thick NbN ground plane on Si wafer. The ground plane was defined to moat pattern and etched by RIE. The 200-nm-thick SiO film is evaporated for isolation between the ground plane and the base electrode. Contact holes between the ground plane and the base electrode were formed using the liftoff technique as shown in Fig.1. The Cu film was evaporated and patterned by ion beam etch. After the resist removing process and the surface cleaning of the Cu film, the trilayer consisting of the 150-nm-thick NbN base electrode, AlN tunnel barrier and the 60-nm-thick NbN counter electrode was deposited *in-situ*. Subsequent to the patterning of the trilayer, the 200-nm-thick SiO film was evaporated and lifted off for planarization. Then the junction definition was carried out. The 200-nm-thick SiO film was evaporated for isolation between the base electrode and the wiring layer and lifted off. Contact holes between between the base electrode and the wiring layer were formed by RIE. Finally, the 400-nm-thick NbN film was deposited and patterned as a wiring layer.

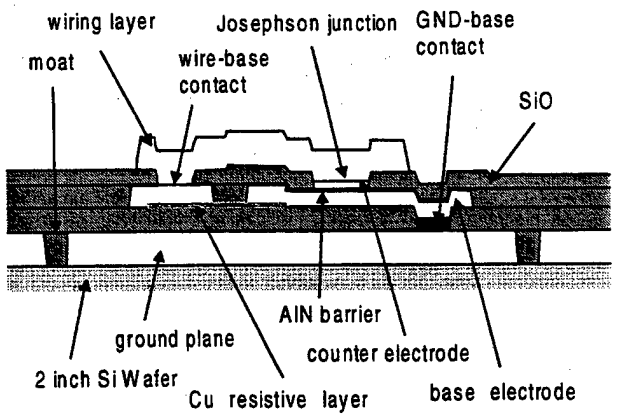

Fig. 1. Schematic cross section of all-NbN integrated circuit based on NbN/AlN/NbN tunnel junction.

III. Results And Discussion

A. Properties of overdumped junctions

The basic element of our all-NbN SFQ circuit is an overdumped NbN/AlN/NbN tunnel junction with a Cu shunted resistor. The thickness of the Cu film was determined to take the McCumber factor $\beta_c \leqq 1$. To calculate β_c, we estimated the specific capacitance of the NbN/AlN/NbN junction to be 56 fF/μm^2 with a critical current density J_c of 2.2 kA/cm^2 at 4.2 K. The junction area A was 3×3 μm^2, and $I_c=J_cA$=200 μA with J_c=2.2 kA/cm^2. By using these parameters, the sheet resistance of the Cu film was calculated to be 3.4 Ω for obtaining β_c =1. This gives the thickness of the Cu film to be 12 nm according to the relation between the thickness and the sheet resistance of Cu film.

Fig. 2 shows the current-voltage (I-V) characteristics of an overdumped NbN/AlN/NbN junction at 4.2 K. Although non-hysteretic I-V characteristics are observed, the sheet resistance of the Cu film estimated from the junction resistance is 4.8 Ω, which is larger than the designed value of 3.4 Ω. This resulted from the reduction of the thickness by ion beam cleaning before the deposition of the NbN/AlN/NbN trilayer.

B. Sheet inductance of NbN stripline

We estimated the sheet inductance of the NbN stripline by measuring the direct coupled superconducting quantum interference device (SQUID) consisting of a ground plane, two Josephson junctions, and a wiring layer with 5-μm-width stripline. An external magnetic field was applied by injecting dc currents into the stripline. Fig. 3 shows the I_c modulation patterns of the dc-SQUIDs with a stripline length of a) 10 μm and b) 15 μm. The coupling inductance is estimated to be 3.9 pH and 5.1 pH from Figs. 3 a) and b), respectively. Therefore, the sheet inductance is evaluated to be 1.2 pH.

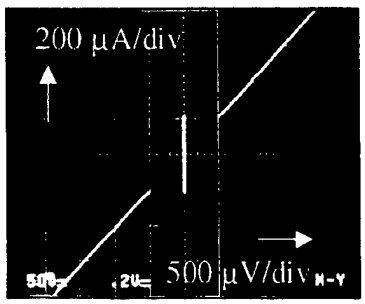

Fig. 2. Current-voltage characteristic of an overdumped Josephson junction consisting of a NbN/AlN/NbN tunnel junction and a Cu shunting resistor.

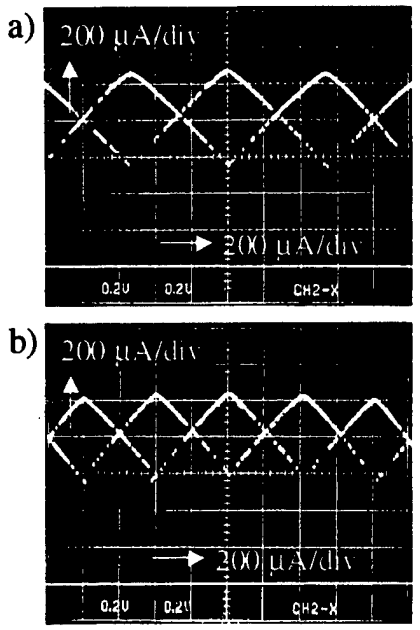

Fig. 3. I_c modulation patterns of the direct coupled dc-SQUID at 4.2 K. Stripline length is a) 10 μm and b) 15 μm.

C. Design and testing of all-NbN SFQ circuits

We designed and fabricated the circuits consisting of dc/SFQ converters, Josephson transmission lines (JTLs), and T flip-flop based SFQ/dc converters. The circuits were based on the Rapid Single Flux Quantum (RSFQ) logic cell [1]. The parasitic inductance was experimentally estimated to be around 0.6 pH from a SQUID measurement. We assumed the loop inductance containing three Josephson junctions to be larger than 5 pH. We designed the circuit using the junction with a J_c of 2.2 kA/cm^2 at 4.2 K. The minimum size of the junction is limited to be 2 × 2 μm^2 by our photolithography technology, indicating that the minimum I_c is 90 μA. The dc/SFQ converter and JTL showed more than ±40% bias margins, and the SFQ/dc converter showed around a ± 20% bias margin according to the circuit simulation by WinS.

Fig. 4 is an SEM image of the fabricated circuit. The dc/SFQ converter, the JTL, and the SFQ/dc converter are serially connected. The J_c of the junctions was 1.2 kA/cm^2, which is smaller than the designed value of 2.2 kA/cm^2. There are six ports, where an input pulse and dc bias currents are supplied from port 1 and ports 2-5. Output voltages are detected from port 6. Fig. 5 shows the test result of the circuits at 4.2 K. Output voltages appear at the leading edge of an input pulse and disappear at the leading edge of the next coming input pulse. This indicates correct operation of the SFQ/dc and T flip-flop based SFQ/dc converter. We investigated the operation margin of the circuit for the input

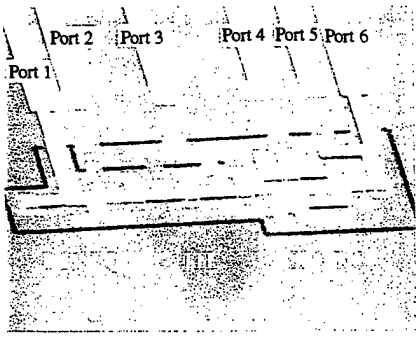

Fig. 4. SEM image of fabricated test circuits

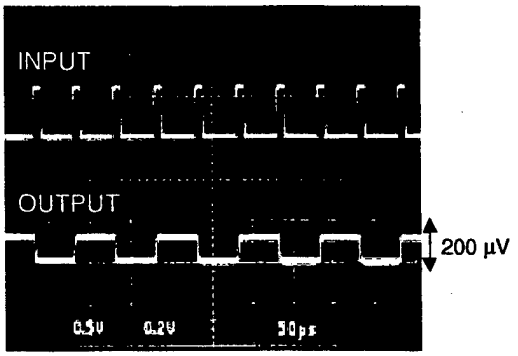

Fig. 5. Test result of the circuit consisting of dc/SFQ converter, JTL, and T-flip flop based SFQ/dc converter at 4.2 K.

pulse level and the dc bias current. The circuit showed an operation margin of more than ±40% for the input pulse level and±20% for the bias current from ports 4 and 5. However, the operation margin for the bias current from ports 2 and 3 was relatively low at 15%. We guess that this is due to the local variation of I_c rather than the small J_c of the junctions.

IV. Conclusion

We have presented the first report on the operation of all-NbN SFQ circuits fabricated on Si wafer. The circuit parameters such as the specific capacitance of the junction and the sheet inductance of the NbN stripline were investigated by the dc-SQUID measurement. The specific capacitance at a J_c of 2.2 kA/cm^2 and the sheet inductance were estimated to be 56 fF/μm^2 and 1.2 pH at 4.2 K, respectively. The overdumped junctions were fabricated by inserting the 12-nm-thick Cu films parallel to the NbN/AlN/NbN tunnel junctions. We confirmed the perfect operation of the serial circuit of the dc/SFQ converter, the JTL and the T flip-flop based SFQ/dc converter with a bias margin of more than ±15% at 4.2 K. For the operation at 10 K, the circuit layout has to be changed slightly taking account of the change of the inductance between 4.2 K and 10 K.

Acknowledgment

The author would thank A. Kawakami and Dr. Y. Uzawa for useful discussion.

References

[1] K. Likharev and V. K. Semenov, "RSFQ logic/memory family: a new Josephson junction technology for sub-terahertz clock frequency digital systems," *IEEE Trans. on Appl. Supercond.* Vol. 1, 3 (1991).

[2] J. M. Rowell, "Materials and Refrigeration Issues for Josephson Digital Technology," *FED Report, January* 1997.

[3] A. Shoji, M. Aoyagi, S. Kosaka, F. Shinoki, and K. Hayakawa, "Niobium nitride Josephson tunnel junctions with magnesium oxide barriers," *Appl. Phys. Lett.*, Vol. 46, 1098 (1985).

[4] G. L. Kerber, L. A. Abelson, R. N. Elmadjian, G. Hanaya, and E. G. Ladizinsky, "An Improved NbN Integrated Circuit Process Featuring Thick NbN Ground Plane and Lower Parastic Circuit Inductance," *IEEE Trans. on Appl. Supercond.*, Vol. 7, No. 2, 2638 (1997).

[5] Z. Wang, A. Kawakami, Y. Uzawa, and B. Komiyama, "Superconducting properties and crystal structures of single-crystal niobium nitride thin films deposited ambient substrate temperature," *J. Appl. Phys.* Vol. 79, 7837 (1996).

[6] Z. Wang, A. Kawakami, and Y. Uzawa, "NbN/AlN/NbN junctions with high current density up to 54 kA/cm^2," *Appl. Phys. Lett.*, Vol. 70, 114 (1997).

[7] Z. Wang, H. Terai, A. Kawakami, and Y. Uzawa, "Characterization of NbN/AlN/NbN tunnel junctions," *IEEE Trans. on Appl. Supercond.*, to be published.

[8] Z. Wang, H. Terai, A. Kawakami, and Y. Uzawa, "Characterization of NbN/AlN/NbN tunnel junctions," Report to ISEC'99, unpublished, June 1999.

High-speed and Medium-speed Testing of the RSFQ Multiplexer and Demultiplexer

Lizhen Zheng, Steve Whiteley, Xiaofan Meng, Theodore Van Duzer

A 1:8 RSFQ demultiplexer(DEMUX) and an 8:1 RSFQ multiplexer(MUX) were designed, simulated and optimized for 20 GHz operation. The 1:8 DEMUX is a data-driven self-timed combination of seven basic 2-bit DEMUX units and has a theoretical dc bias margin of (-20%, +20%). The basic 2-bit DEMUX is a self-clocked dual-rail T flip-flop. The 8:1 MUX takes eight single-rail inputs and merges them toward a higher rate output, and the complementary output is recovered. The theoretical dc bias margin of the 8:1 MUX is (-29%, +29%). The low-speed verifications of the 2-bit DEMUX with an experimental dc bias margin of (-15%, +15%) and the 2-bit MUX with an dc bias margin of (-7%, +7%) were reported in a previous paper. In this paper, we plan to report experimental progress on direct high-speed and medium-speed testing of the MUX and the DEMUX. A correct function of the 1:4 DEMUX was observed up to 9.2 GHz. Medium-speed testing result was achieved for the 2:1 MUX. Efforts were also made toward on-chip high-speed testing of a 2-bit DEMUX up to 20 GHz. A 20 GHz data-driven self-timed on-chip test system previously demonstrated in our laboratory will be used to evaluate the circuit's high-speed operation. The circuits are fabricated using the 1 KA/cm^2 niobium process at both HYPRES and in our own laboratory.

High Speed Operation of RSFQ Circuits up to 30GHz

F. Furuta, Y. Suzuki, H. Hasegawa, E. Oya, A. Fujimaki and H. Hayakawa
Department of Quantum Engineering, Nagoya University
Furo-cho, Chikusa-ku, Nagoya, 464-8603, JAPAN

Abstract--We have experimentally demonstrated high-speed operation of RSFQ circuits using on-chip testing system and confirmed normal operation up to 30GHz. The system includes high frequency pulse generators and shift-registers serving as an interface circuit between high-speed internal signals and low-speed external signals. We adopted two ladder-type pulse generators. One generates clock pulses of 10GHz, and the other generates 25GHz. Increasing bias currents of JTLs, clock pulses can be generated at higher frequency. By using the system, a shift register and a T flip-flop(T-FF) gate are examined. The circuits were fabricated by NEC standard process based on the Nb/AlOx/Nb junction technology with Jc=2.5kA/cm^2. We optimized circuit parameters by using Monte Carlo simulation. In addition, the effect of parasitic inductances can be reduced by decreasing Ic. As a result, the systems for SR and T-FF worked correctly up to 30GHz and 27.5GHz, respectively. The SR and T-FF have wide bias margins of ±39% and ±20%, respectively. We confirmed that the bias margins of SR are independent of operation frequency. The limits of operation frequency are thought to be much higher than 30GHz.

I. Introduction

SFQ logic[1] circuits have a high potential and are promising devices for high-speed digital systems because of the high operating speed up to sub-tera hertz and the low power consumption. In order to develop such digital systems, it is necessary to demonstrate and evaluate the circuits on high-frequency operation above several tens gigahertz.

However, it is difficult to interchange high-frequency signals between SFQ logic circuits under test, "CUT" and external measuring systems because of low signal level of SFQ logic such as ~100μV. Thus, the interface element of both systems is required.

On-chip testing system[2] includes the logic circuit as CUT and the interface circuit, which are integrated on a same chip. Key elements of the interface circuit are shift-registers, "SR", in which input data are written by applying low-frequency, "LF" clock pulses. The data are read out by high-frequency, "HF" clock pulses and sent to CUT. On the other hand, output data from the CUT are stored by HF pulses and read out by LF pulses. HF clock pulses are given to CUT as well as SR's in order to operate CUT at HF. Several on-chip testing systems have been proposed, designed and tested up to 20GHz[3] or 35GHz[2]. However, their circuits do not have large margin at their highest operation frequency. Fortunately, the advanced fabrication technology developed by NEC[4][5] with Jc=2.5kA/cm^2 enables us to operate the SFQ system at higher frequency and with larger bias margins.

In this paper, we report the high-frequency operation of the key element of interface, SR and T-FF using the on-chip testing system up to 30GHz and the evaluation of bias margins of their circuits. In addition, we mention the way of circuit design for larger margin.

II. Outline of the System

Figure 1 shows the block diagram of the on-chip testing system in this work. As shown in fig. 1(a), in order to generate high frequency pulses, we adopted two ladder type pulse generators[3] which consist of JTLs with two difference lengths, confluence buffers, "CB" and splitters, "SP". One generates clock pulses of 10GHz and the other generates 25GHz. One SFQ pulse as a trigger comes into

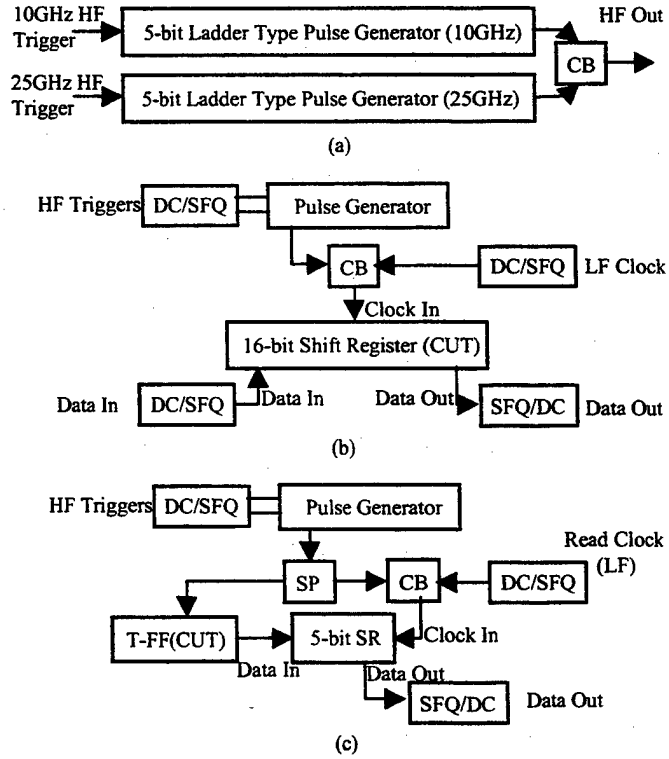

Fig. 1 (a) Pulse generator which consists of two ladder-type pulse generators. Each generates five pulses at 10GHz or 25GHz. (b) On-chip testing system for SR. (c) On-chip testing system for T-FF.

Manuscript received April 30, 1999.
This work is supported by Research on Innovative Information Processing Using Single Flux Quantum under the project "Special coordination Founds for promoting science and technology.

the ladder type generator and is copied into several pulses by the splitters. The pulses are delayed by JTLs and joined by the confluence buffers. As a result, train of five SFQ pulses is created by each generator. The correct operation of pulse generators can be confirmed easily by SFQ/DC converter based on T-FF despite high frequency since the number of HF pulses generated is five that is, odd number. Increasing bias currents of JTLs, clock pulses can be generated at higher frequency. We estimate the frequency of the pulse generators by not only numerical simulation, JSIM[6] but also measurement of average voltage of a ring oscillator which is integrated on the same chip with the pulse generators. LF clock pulses are generated at DC/SFQ converter for LF by applying timing pulse from external pulse generator and joined to outputs of other pulse generators through confluence buffers. In the way, we can generate clock pulses on the three different frequency bands, that is, LF, 10GHz and 25GHz. Thus, we can evaluate circuits at wide frequency band without large variation in biases of JTLs which compose pulse generators.

Fig. 1(b) and (c) show the test systems of a SR and a T-FF, respectively. In former, we jointed an input SR and an output SR to another SR of CUT and replaced the three SRs with only one long SR, 16-bit SR in order to simplify the system. A train of input data is sent to "data in" of the SR and loaded and shifted by applying seven LF clock pulses to "clock in" of SR. Next, five HF pulses shift the data train stored. Finally, the stored data is read out by LF clocks. On normal operation, applying four read-out-clock pulses, the data must appear at "data out" of SR.

In T-FF, the five HF clock pulses are copied by a splitter and applied to "clock-in" of a 5-bit output-SR and a T-FF as a CUT. The output pulses from T-FF are sent to "data-in" of the SR and stored at the same time. The stored data of SR is read out by application of five LF clock pulses to "clock-in" of the SR.

III. Design

The circuit was designed under Jc=2.5kA/cm^2, minimum junction size of 4μm^2 and process variation of Ic 1σ=3% and fabricated by NEC standard process based on the Nb/AlOx/Nb junction technology. The photomicrograph of the systems of SR and T-FF are shown in upper and lower of fig. 2, respectively.

On the stage of design of the system, we considered two points in order to increase operation margins. One is the effect of process variation and the other is that of parasitic inductances. They cause the decrease of bias margins and yields of fabricated circuits.

In order to reduce the effect of process variations, we optimized circuit parameters by adopting Monte Carlo simulation[7]. On the simulation, we fed JSIM with pseudo-random numbers generated by original software. The local Ic process variation of 1σ=3% and R of 1σ=5%

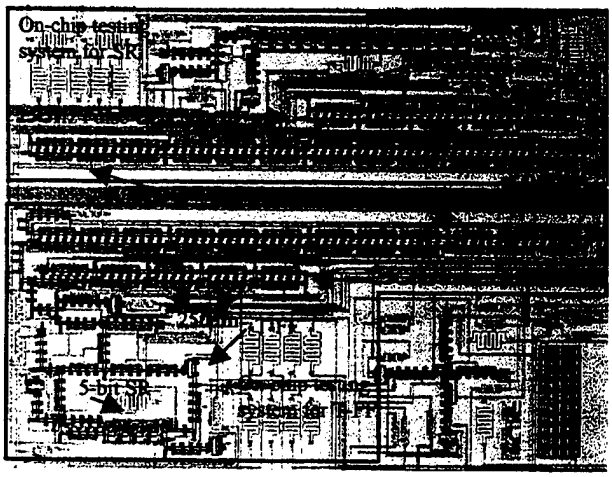

Fig. 2 Photomicrograph of the fabricated circuit. The on-chip testing systems for SR and T-FF are integrated in upper area and lower area, respectively.

were assumed according to specifications of NEC standard process. By optimizations, the final yield of 100% was numerically obtained on our assumption. At the same time, we enlarged critical margins of the circuits by using JSIM.

On the other hand, in order to reduce the effect of parasitic inductances, we increase normal inductances of circuits and reduce critical currents of JJs, since the product of LIc determines the function of a cell in SFQ logic. As a result, we can reduce the ratio of parasitic inductance to total one. In addition, we evaluated the parasitic inductances by measuring SQUID loops. The results were taken into consideration on simulation. The disadvantage of the way is increase of circuit area and propagation delay due to large circuit area.

IV. Experimental Result

Experimental results of on chip testing systems for SR at operation speed of 30GHz and T-FF at 27.5GHz are shown in Fig. 3(a) and (b), respectively. The results indicate that both systems operate correctly.

We also evaluated bias margins of SR-clock and T-FF and show them in fig. 4(a) and (b), respectively. The wide SR-clock bias margin of ±39% was obtained and agree well with the result of numerical simulation. The bias margin of SR-data was ±36.5%. As shown in the fig. 4(a), we confirmed the bias margin of SR-clock are independent of operation frequency. Unlike synchronous circuits, data-flow circuits such as the system for SR we designed are free from the limit of operation frequency. Thus, we consider that the frequency limits of SR functionality will be much higher than 30GHz.

On the other hand, The T-FF has the bias margin of ±20% and is lower than that of numerical simulation. As shown in fig. 4(b), increasing operation frequency, the margin of numerical simulation becomes lower. The reason is that the system for T-FF is synchronous circuit. Variation of the

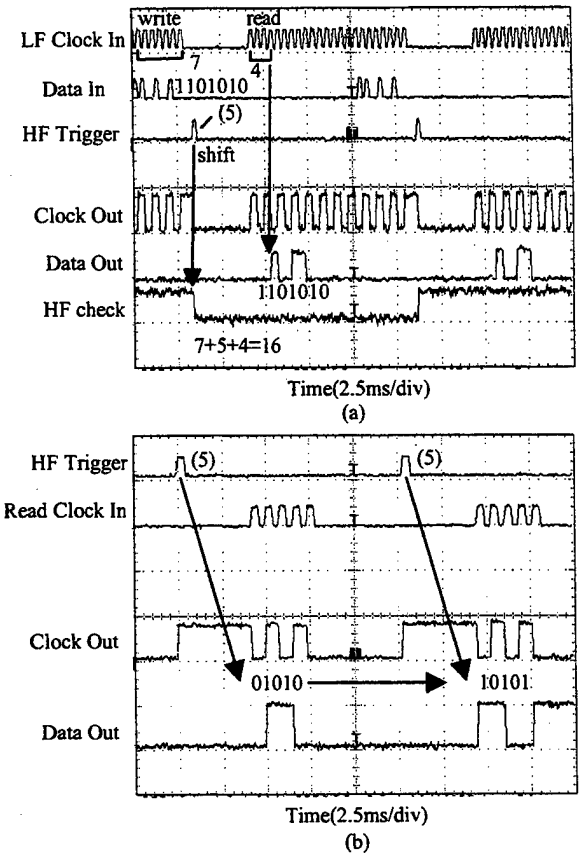

Fig. 3 Experimental results of the on-chip testing system for (a) SR and (b) T-FF.

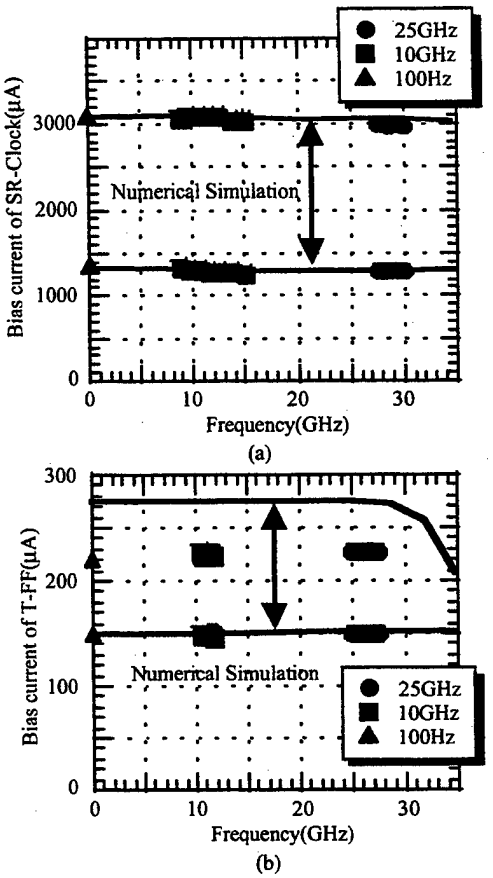

Fig. 4 Measured bias margins of (a) SR-clock and (b) T-FF. Those obtained from numerical simulation are also plotted.

bias current of T-FF affects the delay of the gate, as a result, the lag of arrival time between the clock into SR and output from T-FF increases. However, we cannot confirm the decrease of margins. The difference between experimental result and numerical simulation is due to parasitic inductances of T-FF and global variation of Jc. It is necessary to re-measure inductances of T-FF and re-designed.

V. SUMMARY

We have designed on chip testing systems and experimentally demonstrated operation of SR and T-FF at high frequency up to 30GHz and 27.5GHz, respectively. We optimized of circuit parameter by using Monte Carlo simulation and increased circuit inductances in order to enlarge circuit bias margins and yields. As a result, the systems for SR and T-FF have large bias margins of ±40% and ±20%, respectively.

REFERENCES

[1] K. K. Likharev and V. K. Semenov, "RSFQ logic /memory family: A new Josephson-junction technology for sub-terahertz-clock-frequency digital systems", IEEE Trans. Appl. Superconduct., vol. 1, pp. 3-28, Mar. 1991

[2] Alex F. Kirichenko and Oleg A. Mukhanov, "Advanced On-chip Test Technology for RSFQ Circuits", IEEE Trans. Appl. Superconduct., vol. 7, pp. 3438-3441, 1997

[3] Zhong J. Deng, Nobuyiki Yoshikawa, Stephen R. Whitely and Theodore V. Duzer, "Data-Driven Self-Timed RSFQ Digital Integrated Circuit and System", IEEE Trans. Appl. Superconduct., vol. 7, pp. 3634-3637, 1997

[4] H. Numata, S. Nagasawa and S. Tahara, "Fabrication process for sub-micron Josephson junctions", Extended Abstracts of 1993 Int. Superconductive Electronics Conf. (Boulder, 1993) pp.280-281.

[5] S. Nagasawa, Y. Hashimoto, H. Numata and S. Tahara, "A 380ps, 9.5mW Josephson 4-Kbit RAM operated at a high bit yield", IEEE Trans. Appl. Superconduct., vol. 5, pp. 2447-2452, Jun. 1995.

[6] E. S. Fang and T. V. Duzer, "A Josephson integrated circuit simulator (JSIM) for superconductive electronics application", Extended Abstracts of 1989 Int. Superconductive Electronics Conf., (Tokyo, 1989) pp. 407-410.

[7] R. Spence, R. Singh Soin, "Tolerance design of electronic circuits", Addison-Wesley, 1988

Phase-Locked Operation of RSFQ Ring Oscillators

Cesar A. Mancini and Mark F. Bocko
Department of Electrical and Computer Engineering, University of Rochester, Rochester, NY 14627

Abstract— **Ring oscillators are the traditional on-chip clock source for RSFQ mixed-signal and digital circuits. Their long-term frequency stability is essential for certain signal processing applications such as the sampling clock for an A/D converter or the output clock of a D/A converter. However conventional bias schemes lead to excessive drift in the frequency. Embedding the ring oscillator in a phase-locked loop (PLL) circuit allows it to inherit the frequency stability of an external reference source. An RSFQ circuit comprised of a ring oscillator, a divide-by-2^{20} prescaler and a resynchronizer D flip-flop was fabricated using the standard 1kA/cm^2 niobium foundry service from Hypres. The circuit was stabilized using a low-frequency PLL with a bandwidth of 6 Hz. The output of the phase detector in the PLL was used to produce a feedback current that stabilized the frequency of the ring oscillator at around 8 GHz. The frequency spectrum of the RSFQ scaled oscillator output was measured in open and closed-loop configurations. Compared to the open-loop phase noise spectrum the closed-loop spectrum showed a decrease of 30 dB of the oscillator phase noise at an offset of 1 Hz from the divided-down carrier frequency of 4.1 kHz. This agreed with the classical phase-locked loop model for the system. The long-term frequency drift of the RSFQ clock was determined by the stability of the oven-controlled quartz oscillator used as the reference in the PLL.**

I. Introduction

Digital signal processing blocks, such as FIR filters and digital mixers, and mixed-signal interface blocks such as A/D and D/A converters, are perceived as one of the main applications of superconducting electronics. These blocks rely on clock sources with long-term frequency stability for their correct operation.

The level of integration achievable so far implies that the successful operation of a complete system will have to employ multi-chip-module technologies as well. The necessity of an efficient mechanism for data exchange between chips will likely lead to the use of synchronous communication buses. Normally the on-chip clock is several times faster than the bus clock and the two clocks must be phase-locked to each other.

Manuscript received April 30, 1999.
This work was supported in part by the University Research Initiative at the University of Rochester, sponsored by the Army Research Office under grant DAAL03-92-G-0012

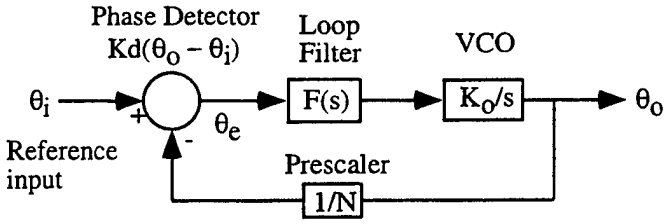

Fig. 1. Model of a phase-locked loop

Therefore, the implementation of these signal processing systems with RSFQ circuits, capable of tens or even hundreds of Gigahertz clock rate operation will require an on-chip clock source that meets the stability requirement and that can be phase-locked to an external clock signal.

Due to its simplicity and robustness, the ring oscillator (RO) has been the most widely used on-chip clock source in RSFQ circuits. However, the traditional biasing schemes used so far are not sufficient to meet the long-term frequency stability requirement. Furthermore, it has been shown that phase noise, or jitter, in ROs is significantly higher than other sources [1], such as flux-flow oscillators [2]. This might hamper system performance due to the hazard of timing constraint violations.

In this paper we demonstrate that by embedding the ring oscillator in a phase-locked loop (PLL) feedback system we can achieve phase-lock to an external low-frequency source and also long-term frequency stability. In addition, the intrinsic phase noise or jitter of the RO can be dramatically reduced.

II. Design of the PLL system

Fig. 1 shows the typical components of a phase-locked loop circuit [3]. The voltage controlled oscillator (VCO) corresponds to the RO. The prescaler makes the output frequency of the RO equal to the frequency of the reference source and is also on-chip along with the RO. The remaining components in the loop are implemented with room temperature electronics. A commercially available

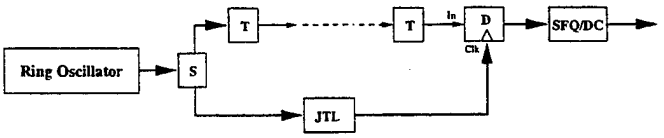

Fig. 2. Block diagram for the ring oscillator and prescaler circuit. The block labeled "S" denotes a splitter, the "T" block a T flip-flop, and the "D" block a D flip-flop. The SFQ/DC block toggles between 0 and $200\mu V$ for each incoming SFQ pulse.

lock-in amplifier (LIA) serves the functions of the phase detector and the loop filter.

A. Ring oscillator and prescaler design

The RO and prescaler circuit is depicted in Fig. 2. It consists of a ring oscillator (RO), followed by a chain of T flip-flops (TFF) and a D flip-flop (DFF) cell. Each TFF divides the frequency by one half. Therefore a chain of N flip-flops divides the frequency by 2^N. The DFF cell takes its data input from the output of the TFF chain, and its clock input from the ring oscillator. The DFF cell is in close physical proximity to the RO, so that the delay of the clock signal is small compared to the clock period. The SFQ/DC converter provides a conversion to voltage levels that can be measured with conventional room temperature electronics; it toggles between 0 and $200\mu V$ for each incoming SFQ pulse.

The RO consists of 25 JTL stages in addition to a confluence buffer and a splitter. The bias current can be adjusted to obtain a frequency of oscillation between 5 to 12GHz. The frequency range of room temperature electronics needed to amplify and analyze the output signal is on the order of tens of kHz. This sets the minimum frequency division factor to about 10^6. From this consideration the number of TFF was set to 20, such that the division factor is $2^{20} = 1,048,576$. An additional frequency division factor of 2 is obtained from the SFQ/DC converter.

Each TFF introduces a time delay and possibly additional jitter to the frequency divided output. In order to minimize this effect, the output of the TFF chain is stored temporarily in the DFF cell, and then released when a pulse from the RO arrives at the clock input of the DFF. The delay introduced by the JTL is small compared to the round-trip delay of the RO; it can also be adjusted in order to avoid timing violations in the DFF cell.

B. Circuit Layout and Fabrication

The ring oscillator and prescaler sections were assembled using cells that were already designed, fabricated and tested for previous designs [4]. The circuit parameters of these cells are optimized for maximum yield [5] according to parameter-variation data supplied by the foundry service. Physical layouts were done using the Cadence Virtuoso Layout Editor [6], and GDSII mask data was supplied to the foundry. The fabrication was done by Hypres Inc. using their standard $1kA/cm^2$ Niobium-based superconducting process [7].

C. Room temperature electronics

The room temperature portion of the PLL system is shown in Fig. 3. The RO and prescaler circuits are biased using DC power supplies connected to a bias box. The output of the ring oscillator is amplified using a PAR113 amplifier. The amplified signal is then fed to the input of a PAR 5204 Lock-In Amplifier (LIA) and an external reference is used. This reference is an HP3325A frequency synthesizer. The 1 Volt full scale in-phase output of the LIA is used to adjust the bias current of the ring oscillator. A 100kΩ resistor is used as a voltage-to-current converter. The input impedance of the bias current input of the ring oscillator is less than an ohm. Therefore the total current is simply the superposition of the DC bias current and the feedback current.

The time constant of the LIA directly determines the bandwidth of the loop and also the transient response. This time constant is set to the value that results in a critically damped response of the loop. A second LIA, an Ithaco 3961B, is connected using the same inputs as the first LIA. The time constant for this LIA is set at a much smaller value than the time constant of the first LIA. The in-phase output of this second LIA is then connected to an HP3561A spectrum analyzer. The role of the second LIA is to obtain the unfiltered output directly following the phase detector, which is not available in the first LIA.

III. Experimental results

The spectrum of the prescaled output of the RO when the feedback loop is open is shown in Fig. 4. The spectrum after the feedback loop is closed is shown in Fig. 5. The time constant in the LIA was set to 3ms. This last figure clearly shows a dramatic decrease of the phase modulation skirts. The narrower linewidth is a clear sign of stable phase-locked operation. From the SFQ/DC output

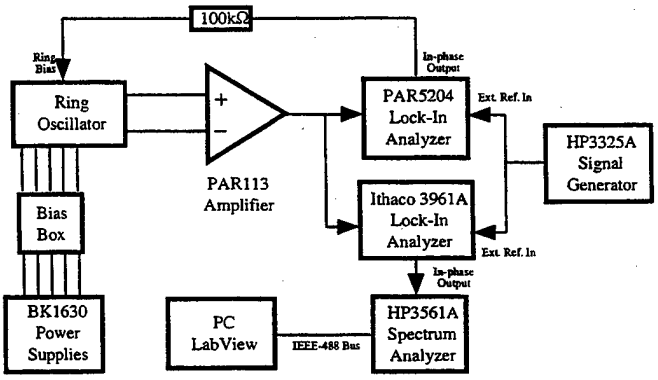

Fig. 3. Block diagram of the phase-locked detector measurement setup.

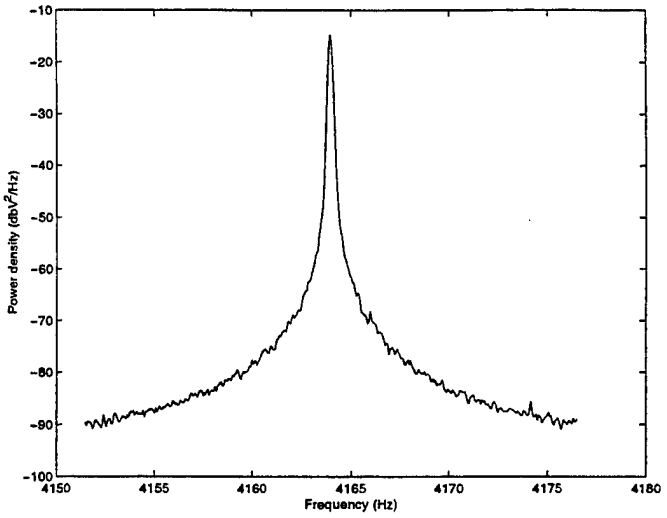

Fig. 4. Spectrum measurement of the fundamental frequency ring oscillator output prescaled by 2^{21}.

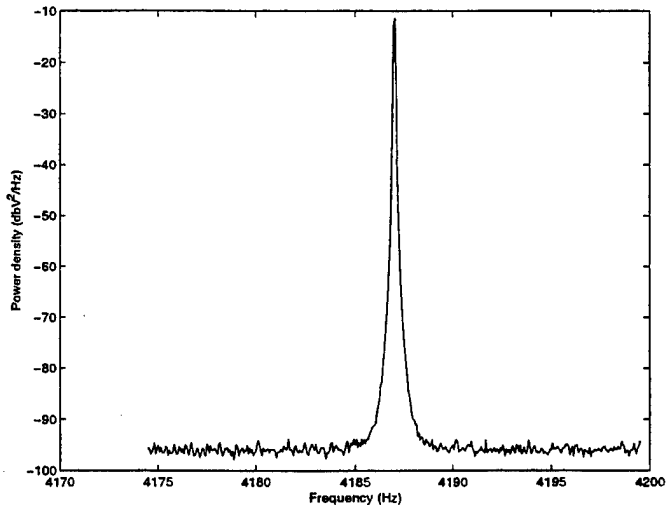

Fig. 5. Spectrum measurement of the ring oscillator output prescaled by 2^{21} when phase-locked to reference source.

frequency we obtain that ring oscillator output frequency is 8.8 GHz.

Fig. 6 shows the spectrum of the LIA output, which is the true phase noise spectrum of the feedback configuration. The portion of the spectrum above 8 Hz represents the range of frequencies under which the loop is able to counteract phase fluctuations. Beyond the loop bandwidth the loop is open, the ring oscillator was "on its own".

When compared to the open-loop phase noise spectrum, the closed-loop spectrum showed a decrease of 30 dB of the oscillator phase noise at an offset of 1 Hz from the prescaled close-loop carrier frequency of 4.187 kHz.

IV. Summary

We have designed and characterized an 8.8 GHz phase-locked clock source for RSFQ circuits. This source has

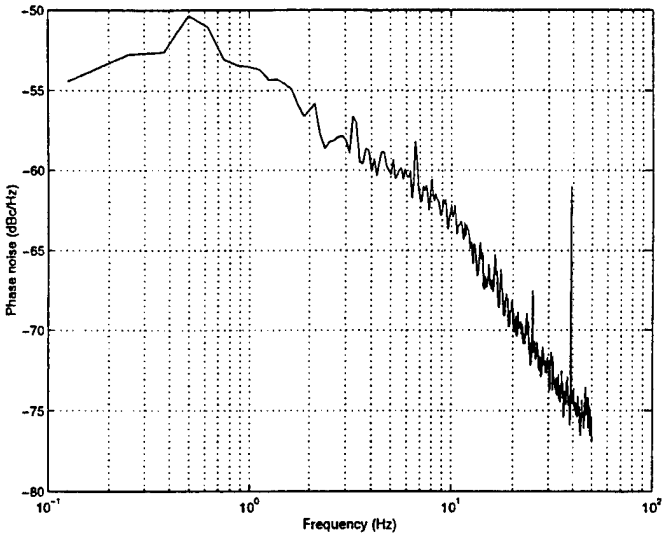

Fig. 6. Phase noise spectrum measurement of the divide by 2^{21} ring oscillator output when phase-locked to a reference source

lower jitter than the intrinsic jitter of the ring oscillator and the long-term frequency stability of the external reference source. The traditional phase-locked loop theory was used in this design and it was found that the experimental results were consistent with this theory.

References

[1] C. A. Mancini and M. F. Bocko, "Short-term frequency stability of RSFQ ring oscillators," *to be published in Tran. Appl. Supercond.*, 1999.

[2] V. P. Koshelets and et. al., "Flux-flow oscillators for sub-mm wave integrated receiver," *to be published in Tran. Appl. Super.*, 1999.

[3] D. Wolaver, *Phase-Locked Loop Circuit Design.* Prentice Hall, 1991.

[4] A. M. Herr, C. A. Mancini, N. Vukovic, M. F. Bocko, and M. J. Feldman, "15GHz operation of 64-bit circular shift registers," *IEEE Trans. Appl. Supercond.*, vol. 8, no. 3, pp. 120–124, 1997.

[5] Q. P. Herr and M. J. Feldman, "Multiparameter optimization of RSFQ circuits using the method of inscribed hyperspheres," *IEEE Trans. Appl. Supercond.*, vol. 5, pp. 3327–3340, June 1995.

[6] Cadence Design Systems, Inc., San Jose, CA, *Cadence Openbook*, 1997.

[7] Hypres, Inc., Elmsford, NY 10523, *HYPRES Niobium Process Flow and Design Rules*, 1993.

Operating Margins for a Superconducting Voltage Waveform Synthesizer

S. P. Benz, C. A. Hamilton, and C. J. Burroughs
National Institute of Standards and Technology, 325 Broadway, Boulder, CO 80303-3328 USA

Abstract—Operating margins for a bipolar superconducting voltage waveform synthesizer were measured. Current ranges were determined for 101 equally spaced dc voltage steps between –18.6 and +18.6 mV. The measured voltages of these steps deviated from the expected voltages by less than ±0.6 μV.

I. Introduction

We are developing a superconducting Josephson digital-to-analog converter as an accurate time-dependent voltage waveform synthesizer with precise spectral output for both amplitude and frequency [1]-[4]. The original circuit of the pulse-driven Josephson digital-to-analog converter uses an input drive of pulses [1]-[2]. Unfortunately, this technique is limited to the generation of unipolar ac waveforms. We recently demonstrated that bipolar waveforms could be synthesized by using a combined input drive consisting of a two-level bias representing the digital code and a sine wave [3]-[4]. This combined input drive provides a six-fold increase in output voltage compared to the original circuit using the same high-speed digital code generator. Bipolar ac generation is an important step toward achieving practical output voltages greater than or equal to 1 V.

In this paper, we confirm the functionality of the bipolar voltage waveform synthesizer by measuring the time-averaged dc voltage of an array of junctions for 101 different patterns of a 100 bit-long code. We demonstrate that the operating current margins are greater than 1.1 mA for every one of 101 equally spaced dc voltages between –18.6 and +18.6 mV. We show that the measured voltage agrees with the expected theoretical voltage within ±6 parts in 10^6. We discuss measured harmonic spectra of sine waves that were synthesized using the optimized bias conditions determined from the 100 bit codes. Undesirable harmonics in these ac waveforms were reduced to 80 dB below the fundamental.

II. Bipolar Voltage Generation

In this section we describe how bipolar ac and dc voltages are generated. When a Josephson junction is biased with a sinusoidal microwave signal $I_{ac}\sin(2\pi ft)$, with frequency f and amplitude I_{ac}, its dc voltage-current characteristic exhibits constant voltage steps at $V_n = n\Phi_0 f$. The flux quantum $\Phi_0 = h/2e$ is the ratio of Planck's constant and twice the electron charge. The step voltage is the time-averaged value of many junction voltage pulses. The quantum step number n is an integer 0, ±1, ... that corresponds to the number and polarity of quantized voltage pulses per period of the sinusoidal drive $1/f$. The time integral of every pulse is precisely equal to the flux quantum. In Fig. 1, we show that the center of the current range of the ±nth step is selected by appropriately choosing bias current ±I_o..

Manuscript received April 30, 1999. This work was supported in part by The Office of Naval Research Gov. Order No. N00014-99-F0127.
Contribution of the U.S. Government, not subject to U.S. copyright.

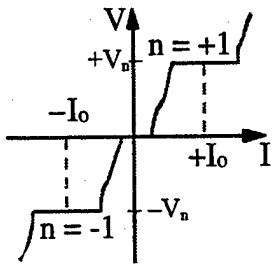

Fig. 1. Simulated voltage-current curve of a sinusoidally driven, resistively shunted Josephson junction showing constant voltage steps.

Bipolar pulse-quantized waveforms are generated by direct control of individual pulses of both polarities, such as those on the $+n$ and $-n$ steps. Pulses of either polarity can be selected by rapidly switching the dc current bias between these steps at a rate comparable to and synchronized with the sinusoidal drive frequency. Time-averaged dc voltages between the values $+V_n$ and $-V_n$ are generated by repeating periodic sequences of high and low biases to generate the appropriate number and polarity of pulses. The appropriate pulse sequence for a given voltage is created by using a digital code that specifies the timing of the high $+I_o$ and low $-I_o$ current biases. Thus, the sine wave frequency determines the maximum and minimum voltages that can be synthesized, whereas the digital code specifies the particular voltage within this range. In general, any dc voltage $(p-q)V_n/(p+q)$ can be generated using a digital code with p 1's and q 0's. For example, a periodically repeated 10 bit code of six 1's and four 0's yields a time-averaged voltage $+0.2V_n$. A code of all 0's gives the minimum output voltage $-V_n$.

Similarly, time-dependent periodic voltage waveforms are synthesized by repeating more complex bit patterns. The peak amplitude of these bipolar ac waveforms is $+V_n$. Figure 2(a) shows an example of how a sine wave is generated using a two-level digital code. The sine wave peak amplitude corresponds to the highest density of 1's. The nodes correspond to an equal density of 1's and 0's.

Figure 2(b) shows a block diagram of the method used to synthesize a sine wave of frequency f_1 or any other bipolar periodic waveform $S(t)$ using quantized pulses. The modulator algorithm is a computer program that digitizes the input waveform and creates a digital code $S(i)$ of length N_s at a sampling frequency f_s. The digital code generator re-creates this two-level code as a bipolar output voltage in real time $S_D(t)$ by clocking its memory at the sampling frequency. The two-level high-speed code is combined with a sinusoidal drive of frequency f using a directional coupler, indicated by "C". The sinusoidal drive frequency must be locked to the code generator's clock in order to prevent phase drift between the two drive signals. The combined signal is used to current-bias the Josephson quantizer consisting of either a single junction or an array of junctions. A three-pole low-pass Butterworth filter is used to remove unwanted

quantization noise from the spectrum of the quantizer output signal $S_J(t)$, leaving the desired waveform $S'(t) \approx S(t)$. Knowledge of the digital code, the drive frequency, and the number of junctions in the array is sufficient to precisely calculate the output waveform.

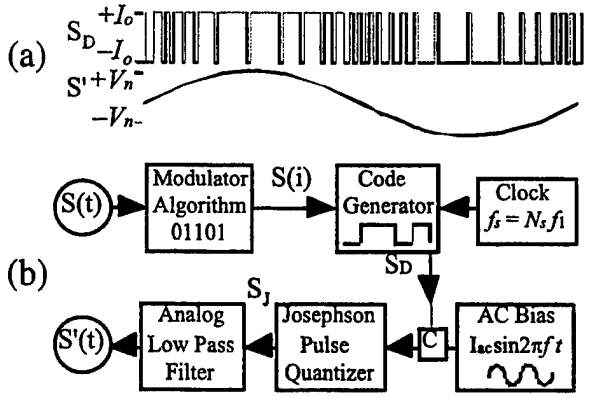

Fig. 2. (a) A two-level high-speed bias corresponding to the digital code of a synthesized sine wave S'. (b) A block diagram of the synthesized bipolar voltage source based on a Josephson junction pulse quantizer. "C" designates a directional coupler.

The sinusoidal frequency should be at precisely half-integral multiples of the sampling frequency $f = mf_s/2$, where the integer $m \geq 2$ [4]. The optimum operating margins occur when m is an odd integer and when the sine and clock signals are "in phase," that is, when transitions between different bits of the code signal are in the opposite direction from the rising or falling edge of the sine wave. Under these frequency (odd m) and phase conditions, all of the steeply rising edges are removed from the combined input code, provided that the code is separated into three pairs of consecutive bits, Low (00), Medium (01), and High (11). The (10) pattern is excluded because it produces steeply rising edges. Both the dc and ac input waveforms presented in this paper were generated under these conditions.

III. DC Voltage Measurements

The operating current range of the bipolar voltage synthesizer can be determined by measuring the current range of dc voltage steps that correspond to different digital codes. The range that is common to all codes is the total operating current range of the device. We investigated a small set of 101 codes for a 100 bit pattern to demonstrate the functionality of the bipolar synthesizer.

Measurements were performed on an array of 1000 Nb-PdAu-Nb Josephson junctions distributed along a 7 mm length of 50 Ω Nb coplanar waveguide [5]. The critical current of each junction in the array is about 4.1 mA, and the resistance of each junction is about 3.8 mΩ. The transmission line is terminated with a 50 Ω PdAu resistor. Four-point measurements of the array are made using four bias taps. Each tap has a 50 Ω resistor close to the transmission line.

The array was driven with a 9 GHz sine wave, and the digital code generator was clocked at 2 GHz (m = 9). The code generator's rise time is 30 ps, about 25 % of the sine period. A digital voltmeter was used to measure the voltage of 101 equally spaced dc voltages between +18.6 and –18.6 mV.

We generated alternating positive and negative voltages starting with the maximum (all 1's) and minimum (all 0's) and decreasing toward 0 V (alternating 01 pattern). For each iteration, the positive and negative voltage patterns were changed by appending 01 to the right end of each 100 bit-long code. The resulting measurement sequence was +18.6, –18.6, +18.2, –18.2, ..., +0.4, –0.4, 0 mV. Each pattern corresponds to different harmonic components of the input. Each voltage can be generated using a number of different patterns, each with its own harmonic signature. Thus, the 101 patterns measured here are only a subset of all possible patterns for these particular voltages, even within the set of 100 bit-long codes.

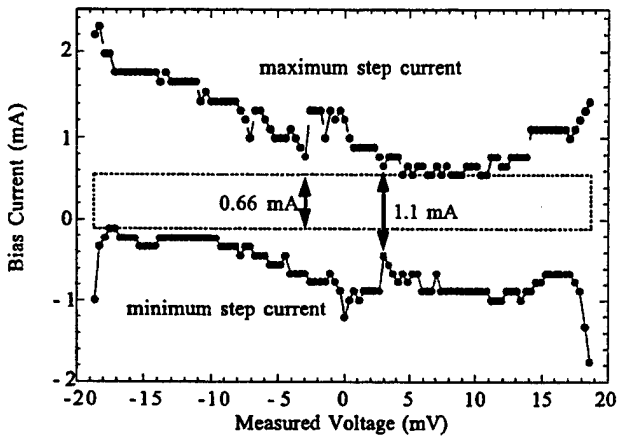

Fig. 3. Maximum and minimum bias currents as a function of the measured voltage showing the current range for 101 digitally synthesized patterns of a 100 bit code. The 1000 junction array was biased with a 9 GHz sine wave, and the code generator was clocked at 2 GHz. The dashed box indicates the common operating current range of all 101 patterns.

Figure 3 shows the current range of each pattern as a function of the measured voltage. The step edges were determined using a large 6 standard deviation search criterion. The voltmeter averaged each voltage measurement over 20 power line cycles. The current range for all 101 patterns is greater than 1.1 mA. The smallest current range occurs for the pattern corresponding to about 3 mV. Although the current range of all steps is greater than 1.1 mA, the combined operating range for all 101 patterns is only 0.66 mA, as indicated by the dashed box in Fig. 3.

Figure 4 shows the measured voltage deviation from the expected voltage with the thermal voltage subtracted for the 101 different 100 bit patterns. The *measured* voltage for each pattern is the *average* of all points on each step when the voltage was measured over the full current range of the step in 100 μA increments (≥ 11 points each). The *expected* voltage is the voltage $(p-q)Nnf\ [K_{J\text{-}90}\ (p+q)]^{-1}$ calculated using the Josephson constant $K_{J\text{-}90}$ = 483 597.9 GHz/V and the number of junctions N. The thermal voltage is estimated from consecutive patterns with voltages of opposite polarity. The thermal voltage drift over the 75 minute measurement is about 1.3 μV. The measured voltage agrees with the expected voltage within ±0.6 μV, or ±6 parts in 10^6 of the

full-scale voltage for this 100 mV range. However, the analog-to-digital linearity of the nanovoltmeter is only 50-66 nV for our 20 mV measurements. This suggests that the average measured voltage contains points where the step is not flat, probably near the edges. Thus a finer search criterion (<6 standard deviations) should be used to determine the step edges, and the midpoint of the steps should be used to determine the best average voltage.

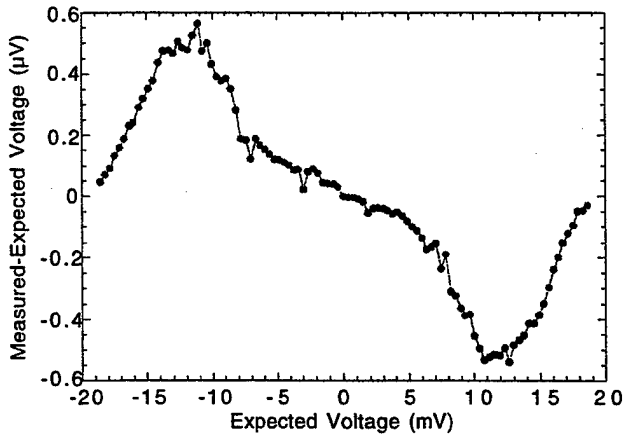

Fig. 4. Deviation of the average measured voltage from the expected voltage with the thermal voltage subtracted for 101 different patterns of a 100 bit code.

IV. Discussion

Since the voltage comparison data suggest that the steps are not flat, the true operating current range may be even smaller. However, even the "best" data above achieve the optimum operating current range (0.66 mA) for only a narrow range of bias conditions. These other important bias conditions determine the complete operating margins of the array and include the sine wave amplitude, the code generator amplitude, and the relative phase delay between the generator and the sine wave. For this set of codes, two patterns were extremely sensitive to the generator amplitude and phase delay, producing a non-zero current range for all 101 patterns only at single generator amplitude. The phase delay was adjusted four times during the measurement set (13 ps total shift) for optimum performance. This suggests that other patterns, either of 100 bit length for the same voltages or longer patterns yielding finer voltage resolution, may have zero operating current range.

Measurements of synthesized low-frequency ac waveforms, in particular a sine wave with 524 288 bits, confirm the lack of operating margins for very long bit patterns. Operating margins exist only if all bias parameters can be varied over a finite range with no change in the output. For these waveforms, we find only a single set of bias conditions that yields the lowest unwanted harmonics [3]. For example, a 3.8 kHz sine wave synthesized using the above "optimized" parameters successfully reduced higher harmonics to -80 dB (carrier), about 50 dB lower than the code generator output, as has been demonstrated previously [2], [3]. The 9 GHz input sine wave amplitude could be varied from −10 to −10.6 dBm. The phase could be shifted by about 4 ps. But single values for the code generator amplitude and offset (100 μV increments) were required to minimize the harmonics.

V. Conclusions

The dc voltage measurements of different patterns and the spectral measurements of ac voltage waveforms both demonstrate the difficulty in achieving operating margins for this broadband circuit. Depending on the digital code pattern, the input waveform contains different harmonics over the range from dc to 9 GHz. Any distortion of these harmonics will distort the input waveform and decrease the operating margins. The most likely cause of our poor operating margins are that the resistive bias taps are inadequate as low pass filters. In future circuit designs we hope to improve the broadband design of our circuit by developing lumped superconducting low-pass filters and arrays, whose dimensions are smaller than one-fourth of the wavelength of the sine wave drive frequency.

Acknowledgment

We thank L. A. Christian and R. Ono for helpful conversations.

References

[1] S.P. Benz and C.A. Hamilton, "A pulse-driven programmable Josephson voltage standard," Appl. Phys. Lett., vol. 68, pp. 3171-3173, May 1996.

[2] S.P. Benz, C.A. Hamilton, C.J. Burroughs, T.E. Harvey, L.A. Christian, and J.X. Przybysz, "Pulse-driven Josephson D/A Converter," IEEE Trans. Appl. Supercond., vol. 8, pp. 42-47, June 1998.

[3] S.P. Benz, C.A. Hamilton, C.J. Burroughs, and T.E. Harvey, "AC and dc bipolar voltage standard using quantized pulses," IEEE Trans. Instrum. Meas., vol. 48, April 1999.

[4] S.P. Benz, C.J. Burroughs, T.E. Harvey, and C.A. Hamilton, "Operating conditions for a pulse-quantized AC and DC bipolar voltage source," in Proc. of the 1998 Applied Superconductivity Conf., IEEE Trans. Appl. Supercond., vol. 9, June 1999, in press.

[5] S.P. Benz, "Superconductor-normal-superconductor junctions for programmable voltage standards," Appl. Phys. Lett., vol. 67, pp. 2714-2716, Oct. 1995.

An Asynchronous SFQ-pulse Arbiter for High Performance Digital Applications

Shinichi Yorozu, Dmitry Zinoviev *, and Shuichi Tahara

Fundamental Research Laboratories, NEC Corporation, 34 Miyukigaoka, Tsukuba, Ibaraki 305-8501, Japan
*Physics and Astronomy Department, SUNY at Stony Brook, Stony Brook, New York 11794-3800, USA

***Abstract*— We have developed a novel arbiter circuit for RSFQ digital applications. The circuit synchronizes two asynchronous incoming signals with the internal clock signal. This can be important in high-end digital computer systems. Even if the input signals arrive at the same time, the output of the arbiter is guaranteed to be sequential.**

The arbiter consists of a clock generator, based on a ring oscillator, and data latches, a total of 16 Josephson junctions. The frequency of the synchronizing clock source can be easily tuned by changing the dc bias in the loop. A dynamic simulation shows that if implemented in 2μm Niobium-trilayer technology, the oscillating period can be as low as 5 ps, and the average latency of the arbiter is less than 10 ps.

I. Introduction

Superconducting RSFQ circuits have demonstrated advantages in high-performance processing in the tens-to-hundreds of gigahertz domain. This kind of high performance cannot be provided by any semiconductor circuits, especially in large-scale [1]. At such high speeds, it is almost impossible to distribute global clock signal without skew, so we should switch the circuit-design methodology from global timing approach to local/asynchronous timing approach (e.g. [2]).

Generally, in digital systems, signal arbitration function is very important. For example, in multiprocessor systems, two processors may request one resource at the same time, and the system must choose which request to serve first and which one to block. The arbitration circuit should have low latency and high throughput, be able to separate two signals even when they arrive at the same time, and have small footprint on a chip.

We propose an RSFQ arbiter for high-performance digital superconductor systems. This arbiter provides the features mentioned above, and requires neither global timing nor synchronizing the internal oscillator with any other external clock source.

II. Operation

Fig. 1 shows the block diagram of a two-input arbiter circuit.

The circuit consists of two data latches (D flip-flops) and a local clock generator. Each data latch has one data input port "I", one clock port "T", and one output port. When a service request arrives to port "I", it is stored in the latch. The latch is periodically polled by the timing signal, and if a request has been stored in it, an SFQ pulse is produced at the output "O". The infinite sequence of the polling SFQ pulses is generated locally by a ring oscillator. Since at any give time moment there is only one clock pulse in the oscillator, no two requests can be propagated to the outputs of the arbiter at the same time. It is important to notice that although the separation in time is not done on a first-in-first-out (FIFO) basis, the output

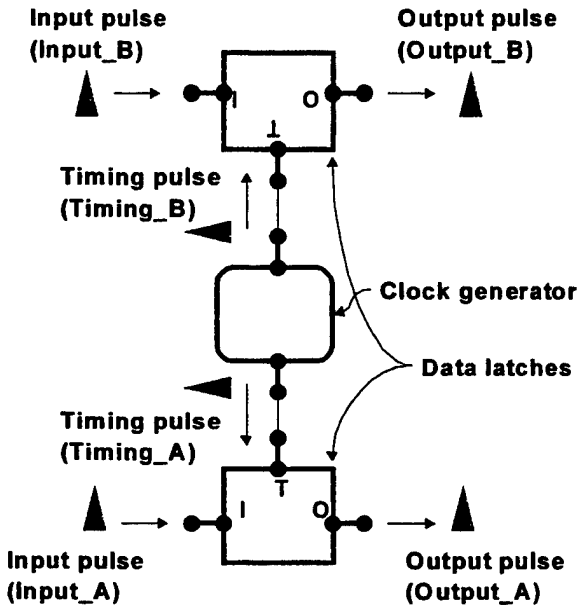

Fig. 1. Block diagram of the arbiter

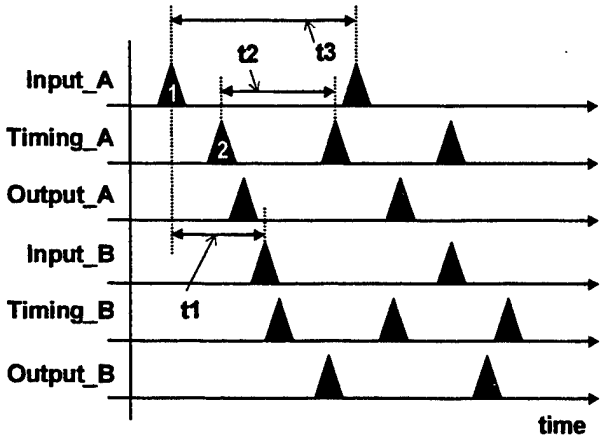

Fig. 2. Timing sequence of the arbiter circuit operation

Manuscript received April 30, 1999.

of the arbiter is guaranteed to be sequential. Fig. 2 shows timing diagram of the arbiter. Here, t1 indicates the difference in arrival times of the input signals, t2 indicates the period of the local clock generator, and t3 shows the period of the input signal. After time t_{hold} from the arrival of input signal "1", the signal is held in the latch. It is kept there until the clock signal "2" arrives. After time $t_{release}$ from the arrival of the clock signal, the latch outputs an SFQ pulse.

The arbiter has two important properties. The first is the dependence of its behavior on the difference in arrival times (t1 in Fig. 2). If the difference in arrival times of the two signals satisfies the following condition:

$$t1 > t2/2, \quad (1)$$

then the circuit separates the output signals in time on a first-in-first-out basis. Otherwise, any particular order of the output signals cannot be guaranteed.

The second important property is the maximum throughput 1/t3 which depends on the processing time of the latches. And t3 must satisfy the following condition to guarantee correct operation:

$$t3 \geq t_{hold} + t2 + t_{release} \quad (2)$$

If condition (2) is not satisfied, bit errors may occur, so the guaranteed maximum throughput of the arbiter circuit is

$$T = (t_{hold} + t2 + t_{release})^{-1} \quad (3)$$

III. RSFQ Implementation

Fig. 3 shows the schematics of our RSFQ implementation of the arbiter.

When an input signal comes from input INPUT_A, it is stored as an SFQ in the interferometer J1-L1-L2-J2.

When an SFQ is stored in loop J1-L1-L2-J2, Josephson junction J2 of the comparator J2-J3 is overbiased by the circulating persistent supercurrent, so when the clock pulse arrives, Josephson junction J2 is switched. Otherwise, junction J3 with the smaller value of the critical current is switched.

Because of the very asynchronous nature of the circuit, we cannot make any assumptions about the difference in arrival times of the request and of the clock signal. Therefore, the arbiter must be able to operate in a mode when these two signals arrive simultaneously or almost simultaneously. In this case, both junctions J2 and J3 will be switched [5], and yet another Josephson junction is necessary to compensate the undesirable 4π phase leap.

The clock signal for the comparator is provided by the clock generator which is a ring oscillator built up of a Josephson transmission line. The two-junction interferometer J4-L3-L4-J5 (L3<<L4) can store a single flux quantum which induces clockwise persistent current in the loop. At most one SFQ pulse exists in the ring. At the beginning of the operation, dc current DCBias1 overbiases Josephson junction J4, so that one SFQ pulse is injected into the ring and one single flux quantum is stored in the interferometer. After

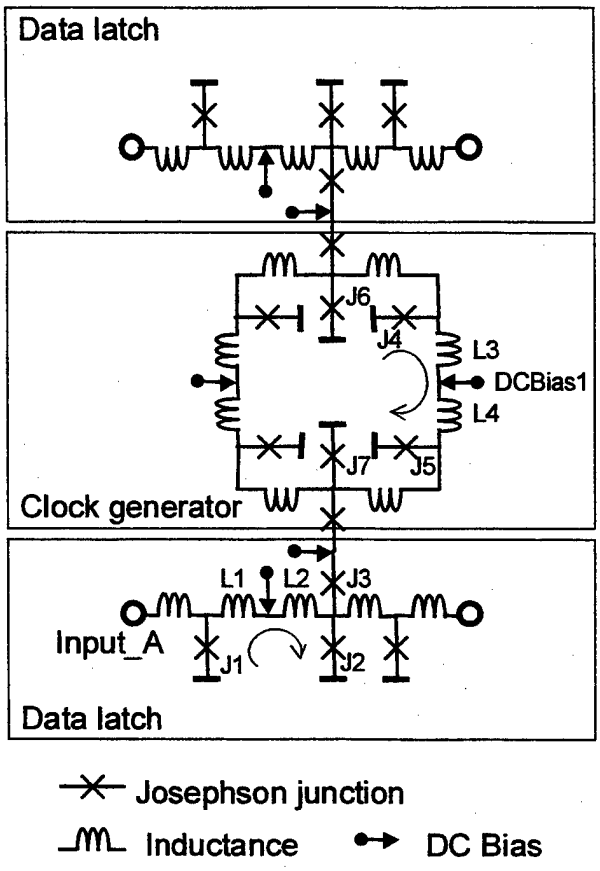

Fig. 3. Circuit diagram of the arbiter

switching J4, the circulating persistent supercurrent reduces the total current through J4 and protects it from further generation. When the SFQ pulse in the ring makes a full rotation, it switches Josephson junction J5, the loop current in the interferometer vanishes, and Josephson junction J4 is switched again thus restarting the oscillation. Josephson junctions J6 and J7 are used to split the clock signal and deliver it to the latches. The period of the polling t2 can be easily changed in vast range by varying the dc bias current in the oscillator, provided that (2) holds.

We have simulated the circuit and optimized its parameters

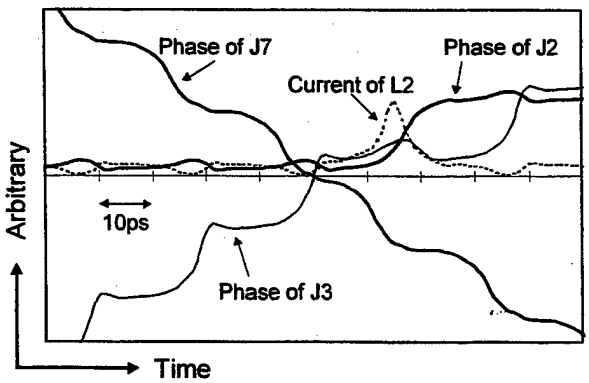

Fig.4 . Dynamic simulation result

TABLE 1. ARBITER PERFORMANCE

Technology	Hold time (ps)	Release time (ps)	t2 (ps)
2.0μm (NEC)	2.95	1.44	10.54
0.8μm (future)	1.11	0.54	3.94

using PSCAN physical-level simulator and "Cowboy" optimization tool (both programs developed in SUNY). Fig. 4 shows the dynamic simulation of the circuit. If a request is stored in the loop J1-L1-L2-J2, the phase of Josephson junction J2 changes leaps by 2π but the phase of J3 does not leap. Table 1 shows the simulated performance of this circuit. The dc bias current in the latch was 70% of the critical current of the Josephson junction J1.

For this circuit, if implemented using to NEC standard process [3], the theoretical maximum throughput is 66 Gbps according. Migration to a hypothetical 0.8 μm minimal feature size technology [4] would increase the throughput to 178 Gbps. Fig. 5 shows the microphotograph of the arbiter fabricated using NEC standard fabrication line.

IV. DISCUSSION

The proposed arbitration circuit can be easily generalized to the case of more than two input signals. Fig. 6 shows a block diagram of such generalization. In this case, however, the increasing number of request latches increases time t2, but the time resolution does not change. So, the maximum possible input request rate respectively decreases.

Notice that in the case of 2^N inputs, the ring oscillator can be replaced by a tree of T flip-flops.

V. CONCLUSION

We have proposed a novel arbitration circuit for RSFQ digital applications. This circuit separates signals in time by synchronizing them with a fast internal clock source. It consists of a clock generator, based on a ring oscillator, and request latches, and it uses a total of 16 Josephson junctions.

The frequency of the synchronizing clock source can be easily tuned by changing the dc bias in the loop. The dynamic simulation show that the oscillating period can be as low as 10 ps, and the average latency of the arbiter fabricated using NEC standard fabrication process is less than 20 ps.

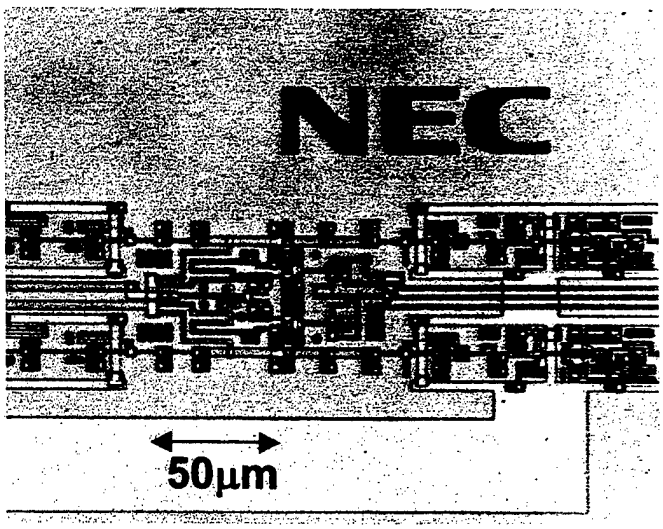

Fig. 5. Photograph of fabricated circuit using NEC standard process

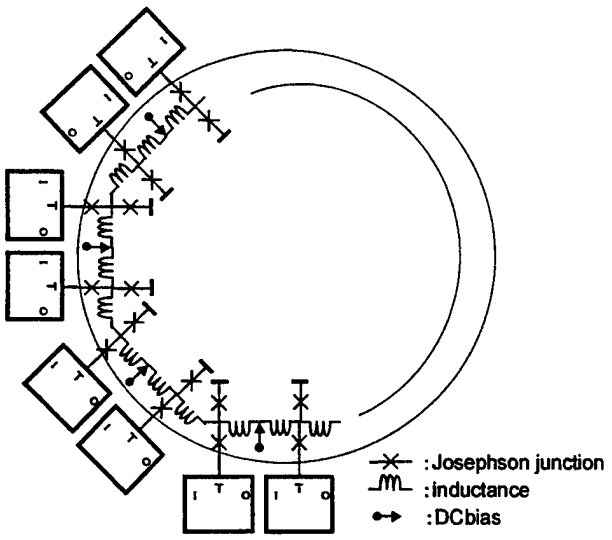

Fig. 6. Arbiter circuit for multiple input

ACKNOWLEDGMENT

We would like to thank Prof. K. Likahrev, M. Tanaka, H. Numata, and Y. Kameda for their collaboration in this work.

REFERENCES

[1] K. Likharev, and V. Semenov, "RSFQ logic/memory family: A new Josephson-junction technology for sub-terahertz-clock-frequency digital systems", *IEEE Trans. on Appl. Superconductivity*, vol. 1, 1991, p.3-28.

[2] P. Patra, S. Polonsky, and D. Fussell, "Delay insensitive logic for RSFQ superconductor technology," in Proc. International Symposium on Advanced Research in Asynchronous Circuits and Systems, IEEE Computer Society Press, Apr. 1997, pp.42-53.

[3] S. Nagasawa, Y. Hashimoto, H. Numata, and S. Tahara, "A 380ps, 9.5mW Josephson 4-Kbit RAM Operated at a High Bit Yield", *IEEE Trans. Appl. Superconductivity*, vol. 5, p.2447-2452, 1995.

[4] K. Likharev, "Recent Progress and Prospects of Superconductor Digital Technology", *FED Report*, Jan. 1997.

[5] T. Filippov, V. Semenov, and K. Likharev, "Signal Resolution of SFQ Comparators", *IEEE Trans. Appl. Superconductivity*, vol. 5, p.2240-2243, 1995.

Design of a 10 GHz High-voltage Driver Operating with SFQ Inputs

N. Harada, A. Yoshida, and N. Yokoyama
Fujistu Ltd.

Abstract—Design and simulation results are described with respect to a high-speed superconducting latching driver for superconductor - semiconductor interfaces toward the creation of an SFQ processing. The driver can produce an output of 7.5 mV from an SFQ input pulse, and has an ability of operating at clock frequencies of up to 10 GHz.

I. Introduction

A superconducting RSFQ digital system is attractive because of its high-speed processing capability and low power dissipation. Since the operating environment of SFQ systems is quite different from room-temperature electronic systems, an interface is necessary to communicate with room-temperature systems. A superconducting high-voltage driver is one of the key components of an interface. There are two approaches to constructing a driver, one is a non-latching driver and another is latching driver. The non-latching driver consists of combinations of SFQ/dc converter, current amplifier, and series connected SQUID amplifiers[1]. This needs only a DC voltage source, however, a lot of junctions are necessary to obtain a high output amplitude due to the low output of a SQUID and the lack of drivability of SFQ circuits with inductive loads. A latching driver consists of an SFQ/latch converter and stacked amplifiers[2]. A relatively high output amplitude is possible with small number of junctions in the latching driver.

Although a lot of Josephson ICs based on latching operation have been developed, it was difficult to increase the clock frequency higher than several gigahertz. Recently, the UC Berkeley group exhibited operation at 10 Gbps of latching circuits[3,4]. Their work opened up the possibility of a latching circuit in the region over 10 GHz.

In this paper, we investigate an Nb-based latching driver using circuit simulation to pursue 10 GHz operation, and the ability to construct high-speed SFQ - semiconductor interfaces.

II. SFQ - Semiconductor Interface Configuration

Manuscript received April 30, 1999.
This study was performed through Special Coordination Funds for promoting Science and Technology of the Science and Technology Agency of the Japanese Government.

For SFQ - semiconductor interfaces, functions such as voltage amplification, pulse-logic to level-logic conversion, clock frequency conversion, and synchronization with room-temperature systems are required. The basic configuration of an interface for an Nb-based SFQ system is shown in Fig. 1. It consists of a superconducting demultiplexer(DEMUX), drivers, transmission cables which connect the low-temperature system with the room-temperature system, semiconductor pre-amplifiers, decision circuits(DEC), and demultiplexers. Superconducting drivers are necessary to convert the SFQ pulse to a voltage signal which can drive room-temperature semiconductor pre-amplifiers.

An interface system with a high bit rate makes it possible to reduce the number of parallel data cables between the low-temperature and room-temperature systems, thus reduce the thermal flow into cryo-system. Since the maximum bit rate of commercially available semiconductor parts such as amplifiers, DEC, and DEMUX is 10 Gbps now, the maximum bit rate of a practical interface system would be 10 Gbps.

The interface voltage among the driver and pre-amplifier is determined by the desirable bit error rate(BER) of an interface system, and other conditions such as pre-amplifier gain, sensitivity of the decision circuit, and so on. There is the following relation between BER and signal-to-noise ratio(SN)[5].

$$BER = 0.5\{1-erf[(SN/2)^{1/2}/2]\} \quad (1)$$

Assuming that thermal noise at the input of pre-amplifier is the dominant noise source, noise voltage is expressed as

$$\langle v_n \rangle = (4kTR\Delta f)^{1/2}. \quad (2)$$

If we allow one error in a year in a 100 GHz clock SFQ system, the BER should be smaller than 3×10^{-18}, then the SN must be larger than 24 dB. When $R = Z_0 = 50\ \Omega$, bandwidth $\Delta f = 10$ GHz, the noise voltage becomes 0.13

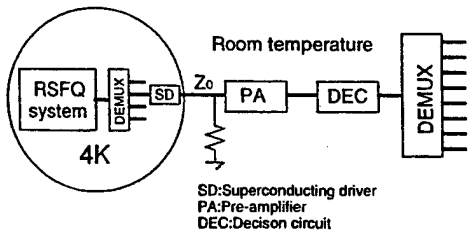

Fig. 1 Basic configuration of an electronic SFQ - semiconductor interface.

TABLE I

COMPARISON ON DRIVERS WITH THREE TYPES OF INPUT COMPONENTS

Input part	capacitor (2 pF)	resistor (1 Ω)	junction (I_c of 120 μA)
Bias margin	360 μA ± 11%	355 μA ± 13%	305 μA ± 28%
Delay time	6.5 ps	5.1 ps	5.4 ps

$mV_{p\text{-}p}$. Assuming a pre-amplifier noise-figure of 7 dB, the minimum interface voltage to keep the SN at the pre-amplifier output larger than 24 dB is estimated to be 4.5 $mV_{p\text{-}p}$. To attain this amplitude with a reasonable number of junctions, a latching driver is suitable as the interface.

III. Driver Circuit Design

A. Driver Configuration

The schematics of our proposed latching driver, which can produce steady-state voltage from an SFQ input is shown in Fig. 2. In a driver of this type, a device is necessary to maintain the voltage difference V_{BA} between the SFQ circuit and latching circuit. We assumed three types of driver, having a capacitor, a resistor, and a Josephson junction as the input component, and compared the bias margin and delay time of the driver at a clock frequency of 1 GHz using circuit simulations. We assumed a junction critical current density of 2.5 kA/cm^2. Delay time is defined as the time interval between the arrival of an SFQ pulse and the time the output reaches 10% of its steady state. The constants of the input components are optimized so as to maximize the bias margin. Table I summarizes the results. Delay time comparison does not show a large difference, however, the driver with the Josephson junction as an input device has the largest bias margin of ±28%. Thus, we consider this type of driver design in the following sections.

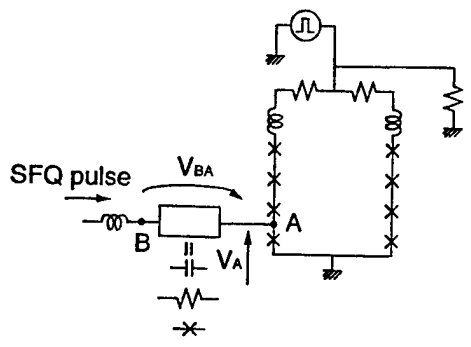

Fig. 2 Schematic of latching driver with different input components.

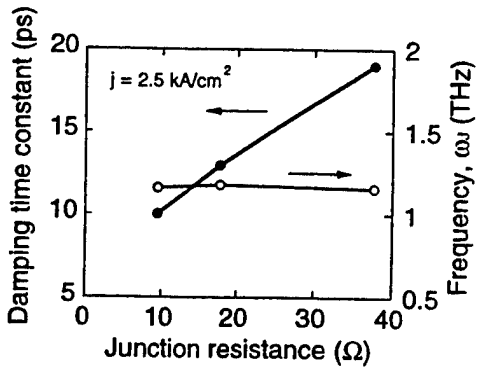

Fig. 3 Dependence of damping time constant and oscillation frequency during the resetting period of the driver on junction resistance.

B. Oscillation Frequency and Damping Time Constant During the Resetting Period

The time necessary to reset the junction from the voltage state to the zero-voltage state is one of the main factors which limit the clocking frequency of a latching circuit. During the resetting period, the output voltage oscillates and decreases at some damping time constant. Bias current should be kept at a low level for a sufficiently longer time than the damping time constant to insure normal operation in the next cycle. For single junctions, since the damping time constant is proportional to junction resistance R, reducing R by connecting a shunt resistor to a junction in parallel shortens the time constant. We performed a circuit simulation on the driver similar to that in Fig. 2 but each junction has a shunt resistor. The dependence of damping time constant and oscillation frequency ω_J on junction resistance are shown in Fig. 3. It can be seen that shunt resistor also shortens the time constant in the driver. On the other hand, oscillation frequency is almost equal to plasma frequency of each junction and hardly depends on resistance.

C. Estimation of Clock Frequency Limit

The punchthrough phenomenon also determines the upper limit of the clock frequency. The punchthrough probability for a single junction is expressed by the relation,

$$P \sim \exp[-\omega_J T_{OFF}], \quad (3)$$

where ω_J is the oscillation frequency during the resetting period and T_{OFF} is the dwell time at which the bias current is at a low level[6]. For example, to keep the probability lower than 3×10^{-18},

$$\omega_J T_{OFF} > 40. \quad (4)$$

Punchthrough analysis on the driver circuit is difficult because of the large number of parameters and is not understood in this time. Since oscillation frequency of the driver is same as single junction, we estimate the upper limit of the clock frequency for the driver using the above criterion as the first step. Fig. 4 shows ω_J and the minimum dwell time necessary to satisfy the criterion as a function of junction current density. Assuming a trapezoid bias with a 30% low level period, the limit of clock frequency is

estimated to be 8.6, 12.2, and 16.3 GHz for j = 2.5k, 5k, 10kA/cm^2 respectively.

D. Delay Time and Rise Time

Delay time and output rise time hardly depend on shunt resistance, but depend on critical current density as shown in Fig. 5. By increasing current density, both delay and rise time are improved. This makes the design on clock timing easy and also allows us to increase the clock frequency.

IV. Yield Evaluation by Monte-Carlo Analysys

Since this type of driver circuit uses synchronized switching of connected junctions, too large variation in a junction parameter may prevent normal circuit operation. We performed a monte-carlo analysis to confirm the possibility of normal operation under parameter variations. We assumed local parameter variation with a standard deviation of 3% for resistance, inductance, and junction critical current. Bias clock frequency was set at 10 GHz. A Monte-Carlo simulation was made 50 times and each step continued in 10 clock cycles, 1 ns. The analysis showed 90 % normal operation, that is, all junctions go to the voltage state by the SFQ input and go zero-voltage state by bias current resetting. Fig. 6 shows an example of an output waveform of the driver including local parameter variations at 10 GHz. An output amplitude of 7.5 mV was obtained.

V. Summary and Conclusions

We investigated a superconducting latching driver for an Nb-based RSFQ - semiconductor interface by circuit simulation. The driver can produce a 7.5 mV output from an SFQ pulse with a small delay time. Characteristic oscillation frequency of the driver is as same as that of single junction, suggesting the possibility of over-10 GHz clock operation. A Monte-Carlo analysis considering local parameter variation showed that the driver can operate normally with yield of 90%.

Acknowledgment

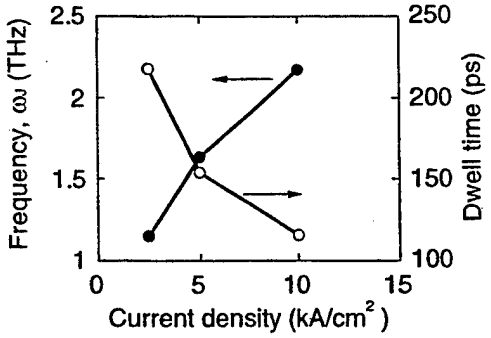

Fig. 4 Oscillation frequency ω_J of the driver and the minimum dwell time necessary to satisfy the criterion $\omega_J T_{OFF} > 40$ as a function of junction current density.

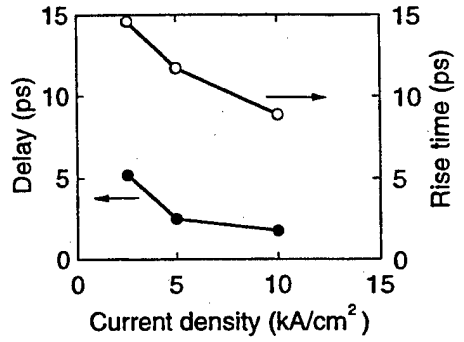

Fig. 5 Dependence of delay time and output rise time of the driver on junction current density.

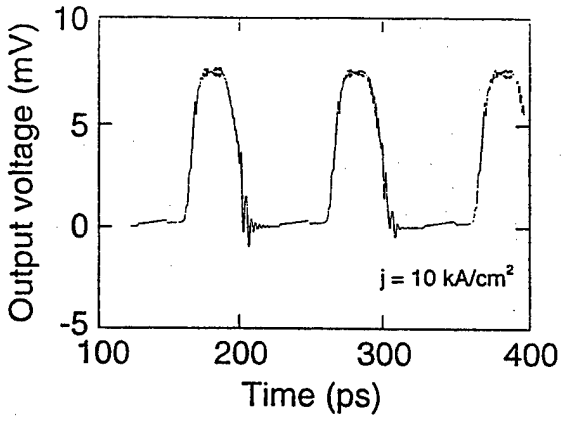

Fig. 6 An example of output waveform of the driver including local parameter variation at 10 GHz.

We would like to thank Drs. H. Suzuki, Y. Ishimaru, and T. Hato for useful discussions, guidance and advice.

References

[1] S. V. Rylov, "DC-powered high-voltage driver for RSFQ logic family", proceedings of ISEC'93, pp. 110-111, 1993.

[2] J. X. Przybysz, J. H. Kang, D. L. Miller, S. S. Martinet, and A. H. Worsham, "Interface circuits for input and output of gigabit per second data", proceedings of ISEC'95, pp. 304-306, 1995.

[3] M. Jeffery, W. Perold, and T. Van Duzer, "Superconducting complementary output switching logic operating at 5-10 Gb/s". Applied Physics Letters, vol. 69, No. 18, pp. 2746-2748, October 1996.

[4] A. M. Bhat, S. R. X. Whiteley, and T. Van Duzer, "High current density Nb/Al-AlOx/Nb Josephson junctions and their implementation in a high speed digital amplifier", IEEE Transactions on Applied Superconductivity, in press.

[5] A. Yariv, *Introduction to opticalelectronics*, 3rd ed., Holt, Rinhert and Winston, Inc., 1985.

[6] E. P. Harris, and W. H. Chang, "Punchthrough in Josephson logic devices", IEEE Transactions on Magnetics, vol. MAG-17, No. 1, pp. 603-606, January 1981.

A Single Flux Quantum Cryogenic Random Access Memory

Alex F. Kirichenko, Oleg A. Mukhanov, and Darren K. Brock
HYPRES, Inc., 175 Clearbrook Rd., Elmsford, NY 10523, USA

Abstract—We report on the design of a superconductive Cryogenic Random Access Memory (CRAM). The 16-Kb RAM consists of four 4-Kb sub-arrays (blocks). It will have a 400 ps access time (latency) and a 100 ps cycle time (throughput). The input data and address are distributed using a high-speed RSFQ pipelined demultiplexer. The output data is collected with an RSFQ pipelined multiplexer. The entire 16-Kb RAM chip will dissipate 2.4 mW. We also discuss the projection for this design, using a future sub-micron fabrication process to achieve a 1-Mb capacity with a 40 ps throughput, required for HTMT (PetaFLOPS computing) project.

I. Introduction

The lack of fast Cryogenic Random Access Memory (CRAM) with sufficient capacity and high throughput has impeded the progress of superconductive electronics in digital applications. To date, the most successful superconductive RAM implementation was one from NEC [1]. The design approach used in the NEC memories combined SFQ memory cells and ac-powered voltage-state Josephson periphery circuits. The use of the large external ac-power limited the clock cycle to about 1 GHz, making the RAM throughput insufficient to match fast, dc-powered RSFQ logic. Until now, there have been no reported dc-powered RAMs.

As a fundamental constant, a quantum of magnetic flux is quite suitable for use as a data unit. The ability of flux quanta to be stored and transferred almost without dissipation allows the development of various circuits with internal memory and further to connect them into deeply pipelined devices. While RSFQ logic designs successfully exploit these features, RAM designs cannot fully use them.

The very idea of random access to a memory matrix contradicts a pipelined approach, because of the necessity to deliver select signals to random memory cells in a short period of time. The only way to transfer an SFQ pulse over a long distance at the speed of light is to use soliton transmission along a microstrip line; however, an SFQ soliton propagation is affected by unavoidable interaction with RAM cells. Alternatively, active Josephson Transmission Lines (JTLs) can be used to reproduce the dissipating SFQ soliton. However, JTLs are slower and take more space. Thus, an SFQ pulse is not suitable to perform the select process. This leads us to implement the traditional select scheme using dc-currents delivered via microstrip lines. However, we should avoid ac-powered voltage-state Josephson circuitry which causes problems in synchronization, power dissipation, and cross-talk. Thus, the main challenge of the CRAM design is to design voltage-state periphery circuits without the external AC powering.

Manuscript received May 7, 1999.
This work was supported in part by the US BMDO/NSA under contract # F49620-99-C-0018 and JPL/NSA under contract # 1205056.

II. CRAM Architecture

A. General Block Diagram

Among all known RAM approaches, the row-access memory architecture is the fastest. In semiconductor technologies, the row-access architecture is implemented using the fastest bipolar processes. This design simplifies the access by reducing the number of select lines, and allows operation on an entire block (or word) of data, providing fast parallel access.

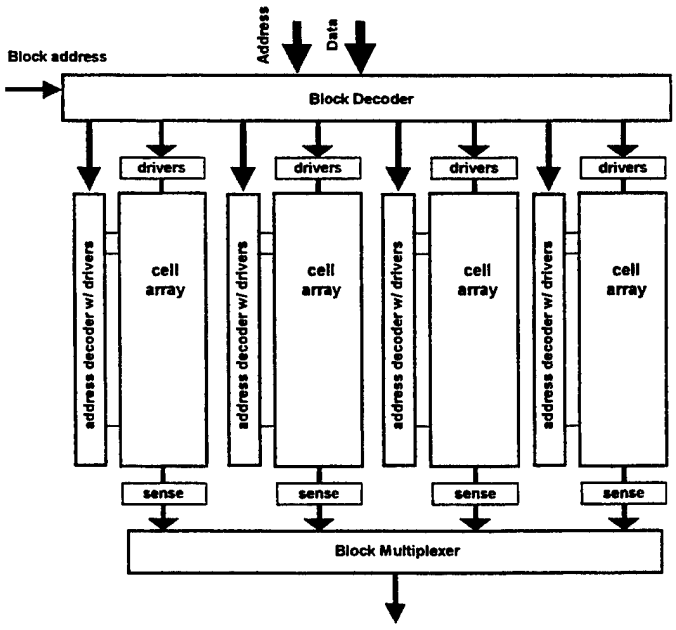

Fig. 1. A block diagram of the proposed RAM chip combining four blocks of memory arrays, block decoder, Y-decoders, select line drivers, sense gates, and output block multiplexer.

Our superconductive SFQ CRAM is constructed from SFQ memory cell arrays, dc/SFQ decoders, current drivers, sensing gates, and a block demultiplexer and multiplexer. The general structure of the RAM chip is in Fig. 1. In order to increase throughput, the 16-Kb RAM chip is divided into four 4-Kb sub-matrices (blocks). Each block comprises a 128 x 32-bit matrix having a row access. Each row of this matrix (seen in Fig. 2) contains a 32-bit word, which forms an accessible unit of data. A block demultiplexer distributes input data between blocks, while a block multiplexer (or merger) provides the output data.

The input to the RAM is a 42-bit sequence consisting of a 32-bit data word (for the WRITE operation only), a 9-bit address, and a 1-bit instruction (R/W) to indicate whether a value should be read written. The 9-bit address splits on two parts, - a 2-bit block (Y) address and a 7-bit row (X) address. The block demultiplexer sends a 40-bit data to a corresponding 4-Kb block.

B. A 4-Kb CRAM Block

Fig. 2 shows a more detailed schematic of the 4-Kb memory block. Access to memory cells is provided with magnetically coupled microstrip lines. Select line current drivers generate dc-signals that propagate along the microstrip line with the speed of light. A sensing gate converts a dc-current readout signal to an SFQ pulse.

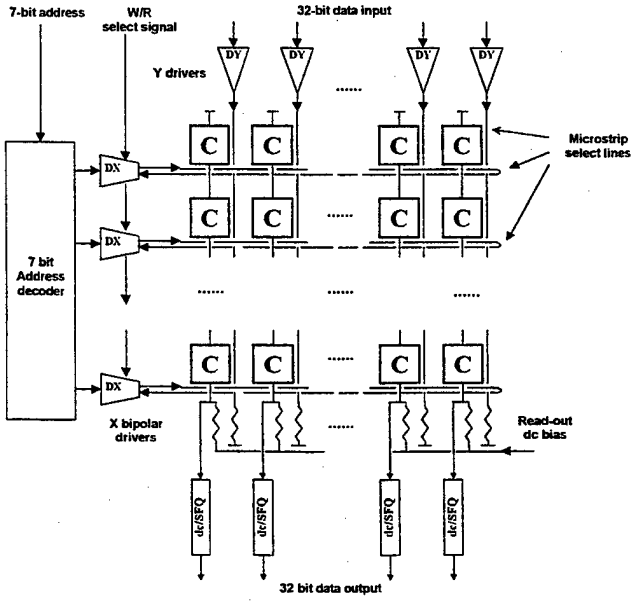

Fig. 2. Single block of RAM including an address decoder and drivers, a 32x128 memory cell array, X drivers, and output sensing dc-to-SFQ converter.

Each WRITE operation is preceded by an erase or WRITE0 operation. This function consumes an extra clock period to clear an entire row of the memory; but, at the same time, it allows us to simplify the overall RAM design and the operation cycle. The result is a higher integration scale and faster access time.

C. Memory Cell

We studied several SFQ cells for this memory. From these, we have chosen a modified version of VT memory cell [2] with non-destructive readout and current control (see Fig. 3). A single cell occupies an area of 40 x 45 μm^2. A 128 x 32-cell array of these cells occupies an area of 5.2 mm x 1.4 mm.

All read-out SQUIDs in a column are sequentially connected and biased with one dc-bias current. A sensing device is placed at the end of each of these columns. If the SQUID switches to the resistive state during the READ operation, the sensing device will detect a dc-voltage and transform it into an SFQ pulse.

Simulation shows excellent operating margins for this cell. The minimal critical current margin is 28%. The control current amplitude margins are above 30%. The DC bias current of the readout SQUIDs has 25% margins. In addition, the simplicity and reliability of this cell are very suitable for the large integration scale memories.

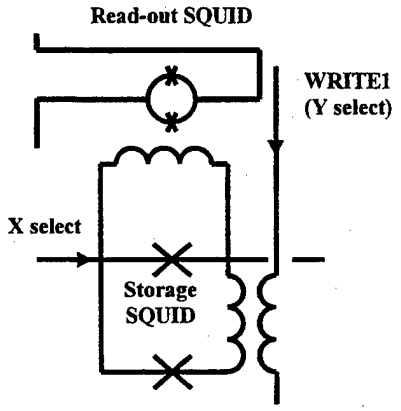

Fig. 3. A SFQ memory cell with dc-powered row-accessible selection.

This row-access architecture allows us to get rid of one extra select signal reducing the space occupied by the cell, while also solving the half-select problem and eliminating the need of bipolar Y-drivers. The memory cell access table for the RAM cell operation is seen in Table 1. The sign before the select line name indicates the control current direction.

TABLE I
MEMORY CELL ACCESS TABLE FOR NDRO RAM DESIGN

Operation	Select lines	Access
WRITE 1	+X+Y	Bit
WRITE 0	-X	Word
READ	+X	Word

D. Current Drivers

The main challenge in designing the current drivers is the necessity of confining them to a reasonable area. Due to the total physical RAM size, the size of the current drivers themselves is limited to 45 μm in width. We have already designed the layout of the SFQ/dc converters to meet this 45 μm condition. These converters are capable of operating at a 20 GHz data rate generating 0.3 mV output dc voltage. In combination with current amplifiers, these devices will supply sufficient drive for the select line current (~0.2 mA).

In contrast to Y-line, the X select line (see Fig. 2) requires bipolar current drivers. In this case, we have implemented a different approach. Specifically, unshunted Josephson junction based drivers are to be implemented here. We have considered both HUFFLE-based and relaxation-oscillation type circuits. We designed, fabricated, and tested an amplifier for the current driver. Fig. 4 shows a schematic of this circuit. The large inductance loop connects two relaxation-oscillation-driven pairs. The dc current from the current source is pushed into and out of the inductance loop, which is magnetically coupled to dc SQUID chain.

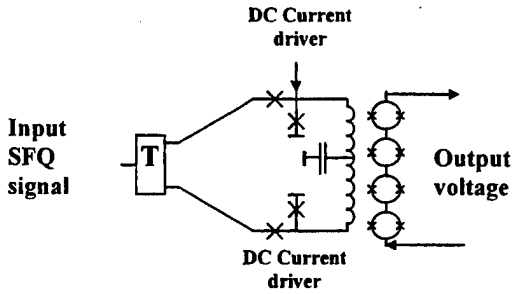

Fig. 4. Amplifier based on dc current drivers.

Fig. 5 shows successful test results of this amplifier used for the dc-current drivers. The driver demonstrates a gain of 15 at low-frequencies. In simulation, the driver worked at a 25 GHz frequency.

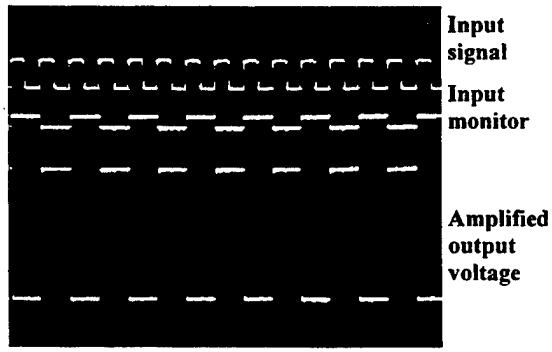

Fig. 5. Low-frequency test results of output amplifier. The output voltage amplitude is 3 mV, in contrast to the conventional SFQ/dc converter (0.2 mV).

E. Address Decoder

The address decoder is the most important part of the RAM. In our approach, the size of the decoder is critical. In previous research, we have designed and successfully tested compact decoder based on ac-powered voltage-state logic [3]. We redesigned it to dc-powered combination of voltage-state and SFQ logic.

This new decoder design consists of an address bus signal generator and 128 decoder cells (Fig. 6). The address generator transforms the address into a dc current dual-rail representation and transfers these currents to an address bus. The address bus consists of two groups of microstrip lines, seven lines in each.

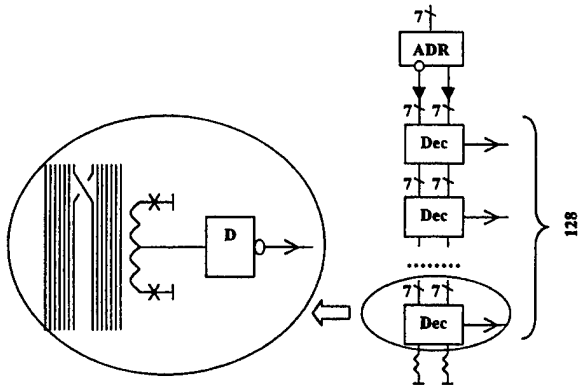

Fig. 6. A 7-bit address decoder.

Fig. 7 shows a single cell of the decoder. Each cell in the decoder has its own unique combination of direct and inverted lines. This configuration is achieved by swapping two different lines in every cell. The right seven lines are magnetically coupled to a SQUID which performs the OR operation. If a dc current persists in any of these 7 lines, the SQUID generates an SFQ pulse. Thus, any address, only one cell among 128 will have no currents in the right group of lines. So, by inverting the cell's output we get an output signal corresponding to address.

The address generator exploits single-ended current drivers to transform addresses from SFQ to dc-current representation. As a result, the address moves down in each block of RAM with the same delay as the data (see Fig. 2). This property might allow us to organize a ballistic pipeline structure, improving the RAM throughput.

F. CRAM Parameters

A major feature of our approach is an access time that is several clock periods, implemented by a pipeline structure. As in Fig. 1, there are three major parts of the RAM: the block decoder, the RAM blocks, and the block multiplexer. Each of these works independently and can be considered as a pipeline stage. The address decoder (Fig. 2) works in two clock cycles. All together this produces a four-clock-cycle pipeline structure of the RAM.

The speed of signal propagation along a microstrip line is close to the speed of light. For a microstrip line with SiO_2 insulator, it is $\sim 6 \cdot 10^7$ *m/s*. The size of the memory array (128 x 50 μm ~ 6 mm) gives us a 100 ps delay time, which compounds to a 10 GHz clock rate (or throughput). The combination of SFQ and current-loop representation allows us to synchronize data flow in different pipeline stages. The travel times of all paths in a single block of the RAM (Fig. 2) are equal to 100 ps, while the delays of all cells and circuits, described above, are less than 20 ps. This might allow us to increase throughput by organizing pipeline access within a 100 ps time interval.

Thus, this 16-Kb RAM design has a four-cycle pipeline structure with 10 GHz throughput and 400 ps access time.

The projected size of the complete RAM chip would be 1 cm x 1 cm and the power dissipation about 2.4 mW. The entire design is estimated to require less than 60,000 Josephson junctions.

III. HTMT Implementation

HTMT (Hybrid Technology Multi-Threaded) architecture has been proposed for a petaflops computer [4]. The HTMT architecture combines semiconductor, optical, and superconductor technologies in a single-system structure. This is essentially a shared-memory architecture employing liquid-helium-cooled superconductive processors and data buffers (CRAM), liquid-nitrogen-cooled SRAM semiconductor buffers, a semiconductor DRAM main memory, and optical holographic storage. The superconductor CRAM is a buffer for the SRAM, which is itself a buffer for the DRAM. Superconductor processors will be ready to read a local CRAM in 10 clock cycles, but latency for reading a location in semiconductor SRAM will exceed 500 cycles. Therefore, the processors must be able to access the CRAM, but not the SRAM.

Previously explored solutions for cryogenic memories have been inadequate for operation at the petaflop level. Scaling down the fabrication process linewidth from the present 3.5 μm to 0.8 μm, will enable us to meet the petaflop CRAM chip requirements.

Table II shows the comparison between what we are capable of doing now and what is expected from CRAM in the HTMT project. We scaled the minimal Josephson junction size down to 0.8 μm (presumed fabrication process for HTMT project) and estimated the characteristics for the CRAM. In order to provide the shared memory access, the HTMT CRAM has to have extra atomic operations in its instruction set. The most convenient for our architecture is a SWAP operation, which comprises the combination of READ and WRITE.

To provide an interface to the external processes, the CRAM will have some additional data packet forming logic.

TABLE II
SPECIFICATIONS FOR THE HTMT CRAM VS. THE 16 KB CRAM

Specs:	This CRAM	CRAM for HTMT
Capacity	16 Kb	1 Mb
Word	32 bit	64 bit
Access time	400 ps	330 ps
Cycle time	100 ps	30 ps
Number of blocks	4	256
Number of cells in block	128x32	64x64
Number of JJs	60K	4M
Cell size	50x50 μm^2	10x10 μm^2
Chip size	1x1 cm^2	2x2 cm^2
Minimal JJ size	3.5 μm	0.8 μm
Atomic operations	W0, W1, RD	W0, W1, RD, SWP

IV. Conclusion

We have presented the fully dc-powered design of a 16 Kb RAM based on combination of dc-powered voltage-state and SFQ elements. The RAM will occupy a 1 cm x 1 cm chip, dissipate 2.4 mW power, and have a 400 ps access time and 100 ps cycle time (embodying four pipeline stages).

Acknowledgment

We are thankful to Prof. K. Likharev of SUNY at Stony Brook for helpful discussions.

References

[1] S. Nagasawa, Y. Hashimoto, H Numata, and S. Tahara, "High-frequency clock operation of Josephson 256-word x 16-bit RAMs," *IEEE Trans. Appl. Supercond.*, vol.9, 1999.

[2] S. Nagasawa, Y. Hashimoto, H Numata, and S. Tahara, "A 380ps 9.5mW Josephson 4-Kbit RAM operating at a high bit yield," *IEEE Trans. Appl. Supercond*, vol.5, p.2447, 1995.

[3] P.F. Yuh, "A 2-kbit superconducting memory chip," *IEEE Trans. Appl. Supercond.*, vol.5, p.3013, 1993.

[4] M. Dorozhevets, P. Bunyk, D. Zinoviev, and K. Likharev, "PetaFLOP RSFQ system design," *IEEE Trans. Appl. Supercond.*, vol.9, 1999.

Microwave Coupling of SINIS Junctions in a Programmable Josephson Voltage Standard

Ralf Behr, Holger Schulze, Franz Müller, Johannes Kohlmann, and Jürgen Niemeyer
Physikalisch-Technische Bundesanstalt, Braunschweig, Germany

Igor Y. Krasnopolin
Russian Research Institute for Metrological Service, Moscow, Russia

Abstract—Using the reliable Nb-AlO$_x$ technology, series arrays of nonhysteretic Superconductor - Insulator - Normal metal - Insulator - Superconductor (SINIS) Josephson junctions have been fabricated with critical voltages of about 100 μV. These arrays are used as 1 V inherently stable Josephson voltage standard circuits at a microwave frequency of 70 GHz. The microwave power required to obtain a suitable 1 V step for calibration purposes is very low because of an active contribution of the SINIS junctions which are embedded in a low-impedance stripline. Measurements concerning the phase locking of junctions in long microstriplines are presented.
A programmable voltage standard or a D/A converter with fundamental accuracy can be realized with a binary sequence of nonhysteretic junctions. Due to the microwave attenuation of an SINIS series array without current bias a new concept for providing all junctions with homogeneous microwave power is needed.

I. Introduction

This paper describes recent progress achieved in Josephson programmable voltage standards and D/A converters at PTB. PTB has started to develop programmable voltage standards (*fast dc voltage*) and D/A converters based on a binary sequence of series arrays with nonhysteretic junctions as first proposed by Hamilton et al. [1]. When irradiated with a microwave frequency f, each junction exhibits constant voltage steps at $V = nf/K_{J\text{-}90}$, where $K_{J\text{-}90} = 483597.9$ GHz/V is the Josephson constant and n the quantum step number, which is $n = 0$, 1 or -1. The voltage of each series array containing $N = 2^k$ junctions (kth bit) is

$$V = nNf/K_{J\text{-}90}. \quad (1)$$

Any output voltage in steps of $f/K_{J\text{-}90}$ can be selected by choosing appropriate bias currents for the array segments, because the voltages of segments add in series. For fast bias operation of this circuit the microwave power has to be adjusted so as to simultaneously maximize the step widths $n = 0$ and $n = \pm 1$ for all segments.

Manuscript received April 26, 1999.
This work is supported in part by the Bundesministerium für Bildung und Forschung (BMBF), Germany (ref. no. 13N6835, 13N7259) and the European Community (ref. no. SMT4-CT98-2239).

The use of SINIS junctions offers the advantage of high characteristic voltages $V_c = I_c R_n$ in the range from 50 μV to 200 μV [2]. I_c is the critical Josephson current and R_n the normal resistance of the junction. Due to the high characteristic voltages, the junctions can be operated at microwave frequencies of 70 GHz, leading to a number of 8192 junctions necessary to achieve the 1 V level (14 bit). On the other hand SINIS junctions in a low-impedance stripline have a high attenuation [3]. This requires an elaborate microwave design and an elaborate arrangement of the bias connections. A homogeneous power distribution to all junctions is needed for phase-locking to the microwave frequency applied.

II. Fabrication

Kupriyanov et al. [4] proposed SINIS junctions as a means of optimizing the characteristic voltage V_c for electronic applications. A lot of work has recently been carried out to investigate the potential of SINIS junctions, e.g. [5]-[7]. Depending on the oxidation parameters and the thickness of the normal layer, the critical current density and normal resistance can be adjusted. SINIS junctions have been fabricated with moderate Josephson current densities $j_c \approx 130$ A/cm^2 and normal resistances $R_n \approx 100$ mΩ to obtain a

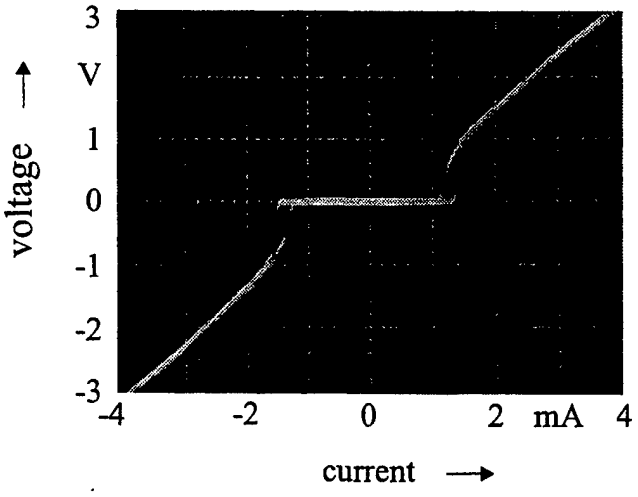

Fig. 1: IVC of an SINIS series array with 8192 junctions.

characteristic voltage of about 130 μV. The reliable Nb-AlO$_x$ technology is used, thus transferring the technological processes used for the very similar fabrication of SIS junctions for the 10 V Josephson voltage standard arrays [8], [9].

Besides a nonhysteretic current-voltage characteristic (IVC) a small parameter spread is crucial for the behavior of long series arrays under microwave irradiation. In Fig. 1 the IVC of an SINIS series array with 8192 junctions is shown to demonstrate the small parameter spread.

III. Experimental Results

A. Attenuation of SINIS Junctions in a Low Impedance Stripline

The attenuation of long SINIS series arrays in a stripline can be estimated on the basis of the RSCJ model. According to Kautz [10] the attenuation of a single junction is

$$\alpha_j = 10 \log_{10} [1 - 3/(4\pi R_n Z_0 f^2 C^2)] \qquad (2)$$

where Z_0 is the impedance of the microwave stripline, f the frequency and C the capacitance of the junctions. At f = 70 GHz the stripline has an impedance of 5 Ω and the capacitance of the junctions is found to be 50 pF. With these values an attenuation of $\alpha_j \approx 5 \times 10^{-2}$ dB per junction can be calculated. 1000 SINIS junctions in a low impedance stripline, therefore, attenuate an external microwave by 50 dB. Despite this high attenuation, it was found that a Shapiro step is formed in long series arrays with 1700 SINIS junctions. The step has a width of $\Delta I \approx 0.16\, I_c$ and has proved to be suitable for calibration purposes [11]. An explanation for this could be the active contribution of the SINIS junctions. This seems plausible, because, first, Josephson junctions are voltage driven oscillators that can mutually couple if the junction number is large enough and if the parameter spread is sufficiently small [12]. Secondly, series arrays of overdamped junctions can be a coherent microwave source if the junctions are phase-locked [13].

To verify the estimated attenuation and the assumption of an active contribution of the junctions to the microwave distribution, different series sub-arrays arranged in the stripline as shown in Fig. 2a were investigated.

The step width of the n = 1 Shapiro step in dependence on the microwave power applied to the finline antenna was measured. In Fig. 2b the microwave power has been plotted for several series sub-arrays. For sub-array 1 with 180 junctions on both sides of the finline antenna much less power is needed than for sub-array 2 and sub-array 3. The attenuation of the stripline is too high to obtain a Shapiro step in sub-arrays 4 and 5. In all measurements the voltage is measured between pads 1 and 6 and the current is supplied to

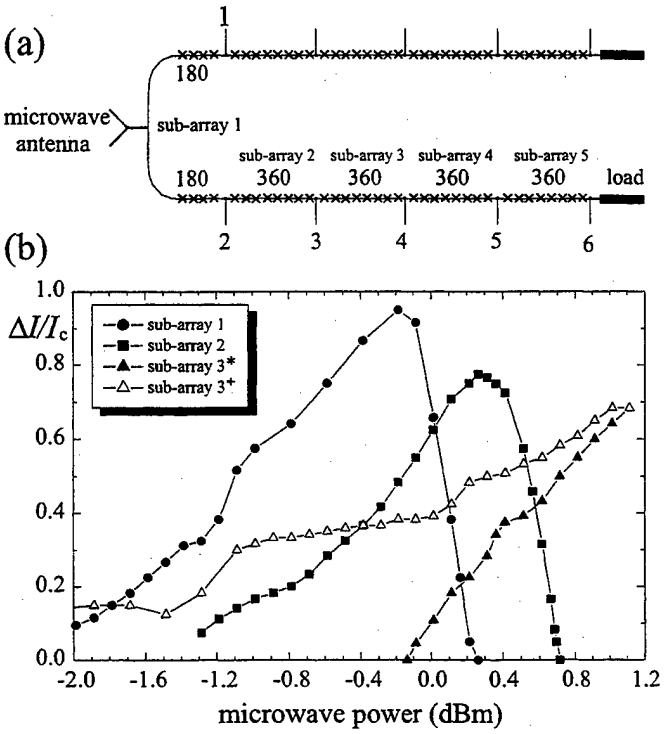

Fig. 2: (a) Arrangement of series sub-arrays in a stripline. (b) Measurements of the step width of the n = 1 step of several sub-arrays. (*) current connections to pads 3 and 4, (+) current connections to pads 1 and 4. See text for further explanation.

the sub-array under investigation, e.g. pads 3 and 4 for sub-array 3.

The shift of the rise of the step width for sub-arrays 2 and 3 in comparison with sub-array 1 is a direct measure of the attenuation for 180 and 540 junctions. When a shift of 8 dB is inferred for sub-arrays 2 and of 14 dB for sub-array 3, extrapolation to 1000 junctions results in 33 dB and 44 dB, which is in agreement with the estimated 50 dB.

When the current and voltage pads are changed, for example pads 1 and 6 for current and pads 3 and 4 to measure the step width of array 3, a Shapiro step at very low power can be observed with a nearly constant step width in the range from -1 to 0 dBm. By increasing the power the maximum step width of the initial current-voltage connections is achieved.

B. Stimulated Microwave Generation of SINIS Series Arrays

Stimulated microwave generation by internal phase locking has been directly demonstrated using a large array with 1512 junctions as an oscillator and a small array (48 junctions) as a detector [3], see Fig. 3. Both arrays are embedded in a single stripline. Measurements have shown that microwave generation starts at a threshold of about 100 SINIS junctions [14] and gets more distinct in large arrays where resonances come into play, to an increasing extent.

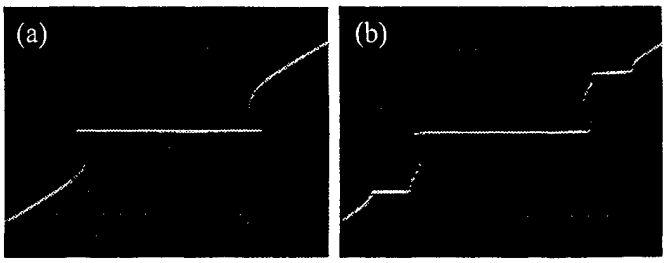

Fig. 3: Current-voltage-characteristic of a 48-junction sub-array at the end of a series array of 1560 SINIS junctions to detect the microwave power generated by the adjacent 1512 junctions. The bias current applied to the oscillator is (a) $I_0 < I_c$; (b) $I_0 = 1.31$ mA $> I_c$. Horizontal scale: 0.5 mA/div, vertical scale: 5 mV/div.

C. Layout of Binary Series Arrays

It is obvious that a small series sub-array cannot be placed at the end of a stripline, behind a large number of junctions, because of the high attenuation of the SINIS junctions in a low-impedance stripline. A very simple layout has, therefore, been chosen: the microwave power from the finline antenna is split into eight paths, one with the bits $k = 0$ to $k = 5$ and all other bits with a separate stripline path. That means that the longest series array with 4096 junctions is arranged in one path only, on the assumption that the external microwave power is distributed by the contribution from the junctions.
Only a few wafers with series arrays with a binary divisions have so far been fabricated. The relative parameter spread is very good, but the absolute values of the characteristic voltage are sometimes below 100 μV and the impedance of the stripline changes from run to run. First experiments show that in all segments Shapiro steps appear, but, unfortunately, the step of the 4096 junctions has a slope or is chaotic.

IV. Conclusions

Large SINIS series arrays have been fabricated with very small parameter spread. Embedded in low-impedance striplines, arrays with up to 2048 junctions can be driven by very low external microwave power because of the active contribution of the junctions. First experiments with series sub-arrays with more than 2048 junctions in a single stripline have shown chaotic behavior of Shapiro steps. Further investigations are required to study the influence of V_c and Z_0 on the active contribution to the microwave distribution.

References

[1] C. A. Hamilton, C. J. Burroughs, and R. L. Kautz, "Josephson D/A Converter with Fundamental Accuracy", *IEEE Trans. Instrum. Meas.*, vol. 44, pp. 223-225, Apr. 1995.
[2] H. Schulze, R. Behr, F. Müller, and J. Niemeyer, "Nb/Al/-AlO_x/Al/AlO_x/Al/Nb-Josephson Junctions for Programmable Voltage Standards", *Appl. Phys. Lett.*, vol. 73, pp. 996-998, Aug. 1998.
[3] H. Schulze, F. Müller, R. Behr, J. Kohlmann, J. Niemeyer, and D. Balashov, "SINIS Josephson Junctions for Programmable Josephson Standard Circuits", *IEEE Trans. Appl. Supercond., in press, 1999.*
[4] M. Yu. Kupriyanov and V. F. Lukichev, "Influence of Boundary Transparency on the Critical Current in "dirty" SS'S Structures", Sov. Phys. JETP, vol. 67, pp. 1163-1168, June 1988.
[5] M. Maezawa and A. Shoji, "Overdamped Josephson Junctions with Nb/AlO_x/Al/AlO_x/Nb Structure for Integrated Circuit Application", *Appl. Phys. Lett.*, vol. 70, pp. 3603-3605, June 1997.
[6] H. Sugiyama, A. Yanada, M. Ota, A. Fujimaki, and H. Hayakawa, "Characteristics of Nb/Al/AlO_x/Al/AlO_x/Nb Junctions Based on the Proximity Effect", *Jpn. J. Appl. Phys.*, vol. 36, pp. L1157-L1160, Sept. 1997.
[7] D. Balashov, H. Schulze, F.-Im. Buchholz, M. I. Khabipov, W. Kessel, and J. Niemeyer, "Superconductor-insulator - normalconductor - insulator - superconductor (Nb/Al_xO_y/Al/Al_xO_y/Nb) Process Development for Integrated Circuits Applications", *Supercond. Sci. Technol.*, vol. 11, pp. 1401-1407, 1998.
[8] F. Müller, R. Behr, J. Kohlmann, R. Pöpel, J. Niemeyer, G. Wende, L. Fritzsch, F. Thrum, H.-G. Meyer, and I. Y. Krasnopolin, "Optimized 10-V Josephson Series Arrays: Fabrication and Properties", *in Proc. ISEC'97, Extended Abstracts*, vol. 1, pp. 95-97, June 1997.
[9] J. Kohlmann, F. Müller, P. Gutmann, R. Pöpel, L. Grimm, F.-W. Dünschede, W. Meier, and J. Niemeyer, "Improved 1-V and 10-V Josephson Standard Arrays", *IEEE Trans. Appl. Supercond.*, vol. 7, pp. 3411-3414, June 1997.
[10] R. L. Kautz, "Design and Operation of Series-Array Josephson Voltage Standards", *Proc. of the International School of Physics "Enrico Fermi", Course CX*, North-Holland (1992).
[11] R. Behr, H. Schulze, F. Müller, J. Kohlmann, and J. Niemeyer, "Josephson Arrays at 70 GHz for Conventional and Programmable Voltage Standards", *IEEE Trans. Instr. Meas.*, vol. 48, no. 2, 1999.
[12] K. Wiesenfeld, P. Colet, and S. Strogatz, "Synchronisation Transitions in a Disordered Josephson Series Array", *Phys. Rev. Lett.*, vol. 76, pp. 404-407, Jan. 1996.
[13] P. A. A. Booi and S. P. Benz, "High Power Generation with Distributed Josephson Junction Arrays", *Appl. Phys. Lett.*, vol. 68, pp. 3799-3801, June 1996.
[14] H. Schulze et al., to be published, 1999.

POSTER SESSION I

Group 2 - SQUIDs

Transport and Noise Properties of High T_c Bicrystal Junctions

K. Enpuku, T. Minotani, F. Shiraishi and S. Ohta
Department of Electronic Device Engineering, Kyushu University, Fukuoka 812-8581, Japan

Abstract—Transport properties of $YBa_2Cu_3O_{7-x}$ bicrystal junctions are studied from the relationship between a critical current I_c and a resistance R of the junction. The relation is obtained when misorientation angle of the junction is changed from 24 to 36.8 degrees. The experimental result can be well explained when two effects are taken into account in the tunneling of electrons, i.e., resonant tunneling of quasiparticles via localized states in an insulating barrier and d-wave symmetry of the superconducting order parameter. Low frequency $1/f$ noise of the junction is also measured, and the fluctuations of I_c and R are obtained as a function of junction parameters. A simple model of the barrier height fluctuation due to the capture and emission of electrons in the localized states can quantitatively explain the experimental results. The present model can consistently explain both the transport and noise characteristics of the bicrystal junction.

I. Introduction

Bicrystal junctions have been used for highly sensitive superconducting quantum interference device (SQUID). Since a critical current I_c and a resistance R of the junction depend on a misorientation angle of a substrate, their angular dependencies have been studied in order to optimize the junction parameters for the SQUID application [1], [2]. However, transport mechanism that gives the dependencies has not yet been clarified.

It is theoretically suggested that the transport properties of the junction are affected by the two effects. One is the resonant tunneling of quasiparticles via localized states in the barrier [3], [4], and the other is the effect of the *d*-wave symmetry of the superconducting order parameter on the tunneling of Cooper pairs [5], [6]. Furthermore, it is suggested that capture and emission of the quasiparticle in the localized states causes the so-called $1/f$ noise of the junction [3], [7]. Therefore, these theoretical predictions should be quantitatively compared with experiments in order to clarify the transport mechanism of the bicrystal junction.

In this paper, we discuss the properties of the bicrystal junction, such as the I_c–R relation, temperature dependence of I_cR, and the fluctuations of I_c and R. We show that experimental results of these properties agree reasonably well with theoretical predictions.

Manuscript received April 15, 1999

II. Transport Properties

When we take into account both direct and resonant tunneling of quasiparticles, conductivity of the junction σ is given by [3], [4]

$$\sigma = \sigma_{do}\exp(-2ad) + \sigma_{ro}\exp(-ad), \quad (1)$$

where d is the thickness of the barrier, $1/a$ is a decay length, σ_{do} and σ_{ro} are parameters. Note that the first and the second terms represent the conductivity due to direct and resonant tunneling, respectively.

It is pointed out that the *d*-wave symmetry of the superconducting order parameter affects the tunneling of the Cooper pairs [5], [6]. In this case, critical current density j_c becomes dependent on the misorientation angle θ of the substrate. Taking account of this effect, we can obtain the expression for j_c as

$$\begin{aligned} j_c(\theta,T,d) &= j_{co}(\theta,T)\exp(-2ad) \\ &\approx K(T)\cos(1.9\theta)\exp(-2ad), \end{aligned} \quad (2)$$

For the theoretical prediction for $j_c(\theta,T)$, we use the expression given by (104) in [5]. Using (104), we can calculate the θ-dependence of j_{co} numerically. The last expression in (2) can be obtained by approximating the numerical result of $j_{co}(\theta,T)$ with a cosine function. The approximation can be shown to become accurate at high temperatures. Using (1) and (2), we can obtain the relationship between I_c and R as

$$1/R = C_1 I_c/\cos(1.9\theta) + C_2\sqrt{I_c/\cos(1.9\theta)}\,. \quad (3)$$

where $C_1=\sigma_{do}/K(T)$, $C_2=\sigma_{ro}(A_j/K)^{1/2}$, and A_j is a junction area.

In Figs. 1(a) and 1(b), experimental results are compared with (3). Here, the experimental results are obtained at T=77 K from bicrystal junctions with misorientation angles of 24°<θ<36.8° [2]. Thickness of the film and junction width is nominally 150 nm and 2 μm, respectively. In Fig. 1(a), a solid line is calculated by taking into account *only* the effect of the resonant tunneling of the quasiparticle, i.e., we tentatively assumed cos(1.9θ)=const.=1 in (3). Parameters of C_1=2100 S/A and C_2=15 S/A$^{1/2}$ are chosen. As shown, theoretical curve explains the experimental results reasonably well, except for the case of θ=36.8°. From (3), we can estimate the ratio between direct and resonant tunneling of quasiparticles. In the present samples, contribution of direct tunneling becomes larger for I_c>50 μA, while contribution of resonant tunneling becomes larger for I_c<50 μA.

As shown in Fig. 1(a), the data obtained for the case of θ=36.8° considerably deviate from the analytical result. In order to discuss this large deviation, we *add* the effect of the *d*-wave symmetry of the superconducting order parameter. In Fig. 1(b), a solid line is calculated from (3) by including the term of cos(1.9θ). Parameters of C_1 = 1650 S/A and C_2 = 7.5 S/A$^{1/2}$ are used in this case. As shown, the line is in good agreement with the experimental results for all misorientation angles. As can be seen from (2), reduction of j_c due to the *d*-wave symmetry becomes more significant when the angle θ becomes larger. Therefore, the data for the case of θ = 36.8° are considerably affected by this effect.

In Fig. 2, closed triangles show the measured temperature dependence of I_cR for the θ=30° junction. As mentioned above, resonant tunneling of quasiparticles decreases the value of R, while I_c is decreased by the *d*-wave symmetry of the order parameter. A broken line denoted by I_cR_{dt} shows the expected value if the resonant tunneling can be neglected: resistance R_{dt} due to direct tunneling is estimated to be about 2 times larger than the measured resistance R in the present sample. A broken line denoted by $I_cR_{dt}/\cos(1.9\theta)$ represents the expected value when both effects can be neglected: the factor of cos(1.9θ) becomes 0.54 for the case of θ=30°.

From the value of I_cR_{dt} shown in Fig. 2, we can estimate the energy gap Δ by using the theoretical expression for the tunneling in *d*-wave superconductors, which was given by (104) in [5]. Circles in Fig. 2 show the estimated temperature dependence of $\Delta(T)$. The solid line shows the dependence of $\Delta(T)=\Delta(0)[1-(T/T_c)^4]$ with $\Delta(0)$=6.7 meV and T_c=90 K. As shown, the temperature dependence of Δ agrees well with this line.

III. Noise Properties

It has been pointed out that there exist some localized states in the barrier, which can capture the quasiparticle. The quasiparticle is trapped in those states for a certain time and escapes from the states due to thermally activation. This capture and emission of the quasiparticle in the localized states causes the barrier height fluctuation, and results in the fluctuations of σ and j_c [3], [7]. From (2), fluctuation of the critical current density δj_c can be given by

$$\delta j_c / j_c = -2da(\delta a / a) = -\ln\left|K\cos(1.9\theta)/j_c\right|(\delta a/a), \quad (4)$$

where the barrier height fluctuation is represented by the fluctuation of the decay length $1/a$. From (4), power spectrum density of the critical current fluctuation S_{Ic} can be given by

$$S_{Ic} = N A_e^2 j_c^2 (2ad)^2 S_a / a^2$$
$$= \alpha^2 I_c^2 \left[\ln\left(K\cos(1.9\theta)/j_c\right)\right]^3 / A_j, \quad (5)$$

where $\alpha^2=(nA_e^2/2a)(S_a/a^2)$, S_a is the power spectrum density of the fluctuation of a, A_e is an effective area where barrier

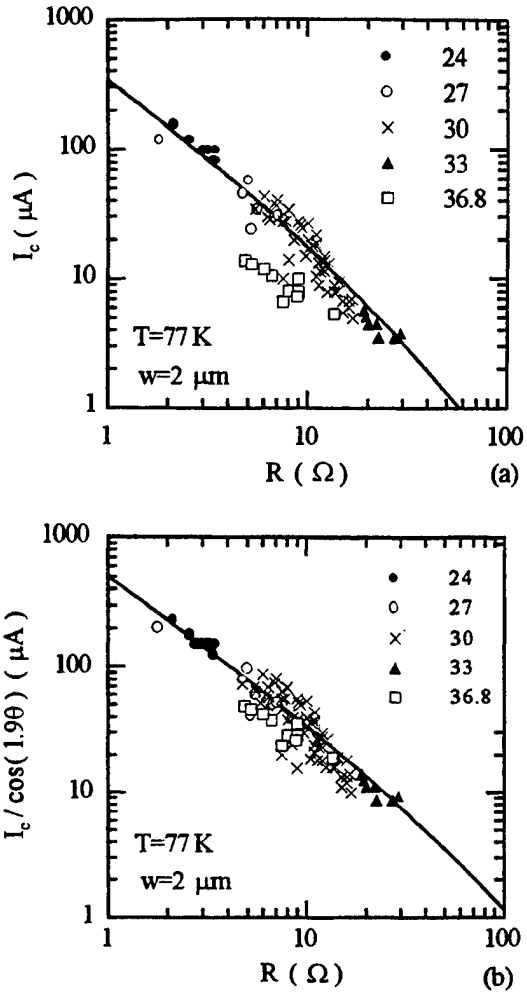

Fig. 1. (a) Relationship between I_c and R of the bicrystal junction at T=77 K. The solid line is calculated from (3) by neglecting the term of cos(1.9θ). (b) Relationship between I_c/cos(1.9θ) and R. The solid line is calculated from (3) by including the term of cos(1.9θ), i.e. the effect of the *d*-wave symmetry.

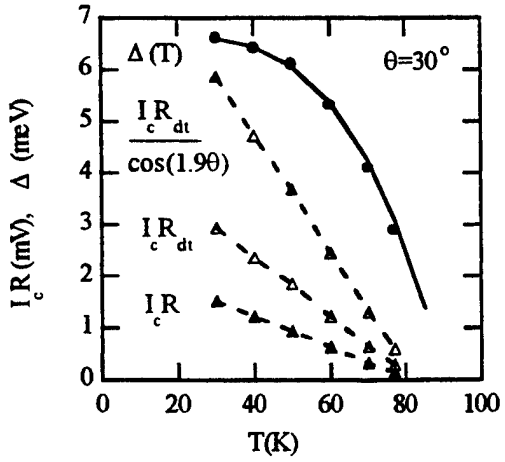

Fig. 2. Temperature dependence of I_cR for the θ=30° junction. The solid line shows the relation of $\Delta(T)=\Delta(0)[1-(T/T_c)^4]$ with $\Delta(0)$=6.7 meV and T_c=90 K.

height locally changes when the quasiparticle is trapped in a single localized state, $N = nA_j d$ is the total number of the fluctuation sites, and n is the volume density of the site.

Making a similar analysis, we can obtain the power spectrum of the fluctuation of the resistance S_R as

$$S_R = \alpha^2 R^2 \left[1 + C_1 I_c R / \cos(1.9\theta)\right]^2 \times \left[\ln\left(K \cos(1.9\theta)/j_c\right)\right]^3 / 4 A_j, \qquad (6)$$

In Fig. 3(a), experimental results of the critical current fluctuation are compared with the theoretical result. The dependence of the normalized fluctuation $A_j^{1/2} S_{Ic}^{1/2}/I_c$ on the critical current density $j_c/\cos(1.9\theta)$ is shown. As shown, the normalized fluctuation $A_j^{1/2} S_{Ic}^{1/2}/I_c$ becomes dependent on the critical current density $j_c/\cos(1.9\theta)$. A solid line in the figure is calculated from (5) with parameters of $\alpha = 14.6 \times 10^{-12}$ and $K = 5.6 \times 10^5$ A/cm^2. As shown, the analytical result is in good agreement with the experiment.

As shown in Fig. 3(a), the normalized fluctuation $A_j^{1/2} S_{Ic}^{1/2}/I_c$ increases with the decrease of $j_c/\cos(1.9\theta)$. The increase becomes considerable when the current density is small. This result means that the fluctuation of the critical current $S_{Ic}^{1/2}$ does not decrease in proportional to I_c, but remains high when I_c becomes small. When the current density becomes large, on the other hand, the normalized fluctuation approaches to the value of $A_j^{1/2} S_{Ic}^{1/2}/I_c = 45 \times 10^{-12}$ cm/Hz$^{1/2}$. For the junction area of $A_j = 0.3$ μm^2, we obtain the relation $S_{Ic}^{1/2}/I_c = 8.2 \times 10^{-5}$/Hz$^{1/2}$ at $f = 1$ Hz, which is consistent with the previous report [8].

In Fig. 3(b), the dependence of the normalized fluctuation $A_j^{1/2} S_R^{1/2}/R$ on the resistivity RA_j is shown. As shown, normalized fluctuation increases with the increase of the resistivity. A solid line denoted by (i) is calculated from (6) with parameters of $\alpha = 14.6 \times 10^{-12}$ and $K = 5.6 \times 10^5$ A/cm^2 which are the same values used for the case of the critical current fluctuation shown in Fig. 3(a). Although the absolute value is a little higher than the experiment, the dependence of $A_j^{1/2} S_R^{1/2}/R$ on the resistivity agrees reasonably well. If the parameter α is a little decreased to $\alpha = 10 \times 10^{-12}$, quantitative agreement becomes much better, as shown by a solid line denoted by (ii).

The broken line in the figure shows the relation $A_j^{1/2} S_R^{1/2}/R = 3.2 \times 10^{-5} (RA_j)^{1/2}$. This line corresponds to the empirical relation of $S_R^{1/2}/R = 3.2 \times 10^{-5} R^{1/2}$ at $f = 1$ Hz, which was obtained experimentally in [9]. As shown, the experimental results and (6) agree with this empirical relation reasonably well.

IV. Conclusion

It was shown that I_c-R relation of the bicrystal junction can be explained when resonant tunneling of the quasiparticle and d-wave symmetry of the order parameter are taken into account. A simple model of the barrier height fluctuation can consistently explain the fluctuations of I_c and R.

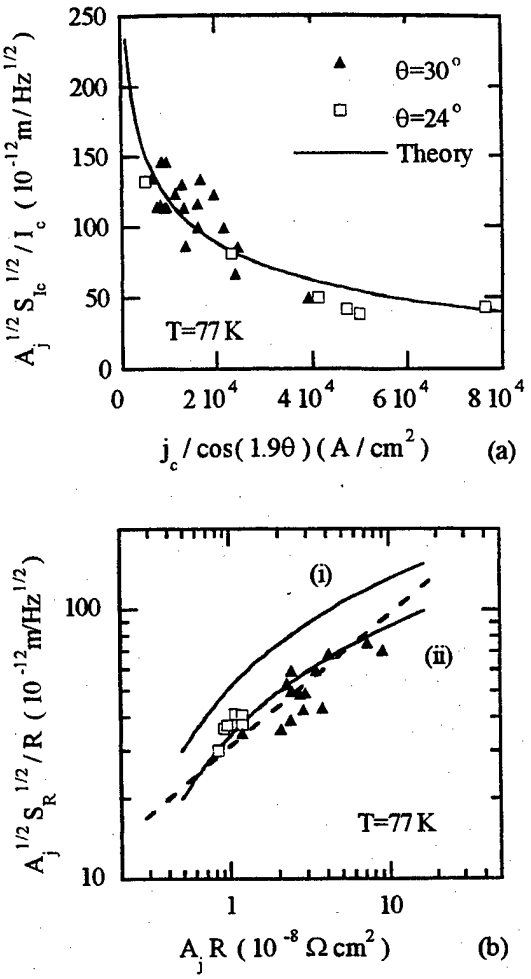

Fig. 3. Comparison between analysis and experiment of (a) critical current fluctuation, and (b) resistance fluctuation. The solid lines are calculated from (5) and (6). A broken line in (b) shows the relation of $A_j^{1/2} S_R^{1/2}/R = 3.2 \times 10^{-5} (RA_j)^{1/2}$.

References

[1] T. Minotani, S. Kawakami, T. Kiss, Y. Kuroki and K. Enpuku, Jpn. J. Appl. Phys. **36** (1997) L1092

[2] T. Minotani, S. Kawakami, Y. Kuroki and K. Enpuku, Jpn. J. Appl. Phys. **37** (1998) L718.

[3] J. Halbritter, J. Appl. Phys., **58** (1985) 1320.

[4] R. Gross, L. Alff, A. Beck, O. M. Froehlich, D. Koelle and A. Marx, IEEE Trans. Appl. Supercond., **7** (1997) 2929.

[5] Y. Tanaka and S. Kashiwaya, Phys. Rev. B. Condens. Matter, **56** (1997) 892.

[6] H. Hilgenkamp and J. Manhart, Appl. Phys. Lett. **73** (1998) 265.

[7] C. T. Rogers and R. A. Buhrman, IEEE Trans. Magn. **MAG-21** (1985) 126.

[8] M. Kawasaki, P. Chadhari and A. Gupta, Phys. Rev. Lett. **68** (1992) 1065.

[9] A. Marx and R. Gross, Appl. Phys. Lett. **70** (1997) 120.

High-T_c Ramp-edge Junctions and DC SQUIDs with a Ga-doped YBCO Barrier

I-Hun Song*, Eun-Hong Lee, and Seok-Yeol Yoon
Microelectronics Laboratory, Samsung Advanced Institute of Technology, P.O.Box 111, Suwon 440-600, Korea

Gwangseo Park
Department of Physics, Sogang University, C.P.O.Box 1142, Seoul 100-611, Korea

Abstract— We report on high-T_c ramp-edge junctions and DC SQUIDs (superconducting quantum interference devices) with a Ga-doped YBCO barrier. The interface resistances of the junctions were drastically reduced by *in-situ* RF plasma cleaning treatment. The plasma gas and pressure were Ar, O_2 and 50~100 mTorr, respectively. The lattice images of the interface of the junctions were analyzed by high resolution transmission electron microscopy. The effects of RF plasma treatment and barrier layer material on the junction properties were systematically investigated. These junctions were fabricated uniformly and reproducibly, and they displayed clear RSJ-like *I-V* characteristics with high values of I_cR_n products at 65 K. DC SQUIDs fabricated with the Ga-doped YBCO junctions exhibited excellent voltage modulations in response to applied fields at 65 K.

I. Introduction

Various barrier materials have been investigated for the formation of reliable superconductor-normal-superconductor (SNS) ramp-edge Josephson junctions (JJs) for high-T_c superconducting digital circuits [1]-[3]. In the case of ramp-edge type junctions, the junction properties can be controlled by changing the barrier conditions so that the choice of the barrier materials are very critical to ensure high quality junctions. Doped YBCO barriers exhibit very little interface resistance with YBCO electrodes because of the excellent match of their lattice constants and thermal expansion coefficients [2], [4]. Some groups have produced Co-doped YBCO junctions with practical I_cR_n values [5]. However, more stable and reliable barrier materials need to be developed for digital circuit applications.

In this letter, we used a 7 % Ga-doped $YBa_2Cu_{2.79}Ga_{0.21}O_{7-\delta}$ (YBCGO) as a barrier layer in ramp-edge junctions to study the effect of doping on the electrical transport properties of the barriers. The higher valence of Ga compared to that of Cu causes a reduction of the density of localized state [6]. The substitution of Cu in the chain layer by Ga in YBCO results in an increase in the bulk resistivity. It is expected from the relatively large resistivity of the YBCGO barrier that Ga-doped YBCO junctions are likely to approach the high values of R_nA and I_cR_n product.

Manuscript received April 30, 1999.
*Also at the Dept. of Physics, Sogang University, Electronic mail : ihsong@sait.samsung.co.kr

II. Experimental

Multilayer films for ramp-edge junctions were deposited on $LaAlO_3$ substrates by pulsed laser deposition. The detailed fabrication method used to produce the junction is described in [7]. Prior to the deposition of barrier layer, the surface of the ramp-edge is cleaned using an *in-situ* RF plasma treatment with low energy. YBCGO used as the metallic barrier is deposited as an epitaxial film under the same conditions as those used for YBCO. The thickness of YBCGO barriers was varied in the range of 100~400 Å. For the barrier layer growth, the laser repetition rate of 1 Hz was employed to enhance the nucleation. YBCO top electrode was also *in-situ* deposited sequentially, the chamber was backfilled with oxygen to 500 Torr during cooling down. The cross-sectional lattice images of the junctions were analyzed by high resolution transmission electron microscopy (TEM). DC SQUIDs, one of the simplest application of the ramp-edge junctions, were fabricated with the Ga-doped YBCO junctions.

III. Results and Discussion

The resistivity of YBCGO film decreases linearly as the temperature decreases down to 50 K and the film reaches to the transition temperature (T_c) around 20 K [7]. This implies that YBCGO is a good candidate as a barrier material since it has a metallic property with fairly large resistivity under conditions similar to those used for YBCO growth. The crystal structure of the YBCGO/STO/YBCO multilayer films and surface morphology of the junctions were already studied by X-ray diffraction and atomic force microscopy [8].

The interfaces at the bottom and top YBCO contact layers are very important because the junction properties are strongly depend on the interface resistance. In order to reduce such resistance, we introduced an *in-situ* RF plasma cleaning treatment. Fig. 1 shows the resistance vs temperature for several no barrier samples with different plasma treatment conditions. We observed long tails to the superconducting state with various plasma conditions. The interface resistance did not decrease with an O_2 plasma treatment while Ar plasma was effective for the removal of interface resistance. In order to examine the interface resistance, we fabricated YBCO/YBCO contacts of the ramp-edge structure without any barrier layer. The critical current density of this contact was higher than $1x10^6$ A/cm^2 at 77 K. This suggests that most of the contaminations, residues and ion beam damages

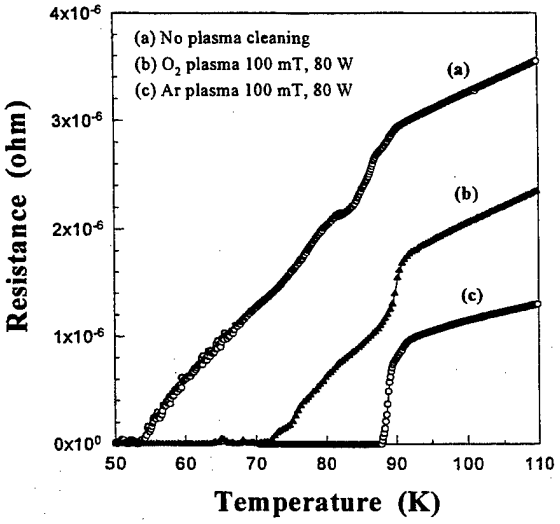

Fig. 1. The resistance vs temperature for several no barrier samples with different RF plasma treatment conditions.

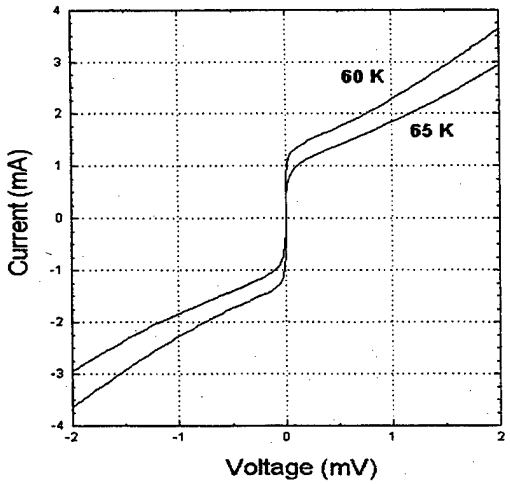

Fig. 3. The current-voltage characteristics of the junction with a 200-Å-thick YBCGO barrier at 60 and 65 K. They show typical RSJ-like behavior.

induced during the initial patterning were almost removed by the *in-situ* Ar plasma treatment.

Fig. 2 shows a cross-sectional TEM image of the Ga-doped YBCO junctions. The interface lines are very clear and the c-axis lattice fringes of the top and bottom YBCO layers are observed uniformly. High resolution TEM works is under way to elucidate what happens to the interface layer of YBCGO barrier. The angle of ramp-edge is characterized to be about 30°.

Fig. 3 shows the current-voltage (I-V) characteristics of the junction with a 200-Å-thick YBCGO barrier at 60 and 65 K. They showed typical resistively shunted junction (RSJ)-like behavior. As the temperature decreased, bending in the *I-V* curve became smaller and the *I-V* characteristics showed flux-flow-like behavior below 20 K. Meanwhile, at much higher temperature, the *I-V* characteristics of junctions with thinner than 100-Å-thick barrier also displayed flux-flow-like behavior. This suggests that the crossover from a RSJ-like behavior to a flux-flow-like behavior is strongly dependent on the magnitude of the critical current (i.e., the large junction limit) rather than the temperature which is close to the critical temperature of the barrier material. When the thickness of the YBCGO barrier is 200 Å, the estimated value of $R_nA = \rho_n d$ = 650 μΩ·cm × 2×10^{-6} cm = 1.3×10^{-9} Ω·cm^2. This result indicates that those junctions does not have any significant interface resistance. The temperature dependence of R_n of the junctions generally follows that of the barrier material. When the temperature increased, R_n of the Ga-doped YBCO junctions increased slightly. The I_cR_n values are about 480 μV and 360 μV at 60 K and 65 K, respectively.

We designed and fabricated the elementary single flux quantum (SFQ) circuit consisting of readout SQUID and

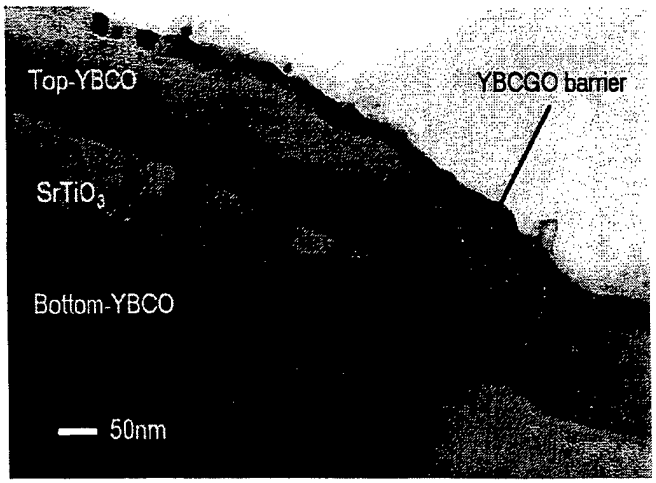

Fig. 2. A cross-sectional TEM image of the complete YBCO/YBCGO/YBCO edge geometry for 200-Å-thick Ga-doped YBCO barrier.

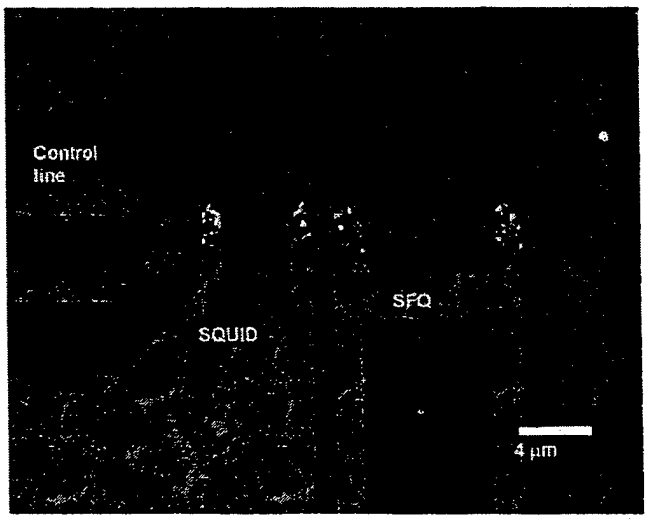

Fig. 4. An optical image of the SQUID and SFQ circuit with Ga-doped YBCO ramp-edge junctions.

magnetic field control line using the Ga-doped YBCO ramp-edge junctions with a 200-Å-thick barrier. Fig. 4 shows a optical image of the SQUID and SFQ cell. The readout SQUID has a control line which has a magnetic coupling, and the design is made in such a way to achieve a maximum magnetic coupling under the constraint of the minimum line spacing required for a safe multilayer junction process. The junction width of the SQUID and SFQ were about 2 and 3 μm, respectively.

Fig. 5 shows the voltage modulation of the DC SQUID with Ga-doped YBCO junctions barrier in a magnetic field at 65 K. When the magnetic field is applied by the control line in the direction perpendicular to the SQUID, the magnetic modulation exhibits an obvious periodic behavior. The observed modulation period ΔI_{con} was about 1.8 mA. From the period of voltage modulation, the mutual inductance m between the readout SQUID and the control line could be calculated through $m = \Phi_o/\Delta I_{con}$ where Φ_o is a flux quantum (Φ_o = 2.07 mA·pH) [5]. The mutual inductance was 1.15 pH and we could determine the adequate bias state of readout SQUID for measuring the SFQ logic circuits. The maximum amplitude of V-Φ modulation was about 10 μV at a bias current of $1.4I_c$. Detailed performance of the SQUID and SFQ circuits will be the subject of a forthcoming paper.

IV. Conclusion

We have successfully fabricated high-T_c ramp-edge junctions and SQUIDs with a new Ga-doped YBCO barrier. Very little interface resistance has been obtained using an Ar plasma cleaning treatment. The interface lines and the c-axis lattice fringes of the top and bottom YBCO layers are observed uniformly by the cross-sectional TEM image.

The RSJ-like behavior of I-V characteristics was clear evidences of the Josephson behavior of the YBCGO junctions. The junctions by Ga-doping resulted in an enhancement of the I_cR_n values, up to 360 μV at 65 K for a 200-Å-thick $YBa_2Cu_{2.79}Ga_{0.21}O_{7-\delta}$ barrier. DC SQUIDs fabricated with the Ga-doped YBCO junctions exhibited excellent voltage modulations in response to applied fields at 65 K.

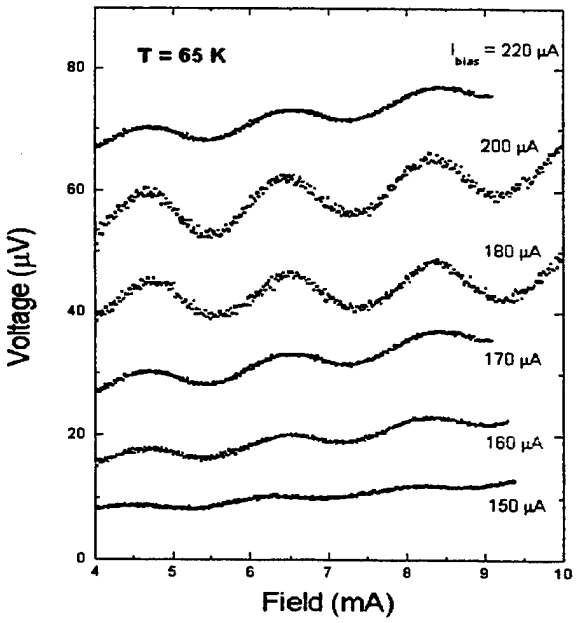

Fig. 5. The voltage-flux characteristics of the ramp-edge DC SQUID with a YBCGO barrier as a function of bias currents in a magnetic field at 65 K.

Acknowledgment

We would like to thank Dr. Gyeong-Su Park for TEM analysis. We also acknowledge Dr. Joonhee Kang and Dr. Kookrin Char for helpful discussions.

References

[1] W. H. Mallison, S. J. Berkowitz, A. S. Hirahara, M. J. Neal, and K. Char, "A multilayer YBCO Josephson junction process for digital circuit applications", *Appl. Phys. Lett.*, vol. 68, pp. 3808-3810, 1996.

[2] K. Char, L. Antognazza, and T.H. Geballe, "Study of interface resistances in epitaxial $YBa_2Cu_3O_{7-x}$/barrier/ $YBa_2Cu_3O_{7-x}$/ junctions", *Appl. Phys. Lett.*, vol. 63, pp. 2420-2422, 1993.

[3] M. G. Forrester, B. D. Hunt, J. D. McCambridge, D. L. Miller, J. X. Pryzbysz, J. Talvacchio, and R. M. Young, "Multilayer edge SNS SQUIDs for digital circuits", *IEEE Trans. on Appl. Supercond.*, vol. 7, pp. 3613-3616, 1997.

[4] M. A. J. Verhoeven, G. J. Gerritsma, H. Rogalla, and A. A. Golubov, "Ramp-type junction parameter control by Ga doping of $PBa_2Cu_3O_{7-x}$ barriers", *Appl. Phys. Lett.*, vol. 69, pp. 848-850, 1996.

[5] B. D. Hunt, M. G. Forrester, J. Talvacchio, J. D. McCambridge, and R. M. Young, "High-T_c superconductor/normal-metal/superconductor edge junctions and SQUIDs with integrated groundplanes", *Appl. Phys. Lett.*, vol. 68, pp. 3805-3807, 1996.

[6] Y. Xu and W. Guan, "Hopping conductivity in the PrBaCuGaO system", *Physica C*, vol. 206, pp. 59-69, 1993.

[7] I. H. Song, E. H. Lee, S. Park, I. Song, and G. Park, "High-T_c multilayer edge junctions with a Ga-doped YBCO barrier", *Appl. Supercond.*, vol. 158, pp. 579-582, 1997.

[8] I. H. Song, E. H. Lee, B. M. Kim, I. Song, and G. Park, "High-T_c edge junctions with a Ga-doped YBCO barrier and interface resistances", *Appl. Phys. Lett.*, vol. 74, pp. 2053-2055, 1999.

High-Tc SQUIDs on bicrystal substrate with low permittivity

Mizushi Matsuda, Syotaro Ono, Koichi Kato, Koichi Yokosawa*,
Hiroshi Oyama**, and Shinya Kuriki**

Muroran Institute of Technology, Muroran 050-8585
*Central Research Laboratory, Hitachi Ltd., Tokyo 185-8601
**Research Institute for Electronic Science, Hokkaido University, Sapporo 060-0812

Abstract— We fabricated high-Tc SQUIDs on the LSAT substrate with low permittivity. Cross-over structure, which is observed in the I-V characteristics of the SQUID on the STO substrate, cannot be observed in those on LSAT. Obtained V-Φ characteristics were not symmetric for positive and negative bias currents. Numerically calculated V-Φ characteristics with asymmetric values of Ic and Rn between two junctions, agreed well with the experimental ones for the SQUID.

I. Introduction

In fabricating a bicrystal junction Superconducting Quantum Interference Device (SQUID), $SrTiO_3$ (STO) has been commonly used as a substrate for $YBa_2Cu_3O_{7-\delta}$ (YBCO) film deposition due to its ability to support high quality film. However, its large dielectric constant, ε_r=1930 at 77K, can produce significant parasitic capacitance across the SQUID loop and across the junctions. Such parasitic capacitance can induce some changes in the current-voltage (I-V) characteristics of the SQUID such as the occurrence of the cross-over structure between the curves at $n\Phi_0$ and $(n+1/2)\Phi_0$ due to the resonant current step. The presence of this structure can degrade the modulation voltage of the SQUID.

In this report, we describe our preliminary results for the SQUIDs on $[LaAlO_3]_{0.3}[Sr(Al,Ta)O_3]_{0.7}$ (LSAT) bicrystal substrates having low permittivity. We also discuss the effects of asymmetric parameter difference between two junctions, such as Ic and Rn.

Manuscript received April 30, 1999.
This work was supported in part by a Granted-in-Aid for Scientific Research from the Ministry of Education.

II. Experiments

The SQUIDs were fabricated on c-axis oriented YBCO films. The films of 200-250nm thick were deposited by a pulsed laser deposition or an e-beam evaporation method on 10mmx10mm LSAT bicrystal substrates with a misorientation angle of 24° or 30°. The films were etched physically in Ar plasma by using standard photolithography technique, into the geometry illustrated in Fig. 1. The SQUID has two parallel strips of 5-10μm width and a long hole parallel to the bicrystal line. The hole length and width are 40-80 and 10-20μm, respectively. The 2-3μm wide bridges including grain boundary junctions were located at the both side of the hole. Two separate pickup coils will be connected to the right and left ends of the upper and lower strips[1]. In this geometry, high coupling of more than 80% was obtained[2]. The inductance values estimated using the coplanar stripline formula which includes the kinetic inductance[3] are about 50-120pH.

For comparison, SQUIDs with the similar configuration were made on STO bicrystal substrate with a misorientation angle of 30°.

The electrical measurements were carried out in an rf shielded room. The SQUID was mounted on a probe and immersed in liquid nitrogen in a dewar surrounded by a μ-metal shield.

III. Results

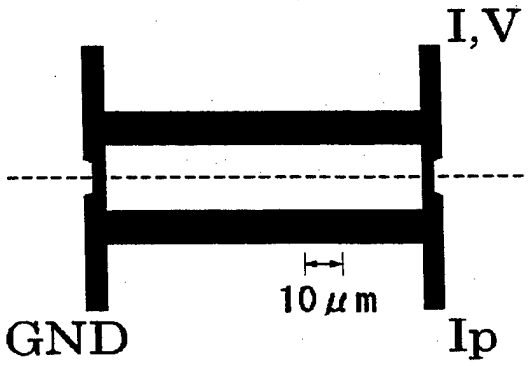

Fig.1. Typical configuration of SQUID devices

III. Results

Figure 2 (a) and (b) show the I-V characteristics at 77K for fabricated SQUIDs on a STO bicrystal substrate with 30° misorientation angle and on a LSAT bicrystal substrate with 24°, respectively. Here, the I-V characteristics were measured using the lead of I,V and GND (as illustrated in Fig. 1) with a flux generated by the injection current of Ip. Ip simulated the supercurrent flowing from the pickup coil to the SQUID. Cross-over structure of the two I-V curves at a flux of $\Phi=n\Phi_0$ and $\Phi=(n+1/2)\,\Phi_0$, which may be the consequence of a resonant phenomenon with large parasitic capacitance, is prominent for the SQUID on a STO substrate. On the other hand, we cannot see such a structure in those on LSAT probably due to low permittivity of the substrate. These characteristics agreed reasonably with the results of the numerical simulation based on the lump circuit model[4], including the parasitic capacitance with the assumed values of ε_r=1930 (STO) and ε_r=80 (LSAT) at 77K, and the SQUID inductance of 120pH.

Figure 3 (a) shows the V-Φ characteristics of the SQUID on LSAT for different bias currents at 77K. These were not symmetric for positive and negative bias currents. Deviations from the symmetric characteristics seems to be larger for larger bias current. Possible explanation is the unbalance of junction parameters, which produces the equivalent flux by a bias current. Numerically calculated V-Φ characteristics of this SQUID at 77K are shown in Fig. 3 (b), where the SQUID parameters of $\beta_L(=2LIc/\Phi_0)$=3.16, β_c $(=2\pi IcRn^2C/\Phi_0)$=0.07, and $\Gamma(=2\pi k_BT/Ic\Phi_0)$=0.18 are assumed. We also assumed the asymmetric critical current ratio of Ic_1/Ic_2=3/2 and normal resistance ratio of Rn_1/Rn_2=2/3 between two junctions, according to the measurement results after cutting the inductance loop. As shown in this figure, simulated characteristics agree well with the experimental ones for the SQUID. We have not clarified the cause for such an unbalance between junctions

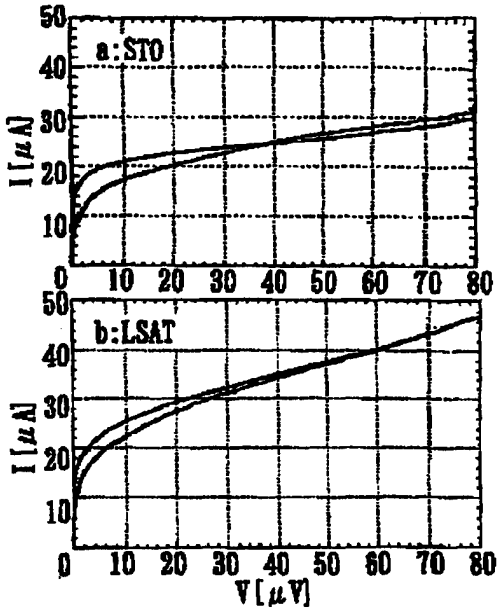

Fig.2. Current-voltage characteristics of fabricated SQUIDs on a (a) STO bicrystal substrate with 30° misorientation angle and a (b) LSAT substrate with 24°, at 77K.

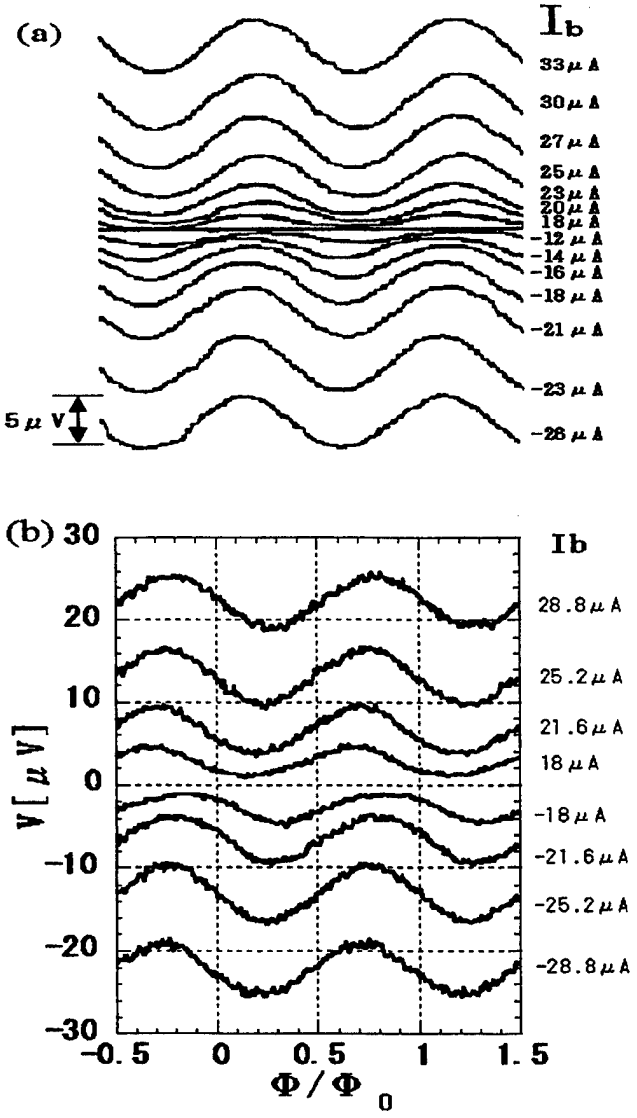

Fig.3. Measured (a) and numerically calculated (b) voltage-flux characteristics for a SQUID with asymmetric junction parameters on LSAT for different bias currents at 77K.

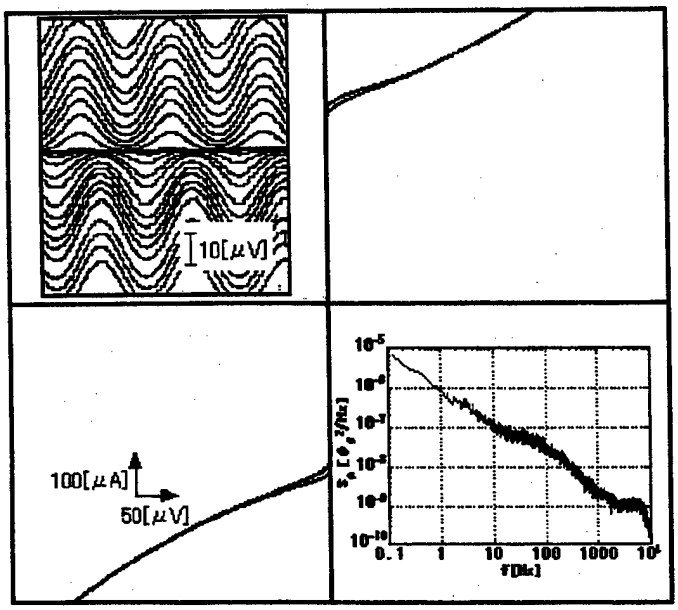

Fig.4. Current-voltage and voltage-flux (upper inset) characteristics, and the spectral density of the flux noise (lower inset) for a SQUID on LSAT.

yet, but it is likely due to physical damage during the etching process of junctions.

Figure 4 shows the I-V, V-Φ and noise characteristics of a SQUID having rather smaller inductance of 50pH on a LSAT bicrystal substrate with 30° misorientation angle. The values of IcRn product and β_L are about 240μV and 9.6, respectively. Obtained modulation voltage ΔV of 17μV is consistent with the calculated value of 19μV from the following equation[5],

$$\Delta V = \frac{4}{\pi}\frac{IcRn}{1+\beta_L}\exp\left(\frac{-3.5\pi^2 k_B TL}{\Phi_0^2}\right).$$

The level of measured flux noise in the white noise region is about $3\times10^{-5}\Phi_0/\sqrt{\text{Hz}}$, limited by a preamplifier noise.

ACKNOWLEDGMENT

The authors thank Mr. H.Takashima and Dr. M.Koyanagi of Electrotechnical Laboratory for film preparation.

REFERENCES

[1] K. Yokosawa, R.S. Ahmad, E. Maruyama, S. Kuriki, D. Suzuki, and M. Koyanagi: Ext. Abstr. Int. Superconductivity Conf., 1997, Berlin, pp. 7-9.

[2] E. Maruyama, S. Kuriki, K. Yokosawa, R.S. Ahmad, D. Suzuki, and M. Koyanagi: Jpn. J. Appl. Phys., Vol.37, pp. L722-L724, 1998.

[3] K. Yoshida, M.S. Hossain, T. Kisu, K. Enpuku, and K. Yamafuji: Jpn. J. Appl. Phys., Vol.31, pp. 3844-3850, 1992.

[4] M. Matsuda, M. Kubo, S. Kuriki, K, Masuzawa, and R.S. Ahmad: Advances in Superconductivity IX, Springer-Verlag Tokyo, 1997, pp. 1221-1224.

[5] K. Enpuku, Y. Shimonuma, and T. Kisu: J. Appl. Phys., Vol.73, pp. 7929-7935, 1993.

Peculiarities of rf SQUID Response in Finite Magnetic Field

E. Il'ichev, V. Schultze, R. P. J. IJsselsteijn, R. Stolz, V. Zakosarenko, H. E. Hoenig, and H.-G. Meyer
Institute for Physical High Technology, Department of Cryoelectronics, P.O. Box 100239, D-07702 Jena, Germany

M. Siegel
Institut für Schicht und Ionentechnik, Forschungszentrum Jülich GmbH, D-52425 Jülich, Germany

Abstract–Single-layer washer-type high-T_C $YBa_2Cu_3O_{7-x}$ rf SQUIDs with grain boundary Josephson junctions as well as low-T_C Nb rf SQUIDs with Nb-Al_2O_3-Nb tunnel junctions have been investigated in finite magnetic fields. It was shown experimentally that the suppression of the critical current of the Josephson junction due to the magnetic field leads into a modulation of the amplitude of the SQUID output signal. The role of the „parasitic" junction of high-T_C rf SQUIDs which is formed by the grain boundary running through the washer of the SQUIDs on bicrystal substrates has also been clarified. The drop of the SQUID signal at a finite magnetic field is originated by the penetration of the magnetic field into the parasitic junction. This drop starts at a magnetic field equal to the first critical field H_{c1}. Based on these results a direct radio-frequency method for the determination of H_{c1} for long Josephson junctions has been developed.

I. Introduction

The stable operation in finite magnetic fields H is one of the crucial requirements for real applications of SQUID-based devices. For example, in the simplest case SQUID magnetometers are designed as so-called washer type SQUIDs. Due to the large demagnetization factor of a washer even small external magnetic fields can (i) promote the nucleation and subsequent displacement of the vortices near the edges of the washer and (ii) suppress the critical current I_C of the junction following a Fraunhofer-like dependence $I_C(H)$. Both effects have been experimentally investigated for dc SQUIDs. It was shown that these effects lead to magnetic hysteresis [1,2], to random telegraph noise [3], and to depression of the amplitude of the voltage-flux characteristic (see, for example, Fig. 8 in [4]).

For rf SQUIDs the situation is not so clear. To our knowledge the influence of $I_C(H)$ on the rf SQUID output signal was investigated neither experimentally nor theoretically. Moreover, single layer rf SQUIDs as often used for applications, contain additional „weak places" in the main quantization circuit. When bicrystal substrates are used for rf SQUID fabrication, an additional long junction crosses the washer (see Fig. 1). For SQUIDs based on step-edge junctions this weak place is produced by the step on the substrate which is in series with the main Josephson junction. These places with a smaller critical current density should *a priory* play an important role for the SQUID operation in finite magnetic fields.

In this work we present the experimental investigation of rf SQUIDs in finite magnetic fields. To clarify the influence of the above mentioned additional weak places in the high-T_C rf SQUIDs, also low-T_C SQUIDs are investigated for comparison. Below we show, that the output signal is strongly disturbed only for high-T_C rf SQUIDs containing weak places in the washer. The suppression of the critical current of the Josephson junction by the magnetic field leads to a modulation of the amplitude of the rf SQUID output signal. Based on the obtained results a radio-frequency method for the determination of the first critical field H_{C1} for long Josephson junctions has been developed.

II. Fabrication and Measuring Setup

The low-T_C rf-SQUID have been fabricated using $Nb/AlO_X/Nb$ technology. First the niobium lower wiring is deposited and patterned to define the SQUID washer with a slit of 10 μm. Then a $Nb/AlO_X/Nb$ trilayer is deposited and patterned by a lift-off process. The trilayer has a critical current density of 200 A/cm^2 and a capacitance of 4.7 μF/cm^2. The junction areas (6 x 6 μm^2) and vias to the lower wiring were defined by protecting the contact areas with a photoresist during the anodization of the remaining area. Two layers of SiO (400 nm each) were used as additional isolation to reduce the parasitic capacitance between lower and upper wiring. On top of these isolation layers the Mo shunt layer and the upper superconducting wiring of Nb were deposited and patterned by lift-off processes. The entire structure was covered by a thin protecting layer of SiO. A sketch of the low-T_C rf SQUID is presented in Fig. 1 (a).

For high-T_C rf SQUID $YBa_2Cu_3O_{7-x}$ films have been used. All $YBa_2Cu_3O_{7-x}$ layers are grown using the pulsed laser deposition technique on (100) oriented $SrTiO_3$ bicrystal substrates with misorientation angles 36° (18°/18° and 0°/36°) and 45° (22.5°/22.5°). Typical values for J_C and T_C of these films are 2 x 10^6 A/cm^2 and 89 K, respectively. The films, with thickness t = 40-70 nm, were patterned by Ar ion-beam etching into 4 x 4 mm^2 or 5 x 5 mm^2 square washer SQUID structures. The widths of the junctions were b = 1-2 μm. The washer holes had a side-length of d = 50 μm, leading to a geometrical inductance $L = 1.25\,\mu_0 d \approx 80$ pH (Fig. 1 (b)).

SQUIDs were coupled to a tank circuit with inductance L_T and capacitance C through a mutual inductance $M = k(L \cdot L_T)^{1/2}$, where L is the SQUID inductance and k is a coupling coefficient (see Fig. 1 (c)). The driving radio-frequency current I_{rf} as well as a sweep current I_{dc} are

supplied to the tank circuit. The radio-frequency voltage V across the circuit was measured using an amplifier at room temperature with a high input impedance. The amplitude and phase of this voltage were detected by a vector-analyzer and recorded as a function of either I_{dc} or the amplitude of I_{rf}.

We used several tank circuits with inductances of 0.3...0.8 μH and with resonance frequencies of 9...40 MHz. The unloaded quality factor Q has been measured for all tank circuits at various temperatures and values of $80<Q<200$ were obtained. The SQUIDs were placed inside of a five-layer mumetal magnetic shielding in a gas-flow cryostat at temperatures in the range of $4.2<T<90$K.

The $I_C(H)$ dependencies were measured using a standard four probe technique and a calibrated solenoid. These measurements were also performed inside the magnetic shielding.

III. Results and Discussion

Fig. 2 shows the typical picture for the output signal of a high-T_C rf SQUID on a bicrystal substrate for a large range of external magnetic field values. In this scale oscillations of the rf SQUID output signal are not visible. For low amplitudes of the external magnetic field usual oscillations of the voltage-flux characteristic are observed. Note that the same behavior has been observed for washer type SQUIDs with step-edge Josephson junctions [5]. In [5] it was assumed that this drop of the output voltage can be accounted for by the $I_C(H)$ dependence. To clarify this issue we have performed special experiments with low-T_C rf SQUIDs based on standard Nb/AlO_X/Nb Josephson junctions. In Fig. 3 the output signal of a low-T_C rf SQUID is presented. The modulation of the amplitude of the output voltage is clearly visible, without any abrupt drop even for larger magnetic fields.

For both effects, the modulation of the rf SQUID output voltage and the abrupt drop of this voltage for high-T_C rf SQUIDs at large external magnetic field, no quantitative models exist. Nevertheless, the picture for the modulation of the rf SQUID output voltage qualitatively seems to be clear. An increase of the external magnetic field leads to a change of the critical current following the $I_C(H)$ dependence and thus to a change in the damping of the tank circuit. Therefore, a change of the output voltage can be expected. The value of the external magnetic field, which produces one flux quantum Φ_0 in Josephson junction can be estimated as follows. Taking into account that the size of the low-T_C SQUID hole is d=25μm (see Fig. 1, a) and the junction area is 6x6 μm^2 one can obtain that one fluxon in the junction is equivalent to approximately $13\Phi_0$ in the SQUID hole. Indeed, this relation we have observed in the experiment (see Fig. 3). Therefore, there are no doubts that the observed modulation of the rf SQUID output voltage is accounted for by $I_C(H)$ dependence.

We assumed that the drop of the high-T_C rf SQUID signal is originated by the penetration of the magnetic field into the parasitic junction of the high-T_C rf SQUIDs. This junction is formed by the grain boundary running through the washer of the SQUIDs on bicrystal substrates (see Fig. 1).

To clarify this issue the following experiments have been performed. First we choose a rf SQUID with the drop of the output signal at a relatively small amplitude of the external magnetic field, so that the SQUID oscillations are clearly visible (see Fig. 4, upper curve). For this SQUID a symmetric 45° bicrystal substrate has been used. Then the Josephson junction was cut by a laser beam and the measurements were repeated (see Fig. 4, bottom curve).

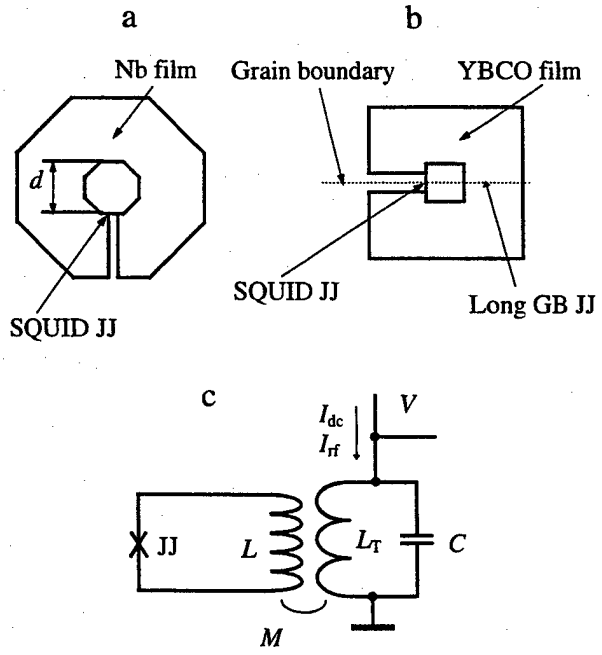

Fig. 1. a) Schematic representation of a low-T_C rf SQUID. The Josephson junction is denoted by JJ, d is the size of the SQUID hole (see text). b) Schematic representation of a high-T_C rf SQUID. c) Schematic of the measurement setup. All denotations are explained in the text.

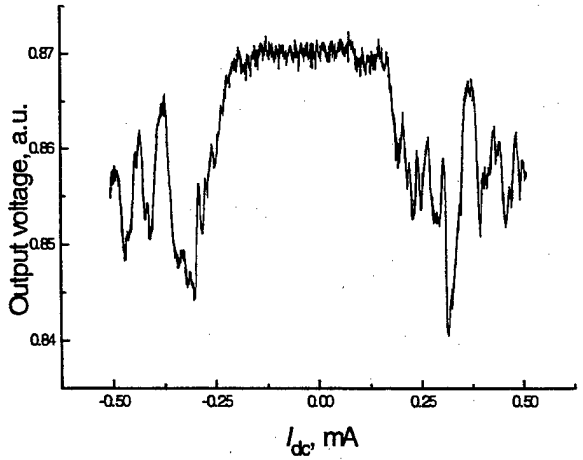

Figure 2. The output signal measured at T=10 K as a function of the dc current I_{dc}, for an $YBa_2Cu_3O_{7-x}$ rf SQUID containing a symmetric 36 degree [001]-tilt grain boundary

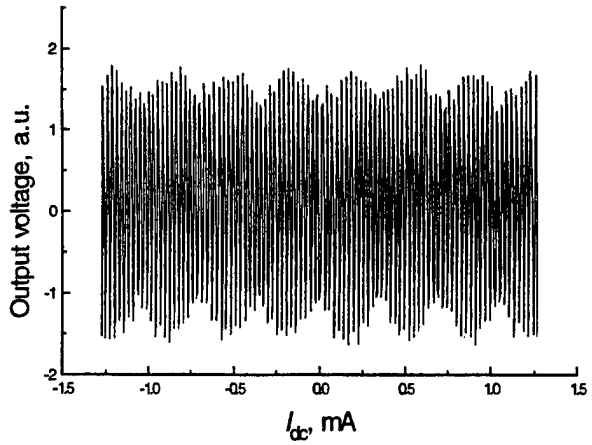

Fig. 3. The output signal measured at T=4.2 K as a function of the dc current I_{dc}, for a Nb rf SQUID.

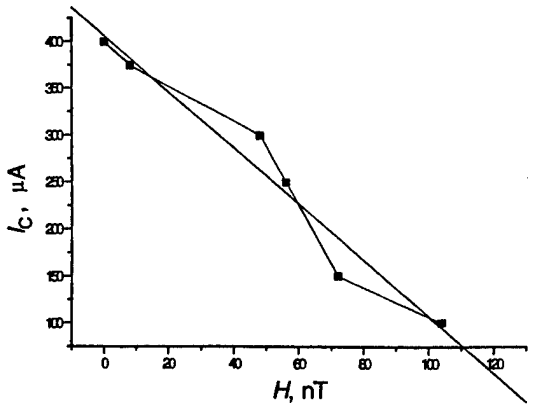

Fig. 5. Critical current of the long Josephson junction (see Fig. 1) as a function of applied magnetic field.

It is clearly seen from Fig. 4 that there are no SQUID oscillations without the short Josephson junction (bottom curve). Nevertheless, the drop remains and its position is not changed. Therefore this drop is not originated by the short Josephson junction, and is due to the penetration of the magnetic field in the parasitic Josephson junction.

Using the data (Fig. 4) the first critical field H_{c1} can be estimated for the long junction. The effective SQUID pickup loop area is $A_{eff}\approx 0.8\cdot d\cdot D$ [6], where d is the edge length of the square hole in the washer and D the outside dimension of the washer. Taking into account that $H_{c1}=n\cdot\Phi_0/A_{eff}$, where n is a number of fluxons in the SQUID loop when the drop occurs. This number can be obtained from the upper curve in Fig. 4. It results in a value of $H_{c1}\approx 71$ nT.

It is well known that the extrapolation of the linear part of the $I_C(H)$ dependence gives a thermodynamic critical field H_{c0} (Fig. 5). With this $H_{c1}=(2/\pi)\cdot H_{c0}$ [7] can be calculated. So, using H_{c0} obtained from Fig.5 we have estimated $H_{c1}\approx 70$ nT.

H_{c1} can also be calculated using a model developed in [1]. In the frame of this model the threshold magnetic field below which no vortex entrance to the washer could occur, is:

$$H_{th}=\left[\left(\frac{2\pi}{3}\right)^3\frac{\Phi_0}{R^2}H_{ch}{}^3\right]^{1/4},$$

where R is the radius of the washer and $H_{ch}=(2\pi J_c\, d)/c$ is so-called characteristic field. For our sample the critical current density J_c is calculated from direct measurements of $I_C(0)$. The calculation gives $H_{th}\approx 68$nT.

Therefore the methods of H_{c1} determination based on (*i*) $I_C(H)$ measurements, (*ii*) $I_C(0)$ measurements and calculation of the field concentration effect, and (*iii*) our new radio-frequency method described above give the same results.

IV. Conclusions

We have shown that in finite magnetic fields the $I_C(H)$ dependence leads to a modulation of the rf SQUID output signal. The abrupt drop of the high-T_C rf SQUID signal is originated by the penetration of the magnetic field into the weak places of the high-T_C rf SQUIDs ring. Based on this last result a direct radio-frequency method for the determination of H_{c1} for long Josephson junctions has been developed.

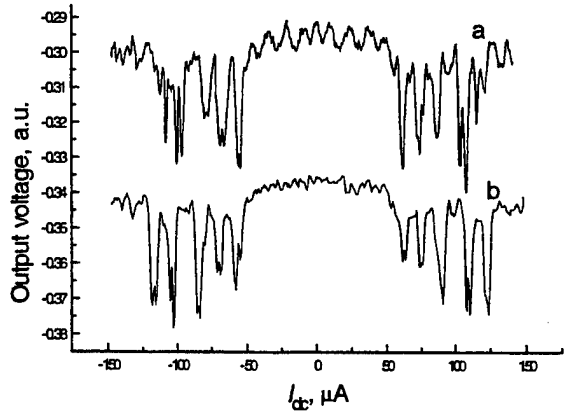

Fig. 4. a) The output signal measured at T=4.2 K as a function of the dc current I_{dc}, for an $YBa_2Cu_3O_{7-x}$ rf SQUID containing a symmetric 45 degree [001]-tilt grain boundary. Curve (b) presents the same measurements after cutting the short Josephson junction

Acknowledgments

Financial support by the DFG (Ho 461/3-1) and INTAS (No 11459) are gratefully acknowledged.

References

[1] J. Z. Sun, W. J. Gallagher, R. H. Koch, Phys. Rev. B **50**, 13 644 (1994).
[2] M. N. Keene, N. J. Exon, R. G. Humphreys, and N. G. Chew, J. Appl. Phys., **79**, 8783 (1996).
[3] J. Gail, M. Mück, and C. Heiden, Appl. Phys. Lett., **73**, 2663, (1998).
[4] P. Seidel *et al.* IEEE Trans. of Appl. Supercond. **3**, No. 1, 2353, (1993).
[5] V. N. Glyantsev, Y. Tavrin, W. Zander, and M. Siegel, Supercond. Sci. Technol. **9**, A105, (1996).
[6] The effective area of our SQUIDs has been measured for several sizes of the washer hole and this formula has been obtained. The deviation from the so-called Ketchen expression $A=1.1\cdot d\cdot D$ is due to the uncovered slit in the washer.
[7] A. Barone and G. Paterno, Physics and Applications of the Josephson Effect, (Wiley, New York, 1982)

Low-frequency noise and linearity of $YBa_2Cu_3O_7$ dc SQUID magnetometers in static magnetic fields

S. Krey, H.-J. Barthelmess, and M. Schilling
Universität Hamburg, Institut für Angewandte Physik und Zentrum für Mikrostrukturforschung,
Jungiusstraße 11, D-20355 Hamburg, Germany

***Abstract*—We have investigated the low-frequency noise of a field-cooled dc SQUID magnetometer from $YBa_2Cu_3O_7$ in magnetic fields up to 200 μT, both before and after it was patterned with holes to reduce the maximum structural width of the pickup-loop. We find, that even in low fields the noise of the unpatterned magnetometer steadily increases with the applied field. However, after the patterning for the holes, the noise remains at the zero field level up to a threshold field of 35 μT and is always less than in the unpatterned case. This threshold field is also found in field dependent measurements of the total harmonic distortion. Moreover, the influence of the patterning on the effective area of the magnetometer is discussed.**

I. Introduction

A severe obstacle for many practical applications of SQUID magnetometers from high temperature superconductors (HTS) has long been the increase of low-frequency noise when the magnetometer is operated in an ambient magnetic field like the earth's field of about 50 μT. This excess noise is caused by the thermally activated random hopping of magnetic flux vortices between their pinning sites [1]. The vortices are either created when the magnetometer is cooled below its critical temperature T_c in an ambient field, or they are introduced into the film by the Lorentz force from shielding currents [2]. The spectral density S_Φ of the flux noise typically scales with $1/f$ as a function of the frequency f and therefore adversely affects low-frequency applications like biomagnetism or geophysical measurements. Since the number of vortices is proportional to the applied field B_0, S_Φ is expected to scale linearly with B_0. Moreover, the amount of noise is strongly dependent on the epitaxial quality of the involved superconducting thin-films [3], [4]. Noise measurements in dependence on the applied field have been reported for bare dc SQUIDs [5], [6], directly-coupled magnetometers [5], [7]–[9], rf SQUIDs [10], [11] and magnetometers from HTS multilayers [12].

Recently, Dantsker *et al.* made several suggestions for the design of HTS SQUID devices in order to reduce the amount of trapped flux. They are based on the reduction of the linewidth of the SQUID body, so that it becomes energetically unfavourable for flux to enter the film. An estimation for the threshold field of flux entry is given by

$$B_T = \frac{\pi \Phi_0}{4w^2}, \qquad (1)$$

where w is the linewidth of the film [13], [14]. Most groups have favoured the slotted design, where the SQUID is provided with many parallel slots which divide the SQUID body in narrow filaments to increase B_T. Here, we present measurements on a directly-coupled magnetometer, both before and after it was patterned with holes to reduce the maximum structural width of the pickup-loop. To our knowledge, these are the first measurements, which directly compare the effects of this kind of patterning for the same device. The comparison of different devices may be misleading, because of a variable microstructural or epitaxial quality of the involved superconducting thin-films. Additional measurements of the total harmonic distortion (THD) characterize the linearity of the magnetometer with holes in dependence on the applied field.

II. Device Preparation

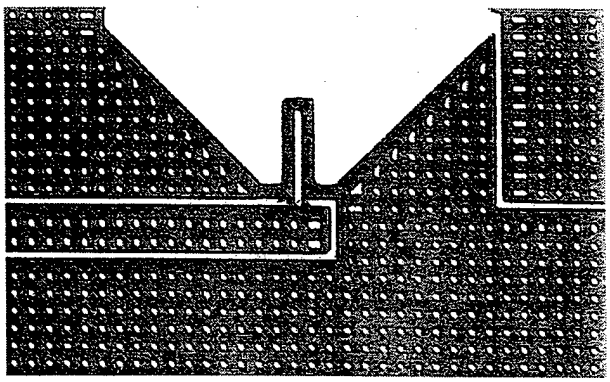

Fig. 1. Micrograph of the magnetometer part around the SQUID-loop after it was patterned with holes. The holes have a diameter of about 4 μm and the linewidth between them is about 5.2 μm.

Our directly-coupled dc SQUID magnetometers are prepared from a single epitaxial $YBa_2Cu_3O_7$ thin-film on a symmetrical (100) $SrTiO_3$ bicrystal with 24° misorientation angle. We typically use films of 120 nm thickness, which are deposited by KrF excimer laser deposition.

Manuscript received April 30, 1999.
This work was supported by the Bundesministerium für Bildung, Wissenschaft, Forschung und Technologie, Federal Republic of Germany under Contract No. 13N7323-8

TABLE I
TRANSPORT PROPERTIES OF THE INVESTIGATED MAGNETOMETER AT $T=77\,\mathrm{K}$, BEFORE AND AFTER THE PATTERNING OF THE HOLES.

		before	after	
Voltage swing	ΔV	26	27	μV
Critical current[a]	I_0	107	76.5	μA
Normal resistance[a]	R_n	2.1	2.8	Ω
Sensitivity	B/Φ	9.203	8.980	nT/Φ_0
Effective area	$A_{\mathrm{eff}}=\Phi/B$	0.225	0.230	mm^2

[a]Values given per junction.

After the patterning with conventional photolithography and argon plasma etching, the magnetometers are treated in an oxygen plasma. Finally, the contact pads are covered with silver to reduce the contact resistance. The magnetometer layout is similar to the one introduced by Lee *et al.* [15] with a washer-type pickup-loop of an outer dimension of 8.3 mm and an inner hole size of $3\times3\,\mathrm{mm}^2$. The SQUID-loop has an outer area of $16\times56\,\mu\mathrm{m}^2$ and an inner hole of $4\times50\,\mu\mathrm{m}^2$, from which we calculate an inductance of 60 pH, including the kinetic contribution. The bicrystal junctions are nominally $3\,\mu$m wide. After the first characterization of the magnetometer with solid pickup-loop, it was patterned a second time using a net-like photomask. We obtained a linewidth of about $5.2\,\mu$m and circular holes with a diameter of about $4\,\mu$m across the whole pickup-loop. Fig.1 depicts a micrograph of the region around the SQUID-loop.

III. MEASUREMENTS

All measurements were performed in liquid nitrogen inside of a triple mumetal shield. The magnetic field B_0 was applied with a Helmholtz coil, that was supplied by a large capacity lead-acid battery and an appropriate resistor. The flux density noise resulting from the current noise in the coil is less than $85\,\mathrm{fT}/\sqrt{\mathrm{Hz}}$ at 3 Hz and $B_0=100\,\mu$T and does not significantly contribute to the measured noise values. The noise measurements were made in fluxed-locked-loop (FLL) mode with bias current reversal to reject the low-frequency noise from critical current fluctuations in the junctions. In all field dependent measurements the magnetic field was applied while the magnetometer was heated above T_c, and it remained on during the cooling and the measurements. Hence, no shielding currents were generated as in a switching process. The magnetometer properties before and after the second patterning step for the holes are listed in Table I. After the treatment, I_0 and R_n were somewhat changed, presumably due to a slight oxygen loss in the junctions, since no second plasma oxidation was carried out. Surprisingly, the patterning had only a minor effect on the sensitivity of the device. The effective area increased by about 2%, although the character of input coupling completely changed. With the solid pickup-loop, flux is focused to some extent into the loop by the Meißner effect. In the patterned device, however, this effect is substituted by the flux quantization, which keeps the flux in the holes constant at integer flux quanta. Thus, flux changes must be partly focused into the pickup-loop again. Obviously, there is no significant quantitative difference between both effects. However, a difference is found in field dependent measurements. For the solid device, we find a slight increase of the effective area with a variation of about $\partial A_{\mathrm{eff}}/\partial B\simeq1.6\times10^{-4}\,\mathrm{mm}^2/\mu\mathrm{T}$, whereas it is a decrease by nearly the same value $-1.5\times10^{-4}\,\mathrm{mm}^2/\mu\mathrm{T}$ for the patterned device. The reason for this behaviour is not yet clear. This effect leads to a nonlinear response of the magnetometer and therefore contributes to its THD. However, a calculation for $B_0=100\,\mu$T and a signal amplitude of 10 nT yields THD ≈-110 dB, which is much less than the measured values discussed below.

A. *Low-frequency noise in static magnetic fields*

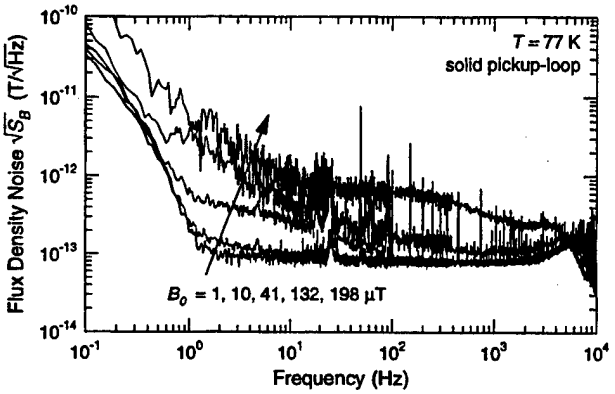

Fig. 2. Flux density noise spectra of the unpatterned magnetometer for different cooling fields B_0.

Fig. 2 depicts several flux density noise spectra for the unpatterned magnetometer in different cooling fields B_0. We find an increasing low-frequency noise with B_0 from the growing number of trapped vortices in the film. The spectra for $B_0=41\,\mu$T and $198\,\mu$T include a Lorentzian contribution, caused by the random telegraph signal (RTS) from a predominant two-level fluctuator. Fig. 3 shows the noise values at the frequency 3 Hz in dependence on B_0, before and after the holes were patterned into the pickup-loop. In the unpatterned case, the low-frequency noise increases with B_0 even for the lowest cooling fields, whereas it remains approximately constant below a threshold field $B_T\simeq35\,\mu$T in the patterned case. Moreover, we find, that for all values of B_0, the magnetometer with holes remains markedly less noisy than without the holes. In the unpatterned case, the noise below B_T presumably results from the motion of vortices near the SQUID-loop, which is directly coupled into the SQUID, since the indirect component from noise currents in the pickup-loop is strongly suppressed by the poor coupling between the inductances of the pickup-loop and the SQUID [13]. In both cases, we observed a significant increase of noise above B_T. We attribute this to flux entry into the SQUID-loop, although a somewhat larger thresh-

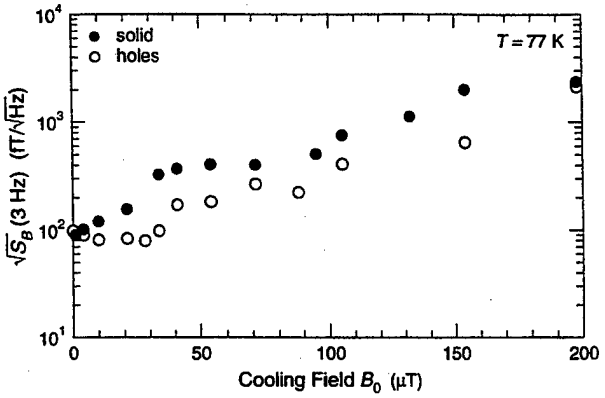

Fig. 3. Flux density noise at 3 Hz vs cooling field B_0 for the directly coupled magnetometer, before (•) and after it was completely patterned with holes (o).

old field of 42 μT for the measured width $w = 6.2\,\mu$m is expected from (1). In particular in the unpatterned case, the noise values above the threshold field remain on a nearly constant level up to $B_0 \simeq 80\,\mu$T. This noise was caused by the dominating RTS from a single fluctuator and therefore does not scale with B_0. For higher values of B_0, it is covered by the noise of the remaining vortices.

B. *Linearity*

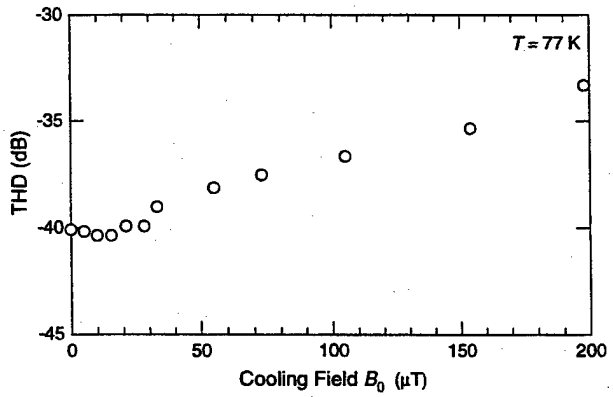

Fig. 4. Measured total harmonic distortion (THD) of the patterned magnetometer in dependence on the cooling field B_0 for a sinusoidal magnetic signal with the amplitude $\Delta B = 10$ nT and the frequency $f = 518$ Hz.

Nonlinear behaviour of a SQUID magnetometer can result from the inelastic motion of vortices in the magnetometer body [16]. Thus, the degree of nonlinearity is expected to depend on the number of vortices and therewith on the cooling field. To measure the magnetometer linearity, we applied a sinusoidal magnetic signal with a peak-to-peak amplitude of 20 nT and the frequency $f = 518$ Hz. The output voltages from the signal source and the FLL electronics were electronically subtracted, to obtain a maximum suppression of the harmonics of the test signal. The residual signal was measured with a spectrum analyzer. Fig. 4 shows the amount of THD of the patterned magnetometer in dependence on the cooling field. The THD values show a very similar dependence on B_0 as is found in the noise measurements. The THD remain nearly constant for fields below a threshold and increased for cooling fields beyond this value, whereby the threshold field agrees well with the value found in the noise measurements. We therefore conclude, that the nonlinearity of the field-cooled magnetometer is caused by the motion of the vortices.

IV. Conclusions

In conclusion, we have shown, that the noise of a SQUID magnetometer cooled in a magnetic field can be significantly lowered by reducing its linewidth through holes in the pickup-loop. The observed threshold field is attributed to flux entry into the SQUID-loop, which should be made narrower in future layouts. The patterning does not significantly affect the effective area of the device. The magnetometer THD is dependent on the cooling field.

References

[1] M.J. Ferrari, M. Johnson, F.C. Wellstood, J. Clarke, D. Mitzi, P.A. Rosenthal, C.B. Eom, T.H. Geballe, A. Kapitulnik, and M.R. Beasley, Phys. Rev. Lett. **64**, 72 (1990).

[2] J.Z. Sun, W.J. Gallagher, and R.H. Koch, Phys. Rev. B **50**, 13664 (1994).

[3] M.J. Ferrari, M. Johnson, F.C. Wellstood, J. Clarke, P.A. Rosenthal, R.H. Hammond, and M.R. Beasley, Appl. Phys. Lett. **53**, 695 (1988).

[4] R. Scharnweber, N. Dieckmann, and M. Schilling, Appl. Phys. Lett. **70**, 2189 (1997).

[5] A.H. Miklich, D. Koelle, T.J. Shaw, F. Ludwig, D.T. Nemeth, E. Dantsker, J. Clarke, N.McN. Alford, T.W. Button, and M.S. Colclough, Appl. Phys. Lett. **64**, 3494 (1994).

[6] M.I. Faley, U. Poppe, K. Urban, H. Hilgenkamp, H. Hemmes, W. Aarnink, J. Flokstra, and H. Rogalla, Appl. Phys. Lett. **67**, 2087 (1995).

[7] J.M. Schmidt, L.P. Lee, A. Matlashov, M. Teepe, V. Vinetskiy, R. Cantor, and M.S. DiIorio, Proceedings of Biomag 96, Santa Fe, February 16–21, 1996.

[8] R.H. Koch, J.Z. Sun, V. Foglietta, and W.J. Gallagher, Appl. Phys. Lett. **67**, 709 (1995).

[9] F.P. Milliken, S.L. Brown, and R.H. Koch, Appl. Phys. Lett. **71**, 1857 (1997).

[10] C.P. Foley, S. Lam, K.E. Leslie, K.-H. Müller, R.A. Binks, L. Macks, and G.J. Sloggett, Proceedings of the 6th Int. Superconductive Electronics Conference (ISEC'97), Berlin, June 25–28, 1997.

[11] J. Borgmann, P. David, R. Otto, J. Schubert, and A.I. Braginski, Appl. Phys. Lett. **74**, 1021 (1999).

[12] S. Krey, B. David, R. Eckart, and O. Dössel, Appl. Phys. Lett. **72**, 3205 (1998).

[13] E. Dantsker, S. Tanaka, P.-Å. Nilsson, R. Kleiner, and J. Clarke, Appl. Phys. Lett. **69**, 4099 (1996).

[14] E. Dantsker, S. Tanaka, and J. Clarke, Appl. Phys. Lett. **70**, 2037 (1997).

[15] L.P. Lee, J. Longo, V. Vinetskiy, and R. Cantor, Appl. Phys. Lett. **66**, 1539 (1539).

[16] R.H. Koch, M.B. Ketchen, W.J. Gallagher, R.L. Sandstrom, A.W. Kleinsasser, D.R. Gambrel, T.H. Field, and H. Matz, Appl. Phys. Lett., **58**, 1786 (1991).

Low Frequency Flux Noise in YBCO dc SQUIDs Cooled in Static Magnetic Fields.

M.P. Sager*, P.R.E. Petersen*†, T. Holst, Y.Q. Shen, and J. Bindslev Hansen*.

NKT Research Center, Priorparken 878, DK-2605 Brøndby, Denmark.

*Department of Physics, Technical University of Denmark, DK-2800 Lyngby, Denmark.

†Department of Clinical Neurophysiology, Rigshospitalet, Blegdamsvej 9, DK-2100 Copenhagen, Denmark.

Abstract—The low frequency flux noise in bicrystal and step-edge $YBa_2Cu_3O_x$ dc SQUIDs has been investigated. The width, w, of the superconducting strips forming the SQUID frame was varied from 4 to 42 μm. The SQUIDs were cooled in static magnetic fields up to 150 μT. Two types of low frequency noise dominated, namely $1/f$-like noise and random telegraph noise giving a Lorentzian frequency spectrum. The $1/f$ noise performance of the w = 4, 6, and 7 μm SQUIDs was almost identical, while the SQUIDs with w = 22 and 42 μm showed an order of magnitude higher noise levels. Our analysis of the data suggest an exponential increase of the $1/f$ noise vs. the cooling field, exhibiting a characteristic magnetic field around 40 μT.

I. Introduction

For many applications of the dc SQUID, a low value of the low frequency noise is desired. In general, HTS SQUIDs suffer from increased low frequency flux noise when operated in an ambient magnetic field in the μT-range. This has been explained in the framework of thermally activated motion of flux vortices trapped in local pinning sites in the superconducting film forming the SQUID body [1]. Mainly two types of low frequency noise are observed: $1/f$-like noise and random telegraph noise giving a Lorentzian power spectrum. According to [1], both the $1/f$ noise and the random telegraph noise originate from the fluctuating trapped flux vortices. Random telegraph noise arises if a single long range hopping process between two pinning sites dominates, while $1/f$ noise results from the summation of many uncorrelated short range random telegraph noise processes. However, by keeping the strip linewidth of the SQUID body narrow (in the order of a few μm), the low frequency flux noise has been substantially reduced [2]. This allows for unshielded operation of the SQUID in the Earth magnetic field of around 50 μT. In this paper we present a systematic study of the low frequency flux noise in dc SQUIDs of varying strip width, cooled in static magnetic fields of up to 150 μT.

II. Experimental Procedures

Ten single layer frame-like dc SQUIDs have been investigated. Seven of these were based on 36.8° misorientation angle $SrTiO_3$ bicrystal Josephson junctions, while the other three were based on MgO step-edge junctions. The SQUIDs were patterned into a 200 nm thick $YBa_2Cu_3O_x$ film deposited by pulsed laser ablation. All SQUIDs have a nominal inductance of ~100 pH. The geometrical design of the junction region was identical for all SQUIDs, only the width of the SQUID frame has been varied from w = 4 to 42 μm, see Fig. 1. During measurements the SQUIDs were placed in a Helmholtz coil arrangement located inside a four layer μ-metal shield with a background field < 5 nT. The Helmholtz coil was powered by a sealed lead acid battery. The background field noise from the coil when powered was below 30 $fT/Hz^{1/2}$ at 1 Hz, which is far below the sensitivity of the investigated SQUIDs (~5 $pT/Hz^{1/2}$at 1 Hz). Atmospheric air was pumped through the sample holder into the small cavity containing the SQUID, thus displacing the liquid N_2. In this way, the temperature could be cycled above the transition temperature and back to 77 K in around 20 sec. The SQUIDs were operated in a flux modulated, flux-locked loop by the NKT SQUID CATCHER™ control electronics. A standard bias reversal scheme was used to suppress the low frequency noise originating from the critical current fluctuations in the Josephson junctions [3]. The noise spectra were recorded by a FFT spectrum analyser using 1000 linear averages for each measurement.

III. Results

Fig. 2(a) and 2(b) show the increase in the flux noise level, $\Delta S_\Phi(1Hz) = S_\Phi(1Hz) - S_\Phi(500Hz)$, as a function of the cooling field B for a bicrystal and a step-edge SQUID, respectively. The white noise level at 500 Hz was measured in the actual fields. In order to gain good statistical information of the noise level, five thermal cycles were carried out for each cooling field and after each cooldown four sequential spectra were recorded.

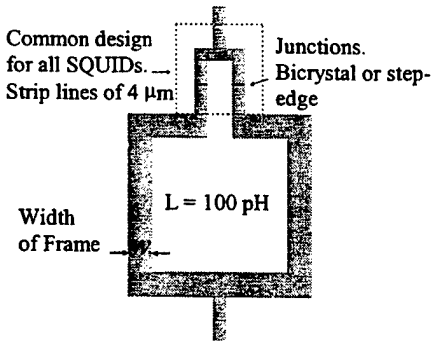

Figure 1. Schematic view of the frame-like dc SQUIDs investigated.

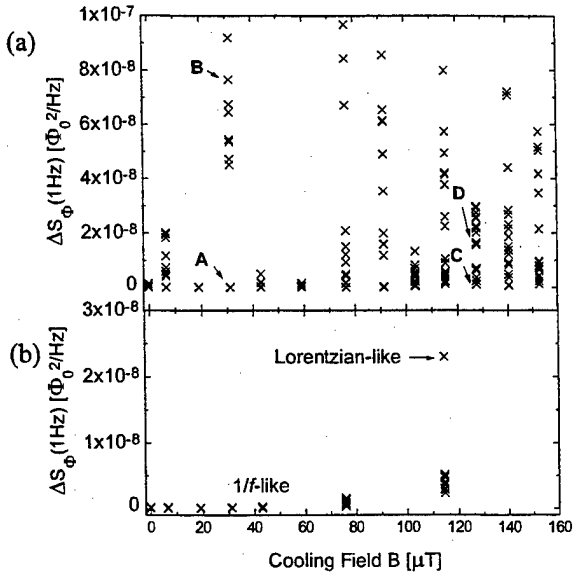

Figure 2. Increase in flux noise at 1 Hz vs. cooling field for two different SQUIDs with, w = 4 μm. (a) SQUID with a high probability of observing Lorentzian-like noise. The points A, B, C, and D refer to Fig. 3. (b) SQUID with a low probability of observing Lorentzian-like noise. In each cooling field a total of 20 measurements during five thermal cycles were recorded.

The two SQUIDs had very similar parameters and differ only in the technology used to form the Josephson junctions. However, as seen from Fig. 2, the two SQUIDs had very different probabilities of showing Lorentzian-like noise. Analysis of the noise spectra corresponding to each cross in Fig. 2(a) revealed that low noise levels were characterised by either a flat or 1/*f*-like power spectrum, whereas the higher noise levels were Lorentzian-like. In general, it was also observed that the 1/*f* noise levels were quite reproducible in successive cooldowns, whereas the Lorentzian-like noise seemed to attain any value at any cooling field. In Fig. 3, the noise spectra corresponding to the labelled crosses in Fig. 2(a) are presented.

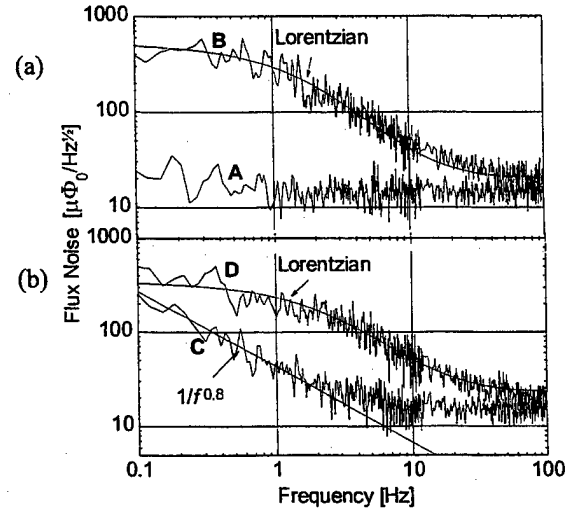

Figure 3. (a) Noise spectra corresponding to points A and B in Fig. 2(a). For this cooling field the spectra were either flat or Lorentzian-like. (b) Noise spectra corresponding to points C and D. For this cooling field the spectra were either 1/*f*-like or Lorentzian-like.

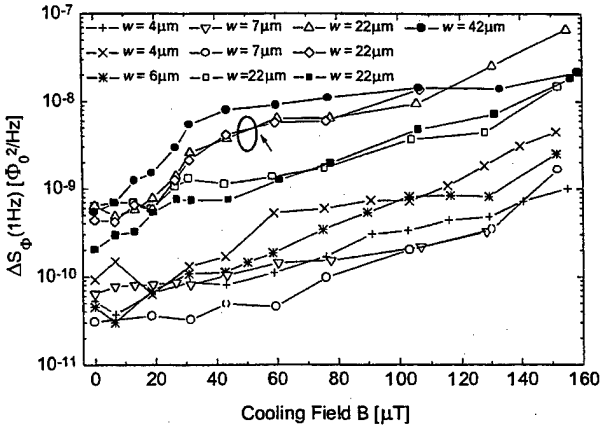

Figure 4. Increase in flux noise at 1 Hz vs. cooling field for ten SQUIDS of various widths, w, shown on a semi-logarithmic scale. Each point is an average of six measurements. $\Delta S_\Phi(1\text{Hz}) = S_\Phi(1\text{Hz}) - S_\Phi(500\text{Hz})$.

We chose to base a systematic study of trends in the low frequency noise on the more reproducible 1/*f* noise levels. Therefore, the presented noise curves have been obtained by several thermal cycles at each field until a reproducible 1/*f* noise level was obtained. All measurements giving Lorentzian-like spectra were rejected. In Fig. 4, the noise curves of the ten SQUIDs are presented on a logarithmic scale. Each point is an average of six measurements recorded during two cooldowns fulfilling the requirements described above.

As seen in Fig. 4, the noise curves of the w = 4, 6, and 7 μm SQUIDs are almost identical. In general, the 1/*f* noise at 1 Hz of these SQUIDs was around 10^{-10} Φ_0^2/Hz when cooled in 50 μT, and between $2\text{x}10^{-10}$ and $7\text{x}10^{-10}$ Φ_0^2/Hz when cooled in 100 μT. The SQUIDs with w = 22 μm and 42 μm had higher noise levels, roughly increased by a decade in all fields. Two of the w = 22 μm SQUIDs had slits on the inner rim, which could be a reason for the increased noise level, compared to the two other w = 22 μm SQUIDs (the noise curves of the two w = 22 μm SQUIDs with slits are indicated with an arrow on Fig. 4). The SQUIDs with slits originally belonged to an experiment investigating edge effects, which will not be discussed further in this context.

IV. Discussion

For most of the samples, the noise curves presented in Fig. 4 look linear, in particular for cooling fields in excess of ~30 μT. For small cooling fields, the recorded noise level at 1 Hz was comparable to the white noise level, which made the determination of the 1/*f* noise level more uncertain. Linear regression analysis of the curves in Fig. 4 was carried out with good results, except for the data belonging to the w = 42 μm SQUID. Fig. 5 shows the best linear fit of one of the w = 22 μm SQUIDs of Fig. 4 (solid squares) compared to the same data shown on a double logarithmic scale. Clearly, an exponential fit accounts better for the experimental data than a power law fit. On the contrary, the noise curve of the w = 42 μm SQUID, which is the most washer-like SQUID

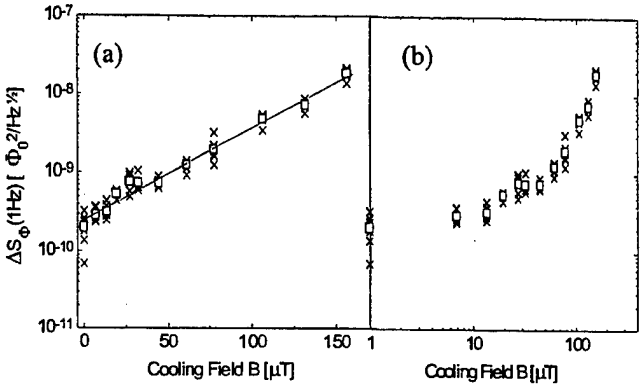

Figure 5. Noise curve of a w = 22 μm SQUID shown (a) in a semi-logarithmic plot with a linear fit, and (b) in a double logarithmic plot. Zero-field data are shown at the vertical axis. The open squares are averages of the six measurements (crosses) carried out in each field.

investigated, appears linear in a double logarithmic plot (see Fig. 6), implying $\Delta S_\Phi \propto B^\alpha$, where $\alpha \approx 1.1$ from linear regression analysis. A linear dependence of the $1/f$ noise versus cooling field has previously been reported by Miklich et al. for washer SQUIDs [4], and by Dantsker et al. for SQUID structures containing a ~50 μm strip line [2].

The linear regression analysis of the noise curves in Fig. 4 yields the fitting parameters S_0 and B_0 of the empirical expression $\Delta S_\Phi(1\text{Hz}) = S_0 \exp[B/B_0]$. In Fig. 7, the parameters B_0 and S_0 are plotted together with the uncertainties obtained from the fits versus the film area of the SQUIDs. As seen, B_0 shows little dependence of the film area and hence the width of the SQUID frame. On the other hand S_0 seems to be proportional to the film area. A magnetic threshold field of the order $B_T = \pi\Phi_0/(4w^2)$, as predicted by J.R. Clem [5], was not observed.

In conclusion, the measurements suggest that the $1/f$ flux noise in small SQUIDs made from narrow strip lines increases exponentially with the cooling field with $S_0 \cong 0.06\ \Phi_0^2/(\text{Hzm}^2) \times$ Film Area. The exponential form implies that flux is trapped in the film even in very small fields, which could be explained by the presence of strong pinning centres occupied by thermally induced vortex-

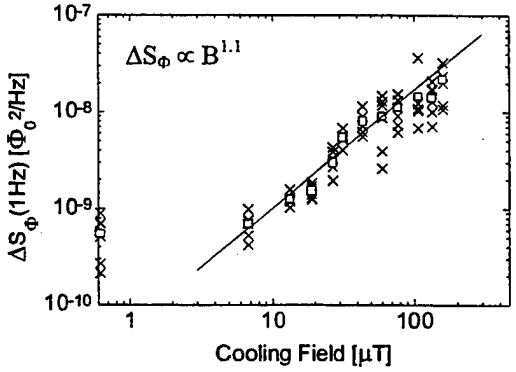

Figure 6. Noise curve of a w = 42 μm SQUID shown in a double logarithmic plot. Zero-field data are shown on the vertical axis. Open squares are averages of the six measurements (crosses) at each field. The solid line is the best linear fit yielding a slope of 1.1, when disregarding the zero-field data.

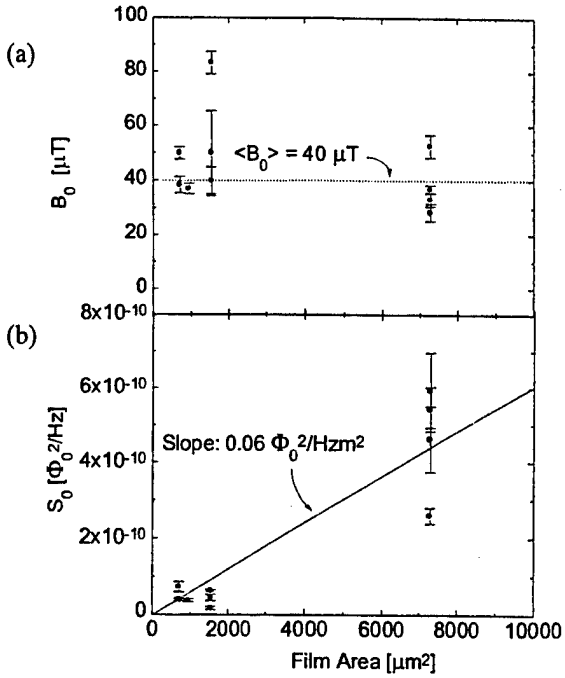

Figure 7. (a) Plot of the slope parameter B_0 and (b) the prefactor S_0 versus film area of the SQUIDs. S_0 and B_0 were obtained from linear regression analysis of the noise curves in Fig. 4. The w = 42 μm SQUID have been omitted.

antivortex pairs. This may be the reason why our samples probably do not fulfil the criteria on which the theoretical prediction of B_T is based. If the trapped flux per unit area is constant, one would expect that the prefactor S_0 scales with the film area as our data suggest. Regarding the characteristic field $B_0 \approx 40$ μT, it is not yet clear how to interpret and estimate it [6].

ACKNOWLEDGMENT

We thank John R. Clem for communicating his unpublished results and Rolf Jensen for technical assistance. P.R.E. Petersen thanks the Danish Research Councils for funding through the Danish Centre for Biomedical Engineering.

REFERENCES

[1] M.J. Ferrari, M. Johnson, F.C. Wellstood, J.J. Kingston, T.J. Shaw, J. Clarke, *Magnetic Flux Noise in Copper Oxide Superconductors*, Jour. Low Temp. Phys., Vol 94, 1, 1994, pp. 1-15.

[2] E. Dantsker, S. Tanaka, J. Clarke, *High-T_C super conducting quantum interference devices with slots or holes: Low 1/f noise in ambient magnetic fields.*, Appl. Phys. Lett., 70 (15), 1997, pp. 2037-2039.

[3] J. Clarke., *SQUID Fundamentals*, NATO ASI series, Series E: Applied Science – Vol. 329, SQUID Sensors: Fundamentals Fabrication and Applications, (1995).

[4] A.H. Miklich, D. Koelle, T.J. Shaw, F. Ludwig, D.T .Nemeth, E. Dantsker, J. Clarke, N. McN. Alford, T.W. Button, M.S. Colclough, *Low-frequency excess noise in $YBa_2Cu_3O_{7-x}$ dc superconducting quantum interference devices cooled in static magnetic fields.* Appl. Phys. Lett., 64 (25), 1994, pp. 3494-3496.

[5] J.R. Clem, Iowa State University, personal communication, 1999.

[6] M.P. Sager, P.R.E. Petersen, T. Holst, Y.Q. Shen, J. Bindslev Hansen, and J.R. Clem, to be published.

Direct coupled YBCO dc SQUID magnetometers

P.R.E. Petersen*+, Y.Q. Shen, M.P. Sager*, T. Holst, B.H. Larsen, and J. Bindslev Hansen*

NKT Research Center, Priorparken 878, DK-2605 Brøndby, Denmark.

*Department of Physics, Technical University of Denmark, DK-2800 Lyngby, Denmark.

+Department of Clinical Neurophysiology, Rigshospitalet, Blegdamsvej 9, DK-2100 Copenhagen, Denmark.

Abstract—$YBa_2Cu_3O_{7-x}$ magnetometers have been made on 10 mm *10 mm MgO substrates by directly coupling the magnetometer pick-up loop to a dc SQUID with narrow strip lines. The dc SQUIDs were made with $YBa_2Cu_3O_{7-x}$ step-edge Josephson junctions. The layout of the magnetometer pick-up loop was chosen as a compromise between maximising the loop effective area and minimising the loop inductance. The SQUID was designed to have $L_S \sim 100$ pH in order to obtain $\beta_L = 2I_0 L_S/\Phi_0 \approx 1$ with the single junction critical current $I_0 \sim 10$ μA. We have made magnetometers with white noise levels down to 55 fT/Hz$^{1/2}$ and a 1/*f*-knee at 1 Hz (ac-biased). Noise measurements were made on a field-cooled magnetometer. The noise measured at 1 Hz when cooled in "zero field" was 175 fT/ Hz$^{1/2}$. When cooled in magnetic fields of B = 50 μT and B = 100 μT we measured the noise at 1 Hz to 430 fT/ Hz$^{1/2}$ and 1.3 pT/ Hz$^{1/2}$, respectively

I. Introduction

The aim of this work was to fabricate magnetometers with minimised zero-field low frequency excess noise and to increase the immunity of the fabricated magnetometers to cooling in static magnetic fields. The magnetometers were patterned in an approximately 200 nm thick $YBa_2Cu_3O_{7-x}$ film deposited by pulsed laser deposition on MgO substrates. The resist masks used for patterning were made with electron beam lithography for two of the magnetometers (#1 and #3) and with UV lithography for the third magnetometer (#2). The patterning was made by Ar^+-ion beam etching. The dc SQUIDs of the magnetometer were made with step-edge Josephson junctions [1],[2].

II. Design Considerations

Experimental work on SQUIDs with differently patterned washers by Dantsker et al. [3] and on direct coupled magnetometers with narrow strips by Cho et al. [4], have shown that the use of narrow strips increases the immunity to cooling in static magnetic fields, as predicted by J.R. Clem.

Noise measurements by M.P. Sager et al. [5] on field cooled frame SQUIDs with narrow strips confirmed that the 1/*f*-noise is significantly lower than the noise level measured for SQUIDs made with wider strips. For frame SQUIDs with strips narrower than 7 μm no significant increase in the 1/*f*-noise was observed when cooled in magnetic fields less than 50 μT.

According to numerical simulations by Tesche and Clarke the optimum energy resolution ($\propto S_\Phi/2L_S$) is obtained when β_L is close to unity [6]. To obtain $\beta_L = 2I_0 L_S/\Phi_0 \approx 1$ with the single junction critical current $I_0 \sim 10$ μA, the SQUID frame inductance L_S should be of the order $L_S \sim 100$ pH. Numerical simulations by Enpuku et al. [7] have shown that the V-Φ curve of the SQUID is degraded with increasing L_S due to thermal noise. The voltage modulation depth ΔV_{mod} is related to L_S and β_L in the following way [7]:

$$\Delta V_{\mathrm{mod}} = \frac{7}{\pi^2}\frac{I_0 R_N}{1+\beta_L}\left(1-3.57\frac{\sqrt{k_B TL}}{\Phi_0}\right) \qquad (1)$$

Using the above-mentioned parameters for I_0, β_L, and L_S and assuming that $R_N \sim 2$ Ω, we get a modulation depth $\Delta V_{mod} \approx 3$ μV at $T = 77$ K

The inductance of the SQUID frame L_S is given as: $L_S = L_M + L_{kin}$, where $L_M = L_{frame} + L_{slit}$ is the magnetic inductance of the frame part and slit part of the SQUID and L_{kin} is the kinetic inductance of the frame (see Fig. 1).

The inductance of a square frame may be estimated as [8]:

$$L = \frac{2\mu_0 l}{\pi}\left(\ln\left(\frac{l}{b}\right)+\frac{1}{2}\right), \qquad (2)$$

where μ_0 is the permeability of free space and the quantities l and b are defined in Fig. 1.

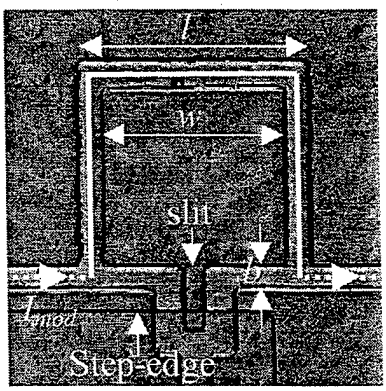

Figure 1. Picture showing the SQUID frame. The modulation current I_{mod} passes through the upper 7/10 part of the SQUID frame as indicated by the full white line. The dimensions of the SQUID frame are: l = 50 μm, w = 40 μm and b = 5 μm.

As seen in Fig. 1, the geometry of the slit part of the SQUID is somewhere in between a frame and a washer. We therefore assume that the inductance of the slit part is within an interval where the minimum value is determined as for a washer i.e. $1.25\mu_0$ times the width of the slit [9] and the maximum value is determined by (2).
For $w >> b$ with b being the strip width the kinetic inductance can be estimated as [10]:

$$L_{kin} = \mu_0 \lambda^2 \frac{4(l-b)}{w\,t}, \qquad (3)$$

where λ is the penetration depth and t is the thickness of the superconducting film. The penetration depth for $YBa_2Cu_3O_{7-x}$ at 77K is taken to $\lambda = 530$ nm.

A series of SQUIDs with different frame size was fabricated with the purpose to measure the inductance of the different frames. The SQUID frame inductance was measured by applying the modulation current directly through the SQUID frame as indicated in Fig. 1. The effective inductance of the SQUID frame was determined as: $L'_{frame} = \Phi_0/(k\, I_{period}) \approx L_{frame}$, where k is the fraction of the frame that the modulation current passes through and I_{period} is the value of the modulation current that generates one flux quantum in the SQUID. For the SQUID shown in Fig. 1, we modulate through ~7/10 part of the SQUID frame i.e. k = 7/10 and we measured I_{period} to be 26 μA. This corresponds to an inductance L'_{frame} = 114 pH which is close to the value of L_{frame} = 112 pH estimated by (2) for the square part of the frame. Note that the kinetic inductance does not contribute to the magnetic response of the SQUID frame, since it represents the inertia of the supercurrent.

The design of the magnetometer pick-up loop was chosen as a compromise between maximising the effective area of the magnetometer pick-up loop and minimising the loop inductance. The outer dimensions of the magnetometer was chosen as 9 mm *9 mm leaving a narrow edge of the 10 mm *10 mm MgO substrate free of $YBa_2Cu_3O_{7-x}$ in order to avoid edge effects. Magnetometers have been fabricated with two different designs of the magnetometer pick-up loop. The inductance of the magnetometer pick-up loop $L_{pick\text{-}up}$ was estimated by (2).

III. Noise Measurements

Noise spectra for the magnetometers #1, #2 and #3 cooled in a magnetic field $B \approx 0$ μT have been recorded. Furthermore the noise spectra for #3 cooled in B = 50 μT and B = 100 μT were recorded. Table I summarises data on #1, #2 and #3.

A. "Zero Field" Measurements

To measure the "zero-field" noise spectra the magnetometers were placed in a four layer μ-metal can. The dc background field inside the can was below 5 nT in the direction normal to the magnetometer and below 100 nT in the magnetometer plane. The noise spectra for #1 and #2 measured in "zero field" are shown in Fig. 2.

TABLE I

DATA ON #1, #2 AND #3

Sample	I'_0	R_N	ΔV_{mod}	L_{frame}	L_{slit}	L_{kin}	β_L	$L_{pick\text{-}up}$
	μA	Ω	μV	pH	PH	pH	-	nH
#1	6.6	10	11.2	107	6-20	8	0.9	12.5
#2	13.7	1.5	6.9	112	6-15	8	1.8	11.5
#3	21.5	15.5	8	107	6-20	8	2.8	12.5

Due to noise rounding of the measured single junction critical current I_0 we estimated it as: $I'_0 \approx \frac{I_{bias,max}}{2} + \frac{k_B T}{\Phi_0}\left(1 + \sqrt{\frac{I_{bias,max}}{k_B T/\Phi_0}}\right)$ where $I_{bias,max}$ is the bias current where the modulation depth ΔV_{mod} is maximised [11]. L_{frame} and $L_{pick\text{-}up}$ are estimated by (2) and L_{kin} by (3). To calculate β_L we have used the maximum value of L_{slit}.

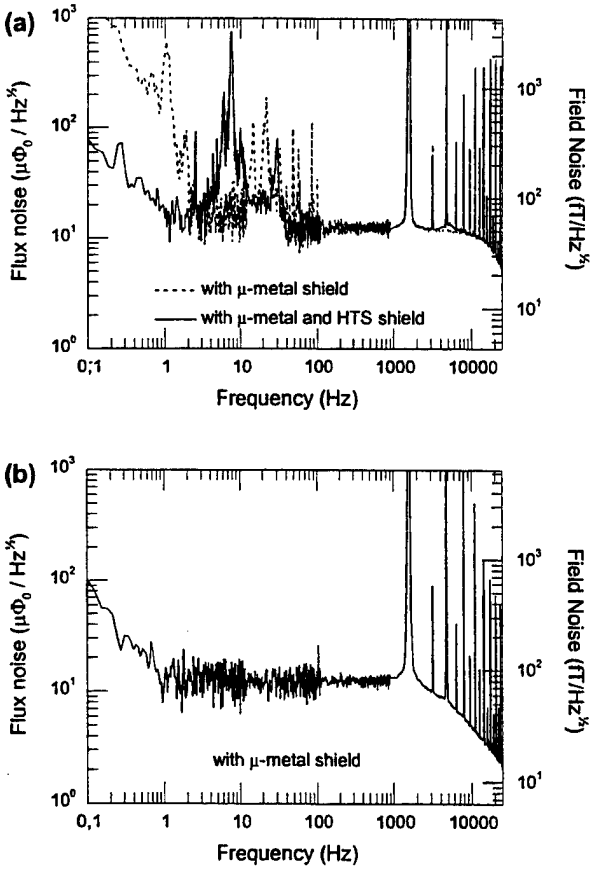

Figure 2 Noise spectra for #1 (a) and #2 (b). The noise measured in the frequency range 3 – 30 Hz in (a) is dominated by vibration noise. Note that the field noise axis in (b) is different from the field noise axis in (a) due to the different field sensitivity of the magnetometers.

The magnetic field sensitivity for the two designs was measured by applying a magnetic field generated by a calibrated coil with four windings. The field sensitivity was different for the two different designs of the magnetometer pick-up loop. The magnetic field sensitivity measured for #1 and #3 was 4.3 nT/Φ_0 and for #2 it was 6.4 nT/Φ_0. This corresponds to an effective area of 0.48 mm^2 and 0.32 mm^2, respectively. For both #1 and #2, we measured a white flux noise level of 12.4 $\mu\Phi_0/Hz^{1/2}$, yielding a white field noise level of 55 $fT/Hz^{1/2}$ and 80 $fT/Hz^{1/2}$, respectively.

The dotted line in Fig. 2(a) is the noise spectrum recorded for #1 when cooled in a high temperature superconducting shield inside the four layer μ-metal can. The HTS shield was a $Bi_2Sr_2CaCu_2O$ cylinder with one end closed. The HTS shield must be completely immersed into liquid N_2 before liquid N_2 flows into the cylinder and cools the magnetometer ensuring that the HTS shield is in the superconducting state when the magnetometer is cooled.

B. Measurements on a field-cooled magnetometer

To perform the measurements on field cooled magnetometers an Helmholtz coil arrangement was placed inside the μ-metal can. The low frequency background noise level of the Helmholtz coil arrangement used to generate the magnetic field for the measurements on the field-cooled magnetometer was below 30 $fT/Hz^{1/2}$ at 1 Hz. The magnetometer chosen for these measurements was #3. Fig. 3 shows the noise spectra for #3 when cooled in the background field and B = 50 μT and B = 100 μT, respectively. As seen this does not change the white noise level but the low frequency excess noise measured at 1 Hz increases from 175 $fT/Hz^{1/2}$ when cooled in zero-filed to 430 $fT/Hz^{1/2}$ when B = 50 μT and to 1.3 $pT/Hz^{1/2}$ when B = 100 μT. The measurements on #3 were made using a modulation coil with four windings. Later we observed that the white noise level was notably reduced when the magnetometers are modulated directly through the SQUID frame.

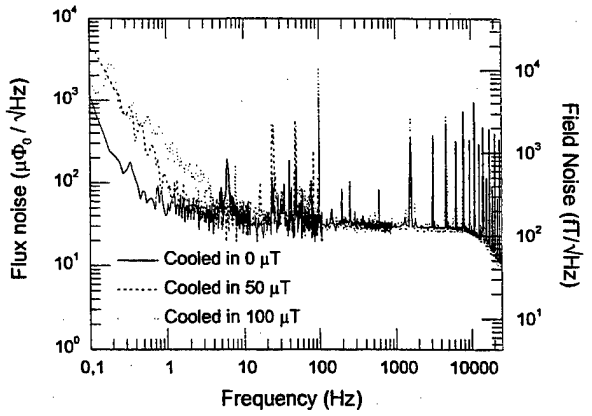

Figure 3 Noise spectrum for #3 when cooled in B = 0 μT, B = 50 μT and B = 100 μT, respectively. A seen this does not increase the white noise level whereas the 1/*f*-noise increases with roughly a decade.

The preamplifier noise level of the SQUID read-out electronics has been determined. For #1, #2, and #3 the preamplifier noise levels were estimated to ~14.5 $\mu\Phi_0/Hz^{1/2}$, ~16.7 $\mu\Phi_0/Hz^{1/2}$ and ~30 $\mu\Phi_0/Hz^{1/2}$, respectively. The measured white noise levels are 12.4 $\mu\Phi_0/Hz^{1/2}$ for both #1 and #2 and 37 $\mu\Phi_0/Hz^{1/2}$ for #3.

SUMMARY

We have reproducibly made magnetometers with a white noise level at ~55 $fT/Hz^{1/2}$ and a 1/*f*-knee at ~1 Hz when ac-biased. Noise measurements have been made on a field-cooled magnetometer. Cooling in magnetic fields of B = 50 μT and B = 100 μT did not increase the white noise level, but the position of the 1/*f*-knee increased to ~5 Hz and ~10 Hz, respectively. The noise measured at 1 Hz when cooled in $B \approx$ 0 μT, B = 50 μT and B = 100 μT, respectively are: 175 $fT/Hz^{1/2}$, 430 $fT/Hz^{1/2}$ and 1.3 $pT/Hz^{1/2}$, indicating that the white noise levels are dominated by preamplifier noise.

ACKNOWLEDGMENT

We thank Can Superconductor, Ltd. for providing us with the $Bi_2Sr_2CaCu_2O$ shield and Rolf Jensen for technical assistance. P.R.E. Petersen thanks the Danish Research Councils for funding through the Danish Centre for Biomedical Engineering.

REFERENCES

[1] Y.J. Feng, Y.Q. Shen, J. Mygind, N.F. Pedersen, and P.H. Wu "Current-voltage characteristics of $Yba_2Cu_3O_7$ step edge junctions on MgO subtrates," Physica C **282-287** p.2459 (1997)

[2] S. Lam and C.P. Foley "Noise properties of High-Quality Step-Edge YBCO Josephson Junctions," Proc. Intl. Superconductive Electronics Conf. (ISEC'95), Nagoya, Japan (1995)

[3] E. Dantsker, S. Tanaka, and J. Clarke "High-T_C superconducting quantum interference devices with slots or holes: Low 1/f noise in ambient magnetic fields," Appl. Phys. Lett. **70**, (15), pp2037 – 2039 (1997).

[4] H.-M. Cho, R. McDermott, B. Oh, K.A. Kouznetsov, A. Kittel, j.H. Miller Jr. , and J. Clarke "Low Frequency Noise in Field Cooled, Directly Coupled Magnetometers," Applied Superconductivety Conference 1998, (ASC'98), to be published.

[5] M. Sager, P.R.E. Petersen, T. Holst, Y.Q. Shen, and J. Bindslev Hansen, ibid

[6] C.D. Tesche and J. Clarke "dc SQUID: Noise and Optimization," J. Low Temp. Phys. **29**, p.301, (1977)

[7] K. Enpuku, Y. Shimomura, and T. Kisu "Effect of thermal noise on the characteristics of a high T_C superconducting quantum interference device", J. Appl. Phys. **73** (11) pp. 7929-7934 (1993).

[8] M. Ketchen. "Integrated thin-film dc SQUID sensors" IEEE Trans. Magn. **MAG-23**, 1650 (1987).

[9] J.M. Jaycox and M.B. Ketchen, "Planar Coupling Scheme for Ultra Low Noise dc-SQUIDs", IEEE Trans. Magn. **MAG-17**, 400 (1981).

[10] R. Meservey and P. Tedrow "Measurement of kinetic inductance of superconducting linear structures," J. Appl. Phys. **40**, p.2028 (1969).

[11] R.F. Voss "Noise characteristics of an ideal shunted Josephson Junction," J. Low Temp. Phys. **42**, pp.151-163 (1981)

Multipurpose LTS SQUID Sensors

R. Stolz, L. Fritzsch, and H.-G. Meyer
Institute for Physical High Technology, Dept. of Cryoelectronics, P.O. Box 100239, D-07702 Jena, Germany

Abstract — We have developed highly sensitive SQUID-based magnetometers and gradiometers, fabricated in a standard $Nb/AlO_X/Nb$ technology. The SQUID itself is designed as a current sensor having an input coil and a feed back coil. The number of turns of the input coil can be adjusted to ensure optimal coupling to the pickup loops with an inductance in the range of 5 nH to 300 nH.

Several types of planar pickup loop configurations have been realized. The magnetometer has a pickup loop with a size of 1 cm × 1 cm. With a typical white noise level better than $4\ \mu\Phi_0/Hz^{1/2}$ and an effective area of 2.6 mm^2 a field resolution of $3.2\ fT/Hz^{1/2}$ results for the magnetometer. Two loops connected in series with an area of 2 cm × 2 cm each and a baseline of 4 cm were used in the gradiometer. We measured 7.5 mm^2 effective area for each loop and a field gradient resolution of $36\ fT/m{\cdot}Hz^{1/2}$ corresponding to a field resolution in the loop of $1.6\ fT/Hz^{1/2}$.

I. Introduction

SQUIDs (Superconducting QUantum Interference Devices) as the most sensitive magnetic field or field gradient sensors are used for investigations of biomagnetic and geomagnetic signals, material investigation, and in several exclusive fields of measurements. To measure these signals with small amplitudes usually pickup loops with dimensions of few centimeters are coupled to the SQUID via a flux transformer. Depending on the subject to be investigated various configurations of pickup loops can be used, for instance, a magnetometer configuration or a gradiometer configuration of first, second or a higher order [1]. These pickup loops have inductances in the range of several hundreds of nanohenry.

When the pickup loops are properly coupled to the SQUID, one obtains an extremely sensitive magnetometer or gradiometer. The magnetic field or field gradient in the pickup loop is converted to flux in the SQUID. For a magnetometer the conversion factor between the magnetic field B_{ext} and the flux in the SQUID Φ_{SQ} is called effective area $A_{eff} = \Phi_{SQ} / B_{ext}$. For the first order gradiometer the corresponding factor is the effective volume $V_{eff} = \Phi_{SQ} / (dB/dx)$. These values are important parameters of the field sensors.

Most of the commercially available SQUID gradiometers or magnetometers use three-dimensional structures with wire wound pickup loops. The integrated thin film planar gradiometer was introduced in the early 1980's. The integrated pickup loops make use of the precision of lithography to achieve a high balance of the gradiometers. In the present work we will consider only integrated thin film structures.

The simplest way is to use the SQUID itself as a pickup structure. The flux focusing effect in the washer increases the effective area of the SQUID [2]. By using two washers in parallel or in series one can build a gradiometer of first order. The drawback of such layouts is the small effective area because of the limitation to the SQUID inductance and hence to its dimensions. In the next design a relatively large pickup loop is directly connected to the SQUID working as a current sensor [3]. This layout is also not effective with respect to the mismatch of the inductances.

More complicated layouts can achieve a larger effective area. By splitting the pickup loop in n fractions the inductance of the loop is decreased by a factor of about n^2 [4], [5] while the effective area is decreased only by a factor of n. The calculation of the SQUID inductance and the effective area of such multi-turn SQUID is given elsewhere [5]. For a pickup loop with a large geometrical dimension the optimal number of fractions can be rather high.

Another layout with a good coupling between pickup loop and SQUID without increasing the SQUID inductance is the coupling via a flux transformer. A simple variant of this widely used design consists of a superconducting washer with a slit closed by two Josephson junctions. The pickup loop is coupled to the SQUID via a n-turn input coil on top of the washer [1].

Here we present a more complicated layout of low T_c (LTS) SQUID consisting of eight washers with eight input coils. Pickup loops with inductances in the range from 5 nH to 300 nH can be optimally coupled to the SQUID. The SQUIDs with various pickup loops were fabricated and investigated.

II. SQUID Fabrication and Layout

The LTS-dc-SQUID Sensors have been fabricated using the 9 layer $Nb/AlO_X/Nb$ technology developed at the IPHT Jena. The process is carried out as follows: First the niobium lower wiring is deposited over the entire wafer (3 inch up to 4 inch) and patterned to define the SQUID washer (with a slit of 10 µm). Then a $Nb/AlO_X/Nb$ trilayer is deposited and patterned. We use the trilayer with the critical current density of 200 A/cm^2. The junction capacitance is 4.7 $\mu F/cm^2$. The junctions (typical 3.2 µm x 3.2 µm) and all areas where the wiring later will be contacted are defined by protecting them with a photoresist and anodizing the remaining area of the lower niobium film. Two layers of SiO (each of 400 nm) are deposited on the anodized Nb to reduce the parasitic capacitance between the input coil and the SQUID and to decrease the probability of shorts between conducting layers. On top of these isolation layers the Mo shunt layer is deposited and

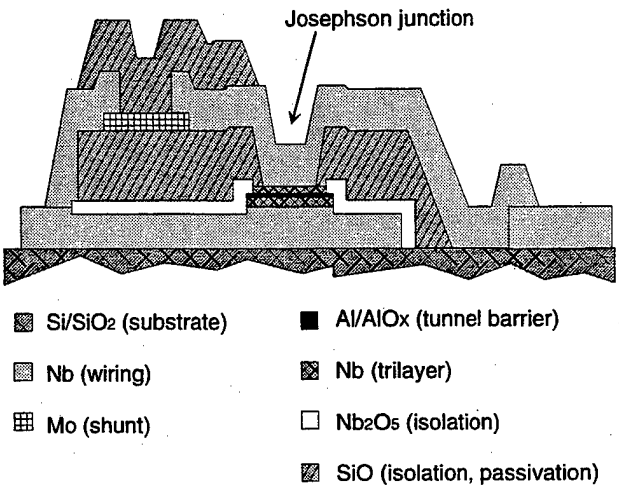

Fig. 1. Scematic representation of the crossection of the central part of the SQUID with the connections of each pair of washers in the corners. The layer thickness is not in scale.

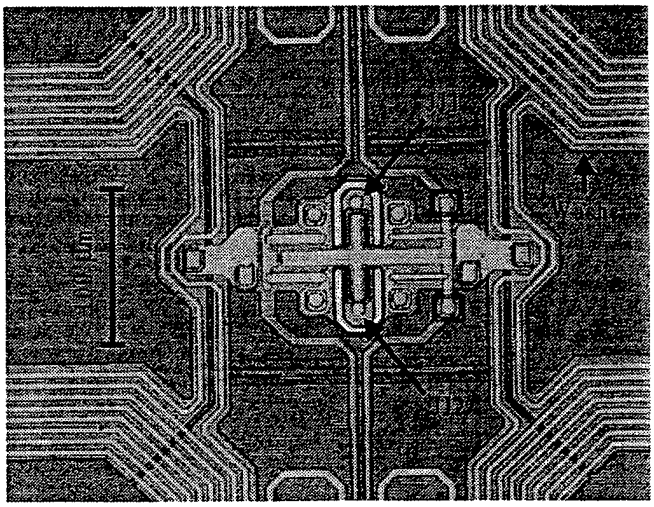

Fig. 3. Photo picture of the central part of the SQUID with the connections of each pair of washers in the corners and parts of 7-turns input coil on the washers.

patterned. The Mo film with a thickness of 100 nm has a sheet resistance of 0.8 Ohm/□ results. The shunt resistors are connected by using the upper superconducting wiring of Niobium which is deposited in the next step. This wiring defines also the input coils, some of the contact pads and the interconnections. The entire wafer (except for the contact pads) is covered by a thin layer of SiO to ensure resistance to moisture and thermal cycling.

All depositions are made by dc magnetron sputtering except for the SiO films which are evaporated. Most of the patterning are made using a lift-off stencil except the two wirings patterned by Ar ion etching. The crossection of the central part of the SQUID with Josephson junction and shunt is shown in Fig.1.

The SQUID itself should not affect the balance of gradiometers, so it has to be insensitive to the external magnetic field or field gradient. Therefore, our SQUID is designed as a highly symmetrical structure. It consists of four pairs of washers connected in parallel. The washers in the pairs are connected in series and forming a first order gradiometer. Each of the all in all eight SQUID washers has an inductance of $L_W = 580$ pH. It results in the SQUID inductance well

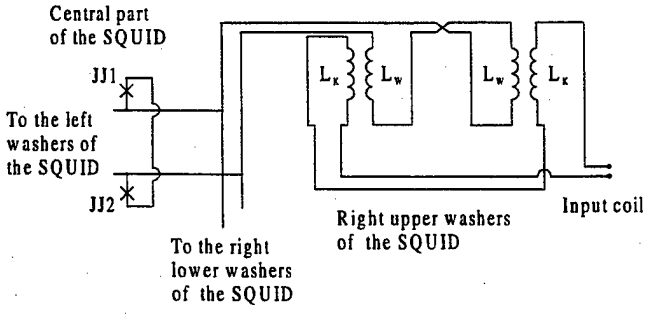

Fig. 2. Part of the equivalent circuit of the SQUID (without the parasitic inductances). JJ1 and JJ2 are the Josephson junctions, L_K is a part of the input coil located on one SQUID washer.

below 300 pH.

The pickup loop is coupled to the SQUID via the input coil placed on the top of all eight washers. The inductance of the input coil should match the pickup loop inductance. It varies in the range of 5 nH up to 300 nH using 1 to 8 turns. The equivalent circuit of the SQUID is partially shown in Fig. 2. This figure shows the connections of one pair of washers to the Josephson junctions and a part of the input coil coupled to these washers. The connection to this pair of in series connected washers can be found in the Fig. 3 in the right upper corner. The Josephson junctions are denoted as JJ1 and JJ2.

To prevent the penetration of flux vortices in the superconducting film during the operation in the earth magnetic field all of the superconducting structures have a width of less than 60 μm. To expell a possibly frozen flux the SQUID can be heated above the critical temperature by using an on-chip resistor of 150 Ω. A current of 20 mA trough the resistor is sufficient to bring the SQUID to the normal state.

There are some additional coils with resistor arrays which may be used to realize additional positive feedback and bias current feedback [5] via bond connections.

The impedance of the input coils with various number of turns n was measured with ac signal. The experimental results can be fitted by the following formula:

$$L_{in} = 25.54\ (\text{nH}) + n \cdot 1.64\ (\text{nH}) + n^2 \cdot 4.61\ (\text{nH}). \qquad (1)$$

The first term is the inductance of the current leads and the measuring setup. The second term is the stripline inductance of the input coil located on top of the SQUID washers. It is proportional to the length of the coil and with that proportional to the number of turns n. The term proportional to n^2 represents the magnetic coupling of the input coil to the SQUID washers.

The eight-turns coil has a total inductance of 308 nH. The measured mutual inductance between this input coil and

SQUID is M_{in} = 10.4 nH and between SQUID and feedback coil M_{FB} = 115 pH.

The SQUID can be used either as a current sensor having an equivalent white flux noise of 6 $\mu\Phi_0/Hz^{1/2}$ and a current resolution of 1.2 $pA/Hz^{1/2}$, or as a universal flux sensor with various designs of magnetometers and gradiometers. The response of several SQUIDs to a uniform magnetic field was tested using a Helmholtz coil system. For all SQUIDs the response corresponds to the parasitic area smaller than 30 μm^2.

III. SQUID WITH A MAGNETOMETER PICKUP LOOP

A square pickup loop with an area of 1 cm × 1 cm is coupled to the SQUID with a 4-turns input coil. The effective area of this magnetometer is 2.6 mm^2, again measured using a Helmholtz coil system.

The voltage modulation depth is between 30 μV and 50 μV. We measured a field resolution of better than 3.2 $fT/Hz^{1/2}$ with white flux noise levels below 4 $\mu\Phi_0/Hz^{1/2}$. For mechanical protection and safe handling the magnetometers is placed in a fiberglass capsule having a diameter of 19 mm and a thickness of 3 mm.

IV. SQUID WITH GRADIOMETER PICKUP LOOPS

Two types of gradiometers are realised with our universal SQUID. The first gradiometer consists of two loops connected in series each with an area of 1 cm × 1 cm. The baseline is 1 cm. In the second case two loops with an area of 2 cm × 2 cm are connected in series. The baseline of this gradiometer is 4 cm. The effective volume of the gradiometers was determined experimentally from the response of the device to the magnetic field generated by a small coil placed outside the cryostat at various distances to the gradiometer.

For the first type of gradiometer we used a SQUID with a 6-turns input coil. The measured effective volume is 21 mm^3. This corresponds to the effective area of 2.1 mm^2 of one loop of the gradiometer. The magnetic field gradient resolution is 0.6 $pT/m \cdot Hz^{1/2}$ and the field resolution in one loop of 6 $fT/Hz^{1/2}$. This gradiometer is also mounted in a fiberglass capsule having a diameter of 27 mm and a thickness of 3 mm.

For the second type of gradiometer the SQUID with a 7-turns input coil was used. It has an effective volume of 285 mm^3. For a baseline of 4 cm this is an effective area of 7.1 mm^2 of one loop of the gradiometer. The measured white noise level of several SQUIDs was in the range of 5 $\mu\Phi_0/Hz^{1/2}$ up to 10 $\mu\Phi_0/Hz^{1/2}$. Therefore, the magnetic field gradient resolution is 36 $fT/m \cdot Hz^{1/2}$ up to 72 $fT/m \cdot Hz^{1/2}$, what corresponds to a field resolution in one gradiometer loop of 1.45 $fT/Hz^{1/2}$ up to 2.9 $fT/Hz^{1/2}$. First measurements in an uniform field showed a balance in the range of 10^4/m up to 10^3/m.

The gradiometers could work in an unshielded environment in the laboratory using a direct coupled electronics [5] with a bandwidth of 1 MHz.

V. CONCLUSIONS

We have presented an universal SQUID sensor insensitive to external magnetic field with an input coil having an inductance from 5 nH up to 300 nH. The SQUID can be used as a current sensor with purely inductive input impedance and a current resolution of 1.2 $pA/Hz^{1/2}$. Using pickup loops of various configurations we have built gradiometers and magnetometers with this universal SQUID having an appropriate number of turns of the input coil. A magnetometer SQUID with a chip size of 1 cm × 1 cm has magnetic field resolution of 3.2 $fT/Hz^{1/2}$. The gradiometers have a chip size of 2 cm × 1 cm and 6 cm × 2 cm a field gradient resolution of 0.6 $pT/m \cdot Hz^{1/2}$ and 36 $fT/m \cdot Hz^{1/2}$, respectively.

REFERENCES

[1] M. B. Ketchen, W. M. Goubau, J. Clarke, and G. B. Donaldson, *J. Appl. Phys., vol 49*, pp. 4111-4116, 1978.

[2] M. B. Ketchen, W. J. Gallagher, A. W. Kleinsasser, S. Murphy, and J. R. Clem, in the *Proceedings of the 1985 Berlin SQUID Conference*, edited by H.-D. H. Hahlbohm and H. Lubbig (de Gruyter, Berlin), pp. 865-871, 1985.

[3] J. E. Zimmermann, *J. Appl. Phys.*, vol. 42, pp. 4483-4487, 1971.

[4] D. Drung, R. Cantor, M. Peters, H. J. Scheer, and H. Koch, *Appl. Phys. Lett.*, vol. 57, pp. 406-408, 1990.

[5] D. Drung, R. Cantor, M. Peters, T. Rhyänen, and H. Koch, *IEEE Trans. Magn.*, MAG-27, pp. 3001-3004, 1991.

Field sensitivity limitation due to pick-up coil resonances

Heikki Seppä and Mikko Kiviranta
VTT Automation, Measurement Technology, P.O. Box 1304, 02044 VTT, Finland
http://www.vtt.fi/aut/mit/

Abstract— **The existence of the pick-loop in the SQUID circuit modifies the dynamics and increases the noise. We show that the noise related to the damping of the input coil resonances or the microwave terminations markedly deteriorates the field resolution at least in the magnetometer having a large pick-up loop. We optimise the field resolution of the SQUID magnetometer including both the intrinsic noise sources and the mixed down noise related to the microwave termination.**

I. Introduction

The SQUIDs are mainly applied in biomagnetic measurements, where the magnetic field or its gradients are monitored. [1] To achieve a high field sensitivity large pick-up loops are used. Most cases the pick-up loop is designed independently of the SQUID design. Only the inductance of the pick-up loop is matched to the input inductance of the SQUID. The basic idea is to maximize the applied flux in the SQUID ring. The inductance matching is obtained either with a single loop or splitting the antenna into parallel sub-loops decrease the output inductance of the antenna.

In this paper we show that the field resolution of the magnetometer is fundamentally connected with the pick-up loop design. The reason is that a low noise SQUID system requires damping of all resonances and an appropriate termination of the microwave transmission lines [1]. Since the characteristic wave impedance is proportional to the pick-up loop area, the noise arising from the termination is associated with the pick-up loop design. The larger the antenna the higher is the noise related to the microwave termination. In this paper we show that the full and simultaneous optimization of the SQUID and the pick-up loop is necessary.

II. Optimization

Figure 1 shows the schematic diagram of the integrated magnetometer, where the signal coil consists of n turns and the pick-up loop is composed of m slices connected in parallel. There are many ways to accomplish the SQUID layout but we use this simple geometry to simplify our calculations. In addition, our new SQUID design based on

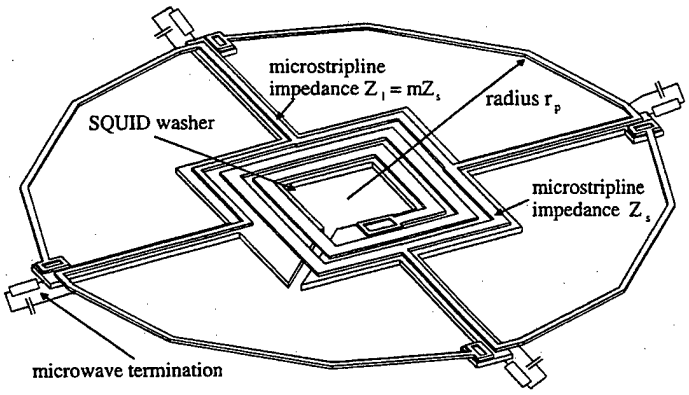

Figure 1 – Layot of the SQUID magnetometer. The large pick-up loop consists of several parallel sub-loops and the signal coil forms the spiral microstripline on the SQUID washer.

the un SQUID (unshunted SQUID) resembles that shown in Fig. 1.[2] We assume that a low noise SQUID can only be obtained by damping all the resonances introduced by the SQUID itself and its field sensing elements. In the construction shown in Fig. 1, an appropriate damping is achieved simply by terminating the microstriplines formed by the overlaps between adjacent slices. In addition, to prevent reflections at the edge of the washer the characteristic impedance of the signal coil should be m times smaller than that of the overlaps.

The appropriate termination eliminates the excess noise related to the resonances but it creates high frequency noise currents which enter the SQUID loop. Owing to the nonlinear characteristic, Josephson junctions mix high frequency noise down to low frequencies. If microwave lines are terminated, also the LC-resonance of the flux transformer becomes well damped and no other damping elements are required.

The magnetic field B threading the pick-up loop changes the flux in the SQUID ring as

$$\Phi_a^2 = \frac{m^2 n^2 L_w^2 B^2 A^2}{L_l^2 \left(1 + m^2 n^2 L_w / L_l + m^2 L_{par} / L_l\right)^2} , \qquad (1)$$

where L_w is the inductance of the SQUID washer and L_l that of the single turn pick-up loop, respectively. The to-

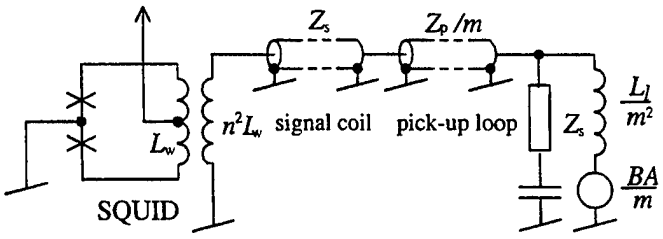

Figure 2 – Block diagram of the coupled SQUID. The signal coil and the overlaps between adjacent sub-loops in the pick-up loop are modeled with transmission lines.

tal stray inductance related to the microstriplines formed by the signal coil and the SQUID washer and the microstiplines formed by the overlaps of the adjacent sectors is denoted L_{par}. The effective area sensing the magnetic field B is A.

Block diagram of the coupled SQUID is shown in Fig. 1. The microwave terminations cause high frequency flux noise in the SQUID ring which is mixed down to low frequencies by the Josephson junctions. To eliminate reflection the termination at the end of each sub-loop should be $Z_p = mZ_s$, where Z_s the characteristic wave impedance of the signal coil.

If the SQUID ring is disturbed by high frequency flux Φ_{rf} then the junctions convert it to low frequencies as $\left\langle \Phi_{lf}^2 \right\rangle = (\pi/2)^2 \beta^2 \cos^2(\pi\Phi_b/\Phi_0) \left\langle \Phi_{rf}^2 \right\rangle$, if $\beta \ll 1$, where $\beta = 2LI_c/\Phi_0$ is the normalized SQUID inductance. If $\Phi_b = \pi\Phi_0/4$, then $\left\langle \Phi_{lf}^2 \right\rangle \approx \beta^2 \left\langle \Phi_{rf}^2 \right\rangle$. The mixed down noise can be given in the form

$$\left\langle \Phi_{n,pick}^2 \right\rangle \approx \frac{4k_BT\beta^2}{Z_s} \frac{n^2L_w^2}{\left(1 + m^2n^2\frac{L_w}{L_l} + m^2\frac{L_{par}}{L_l}\right)^2} . \quad (2)$$

It is well know that the intrinsic noise of the SQUID can be given in the form

$$\left\langle \Phi_{n,sq}^2 \right\rangle \approx 2\alpha\gamma k_BTL\sqrt{LC} , \quad (3)$$

where constant α depends on the SQUID type and $\gamma = \left(\beta^{-2} + 4\sqrt{\beta}\right)/5$ approximates the influence of the β parameter to the SQUID noise [3]. The screened SQUID inductance and the capacitance of the Josephson junction are denoted as L and C. In the conventional dc SQUID optimized with respect to β_c, and β parameters, $\alpha = 12$. The numerical simulations for our un SQUID predict $\alpha = 4 - 5$. [4] Setting $\Phi_a^2 = \left\langle \Phi_{n,sq}^2 \right\rangle + \left\langle \Phi_{n,pick}^2 \right\rangle$, we get

$$\left\langle B_n^2 \right\rangle = \frac{\Psi}{m^2}\left(\frac{\beta^2}{\alpha Z_s} + \frac{L^{\frac{3}{2}}\gamma\sqrt{C}\left(1 + m^2\left(n^2\frac{L_w}{L_l} + \frac{L_{par}}{L_l}\right)\right)^2}{2n^2L_w^2}\right) \quad (4)$$

where L is the SQUID inductance screened by the pick-up loop (see Eq. (6)) and

$$\Psi = \frac{4\alpha k_BTL_l^2}{A^2} . \quad (5)$$

If the number of turns in the spiral-type signal coil is high, the total length of the coil is $2w_s\Omega n^2$, where the pitch is $2\Omega w_s$ and w_s is the width of the transmission line. The capacitance across the SQUID ring is also increased by the transmission line, but because we assume that the SQUID operates in so called double loop mode, this does not markedly increase the noise of the SQUID.[5]

Since $Z_s = Z_p/m$, then $\ell_p = m\ell_s$, where ℓ_s and ℓ_p denote the inductance per unit length in the signal coil and the pick-up loop, respectively. In addition, $Z_s = \sqrt{\ell_s/c_s} = c_\epsilon\ell_s/\sqrt{\Theta}$, where $\Theta = 1 + \lambda_L^2/(ht_{ef})$, and $\ell_s = \mu_0h\Theta/(w_sK_s)$. K_s is the fringe field factor and c_ϵ is the speed of the signal in the transmission line. The London penetration depth is λ_L. The thickness of the insulation barrier is h and that of the superconducting film t_{ef}.[6]

The field resolution related to the intrinsic SQUID noise depends strongly on the SQUID inductance. Following the schematic diagram given in Fig. 2 L can be expressed as a function of the washer inductance L_w as follows:

$$L = L_w\frac{L_p + \ell_{sw}n^2m^2}{L_p + (L_w + \ell_{sw})m^2n^2} , \quad (6)$$

where $L_p = m^2r_p\ell_s + L_l$ and $\ell_{sw} = 2w_s\Omega\ell_s$ Now

$$\left\langle B_n^2 \right\rangle = \frac{\Psi}{m^2}\left(\frac{\beta^2}{\alpha Z_s} + \frac{L_w^{3/2}\gamma\sqrt{C}}{2n^2L_l^2}\frac{\sqrt{m^2n^2\left(1 + \frac{\ell_{sw}}{L_w}\right) + \frac{L_p}{L_w}}}{\left(n^2m^2\frac{\ell_{sw}}{L_w} + \frac{L_p}{L_w}\right)^{-3/2}}\right) \quad (7)$$

We next optimise the field resolution in respect to the number of the turns in the signal coil. If we assume that $L_w \gg \ell_{sw}$, then

$$n_{opt}^2 \approx \frac{L_p}{2m^2\ell_{sw}}\left(1 + 3\frac{\ell_{sw}}{L_w}\right) \quad (8)$$

and the resolution becomes

$$\left\langle B_n^2 \right\rangle \approx \frac{\Psi\beta^2}{\alpha Z_sm^2} + \frac{4\Psi\gamma\sqrt{C\ell_{sw}}}{3L_l}\left(1 + \frac{m^2r_p\ell_s}{L_l}\right)\left(1 + \frac{3\ell_{sw}}{2L_w}\right) \quad (9)$$

The optimisation with respect to m leads to

$$m_{opt}^2 \approx \frac{L_l\beta}{\sqrt{r_p\ell_s\alpha Z_s\gamma\sqrt{C\ell_{sw}}}}\left(1 - \frac{3}{4}\frac{\ell_{sw}}{L_w}\right) \quad (10)$$

Setting $Z_s = \sqrt{\ell_s/c_s} = c_\epsilon\ell_s/\sqrt{\Theta}$ we find

$$\left\langle B_n^2 \right\rangle \approx \frac{3\alpha E\gamma\sqrt{C\xi}}{r_p^3}\left(1 + \frac{\xi}{L_w} + \sqrt{\frac{4\beta_L^2r_p}{\gamma\alpha c_\epsilon}\left(1 + \frac{\xi}{L_w}\right)\sqrt{\frac{\Theta}{\xi C}}}\right) \quad (11)$$

where $\xi = 3\Omega\mu_0 h\Theta/K_s$ and $E = \chi\mu_0 k_B T$. The inductance of the circular loop is given in the form $L_l = 2\chi\mu_0\pi r_p$, where r_p is the radius and χ depends on the thickness of the stripline ($\chi \sim 4$). Equation (11) indicates that the better the field resolution the higher the SQUID washer inductance L_w. On the other hand 1/f noise resulting from the critical current fluctuations is smaller the smaller the inductance and thus

$$L_w = \theta\xi = \theta\frac{3\Omega\mu_0 h}{K_s}\left(1+\frac{\lambda_L^2}{ht_{ef}}\right), \qquad (12)$$

where $\theta = 3-6$ is a good compromise.

For small pick-up loops, $r_p < 0.03\alpha c_\epsilon\sqrt{\mu_0 hC}$, the field resolution can be given as

$$\langle B_n^2\rangle \approx \frac{5\alpha E}{r_p^3}\sqrt{\frac{\mu_0\Omega C}{K_s}\left(h+\frac{\lambda_L^2}{t_{ef}}\right)}. \qquad (13)$$

Equation (13) shows that the insulation barrier h between superconducting layers should be as thin as possible until the resolution will be limited by the London penetration depth.

The field resolution can be improved by enlarging the pick-up loop area. The noise from the microwave termination becomes dominant and thus the optimisation leads to a low β device. If we optimise Eq.(11) with respect to β, we find $\beta^{opt} \approx 0.64\left(\alpha c_\epsilon\sqrt{\Omega\mu_0 hC}/r_p\right)^{1/9}$ and

$$\langle B_n^2\rangle \approx \frac{5\chi\mu_0 k_B T}{r_p^{5/2}}\sqrt{\frac{\alpha}{c_\epsilon}\sqrt{\frac{C\Omega\mu_0 h}{K_s}\left(1+\frac{\lambda_L^2}{ht_{ef}}\right)}}. \qquad (14)$$

The resolution can be now minimized by adjusting the thickness of the barrier $h^{opt} = \lambda_L^2/t_{ef}$ and finally we get

$$\langle B_n^2\rangle \approx \frac{7\chi\mu_0 k_B T}{r_p^{5/2}}\sqrt{\frac{\alpha}{c_\epsilon}\sqrt{\frac{C\Omega\mu_0}{K_s}\frac{\lambda_L^2}{t_{ef}}}}. \qquad (15)$$

The result shows that the field sensor favors thick superconducting films where the London penetration depth is as small as possible.

The optimisation can be done as follows: First, the thickness of the insulation barrier h should be minimized while the thickness of the superconducting films t_{ef} is maximized. Second, the SQUID washer inductance should be selected so that the parameter θ exceeds unity. The radius of the pick-up loop r_p should be chosen depending on the required field resolution. Finally, the number of sub-loops in the pick-up loop m and the number of turns in the signal coil n can be found from the following equations

$$m_{opt}^2 \approx \frac{15\beta w_s\Omega}{2L_w^{5/4}}\sqrt{\frac{\chi\mu_0 L_l}{\gamma\alpha c_\epsilon}\sqrt{\frac{\Theta}{C}}}\left(1-\frac{1}{2\theta}\right), \qquad (16)$$

$$n_{opt}^2 \approx \frac{r_p}{4w_s\Omega}\left(1+\frac{2\pi\chi K_s}{m_{opt}^2\Theta}\frac{w_s}{h}\right)\left(1+\frac{2}{\theta}\right). \qquad (17)$$

Since the parasitic capacitance arising from the microstriplines does not increase the noise, the thickness of the insulation layer h should be as thin as possible to minimise the stray inductance. However, a thin insulation layer does not cover steps well enough; in practice, it should exceed the thickness of the lower superconducting film. Thus we get a simple guideline $h \gtrapprox t_{ef} \approx \lambda_L$.

If $\lambda_L = 80$ nm, $\chi = 4$, $t_{ef} = 100$ nm, $C = 1$ pH, $c_\epsilon = 10^8$ m/s and $\alpha = 12$, Eq.(15) predicts that the ultimate field resolution is about 0.05 fT/$\sqrt{\text{Hz}}$ with a pick-up loop of radius 10 mm. In this case $\beta \approx 0.5$. The un SQUID having $\alpha \approx 4$ provides only slihgly better field resolution than the conventional dc SQUID ($\alpha = 12$).

III. Conclusion

We have shown that the simultaneous optimization of the SQUID and the pick-up loop parameters enables us to improve the field resolution. Since in our model the effective capacitance across the SQUID loop resulting from the transmission lines is accepted without noise rise, the system favors the transmission lines having low characteristic impedance. Consequently, the transmission lines produces a large capacitance across the SQUID dividing the SQUID ring into the two parts at high frequencies. The SQUID having a large pick-up loop actually operates in the double-loop mode and the field noise is limited by the thermal noise from the microwave terminations. That noise can be minimized by reducing β parameter until the intrinsic noise of the SQUID becomes important. For the given pick-up loop area the ultimate limitation for the field resolution is due to the London penetration depth.

References

[1] T. Ryhänen, H. Seppä, R. Ilmoniemi, and J. Knuutila *J. Low Temp. Phys.*, **46**, 345–678, 1989.

[2] H. Seppä, M. Kiviranta, V. Virkki, L. Grönberg, J. Salonen, P. Majander, I. Suni, J. Knuutila, J. Simola and A. Oittinen, *Extended abstracts of ISEC '97*, PTB, 38116, Braunschweig, Germany (preprint: www.iki.fi/~msk/isec97).

[3] C.D Tesche, *J. Low Temp. Phys.* **44**, 119 (1981).

[4] M. Kiviranta and H. Seppä. "Noise simulation of the un SQUID", *Appl. Supercond.*, in press. (preprint: www.iki.fi/~msk/isec97).

[5] T. Ryhänen, H. Seppä, and R. Cantor, *J. App. Phys.*, **71** (12) 6150, June 1992.

[6] W. H. Chang, *J. Appl. Phys.* **50** (12), Dec. 1979.

Comparison of dc SQUID readout methods based on positive feedback

Mikko Kiviranta and Heikki Seppä
VTT Automation, Measurement Technology
Otakaari 7B, 02150 Espoo, Finland

Abstract— **Positive local feedback can be used to facilitate noise matching between a sensor (e.g. SQUID, single electron transistor, bolometer) and a preamplifier. The possible feedback topologies are introduced and two techniques for dc SQUID readout are compared. The techniques result in similar theoretical noise and flux range performance, but the current readout is more convenient from the practical point of view.**

I. Introduction

The challenge in the design of the dc SQUID readout is to obtain a system whose noise is limited by the SQUID instead of the readout electronics. The noise temperature at the low-T_c SQUID output is in the order of 20 K (assuming here 50 pV/$\sqrt{\text{Hz}}$ at 2 Ω). This noise temperature is easily achieved with room-temperature FET-input amplifiers (eg. AD743: $T_{n,\text{opt}} = 0.8$ K, $R_{\text{opt}} = 460$ kΩ) but not so readily with bipolar amplifiers (eg. AD797: $T_{n,\text{opt}} = 65$ K, $R_{\text{opt}} = 450$ Ω). A further problem is that the amplifiers reach the above-mentioned noise temperatures only when the source impedance equals R_{opt}; at non-optimal source R_d the effective noise temperature is degraded as

$$T_n = \frac{1}{2} T_{n,\text{opt}} \left(\frac{R_d}{R_{\text{opt}}} + \frac{R_{\text{opt}}}{R_d} \right), \qquad (1)$$

where $T_{n,\text{opt}} = u_n i_n / 2k_B$ and $R_{\text{opt}} = u_n / i_n$ can be expressed in terms of spectral densities of the equivalent voltage (u_n) and current (i_n) noise generators at the amplifier input.

Matching the source impedance with the amplifier has traditionally been attempted by use of a transformer. Modulation is needed in this approach if one wishes to register dc signals. If bias reversal techniques are utilized [8], modulation is available as a by-product anyway. More recently, increase of the SQUID R_d has been aimed for by non-standard shunting of the junctions [3] or by use of various feedback topologies. The method of positive feedback was patented in the context of radio receivers by E. H. Armstrong in 1914, utilized in a simple manner with SQUIDs by Clarke et al. [4] and advocated more recently by Drung et al. [5] under the name APF. A slightly different method (noise cancellation, NC) has been proposed in the context of dc SQUIDs by Seppä et al. [1][2]. The feedback methods have an advantage over a simple transformer because they also increase the gain and thus the noise temperature at the SQUID output (without degradation of the S/N ratio). This is achieved because the signal is regeneratively fed back through the amplification mechanism of the SQUID.

[0]Manuscript received May 5th, 1999.

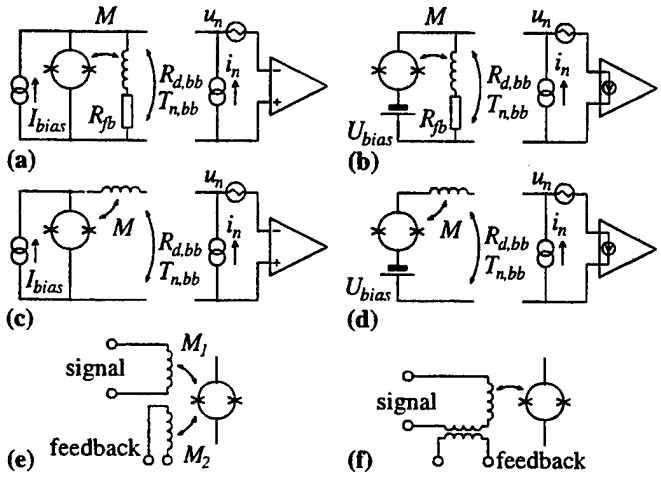

Figure 1 – Feedback topologies at SQUID output: voltage sampling, voltage readout **(a)**; voltage sampling, current readout **(b)**; current sampling, voltage readout **(c)**; and current sampling, current readout **(d)**. Feedback topologies at SQUID input: shunt **(e)** and series **(f)**.

II. Noise matching properties

There is a large variety of possible feedback topologies, including

$$\left.\begin{matrix}\text{positive}\\ \text{negative}\end{matrix}\right\} \left.\begin{matrix}\text{V-sampling}\\ \text{I-sampling}\end{matrix}\right\} \left.\begin{matrix}\text{V-readout}\\ \text{I-readout}\end{matrix}\right\} \left.\begin{matrix}\text{shunt input}\\ \text{series input}\end{matrix}\right\},$$

where the terminology of standard amplifier theory (eg. [9]) is used. Furthermore, the feedback methods can be applied to any device capable of providing power gain and the fed back quantity may be e.g. magnetic flux (SQUIDs), electric charge (single electron transistors or SETs) or temperature (bolometers) [6][7]. A few of the alternatives for feedback topology are depicted in the Fig. 1.

We a linearized response for the bare SQUID at a given point of operation, characterized by dynamic resistance $R_{d,\mathrm{sq}} = \partial V/\partial I$ and transfer gain $G_{V,\mathrm{sq}} = \partial V/\partial \Phi$ (or $G_{I,\mathrm{sq}} = G_{V,\mathrm{sq}} = (\partial V/\partial \Phi)/R_{d,\mathrm{sq}}$). The SQUID and its local feedback circuit are considered as a black box characterized by its responses $R_{d,\mathrm{bb}}$ and $G_{V,\mathrm{bb}}$ or $G_{I,\mathrm{bb}}$ to small test signals.

The noise temperature at either the black box or bare SQUID output can be defined in two equivalent ways:

$$T_n = \frac{\Phi_n^2 G_V^2}{4k_B R_d} = \frac{\Phi_n^2 G_I^2 R_d}{4k_B}$$

where ϕ_n is the flux noise at the SQUID input. The response functions are modified due to the feedback in the voltage-sampling cases as

$$R_{d,\mathrm{bb}} = \frac{R_{d,\mathrm{sq}}}{1-\gamma_V}, \quad G_{V,\mathrm{bb}} = \frac{G_{V,\mathrm{sq}}}{1-\gamma_V}, \quad G_{I,\mathrm{bb}} = G_{I,\mathrm{sq}} \ ,$$

where $\gamma_V = G_{V,\mathrm{sq}} M/R_{\mathrm{fb}}$, and in the current-sampling cases as

$$R_{d,\mathrm{bb}} = R_{d,\mathrm{sq}}(1-\gamma_I), \quad G_{V,\mathrm{bb}} = G_{V,\mathrm{sq}}, \quad G_{I,\mathrm{bb}} = \frac{G_{I,\mathrm{sq}}}{1-\gamma_I} \ ,$$

where $\gamma_I = G_{I,\mathrm{sq}} M$. The noise temperature at the black box output becomes

$$T_{n,\mathrm{bb}} = \frac{T_{n,\mathrm{sq}}}{1-\gamma_V} \quad \text{or} \quad T_{n,\mathrm{bb}} = \frac{T_{n,\mathrm{sq}}}{1-\gamma_I} \qquad (2)$$

where γ_V is to be used in the voltage-sampling and γ_I in the current-sampling cases.

The noise matching a room-temperature amplifier to a SQUID reduces now to the problem of finding a feedback topology that yields higher noise temperature at black box output, Eq. 2, than the noise temperature due to the amplifier , Eq. 1. Because γ_V and γ_I can change sign depending on the Φ - point of operation, both positive ($T_{n,\mathrm{bb}} > T_{n,\mathrm{sq}}$) and negative ($T_{n,\mathrm{bb}} < T_{n,\mathrm{sq}}$) feedback is possible. On the slope with positive feedback voltage sampling increases $R_{d,\mathrm{bb}}$ and is thus advantageous for SQUID readouts, whereas current sampling tends to decrease $R_{d,\mathrm{bb}}$ which is sometimes advantageous in SET readouts. Both voltage sampling and current sampling can be used simultaneously to allow control of $R_{d,\mathrm{bb}}$ and $T_{n,\mathrm{bb}}$ independent of each other. In the case of voltage readout Drung has called this technique 'Bias Current Feedback [10]. Making the feedback circuit frequency-dependent would allow matching even when R_d and T_n depend on frequency.

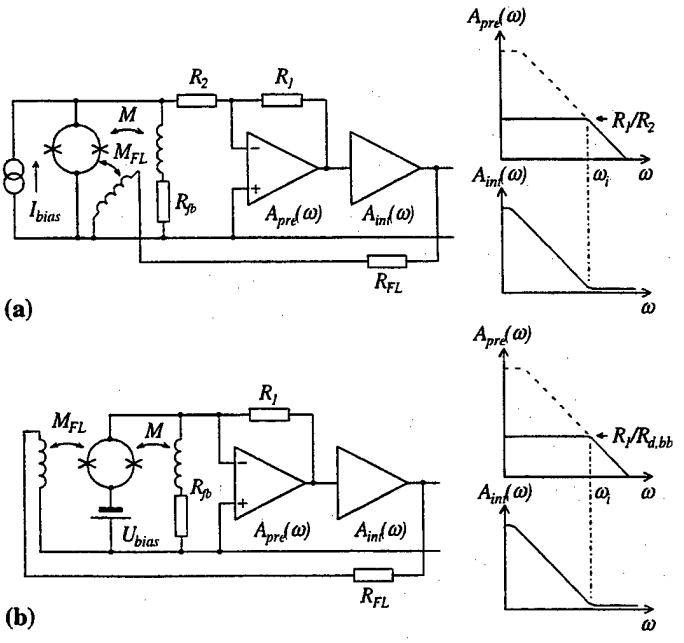

Figure 2 – A realization of flux locked loop in the case of voltage readout (a) and current readout (b). Frequency responses of the available preamplifier $A_{\mathrm{pre}}(\omega)$ and the integrator $A_{\mathrm{int}}(\omega)$ are assumed to be similar in both cases. For stable closed-loop operation the combined frequency response must have phase shift (related to the slope of $A(\omega)$ by Kronig-Kramers [Bode] relation) less than 180^o when open-loop gain >1.

An additional noise source is the resistor R_{pf} , which is needed if voltage sampling in flux feedback (SQUID) or current sampling in charge feedback (SET) is desired. In the SQUID case it is advantageous to reduce both M and R_{pf} until feedback circuit begins to load the SQUID too much. It can be shown that the requirement $R_{\mathrm{pf}} > R_{d,\mathrm{sq}}$ leads to deterioration of the theoretical energy resolution [11] $\varepsilon = 6.7 k_B T (L/R)$ by a factor of > 2.

Because a capacitive analogy of a multi-turn transformer does not exist, the achievable γ_I in the charge-feedback (SET) case is quite limited. The SET case is somewhat analogous to the case in [4]: the effective M cannot exceed the SQUID loop inductance, which is equivalent of having a feedback coil with only one turn.

III. Operation in flux-locked loop

Typically SQUID magnetometers are operated in flux locked loop (Fig. 2), in which negative flux feedback is used to linearize the flux response. An important figure-of-merit is the signal flux range as a function of frequency. An equivalent figure-of-merit is the slew rate, which is independent of frequency if the simple integrator is used for $A_{\mathrm{int}}(\omega)$. It is clearer to use the parameter of direct interest, however, if a more complex frequency reponse such

as double-pole or 3/2-pole integrator is used.

The controller loses lock when the applied flux Φ_a, which is a sum of the signal flux Φ_s and feedback fluxes, exceeds $\pm\Phi_0/4$. Using the notation of Fig. 2 one gets in the case of current readout (or NC)

$$\Phi_a \approx \frac{\Phi_s}{1-\gamma_I \frac{R_1}{R_{fb} A_{\mathrm{pre}}(\omega)} + \frac{R_1}{R_d} G_V A_{\mathrm{int}}(\omega) \frac{M_{\mathrm{FL}}}{R_{\mathrm{FL}}}}.$$

The negative term in the denominator can be identified with the positive feedback at high frequencies where the preamplifier cannot keep the virtual ground at its input and the SQUID becomes current biased rather than voltage biased. Arranging a high-frequency cutoff to the M_{FB}-R_{FB} circuit and thus making γ_I frequency-dependent allows non-diverging operation even in the case $\gamma_I \geq 1$. The consequent rise of the noise level above the cutoff frequency does no harm in typical applications, in which low-noise readout is needed only at low frequencies, and the wide controller bandwidth is used only to make the system tolerant to magnetic interference. In such circumstances optimal solution would be to arrange *local* feedback to be positive (to reduce noise) only in the actual signal band, and make it negative (to increase flux range) at higher frequencies. This way the preamplifier noise is fed back to the SQUID loop over the actual signal bandwidth only, which makes it easier to satisfy the requirement that the RMS flux noise in the SQUID loop must be $\ll \Phi_0$.

In the case of voltage readout (or APF)

$$\Phi_a \approx \frac{\Phi_s}{1-\gamma_V + \frac{R_1}{R_2} G_V A_{\mathrm{int}}(\omega) \frac{M_{\mathrm{FL}}}{R_{\mathrm{FL}}}}.$$

The negative term in the denominator makes the system unstable when $\gamma_V \gtrsim 1$ either in open loop at all frequencies or in closed loop at high frequencies where the negative flux feedback cuts off. Unfortunately, this is the desired point of operation to minimize the amplifier noise. A high-frequency M_{FB}-R_{FB} cutoff would result in a stable operation in flux-locked loop but not in open loop.

If similar amplifiers are available, both voltage readout and current readout lead to similar flux range. The black box flux range reduction by the factor $1/(1-\gamma_V)$ in the voltage readout case is compensated by increase of the controller gain by the same factor in the flux locked loop.

IV. Conlusion

Positive feedback techniques with abbreviations such as APF, NC, BCF can be viewed in the framework of the standard noise matching problem, when the device characteristics are modified in the way described by the standard amplifier theory. The techiques can be generalized to any device capable of providing power gain.

The APF and NC techniques for SQUIDs appear to have similar noise and flux range (slew rate) performance. In the NC, however, part of the negative feedback (current) is active already when the flux loop is open, which allows easy adjustment of the operating point and γ. In the APF, operation in the open flux loop mode is more difficult because de-linearizing and potentially unstabilizing impact of positive feedback is present, and only after closing the flux loop the negative feedback takes effect.

Both methods benefit from the use of a cooled FET [2] as feedback control resistor because it allows adjustment of γ independ of the point of operation of the bare SQUID.

References

[1] H. Seppä, A. Ahonen, J. Knuutila, J. Simola and V. Vilkman, "Dc-SQUID electronics based on adaptive positive feedback: experiments", *IEEE Trans. Magn,* vol. MAG-27, no. 2, p. 2488, March 1991.

[2] H. Seppä, "Dc-SQUID electronics based on adaptive noise cancellation and a high open-loop gain controller", in *Superconducting devices and their applications,* Springer proceedings in physics vol. 64, p. 346, 1992.

[3] H. Seppä, M. Kiviranta and L. Grönberg, "Dc SQUID based on unshunted Josephson junctions: experimental results", *IEEE Trans. Appl. Supercond,* vol. 5, no. 2, p. 3248, June 1995.

[4] J. Clarke and J. L. Paterson, "Josephson-junction amplifier", *Appl. Phys. Lett,* vol. 19, no. 11, p. 469, December 1971.

[5] D. Drung, R. Cantor, M. Peters, H. J. Scheer and H. Koch, "Low-noise high-speed cd SQUID magnetometer with simplified feedback electronics", *Appl. Phys. Lett,* vol.57, no. 4, p. 406, July 1990.

[6] J. C. Mather, "Bolometer noise: nonequilibrium theory", *Applied Optics,* vol. 21, no. 6, p. 1125, March 1982.

[7] A. T. Lee, P. L. Richards, Sae Woo Nam, B. Cabrera and K. D. Irwin, "A superconducting bolometer with strong electrothermal feedback", *Appl. Phys. Lett,* vol. 69, no. 12, p. 1801, September 1996.

[8] M. Lam Chok Sing, C. Dolabdjian, C. Gunther and D. Bloyet, *Rev. Sci. Instrum,* vol. 67, no. 3, p. 796, March 1996.

[9] J. Millman, *Microelectronics,* chapter 12, McGraw-Hill 1979.

[10] D. Drung, "Advanced SQUID read-out electronics", in *SQUID sensors: fundamentals, fabrication and applications,* H. Weinstock (ed.), p. 92, Kluwer 1996.

[11] T. Ryhänen, H. Seppä, R. Ilmoniemi and J. Knuutila, "SQUID magnetometers for low-frequency applications", *J. Low Temp. Phys,* vol. 76, nos. 5/6, p. 328, September 1989.

Optimisation of the SQUID Read-Out Circuit for Cryogenic Particle Detector

Sergey V. Uchaikin, CRESST Collaboration

Max-Planck Insitut für Physik, Föhringer Ring, 6, München, D-80805, GERMANY
Joint Institute for Nuclear Research, Dubna, 141980, RUSSIA

The transfer function and noise performance of the SQUID read-out circuit for the cryogenic particle detector with superconducting phase transition thermometer are analysed. The noise equivalent circuit is designed. Effects of the electrothermal and thermal feedback on the noise and dynamic properties are discussed. The procedure to determine the optimum signal to noise ratio is developed.

High-Tc SQUID Microscope with sample chamber

Saburo Tanaka, Osamu Yamazaki, Ryoji Shimizu and Yusuke Saito
Ecological Engineering, Toyohashi University of Technology
1-1 Hibarigaoka Tempaku-cho Toyohashi Aichi 441-8580, Japan

Abstract— We have designed and constructed a high-Tc superconducting quantum interference device (SQUID) microscope with a sample chamber isolated by a shutter. It can image magnetic distributions of samples at both room temperature and 77 K. According to our scheme, the separation of the sample from the SQUID can be less than several micrometers, in principle. We have successfully imaged a trapped flux in a $YBa_2Cu_3O_{7-y}$ thin-film ring at 77 K and a printouts of a laser printer at room temperature.

I. INTRODUCTION

It is important to image weak magnetic fields by a superconducting quantum interference device (SQUID) microscope not only for non-destructive evaluation (NDE) but also for studies in physics such as vortex dynamics [1-6]. Although a high-Tc SQUID is typically one order of magnitude less sensitive than a 4.2 K low-Tc SQUID, there are many advantages of using high-Tc SQUIDs such as easy thermal insulation, easy handling and low running cost [7,8]. High-Tc SQUID microscopes reported to date are classified into two types; one is for cold samples (77K) and the other is for room temperature-samples. Black and coworkers pioneered the use of high-Tc SQUIDs operated at liquid N_2 temperature to evaluate cold samples [9,10]. Recently, a high-Tc SQUID microscope for room-temperature samples has been developed and used for biological applications [11,12]. In the SQUID microscope for cold samples, the accumulation of ice on the sample is one of the major problems because the SQUID and the sample are immersed in liquid nitrogen. An obvious disadvantage of the system is that the time required for thermal cycling is long. In the SQUID for room-temperature samples, there is no icing problem, but the separation of the sample from the SQUID can not be less than several ten micrometers, because of the presence of a window isolating the sample from the cold SQUID in vacuum. We have developed a high-Tc SQUID microscope with a sample chamber isolated by a shutter gate. After pumping both the cryostat and the sample chamber, the shutter is opened and the sample is positioned as close as possible to the SQUID. Thus the microscope becomes "windowless". According to our scheme, the temperature of the sample can be changed and the distance between the sample and the SQUID can be reduced to several micrometers, in principle [13]. After finishing the evaluation, the shutter will be closed again. We present here the design of our windowless high-Tc SQUID microscope and some results of 2D field images.

Manuscript received April 30, 1999.

II. CONSTRUCTION OF MICROSCOPE

We used a $YBa_2Cu_3O_{7-y}$ (YBCO) SQUID magnetometer for the system. This SQUID is a product of Sumitomo Electric Ind., Ltd [14]. The junctions utilized in the SQUID are of the step-edge type. The washer size of the SQUID is about 2.5 mm x 2.5 mm and the effective area is 0.11 mm^2. The inner hole is rectangular and its size is 5 μm x 200 μm.

The configuration of the microscope is shown in Figs.1 and 2. Most parts of the cryostat are made of G-10 fiberglass and Delrin. They are nonmetallic except for a copper reservoir, liquid N_2 filling tubes and stainless steel bellows. The size of the cryostat is 250 mm in diameter and 280 mm in height.

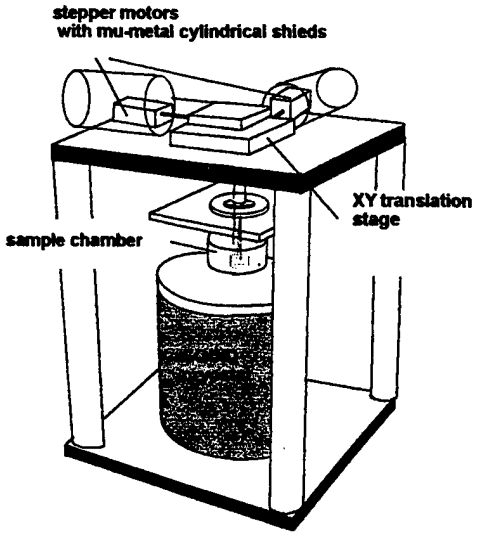

Fig. 1 Side view of microscope. The sample chamber is connected to the cryostat, which includes a high-Tc SQUID chip. The sample holder is suspended from the XY translation stage. The stage can be driven by stepper motors. The frame consists of ϕ50 x 500 mm Derlin columns and 20 mm-thick 420 x 420 mm^2 aluminum alloy plates.

The cryostat contains a liquid N_2 copper reservoir, the volume of which is 0.8 liters. The reservoir is superinsulated by 30

layers of single-sided aluminum evaporated mylar sheet. The inside of the cryostat can be evacuated by a vacuum pump and sealed off by an o-ring valve. The SQUID chip is silver pasted on top of a sapphire rod thermally anchored with the liquid N_2 reservoir. This cryostat can keep liquid N_2 for 17.5 hours. The SQUID is 50 mm far from the metallic reservoir. A modulation coil and a heater are installed in the upper end of the sapphire rod. A copper wire step-up transformer is glued tightly to the top of the copper reservoir. Electrical contacts to the SQUID chip are made by applying conductive silver paint to the bonding pads and the side of the SQUID chip.

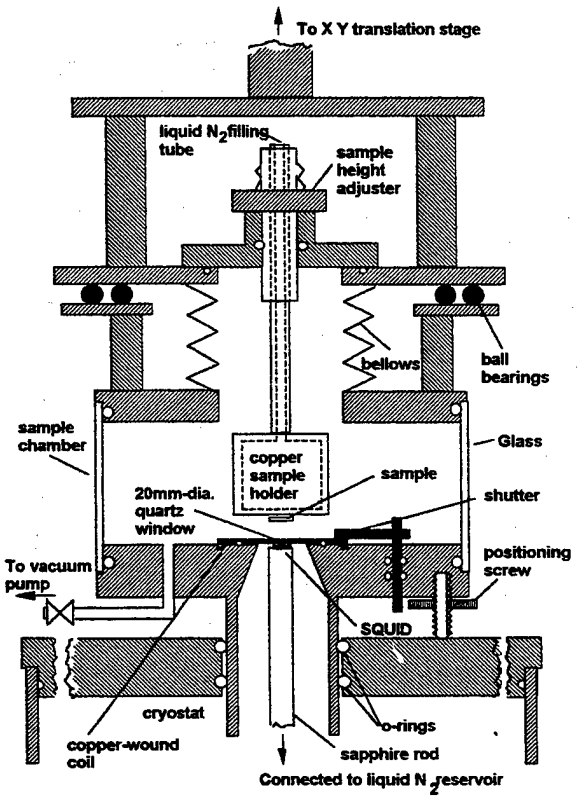

Fig.2 Detailed side view of sample chamber. The sample chamber and the cryostat can be separately evacuated. The shutter gate is installed between them. Motion can be controlled from the outside. The copper sample holder can be cooled by filling it with liquid nitrogen.

The size of a sample chamber is 100 mm diameter x 60 mm height. The details of the chamber are shown in Fig. 2. The chamber consists of top and bottom fiberglass discs with a hole at the center and a quartz cylindrical glass. These discs are sealed by o-rings. The bottom plate is coupled to the top plate of the cryostat through a fiberglass tube. The chamber with the cryostat looks like a "double-decker." The position of the sample chamber can be changed by turning three positioning screws set at the bottom of the sample chamber. A sample holder made of copper, which contains 10 ml of liquid N_2, is centered on top of the chamber via stainless steel bellows. The vertical position of the holder can be adjusted by a height adjuster. The upper end of the bellows is connected to an aluminum alloy disc, which is placed on a flat plate via steel ball bearings. Thus, the disc with the sample holder can be moved smoothly in the X and Y directions with low friction. A 20 mm-diameter quartz vacuum window shutter, which can be opened and closed from outside the sample chamber, is installed on the bottom disc. When it is closed, one can independently evacuate the sample chamber from a vacuum pump-out flange. A 20 mm-diameter copper-wound coil, which can generate a known magnetic field to the sample, is equipped around the window hole.

The sample holder is connected to an XY translation stage placed on an upper 20 mm-thick aluminum alloy table supported by four 60 mm-diameter Delrin columns. The stage is made of aluminum alloy and driven by stepper motors, and is surrounded by a 1 mm-thick mu-metal cylindrical shield to suppress noise generated by the stepper motors. The minimum step size is 1.4 μm. The wobbling of the X direction screw is somewhat large and about 100 μm, though that of Y direction is less than 10 μm. The maximum scan range is 10 x 10 mm^2 and the maximum scan speed is 1.2 mm/s.

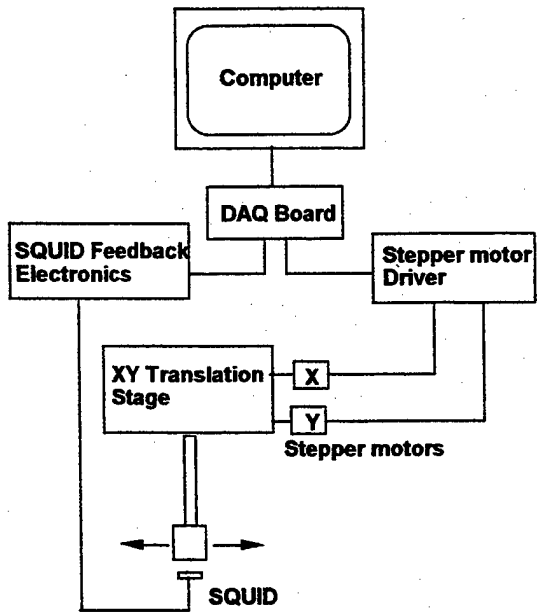

Fig.3 Schematic layout of electronics and data acquisition system. The signal voltage is coupled to an A/D interface board (NI-1200) and stored in a Macintosh 7200/90 computer. The program controlling the system is homemade and based on LabVIEW 4.0 (National Instruments).

The SQUID is operated in a flux-locked loop with a flux modulation frequency of 100kHz. R_f/M_f is $1.7V/\phi_0$, where R_f is the feedback resistance of the system and M_f is the mutual inductance between the SQUID and the modulation coil. The magnetic flux noise $S\phi^{1/2}(f)$ is $80\mu\phi_0/Hz^{1/2}$ at 1Hz and $40\mu\phi_0/Hz^{1/2}$ in the white noise region. The schematic layout

of the electronics and the data acquisition system is shown in Fig. 3. The output voltage Vout of the SQUID electronics is low-pass filtered at a frequency of 10 Hz. The signal voltage is coupled to an A/D interface board (NI-1200) and stored in a Macintosh 7200/90 computer. The computer also supplies pulses to the stepper motors that drive the translation stage. The program controlling the system is homemade and based on LabVIEW 4.0 (National Instruments). The signal data are converted into false color contour image by the imaging software "Spyglass".

III. EXPERIMENTAL ANDDISCUSSION

We performed all of the measurements in a magnetically shielded room with a shielding factor of –50 dB for 0.1 Hz. A YBCO superconducting thin-film ring with outer dimensions of about 1.3x1.4 mm^2 and inner dimensions of about 0.7x0.8 mm^2 was prepared for imaging. It was put on the copper holder by applying a silver paste, which made good thermal contact. After pumping out the cryostat, SQUID was cooled down by filling liquid N_2 to the reservoir. Then the sample chamber was separately evacuated so that the pressure of the chamber became the same as that of the SQUID cryostat. Opening the shutter, the positioning screws were mated so that the SQUID and the sample became parallel and as close as possible to each other. The separation of the sample from the SQUID was about 100 μm. Firstly, the sample was scanned at room temperature in the range of 4.5x4.5 mm^2. The scan rates along the X and Y axes were 1.11 mm/s and 0.225 mm/step, respectively. The sampling rate was 10/s in the X axis scan. This implies that the number of data is 40x20 points. Figure 4(a) shows a 2D magnetic field image of the sample at room temperature. A field inhomogeneity from lower left corner to upper right corner exists. This inhomogeneity may be caused by the remanent field from the metallic components comprising the microscope, such as steel ball bearings or stainless steel bellows. The field variation from the minimum to the maximum in the region is about 60 nT. The YBCO thin-film ring was cooled to 77 K and then scanned over. No magnetic field was applied to the sample while cooling. The produced 2D image is shown in Fig. 4(b). The shape of the sample is shown on the right in the same scale. The trapped flux inside the ring could be clearly seen, though no field was applied while cooling. The magnetic field generated by the trapped flux is about 60 nT, which corresponds to $14\phi_0$, where ϕ_0 is a flux quantum. This trapped image is caused by the inhomogeneity of the environmental field. The jagged line along the Y axis is due to the backlash from the X direction. The reasons why the image is rounded and its size is larger than the real sample are explained by the size of the SQUID (2.5 mm x 2.5 mm) and the separation of the sample from the SQUID. Since the space resolution is restricted by the sensing area of the SQUID, it should be small to obtain good space resolution.

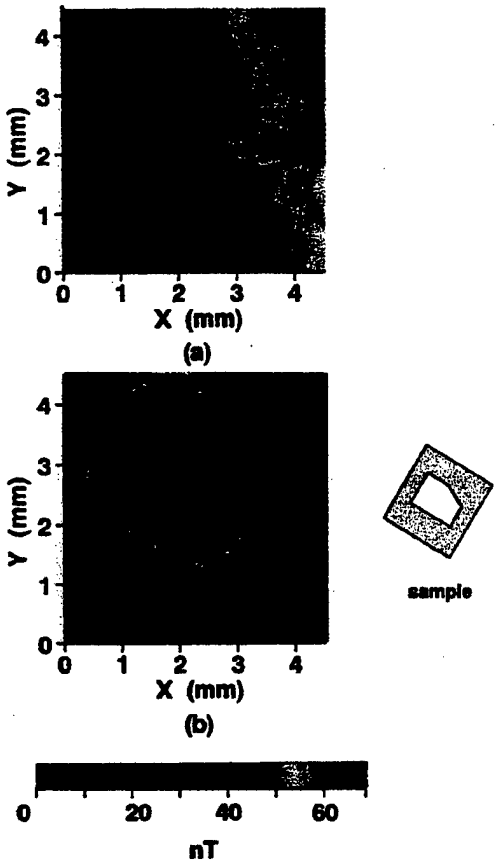

Fig.4 (a) 2D magnetic field image of YBCO thin-film ring at room temperature. Field distribution is caused by remanent field from metallic components comprising the microscope. (b)Field image of YBCO ring at 77 K. The magnetic field generated by the trapped flux is about 60nT, which corresponds to $14\phi_0$.

We could not reduce the distance between the SQUID and the sample to less than 100 μm because of the difficulty in closing them in parallel, though the distance can be less than several micrometers in principle. Therefore, the field image in the hole is broadened and the area looks larger than that of the real sample. To solve this problem, the adjusting mechanism should be improved. After the measurement, the sample holder was warmed up to room temperature by inserting a wire heater into the sample holder. It took only 5-6 minutes to warm it up. Problems such as icing were not observed.

We tried to scan a stripe-shaped printout of a laser printer, which ink contained magnetic particles. In order to obtain good resolution, the printout sample was almost touched to the SQUID. The scan range was 2 mm x 2 mm. The resulting image is shown in Fig. 5. The separation of the original pattern is 0.9mm and width of the solid area is 0.3 mm. In this case, the broadness of the pattern was improved. This means that the separation between the sample and the SQUID is an important factor to obtain a good space resolution.

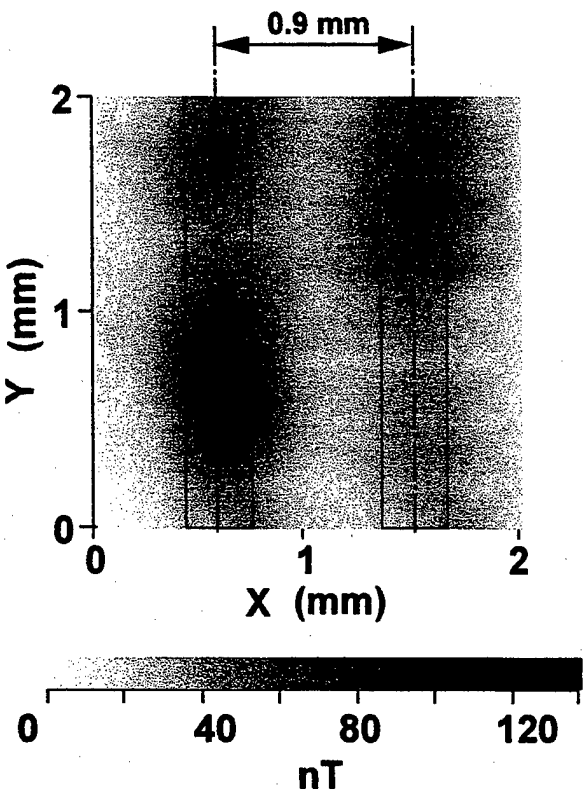

Fig. 5 Image of a printout line pattern of laser printer *Canon Laser Shot* and it's original pattern. The ink contains magnetic particles. The line separation is 0.9 mm. Dotted line shows the solid pattern area and the width is 0.3 mm.

IV. Conclusion

A high Tc SQUID microscope with a sample chamber isolated by a shutter was constructed. According to our scheme, the separation of the sample from the SQUID can be several micrometers, in principle. The other advantage of the system is that the required time for thermal cycling can be reduced without icing. Samples were measured at both room temperature and 77 K. A trapped flux in a YBCO thin-film ring could be imaged. By bringing in partially contact the sample on the SQUID, the space resolution was improved. When we imaged a magnetic printout line pattern with separation of 0.9mm, the broadness of the pattern was dramatically improved.

Acknowledgment

We thank Mr. M. Kanamori for writing the LabVIEW program. This work was partially supported by a Grant-in-Aid for Scientific Research on Priority Area (A) from the Ministry of Education, Science, Sports and Culture of Japan.

References

[1] G. Donaldson, S. Evanson, M. Otaka, K. Hasegawa, T. Shimizu, and K. Takaku, "Use of SQUID magnetic sensor to detect aging effects in duplex stainless steel," British Journal of NDT, **32,** pp. 238, 1990.

[2] H. Weinstock, "Prospects on the application of HTS SQUID magnetometry to nondestructive evaluation (NDE)," Physica C, **209,** pp. 269, 1993.

[3] C. C. Tsuei, J.R.Kirtley, C.C.Chi, Lock See Yu-Jahnes, A.Gupta, T.Shaw, J.Z.Sun and M.B.Ketchen, "Pairing symmetry and flux quantization in, a tri-crystal superconducting ring of YBa2Cu307", Phys. Rev. Lett. **73,** pp. 593, 1994.

[4] L. N. Vu, M. S. Wistrom, and D. J. Van Harlingen, "Imaging of magnetic vortices in superconducting networks and clusters by scanning SQUID microscopy". Appl. Phys. Lett. **63,** pp. 1693, 1993.

[5] N. Kasai, N. Ishikawa, H. Yamakawa, K. Chinone, S. Nakayama, and A. Odawara, "Nondestructive detection of dis-locations in steel using a SQUID gradiometer," IEEE Trans. Appl. Supercond. **7,** pp. 2315, 1997.

[6] T.Morooka, S.Nakayama, A.Odawara, M.Ikeda, S.Tanaka, and K.Chinone, "Micro-imaging System Using Scanning DC-SQUID Microscope" To be published in IEEE Trans. Appl. Supercond. 1999.

[7] S.Tanaka, H.Itozaki, H.Toyoda, N.Harada, A.Adachi, K.Okajima, and H.Kado: "Four-channel YBa2Cu3O7-y dc SQUID Magnetometer for Biomagnetic Measurement", Appl. Phys. Lett. **64,** pp. 514, 1994.

[8] J. P. Wikswo, "SQUID magnetometers for biomagnetism and nondestructive testing: Important questions and initial answers."IEEE Trans. Appl. Supercond. **5,** pp. 74, 1995.

[9] R. C. Black et al., "Magnetic microscopy using a liquid nitrogen cooled YBCO SQUID", Appl. Phys. Lett. **62,** pp. 2128, 1993.

[10] R. C. Black et al., "Eddy-current microscopy using a 77 K superconducting sensor", Appl. Phys. Lett. **64,** pp. 100, 1994.

[11] T. S. Lee, G. Dantsker, and John Clarke, "High-transition temperature SQUID microscope," Rev. Sci. Inst. **67,** pp. 4208, 1996.

[12] T.Shaw, K.Schlenga R. McDermott, John Clarke, J.W.Chen, S.-H.Kang, and J.W.Morris, Jr., "High-Tc SQUID microscope Study of the Effects of Microstructure and Deformation on the Remanent Magnetization of " To be published in IEEE Trans. Appl. Supercond. 1999.

[13] S. Tanaka, O. Yamazaki, R. Shimizu, Y. Saito, "Windowless High Tc Superconducting Quantum Interference Device Microscope", To be published in Jpn. J. Appl. Phys. 1999.

[14] Catalog on web page: http://squid.sei.co.jp, E-mail: squid@info.sei.co.jp

Study into the Feasibility of SQUID Sensors for Use in Geophysical Exploration

G Macmillan and P de Groot
Dept of Physics and Astronomy, University of Southampton, SO17 1BJ, UK.

Y Zhuravlev and D Rassi
School of Health Science, University of Wales Swansea, SA2 8PP, UK.

Abstract.— The high sensitivity of modern high temperature SQUID sensors offers the potential for application in geophysical exploration. We have investigated the performance of the latest HTM100 SQUID sensors (as supplied by Tristan Technology) for use in magnetotellurics (MT) and electromagnetic induced (EM) methods. The HTM100 performance is compared to that of other high T_c and low T_c SQUIDs and fluxgate magnetometers. Data will be presented of SQUID performance, both from laboratory and field environments. The progress towards geophysical application and the aspects still requiring attention before fully integrated systems are available will be discussed.

I. Introduction

The use of high transition temperature SQUIDs as magnetic detectors in MT and EM is becoming a practical proposition with the recent improvements in the sensitivity and noise immunity of these sensors. The principal requirement for such applications is the stable and low-noise operation of the SQUID system whilst subject to the earth's magnetic field and other environmental magnetic disturbances.

There has been much documentation on the critical current (I_c) of Josephson junctions being dependent upon the magnetic flux penetrating the junction [1]. Hence the earth's magnetic field can adversely affect the performance of high-T_c dc SQUIDs, due to the Fraunhofer-type field dependence of the critical current in the Josephson junctions.

Tristan Technologies Inc. supply high-T_c SQUID sensors (HTM100) that are specified to work well in a magnetically unshielded location. The intrinsic noise of the HTM100 sensors was quoted to be about 100 fT $Hz^{-1/2}$ at 1 Hz and 20-30 fT $Hz^{-1/2}$ white noise above 100 Hz in zero field. Further data on the sensor performance in simulated field tests were obtained from Faley *et al.* [2]. These results were obtained by placing a $SmCo_5$ magnet close to the sensor inside magnetic shielding; giving some idea of their performance in an open field, although only actual field tests can confirm their true open field performance.

Manuscript received April 30, 1999.

This work was supported by the EPSRC.

In this work we have characterised the performance of the SQUID sensors in zero magnetic field and compared it to that of the Mag-03 fluxgate magnetometer (Bartington Instruments.) Similar measurements were then repeated in a rural location in South Wales far from major conurbations and roads. In these field tests the SQUID sensors operated within the earth's magnetic field and the magnetotelluric signals.

SQUID magnetometers must be compared with fluxgates and other sensitive magnetometers including proton precession and alkali vapour magnetometers, although probably the most widely used magnetic sensor in geophysical applications are modern induction coils that claim resolution as low as 100 fT $Hz^{-1/2}$ at 1 Hz, and a white noise figure of around 30 fT $Hz^{-1/2}$ from 10 Hz up to around 100 Hz. High temperature SQUID magnetometers can match these figures, offer better linearity and have the added advantage of their considerably smaller size and weight. With three orthogonal SQUID magnetometers mounted in a single cryostat, deployment of the instrument would be much simpler than three induction coils. A small cryostat containing about 2 litres of liquid nitrogen could have a hold time of the order of several weeks. This gives high-T_c SQUIDs an advantage over their otherwise superior low temperature counterparts, where a similar helium cryostat would have a hold time of roughly a day. It is evident that if the performance of high-T_c sensors were sufficient, they would form the best choice in applications where portability, remoteness and practicality are serious issues.

II. Laboratory and Field Set-up

To test the sensors fully they were first assessed in the laboratory protected from magnetic interference, both static and dynamic, by using three mu-metal shields per sensor. The earth's magnetic field of approximately 50 μT was reduced by over two orders of magnitude inside the magnetic shielding. These measurements provided the baseline performance of the sensors. Bartington Instruments provided data on similar tests in triple shielding with their lowest noise triple axis fluxgate sensors.

Because the measurement bandwidth in geophysical prospecting can range from kHz down to mHz, two different types of measurement were performed. Long time-base data were collected at a rate of one sample per second for up to 1000 seconds. The plotting of this data (magnetic field versus time) provides information on a time interval of 'field drift' of the magnetometer. Data were also collected at a sampling rate of 1000 Hz for ten seconds in order to construct power spectra allowing more detailed analysis of sensor performance. Here the field drift results have been presented since they can be directly compared to the fluxgate data. The triple shielded power spectrum information confirmed the manufacturer's specification of the HTM100 SQUID sensors.

The fieldwork was performed in a similar way, except the data sampling rate was 300 Hz with three times oversampling (actual sampling rate 900Hz with each set of 3 points being averaged.) We set the sensors up in a gradiometer arrangement. The system was supplied with the standard Conductus iMC-303 control electronics. A glassfibre nitrogen cryostat and Tufnol sensor holder were constructed ensuring that no ferrous metallic components were used. The entire system, including data collection and controller were converted to battery power to enable operation in the field. The glassfibre cryostat was placed inside a wooden box that was stabilised on level ground. It is essential to minimise any physical movement of the magnetometer as a 0.01 ppm change in the orientation of the sensor within the earth's magnetic field can cause a change of around 0.5 pT which is of the same order of magnitude as the signals to be measured. Vibration of the system (*e.g.* due to wind) can easily produce such minute changes in orientation. It should be noted, however, that wind and other sources of vibration normally occur at low frequencies and result in an overall increase in the 1/f region of the noise spectrum of the sensor.

It is important to note that the power spectra of the triple shielded sensors obtained in the laboratory were for individual sensor output, whereas the power spectra recorded in the field are of the subtracted difference between the two gradiometer channels. The point of taking the difference between the two channels is to remove the large background magnetotelluric disturbances that are filtered out when triple shielded in the laboratory.

III. Experimental Results

The zero-field characterisation of the high-T_c SQUID sensors and comparison with fluxgate data are shown in Fig. 1. The results obtained in a shielded environment show magnetic field drift of the two HTM100 SQUID sensors over a period of 300 seconds. Over ten runs, the peak-to-peak field drift of the smoothed data was around 20 pT. The corresponding drift for the fluxgate was very close to 100 pT.

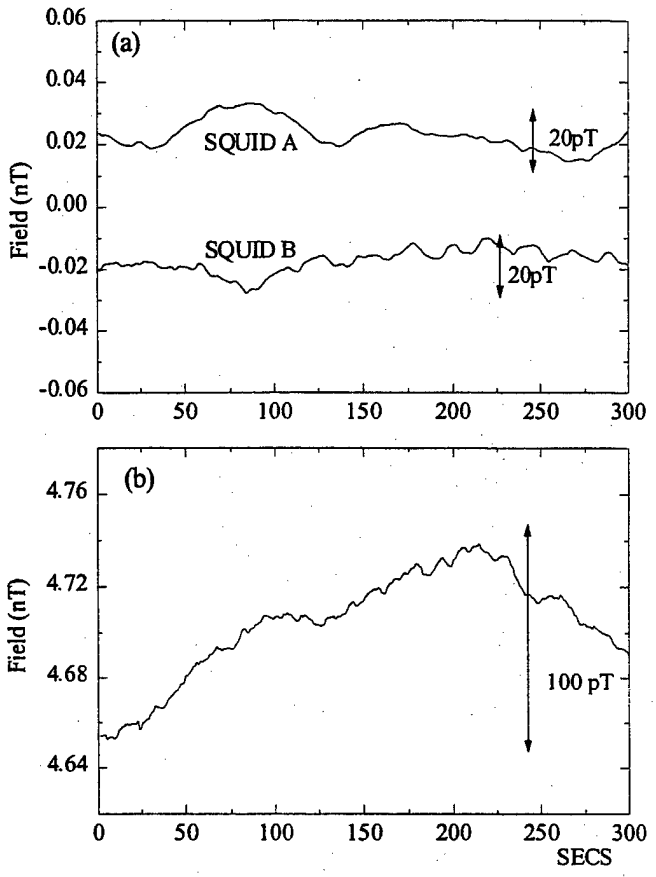

Figure 1. (a) Field Drift of SQUIDs (b) Field Drift of Fluxgate.

A typical power spectrum of the HTM100 sensor (operated inside three shields) is shown in Fig. 2. As can be seen, the intrinsic noise is about 200 fT $Hz^{-1/2}$ at a frequency of 1 Hz dropping to a white noise level of around 20-30 fT $Hz^{-1/2}$. This power spectrum compares well with that of the most up to date induction coils as detailed in reference [3].

The sensors were calibrated inside a square Helmholtz coil set (side 3.70 m, separation 2.02 m). It was found that the calibration supplied by Tristan Technologies Inc. was accurate to within 1%. Fig. 3 shows the output of the SQUID gradiometer (*i.e.* two sensors connected in series opposition) during the field tests. Fig. 3 has three curves showing the output from the two sensors and their difference.

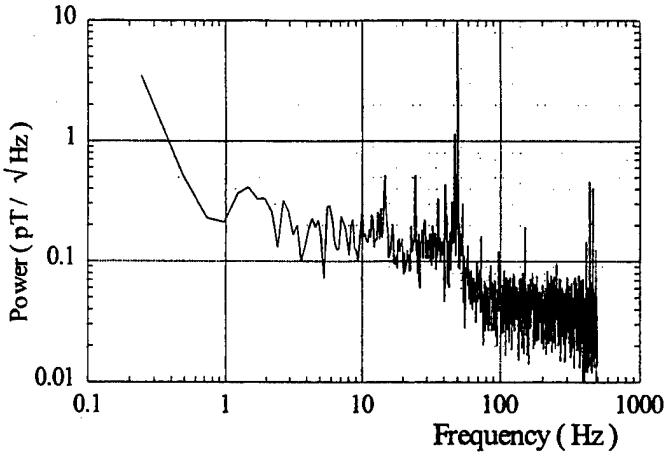

Figure2. Typical Zero Field Power Spectrum of SQUID sensor.

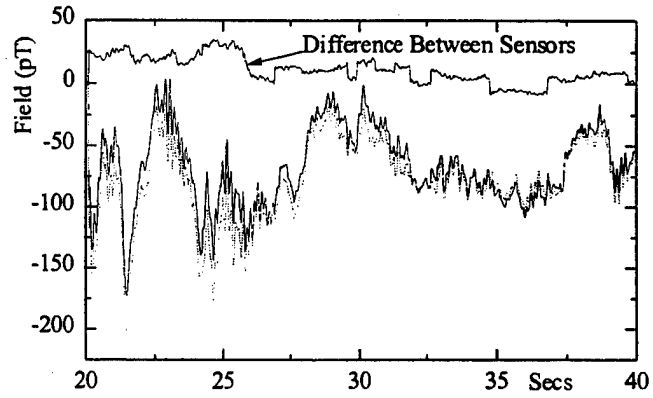

Figure 3. Output of Both Sensors and Their Difference.

A typical power spectrum of the difference between the two sensor outputs during the field tests is shown in Fig. 4. It can be seen that the 1 Hz noise level is of the order of 1 pT $Hz^{-1/2}$dropping to a white noise of around 42 fT $Hz^{-1/2}$.

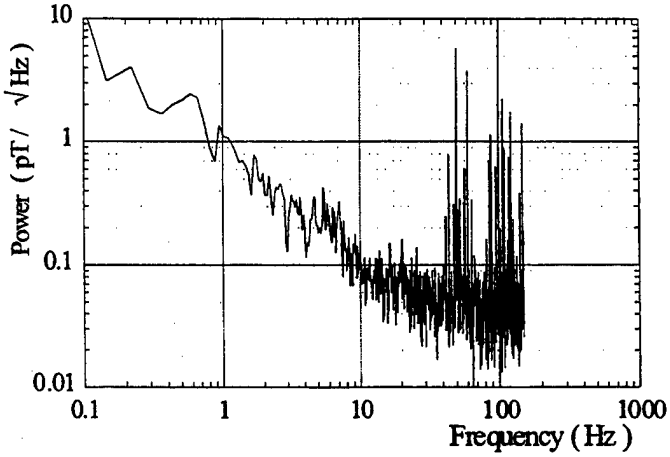

Figure 4. Typical Power Spectrum Taken in the Field

IV. Conclusions

We have characterised the HTM100 sensors, both in the lab and in an open field environment. It is possible to note that there is very little difference in terms of their performance in the two environments. This shows that the sensors work well whilst immersed in the earth's magnetic field. We can confirm that above 10 Hz the HTM100's work almost equally as well whether shielded or not.

On a practical note, induction coils are simpler to construct and operate, but SQUIDs have an advantage where 3-axis portability is a consideration due to the possibility of making much smaller and lighter systems. The HTM100 sensors are also superior to fluxgate sensors at frequencies above 1 Hz where a higher resolution survey is required. In a recent paper by Carr [4], induction coils, Hall sensors, magnetoresistors, fluxgates and SQUIDs are compared for their use and practicality in the field of non-destructive evaluation; similar considerations apply in the present case.

Our tests of the HTM100 high-T_c SQUID sensors have established that their performance is of a standard that warrants further investigation in the form of actual geophysical prospecting. We are currently developing the necessary instrumentation and will report on it's deployment.

References

[1] Miklich A H, Koelle D, Shaw T J, Ludwig F, Nemeth D T, Dantsker E, Clarke J, McN.Alford N, Button T W and Colclough M C 1994 *Appl. Phys. Lett.* **64** 3494.

[2] Faley M I, Poppe U, Urban K, Zimmerman E, Glaas W, Halling H, Bick M, Krause H-J, Paulson D N, Starr T and Fagaly R L Submitted to *IEEE Trans. Appl. Supercond.*

[3] Keller G V 1997

http://www.edge-online.org/archive/apr1497.html.

Principles of time-domain electromagnetic (TDEM) sounding.

[4] Carr C and Macfarlane J C 1999 *Insight* **41** No.1 20.

Acknowledgment

D. Rassi is a Royal Society Industry Fellow.

Characterization of a dc-SQUID Based Accelerometer Circuit for a Superconducting Gravity Gradiometer

R. Scharnweber and John M. Lumley
Oxford Instruments, Scientific Research Division, Research Instruments (Cambridge),
Newton House, Cambridge Business Park, Cowley Road, Cambridge CB4 4WZ, UK.

Abstract—A demonstrator set-up to test superconducting components has been designed and fabricated in order to characterize their functionality for use in a superconducting gravity gradiometer. The displacement of a freely oscillating levitated niobium proof mass in this acceleration transducer is measured inductively and read out by a direct current superconducting quantum interference device (dc-SQUID). It has been confirmed experimentally that the oscillation frequency depends on the current of the levitation magnet that is operated in persistent current mode. The results allow us to establish testing and operational procedures that can be used in a more complex multi-channel system to confirm functionality and to adjust the levitated proof mass.

I. Introduction

Gravity measurements have been used successfully for more than a century for various applications. Because of the Einstein's Equivalence Principle, one of the simplest instruments to detect a gravity signal is an accelerometer formed by a proof mass suspended by a weak spring and confined to one linear degree of freedom. Gravity signals as well as acceleration signals parallel to the axis of motion in this instrument will cause a linear displacement of the proof mass. In order to distinguish between the gravity and the acceleration components of an unknown signal, a gravity gradiometer consisting of two separate accelerometers has to be used. A sufficient suppression of the common mode signal caused only by acceleration allows gravity measurements to be taken with such an instrument mounted on a moving platform.

The application of superconducting technology provides a possibility to overcome the challenge of reading out the extremely small signals of gravity detectors. Theoretical considerations and experimental results on a superconducting gravity gradiometer (SGG) where a direct current superconducting quantum interference device (dc-SQUID) is used to read out the displacement of superconducting proof masses have been reported in [1]. The ultimate instrument sensitivity achievable with this SGG has been estimated to be better than 10^{-3} E/√Hz (1 E ≡ 1 Eötvös ≡ 10^{-9}/s^2) [2].

This contribution describes experimental results obtained with a simple superconducting accelerometer circuit, on the way towards the construction of a multi-channel SGG for space operation.

Manuscript received April 30, 1999.
This work was supported in part by ESA under contract #10393/93/NL/PB.

II. Experimental Set-up

A superconducting coil with a self-inductance of $L_i \approx$ 50 mH is operated as a magnet to levitate a 20 g niobium proof mass. The shape of the proof mass is an almost hollow cone of 3 cm diameter with an opening angle of 120°, matched to the shape of the levitation coil and therefore self centering in the earth's gravity field.

A schematic circuit diagram of the accelerometer is shown in Fig. 1. After external adjustment of the levitation current fed in across a heat switch HS 1, the levitation magnet can be operated in persistent current mode. A second heat switch, HS 2, in an intermediary transformer circuit to the input coil of the dc-SQUID may be activated to minimize the offset flux in this coupling circuit that is caused during the charging of the levitation current. Displacement of the levitated proof mass causes a change of the inductance of the levitation coil that is used as sensing coil as well. The resulting additional screening current in the levitation circuit is inductively coupled into the SQUID via the intermediary transformer coupling circuit. The dc-SQUID and all superconducting circuitry are mounted in two separate magnetically screened niobium cans [3].

For the preliminary experiments reported here, the complete demonstrator instrument was operated inside a superconducting lead shield immersed in liquid helium. However, the design of the accelerometer considers also the possibility of an upgrade for operation in vacuum or with helium as temperature exchange gas.

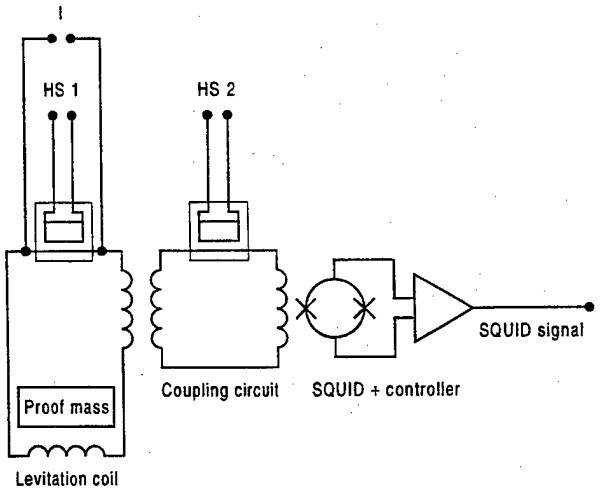

Fig. 1. Schematic circuit diagram of accelerometer test set-up.

III. Results

A. Heat Switches

In order to find the threshold current to drive the heat switches, a triangular shaped current signal was fed into the levitation circuit that caused a flux shift of a few flux quanta Φ_0 in the SQUID. The heat switch HS 1 was driven by a current well beyond its estimated operation level while HS 2 was cold. Because of the current sweep, a horizontal shift of the sinusoidal flux-to-voltage modulation of the dc-SQUID was observed on the oscilloscope. A reduction of the current in heat switch HS 1 below 7 mA stopped the flux sweep, indicating a persistent current trapped in the levitation circuit. In a similar experiment, the external current to charge the levitation coil was swept across the warm heat switch HS 1 while the current to activate heat switch HS 2 was turned up slowly. The effect of uncoupling the SQUID from the levitation circuit was observed in the sweeping flux-to-voltage modulation signal that suddenly became static. Due to the better thermal coupling to the mounting plate, a higher threshold current of 19 mA was found for heat switch HS 2.

B. Levitation

Turning up the levitation current and watching the SQUID output signal at the same time showed a linear increase of the flux signal up to a current of 150 mA. Beyond this value, the signal suddenly started to fluctuate. Time traces of this fluctuation signal were measured with the SQUID operated in FLL mode and the levitation circuit in persistent current mode. They show sinusoidal oscillation signals of the levitated proof mass as depicted in Fig. 2. The oscillation frequency as a function of the persistent current in the levitation coil is shown in Fig. 3. An asymptotic increase of the resonance frequency indicates a higher stiffness of the spring constant towards the threshold of the levitation current to lift the proof mass.

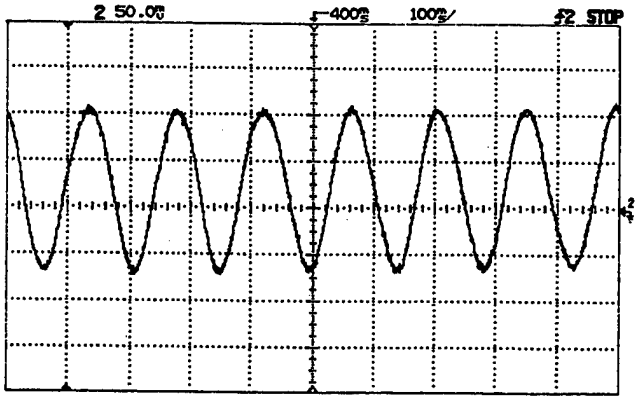

Fig. 2. Time trace of SQUID output detecting proof mass oscillation for a levitation current of 1 A, stored as persistent current. The scale of the x-axis (time) is 0.1 s/div, the scale of the y-axis (flux detected by the SQUID) is 0.05 Φ_0/div.

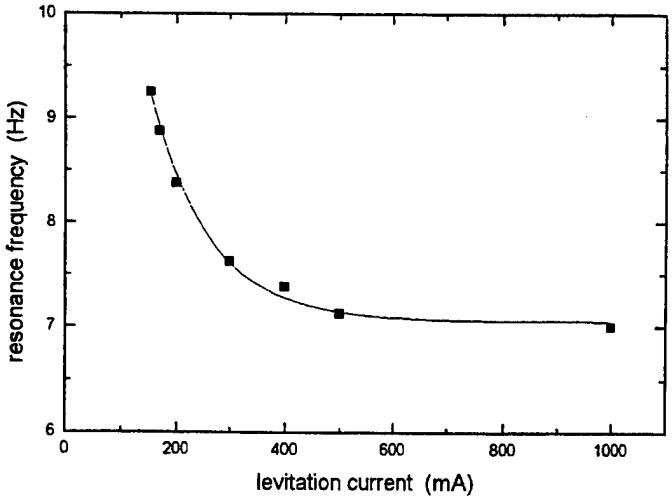

Fig. 3. Resonance frequency of proof mass oscillations as a function of the levitation current. The threshold current for levitation is 150 mA.

Large oscillations of the levitated proof mass, caused by a transient excitation show that there is a damping factor in the system due to the movement of the proof mass in liquid helium. The oscillations did not disappear completely, even after several hours, because of the excitation due to gas bubbles in the boiling helium. A shift of the offset flux was not observed in the same time, indicating the stable persistent current operation of the levitation circuit.

C. Noise Measurements

A spectrum of the flux noise measured by the SQUID without any current charged into the levitation coil is shown in Fig. 4. The white noise floor level is 10 $\mu\Phi_0/\sqrt{\text{Hz}}$. Several oscillation modes can be observed between 3 Hz and 30 Hz. They can be explained by gas bubbles and microphonic effects of the set-up supporting the levitation coil, excited by vibrations of the laboratory building.

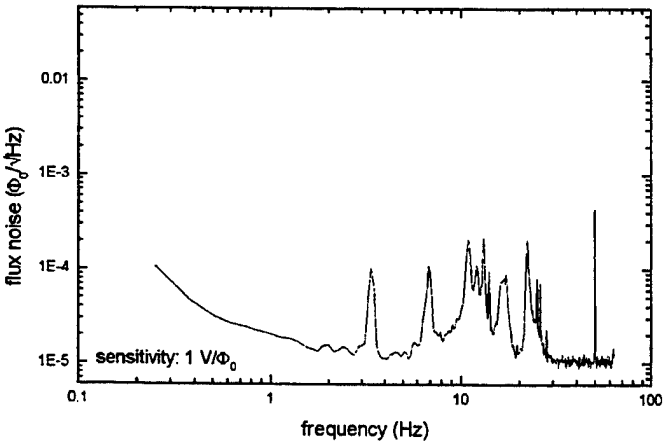

Fig. 4. Flux noise spectrum of the system background noise. The white noise level is 10 $\mu\Phi_0/\sqrt{\text{Hz}}$.

Fig. 5 shows flux noise spectra measured for the levitated proof mass. The main oscillation mode and the shift of its frequency depending on the levitation current are clearly visible. A more detailed analysis in comparison with the background noise spectrum shows another oscillation mode around 22 Hz that shifts towards higher frequencies for higher levitation currents, in contrast to the main mode that shifts to the opposite direction. A further mode during levitation that is not present in the background noise spectrum can be observed at 34 Hz, independent of the levitation current within the range of investigation. The main oscillation mode is caused by the vertical translation of the proof mass. The two other modes can be explained by the horizontal translation and the rotation about a horizontal axis, respectively. Due to the rotational symmetry of the proof mass, a rotation about the vertical axis is not expected to cause a signal in the SQUID.

For an estimate of the instrument sensitivity of the accelerometer, the transfer function between acceleration and flux signal has to be determined. An improved set-up is currently under construction, where the accelerometer is mounted in a shaker that provides a controlled acceleration signal of variable frequency and amplitude.

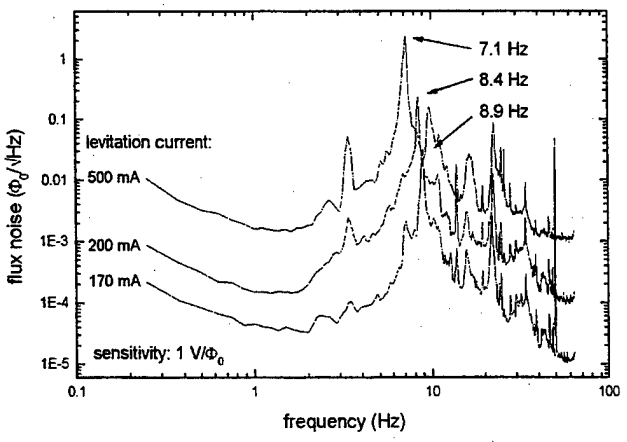

Fig. 5. Flux noise spectra of proof mass oscillations for different levitation currents. The frequency of the main resonance peak is indicated. For easier comparison, the spectra for 200 mA and 500 mA have been multiplied by a factor of 10 and 100, respectively.

IV. Conclusions

A superconducting accelerometer with dc-SQUID read-out has been built in order to investigate components and establish test procedures for the construction of a multi-channel SGG for space operation. Threshold currents for the heat switches have been determined. The superconducting circuitry allows the levitation magnet to be operated in persistent current mode. The levitation of the proof mass has been studied experimentally. Noise measurements reveal three oscillation modes, whose frequencies depend on the current in the levitation coil. A characterization of the transfer function between acceleration and flux signal is planned. This will lead to an estimate of the sensitivities for both the accelerometer as well as the more complex SGG.

Acknowledgment

We thank D. Thompson, R. Tomba, and M. Butterly for their machining work and P. Pope for his support on the fabrication of superconducting joints.

References

[1] H.A. Chan, M.V. Moody, and H.J. Paik, "Superconducting gravity gradiometer for sensitive gravity measurements. I. Theory," *Phys. Rev. D*, vol. 35, pp. 3551-3571, June 1987; H.A. Chan and H.J. Paik, "Superconducting gravity gradiometer for sensitive gravity measurements. II. Experiment," *Phys. Rev. D*, vol. 35, pp. 3572-3597, June 1987.

[2] M.V. Moody, H.A. Chan, and H.J. Paik, "Superconducting gravity gradiometer for space and terrestrial applications," J. Appl. Phys, vol 60, pp. 4308-4315, December 1986.

[3] R. Scharnweber and John M. Lumley, "High Resolution Multipurpose dc-SQUID Applications System," presented at Appl. Supercond. Conf. (ASC), Palm Desert CA, September 1998.

POSTER SESSION I

Group 3 - Analog

Microstrip Coupled SNS Josephson Junctions on p-Type InAs

K. Biedermann, T. Matsuyama, and U. Merkt
Institut für Angewandte Physik und Zentrum für Mikrostrukturforschung, Universität Hamburg,
Jungiusstraße 11, D-20355 Hamburg, Germany

Abstract—We investigate the high frequency (rf)-coupling of two Nb/InAs(2DES)/Nb Josephson junctions coupled by a superconducting microstrip. One junction acts as a transmitter the other one as a receiver. We report on the influence of the transmitter junction on the critical current and on the Fiske resonances of the receiver junction for different geometrical designs.

I. Introduction

In recent years a lot of progress has been made in the fabrication and understanding of mesoscopic semiconductor/superconductor weak links [1]. Of particular interest is the ac-Josephson effect which leads to rf-radiation with frequencies in the GHz range. This opens the possibility to use Jospehson junctions as local oscillators for the investigation of other mesoscopic systems. Our junctions have high I_cR_n products of about 1 mV [2] from which we estimate a high power of 1 μW of the emitted radiation. The second aspect, which makes our junctions especially interesting for investigations of the ac-Josephson effect, is their integrated resonator formed by an overlap of two Nb electrodes with an anodic oxide in between them. We investigate the characteristics of the resonator by studying the magnetic-field dependence of the Fiske resonances in the current-voltage characteristics (CVCs). It agrees well with an adopted resistively shunted junction (RSJ) model [3].

II. Sample Preparation

The preparation of a single Nb/InAs(2DES)/Nb junction is described in [4]. Fig.1 depicts the two different designs of coupled junctions studied here. The preparation of the two designs is very similar, therefore we describe exemplarily the preparation of the design shown in Fig.1(a). First, a Nb electrode is sputtered on the InAs substrate and subsequently it is anodically oxidized yielding an oxide thickness of h = 30-120 nm. This electrode is the common lower electrode for both junctions and the lower electrode of the microstrip. The thickness h of the oxide defines the channel lengths of both junctions and also the thickness of the dielectric of the microstrip. Then a second Nb film is deposited forming the receiver junction by overlapping the oxide at one end. To avoid a superconducting short circuit between the second and third sputtered Nb electrode, the receiver is also oxidized at the end of its overlap. At last, the third Nb film is sputtered which forms the transmitter junction and whose overlap is galvanically coupled to the upper electrode of the microstrip. The junction widths vary between 5 μm and 100 μm.

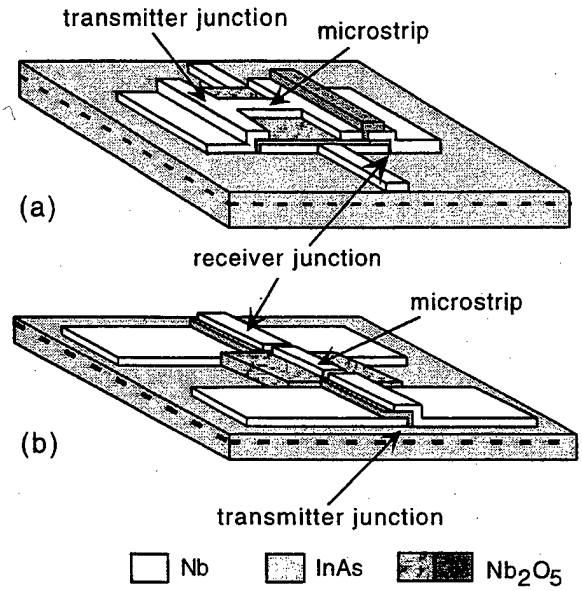

Fig. 1: Schematic view of the different designs: (a) galvanically coupled microstrip and (b) microstrip capacitively coupled to the transmitter junction.

III. Microstrip Design

The electromagnetic wave is guided from the transmitter to the receiver by a superconducting microstrip. Our goal is to radiate resonantly into the integrated resonator of the receiver junction. This implies that the width of the receiver junction is equivalent to $n \cdot \lambda/2$ (n integer) of the transmitted wavelength λ. The length of our microstrip is $\lambda/8$ to prevent that the microstrip itself acts as a resonator. The impedance Z_L of the microstrip is adjusted to the normal resistance R_n of the transmitter junction to couple the emitted radiation with the least reflection into the microstrip. The impedance is determined in the static approximation where the phase velocity is independent of the frequency. The phase velocity is given by the Swihart velocity c' [5], which depends on the thickness h of the dielectric, the penetration depth λ_L, and the film thickness t. We model our microstrip as an ideal capacity due to

We acknowledge financial support of the Deutsche Forschungsgemeinschaft via the Sonderforschungsbereich 508 "Quantenmaterialien — laterale und hybride Strukturen".

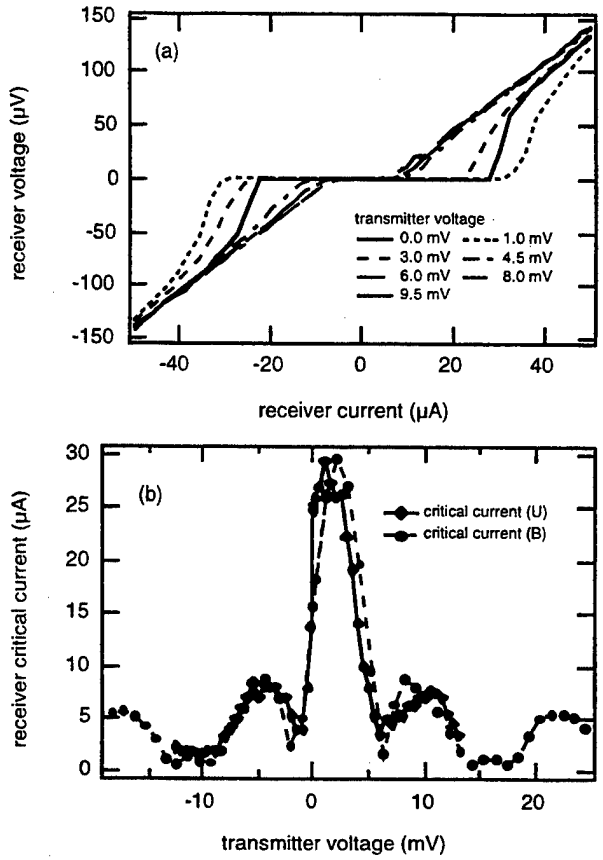

Fig. 2: (a) Current-voltage characteristics of the design in Fig.1(a) for different transmitter bias voltages at 1.7 K. (b) Critical current (solid line) and Fraunhofer pattern (dashed line) of the receiver junction for a perpendicular magnetic field. The x-axis of the Fraunhofer pattern is scaled by a single numerical factor.

the small thickness h = 30-120 nm of the dielectric which is much smaller than the width w = 1 μm of the upper electrode of the microstrip. With these approximations the impedance of the microstrip is real and is given by $Z_L = h/\varepsilon_0\varepsilon_r c' w$ [6]. In our design the impedance is about 5 Ω and is of the same magnitude as the normal resistances R_n of our junctions that vary between 1 Ω and 10 Ω.

IV. Experimental Results

We have measured the current-voltage characteristics (CVCs) of the receiver junction while the transmitter junction is current biased at a constant voltage. This voltage defines the frequency of the radiation intended to be transfered by the second Josephson equation. The respective power level is given by the product of the bias voltage and the bias current of the transmitter. A change of the bias voltage changes the frequency and the power level. In Fig.2(a) the CVCs of the receiver junction are shown for different bias voltages of the transmitter. An influence on the critical current of the receiver is clearly visible. In Fig.2(b) the critical current of the receiver is shown versus the bias voltage of the transmitter junction. The critical current is modulated as expected for rf-coupling or a magnetic influence. To check whether the effect is due to rf-coupling or an inductive influence we have measured the Fraunhofer pattern of the receiver junction. It is shown in Fig.2(b) with the magnetic field applied perpendicularly to the junction. The x-axis for the Fraunhofer pattern is scaled by a single factor resulting in traces which are equal in period and height. From this we deduce an inductive influence from the transmitter onto the receiver junction. Another observation, which indicates an inductive influence, is that the effect on the critical current is still visible for bias voltages exceeding the gap voltage. For these voltages the ac-components should be suppressed. For the design in Fig.1(b) the corresponding measurements are shown in Fig.3. In contrast to the design in Fig.1(a) the receiver shows hysteretic behavior. In Fig.3(a) only the negative branch of the CVC is plotted measured from negative to positive voltages. Due to its large width of 100 μm the receiver of this design shows transverse Fiske resonances in the differential CVC for receiver voltages below 1mV. The voltage positions correspond to the model in [3]. The dependence of the critical current and the return current on the transmitter bias voltage is plotted in Fig.3(b). The maximum of the critical current is shifted to positive transmitter voltages presumably as a result of flux

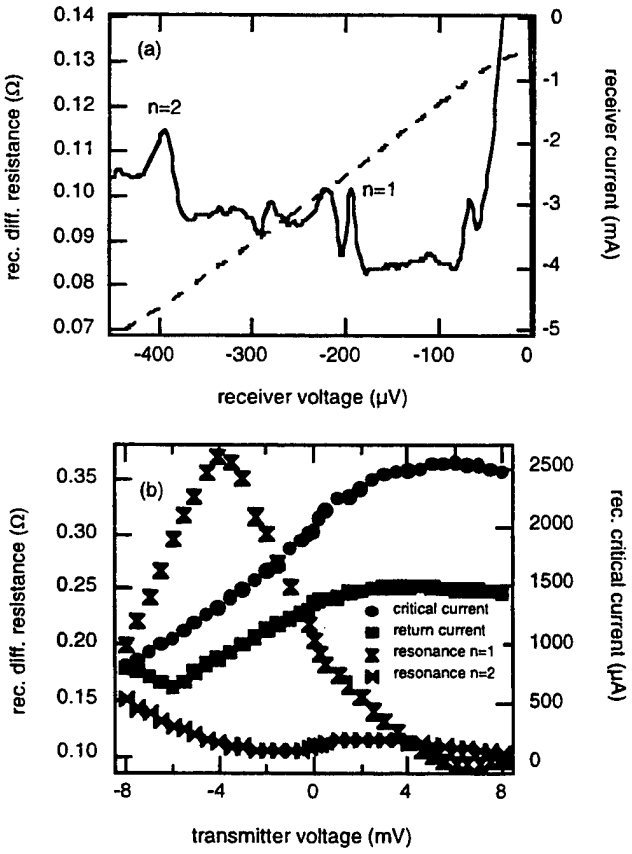

Fig. 3: (a) Direct (dashed line) and differential (solid line) CVC of the receiver junction of the design in Fig.1(b) at a bias voltage of the transmitter junction of +4 mV. The receiver shows Fiske resonances in the differential CVC marked by their order n=1 and n=2. (b) Dependence of the critical current and return current from the bias voltage of the transmitter. Additionally, the maxima of the Fiske resonances in the differential CVCs are plotted.

penetration. The shapes of the curves are very similar to a Fraunhofer pattern. Measurements in small magnetic fields for a direct comparison are not yet made. Also depicted in Fig.3(b) is the maximum of the resonances of order n=1 and n=2 in the differential CVCs as a function of the bias voltage of the transmitter. The bias-voltage dependence of the resonances is very similar to the magnetic-field dependence in [3]. For zero field no transverse modes exist. In Fig.3(b) this situation corresponds to the maximum of the critical current at a transmitter voltage of +6 mV. The n=1 resonance occurs earlier than the n=2 resonance and its maximum closely coincides with the minimum of the critical current as expected from the model [3]. Even in the absence of a measured Fraunhofer pattern we are able to estimate the effective magnetic field at the position of the receiver generated by the transmitter. This is illustrated in Fig.4. In the Fraunhofer pattern the first minimum corresponds to one flux quantum $\phi_0 = 2.07 \cdot 10^{-15}$ Tm^2. The respective magnetic field is given by $B = \phi_0/A$ where A is the penetrated area. In our case $A = 20 \cdot 100$ $\mu m^2 = 2 \cdot 10^{-9}$ m^2 corresponds to the area of the overlap of the receiver junction. From this we calculate a magnetic field $B = 1.3 \cdot 10^{-6}$ T. This we compare with the magnetic field $B = (\mu_0/2\pi) \cdot I/R$ at a distance R of an infinitely long current carrying wire. Here c is the speed of light. The distance R = 105 μm is taken from the middle of the transmitter to the middle of the receiver (see Fig.4). The current $I = 4.83$mA is given by the sum of the current for a transmitter voltage of +6 mV and, by chance, of –6 mV which corresponds to the maximum and minimum of the critical current in Fig.3(b), respectively. This leads to a magnetic field $B = 9.2 \cdot 10^{-6}$ T. The difference between both fields is approximately a factor of 7 which can possibly be explained by flux-focussing effects, since for our junctions the area A obtained from the measured Fraunhofer pattern and the geometrical area differ by a factor of the same magnitude.

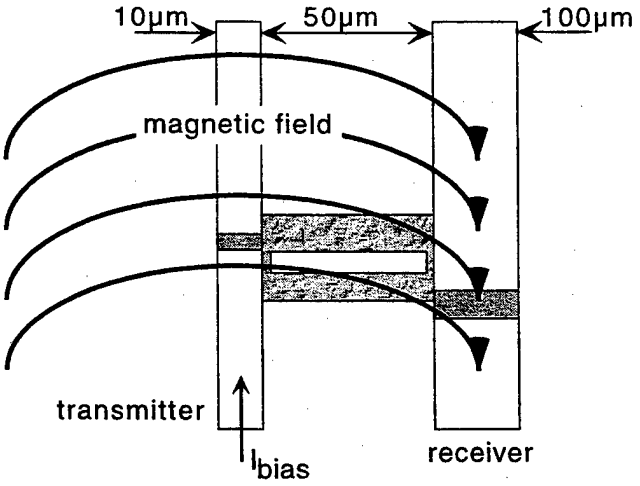

Fig. 4: Topview of the design in Fig.1(b). Due to the current bias of the transmitter an effective magnetic field is generated at the position of the receiver.

V. Conclusions

We have investigated the coupling of two Josephson junctions on p-type InAs. We observe an effect on the critical current and on the Fiske resonances of the receiver for both of our designs if we change the bias voltage of the transmitter. Comparison with measurements in magnetic fields and simple geometrical approximations lead us to conclude on an inductive interaction which masks a possible rf-coupling. We suggest that detectors not as sensitive to magnetic fields as Josephson junctions would be more appropriate to study the characteristics of our junctions as local oscillators. A possible device could be a single quantum dot.

References

[1] B. J. van Wees and H. Takayanagi, *Mesoscopic Electron Transport,* ed. L. P. Kouwenhoven, G. Schön and L. L. Sohn, Kluwer, Dordrecht, 1996.

[2] A. Chrestin and U. Merkt, "High characteristic voltages in Nb/p-type InAs/Nb Jospehson junctions," *Appl. Phys. Lett.*, vol. 70 (23), pp. 3149-3151, June 1997.

[3] K. Biedermann, A. Chrestin, T. Matsuyama and U. Merkt, "Magnetic-field dependence of Fiske resonances in Nb/p-type InAs/Nb weak links," *Applied Superconductivity*, vol. 5 (7-12), pp. 255-260, 1998 [Proc. Sixth Int. Superconductive Electronics Conference, pp. 185-187, 1997].

[4] A. Chrestin and U. Merkt, "Evidence for a proximity-induced energy gap in Nb/InAs/Nb junctions," *Phys. Rev. B*, vol. 55 (13), pp. 8457-8465, April 1997.

[5] J. C. Swihart, "Field Solution for a Thin-Film Superconducting Strip Transmission Line," *J. Appl. Phys.*, vol. 32 (3), pp. 461-469, March 1961.

[6] R. K. Hoffmann, *Integrierte Mikrowellenschaltungen,* Springer, Berlin 1983.

Measurements of the dielectric properties of strontium titanate at submillimetre wavelengths using Josephson junction driven oscillators

P. F. McBrien, W. E. Booij, F. Kahlmann, M. G. Blamire and E. J. Tarte
I. R. C. in Superconductivity, University of Cambridge, Cambridge, CB3 0HE, UK

E. J. Romans and C. M. Pegrum
Department of Physics and Applied Physics, Strathclyde University, Glasgow, G4 0NG, UK

Abstract—Measurements of the dielectric constant ε_R of thin film $SrTiO_3$ made using Josephson junction driven oscillators are reported. ε_R for a 100nm $SrTiO_3$ film was found to vary between 120 and 245 in the temperature range 4.2K to 65K and to be independent of frequency from 50GHz to 340GHz.

I. Introduction

Josephson junctions coupled to external microstrip resonators provide an ideal method of measuring dielectric properties. The Josephson oscillations drive the resonator and the junction acts as a detector enabling a straightforward determination of resonator characteristics. Previous studies of both low T_C [1] and high T_C [2], [3] Josephson junctions coupled to resonators have placed emphasis on measuring the surface resistance of the materials concerned. However, this technique also provides a relatively simple way of characterising dielectric films in structures relatively close to final device designs.

There are few alternative oscillators in the frequency range 50GHz to 1THz, and correspondingly few measurements of the dielectric properties of thin films of $SrTiO_3$ in this region. Thin films of $SrTiO_3$ are of interest because they provide the potential for tuneable microwave circuits due to the dc bias dependence of ε_R[4]. In this paper grain boundary $YBa_2Cu_3O_7$ Josephson junctions coupled to a range of sizes of external microstrip resonator are reported, enabling measurement of the ε_R of $SrTiO_3$ in the frequency range 50GHz to 340GHz, and the temperature range 4.2K to 65K.

II. Theory

The Josephson junction is a voltage tuned microwave oscillator with a frequency f given by,

$$f = V/\Phi_0 \tag{1}$$

where V is the voltage and Φ_0 is the flux quantum. A transmission line open at both ends driven by these oscillations has a pure real impedance at resonance when its length a is equal to half integer multiples of the wavelength of the applied microwaves. Thus the wavenumber β at resonance is

$$\beta = n\pi/a \tag{2}$$

where n is the order of the resonance. At resonance the real impedance is in parallel to the junction resistance, so the dc current seen in the junction current voltage (IV) characteristic is reduced because some microwave power is coupled out of the junction into the resonator.

Manuscript received 28 April 1999.
This work was supported by the UK Engineering and Physical Sciences Research Council and the Defence Evaluation and Research Agency.

Generally, a transmission line has a complex propagation constant γ[5], where,

$$\gamma = \alpha + j\beta = \sqrt{(R'+j\omega L')(G'+j\omega C')} \tag{3}$$

Here, L' and C' are the inductance and capacitance per unit length of the tranmission line and R' and G' represent the finite resistive and conductive losses per unit length. ω is the angular frequency of the oscillations. If these losses are small then the attenuation constant α of the line is negligible and the dispersion relation is

$$\beta = \omega\sqrt{L'C'}\left(1 - \frac{R'G'}{4\omega^2 L'C'} + \frac{G'^2}{8\omega^2 C'^2} + \frac{R'^2}{8\omega^2 L'^2}\right) \tag{4}$$

III. Experiments

A bilayer consisting of 200nm $YBa_2Cu_3O_7$ and 100nm $SrTiO_3$ was deposited using pulsed laser ablation onto a 24° misorientated $SrTiO_3$ bicrystal substrate. The bilayer was then patterned using standard photolithographic techniques and Ar^+ milling. Following this step the junction IV characteristics were measured. Next a 160nm thick gold top electrode for the tranmission lines was sputtered and patterned by lift-off.

The resonator design is shown in Fig. 1. Five different resonators of lengths 25, 50, 75, 100 and 125μm were tested. The width of the track containing the junction was 2μm. The resonator was tapered towards this track so as to impedance match the two structures. The inductance and capacitance per unit length of the resonator are therefore [6],

$$L' = \frac{\mu_0}{a}(t + d_s + \lambda_L \coth(h/\lambda_L)) \tag{5}$$

$$C' = \varepsilon_0\varepsilon_R a/t \tag{6}$$

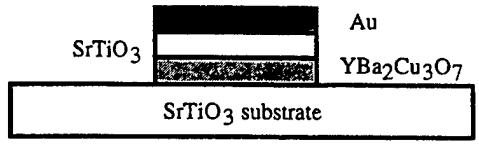

Cross sectional view

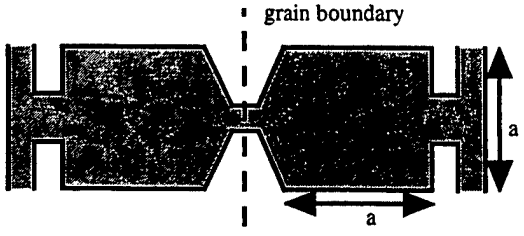

Planar view

Fig.1. The resonator design, not to scale.

Here, μ_0 and ε_0 are the permeability and permittivity of free space, t is the thickness of the dielectric, λ_L and h are the London penetration depth and thickness of the $YBa_2Cu_3O_7$ and $d_S=(\delta_S/2)(\sinh(2b/\delta_S)-\sin(2b/\delta_S))/(\sinh^2(b/\delta_S)+\sin^2(b/\delta_S))$ where b is the gold thickness and δ_S is the gold skin depth. Equation (5) is valid when $\lambda_L \sim h$ and $b \sim \delta_S$.

Differential resistance measurements were made using a lock-in amplifier with a standard ac modulation technique.

IV. Results

Typical junction parameters at 4.2K are illustrated by those of the junction coupled to the 50μm resonator for which the critical current was 740μA and the resistance was 1.14Ω after gold deposition. The *IV* characteristic of this device at 4.2K before and after gold deposition is shown in Fig. 2. Transmission line resonances can clearly be seen in the *IV* characteristic after gold deposition.

The resonances were seen more clearly in a differential resistance (*dV/dI*) measurement. The resonance, which is at a dip in the *IV* characteristic, is at a position of maximum gradient in the *dV/dI* versus voltage curve. In some cases it was necessary to apply a small magnetic field to suppress the junction critical current. This prevented the junction switching out to a voltage beyond that of the position of the first order resonance. The *dV/dI-V* and the *IV* characteristic (measured simultaneously) for the junction coupled to the 75μm resonator at 4.2K and a magnetic field of 8.1μT are shown in Fig. 3. Four resonances are clearly visible. The positions of the resonances did not vary with applied magnetic field and changed with length of resonator demonstrating that they were neither Fiske[7] nor flux flow resonances, both of which propagate in the junction cavity itself. Equations (1) and (2) can be used to detemine the angular frequency and wavenumber of the resonance. A plot of wavenumber versus frequency, the dispersion relation, for the various devices measured at 4.2K is shown in Fig. 4.

IV and *dV/dI*-V characteristics were measured at temperatures up to 65K for the 50μm, 75μm and 100μm resonators where the first resonance was no longer visible. Thermal noise rounding of the critical current produces a broad peak in the *dV/dI-V* characteristic which can obscure resonances at lower frequencies and higher temperatures. The dispersion relation was found to be linear at all temperatures measured.

The line in Fig. 4. is a fit to (4), using $(L'C')^{1/2}$ obtained from the gradient of the measured dispersion relation. The other parameters needed are the surface resistance and the dielectric losses. The total surface resistance is the sum of the

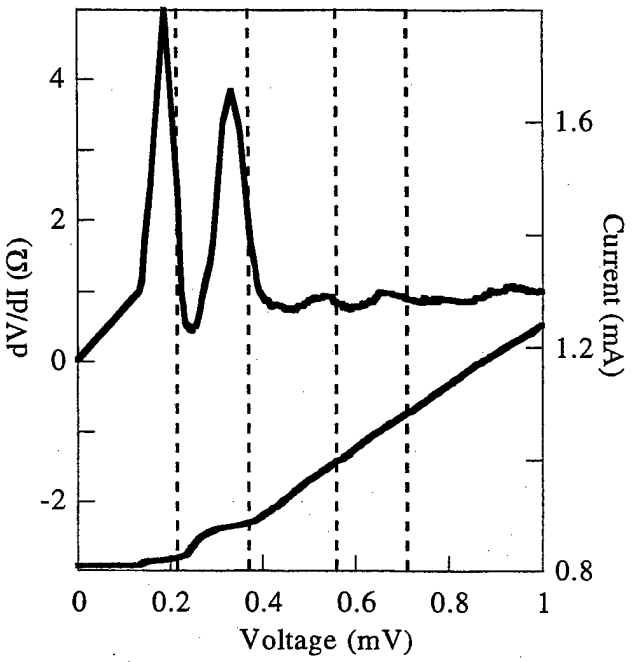

Fig. 3. The *IV* (lower curve) and *dV/dI-V* (upper graph) characteristic of the junction coupled to the 75μm resonator at 4.2K in a 8.1μT magnetic field. The first 4 resonances are indicated by the vertical lines.

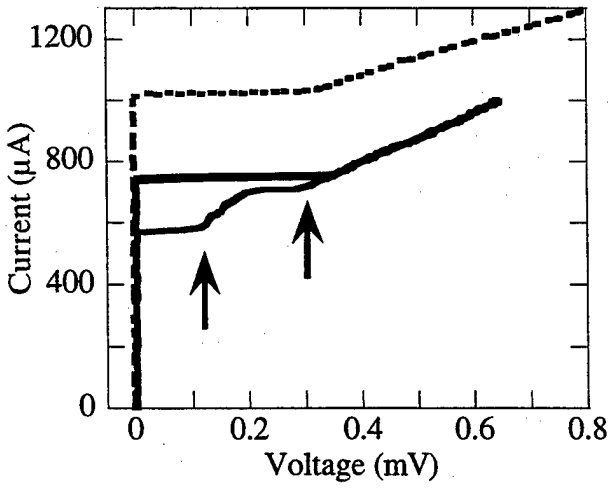

Fig. 2. The IV characteristic of the junction coupled to the 50μm resonator at 4.2K before gold deposition (dashed line) and after gold deposition (solid line). The resonances are indicated by arrows.

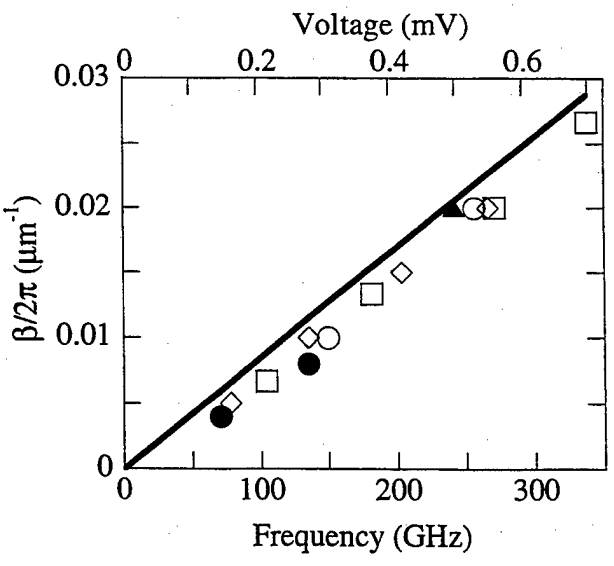

Fig. 4. The dispersion relation at 4.2K. (▲) is the 25μm resonator, (o) the 50μm resonator, (□) the 75μm resonator, (◇) the 100μm resonator and (●) is the 125μm resonator. The line is a fit to (4).

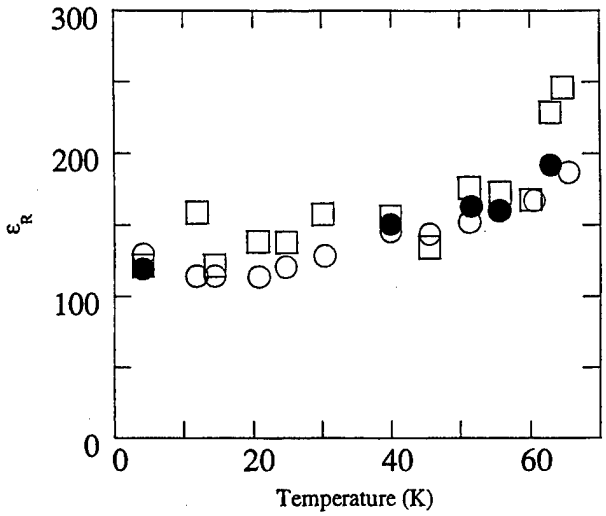

Fig. 5. ε_R versus temperature for the $SrTiO_3$ film. The points were taken from the first order resonances in the 50μm (o), 75μm (•) and 100μm (□) resonators, corresponding to frequency ranges from 116GHz to 150GHz, 77GHz to 103GHz and 50GHz to 77GHz respectively.

contribution from the $YBa_2Cu_3O_7$ and the gold. The gold surface resistance R'_{Au} is $(\omega\mu_0/2\sigma a^2)^{1/2}$ and the $YBa_2Cu_3O_7$ surface resistance $R'_{YBCO} \propto \omega^2$ with R'_{YBCO}=25mΩ at 100GHz[3]. Dielectric losses are given by $G'=\omega C' tan\delta$ with $tan\delta$=0.06 from[8], which is a typical value for the loss tangent of $SrTiO_3$ at f~1GHz.

Combining (1), (2), (4), (5) and (6) to give

$$\varepsilon_R = \Phi_0^2/(4a^2V_1^2\mu_0\varepsilon_0(t+d_S+\lambda_L \coth(h/\lambda_L))/t) \quad (7)$$

where V_1 is the voltage of the first resonance enables ε_R to be calculated if the temperature dependences of λ_L and δ_S are known. The two fluid model was used for $\lambda_L(T)$ where $\lambda_L(T)=\lambda_L(0)/(1-(T/T_C)^4)^{1/2}$ with $\lambda_L(0)$=140nm[9]. From the gold conductivity σ the skin depth at the resonant frequency was calculated using $\delta_S=(2/\sigma\omega\mu_0)^{1/2}$, with σ(4.2K) = 4.2×10^7 $\Omega^{-1}m^{-1}$. This was 280nm for the first order resonance in the 100μm device at 78GHz. Hence a plot of ε_R versus temperature was obtained, and is shown in Fig. 5.

V. Discussion

Typical loss parameters do not introduce curvature into the dispersion relation, as shown by both the measured data and the calculation from (4) shown in Fig. 4. Also, the linear dispersion relation shows that ε_R is independent of frequency in the range 50GHz to 340GHz. However, there is an offset in the data which is not explained by (4).

The value of ε_R measured is comparable to measurements of ε_R for $SrTiO_3$ films at low frequencies[4], [10] and at 1.5GHz to 2.5GHz[8]. The temperature dependence of ε_R is similar to that measured previously for $SrTiO_3$ thin films[4], [8] and [10]. The dielectric constant increases with increasing temperature but a peak is not observed as measurements above 65K were not possible.

By applying a dc bias to the gold top electrode the technique could be extended to measure the bias dependence of ε_R. Other ferroelectrics films with a lattice parameter compatible with $YBa_2Cu_3O_7$, for example $Ba_xSr_{1-x}TiO_3$, $SrBi_2Ta_2O_9$ or $PbZr_xTi_{1-x}O_3$, could also easily be measured.

VI. Conclusion

A $YBa_2Cu_3O_7/SrTiO_3$/Au microstrip transmission line resonator coupled to a Josephson junction has been used to measure the dielectric constant of thin film $SrTiO_3$ between temperatures of 4.2K and 65K and in a frequency range from 50GHz to 340GHz. The dielectric constant was found to vary between 120 and 245. The method was found to give reproducible results for a range of different resonator sizes coupled to different Josephson junctions, thereby demonstrating the suitability of this technique for dielectric characterisation.

References

[1] B. Bi, K. Wan, W. Zhang, S. Han, and J. E. Lukens, "Josephson Junction Driven submillimeter wave microstrip resonator." *IEEE Trans. App. Sup*, 1991. vol. 1(4): p. 145-149.

[2] J. Edstam, P. A. Nilsson, E. A. Stepantsov, and H. K. Olsson, "100 GHz Oscillations On Monolithic High-Tc Chip." *Appl. Phys. Lett.*, 1993. vol. 62(8): p. 896-898.

[3] J. Edstam and H. K. Olsson, "Josephson Broad-Band Spectroscopy to 1 THz." *Appl. Phys. Lett.*, 1994. vol. 64(20): p. 2733-2735.

[4] Y. A. Boikov and T. Claeson, "High tunability of the permittivity of YBa2Cu3O7-delta/SrTiO3 heterostructures on sapphire substrates." *Jnl. Appl. Phys.*, 1997. vol. 81(7): p. 3232-3236.

[5] S. Ramo, J. R. Whinnery, and T. Van Duzer, "Fields and Waves in Communication Electronics." . 1984, New York: John Wiley.

[6] T. P. Orlando and K. A. Delin, "Foundations of Applied Superconductivity." . 1990, New York: Addison- Wesley.

[7] E. J. Tarte, G. A. Wagner, R. Somekh, F. Baudenbacher, P. Berghuis, and J. E. Evetts, "The Capacitance of Bicrystal Josephson Junctions Deposited on SrTiO3 substrates." *IEEE Trans. Appl. Supercon.*, 1997. vol. 7(2): p. 3662.

[8] M. J. Dalberth, R. E. Stauber, J. C. Price, C. T. Rogers, and D. Galt, "Improved low frequency and microwave dielectric response in strontium titanate thin films grown by pulsed laser ablation." *Appl. Phys. Lett.*, 1998. vol. 72(4): p. 507-509.

[9] C. W. Schneider, R. E. Somekh, J. E. Evetts, D. J. C. Walker, I. M. Watson, F. Baudenbacher, *et al.*, "Inductive measurements of λ(T) of bare YBCO films and the proximity effect in YBCO/normal metal bilayers." *IEEE Trans. Appl. Supercon.*, 1995. vol. 5(2): p. 1432-1435.

[10] H. M. Christen, J. Mannhart, E. J. Williams, and C. Gerber, "Dielectric Properties Of Sputtered SrTiO3 Films." *Phys. Rev. B.*, 1994. vol. 49(17): p. 12095-12104.

Study of the Magnetic Tuning Effect in HTS Coplanar Resonators

T. Nurgaliev, S. Miteva
Institute of Electronics BAS, 72 Tzarigradsko chaussee, 1784 Sofia, Bulgaria

A. Jenkins, D. Dew-Hughes
University of Oxford, Parks Road, OX1 3PJ, UK

Abstract - Formulas for calculating of the resonance frequency and the microwave (MW) losses in HTS thin film coplanar waveguide resonators containing a tangentially magnetized ferrite layer were obtained by using the perturbation method. The problem of achievement of a maximum sensitivity of the resonance frequency to the field intensity and the problem of diminishing of the MW losses contributed to the resonator by the magnetostatic waves were analyzed.

I. INTRODUCTION

Magnetically tunable HTS thin film microwave (MW) devices are formed on the basis of layered structures, which include superconducting electrodes, a tuning ferrite layer and dielectric substrates [1]-[4]. The components of the structure affect the degree of the tunability of the device and the MW losses in it. A detailed investigation of these factors is important for interpretation of the experimental data and for optimization of the tunable device geometries.

This paper deals with the investigation of the magnetic tuning effect and the MW losses in HTS coplanar waveguide (CPW) resonator of a general geometry, consisting of HTS electrodes, a tangentially magnetized ferrite layer and dielectric substrates.

II. THE RESONANCE FREQUENCY AND THE MW LOSSES

The structure considered is shown in Fig.1. High temperature superconducting CPW resonator 2 is situated on the top of dielectric substrate 1 and is separated by dielectric spacer 3 from ferrite layer 4 with its substrate 5. The length l and the width w_f of the structure are assumed to be considerably greater than the width of the central conductor w and the distance w_1 between the ground plane electrodes in HTS CPW resonator geometry. The structure is placed in free space with relative permittivity ε =1 (media 0 and 6 in Fig.1). The thicknesses of layers 1 - 5 and the relative permittivities of media 1 and 3 - 5 are assumed to be t_1 - t_5 and ε_1, ε_3 - ε_5, respectively. The permeabilities of all media except the ferrite one are μ=1. The ferrite medium is characterized by permeability tensor μ [5]. External DC magnetic field H_e lies in the plane of the structure and forms an angle φ with the CPW direction. The primary and the secondary coordinate systems x, y, z and x', y', z', the $0z$ and $0z'$ axes of which are oriented parallel to the CPW resonator and to the applied field directions, respectively (see Fig.1), were used to investigate the problem.

In an initial step an auxiliary resonator configuration with a dielectric layer 4 with permittivity ε_4 and permeability $\mu_4 = 1$ instead of a ferrite one was considered. In this approach the complex resonance frequency f_n can be expressed as

$$f_n = f_{0n}[1 + 0.5itg(\delta_e)], \quad (1)$$

where $f_{0n} = [n/(2l)](L_eC_o)^{-1/2}$; $i^2 = -1$; $C_0 = 4\varepsilon_e\varepsilon_0G(k)$ and $L_e = \mu_0/[4G(k)]$ are the capacitance and the external inductivity of CPW per unit length; $G(k)$ is the parameter which depends on the dimensions of the structure; μ_0 and ε_0 are the magnetic and dielectric constants of vacuum; ε_e and $tg(\delta_e)$ are the effective dielectric constant and the effective loss tangent of the layered structure [6], which depend on the geometry of the structure, and the electric parameters of the layers; n =1, 2, 3, ... are the numbers of the modes.

In the following step the MW losses and the change of the resonance frequency caused by the complex kinetic inductance of the HTS electrodes were taken into account. This inductance is related to the magnetic penetration depth λ and the surface resistance R_s of the HTS material, which depend linearly on the applied field intensity H_e when the temperature is not very close to the critical one [7]:

$$R_s = R_{sc} + p_1H_e, \quad \lambda = \lambda_l + p_2H_e, \quad (2)$$

where R_{sc} and λ_L are the characteristic surface resistance and London penetration depth, respectively; p_1 and p_2 are the coefficients related to the dynamic parameters of the magnetic fluxons in HTS material.

In the final step a perturbation of the resonator parameters, caused by the permeability of ferrite layer 4 was considered and the following formulas for calculating of the real and the imaginary part of the resonance frequency were determined by using the perturbation method:

$$f_{pn} = f_{0n}\left(1 - \frac{N_1\lambda}{2t_2}\frac{\mu_0}{L_e} - m_1\right), \quad (3)$$

$$\delta f_{pn} = \frac{1}{2}f_{0n}\left(tg(\delta_e) + N_1\frac{R_{sc}}{2\pi t_2L_ef_{0n}} + 2m_2\right), \quad (4)$$

Manuscript received April 30, 1999.
This work was supported by the Bulgarian Academy of Sciences and the British Royal Society under the Joint - Research Project "Magnetic tuning effect in high temperature superconducting thin film resonator structures with ferrite components".

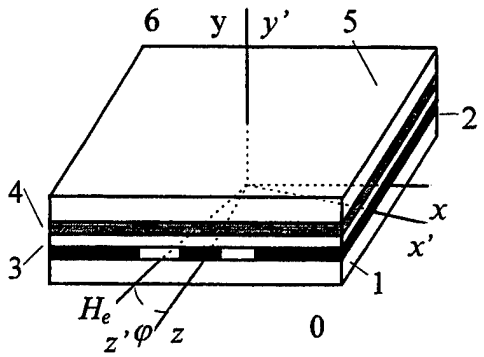

Fig.1. Geometry of the CPW resonator structure: 0 and 6 - free space; 1 - dielectric substrate; 2 - HTS thin film electrodes; 3 - dielectric spacer; 4 - ferrite layer; 5 - substrate of the ferrite layer.

$$m_1 = S\frac{f_s f_M (f_{fm}^2 - f_{0n}^2)(G_x \cos^2\varphi + n_1 G_y)}{(f_{fm}^2 - f_{0n}^2)^2 + \alpha^2 f_{0n}^2 (f_M + 2f_H)^2}, \quad (5)$$

$$m_2 = S\frac{\alpha f_{0n} f_M (f_s^2 + f_{0n}^2)(G_x \cos^2\varphi + n_2 G_y)}{(f_{fm}^2 - f_{0n}^2)^2 + \alpha^2 f_{0n}^2 (f_M + 2f_H)^2}, \quad (6)$$

$$S = \frac{w f t_3 \mu_0}{8 w^2 L_e}, \quad n_1 = \frac{f_H}{f_s}, n_2 = \frac{f_H^2 + f_{0n}^2}{f_s^2 + f_{0n}^2},$$

where $f_s = (f_H + f_M)$; $f_M = \gamma_e H_M/(2\pi)$; $f_H = \gamma_e H_e/(2\pi)$; $H_M = M/\mu_0$; M is the saturation magnetization; γ_e is the gyromagnetic ratio; $f_{fm} = [f_H(f_H + f_M)]^{1/2}$ is the ferrimagnetic resonance (FMR) frequency of the tangentially magnetized film; α is the damping parameter; N_1 is a parameter, which depends on the geometry of the electrodes and the magnetic penetration depth [8]; G_x and G_y are parameters, which depend on the MW current distribution in the electrodes. The perturbation method leads to correct results if the change of the parameters due to the perturbation is small [5]. That is satisfied when the absolute values of the parameters m_1 and m_2 in (3-4) are considerably smaller than one.

III. Analysis and Discussion

The term with m_1 in (3) possesses a negative sign when the magnetic field is not too strong

$$H_e < H_r = -0.5H_M + 0.5\sqrt{(H_M)^2 + (2f_{0n})^2} \quad (7)$$

and the sign is positive when $H_e > H_r$. As a result, the resonance frequency is shifted to higher values if $H_e < H_r$ and to lower ones - if $H_e > H_r$. A maximal field sensitivity of the resonance frequency (a maximum tuning effect) can be expected when $\varphi = 0$ and when the difference between the resonance frequencies f_{fm} and f_{0n} is not too large.

The obtained formulas were used to calculate the MW characteristics of some resonator structures. The parameters of the HTS film were chosen to be close to those of a high

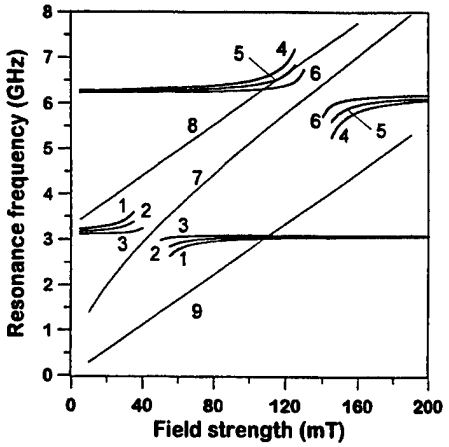

Fig.2. Dependencies of the resonance frequency f_{p1} of the CPW resonators 1 (curves 1 - 3) and 2 (curves 4 - 6) on the external magnetic field strength $\mu_0 H_e$ calculated for the field orientation angles $\varphi = 0$ (curves 1, 4), $\varphi = \pi/4$ (curves 2, 5) and $\varphi = \pi/2$ (curves 3, 6). Curve 7 shows the field dependence of the FMR frequency in the tangentially magnetized film and it coincides with the upper and lower frequency limits of the volume and surface MSW, respectively. Curves 9 and 8 show the lower frequency limit of the volume MSW ($\varphi = \pi/2$) and the upper frequency limit of the surface MSW ($\varphi = 0$), respectively.

quality YBCO film (at T=77 K) prepared on $LaAlO_3$ substrate; $t_1 = 0.5$ mm; $\varepsilon 1 = 24.5$; $tg(\delta_1) = 2\ 10^{-5}$; $t_2 = 0.3$ μm; $R_{sc} = 0.3$ mΩ (resonator 1 with $l = 6$ mm, $f_{p0} \approx 3$ GHz) and $R_{sc} = 0.6$ mΩ (resonator 2 with $l = 3$ mm, $f_{p0} \approx 6$ GHz); $\lambda_l = 0.35$ μm; $p_1 \approx p_2 \approx 0$. As a ferrimagnetic material was considered a YIG layer on a gadolinium-gallium-garnet (GGG) substrate: $t_4 = 15$ μm; $\varepsilon_4 = 16.7$; $tg(\delta_4) = 5\ 10^{-5}$ [9]; $\alpha = 2\ 10^{-4}$ [5]; $M = 235$ mT at 77 K [3]; $t_5 = 0.5$ mm; $\varepsilon_5 = 12$; $tg(\delta_5) = 2\ 10^{-4}$ [9]. The parameters of the dielectric spacer were following: $t_3 = 0.05$ mm; $\varepsilon_3 = 2.4$; $tg(\delta_3) = 2\ 10^{-5}$ The planar dimensions of the CPW resonator were picked up to be $w = 0.4$ mm, $w_1 = 0.6$ mm, $w_f = 3$ mm. In HTS CPW structures the MW current is mainly concentrated in edge areas (with a depth λ_l) of the electrodes. In our case for sake of simplicity the current was assumed to be distributed uniformly over the cross sections of the 4 narrow strips with dimensions t_2 x λ_l, placed at the edges of the central and the ground plane electrodes.

The field dependence of the resonance frequency f_{p1} of CPW resonators 1 and 2, calculated from formula (3) for three different orientations of the external magnetic field H_e in the plane of the structure are shown in Fig.2. In the same figure one can see the field dependence of the magnetic resonance frequency f_{fm} of the tangentially magnetized ferrite layer. It is seen, that when $H_e < H_r$ the resonance frequency is shifted towards higher frequency values whereas the converse is true for the case when $H_e > H_r$. It is interesting to note, that the resonance frequency f_{p1} depends significantly on the field orientation as well. Dependencies of the resonance frequencies f_{p1} on the field orientation angle φ for resonator 1 are shown in Fig.3. For the angles $\varphi < \pi/6$ and $\varphi \sim \pi/2$ these dependencies are not so pronounced as for the angles $\pi/6 < \varphi$

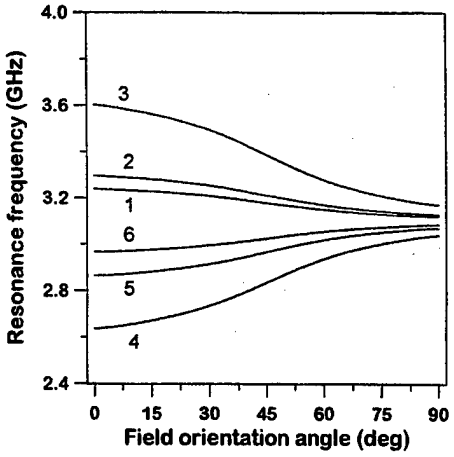

Fig.3. Dependence of the resonance frequency of CPW resonator 1 on the field orientation angle φ computed from formulas (3) for the field strengths $\mu_0 H_e$ = 10, 20, 35, 55, 65, 80 mT (curves 1 - 6, respectively).

$< \pi/3$. When the complex resonance frequency is known the quality factor Q_{pn} can be calculated as well: it was found to be about 1700 for resonator 1 when $H_e << H_r$. It can be shown that the quality factor depends both on the field intensity and the field orientation angle and decreases in the FMR region $f_{fm} \sim f_{01}$, where an increasing of MW losses contributed into the resonator by the ferrite film occurs.

Let us now briefly analyze the conditions of appearing of the MW losses in the resonator due to the excitation of magnetostatic waves (MSW). The frequency of MSW depends on the wavevector and on the angle between the wavevector and the field directions. For $\varphi = 0$ the surface MSW propagating in $0x$ direction can be excited in the resonator structure, shown in Fig.1. The spectrum of these surface MSW are limited by the frequencies [10]

$$f_{fm} \le f \le f_H + 0.5 f_M . \qquad (8)$$

The lower and upper frequency limits of such waves are shown in Fig.2 by curves 7 and 8, respectively. An increasing of the angle φ leads to a decreasing of the upper frequency limit of the surface MSW and at $\varphi = arctan(f_H/f_m)^{-1/2}$ the propagation of surface MSW in the $0x$ direction becomes impossible [10]. For higher values of the angle φ an excitation of the volume MSW is possible. The spectrum of these waves is limited by frequencies [10]

$$f_H \le f \le f_{fm} . \qquad (9)$$

The limiting curves 9 and 7 for the frequencies of the volume MSW are given in Fig.2 as well. It was shown above that a maximum magnetic tuning effect in the considered CPW resonators can be achieved for the field orientation $\varphi = 0$. For such resonators the MW losses caused by an excitation of the surface MSW in the ferrite film will be minimum if $H_e > H_r$: in this case the frequencies of the surface MSW are higher than f_{p1} (see Fig.2) and a transmission of the energy from the resonator to MSW is impossible. For lower external fields $H_e < H_r$ some improvement of the quality factor can be achieved with an increasing of the angle φ. This leads to a decreasing of the upper limit of MSW frequencies and to worsening of the coupling degree of the resonator with the MSW. It is also seen from Fig.2 that when $\varphi = \pi/2$, the functioning of the resonator in the field region $H_e < H_r$ is more preferable, as the resonance frequency f_{p1} will be higher than that of the volume MSW. It can be also noted, that the frequency band of surface MSW gets narrower with the increasing of the magnetic field strength and therefore the resonators with higher resonance frequencies can function out of spectrum MSW and in good tuning conditions even if $\varphi = 0$ and $H_e < H_r$ (see curves 4 and 5 for the second resonator in Fig.2).

IV. Conclusion

In conclusion the MW characteristics of HTS CPW resonator structures containing a tangentially magnetized ferrite layer were investigated using the perturbation method. The formulas, relating the complex resonance frequency of the resonator to the complex permittivity, permeability and kinetic inductance of the layers of the structure were obtained and analyzed. It was shown that i) a tuning of the resonance frequency can be performed by a variation of the magnetic field strength or the orientation angle of the field; ii)a maximum sensitivity of the resonance frequency to the external magnetic field strength is achieved when the field is oriented along the resonator direction; iii) a diminishing of the MW losses due to MSW excitation in the ferrite film is possible by an appropriate choice of the field strength and the field orientation.

References

[1] M. Tsutsumi, T. Fukusako, and H. Shimasaki, "Magnetically tunable superconductor filters using yttrium iron garnet films," *IEEE Trans. Magn.*, vol. 31, pp. 3467 - 3499, Nov. 1995.

[2]. G. F. Dionne, D. E. Oates, D. H. Temme, J. A. Weiss, "Ferrite-superconductor devices for advanced microwave applications," *IEEE Trans.Microwave Theory Tech.*, vol. 44, pp. 1361 - 1369, July 1996.

[3] T. Fukusako, M. Tsutsumi. "Superconducting microstrip resonator with yttrium iron garnet single crystals," *IEEE Trans. Microwave Theory Tech.*, vol. 45, pp. 2013 - 2017, Nov. 1997.

[4] G. F. Dionne, D. E. Oates, "Tunability of microstrip ferrite resonator in the partially magnetized state," *IEEE Trans. Magn.*, vol. 33, pp. 3421 - 3423, Sept. 1997.

[5] A. G. Gurevich, *Magnetic resonance in ferrites and antiferromagnetics.* Moscow: Nauka, 1973.

[6] C. M. Jackson, T. Pham, Z. Zhang, A. Lee, C. Pettiete-Hall, "Model for a novel CPW phase shifter," *1995 IEEE-MTT-S Dighest*, TH3F-G3, pp. 1439-1442.

[7] J. R. Powel, A. Porch, R. G. Humphreys, F. Wellhofer, M. J. Lancaster, C. E. Gough, "Field temperature and frequency dependence of the surface impedance of $YBa_2Cu_3O_7$ thin films," *Phys.Rev.B.*, vol. 57, pp. 5474 - 5484.

[8] W. Rauch, E. Gornik, "Microwave properties of $YBa_2Cu_3O_{7-x}$ thin films studied with coplanar transmission line resonators", *J.Appl.Pys.*, vol. 73, pp.1866 - 1872, Feb. 1993.

[9] P. Mukhopadhyay, "High - T_c films on GGG substrates," *Supercon.Sci.Technol.*, vol. 7, pp. 298 - 299, 1994.

[10] R. W. Damon, J. K. Eshbach. "Magnetostatic modes of a ferromagnet slab", *J. Phys. Chem. Solids*, vol. 19, pp. 308 -320, 1961.

Experimental Observation and Simulation of Unusual Microwave Response for the Superconducting Microstrip Resonator at Small DC Magnetic Field

C. K. Ong, X. S. Rao, B. B. Jin[1]
Centre for Superconducting and Magnetic Materials, Department of Physics,
National University of Singapore, Singapore 119260

Abstract----An unusual microwave response of surface impedance Z_s of high-T_c thin film at an applied small DC magnetic field (B_{dc}) at 77K, namely the decrease of Z_s is observed with microstrip resonator technique. The resonant frequency is 1.107GHz. The direction of B_{dc} is parallel and perpendicular to the ab plane. B_{dc} ranges from 0 to 200G. It is found that change of surface resistance (R_s) at B_{dc} parallel to ab plane, first decrease with B_{dc} and then increase above a crossover field. The R_s behaviour for B_{dc} perpendicular to the ab plane is the same but with a different crossover field. The two behaviours can be collapsed to one curve by scaling the crossover fields. The changes of surface reactance X_s correlated linearly with the changes of R_s in the ranges of B_{dc}. The ratios r_H of changes of R_s and X_s ($r_H=\Delta R_s/\Delta Xs$) are 0.5 at B_{dc} less than crossover field and 0.1 at B_{dc} greater than crossover field. The measurements also show that the crossover field is independent on rf input power. A phenomenological model is also proposed to explain this unusual behaviour. By adjusting fitting parameters the computed results agree with the experimental results qualitatively.

I. Introduction

It is an important subject to measure the field dependence of surface impedance (Z_s) of high-T_c superconducting (HTS) thin films[1]-[11]. The basic behaviour of Z_s is the surface resistance (R_s) and surface reactance (X_s) increase monotonically with applied rf or dc magnetic field. The results showed that microwave losses may be caused by weak links in the low rf field and magnetic hysteretic losses in high rf field [1]-[3]. The power handling of the devices may be limited by local heating at non-superconducting defects[6]. The parameters of high-frequency vortex dynamics can also be deduced from the experimental data [7]. These results are helpful in the understanding of the superconducting mechanism and limit of power handling of microwave devices.

Recently, some anomalous microwave responses, i.e. surface resistance R_s and surface reactance X_s not increasing monotonically with applied rf or dc magnetic field, are reported which are not well explained so far [8-11]. In this paper we present our experimental observations on anomalous R_s and X_s behaviours at 77K in weak applied DC magnetic field B_{dc} (parallel and perpendicular to c-axis) with a HTS meandering microstrip resonator. The field dependence of R_s at different input power is also measured. Some simulations are carried out to explain the anomalous behaviours.

II. Experimental Results

The double-sided YBCO thin films were prepared by on-axis pulsed-laser deposition (PLD) technique on polished $LaAlO_3$ (100) substrates with size of 15×10×0.5 mm^3. The films have a strong preferential orientation with the *c*-axis. The surface resistance, measured with dielectric resonator, is about 1 mΩ at 10.66 GHz before patterning. The microstrip resonator was patterned with conventional chemical etching method. Details of the film deposition and characterisation, design and fabrication of the microstrip resonators can be found in Ref. [12].

The microwave responses were measured using a vector network analyser and the dc magnetic field was applied using a copper solenoid. It is worth pointing out that there is no remnant field effect in the measurements since the experimental set-up are all made of Teflon except for the

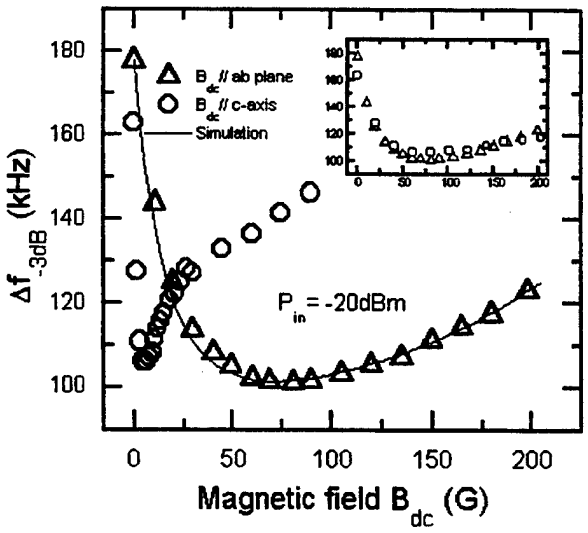

Fig.1 3dB bandwidth Δf_{-3dB} versus B_{dc} at input power –20dBm. Triangles and circles represent B_{dc} parallel to ab plane and c-axis, respectively. The solid line represents the simulation. The inset shows the scaling behavior of field dependence of Δf_{-3dB}.

[1] On leave from Dept. of Electronic Engineering, Nanjing Univ. of Posts and Telecommunications, Nanjing, China

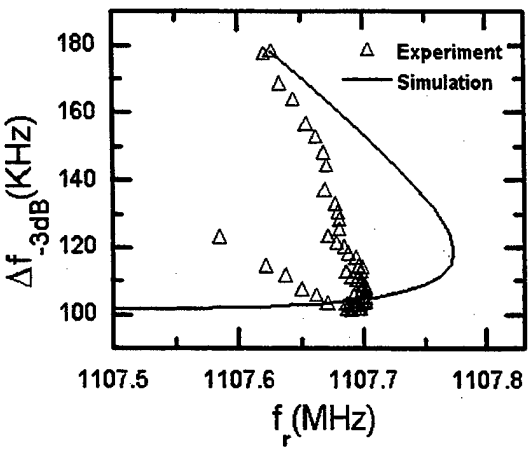

Fig.2 Δf_{-3dB} versus resonant frequency at varing B_{dc} at input power -20dBm. The symbol and solid line represent the experimental results and simulation

copper solenoid

Fig.1 shows the data for 3dB bandwidth (Δf_{-3dB}) of the resonant curves versus B_{dc} for the sample in a zero-field cooled state. In our measurements the coupling to the resonator is very weak. It will bring minor errors to replace unloaded quality factor (Q_U) with Q_L. Hence, Q_L is inversely proportional to surface resistance (R_s), that is, Δf_{-3dB} is proportional to R_s. The measurements were carried out at fundamental frequency with input power -20dBm in liquid nitrogen temperature. From the fig.1 we can find that at first R_s is dramatically decreased by B_{dc} for both B_{dc} parallel or perpendicular to c-axis. The relative change of R_s is greater than 35%. The curves for the two orientations are similar. The only difference is the location of the minima of R_s, which may be caused by serious demagnetisation effect. The inset of Fig.1 shows the data for B_{dc} parallel to c-axis are normalised with B_{dc} corresponding to minimum of R_s for B_{dc} perpendicular to c-axis. The two curves almost collapse to one, i.e., the field dependence of R_s is a scaling behaviour for different orientations B_{dc}. So, the mechanisms governing the

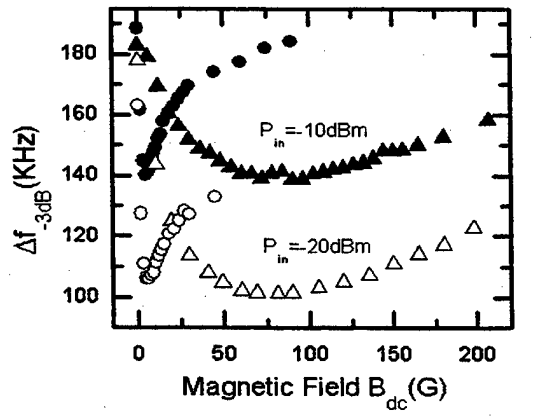

Fig.3 Δf_{-3dB} versus B_{dc} at input power -20dBm.(open) and –10dBm (solid). The triangles and circles represent B_{dc} parallel to ab plane and c-axis, respectively. No obvious shift of the crossover field is observed.

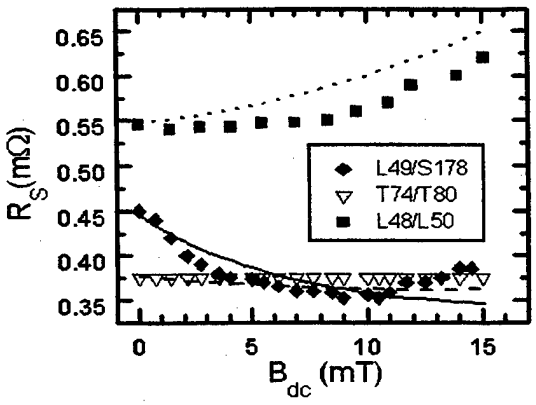

Fig.4 R_S versus B_{dc} for three samples in Hein et al paper. The symbols and lines represent the experimental results and simulation, respectively.

anomalous microwave response are independent of the different orientation of B_{dc}.

Fig.2 shows the relation between Δf_{-3dB} and resonant frequency f_r. Because the change of f_r is proportional to the change of X_s, the figure demonstrates the correlation between R_s and X_s. The two factors of the slope of the curve represents the ratio of changes of R_s and X_s, i.e. the dimensionless parameter r_H, where $r_H = \Delta R_s(B_{dc})/\Delta X_s(B_{dc})$. Some papers have illustrated that this parameter can be used as a characteristic signature for differentiating the mechanisms[13]-[16]. The different r-values represent different mechanism dominating the response. In our measurements, r_H~0.5 below the crossover field and r_H~ 0.10 above crossover field. So, we conclude that two mechanisms dominate the microwave response at weak B_{dc}.

Similar results are observed as the input power is varied. Fig.3 shows Δf_{-3dB} versus B_{dc} with different orientations when the input rf power is –10dBm and –20dBm. We do not observe the shift of the crossover field within the accuracy of the measurements.

III. SIMULATION

Up to now, the previous mechanisms, which can explain field dependence of Z_s, can not be used for this anomalous behaviour. Several groups proposed that magnetic field-induced recovery of superconductivity might account for the anomalous microwave response[9]-[11],[17]-[18]. As we know a spin-flip process exists in the interaction between mobile charge-carriers and magnetic impurities. In superconductor, It will lead to the pair-breaking, that is, to the destruction of Cooper pairs. So, the superconducting properties are strongly affected by the presence of magnetic impurities. An external magnetic field forces the localized magnetic moments, which exists in HTS thin films, to align and frustrates the spin-flip scattering, then leads to a reduction of pair breaking. According to two-fluid model the increase of pair electrons can lead to the decrease of R_s and X_s. A phenomenological model is proposed based on this

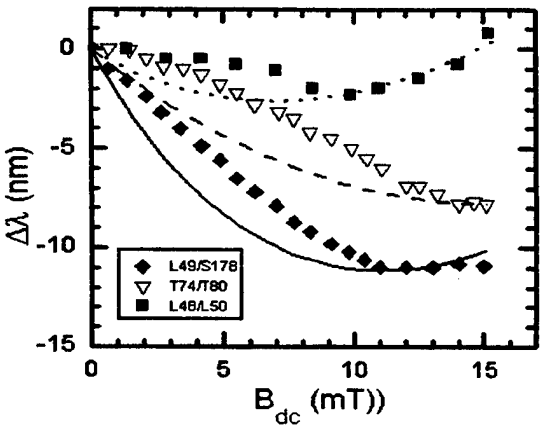

Fig.5 The penetration depth versus B_{dc} for three samples in Hein et al paper. The symbols and lines represent the experimental results and simulation, respectively.

frame[19]. In this model we think some of the normal electrons change to superconducting electrons. The density of superconducting electrons (n_s) in small B_{dc} can be expressed as $n_s(T,B)=n_s(T)[1+\alpha(1-\exp(-B_{dc}/B_c))]$ where $n_s(T,B)$ and $n_s(T)$ represent the density of superconducting electrons with and without B_{dc}, respectively. α and B_c are fitting parameters. According to experimental results, two mechanisms dominate our microwave response. So, we assume that another mechanism comes from weak links, which are always likely in HTS thin film. Combining the coupled-grain model we can calculate the changes of Z_s[20]-[21]. The details can be found in Ref.[19]. The solid lines in Fig.1 and Fig.2 represent parts of the simulations. Only the case of B_{dc} parallel to ab plane is computed because no demagnetization effect needed to be considered. This can simplify our calculations. We also apply our model to simulate the experimental results carried out by Hein et al[9]. The simulation results are demonstrated in Fig.3 and Fig.4. All simulations are able to agree with the measurements qualitatively by properly choosing a set of fitting parameter [19].

IV. Conclusions

We have observed the anomalous R_s and X_s behaviours in the presence of a weak dc magnetic field with microstrip resonator technique. The crossover field are independent on rf input power. The mechanisms governing the anomalous response are independent of orientation of B_{dc}. A phenomenological model is proposed based on assumption of field recovery of superconducting, two-fluid model and couple-grain model. Qualitative agreement can be obtained between the experiments and simulations.

References

[1] P.P.Nguyen, D.E.Oates, G.Dresselhaus, M.S.Dresselhaus, Phys. Rev. B48, 6400 (1993).
[2] P.P.Nguyen, D.E.oates, G.Dresselhaus, M.S.Dresslhause, A.C.Anderson, Phys. Rev. B51, 6686(1995)
[3] D.E.Oates, P.P.Nguyen, Y.Habib, G.Dresselhaus, M.S.Dresselhaus, G.Koren, and E.Polturak, Appl. Phys. Lett. 68, 705 (1996).
[4] J.C.Gallop, A.L.Cowie and L.F.Cohen, Inst. Phys. Conf. Ser. No 158, 65 (1997).
[5] M.Tsindlekht, M.Golosovosky, D.Davidov, and A.F.Jacob, IEEE trans. Appl. Supercond. 7, 1295 (1997).
[6] M.Hein, W.Diete, M.Getta, S.Hensen, T.Kaiser, G.Muller,H.Piel and H.Schlik, IEEE Trans. Appl. Supercond. 7', 1264 (1997).
[7] M.Golosovsky, M.Tsindlekht, and D. Davidov, Supercond. Sci. Technol. 9, 1 (1996).
[8] D.P.Choudhury, B.A.Willemsen, J.S.Derov, and S.Sridhar, IEEE Trans. Appl. Supercond. 7, 1260(1997)
[9] M.A.Hein, C.Bauer, W.Diete, S.Hensen, T.Kaiser, V.Z.Kresin and G.Muller, J. Supercond. 10, 485 (1997).
[10] A.P.Kharel, A.V.Velichko, J.R.Powell, A.Porch,M.J.Lancaster and R.G.Humphreys, Phy. Rev. B58, 11189 (1998).
[11] A.P. Kharel, K.H.Soon, J.R.Powell, A.Porch, M.J.Lancaster, A.V.Velichko, and R.G.Humphreys, ASC'98, USA (1998).
[12] X.S.Rao, C.K.Ong, P.Chen, S.Y.Xu, and Y.P.Feng, submitted.
[13] J.Halbritter, J. Superconductivity 8, 691(1995)
[14] J.Halbritter, J. Superconductivity 8, 91(1997)
[15] J.S.Herd, D.E.Oates, J.Halbritter, IEEE Trans. Appl. Supercond. 7, 1299(1997)
[16] M.A.Golosovsky, H.J.Snortland and M.R.Beasley, Phys. Rev.B51, 6462 (1995)
[17] V.Z.Kresin, S.A.Wolf, Yu. N. Ovchinnikov, J. Supercond. 9, 431 (1996).
[18] A.Bill, S.A.Wolf, Yu.N. Ovchinnikov, V.Z.Kresin, Physica C 298, 231(1998)
[19] B.B.Jin, X.S.Rao, C.Y.Tan and C.K.Ong, in press
[20] T.L.Hylton, A.Kapitulnik, M.R.Beasley, J.P.Carini, L.Drabeck and G.Gruner, Appl. Phys. Lett. 53, 1343(1988)
[21] C.Attanasio, L.Maritato and Ruggero Vaglio, Phys. Rev. B 43, 6128 (1991)

Superconductor-Semiconductor-Superconductor (S/N/S) Interferometers with Phase Sensitive Conductance at V = 0 and V = Δ/e.

J. Kutchinsky, Rafael Taboryski~, Jørn Bindslev Hansen,
Department of Physics, Technical University of Denmark, Build. 309, DK-2800 Lyngby, Denmark
~Presently at: Danish Institute of Fundamental Metrology, Build. 307, DK-2800 Lyngby, Denmark.

Morten Wildt, Claus B. Sørensen, and Poul Erik Lindelof.
Niels Bohr Institute, University of Copenhagen, Universitetsparken 5, DK-2100 Copenhagen Ø, Denmark.

Abstract – We report measurements on phase sensitive conductance in interferometers of superconductor-semiconductor-superconductor (S/N/S) structures of aluminum on degenerate GaAs. The samples were fabricated in a planar geometry with high transparency superconducting contacts of Al deposited on highly diffusive and surface δ-doped n++-GaAs. The I-V and dV/dI vs. V characteristics exhibit resistance minima at V = 2Δ/ne, the so-called sub-harmonic energy gap structure (SGS) originating from multiple Andreev reflections. We have studied the flux dependence of the differential resistance, dV/dI. Clear h/2e-periodic oscillations are observed in the dV/dI vs. Φ curves around V = 0 and around V = Δ/e. We interpret this voltage dependent SQUID-like effect as a result of enhanced phase coherence for Andreev reflected electron-hole pairs propagating diffusively in the GaAs region.

I. Introduction

In recent years the study of the proximity effect observed at the interface between superconductors and normal metals (N-S interfaces) has been revived. As a result of such efforts that lie within the main stream of mesoscopic physics, a new understanding of the proximity effect based on the Andreev reflection process at N-S interfaces has emerged. The characteristic energy-dependent length scales both in equilibrium and for the non-equilibrium phenomena induced when a current is driven through an N-S interface have been clarified and so has the role of Andreev bound states in carrying phase coherent currents in S-N-S junctions.

II. Theory

The Andreev reflection is a second order quantum mechanical process: an electron incident on the N-S boundary with a quasiparticle excitation energy ε above the Fermi energy, may be transmitted as a Cooper pair in the superconductor, if a hole-like particle with energy $-\varepsilon$ is retroreflected along the path of the incoming electron [1]. For a superconductor-oxide-normal metal (S-I-N) interface, with a very thin oxide layer, or for an superconductor-semiconductor interface with a negligible Schottky barrier this leads to an increased conductance, which is observed as an excess current at high voltage bias ($V > 2\Delta/e$). For S-N-S junctions a sub-harmonic energy gap structure (SGS) is normally observed in the I-V curves as peaks in the conductance for $V = 2\Delta/ne$ with $n = 1,2,3,....$ A semiclassical model of the SGS based on multiple Andreev reflections has long been known [2]. However, this model completely neglects scattering and the effect of coherent states in the normal region. Recently also coherent transport in short S-N-S junctions has been taken into account [3].

The superconductor energy gap Δ obviously defines the voltage scale for the sub-harmonic energy gap structure and it also determines the Josephson frequency, $\omega_J = 2eV/\hbar$. The present models for SGS in S-N-S junctions assume, that at all voltages considered the transit time across the normal region is short compared to the inverse Josephson frequency. For a conductor in the diffusive regime the average transit time over the length L is $t = L^2/D$, where D is the diffusion constant. Therefore, the junction must be short compared to the length $L_\Delta = (\hbar D/\Delta)^{1/2}$.

The coherent charge transport across the N-S interface is due to the Andreev reflection process, which couples the single particle states at energies $\mu_s \pm \varepsilon$ where μ_s is the chemical potential of the superconductor. In a diffusive system, the energy difference 2ε between the states becomes the limiting factor for how far from the N-S interface the states can remain phase-coherent. Over a time period t after the Andreev reflection, an initially coherent pair of quasi-particles (one electron-like and the other hole-like) will develop a phase-difference $\delta\phi = 2\varepsilon t/\hbar$. During this time the particles will diffuse an average distance $L = (Dt)^{1/2}$. This defines the relevant energy scale for dephasing of the initially coherent pair-state: $\varepsilon_c = \hbar D/L^2$, also called the Thouless energy (the correlation energy). If phase-breaking processes are included, the phase-breaking diffusion length ℓ_ϕ enters into the expression for the correlation energy $\varepsilon_c = \hbar D(1/L^2 - 1/\ell^2)$. With increasing distance from the interface the coherent window becomes narrower. By definition, the coherence length in the diffusive normal region, $\xi_N = (2\pi k_B T/(\hbar D) + 1/\ell_\phi^2)^{-1/2}$ corresponds to the range over which the states are coherent in the thermal energy window between $\pm 2\pi k_B T$. Therefore the critical current I_c is determined by states with energies of the order of the thermal energy.

Manuscript received April 30, 1999. This work was supported by the Danish Technical Research Council, the Velux Foundation, the III-V Nanolab, and the CNAST center program.

III. Experimental techniques

A. Material growth and characterization

The samples were fabricated as follows: a 200 *nm* thick layer of degenerate GaAs was grown in a VARIAN molecular beam epitaxy chamber on an undoped GaAs substrate. The GaAs was doped with Si to 4.4×10^{18} cm^{-3} and capped with five Si monolayers (δ-doping) separated by 2.5 *nm* of GaAs. Each of the δ-doped layers contained 5×10^{13} Si atoms per cm^2. These layers reduce the width of the Schottky barrier at the superconductor-semiconductor interface, which was formed by depositing 200 *nm* of Al *in-situ* after the GaAs had cooled down. The result was a highly transparent superconductor-semiconductor interface with a measured contact resistivity between Al and GaAs for the best material of $\rho_c = 8\times10^{-13}$ Ωm^2. From the excess current in devices made from this material we estimate a barrier transmission coefficient based of $T_n = 0.5$. On the other hand, an estimate based on the contact resistivity gives $T_n = (3\rho_c/(\ell\rho) + \frac{1}{2})^{-1} = 0.15$, where $\ell \approx 50$ *nm* and $\rho \approx 8\times10^{-6}$ Ωm is the mean free path and resistivity of the semiconductor. This discrepancy may be explained if we assume that the effective contact area is a factor of 0.4 smaller than the nominal contact area. $T_n = 0.15$ is a lower limit for the transmission coefficient. The contact resistivity depends critically on the MBE growth parameters. The GaAs had a carrier density of $n = 4.8\times10^{18}$ cm^{-3} and a diffusion constant $D = 0.016$ m^2/s. For an electrode separation of $L = 1$ μm this gives a Thouless energy of $\varepsilon_c = \hbar D/L^2 = 10.4$ μeV. In an independent measurement the phase-breaking diffusion length was determined by means of the weak localization effect [4] and found to be $\ell_\phi \approx 5$ μm at 0.24 K, the base temperature of the cryostat. The resulting normal metal coherence length at 0.24 K is therefore $\xi_N \approx 0.28$ μm. The Al film had a superconducting transition temperature close to the bulk value T_c=1.2 K. For individual devices the superconducting energy gap ranged from Δ=170 μeV to 178 μV clustered around the bulk value of 175 μeV.

B. Device processing

First, 18 μm wide mesa structures in the Al and GaAs layers were etched with separate current and voltage contacts for four point measurements. Second, the S-N-S structures were fabricated by removing Al in selected areas by the use of electron beam lithography with standard PMMA resist and wet etching [5]. The devices were either shaped as simple Josephson junction type of slits with width *L*, or as flux-sensitive interferometers where one of the Al electrodes was shaped as an open loop, see the inset of Fig. 2.

C. Measurement system

The samples were characterized electrically in a ^{3}He cryostat with a base temperature of 0.235 *mK*. The measurement leads pair were filtered and twisted. The *I/V* and *dV/dI* vs. *V* characteristics of the devices were measured by applying a low frequency ac modulation current superimposed on a dc bias. The ac voltage was measured with a lock-in amplifier. The overall resistance of the devices was of the order of 1–10 Ω depending on the geometry. The ac current amplitude was kept as low as possible to gain optimal resolution in the dc measurement without compromising the signal to noise ratio of the ac measurement. Approximately 200 *nA* rms. ac excitation amplitude was chosen. A magnetic field was applied from a superconducting solenoid powered by a high resolution current source.

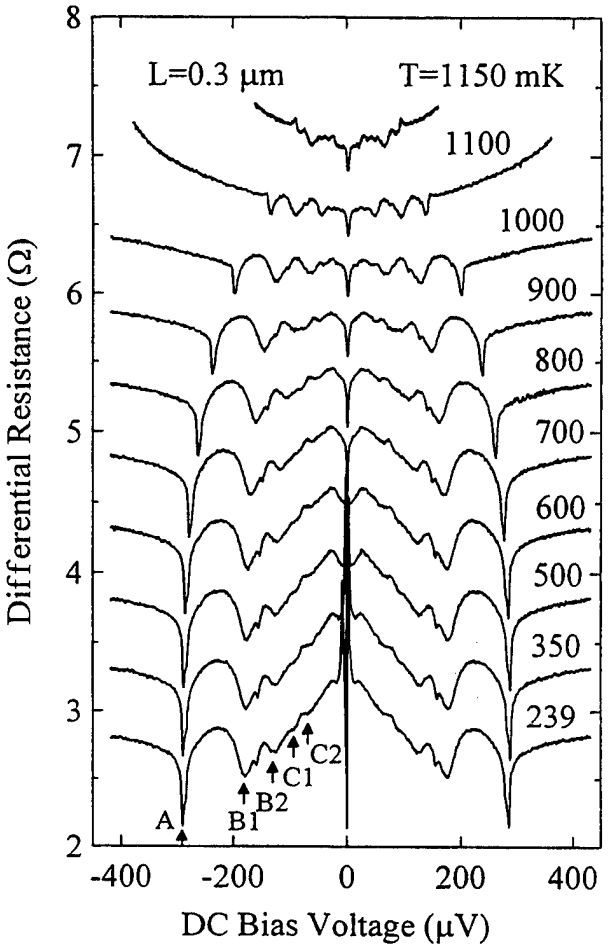

Fig. 1 Differential resistance vs. voltage for a simple Josephson junction. The minima in the differential resistance at $V = 2\Delta/ne$ associated with the sub-harmonic energy gap structure are marked A, B and C corresponding to n = 1,2 and 4. The n = 2 and n=4 structures are split.

IV. Experimental results

Figure 1 shows the dV/dI vs. V curves at a number of temperatures for a simple Josephson junction sample with L = 0.3 μm. The sub-harmonic energy gap structure, SGS, is seen as a series of local minima in the differential resistance. In the existing theories the SGS is predicted at DC bias voltages $V = \pm2\Delta/ne$, where n takes on all positive integer

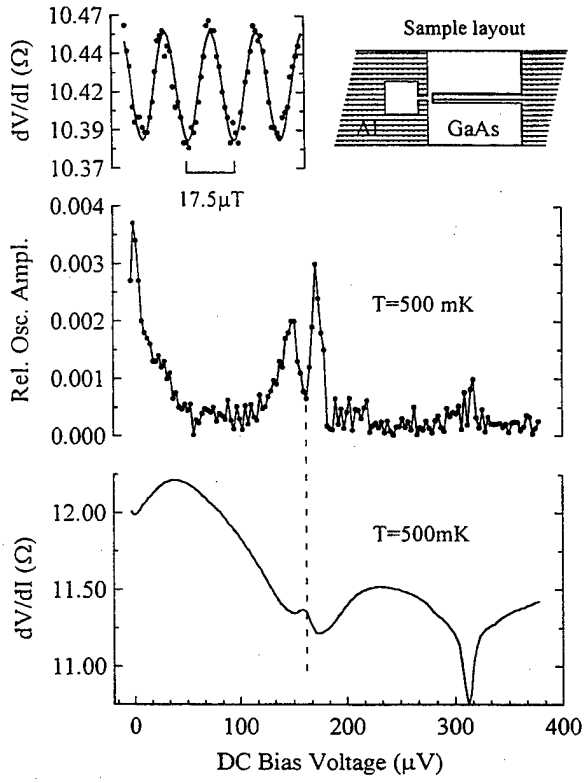

Fig. 2 Upper left: oscillations in the differential resistance taken at the highest $V = \Delta/e$ peak seen in the middle panel. Upper right: sample lay-out. The oscillation period corresponds to h/2e. Middle and bottom: comparison between the differential resistance and the relative oscillation amplitude, both plotted as a function of voltage.

values. As seen the SGS is observed at n = 1,2,4 i.e. only at even sub-gap positions. The experimental fact that only even SGS is seen may indicate that phase-coherence between the electron-like quasiparticles and the Andreev reflected holes plays an important role for the SGS. For even n, Andreev reflected quasiparticles emerge pair wise at the same energy, thereby providing phase-coupling of the two superconductors via coherent energy windows. For $V = \Delta/e$ (n = 2) the coherent energy window emerging from one superconductor probes the quasiparticle density of states singularity at $\varepsilon = \Delta$ in the other superconductor. Quasiparticles injected into the normal conductor at $V = \pm\Delta/e$ will remain phase-coherent with their Andreev reflected counterparts. In the interferometer experiment shown in Fig.2 the current carried by coherent states is distinguished from the background current by application of a magnetic field perpendicular to the loop plane [6]. The magnetic flux threading the loop imposes a phase-difference across the slit between the arms of the loop. As the voltage exceeds $\varepsilon_c/e \approx 10.4\ \mu V$, the oscillations disappear below experimental resolution. However, the oscillations reappear at higher bias around the superconducting energy-gap $V = \Delta/e$ corresponding n = 2. The n = 4 SGS could not be resolved in the interferometer experiment where the distance between the split electrode and the counter-electrode was roughly 1 μm. This experiment clearly indicates that phase-coherent transport plays an important role at the SGS bias positions.

V. Conclusions

In conclusion, we have observed the sub-harmonic energy gap structure (SGS) originating from multiple Andreev reflections in the dV/dI vs. V curves of diffusive Al/GaAs/Al SNS junctions with highly transparent interfaces. This structure could be related to the phase-coherent transport observed in a flux sensitive interferometer at finite voltage bias $V = 2\Delta/2e$.

References

[1] T.M.Klapwijk, G.E.Blonder, and M.Tinkham, Physica (Amsterdam) **109-110B+C** 1657 (1982); G.E.Blonder, M.Tinkham, and T.M.Klapwijk. Phys.Rev. B **25**, 4515 (1982).

[2] M.Octavio, M.Tinkham, G.E.Blonder, and T.M.Klapwijk, Phys.Rev. B **27**, 6739 (1983); K.Flensberg, J.Bindslev Hansen, and M.Octavio, Phys.Rev. B **38**, 8707 (1988).

[3] E.Sheer, P.Joyez, D.Esteve, C.Urbina, and M.Devoret, Phys.Rev.Lett. **78**, 3535, (1997).; E.N.Bratus, V.N.Shumeiko, and G.Vendin, Phys.Rev.Lett. **74**, 2110 (1995); J.C.Cuevas, A.Martin-Rodero, and A. Levy-Yeyati, Phys.Rev. B **54**, 7366 (1996); A.V.Zeitsev and D.V.Averin, Phys.Rev.Lett. **80**, 3602 (1998).

[4] J.Kutchinsky, R.Taboryski, C.B.Sørensen, A.Kristensen, P.E.Lindelof, J.Bindslev Hansen, C. Schelde Jacobsen, and J.L.Skov, Phys.Rev.Lett. **78**, 931 (1997).

[5] R.Taboryski, T.Clausen, J.Bindslev Hansen, J.L.Skov, J.Kutchinsky, C.B.Sørensen, and P.E.Lindelof, Appl.Phys.Lett, **69**, 656 (1996); R.Taboryski, T.Clausen, J.Kutchinsky, C.B.Sørensen, P.E.Lindelof, J.Bindslev Hansen, and J.L.Skov, IEEE Trans. Appl. Sup. **7**, 2809 (1997).

[6] A.Dimoulas, J.P.Haida, B.J.v.Wees, T.M.Klapwijk, W.v.d.Graaf, and G.Borghs, Phys.Rev.Lett., **74**, 602 (1995); J.Kutchinsky, R.Taboryski, O.Kuhn, C.B.Sørensen, P.E.Lindelof, A.Kristensen, J.Bindslev Hansen, C.Schelde Jacobsen, and J.L.Skov, Phys.Rev. B **56**, R2932 (1997).

Extremely Underdamped Josephson Junctions for Macroscopic Quantum Experiments

B.Ruggiero, E.Esposito, C.Granata, M.Russo, and P.Silvestrini
Istituto di Cibernetica del CNR, I-80072 Arco Felice, Naples, Italy
Macroscopic Quantum Mechanics Group, INFN I-80126, Naples, Italy

Abstract-Macroscopic quantum effects in Josephson systems have attracted interest in the scientific community both for the physics involved and in view of applications setting the ultimate limits of many quantum devices. In this context here we present a new design of extremely underdamped Josephson junctions either for use in new experiments in the quantum limit and for devices using the switching dynamics of the junction, when a low noise level is mandatory. High resistance molybdenum meander lines integrated with the junction allow one to increase the insulation of the sample from its electromagnetic environment. We report an experimental study of the effective dissipation relevant in the thermally activated supercurrent decay presenting evidence of a substantial reduction of the dissipation level at low temperature.

I. INTRODUCTION

Quantum devices based on the Josephson effect require a very low dissipation level for their applicability. In the experiments on macroscopic quantum effects[1]-[8], the authors give different conclusions about the dissipation level reached. All these experiments use special noise reduction configurations tailored on the particular situation, which may influence the system dissipation. In many configurations the dissipation is determined by the complex impedance of the load line at the plasma frequency and this leads to an effective dissipation resistance of a few hundred of ohms or less[1],[2] In other cases the dissipation is related to intrinsic processes such as the quasiparticle tunneling resulting in high values of the effective resistance[3],[6],[7]. Favourable configurations are obtained by integrating high-value resistors close to the junction, in order to decouple the system from the external environment[4],[7]. This is typically obtained by locating limiting resistors close to the junction, but the associate stray capacitance may reduce the real part of the complex impedance at the relevant plasma frequency. In devices using the switching properties of a complex configuration of several Josephson junctions, an extremely low dissipation as well as a very low noise level is mandatory. The usual noise configuration would be too complex in real device of that kind and a more compact solution is desirable.

We propose a technique to control the effective dissipation by integrating in a compact way molybdenum resistors wiring with the junction. The resistors are provided by 20 μm-wide thin films sputtered during the fabrication process, and located as close as possible to the junction. The meander shaped resistive lines provide an "in-situ filtering stage", which strongly reduces the external noise coming into the junction. We report an experimental study of the effective dissipation relevant in the thermally activated supercurrent decay of "these self-filtered" $Nb/AlO_x/Nb$ junctions, giving evidence of a substantial improvement of the dissipation level at low temperatures. As result, the junction is decoupled from the external environment and circuit up to high frequency, and the dissipation is determined by the value of the molybdenum resistors. This renders the proposed technique useful for low noise applications of Josephson junctions, where highly integrated filters are recommended, as well as in view of new experiments in the quantum limit, where a very low dissipation is required.

II. EXPERIMENTS AND DISCUSSIONS

The samples were fabricated with all-refractory niobium technology. The $Nb/AlO_x/Nb$ trilayer was deposited by dc-magnetron sputtering. The base and top Nb electrodes were 220 nm and 50 nm thick respectively. They were deposited at a rate of 1.5 nm/sec. The Al film, 10 nm thick, was exposed to an Oxygen pressure of $2.5x10^{-6}$ Pa at room temperature for 1h to form the tunneling barrier. A passivated Si wafer was used as substrate. The whole trilayer geometry is defined by a lift-off process. The junction insulation was provided by an anodization step and a thermally evaporated SiO layer. The anodic Nb_2O_5 layer was grown with a constant current at a rate of 0.5 nm/sec. The molybdenum meander resistors were formed by dc-magnetron sputtering and defined by lift-off technique. The sheet resistance of the 200 nm thick Mo film, deposited at a rate of 1.3 nm/s is 0.5 Ω/sq. at T=4.2 K. Finally 450 nm Nb wiring was deposited and then defined by lift-off technique. Such a procedure has routinely allowed the fabrication of all refractory niobium junctions exhibiting a very low leakage current with a quality factor V_m>80 mV at T=4.2 K and quite uniform critical current density J_c. We produced window-type junctions of area A=5x5 μm^2 and A=10x10 μm^2.

This design gave us the possibility to measure the junction when it is connected to the environment through current and voltage leads made of molybdenum meander resistors (configuration A). Furthermore, we could compare measurements of the same junction when it is simply connected through its current and voltage pads

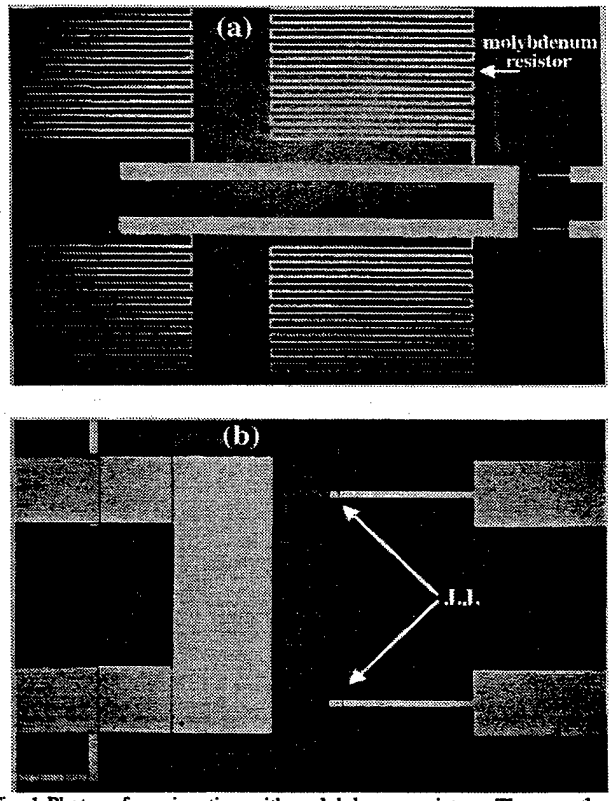

Fig. 1 Photos of our junction with molybdenum resistors. The meander shaped resistors, R_M=6.5 kΩ, inserted into the current and voltage leads, improve the insulation from the electromagnetic environment.

(configuration B). A photo of the sample is shown in Fig.1.

All the measurements were performed in a pumped liquid ^{4}He cryostat with three μ-metal shields and two copper layers to reduce electromagnetic noise. The electrical connections to room temperature went through home-made miniature twin axial cables. The quasiparticle resistance, R_{qp}, tends to saturate at T<2 K due to leakage current in the junction. The measured meander resistance was R_M(4.2 K ÷ 1.2 K)= 6.5 kΩ. We selected junctions with a low critical current density J_c in order to have an extremely low intrinsic dissipation level. The data presented here refer to a junction with J_c≅ 48 Acm^{-2} at T=4.2 K and A≅10x10 μm^2. The capacitance C, as measured from the Fiske step voltage, was C=18±3.6 pF. The Josephson critical current I_c as functions of the temperature T and the superconducting gap Δ, were independently measured (Δ=1.37 ± 0.01 meV at T=4.2 K).

To determine the noise condition as well as the dissipation level for our system, we have measured the switching current distribution as a function of the bias current, P(I), in the temperature range 1.2 K ÷ 4.2 K.

The measurements were performed by standard time fly technique[6]. We compare data taken biasing the junction through the 13 kΩ molybdenum lines (configuration A) and through the usual wiring (configuration B). The ramp generator as well as the preamplificator stage were battery-powered. We biased the junction through a 100 kΩ limiting resistor with a triangular-shaped wave form at frequencies ranging from 100 Hz up to 1 kHz. The synchronism of the ramp generator was delayed and sent to start input of a time-to-amplitude-converter (TAC). The junction voltage was amplified and sent to a discriminator that provides the stop signal for the TAC at the time of the switching out of the zero voltage state. The TAC then provides a voltage signal proportional to the time elapsed between the start and stop input that was sent to an analog to digital converter. A count is assigned to the channel corresponding to the switching time. After each measurement the current ramp has been measured to get dI/dt, which multiplied for the TAC time scale gave the current resolution. In this way we measured experimental histograms equivalent to the switching current distributions.

The results for the two different configurations are reported in Figs.2 and 3.

The measured distribution width $\sigma=(\langle I^2\rangle-\langle I\rangle^2)^{1/2}$ as function of T is shown in Fig.2. The fitting values of the effective resistance R as obtained by each measured P(I) is reported in Fig.3 as function of temperature T. We remark that data were splitted in two different sets for the two different configurations and the fitting value of the effective resistance at low temperatures was different: R=15 kΩ (configuration A) while R=1 kΩ (configuration B). We therefore conclude that the molybdenum meander resistors in the current and voltage lines decouple efficaciously the system from the external circuit and they determine the effective dissipation at low temperature. It is worth to note that the effective resistence shows an exponential temperature dependence due to the activation of the quasiparticle over the superconducting gap Δ, confirming that the effective dissipation is dominated by intrinsic mechanisms: $1/R=1/R_0 \exp(\Delta(T)/K_BT)+1/R_{sat}$. Here R_0= 1 Ω is fixed, while the saturation resistance R_{sat} was different for the two configurations: R_{sat}=15 kΩ (configuration A) and R_{sat}=1 kΩ (configuration B). In Fig.2 the theoretical curves are obtained within the Kramers theory[9] in the extremely-low-damping limit, with the junction parameters (I_c, Δ, and C) independently measured, while the R versus T dependence is assumed to be: $1/R=1/R_0\exp(\Delta(T)/K_BT)+1/R_{sat}$. The fitting temperature is equal to the bath temperature, indicating that any residual amount of external noise is negligible in our measurements. Different curves refer to different saturation resistance at low temperatures.

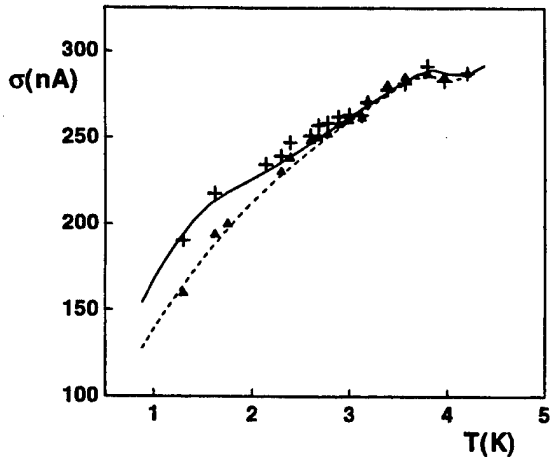

Fig.2 Experimental data for the distribution width σ versus T for configuration A (crosses) and configuration B (triangles). Data are compared with the theoretical predictions within the Kramers theory[9]. The relevant junction parameters are independently measured (C=18 ± 3.6 pF, I_C=48 ± 0.5 μA at T=4.2 K, I_C=55 ± 0.5 μA at T=1.2 K, and Δ=1.37 ± 0.01 meV at T=4.2 K). The R vs T dependence is obtained by Fig.3 as: $1/R=1/R_0\exp(\Delta(T)/K_BT)+1/R_{sat}$, with R_0= 1 Ω and the saturation resistance R_{sat}=15 kΩ (full curve) and R_{sat}=1 kΩ (dashed line).

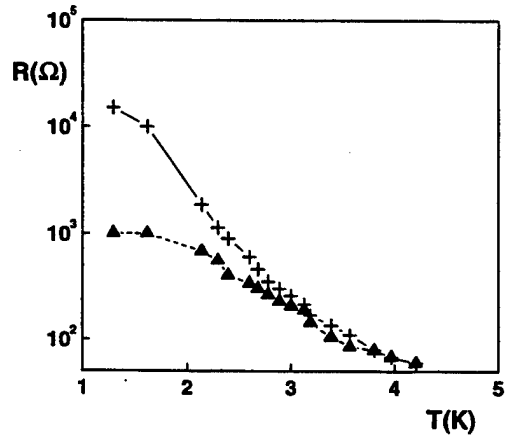

Fig.3 Fitting values of the effective resistance R versus T as obtained from measured P(I) for configuration A (crosses) and for configuration B (triangles). The theoretical curves are the expected dependences for effective resistance as dominated by intrinsic mechanisms: $1/R=1/R_0\exp(\Delta(T)/K_BT)+1/R_{sat}$ (R_0= 1 Ω). The saturation resistance is: R_{sat}=15 kΩ (full line) and R_{sat}=1 kΩ (dashed line).

III. CONCLUSIONS

In conclusion, we have presented a new design of extremely underdamped Josephson junctions to integrate in a compact way molybdenum resistors wiring with the junction. These resistive molybdenum lines do decouple the sample from the external circuit and the electromagnetic environment. The resistance relevant in the thermally-activated supercurrent decay of $Nb/AlO_x/Nb$ Josephson junction shows a substantial improvement of the dissipation level at low temperature. This renders the proposed technique useful for devices using the switching properties of Josephson junctions, when integrated filters are recommended, as well as in view of new experiments in the quantum limit, where a very low dissipation is required[10]. In the millikelvin range of temperture a different material, such as AuPd, is required. Work is in progress to further decrease the effective dissipation by suitable choice of the geometrical pattern of the resistors.

ACKNOWLEDGMENTS

The authors are grateful to V.G. Palmieri, M. Cirillo, and L. Serio for help in the experimental set-up and thank to G. Testa for numerical simulations. This work is partially supported by Istituto Nazionale Fisica Nucleare under the MQC project.

REFERENCES

e-mail: silvestrini@fisps.cib.na.cnr.it

[1] J.M. Martinis, M.H. Devoret and J. Clarke, Phys. Rev. B **35**, 4682 (1987); and references therein

[2] D.B. Schwartz, B. Sen, C.N. Archie and J.Lukens, Phys. Rev. Lett. **57**, 1547 (1985).

[3] R. Rouse, S. Han, and J.E. Lukens, Phys. Rev. Lett. **75**, 1614 (1995).

[4] L.S.Kuzmin and D.B. Haviland, Phys. Rev. Lett.. **67**, 2890 (1991);

[5] D. Vion, P.F. Orfilia, P. Joyez, D. Esteve, and M.H. Devoret, J.Appl.Phys. **77**, 2519 (1995)

[6] P. Silvestrini, R. Cristiano, S. Pagano, O. Liengme and K.E. Gray, Phys. Rev. Lett. **60**, 844 (1988); B. Ruggiero, P. Silvestrini, C. Granata, V.G. Palmieri, A. Esposito, and M. Russo, Phys. Rev. B **57**, 134 (1998).

[7] P. Silvestrini, V.G.Palmieri, B.Ruggiero, and M. Russo, Phys. Rev. Lett. **79**, 3046 (1997.

[8] M.H. Devoret, D. Esteve, and C.U. Urbina, Nature **360**, 547 (1992); see also Proc. of International Workshop on "Macroscopic Quantum Tunneling and Coherence", Special Issue of J. of Superconductivity, P.Silvestrini, B.Ruggiero, F.Petruccione, and A. Barone Eds. (1999, in press).

[9] M. Buttiker, E.P. Harris and R. Landauer, Phys. Rev. B **28**, 1268, (1983); H.A. Kramers, Physica **7**, 284 (1940).

[10] A.D. Caldeira and A.J. Leggett, Phys. Rev. Lett. **46**, 211 (1981).

Third Harmonics Generation from Y-Ba-Cu-O Bicrystal Josephson Junctions in Coplanar Waveguides

H. Shimakage,[a)] J. C. Booth, L. R. Vale, and R. H. Ono
National Institute of Standards and Technology, Boulder CO 80303 USA

Abstract—We report harmonic generation from a bicrystal Josephson junction fabricated in the middle of a 50 Ω coplanar waveguide (CPW). Microwave radiation was injected at one end of the CPW transmission line, and the fundamental and second and third harmonic powers were measured. A decrease of the fundamental transmitted power related to thermal breakdown was observed. The third harmonic output power from the junctions was a complicated function of the input power, showing many non-third order effects.

I. Introduction

In this paper, we report results on microwave harmonic generation from Y-Ba-Cu-O bicrystal junctions. Such measurements are useful in comparing models for nonlinear behavior in high-T_c RF devices.

High-T_c passive devices such as microwave filters are candidates for commercial applications [1]. The advantage of a high-T_c filter is the very high Q-value compared with normal metal designs, which results from low loss in the superconductor [2]. There are difficulties modeling and designing devices using high-T_c thin films. For example, high-T_c materials exhibit nonlinear effects, producing undesirable high-order harmonics and intermodulation products in filters. Therefore studies about nonlinearity are essential for applications.

In the weakly coupled grain model for superconducting thin films [3], the film is described as a network of grain boundaries, each of which acts as a Josephson junction. Yoshida et al. showed the residual surface resistance to be in agreement with this model experimentally [4]. Habib et al. demonstrated the nonlinearity of a Josephson junction by placing it in the center of a stripline resonator [5]. Our group has evaluated nonlinearity by third-order intercept techniques [6], and developed a model using nonlinear inductance [7] in high-T_c thin films.

For the experiments described here, a YBCO bicrystal junction is fabricated in the center of a coplanar waveguide. The input signal is applied at one end, and the first-, second-, and third harmonic outputs are measured at the opposite end using a cryogenic microwave probe station. The fundamental signal transmission behavior and third-harmonic generation characteristics will be discussed.

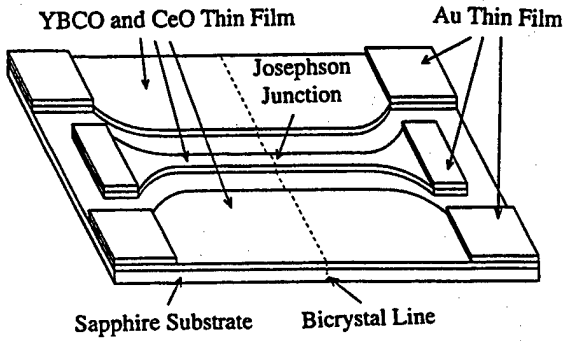

Fig. 1. Schematic drawing of the sample with the bicrystal Josephson junction fabricated in the center of coplanar waveguide.

II. Experiments

A. Junction fabrication

A schematic drawing of the device is shown in Fig. 1. The thin films were grown by pulsed-laser deposition on sapphire bicrystal substrates with buffer layers. The 20 nm CeO_2 buffer layers were grown at a substrate temperature of 800 °C, an oxygen pressure of 53 Pa (400 mTorr), and a repetition rate of 1 Hz. The 140 nm Y-Ba-Cu-O thin films were grown at a substrate temperature of 770 °C, an oxygen pressure of 103 Pa (770 mTorr), and a repetition rate of 10 Hz. The typical critical temperature of the unpatterned film was 89 K. The films were patterned into CPWs using standard photolithography and ion beam etching. The bicrystal line was aligned to the center of the CPW. To reduce contact resistance between the Y-Ba-Cu-O and the probe tips, 150 nm Au contact pads were fabricated by a lift-off process. The center line widths of the CPWs are 92 μm, 64 μm, 32 μm and 16 μm. They are designed to have 50 Ω characteristic impedance to match the external circuit impedance. The length of the line is fixed at 1 mm.

Manuscript received April 30, 1999.
[a)]Permanent address: Kansai Advanced Research Center, Communication Research Laboratory, 588-2 Iwaoka Kobe, 651-2401 Japan
Contribution of the U. S. Government and not subject to copyright.

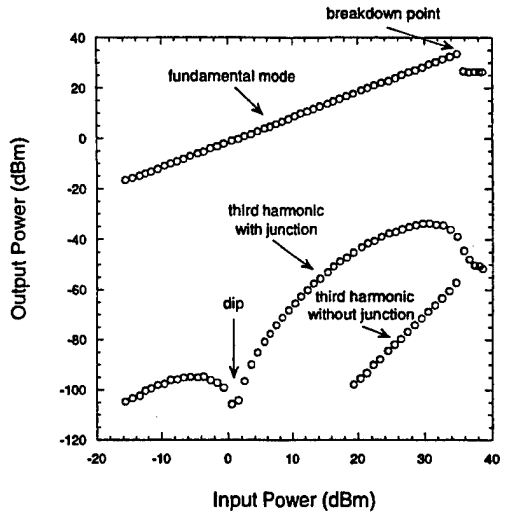

Fig. 2. Fundamental signal output and the second and third harmonics as a function of input power. The line width is 32 μm, and substrate temperature is 60 K.

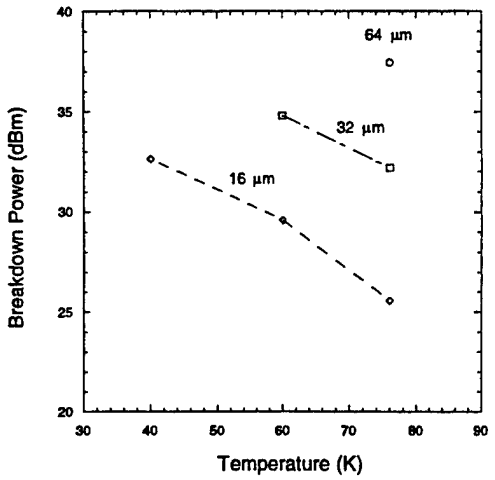

Fig. 3. Temperature dependence of the breakdown power. The higher substrate temperature results in lower breakdown power, and the wider lines have a higher breakdown power.

B. Microwave measurement

The measurement system is described in detail in [7]. The sample is mounted on a cold head, which is cooled using liquid Helium. The temperature is well controlled using a PID controller, ranging from 40 K to 85 K. A continuous signal from a network analyzer is amplified approximately 40 dB, then goes through a 20 dB directional coupler for input power measurement. After passing through a 3 GHz low-pass filter, the signal is introduced to the CPW using high bandwidth coplanar probes. The output signal from the Josephson junction is extracted from the other end of the CPW. The harmonic signals are sampled using a second 20 dB directional coupler. The signals go through a 6 GHz high-pass filter and are measured using a spectrum analyzer. Before measurement of the bicrystal sample, we measured the third harmonics from a CPW without a Josephson junction, fabricated on the same chip. This third-harmonic power was more than 10 dB lower than that of a CPW with a junction. Therefore, most of the third-harmonic output on the samples we now discuss is thought to be from the bicrystal Josephson junction and not from the CPW line.

III. Results and Discussion

A. Fundamental signal output

Fig. 2 shows the fundamental signal and third-harmonic outputs of the 32 μm wide junction at 60 K. The third-harmonic output using the CPW line without Josephson junction is also plotted. We fit the fundamental output with a line of slope unity. For the same size CPW line without Josephson junction, this fitting was same within the measurement uncertainty, implying that the insertion loss due to the Josephson junction is very low. However, a sudden breakdown can be seen at 32 dBm in Fig. 2. This behavior also appeared at other temperatures and in the waveguides with different widths, but did not appear in the waveguides without junctions. The breakdown power is shown in Fig. 3 as a function of temperature and junction width. The higher substrate temperature results in lower breakdown power, and the wider lines have a higher breakdown point power. Because of the output power limit from the power amplifier, the results both for the 92 μm CPW and for the other lines at low temperature do not show the breakdown power. Using the formula $P=I^2Z_0/2$, we roughly estimated the high frequency current using the characteristic impedance of $Z_0=50\ \Omega$. For the 16 μm width at 60 K, the average breakdown current was estimated to be 84 mA. This value is many times larger than we expect for the critical current of a 16 μm junction on a 24° bicrystal [8]. We attribute this phenomenon to exceeding the critical current of the CPW line, perhaps reduced by heating due to small local dissipation at the junction.

B. Third-harmonic power

A dip of the third-harmonic power can be seen near 0 dBm in Fig 2. Fig. 4 shows the third-harmonic power for the 64 μm line width CPW at 40, 60, and 76 K. The dip points were 5.5 dBm at 40 K and 2.6 dBm at 60 K. The dip cannot be seen at 76 K due to the spectrum analyzer noise limit. This behavior was observed in junctions with other widths. We confirmed that the location of the power dip increases with increasing line width. We also estimated the high frequency current to be 11.9 mA at 40 K and 8.5 mA at 60 K. These values are close to the estimated critical current of a 64 μm wide Josephson junction [8]. The power at the dip as a function of substrate temperature is illustrated in Fig. 5. The power at the dip of wider CPW is higher than that of smaller

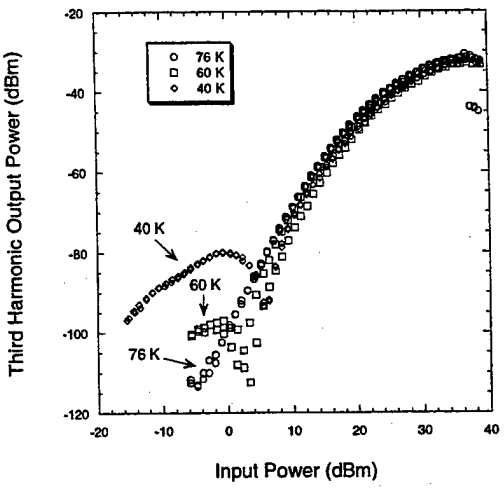

Fig.4. Third-harmonic power as a function of input power. The line width of the coplanar waveguide is 64 μm, and the substrate temperatures are 40, 60, and 70 K. The dips were observed at input powers of 5.5 dBm at 40 K and 2.6 dBm at 60 K.

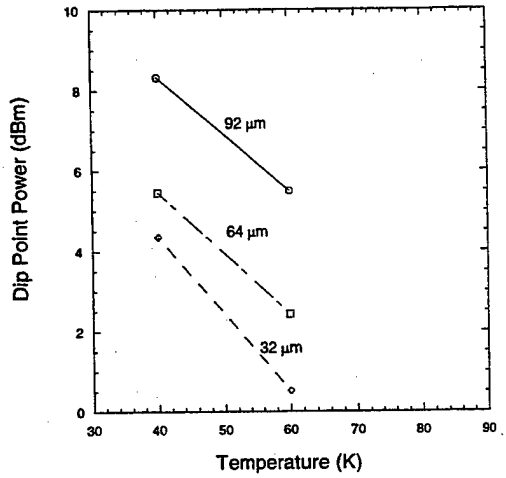

Fig. 5. Dip point power as a function of substrate temperature. The dip point power of wider coplanar waveguides is bigger than that of smaller ones.

ones, suggesting that this is related to the junctions critical current.

The behavior above the dip has little temperature dependence and the slope is decreasing with increasing input power, as seen in Fig. 4. In the CPW without a junction, the third-harmonic power has a slope of 3 when plotted logarithmically vs. input power, and the higher substrate temperature results in lower third-harmonic power [9]. Furthermore, the temperature dependence at powers below the dip is opposite of that of a plain thin film in the measured power range. To understand this further we are working with both shunted-junction models and the nonlinear Josephson kinetic inductance.

IV. Conclusion

We reported the behavior of fundamental signal transmission and third harmonic generation in YBCO coplanar waveguides with imbedded bicrystal Josephson junctions. The fundamental signal transmits through the Josephson junction with low attenuation. However breakdown of the transmission appeared at high input signal power. We estimated the high frequency current, and concluded that the breakdown was related with the critical current density of the film itself. In the measurement of the third harmonic, a dip in the output power was observed. The temperature dependence of the third harmonic is quite unlike that of CPW lines without junctions. The details of this behavior will be analyzed by further studies of the temperature and linewidth dependence and by numerical modeling.

References

[1] J. Galop, "Microwave application of high-temperature superconductors," *Supercond. Sci. Tech.*, vol. 10, pp. A120-A141, 1997.

[2] C. Wilker, Z.-Y. Shen, P. Pang, D. W. Face, W. L. Holstein, A. L. Matthews and D. B. Laubacher, "5 GHz high-temperature-superconductor resonators with high Q and low power dependence up to 90 K," *IEEE Trans. Microwave Theory Tech.*, vol. 39, no. 9, pp. 1475-1479, September 1991.

[3] T. L. Hylton, A. Kepitumik and M. R. Beasley, "Weakly coupled grain model of high-frequency losses in high T_c superconducting thin films," *Appl. Phys. Lett.*, vol. 53, no. 14, pp. 1343-1345, 1988.

[4] K. Yoshida, K. Nagasawa, T. Kiss, H. Shimakage and Z. Wang, "Residual Surface Resistance of $YBa_2Cu_3O_x$ Thin Films – Weakly Coupled Grain Model," *IEEE Trans. Appl. Supercond.*, vol. 7, no. 2, pp. 1253-1256, June 1997.

[5] Y. M. Habib, E. O. Oates, G. Dresselhaus, M. S. and Dresselhaus, "Power Dependence of Microwave Zs in High-T_c Josephson Junctions: Measurements and Modeling," *IEEE Trans. Appl. Supercond.*, vol. 7, no. 2, pp. 2553-2557, June 1997.

[6] J. C. Booth, J. A. Beall, R. H. Ono, F. J. B. Stork, D. A. Rudman and L. R. Vale, "Third Order Harmonics Generation in High-Temperature Superconducting Coplanar Waveguides at Microwave Frequencies," *Appl. Supercond.*, vol. 5, nos 7-12, pp. 379-384, 1998.

[7] J. C. Booth, J. A. Beall, D. A. Rudman, L. R. Vale and R. H. Ono, "Geometry Dependence of Nonlinear Effects in High Temperature Superconducting Transmission Lines at Microwave Frequency," *J. Appl. Phys.*, in press.

[8] L. R. Vale, R. H. Ono and D. A. Rudman, "$YBa_2Cu_3O_{7-x}$ Josephson Junctions on Bicrystal Al_2O_3 and $SrTiO_3$," *IEEE Trans. Appl. Supercond.*, vol. 7, no. 2, pp. 3193-3196, June 1997.

[9] J. C. Booth, J. A. Beall, D. A. Rudman, L. R. Vale, and R. H. Ono, "Simultaneous Optimization of the Linear and Nonlinear Microwave Response of YBCO Films and Devices," *IEEE Trans. Appl. Supercond.*, in press.

Microwave Properties of Tunable $TE_{01\delta}$ mode Sapphire-loaded Cavity Resonators with $YBa_2Cu_3O_{7-\delta}$ Endplates

Sang Young Lee, H.J. Kwon, J. H. Lee, W. I. Yang, Jin Kook Kim*, W.H. Lee* and Jung Hur*
Department of Physics and Center for Advanced Materials and Devices
*Department of Electronic Engineering
Konkuk University, Seoul 143-701, Korea

Abstract—A sapphire-loaded cavity resonator with $YBa_2Cu_3O_{7-\delta}$ (YBCO) endplates and the $TE_{01\delta}$ mode resonant frequency (f_0) of about 19 GHz at 77 K were prepared and their microwave properties were investigated at low temperatures. Unloaded Q (Q_0) of the $TE_{01\delta}$ mode resonator appeared to be more than 1000000, 600000 and about 300000 at 30 K, 60 K and 77 K, respectively, at $f_0 \sim 19.56$ GHz with the sapphire rod sandwiched between two YBCO endplates. Q_0 appeared to decrease as the gap distance (s) between the sapphire rod and the top endplate increases for the resonator with YBCO endplates at 30 K, which was in contrast with the increase of Q_0 for increasing s for the cavity resonator with copper endplates. Microwave losses from the surrounding copper walls appeared to reduce Q_0 of the $TE_{01\delta}$ mode resonator with YBCO endplates significantly at low temperatures. Experimental values of the $TE_{01\delta}$ mode resonant frequencies appeared to agree well with both the calculated values from analytic expressions and the simulated values from a commercial software within 1.3 %. Variations in f_0 upon the gap distance were more than 4.8 % between s = 0 mm and 1 mm, with Q_0 of the $TE_{01\delta}$ mode resonator about 770000, 530000 and 350000 at s = 1 mm at 30 K, 60 K and 77 K, respectively.

I. Introduction

Microwave technologies based on high temperature superconductor (HTS) films have been proved useful in realizing devices with high performance, which include oscillators with extremely low phase noise [1] as well as filters with very small insertion loss and high power handling capability. Tunable microstrip resonators based on YBCO microstrip and $SrTiO_3$ (STO) have been studied by many researchers, where dependence of the dielectric constant of STO on the applied electric field are used for changing the resonant frequency (f_0) [2]. However, due to the high dielectric loss of STO and the loss from the YBCO microstrip, the observed Q was relatively low, with the value of about 200 at 80 K. Meanwhile, HTS films, when used as the endplates of a cylindrical dielectric-loaded cavity resonator, enables us to make a tunable resonator with very high Q. There are reports on $TE_{01\delta}$ dielectric-loaded resonators with very high Q, where YBCO or Thallium-based films are used to form the endplates of the cylindrical cavity with a sapphire rod placed inside as a dielectric with low loss [3]. Furthermore, tuning of f_0 can be realized over a wide frequency range without significant degradation of Q by using $TE_{01\delta}$ mode resonator based on HTS.

Here we report on the properties of a $TE_{01\delta}$ mode cavity resonator based on YBCO films and a sapphire rod wide frequency range without significant degradation of Q by using $TE_{01\delta}$ mode resonator based on HTS. Tuneability of the $TE_{01\delta}$ mode resonator as well as the dependence of the unloaded Q (Q_0) on f_0 was studied for two different cases: one for the resonator based on YBCO films and sapphire and the other one with YBCO films replaced by oxygen-free high quality copper (OFHC) plates.

II. Experimental

A. Preparation of a Sapphire-loaded Cavity Resonator

Fig. 1 shows a diagram of an open-ended parallel plate resonator with a movable top endplate, which we prepared for this experiment. In the figure, a sapphire rod is placed at the center of a YBCO bottom plate with a YBCO plate at the top. The sapphire rod is glued to the YBCO film at the bottom using an epoxy with low microwave loss. The YBCO film at the bottom was grown on both sides of a (100) $LaAlO_3$ substrate while the YBCO film at the top was grown on a CeO_2-buffered r-cut sapphire (CbS) substrate. Both films have the thickness of ~ 0.3 μm and their T_C's are higher than 88 K with the transition width less than 0.8 K. The cavity has the dimensions of 15 mm x 15 mm for the diameter and the height, respectively, with the corresponding values of 5 mm x 5 mm for the sapphire rod. The sapphire rod is c-axis oriented high purity single crystal from CrysTec in Germany.

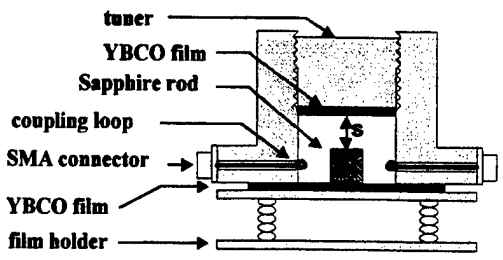

Fig. 1. A diagram of our sapphire-loaded cavity resonator with a movable top plate

Manuscript received April 29, 1999
This work was supported by Korean Ministry of Information and Communications and Ministry of Science and Technology.

The cavity is made of OFHC. To consider thermal contraction of the cavity at low temperatures, the diameter of the YBCO film at the movable top is set to 14.85 mm at the room temperature with the value 0.15 mm smaller than the inner diameter of the cavity.

B. Measurement Procedures

In Fig. 1, the input and output lines were weakly coupled to the resonator and, for TE mode excitations, loop couplings were used. SMA connectors were used for all connections. The data were collected using a HP8510C network analyzer as the temperature was raised. Change in f_0 was realized by moving the top endplate and thereby changing s, the gap between the sapphire rod and the cavity top plate. In identifying the $TE_{01\delta}$ mode resonance signal, we compared experimentally observed f_0 with both the calculated and simulated ones [4]. At 293 K, with $\varepsilon_r = 9.4$ used for the dielectric constant of the sapphire rod, the $TE_{01\delta}$ mode f_0's are 19.448 GHz, 19.497 GHz and 19.697 GHz for the experimental, calculated and simulated values, respectively, with the differences of less than 1.3 % among each other. At temperatures between 30 K and 80 K, the $TE_{01\delta}$ mode f_0 appeared to be ~ 19.56 GHz, which agrees well with the calculated value of 19.58 GHz obtained from analytic expressions for the field distributions inside the cavity [4]. $\varepsilon_r = 9.32$ was used for the dielectric constant of the sapphire at 77 K. Q_L was measured using the conventional 3-dB method. For the weakly coupled case, $Q_0 \approx Q_L$.

III. Results and Discussions

Fig. 2 shows Q_0 vs T data for different values of the gap distance s for the cavity resonator with YBCO endplates (henceforth called 'the YBCO resonator'), with the inset displaying f_0 vs s data. In the figure, Q_0 appears to be ~ 1000000 with f_0 = 19.57 GHz at 30 K and s = 0 mm. The observed high Q_0 is attributed to the very low surface resistance (R_S) of the YBCO films as well as the extremely low loss tangent (tanδ) of the sapphire at low temperatures. Using the observed Q_0 of ~ 1000000, we calculated the effective surface resistance (R_S^{eff}) of the YBCO films, which turned out to be ~ 0.27 mΩ. For calculating R_S^{eff}, tanδ ~ 10^{-7} was used for sapphire and the intrinsic surface resistance (R_S) of the YBCO film at the bottom was assumed equal to the R_S of the YBCO film at the top. At 60 K and 77 K, Q_0's of the YBCO resonator remained as high as ~ 600000 and ~ 300000, respectively, which give R_S^{eff}s of 0.49 mΩ and 1 mΩ, respectively. That also means, R_S^{eff} would be as small as ~ 0.13 mΩ and 0.26 mΩ at 10 GHz at 60 K and 77 K, respectively. In the inset of Fig. 2, it is noted that f_0 changes more abruptly according to s at smaller s. For instance, there is variations of ~ 0.94 GHz in f_0 between s = 0 mm and s = 1 mm, while it is ~ 0.42 GHz between s = 1 mm and 2 mm. This is due to that field distributions inside the cavity are

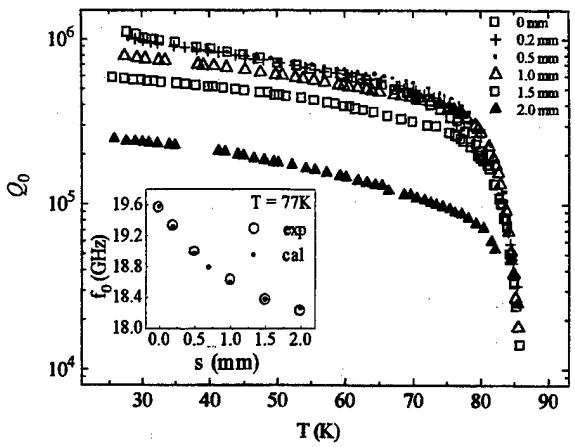

Fig. 2. Dependence of Q_0 on the temperature for different values of s for the YBCO resonator. Inset: Dependence of the experimental (open circle) and calculated (dot) $TE_{01\delta}$ mode resonant frequencies on the gap distance for the YBCO resonator.

modified more according to s at smaller s. The observed f_0's also appear to agree well with the calculated ones, as seen in the inset. In Fig. 2, one interesting thing to point out is that Q_0 appears smaller as s increases at 30 K. This observation is in contrast with the increase of Q_0 for increasing s for the OFHC resonator. In Fig. 3, we display Q_0 vs s data for the YBCO resonator at 30 K, 60 K and 77 K, with the inset showing the data for the OFHC resonator at the room temperature. In the figure, Q_0 appears to decrease as s increases at 30 K for the YBCO resonator with Q_0 = 1020000 and 960000 at s = 0 mm and 5.5 mm, respectively. Meanwhile, Q_0 increased from 12000 at s = 0 mm to 17000 at s = 7 mm for the OFHC resonator. The observed results for the OFHC resonator is attributed to that the magnitude of the magnetic field at the cavity surface becomes smaller for larger s, resulting in smaller signal loss at the cavity surfaces. Also decreasing Q_0 for increasing s is attributed to the fact that losses from the YBCO surface is less significant than the losses from the side walls made of OFHC. Interestingly, at 60 K and 77 K, the dependence of Q_0 on s appeared somewhat complicated with Q_0 increasing according to s up to s = 0.5 mm and decreasing as s increased further. For explaining the unique behaviors observed at 60 K and 77 K, we calculated Q_0's for different values of s using the calculated values of R_S^{eff} = 0.27 mΩ, 0.49 mΩ and 1 mΩ for the YBCO film at 30 K, 60 K and 77 K, respectively. It is noted here that tanδ = 10^{-7} and σ = 5.22 x 10^8 S/m was used for the loss tangent of the sapphire and the conductivity of the OFHC, respectively, throughout the calculation. Detailed procedures for calculating R_S^{eff}s and Q_0's are described elsewhere [5]. From the calculation, Q_0 appeared to decrease as s increases with Q_0's of 980000 and 810000 at s = 0 mm and 0.5 mm, respectively. Meanwhile, at 77 K, the calculated Q_0 appeared to increase between s = 0 mm and 0.5 mm with Q_0 ~ 300000 and 320000 at s = 0 mm and 0.5 mm, respectively, allowing a qualitative agreement between the experimental and calculated Q_0 vs T data. Also, at 60 K, the

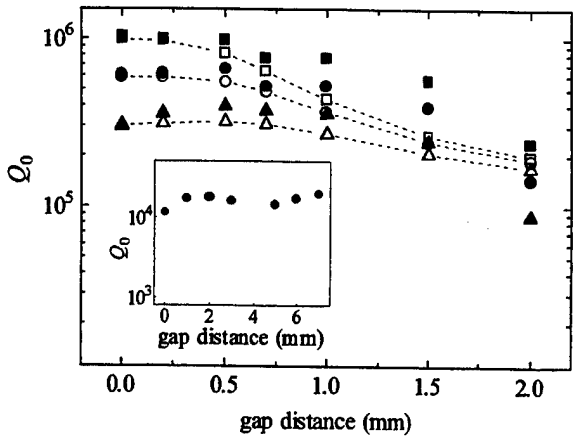

Fig. 3. Dependence of the experimental (filled) and calculated (open) $TE_{01\delta}$ mode Q_0 on the gap distance for the resonator with YBCO endplates at 30 K (square), 60 K (circle) and 77 K (triangle). The dotted lines are guides to eyes. Inset: Dependence of the $TE_{01\delta}$ mode Q_0 on the gap distance for the resonator with OFHC endplates at 293 K. Other mode appears near the $TE_{01\delta}$ mode for s > 2 mm, resulting in more errors in Q_0.

calculated Q_0's are 582000 and 589000 at s = 0 mm and 0.2 mm, showing a slight increase in Q_0 as s increases. In Fig. 3, the calculated Q_0 vs s data are compared with the experimental ones, where good agreements are found up to s = 0.7 mm. For s > 1 mm, calculated Q_0's are less accurate because analytic expressions for field distributions becomes less accurate at higher s. The data in Figs. 2 and 3 show the merits in using the YBCO resonator as a tunable resonator with very high Q. As far as tuning of f_0 is concerned, we have no significant advantages in using the YBCO resonator with the tuning range comparable to the corresponding value for the OFHC resonator. However, Q_0 of the YBCO resonator appears to be improved significantly compared to the one of the OFHC resonator. For instance, between s = 0 mm and 1 mm, Q_0's are more than 300000 with variations of 0.94 GHz (~ 4.8 %) in f_0 at 77 K for the YBCO resonator. Meanwhile there are variations of 5600 in Q_0 from 17000 to 11600 and 0. 98 GHz in f_0 for the OFHC between s = 1 mm and 0 mm at T = 300 K. Our results are also compared with the observed results from tunable microstrip YBCO resonators based on BST or STO, where Q_0 of several hundreds at 80 K have been reported with the tuning range of about 4 % [2]. It is also noted that the YBCO resonator can be used in making a tunable oscillator with very low phase noise, considering the high Q_0 of the $TE_{01\delta}$ mode YBCO resonator and the relatively large frequency tuning range.

Summarizing, the $TE_{01\delta}$ mode sapphire-loaded resonators with YBCO endplates appeared to have Q_0 of ~ 1000000 and 400000 at 30 K and 77 K, respectively, with f_0 ~ 19.56 GHz. Also, the frequency tuning range of about 0.94 GHz was observed upon moving the top YBCO endplate of the cavity resonator by 1 mm. Q_0 vs the gap distance data appeared different between the YBCO resonator and the OFHC resonator, for which an explanation is provided based on the microwave losses from both the YBCO endplates and the surrounding OFHC walls. High Q_0 as well as the large tuning range observed from the YBCO resonator shows that the sapphire-loaded YBCO resonator can be used in making a tunable oscillator with very low phase noise.

ACKNOWLEDGMENT

We thank Dr. B. Oh and Dr. S. H. Moon in LGCIT for providing a YBCO film used for this experiment.

REFERENCES

[1] I.S. Ghosh, N. Tellman, D. Schemion, A. Scholen, and N. Klein, "Low phase noise microwave oscillators based on HTS shielded dielectric resonator", IEEE Trans. on Applied Supercond., vol. 7, pp. 3071-3074, June 1997.

[2] A. T. Findikoglu, Q. X. Jia, D. Reager, I. H. Campbell, C. B. Mombourquette, D. McMurry and X. D. Wu, "Electrically tunable coplanar transmission line resonators using $YBa_2Cu_3O_{7-x}/SrTiO_3$ bilayers", Appl. Phys. Lett., vol. 66, pp. 3674-3676, June 1995.

[3] Z.-Y. Shen, C. Wilker, P. Pang, W. L. Holstein, D. Face and D. J. Kountz, "High T_C superconductor-sapphire microwave resonator with extremely high Q-value up to 90 K", IEEE Trans. on Microwave Theory and Tech., vol. 40, pp. 2424-2432, Dec. 1994.

[4] See e.g., Sang Young Lee, H.J. Kwon, J.H. Suh, J.H. Lee, Jung Hur and V.B. Fedorov, "Effects of the finite HTS film thickness on the resonant frequency of the axially symmetric $TE_{01\delta}$ mode of a parallel plate dielectric resonator", to be published in IEEE Trans. on Applied Supercond., June 1999, for more details on the calculated result. The simulated results were obtained using "Micro-Stripes", a trademark of Kimberley Communications Consultants, Ltd., in UK.

[5] Sang Young Lee, H.J. Kwon and V. B. Fedorov, unpublished.

Preparation of All Oxide Ferromagnetic / Ferroelectric / Superconducting Hetero Structures for Advanced Microwave Applications

Shigeki HONTSU , Hiroaki NISHIKAWA , Harutaka NAKAI and Junya ISHII
Faculty of Biology-Oriented Science and Technology, Kinki University, Uchita-cho, Naga-gun, Wakayama 649-6493, Japan

Masaya NAKAMORI
Department of Electric Engineering, Kumano Technical College, Arima-cho, Kumano, Mie 519-4395, Japan

Akira FUJIMAKI
Department of Electronics, Nagoya University, Furo-cho, Chikusa-ku, Nagoya 464-8603, Japan

Yasumasa NOGUCHI
Kinki University, Kowakae, 3-4-1, Higashi-Osaka, Osaka 577-8502, Japan

Hitoshi TABATA and Tomoji KAWAI
The Institute of Scientific and Industrial Research, Osaka University, Mihogaoka, Ibaraki, Osaka 567-0047, Japan

Abstract—As candidates of the functional layers, 3d-transition-metal oxides with perovskite structures show some interesting properties, such as ferromagnetism, ferroelectricity and superconductivity. Accordingly, the combinations of these properties create new tunable microwave devices. Ferromagnetic / ferroelectric / superconducting multi-structures, such as $La_{0.70}Sr_{0.30}MnO_3$ (LSMO) / $Pb(Zr_{0.52}Ti_{0.48})O_3$ (PZT) / $YBa_2Cu_3O_{7-y}$ (YBCO) and YBCO / PZT / LSMO, have been fabricated by ArF excimer laser deposition on a $LaSrGaO_4$ (LSGO) [001] and $(La_{0.30}Sr_{0.70})(Al_{0.65}Ta_{0.35})O_3$ (LSAT) [001] substrates. The resulting films of these trilayers have highly *c*-axis oriented structure. Epitaxial YBCO films formed on the PZT/LSMO//LSAT have a zero resistance temperature of 87K. Moreover, *D-E* and *M-H* hysteresis loop are observed for the LSMO/PZT/YBCO//LSGO structure using a conventional Sawyer-Tower circuit and a superconducting quantum interference device (SQUID). The remanent polarization and coercive field of PZT layer are obtained to be 19μC/cm² and 275kV/cm at 70K, respectively. The remanent magnetic moment and coercive magnetic field are about 2.6 μ_B/site and 50Oe at 78K, respectively. These results here suggest that the LSMO/PZT/YBCO structures are favorable for use in the superconducting microwave applications, such as tunable phase shifters and filters.

I. INTRODUCTION

High temperature superconducting microwave circuits with the low surface resistance have been demonstrated for passive microwave elements such as filters, antennas and delay lines. To small, lightweight and low-loss microwave components, possible applications include tunable filters, tunable resonant antennas and phase shifters. The electrically controlled superconductor / ferroelectric microwave components such as $YBa_2Cu_3O_{7-y}$ (YBCO) / $SrTiO_3$ (STO)[1] and YBCO / $Ba_{1-x}Sr_xTiO_3$ (BSTO)[2] can be used to tunable filters and oscillators. Also, the magnetically controlled superconductor / magnetic microwave components such as YBCO / Ferrite[3] and YBCO / $Y_3Fe_5O_{12}$(YIG)[4] could build on filters and phase shifters for phased–array radars and communications system with electronically steerable or adaptable antennas. These tunable microwave devices can be designed to change either of the effective dielectric constant (ε_r) of the ferroelectric layer by an applied electric field or the effective permeability (μ_r) of magnetic layer by an applied magnetic field. Namely, the dielectric permittivity ε_r of a ferroelectric or the permeability μ_r of a magnetic close to the Curie point varie considerably with an applied electric field or magnetic field, respectively. As a result, the resonance frequency f_0 ($=1/2\pi\sqrt{LC}$) or phase velocity v_p ($=1/\sqrt{LC}$) can be tuned, because the capacitance C varied by the electric field and the inductance L varied by the magnetic field can be changed. If ε_r (or C) and μ_r (or L) of microwave device can be simultaneously changed, f_0 and v_p determined by the product L and C are very large. Furthermore, the characteristic impedance Z_0 ($=\sqrt{L/C}$: L divided by C) which is important problem for the phase shifters can be kept constant. Thus, the insertion loss generating between the device and transmission line can be decrease. The report on the microwave device to change both L and C has not been seen.

In order to make tunable microwave devices, it may be advisable to use 3d transition-metal oxides, because the 3d transition-metal oxides with perovskite structures show some interesting properties, such as ferromagnetism, ferroelectricity and superconductivity. Cu-oxide exhibits superconductivity, Ti-oxides show dielectricity and ferroelectricity, and Mn-, Co- and Fe-oxides show novel magnetism. Thus, ferromagnetic / ferroelectric / super-conducting heterostructures are suitable for the new tunable microwave devices.

In this paper, as a basic research for the realization of the advanced tunable microwave device, we report the fabrication of $La_{0.70}Sr_{0.30}MnO_3$ (LSMO) / $Pb(Zr_{0.52}Ti_{0.48})O_3$

(PZT) / YBCO , YBCO / PZT / LSMO trilayer structures using ArF excimer laser deposition. We have also measured ferroelectrical properties of PZT, ferromagnetical properties of LSMO and superconducting properties of YBCO film in LSMO / PZT / YBCO structures.

II. Experimental

Thin films of YBCO, LSMO and PZT were deposited by a laser ablation, ArF excimer laser (λ=193nm, τ=20ns) with the 1~7 Hz pulse repetition rate was used. Ceramic targets with the same stoichiometric composition as the films were ablated by laser beam with energy density of ~1J/cm^2 within a spot size of 1×1mm^2. In our experiments the deposition was carried out in an oxygen pressure (containing 8% O_3) of about 3mTorr for YBCO films, 40mTorr for the PZT films and 20mTorr for the LSMO films. Different substrate temperatures *Ts* were used during the deposition and the following values were chosen: for YBCO-*Ts*=640°C, for PZT-*Ts*=540°C, for LSMO-*Ts*=680°C, respectively. The laser repetition rate was increased step by step from 1 Hz by 2 Hz every 20min, and finally the rate went up to 7 Hz to obtain the desire thickness. Typical average deposition rates were 10Å/min for YBCO, 8Å/min for PZT and 15Å/min for LSMO film.

(001)-$LaSrGaO_4$ (LSGO) and (001)-$(La_{0.30}Sr_{0.70})(Al_{0.65}Ta_{0.35})O_3$ (LSAT) substrates with size of 10×10×0.5mm^3 were used. These substrates are very suitable for epitaxial growth of YBCO thin films since the lattice mismatch is less than 1%, and are a dielectric with low microwave losses (tan $\delta \cong 10^{-4}$) which makes it attractive for microwave applications.

The crystallographic properties were evaluated by an X-ray diffraction (XRD). The resistivity of the YBCO films was measured by the conventional four-probe method and magnetization for the LSMO films was measured by a superconducting quantum interface device (SQUID). Also, the ferroelectric property for the PZT film was investigated by a conventional Sawyer-Tower circuit and LCR meter.

III. Results and Discussion

Typical θ-2θ XRD patterns of LSMO(1000Å) / PZT(1800Å) / YBCO(600Å) // LSGO(001) and YBCO (2000Å) / PZT(300Å) / LSMO(300Å) // LSAT(001) were shown in Fig.1. The (00*l*)-YBCO and (00*l*)-PZT peaks indicate a *c*-axis orientation of these layers. Since the lattice constants of LSMO are very close to those of LSAT substrate. The (00*l*)-LSMO peaks is not observed for the LSAT substrate. On the other hand, (00*l*)-LSMO peaks observed for LSGO substrate, thus, we consider that the LSMO layers are *c*-axis perpendicular to the substrate surface.

Figure 2 shows the resistance vs. temperature (*R*-*T*) curve of the LSMO / PZT / YBCO trilayer on the LSGO (001) substrate. The critical temperature *Tc* was 87K. This resistance is measured by contacting in parallel LSMO and YBCO layer. LSMO has high conductance below the paramagnetic insulator-ferromagnetic metal transition temperature[5]. Therefore, the temperature dependence of resistance in this trilayer shows combined resistance in parallel of LSMO and YBCO layer at the temperature above *Tc* of YBCO.

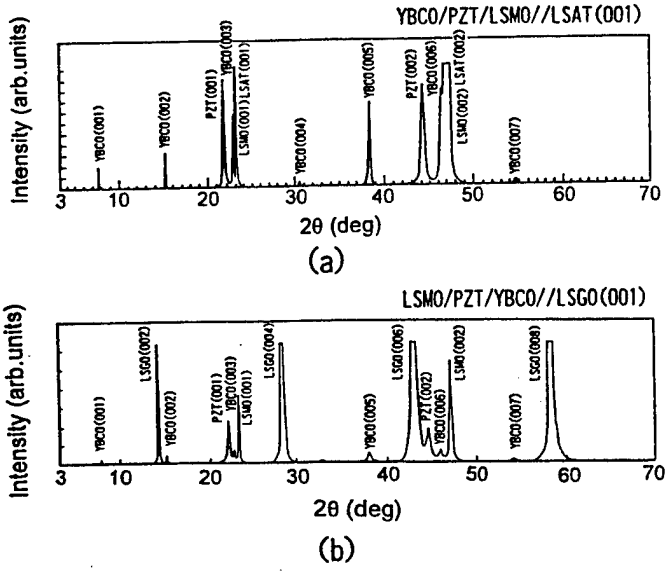

Fig.1 The typical XRD patterns of (a) YBCO(2000Å) / PZT(300Å) / LSMO(300Å) film on LSAT(001) substrate and (b) LSMO(1000Å) / PZT(800Å) / YBCO(600Å) film on LSGO(001) substrate.

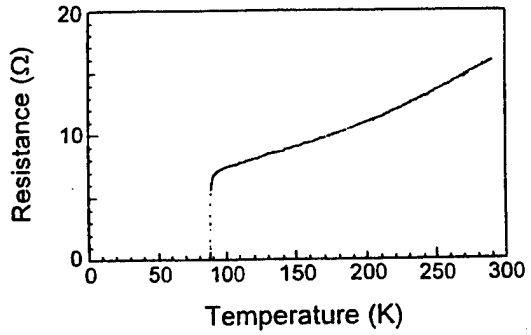

Fig.2 Temperature dependence of LSMO and YBCO parallel resistance in LSMO/PZT/YBCO trilayer on LSGO substrate.

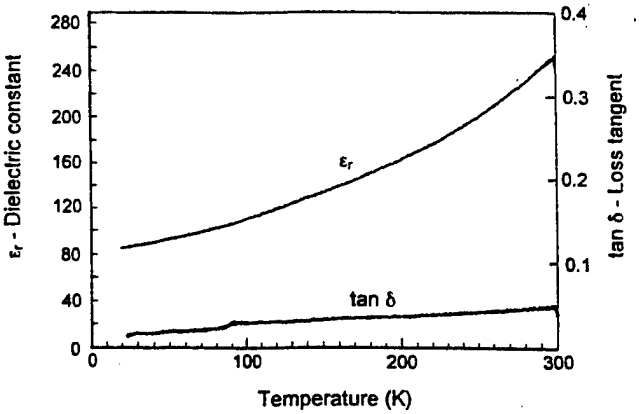

Fig.3 Temperature dependences of relative dielectric constant (ε_r) and loss tangent (tan δ) of PZT film with a LSMO/PZT/YBCO structure.

Figure 3 shows temperature dependencies of relative dielectric constant (ε_r) and dielectric loss (tan δ) measured at frequency of 100kHz and electric field of 50kV/cm. The value of dielectric constant (ε_r) was about 220 at 280K, decreases gradually with decreasing temperature, and showed about 100 at 77K. On the other hand, dielctric loss (tan δ) was smaller than 0.05 over the measured temperature range.

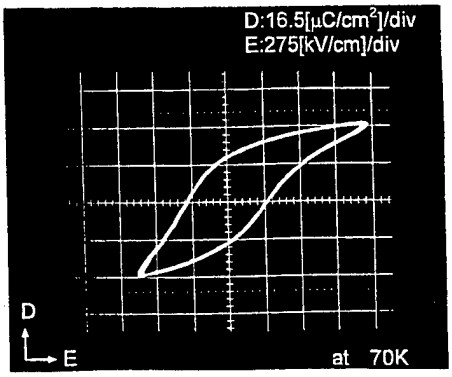

Fig.4 *D-E* hysteresis loop of PZT film in LSMO/PZT/YBCO structure on LSGO substrate at a temperature of 70K.

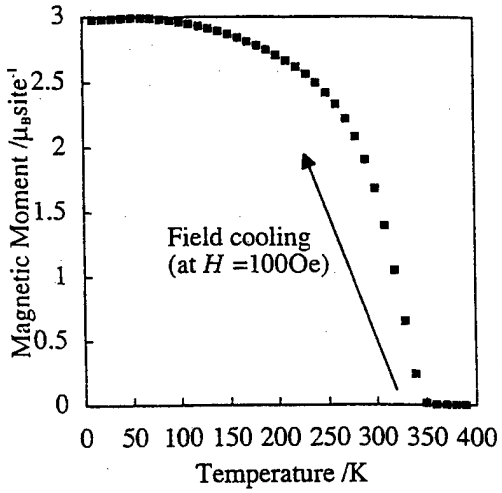

Fig.5 Temperature dependence of magnetic moment for the LSMO/PZT/YBCO trilayer film on LSGO substrate.

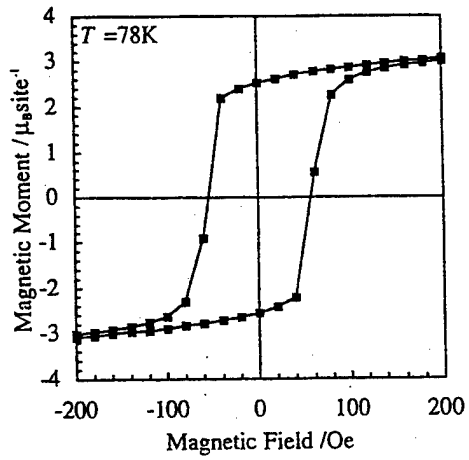

Fig.6 *M-H* hysteresis curve of the LSMO film in LSMO/PZT/YBCO structure at a temperature of 78K The sweep of magnetic field is ±10 kOe while only the result in ±200 Oe is shown in figure.

The ferroelectric properties of PZT film of the LSMO/PZT/YBCO trilayer were measured by using the Sawyer-Tower circuit. Figure 4 shows typical *D-E* hysteresis loop of PZT layer at a frequency of 60Hz. The remanent polarization and coercive field were 19μC/cm^2 and 275 kV/cm at 70K, respectively.

Temperature dependence of magnetic moment was measured under a magnetic field of 100 Oe, which is applied parallel to the LSMO (100) direction. This magnetic field was reported to be sufficient to saturate the magnetictization of LSMO[6]. With decreasing temperature, the magnetic moment increases at blow 350K (Fig.5). This temperature of 350K is well corresponding to magnetic Curie temperature of $La_{0.70}Sr_{0.30}MnO_3$ bulk[7]. The *M-H* hysteresis curve of the LSMO film at 78K is shown in Fig.6. The remanent magnetic moment (*Mr*) is 2.6 μ_B/site and coercive field (*Hc*) is 50 Oe.

IV. SUMMARY

We have fabricated ferromagnetic / ferroelectric / superconducting heterostructures for the electrically and magnetically tunable microwave devices by pulsed laser ablation technique. Electrical properties of an individual film have been measured. As a result, the YBCO film exhibits superconductivity below *Tc*=87K. Also, clear ferroelectric properties of PZT film were observed. The value of dielectric constant (ε_r) was about 220 at 280K, decreased gradually with decreasing temperature, and showed about 100 at 77K. On the other hand, dielctric loss (tan δ) was smaller than 0.05 over the measured temperature range. The remanent polarization and coercive field for the *D-E* hysteresis curve were 19μC/cm^2 and 275 kV/cm at 70K. Further more, we investigated the ferromagnetic property of the LSMO film. LSMO film showed ferromagnetic properties blow 350K, and clear ferromagnetic hysteresis loops even at 78K. The remanent magnetic moment and coercive field were 2.6 μ_B/site and 50 Oe, respectively. These results here suggest that the LSMO/PZT/YBCO structures are favorable for use in the superconducting microwave applications, such as tunable phase shifters and filters.

REFERENCES

[1]S.S.Gevorgian, D.I.Kaparkov, O.G.Vendik, *IEE Proc. –Microw. Antennas Propag.*, Vol.**141**, No.6, 1994, pp.501—503

[2]R.A.Chakalov, Z.G.Ivanov, Yu.A.Boikov, P.Larsson, E.Carlsson, S.Gevorgian, T.Claeson, *Physica C* , **308**, 1998, pp..279—288

[3]G.F.Dionne, D.E.Oates, D.H.Temme, J.A.Weiss, *IEEE Tans .Microwave Theory Tech.* Vol.**44**, No.7, 1996, pp.1361—1368

[4]D.E.Oates, A.Piqué, K.S.Harshavardhan, J.Moses, F.Yang, G.F.Dionne, *IEEE Tans. on Applied Supercond.*, Vol.**7**, No.2, 1997, pp.2338—2342

[5] G.H.Joker , J.H.VanSanten, *Physica* **16** , 1950, pp..337.

[6]Z.Trajanovic, C.Kwon, M.C.Robson,K.C.Kim, M.Rajeswari, R.Ramesh, T.Venkatesan, S.E.Lofland, S.M.Bhagat, D.Frk, *Appl.Phys. Lett.*. **69** , 1996, pp. 1005

[7] A.Urushihara, Y.Moritomo, T.Arima, A.Asamitsu, G.kido and Y.Tokura, Phy. Rev., Vol.**B**51, 1995, pp.14103-14109.

POSTER SESSION I

Group 4 - Detectors and Mixers

Development of transition-edge microbolometers for space applications

A. Luukanen and H. Sipilä
Metorex International, P.O. Box 85, FIN-02631 Espoo, Finland

K. Kinnunen, A. Manninen, A. Nuottajärvi, J. Pekola, and S. Pöyhönen
University of Jyväskylä, Department of Physics, P.O. Box 35, FIN-40351 Jyväskylä, Finland

I. Suni and J. Salmi
VTT Electronics, P.O. Box 1101, FIN-02044 VTT, Finland

Abstract—Recent years have seen the development of transition-edge microbolometers, which utilize the sharp superconducting transition of a low-temperature superconductor. Our group has developed the technology for future applications of the European Space Agency (ESA). The temperature-sensing element consists of a Ti/Au bi-layer, and by varying the thickness of the films, we have been able to tune the T_c of the film from 200 mK to 420 mK. In the case of the microcalorimeter, the x-ray absorber consists of a 2 μm thick Au layer, and electrical contacts to the detector are made with superconducting Ti lines. In this paper we present the measured properties of the thermometer, where we have observed sharp superconducting transitions with the parameter α=d(log R)/(d log T) describing the sharpness of the transition reaching a value of ~2000. We have also investigated the aging effects caused by interdiffusion in the two metal layers in Al/Cu and Ti/Au films. In the case of Ti/Au films the results are encouraging.

I. INTRODUCTION

If a superconducting film is biased to the midpoint of its superconducting transition, very small changes in temperature will have significant effect on the resistance of the film. This naturally is well suited for extremely sensitive bolometers or calorimeters.

II. OPERATIONAL PRINCIPLE

A transition-edge microcalorimeter [1],[2] consists of a bi-metal thermometer in good thermal contact with an x-ray absorber, and weakly coupled to the heat sink. As an incident x-ray deposits its energy in the absorber volume, the temperature of the electron system changes by $\Delta T=E_\gamma/C$, where E_γ is the energy of the absorbed quantum, and C is the total heat capacity of the detector. This temperature rise is sensed with a superconducting bimetal film voltage biased to the midpoint of its superconducting transition. This reduction in the bias current is sensed with a SQUID ammeter connected in series with the detector.

Manuscript received April 30, 1999.
This work has been supported by the European Space Agency (ESTEC contract No. 12835/98/NL/SB)

The energy of the absorber x-ray is given by

$$E_\gamma = V_b \int \Delta I dt . \quad (1)$$

The detector temperature is maintained within the superconducting transition by electrothermal feedback, whose strength can be described with parameter $l=P_b\alpha/GT_c$, where $P_b=V_b^2/R$ is the bias heating power, α=d(log R)/d(log T) is logarithmic derivative of the detector R-T -curve at the transition at T_c, G is the thermal conductance between the detector and the heat sink. The steady-state thermal conductance at operating temperature can be calculated from 2-D Laplace's equation, which is at low frequencies [3]

$$G = 2\pi\kappa(T_c)d \ln\left(\frac{w_m}{w_d}\right)^{-1} , \quad (2)$$

where $\kappa(T)$ is the temperature dependent thermal conductivity, d is the thickness and w_m is the pitch of the membrane. The detector pitch is denoted by w_d. Electrothermal feedback reduces the detector time constant to an effective value of $\tau_e=\tau_0/(1+l)$, where τ_0=C/G is the thermal time constant of the detector. Also the Johnson noise of the detector is suppressed at low frequencies.

Intrinsic noise of the detector consists of enthalpy fluctuations between the detector and the heat sink, commonly known as phonon noise, Johnson noise from the detector resistance, excess low frequency noise and noise of the preamplifier. The noise introduces inaccuracy in the energy measurement process, thus causing a spread ΔE (FWHM) in the value of the measured energy. It can be shown [4], that for an x-ray calorimeter, the fundamental limit for energy resolution is

$$\Delta E_{FWHM} = 2.36\sqrt{k_B T^2 C} \quad (3)$$

when no ETF is present in the system. In the case where ETF is utilized, the limit for energy resolution becomes

$$\Delta E_{FWHM} = 2.36\sqrt{\frac{k_B T^2 C\sqrt{8n}}{\alpha}} , \quad (4)$$

where $n=d\log P_b/d\log T$. However, recent experiments [5], [6] have shown, that operation near the maximum value of α introduces excess noise (scaling with α) to the system. The exact explanation for this effect is still unknown, but might be a result of internal thermal non-equilibrium effects. In

many of the recent experiments [4], [6] the best resolution has indeed been obtained with only moderate ETF, indicating that the excess noise degrades the performance of the detector when biased close to maximum α.

Very large values of α also lead to significant challenges in detector design. In order to reach good energy resolution, it is advantageous to design the absorber heat capacity so that the maximum x-ray energy to be measured produces a significant change in detector temperature. In the extreme case, if biased to the center point of the transition, the detector should go to almost normal state. Assuming that the total heat capacity of the detector is dominated by the heat capacity of the absorber, the minimum required heat capacity for the absorber is

$$C_{\min} = \frac{E_\gamma \alpha}{T_c}. \qquad (5)$$

Thus for a detector with α=1000, T_c=150 mK, designed for 5.9 keV x-rays the minimum heat capacity is 6 pJ/K. If the detector pitch is 400 μm, the required thickness for Au absorber would be ~4 μm. Thus with very sharp transitions, the heat capacity requirement may result to unpractical detector designs, as well as excessive internal noise at operating point. Instead of aiming for very sharp transitions, one should try to produce detectors with good linearity, moderate transition width and practical absorber heat capacity.

III. DETECTOR FABRICATION

The microcalorimeters were fabricated on 300 nm thick SiN membranes. These free standing membranes were defined to a nitridized silicon wafer by anisotropic etching in aqueous KOH solution. The thermometer structures were then patterned on to the membranes using electron beam lithography. The thermometer metal films were deposited in an UHV electron-beam evaporation system using two-angle evaporation techniques, after which 300 Å of SiO was deposited using a thermal evaporation system.

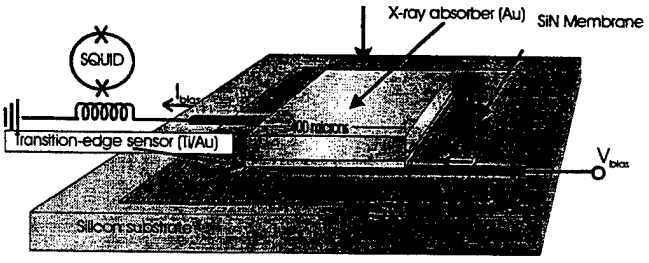

Fig. 1: Structure of the transition-edge microcalorimeter and schematic of the biasing circuit.

The purpose of this silicon monoxide film is to provide electrical insulation between the thermometer and the absorber, and reduce the proximity effect of the thick normal metal absorber on the thermometer. The 2 μm absorber film was then deposited in the UHV system, and a Si mechanical mask was used to pattern the absorber.

In this phase of the project, we have only experimented with Cu absorbers which are much easier to deposit, but have significantly smaller efficiency for 5.9 keV x-rays.

IV. THERMOMETER PROPERTIES

A lot of effort was used to find the best materials for the transition-edge thermometer. As criteria, the TES films should be very stable with little interdiffusion of the two metals taking place at room temperature. The obtainable range of critical temperatures should be between 100 to 300 mK, the superconducting transition should be sharp, linear and repeatable, and the films should be easy to deposit. In the first phase, we investigated the combination of Al/Cu. The transition temperature was rather easy to tune, with a fairly large α between 200 and 500. However, these films exhibited drastic aging effects at room temperature, with the sample resistance increasing by several percents within a few days. Also the films failed to go to superconducting state after a few weeks of storage at room temperature. Fig. 2 illustrates the aging of Al/Cu samples at room temperature

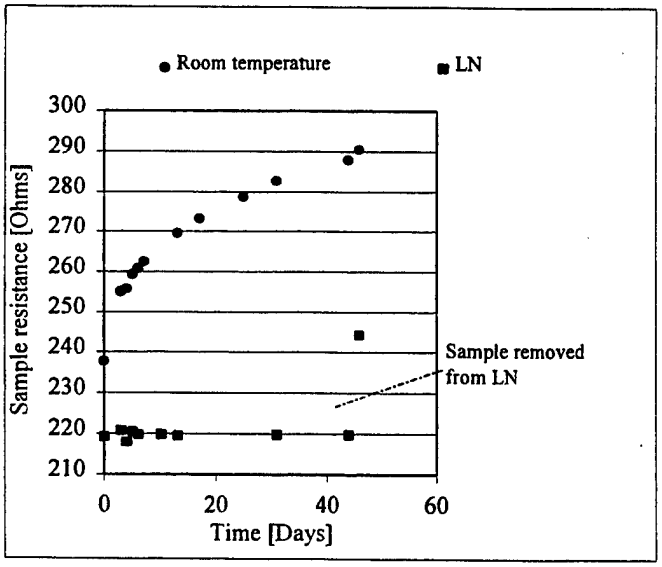

Fig. 2: Aging of Al/Cu samples at room temperature (diamonds) and at 77 K (squares).

and at LN temperature.

Results indicated that Al/Cu thermometers were inherently unstable, and could only be stored at LN temperature.

Next experiments were done on Ti/Au bilayers. This combination displayed much less aging effect in terms of resistance creep at room temperature. In order to determine the diffusion rate in these films, we made tests on the samples by heating them to elevated temperatures, and monitoring the

resistance of the sample. The heating tests indicated, that as the sample is heated to at temperature above 100 °C, rapid grain-boundary diffusion causes the sample resistance to increase rapidly. After the grain-boundary diffusion is saturated, the much slower lattice diffusion becomes dominant, and the sample becomes very stable, with a change in room temperature resistance of only 10 ppm/year. Also the effect of curing the sample at 100 °C was measured. Fig.4 shows the measured transitions of a Ti/Au sample before and after a 1 hour bake. The T_c of the film had changed by 2 %, and α had increased from ~300 to over 400. In an other cured sample a record α~2000 was measured, indicating that curing can be used to reduce the transition width of the bilayer. The aging of the films stored at room temperature was also measured. Two successive measurements of the transition separated by 3 months of storage at room temperature showed about 4 % change in T_c and a 3 -fold increase in α, although most of the increase in transition width could be explained by lower noise in the measurement setup.

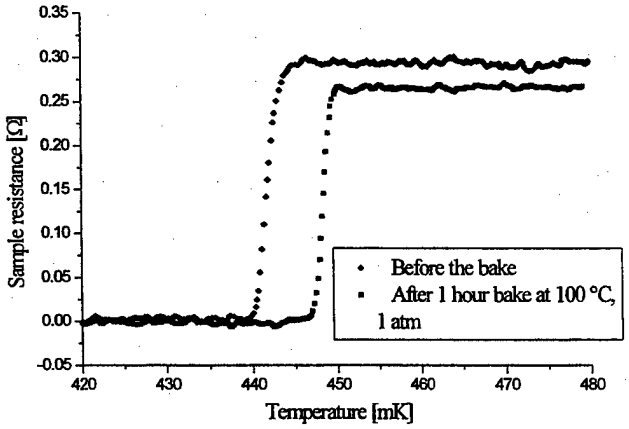

Fig. 3: The superconducting transition of a (400 μm)² Ti/Au sample before and after an 1 hour bake at 100 °C

V. X-RAY MEASUREMENTS

At the time of writing, the first x-ray measurements are about to be measured. We have successfully installed a VTT SQUID with noise cancellation electronics [7] operating at 1 K to the cryostat, and in the near future this SQUID will be replaced by a SQUID with Pd shunt resistors, capable of operating at 100 mK. Fig. 5 shows a superconducting transition of the same sample as in Fig.4, but this time measured with the SQUID.

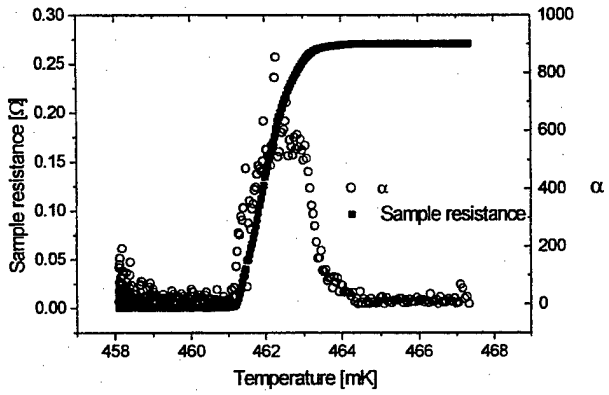

Fig. 4: Superconducting transition of a Ti/Au sample measured with a SQUID. Calculated values for α are marked by circles

ACKNOWLEDGMENT

This work has been funded by the European Space Agency (ESTEC contract No. 12835/98/NL/SB).

REFERENCES

[1] A. T. Lee, P.L Richards, S. W. Nam, B. Cabrera, and K. D. Irwin,"A superconducting bolometer with a strong electrothermal feedback," *Appl. Phys. Lett.*, vol. 69, pp. 1801-1803, September 1996.

[2] K. D. Irwin, "An application of electrothermal feedback for high resolution cryogenic particle detection", *Appl. Phys. Lett.*, vol. 66, pp. 1998-2000, April 1995.

[3] M .M. Leivo and J. P. Pekola, "Thermal characteristics of silicon nitride membranes at sub-kelvin temperatures", *Appl. Phys. Lett.*, vol. 72, pp.1305-1307, March 1998.

[4] K. D. Irwin, G. C. Hilton, D. A. Wollman and J. M. Martinis, "X-ray detection using a superconducting transition-edge sensor microcalorimeter with electrothermal feedback", *Appl. Phys. Lett.*, vol. 69, pp.1945-1947, September 1996.

[5] S.-F. Lee, J. M. Gildemeister, W. Holmes, A. T. Lee, and P. L. Richards, "Voltage-biased superconducting transition-edge bolometer with strong electrothermal feedback operated at 370 mK", *Appl. Opt.* , vol. 37, pp.3391-3397, June 1998.

[6] H. F. C. Hoevers, A. C. Bento, M. P. Bruijn, M. Frericks, F. B. Kiewiet, W. A. Mels and P. A. J. Korte, "Performance of hot-electron bolometers for infrared photometry and x-ray microcalorimetry", *unpublished.*

[7] M. Kiviranta and H. Seppä, "DC-SQUID electronics based on the noise cancellation scheme", IEEE Transactions on Applied Superconductivity vol. 5, pp. 2146 - 2148, 1995.

Molybdenum-Gold Proximity Bilayers as Transition Edge Sensors for Microcalorimeters and Bolometers

T. C. Chen[1,4], F. M. Finkbeiner[2,3], A. Bier[1,4], B. DiCamillo[1,4]
[1]Global Science & Technology Inc., Greenbelt, MD 20770, USA.
[2]Department of Astronomy, University of Maryland, College Park, MD 20742, USA.
[3]NASA/Goddard Space Flight Center, Code 662, Greenbelt, MD 20771, USA.
[4]NASA/Goddard Space Flight Center, Code 685, Greenbelt, MD 20771, USA.

***Abstract*—Mo/Au proximity bilayers as transition edge sensors (TES) are promising candidates for low-temperature thermometry. The transition temperature of the bilayers can be easily tuned between 50 and 600 mK, yielding sensors which can be used in a variety of calorimetric and bolometric applications. With phase transition widths of less than 1 mK, Mo/Au TESs show very high temperature sensitivity (d(logR)/d(logT)~2500). Also, Mo/Au TESs show improved thermal and chemical stability compared to most other bilayer configurations. Fabrication issues and detector performance of Mo/Au TES on Si_3N_4 membranes are discussed.**

I. Introduction

In general, a microcalorimeter or bolometer consists of an absorber with heat capacity C(T) and a temperature dependent resistance (thermometer) linked to a heat bath through a thermal conductance G(T). The incoming radiation heats the absorber which causes a change in the resistance of the thermometer. The resistance change can be measured as a voltage or current change, depending on the biasing method. The thermometer is characterized by its fractional resistance change with temperature, α, which is defined by $\alpha = d(\log R)/d(\log T)$.

As a measure of the temperature sensitivity of the thermometer, α plays a key role in the detector performance: a high value of α leads to a high detector responsivity, and noise performance near the thermal fluctuation limit.

Our transition edge sensors (TES) show maximum α values of 2500,which is an improvement over commonly used standard semiconductor thermistor thermometers by a factor of 400. Given such a high sensitivity, our TES can operate in extreme electrothermal feedback (ETF) which dramatically improves detector stability, dynamic range, and response time [1].

Conceptually, a TES is a superconducting material biased within the transition from normal to superconducting state. By using normal-superconducting metal bilayers instead of elementary superconductors, the transition temperature (T_c) of a bilayer can be tuned to the desired operating point and very small transition widths (dT_c) are achievable [2].

Within the last year, we started to investigate a new type of TES, a molybdenum/gold (Mo/Au) proximity bilayer, which shows improvements in chemical, electrochemical, and thermal stability compared to previous bilayer combinations [3]. Therefore, the Mo/Au bilayer TES promises long-term stability. Furthermore, a TES microcalorimeter or bolometer can be produced using standard microlithographic techniques without any degradation of its detector performance.

In ETF operation, our Mo/Au TES sensor is voltage biased within its transition and temperature biased well above the bath temperature T_b (i.e. $T_b << T_c$). At the bias point the electrical resistance of our TES is typically 10 mΩ -100 mΩ. Any resistance change is detected by a highly sensitive SQUID via the current change through the TES.

ETF effectively counteracts any temperature (and therefore resistance) excursion from the bias point by introducing or reducing power via the electrical circuit. Therefore, our TES has the ability to self-bias within its superconducting transition and can operate on a much shorter effective time scale than its intrinsic thermal time constant (τ_0 = C/G). The relationship between the effective time constant (τ_{eff}) and τ_0 is given by $\tau_{eff}=(n / \alpha)\tau_0$, where n = 4 for silicon nitride (Si_3N_4) [4].

II. TES Applications

There are several ongoing investigations at NASA/Goddard employing Mo/Au TES on Si_3N_4 membrane detector technology. We present the following applications: TES as thermometer for x-ray calorimetry, TES as thermometer for Far-IR bolometry, and monolithic stripline bolometer with TES thermometer. The choice to fabricate the TES on Si_3N_4 is to reduce the G(T) and C(T) of the detector configuration. The G(T) is tuned for each application by perforating the Si_3N_4 membrane around the device.

The parameters for the TES detector element are chosen by performing an optimization between the sensitivity of the device, its speed, and its thermal environment. The sensitivity is related to the achievable value of α and the conductivity G(T) between the thermistor and the bath - higher α and lower G(T) generally implies a more sensitive detector. The time constant of the device is related to C(T), α, and the G(T). A lower bath temperature usually allows the design of sensitive detectors.

Since a TES is to be operated within its transition, a given α and energy range set the upper limit to the total C(T); whereas the G(T) is given by the total C(T) and the desired response time of the detector.

A. X-ray TES

High resolution x-ray spectroscopy is an important tool in the understanding of some of the most energetic phenomena in

the universe, involving, for examples, quasars and active galactic nuclei. The design of our TES microcalorimeters is targeted for high energy sensitivity and fast detector response for energies ranging between 1 keV and 10 keV. In order to obtain the necessary C(T) and provide effective x-ray absorption and thermalization, bismuth/copper multilayers are added (2 μm to 10 μm) as absorbers on top of the TES devices. In addition, operation temperatures of less than 0.1 K boost the detector sensitivity. For design parameters, refer to Row A in Table I.

B. FAR-IR TES

Over the last few decades, millimeter-wave and far-infrared astronomy have increased our understanding of Galactic processes, large-scale structure, and the early history of the cosmos. This has been enabled by continuing improvements in observational methods and in instrumentation. One area in which instrumentation can be further improved is detector sensitivity - many measurements are not photon noise limited. The most sensitive detectors at present for far-infrared broadband measurements are bolometers. The sensitivity of these devices can be improved by a factor of 30 using TES thermometers instead of traditional doped semiconductor thermistors. For design parameters, refer to Row B in Table I.

C. STRIPLINE TES

More than 99% of the photons in the universe lie within the millimeter and sub-millimeter wavelength bands. Emitted by diffuse sources, the radiation can be characterized by three properties: its frequency spectrum, its brightness and its polarization. Of these three properties, the spectrum of the sources is the best known. The intensity power spectra of the sources at small angular scales where the most interesting cosmological information is to be found is less known. The polarization state of each of the sources remains unknown at any angular scale.

The monolithic stripline bolometer is composed of the following elements: a polarization selective "launcher" - designed to couple the TE_{10} mode from square or rectangular waveguide to a stripline transmission line, a band-defining filter realized in stripline, a resistive termination in a thermally isolated section of stripline, and an integrated TES microbolometer which measures the temperature rise in the termination. For design parameters, refer to Row C in Table I.

TABLE I. Design parameters for presented TES detectors.

	$C(T_b)$ [J/K]	$G(T_b)$ [W/K]	τ_{eff} [ms]	T_b [K]
A.	1×10^{-11}	1×10^{-9}	0.1	0.1
B.	1×10^{-12}	5×10^{-12}	1 – 10	0.3 – 0.4
C.	5×10^{-12}	1×10^{-11}	2	0.3

III. FABRICATION

Fabrication begins with the deposition of 0.5 μm of low stress Si_3N_4 on both sides of a double-side polished <100> silicon wafer by low pressure chemical vapor deposition. The starting silicon substrate ranges in thickness between 200 μm - 400 μm. Holes the size of the desired free standing area of the Si_3N_4 membranes are etched using reactive ion etch (RIE) in the nitride on the back side of the wafer. This is done by photolithographically patterning a photoresist (PR) etch mask, etching the nitride through the PR, and removing the PR in oxygen plasma. The wafer is then placed in anisotropic KOH chemical etch (80°C, 45% solution) to form the free standing Si_3N_4 membranes.

In an ultra-high vacuum deposition system, the Mo/Au bilayers are thermally deposited by electron beam evaporation at a base pressure of 1×10^{-10} Torr. The molybdenum (Mo) layer is deposited first at a rate of 0.5 nm/sec on the Si_3N_4 wafer at a temperature of 500°C. Under these conditions, our thin Mo films (40 nm – 70 nm) show low film stress and sharp transitions at about 700 mK. Without breaking vacuum, the gold (Au) layer (100 nm- 300 nm) is deposited next at a rate of 0.1 nm/sec on the Mo layer at temperatures between 10°C and 200°C. We intend to investigate other methods of bilayer deposition including sputtering both Mo and Au and sputtering Mo and e-beam Au.

The Mo/Au bilayer structure is defined on the Si_3N_4 membrane using photolithographic techniques aligning to the back of the wafer and chemically etching the Au in gold etch ($KI:I_2$:DIW) and the Mo in molybdenum etch ($HNO_3:H_2SO_4$:DIW). The contact leads and the bonding pads are produced in a series of masking, deposition, and lift-off steps. For lift-off, we use Futurrex NR5-6000PY PR which produces overhang structures of 3 μm and removes in acetone. Currently, the contact leads are aluminum (Al) which when in extended contact with Au corrodes to form a compound known as the 'purple plague'. We intend to investigate using niobium (Nb) or granular Al as the contact material. In the case of Nb, the leads will be sputtered and formed using lift-off. See Fig. 1 for a TES device fabricated as described.

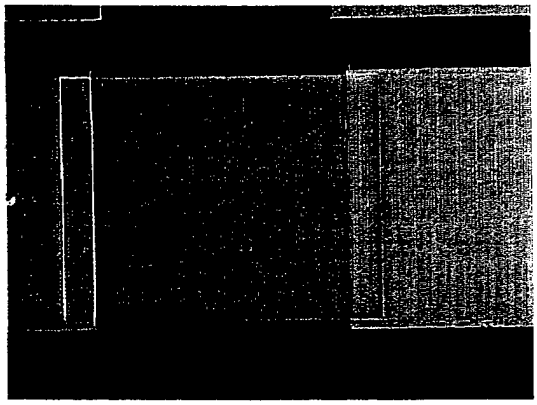

Fig. 1. 500 x 500 μm Mo/Au TES with Al leads on Si_3N_4 membrane.

Perforations are made in the free standing Si_3N_4 membrane to control the G(T) of the device using RIE. The absorber is placed on top of the TES structure using photolithography and

lift-off techniques. The absorbing material and the thickness of absorber is dependent on the specific application.

Heat treatment studies on Mo/Au bilayers were conducted in order to test and prove their processibility. The Mo/Au bilayer system was annealed at temperatures in excess of the actual temperature range and duration within a standard microlithographic process. Comparisons of test results before and after the heat treatment revealed no significant change in the T_c and dT_c of the Mo/Au bilayers.

IV. Readout & Results

Mo/Au bilayer characterization and detector test runs are carried out in an Oxford dilution refrigerator and in an IR Lab ^{3}He refrigerator. The dilution refrigerator is used for experiments in the temperature range between 50 mK and 300 mK, while the ^{3}He refrigerator covers the range between 300 mK and 1 K. As part of the bilayer characterization, the T_c and dT_c of a bilayer strip are obtained by recording its resistance as a function of temperature (RFT). The resistance of a Mo/Au bilayers strip is read out in a 4-wire scheme by an ac resistance bridge during a temperature sweep. With the current experimental setup, resistance changes down to a fraction of a mΩ and temperature changes of about 0.1 mK - 0.2 mK can be resolved.

Test results on our Mo/Au bilayer strips indicate very good tunability and sufficient reproducibility of T_c and very steep transitions of 1 mK and smaller. We have produced bilayers with T_c's between 100 mK and 600 mK and maximal values of α of about 2500. Fig. 2 presents a RFT of a typical phase transition with a dT_c of less than 1 mK, and an α value of 2300 at the steepest part of the transition. For T_c ranging between 200 mK and 300 mK, the total distribution of T_c on a 4" wafer was found to be less than +/- 8 mK. In addition, critical current measurements were carried out. First results showed values for the critical current density J_c between 100 A/cm^2 and 160 A/cm^2 at T/T_c=0.9, which is in well agreement with theoretical J_c-models of very thin superconducting films.

To date, our TES detectors are readout by dc SQUID systems. First detector tests have already been performed in the dilution refrigerator using commercially available dc SQUID sensors (from Conductus) which have input inductances of 600 nH. Two sensors are installed in the ^{4}He bath of the dilution refrigerator. A magnetically shielded twisted pair of superconducting NbTi wires provide the electrical connection between the TES circuit and the SQUID sensor which is inside a superconducting Nb shield.

A typical IV-curve of a TES microcalorimeter with Al leads shows two distinct voltage ranges where the slope dI/dV is negative, representing bias conditions within phase transitions. The range at the higher bias voltage is related to the phase transition of the Mo/Au bilayer. The one at the lower voltage represents the phase transition of the contact areas of the Al leads and the TES Au layer. This region is presumably due to the formation of the 'purple plague'. Preliminary results on first x-ray irradiation experiments indicated an energy resolution of about 115 eV at 3 keV for that type of detector (i.e. Mo/Au TES with Al leads). The detector was voltage biased within the Mo/Au transition.

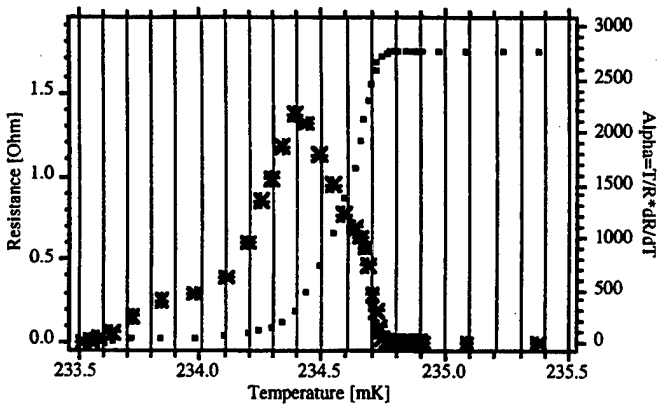

Fig. 2. RFT curve and corresponding α of a Mo/Au superconductive phase transition.

V. Conclusion

Mo/Au proximity bilayers as transition edge sensors are ideal for bolometric and calorimetric applications requiring low-temperature thermometry. Fabricating the TES on patterned Si_3N_4 membrane substrate reduces the thermal conductance and the heat capacity of the devices. Mo/Au bilayers have shown very sharp transitions of less than 1 mK and are, therefore, highly temperature sensitive. Our goal is to proceed with the development of TES bolometers and microcalorimeters suspended by silicon nitride membrane structures.

Acknowledgment

We thank the 'X-ray TES Group' at NASA/Goddard including M. Li, D. B. Mott, C. K. Stahle, C. M. Stahle, and N. Tralshawala for helpful discussions and assistance in fabrication. We thank D. Cottingham, G. Hinshaw, S. Meyer, R. F. Silverberg, G. W. Wilson, and E. Wollack for helpful discussions and great ideas. This work is carried out at the Detector Development Laboratory at NASA/Goddard.

References

[1] K. D. Irwin, *Appl. Phys. Lett.*, vol. 66, p. 1998, 1996.

[2] K. D. Irwin, G.C. Hilton, J.M. Martinis, B. Cabrera, *NIM A*, vol. 370, p. 177, 1996.

[3] F. M. Finkbeiner, T. C. Chen, S. Aslam, E. Figueroa Feliciano, R. L. Kelly, M. Li, D. B. Mott, C. K. Stahle, C. M. Stahle, Proc. Applied Superconductivity Conference '98, IEEE Trans. Appl. Superc.(in press).

[4] S. H. Moseley, J. C. Mather, D. McCammon, J. Appl. Phys., vol. 56, p. 1257, 1984.

Nonequilibrium Kinetic Inductive Response of Y-Ba-Cu-O Photodetectors

Carlo Williams, Roman Adam, and Roman Sobolewski*
Department of Electrical and Computer Engineering and Laboratory for Laser Energetics
University of Rochester, Rochester, NY 14627-0231 USA

Oliver Harnack
Institute for Thin Film and Ion Technology, Research Center Jülich, D-52425 Jülich, Germany

Abstract—We present a comprehensive study of the light-induced transient nonequilibrium kinetic inductive response of high quality, epitaxial Y-Ba-Cu-O (YBCO) thin films. The test structures consisted of 20- to 30-μm-wide coplanar strip (CPS) transmission lines with 7- to 10-μm separation, patterned in 100-nm thick YBCO films grown on MgO and $LaAlO_3$ substrates. Each CPS structure contained a 5-μm-wide, 7- to 10-μm-long microbridge. The photoresponse of the microbridge, biased below the critical current and excited by 130-fs laser pulses, was measured using a cryogenic subpicosecond electro-optic sampling system. The physical origin of the photoresponse is attributed to the nonequilibrium quasiparticle generation and recombination effect, and fitted with the Rothwarf-Taylor model. Our measurements show a 2-ps-wide bipolar voltage transient in the entire tested temperature and current bias ranges. We regard the measured response times to be the intrinsic dynamics of a YBCO superconductor, making it a suitable material for THz digital and communication applications.

I. Introduction

Photoexcitation studies of thin film high-T_c superconductors have attracted considerable attention due to its promising applications as fast, broadband photodetectors and mixers. To this end, epitaxial Y-Ba-Cu-O (YBCO) has received most of the attention. Early experiments have shown the photoresponse of YBCO microbridges that were biased in the superconducting state at temperatures well below T_c to be as fast as 1.5-ps long [1]. Recently, with an improved microbridge structure, we observed intrinsic photoresponse of the YBCO microbridge [2]. The physical origin of the photoresponse was attributed to the nonequilibrium quasiparticle generation and recombination effect. Although these experiments show YBCO to be a viable material for high-speed photodetectors with intrinsic bit rates exceeding 300 Gbits/s, there are still ongoing experiments to fully understand the nonequilibrium processes in high-T_c superconductors.

Manuscript received May 1 1999.
E-mail: cwilliam@ece.rochester.edu
* Also at the Institute of Physics, Polish Academy of Sciences, PL 02668 Warsaw, Poland.
This work was supported by the Office of Naval Research Grant No. N00014-98-1-0080. R. Adam acknowledges financial support from the Frank Horton Graduate Fellowship Program.

We present here our further studies of the light-induced transient nonequilibrium kinetic inductive response of high quality, epitaxial YBCO thin films.

II. Experiment

The test structures consisted of coplanar strips (CPS) patterned in 100-nm thick YBCO thin films grown on MgO and $LaAlO_3$. The structures on MgO consisted of 8-mm-long, 20-μm-wide lines with a 10-μm-wide gap. Each CPS structure contained a 5-μm-wide, 10-μm-long microbridge. On the $LaAlO_3$ substrate, the lines were 4-mm long and 30-μm wide with a 7-μm separation, and each structure had a 5-μm-wide, 7-μm-long microbridge. The microbridges were characterized by a zero-resistance transition temperature $T_{c0} >$ 88 K and critical current density $J_c > 1$ MA/cm^2 at 77 K. To study the nonequilibrium kinetic photoresponse, the bridge was current–biased in the superconducting state at varying values below the critical current and at different temperatures below T_c. The dependence of photoresponse amplitude on the excitation optical power was also investigated.

Measurements were acquired using a cryogenic electro-optic (EO) sampling system that is capable of measuring ultrafast electrical transients with a temporal resolution of 200-fs and a voltage sensitivity of 150-μV [3]. The sample being measured was covered with a $LiTaO_3$ crystal to facilitate EO measurements and then mounted on a copper block heat exchanger inside a continuous-flow helium cryostat. One end of the coplanar strip was wire-bonded to a 50-Ω semi-rigid coaxial cable, while the other end was grounded. This arrangement allowed us to directly observe the switched-state photoresponse on a 20 GHz sampling oscilloscope, which also aided to optimize the EO measurements [2]. Additional wiring to the coplanar strips provided means to obtain current-voltage characteristics of the microbridge at the different measuring temperatures.

A commercial Ti:sapphire laser provided 100-fs-wide optical pulses (790-nm wavelength) at 76-MHz repetition rate, that were split into two beams. One beam was frequency doubled to 395-nm and focused to a 10-μm spot to excite the microbridge. By calculating the amount of light absorbed in our optical beam path, we estimated that the power actually delivered to the microbridge was only 60 μW, which was the equivalent of 1 μJ/cm^2, and was low enough to induce below 0.3 K permanent heating of the bridge area [1]. The second

(sampling) beam traveled through a computer-controlled delay path and was focused to a 10-μm position inside the $LitaO_3$ crystal and between the gap of the coplanar transmission lines. The sampling beam sensed the birefringence change in the $LiTaO_3$ crystal induced by the transient electric field of the microbridge photoresponse. The computer controlled delay of the sampling beam relative to the excitation beam allowed us to resolve the time evolution of the photoresponse voltage signal. It is important to note that the time resolution of our EO sampler is well below the characteristics of the transients reported here.

III. Results and Discussion

A. Nonequilibrium Kinetic Inductance Mechanism

According to the nonequilibrium kinetic model [4], a photoinduced change in the Cooper-pair density gives rise to a voltage transient

$$V = I(dL_{kin}/dt), \tag{1}$$

where I is the bias current. L_{kin} is the kinetic inductance and is related to the superfluid fraction of electrons f_{sc} as,

$$L_{kin} = \frac{1}{\varepsilon_0 \omega_p^2} \frac{l}{wd} \frac{1}{f_{sc}}, \tag{2}$$

where ε_0 is the vacuum permitivitty, $\omega_p = 1.67\text{x}10^{15}\text{s}^{-1}$ is the plasma frequency of YBCO, and l, w, d are the bridge length, width, and film thickness, respectively.

To analyze the nonequilibrium response of superconductors, one can use the Rothwarf-Taylor (R-T) equations [5]. The nonlinear equations represent the interplay between the nonequilibrium quasiparticles (QP) and phonons with an energy greater than or equal to twice the superconducting gap (called 2Δ phonons);

$$\begin{aligned} \frac{dN_{QP}}{dt} &= I_{QP} - RN_{QP}^2 + \frac{2}{\tau_B} N_\omega \\ \frac{dN_\omega}{dt} &= I_\omega + \frac{1}{2} RN_{QP}^2 - \frac{1}{\tau_B} N_\omega - \frac{1}{\tau_{es}} (N_\omega - N_{\omega T}), \end{aligned} \tag{3}$$

where N_{QP}, N_ω, and $N_{\omega T}$ are the numbers per unit volume of QP's, 2Δ phonons, and equilibrium thermal phonons respectively. I_{QP} is the external generation rate (optical pulse) for the QP's, I_ω represents the 2Δ phonon generation rate, R is the recombination rate for the QP's into Cooper pairs, and τ_B and τ_{es} are the phonon pair-breaking and the phonon escape times, respectively. The R-T equations are best suited to describe the conditions in the superconductor far below T_c, and for moderate to strong external perturbations. The equations are used to derive N_{QP} and N_ω, which can then be used to calculate the superfluid fraction:

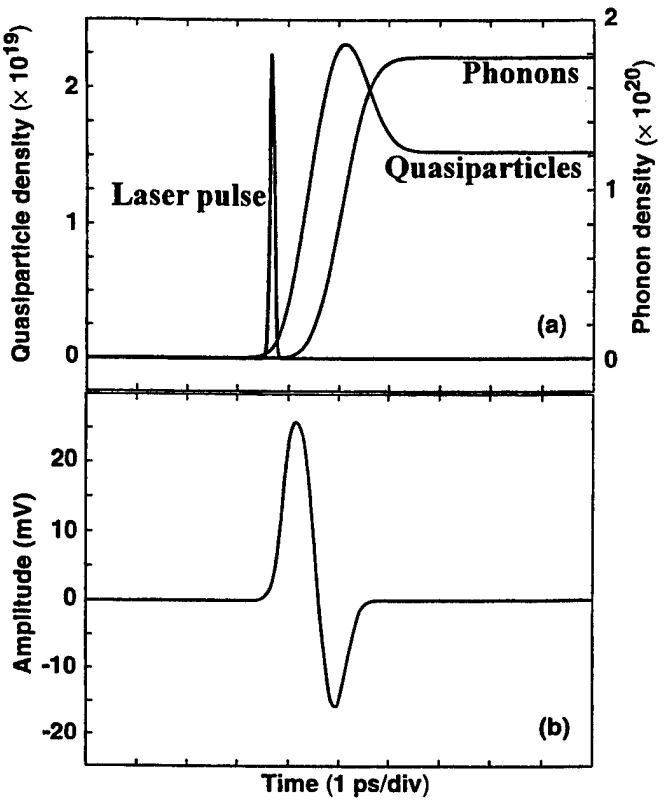

Fig. 1. (a) Solutions to the R-T equations that calculates the dynamics of the quasiparticle and phonon density after being excited by a short laser pulse. (b) The simulated nonequilibrium kinetic transient voltage using the solutions from the R-T equations.

$$f_{sc} = (N_0 - N_{QP})/N_0, \tag{4}$$

where N_0 is the total density of electrons in the sample.

Fig. 1(a) shows the solution for the R-T equations, (3), that calculated N_{QP} and N_ω. Fig. 1(b) then shows the simulated nonequilibrium kinetic inductive transient voltage using the solutions from the R-T model, (4), (2), and (1).

B. Measurements

Fig. 2 shows typical transients measured when the microbridge was biased in the superconducting state. The dotted line is a measured response from a structure fabricated on $LaAlO_3$ and the solid line is the measured response from a structure on MgO substrate. In both traces the microbridge was biased at $0.8I_c$ at a temperature of 60 K and 70 K for the $LaAlO_3$ and MgO sample, respectively.

The main, bipolar feature of the photoresponse waveform is characteristic for the nonequilibrium kinetic inductive response [6] with the positive part representing the Cooper pair breaking process and the negative part corresponding to the pair recombination. When compared to the calculated traces in Fig. 1(b), we note that the R-T model explains the main oscillation of the transient, but fails to explain the post-oscillation overshoot and the subsequent apparent

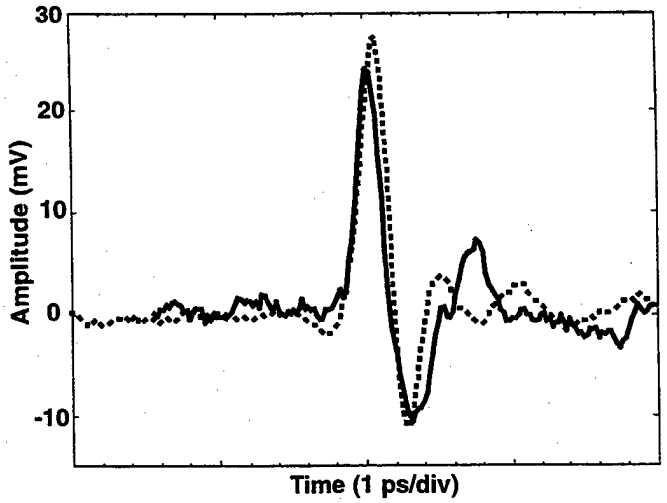

Fig. 2. Measured transient voltage of bridges fabricated on $LaAlO_3$ at 60 K (dotted line) and on MgO substrate at 70 K (solid line). In both cases the bridge was biased at $0.8I_c$.

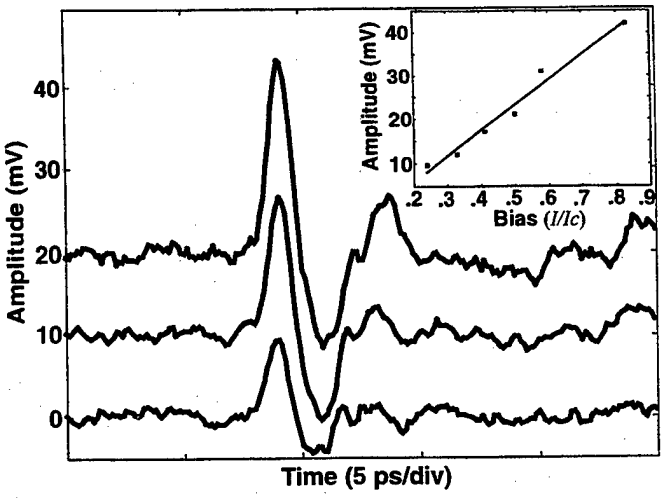

Fig. 3. Microbridge voltage transient response as the bias current is varied from 0.6 (top), 0.4 (middle), to 0.2 (bottom) of I_c, while the temperature and excitation power were held constant at 70 K and 60 μW respectively. The inset summarizes all photoresponse measurements taken as a function of the bias current.

ringing. We note that the main part of the transient is approximately 2-ps-wide, with the recombination part being essentially as fast as pair breaking; thus, clearly showing no phonon-trapping effect present in the photoresponse of YBCO.

Fig. 3 shows the behavior of the voltage transient as the bias current is changed, and the illumination power and temperature are held constant. The waveforms are offset for viewing clarity. From the top to the bottom, the waveforms were obtained with $0.6I_c$, $0.4I_c$ and $0.2I_c$ bias current, respectively. The bipolar part of the waveforms was observed to be a constant 2-ps-wide transient throughout the bias current range. The amplitudes of the positive and negative parts of the main transient, and the post-oscillation overshoot decreased with decreasing bias current. The inset summarizes the photoresponse amplitude of the positive component of transient to the current-biasing conditions for the entire test range. The linear dependence of the voltage transient amplitude on the current bias agrees with (1).

A dependence of the voltage transient amplitude on excitation power was also investigated. The amplitude was observed to increase with increasing switching power, consistent with the R-T model, and the main transient was measured to be 2-ps-wide for the entire test range of 50 to 200 μW incident on the sample.

V. CONCLUSION

We reported time resolved photoresponse measurements of high quality epitaxial thin films biased in the superconducting state at temperatures below the transition temperature. The origin of the response is attributed to the nonequilibrium kinetic inductance mechanism described by the R-T equations which qualitatively explain the main bipolar feature, but not the post-pulse overshoot and the apparent subsequent ringing. More theoretical work is needed to this end.

Our measurements showed a typical 2-ps-wide voltage transient for the entire bias current and excitation power test range. The ultrafast transient response time of YBCO microbridge demonstrates its viability as a high speed photodetector and its suitability for THz digital and communication applications.

REFERENCES

[1] F. A. Hegmann, D. Jacobs-Perkins, C.-C. Wang, S. H. Moffat, R A. Hughes, J. S. Preston, M. Currie, P. M. Fauchet, T. Y. Hsiang, and R. Sobolewski, "Electro-optic sampling of 1.5-ps photoresponse signal from $YBa_2Cu_3O_{7-\delta}$ thin films," *Appl. Rev. Lett.*, vol. **67**, pp. 285-287, July 1995.

[2] M. Lindgren, M. Currie, C. Williams, T. Y. Hsiang, P. M. Fauchet, R. Sobolewski, S. H. Moffat, R. A. Hughes, and J. S. Preston, "Intrinsic picosecond response times of Y-Ba-Cu-O superconducting photodetectors," *Appl. Phys. Lett.*, vol. **74**, pp. 853-855, February 1999.

[3] M. Lindgren, M. Currie, C. Williams, T. Y. Hsiang, P. M. Fauchet, R. Sobolewski, S. H. Moffat, R. A. Hughes, and J. S. Preston, "Ultrafast photoresponse in microbridges and pulse propagation in transmission lines made from high-T_c superconducting Y-Ba-Cu-O thin films," *IEEE J. Sel. Top. Quantum Electron.*, vol. **2**, pp. 668-678, September 1996.

[4] F. A. Hegmann, and J. S. Preston, "Origin of the fast photoresponse of epitaxial $Yba_2Cu_3O_{7-\delta}$ thin films," *Phys. Rev. B*, vol **48**, pp. 16023-16039, December 1993.

[5] A. Rothwarf and B. N. Taylor, "Measurement of recombination lifetimes in superconductors," *Phys. Rev. Lett.*, vol. **19**, pp. 27-30, July 1967.

[6] N. Bluzer, "Temporal relaxation of nonequilibrium in Y-Ba-Cu-O measured from transient photoimpedance response," *Phys. Rev. B.*, vol **44**, pp. 10222-10233, June 1991.

Optimization of a 115 GHz Waveguide Mixer Based on HTS Josephson Junction

Oliver Harnack, Marian Darula, Jens Scherbel, Jan-Klaas Heinsohn, Michael Siegel
Institut für Schicht- und Ionentechnik, Forschungszentrum Jülich, D-52425 Juelich, Germany

Dirk Diehl, Peter Zimmermann
Institution Radiometer Physics GmbH, D-53340 Meckenheim, Germany

Abstract—A waveguide mixer based on a Josephson junction made from a high-temperature superconductor has been analyzed at the frequency of 90 GHz and 115 GHz. The mixer consisted of a single-grain-boundary bicrystal junction which was integrated with a bow-tie antenna and a microstrip filter structure fabricated on a MgO substrate. Two different designs of mixer block were tested. Using the first design the best noise performance was measured at a local oscillator (LO) frequency of about 90 GHz. At the projected LO frequency of 115 GHz significant deterioration of performance was observed. A computer simulation of the mixer chip and substrat channel structure was performed using the 3d simulation program HFSS. A sufficient RF signal rejection by the filter structure was confirmed at 90 GHz. After a simulation cycle for 115 GHz the substrate channel in the mixer block was modified. Using this second design we measured a double-side-band mixer noise temperature of 1090 K at 10 K operating temperature which is the best performance of a HTS Josephson mixer to date obtained at this frequency and temperature.

I. Introduction

Three concepts of superconducting mixers for sub-mm wave receivers are presently under investigation: mixers based on quasiparticle tunneling (SIS), mixers where Josephson effect is explored (Josephson mixer) and mixers utilizing bolometric effects. The latter two can be fabricated using either low-temperature or high-temperature superconductors (HTS). The HTS Josephson mixer offers the possibility of high-temperature operation at very low local oscillator power levels (of the order of a few nanowatts) and thus to compete with cooled Schottky mixers. The goal of our work is to develop a receiver on the basis of a HTS Josephson mixer operating at 115 GHz. This frequency is of particular interest for gas spectroscopy, e.g. for environmental monitoring applications. Here, we report on results obtained during the optimization of the radio frequency (RF) structure of a Josephson mixer.

Manuscript received April 30, 1999.

This work was supported in part by the German Ministry of Education and Research (BMBF, 13N7321/5-6)

II. The Receiver Setup

A. *The RF setup*

The core of the RF setup used in our experiments was a waveguide mixer block, schematically shown in Fig.1 (a). The mixer block was mounted inside a cryostat. A simple beam splitter was used to combine the signal and the LO signal. The signal beam was picked-up by the horn antenna of the mixer block and guided to the mixer chip which was located in a narrow substrate channel perpendicular to the waveguide. Mechanical backshort and E-plane tuners, adjustable from the outside of the cryostat, allowed a precise control of impedance matching between the mixer and the waveguide environment. The 1.4 GHz intermediate frequency (IF) signal was amplified by an external room-temperature amplifier and limited by a bandpass filter with a bandwidth of 400 MHz. The noise temperature of the IF chain determined using hot/cold method was 130 K.

B. *Design and fabrication of the mixer chip*

A photograph of the mixer chip is shown in Fig. 1(b). The

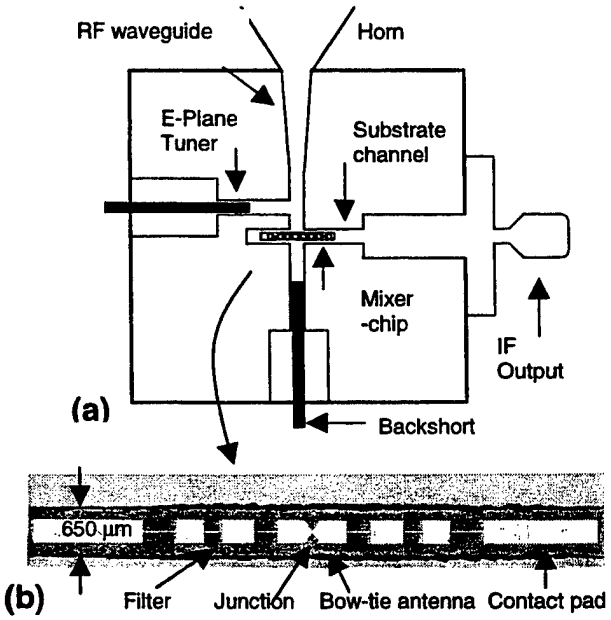

Fig.1 (a) Schematic of wave-guide mixer block with the Josephson junction mixer. (b) Photograph of the mixer-chip.

mixing element is located in the center, and it is integrated with the bow-tie antenna and the filter structure [1]. The stop-band filter prevents leakage of RF signal from the mixer to the terminals, but it lets the IF signal passing through. A rough estimation of dimensions of the filter structure can be done by applying approximations for impedance of microstrip lines. However, as shown below, such approach suffers from a large error as it neglects the influence of the substrate channel.

The mixer was a single HTS grain-boundary Josephson junction fabricated a bicrystal (24°) substrate from MgO which has a dielectric constant of ε_r=9.6. Pulsed laser deposition method was used for growing 50 to 100-nm-thick $YBa_2Cu_3O_{7-\delta}$ (YBCO) films. In addition, a 50-nm-thick gold layer was deposited in-situ on top of the YBCO film. Standard optical lithography and the ion beam etching (IBE) method were used to pattern the film and to create the filter structure with the junction in the form of a 1-μm-wide bridge in the center. The gold shunt was then removed from the area of the bridge using IBE and the structure was passivated by an evaporated SiO_x layer. The substrate was mechanically polished to reduce the thickness of the substrate down to 150 μm. This is necessary in order to avoid losses due to the generation of substrate modes.

The Josephson junctions fabricated using the described process had critical currents (I_c) of about 10 to 100 μA and normal resistance (R_n) between 10 and 15 Ω at 10 to 20 K.

III. Mixer Optimization

A. Noise measurement at 90 GHz

In the first series of experiments, the receiver and the mixer were characterized in the W-band frequency range. The receiver noise temperature T_{rec} and the conversion efficiency η were determined using the hot/cold method. A typical experimental result obtained at 90 GHz LO frequency is shown in Fig. 2. A double-side-band (DSB) receiver noise temperature of 2900 K, a conversion efficiency (not corrected to the IF impedance mismatch) of η=-10 dB, and a mixer noise temperature of 1600 K was measured at an operating temperature of 20 K. The optimal bias point was approximately in the middle between the zeroth and first Shapiro steps. Details about these experiments can be found elsewhere [2].

Using the same experimental setup we measured the noise at 115 GHz. However, significant deterioration of the receiver noise performance was observed.

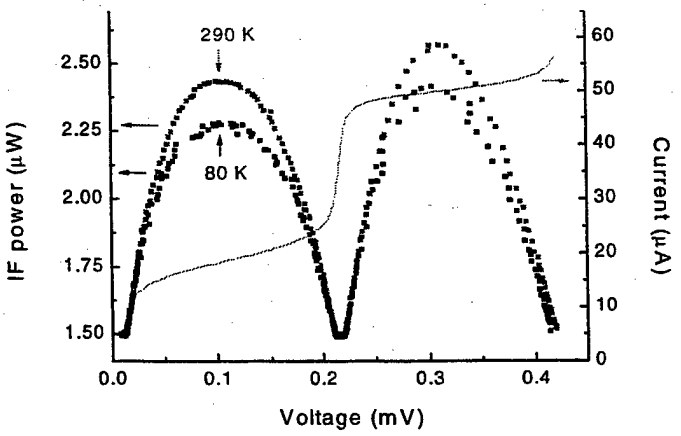

Fig.2 The current-voltage characteristic of Josephson mixer pumped at 90 GHz and corresponding IF hot/cold response. Operating temperature was 20 K.

B. Simulation of the filter structure

In order to identify the reason of performance degradation at 115 GHz, we analyzed the performance of the filter structure over a broad frequency range.

Figure 3 displays the definition of the filter structure (placed inside the substrate channel) used in the calculations. Because of the metallic connection of the filter on MgO substrate to the RF ground in the substrate channel, with small distance to the channel walls, it was not possible to apply analytical approximations for unscreened microstrip or suspended substrate. The theoretical analysis requires a 3-dimensional (3d) microwave simulation, and for this purpose the program HFSS [3] was used. The 3d simulation has the advantage that it accounts not only for quasi-TEM waves in the microstrip, but also for waveguide substrate modes. Using the HFFS program we could calculate the wave distribution of the structure and the transmission coefficient S21 of the filter. The result is presented in Fig. 4, curve (a). We observe, that with the first design the best filter performance, i.e., the highest damping is expected in the vicinity of 70 GHz. At 90 GHz the damping is still high enough so that the operation of the mixer is not negatively affected. In contrast, at 115 GHz the filter provides no isolation in accordance with our experimental result.

Using the same program we could investigate the influence of the substrate channel dimensions on the performance of the filter. This permitted us to carry out the optimization. We found that the slight modification of the dimension (second design in Fig. 3 caused a shift of frequency of maximal

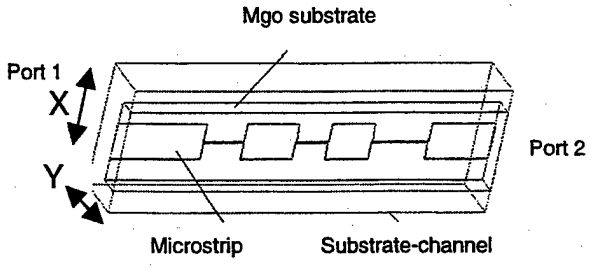

Fig.3 Definition of the geometrical structure of microsrip-filter on the MgO substrate in the substrate channel for HFFS simulation. First design: X=1000μm, Y=400μm, second design: X=650μm, Y=310μm,

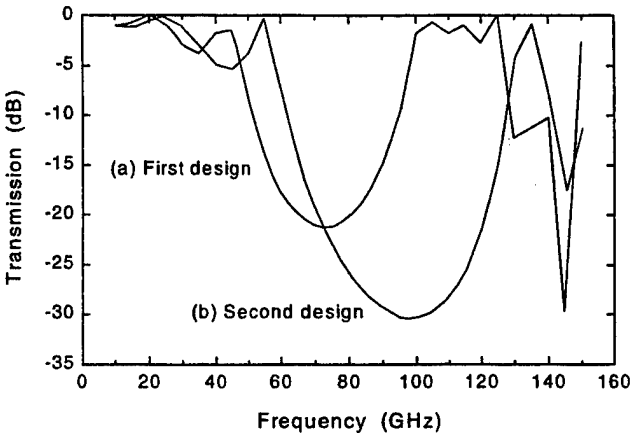

Fig.4 HFSS simulation of the transmission (s12) of the filter in the filter channel. (a) original design, (b) design with modified filter channel.

damping to approximately 100 GHz as shown in Fig. 4, curve (b). The simulation predicted an isolation better than –28 dB at 115 GHz, in contrast to -16 to -17 dB at 90 GHz using the first design.

C. *Noise measurements with modified mixer block*

The mixer block has been modified based on the results of simulations described above. The mixer chip, with a Josephson junction having approximately the same parameters like the sample measured at 90 GHz, was mounted into the modified mixer block and the measurement of the noise temperature was carried out. The result is shown in Fig. 5. We obtained a receiver noise temperature of 2420 K and a conversion efficiency η=10.1 dB (not corrected for the IF impedance mismatch) at an operating temperature of 10 K. After correction for the IF noise contribution the mixer

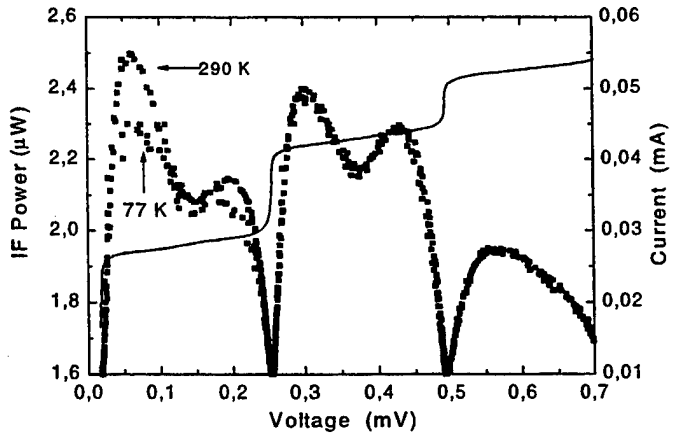

Fig.5 The current-voltage characteristic of Josephson mixer pumped at 115 GHz and corresponding IF hot/cold response. Operating temperature was 10 K.

noise temperature was 1090 K which is the best performance of a HTS Josephson mixer reported to date at 115 GHz and 10 K. The RF bandwidth was not checked in detail. Since the the stop-bandwidth of the RF filter is broader than that of the first design (which showed DSB operation [2]) we assume DSB operation also for the second design.

According to the simulation shown in Fig. 4 (b) the filter should operate properly also at 90 GHz. A measurement at 90 GHz confirmed the operation of the mixer at this frequency with the noise temperature T_{rec}=3000 K.

An optimization of the performance of the mixer element itself has to be done as a next step. Simulations of the noise properties of the Josephson mixer reported earlier [4] have shown that a DSB mixer noise temperature of about 20 times the operating temperature are expectable. The measured noise temperatures at 90 GHz are about 4 times and the results at 115 GHz are about 5 times close to this limit. An increase of the I_cR_n product of our junctions will certainly further increase the conversion and noise performance of the Josephson mixer.

IV. Conclusion

We presented our work on the RF optimization of a 115 GHz receiver using a HTS Josephson junction mixer. The optimization was performed in two steps. The first design of the mixer block and mixer chip resulted in a good mixer operation at 90 GHz, but a strong degradation of the noise performance was observed at 115 GHz. The 3d microwave computer simulation of the mixer chip in the substrate channel showed that the RF filter characteristics was responsible for bad performance at 115 GHz. Based on the simulation results a change of dimensions of the substrate channel was performed. Experimental results confirmed a substantial improvement of operation of the receiver at 115 GHz. A DSB receiver noise temperature of 2420 K and a mixer noise temperature of 1090 K was measured at an operating temperature of 10 K.

References

[1] The antenna and filter design was provided by E. Tong.

[2] O. Harnack, S. Beuven, M. Darula, H. Kohlstedt, M. Tarasov, E. Stephansov, and Z. Ivanov, "HTS mixers based on the Josephson effect and on the hot-electron bolometric effect", *IEEE Trans. on Appl. Supercond.* in press.

[3] Software package: "High Frequency Structure Simulator", Ansoft Corporation, Pittsburg, PA, ver. 6, 1999.

[4] R. J. Schoelkopf, "Studies of noise in Josephson-effect mixers and their potential for submillimeter heterodyne detection", Ph.D. dissertation, CalTech., 1995 (unpublished)

Submicron-Long HTS Hot-Electron Mixers

Oliver Harnack[1], Boris Karasik, William McGrath, Alan Kleinsasser, Jeff Barner

Center for Space Microelectronics Technology, Jet Propulsion Laboratory,
California Institute of Technology, Pasadena, CA 91109, USA

[1]On leave from Institute for Thin Film and Ion Technology, Research Center Juelich, 52425 Juelich, Germany

Abstract—We have measured the device length and temperature dependence of the intermediate frequency (IF) bandwidth and noise of hot-electron bolometer (HEB) mixers made from a high-T_c superconductor. Mixer devices with lengths (L) between 50 nm and 1 μm were fabricated from 25 - 35 nm thick YBCO films on MgO and sapphire substrates. Bandwidth measurements were done using signal and local oscillator (LO) frequencies in the range 1-20 GHz. At low operation temperatures the IF bandwidths were about 100 MHz and several 100 MHz for devices on MgO and sapphire, respectively. At higher operation temperatures, where self-heating disappeared and flux-flow effects define the shape of the IV characteristic, the measured IF bandwidth increased significantly. The temperature and IF dependence of absolute conversion efficiencies determined from noise measurements are in good agreement with the bandwidth data. At 2.7 GHz LO frequency the single-side-band mixer noise temperatures of a 50 nm long HEB on MgO was about 8000 K.

I. Introduction

The hot-electron bolometer (HEB) mixer made from a high-T_c superconductor (HTS) was introduced recently as a competing alternative to a Schottky-diode mixer. The HTS HEB mixer would require 100-times less LO power and thus would be a desirable candidate for long-term atmospheric remote-sensing and planetary missions. The required operating temperatures between 65 K and 75 K can be achieved with available space-qualified coolers.

The HEB mixer consists of a small volume of HTS material between normal metal contacts (Fig. 1). Electrons in the volume can be heated by absorbed RF radiation and transport current. Nonequilibrium "hot" electrons (e*) transfer their energy to the lattice (ph*) during a very short electron-phonon relaxation time $\tau_{e\text{-}ph}$, which is about 1-2 ps at 80-90 K in $YBa_2Cu_3O_{7-\delta}$ (YBCO) [1-3]. The performance of the mixer depends strongly on the total thermal conductance for heat removal from the phonon sub-system. Heat can be removed by escape of the phonons to the substrate (τ_{es}) or, as suggested in [4], by diffusion of phonons to the normal metal contacts (τ_{diff}). Modeling of the performance of HTS HEB mixers showed that the increased thermal conductance provided by phonon diffusion would result in significantly larger band widths at IF's dominated by phonon processes, and lower noise temperatures at IF's dominated by hot-electron effects. In addition, the IF response would depend strongly on the micro-bridge length [4]. In order to make phonon diffusion a dominant thermal process, submicron device lengths are required.

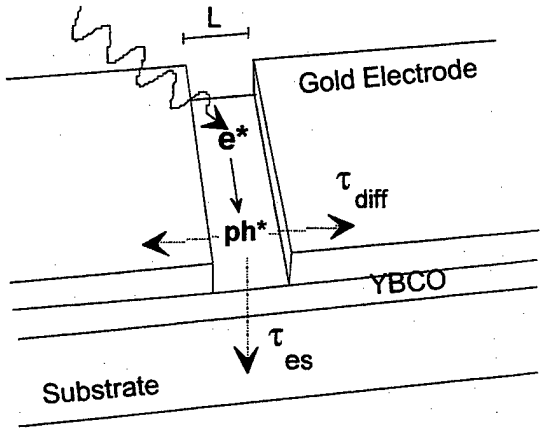

Fig. 1: Schematic of a HTS hot-electron bolometer mixer.

Heat removal through the film-substrate boundary is determined by the thermal boundary resistance (R_{bd}) and the heat diffusion in the substrate. Two substrates with good dielectric properties and high thermal conductivity on which high quality HTS films can be grown are magnesium oxide (MgO) and sapphire. MgO provides a low R_{bd} of about 5.3×10^{-4} K cm^2/W, while Al_2O_3 gives 1.1×10^{-3} K cm^2/W [5]. The perovskite-like substrates $LaAlO_3$, $SrTiO_3$ and $YAlO_3$ are less favorable due to their dielectric and thermal properties.

The goal of our work was to fabricate submicron-long YBCO HEB mixers on MgO and sapphire substrates and to determine their intrinsic thermal relaxation times as inferred from the 3-dB IF bandwidth. Additionally, noise measurements at low frequencies were done to provide data on the absolute conversion efficiency and on the LO pumping level required to minimize the mixer noise temperature.

II. Sample Fabrication

For the fabrication of HEB mixers, YBCO films with thickness of about 25-35 nm were grown on MgO and sapphire substrates using the laser deposition method. On sapphire substrates, a 30 nm CeO_2 buffer layer was used between the substrate and the YBCO film. Inductive T_c-

Manuscript received April 30, 1999.
This work was supported in part by NASA through the JPL Director's Research and Development Fund and Office of Space Science. Funding for O. H. was provided by the HSP III program of the German Academic Exchange Service (DAAD). Email: o.harnack@fz-juelich.de

measurements showed critical temperatures of 89-90 K for YBCO films on sapphire substrates and 84-86 K for films on MgO substrates with transition widths <2K for both substrate types. After patterning the films into 1 μm wide microbridges integrated with bow-tie antennas, a small-area window (50 nm to 500 nm length) was defined across the bridge using e-beam lithography. After removing the gold layer from the window using the ion beam etching (IBE) method, a SiO_x protection layer was deposited by thermal evaporation.

III. Bandwidth Measurements

A. Measurement setup and technique

The measurement system was recently described in detail in [6]. Two sweep oscillators in the frequency range 0.1-26 GHz were used as LO and signal source respectively. The downconverted signal in the range 10 MHz to 10 GHz was directly measured by using a spectrum analyzer. For the bandwidth measurement the LO signal power was adjusted to maintain a constant bias point.

B. IF characteristics of devices on MgO

As shown in Fig. 2, the IF bandwidth of a 50 nm long HEB mixer on MgO depends strongly on the temperature. The IF bandwidth at 50 K was about 100 MHz, increasing to about 2 GHz as the temperature was raised to 83 K. At the same time the conversion efficiency at low IF dropped by several dB (data at 50 K and 62 K should not be included in this direct comparison, since the available LO power was not sufficient to pump the device optimally. Thus the optimal conversion efficiency was probably several dB higher). However, the conversion efficiency at 73 K and 1 GHz IF is about 5 dB higher than for this IF at 65 K.

At the lowest temperature, we clearly see a –20 dB/dec slope at IF>100 MHz and the hot-electron plateau starting around 2 GHz. This device behavior at low temperature is well-characterized by the two-temperature model [7]. Measurements with 200 nm and 400 nm long devices gave very similar results and the theoretically predicted L^{-2}-dependence [5] of the IF bandwidths was not observed. The current-voltage characteristics (IVC) show that self-heating effects are present at 50-65 K and, as the temperature becomes closer to T_c, flux-flow-like rounding starts to dominate the shape of the IVCs. Flux-flow effects can provide nonlinearities [8], which possibly generate an IF response in addition to the hot-electron mixing response and effectively extend the IF bandwidth as seen at T>70 K. However, it has been shown that the nonlinearity due to flux creep which is the dominant source of d.c. resistivity in the superconducting state, becomes unimportant as the operating frequency exceeds the depinning frequency, which is in the range 10-100 GHz at temperatures close to T_c [8]. We also performed IF bandwidth measurements at 100 GHz and 300 GHz. The results indeed showed that the large IF bandwidth seen at high temperatures (Fig. 2) revert to the low-temperature IF bandwidth as the operating frequency increases above about 100 GHz [6].

C. IF characteristics of devices on CeO_2/sapphire

A 50 nm long HEB mixer on CeO_2 showed higher IF bandwidths and a quite different scaling of the IF response with temperature. (Fig. 3, the data were averaged and the curves were offset relative to each other for better visibility). At low temperature, the bandwidth is 450 MHz and increases to 2.4 GHz at 83 K. A clear roll-off with a –20 dB/dec slope starting at IF>1.5 GHz is observed over the whole temperature range. A two-temperature model fit to the roll-offs would give a even weaker temperature dependence. Measurements with 80 nm and 300 nm long devices showed a similar behavior. Again, no L^{-2}-dependence of the IF bandwidths was observed. In contrast to the case MgO, the

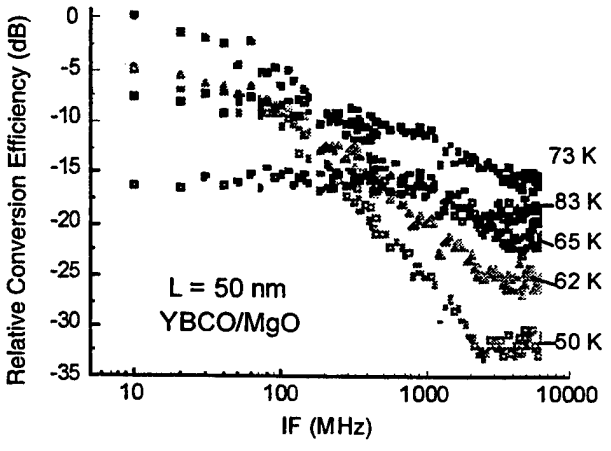

Fig. 2: IF response of a 50 nm long HEB mixer on MgO, measured at different temperatures.

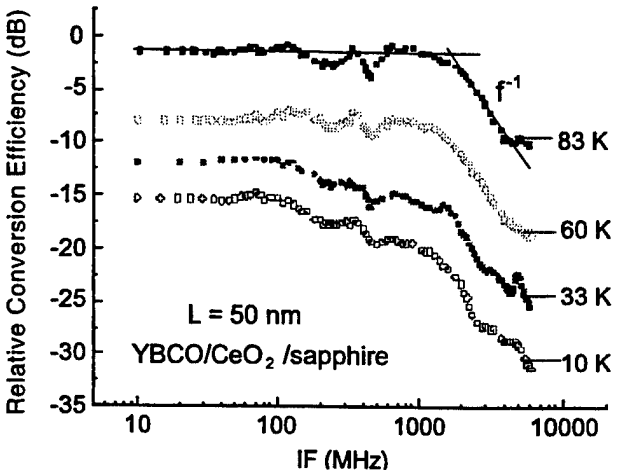

Fig. 3: IF response of a 50 nm long HEB mixer on CeO_2/sapphire measured at different temperatures

conversion efficiency did not change significantly with temperature.

IV. Noise Measurements

A) *Setup*

Noise measurements were done by using a calibrated HP noise diode as a signal source. The effective temperature T_N of the diode signal was 1100 K at the mixer port and the receiver noise temperature was calculated by using the Y-factor method. The LO frequency was chosen to be 2.7 GHz in order to keep the technical requirements simple. A broadband 10 MHz-1 GHz amplifier was used to amplify the IF signal and different bandpass filters were used to define the IF bandpass for the noise measurements.

B) *Results*

Figure 4 shows the result of the noise measurement at a temperature of 65 K and at an IF of 120 MHz. After correcting the data for the IF-system noise contribution, the single-side-band (SSB) mixer noise temperature was about 8000 K and the SSB conversion efficiency η at the same bias point was -9.5 dB. In order to obtain the lowest noise temperature, the LO power had to be increased up to a level where the hysteresis due to self-heating effects was suppressed. Decreasing of the LO power level resulted in a significant in-crease of the output noise and smaller Y-factors. Table I shows the results of noise measurements at different temperatures and IF frequencies. At the low IF a decrease of η of about 2.1 dB can be seen as the temperature is increased from 65 K to 70 K. This drop qualitatively agrees with the IF characteristics shown in Fig. 2. At the same time, the mixer noise temperature increases slightly with temperature.

Keeping the temperature at 65 K we note that η drops about 4.4 dB as the IF changes from 120 MHz to 1 GHz. At 70 K this drop is only about 0.8 dB. This is also in qualitative agreement with the measured IF characteristics. At 65 K the difference in noise temperatures of only 0.8 dB suggests that the mixer noise bandwidth is larger than the signal bandwidth. The mixer output noise is quite constant with temperature for an IF of 1 GHz but increases remarkably with decreasing temperature for an IF of 120 MHz, which suggests stronger mixing performance.

TABLE I

RESULTS OF NOISE MEASUREMENTS WITH A 50 NM HEB ON MgO

IF [MHz]	T_{MIX} (65 K) [K]	η (65 K) [dB]	T_{MIX} (70 K) [K]	η (70 K) [dB]
120	8000	-9.5	8600	-11.6
1000	9700	-13.9	6650	-12.4

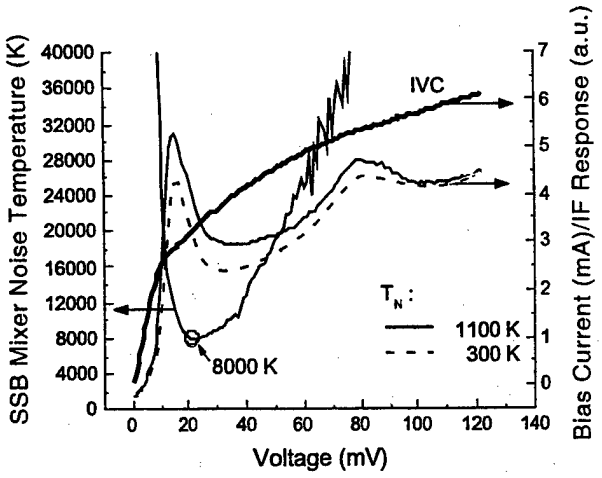

Fig. 4: Noise measurement using a 50 nm long mixer on MgO at 65 K and f_{LO}=2.7 GHz. The IF center frequency was 120 MHz and the filter bandwidth was 100 MHz.

V. Conclusion

We measured the IF bandwidths of sub-μm long HEB mixers on MgO and CeO_2/sapphire substrates. An L^{-2} dependence of the IF bandwidth was not observed for our type of device geometry. In terms of available IF bandwidth, HEB mixers on CeO_2/sapphire are most promising. The SSB mixer noise temperatures are several-times higher than expected if phonon diffusion was present in our mixers. Additional experiments with different device geometries are required to further investigate the missing phonon diffusion.

References

[1] M. Lindgren, V. Trifonov, M. Zorin, M. Danerud, D. Winkler, B.S. Karasik, G.N. Gol'tsman, and E.M. Gershenzon, *Appl. Phys. Lett.* **64**, 3036 (1994).

[2] M. Danerud, D. Winkler, M. Lindgren, M. Zorin, V. Trifonov, B.S. Karasik, G.N. Gol'tsman, and E.M. Gershenzon, *J. Appl. Phys*, **76**, 1902 (1994).

[3] A.D. Semenov, R.S. Nebosis, Yu.P. Gousev, M.A. Heisinger, and K.F. Renk, *Phys. Rev.* B **52**, 581 (1995).

[4] B.S. Karasik, W.R. McGrath, and M.C. Gaidis, *J. Appl. Phys.* **81**, 1581 (1997).

[5] A.V. Sergeev, A.D. Semenov, P. Kouminov, V. Trifonov, I.G. Goghidze, B.S. Karasik, G.N. Gol'tsman, and E.M. Gershenzon, *Phys. Rev. B* **49**, 9091 (1994).

[6] O. Harnack, B.S. Karasik, W.R. McGrath, A.W. Kleinsasser, J.B. Barner, to be published *in Proc. 10th Int. Symp. Space THz Technol.*, Charlottesville, 16-18 March 1999.

[7] M. Lindgren, M.A. Zorin, V. Trifonov, M. Danerud, D. Winkler, B.S. Karasik, G.N. Gol'tsman, E.M. Gershenzon, *Appl. Phys. Lett.* **65**, 3398 (1994).

[8] M. Golosovsky, M. Tsindlekht, and D. Davidov, *Supercond. Sci. Technol.* **9**, 1 (1996).

A Nanoscale YBCO Mixer Optically Coupled with a Bow Tie Antenna

Fredrik Rönnung, Sergey Cherednichenko and Dag Winkler
Dept. of Microelectronics and Nanoscience, Chalmers University of Technology, Göteborg, Sweden

Gregory N. Gol'tsman
Dept. of Physics, Moscow State Pedagogical University, Moscow, Russia

Abstract – Bolometric response of $YBa_2Cu_3O_{7-\delta}$ (YBCO) hot-electron bolometers (HEB) to near-infrared radiation was studied. Devices were fabricated from a 50 nm thick film and had in-plane areas of 10×10 μm², 2×0.2 μm², 1×0.2 μm², and 0.5×0.2 μm². We found that nonequilibrium phonons cool down more effectively for the bolometers with smaller area. For the smallest bolometer the bolometric component in the response is 10 dB less than for the largest one.

I. INTRODUCTION

Heterodyne detection of electromagnetic radiation in the submillimeter and the far infrared range is important in a number of research fields, such as radioastronomy, atmospheric physics and chemistry. Semiconductor based detectors (Schottky diodes) are not so useful in this range due to their high noise temperature and demand for high local oscillator (LO) power. Superconductor-insulator-superconductor (SIS) quasiparticle mixers have a performance close to the quantum limit but deteriorate at frequencies higher than the superconductor energy gap ($h\nu=2\Delta$), which for niobium is ~750 GHz. Recent years, heterodyne recievers utilizing the hot-electron effect in low-temperature superconductors [1] have proved to be superior these other competing technologies for terahertz frequencies. An intermediate frequency (IF) bandwidth of 10 GHz and a double sideband noise temperature of the order $20h\nu/k_B$ have been reached for low-T_c materials [2-4]. This noise temperature is an order of magnitude lower than that of Schottky diodes.

Considering high-T_c materials for HEB mixers, we cannot expect to compete with low-T_c superconductors with regard to sensitivity. An obvious advantage of the YBCO HEB is that it operates at liquid nitrogen temperature. Besides this, the IF bandwidth has been estimated from time domain measurements to be ≈130 GHz [5]. Optical mixing in YBCO has been demonstrated up to 18 GHz [6], limited only by read-out electronics. Such a large bandwidth becomes very important in the terahertz frequency range because of the lack of tunable LO sources for these wavelengths. Calculations show [7] that the YBCO HEB would out-perform Schottky diodes both in view of LO power requirements and the noise temperature level. These properties taken together makes the YBCO HEB useful in space-borne applications.

Manuscript received May 4, 1999.

This work was supported by the Swedish Foundation for Strategic Research and Russian Program on Condensed Matter (Superconductivity Division) under Grant No. 3.4.

Since the YBCO HEB mixer operates on the basis of nonequilibrium effects, a major obstacle in its realization is the presence of a bolometric component in the resistive response of an YBCO film. This component significantly increases the conversion loss and noise temperature. Furthermore, the bolometric response is a function of phonon heating in the film, and it may thus be diminished by improved heat exchange through the film/substrate interface. This is accomplished by decreasing the acoustic mismatch between film and substrate and by making use of thinner films. Another effect that contributes to the total thermal resistance at the interface is heating of the substrate underneath the film. With smaller device area we will obtain a gradual transition from one-dimensional to three-dimensional heat diffusion in the substrate. This in combination with the use of a substrate with large thermal conductivity will keep the area underneath the mixer closer to the bath temperature.

This work is devoted mainly to the study of the dependence of the cooling rate of phonons on the bolometer size.

II. DEVICE FABRICATION

We manufactured bolometers with different in-plane area (see Table I), which were integrated into planar bow tie antennas. YBCO films with a thickness of 50 nm were deposited onto $LaAlO_3$ substrates by standard pulsed laser deposition technique. After deposition, the films had a superconducting transition temperature of ≈88 K. X-ray diffraction showed that the films were predominantly c-axis oriented. Bolometer and antenna structures were patterned using electron-beam lithography and argon ion milling. After processing, the devices had a transition temperature of ≈87 K.

TABLE I. PHYSICAL AND ELECTRICAL PROPERTIES OF SAMPLES #1 THROUGH #4.

Sample Number	Length, l [μm]	Width, w [μm]	T_c [K]	j_c [10^6 A/cm²]
1	10	10	87	5.2
2	0.2	2	87	6.7
3	0.2	1	87	4.8
4	0.2	0.5	87	2.0

III. EXPERIMENTAL SETUP

The experimental setup is shown in Fig.2. A semiconductor laser (1.56 μm wavelength) coupled to a single-mode fiber was used as a radiation source. The radiation power in the fiber was 1.4 mW. An optical isolator added 3 dB loss. The intensity of the laser radiation was modulated by a high-frequency signal generator. The modulated part of the total radiation intensity was about 10%. The bolometer was driven into resistive state by a dc bias current. The bolometer response was measured with a Tektronix 494AP spectrum analyzer for modulation frequency from 0.2 MHz to 2000 MHz. For frequencies higher than 300 MHz additional amplifiers with a total gain of 30 dB were used. Measurements were performed at 77 K using the bias current that corresponded to the largest responsivity.

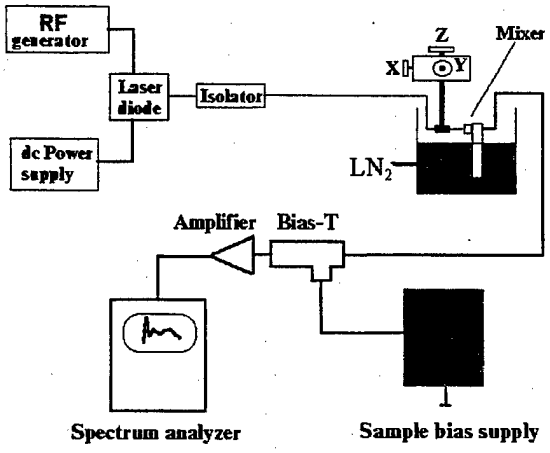

Fig 1. The experimental setup.

IV. RESULTS AND DISCUSSION

The photoresponse of different bolometers versus modulation frequency is shown in Fig.2. The curves are made to cross each other at frequency 300 MHz for comparison.

For sample #1 in the frequency range from 1 MHz to 10 MHz there is a gradual decrease of the response according to $f^{-0.3}$, where f is the modulation frequency. At frequencies larger than 40 MHz this dependence changes to f^{-1}, which characterizes a roll-off process with a single relaxation time. Such an evolution of the response agrees well with the observation made earlier [8] for bolometers of the same size. Samples #1 and #2 demonstrate practically the same dependence of the response on the modulation frequency. The response of the sample #3 shows a 5 dB smaller decrease in the low frequency bolometric range. For this sample the response remains constant for f<1 MHz, decreases according to $f^{-0.3}$ at larger frequencies, and follows a f^{-1} law at f>40 MHz. For sample #4 that has the smallest bolometer area the magnitude of the response remains constant until 60 MHz (within 3 dB) and then rolls off according to f^{-1}.

Several studies of hot-electron detectors from thin YBCO films have been made in the optical and millimeter wavelength ranges [6-12]. Both bolometric and nonbolometric components have been identified in the resistive response. The nonbolometric component controls the early stage of relaxation after pulse excitation or, in the case of modulated continuous wave excitation, the frequency dependence of the response at high modulation frequency (above 2 GHz) [5,6]. The nonbolometric component corresponds to the heating up and cooling down of quasiparticles. The quasiparticle cooling rate is controlled by the reciprocal electron-phonon interaction time $(\tau_{e\text{-}ph})^{-1}$ in the resistive state of the superconductor. Recent direct measurements have shown that in thin YBCO films at 80 K this time equals 1.1 ps [5], i.e. the electron temperature can be modulated with a frequency as large as 140 GHz.

The bolometric component of the response is related to the heating of both the phonons and electrons in the film. If the film thickness d is smaller than $l_{ph,f}/\alpha_{f\text{-}s} \approx 500$ nm [13], where $l_{ph,f}$ is the phonon mean free path in the YBCO film and $\alpha_{f\text{-}s}$ is the transparency of the film/substrate interface for thermal phonons, thermal diffusion in the film towards the substrate can be neglected. Hence, the rate of phonon cooling is determined by the heat exchange rate through the film/substrate interface. It has been shown [13] that the total heat exchange rate depends not only on the rate of phonon escape $(\tau_{esc})^{-1}$ from the film into the substrate but also on the rate of reverse flow $(\tau_R)^{-1}$ of phonons back from the substrate to the film. Depending on the substrate material, for a 50 nm thick film the phonon escape time varies from 2 ns to 5 ns [13, 6], which corresponds to roll-off frequencies from 80 MHz to 30 MHz. The reverse phonon flow slows down the cooling of phonons in the film and results in the gradual decrease of the bolometric component of the response at small modulation frequencies according to f^{-m}, where m is between 1/2 and 1/3. The characteristic time of the phonon return to the film can be estimated as $\tau_R \approx \tau_{ph,s}/(\alpha_{s\text{-}f})^2$ where $\tau_{ph,s}$ is the phonon scattering time in the substrate and $\alpha_{s\text{-}f}$ is the transparency of the interface for phonons in the direction

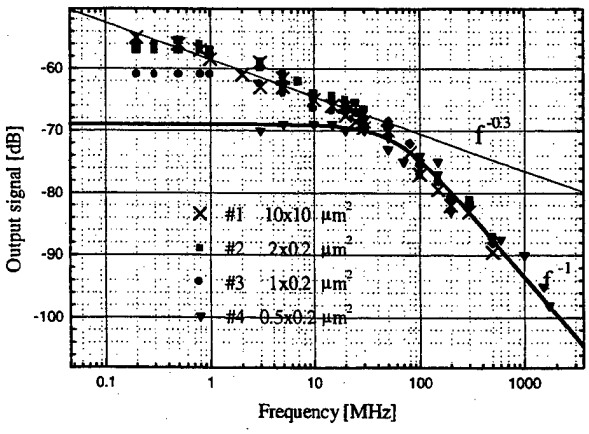

Fig.2. IF spectrum of different YBCO HEB samples.

from the substrate to the film. Corresponding characteristic length is $l_R=(D_s\tau_R)^{1/2}=l_{ph,s}/\alpha_{s-f}$ where D_s is the phonon diffusivity in the substrate and $l_{ph,s}$ is the phonon mean free path in the substrate. The length l_R is the mean distance over which a phonon travels in the substrate until it returns to the film. The reverse flow of phonons can be minimized making use of substrates with larger heat conductivity, i.e. larger $\tau_{ph,s}$ and $l_{ph,s}$, and also by decreasing the in-plane sizes of the bolometer down to a magnitude less than l_R. Using $\tau_{ph,s}\approx 42$ ps and $\alpha_{s-f}\approx 0.059$ [13] we estimate $l_R=0.4$ μm for our samples. Our estimate corresponds well to the area (0.5×0.2 μm^2) of the bolometer #4 that demonstrates a flat response in the frequency range from 2 to 60 MHz.

In the absence of the reverse flow of phonons from the substrate to the film, the response of HEB follows predictions of the two-temperature model [14] even at lowest modulation frequencies used in our experiment (see the solid line in Fig.2). The frequency dependence of the conversion loss in the heterodyne regime is controlled by the frequency dependence of the responsivity [1]. Therefore the conversion loss in the hot-electron mode scales with the magnitude of the bolometric component. This suggests that at frequencies larger than 30 MHz and, consequently, in the hot-electron mode the conversion loss for a submicron YBCO HEB mixer should be ≈5 dB and ≈10 dB less, than for a 1 μm and 2 μm wide HEB mixer, respectively.

Further decrease of the conversion loss can be achieved due to additional improvement of the heat removal from the bolometer. One possibility is to decrease the film thickness and, consequently, shorten the phonon escape time. Another direction is to utilize the diffusion of nonequilibrium phonons from the bolometer to contacts. This mechanism of phonon cooling has been discussed in [7]. Authors theoretically estimated out-diffusion time τ_{diff} for a 0.2 μm long bolometer. They found $\tau_{diff}=260$ ps that is an order of magnitude less than τ_{esc} for a 50 nm thick film. The effective cooling time due to both cooling mechanisms can be estimated as $(\tau_{esc}^{-1}+\tau_{diff}^{-1})^{-1}$ which results in a 240 ps overall cooling time and a corresponding roll-off frequency of 650 MHz. In comparing modulation frequency dependence of the response we did not find a noticeable difference between roll-off frequencies of bolometers with the length 10 μm and 0.2 μm (devices #1 and #3). The absence of the diffusion contribution to the phonon cooling rate in our samples can be attributed to defects and impurities that are not considered in [7] but may decrease the diffusivity of phonons.

A crude estimation of the responsivity based on the absorbed power as read from the difference between the pumped and the unpumped *IV*-curve, gave a value at 10 MHz of 1.8×10^3 V/W. From the absorbed power for the largest device, which is without the bow tie antenna, the average power density incident on the devices was determined and the antenna gain was calculated to ~4.5 dB.

V. CONCLUSION

We have studied the response of YBCO hot-electron bolometers of different sizes to modulated laser radiation. We found that the decrease of the in-plane size of the bolometer below 1 μm resulted in the disappearance of the $f^{-0.3}$ dependence of the bolometric component in the response. It means that for a bolometer with such a small area the bolometric response is flat at frequencies smaller than the roll-off frequency corresponding to the phonon escape time, and above this frequency follows according to the two-temperature model. The obtained results suggest that the use of the submicron bolometer as mixer in the hot-electron mode should result in an increase of the conversion efficiency of the order 10 dB compared to larger bolometers.

ACKNOWLEDGMENT

All devices were fabricated in the Swedish Nanometer Laboratory.

REFERENCES

1 E.M.Gershenzon, G.N.Gol'tsman, I.G.Gogidze, Yu.P.Gousev, A.I.Elant'ev, B.S.Karasik,and A.D.Semenov, Sov. J.Superconductivity 3, 1582 (1990).

2 B.S.Karasik, A.Skalare, R.A.Wyss, W.R.McGrath, B.Bumble, H.G.Le.Duc, J.B.Barner, and A.W.Kleinsasser, 6th IEEE Int.Conf. on THz Electronics, 3-4 Sept, 1998, Leeds, UK.

3 P.Yagoubov, M.Kroug, H.Merkel, E.Kollberg, G.Gol'tsman, S.Svechnikov, G.Gershenzon, Appl.Phys.Lett. **73**, (19), 2814, 1998.

4 J. Schubert, A. Semenov, G. Gol'tsman, H.-W. Huebers, G. Schwaab, B. Voronov, E. Gershenzon, 10th Int. Symposium on Space Terahertz Technology, Charlottesville, USA, March 1999.

5 M.Lindgren, M.Currie, C.Williams, T.Y.Hsiang, P.M.Fauchet, R.Sobolewsky, S.H.Moffat, R.A.Hughes, J.S.Preston, F.A.Hegmann, subm.Appl.Phys.Lett. Sept. 1998.

6 M.Danerud, D.Winkler, M.Lindgren, M.A.Zorin, V.Trifonov, B.S.Karasik, G.N.Gol'tsman, E.M.Gershenzon, J.Appl.Phys. **76** (3), 1994.

7 B.S.Karasik, W.R.McGrath, and M.C.Gaidis, J.Appl.Phys. **81** (3), pp.1581-1589, 1997.

8 M.Lindgren, V.Trifonov, M.A.Zorin, M.Danerud, D.Winkler, B.S.Karasik, G.N.Gol'tsman, E.M.Gershenzon, Appl.Phys.Lett., **64**(22), 1994.

9 Yu.P.Gousev, A.D.Semenov, E.V.Pechen, A.V.Varlashkin, R.S.Nebosis, and K.F.Renk, Appl.Phys.Lett. **69**(5), 1996.

10 M.J.Burns, A.W.Kleinsasser, B.Karasik, M.Gaidis, and W.R.McGrath, Proc. of the 8th Int. Symp. on Space Terahertz Tech., Pasadena , USA, 1997.

11 V.Trifonov, B.S.Karasik, M.A.Zorin, G.N.Gol'tsman, E.M.Gershenzon, M.Lindgren, M.Danerud, D.Winkler, Appl. Phys. Lett. **68**, 1418 (1996).

12 C.-T.Li, Mark Lee, B.S.Deaver, Jr, R.M.Weikle II, Proc. of the 9th Int. Symp. on Space Terahertz Tech., Pasadena , USA, 1998.

13 A.V.Sergeev et al, Phys.Rev.B, **49**(13), pp.9091, 1994.

14 N.Perrin and C.Vanneste, Phys. Rev. B**28**, 5150 (1983).

Large Area $YBa_2Cu_3O_{7-x}$ Bolometers on Si Substrates

L. R. Vale and R. H. Ono,
National Institute of Standards and Technology, Boulder, CO 80303

D. G. McDonald and R. J. Phelan,
Boulder Metric, Inc. Boulder, CO 80303

Abstract–We have developed $Yba_2Cu_3O_{7-x}$ (YBCO) thermometers for large area (4 mm x 4mm) electrical substitution bolometers. We passivated the YBCO with a thin Au layer and demonstrated a noise equivalent temperature (NET) of 4 nK $Hz^{-1/2}$. We then used a resistor layer of NiCr alloy deposited directly on the thermometer to perform optical measurements of the bolometer in the cryostat. Optical measurements show an electrical noise equivalent power (NEP) of 87 pW $Hz^{-1/2}$ with a large thermal conductance of $1.87x10^{-3}$W/K. These thermometers may be used as a real-time measurement radiometer.

I. Introduction

We report on the fabrication of a high temperature superconducting (HTS) bolometer for a radiometer operating at liquid nitrogen temperature that can be used in the infrared, visible, and ultraviolet regions of the electromagnetic spectrum. The application of this bolometer requires a large thermal conductance combined with low noise. The sensitivity of the bolometer depends on the thermal conductance G to the reservoir and the noise of the thermometer. Our goal was an electrical noise equivalent power (NEP) of 100 pW $Hz^{-1/2}$ at a chopper frequency of 10 Hz.

Our composite bolometer consists of a $(4\ mm)^2$ membrane of Silicon (Si), with YBCO and buffer-layer thin films grown by pulsed-laser deposition, and a thin film heater which will be used for calibration by the electrical substitution-of-power method. The large area membrane detector is unique for calibrated HTS radiometers because of the large G and simultaneously low noise temperature. We will discuss the fabrication issues which presented the greatest challenges to successful device performance: achieving thermal isolation of the detector by Si back etching, uniform strain-free deposition of large area YBCO films on Si, and electrical isolation of the large area detector from the heater.

II. Fabrication

The YBCO is grown to a maximum thickness of 50 nm to minimize the mechanical stress inherent in YBCO grown on Si. Previous studies have shown the sensitivity to environmental degradation of YBCO films on Si, due to stress induced by differential thermal expansion [1]. This is seen as a decrease in the film's critical temperature and current density. We have previously demonstrated low noise in large area YBCO devices on Si [2]. However, we have observed that standard photolithographic processing can deteriorate these devices and result in an anomalous increase in voltage noise of current-biased YBCO devices on Si. Our application required further processing and a need to insulate the YBCO from the subsequent heater layer.

The vertical structure of the devices we fabricated is shown in Fig. 1. The bolometer fabrication begins with a B-doped Si substrate upon which we deposit 200 nm of epitaxial yttria-stabilized zirconia (YSZ) and 20 nm CeO_2 (CeO) as buffer layers to prevent interaction between the Si and the YBCO film (Fig. 1a). The fabricated thermometer would then be followed by the deposition and fabrication of a heater layer, which would be electrically isolated from the YBCO thermometer. The need for passivation with long term stability and for electrical isolation for the YBCO, resulted in an investigation of a variety of insulator layers. We worked with room-temperature grown amorphous films and epitaxial *in situ* films of yittria stabilized zirconia and CeO to protect the YBCO. Unfortunately, the amorphous films themselves were easily damaged and not pinhole-free, thus not able to protect the underlying YBCO from subsequent patterning effects. We then developed a process (based on a passivation process that we use successfully on YBCO films on substrates other than Si [3]) for depositing *in situ* epitaxial passivating $SrTiO_3$ (STO) films using a mechanical mask that also allowed for the deposition of *in situ* Au contacts. Unfortunately, the STO layer made it difficult to fully oxygenate the underlying YBCO on Si and resulted in thermometer devices demonstrating a higher noise level.

Our previous studies on long term stability of passivated vs. non-passivated Josephson junctions using Au normal metal layers [3] plus other studies on the use of Ag on YBCO for passivation [4,5] encouraged us to try this technique for the 50 nm YBCO films on Si. We followed the YBCO deposition with an *in situ* layer of 20 nm thick Au deposited by sputtering at 100 °C (Fig. 1b). This Au layer does cause

*Contribution of the U.S. Government and not subject to copyright.

an electrical shunt to the YBCO, but it is resistant to processing effects and has the added benefit of providing *in situ* contacts for the voltage and current leads. Passivation of the YBCO was confirmed with measurements of the noise equivalent temperature (NET) of the thermometer, before and after processing, which remained unchanged. Another added benefit of this *in situ* Au passivation technique is its effect on the thermometer NET which appears to be the lowest value yet reported for a device of this type and is of order 4 nK $Hz^{-1/2}$ [5].

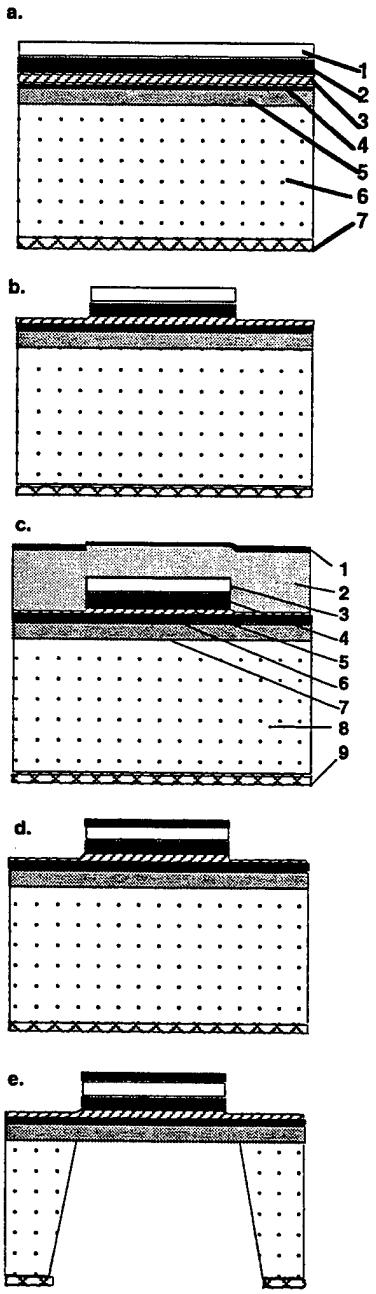

Fig. 1. Vertical structure and fabrication sequence. (a) The layer sequence grown in situ is: 1- Au, 2-YBCO, 3-CeO, 4-YSZ, 5-Boron doped Si, 6-Si (100), and 7-SiO_2. (b) shows the structure after patterning the thermometer (Au/YBCO). (c) shows the sequence with a deposited insulator and heater/absorber: 1-NiCr or AuPd, 2-DPXN, 3-Au, 4-YBCO, 5-CeO, 6-YSZ, 7-B-Si, 8-Si, and 9-SiO_2. (d) shows the use of a directly grown absorber layer and (e) shows the result after membrane etching.

With the passivation and long term stability of the YBCO achieved, we now required electrical isolation of the thermometer from the electrical substitution heater. We tested a number of different spin-on and vapor deposited polymer films, as well as evaporated or pulsed laser deposited materials. We used a vapor deposition polymerization process of Polyparaxylylene (DPXN) because of its excellent insulating qualities (Fig. 1c). NiCr or AuPd heater layers, seen as the meander line in Fig. 2, were patterned by liftoff on these polymer films. Subsequent processing included KOH etching of the back side of the Si (for 2.5 hours) to produce the 2.8 μm B-Si supporting membrane (Fig. 1e) that we required for our high conductance, high speed bolometer. The 0.5 μm-1 μm thick layers of DPXN material resulted in a mechanical strain that ruptured the 2.8 μm thick B-Si when the membrane was cooled to liquid nitrogen temperatures for testing. The trade-off between perfect electrical isolation and mechanical strain with thick insulator films over the relatively large 4 mm x 4 mm area required for the calibration heater remains problematic. Alternatively, we deposited a 12 nm thick absorbing NiCr layer directly on the normal-metal passivated YBCO thermometer (Fig. 1d), which allowed us to make optical measurements to verify the properties of the bolometer. The completed bolometer (Fig. 2), which was thermally isolated on the 2.8 μm thick B-doped membrane, was mounted in the cryostat and measured.

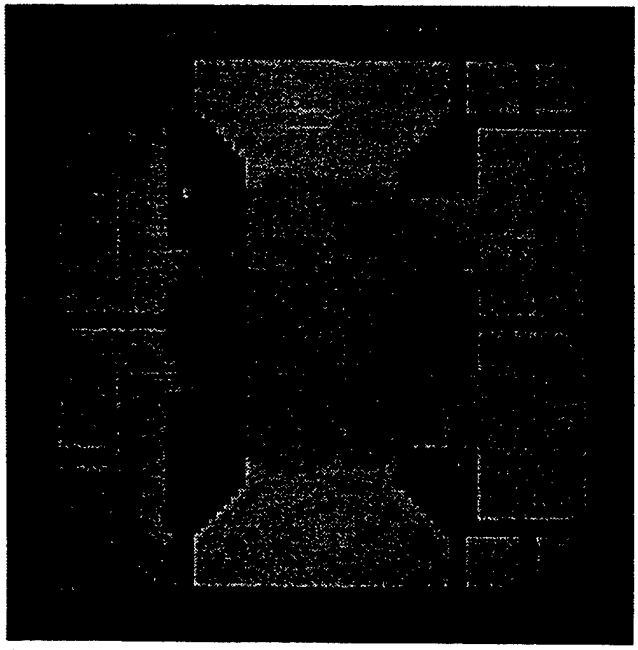

Fig. 2. Photograph of the completed bolometer chip which is 14 mm on a side.

III. Results

The bolometer described here ,with the NiCr absorber, was measured in the cryostat using a 670 nm wavelength power-stabilized diode laser scanned over the entire thermometer area. With a time constant of 16.8 ms, this device had an optical NEP of 87 pW $Hz^{-1/2}$ which is notably small for a device with a large thermal conductance of 1.87×10^{-3} W/K, and exceeded our intended goal of 100 pW $Hz^{-1/2}$. The specifics of the measurement technique and recorded data table are reported in detail in Ref. [6]. We have demonstrated the combination of a large thermal conductance with an excellent low noise thermometer that provides for a large dynamic range radiometer.

IV. Conclusions

The bolometer is notable for its combination of low noise and large thermal conductance. Further work is needed to optimize insulator thickness and reduce mechanical strain on the membranes, these improvements would allow the fabrication of the electrical substitution heater that is necessary for calibration of the bolometer. The thermometer performance is sufficiently encouraging that we plan to fabricate these devices using Si-on-insulator (SOI) substrates. We can then take advantage of the demonstrated low noise and improve the NEP by reducing the thermal conductance. The resulting loss of speed can be compensated by negative electrothermal feedback. The resulting bolometer can then be used in more generic applications of long-wavelength infrared detectors.

References

[1] H. Brehner, K. Ruhrnschopf, G. Wedler, and W. Rauch, "Surface reactions and long time stability of YBCO thin films," *Physica C* 208, pp. 419-424, 1993

[2] D.G. McDonald, R. J. Phelan, L.R. Vale, R.H. Ono, J.P. Rice, et al, "Noise from YBCO films: Size and Substrate Dependence," *IEEE Trans. Appl. Supercond.* 7, pp. 3091-3095, 1997.

[3] L.R. Vale, R.H. Ono, and D.A. Rudman, "YBCO Josephson Junctions on Bicrytsal Al_2O_3 and STO Substrates," *IEEE Trans. Appl. Supercond.* 7, pp. 3193-3196, 1997.

[4] C.A. Chang, "Effects of Ag and Au on the YBCO superconducting thin films with the use of Ag/Cu/BaO/Y_2O_3 structures," *Appl. Phys. Lett.* 52, pp. 924-926, 1988.

[5] C.A. Chang, "Reduced moisture induced degradation of YBCO films by silver and high deposition temperatures," *Appl. Phys. Lett.* 53, pp. 1113-1115, 1988.

[6] D.G. McDonald, R. J. Phelan, L.R. Vale, R.H. Ono, and D.A. Rudman, "Passivation, Transition Width and Noise for YBCO Bolometers on Si," to be published in *IEEE Trans. Appl. Supercond.*, 1999.

Characterizations of Planar Log-periodic Antennas at Low Temperatures using HTS Josephson Junctions

Jian Chen
Research Institute of Electrical Communication, Tohoku University, Sendai 980-8577, Japan
CREST, Japan Science and Technology Corporation, Japan
Downs Laboratory of Physics 320-47, California Institute of Technology, Pasadena, CA 91125, USA

Eeisuke Kobayashi
Research Institute of Electrical Communication, Tohoku University, Sendai 980-8577, Japan

Kensuke Nakajima
Research Institute of Electrical Communication, Tohoku University, Sendai 980-8577, Japan
CREST, Japan Science and Technology Corporation, Japan

Tsutomu Yamashita
New Industry Creation Hatchery Center, Tohoku University, Sendai 980-8579, Japan
Research Institute of Electrical Communication, Tohoku University, Sendai 980-8577, Japan
CREST, Japan Science and Technology Corporation, Japan

Jonas Zmuidzinas
Downs Laboratory of Physics 320-47, California Institute of Technology, Pasadena, CA 91125, USA

Abstract — Using the Josephson oscillations of high-temperature superconducting (HTS) grain boundary Josephson junctions (GBJJs), we have characterized HTS planar log-periodic antennas from 4.2K to the critical temperature of the GBJJs. The antennas were designed to operate from 25GHz to 3.2THz for a broadband receiver. As a result, several resonant steps were obtained in the dynamic resistance (*dV/dI*) - voltage (*V*) curves and the steps can be quite well explained by geometric resonances of the antenna.

I. Introduction

There are many groups using planar log-periodic antennas to improve the responses of the receivers [1]-[3] and the output power of the generators [4] at millimeter and submillimeter wave bands. General speaking, this kind of self-complementary antenna has a frequency-independent property over a broad band [5]. However, there are no extensive experimental studies, especially at low temperatures where superconducting devices were used. Here, using Josephson oscillation effects and high-temperature superconducting (HTS) grain boundary Josephson junctions (GBJJs) integrated with the HTS planar log-periodic antennas, the characterizations of the planar log-periodic antennas at low temperatures are reported.

Manuscript received April 30, 1999.
J.C. thanks the support of the overseas dispatch by the Ministry of Education, Science, Sports, and Culture, Japan.

II. Experimental

$YBa_2Cu_3O_{7-x}$ (YBCO) thin films with a thickness of 200nm were deposited on MgO bicrystal substrates using a pulsed laser ablation method [1]. The GBJJs (with widths (W) of 3 to 10 μm) and the planar log-periodic antennas were fabricated using an ion milling method. The critical temperature of the GBJJs is about 70K. The antennas were designed to operate from 25GHz to 3.2THz for a broadband receiver [5]. An optical microscope photo of a YBCO GBJJ integrated with an antenna is shown in Fig. 1. A lock-in

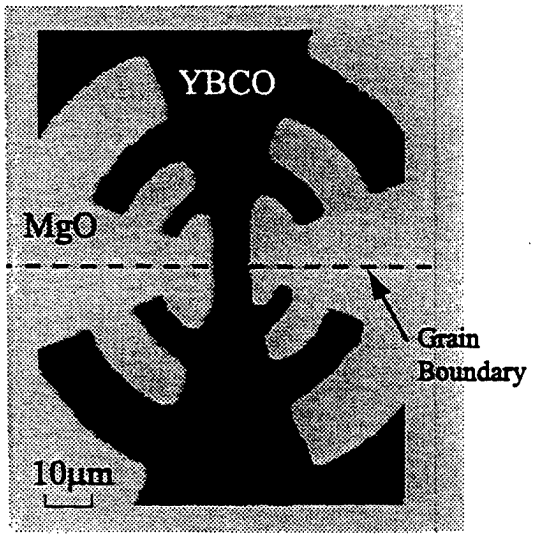

Fig. 1 Optical microscope photo of a YBCO GBJJ integrated with a YBCO planar log-periodic antenna.

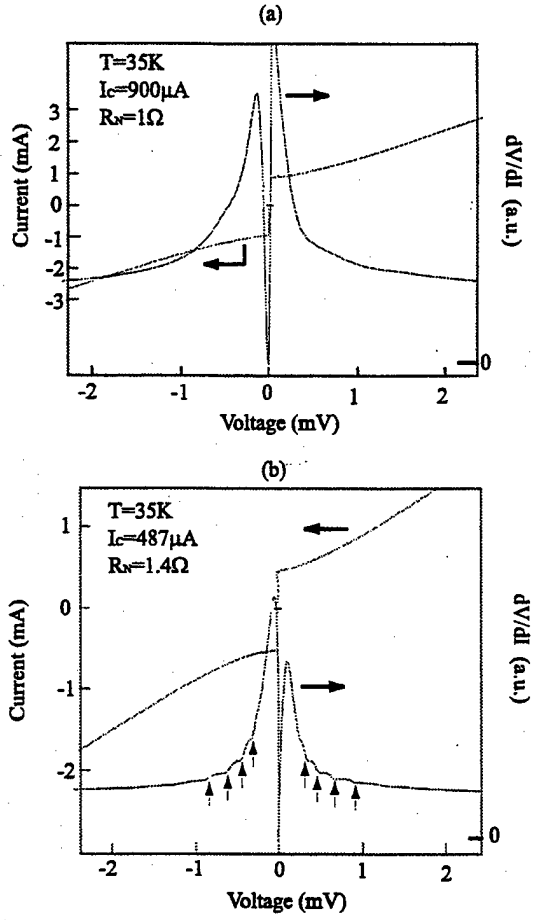

Fig. 2 *I* –*V* curves and *dV/dI* – *V* curves for the GBJJs integrated without (a) and with (b) the planar log-periodic antenna at *T* of 35K.

amplifier was used to measure the dynamic resistance (*dV/dI*) of the GBJJs. The sample holder had a two layer μ-metal cylinder shielding and was kept at different heights in a liquid helium Dewar to control the operation temperature (*T*) above 4.2K.

III. Results and Discussion

Fig. 2 shows the typical current (*I*) - voltage (*V*) curves and dynamic resistance (*dV/dI*) - *V* curves for the GBJJs integrated without (a) and with (b) the planar log-periodic antenna at *T* of 35K. The GBJJs show the resistively shunted-junction (RSJ) behaviors from 4.2K to 70K. Several resonant steps, shown by arrows in Fig. 2(b), were observed in the *dV/dI* – *V* curve only for the GBJJ integrated with the antenna. This implies that this phenomenon should be due to the antenna together with the GBJJ. Also, the voltage positions of the steps do not change when a GBJJ with a different width is used, or when the temperature of the GBJJs is changed from 4.2K to the critical temperature (about 70K).

For Fiske steps in *I-V* curves of junctions, the constant voltage steps V_n can be expressed by [6]

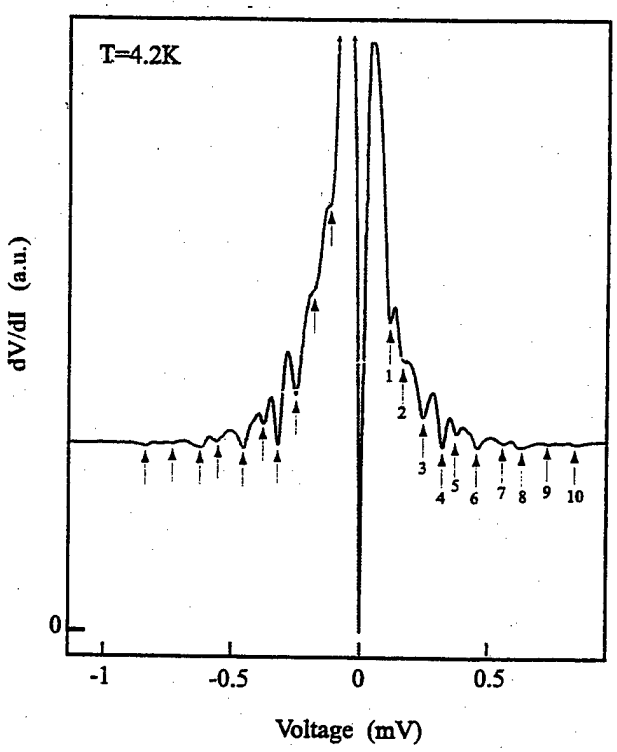

Fig. 3 *dV/dI* - *V* curve for a GBJJ integrated with a log-periodic antenna at *T* of 4.2K.

$$V_n = n\,(h/2e)(\upsilon/2W) \qquad (n=0, \pm1, \pm2, \pm3 \cdots), \qquad (1)$$

where *h*, *e* and υ are the Planck's constant, the electron charge, and the propagation velocity of the electromagnetic waves in the junctions. The intervals for the Fiske steps, which are due to the junctions only, should be at even intervals and dependent on the width of the GBJJs. In our case, the intervals between the steps, as shown by the arrows in Fig. 2(b), are not at even intervals and independent on the *W*. Thus the observed steps can not be Fiske steps.

Fig. 3 shows a *dV/dI*- *V* curve for a GBJJ integrated with a planar log-periodic antenna at *T*=4.2K. To study the steps in detail, we picked up the voltages (V_n) of the steps as shown by the arrows in Fig. 3 and calculated the respective frequencies (f_n) using the Josephson relationship:

$$V_n = hf_n/2e\,. \qquad (2)$$

The results are listed in Table 1. Also, the geometric oscillation frequencies in the antenna were calculated assuming $\lambda/2$ resonator at the edges of the teeth in the antenna and compared them with the frequencies listed in Table 1. It was found that each resonant steps shown in Fig. 3 and Table 1 can be associated with geometric oscillations at the edges of the teeth in the antenna, as shown in Fig. 4. As a Josephson junction is a broadband oscillator and/or detector, HTS GBJJs can irradiate and detect the electromagnetic wave from very low frequency to several THz at least [1]. This association suggests that the steps we are observing in the *I* – *V* or (*dV/dI*) - *V* curves arise from the frequency dependence at the terminal impedance at the antenna. This effect should be considered in applications.

TABLE 1

Voltages and frequencies for the resonant steps as shown by arrows in Fig. 3.

No. (n)	Voltage V_n (mV)	Frequency f_n (GHz)
1	0.11	53.1
2	0.17	82.1
3	0.24	118.0
4	0.31	150.0
5	0.37	177.6
6	0.45	219.8
7	0.54	260.0
8	0.62	299.5
9	0.73	352.6
10	0.84	405.7

IV. Conclusion

Using Josephson oscillation effects and YBCO GBJJs integrated with the YBCO planar log-periodic antennas, the antennas were characterized above 4.2K. As a result, several resonant steps were obtained in the dV/dI - V curves and the steps can be quite well explained by geometric resonances of the antenna. This means in fact the antennas have frequency-dependent properties and this effect should be considered. Also, It was found that the Josephson effects of the HTS junctions could be simply used to characterize the planar antennas at low temperatures.

Acknowledgment

It is a pleasure to express our appreciation to H. Myoren and T. Endo for their helps with experiments, H.B. Wang and Y. Mizugaki for useful discussions and J. Kawamura for reading the manuscript.

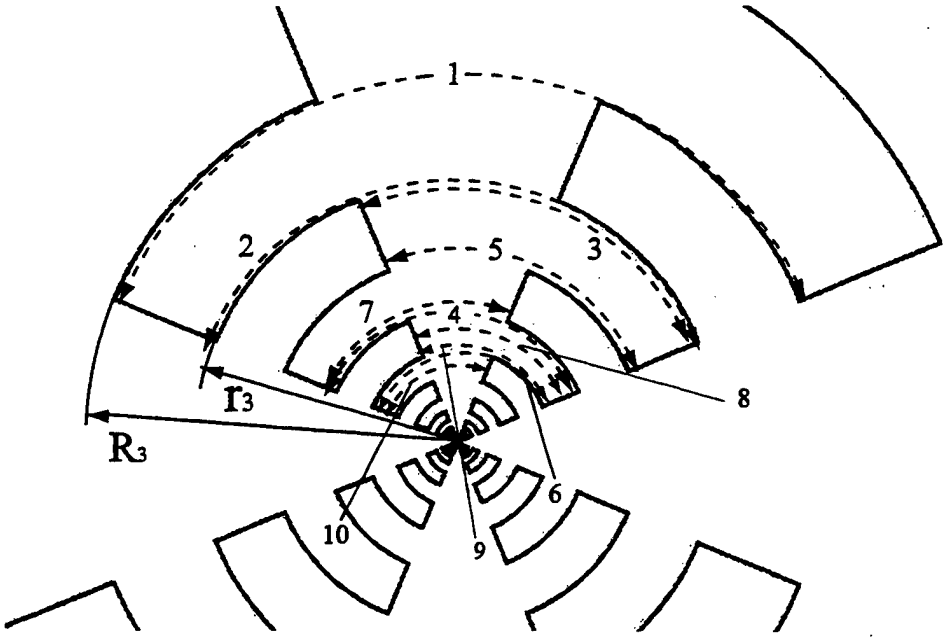

Fig. 4 The $\lambda/2$ geometric resonant lengths, shown by the dotted lines with arrows, at the edges of the teeth in the antenna. The number shown in here is corresponding to that in Fig. 3 and Table 1.

References

[1] J. Chen, E. Kobayashi, H. Myoren, K. Nakajima, T. Yamashita, S. Linzen, F. Schmidl, and P. Seidel, "Submillimeter wave detection and mixing experiments using high temperature Josephson junctions," *Proc. of SPIE (The 4th International Conference on Millimeter and Submillimeter Waves and Applications)*, vol.3465, pp.200-205, 1998.

[2] Y. Uzawa, Z. Wang, and A. Kawakami, "Terahertz NbN/AlN/NbN mixers with Al/SiO/NbN microstrip tuning circuits," *Appl. Phys. Lett.*, vol. 73, pp.680-682, August 1998.

[3] E. N. Grossman, D. G. McDonald, and J. E. Sauvageau, "Far-infrared kinetic-inductance detectors," *IEEE Trans. Magn.*, vol. 27, pp.2677-2680, March 1991.

[4] A. Kawakami, Y. Uzawa, and Z. Wang, "Josephson array oscillators with microstrip resonators," *IEEE Trans. Appl. Supercon.*, vol. 7, pp. 3126-3129, June 1997.

[5] V. H. Rumsey, *Frequency Independent Antennas*. New York, 1966 Academic Press.

[6] A. Barone, and G. Paterno, *Physics and Applications of Josephson Effect,* Wiley, New York, 1982.

Mesoscopic SNS Mixers Using Negative Resistance at Low Voltage

Toshiaki Matsui and Hiroshi Ohta
Communications Research Laboratories, Ministry of Posts & Telecomm., Koganei-shi, Tokyo 184-8795, Japan

Abstract— The current carried by the bound quasi-particles in the N-region of a mesoscopic SNS weak-link has a dc and cosine components. The dc current component depends on the pair charge (-2e) transferred by each Andreev reflection at an NS interface. The pair-charge transfers decrease due to reduction of the allowed number of Andreev reflection when the voltage increases. It is the origin of the negative differential resistance at low bias voltage observed in I-V curves of SNS junctions. The quasi-particle states carrying the supercurrent in the N-region can sensitively be influenced by external high-frequency fields. In an experiment of the mesoscopic SNS mixer, prominent IF signal peaks are observed at low bias voltage. The each IF signal peak appeared in the broad bias voltage region, which is correspond to the broadness of the negative differential resistance region at low bias voltage. The SNS mixer operation at low voltage is promising for application to low-noise mixer in submillimeter wave region.

I. Introduction

Negative resistance at low voltage in the mesoscopic SNS junction is theoretically described in terms of multiple Andreev reflections (MAR) [1][2]. The negative resistance regions are observed as the hysteretic structures in the I-V curves when the superconducting weak-link is driven by a current bias source with high impedance. The hysteretic structures in the I-V curves have masked the physical effect and prevented detail understandings of the SNS junctions. In the history of the experimental research on SNS junctions, the structures must have been observed as voltage jumps in many experiments of the well-formed Nb point contact junctions [3][4]. Unfortunately, there had been no theory to give a positive evaluation as a superconducting device [4][5]. Many important data might be thrown away or not be mentioned properly.

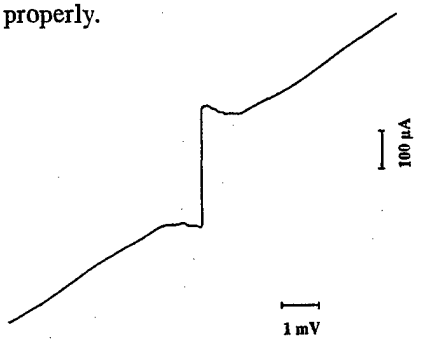

Fig. 1. I-V curve of the mesoscopic SNS junction driven by a voltage bias Source. Negative resistance structures are observed at low voltage region.

Manuscript received May 16, 1999.

We have reported SNS mixers using negative resistance at subharmonic gap voltages [6]-[9]. The negative resistance regions at low bias voltages are often observed in the I-V curves when the mesoscopic SNS junctions are driven by the voltage bias source with low impedance. Fig. 1 shows an example of I-V curves of the mesoscopic SNS junction at 4.2 K. Application of negative resistance regions is reported, [9][12][13].

In this paper, we try to demonstrate a mesoscopic SNS mixer using negative resistance at low bias voltage. Recent theoretical and experimental results will be described.

II. Current Carrying State of SNS Junctions

Charge transport in the SNS (Superconductor / Normal–metal / Superconductor) junction is described in terms of MAR at the two SN interfaces [1][2][9]-[11]. The quasi-particles in the N (normal metal) region of a mesoscopic SNS junction are bounded between the pair-potential and satisfy the quantization condition [10], [11] similar to the Bohr-Sommerfeld quantization condition of an electron bounded between the potential walls. The general theory has unified a clean-limit weak link, a dirty-limit weak link and a tunnel Josephson junction [2][11].

Pair transfer by MARs in mesoscopic SNS junction is shown in Fig. 2. In the N region, when an electron (-e) from the left side moves to the right wall and hits the wall, the incident electron cannot become a Cooper pair moving to the right direction without the partner electron, which generates a hole (+e) behind. The hole (+e) propagates to the left direction, and at the left wall it is changed into an electron (-e) propagating to the right direction, which produces a hole pair moving to left direction. A pair charge (-2e) is transferred by the Andreev reflection at each SN interfacewall. Mesoscopic SNS junctions with very short

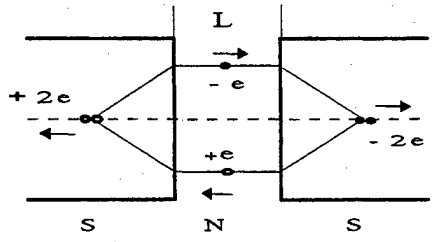

Fig. 2. Charge transport in mesoscopic SNS junction. The clockwise trajectory composed of electron- and hole-like quasi-particles carries the current to the left direction.

weak-link-length can be treated using a model similar to the orbit of the hydrogen atom. According to the semiclassical quantization condition, the energy spectrum of the Andreev bound state in a mesoscopic weak-link consists of a discrete set of levels written in the form of

$$\varepsilon^{\pm} = \pm\Delta\sqrt{1-T\sin^2\left(\frac{\phi}{2}\right)}, \qquad (1)$$

where (+) & (-) are correspond to the two different current-carrying states of clockwise and counterclockwise trajectories respectively. The energy is measured from the Fermi level. If the transmission coefficient, T, of the normal region is unity (T≈1) and the weak-link length of the SNS junction is short enough (L < ξ), then (2) reduces to $\varepsilon^{\pm} \approx \pm\Delta\cos\phi/2$.

The energies of the two current-carrying states given by (1) coincide at the phase difference $\phi = \pi$, the energy level crossing occurs between the two states. The trajectories of electrons and holes may be switched into the opposite directions by the scattering effect in the normal region, N. If the perturbation to the two trajectories is increased, the two current-carrying states can lift the degeneracy, which will lead to splitting apart in energy and the appearance of a small gap in the energy spectrum [2], [9]-[11].

A. Zener tunneling in SNS weak-links

The energy-phase diagram of the two current-carrying states in the mesoscopic weak-links is schematically shown in Fig. 3. The first possible state corresponds to the original trajectory crossing the ϕ-axis at $\phi=\pi$ from the rout 1 to the rout 2 in Fig. 3, and the probability, P, of the transition across an energy gap in the mesoscopic N region is given by the formula for Zener tunneling [2], [9], [14];

$$P = \exp\left[\frac{-\pi R\Delta}{eV}\right], \qquad (2)$$

where, R=1–T. The other possible state corresponds to changing the original-trajectory to another-trajectory without crossing the energy gap at the point of $\phi = \pi$, which is shown by the route 1-3 in Fig. 3.

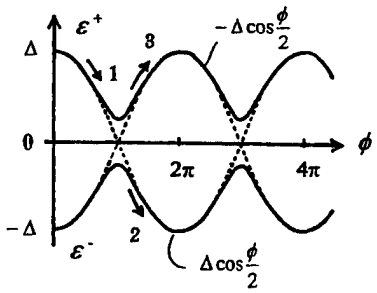

Fig. 3. The energy-phase (ε – ϕ) diagram of the two current carrying states in the mesoscopic SNS junction.

The net current is given by a difference between currents of the two current-carrying states.

When the barrier region is made of insulator, R≈1, then V <<πRΔ/e, tunneling probability, P, is almost 0. Electrons in the barrier region occupy the same split-level without tunneling at the energy gap. In this case, the route from 1 to 3 will be preferred. The current transport exchanges the two current-carrying states at every point of $\phi = (2n-1)\pi$, where n=1,2,3... . In this case, $\delta\varepsilon = \varepsilon^- - \varepsilon^+ = -2\Delta\cos\phi/2$ for $0<\phi<\pi$ and $2\Delta\cos\phi/2$ for $\pi<\phi<2\pi$. Without Zener tunneling, current-phase relation is proportional to $\sin\phi/2$ for $0<\phi<\pi$ and $-\sin\phi/2$ for $\pi<0<2\pi$. Current-phase relation can be given by

$$I \approx \frac{8}{3\pi} I_m \sin\phi. \qquad (3)$$

This is the current-phase relation of the Josephson effect.

When V >>πRΔ/e, tunneling probability, P, is almost 1. Electrons in N region transport current across the energy gap; Zener tunneling (breakdown) is shown in Fig. 2 at the $\phi=\pi$ from 1 to 2. In this case, $\delta\varepsilon = \varepsilon^- - \varepsilon^+ = -2\Delta\cos\phi/2$ for $0<\phi< 2\pi$ and current-phase relation is proportional to $\sin\phi/2$ for $0<\phi<2\pi$. With Zener tunneling [9], the current-phase relation can be given by

$$I \approx \frac{4}{\pi} I_m - \frac{8}{3\pi} I_m \cos\phi. \qquad (4)$$

The pair current carried by the Andreev bound state in a mesoscopic SNS weak-link has a dc and cosine components. The phase-dependent pair-current in (3) & (4) has the same amplitude. The Josephson effect observed in the SNS weak-links is theoretically explained by (4). In the following sections, interactions between charge transfer in SNS weak-links and microwave irradiation is discussed.

III. Negative Resistance in I-V Characteristics

The trajectory does not close any more when a finite bias-voltage is applied to the SNS junction. Including a small energy gap in mesoscopic N region, the energy band diagram of SNS weak-links is shown in Fig. 4. In Fig. 4, potential difference V is settled at the slightly higher than the 11th subharmonic gap voltage; V= (1/11)(2Δ/e)+0. Charge transfer induced by MAR and Zener tunneling at finite voltage state is shown using an energy band diagram of an SNS junction. Holes are transferred to the left direction in valence band and electron transferred to the right direction in the conduction band in N region. Zener tunneling across the energy gap in N region generates a set of an electron and a hole with opposite momentum. In the case, pair charge (2e) is transferred by each Andreev reflection at an NS interface. Finally, an electron and a hole are transferred into the band edge of superconducting electrodes.

A. Microwave amplification by negative differential resistance at low voltage

The dc current component of total current of the SNS junctions depends on the pair charge (-2e) transferred by each Andreev reflection at an NS interface. Large number of multiple Andreev reflections carry high-density pair current at low voltages. The pair-charge transfers decrease due to reduction of the allowed number of Andreev reflection in the mesoscopic SNS junction when the voltage increases. It is the origin of the negative differential resistance at low bias voltage observed in I-V curves of SNS junctions. Negative differential resistance at low voltage region on I-V characteristics is shown in Fig. 5. Bias voltage was stable even in negative-resistance region because we used a voltage bias source with low output impedance. The SNS junction with $I_m \approx 20\ \mu A$, $R_j \approx 100\ \Omega$ at liquid helium temperature was irradiated with noise from a 50 Ω termination at room temperature through a coaxial cable. Noise power reflected from the SNS junction was separated by a circulator from incident noise coming from the 50 Ω termination, and amplified by a preamplifier and measured by the spectrum analyzer. The 3.7–4.2 GHz frequency band was used for this experiment. Receiving power in left vertical axis in Fig. 5 shows the reflected noise power for bias voltages. Losses of coaxial cable, circulator, and the others were calibrated by the noise power level at zero voltage, which is a short terminal. The 7 dB gain is observed at the peak of receiving power.

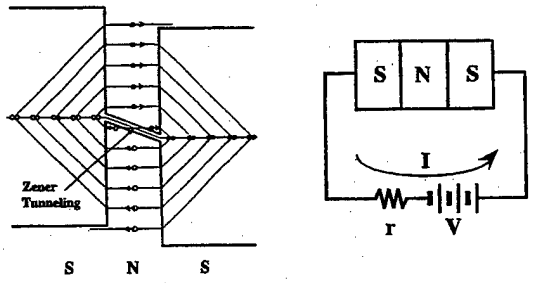

Fig. 4. Multiple Andreev reflections at the subharmonic gap voltage of V=(1/11)(2Δ/e)+0, in resonance case. Pair current carryng by the MARs increase at lower voltage due to increase of allowed number of Andreev reflections

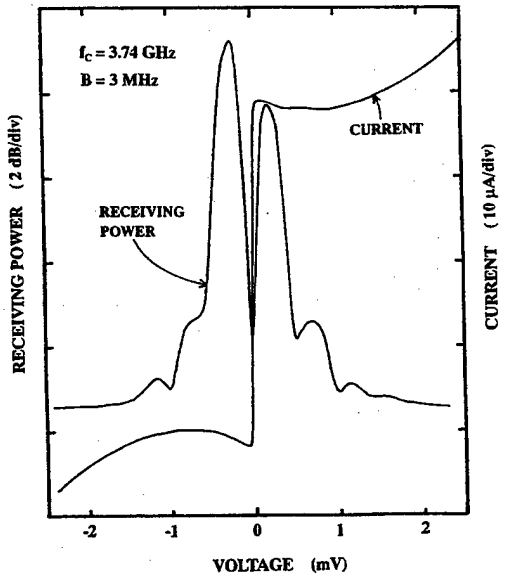

Fig. 5. Microwave amplification by negative differential resistance at low voltage. Symbols of a, b, c, d and e on P_{out} correspond to those on I-V curves. The 6 dB gain is observed at the peak of P_{out}.

B. Millimeter wave response

External high-frequency fields can sensitively influence the quasi-particle states carrying the supercurrent in the N-region. Fig. 6 shows I–V characteristics under the irradiation of 112.5 GHz millimeter-waves. From bottom curve up, curves are at the relative power levels; no rf, room temperature termination, increase of millimeter wave power. Without irradiation, negative differential resistance was observed at low voltage in the I-V curve. Millimeter wave irradiation effected on the low voltage region, however, Josephson current-step did not appear clearly. Fig. 7 shows differential conductance (dI/dV-V) for different power levels. The Josephson current-steps, at the voltage series of $V_m = m(\hbar\omega/2e)$; m=1.2.3..., are superimposed on the conductance modulation induced by the external radiation.

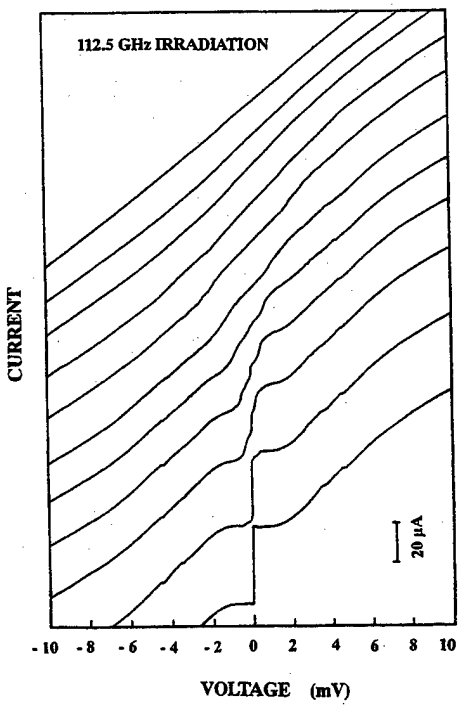

Fig. 6. Millimeter wave response of SNS junction.

at the voltage series of $V_m=m(\hbar\omega/2e)$; m=1.2.3... The simple resistive shunted junction (RSJ) model can not describe this experimental observation.

IV. Mixer Experiment

A SNS weak-links was positioned in a quarter height waveguide (WR-10) of a mixer block. Two Gunn PLL oscillators were used to supply millimeter wave signal and local frequencies. The SNS mixer was held and cooled in liquid helium (4.2K). Millimeter waves were fed through a waveguide, and the signal of intermediate frequency f_{IF} coming out from the mixer was amplified by a low noise IF amplifier and measured by a spectrum analyzer. DC bias for the mixer was supplied by the low impedance voltage bias source. Prominent IF signal peaks are observed at low bias voltage around 0 ± 1.5 mV. Mixer IF output vs. bias voltage is show in Fig. 7, where rf signal frequency is 105 GHz and IF signal frequency is 4 GHz.

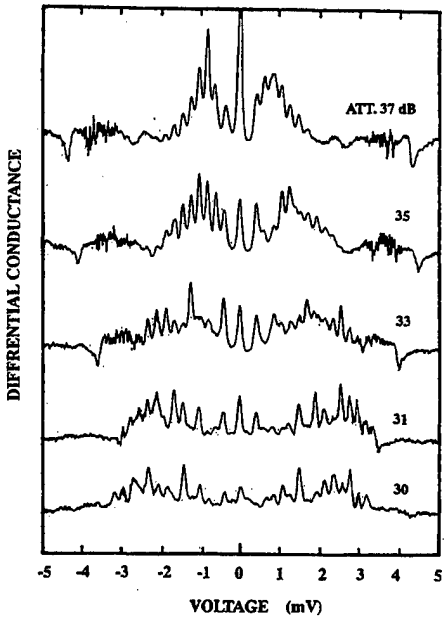

Fig. 7. Differential conductance for bias voltage under the millimeter wave irradiation

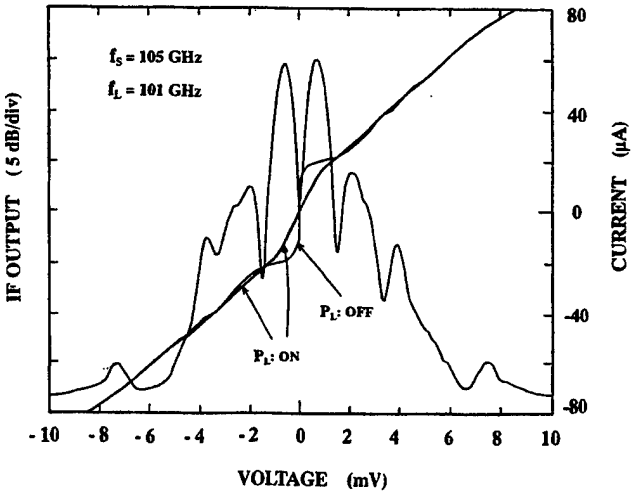

Fig. 8. Mixer IF output vs. bias voltage, f_S=105 GHz, f_{IF}=4 GHz. Prominent IF peak appeared in broad voltage region at low bias voltage.

V. Conclusion

Pair-current of a mesoscopic SNS weak-link has a dc and cosϕ components. Charge transport in the mesoscopic SNS weak-link is really sensitive to the external radiation. Radiation from coaxial termination was efficiently amplified at the low voltage negative resistance (LVNR) region. In the mixer experiment at 105 GHz, prominent IF signal peaks apppeared in the broad bias voltage region, which is corresponding to the LVNR region. The experimental results sugest that there is an efficient interaction between the electron-wave characterised by the Andreev bound state and the microwave field coupled to the mesoscopic SNS weak-link. The mixer operation at the LVNDR region could also be very promising for application to low noise mixers in submillimeter waves.

References

[1] R. Kümmel, U. Gunsenheimer and P. Nicolsky, "Andreev scattering of quasi-particle wave packets and current-voltage characteristics of superconducting metallic weak links," *Phys. Rev. B*, vol. 42, pp. 3992-4009, Sept. 1990.

[2] D. Averin and A. Bardas, "Ac Josephson effect in a single quantum channel," *Phys. Rev. Letters*, vol. 75, pp. 1831-1834, Aug. 1995.

[3] J. E. Zimmerman, "A review of the properties and aplications of superconducting point contacts", *Proc. 1972 Applied Superconductivity Conference*, IEEE Pub. No. 72 CHO 682-5-TABSC, pp. 544-561, 1972.

[4] T. A. Fulton and L. N. Dunkleberger, "Origin of hysteresis in the I-V curves of point –contact junctions", J. Appl. Physics vol. 45, pp. 2283-2285, 1974.

[5] A. Barone and G. Paterno, *Physics and Applications of the Josephson Effect*, John Wiley & Sons, 1982, pp. 185-186.

[6] H. Ohta and T. Matsui, "Microwave and millimeter-wave mixers using negative differential resistance due to Andreev reflection in superconducting weak links," *Physica C*, vol. 185-189, pp. 2581-2582, July 1991.

[7] T. Matsui and H. Ohta, "Mixer of short weak link using a resonance effect due to multiple Andreeev reflections at subgap voltages", *IEEE Trans. Applied Superconductivity*, vol. 5, pp. 3300-3303, June 1995.

[8] T. Matsui and H. Ohta, "Observed photon-assisted process in mesoscopic SNS mixers", *IEEE Trans. Applied Superconductivity*, vol. 7, pp. 2578-2581, June 1997.

[9] T. Matsui and H. Ohta, "Millimeter- and submillimeter-wave Negative Resistance SNS mixers", *IEEE Trans. Applied Superconductivity*, in press.

[10] H. Ohta and T. Matsui, "Nanometer SNS junctions as quantum-well devices," IEEE Trans. Applied Superconductivity, vol. 7, pp. 2814-2817, June 1997.

[11] H. Ohta and T. Matsui, *Physics and Application of Mesoscopic Josephson Junctions*, "Semiclassical picture of mesoscopic SNS junctions", The Physical Society of Japan, in press.

[12] A. M. Luiz, L. A. A. Pereira and R. Nicolsky, "Heterodyne detector using a SNS junction," *IEEE Trans. Applied Superconductivity*, vol. 7, pp. 3719-3721, June 1997.

POSTER SESSION I

Group 5 - Junctions and Fabrication

Fabrication and Properties of Nb/AlO$_x$/Nb Self-Shunted Josephson Junctions With High Critical Current Densities

Vijay Patel, Sergey K. Tolpygo, W. Chen, and J.E. Lukens
Department of Physics and Astronomy, State University of New York at Stony Brook, Stony Brook, NY 11794-3800

Abstract—We report on the fabrication and characterization of deep submicron Nb/AlO$_x$/Nb Josephson tunnel junctions with critical current densities up to 3 mA/μm^2. At these current densities, the junctions become nonhysteretic, so their implementation in digital circuits allows for both a significant improvement in performance and simplification of the fabrication. The self-shunting is due to a significant fraction of current occurring through multiple Andreev reflection (MAR) channels. The noise properties of the junctions and the effect of microwaves (20 and 100 GHz) on I-V characteristics are also studied and discussed. The low frequency noise has a Debye-Lorentz lineshape and is due to the conductance fluctuations caused by only a few (1-3) electron traps in the barrier.

I. Introduction

Nb/AlO$_x$/Nb Josephson tunnel junctions are currently the basis of digital and analog superconductor electronics due to extremely low parameters spreads, high yield and reliability which can be achieved with such state-of-the-art fabrication processes as, e.g., PARTS [1]. For digital circuits, it is well known that both the ultimate operation frequency and the possible level of integration grow in proportion to the critical current density J_c of Josephson junctions comprising the circuit. For example, a divide-by-two operation up to 770 GHz has recently been demonstrated for a SFQ T-flip flop with 2.5 mA/μm^2 (250 kA/cm^2) Josephson junctions [2]. Many other characteristics of various Josephson-effect-based superconducting circuits are expected to improve with increase in the critical current density, e.g., the maximum power of Josephson junction array oscillators, noise performance of dc SQUIDs, etc.

Yet another feature important for electronics is that at sufficiently high critical current density self-shunting becomes sufficient to render the junctions overdamped and exhibit nonhysteretic *I-V* characteristics. The use of such self-shunted devices in multijunction circuits can, in addition to performance improvement, provide a significant simplification of the fabrication process because the shunt resistor fabrication step becomes unnecessary.

Mechanisms of current transport in high-J_c junctions are of considerable interest in their own right. The main features are the fast growth of the subgap conductance G_{sg} with increasing J_c and the appearance of pronounced structures in *I-V* characteristics known as subgap steps. G_{sg} nearly approaches the normal state conductance G_N when J_c reaches about 2 mA/μm^2. Formally, this increase in G_{sg} causes a decrease in McCumber-Stewart parameter $\beta_c \equiv 2\pi I_c C/G_{sg}{}^2\Phi_0$ with increasing transparency of the oxide barrier. When β_c becomes less than unity the junctions become overdamped and thus nonhysteretic. Here I_c is the critical current, C the junction capacitance, and Φ_0 the flux quantum. These experimental facts have been known for quite some time. However, the physical reasons for these dramatic changes in transport properties are not fully understood even though several explanations have been proposed based on multiple Andreev reflections (MAR), self-coupling of Josephson radiation, and multiparticle tunneling [3],[4]. One of the most popular is a pinhole model according to which, as the tunnel barrier gets thinner, the properties become dominated by microshorts or pinholes in the barrier, acting as a large number of SNS or SS'S junctions, in which transport is due to MAR .

In order to get more insight into the transport mechanisms in high-J_c Josephson junctions, in this work we have studied the *I-V* characteristics, noise properties, and the effect of microwave irradiation on Nb/AlO$_x$/Nb tunnel junctions with critical current densities up to 3 mA/μm^2.

II. Junction Fabricaton

The deep-submicron junctions (area < 0.1 μm^2) used in this work were fabricated using an advanced planarized process developed here at Stony Brook [5],[6]. The process combines conventional contact photolithography with electron-beam lithography (EBL) which permits a minimum feature size of less than 0.2 μm for all layers. This allows us, for example, to reduce the area of the base electrode (BE) and thus the BE – wiring layer overlap, the primary cause of parasitic capacitance. A Nb/AlO$_x$/Nb trilayer is deposited on a 50 mm diameter oxidized Si wafer by DC magnetron sputtering with 150 nm thick base (BE) and counter electrodes (CE). The AlOx barrier is formed by oxidation of an 8 nm thick Al interlayer at room temperature, and the total O_2 exposure (pressure×time) determines J_c [7]. For high current densities (small exposures) the run-to-run reproducibility of J_c becomes a major concern. In three separate runs oxidation at 1.0 mTorr of O_2 for 10 min. gave J_c in the range 2.1-2.5 mA/μm^2. All layers were patterned using PMMA/P(MMA/MAA) bilayers as both EBL resist and DUV resist for contact printing. A 50 nm thick layer of RF-sputtered SiO_2 (quartz) is lifted off to form an etch mask for the CE. The junction is defined by a reactive ion etch (RIE) of the Nb CE in SF_6 plasma. A 120 nm quartz etch mask is then lifted off for the BE, which gets defined by a wet etch of the Al interlayer followed by another RIE of the Nb base layer. 550 nm of quartz is then deposited to form the dielectric layer which is planarized using chemical-mechanical polishing. The residual 5-10 nm of quartz remaining after planarization

Manuscript received April 30, 1999.
This work is supported by ONR and AFOSR .

on top of the CE is removed using a $CHF_3 + O_2$ oxide etch which exposes the top of the junctions. Finally a 200 nm thick Nb wiring layer is lifted off. Data on reproducibility, yield, and parameter spreads across the wafer can be found in [5].

III. Experimental Results

A. *Current-Voltage Characteristics*

Fig. 1 shows the typical *I-V* characteristics and differential conductance $G = dI/dV$ of a self-shunted junction with $J_c = 2.1$ mA/μm^2. The common features of all *I-V*s are the absence of hysteresis, large excess current, and a rich structure (peaks) in the conductance at subgap voltages.

Some of the conductance peaks (steps on *I-V*) are clearly of the ac Josephson effect origin: they form a nearly equidistant series, their amplitude strongly depends on the applied magnetic field, and they are more pronounced in smaller size junctions. We suggest that these are caused by interaction of the junction with a resonator formed by a section of bias/voltage leads. This section presents a low-loss high impedance transmission line loaded by junction at one end and nearly open-ended at another one. The stronger resonances in smaller junctions are due to a better impedance matching. A detailed analysis of self-detection of resonant modes excited by Josephson oscillations in resistively shunted and unshunted junctions can be found in [8].

Another group of peaks is not related to the Josephson effect. These become more visible when the critical current is fully suppressed by a parallel magnetic field as shown in Fig. 2. These peaks appear at submultiple of the gap voltage $V_n = 2\Delta/n$, n = 1,2... [5]. The common explanation of these subharmonic peaks is multiple Andreev reflections of quasiparticles in current channels formed by "microshorts" or "pinholes" in oxide tunnel barrier [3]. Since the barrier thickness at our current densities is only one or two monolayers, these microshorts are likely to be atomic size NbAlNb channels formed due to existence of oxygen vacancies. The dimensions of these shorts are much smaller than the coherence length and the mean free path, so each can be viewed as a ballistic channel with a small number of transverse modes. The theory of ac Josephson effect for such ballistic channels has recently been developed [9]. One of the predictions of this theory is a large excess current (I_{ex}) which at low temperatures reaches $(2/\pi)I_c$. This excess current is due to a non-sinusoidal current-phase relation at finite voltages, which results in a nonzero time average of Josephson oscillations. For the junction in Fig. 1, the extrapolation of the linear *I-V* part above the gap voltage gives I_{ex} = 40 μA, in agreement with $(2/\pi)I_c$ (I_c= 62 μA for this junction).

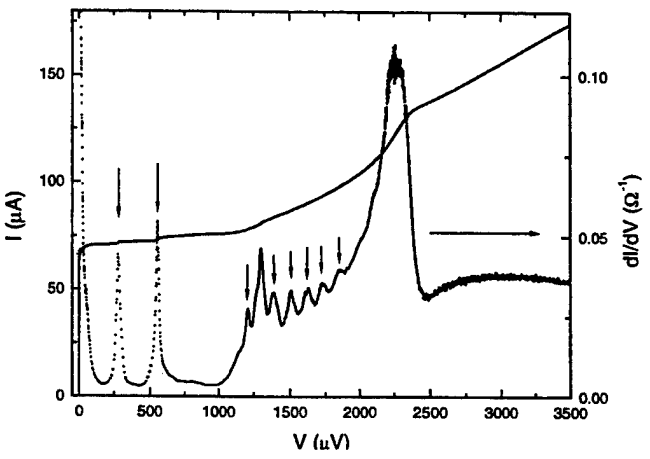

Fig.1 IV Characteristic and differential conductance of a 0.06 μm^2 junction at T = 4.2K. The arrows indicate peaks due to resonances in the leads excited by Josephson oscillations.

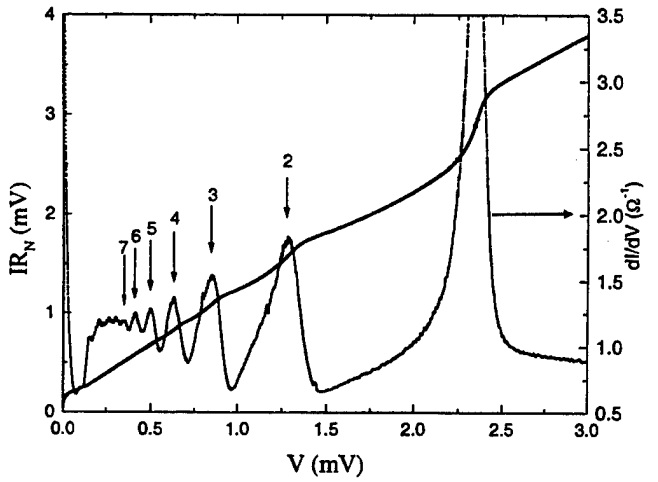

Fig. 2. Quasiparticle IV characteristic and differential conductance of a 0.5x0.5 μm^2 junction at T = 1.8 K. The MAR peaks at $2\Delta/n$ are clearly seen and are indicated by arrows for n up to 7.

The upper limit on the number of open channels can be estimated by assuming that all the junction conductance is due to microshorts. Then the number of the channels is $N = G_N/G_Q$, where $G_Q = 2e^2/h$. For the junction in Fig. 1, this gives $N \approx 400$ corresponding to the average distance between the microshorts ~ 12 nm and the total area occupied by microshorts of less than 0.1 % of the junction area. The critical current of the N channels at $T << T_c$ should be $Ne\Delta/\hbar$ [10] which is a factor of 2 larger than the experimentally observed. This indicates that the number of conducting channels is actually smaller. A more quantitative description based on a joint analysis of both the subgap conductance and the temperature dependence of the critical current will be presented elsewhere.

B. *Effect of Microwave Irradiation*

Fig. 3 shows the effect of microwave radiation on a 0.09 μm^2 junction at 20 GHz and 102 GHz (inset). A large number of Shapiro steps are clearly seen even at voltages well above the superconducting gap. Two other features deserve to be mentioned. First, while the 2Δ step gets fully suppressed at relatively low rf powers, the step at Δ becomes more pronounced at higher powers. Second, at sufficiently high powers, the excess current gets almost completely suppressed

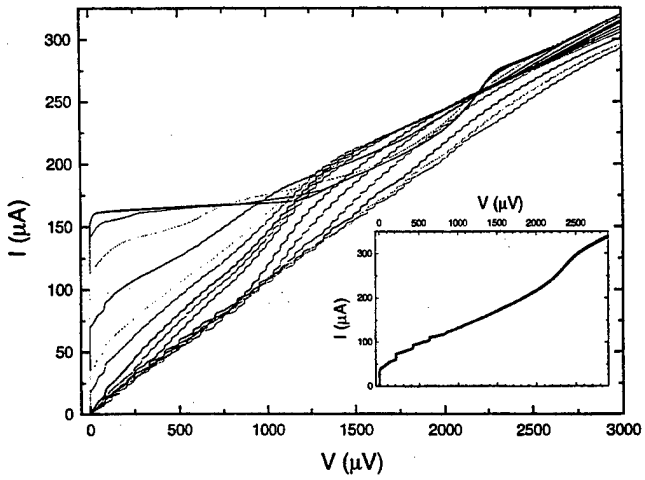

Fig.3. *I-V* characteristics of a 0.09 μm² junction in presence of 20 GHz microwave radiation at $T = 4.2$ K. The different curves correspond to different applied microwave power. The inset shows the *I-V* with 102 GHz radiation at $T = 1.8$ K. A small magnetic field was applied to reduce the critical current.

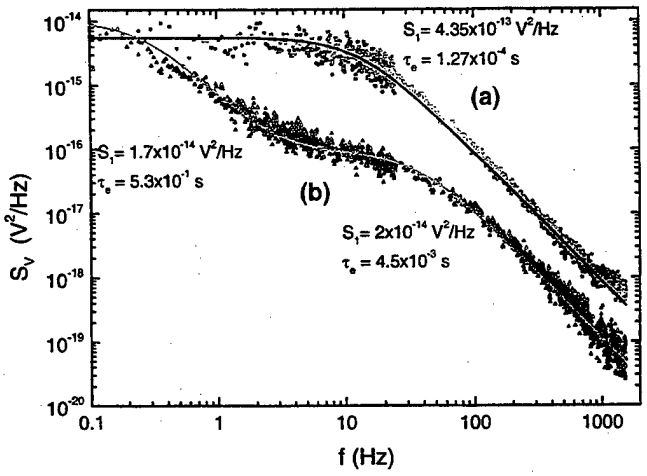

Fig. 4. Spectral density of voltage noise for two ~ 0.06 μm² junctions at $T =$ 1.3 K. The parameters are $I_b = 148$ μA, $V = 3.15$ mV, $R_N = 30$ Ω for (a) and I_b = 162 μA, $V = 3.09$ mV, $R_N = 26.5$ Ω for (b). The solid lines are fits to one or two Lorentzians of eq. (1).

contrary to what happens in the presence of a magnetic field (see, e.g. Fig. 2). The rf power at 102 GHz was not sufficient to study these effects.

C. *Low Frequency Noise*

Fig. 4 shows the typical low frequency voltage noise spectral density (S_V) of two 0.06 μm² junctions at $T = 1.3$ K. Both junctions were biased above 2Δ so that the measured voltage noise has negligible contribution from critical current fluctuations and conductance fluctuations are dominating. In the bandwidth investigated (2 kHz) the noise typically consisted of one or two Lorentzians. It is usually assumed that this type of noise it due to discrete conductance fluctuations caused by localized states in the barrier [11]. The spectrum of this random telegraph noise is known to be

$$S_V = S_I \tau_e [1+(2\pi f\tau_e)^2]^{-1} \quad (1)$$
$$S_I = S_0\tau_e (\tau_1+\tau_2)^{-1}$$

where τ_1^{-1} and τ_2^{-1} are characteristic rates of filling and emptying the traps, $\tau_e^{-1} = \tau_1^{-1} + \tau_2^{-1}$, and S_I is the total integrated power [12]. The fits to the lineshape (1) with only one (a) and two (b) Lorentzians are shown in Fig. 4. If we assume conductance fluctuations, the minimum resistance change between the high- and low-conductance states can be estimated from S_I as $\Delta R_{max} = 2S_I^{1/2}/I_B$ which, for the junctions and temperatures studied, lies between 1 and 10 mΩ. Note that the blocking of a single ballistic channel would cause a much large resistance change $R_N^2 G_Q$ about 50-70 mΩ. A detailed study of the temperature and bias dependence of the noise is currently underway and will be presented elsewhere.

IV. Conclusions

We have fabricated and studied high critical current density (2.1 mA/μm²), small area (< 0.1 μm²) Nb/AlO$_x$/Nb Josephson junctions with non-hysteretic *I-V* characteristics. The junctions clearly demonstrate strong Josephson oscillations well above the gap voltage which makes them nice candidates for many microwave and high speed digital applications.

References

[1] M. Ketchen, D. Pearson, A.W. Kleinsasser, C.-K. Hu, M. Smyth, J. Logan, K. Stawiasz, E. Baran, M. Jaso, T. Ross, K. Petrillo, M. Manny, S. Basavaiah, S. Brodsky, S.B. Kaplan, W.J. Gallagher, and M. Bhushan, "Sub-μm, planarized, Nb-AlO$_x$-Nb Josephson process for 125 mm wafers developed in partnership with Si technology," *Appl. Phys. Lett.*, vol. 59, pp. 2609-2611, November 1991.

[2] W. Chen, A.V. Rylyakov, V. Patel, J.E. Lukens, and K.K. Likharev, "Superconductor digital frequency divider operating up to 750 GHz," *Appl. Phys. Lett.*, vol. 73, pp.2817-2819, November 1998. W. Chen, A.V. Rylyakov, V. Patel, J.E. Lukens, and K.K. Likharev, "Rapid Single Flux Quantum T-Flip Flop operating up to 770 GHz," *IEEE Trans. Appl. Supercond.*, June 1999, in press.

[3] A.W. Kleinsasser, R.E. Miller, W.H. Mallison, and G.B. Arnold, "Observation of multiple Andreev reflections in superconducting tunnel junctions," *Phys. Rev. Lett.*, vol. 72, pp. 1738-1741, March 1994.

[4] N.R. Werthamer, "Nonlinear self-coupling of Josephson radiation in superconducting tunnel junctions," *Phys. Rev.*, vol. 147, pp. 255,1966.

[5] Vijay Patel and J.E. Lukens, "Self-shunted Nb-AlOx-Nb Josephson junctions," *IEEE Trans. Appl. Supercond.*, June 1999, in press.

[6] D.J. Flees, "Experimental studies of band-structure properties in Bloch transistors," Ph.D. Dissertation, State University of New York at Stony Brook, August 1998.

[7] R.E. Miller, W.H. Mallison, A.W. Kleinsasser, K.A. Delin, and E.M. Macedo, "Niobium trilayer Josephson tunnel junctions with ultra-high critical current densities," *Appl. Phys. Lett.* , vol. 63, pp. 1423-1425, September 1993.

[8] K.K. Likharev, *Dynamics of Josephson Junctions and Circuits*, Gordon and Breach, 1986, ch.12.

[9] D. Averin and A. Bardas, "ac Josephson effect in a single quantum channel," *Phys. Rev. Lett.*, vol. 75, pp. 1831-1834, August 1995. D. Averin and A. Bardas, "Adiabatic dynamics of superconducting quantum point contacts," *Phys. Rev. B.*, vol. 53, pp. R1705-R1708, January 1998.

[10] C.W.J. Beenakker, and H. van Houten, "Josephson current through a superconducting quantum point contact shorter than the coherence length," *Phys. Rev. Lett.*, vol. 66, pp. 3056-3059, June 1991.

[11] C.T. Rogers and R.A. Buhrman, "Nature of single localized electron states derived from tunneling experiments," *Phys. Rev. Lett.*, vol. 55, pp.859-862, August 1985.

[12] S. Machlup, " Noise in semiconductors : spectrum of a two parameter random signal," *J. Appl. Phys.*, vol. 25, pp.341-343, March 1954.

Enhancement of the dc supercurrent in double-barrier Nb/Al-AlO$_x$-Al-AlO$_x$-Nb junctions

I. P. Nevirkovets[1,2] and J. B. Ketterson[1,3]
[1]Northwestern University, Department of Physics and Astronomy, Evanston, Illinois 60208
[2]Institute for Metal Physics, National Academy of Sciences of the Ukraine, UA-252680 Kyiv-142, Ukraine
[3]Northwestern University, Department of Electrical and Computer Engineering, Evanston, Illinois 60208

Abstract—We have carried out experiments on Nb/Al-AlO$_x$-Al-AlO$_x$-Nb double-barrier junctions with a "dirty" middle Al layer. At low temperatures, the devices displayed a critical current larger than that possible for a system considered as a simple, series-connection, of two (Nb/Al-AlO$_x$-Al and Al-AlO$_x$-Nb) junctions, and a novel subgap structure. The behavior is explained as a manifestation of the Andreev bound states appearing in the double-barrier devices.

I. Introduction

Recently, the SINIS type junctions have demonstrated their potential as switching elements for superconductive digital circuits [1],[2], voltage standards [3], and microrefrigerators [4]. In particular, the Nb/Al-AlO$_x$-Al-AlO$_x$-Nb devices displayed a characteristic voltage of order 0.1 mV and non-hysteretic behavior at a temperature of 4.2 K. Up to now, most of the work was devoted to fabrication and application aspects of the devices. However, the lack of experimental and theoretical work on the underlaying physical mechanisms of the electron transport prevents further optimization of the device characteristics.

In this work, we report the results of an experimental investigation of the current-voltage characteristics (IVC's)of the double-barrier Nb/Al-AlO$_x$-Al-AlO$_x$-Nb devices which suggest that the current through the devices can not be presented as a two-step sequential tunneling process. We have found peculiarities that suggest that the electron transport through the double-barrier structure is coherent and is probably established by the Andreev bound states [5]. Therefore, the MacMillan's proximity effect theory[6] can not be directly used to describe the supercurrent in such devices, as assumed by Capogna and Blamire [7].

II. Device characterization

The Nb/Al-AlO$_x$-Al-AlO$_x$-Nb structures were fabricated by a conventional whole-wafer dc magnetron deposition process. Both oxidized Si and R-plane sapphire substrates were used, and 10 μm × 10 μm two-terminal devices were fabricated. The thickness of the external Nb electrodes was 100 nm for all the devices. Usually, for barrier formation, we used Al films deposited under conditions that yield a residual resistance ratio $R(300K)/R(10K) > 3$ (for the 80 nm thick films). Such films will be referred to as "clean". Usually, in Nb/Al junction technology, a little attention is paid to the quality of the Al films. However, we have found that a significant modification of the IVC occurs when using "dirty" Al films in the middle electrode of the double-barrier Nb/Al-AlO$_x$-Al-AlO$_x$-Nb junctions. Here we consider devices in which the Al electrode was deliberately contaminated by introducing 1×10^{-5} torr of O_2 during sputtering of the Al. The Al used to form the bottom junction was always "clean", whereas for the top junction both "dirty" Al and composite ("dirty" Al covered with "clean" Al) electrodes were used. The tunnel barriers were formed by thermal oxidation of Al in pure oxygen, identically for the bottom and top barriers, to provide a specific tunneling resistance (defined for a single junction from the stack) in the range 10^{-7}-10^{-6} Ωxcm^2. The devices were characterized by measuring their IVC's between the bottom and top Nb electrodes.

III. Results and descussion

The junctions with "dirty" Al electrode revealed more complicated behavior than similar devices with a "clean" Al electrode. Fig. 1 shows the IVC of a Nb/Al-AlO$_x$-Al-AlO$_x$-Nb

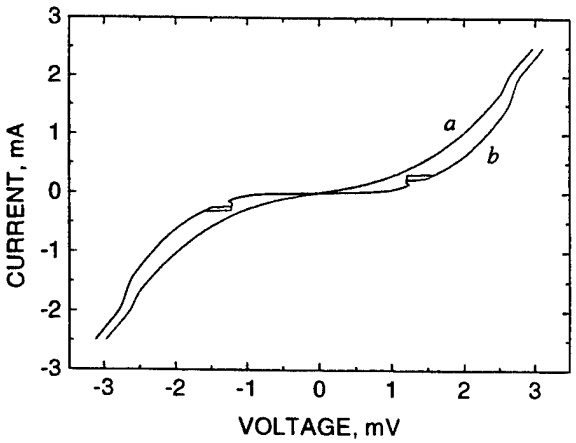

Fig. 1. Typical IVC of a Nb/Al-AlO$_x$-Al-AlO$_x$-Nb device on the Si substrate with a a 14 nm "dirty" Al electrode. Curves (*a*) and (*b*) are measured at T=4.2 K T=4.2 K and 1.8 K, respectively.

Manuscript received April 30, 1999.
This work was supported by the Northwestern Materials Research Center under the NSF MRSEC program, Grant No. DMR9309061.

device with a "dirty" middle electrode with the thickness d_m=14 nm at T=4.2 K (curve *a*) and T=1.8 K (curve *b*). The IVC at T=4.2 K displays only the sum-gap feature at $V=2\Delta_{Nb}/e$ and is smooth in the subgap region. This behavior is typical of similar devices reported in [8],[9]. However, as the temperature is lowered (below ~3K), a peculiarity appears in a narrow interval in the neighborhood of $V=\Delta_{Nb}/e$,which has a step-like shape. The position of the step moves towards lower voltages as the temperature is decreased, while the current increases (see Fig. 2). Note that the dc Josephson current does not appear at the same time, and it is much smaller than the step height even at low temperatures (the experimental setup allowed temperatures as low as T=1.8 K). At sufficiently low temperature a hysteretic behavior and negative-voltage switching appears (IVC at T=1.8 K in Figs. 1 and 2). The shape of the step is sensitive to a small magnetic field. A magnetic field suppresses the step, so that by H=100 G it disappears completely.

As the thickness of the Al layer, d_m, decreases and the barrier transparency increases, the structure of the step becomes more complex, and, at the same time, less sensitive to a magnetic field. Below we consider a device fabricated on a sapphire substrate with the thickness of the middle ("dirty") Al electrode d_m=7 nm. The IVC of the device is shown in Fig. 3 at T=4.2 K (curve *a*) and T=1.8 K (curve *b*). At T=4.2 K, the device has an I_c~17μA, which is not resolved on the scale of the plot, and nonhysteretic behavior. At T=1.8 K, the dc Josephson current is I_c=2.38 mA and the IVC is hysteretic. This value is too large if we consider the double-barrier device as a series connection of the two junctions, Nb/Al-AlO_x-Al and Al-AlO_x-Nb [10]. In this paper, we focus the discussion for a possible mechanism of the supercurrent enhancement.

Consider the $I_c(T)$ dependence of the device (see Fig. 4, solid circles). The sharp raise of the critical current at T<3 K correlates with the temperature dependence of the Al energy gap, Δ_{Al}, derived from the subgap steps 1 and 2 (see curve *b*

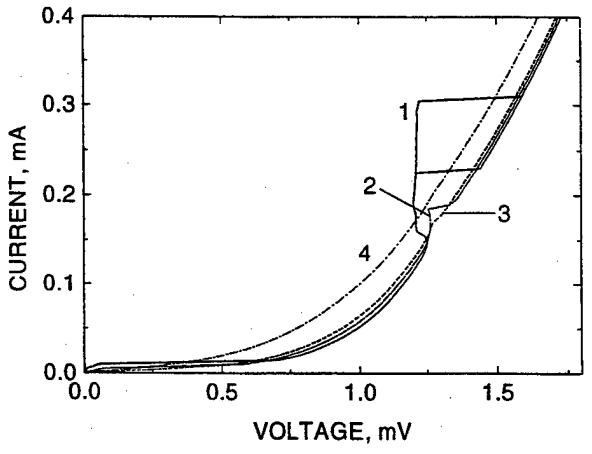

Fig. 2. Initial portion of the IVC of a device identical to that presented in Fig. 1 at different temperatures and zero magnetic field. Curves 1-4 are for T=1.8, 1.9, 2.2, and 2.5 K, respectively.

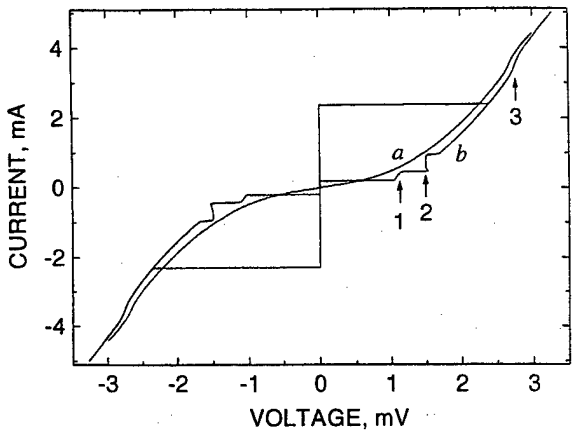

Fig. 3. IVC of a junction with d_{Al}=7 nm at T=4.2 (*a*) and 1.80 K (*b*). Steps 1-3 in the curve *b* correspond to the voltage $V=(\Delta_{Nb}-\Delta_{Al})/e$, $\Delta_{Nb}+\Delta_{Al})/e$, and $2\Delta_{Nb}/e$, respectively.

in Fig. 3), which is shown in Fig. 4 by the open circles. Arguments that the steps 1 and 2 in Fig. 3 correspond to the voltages $V=(\Delta_{Nb}-\Delta_{Al})/e$ and $V=(\Delta_{Nb}+\Delta_{Al})/e$, respectively, are presented in [10],[11]. In Fig. 4, the temperature dependence of the gap sum voltage, V_s, normalized by the electron charge e (step 3 in Fig. 3), is also plotted. The position of the step was determined from the peak of the derivative dV/dI. For ease of comparison with $\Delta_{Al}(T)$, the $V_s(T)/e$ dependence is shifted along the energy axis by 2.51 meV to lower energy. Unlike the $I_c(T)$ and $\Delta_{Al}(T)$ dependences, this dependence shows no sharp raise at low temperature. This indicates that the Al energy gap probably vanishes at the gap sum voltage, which is then simply equal to $V=2\Delta_{Nb}/e$.

Such a behavior is not expected if the Al energy gap is the equilibrium energy gap described by the BCS temperature dependence. Rather, the structures related with Δ_{Al} (steps 1 and 2 in Fig. 3) are induced at $V<2\Delta_{Nb}/e$.

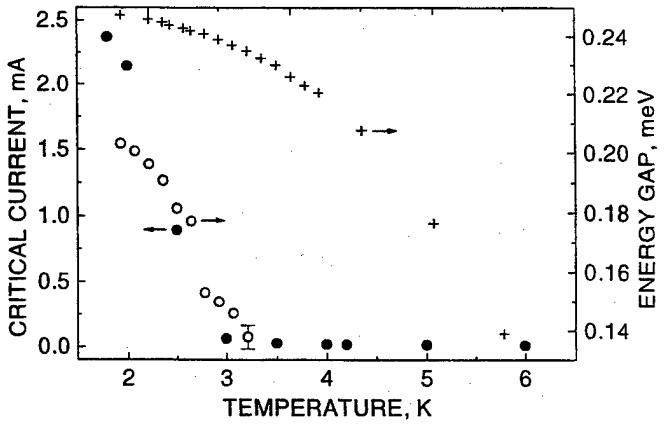

Fig. 4. $I_c(T)$, $\Delta_{Al}(T)$, and $2\Delta_{Nb}(T)$ dependences (solid circles, open circles, and crosses, respectively) for the device with d_{Al}=7 nm (cf. Fig. 3). Error bars are the same for all the points in the $\Delta_{Al}(T)$ dependence; only one error bar is shown for clarity. The $2\Delta_{Nb}(T)$ dependence is shifted along the energy axis to the lower energy by 2.51 meV.

Apparently, the subgap structure in Figs. 1-3 implies a modification of the electronic spectrum in the middle electrode, which occurs in an energy interval near $V=\Delta_{Nb}/e$. The two experimental features: (a) sensitivity of the subgap structure to a magnetic field, and (b) its appearance in the same temperature interval where the $I_c(T)$ dependence has a sharp raise (in the case presented in Figs. 3,4), suggest that the subgap structure is related with the phase coherent electron transport. It is shown in [5] that the Andreev bound states (ABS) may appear in junctions with a SIS'IS (SINIS) structure (here S, I, and N are superconductor, insulator, and normal metal, respectively), if the superconductor S' has a lower critical temperature than S. The ABS provide an additional channel of electron transport, and therefore, the critical current of the double-barrier junction may be increased compared with the single-barrier junction (provided the barrier transparency is identical). At finite voltage, the ABS should display themselves as singularities in the junction conductivity. We suggest that the novel subgap structure described above is a manifestation of the ABS.

IV. Conclusion

If the above assumption is correct, it implies that Nb/Al-AlO_x-Al-AlO_x-Nb junctions are suitable to design three-terminal switching devices with the configuration described in [12], in which the critical current can be controlled by changing the occupation of the ABS [13] with a current lead attached to the middle Al layer.

On the theoretical side, it is clear that the double-barrier junctions reveal a complicated behavior that cannot be described within a simplified model [6], as it was supposed in [7]. More elaborate theoretical model which involves both coherent and nonequilibrium effects is therefore necessary.

References

[1] M. Maezawa and A. Shoji, "Overdamped Josephson junctions with Nb/AlO_x/Al/AlO_x/Nb structure for integrated circuit application," *Appl. Phys. Lett.* vol. 70, pp. 3603-3605, June 1997.

[2] H. Sugiyama, A. Yanada, M. Ota, A. Fujimaki, and H. Hayakawa, "Characteristics of Nb/Al/AlO_x/Al/AlO_x/Nb junctions based on the proximity effect", *Jpn. J. Appl. Phys.*, vol. 36, pp. L1157-L1160, September 1997.

[3] H. Schulze, R. Behr, F. Mueller, and J. Niemeyer, "Nb/Al/AlO_x/Al/AlO_x/Nb Josephson junctions for programmable voltage standards," *Appl. Phys. Lett.*, vol.73, pp. 996-998, August 1998.

[4] A. J. Manninen, M. M. Leivo, and J. P. Pekola, "Refrigeration of a dielectric membrane by superconductor/insulator/normal-metal/insulator/superconductor tunneling," *Appl. Phys. Lett.*, vol. 70, pp. 1885-1887, April 1997.

[5] I. P. Nevirkovets and S. E. Shafranjuk, "Resonant Josephson tunneling in S-I-S'-I-S multilayered devices", *Phys. Rev. B*, vol. 59, pp. 1311-1317, Jauary 1999.

[6] W. L. McMillan, "Tunneling model of the superconducting proximity effect," Phys. Rev. vol. 175, pp. 537-542, November 1968.

[7] L. Capogna and M. G. Blamire, "Superconducting proximity effect through high-quality high-conductance tunnel barriers," *Phys. Rev. B*, vol. 53, pp. 5683-5687, March 1996.

[8] M. G. Blamire, E. C. G. Kirk, J. E. Evetts, and T. M. Klapwijk, "Extreme critical-temperature enhancement of Al by tunneling in Nb/AlO_x/Al/AlO_x/Nb tunnel junctions," *Phys. Rev. Lett.*, vol. 66, pp. 220-223, January 1991.

[9] I. P. Nevirkovets, "Modification of current-voltage characteristics of double-barrier tunnel junctions under influence of quasiparticle extraction," *Phys. Rev. B*, vol. 56, pp. 832-837, July 1997.

[10] I. P. Nevirkovets, J. B. Ketterson, and S. Lomatch, "Anomalous critical current in double-barrier Nb/Al-AlO_x-Al-AlO_x-Nb devices," *Appl. Phys. Lett.*, vol. 74, pp. 1624-1626, March 1999.

[11] I. P. Nevirkovets, J. B. Ketterson, S. E. Shafranjuk, and S. Lomatch, "Manifestation of Andreev bound states of double-barrier Nb/Al-AlO_x-Al-AlO_x-Nb tunnel junctions," unpublished.

[12] I. P. Nevirkovets, M. G. Blamire, and J. E. Evetts, "Three-terminal Josephson device with direct bias-current controlled phase difference," *IEEE Trans. Appl. Supercond.*, vol. 5, pp. 3106-3108, June 1995.

[13] L.-F. Chang and P. F. Bagwell, "Control of Andreev-level occupation in a Josephson junction by a normal-metal probe," *Phys. Rev. B*, vol. 55, pp. 12678-12690, May 1997.

Submicron Nb/Al-AlOx/Nb Tunnel Junctions With High Critical Current Densities

Xiaofan Meng, Anupama Bhat, Lizhen Zheng, Andre Wong, and Theodore Van Duzer
Department of Electrical Engineering and Computer Sciences, University of California at Berkeley
Berkeley, CA 94720, USA

Abstract--We describe the fabrication and properties of high critical current density micron and submicron Nb/Al-AlO$_x$/Nb tunnel junctions. Using a 10:1 reduction wafer stepper with I-line photoresist, we obtained a minimum linewidth of 0.6 μm and junctions as small as 0.3 μm^2. The critical current densities are between 10 and 20 kA/cm^2. The measured critical current spreads are small. This is due to low-temperature, low-stress ECR (Electron Cyclotron Resonance) based PECVD (Plasma Enhanced Chemical Vapor Deposition) SiO$_2$ insulation layers, stress-free Nb electrodes and light anodization around junction areas. The junctions have potential applications in very high-speed superconducting digital circuits and submillimeter microwave devices.

I. Introduction

Nb/AlO$_x$/Nb Josephson junctions are candidates for future ultrahigh performance computer and communication applications due to their high intrinsic switching speed and low power dissipation. To increase speed, it is necessary to reduce junction size and increase critical current density. Reducing junction size can also increase the integrated circuit density. When the junction size approaches submicron ranges, it poses a big challenge to the Nb/AlO$_x$/Nb junction process technology. One major problem is photolithography of submicron patterns. Also, it is very difficult, if not impossible, to open an even smaller contact window through the dielectric layer above the submicron junction. And small junctions are more sensitive to the film stress and process damage. Several groups have developed new processes for submicron junctions; among them are e-beam lithography, focused ion-beam patterning, and chemical-mechanical polishing (CMP) planarization [1]-[3].

We have previously reported a Nb/AlO$_x$/Nb junction process with very low critical current spreads. The critical current densities were between 1 to 10 kA/cm^2. The smallest junction size was 1.6 μm × 1.6 μm [4]-[6]. In this paper we introduce our new progress on submicron and high critical current density junctions. The critical current densities were between 10 to 20 kA/cm^2. The smallest junction area is 0.3 μm^2. In Part II we describe the fabrication procedure of the submicron Nb/AlO$_x$/Nb junctions. In Part III we describe the properties of the junctions. Part IV is the conclusion.

Manuscript received April 30. 1999.

II. Fabrication Procedure

A. *Process Steps*

Fig. 1 shows the process steps for micron and submicron Nb/AlO$_x$/Nb junctions. A Nb/AlO$_x$/Nb trilayer was deposited on a thermally oxidized four-inch silicon wafer surface using dc sputtering (Fig. 1a). The trilayer was then patterned and etched to isolate junction areas. Deviating from our normal process, we only etched a small ring around the junction (Fig. 1b). Before removing the photoresist, a light anodization was performed to form a thin layer of Nb_2O_5 on the sidewalls of the junction and a thin double layer of Nb_2O_5 and Al_2O_3 around the junction (Fig. 1c). The next step is to pattern and etch the junction base electrode. Also in a deviation from the normal process, we used whole trilayers as the base electrodes. Since it has relatively large area, the tunneling conductance makes the trilayer behave similar to a single layer electrode. This requires etching the three layers instead of one base electrode (Fig. 1d). After base electrode patterning an ECR PECVD SiO_2 film was deposited on the top as a dielectric layer (Fig. 1e). This was followed by junction contact window patterning and etching (Fig. 1f), Nb wire layer deposition (Fig. 1g), and the wire layer patterning and etching (Fig. 1h). Finally an Al-Ti-Au film was deposited by an e-beam evaporation and the contact pads were formed by lift-off. Table I lists the layer thickness and process methods.

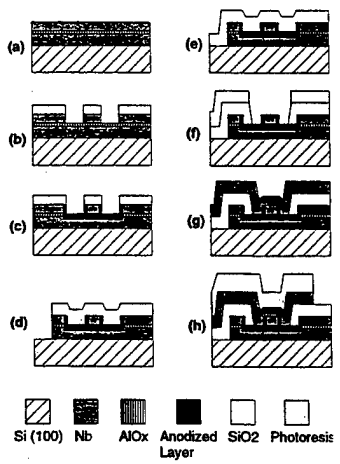

Fig. 1 Schematics of the process steps.

TABLE I
Nb TUNNEL JUNCTION LAYERS

Layers	Materials	Thickness (Å)	Process Methods
Base-electrode	Nb	2000	dc sputtering and RIE
Barrier	Al/AlO_x	90	dc sputtering and thermal oxidation
Counter-electrode	Nb	600	dc sputtering and RIE
Insulator	SiO_2	2000	ECR PECVD and RIE
Wire	Nb	3000	dc sputtering and RIE
Contact pads	Al	100	E-beam evaporation and lift-off
	Ti	100	
	Au	2000	

B. *Nb films and Nb/AlO$_x$/Nb Trilayers*

The quality of the Nb films and $Nb/AlO_x/Nb$ trilayers is essential for submicron junctions. We use a specially designed dc magnetron sputtering system to deposit the films. The system has a loadlock and a main chamber with Nb and Al targets, allowing for a complete trilayer process without breaking vacuum. The base pressure of the main chamber is 7×10^{-8} Torr. Eight-inch diameter targets with unique off-axis rotating magnets are used to improve the film uniformity. The thickness variations of the Nb and Al films over a four-inch wafer are less than ±2%. The surface roughness of a Nb film is about 8 Å, as measured by an AFM.

The stress of Nb films also affects the quality of submicron junctions. Fig. 2 shows the film stress vs. Ar pressure. When the Ar pressure increases, the stress changes from negative (compressive) to positive (tensile). We control the Ar pressure during dc sputtering to make nearly stress-free Nb films.

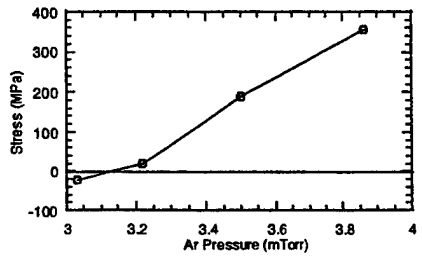

Fig. 2 Nb film stress vs. Ar pressure.

C. *ECR PECVD SiO$_2$*

We have developed a low-temperature, low-stress ECR PECVD silicon oxide process for junction insulation. High quality ECR oxide films can be deposited at near room temperature with very low stress. The surface roughness of the films is below 10 Å, as measured by an AFM. The thickness variation of ECR PECVD SiO_2 across a four-inch wafer is only ±1%. The stress of the films is below 100 MPa (compressive). Since the ECR microwave plasma has a much higher density and a very low ion energy compared with the traditional RF plasma, the ECR PECVD system can deposit SiO_2 at a high deposition rate and a low substrate temperature with very low damage to underlayers [5].

D. *Photolithography*

We use a 10:1 reduction wafer stepper with I-line (365 nm) photoresist for photolithography. The CD and alignment accuracy can be controlled to 0.1 μm. The smallest linewidth is 0.6 μm and the minimum junction size is 0.3 μm^2. An e-beam mask with a maximum variation of 0.05 μm for junction area definition was used. After 10:1 reduction, the variation from the mask is only 0.005 μm, which is 1% in area for a 1 μm^2 junction. The 10:1 reduction wafer stepper and the e-beam masks minimize junction area variation.

E. *Reactive Ion Etch*

The films are etched by Reactive Ion Etching (RIE) using CF_4, CHF_3, and O_2 gases. The etching profile, endpoint, and selectivity controls are more critical for submicron junctions. Table II lists the etching conditions for the various layers. For the Nb counterelectrode and SiO_2, the sidewall slope is 80°-85°. For the Nb baseelectrode and wire layers, the sidewall slope is 45°-55°. We also use an optical end-point detector to monitor the F ion emission spectrum, which enable us to control the overetch within 15-20%.

TABLE II
RIE CONDITIONS FOR DIFFERENT LAYERS

Layers	Gas flow rate (sccm)	Pressure (mTorr)	Power (W)	Etch rate (Å/s)	Sidewall slope
Nb CE	CF_4: 100	50	30	Nb: 120 SiO_2: 12	80°
Nb BE	O_2 : 7 CF_4: 100	150	50	Nb: 420 SiO_2: 50	45°-55°
Nb wire	O_2 : 7 CF_4 : 100	300	100	Nb: 750 SiO_2: 150	45°-55°
SiO_2	O_2 : 8 CHF_3 : 72	50	120	SiO_2: 300 Nb: 100	80°-85°

F. *Anodization*

After trilayer formation we pattern and etch the Nb counterelectrode down to the Al_2O_3 barrier. Unlike the conventional process which etches away all of the counter-electrode except the junction area, we only etch a few micron ring around the junction. Then we perform light anodization in an electrolyte of propylene glycol, ammonium pentaborate and DI water with a voltage of 20 V to form a thin layer of

Nb_2O_5 on the junction sidewall and double layers of Al_2O_3 and Nb_2O_5 around the junction. Since voltage of 1 V can convert 9 Å Nb into 20.7 Å Nb_2O_5 and 8.3 Å Al into 12 Å Al_2O_3, we estimate that the thickness of the Nb_2O_5 layer on junction sidewall is 414 Å, and the thickness of the double layer is 320 Å. The thin anodized oxide layers can protect the junction from processing damage and eliminate pinholes. It also makes the submicron junction process much easier because the contact window can be larger than junction area. Fig. 2a shows an AFM 3-D image of a submicron junction after anodization. Fig. 2b shows a microphotograph of a complete junction with anodization area and contact window. According the experimental evaluation of the $Nb/AlO_x/Nb$ junction capacitance [7], a capacitance of 20 fF was estimated from the junction area of 0.3 μm^2 and J_c of 12 kA/cm^2. Assuming that the contact window area is 1 μm^2, a capacitance of 4 fF was estimated from the parallel-plane capacitance fomula which is much smaller than the junction capacitance.

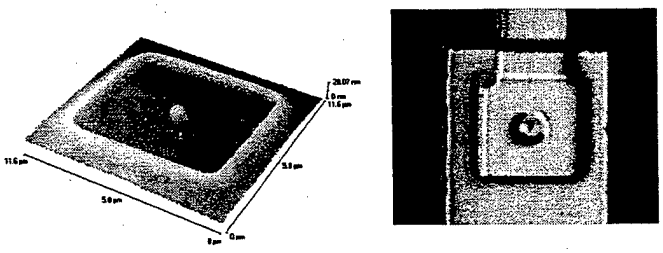

(a) (b)

Fig. 3(a) AFM 3-D image of a submicron junction after anodization. (b) Microphotograph (2000 ×) of a complete junction with anodized area and contact window, the window is larger than the junction.

III. Results and Discussion

The junction barriers were formed by room temperature thermal oxidation in the loadlock chamber. The oxygen pressure ranges from 10 to 1100 mTorr. The oxidation time was 10 min. to 30 min. Fig. 4 plots the critical current density J_c vs. the oxygen exposure E (E is the product of the O_2 pressure and the oxidation time). The $J_c(E)$ follows the universal power law dependence [8] with $J_c \propto E^{-5.5}$.

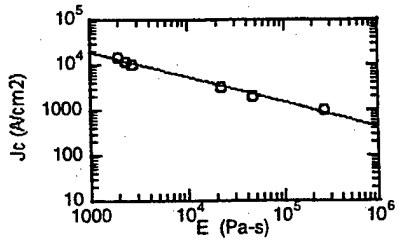

Fig. 4 The critical current density J_c vs. the oxygen exposure E.

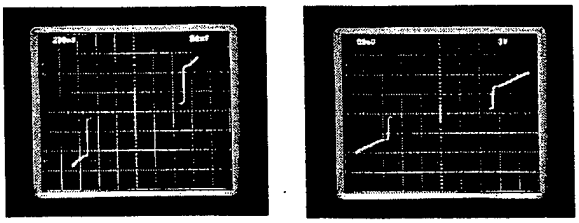

(a) (b)

Fig. 5 I-V characteristics for (a) a submicron junction (x-axis: 1 mV/div, y-axis: 50 μA/div); (b) 50 series junctions, the junction size is 1.5 μm × 1.5 μm (x-axis: 50 mV/div, y-axis: 200 μA/div).

Fig. 5a shows the I-V curve for a submicron junction of 0.3 μm^2. The J_c for the junction is 12 kA/cm^2. The junction barrier was oxidized in 10 mTorr pure oxygen for 30 min. The junction quality factor V_m ($I_c \times R_{2mV}$) is 12 mV. Fig. 5b shows the I-V curve for 50 series junctions of dimensions 1.5 μm × 1.5 μm. The critical current I_c spread (maximum to minimum) is only 1%, which is extremely small, considering the small junction size and high critical current density.

IV. Conclusion

We have fabricated high quality micron and submicron $Nb/Al\text{-}AlO_x/Nb$ Josephson junctions with high critical current density (10-20 kA/cm^2). The V_m for a 0.3 μm^2 junction with a J_c of 12 kA/cm^2 is 12 mV. The I_c spreads (maximum to minimum) for an 1.5 μm × 1.5 μm junction (12 kA/cm^2) array of 50 junctions is only 1%. The junctions have potential applications in very high-speed superconducting digital circuits and submillimeter microwave devices.

References

[1] M. B. Ketchen, D. Pearson, A. W. Kleinsasser *et al.*, *Appl. Phys. Lett.* vol. 59, pp. 2609-2611, Nov. 1991.

[2] Z. Bao, M. Bhushan, S. Han, and J. Lukens, *IEEE Trans. Appl. Superconduct.* vol. 5, pp. 2731-2734, June 1995.

[3] H. Akaike, T. Watanabe, N. Nagai, A. Fujimaki, and H. Hayakawa, *IEEE Trans. Appl. Superconduct.* vol. 5, pp. 2310-2313, June 1995.

[4] Xiaofan Meng, Huaming Jiang, Anupama Bhat, and Theodore Van Duzer, "Precise control of critical current and resistance in a Nb/AlO_X /Nb integrated circuit process," *Extended Abstracts of the 6th International Superconductive Electronics Conference, ISEC'97,* vol. 2, pp. 164-166, Berlin, Germany, June 1997.

[5] Xiaofan Meng, Anupama Bhat, and Theodore Van Duzer, "Very small critical current spreads in Nb/AlOx/Nb integrated circuits using low temperature and low stress ECR PECVD silicon oxide films", *1998 Applied Superconductivity Conference,* Palm Desert, California, Sept. 13-18, 1998.

[6] Anupama Bhat, Xiaofan Meng, Stephen Whiteley, Mark Jeffery, and Theodore Van Duzer, "A 10 GHz digital amplifier in an ultra-small-spread high J_c Nb/AlO_x-Al/Nb integrated circuit process," *1998 Applied Superconductivity Conference,* Palm Desert, California, Sept. 13-18, 1998.

[7] T. Van Duzer and C. W. Turner, *Principles of Superconductive Devices and Circuits,* 2nd ed., Prentice Hall PTR, 1999, p. 193.

[8] A. W. Kleinsasser, R. E. Miller, and W. H. Mallison, "Dependence of critical current density on oxygen exposure in Nb-AlO_x-Nb tunnel junctions", *IEEE Trans. Appl. Superconduct.,* vol. 5, pp. 26-30, 1995.

SINIS Fabrication Process for Realizing Integrated Circuits in RSFQ Impulse Logic

D. Balashov *), M. I. Khabipov *), **), F.-Im. Buchholz, W. Kessel, J. Niemeyer

Physikalisch-Technische Bundesanstalt, Bundesallee 100, D-38116 Braunschweig, Germany

*) Permanent address: IREE Russian Academy of Sciences, Moscow, Russia.
**)Present address: Institut für Physikalische Hochtechnologie (IPHT), Jena, Germany.

Abstract—At PTB, a new type of fabrication process has been developed to verify Rapid Single Flux Quantum (RSFQ) integrated circuits based on intrinsically shunted two-tunnel Josephson junctions (JJs). The process has been realized in LTS implementation using SINIS technology. A variety of single JJs, junction arrays and test circuits have been fabricated and experimentally investigated. The critical current densities of the junctions were set to a nominal value of $j_C = 500$ A/cm^2, with values of the characteristic voltage V_C equal to or larger than 160 μV. The JJs show nearly hysteretic-free behaviour (less than 10%), the intra-wafer parameter spread is smaller than ± 10%. Various basic RSFQ circuits have been realized with operation margins of bias currents of larger than ± 20%.

I. Introduction

In the field of LTS superconducting integrated circuits there is an increasing interest to use internally shunted JJs as active circuit elements based on superconductor-insulator-normalconductor-insulator-superconductor (SINIS) multilayer technology [1-6]. Compared with externally shunted JJs, they offer the possibility of decreasing the circuit area down to the size of the junction area and removing the resistor layer. The reduction of the circuit area in turn will decrease the probability of trapped spurious Single Flux Quanta. These features make SINIS contacts attractive for implementation into integrated circuits: they enable a considerable elevation of the integration level of the circuits. The purpose of this work is to present a new fabrication process developed at PTB for integrated circuitry in RSFQ impulse logic based on SINIS Nb/Al_xO_y/Al/Al_xO_y/Nb multilayer technology.

II. Fabrication Technology

A. Fabrication Process

Fig. 1 illustrates the fabrication process developed. It is based on the PTB production line for the fabrication of shunted JJs in 4-μm Nb/Al_2O_3-Al/Nb trilayer technology [7]. It has been modified and adapted to the special requirements of intrinsically shunted SINIS junctions [6].

Manuscript received April 30, 1999.
PTB participates in several research programs supported by the Deutsche Forschungsgemeinschaft (DFG), Germany (proj. no. NI 253/3-1), the Bundesministerium für Bildung, Wissenschaft, Forschung und Technologie (BMBF), Germany (proj. nos. 13N6835, 13N7259) and in part by the Russian SSP "Superconductivity", and INTAS (proj. no. 97-1712). This work is strongly linked to these programs.

Three-inch thermally oxidized silicon wafers are used as substrates. First, an Nb groundplane is deposited by dc magnetron sputtering and patterned by reactive ion etching (RIE) in a CF_4/O_2 plasma (Fig. 1a). To isolate other parts of

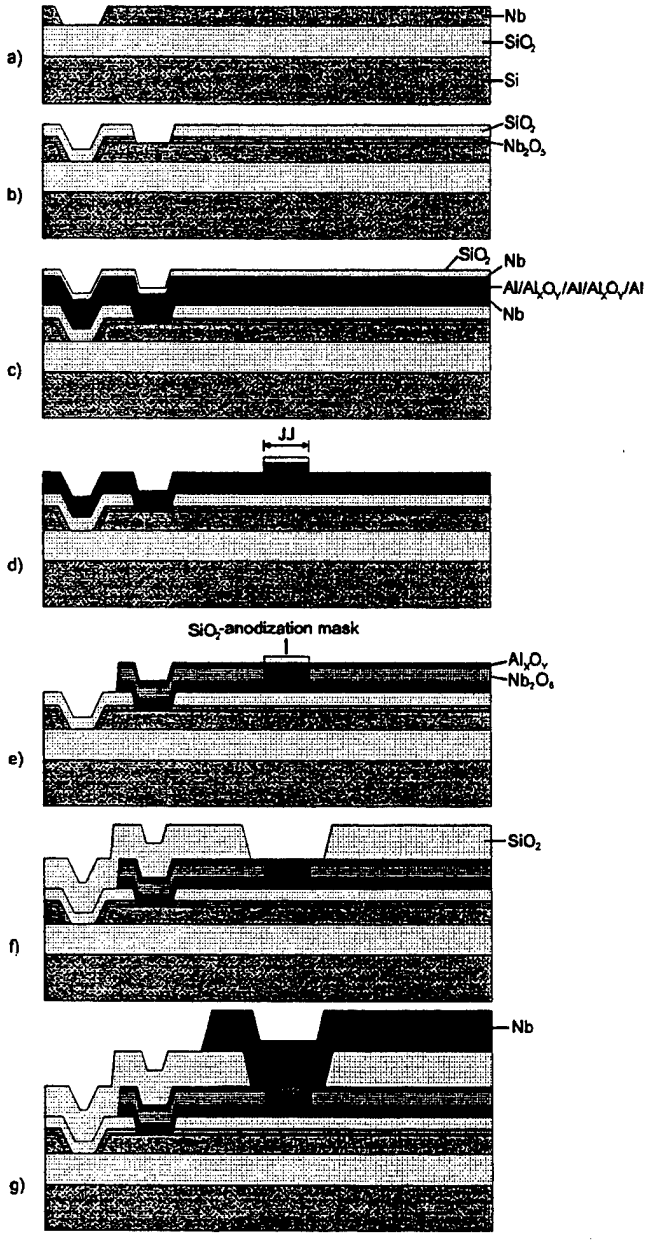

Fig. 1: Processing steps for fabricating intrinsically shunted Josephson junctions in SINIS technology.

TABLE I

SINIS TECHNOLOGY PARAMETERS

Step	Function	Material	SINIS CODE	Thickness in nm
	substrate	Si, SiO_2		
a)	ground	Nb		200
b)	1. groundpl. isol.	Nb_2O_5		50
b)	2. groundpl. isol.	SiO_2		200
	resistors	Cr/Pt/Cr		15/90/15
c),d)	base electrode	Nb	S	200
c),d)	normal metal	Al		10
c),d)	tunnel barrier	Al_xO_y	I	1
c),d)	normal metal	Al	N	10
c),d)	tunnel barrier	Al_xO_y	I	1
c),d)	normal metal	Al		10
c),d)	counter electrode	Nb	S	100
e)	1. multilayer isol.	Al_xO_y		45
e)	2. multilayer isol.	Nb_2O_5		75
f)	3. multilayer isol.	SiO_2		280
g)	wiring	Nb		350
	contact pads	Pd		75

the circuits, wet anodization of the groundplane is used up to a voltage of 27 V (Fig. 1b). The isolation is reinforced by an rf-sputtered SiO_2 layer. In order to connect the groundplane to other metal layers, holes are etched into the double dielectric layer in a CHF_3/O_2 RIE process. The next step (not included in Fig. 1) is the deposition of a Cr/Pt/Cr layer which is etched by Ar-mill to form bias resistors [8]. After this, the $Nb/Al_xO_y/Al/Al_xO_y/Nb$ multilayer is deposited and covered with a thin SiO_2 layer which serves as a mask during anodization and eliminates the undercut of simple photoresist masks (Figs. 1c, d). The areas of the JJs are protected by the photoresist and SiO_2 layer combination, and the Nb counterelectrode is subsequently exterminated outside by an RIE process in CHF_3/O_2 and CF_4/O_2 plasmas with the Al_XO_Y-Al layer acting as an etch stop (Fig. 1e). Then, the sample is anodized up to a voltage of 45 V. The next photomask is used to pattern the Nb base electrode. First, the Al_XO_Y is etched by Ar-mill and then the Nb_2O_5 and Nb layers are etched in a CF_4/O_2 RIE process. An SiO_2 layer is sputtered onto the sample to isolate the edges of the base electrode and strengthen the anodic oxide (Fig. 1f). By etching contact holes into this SiO_2 layer, the thin SiO_2 anodization mask is removed from the junction surface. The holes may be larger than the JJs, because isolation near the junctions is ensured by the anodic oxide. The circuits are completed by sputtering of an Nb wiring layer and by structuring this layer in a CF_4/O_2 RIE process (Fig. 1g). The main parameters of the technology process are summarized in Table I. For the different processing steps indicated, see Fig. 1.

Two types of contacts have been realized between the top Nb wiring layer and the Nb counter electrode of the multilayer junctions. They differ in the sizes of windows within the SiO_2 insulation layer, which are either larger or smaller than the contact area of the junction itself.

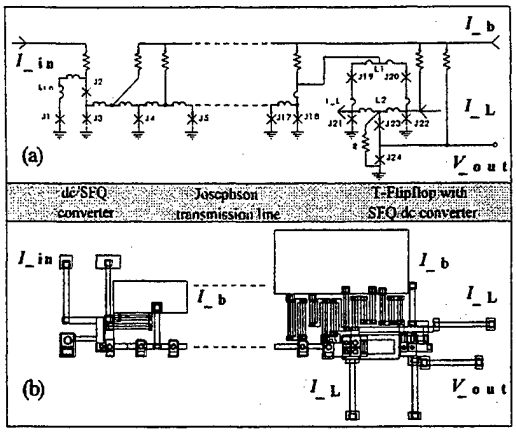

Fig. 2: Schematic diagram (a) and layout (b) of a basic RSFQ circuit.

B. Optimization of Technology

By variation of the oxidation parameters the fabrication process has been improved to give higher values of j_C and V_C. Different thicknesses of the Al_xO_y insulation layers within the multilayer junctions have been obtained by varying the oxidation times of the Al surfaces exposed to oxygen during the single processes of wafer production. They have been chosen between 1 min and 4 min, in each case at a constant oxygen pressure $p = 0.4$ Pa [6]. The values of microstrip sheet inductances L_S have been set to simulated values [9] and optimized by variation of the thickness of the SiO_2 isolation layers corresponding to $L_S = 0.94$ pH (wiring-ground), 0.71 pH (wiring-base), and 0.58 pH (base-ground) with intra-wafer margins of $\Delta L_S = \pm 0.03$ pH.

III. Circuit Design

Basic RSFQ circuits have been realized in different designs and layouts. Fig. 2 shows the schematic diagram (a) and the layout (b) of a circuit configuration comprising dc/SFQ and SFQ/dc converters, a Josephson transmission line (JTL), and a T-flipflop (TFF). The critical current densities of the junctions have been set to a nominal value of $j_C = 500$ A/cm^2. The area of the smallest junctions used in the circuits is $A = 24$ μm^2, and the nominal value of their critical currents is $I_C = 125$ μA. A resistive layer (sheet resistance $R_S = (1.05 \pm 0.07)$ Ω across 3-inch wafers) has been used for the bias current distribution.

IV. Measurements and Results

Single JJs and junction arrays covering a large variety of junction contact areas have been produced and tested. Figs. 3(a), (b) show current-voltage characteristics (IVCs) of a single SINIS junction and of an array of 200 SINIS junctions (contact areas $A = 48$ μm^2), respectively. The critical current of the single junction (Fig. 3(a)) is found to be $I_C = 200$ μA ($j_C = I_C/A = 416$ A/cm²) and its characteristic voltage to be $V_C = I_C \cdot Rn = 160$ μV ($Rn = 0.8$ Ω). The junction exhibits a nearly hysteresis-free IVC (hysteresis: less than 10%).

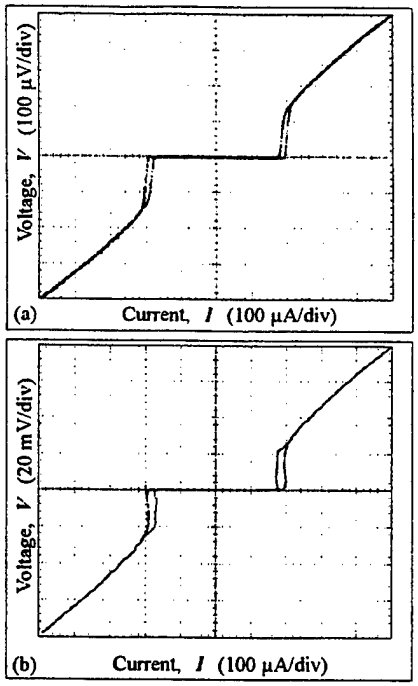

Fig. 3: Current-voltage characteristics of intrinsically shunted Josephson junctions realized in SINIS technology.
a): single junction, (b): series array containing 200 junctions.

The spread of the values of I_C of the junctions within the array is ±2% (see Fig. 3(b)). Using higher voltage amplification, no suppression of I_C of any of the junctions of the array was detected. For j_C, the intra-wafer parameter spread has been experimentally determined to be below ±10%. Higher values of j_C and V_C, up to 1000 A/cm^2 for j_C and up to 230 μV for V_C, were achieved for an oxidation time of 1 min of the Al surface layers within the junctions.

The conversion of the usual type of dc information to SFQ impulses (dc/SFQ), and vice versa (SFQ/dc), has been realized and tested. Fig. 4 illustrates the operation of a circuit containing a dc/SFQ converter, a JTL and a TFF with integrated SFQ/dc converter. At increasing amplitude, two SFQ impulses are generated in each period of the input current (I_{in}, "1") fed to the dc/SFQ converter. Correct operation is detected by the SFQ/dc converter (V_{out}, "2"). The bias current margins have been experimentally determined to be larger than ± 20%. With regard to the different types of wiring connection (see chap. II.), no degradation in circuit operation was detected.

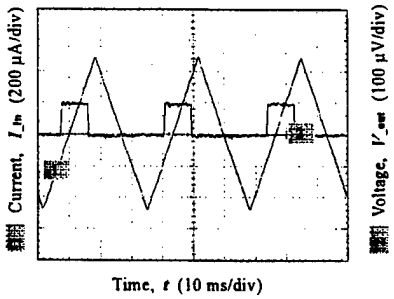

Fig. 4: Operation of a dc/SFQ and SFQ/dc converter circuit.

V. Conclusion

We have developed a new type of fabrication process in SINIS Nb/Al$_x$O$_y$/Al/Al$_x$O$_y$/Nb multilayer technology to verify RSFQ integrated circuits. The process has been developed by modifying the production line in 4 μm Nb/Al$_2$O$_3$-Al/Nb trilayer technology established at PTB. The values achieved for the critical current density of the JJs range up to about j_C = 1000 A/cm^2, those of the characteristic voltage to up to about V_C = 230 μV. The junctions show nearly hysteretic-free current-voltage characteristics (less than 10%), the intra-wafer parameter spread is smaller than ± 10%. Various basic RSFQ circuits have been realized in different designs and layouts comprising dc/SFQ and SFQ/dc converters, Josephson transmission lines, and T-flipflops. The circuit parameters experimentally determined are about 400 A/cm^2 for j_C and about 160 μV for V_C. The range of bias currents at which the circuits show correct functionality is fully covered by the operation margins which are larger than ± 20%. An important objective of future research will be to find out, up to which limits of critical current densities and characteristic voltages SINIS contacts can be realized.

Acknowledgment

We wish to thank R. Dolata and H. Schulze for advice in process optimization, T. Weimann for his commitment in fabricating photomasks, and D. Schubert and H.-P. Duda for engineering and technical assistance. One of the authors (D. B.) is gratefully indebted to the Robert Havemann Foundation.

References

[1] Yu. M. Kupriyanov and V. F. Lukichev, "Influence of boundary transparency on the critical current in "dirty" SS'S structures," *Sov. Phys. JETP*, vol. 67, pp. 1163-1168, 1988.

[2] L. Capogna and M. G. Blamire, "Superconducting proximity effect through high-quality high-conductance tunnel barriers," *Phys. Rev. B*, vol. 53, pp. 5683-5687, 1996.

[3] M. Maezawa and A. Shoji, "Overdamped Josephson junctions with Nb/Al$_x$O$_y$/Al/Al$_x$O$_y$/Nb structure for integrated circuit application," *Appl. Phys. Lett.*, vol. 70, pp. 3603-3605, 1997.

[4] H. Sugiyama, A. Yanada, M. Ota, A. Fujimaki, and H. Hayakawa, "Characteristics of Nb/Al$_x$O$_y$/Al/Al$_x$O$_y$/Nb junctions based on the proximity effect," *Jpn. J. Appl. Phys.*, vol. 36, pp. 1157-1160, 1997.

[5] Schulze, R. Behr, F. Müller, and J. Niemeyer, "Nb/Al/AlO$_x$/ Al/AlO$_x$/Al/ Nb-Josephson junctions for programmable voltage standards," *Appl. Phys. Lett.*, vol. 73, pp. 996-998, 1998.

[6] D. Balashov, F.-Im. Buchholz, H. Schulze, M. I. Khabipov, W. Kessel, and J. Niemeyer, "Superconductor-insulator-normalconductor-insulator-superconductor (Nb/Al$_x$O$_y$/Al/Al$_x$O$_y$/Nb) process development for integrated circuit applications," *Supercond. Sci. Technol.*, vol. 11, pp. 1401-1407, 1998.

[7] R. Dolata, M.I Khabipov, F.-Im. Buchholz, W. Kessel, J. Niemeyer, "Nb/Al$_2$O$_3$-Al/Nb process development for the fabrication of fast-switching circuits in RSFQ logic," in: *Applied Superconductivity 1995*, Inst. Phys. Conf. Ser. no. 148, vol. 2, Bristol: IOP Publishing, 1995, pp. 1709-1712.

[8] R. Dolata, D. Balashov, "Platinum thin film resistors with Cr under- and overlayers for the Nb/AlO$_x$/Nb technology," *Physica C*, vol. 295, pp. 247-250, 1998.

[9] P. Bunyk and S. Rylov, "Automated calculation of mutual inductance matrices of multilayer superconductor integrated circuits," *Ext. Abstr. ISEC'93*, Boulder, CO, USA, 1993.

Electrical characteristics of NbN Josephson junctions with Nb/AlOx/Nb multilayered barriers

T. Iwai, Y. Ninomiya, T. Aoyama, R. Oke, H. Akaike*, A. Fujimaki, and H. Hayakawa

Department of Quantum Engineering, Nagoya University, Furo-cho, Chikusa-ku, Nagoya 464-8603, Japan
*Center for Cooperative Research in Advanced Science & Technology, Nagoya University, Furo-cho, Chikusa-ku, Nagoya 464-8603, Japan

Abstract—We have fabricated and evaluated NbN Josephson junctions with Nb/AlOx/Nb multilayered barriers. The Nb/AlOx/Nb barriers work as a normal layer – insulator – normal layer barrier at 10 K, which realizes overdamped junctions. The junctions showed overdamped behavior at 10 K and the critical current density Jc and the characteristic voltage Vc were as high as 0.44 kA/cm^2 and 180 μV, respectively. The critical current uniformity was also evaluated. The standard deviation, 1-σ was 2.1 % at 4.2 K and 2.8 % at 6.6 K for a series of 64 5 x 5 μm^2 junctions.

I. Introduction

Overdamped NbN Josephson junctions are key elements [1,2] in 10 K superconductor integrated circuits (ICs) based on single flux quantum (SFQ) pulses [3]. The junctions used for ICs are required to have high reliability including high controllability, uniformity and reproducibility of their characteristics because these factors strongly affect yields of circuit fabrication. NbN/MgO/NbN junction [4] with external shunt resistors have been used as such elements so far. However, developments of intrinsically overdamped junctions are needed because they can realize higher density circuit integration and simplify the fabrication process [5,6].

In this work, Nb/AlOx/Nb multilayers are employed as barriers for NbN junctions to realize intrinsically overdamped junctions. The Nb/AlOx/Nb trilayer technology [7] is the most established junction technology and has excellent reliability. Therefore, the NbN junctions are expected to have high reliability. The junctions are also expected to show overdamped behavior because the Nb/AlOx/Nb multilayers behave as normal layer - insulator - normal layer (N-I-N) barriers at 10 K. In this paper, we describe the fabrication and characteristics of NbN junctions with Nb/AlOx/Nb multilayered barriers.

II. Junction Fabrication

Figure 1 shows a schematic view of cross section of a NbN/Nb/AlOx/Nb/NbN junction. The junctions were fabricated as follows. The NbN films with a film thickness of 100 nm were deposited as base layers by rf-magnetron sputtering on 5 cm-diam. Si wafers. The base pressure was less than 2 x 10^{-7} Torr, and the wafers were cooled by water. The films were prepared using Ar gas mixed with N_2. The total gas pressure was 19 mTorr and the partial pressure of N_2 was 8.3 %. The rf power density was 4.5 W/cm^2. The deposition rate of NbN was about 90 nm/min. The NbN films showed the critical temperature Tc of 14 K. The Nb and Al layers as barrier layers were deposited by dc-magnetron sputtering in Ar plasma. The deposition rates of Nb and Al were 85 nm/min and 28 nm/min, respectively. After deposition of the 6-nm-thick Al layers on the lower-Nb layers, the surfaces of the Al layers were exposed to pure O_2 gas to form AlOx barriers. The O_2 pressure was 100 mTorr and the oxidation time was 10 min. The upper-Nb layers were deposited after evacuation of the chamber. In this work, the film thickness of the lower-Nb ranged from 0 to 20 nm and that of the upper-Nb did from 3 to 20 nm. Finally, 200-nm-thick NbN layers as counter electrodes were sputtered.

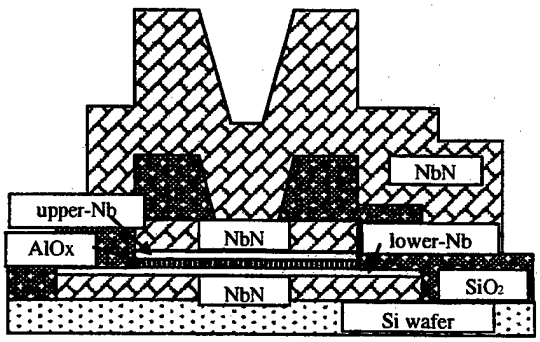

Fig. 1. Schematic cross section of a NbN/Nb/AlOx/Nb/NbN structure.

The junctions were patterned using photolithography and reactive ion etching (RIE). Sputtered SiO_2 films with a thickness of 650 nm were used as insulating layers between the base NbN electrodes and upper NbN wires. Via holes were formed in the insulating layers for electrical contact between the counter electrodes and upper wires when fabricating single junctions. On the other hand, when series junctions were fabricated, chemical mechanical polishing (CMP) process was used. 1.2 or 1.8-μm-thick NbN films were used as upper wires.

III. Result and Discussion

Figure 2 shows the current-voltage (I-V) characteristics at 10 K of an 8 x 8 μm^2 junction with a barrier structure of lower-Nb (0 nm) / AlOx / upper-Nb (3 nm) under the external magnetic field B=0 and B≠0. The junction behaves as an overdamped one. The critical current Ic of the junction is

Manuscript received April 30, 1999.

0.28 mA, which results in the critical current density Jc of 0.44 kA/cm^2. The characteristic voltage Vc is estimated to be 180 μV. The Vc is defined as the product of Ic and R, where R is the junction resistance at a current value of Ic when the Josephson current is completely suppressed by external magnetic field. The Vc is expected to get higher, as the Jc is increased by changing the oxidation conditions of the Al film.

Figure 3 shows the current-voltage (I-V) characteristics at 4.2 K for the junction shown in Fig.2 under the external magnetic field B=0 and B≠0. The hysteresis is observed in I-V characteristics. The Ir/Ic indicating the degree of the hysteresis is 0.46, where the Ir is the reset current at which the junction returns from a voltage state to a zero-voltage state. The Ic is 2.6 mA, from which Jc is estimated at 4.1 kA/cm^2.

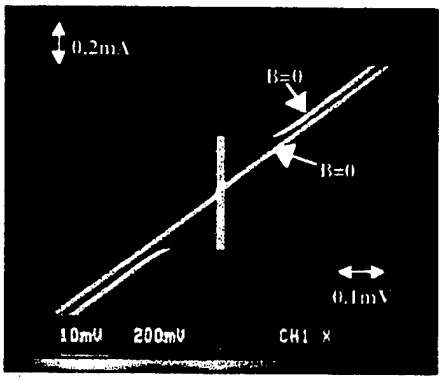

Fig.2. I-V characteristics measured at 10 K of an 8 x 8 μm^2 junction with a barrier of lower-Nb(0nm)/AlOx(6nm)/upper-Nb(3nm) under the external magnetic field B=0 and B≠0.

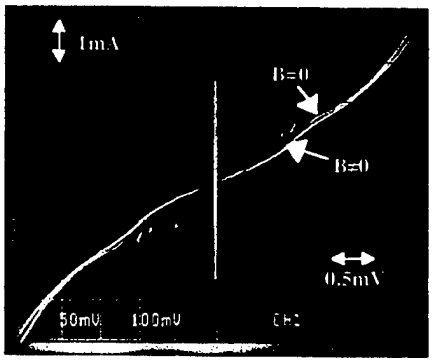

Fig.3. I-V characteristics measured at 4.2 K for the junction shown in Fig.2.

The parameters at 10 K and 4.2 K of junctions fabricated under various Nb thickness conditions are summarized in Table I. At 10 K, all the junctions showed overdamped characteristics. Jc ranged from 0.0047 to 0.44 kA/cm^2 and Vc did from 3.7 to 180 μV. On the other hand, at 4.2 K, Jc was in the range of 0.28 - 4.1 kA/cm^2 and the Ir/Ic in the range of 0.46 - 1.0. It is found that Jc and Vc at 10 K depend on the film thickness of Nb layers more strongly than those at 4.2 K. This suggests that the thickness of Nb layers is a key parameter for controlling the junction characteristics at 10 K. When the junctions are used in ICs, the junctions are required to have the Jc of higher than 1 kA/cm^2 at 10 K. No use of the lower-Nb layer may be a good choice for obtaining high Jc.

Figure 4 shows the dependence of Ic on the temperature for sample B, D and E. The Ic is normalized by the Ic value at 4.2 K for each junction. It is observed that the dependence changes from the exponential decrease to quasi-linear one with decreasing film thickness of Nb layers. This indicates that the Nb layers work as an N layer. As the film thickness of Nb films is decreased, the proximity effect does

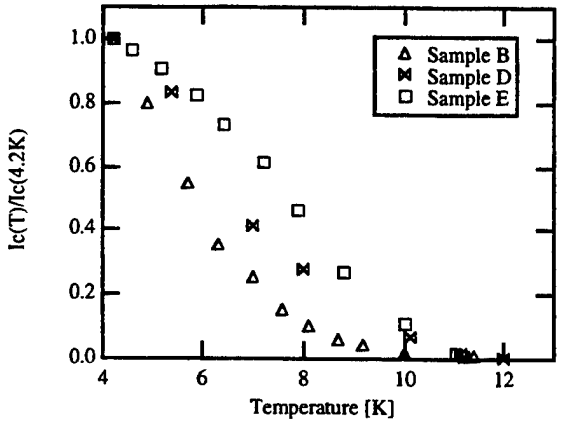

Fig. 4. Dependence of Ic on temperature for several samples listed in Table I.

TABLE I

The parameters at 10 K and 4.2 K for NbN/Nb/AlOx/Nb/NbN Josephson junctions with various thickness of lower and upper-Nb. The junction size is 8 x 8 μm^2.

Sample lower-Nb [nm]/ upper-Nb [nm]	10K			4.2K			
	Jc[kA/cm^2]	Vc[μV]	Ir/Ic	Jc[kA/cm^2]	IcRn[μV]	Vc[μV]	Ir/Ic
A (20/20)	«1	—	—	0.28	160	160	1.0
B(10/20)	0.0047	3.7	1	0.31	190	200	0.95
C (10/10)	«1	—	—	0.31	270	—	0.65
D (0/10)	0.16	36	1	2.3	—	600	0.62
E (0/3)	0.44	180	1	4.1	1300	2050	0.46

not have a great influence on the conduction mechanism.

The uniformity of junctions is one of the most important issues for fabricating superconducting circuits, because it affects the yields or the bias margin of the circuits. The Ic uniformity of the junctions can be easily measured because the junctions exhibit a small hysteresis in I-V characteristics at 4.2 K. Figure 5 (a), (b) and (c) show the I-V characteristics of a series of 64 5 x 5 μm^2 junctions with lower-Nb (0 nm) and upper-Nb (3 nm) at 4.2 K, 6.6 K and 10 K, respectively. The spread of Ic across this array had a standard deviation, 1-σ, of 2.1 % at 4.2K and 2.8 % at 6.6 K. The Jc and average Vc at 10 K for each junction are estimated to be 0.32 kA/cm^2 and ~90 μV, respectively.

IV. Conclusion

The overdamped NbN Josephson junctions for 10 K operation have been fabricated using Nb/AlOx/Nb multilayers as junction barriers. The junctions showed the Jc up to 0.44 kA/cm^2 and the Vc up to 180 μV at 10K. Although the Jc or Vc is not high enough to use the junctions as elements in 10 K ICs at present, it is expected to be improved by optimizing the conditions of AlOx barrier formation or by using the rare metals, such as gold, which have much longer mean-free-path of electrons than Nb, as N layers. The Ic spread was also evaluated using a series of junctions. The standard deviation, 1-σ, was 2.1 % and 2.8 % for a series of 64 junctions with an area of 5 x 5 μm^2 at 4.2 K and 6.6 K, respectively.

Acknowledgment

The work is supported partly by a Grant-in-Aid for scientific research from the Japanese Ministry of Education, Science and Culture and partly by "Breakthrough 21" research projects of Communications Research Laboratory of the Japanese Ministry of Posts and Telecommunications.

References

[1]S. L. Thomasson, A. W. Moopen, R. Elmadjian, J. W. Spargo, L. A. Abelson, and H. W. Chan, IEEE Trans. Appl. Supercond. 3, 2058 (1993).

[2]G. L. Kerber, J. E. Cooper, H. W. Fry, G. R. King, R. S. Morris, J. W. Spargo, and A. G. Toth, J. Appl. Phys. 65, 4853 (1990).

[3]K. K. Likharev and V. K. Semenov, IEEE Trans. Appl. Supercond. 1, 3 (1991).

[4]G. L. Kerber, L. A. Abelson, R. N. Elmadjian, G. Hanaya, and E. G. Ladizinsky, IEEE Trans. Appl. Supercond. 7, 2638 (1997).

[5]H. Akaike, K. Yoshizawa, R. Oke, A. Fujimaki, and H. Hayakawa, Applied Superconductivity, 5, 319 (1997).

[6]Q. Wang, J. Katsuta, T. Kikuchi, S. Kohjiro, and A. Shoji, Applied Superconductivity, 5, 339 (1997).

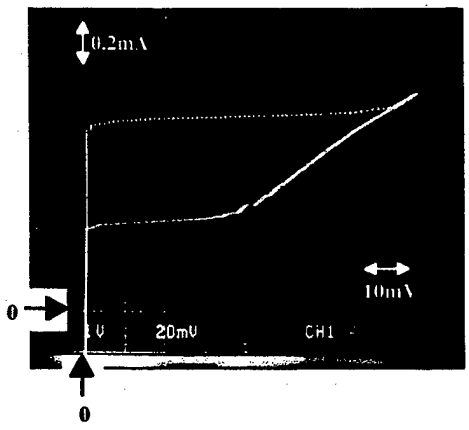

(a) I-V characteristics at 4.2 K. (1-σ=2.1%)

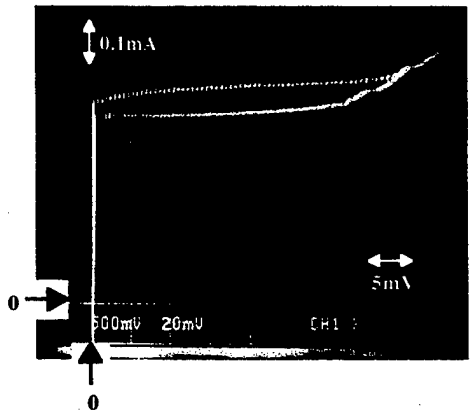

(b) I-V characteristics at 6.6 K. (1-σ=2.8%)

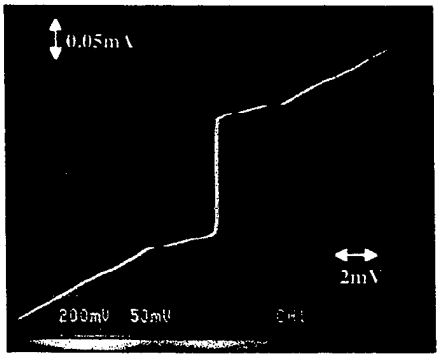

(c) I-V characteristics at 10 K.

Fig.5. I-V characteristics at 4.2 K, 6.6 K and 10 K of a series of 5 x 5 μm^2 junctions with a barrier of lower-Nb(0nm)/AlOx(6nm)/upper-Nb(3nm).

[7]S. Nagasawa, Y. Hashimoto, H. Numata, and S. Tahara, IEEE Trans. Appl. Supercond. 5, 2447 (1995).

Characteristics of NbN/AlN/NbN Tunnel Junctions Operating at 10 K

Zhen Wang, Hirotaka Terai, Akira Kawakami, and Yoshinori Uzawa

Kansai Advanced Research Center, Communications Research Laboratory
588-2 Iwaoka, Iwaoka-cho, Nishi-ku, Kobe, 651-2401 Japan

Abstract—NbN/AlN/NbN tunnel junctions and junction arrays were fabricated on single-crystal MgO and Si substrates for the basic investigation of all-NbN superconductor integrated circuits operating at 10 K temperature. The electrical characteristics of single junctions and junction arrays were measured in a wide temperature range of 4.2-15 K. There is almost no recognizable difference in junction characteristics when the operating temperature varied from 4.2 K to 10 K. The junctions demonstrated a very good junction quality with a high gap voltage (V_g = 4.8 mV), large I_cR_N products (I_cR_N = 2.6 mV), and a small subgap leakage current (R_{sg}/R_N = 6) at 10 K temperature. NbN/AlN/NbN junction arrays were fabricated for estimating the nonuniformity of the junction parameters. I_c nonuniformity for 200 junction array with a high current density (J_c = 11 kA/cm^2) was to be less than ±2 % (1σ).

I. Introduction

NbN tunnel junctions have attracted interest recently as replacements for Nb tunnel junctions used in high frequency and high speed Josephson devices, because NbN has a large gap energy and a relatively high operating temperature of 10 K. However, it is well known that NbN has a very short superconducting coherence length and superconducting properties of NbN thin films are sensitive to its crystal structures [1],[2]. The tunneling properties of all-NbN tunnel junctions, therefore, are strongly dependent on the quality of the superconducting electrode layers and the barrier-electrode interface properties.

We have recently made two advances in developing of high current density and high quality all-NbN tunnel junctions. Firstly, we developed single-crystal NbN thin films deposited on single-crystal MgO substrates at ambient temperature [3]. We also succeeded in using aluminum nitride (AlN) as the tunnel barrier for improving the electrode-barrier interface properties [4]-[6]. Since AlN has a low direct band gap (E_g = 6.2 eV) [7],[8], it is suitable for fabricating high current density tunnel junctions. Although AlN and NbN have a different crystal structure, the NbN/AlN/NbN junctions showed excellent tunneling characteristics with a very high current density [6]. In this paper, we report on the properties of the single NbN/AlN/NbN junction and junction arrays operating in a wide temperature range of 4.2-15 K. We discuss the electrical characteristics, temperature dependence of the junction parameters, and junction uniformity for the basic investigation of all-NbN superconductor integrated circuits.

Manuscript received April 30, 1999.

II. Fabrication

NbN/AlN/NbN tunnel junctions were fabricated on single-crystal (100) MgO and Si substrates using the fabrication processes described elsewhere [4],[5]. NbN and AlN films were prepared by rf magnetron sputtering in a load-lock sputtering system at ambient substrate temperatures. To promote the growth of NbN films at low substrate temperatures, a low total pressure (5 mTorr) and high-power density (6.2 W/cm^2) were used to deposit the NbN films. In order to control the current density, the AlN barriers were deposited in pure N_2 gas at 5 mTorr total pressure. The power density for AlN deposition was 2.3 W/cm^2, and the sample holder was rotated at 15 rpm during the deposition of the AlN barrier. The deposition rate of the AlN film was about 0.55 nm/min.

III. Results and Discussion

A. Temperature Dependence of Junction Parameters

1) Single junctions: The tunneling characteristics for single NbN/AlN/NbN junction and junction array were investigated in a wide temperature region of 4.2-16 K. Fig. 1 shows the I-V curves of a single NbN/AlN/NbN tunnel junction at 4.2 K (a) and 10 K (b) temperature. The junction

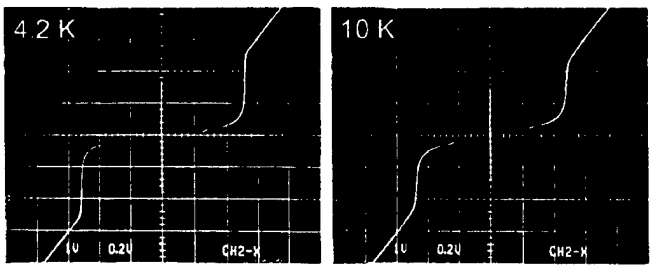

(a) (b)

Fig. 1. I-V curves of a single NbN/AlN/NbN tunnel junction at 4.2 K (a) and 10 K (b) temperature. There is almost no recognizable difference in junction characteristics at both 4.2 K and 10 K.

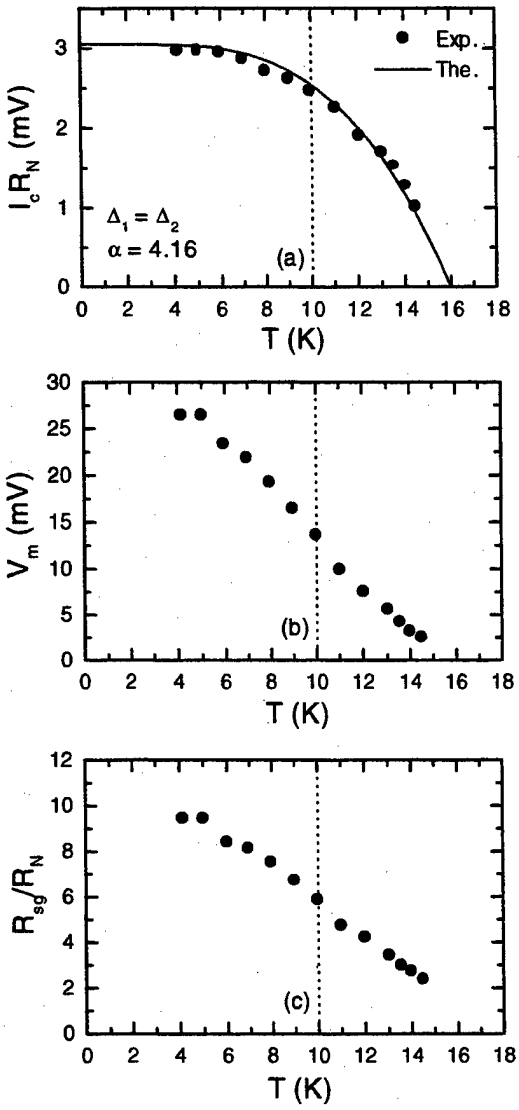

Fig. 2. Temperature dependence of junction parameters for a single NbN/AlN/NbN tunnel junction. The line shown in (a) is calculated from Ambegaokar-Baratoff relation.

size is 4x4 μm^2, and current density is 10.6 kA/cm^2. The junction, as shown in Fig. 1, has a good junction quality with a large gap voltage of about 5 mV and a small subgap leakage current at both 4.2 K and 10 K temperature. The super current I_c can be observed up to 15.3 K at which is very close to the T_c of NbN electrodes.

Fig. 2 shows the temperature dependence of junction parameters: (a) I_cR_N product, (b) subgap quality parameter V_m and (c) R_{sg}/R_N. The subgap leakage factor V_m is defined as the product of I_c and subgap resistance R_{sg}, where R_{sg} is measured at 4 mV. The temperature dependence of I_cR_N product, as shown in Fig. 2(a), has a good agreement with Ambegaokar-Baratoff theoretical relation [9] by assuming $\Delta_1 = \Delta_2$, where Δ_1 and Δ_2 are the superconducting energy gap of the base and counter electrodes. The strong-coupling parameter $\alpha = 4.16$ was given in our past work [3]. The

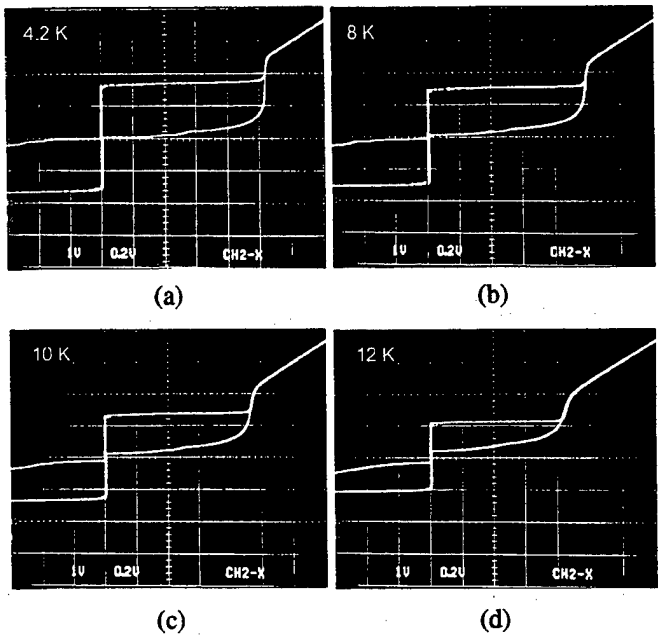

Fig. 3. I-V characteristics of a series array of 200 NbN/AlN/NbN tunnel junctions at different temperature. The junction size is 4x4 μm^2, and current density is 11 kA/cm^2.

subgap quality parameter V_m and R_{sg}/R_N decreased with increase in temperature, but a large value of V_m (~15 mV) and R_{sg}/R_N (~6) was obtained even at 10 K for the junction with a high current density of 10.6 kA/cm^2. In addition to the large I_cR_N product of 2.6 mV at 10 K, our NbN/AlN/NbN tunnel junctions are sufficient to serve as high speed Josephson devices operating at 10 K temperature.

2) Junction array: Fig. 3 shows I-V characteristics of a 200 junctions array at different temperature. The junction size was 4x4 μm^2, and current density was 11 kA/cm^2. The I-V curves demonstrated excellent array characteristics with a good uniformity and temperature dependence. The super current I_c and gap voltage V_g at 10 K, as shown in Fig. 3(c), is kept about 88% value of the I_c and V_g at 4.2 K. There is no evident degradation on the junction array quality when the temperature varied from 4.2 K through 10 K (Fig. 3 (a), (b), (c)). The I_c also has a 70% value of the I_c at 4.2 K even at 12 K temperature. These results indicate that our NbN/AlN/NbN tunnel junctions have an enough capacity for operating at 10 K. temperature.

B. Junction Uniformity

We have fabricated 100, 200 and 400 junction arrays on 15x15 mm^2 single crystal MgO substrates and 2 inch Si wafers for investigating junction uniformity. Fig. 4 is a typical trend chart showing I_c uniformity for 200 NbN/AlN/NbN tunnel junction arrays fabricated on 15x15 mm^2 MgO substrates. The junction size is 4x4 μm^2, and current density is 11 kA/cm^2 at 4.2 K. The supercurrent I_c for 196 junctions justly varied from 1.6 to 1.7 mA, and only 4

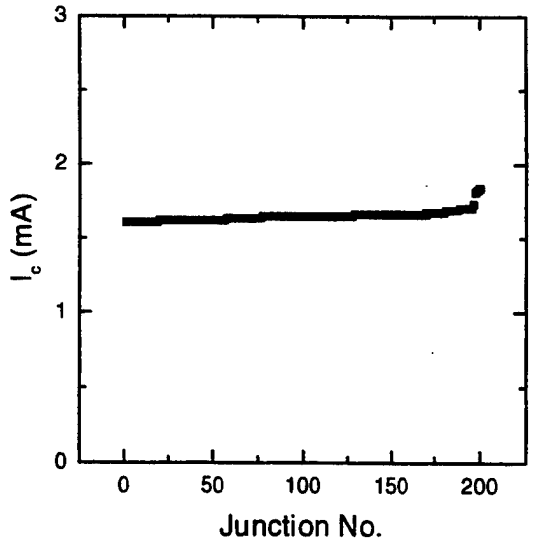

Fig. 4. Trend chart of critical current I_c measured at 4.2 K for 200 NbN/AlN/NbN tunnel junctions fabricated on single crystal MgO substrate. The junction size is 4x4 mm^2, and the current density is 11 kA/cm^2.

junctions had a I_c variation from 1.72 to 1.84 mA. Nonuniformity of the I_c for the 200 junction array was calculated to be less than ±2 % (1σ) by using the dates of Fig. 4. We have also fabricated the NbN/AlN/NbN junction arrays on 2 inch Si wafer. The I_c nonuniformity for 400 junction arrays was about ±4.5 %.

IV. Conclusions

We fabricated NbN/AlN/NbN tunnel junctions and junction arrays on single-crystal MgO and Si substrates, and investigated temperature dependence of junction parameters and I_c nonuniformity. There is almost no recognizable difference in junction characteristics when the operating temperature varied from 4.2 K to 10 K. The junctions demonstrated a very good junction quality with a high gap voltage (V_g = 4.8 mV), large I_cR_N products (I_cR_N = 2.6 mV), and a small subgap leakage current (R_{sg}/R_N = 6) at 10 K temperature. I_c nonuniformity for 200 junction arrays fabricated on MgO was to be less than ±2 %, and for 400 junction arrays fabricated on Si wafer was estimated to be ±4.5 %. We have fabricated and tested superconducting single flux quantum (SFQ) circuits based on the NbN/AlN/NbN junctions fabricated on Si wafer. The operating properties are presented in this conference [10].

References

[1] Y. M. Shy, L. E. Toth, and R. Somasundaram, "Superconducting properties, electrical resistivities, and structure of NbN thin films," *J. Appl. Phys.*, Vol. 44, pp. 5539-5545, December 1973.

[2] G. Oya and Y. Onodera, "Transition temperature and crystal structures of single-crystal and polycrystalline NbNx films," *J. Appl. Phys.*, vol. 45, pp. 1389-1397, 1974.

[3] Z. Wang, A. Kawakami, Y. Uzawa, and B. Komiyama, "Superconducting properties and crystal structures of single-crystal niobium nitride thin films depositedat ambient substrate temperature," *J. Appl. Phys.*, vol. 79, pp. 7837-7842, May 1996.

[4] Z. Wang, A. Kawakami, Y. Uzawa, and B. Komiyama, "High critical current density NbN/AlN/NbN tunnel junctions fabricated on ambient temperature MgO substrates," *Appl. Phys. Lett.*, vol. 64, pp. 2034-2036, April 1994.

[5] Z. Wang, A. Kawakami, Y. Uzawa, and B. Komiyama, "NbN/AlN/NbN tunnel junctions fabricated at ambient substrate temperature," *IEEE Trans. Appl. Supercond.*, vol. 5, pp. 2322-2325, June 1995.

[6] Z. Wang, A. Kawakami, and Y. Uzawa, "NbN/AlN/NbN tunnel junctions with high current density up to 54 kA/cm^2," *Appl. Phys. Lett.*, vol. 70, pp. 114-116, January 1997.

[7] W. M. Yim, E. J. Skofko, P. J. Zanzucchi, J. I. Pankove, M. Ettenberg, and S.L. Gilbert, "Epitaxially grown AlN and its optical band gap," *J. Appl. Phys.*, vol. 44, pp. 292-296 January 1973.

[8] H. Yamashita, K. Fukui, S. Misawa, and S. Yoshida, "Optical properties of AlN epitaxial thin films in the vacuum ultraviolet region," *J. Appl. Phys.*, vol. 50, pp. 896-898, February 1979.

[9] V. Ambegaokar and A. Baratoff, "Tunneling between superconductors", *Phys. Rev. Lett.*, vol. 10, pp. 486-489, 1963. Errata, *Phys. Rev. Lett.*, vol. 11, p. 104, 1963.

[10] H. Terai and Z. Wang, "All-NbN integrated circuits based on NbN/AlN/NbN tunnel junctions," Present in ISEC'99, PI-1.9, June 1999.

Fabrication of Josephson superconductor-normal metal-superconductor series arrays using a focused ion beam

R.W. Moseley*, A. J. Bennett, W.E. Booij, E.J. Tarte, and M.G. Blamire
IRC in Superconductivity, University of Cambridge, Cambridge, CB3 0HE, UK.

Abstract— A new fabrication method for Superconductor-Normal metal-Superconductor (SNS) junctions employing Focused Ion Beam (FIB) patterning of a superconductor-normal metal bilayer, has been used to make series junction arrays. We investigated their current-voltage (I-V) characteristic, and examined their response to microwaves at 4.2 K. Multiple integer Shapiro steps were observed in the I-V response of an array to microwaves. In addition, we found the properties of each junction in a double junction series array did not change in the junction spacing range studied (0.2-8 μm). Modeling the I-V characteristic of large arrays showed the junction variation of the critical current was 20 %.

I. Introduction

We have recently reported a fabrication method to create single SNS junctions [1]. The method consists of using a FIB to remove a portion of superconductor in a superconductor-normal metal thin film wire so as to form a junction. The dimensions of a junction can be controlled to obtain barrier lengths as short as 30 nm and longer than 150 nm. Using the same fabrication parameters we found the reproducibility of a junction with a critical current, I_C, and the normal state resistance, R_N, product ($I_C R_N$ product) to be within 10%. The good reproducibility of our single junctions has led us to investigate the fabrication of junction series arrays. Ultimately, our goal is to make arrays for use in voltage standard and microwave source based applications [2], [3].

In this paper, we present our early development work towards this goal. First we made small series arrays (containing between 2 and 8 junctions) having varied the spacing so we could examine the effect of an array's geometry on its performance. Second we made larger arrays so we could examine the spread of I_C within an array to evaluate its performance for use in future devices.

II. Array Fabrication

Cu (70 nm)/Nb (50 nm) bilayers were deposited onto oxidised Si substrates. To maximise film quality the deposition was performed in an ultra high vacuum magnetron sputter system in sequence without breaking the vacuum at a base pressure of 2 x 10^{-9} mbar. The bilayers were patterned using optical lithography and Ar ion milling to define 1.5 μm wide tracks and connecting contact pads.

The sample was then transferred to a standard FIB (FEI Inc. FIB200) for the junction fabrication. It allows in-situ, high resolution milling (8 nm at a beam current of 1 pA) to a variety of depths, and imaging (6 nm) of the sample. The Ga ion beam had a dwell time of 1.0 μs, a beam spot overlap of 50%, and an acceleration beam voltage of 30 kV throughout the process.

Fig. 1 shows a schematic diagram of a typical array. The junction fabrication process consisted of two stages. First, at a beam current of 10 pA and magnification of 25k (in combination with the 12 bit digital-analogue FIB controller card, this results in a pixel spacing of 3 nm), the width of the junctions, 0.5 μm, were defined by making rectangular perimeter cuts (labeled *a* and *b* in Fig. 1) through the bilayer and into the substrate, electrically isolating the junction from

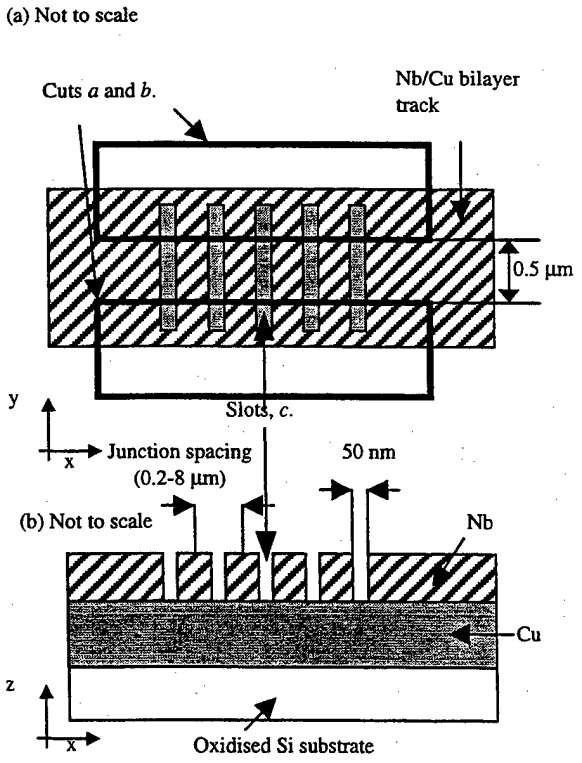

Fig. 1. (a) Plan-view and (b) cross-section schematic diagram of a series junction array. Labels *a* and *b* denote the two isolating cuts, and *c* denote the multiple slots cut, made by the FIB.

Manuscript received April 27, 1999.
This work was supported the UK Engineering and Physical Sciences Research Council.

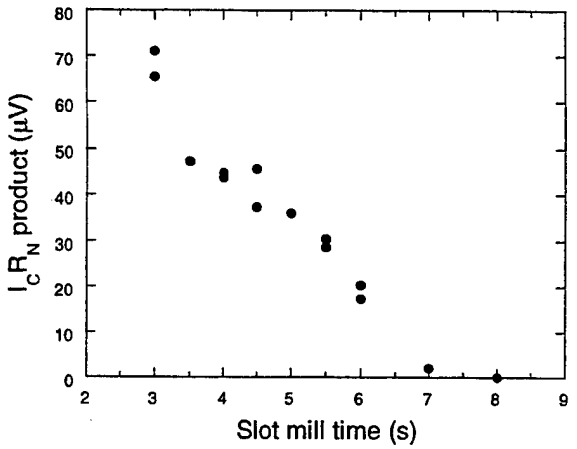

Fig. 2. Graph showing the single junction I_cR_N product (at 4.2 K) dependence of the junction slot (*c* in Fig. 1) mill time for an area of 50 nm x 1 μm.

the edge of the track thereby preventing spurious electrical edge effects from degrading the junction. Second, at a beam current of 1 pA and with a magnification between, 35k (2 nm resolution) and 50k (1.5 nm resolution), the junctions were made. Regularly spaced slots (*c* in Fig. 1) were patterned and removed only the superconducting Nb layer to give junction barrier lengths of 50 nm. We varied the junction spacing between 0.2 μm and 8 μm.

The depth of a cut into the bilayer (*c*) is critical in determining the parameters of an individual junction. Insufficient milling leaves residue superconducting Nb, while over-milling results in no measurable Josephson coupling at 4.2 K. We found that we can control the ion beam sufficiently to make accurate cuts, as demonstrated by the reproducibility in the I_cR_N product. Fig. 2 shows the I_cR_N product of single junctions made using different milled slot times (the milled slot time is proportional to the depth of the slot). For all the junctions discussed here we used a milled slot time of 4 s. This corresponds to the time taken to mill through the Nb layer without damaging the Cu layer underneath.

Fig. 3 shows a secondary electron image, taken in the FIB, of 16 and 30 series junction arrays.

III. Results

A. Studies of small series arrays

All the measurements in this paper were recorded at 4.2K using a custom built probe containing a microwave antenna. Table I displays the overall I_C, R_N, and I_cR_N products for two junction arrays with a variable spacing of between 0.2 and 8 μm and, for comparison, a single junction made on the same sample. The average overall I_cR_N product of the double junctions is 80 μV, within 10 % of the I_cR_N product calculated from two single junctions in series, 84 μV. Under microwave irradiation (13.3 GHz) the sample produced double Shapiro steps [4] in their I-V characteristic at voltages, $n\hbar\omega/2e$ where

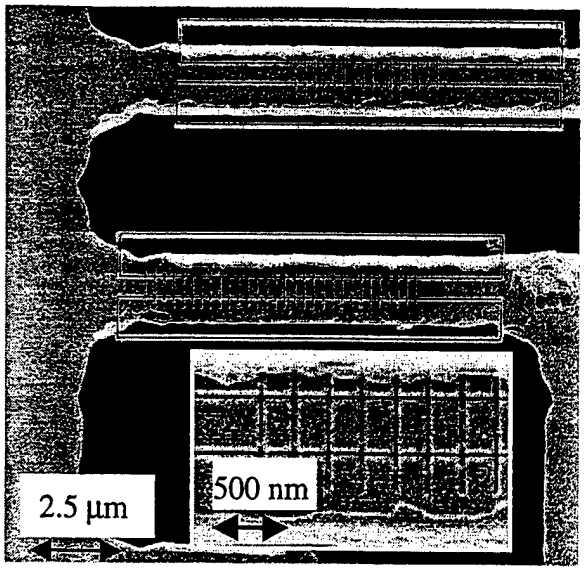

Fig. 3: FIB image of 16 and 30 series junction arrays with a junction spacing of 200 nm. Inset shows an enlargement of an array.

TABLE I

VARIABLE SPACED DOUBLE JUNCTIONS

Junction spacing (μm)	I_c (μA)	R_N (Ω)	I_cR_N (μV)
0.2	320	0.25	80
0.5	300	0.23	69
1	270	0.27	73
8	390	0.25	98
Single junction	350	0.12	42

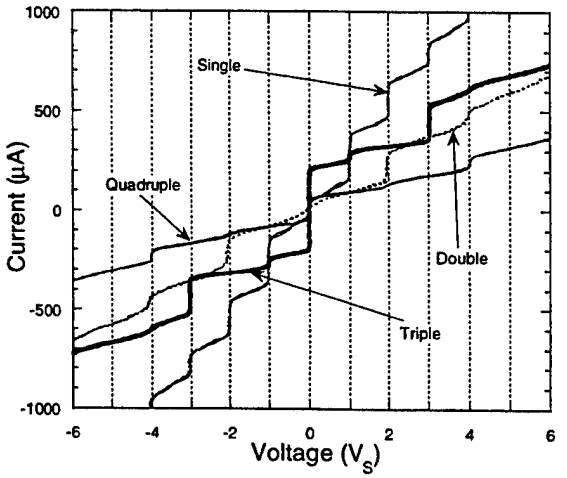

Fig. 4. Graph showing the I-V characteristic responses of 1, 2, 3 and 4 junctions in series to microwaves (13.3 GHz).

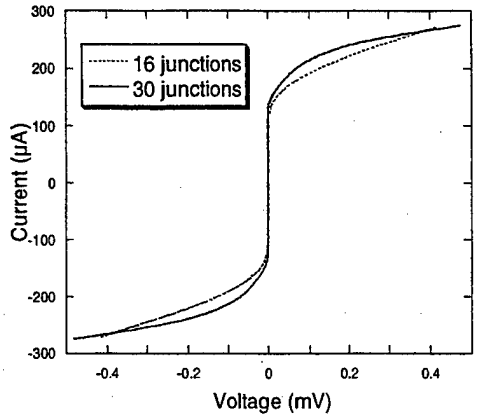

Fig. 5. Graph showing the low voltage I-V characteristics of 16 and 30 series junction.

n= 2, 4, 6..., and ω is the angular frequency of the microwave radiation (Single Shapiro steps, occur at $V_s=\hbar\omega/2e$, commonly seen in the I-V characteristic of a single junction).

Fig. 4 compares the microwave I-V characteristics of 2, 3, and 4 junction arrays with a spacing of 1 μm, and a single junction. The voltage is measured in units of single Shapiro steps, V_s=28 μV. As expected, the I-V characteristic of a single junction has only single steps, and the double junction has double steps. However, for 3 junctions in series we find a series of single and double steps, and for 4 junctions in series there are double steps.

B. Studies of large series arrays

Fig. 5 shows low voltage I-V characteristics of 16 and 30 junction arrays with a junction spacing of 0.2 μm. To model the I-V characteristic of the array, we firstly fitted a polynomial curve to the I-V characteristic of a single junction in its finite, positive voltage state (i.e. $I>I_C$). We assumed the general form of the I-V characteristic of a junction in an array is the same as the fitted individual junction. Then we fitted the I-V characteristic of an array using 3 fitting parameters, the mean I_{C0}, the spread of I_C, σ, of the junctions in the array, and the overall R_N of the array. The overall voltage of the array was found by considering a current flowing through the array, and calculating the voltage contribution of each junction from the polynomial fit, to the overall voltage across the array. Using this method we found the values shown in Table II model the results best.

The 16 junction array responded to microwaves by showing Shapiro steps at voltages of $14V_s$.

IV. Discussion

In the spacing range studied (0.2-8 μm) the overall I_CR_N product of the double junctions did not appear to significantly vary from the sum of two single junction I_CR_N products. The double Shapiro step response of the I-V characteristic to microwaves for each double junction indicates the I_C of both junctions are very similar. Examination of the larger arrays showed I-V responses characteristic of two junctions in an array not locked with the other junctions. We attribute this to a geometrical consequence of the 2 junctions at the ends of the array being in a different environment to the rest of the junctions inside the array.

The I_C spread of the large arrays can be statistically modeled with both arrays having an I_C spread of 20%. We believe we can improve this spread by further improvements to the fabrication process e.g. writing the junctions with better resolution so the accuracy of the barrier lengths can be improved.

TABLE II

STATISICAL ANALYSIS OF THE VARIATION OF I_C IN LARGE ARRAYS

Number of junctions in array	I_{C0} (μA)	σ(μA)	R_N (Ω)
16	225	43	1.3
30	310	65	4

Acknowledgment

The authors thank Gavin Burnell for his help and useful discussions.

References

[1] R.W. Moseley, W.E. Booij, E.J. Tarte, and M.G. Blamire, "Direct writing of low T_C superconductor-normal metal-superconductor junctions using a focused ion beam," paper submitted to *Applied Physics Letters*.

[2] S.P. Benz, and C.A. Hamilton, "A pulse-driven programmable Josephson voltage standard," *Appl. Phys. Lett.*, vol. 68, pp.3171-3173, May 1996.

[3] P. Barbara, A.B. Cawthorne, S.V. Shitov, and C.J. Lobb, "Stimulated emission and amplification in Josephson junctions arrays," *Phys. Rev. Letts.*, vol. 82, pp.1963-1966, March 1999.

[4] S. Shapiro, "Josephson currents in superconducting tunneling: The effect of microwaves and other observations," *Phys. Rev. Letts.*, vol. 11, pp80-82, July 1963.

Transport Properties of Nb/InAs(2DEG)/Nb Josephson Field-Effect Transistors

A. Richter, M. Koch, T. Matsuyama, and U. Merkt
Institut für Angewandte Physik und Zentrum für Mikrostrukturforschung, Universität Hamburg,
Jungiusstraße 11, D-20355 Hamburg, Germany

Abstract—We investigate transport properties of mesoscopic semiconductor/superconductor weak links. The superconducting Nb electrodes of our junctions are coupled by the two-dimensional electron gas (2DEG) of an InAs heterostructure grown on a GaAs substrate. We report on the properties of Josephson field-effect transistors (JoFETs) utilizing these junctions.

I. Introduction

Semiconductor coupled weak links combine the world of superconductivity with the world of semiconductor physics. Via the field-effect it is possible to control the charge density in the semiconductor and hence the superconducting properties of the weak links. The charge transfer can be well understood in terms of Andreev reflection processes taking place at the interfaces between superconductor (S) and semiconductor [1]. Most prominently, these processes result in a subharmonic gap structure (SGS) and an excess current. Andreev reflection means that an incoming electron/hole is retro-reflected as a hole/electron with creation/destruction of a Cooper-pair in the superconductor. Recently, this process has been discussed to be the origin of SGS also in high-T_c Josephson junctions [2].

Gate voltage controlled Josephson junctions, so called Josephson field-effect transistors (JoFETs), have been known for many years [3]. Although they have never gained any role in practical applications they can be very helpful to understand more fundamental aspects in superconducting electronic devices. For example, the influence of asymmetry in superconducting quantum interference devices (dc-SQUIDs) could be observed with JoFETs.

We present the properties of Josephson junctions and JoFETs that are coupled via the 2DEG of an InAs heterostructure grown on GaAs. This integrates superconducting devices on a commercially widespread and physically very important substrate material.

II. Sample Preparation

The InAs heterostructures are grown by solid source molecular beam epitaxy (MBE) on GaAs(001) substrates. The layer sequence and the thicknesses of the distinct layers are given in Fig.1. To overcome the problem of lattice mismatch between InAs (lattice constant a=6.06 Å) and GaAs (a=5.65 Å) a buffer layer has to be grown between the substrate and the electrical active region. In the buffer layer the In content is gradually increased from 0 to 75%. The electrical active region consists of an InAlAs/InGaAs quantum well in which a strained InAs channel layer is inserted. This is intended to get highly transmissive contacts because InAs does not form any Schottky barrier to Nb. The quantum well is separated by a spacer from the Si-doped layer. By thermal activation the donors are ionized and the electrons are trapped inside the quantum well to form the two-dimensional electron gas (2DEG). Because the donors are separated from the channel very high mobilities can be achieved. Our best samples presently already exhibit mobilities of μ=85.000 $cm^2V^{-1}s^{-1}$ and electron densities of N_s=8·10^{11} cm^{-2} at a temperature of T=4.2 K. From these data we calculate an electron mean free path of l_{el} = 1.3 µm.

InAlAs	36 nm	cap
InGaAs	13.5 nm	
InAs	4 nm	channel
InGaAs	2.5 nm	
InAlAs	5 nm	spacer
Si-InAlAs	7 nm	n-doping
InAlAs	400 nm	
buffer	700 nm	buffer
GaAs		substrate

Fig.1: Layer sequence of the InAs heterostructure on GaAs.

A sketch of our JoFET structure is given in Fig.2. First, a

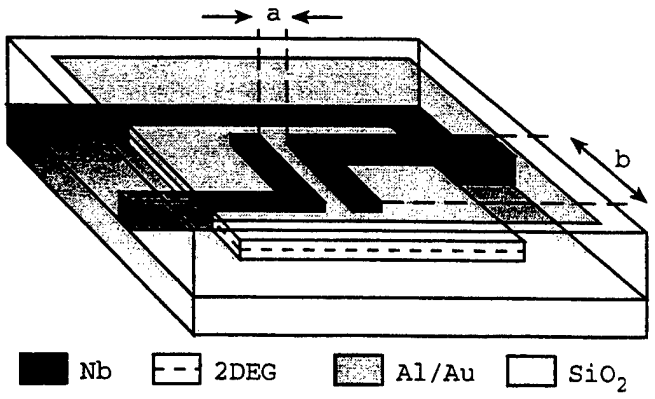

Fig.2: Schematic view of the JoFET.

Manuscript submitted April 22, 1999.
This work is supported by the Deutsche Forschungsgemeinschaft via the Sonderforschungsbereich 508 "Quantenmaterialien – laterale und hybride Strukturen".

200 μm x 200 μm mesa is etched into the heterostructure by reactive ion etching (RIE). Then the junctions are defined by electron-beam lithography. The widths of the current leads are 2 μm in order to prevent magnetic flux penetration. The separation of the source and drain electrodes in the junctions range from a=400 nm to a=1 μm. Their widths are b=20 μm, 10 μm, 8 μm and 5 μm, respectively. We achieve highly transmissive side contacts to the 2DEG by low energy Ar-etching and subsequent in situ sputtering of the 100 nm thick niobium film. Then a 300 nm thick SiO_2 layer is grown as the insulator by plasma enhanced chemical vapor deposition (PECVD). Finally the 400 μm x 400 μm Al/Au gate electrode is deposited by thermal evaporation.

III. Experimental results

We first present the properties of a single contact with a=400 nm, b=8 μm and l_{el}=345 nm (T=4.2 K). The temperature-resistance characteristic of this junction shows a sharp drop of resistivity at T_C=9.2 K, a value which is very close to that of the bulk value of Nb. Critical currents in the current-voltage characteristics appear at T=6 K. Additionally, we clearly observe excess currents at still lower temperatures. In Fig.3(a) we depict the differential resistance vs. source-drain voltage at temperatures T=2.0 K, 2.5 K, ..., 9.5 K. A very pronounced SGS with up to five dips at low temperatures can be seen. The SGS survives even for temperatures where a critical current can no longer be observed. At higher temperatures the features become indistinct to reappear near T_C but more as peak-like structures. Above T_C the SGS disappears. The temperature dependence of the dip positions is presented in Fig.3(b). The solid curves are calculated values for the energy gap $\Delta(t)/\Delta(0)$ of a BCS superconductor with $t=T/T_C$. This shows that the dips shift in accordance with the temperature dependent value of the energy gap. For temperatures near T_C the fit becomes better if the peaks are considered instead of the dips. This suggests a transition of the dominant transport process. At higher temperatures more quasiparticles are generated that provide a negativ contribution to the current. The dip positions cannot be described by the well-known formula $V=2\Delta/(ne)$ with n being an integer given in the OTBK model which is also addressed as ScS model [1]. Moreover, the low temperature value of 2.72 mV which is extrapolated from the outermost peak is quite different from the bulk value of the energy gap for niobium $2\Delta(0)$=3.05 meV. A more satisfying comparison can be achieved within the SNcNS model [4]. In this description N denotes normal conducting layers at the interfaces and c a ballistic constriction between the SN sandwiches. Although not intended, normal layers might form at the interfaces of our junctions by the Ar-etching process prior to the niobium sputtering. In the SNcNS model the proximity of S and N can lead to an induced energy gap Δ_N in the density of states of the N layer. Additional dips are predicted to appear at positions $2\Delta_N/(ne)$, $(\Delta_S+\Delta_N)/(ne)$ and $(\Delta_S-\Delta_N)/(ne)$. For T>0 the $2\Delta_S/(ne)$ series should disappear. This might account for the reduced value of the first dip and the aperiodic dip positions in our junction. We are currently working on a more quantitative description of our data in the framework of the SNcNS model. From the existence of high supercurrents, excess currents, pronounced SGS structures, and products of the critical current times normal state resistance I_CR_N of up to I_CR_N=130 μV at T=1.7 K we infer highly transmissive side contacts between the niobium and the only 4 nm thick InAs layer in our junctions.

In the following we present the properties of a JoFET utilizing a junction with a=600 nm, b=20 μm and l_{el}=1.3 μm (T=4.2 K). The temperature dependence of the resistivity of this JoFET is similar to that of the junction discussed before. At T=1.7 K and for zero gate voltage V_G the critical current is I_C=15.6 μA and the normal state resistance for currents well above the critical current is R_N=5.9 Ω resulting in an I_CR_N product of I_CR_N=90 μV. At positive gate voltages of up to +20 V, i.e. at increased carrier densities in the semiconductor, the critical current and the normal state resistance essentially stay constant. At negative voltages, the critical current starts

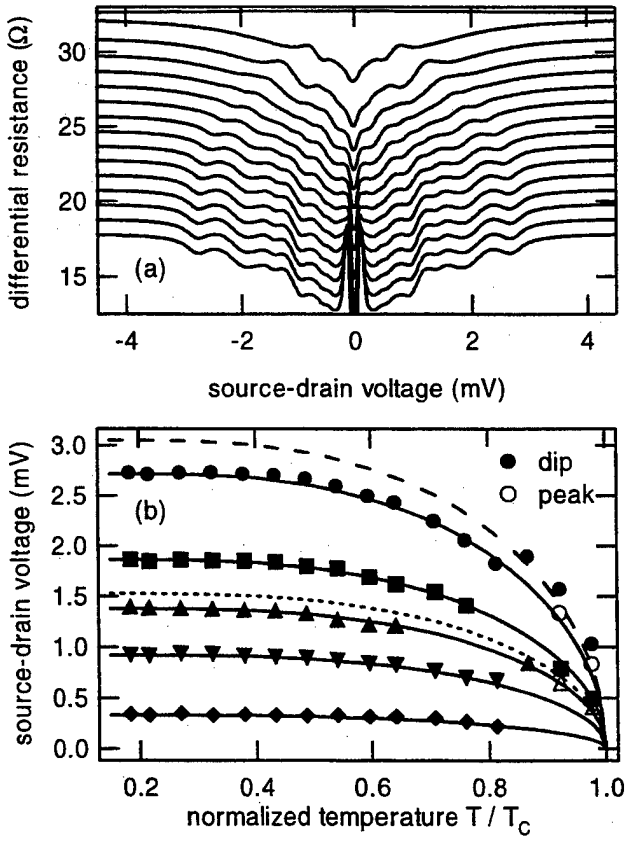

Fig.3: (a) Differential resistance vs. source-drain voltage at T=2.0 K (lowest curve), 2.5 K, ..., 9.5 K (upper curve). For clarity, the traces are successively shifted by 1 Ω. (b) Dip positions vs. normalized temperature $t=T/T_C$. Solid curves are $\Delta(t)/\Delta(0)$ of a BCS superconductor fitted to the lowest temperature values of the respective peaks. The dotted and dashed lines show the bulk values of the Nb gap $\Delta_{Nb}(t)$ and $2\Delta_{Nb}(t)$, respectively.

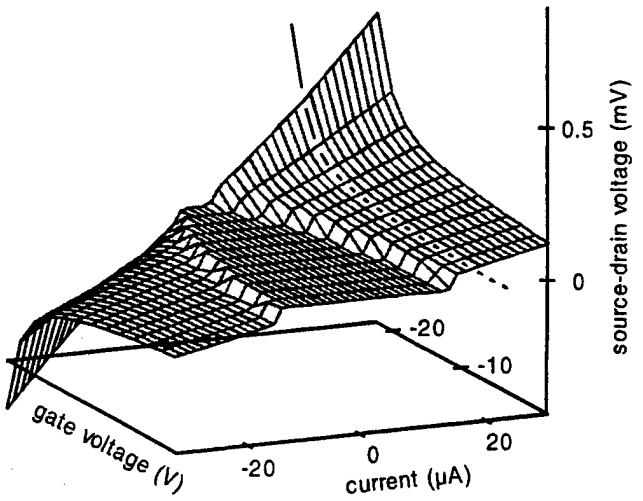

Fig.4: Current-voltage characteristics vs. applied gate voltage of a JoFET with a=600 nm and b=20 μm at T=1.7 K. The dashed line marks the path of gate voltage sweep presented in Fig.5.

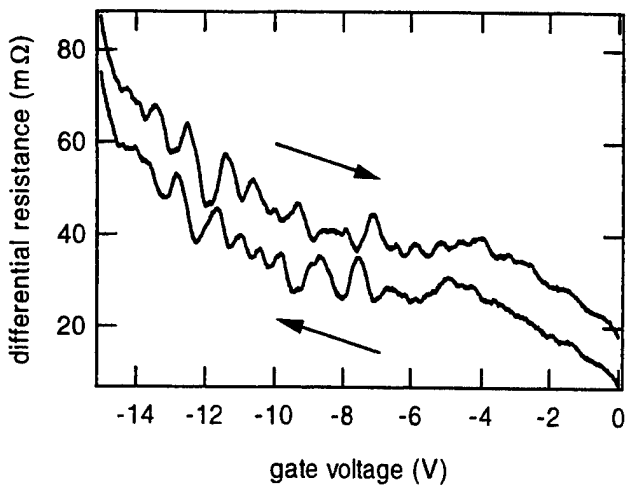

Fig.5: Oscillations in the differential resistance vs. gate voltage. Arrows indicate the sweep direction. The upper curve is offset by +10 mΩ for clarity. The figure shows slightly different peak positions between up and down sweep.

to decrease entering a regime of strong reduction below -22 V (Fig.4). Below about –25 V the critical current is fully suppressed. At the same time the normal state resistance increases significantly. This behavior can be explained by the depletion of charge carriers reducing the conductivity of the heterostructure and the coherence length in the semiconductor. It also agrees with the observation that the SGS structure in the JoFET, which is also very pronounced, does not shift with gate voltage. This means that the values of the superconducting gap and the induced gap remain constant for all gate voltages. The I_CR_N product does not change significantly as long as a critical current can be determined.

A new phenomenon is observed when the differential resistance is measured as a function of the applied gate voltage. For that measurement V_G is sinusoidally modulated by a small amplitude ΔV_G and is swept up and down at a constant bias current $I_B > I_C$ (see Fig.4, dashed line). Such a measurement for ΔV_G=200 mV and I_B=18 μA is shown in Fig. 5. Clear oscillations of the differential resistance can be seen. The positions of the maxima differ slightly for the up and down sweep. This might be due to the strong depletion of the electron system at very high negative voltages leading to a shift in the threshold voltage. A possible explanation for the oscillations can be given in a simple potential barrier picture. Since the Fermi energy in the Nb is much higher than the one in the InAs heterostructure an incoming electron sees the interfaces between super- and semiconductor as potential steps and can therefore be scattered even if its energy is above that of the potential barrier. The transmission probability depends on the electrode separation a and the value of the Fermi wave vector k_F of the electron or the "height" above the step in the semiconducting region, respectively. It becomes maximal for $\pi n/a=k_F$ with n being an integer. The Fermi vector and the barrier height are changed by the applied gate voltage possibly resulting in the more or less periodic oscillations of the differential resistance.

IV. Conclusion

We have prepared Nb Josephson junctions that are coupled by the 2DEG of an InAs heterostructure grown on GaAs. From the existence of high supercurrents, excess currents, pronounced SGS structures, and high I_CR_N products we deduce highly transmissive contacts between the Nb and the 4 nm thick strained InAs layer. The positions of SGS differ from the voltage values $V=2\Delta/(ne)$ presumably as a consequence of an induced energy gap in the density of states of a thin normal conducting layer formed at the interfaces.

In JoFET structures the superconducting properties can be controlled via an applied gate voltage. We observe oscillations in the differential resistance that can be qualitatively explained by a simple potential barrier model.

Acknowledgment

We would like to thank Christian Heyn for his support in the MBE growth.

References

[1] M. Octavio, M. Tinkham, G.E. Blonder, and T.M. Klapwijk, Phys. Rev. B 27(11), pp. 6739-46 (1983)

[2] A. Engelhardt, R. Dittmann, and A.I. Braginski, Phys. Rev. B 59(5), 3815 (1999)

[3] H. Takayanagi and T. Kawakami, Phys. Rev. Lett 54, 2449 (1985)

[4] B.A. Aminov, A.A. Golubov, and M.Yu. Kupriyanov, Phys. Rev B 53(1), pp. 365-73 (1996)

Improvement of uniformity of NbCN/MgO/NbCN Josephson junctions for large scale circuit applications

Hirotake Yamamori and Akira Shoji
Electrotechnical Laboratory, 1-1-4, Umezono, Tsukuba, 305-8568, Japan

Abstract – On-wafer variation of critical current density for NbCN/MgO/NbCN Josephson junctions has been improved by introducing substrate-holder rotation into the deposition of tunnel barriers and base electrodes. From results of AFM observation of surface morphology for NbCN films, it seems that larger grain size in the base electrodes causes lower critical current density for junctions.

I. Introduction

For large-scale circuit application of Josephson junctions, ensuring of high uniformity in their critical current density J_c over a wafer and precise control of its average value are important. For practical application, Josephson junctions with NbCN electrodes have some advantages, e.g., large gap voltages(>5mV) and high critical temperature(>15K). However, there is room to improve uniformity of J_c in comparison with well-developed Nb/AlOx/Nb technology[1], [2]. In this paper, we describe a method to improve uniformity of critical current density for NbCN Josephson junctions with sputter-deposited MgO films as barriers.

II. Experiments

Prior to junction fabrication, we deposited MgO films on Si wafers in an rf-sputtering system(Fig.1) and measured distribution of film thickness over a wafer with an ellipsometer. The diameter of the MgO target was 6 inch and that of Si wafers 3 inch. The Ar gas pressure was 1.33Pa and the incident power 100W. For a film deposited without rotating the substrate-holder, we had a circular thickness distribution as shown in Fig.2(a). Variation of film thickness within 30 mm from the center of the wafer was ± 9.3 % rather large for tunnel barriers. Fig.2(b) shows thickness distribution for a film deposited rotating the substrate holder. By the introduction of substrate-holder rotation, variation of MgO film thickness along a direction parallel to the rotation was reduced to ± 2.3 %. Typical rotation speed of the holder was 10 rpm.

Manuscript received May 1, 1999.

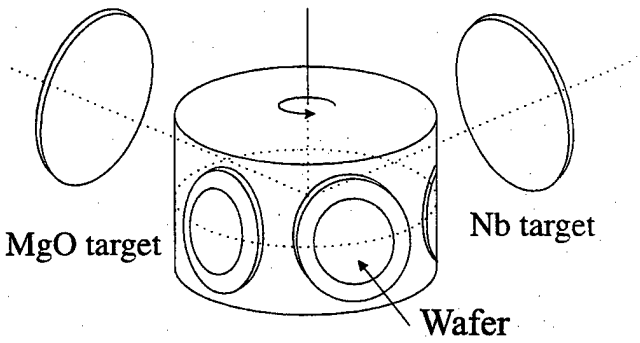

Fig. 1. A schematic view of the rf-sputtering system. Six wafers were placed on the substrate holder and were rotated at 10 rpm during deposition of the MgO and NbCN films.

Based on the experimental results above, we adopted substrate-holder rotation in the MgO barrier formation. In Fig.3, we show typical I–V characteristics for an array of 400 junctions. The on-chip spread of I_c is due to the spread of junction areas, which was caused during photolithography and etching processes. The average I_c value for the 400 junctions was defined as the center value of the spread.

Fig.4 shows J_c values measured along with a direction parallel to the substrate-holder rotation. As seen in this figure, in spite of the use of substrate-holder rotation. measured J_c values varied in a range of 1.5-4.5 kA/cm^2 (± 49.2 %). The large variation of J_c can not be explained by the variation of MgO film thickness shown in Fig.2(b). There is a clear tendency that J_c becomes smaller when the distance of junctions from the center increases.

To improve the uniformity of J_c, we attempted a fabrication of junctions introducing the substrate-holder rotation not only into the barrier deposition but also into the deposition of the base electrode. Fig.5 shows J_c variation for junctions fabricated rotating the substrate holder during both of the deposition of the base electrode and that of the MgO barrier. As shown in Table I, by introducing substrate-holder rotation into the base-electrode deposition, on-wafer uniformity of J_c was much improved.

To reveal the origin of the large variation of J_c in Fig.4, we observed surface morphology of NbCN films

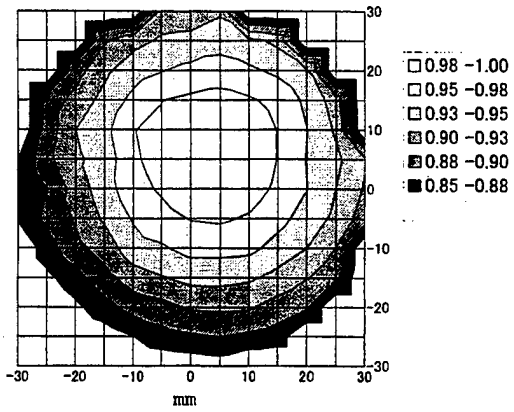

(a) without rotation

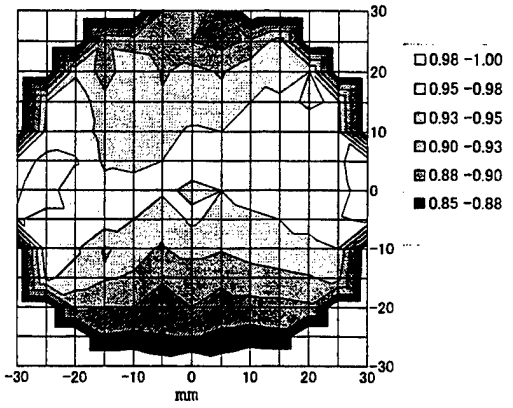

(b) with rotation

Fig. 2. Thickness variation for a MgO film deposited without rotation (a) and that for a film deposited with rotation (b). The thickness variation in direction perpendicular to the rotation in (b) is ± 8.3 %.

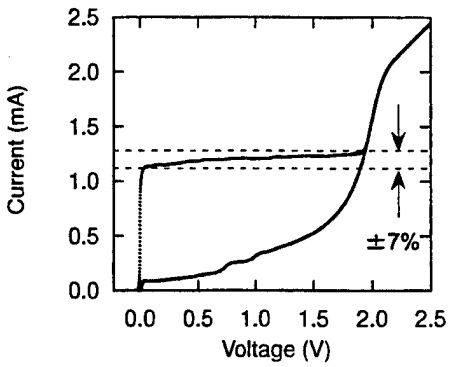

Fig. 3. Current-voltage characteristics for a 400-junction series array at 4.2 K. The size of junction is 3 μm square. Speed of rotation is 10 rpm for MgO barrier and 0 rpm for NbCN electrode. The on-chip variations shown by dashed line is about ± 7 %.

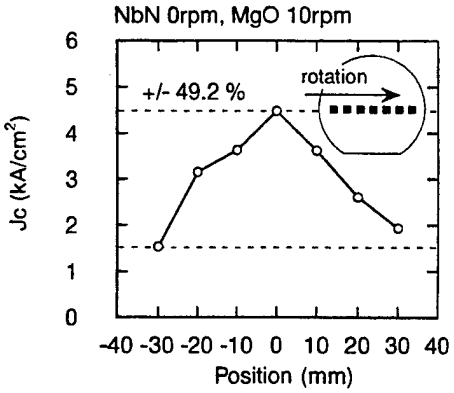

Fig. 4. On-wafer variation of J_c is ±49.2 %. On-wafer variations were calculated by $\delta = \pm(d_{max} - d_{min})/(d_{max} + d_{min})$, where d_{max} and d_{min} denote the maximum and minimum film thickness values, respectively.

TABLE I
VARIATIONS OF CRITICAL CURRENT DENSITY

Rotation (NbCN)	On-wafer variations	On-chip variations
0 rpm	± 42.9 %	± 7 %
10 rpm	± 12.7 %	± 7 %

by atomic force microscopy(AFM). An AFM image observed is displayed in Fig.6. From processing of AFM images with a personal computer, we deduced an average grain size in the films. In Table II, average grain sizes measured at the center of the wafer and at the edge of the wafer for a NbCN film which had been fabricated without substrate holder rotation are summarized with a grain size for a film fabricated with substrate-holder rotation. For NbCN films grown without substrate-holder rotation, grain size slightly increased from the center of the wafer. This tendency corresponds to that of J_c in Fig.4. The grain sizes for NbCN films deposited with substrate-holder rotation were always larger than those for NbCN films fabricated without substrate-holder rotation. This also corresponds to the fact that NbCN/MgO/NbCN junctions with base electrodes fabricated without substrate-holder rotation have relatively lower J_c values than those for junctions with base electrodes fabricated with substrate-holder rotation (Fig.7).

From comparison of grain size values and J_c values in Table II, we presume that larger grain sizes in NbCN base electrodes causes lower critical current densities for junctions although its mechanism is not clear. Influence of crystallographic property of base electrodes to the electrical property of Josephson junctions are also reported in other papers[3]-[5].

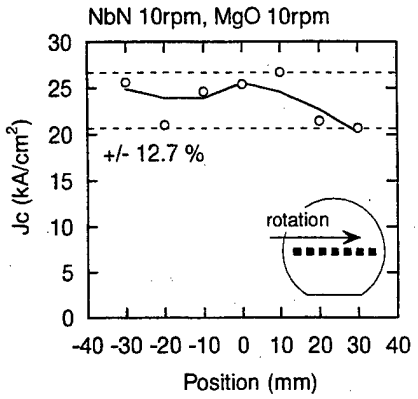

Fig. 5. J_c variations on 3-inch wafer. Not only MgO but also NbCN were deposited with rotation and on-wafer variation of J_c is reduced to ±12.7 %.

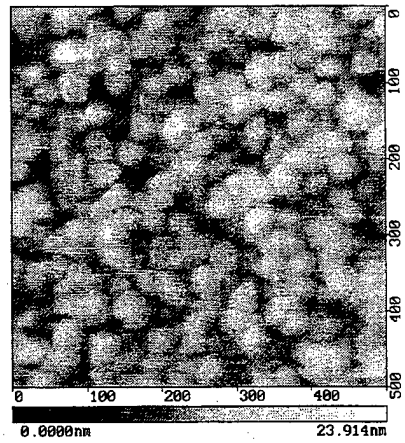

Fig. 6. An AFM image for the surface of NbCN film deposited with rotation at 10 rpm.

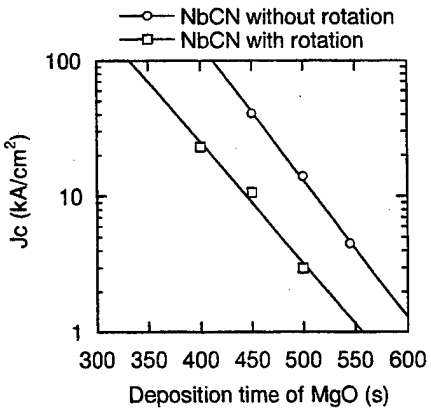

Fig. 7. The relation between critical current density and deposition time of MgO barrier. NbCN electrode deposited with rotation is shown by open circles and that deposited without rotation is shown by open squares. MgO barriers were deposited with rotation for both of them.

TABLE II
GRAIN SIZE OF NBCN FILMS

Rotation (NbCN)	Position	Grain size	J_c
0 rpm	Center	4.0 nm	14.0 kA/cm^2
0 rpm	Edge	4.2 nm	8.5 kA/cm^2
10 rpm	Center	5.6 nm	3.0 kA/cm^2

III. Summary

To improve on-wafer uniformity of J_c for NbCN/MgO/NbCN Josephson junctions, we have introduced substrate-holder rotation into the deposition of MgO barriers and also into the deposition of NbCN base electrodes. As a result, much improvement has been made in the variation of J_c along with a direction parallel to the rotation. From results of AFM observation of surface morphology for NbCN films, it seems that larger grain sizes in NbCN base electrodes causes lower critical current densities for junctions.

Acknowledgment

The authors would like to thank S.Kohjiro and T.Kikuchi for discussions and technical assistance, and T.Maeda for AFM observation.

References

[1] X.Meng, H.Jiang, A.Bhat, and T.Van Duzer, "Precise control of critical current and resistance in a Nb/AlOx/Nb Integrated circuit process," *6th ISEC'97. Ext. Abstr.* vol. 2 pp.164-166, 1997

[2] A.D.Smith, S.L.Thomasson, and C.Dang, "Reproducibility of niobium junction critical currents: statistical analysis and data," *IEEE Trans. on Appl. Supercond.* vol.3, pp.2174-2177, 1993

[3] S.Kominami, H.Yamada, N.Miyamoto, and K.Takagi. "Effects of underlayer roughness on Nb/AlOx/Nb junction characteristics," *IEEE trans. on Appl. Supercond.*. vol.3, pp.2182-2186, 1993

[4] E.C.G.Kirk, M.G.Blamire, R.E.Somekh, and J.E.Evetts, "The influence of Al morphology on quality in Nb/AlOx/Al/Nb epitaxial base layer junctions." *IEEE trans. on Appl. Supercond.*, vol.3, pp.2178-2181. 1993

[5] T.Imamura, T.Shiota, and S.Hasuo, "Fabrication of high quality Nb/AlOx-Al/Nb Josephson junctions: I-Sputtered Nb films for junction electrodes," *IEEE trans. on Appl. Supercond.*, vol.2, pp.1-14, 1992

SNS and SIS Josephson junctions with dimensions down to the sub-micron region prepared by an unified technology

L. Fritzsch, H. Elsner, M. Schubert, and H.-G. Meyer
Institute for Physical High Technology, Dept. of Cryoelectronics, Winzerlaer Str. 10, D-07745 Jena, Germany

Abstract—Several applications of Josephson junctions (JJ) in low temperature superconducting circuits as for instance programmable voltage standards and SFQ logical circuits or SQUID sensors require JJ with sub-μm dimensions.

A method for preparing superconductor-isolator-superconductor (SIS)-JJ as well as superconductor-normal metal-superconductor (SNS)-JJ was developed which allows the preparation of both types of junctions by nearly the same technological process. Titanium is introduced as normal metal for the SNS-JJ. Ti can be anodically oxidized and a technology similar to the well-tried Nb/Al-technology for SIS-JJ can be used for the SNS system, too. By electron-beam exposure of a negativ deep UV (DUV) photoresist (ma-N 2400) a stable resist mask is generated which has to withstand the following three self-aligned process steps: etching of the Nb counterelectrode by RIE, isolation by anodization and lifting of a SiO planarization layer.

By this process SNS (Nb-Ti-Nb) and SIS (Nb-Al/AlO_x-Nb) Josephson junctions with smallest junction areas of 0.49 μm^2 were prepared and characterized by dc-measurements and under the influence of microwave irradiation. The Nb-Ti-Nb junctions have I_cR_n products of 87 μV. They can be used for programmable Josephson voltage standard circuits at frequencies of 70 GHz.

I. Introduction

Josephson junctions with micron and sub-micron dimensions are of considerable interest for SFQ logical circuits or programmable voltage standards in the form of SNS-JJ and as SIS-JJ for SQUID sensors. For SIS-JJ the well-tried Nb/Al process [1], [2] is used in several modifications in order to prepare junctions with sub-micron dimensions. One main technological problem is the encroachment of the anodized Nb film beneath the resist mask. This problem is solved by hardening the resist, use of special anodization mask films or by renounciation of the anodization process [3]-[8].

Small SNS-JJ in micron dimensions are used for instance in programmable Josephson voltage standards. Such circuits, consisting of 32,768 Nb-AuPd-Nb junctions, have been successfully fabricated and tested [9]. Because of the AuPd normal-metal interlayer the isolation of the junctions cannot be made by anodization as in the conventional Nb/Al technology [10]. Therefore some other technological problems arise, especially with the wiring contact to the junction counter electrode, which must be realized through a window in the SiO_2 isolation. Because of the clear technological benefits of the anodization method we looked for a normal metal in the SNS-JJ that can also be anodized.

Manuscript received April 30, 1999.

We have tested titanium as a new material for the normal-metal interlayer in SNS-JJ's. The Ti film can be anodized as in the Nb/Al process [11], [12]. Therefore this well-tried technology can be widely used for the preparation of the Nb-Ti-Nb junctions.

To overcome the mask instability problems with small junction areas during the anodization a separate mask according to [6] is inserted. In our case this mask layer is made of evaporated SiO.

II. Sample Preparation

The process is started with the in-situ deposition of a four-layer film system onto a 3-inch thermally oxidized Si wafer. The film system consists of an Al contact-layer with a thickness of 36 nm. This layer is followed by the Nb base electrode (150 nm thick). The barrier material is Ti in the case of SNS-JJ. Its thickness is in the range of 20 ... 35 nm

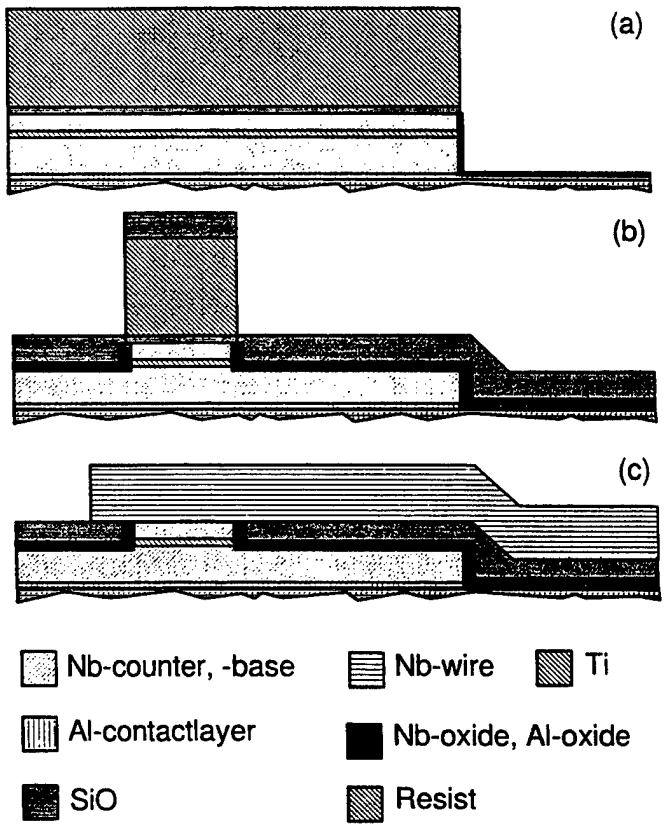

FIG. 1. Schematic diagram of the preparation process of a Nb-Ti-Nb SNS junction. (a) Patterning of the junction base electode and generation of the first sidewall isolation. (b) Definition and isolation of the junction counter electrode, lift-off of a SiO planarization layer. (c) Etching of the SiO anodization-mask layer, deposition and patterning of the upper wiring.

depending on the required I_cR_n product. The barrier for the SIS-JJ is prepared in the conventional way by oxidation of an Al film (thickness 12 nm) in pure oxygen atmosphere in the load-lock of the deposition system. At last the counterelectrode of Nb is sputtered with a thickness of 80 nm. Nb and Al are deposited by dc-magnetron sputtering, Ti by rf-diode sputtering. These four layers are covered by a 50 nm thick SiO-film which is evaporated in a separate deposition chamber after an ion-beam cleaning step. The SiO layer serves as mask for the isolation of the junction sidewalls by anodization.

To define the base wiring the upper four layers are etched down to the Al contact-layer (see Fig. 1a) by reactive ion etching (RIE) using CF_4 gas for SiO and Nb and SF_6 for Ti. The Al/AlO_x barriers of the SIS-JJ are removed by rf-sputter etching in Ar gas. In this first photolithographic step the alignment marks for subsequent electron-beam lithography steps are defined, too. The etching processes are followed by a first soft anodization up to a voltage of 10 V, using the same resist mask. By this anodization the sidewalls of the base electrode and the first 8 nm of the Al contact layer are anodized. This thin AlO_x layer prevents an etching of the Al by the alcaline resist developer during the second lithographic step. This second resist mask defines the junction area and is generated by electron-beam exposure of the DUV resist ma-N 2400 [13], [14]. The resist is 800 nm thick and allows aspect ratios up to three in the structures. The smallest junction areas we realized up to now are 0.7 µm x 0.7 µm. The mask has to withstand three process steps (Fig. 1b). The first one is the definition of the junction area by RIE of the SiO anodization mask and the Nb-counter electrode. The etching stops at the Al/AlO_x barrier. In the case of SNS-JJ the Ti is etched, too. This etching is followed by a second anodization for the isolation of the junctions. The anodization stops as soon as the Al contact layer is completely oxidized. This corresponds to an anodization voltage of about 45 V. In a third step a SiO planarization layer can be evaporated and lifted off. Its thickness has to be choosen so, that the height of the planarizing layer coincides nearly with the height of the anodization-mask layer at the top of the junctions. After removing the resist mask the SiO layer is etched away from the Nb counter electrode by CF_4-RIE. In the last step the Nb wiring is deposited and patterned (Fig. 1c). The resist mask for the wiring definition is generated by electron-beam exposure. Because the alignment marks are covered by the wiring layer, they have to be opened by a preceding standard photolithographic lift-off step. The Nb wiring layer has a thickness of 300 nm and is structured by CF_4-RIE.

III. Measurements

The measurements were made in an unshielded room in a liquid-helium dewar at 4.2 K. The chip itself was magnetically shielded by a tube of soft magnetic material. A representative tunnelling characteristic of a SIS Josephson junction with a designed junction area of 0.7 µm × 0.7 µm is given in Fig. 2. The critical current is 10.5 µA and the corresponding critical current density j_c is about 2.1 kA/cm^2.

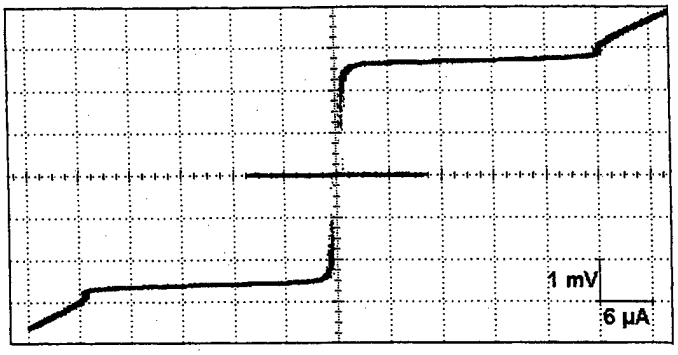

FIG. 2. Current-voltage characteristic of a single 0.7 µm × 0.7 µm Nb-Al/AlO_x-Nb Josephson junction.

Characteristic parameters of tunnel junctions are the I_cR_n- and the I_cR_s -product with 1.06 mV and 19 mV, respectively.

In the case of Nb-Ti-Ni Josephson junctions we have used different thicknesses d of the Ti interlayer. The critical current density as a function of the interlayer thickness can be fitted by $j_c = (360\ \text{mA}/\mu\text{m}^2)\cdot\exp(-d / 4.9\ \text{nm})$. Fig. 3 presents a typical current-voltage characteristic of a Nb-Ti-Nb Josephson junction at 4.2 K. The nominal junction area is 0.7 µm × 0.7 µm with an interlayer thickness of 20 nm. From the measured critical current of $I_c = 3$ mA we calculate the critical current density j_c to about 610 kA/cm^2. The normal state resistance R_n of the junction is 28 mΩ and hence an estimation of the Ti interlayer resistivity yields $\rho_n = 70\ \mu\Omega\text{cm}$. This is in reasonable agreement with measurements on 80 nm thick Ti films which showed at 4.2 K a resistivity in the range of 50 to 200 µΩcm, depending on the residual gas conditions during the deposition.The bulk resistivity of Ti is 54 µΩcm at room temperature.

An important parameter for the junctions dynamic behavior is the characteristic voltage I_cR_n. With our sub-micron Nb-Ti-Nb junctions we achieved a value of $I_cR_n = 87\ \mu\text{V}$. This allows microwave excitation at such frequencies which are relevant for practical applications. Fig. 4 shows Shapiro steps of the zero, first, second and third order with amplitudes in the milliampere range at a drive frequency of 20 GHz. We irradiated this junction also with a micowave field at 75 GHz. Fig. 5 presents the resulting current-voltage characteristic

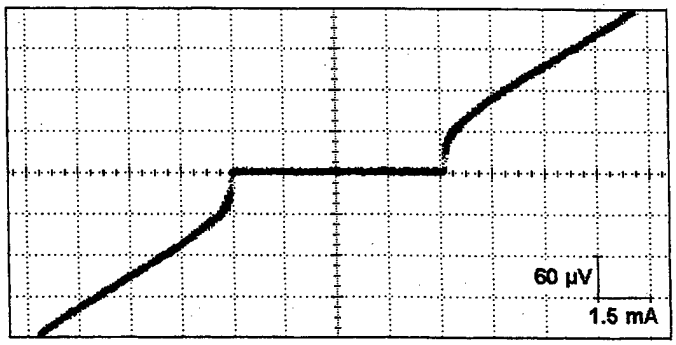

FIG. 3. Current-voltage characteristic of a single 0.7 µm × 0.7 µm Nb-Ti-Nb Josephson junction.The I_cR_n-product is 87 µV.

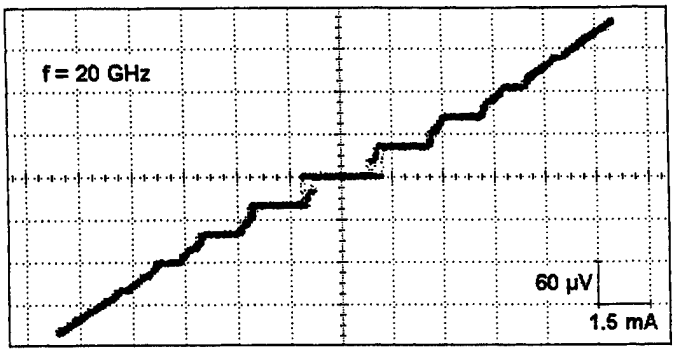

FIG. 4. Current-voltage characteristic of the single 0.7 μm × 0.7 μm Nb-Ti-Nb Josephson junction under influence of 20 GHz irradiation.

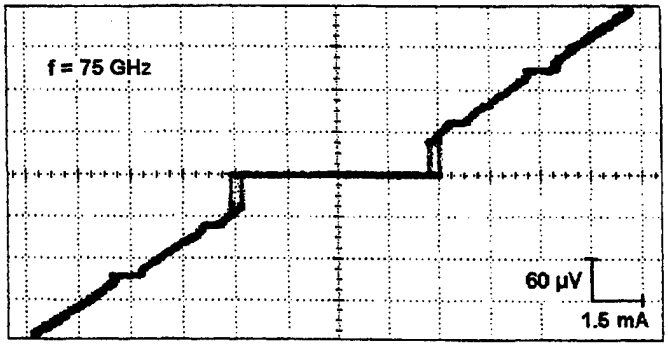

FIG. 5. Current-voltage characteristic of the single 0.7 μm × 0.7 μm Nb-Ti-Nb Josephson junction under influence of 75 GHz irradiation.

characteristic. Constant-voltage steps appear at 77.5 and 155 μV. In this case the lower voltage corresponds to a halfharmonic step. The stepwidths of 400 and 800 μA, respectively, were limited by the ineffective microwave excitation. This type of JJ offers a good potential for the application in programmable Josephson voltage standard circuits driven at frequencies up to 75 GHz.

IV. SUMMARY

SIS and SNS Josephson junctions with sub-micron dimensions were prepared using the well known anodization technique for the junction isolation in both cases. The SNS junctions with Ti normal-metal layer show under microwave irradiation up to frequencies of 75 Ghz wide and stable Shapiro steps. The I_cR_n-product of SNS junctions with an area of 0.7 μm × 0.7 μm is 87 μV. Such junctions may find a promising application both in programmable voltage standard and in SFQ circuits.

REFERENCES

[1] H. Kroger, L.N. Smith, and D.W. Jillie, "Selektive niobium anodization process for fabricating Josephson tunnel junctions," *Appl. Phys. Lett.*, vol. 39, pp. 280-282 , August 1981.

[2] H. Gurvitch, M .A. Washington, and H. A. Higgins, "High quality refractory Josephson tunnel junctions utilizing thin aluminum layers," *Appl. Phys. Lett.*, vol.42, pp. 472-474, 1983.

[3] M. M. T. M. Dierichs, R. A. Panhuyzen, C. E. Honingh, M. J. de Boer, and T. M. Klapwijk, "Submicron niobium junctions for submillimeter-wave mixers using optical lithography," *Appl. Phys. Lett.*, vol. 62, pp. 774-776, February 1993.

[4] L. P. S. Lee, E. R. Arambula, G. Hanya, C. Dang, R, Sandell, and H. Chan, "RHEA (resist-hardened etch and anodization) process for fine.geometry Josephson junction fabrication," *IEEE Trans. Magn.*, vol. 27, pp. 3133-3136, March 1991.

[5] A. H. Worsham, D. E. Prober, J. H. Kang, J. X. Przybysz, and M. J. Rooks, "High-quality sub-micron Nb trilayer tunnel junctions for a 100 GHz SIS receiver," *IEEE Trans. Magn.*, vol. 27, pp. 3165-3167, March 1991.

[6] T. Imamura and S. Hasuo, "A submicrometer Nb/AlO_x/Nb Josephson junction," *J. Appl. Phys.*, vol. 64, pp. 1586-1588, August 1988.

[7] H. Dang and M. Radparvar, "A process for fabricating submicron all-refractory Josephson tunnel junction circuits", *IEEE Trans. Magn.*, vol. 27, pp. 3157-3160, March 1991.

[8] S. E. Huq, M. G. Blamire, J. E. Evetts, D. G. Hasko, and H. Ahmed, "Fabrication of sub-micron whole wafer SIS tunnel junctions for millimeter wave mixers," *IEEE Trans. Magn.*, vol. 27, pp. 3161-3164, March 1991.

[9] S.P. Benz, C.A. Hamilton, C.J. Burroughs, T. E. Harvey, and L. A. Christian, "Stable 1 volt programmable voltage standard," *Appl. Phys. Lett.*, vol. 71, pp. 1866-1868, September 1997.

[10] S.P. Benz, "Superconductor-normal-superconductor junctions for programmable voltage standards," *Appl. Phys. Lett.*, vol. 67, pp. 2714-2716, October 1995.

[11] S. P. Zhao, H. Du, G. H. Chen, Q. S. Yang, "Fabrication and properties of all-refractory Nb/Al-AlO_x-Ti junctions for microbolometers and microrefrigeratores", *Appl. Phys. Lett.*, vol. 72, pp. 3062-3064, June 1998.

[12] L. Fritzsch, M. Schubert, G. Wende, and H.-G. Meyer, "Superconductor-normal-metal-superconductor Josephson junctions with Ti interlayer", *Appl. Phys. Lett.*, vol. 73, pp. 1583-1585, September 1998.

[13] H. Elsner, H.-G. Meyer, A. Voigt, and G Grützner, "Evaluation of ma-N 2400 series DUV photoresist for electron beam exposure", Int. Conf. Micro and Nano-Engineering 98, September 22-24, 1998, Leuven, Belgium. Accepted for publication in *Micro Engng.*, 1999.

[14] Resist ma-N 2400 delivered by: Micro Resist Technology GmbH, Berlin, Germany

Nondestructive Imaging of the Microwave Properties of Superconducting Thin Film Devices and Substrates with a Scanning Microwave Near-Field Microscope

Y.J.Feng*, L.Liu, Q.G.Liu, L.X.You, L.Kang, P.H.Wu
Department of Electronic Science and Engineering, Nanjing University, Nanjing, 210093, P.R.China

Recently, the superconducting microwave devices have found significant applications in high-performance wireless communication system due to their very low losses and high quality factor. For commercializing these microwave devices, one of the major obstacles is the inhomogeneous microwave properties over large-area superconducting thin films. It is quite important to study the local microwave properties, such as the surface resistance of the thin film or the dielectric constant of the substrate over the whole wafer. In this paper, nondestructive microwave scanning techniques have been used to image the local microwave properties of the planar microwave devices. Either a coaxial cavity or an open-ended coaxial transmission line has been used as a probe in our scanning microwave near-field microscope. Quantitative images of the surface resistance of metal film samples as well as the dielectric constant of the substrates have been obtained. Comparisons of the spatial resolutions and the image qualities have been made for these two different kinds of microwave probes. Local surface resistances at 3GHz have been imaged on microwave devices prepared by laser ablated YBaCuO thin films. To study the influence of the patterning process on the spatial variation of the surface resistance, the inhomogeneity of the YBaCuO superconducting thin films at the microwave frequency has been studied systematically on both the wet-etched patterns and the argon ion etched patterns. These results would be helpful in evaluating the performance of the devices.

Material science and surface impedance Z(T,f,H) of Nb and YBCO and their quantitative modeling by the leakage current of weak links

J. Halbritter
Forschungszentrum Karlsruhe
Institut für Materialforschung I
Postfach 3640, 76021 Karlsruhe
Germany

Abstract - In Nb_2O_{5-x}-junctions the critical Josephson current $j_{CJ}(T)$ is accompanied by a small leakage current j_{bl} ($\propto 1/R_{bl}$) and hence, the rf residual losses R_{res} by weak links are small. HTS-in-plane weak links show very much reduced $j_{CJ}(0)$-values compared to theory and a large leakage current j_{bl} of the order of j_{CJ} due to a high density of intermediate states in disordered HTS junction material. The finite $R_{res}(T,f,H)$ by weak links in distances a_J are due to the finite normal conducting leakage current with $R_{bl}(T < 0.8\ T_c) \approx$ const., where the $R_{res}(T)$-dependence is dominated by $j_{CJ}(T) \approx j_{CJ}(0)(1 - T/T_c)$. Quantitative agreement experiment – model is obtained by measured values of a_J($\approx 0.2 - 20$ μm), of R_{bn} ($\approx 1000 - 1$ nΩcm²), and of j_{CJ}($\approx 10^2 - 10^7$ A/cm²) yielding $j_{CJ}R^2_{bl} \approx 10^{-12}$ AΩ²cm². Aside of this agreement the measured T-,f- and H-dependencies $R_{res}(T<0.8T_c,f,H) \approx R^0(1+T/T_c)\ f^\alpha(1+H_{rf}/H_{c1J})$ are modeled quantitatively by a distribution of weak links ($\alpha < 2$) with scaling fields $H_{C1J} \propto \sqrt{j_{CJ}}$. The latter results fits to Josephson fluxons for $j_{CJ} < 10^7$ A/cm² and $H_{rf} <$ mT with short hops according to $\delta X(T,f,H_{rf})/\delta R(T,f,H_{rf}) \approx 2$ observations. Hence, for HTS-samples over 7 orders of magnitude, up to $j_{CJ} \propto \leq 10^7$ A/cm² being much smaller than the intrinsic critical depairing current with $4 * 10^8$ A/cm², a distribution of weak links with their leakage current resistance R_{bl} describes $R(T < 0.8\ T_c, f, H)$ quantitatively.

I. INTRODUCTION

Defects define properties of real materials. This general statement is especially true for rf superconductivity, and even more for HTS's, which are far away from 'single crystals'. Those defects are not known 'a priory' and need extensive material and rf studies but their quantification is the prerequisite for the identification of intrinsic properties. The first consistent quantification of defects relevant for YBCO in rf fields is the goal of this paper. In the case of the metallic superconductor Nb, the studies in the last 30 years finally yielded the coherent model: the prominent defects are oxides extending from the oxide-metal boundary 10 – 100 nm deep into the metal [1,2]. Those Nb-NbO_x-Nb_2O_{5-y}-NbO_x-Nb(x,y < 1)-layers yield weak links, i.e. Josephson junctions in the superconducting state. Those specific defects, their of quantification and the successful identification methods for Nb are summarized in Sect.2 shortly. With this background results on YBCO are summarized in Sect. 3 and discussed in Sect. 4.

II. RESIDUAL RF SURFACE IMPEDANCE RELEVANT DEFECTS

Nb oxidation causes crack corrosion, i.e. oxide filled cracks, which act in the superconducting state as Josephson junctions or weak links (WL). Those WL grow deeper into the Nb for dirtier Nb or for heavier oxidation attack [1]. The weak links are described by the Josephson critical current $j_{cJ}(T)$ and by the normal leakage current resistance R_{bl} staying finite for $T \rightarrow 0$ [1,2]. The WL yield rf residual losses R_{res} [1-5]

$$R(T,f) = R^*_{BCS}(T,f) + R_{res}(T,f). \qquad (1.1)$$

The BCS-like surface resistance $R^*_{BCS} = R^*_{BCS}(T,f,\lambda_{BCS},\zeta_F,l)$ yields the material parameters of the superconducting state, like $2\Delta/kT_c$ or the mean free path l [3]. Also the penetration depth $\lambda(T,f)$ shows deviation from the BCS theory [1]. Those deviations from 'intrinsic properties', identified by measuring and analyzing Z(T,f,H) for various oxidation and Nb conditions combined with interface studies, yielded the 'weak links' with their NbO_x-Nb_2O_{5-y} - interface as the prominent defect [1,2]. The Nb_2O_{5-x}-junctions show a slightly degraded critical Josephson current and Ambegoakar-Baratoff-relation [6a].

$$j_{cJ}(O)R_{bn} \approx \pi\Delta(O)/2e(1+R_o/R_{bl});\ 1/R_{bn} = 1/R_o + R_{bl} \qquad (2.1)$$

by the leakage current $R_{bl} \geq R_o$ in parallel to direct tunneling R_o and with $\Delta(T)$ the superconducting gap, where the oxygen vacancies "y" yield the normal leakage tunnel current and inelastic surface scattering reducing the mean free path.

Whereas $R_{res}(GHz) \approx$ nΩ of Nb are due to strong links in distances $a_J \approx 10$ nm extending only about 10nm deep into bulk Nb [5], the growth of YBCO itself yields weak or strong links extending throughout the material with $R_{bn} \approx R_{bl} \ll R_o$ causing $R_{res}(GHz) \geq$ μΩ. The HTS-junctions follow [6b,c]

$$j_{CJ}R_{bn} = \hbar/2e\tau_J \approx 10^{-12}\text{VΩcm}^2/R_{bn};\quad j_{CJ}R_{bn} \ll \Delta/e \qquad (2.2)$$

with τ_J the Josephson frequency being in HTS preparation dependent, as shown, e.g., by the percolation analysis of the resistivity $\rho(T>T_c)$ [7]

$$\rho = R_{bn}/a_J + p\,(\alpha^i T + \rho^i_{OL}) \qquad (2.3)$$

with the intrinsic values for optimal doping of $\alpha^i = 0.5$ μΩcm/K and $\rho^i_o \approx -40$ μΩcm and $p \geq 1$ the percolation factor describing, e.g., conduction path lengthening. With the Josephson penetration depth

$$\lambda_J(T) = \sqrt{\hbar/2e\mu_o\, 2\lambda_{BCS}(T) j_{cJ}(T)}$$

$$j_{cJ}(T) = j_{cJ}(0)(1 - T/T_c) \qquad (2.4)$$

The rf residual losses for $a_J \gg \lambda_{BCS}$ are given by [4b]

$$R_{res}(T) = R^*_{res} + \frac{2(\omega\mu_0\lambda_{BCS}(T))^2}{1+(\omega\tau_J)^2} * \frac{\lambda_J(T)^{3/2}}{a_J R_{bl}} \quad (1.2)$$

where R^*_{res} describe extrinsic losses, e.g., due to the experimental set-up and $\tau_J(T) \propto 1/R_{bl}$ describes the leakage current losses in the RSJ-model. In 'granular' superconductors at GHz fields $H_{c1J} < H_{c1}$ Josephson fluxons enter weak links, with $H_{c1J} = H_{c1}\,\lambda_{BCS}/\lambda_J$ yielding nonlinearities in R(H) and $j_{cJ}(H)$ [4]:

$$j_{cJ}(H) = j_{cJ}(0)(1+\gamma^*(H/H_{c1J}) + \dots). \quad (3)$$

The analysis of $\delta R(H^{\parallel},T)$, or $\delta R(E^{\perp},T)$, yield crucial information on non-linearities. A unique method to identify and separate nonlinear mechanisms $\delta R \propto H^n$ and $\delta X \propto H^n$ is the use of $r = \delta X(T,f,H)/\delta R(T,f,H)$ with its specific T- and f-dependencies [4b].

III. DEFECTS AND Z(T,F,H)-CHANGES OF $YBa_2Cu_3O_{7-\delta}$ WITH PREPARATION

Above, the importance of Z-changes with preparation has been shown as key for the identification of defects governing Z(T,f,H). For Nb, where the BCS theory acts as frame, it was possible to separate $R_{res} \approx R_{res}(T<T_c/2)$ in an unique way and to identify NbO_x-precipitations and Nb_2O_{5-y}/NbO_x weak links. In contrast for HTS, a theory does not exist, yet. Proposed are s- or d-wave order parameters [9], which, both, successfully fit the Z(T,f)-data between about $0.8T_c$ and T_c[8,9]. For lower temperatures R_{res}(T,f,H)-dependencies, are well fitted by weak links [4,5,9-12], as shown below.

Surface resistance data R(T) of differently prepared YBCO are fitted in Figs. 1-2 by intrinsic theories starting at 300 K or 100 K down to about $T_c/2$. In contrast to low temperature superconductors (LTS), where impurity scattering with $l(T \le T_c)$ = const. holds, in HTS the electron-electron interaction dominates, yielding in R_{BCS}(T,f)-fits a rapid mean free path increase $l(T<T_C) = l(T_C)\exp(\Delta T^*/T)$ with $\Delta T^* \approx 3$ K for epitaxial films [9a,c] and $\Delta T^* \approx 6$ K for single crystals [9a], where $l(T_c)$ and $l_{sat}(T \le 0.8\ T_c)$ depend on position and sample. The l(T)-increase saturates at $l(T \le 0.8\ T_c) \approx a_J/2$ (see Fig. 1a), where weak link residual losses take over. In Fig. 1b for epitaxial films and in Fig. 2 for differently prepared sintered YBCO fits of $R_{res}(T < 0.8\ T_c)$ to Eq.(1.2) are presented. The weak link parameters obtained by percolation analysis using Eq. (2.3) can account for R_{res}(T,f) quantitatively by j_{cJ}-values up to 10^7 A/cm^2 and $R_{bl} \simeq 10\text{-}10^{-4}$ $\mu\Omega$ cm^2 with $j_{cJ}R^2_{bl} \approx 10^{-12}$ VΩcm^2.

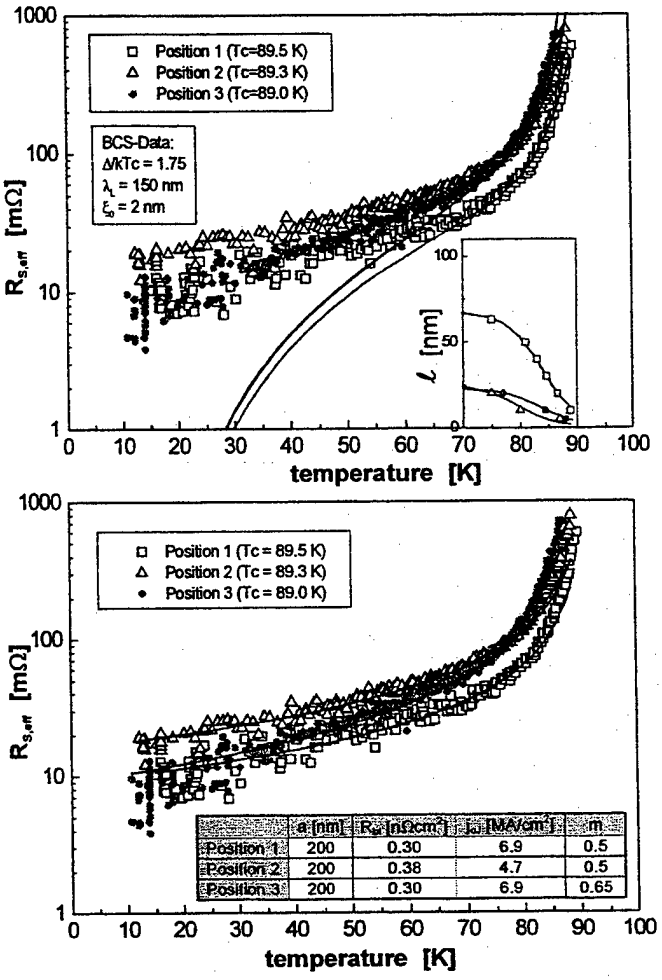

Fig. 1: Surface resistance R(T,145 GHz) of a sputter deposited YBCO film (400 nm YBCO/CeO_2/Saphir [8]). Sputter- and pulsed laser deposited YBCO films show similar R(T) spreads and R_{res}(T) values [10]. The coevaporated films (CVD) are more uniform with ΔT^*- and R_{res}-values agreeing with, e.g., PLD.

1a: The BCS-fit of R(T,145 GHz) from T_c down yields the strong l(T) increases needed at 145 GHz to steepen the R(T)-decrease. Stronger l(T)-increases in the insert yield larger $l_{sat}(T \le 0.8\ T_c)$- values corresponding to smaller R_{res}(T) values.

1b: Weak link fit to $R(T<0.8T_c)$ with the indicated parameters.

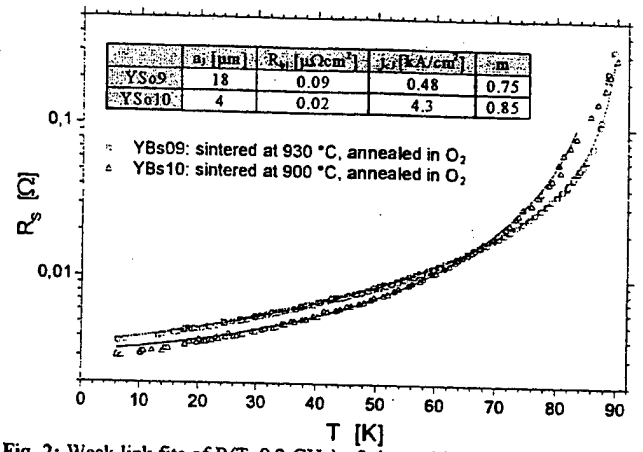

	a_J [µm]	R_{bi} [µΩcm²]	j_{cJ} [kA/cm²]	n
YSo9	18	0.09	0.48	0.75
YSo10	4	0.02	4.3	0.85

Fig. 2: Weak link fits of R(T, 9.2 GHz) of sintered YBCO with the parameters indicated [11].

IV. DISCUSSION

Following [9], R(T) from T_c down to about 0.8 T_c for various samples [8-12] have been fitted quantitatively by the BCS theory with $\lambda_{BCS}(0)$ = 150 nm, ξ_F = 2 nm as dimension of Cooperpairs and $2\Delta/kT_c$ = 3.5 which results in the plotted $l(T<T_c)$ increases saturating at about 0.8 T_c. This fast increase and saturation at about $a_J/2$, like the $2\Delta/kT_c$ = 3.5-value, have been confirmed by relaxation measurement [13]. Similar l(T)-increases are obtained by d – wave fits [9b], and, hence, with the support of [13] we stick to the full BCS-theory. As a sideline, in $\lambda_{BCS}(T,l)$ this l(T)-increase yields the $\lambda(T) \propto 1/\sqrt{1-t^2}$ dependencies of phenomenological two fluid models [8,10,14] being consequently not intrinsic. The l(T) increase of Fig. 1a yields a drastic reduction of the frequency dependence $R_{BCS}(T,f) \propto f^{\alpha}$ from α (0.95 T_c) ≈ 1.5 to α(0.8 T_c) ≈ 0.5 between 10 and 150 GHz and a corresponding reduction of $\lambda_{BCS}(T,f)$ [3].

The finite rf surface resistance in Figs. 1-2 for $T<T_c/2$ indicates rf residual losses $R_{res}(T)$, like in the case of Nb, by weak links [1,2,5]. Fits to Eq. (1) are shown in Figs. 1b and 2, proving the good description of the $R_{res}(T)$-data. The obtained a_J- and $j_{cJ}(0)$-values agree with independent measurements [15]. In addition, $R(T< 0.8\ T_c,f)$ yield one value $j_{CJ}R_{bl}^2 \cong 10^{-12}$ $A\Omega^2cm^2$ if fitted with Eq. (1.2) using measured a_J,- j_{CJ}-, and $R_{bl} \cong R_{bn}$ – values [10,11], i.e. over seven orders of magnitude $R_{res}(T,f)$ yield one $j_{CJ}R_{bl}^2$-value identical with natural and artificial junctions [6]. The j_{cJ}- and R_{bn}-values for best films of 10^7 A/cm² < $4\cdot10^8$ A/cm² and of $10^{-9}\Omega$ cm² > 10^{-11} Ω cm² = R_{Sh} are a factor 50 off the intrinsic critical depairing current or Sharvin resistance R_{sh} prove that the rf residual losses are extrinsic in nature and well described by 'weak' or 'strong' links in YBCO. The quality of YBCO-junctions described by R_{bn}/R_{sh}> 50 and $j_{CJ}R_{bn} \propto 1/R_{bn}$ yield $j_{cJ}(T) = j_{cJ}(0)\ (1-T/T_c)$ confirmed by Figs. 1 and 2 as compared to $j_{cJ}(T<T_c/2) \approx$ const. for Nb with $R_{bn}/R_{Sh} \leq 3$, $j_{CJ}R_{bn} \approx \pi\Delta/2$ and R_{res} (1 GHz) being two to three orders below the typical values of YBCO [2,9]. Those YBCO R_{res} values typical for epitaxial films and single crystals are still well above the intrinsic upper d-wave limit of R^d_{res}(GHz) ≈ 0.1 µΩ [9] increasing fith f^2 $R_{res}(T,f) \propto f^{\alpha}$ of Eq. (1.2) yields a slope between α = 2 for $\omega\tau_J \ll 1$ for 'good' and α = 0 for $\omega\tau_J > 1$ for bad junctions explaining so the plateau in [8,9] by differences in f- and T-depencence of R_{BCS} and R_{res}.

The small, intrinsic field dependencies δR(H), scaling like $(H/H_c)^2$or (H/H_{c1J}) [4,9] are difficult to measure not only because of their smallness but also because according to Figs. 1 and 2 extrinsic, weak link residual losses dominate in YBCO below 0.8 T_c. The intrinsic YBCO fields have values $H_c \simeq$ 1T and $H_{c1} \simeq$ 0.12 T [4]. Accordingly, the observed R(H) increases of [9c] with $H_{c1J} \approx$ 5mT as scaling field in Eq. (3) are extrinsic in nature, namely by weak links. Fields of $H_{c1J} \approx$ 5mT correspond to $j_{cJ} \approx 10^7$A/cm², fitting nicely to our R_{res} results in Fig. 1b for epitaxial films. The above 'weak link networks' show r(T,f) ≈ 1 [12] indicating hysteresis losses [4]. Granular YBCO of Fig. 2 with $j_{CJ} \approx 10^3$ A/cm² yield in δR(H) [12] $H_{C1J} \approx$ 0.1 mT, i.e. $H_{C1J} \approx \sqrt{j_{CJ}}$ which is in line with Josephson fluxon penetration.

V. CONCLUSION

The above analysis gave, for the first time, a consistent description of $R_{res}(T,f)$ and dR_{res}/dH with independently measured weak link parameters like R_{bn}, a_J or j_{cJ} in a j_{cJ}-range of 7 orders of magnitude with one value $j_{CJ}R_{bn} \approx 10^{-12}$ $V\Omega cm^2/R_{bn}$. Up till now, no intrinsic d-wave properties have been found in our surface resistance results being well above the upper d-wave limit for typical YBCO-results. Only good agreement with Nb corrosion or granular Nb film results is found [2].

REFERENCES

[1] J. Halbritter, A 43, 1 (1987) and J. Less-Common Metals 139, 133 (1988) and references therein

[2] a. J. Halbritter, J. Appl. Phys. 68, 6315 (1990) and 71, 393 (1992)
b. J. Halbritter, Proc. 5th Workshop on rf Superconductivity Aug., 1991 (DESY M-922-01), p. 939

[3] J. Halbritter, Z. Phys. 266, 209 (1974) and J. Superconductivity 4, 431 (1991) and 5, 171 (1992)

[4] J. Halbritter, J. Superconductivity 8, 691 (1995) and 10, 91 (1997)

[5] M. Regier et. al., IEEE Trans Appl. Superconductivity 9, (1999)

[6] a. J. Halbritter, J. Appl. Phys. 58, 1320 (1985)
b. J. Halbritter, B 46, 14861 (1992)
c. e. g., R. Gross et al., IEEE Trans. Appl. Supcerconductivity 7, 2929 (1997)

[7] J. Halbritter, Phys. Rev. B 48, 9735 (1993) and Int. J. Modern Physics B3, 719 (1989)

[8] a. T. Jacobs et al., IEEE Trans. Appl. Supercond. 7, 1917 (1997)
b. S. Hensen et al, Phys. Rev. B 56, 6237 (1997)
c. E. Keskin et al., IEEE Trans Appl. Superconductivity 9, (1999)

[9] e.g., M. R. Trunin, J. Superconductivty 11, 381 (1998);
M. Hein, Habilitation thesis (Phys. Uni Wuppertal, 1999), N. Klein, Habilitation thesis (Phys, TH Aachen, 1998

[10] R. Schwab, PhD thesis (Physik, Universität Karlsruhe, 1999), R. Schwab et al., Proc. 23. Inf. Conf. on Infrared and Millimeter Waves, Sept. 1998 (Essex, UK), p. 379

[11] E. Keskin, Diplom-thesis (Physik, Universität Karlsruhe, 1998)

[12] K. Numssen, PhD thesis (Physik, Universität Karlsruhe, 1998)

[13] C.J. Stevens et. al., Phys Rev. Lett. 78, 2212 (1997) and D. Mihailovic et. al., Rev. B 59, 1497 (1999)

[14] e.g., D. Bonn et. al., Phys. Rev. B47, 11314 (1993)

[15] M. Lorenz, H. Hochmuth, private communication – see [9c]

Effect of the CeO_2 Buffer Layer Thickness on the Microwave Properties of YBCO Thin Films

Katherine D. Develos, Masanobu Kusunoki, Masashi Mukaida and Shigetoshi Ohshima
Department of Electrical and Information Engineering, Yamagata University, Yonezawa, Japan

Abstract—We have examined the effect of varying the CeO_2 buffer layer thickness on the microwave surface resistance R_s and surface morphology of YBCO films deposited by pulsed laser deposition. Above the critical thickness value d_c of CeO_2 at ~90 nm, the surface roughness and areal density of outgrowths of the film increased significantly. The YBCO films grown on a CeO_2 with thickness less than d_c were completely c-axis oriented and had lower c-axis length than those grown on a CeO_2 with thickness greater than d_c. The R_s measured via sapphire dieletric resonator technique was significantly lower for the YBCO film grown on CeO_2 with thickness less than d_c. The increase in the R_s value when the buffer layer thickness is greater than d_c is considered to be due to the increased surface outgrowths and presence of a-axis domains in the YBCO film. Changes in the microstructure and orientation of the YBCO films were found out to be strongly influenced by the underlying CeO_2 layer.

I. Introduction

The surface resistance, R_s of high temperature superconducting thin films such as $YBa_2Cu_3O_{7-\delta}$ (YBCO) is orders of magnitude lower than that of normal metals in the microwave frequency region [1]. This makes these materials as excellent candidates for device applications. However, structural perfection and good crystalline properties are paramount parameters for these applications. In the case of YBCO films deposited on a low-loss substrate like Al_2O_3, cerium oxide (CeO_2) films are used as buffer layers to prevent interdiffusion and provide good lattice matching [2]. In a detailed study of the thickness dependence of the CeO_2 surface morphology as observed through atomic force microscopy (AFM), a critical value (hereafter identified as d_c) at ~90 nm has been found [3]. Above this critical value, extensive surface roughening and increase in the areal density of outgrowths occurred. However, the effect of the CeO_2 morphology on the quality or microwave property of YBCO has not yet been examined in detail. In this study, we therefore investigated the dependence of the R_s, measured using sapphire dielectric resonator technique, on the CeO_2 buffer layer thickness. We correlated the R_s results to the YBCO surface morphology as observed by AFM. We also report on the effect of CeO_2 on other characteristics of YBCO, such as orientation and lattice constant.

Manuscript received April 30, 1999.
This work was supported in part by the Grant-in-Aid for Scientific Research on Priority Areas of the Ministry of Education, Science, Sports and Culture.

II. Experimental

The CeO_2 and YBCO films were deposited on r-cut Al_2O_3 ($1\bar{1}02$) by pulsed laser deposition utilizing an ArF excimer laser. The deposition parameters for each case are listed in Table I. The sapphire substrates were mounted on Inconel disc holders using silver paste to provide thermal contact. These were heated to deposition temperature using a lamp heater. Actual deposition temperature was calibrated using an optical pyrometer. The films were characterized by θ-2θ x-ray diffraction (XRD). The R_s of the YBCO films was measured using a sapphire dielectric resonator operating in a cryocooler. The height of the sapphire rod was 3.03 mm and the diameter was 6.50 mm, resulting to a resonance frequency of 22 GHz for the TE_{011} mode. For calibration, one film (YBCO/$LaAlO_3$) with known R_s value was used. A vector network analyzer was used to measure the center frequency f_o and the 3dB points of the resonance curve. The R_s of the films was calculated from the measured unloaded quality factor Q_u. AFM was used to investigate the surface morphology of the films.

TABLE I
DEPOSITION PARAMETERS

Deposition Parameters	CeO_2	YBCO
Laser energy	200	200
Laser repetition rate	1 Hz	1, 5 Hz
Deposition temperature	~700°C	~ 720°C
Film thickness	~20 – 130 nm	~ 550 nm

III. Results and Discussion

A. XRD Results

Using the intensities of the (006) and (200) peaks of YBCO, we used a simple relation to evaluate the amount of c-axis oriented grains in the film:

$$Volume\ fraction\ (\%\ c\text{-}axis) = \frac{I_{(006)}}{I_{(006)} + I_{(200)}} \times 100\% \quad (1)$$

The plot of (1) with respect to CeO_2 film thickness is shown in Fig. 1(a). As is evident from the graph, perfect c-axis alignment was obtained in the case of YBCO films grown on

CeO_2 films with thickness less than d_c. Since all conditions are the same except for the surface morphology of the CeO_2 buffer, it is considered that the increased surface roughness and outgrowths in the buffer layer acted as nucleation sites for a-axis oriented growth of YBCO.

The c-axis length of YBCO films has been found to correlate to the amount of stoichiometric oxygen it contains [4]. From XRD results, the c-axis length can also be computed; the values are plotted against CeO_2 film thickness in Fig. 1(b). The c-axis length is almost constant up to the critical value d_c; on the other hand, an increasing trend is seen at a thickness above d_c, implying higher oxygen deficiency. Correspondingly, we have also confirmed a significant decrease in the value of the critical temperature T_c for YBCO films grown on CeO_2 with thickness above d_c [5].

B. Surface Resistance

We used the following equation to calculate the R_s from the measured unloaded Q_u value [6]:

$$R_s = \left(\frac{\lambda_g}{\lambda_0}\right)^3 \frac{30\pi^2}{1+W}\left\{\frac{\varepsilon_r + W}{Q_u} - tan\,\delta\right\} \qquad (2)$$

Here, λ_0 is the resonant wavelength; λ_g corresponds to the guiding wavelength of an infinitely long dielectric rod waveguide, and W is a function that represents the ratio of electric-field energy stored outside to inside the rod. As an approximation, we set $\tan\delta \approx 0$ in the calculation.

Taking into consideration the preceding XRD results, we measured the R_s of two YBCO films grown on CeO_2 with thickness (a) less than d_c, and (b) greater than d_c. The R_s-T plots adjusted to 10 GHz resonance frequency are shown in Fig. 2. The R_s values of the film grown in (a) are significantly lower than in (b). For comparison, at T = 31 K, the R_s of (a) is 0.27 mΩ while that of (b) is 1.6 mΩ. Thus the optimum range of CeO_2 thickness suitable for YBCO lies below the critical value d_c. This dependence on the thickness of CeO_2 arises from the changes in the surface morphology of the buffer layer itself, which consequently affects the growth of the overlying YBCO film.

C. Surface Morphology of YBCO

Fig. 3 shows the top and three-dimensional AFM images of the YBCO films deposited on CeO_2 buffer layer with thickness below and above d_c, taken over a scan area of 20 μm x 20 μm. In Fig. 3(a), the thickness of the CeO_2 buffer layer is ~26 nm, and the YBCO surface is seen to be characterized by some outgrowths, which we may attribute to misaligned grains or other phases of YBCO. The effect of the surface roughening of CeO_2 when the thickness is above d_c is evident in the AFM images in the case of Fig. 3(b), where we see a significant increase in the surface roughness and areal density of these outgrowths. It has been suggested in earlier studies that a correlation exists between the amount of

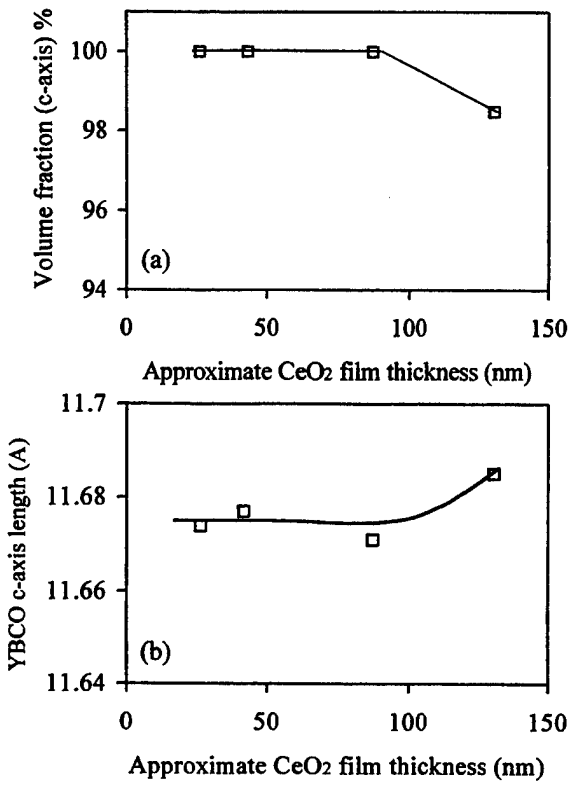

Fig. 1. (a) Plot of the volume fraction of c-axis oriented grains of YBCO against CeO_2 thickness. Greater than d_c, a-axis orientations appeared in YBCO. (b) Plot of YBCO c-axis length with respect to CeO_2 thickness. Increase in c-axis length is seen at thickness greater than d_c.

outgrowths on the film surface and the R_s [7]. The increase in the number of outgrowths of the YBCO film shown in Fig. 3(b) can therefore be associated with the comparatively high R_s value obtained. Furthermore, the existence of a-axis domains (from XRD results) in this film also contributed to the increase of R_s.

Next the surface microstructures of the YBCO films are examined closely over a smaller scan area of 0.5 μm x 0.5 μm. This is shown in Fig. 4, for YBCO films deposited on

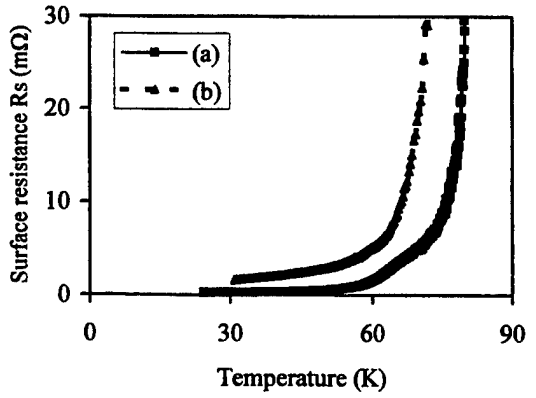

Fig. 2. Surface resistance as a function of temperature of the YBCO films at 10 GHz resonance frequency deposited on CeO_2 buffer layer with thickness (a) ~26 nm, and (b) ~130 nm.

CeO_2 buffer with thickness of (a)~26 nm and (b)~130 nm. The films exhibit an island nucleation and growth mechanism, as previously reported for laser-ablated YBCO films [8]. In Fig. 4(a), the observed microstructure of the YBCO film shows terraces with height of ~1.2 nm, i.e., the approximate c-axis length of YBCO. In contrast, as shown in Fig. 4(b), the YBCO surface is comprised of large, boulder-like islands and has a higher surface roughness.

Correlating the observed morphologies to the previous c-axis length values, it is seen that the YBCO film with higher surface roughness and denser outgrowths is also more oxygen deficient. These results suggest that oxygen incorporation during the transformation of YBCO from tetragonal to orthorhombic phase may be affected by its surface morphology. It is therefore important to maintain the surface smoothness of the YBCO films, and for this purpose, smooth CeO_2 buffer layers (i.e., with thickness less than d_c) must be used.

IV. Conclusions

The effect of the CeO_2 buffer layer thickness on the microwave surface resistance, R_s, and surface morphology of the YBCO films was investigated. The surface morphology of the CeO_2 films as dependent on the thickness affected the qualities of the YBCO films. The YBCO films deposited on CeO_2 with thickness less than d_c were completely c-axis oriented and had lower c-axis length values compared to that grown on CeO_2 with thickness greater than d_c. The R_s values were significantly lower for a YBCO film when the CeO_2 thickness used was less than d_c. Higher R_s value was obtained when the buffer layer thickness was greater than d_c. Observation through AFM showed that the areal density of surface outgrowths for this film had also increased, and together with the presence of a-axis domains, led to the increase in the R_s. Hence, the critical value d_c is the upper limit of the optimum thickness range of the CeO_2 buffer layer to obtain YBCO films with good microwave properties.

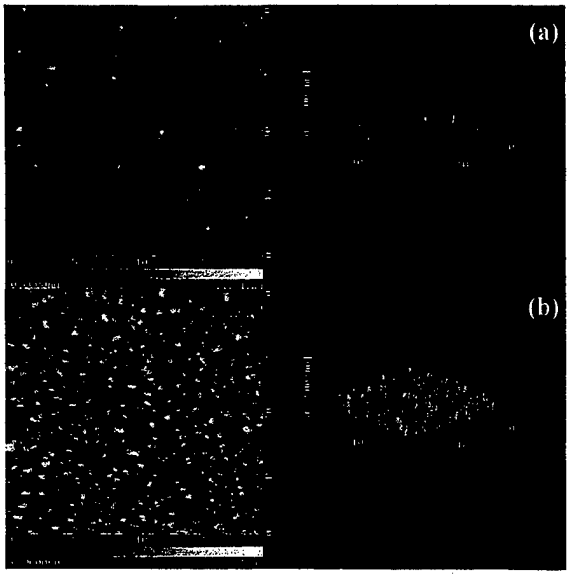

Fig. 3. Top and three-dimensional AFM images of YBCO films on CeO_2 with thickness (a) ~26 nm and (b) ~130 nm. (Scan area: 20 μm x 20 μm; Vertical scale: 500 nm.)

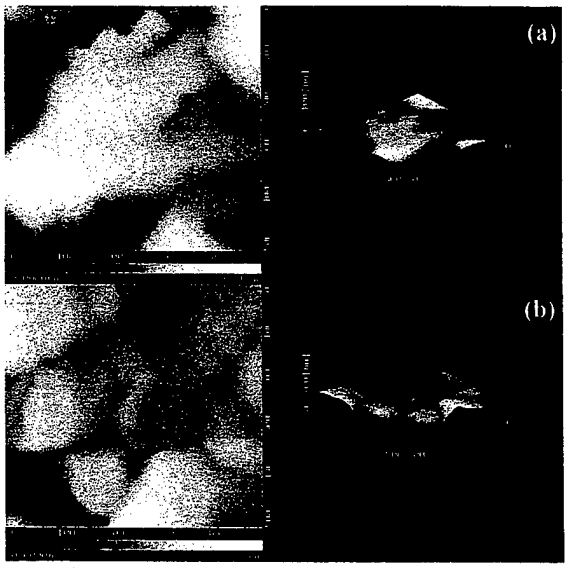

Fig. 4. Top and three-dimensional AFM images of YBCO films on CeO_2 with thickness (a) ~26 nm and (b) ~130 nm. (Scan area: 0.5 μm x 0.5 μm; Vertical scale: 100 nm.)

References

[1] M. J. Lancaster, *Passive Microwave Device Applications of High-Temperature Superconductors*. U.K.: Cambridge University Press, 1997, pp. 314-317.

[2] X. D. Wu, R. C. Dye, R. E. Muenchausen, S. R. Foltyn, M. Maley, A. D. Rollett, A. R. Garcia and N. S. Nogar, *Appl. Phys. Lett.*, vol. 58, pp. 2165-2167, May 1991.

[3] K. D. Develos, M. Kusunoki, and S. Ohshima, *Jap. J. Appl. Phys.*, vol. 37, pp. 6161-6169, November 1998.

[4] K. Nakamura, J. Ye, and A. Ishii, *Physica C*, vol. 213, pp. 1-13, August 1993.

[5] K. D. Develos, M. Kusunoki, and S. Ohshima, "Influence of a CeO_2 buffer layer on the superconducting properties of $YBa_2Cu_3O_{7-\delta}$ on Al_2O_3," *Proceedings of the 11th International Symposium on Superconductivity*, in press.

[6] Y. Kobayashi and M. Katoh, *IEEE Trans. Microwave Theory and Techniques*, vol. MTT-33, pp. 586-592, July 1985.

[7] Y. J. Tian, L. Li, L. P. Guo, J. Z. Liu, Z. X. Zhao, S. F. Xu, H. B. Lu, Y. L Zhou, Z. H. Chen, D. F. Cui and G. Z. Yang, *Appl. Phys. Lett.*, vol. 65, pp. 2356-2358, October 1994.

[8] J. M. Moreland, P. Rice, S. E. Russek, B. Jeanneret, A. Roshko, R. H. Ono, and D. A. Rudman, *Appl. Phys. Lett.*, vol. 59, pp. 3039-3041, December 1991.

A new epitaxial $BaSnO_3$ buffer layer for $YBa_2Cu_3O_{7-\delta}$ thin films on MgO substrates

M. Mukaida, Y. Takano, K. Chiba, T. Moriya, M. Kusunoki and S. Ohshima
Yamagata University, Jonan 4-3-16, Yonezawa, Yamagata 992-8510, Japan

Abstract—45° grain boundaries, which drastically increase surface resistance (R_S) in superconducting $YBa_2Cu_3O_{7-\delta}$ films for microwave devices on MgO substrates are eliminated using new buffer layer of $BaSnO_3$. $BaSnO_3$ buffer layers and $YBa_2Cu_3O_{7-\delta}$ films are grown by ArF pulsed laser deposition. Epitaxial relationships among $BaSnO_3$, $YBa_2Cu_3O_{7-\delta}$ and MgO are confirmed by X-ray φ-scanning. The R_S's of the $YBa_2Cu_3O_{7-\delta}$ films are measured using a dielectric resonator with 22GHz TE011 mode. The epitaxial $YBa_2Cu_3O_{7-\delta}$ films grown on $BaSnO_3$ buffered MgO substrates show lower R_S than $YBa_2Cu_3O_{7-\delta}$ films directly grown on MgO substrates. The $BaSnO_3$ buffer layer which enables $YBa_2Cu_3O_{7-\delta}$ films to grow without 45° grain boundaries at a optimum film growth condition is attractive for microwave applications.

I. INTRODUCTION

Superconductors have superior characteristics of quite low surface resistance (R_S), which is 2 ~ 3 order lower than that of normal metals in high frequency region. By using the characteristics, super low insertion loss multi-cross-coupled filters are expected to be realized. These filters enables low group delay and high-speed data transmission and small size in lower than 100GHz frequency region[1]. However, the usage of liquid Helium for metal superconducting microwave devices hinders the realization.

Discovery of high-T_C oxide superconductors with T_C higher than 77K, got rid of these disadvantages. Many researchers began to study the high-T_C superconducting microwave devices using $YBa_2Cu_3O_{7-\delta}$ films on MgO substrates. However, it is pointed out that there are in-plane misaligned *c*-axis oriented grains in $YBa_2Cu_3O_{7-\delta}$ films on MgO substrates. These are $[100]_{MgO}$ // $[100]_{YBCO}$ (hence forth termed as "0°") $[110]_{MgO}$ // $[100]_{YBCO}$ ("45°") grains. Suzuki *et al.*[2] reported that surface morphologies of films consisting of 0° grains were grain-like patterns, while the 45° grains are smooth and show no grain-like patterns. These misaligned grains have large angle grain boundaries, which cause large losses in microwave characteristics.[3]

Manuscript received April 30, 1999. This work is supported in part by Asahi glass.

In this paper we investigate the in-plane crystalline quality of $YBa_2Cu_3O_{7-\delta}$ films grown on MgO substrates and new buffer layer to control the in-plane crystalline axes of $YBa_2Cu_3O_{7-\delta}$ films grown on MgO substrates.

II. EXPERIMENTAL

A. Substrate preparations

We used four kinds of MgO substrates. These were as polished, freshly cleaved, annealed and Ar ion cleaned MgO substrates. Thermal annealing was performed in vacuum. The MgO substrates were annealed up to 1000°C[4]. Only the Ar ion cleaning was executed in a load-lock chamber connected to the growth chamber just before the $YBa_2Cu_3O_{7-\delta}$ thin film growth. The MgO substrates were irradiated by Ar ions accelerated by 5kV for 10min. After the ion cleaning, the substrate was used to grow a $YBa_2Cu_3O_{7-\delta}$ thin film without breaking vacuum.

B. Growth of thin films

The $YBa_2Cu_3O_{7-\delta}$ and $BaSnO_3$ thin films were grown by a pulsed ArF excimer laser deposition technique. The details of experimental setup and experimental procedures are described elsewhere.[5] The target used in this experiment was a high density sintered $YBa_2Cu_3O_{7-\delta}$ and $BaSnO_3$ ceramic. During deposition, the oxygen pressure was fixed at 53.3 and 5.3Pa with oxygen flow rate of 100 and 10cc/min for $YBa_2Cu_3O_{7-\delta}$ and $BaSnO_3$ films respectively.

C. Characterization of film quality

Preferred orientations of $YBa_2Cu_3O_{7-\delta}$ films were determined by X-ray diffraction (XRD) with Cu-Kα radiation. In-plane orientation of the $YBa_2Cu_3O_{7-\delta}$ films was evaluated by X-ray φ scanning using the (102) plane of $YBa_2Cu_3O_{7-\delta}$. The critical temperature, T_C was measured from a ρ-T curve using a conventional four-probe method. The surface resistance (R_S) of the $YBa_2Cu_3O_{7-\delta}$ films are measured using a dielectric resonator consisted in Al_2O_3 rod with 22GHz TE011 mode in a cryocooler.

III. RESULTS AND DISCUSSIONS

A. Substrate preparation dependence

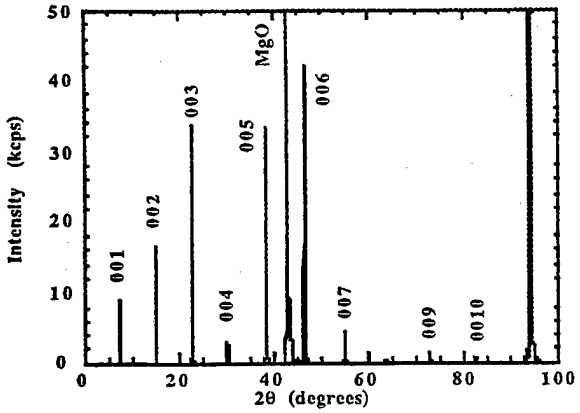

Fig. 1 A typical XRD pattern of $YBa_2Cu_3O_{7-\delta}$ films on MgO substrates.

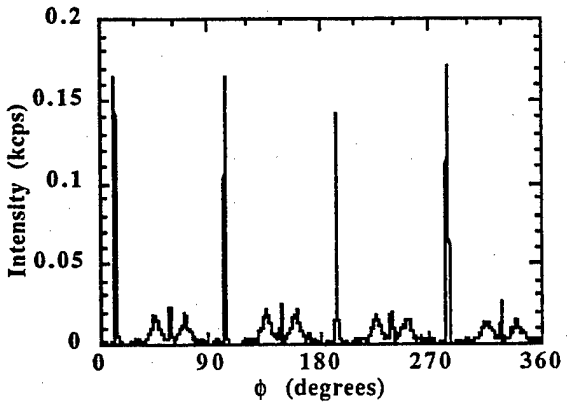

Fig. 2 A typical X-ray ϕ scanning of the $YBa_2Cu_3O_{7-\delta}$ film grown on the MgO substrate.

A typical θ/2θ XRD pattern of a $YBa_2Cu_3O_{7-\delta}$ film grown on an as-polished MgO substrate is shown in Fig.1. Only the 00*l* reflections of $YBa_2Cu_3O_{7-\delta}$ are observed in the XRD pattern. The separation of the Cu-Kα_1 and Cu-Kα_2 radiation can be seen at reflection peaks higher than 003. From these peaks, the *c*-axis lattice constant was calculated to be 11.69Å.

From the results of XRD pattern, the film can be considered to be a high crystalline quality *c*-axis oriented $YBa_2Cu_3O_{7-\delta}$ film. However, the important consideration is the in-plane alignment of the film and the substrate.

Figure 2 shows a typical X-ray ϕ scanning of the $YBa_2Cu_3O_{7-\delta}$ film. In the figure, the peaks correspond to grains with in-plane rotated angle. From the angles, there are three kinds of in-plane rotated grains. One is a grain with a $[100]_{MgO}//[100]_{YBCO}$ in-plane epitaxial relationship. This configuration is referred to a 0° grain. Second is a grain with a $[110]_{MgO}//[100]_{YBCO}$ in-plane epitaxial relationship. This configuration is referred as a 45° grain. The last is a grain

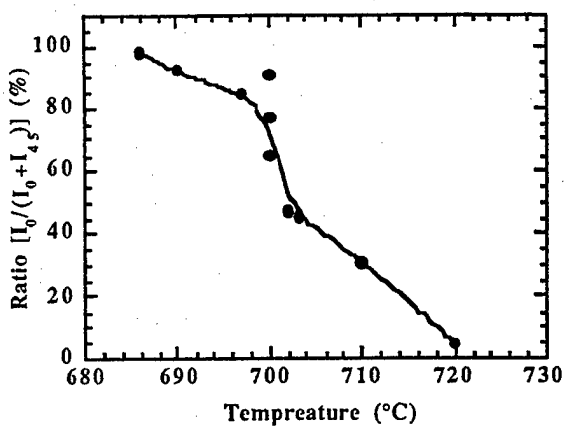

Fig. 3 Temperature dependence of growth of 0° and 45° rotated grains. $YBa_2Cu_3O_{7-\delta}$ films grown at low temperature around 680°C and high around 720°C do not have good superconducting properties.

with broad in-plane angle distributions. These grains originated from contamination exposed in air. Then they are eliminated by cleaning the surface, such as ion cleaning and/or annealing. However, 0° and 45° grains always grow on MgO substrate. Therefore, $YBa_2Cu_3O_{7-\delta}$ films on these substrates will not be suitable for microwave devices because of the resulting high surface resistance R_S.

Next we observed the substrate temperature dependence of in-plane orientation of $YBa_2Cu_3O_{7-\delta}$. Figure 3 shows the temperature dependence of in-plane orientation of $YBa_2Cu_3O_{7-\delta}$ grains on MgO substrates. In the figure, the vertical axis corresponds to the x-ray diffraction intensity ratio of 0° and 45° rotated grains $[I_0/(I_0 + I_{45})]$ observed in X-ray ϕ-scanning. The $[110]_{MgO}$ // $[100]_{YBCO}$ grains increased its amount with the increase of the substrate temperature. From the figure we get only one in-plane oriented grains of the $[100]_{MgO}//[100]_{YBCO}$ at around 680°C and only the $[110]_{MgO}//[100]_{YBCO}$ grains at around 720°C. It is therefore evident that 0° and 45° rotated grains can be controlled by the growth temperature.

However, the growth temperature for the in-plane alignment is achieved is not optimized growth temperature from the superconducting properties point of view. Therefor we used $BaSnO_3$ buffer layers. A typical θ/2θ XRD pattern of $YBa_2Cu_3O_{7-\delta}$ films grown on $BaSnO_3$ buffered MgO substrates is almost the same as Fig. 1 with peaks from $BaSnO_3$. Only 00*l* peaks of the $BaSnO_3$ film were present. The $BaSnO_3$ film is *c*-axis oriented on the MgO substrate. The *c*-axis lattice constant of the film was calculated to be 4.13Å using Nelson-Riley function. For the $YBa_2Cu_3O_{7-\delta}$ films, only the 00*l* reflections of $YBa_2Cu_3O_{7-\delta}$ are also observed from the film. $YBa_2Cu_3O_{7-\delta}$ films grow epitaxially on $BaSnO_3$ buffer layers on MgO substrates with the *c*-axis preferred orientation. The *c*-axis lattice constant of the film was calculated by the same method to be around 11.68Å. Figure 4 shows typical ϕ scanning XRD patterns of the

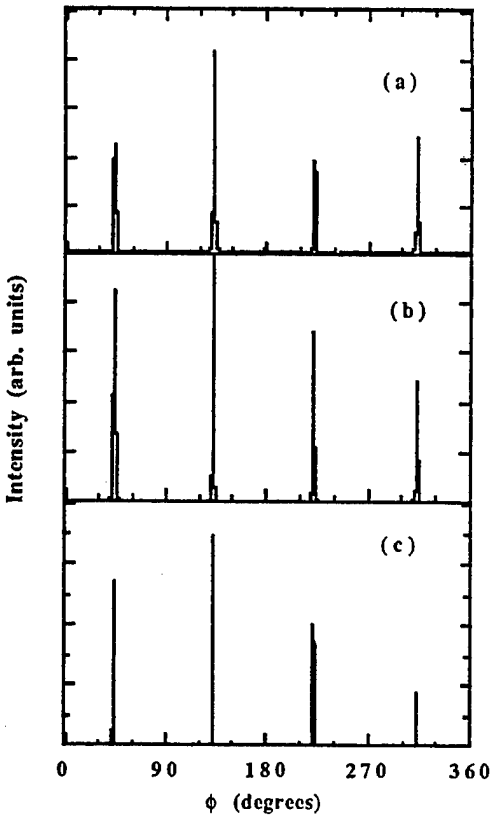

Fig. 4 Temperature dependence of growth of 0° and 45° rotated grains. $YBa_2Cu_3O_{7-\delta}$ films grown at a low temperature around 680°C and a high temperature around 720°C do not have good superconducting properties.

(a)$YBa_2Cu_3O_{7-\delta}$, (b)$BaSnO_3$ films and (c)MgO substrate, respectively. From the figure, epitaxial relationships among the films and the substrate are $[001]_{YBCO}//[001]_{BSO}$, $[100]_{YBCO}//[100]_{BSO}$, $[001]_{BSO}//[001]_{MgO}$ and $[100]_{BSO}//[100]_{MgO}$. It is thus confirmed that the in-plane orientation of $YBa_2Cu_3O_{7-\delta}$ films grown at an optimized growth temperature could be controlled by $BaSnO_3$ buffer layers on MgO substrates.

Finally we compared the surface resistances of $YBa_2Cu_3O_{7-\delta}$ films (a) with and (b) without $BaSnO_3$ buffer layers. Temperature dependence of surface resistances of $YBa_2Cu_3O_{7-\delta}$ films with $BaSnO_3$ buffer layers and $YBa_2Cu_3O_{7-\delta}$ films without $BaSnO_3$ buffer layers grown at the same growth conditions of 710°C are shown in Fig.5. In the figure the lateral axis is normalized temperature by its T_C and the vertical axis is the R_S calculated to the value at10GHz using the f^2 rule. Both surface resistances drop sharply at their T_C. However, the surface resistance of $YBa_2Cu_3O_{7-\delta}$ films without $BaSnO_3$ buffer layers is always one order of magnitude higher than that of $YBa_2Cu_3O_{7-\delta}$ films with $BaSnO_3$ buffer layers. It must be noted that the simple introduction of $BaSnO_3$ buffer layers successfully eliminate the 45° tilted $YBa_2Cu_3O_{7-\delta}$ grain boundaries on low dielectric MgO substrates.

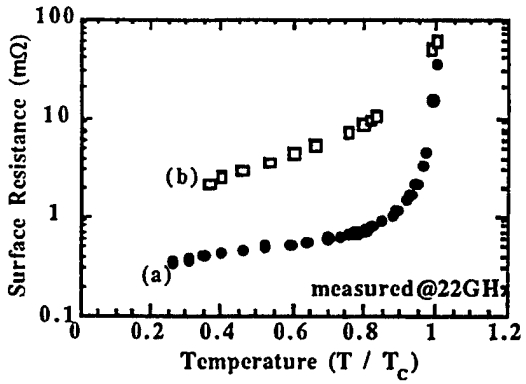

Fig. 5 Temperature dependence of R_S's of $YBa_2Cu_3O_{7-\delta}$ films (a)with and (b)without $BaSnO_3$ buffer layer.

IV. Conclusion

In-plane rotations of $YBa_2Cu_3O_{7-\delta}$ grains were investigated from the substrate surface lattice matching between MgO and $YBa_2Cu_3O_{7-\delta}$. The broad in-plane peaks were considered to be due to the contaminated surface of MgO. Using a MgO substrate with a freshly cleaved, 1000°C annealed and Ar ion cleaned surface, we could eliminate the broad in-plane distributed grains. 0° and 45° rotated grains were observed in 710°C grown $YBa_2Cu_3O_{7-\delta}$ films on MgO substrates.

A new buffer layer of $BaSnO_3$ films with low loss tangent was proposed for controlling in-plane orientation of $YBa_2Cu_3O_{7-\delta}$ films. It is confirmed by x-ray ϕ-scanning that the 45° grain boundaries were eliminated by controlling in-plane orientation of $YBa_2Cu_3O_{7-\delta}$ films using $BaSnO_3$ buffer layers. These $YBa_2Cu_3O_{7-\delta}$ films with $BaSnO_3$ buffer layers showed surface resistance lower by one order of magnitude than that of $YBa_2Cu_3O_{7-\delta}$ films without $BaSnO_3$ buffer layers grown at the same growth condition of 710°C.

Acknowledgment

We would like to thank Mr. K. Aizawa for his technical support and Miss K. Develos for her help with the preparation of this manuscript and discussion. Authors also acknowlege to Mr. D. Okai and Mr. K. Ehata for their fruitful discussions.

References

[1] H. Chaloupka: *Frequenz* vol. 443 (1990) p.141.
[2] M. Suzuki, H. Sakurai, T. Sakurai, M. Nagano and Y. Wakiya, *Advances in Superconductivity III* (Springer-Verlag, Tokyo, 1993) p.969.
[3] S. S. Laderman, R. C. Taber, R. D. Jacowitz, J. L. Moll, C. B. Eom, T. L. Hylton, A. F. Marshall, T. H. Geballe and M. R. Beasley, *Phys. Rev. B* vol. 43 (1991) p. 2922.
[4] T. Minamikawa, T. Suzuki, Y. Yonezawa, K. Segawa, A. Morimoto, and T. Shimizu, *Jpn. J. Appl. Phys.* vol. 34 (1995) p. 4038.
[5] M. Mukaida and S. Miyazawa, *Jpn. J. Appl. Phys.* vol. 32 (1993) p. 4521-4528.

Microscopic model for double-barrier SIS'IS Josephson junctions

A. Brinkman, A. A. Golubov, H. Rogalla
Department of Applied Physics, University of Twente, P.O.Box 217, 7500 AE Enschede, the Netherlands

M. Yu. Kupriyanov
Nuclear Physics Institute, Moscow State University, 119899 GSP Moscow, Russia

Abstract — As is shown in [1], double barrier SIS'IS structures (I is the tunnel barrier, S' is a thin film with $T_{cS'}<T_{cS}$) combine advantages of weak links and tunnel junctions. Namely, they are intrinsically shunted and have therefore non-hysteretic I-V characteristics, while their resistance is controlled by the tunnel barriers rather than by the interlayer material. Such junctions are thus very promising in RSFQ and programmable voltage standard applications. In the present contribution we develop the microscopic model for stationary supercurrent and I_cR_N product in SIS'IS junctions in the general case of an arbitrary $T_{cS'}/T_{cS}$ ratio and arbitrary barriers. In earlier theoretical papers [1,2] only a few limited cases were studied. The influence of interlayer thickness, critical temperature $T_{cS'}$ and of barrier asymmetry on I_cR_N is quantitatively studied within this model. The current-phase relation in different parameter ranges and an influence of the electronic mean free path in the S' interlayer is also discussed. It is shown that data for *Nb/AlOx/Al/AlOx/Nb* junctions from different groups are well described by the theory.

I. Introduction

Recently it has been demonstrated in a series of experimental studies [3]-[5] that double barrier SS'IS'IS'S structures can be considered as promising candidates for the replacement of SIS tunnel Josephson junctions (JJ) in a large scale integrated circuit technology. Moreover these structures have been used successfully for the fabrication of microcircuits for voltage standards (8192 JJ) and simple RSFQ devices (68 JJ) with an on-chip spread of the junction parameters less than 10% [5]-[7].

Unfortunately, even stationary processes in SIS'IS junctions were studied only in a few limited cases [1,2]. In the present contribution we develop the microscopic model for stationary supercurrent and I_cR_N product in SIS'IS junctions in the general case of an arbitrary $T_{cS'}/T_{cS}$ ratio and arbitrary transparency of the barriers. The transport properties of the interlayer are considered both in dirty and clean limits. The results of calculations are compared with experimental data.

II. Theory

A. Microscopic model

To derive the microscopic model for a double barrier structure we assume the thickness of the interlayer between the barriers to be much smaller then the coherence length ($d<< \xi_{S'}=(v_F l_{S'}/6\pi T_{cS})^{1/2}$ where v_F is the Fermi velocity for S' and $l_{S'}$ is the electron mean free path in S').

Manuscript received April 30, 1999. This work was supported in part by INTAS-97-1712 and ISTC 1197 projects

If the conditions of the dirty limit for the interlayer are fulfilled ($l_{S'} << d$, $\xi_{S'}$), then the supercurrent can be derived within the framework of the Usadel equations [8]. We have found (see also [2]):

$$\frac{eI(\varphi)R_N}{2\pi T_{cS}} = \frac{T}{T_{cS}}\sum_{\omega>0}\frac{G_{S'}\Delta_S \sin\varphi}{E_1\Omega\omega}\left[\frac{\Delta_S}{E_1}+\frac{\Delta_{S'}\gamma_{eff}}{\pi T_{cS}}\right], \quad (1)$$

$$\Omega = \frac{\gamma_{eff}\omega}{\pi T_{cS}} + G_S,\ G_{S'} = \frac{\omega\Omega}{\sqrt{\omega^2\Omega^2+\delta^2}},\ \delta = \Delta_S G_S \eta + \frac{\omega\Delta_{S'}\gamma_{eff}}{\pi T_{cS}}$$

Here the summation goes over the Matsubara frequencies $\omega=(2n+1)\pi T$, φ is the phase difference across the junction, $E_1^2 = \omega^2+\Delta_S^2$, $G_S^2=\omega^2/(\omega^2+\Delta_S^2)$, $\eta=(\cos^2(\varphi/2)+\gamma_-^2\sin^2(\varphi/2))^{1/2}$, $\gamma_- = (\gamma_{B1}-\gamma_{B2})/(\gamma_{B1}+\gamma_{B2})$. The suppression parameter γ_{eff} is

$$\gamma_{eff} = \frac{d}{\xi_{S'}}\frac{\gamma_{B1}\gamma_{B2}}{\gamma_{B1}+\gamma_{B2}},\ \gamma_{B1,2} = \frac{2}{3}\frac{l_{S'}}{\xi_{S'}}\left\langle\frac{D_i}{1-D_i}\right\rangle^{-1} \equiv \frac{R_{B1,2}}{\rho_{S'}\xi_{S'}} \quad (2)$$

where $D_{1,2}$ are the barriers transparencies, $R_{B1,2}$ are the boundary resistances and $\rho_{S'}$ is the resistivity of the interlayer. The brackets denote angle averaging. The order parameter in the interlayer $\Delta_{S'}$ is the solution of the selfconsistency equation

$$\Delta_{S'}\left\{\ln\frac{T}{T_{cS'}}+2\pi T\sum_{\omega}\left[\frac{1}{\omega}-\frac{\gamma_{eff}G_{S'}}{\omega\Omega}\right]\right\} = \pi T\sum_{\omega}\frac{G_S G_{S'}\Delta_S \pi T_{cS}}{\omega^2}.$$

Expression (1) is valid for any shape of an atomically sharp interface barrier potential, and $\gamma_B>>d/\xi_{S'}$.

B. Limit of a small suppression parameter

In the case of a small suppression parameter, $d/\xi_{S'} << \gamma_{eff} << \xi_{S'}/d$, equation (1) can be simplified into

$$\frac{eI_S R_N}{2\pi Tc} = \frac{T}{Tc}\sum_{\omega}\frac{\Delta_0^2\sin\varphi}{\sqrt{\Delta_0^2\cos^2(\varphi/2)+\omega^2}\sqrt{\Delta_0^2+\omega^2}}. \quad (3)$$

This current-phase relationship is not sinusoidal anymore but has it's maximum at $\varphi=1.86$ if $T<< T_{cS'}$. This limit was first found by [1] for a normal metal interlayer (see Fig.1). Here we have proved that it holds for any kind of interlayer, namely the critical voltage is independent of the material properties or the thickness of the interlayer and the barriers.

C. Limit of a large suppression parameter

In the practically interesting case of a large suppression parameter and relatively high temperatures

$$\gamma_{eff} >> \frac{T_{cS}}{T},\quad T \geq T_{cS'}+T_{cS'}\left[\frac{\sqrt{T_{cS}(T_{cS}-T_{cS'})}}{\gamma_{eff}T_{cS'}}\right]^{2/3}$$

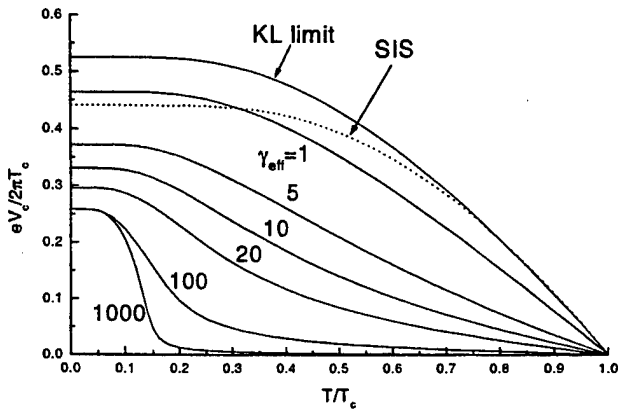

Fig. 1. Temperature dependence of the critical voltage for several values of the suppression parameter for $T_{cS}/T_{cS'}$ = 9.2 / 1.25.

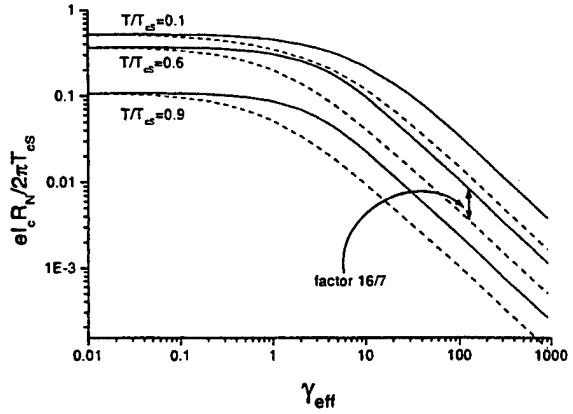

Fig 2. Relation between the normalized critical voltage and the suppression parameter for a double barrier structure with a normal metal interlayer. Solid lines correspond to the clean limit, dotted lines to the dirty limit.

equation (1) reduces to:

$$\frac{eJ_S(\varphi)R_N}{2\pi T_{cS}} = \frac{T}{T_{cS}}\frac{1}{\gamma_{eff}}\sum_{\omega>0}\frac{\Delta_S^2\sin\varphi}{\omega^2+\Delta_S^2}\frac{\pi T_{cS}}{\omega}. \qquad (4)$$

The current-phase relation is now purely sinusoidal. The critical voltage is inversely proportional to the suppression parameter.

Another limiting case in the regime of large suppression parameters is the situation in which $T<<T_{cS'}$. This situation is described by two tunnel junctions in series, each barrier carrying a phase difference of $\varphi/2$ if the barriers are equal.

Fig.1 shows the calculated normalized critical voltage as a function of the reduced temperature for different values of the suppression parameter. This plot is made for a ratio of critical temperatures of $T_{cS}/T_{cS'}$ = *9.2 /1.25* as is the case for *Nb/Al*.

D. Electronic mean free path

The derived microscopic model is based on the assumption that the condition of the dirty limit is fulfilled in the interlayer material. But a recent systematic study [9] of the transport parameters of thin aluminum films in *Nb/Al/AlOx/Al/Nb* tunnel structures shows that they are mainly controlled by the scattering at the interfaces. This demonstrates that the dirty limit assumption is difficult to justify. Therefore we have developed the microscopic model for an interlayer material in the clean limit.

Starting from a set of Gor'kov equations [10], we have found an expression for the temperature Green's functions in a double barrier structure. The supercurrent can then be derived after angle-averaging over the wavevector component $k_{//}$ and summing over the Matsubara frequencies:

$$J_S = \frac{e}{\hbar}\int\frac{d^2k_{//}}{(2\pi)^2}T\sum_{\omega>0}\frac{\Delta_S^2\sin\varphi+\Delta_S\Delta_{S'}\sqrt{\frac{E_1}{E_2}}\frac{d}{\xi_{S'}}W^2\sin\frac{\varphi}{2}}{2W^4E_1^2\left(\cosh\frac{d}{\xi_{S'}}-\cos 2k_Fd\right)+E_3^2}. \qquad (5)$$

Here $E_1^2=\omega^2+\Delta_S^2$, $E_2^2=\omega^2+\Delta_{S'}^2$, $E_3^2=\omega^2+\Delta_S^2\cos^2\varphi/2$ and $W=W_{1,2}/h\nu_F$ is the potential barrier height. The coherence length is now defined as $\xi_{S'}=h\nu_F/2\omega$ and $\Delta_{S'}$ should be determined from the solution of the appropriate selfconsistency equation.

To compare results with the findings of the model for the dirty limit, we define the suppression parameter as $\gamma_{eff} = (W^2d/\xi)/4$, which coincides with the previous definition of γ_{eff}.

For a small suppression parameter ($\gamma_{eff}<<1$) we found (3) again. In this coherent regime the electron mean free path does not play a role in the value of the critical voltage (as does neither one of the material parameters of the interlayer).

In the case of a large suppression parameter and $T>> T_{cS'}$ the supercurrent is again given by (4) multiplied by a factor of *16/7*. Here we see that the coincidence of the two models breaks down but that we can still use the model for the dirty limit as long as we take this correction into account. The crossover between the two models is shown in Fig.2

E. Proximity effect in the composite electrodes

So far we used rigid boundary conditions in our model. This means that the pair potential is assumed to be constant in each layer. In the case of *Nb/Al/AlOx/Al/AlOx/Al/Nb* junctions however, the electrodes consist of the Nb superconductor and a proximized thin normal layer of *Al*. To implement the spatial variation of the pair potential in our model for the double barrier junction we used the method described in [11].

We found that the influence on the critical voltage in the practical regime of large suppression parameters can be described by a single scaling factor. Even for 10 nm thick *Al* layers we found that the result differed less than 10% from the previous results. For thinner *Al* layers, the influence becomes even less.

III. Experimental Results

Most fabrications of double barrier junctions are done in standard process developed for *Nb/Al/AlOx/Al/AlOx/Al/Nb* technology [12]. This technology is well developed for the case of single barrier type devices and *Al* is very suitable as an interlayer because of it's large coherence length (which reduces the suppression parameter).

An example of a theoretical fit to measured data of I_c vs. T is plotted in Fig. 3.

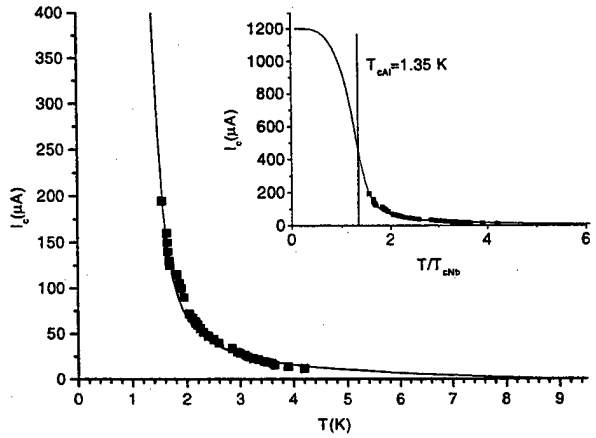

Fig. 3. Experimental data points in an $Ic(T)$ measurement. The solid line is a theoretical fit (γ_{eff}=750, T_{cAl}=1.35 K). The onset shows the entire shape of the theoretical curve.

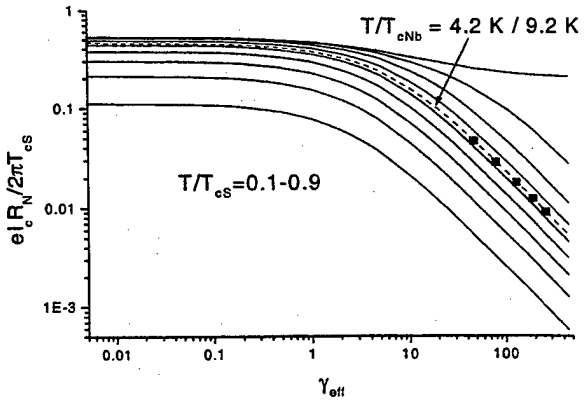

Fig. 4. Dependence of the normalized critical voltage on the suppression parameter for different temperatures, T_{cS}=9.2K and T_{cS}=1.25K, corresponding to the *Nb-Al* case. The squares are experimental data at 4.2 K from [5].

We fabricated this double barrier junction with minor changes to our standard technology for *Nb-Al-AlOx-Al-Nb* junctions [13]. The normal state resistance is extracted from the non-hysteretic current voltage characteristics. In our case of rather thick oxide layers, R_N=1.1 Ω for a 9 μm x 9 μm junction with d_{Al}=7nm. We obtained a value of γ_{eff} =750 for the suppression parameter.

Several double barrier junctions measurements from other groups [5],[14] were found to be well described by the microscopic model. Until now all realized double barrier junctions have suppression parameters much larger than one. Some data which have been extracted from [5] are shown in Fig. 4. This indicates that practical double barrier junctions still only exist in the regime where the supercurrent is inversely proportional to the suppression parameter.

IV. Conclusion

The developed model of double barrier SS'IS'IS'S devices, which takes the proximity effect in the electrodes and the electronic mean free path of the interlayer into account, describes the existing experimental data well.

In the coherent regime of a small suppression parameter the critical voltage becomes independent of the thickness, barrier transparencies and material properties of the interlayer.

In the practical case of a large suppression parameter increasing barrier transparencies or $T_{cS'}$ and decreasing the interlayer thickness will lead to a higher I_cR_N product. Pinholes due to this increase in the barrier transparency do not pose problems if they are smaller than the coherence length of the interlayer material.

The microscopic model predicts that the I_cR_N product can still be very much improved compared to the current status of experimental results (Fig. 4). This implies the possibility for a critical voltage of 1 mV (J_c=10-20 kA/cm^2, γ_{eff}=10) while still having non-hysteretic current voltage characteristics.

Acknowledgment

The authors thank D. Balashov, F-Im. Buchholz, M.I. Khabipov, J. Niemeyer, M. Siegel, H. Kohlstedt, A. Braginskii, V.P. Koshelets, J. Flokstra for stimulating dicussions and D. Veldhuis for his support in fabricating the junctions.

References

[1] M.Yu. Kupriyanov and V.F. Lukichev, Sov. Phys. JETP **67** (6), 1163-1168 (1988).

[2] A.V. Zaitsev, Physica C **185-189**, 2539-2540 (1991).

[3] M. Maezawa, A. Shiji, Appl. Phys. Lett. **70**, 3603,-3605 (1997).

[4] H. Sugiyama, A. Yanada, M. Ota, A. Fujimaki, H. Hayakawa, Jpn. J. Appl. Phys. **36**, L1157-L1160 (1997).

[5] D. Balashov, F-Im. Buchholz, H. Schulze, M.I. Khabipov, W. Kessel and J. Niemeyer, Supercond. Sci. Technol. **11**, 1401- 1407 (1998).

[6] H. Schulze, F. Müller, R. Behr, J. Kohlmann and J. Niemeyer, presented at ASC, report ETB-01 (1998).

[7] M.I. Khabipov, D. Balashov, F-Im. Buchholz, W. Kessel and J. Niemeyer, Preprint (1999).

[8] K.D. Usadel, Phys. Rev. Lett. **25**, 507 (1970).

[9] A. Zehnder, Ph. Lerch, S.P. Zhao, Th. Nussbaumer, E.C. Kirk, Phys.Rev.B **59**, 8875 (1999).

[10] A.A. Abrikosov, L.P. Gorkov and I.E. Dzyaloshinski, (Prentice-Hall, Englewood-Cliffs N.J.), 1963.

[11] A.A. Golubov, E.P. Houwman, J.G. Gijsbertsen, V.M. Krasnov, J. Flokstra, H. Rogalla and M.Yu. Kupriyanov, Phys. Rev. B **51**(2), 1073-1089 (1995).

[12] M.Gurwitch, W.A.Washington and H.A.Huggins, Appl.Phys.Lett. **42**, 472-476 (1983).

[13] D.J. Adlerhof, M.E. Bijlsma, P.B.M. Fransen, T. Weiman, J. Flokstra and H. Rogalla, Physica C **209**, 477-485 (1993).

[14] I.P. Nevirkovets, J.B. Ketterson and S. Lomach, Appl. Phys. Lett. **74**, 1624 (1999).

Investigation of SFQ Integrated Circuits using Nb Fabrication Technology

Hideaki Numata, Michi Tanaka, Yoshihiro Kitagawa, and Shuichi Tahara
NEC Corporation, 34 Miyukigaoka, Tsukuba, Ibaraki, 305-8501, Japan

Abstract — **In NEC's standard process, the minimum junction size is 2 μm and the critical current density (J_C) is 2.5 kA/cm^2. In the process, i-line stepper lithography and reactive ion etching (RIE) with SF_6 gas are used and the standard deviation (σ) of the critical current (I_C) was 0.9% for the 2-μm junctions. This junction uniformity enables integration of more than 10M junctions if an I_C variation of ± 10% permits correct circuit operation. A 512-bit shift register was designed and fabricated by our standard process. Correct 512-bit delay operation was obtained. These results are promising for the large-scale integration of single flux quantum (SFQ) circuits.**

I. INTRODUCTION

We have developed fabrication technology for Nb integrated circuits and it is called NEC's standard process. The process has been used routinely and we obtained successful operation of the circuits such as a 4K-bit RAM [1]. The process is also used to fabricate the circuits designed by many other groups in Japan. These circuits we demonstrated were latching-type circuits. Single flux quantum (SFQ) circuits can operate faster than latching-type circuit [2], so we fabricated an SFQ integrated circuit using our standard process. As our first trial to demonstrate SFQ circuits, we used shift register circuits because of the following reasons. A large-scale shift register can be easily designed by repeating the unit cell without complex timing design. Shift register circuits are serial circuits, so only one defect might spoil the correct circuit operation. Therefore, reliability of the fabrication process will be evaluated. In addition, two serial junctions are often used as a comparator in SFQ circuits. Such two junctions (JA, JB) are used, for example, in an RS-flip-flop [2]; in which a data storage loop contains one of the junctions (JA), and a reset (clock) signal arrives through the other junction (JB). These two junctions operate under racing conditions, and which junction switches depends on the data stored in the storage loop. In the most of the cases, the margin of the comparator is smaller than that of other elements. In an SFQ shift register circuit, the comparator is used every stage. Thus, The capability of our fabrication technology for SFQ integrated circuits will be shown by fabricating a shift register. Moreover, a digital system requires a large-scale and high-speed memory, and an SFQ shift register is one of the candidates for the memory circuit in SFQ digital systems. In this paper, we describe the outline of NEC's standard process and the future prospects of our fabrication technology. We also report the experimental results of the RSFQ shit resister fabricated using our standard process.

Manuscript received May 1, 1999.
This work was partly supported by Special Coordination Funds of the Science and Technology Agency of the Japanese Government.

II. FABRICATION TECHNOLOGY

A. NEC's Standard Process

Fig. 1 shows a schematic cross-section of a device structure fabricated by NEC's standard process. The structure consists of a Nb/Al-AlOx/Nb junction, two Nb wiring layers, a Nb ground plane, and a Mo resistor. The Nb, Al, and Mo films are deposited by DC magnetron sputtering. The interlayer dielectric material is RF sputtered SiO_2.

The LSI fabrication uses 5× i-line stepper lithography with the nine photo-masks listed in Table I. The first mask named GP is used to make the first alignment mark and the ground plane moats. RES is the resistor pattern, and JJ defines the junction counter electrodes. The Al-AlOx layer is patterned using JP, and BAS is used to form the junction base electrodes and the lower Nb wiring layer. The upper wiring layer is formed using COU. GC, RC, and BCC/JCC are used to make contact holes.

In our standard process, there are two key points. One concerns the etching profile of the counter electrodes. We optimized reactive ion etching (RIE) conditions so that the counter electrodes is etched anisotropically and the etching profile is rectangular without etching residue and side etching. Consequently, the high-quality and highly uniform junctions can be obtained [3]. The other concerns the insulation layer between the lower and upper wiring layers. We use a bias sputtering method to deposit the insulation SiO_2 and good step coverage is obtained. Thus, reliable interlayer insulation is achieved.

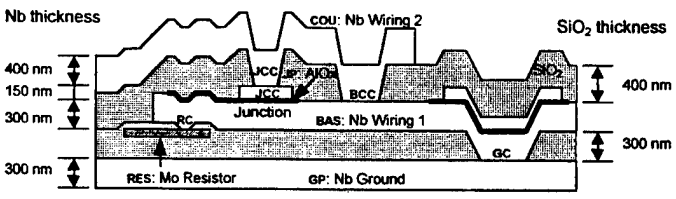

Fig. 1 Schematic cross-section of a device structure fabricated by NEC's standard process.

TABLE I
Photo-masks used in NEC's Standard Fabrication Process

#	Mask name	Layer	Material
1	GP	Ground plane	Nb
2	RES	Resistor	Mo
3	RC	Contact between RES and BAS	SiO_2
4	GC	Contact between GP and BAS	SiO_2
5	JJ	Junction	Nb
6	JP	Junction barrier	Al-AlOx
7	BAS	Base electrode & lower interconnection	Nb
8	BCC / JCC	Contact between BAS and COU / Contact between JJ and COU	SiO_2
9	COU	Upper interconnection	Nb

B. Junction Uniformity and Advanced Technology

In NEC's standard process, the minimum junction size is 2 μm and the critical current density (J_C) is 2.5 kA/cm^2. To increase the circuit density and operating speed of the integrated circuits, we plan to reduce the junction size and increase the J_C in two steps. First, we will reduce the junction size to 1.4 μm and increase the J_C to 5 kA/cm^2. Then we will further reduce the size to 1 μm with J_C of 10 kA/cm^2. The design rule for each reduction is listed in Table II. In order to use the reduction processes to fabricate the integrated circuits, junction uniformity must be took into consideration. Then, we evaluated our fabrication technology from the point of view of junction uniformity. The uniformity of our junctions depends on the Nb fine-etching technique. The experimental values of the standard deviation (σ) for 1000 junctions are also listed in Table II. The junction counter electrodes were formed by two etching methods: conventional RIE with SF_6 gas (the standard process), and electron cyclotron resonance (ECR) plasma etching with SF_6 gas [4]. When SF_6 RIE was used, σ was 0.9%, 2.3%, and 4.7% for the junction sizes of 2 μm, 1.4 μm, and 1 μm, respectively. With SF_6 ECR, σ was improved to 0.8%, 0.7%, and 1.7%, respectively.

TABLE II
Design Rule and Junction Uniformity for Standard and Advanced Processes

Design Rule		Standard	Reduction 1	Reduction 2
Minimum Line		1.5 μm	1.0 μm	0.5 μm
Minimum Spacing		1.5 μm	1.0 μm	0.5 μm
Minimum Via Hole		1.0 μm	0.6 μm	< 0.6 μm
Alignment Margin		0.5 μm	0.3 μm	0.2 μm
Minimum JJ		2.0 μm	1.4 μm	1.0 μm
Current Density (J_C)		2500 A/cm^2	5000 A/cm^2	10000 A/cm^2
Uniformity				
SF6-RIE	σ (1000 JJ)	0.9 %	2.3 %	4.7 %
	$\Delta I_C < \pm 10\%$	10M JJ	50K JJ	25 JJ
SF6-ECR	σ (1000 JJ)	0.8 %	0.7 %	1.7 %
	$\Delta I_C < \pm 10\%$	10M JJ	10M JJ	100K JJ

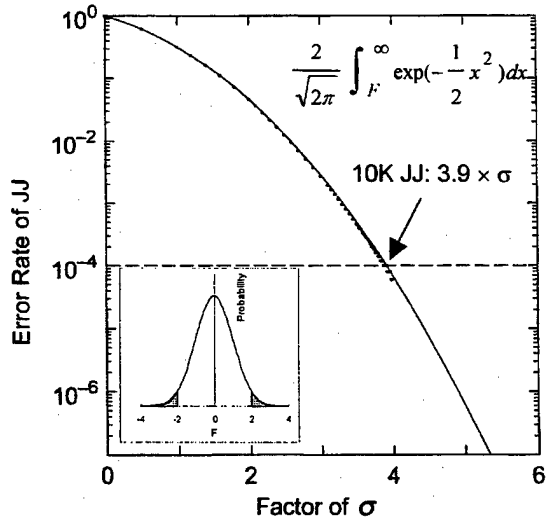

Fig. 2 Plot of a probability integral for normal distribution. The vertical axis shows the error rate of junction whose I_C variation is more than ΔI_C. For the circuits 10K JJs are integrated, the value of F is 3.9 and 3.9 × σ should be less than ΔI_C.

To ensure the correct circuit operation, the I_C values of all junctions must be within the margin of I_C variation (ΔI_C) allowed for the correct circuit operation. A necessary condition for the relationship of σ and ΔI_C is

$$F \times \sigma\,(\%) \le \Delta I_C\,(\%),$$

where F is a factor of σ, that depends on the number of junctions. The value of F is determined using a normal distribution table so that probable number of junctions, whose I_C variation are more than ΔI_C, is less than one. In the case of a circuit in which 10k junctions are integrated, for example, the junction error rate must be less than 10^{-4}. An F of 3.9 are obtained using a probability integral of normal distribution (Fig. 2), consequently 3.9 × σ (%) should be less than ΔI_C. When ΔI_C of ± 10% is assumed, the value of σ must therefore be less than 2.5% for the correct circuit operation.

From the point of view of junction uniformity, our standard technology enables integration of more than 10M 2-μm junctions if ΔI_C of ± 10% is allowed. With ECR plasma etching, it will be possible to integrate 10M 1.4-μm junctions and 100k 1-μm junctions and increase the operating speed of SFQ circuits.

III. SFQ SERIAL MEMORY CIRCUITS

We designed a double-buffered shift register circuit whose equivalent circuit is shown in Fig. 3. One stage of the shift register consists of two buffer loops (loop 1 and loop 2) and the storage loop. Four junctions per stage are used and three DC bias currents (B1, B2, B3) are supplied. Buffer loop 1 contains Jd0, Lba1, and Jba1, and buffer loop 2 contains Jba1, Lbb1, and Jbb1. The storage loop consists of Jbb1, Ld1, and Jd1. Clock signals are propagated through

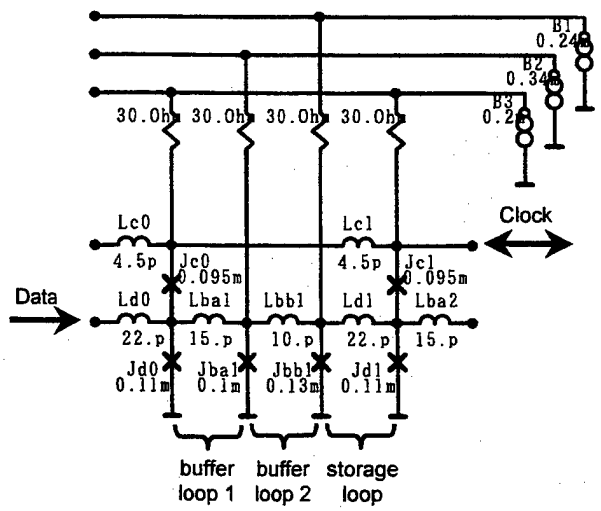

Fig. 3 Equivalent circuit of a 1-bit double-buffered shift register. One stage of the shift register consists of two buffer loops (loop 1 and loop 2) and the storage loop.

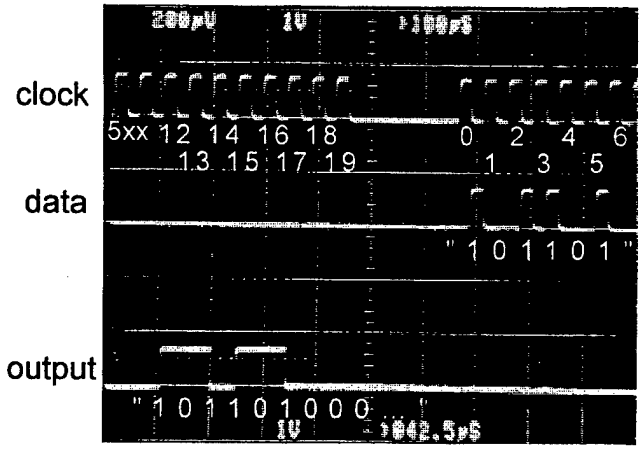

Fig. 4 Functional testing results for the 512-bit shift register circuit. The traces from top to bottom are clock, input data, and output data. The end and the beginning of the 520-pulse clock envelope are shown with a data pattern of "10110100....". The output data was read by the SFQ/DC converter with a T flip-flop.

Lc1. Junctions, Jd1 and Jc1, are under the racing condition. When the data "1" is stored in the storage loop and a clock signal arrives, Jd1 switches, so data "1" is sent to the next stage. When the data "0" is stored and a clock signal arrives, Jc1 switches and the state of the storage loop is not changed. Using the two buffer loops, the shift register can accept a bi-directional clock-signal flow. The circuit operation is similar to the buffered shift register reported by Mukhanov [5]. The circuit parameters were initially determined using PSCAN [6] on an MS-DOS (R) platform, and they optimized using WinS [7] to enable proper operation with wide margins.

We designed a 512-bit shift register using the unit cell and input/output gates. The input gates contained two DC/SFQ converters that generated data and clock SFQ pulses. The DC/SFQ converters were based on the converter reported in [8]. An SFQ/DC converter with a T flip-flop was used as the output gate, and this converter was based on the one described in [2]. In the 512-bit shift register, the clock-signal flow was in the opposite direction to the data flow (counter flow clocking). The circuit contained 2070 junctions.

We fabricated the 512-bit shift register circuit using our standard process and carried out functional testing at 10 kHz. Fig. 4 shows the test results. In Fig. 4, the traces from top to bottom are clock, input data, and output data. A 520-pulse clock envelope and a data pattern of "10110100...." were applied to the shift register. The last and first 20 to 30 clock cycles were observed to confirm proper 512-bit-delay operation. The first input data "1" was applied between the clock 0 and 1, and the first output data "1" was read when the clock 512 was applied. Thus, a 512-bit-delay operation was obtained and the measured margins were ±55%, ±31%, and ±13% for B1, B2, and B3, respectively.

IV. Conclusion

We have developed NEC's standard process, and it has been used routinely to fabricate Nb integrated circuits. In the process, i-line stepper lithography and RIE with SF_6 gas are used and the minimum junction size is 2 μm with a J_C of 2.5 kA/cm^2. For the 2-μm junctions, the σ of I_C was 0.9%. This junction uniformity allows integration of more than 10M junctions if an I_C variation of ± 10 % permits correct circuit operation. We have also developed an advanced fabrication technology to reduce the junction size. The junction size can be reduced to 1.4 μm, with a σ of 2.3% when using standard SF_6 RIE. With ECR plasma etching, a σ of 2.5% was obtained for 1-μm junctions. These results are promising to increase the operating speed of SFQ integrated circuits.

We designed a double-buffered shift register circuits in which four junctions per stage are used. A 512-bit shift register and the input/output gates were designed. The circuit contained 2070 junctions and were fabricated using our standard process. Correct 512-bit delay operation was obtained during functional testing. This work was our first step to demonstrate SFQ integrated circuits. In the next step, we will increase the integration scale and demonstrate the high-speed operation of the shift register. We will also try to increase the operating speed by using advanced fabrication technology.

Acknowledgment

We thank Jun'ichi Sone for his continuous encouragement during this work and Shuichi Nagasawa, Shinichi Yorozu, and Yoshihito Hashimoto for their helpful discussions.

References

[1] S. Nagasawa, Y. Hashimoto, H. Numata, and S. Tahara, "A 380ps, 9.5mW Josephson 4-Kbit RAM operated at a high bit yield," *IEEE Trans. Appl. Superconductivity*, vol. 5, pp. 2447-2452, Jun. 1995.

[2] K.K.Likharev and V. K. Semenov, "RSFQ logic/memory family: a new Josephson-junction technology for sub-terahertz-clock-frequency digital system," *IEEE Trans. Appl. Superconductivity*, vol. 1, pp. 3-28, Mar. 1991.

[3] H. Numata, S. Nagasawa, and S. Tahara, "Fabrication process for sub-micron Josephson junctions," *Extended Abstracts of 4th International Superconductive Electronics Conference*, Boulder, pp. 280-281, 1993.

[4] H. Numata, S. Nagasawa, and S. Tahara, "Fabrication technology for a high-density Josephson LSI using an electron cyclotron resonance etching technique and a bias-sputtering planarization," *Supercond. Sci. Technol.*, vol. 9, pp. A42-A45, 1996.

[5] O. A. Mukhanov, "Rapid single flux quantum (RSFQ) shift register family", *IEEE. Trans. on ASC.*, vol. 3, pp. 2578-2580, Mar. 1993.

[6] S. V. Polonsky, V. K. Semenov, and P. N. Shevchenko, "PSCAN: Personal Superconductor Circuit Analyser," *Supercond. Sci. Technol.*, vol. 4, pp. 667-670, 1991.

[7] V. K. Kaplunenko, "Interactive Simulator for Superconducting Electronics, " to be published in ASC'98 proceedings, EDE-08.

[8] S. V. Polonsky, V. K. Semenov, P. I. Bunyk, A.F. Kirichenko, A. Yu. Kidiyarova-Shevchenko, O. A. Mukhanov, P. N. Shevchenko, D. F. Schneider, D. Yu. Zinoviev, and K. K. Likharev, "New RSFQ Circuits," *IEEE Trans. Appl. Superconductivity*, vol. 3, pp. 2566-2577, Mar. 1993.

Superconductor–semiconductor–superconductor junctions using NbN

Tatsushi Akazaki, Hiroshi Yamaguchi, Junsaku Nitta, and Hideaki Takayanagi
NTT Basic Research Laboratories, 3-1 Morinosato-Wakamiya, Atsugi-shi, Kanagawa, 243-0198 JAPAN

Abstract – We report on the fabrication of the superconductor–semiconductor–superconductor (S–Sm–S) junction formed by two superconducting NbN electrodes and a two-dimensional electron gas (2DEG) in an $Al_{0.7}Ga_{0.3}Sb$/InAs heterostructure and we describe the superconducting characteristics we obtained. A critical current I_C of ~ 0.9 μA at ~ 70 mK was obtained for the first time in the S-Sm-S junction using NbN. Although the T_C of NbN was about 12 K, I_C decreased as increasing temperature, and then disappeared at ~1.7 K. This phenomenon can be qualitatively explained by considering that the 2DEG underneath the NbN changed places with the *pseudo*-superconductor because of proximity-induced superconductivity.

1. INTRODUCTION

In recent years, we have investigated the superconductor–semiconductor–superconductor (S–Sm–S) junctions for device applications as well as the study of mesoscopic Josephson effects. Recently, we have exchanged n-type InAs bulk materials and the p-type InAs inversion layer that we used at the first step for the InAs-inserted-channel $In_{0.52}Al_{0.48}As/In_{0.53}Ga_{0.47}As$ inverted modulation-doped (i-MD) structure with both high sheet-carrier density and high electron mobility [1], [2]. This is because we needed a novel semiconductor material to observe new mesoscopic Josephson effects in the S–Sm–S junction which obeys the clean-limit theory and we also needed to develop a Josephson field effect transistor (JOFET) with good three-terminal operation. We have also used Nb as a superconductor material. This is because the critical temperature T_C and the upper critical field H_{C2} of Nb are sufficient when the measuring temperature is equal to 4.2 K or less and the magnetic field is applied just up to about 0.1 T.

Since Zyuzin et al. theoretically predicted the existence of the Josephson current in the S–Sm–S junction under a very high magnetic field, several theorists have discussed new phenomena in the S–Sm–S junction under very high magnetic fields [3]-[5]. In order to observe these phenomena experimentally, we need to obtain a high H_{C2} superconductor. This is because a superconductor has to keep superconductivity even in a very high magnetic field of, at least, over 10 T. NbN is one of the best candidates for such a superconductor because NbN typically has a T_C of about 15 K and a H_{C2} of over 20 T, and it is easy to make a NbN film using sputtering deposition.

In this paper, we report on the fabrication of the S–Sm–S junction formed by two superconducting NbN electrodes made by using DC magnetron sputtering deposition and a 2DEG in an $Al_{0.7}Ga_{0.3}Sb$/InAs heterostructure. We also describe the superconducting characteristics we obtained.

II. EXPERIMENT and DISCUSSION

A. Junction Fabrication

Figure 1 shows the schematic structure of the S–Sm–S junction formed by two superconducting NbN electrodes and a two-dimensional electron gas (2DEG) in an $Al_{0.7}Ga_{0.3}Sb$/InAs heterostructure (NbN S–Sm–S JJ). The heterostructure was grown by molecular beam epitaxy (MBE) on a semi-insulating (100) GaAs substrate. The 2DEG was formed in the InAs layer. The sheet carrier density n_s and mobility μ of the 2DEG at 77 K were determined at 1.2×10^{12} cm^{-2} and 31,000 cm^2/Vs by Hall measurement. The NbN electrodes were grown by DC magnetron sputtering deposition. NbN electrodes of 80~100 nm thickness were sputtered from an Nb target in an Ar/N_2 atmosphere consisting of 10 sccm Ar and 0.3 sccm N_2 at a total pressure of 4 mTorr, a constant DC current of 0.2 A and a target voltage of 410 V without intentional substrate heating. In this way, we obtained the best T_C of ~13.5 K [6].

We will now briefly describe the NbN S–Sm–S JJ fabrication process. First, patterns for ohmic electrodes were defined employing electron beam lithography. Chemical etching with an NH_4OH-based etchant was used to selectively remove both the 5-nm undoped GaSb cap layer and the 50-nm undoped

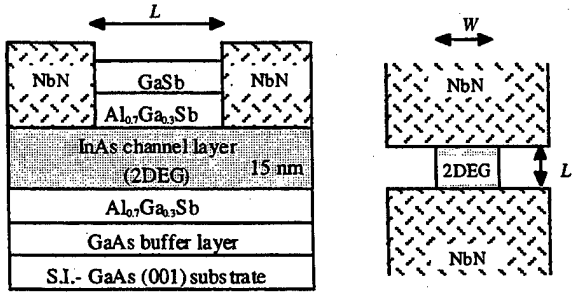

(a) Cross-sectional view (b) Top view

Fig. 1 The schematic structure of the S–Sm–S junction formed by NbN and AlGaSb/InAs heterostructure (NbN S–Sm–S JJ).

Manuscript received April 30, 1998.
This work was supported in part by the NEDO International Joint Research Grant.

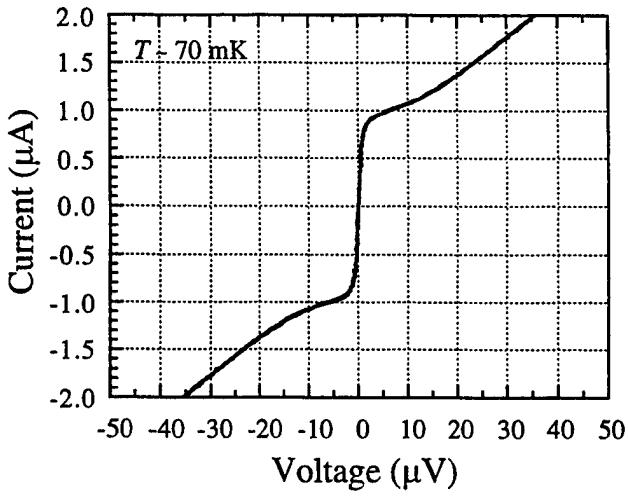

Fig. 2 Typical current - voltage characteristics of the NbN S–Sm–S JJ at ~ 70 mK .

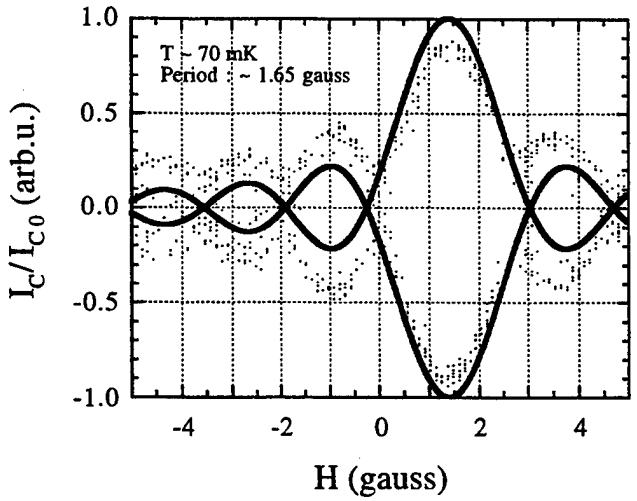

Fig. 3 Measured critical current (circles) and a theoretical Fraunhofer pattern (line) versus magnetic field for the NbN S–Sm–S JJ at ~ 70 mK .

$Al_{0.7}Ga_{0.3}Sb$ Schottky layer. The oxidation layer of the undoped InAs layer was only etched by Ar RF sputter etching in a sputtering chamber, and then 100-nm thick NbN was deposited by DC magnetron sputtering and lifted off. Finally, the unused part of the $Al_{0.7}Ga_{0.3}Sb$/ InAs heterostructure was removed, and then Au pads for wire-bonding were deposited.

B. Junction Characteristics

Figure 2 shows typical *I-V* characteristics of the NbN S–Sm–S JJ with $L = 0.5$ μm and $W = 2.5$ μm at 70 mK. A critical current I_C of about 0.9 μA was obtained for the first time in the S-Sm-S junction using NbN. When a magnetic field is applied, the critical current follows a Fraunhofer pattern, as can be seen in Fig. 3. The periodicity becomes 10 times smaller than that corresponding to one flux quanta inside the junction area. This discrepancy is caused by the flux enhancement due to the flux focusing within this geometry. Figure 4 shows the differential resistance as a function of voltage $dV/dI - V$ at ~10 K. The broad resistance minima within $V \sim \pm 3$ mV is clear evidence of Andreev reflection, even at ~10 K. These results indicate that we obtained good ohmic contact between NbN and InAs.

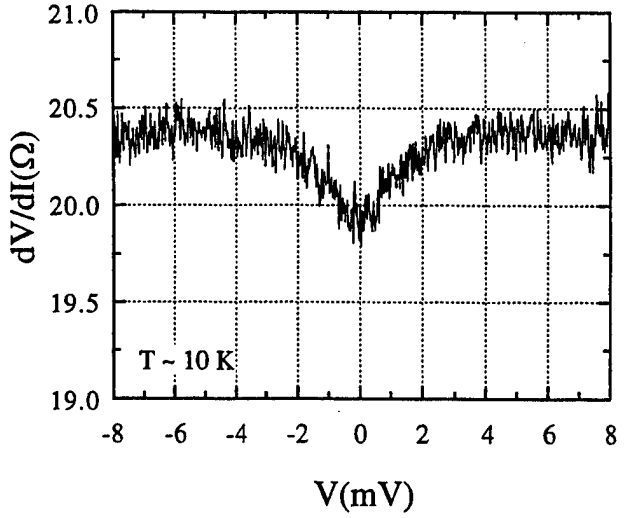

Fig. 4 Differential resistance as a function of voltage at ~ 10 K.

Figure 5 shows the temperature dependence of I_C. The supercurrent disappeared over ~ 1.7 K, even though the T_C of NbN is about 12 K. According to recent superconducting proximity theory [7], [8], the reason for this can be qualitatively understood as follows. In Fig. 6, one scenario is illustrated schematically. Here, S is a superconductor, N_1 is a normal conductor, N_2 is a normal conductor underneath a superconductor, T is measuring temperature, and $E_{Th,N1(N2)}$ is Thouless energy ($=\hbar D/L^2$, D is diffusion constant, and L is the length of a normal conductor of $N_1(N_2)$). We assume that the conductivity of N_1 is much higher than that of N_2, namely $E_{Th,N1} >> E_{Th,N2}$. This assumption is appropriate because both the sheet carrier density and mobility of the 2DEG decrease as the conduction band energy increases with the removal of the Schottky layer. For $T >> E_{Th,N2}$, the proximity-induced superconducting correlation between electrons in N_2 disappears at a short distance from the S/N_2 interfaces, and then the Cooper pairs injected from S into N_2 are immediately destroyed. Consequently, the supercurrent between the two S cannot flow through N_1 and N_2 [Fig. 6(a)]. As T is lowered, the proximity-induced superconductivity expands into N_2, and for $T \sim E_{Th,N2}$, the proximity-induced superconducting correlation survives everywhere in N_2. Consequently, a real gap ε_g in the quasiparticle spectrum starts to develop in N_2, and then N_2 is regarded as a *pseudo*-superconductor S_2. Assuming that N_1 is ballistic for $T \sim E_{Th,N2}$ the supercurrent between the two S_2 starts to flow through N_1, and then increases as T decreases [Fig. 6(b)].

Next, we will discuss the temperature dependence of I_C in

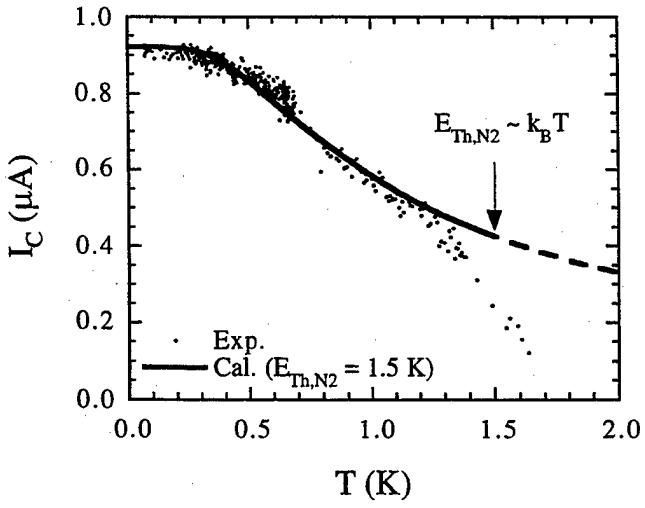

Fig. 5 Temperature dependence of the critical current.

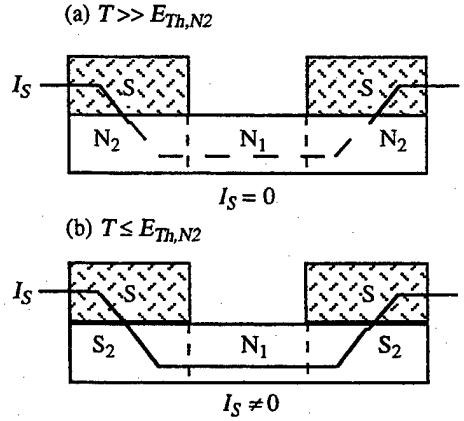

Fig. 6 Schematic diagram of the supercurrent path across the superconductor/semiconductor interface at (a) $T \gg E_{Th,N2}$ and (b) $T \leq E_{Th,N2}$. Here, S is a superconductor, N_1 is a normal conductor, N_2 is a normal conductor underneath a superconductor. S_2 is N_2 becoming a *pseudo*-superconductor due to the proximity effect. I_S is supercurrent.

this S_2–N_1–S_2 junction. The temperature dependence of I_C in an S–ballistic N–S junction is expressed by

$$I_C(T) \propto N \frac{e\Delta}{2\hbar} \tanh\left(\frac{\Delta}{2k_B T}\right), \qquad (1)$$

where N is the number of subbands below the Fermi level, and Δ is the superconducting gap [9], [10]. For the S_2–N_1–S_2 junction, Δ is replaced by ε_g in S_2, which is of the order of $E_{Th,N2}$. Consequently, I_C is proportional to $\tanh(E_{Th,N2}/2k_B T)$. Note that this expression can be applied to only $T \leq E_{Th,N2}$, as we mentioned above. The calculated temperature dependence of I_C is shown in Fig. 5 by the solid line. Here, we assumed $E_{Th,N2}$ = 1.5 K that is close to $T \sim 1.7$ K where the supercurrent disappeared. It is clear that there is agreement between the experimental results and the calculated ones. This agreement suggests that our picture can qualitatively describe the NbN S–Sm–S JJ.

III. Conclusions

We fabricated a superconductor–semiconductor–superconductor junction of two superconducting NbN electrodes using a DC magnetron sputtering deposition and a 2DEG in an $Al_{0.7}Ga_{0.3}Sb$/InAs heterostructure. A critical current I_C of about 0.9 μA was obtained for the first time in the S-Sm-S junction using NbN. Moreover, resistance minima due to Andreev reflection was observed even at ~10 K. These results indicate that we obtained good ohmic contact between NbN and InAs. We also obtained temperature dependence of the critical current. Although the T_C of NbN was about 12 K, I_C decreased as temperature increased, and then disappeared at ~1.7 K. This phenomenon can be qualitatively explained by considering that the 2DEG underneath the NbN changed places with the *pseudo*-superconductor because of proximity-induced superconductivity.

Acknowledgments

We would like to thank Dr. H. Nakano, Dr. J. Rosland, and Dr. Y. Hirayama for their valuable discussions, and also Y. Iguchi for assistance with the data analysis. Furthermore, we wish to thank Dr. S. Ishihara for his encouragement throughout this work.

References

[1] J. Nitta, T. Akazaki, H. Takayanagi, and K. Arai "Transport properties in an InAs-inserted-channel $In_{0.52}Al_{0.48}As/In_{0.53}Ga_{0.48}As$ heterostructure coupled superconducting junction," *Phys.Rev.B*, vol. 46, pp. 14286-14289, 1992.

[2] T. Akazaki, H. Takayanagi, J. Nitta, and T. Enoki, "Josephson field effect transistor using InAs-inserted-channel $In_{0.52}Al_{0.48}As/In_{0.53}Ga_{0.48}As$ inverted modulation-doped structure," *Appl. Phys.Lett.*, vol. 68, pp. 418-420, 1996.

[3] A. Yu. Zyuzin, "Superconductor–normal-metal–superconductor junction in a strong magnetic field," *Phys.Rev.B*, vol. 50, pp. 323-329, 1994.

[4] Y. Takagaki "Transport properties of semiconductor–superconductor junctions in quantized magnetic fields," *Phys.Rev.B*, vol. 57, pp. 4009-4016, 1998.

[5] Y. Ishikawa and H. Fukuyama, "Effects of Magnetic field on Josephson current in SNS System," *J. Phys. Soc. Jpn.*, vol. 68, pp. 954-963, 1999.

[6] T. Akazaki, J. Nitta, and H. Takayanagi, "InAs-inserted-channel InAlAs/InGaAs Inverted HEMTs with NbN Electrodes," *IEEE trans. on Appl. Superconductivity*, in press.

[7] A. A. Golubov, F. K. Wilhelm, and A. D. Zaikin, "Coherent charge transport in metallic proximity structure," *Phys.Rev.B*, vol. 55, pp. 1123-1137, 1997.

[8] A. F. Volkov, P. H. C. Magnée, B. J. van Wees, and T. M. Klapwijk, "Proximity and Josephson effects in superconductor–two-dimensional electron gas planar junctions," *Physica C*, vol. 242, pp. 261-266, 1995.

[9] C. W. J. Beenakker and H. van Houten, "Josephson current through a superconducting quantum point contact shorter than the coherence length," *Phys.Rev.Lett.*, vol. 66, pp. 3056-3059, 1991.

[10] A. Furusaki, H. Takayanagi, and M. Tsukada, "Josephson effect of the superconducting quantum point contact," *Phys.Rev.B*, vol. 45, pp. 10563-10575, 1991.

Full-Scale Integration of Superconductor Electronics for Petaflops Computing

Lynn A. Abelson, Quentin P. Herr, George L. Kerber, Michael Leung, and Thomas S. Tighe
TRW, Space & Electronics Group, Redondo Beach, CA 90278

Abstract—**Ultra-low power and ultra-high speed single-flux-quantum electronics is an enabling technology solution for near-term petaflops computing. The proposed Hybrid Technology Multi-Threaded (HTMT) petaflops-scale computer architecture includes computational modules operating at 100 GHz and an I/O throughput of 32 Petabit/s. In this frequency regime, on-chip interconnect mimics the system interconnect problem. On-chip latency can be minimized with increased gate density by using more levels of metal and smaller line pitch. This may be even more important than increasing the maximum clock rate by using smaller junctions and higher critical current density. Superconductor ICs at an integration level of 100 kgates/cm^2 are proposed for the processors, first level cache, and inter-processor network. Petaflops capacity will require a compact, optimized system-level packaging strategy to achieve the necessary computational density and interconnect bandwidth. Modular packaging and automated circuit testing are required to minimize manufacturing costs. We focus on the critical technology challenges that exist for the IC foundry, packaging, and the I/O data link, and present technology roadmaps to achieve the HTMT requirements.**

I. Introduction

PETAFLOPS COMPUTING represents a thousand-fold improvement over today's largest massively-parallel-processor machines, which are susceptible to fundamental time-of-flight and power dissipation limits. Superconductor electronics (SCE) offers the ultimate high-speed and low-power computing solution. SCE has been identified as an enabling technology for achieving petaflops in the short term, as part of the Hybrid Technology Multi-threaded (HTMT) architecture system. The proposed HTMT system uses hybrid technologies, including processor-in-memory, holographic data storage, optical network communications and superconductor electronics, and a unique multi-threaded architecture. The goal is to achieve petaflops within ten years [1]. A petaflops architecture using conventional electronics, developed within the same timeframe, may have prohibitive power, size and interconnect latency [2].

Various aspects of the SCE circuit design are described in [3], [4], [5]. Technology goals for the superconductor processors (SCP) include: 0.8 μm Josephson junctions with J_c=20 kA/cm^2 to achieve 100 GHz on-chip clock speed, 100 k gates/cm^2 to achieve computational density, 2000 to 5000 pinouts per chip, 50 chips per multi-chip module (MCM) with chip-to-chip bandwidth of 30 Gbps, and 8 million wires out of the liquid helium cryogenic region at a data rate of 8 Gbps. It is estimated that 4 k processors, partitioned among 512 MCMs, comprised of 40 k chips and 100 billion Josephson junctions will be needed.

Manufacture of the full-scale system will require advances in SCE integrated circuit (IC) fabrication, packaging, and high throughput, high-speed cryogenic test capabilities. The authors have examined critical challenges in each of these areas in [6]. In this paper, we focus on two key aspects of the SCE system design: latency and parts count. Low latency, both within and between the processors, is the single most important performance issue and thus drives technology improvement on all levels. Reduced parts count dictates manufacturing complexity and cost. This is particularly critical applied to the datalink between the superconductor cryostat and the room temperature electronics. We present updated technology roadmaps showing the evolution of present technology needed to meet the petaflops-scale computing challenge.

II. IC Technology

Clock rates of 100 GHz are accessible to single-flux-quantum (SFQ) superconductor electronics. Signal propagation is equal to one-third the speed of light on superconductor microstrip lines; even so, interconnect latency dominates gate delay in this frequency regime. Latency can be minimized with increased gate density by using more levels of metal and narrower line pitch. This may be even more important than increasing the maximum clock rate by using smaller junctions and higher critical current density. Various process improvements are listed and evaluated in Table I.

Present Nb-based Josephson junction technology is at 10^4 gates/cm^2 integration level, with feature sizes ranging from 1.5 μm to 3 μm, depending on the foundry [7]. Scaling to petaflops requires more than a ten-fold increase in circuit density (to 100 k gates/cm^2), a decrease in feature size two to three times below present day technology (to 0.8 μm), and additional interconnect and masking levels. The evolution of superconductor IC technology to achieve petaflops and beyond is shown in Table II. Petaflops is achieved with 0.8 μm technology. The most dense chip will have an estimated 10 million, 0.8 μm di-

TABLE I
ADVANCED IC PROCESS CAN REDUCE LATENCY

	Increased Clock Rate	Increased Density
Technology Improvement	Smaller junctions with higher critical current density.	Smaller line pitch. Increased vertical integration.
Benefits	Higher junction impedance. Higher voltage signals.	Reduced latency. [a]
Disadvantages	Larger electrical spreads. Increased latency.	Lower yield.

[a] Latency is measured as the number of clock ticks for signal propagation between a given pair of gates.

Manuscript received May 1, 1999.

This work was performed for the Jet Propulsion Laboratory, California Institute of Technology, and was sponsored by the Defense Advanced Research Projects Agency (DARPA) and the National Security Agency (NSA) through an agreement with the National Aeronautics and Space Administration.

Reference herein to any specific commercial product, process, or service by trade name, trademark, manufacturer, or otherwise, does not constitute or imply its endorsement by the United States Government or the Jet Propulsion Laboratory, California Institute of Technology.

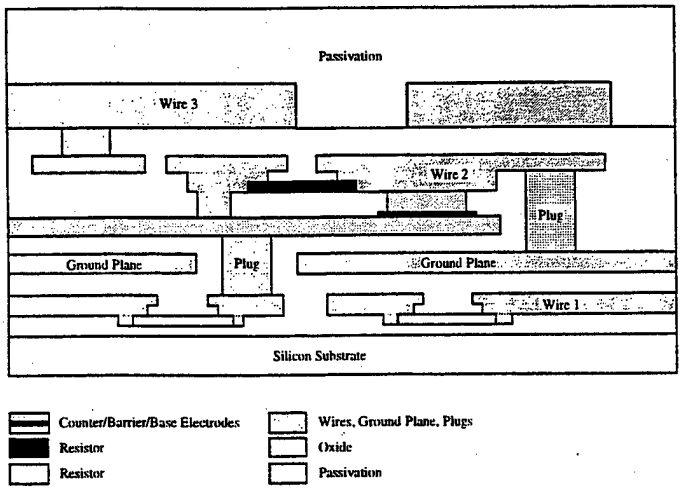

Fig. 1. Notional cross-section of the IC process illustrating salient features of an advanced process, which includes four interconnect levels, planarization, and plugs.

ameter junctions and four wiring layers on a 2 cm × 2 cm die. Chip fabrication exceeds the capability of existing superconductor foundries, but this level of integration has been available for several years in the semiconductor industry [8]. The fabrication tools, including chemical mechanical planarization (CMP) and infrastructure support, are known and readily available which implies that no new technologies or inventions are required to produce superconductor IC chips of equivalent density.

The superconductor IC chip fabrication process will build upon existing experience and concepts that already have been proposed or demonstrated in MSI and LSI superconductor circuits [9], [10], [11]. Fig. 1 is a cross-sectional view of a conceptual IC process that relies extensively on metal and oxide CMP. This process has one ground plane, four wiring layers including base electrode, two resistor layers, self-aligned junction contacts, and vertical plugs or pillars [9] for interconnection vias between wiring layers. The aspect ratio of the vertical plugs is on the order of 1:1, which does not require complex chemical vapor deposition or hot metal deposition processes that are typically used in semiconductor fabrication to fill vias of more extreme aspect ratio. Power lines and biasing resistors are located below the ground plane to isolate the junctions from the effect of magnetic fields and to increase circuit density [10]. The final IC process is likely to include an additional wiring layer and/or ground plane and vertical resistors to reduce the chip real estate occupied by junction shunt resistors.

III. Cryogenic Package and I/O

The ultra-low power associated with SFQ logic means that a compact package may be used, enabling high computational density and interconnect bandwidth. A concept for the package that minimizes interconnect latency is shown in Fig. 2. Marginal improvement in standard electronics packaging such as the use of MCMs and flip-chip bonding die attach are required to realize this design. Issues for manufacturability include minimizing parts count and modularity. Modularity means that individual chips or boards may be easily repaired or replaced. Parts count is especially critical for the I/O data link to room temperature electronics.

TABLE II
IC Technology Roadmap

	1998	2001	2004	2007	SIA 1992
Min. feature size (μm)	1.5	0.8	0.50	0.25	0.50
Junction size (μm)	2.5	0.8	0.80	0.80	-
Critical current (A/cm^2)	2k	20k	20k	20k	-
Gates/chip (logic)	5k	120k	600k	2M	300k
Bits/chip (SRAM)	16k	400k	2M	6M	4M
Chip size (mm^2)	100	400	400	400	250
Wafer diameter (mm)	100	150	150	150	200
Defects per cm^2	<2	<0.2	<0.1	<0.05	<0.1
No. interconnect levels	3	4-5	5-6	6	3
No. of resistor layers	2	2	2	2	-
Planarization	no	yes	yes	yes	yes
Vertical resistors	no	no	yes	yes	-
I/O count	128	2k	2-5k	2-5k	500
Wafer starts per month	12	200	1k	1k	>20k

The configuration shown in Fig. 2 has 512 MCMs in an octagonal arragement. Each MCM, up to 20 cm on a side, has up to 50 SCE chips and eight processor units. Flip-chip bonding is used to attach the chips to the MCM providing high interconnect density, multi-Gbps data rate transmission, automated assembly, and reworkability [12]. The vertical MCMs are edge-mounted to 160 horizontal multi-layer printed circuit boards (PCB) which allows for MCM-to-MCM connections. Adjacent MCMs are connected to each other along their top and bottom edges. The cryogenic network (CNET) allows any processor unit to communicate with any other with less than 20 ns latency [5]. A roadmap for the packaging technology requirements, including specifications for the MCMs, PCBs and flexible ribbon I/O cables is given in Table III.

The interconnect problem includes the data link between the cryostat and room temperature. This link must bridge major differences in both temperature and electrical characteristics.

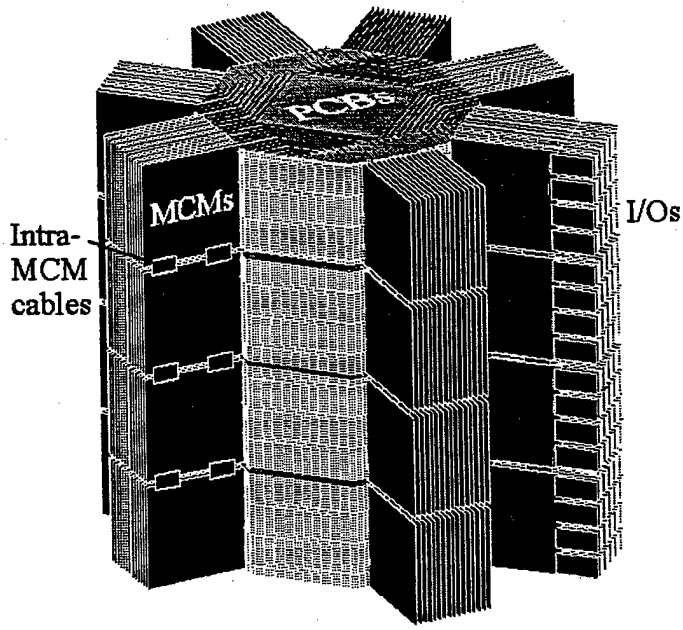

Fig. 2. Packaging concept for HTMT SCP, showing 512 fully integrated MCMs on cylindrical backplane.

TABLE III
PACKAGING TECHNOLOGY ROADMAP

	1998	2001	2004
MCM[a]			
Pad size (μm)	100	75	25
Pad pitch (μm)	150	125	60
Max. pads per chip	3600	5000	12000
Pad density (cm^{-2})	1200	2000	7500
Max. No. Nb layers	5	7	9
Max. No. W layers	20	30	40
Linewidth (μm)	5	3	3
Bandwidth (Gbps/wire)	10	10	30
Chip-to-chip SFQ	No	Yes	Yes
Chips per MCM	24	50	75
Backplane			
Technology	PCB	Ceramic	Ceramic/Flex
Size (cm^2)	30	30	50
Bandwidth (Gbps/wire)	2.5	5	10
I/O ribbon cables			
Pitch (μm)	200	50	10
Cable width (cm)	2.5	5	5
Bandwidth (Gbps)	2.5	5	8
Heat load / wire (mW @ 4 K)	0.4	0.2	0.1

[a] Assuming an MCM Ceramic/Dielectric technology.

Table III assumes ribbon cables for this interface. These cables consist of lithographically defined signal lines on a substrate of polyimide film in a stripline configuration, which have been demonstrated in a cryogenic test station at data rates up to 3 Gbps with minimal heat load, but the present line density is an order of magnitude lower than that required for HTMT [13]. One method for increasing density is to piggy-back the cables, but this increases complexity.

Other implementations of the data link merit consideration. Use of fiber optics to carry information into the cryostat reduces parts count and thermal load. Using wavelength division multiplexing (WDM), each fiber can replace 100 wires. A factor of 1000 reduction in direct thermal load is achieved, as each fiber has 10× less thermal conductance relative to wire cable.

These advantages apply only to data traveling *into* the cryostat. There are known low-power techniques to convert photons to electrical current, but the reverse is not true. Driving optical signals at high frequencies requires lasers or diodes. An average laser channel requires 1 mA of current at 1 V for a power consumption of 1 mW. This compares unfavorably with the present estimate of 50 μW thermal load for each electrical signal line. At the same time, direct modulation of lasers or diodes at 4 K is just one method of transmitting optical data. Another method is to generate the photons at room temperature and amplitude modulate at 4 K. In theory, this promises greatly reduced power consumption within the cryostat. At present, however, a low-power modulation technique at multi-Gbit/s data rates is unproven.

The optimal configuration may use optical fiber to carry data into the cryostat and flexible ribbon cable to carry data out. Initial estimates suggest data flow will be asymmetrical; the data rate in will be greater than data flow out. The benefits of a hybrid configuration therefore may be significant. If the data asymmetry is 4:1, 20 k fibers and 800 k wires are required, with a thermal heat load of only 40 W. This estimate only accounts for the passive heat load. Additional heat will be generated transmitting signals to and from the cryostat because of I^2R heating. Depending on the currents used, this term can dominate.

Evaluation of the data link design is ongoing. With WDM, the different channels within a single fiber need separation. This is usually accomplished using zero-power elements such as prisms or gratings. These elements can be relatively large, and may not fit within the planned size of the cryostat. We have not addressed the power required for the optical receivers, or the thermal energy delivered by the photons themselves. These sources of heat may offset any gains from using the low thermal conductance glass fibers. In addition, if the SRAM/PIM chips are placed at a 77 K stage, the heat generated by the light sources used to drive data down to the 4 K stage may increase required cooling at 77 K to unreasonable levels, even with the increased refrigeration efficiency at that temperature. A more detailed design study can occur once details such as data flow asymmetry are better defined.

IV. CONCLUSION

Superconductor electronics simultaneously offers the high speed and low power needed to achieve petaflops at a reasonable level of circuit density. Inter- and intra-processor latency can be minimized through a high level of chip integration and compact packaging. An advanced IC process will require development of a robust 0.8 μm-junction technology, small-footprint resistors, planarization, and plug technology. A hybrid electrical-optical I/O datalink may reduce complexity.

ACKNOWLEDGMENT

The authors thank Dale Durand and John Spargo of the TRW team, as well as Arnold Silver, Thomas Sterling, Larry Bergman, Kostya Likharev, and Doc Bedard for useful discussions and critical review.

REFERENCES

[1] J. Cohen, "Mix of technologies spurs future supercomputer," *Insights*, pp. 2-11, July 1998.
[2] T. Sterling, "In pursuit of a quadrillion operations per second," *Insights*, pp. 8-11, April 1998.
[3] P. Bunyk, M. Dorojevets, K. Likharev, and D. Zinoviev, "Technical Report 03: RSFQ Subsystem for HTMT Petaflops Computing," online at www.sunysb.edu, December 1997.
[4] M. Dorojevets, P. Bunyk, D. Zinoviev, and K. Likharev, "Petaflops RSFQ System Design," *IEEE Trans. Appl. Supercond.*, in press.
[5] D. Zinoviev, G. Sazaklis, L. Wittie, and K. Likharev, "CNET: RSFQ switching network for petaflops computing," *IEEE Trans. Appl. Supercond.*, in press.
[6] L. A. Abelson, Q. P. Herr, G. L. Kerber, M. Leung, and T. Tighe, "Manufacturability of Superconductor Electronics for a Petaflops-Scale Computer," *IEEE Trans. Appl. Supercond.*, in press.
[7] L. Abelson, "Superconductive process technologies," *Ext. Abstr. 6th Int'l Supercond. Elec. Conf.*, pp. 1-4, June 1997.
[8] Semiconductor Industry Association, *National Technology Roadmap for Semiconductors, 1997 Edition*, San Jose, Calif., online at notes.sematech.org/mcpgs/roadmap4.pdf.
[9] H. Numata, S. Nagasawa, M. Tanaka, and S. Tahara, "Fabrication technology for high-density josephson integrated circuits using mechanical polishing planarization," *IEEE Trans. Appl. Supercond.*, in press.
[10] T. Shiota, S. Kotani, and T. Imamura, "Subterranean power lines in high-density integrated josephson circuits," *IEEE Trans. Appl. Supercond.*, vol 5, no 1, pp. 31-36, March 1995.
[11] L. A. Abelson, R. N. Elmadjian, and G. L. Kerber, "Next generation Nb superconductor integrated circuit process," *IEEE Trans. Appl. Supercond.*, in press.
[12] K. E. Yokoyama, et al., "Robust superconducting die attach process," *IEEE Trans. Appl. Supercond.*, vol. 7, p. 2631, June 1997.
[13] T. S. Tighe, et al., "Cryogenic packaging for multi-GHz electronics," unpublished.

Study of Correlation between the Microstructure and Phase Inhomogeneities of Y-Ba-Cu-O Epitaxial Films and their DC and Microwave Properties

A. K. Vorobiev, Y. N. Drozdov, S. A. Gusev, V. L. Mironov, N. V. Vostokov, E. B. Kluenkov, and S. V. Gaponov
Institute for Physics of Microstructures RAS, 603600, Nizhny Novgorod, GSP-105, RUSSIA

V. V. Talanov
University of Maryland, Center for Superconductivity Research, College Park, MD 20742, USA

Abstract—The influence of various kinds of structure and phase inhomogeneities on electrical properties of YBCO thin films prepared by inverted cylindrical magnetron sputtering has been investigated. A simultaneous analysis of the changes in the microstructure and electrical parameters has allowed to define a contribution of each kind of inhomogeneities in the restriction of the films electrical parameters. It has been found out that the transition temperature depends mainly on deviations of the *c*-axis lattice parameter from its optimum value, the critical current density depends mainly on the out of plain misorientation of the film domains, and the microwave surface resistance depends mainly on the volume of the high-angle misoriented domains. By using an atomic force and scanning tunneling microscopy the regions of YBCO films with modified properties around Cu-rich second phase particles were observed. It is suggested that superconducting properties of these regions are worse than the matrix due to Cu-depletion. Usually the relative area of these inhomogeneities in our films is about 30 % and can occupy up to 50 % and therefore, mostly determines the electrical properties of films. It is suggested that the processes of cation disorder deforming the film lattice play an important role in formation of structure and phase inhomogeneities in YBCO thin films.

I. Introduction

Currently the properties of even the highest quality Y-Ba-Cu-O (YBCO) thin films are mostly determined by their real structure and not by the fundamental properties of this material. The point is that, in the HTS, the superconducting characteristic lengths, the penetration depth and the coherence length, are quite small [1]. Thus, very small microstructural features can affect the superconducting properties in the HTS. In the last years a lot of studies, applied and fundamental, have been devoted to this subject. It was found out that YBCO film electrical properties can sufficiently depend on the following structural and phase inhomogeneities: the boundaries of the twins, grains and microblocs [2], [3]; the domains with high angle misorientation [4] and *a*-oriented domains [5]; the domains with oxygen nonstoichiometric [6]; the stacking faults [7], the cation disorder in the YBCO cell [8], [9]; secondary phase particles [10]. It is obvious that for development of advanced techniques of high quality YBCO films preparation it is necessary to know how much each kind of inhomogeneities affects certain electrical parameters of films during optimization of deposition conditions. However, to date this problem is completely unsolved. In comparison with other inhomogeneities, the influence of the secondary phase particles on the electrical properties of YBCO films was little investigated. Meanwhile, the presence of the Cu-rich and Y-rich secondary phase particles is a characteristic feature of YBCO films with high electrical properties. It depends on the optimum of YBCO film superconducting properties is located in the area of compositions enriched by copper and yttrium [6], [11]-[13]. Obviously, the presence of the secondary phase particles affects the YBCO film electrical properties through reduction of the effective area of a film cross-section. As a rule, Cu-rich particles occupy about 10-20 % of film surface [14]. However, this area is much more, if we take into account the formation around the Cu-rich particles of the film regions with modified properties [10]. In this paper the results of the analysis of the influence of microstructure and secondary phase inhomogeneities on the DC and microwave properties of YBCO thin films during optimization of deposition conditions is presented and discussed.

Manuscript received April 30, 1999.
This work was supported in part by the Russian State Committee for Science and Technology under Grants No. 98064, No 3.45 and by the Russian Foundation for Basic Research under Grant No. 99-02-16139.

II. Experiment

YBCO thin films were made *in-situ* by inverted cylindrical magnetron sputtering. In the study of the influence of microstructural inhomogeneities two series of YBCO thin films were analyzed: the films obtained on sapphire substrates with YSZ buffer layers during optimization of the deposition temperature T_d [10] and the films obtained on YSZ substrates during optimization of the gas mixture pressure p [15]. The electrical properties of YBCO films were characterized by the values of the temperatures of the onset ($T_{c\,on}$) and the end ($T_{c\,off}$) of superconducting transition, the critical current density at 77 K (J_c) and the microwave surface resistance at 77 K and 10 GHz (R_{eff}). By using X-ray analysis the following kinds of the film microstructural parameters were quantitatively measured: the *c*-axis lattice parameter, *out of plain* misorientation of the *c*-axis of the domains (*FWHM(005)YBCO*), the volume of 45°-misaligned *in plain* grains (I_{45}/I_0) and the volume of the *a*-oriented grains ($I_{(200)}/I_{(006)}$). The properties of the film regions around Cu-rich particles were studied at room temperature by atomic force microscopy (AFM) and scanning tunneling microscopy (STM) on YBCO films with optimized electrical properties obtained on $NdGaO_3$ substrates.

III. Results and Discussions

A. Inhomogeneities of microstructure

A simultaneous analysis of the changes in the microstructure parameters and electrical properties of YBCO films under deposition conditions [10], [15] made it possible to define a contribution of each kind of microstructure inhomogeneities in the restriction of the films electrical parameters.

In the investigated ranges of T_d and p the changes of the $T_{c\,on}$ and $T_{c\,off}$ values correlate mainly with deviations of the c-axis lattice parameter from its optimum value. Hence, the observed $T_{c\,on}$ and $T_{c\,off}$ values are caused mainly by the properties of grains rather than boundaries. The $T_{c\,on}$ and $T_{c\,off}$ values of YBCO films versus the c-axis lattice parameter values are given in Fig. 1. The lattice distortion and the corresponding reduction of $T_{c\,on}$ and $T_{c\,off}$ values is the result of cation disorder processes: Ba-Y substitution [8] and Cu-vacancy formation [9]. The cation disorder occurs at low T_d because of low mobility of adatoms [7], at higher T_d because of an increasing area of film regions with Cu-depletion around Cu-rich particles [10], and at low p because of changes of the film cation composition [16].

In the investigated ranges of p and T_d up to 720 °C [10] the behavior of J_c correlates mainly with the changes of *FWHM(005)YBCO* values. Hence, the observed J_c values are caused mainly by the *out of plain* misorientation of the c-axis of the YBCO film domains. The J_c values of YBCO films versus *FWHM(005)YBCO* values are given in Fig. 2. An exponential dependence of J_c on *FWHM(005)YBCO* has been also found out in [3]. Higher *FWHM(005)YBCO* values, and the corresponding decrease of the J_c values, is the result of a greater lattice mismatch between the film and the substrate at low T_d and p because of the cation disorder, and the result of the *out of plain* misorientation of the domains of YSZ buffer layers.

The R_{eff} values of YBCO films versus T_d up to 720 °C are given in Fig. 3. It can be seen that in the investigated ranges of T_d the behavior of R_{eff} correlates mainly with the changes of I_{45}/I_0 and $I_{(200)}/I_{(006)}$ and, more poorly, with *FWHM(005)YBCO* (dashed line in Fig. 3) [10]. Hence, the observed R_{eff} values are caused mainly by the volume of the high-angle misoriented domains of YBCO films. This result corresponds to the results described in [4]. The higher I_{45}/I_0 and $I_{(200)}/I_{(006)}$ values, and the corresponding increase of R_{eff} values, is the result of a greater lattice mismatch between the film and the substrate at low T_d because of the film lattice distortion in the result of the cation disorder processes.

B. Inhomogeneities in the secondary phases regions

Fig. 4 demonstrates a typical AFM image of the surface of the investigated YBCO films with the highest electrical properties. The light areas correspond to the Cu-rich secondary phase particles. Besides, the spiral growth pyramids (marked by arrow) can be seen [17]. Near the Cu-rich particles the regions of YBCO film have a lower thickness. It can be seen

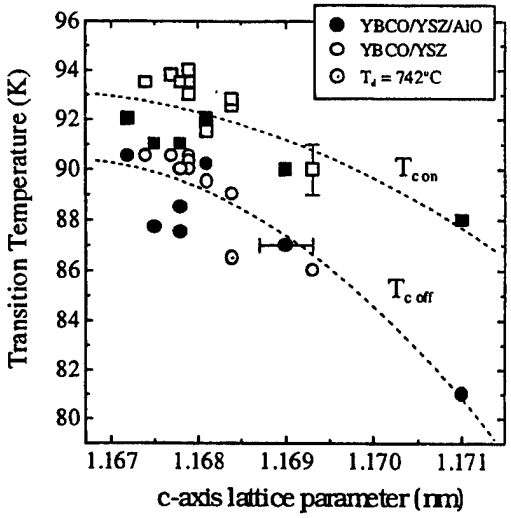

Fig. 1. Temperatures of onset- ($T_{c\,on}$) and end ($T_{c\,off}$) of the superconducting transition of YBCO films versus c-axis lattice parameter. Open symbols correspond to the films obtained during optimization of deposition temperature [10], solid symbols – the films obtained during optimization of gas mixture pressure [15]. Dashed lines are least-squares fit.

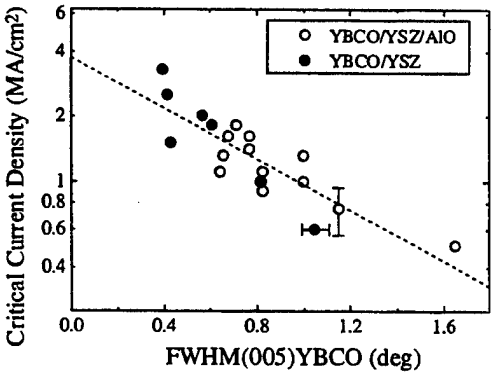

Fig. 2. Critical current density of YBCO films at 77 K versus FWHM(005)YBCO. Open symbols correspond to the films obtained during optimization of deposition temperature [10], solid symbols – the films obtained during optimization of gas mixture pressure [15]. Dashed line is least-squares fit.

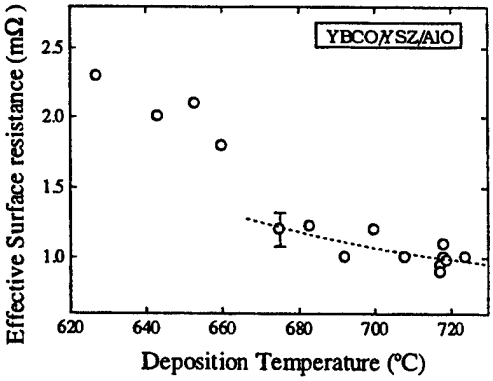

Fig. 3. Effective surface resistance of YBCO films (at 77 K and 10 GHz) versus deposition temperature [10]. Dashed line is least-squares fit.

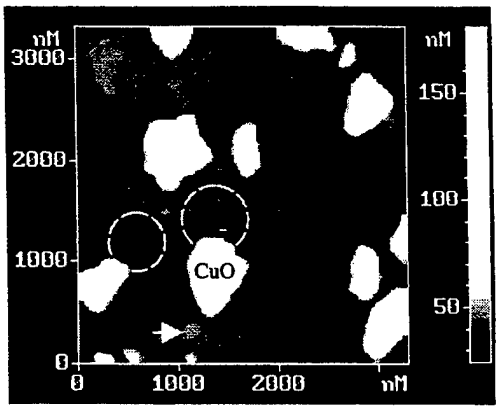

Fig. 4. AFM picture of YBCO film with highest electrical properties. The arrow points to the spiral growth pyramids, circles to the areas of shape distortion of growth pyramids.

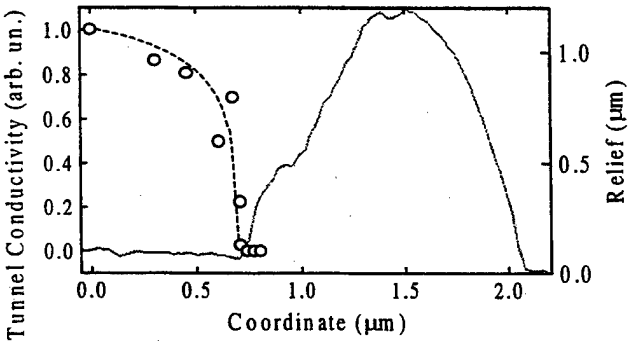

Fig. 5. Data of STM study of YBCO film with highest electrical properties: the relief of Cu-rich secondary phase particle and neighboring film area (solid line); the surface distribution of tunnel conductivity of film near Cu-rich particle (dashed line).

through the shape distortion of growth pyramids (marked by circles). The sizes of these regions are up to 500 nm. A similar effect has been observed in [18] and can be explained by Cu-depletion due to increasing probability of capture of Cu-adatoms by Cu-rich particles during film growth [10]. Fig. 5 shows the results of STM study of YBCO thin films. It is seen that relative tunnel conductivity decreases from maximum value to zero in approach to the edge of Cu-rich particles. The sizes of the regions of the appreciable changes of tunnel conductivity are about 500 nm, which coincides with the sizes of the regions of shape distortion of growth pyramids (Fig. 4). We believe that the tunnel conductivity is reduced by Cu-depletion of YBCO film regions near Cu-rich particles. According to [9] these regions have lower superconducting properties. According to our calculations based on the microkinetics analysis of film growth [10], the total area of Cu-rich particles and Cu-depletion film regions increases with an increase of the deposition temperature and at $T_d \approx 740$ °C reaches 55 %. Thus, the ihomogeneities caused by the Cu-rich particles form a matrix and all electrical properties of YBCO films degrade drastically [10].

IV. Conclusion

The electrical properties of YBCO thin films depend on microstructural parameters during optimization of deposition conditions as follows: the transition temperature depends mainly on deviations of the *c*-axis lattice parameter from its optimum value, the critical current density depends mainly on the *out of plain* misorientation of the film domains, and the microwave surface resistance depends mainly on the volume of the high-angle misoriented domains. Around Cu-rich particles there are regions of films with sizes up to 500 nm which have a modified relief and tunnel conductivity. It is suggested that the superconducting properties of these regions are worse due to Cu-depletion and, therefore, they can strongly affect the YBCO film properties. The processes of cation disorder deforming the film lattice play an important role in formation of structure and phase inhomogeneities in YBCO thin films.

References

[1]. J. Evetts, ed. *Concise Encyclopedia of Magnetic and Superconducting Materials*, Pergamon Press, Ltd., N.Y., 1992.

[2]. P. Chaudhari, J. Mannhart, D. Dimos, C. C. Tsuei, J. Chi, M. M. Oprisko, and M. Scheuermann, *Phys. Rev. Lett.*, vol. 60, N. 14, 1998, pp. 1653-1656.

[3]. M. Strikovsky, G. Linker, S. Gaponov, L. Mazo, O. Mayer, *Phys. Rev. B*, vol. 45, N. 21, 1992, pp. 12 522-12 526.

[4]. S. S. Laderman, R. C. Taber, R. D. Jacowitz, J. L. Moll, C. B. Eom, T. L. Hylton, A. F. Marshall, T. H. Geballe, and M. R. Beasley, *Phys. Rev. B*, vol. 43, N. 4, 1991, pp. 2922-2933.

[5]. Y. J. Tian, L. Li, L. P. Guo, J. Z. Liu, Z. H. Zhao, S. F. Xu, H. B. Lu, Y. L. Zhou, Z. H. Chen, D. F. Cui, and G. Z. Yang, *Appl. Phys. Lett.*, 65(18), 1994, p. 2356-2358.

[6]. N. G. Chew, J. A. Edwards, R. G. Humphreys, J. S. Satchell, S. W. Goodyear, B. Dew, N. J. Exon, S. Hensen, M. Lenkens, G. Muller and S. Orbach-Werbig, *IEEE Trans. Appl. Supercond.*, v. 5, N. 2, 1995, p. 1167-1172.

[7]. A. C. Westerheim, Alfredo c. Anderson, D. E. Oats, S. N. Basu, D. Bhatt, M. J. Cima, *J. Appl. Phys.*, 75(1), 1994, pp. 393-403.

[8]. V. Matijasevic, P. Rosenthal, R. H. Hammond, M. R. Beasley, and K. Shinohara, edited by R. Kossowsky, B. Raveau, D. Wohlleben, and S. K. Patapis (Kluwer Academic, Dordrecht, Netherlands, 1992), p. 557.

[9]. T. Yoshitake, W. Hattori, and S. Tahara, *J. Appl. Phys.*, 84(4), 1998, pp. 2176-2180.

[10]. Yu. N. Drozdov, S. V. Gaponov, S. A. Gusev, E. B. Kluenkov, Yu. N. Nozdrin, V. V. Talanov, B. A. Volodin, and A. K. Vorobiev, *Supercond. Sci. Technol.*, 9(1996), pp. A166 – A169.

[11]. E. Waffenshmidt, K. H. Waffenshmidt, F. Arndt, E. Boeke, J. Musolf, X. He, M. Hueken, and K. Heime, *J. Appl. Phys.*, 75(8), 1994, pp. 4092-4096.

[12]. B. Schulte, M. Maul, P. Haussler, H. Adrian, *Appl. Phys. Lett.*, 62(6), 1993, pp. 633-635.

[13]. J. Hudner, O. Thomas, E. Mossang, P. Chaudouet, F. Weiss, D. Boursier, and J. P. Senateur, M. Ostling, A. Gaskov, *J. Appl. Phys.*, 74(7), 1993, pp. 4631-4642.

[14]. C. N. L. Johnson, U. Helmersson, L. D. Madsen, S. Rudner, and L.-D. Wernlund, *J. Appl. Phys.*, 77(12), 1995, pp. 638-6393.

[15]. Yu. N. Drozdov, S. V. Gaponov, S. A. Gusev, E. B. Kluenkov, Yu. N. Nozdrin, V. V. Talanov, A. K. Vorobiev, *IEEE Trans. on Appl. Supercond.*, vol. 7, N. 2, 1997, pp. 1642-1645.

[16]. M. N. Drozdov, S. V. Gaponov, S. A. Gusev, E. B. Kluenkov, V. I. Luchin, D. V. Masterov, S. K. Saykov, and A. K. Vorobiev, *IEEE Trans. on Appl. Supercond.*, in press.

[17]. S. J. Pennycook, M. F. Chisholm, D. E. Jesson, R. Feenstra, S. Zhu, X. Y. Zheng and D. J. Lowndes, *Physica C*, 202 (1992), pp. 1-11.

[18]. J. A. Alarco, G. Brorsson, H. Olin, and E. Olsson, *J. Appl. Phys.*, 75(6), 1994, pp. 3202-3204.

Oral Session 5

HTS Josephson Junctions

Use of C-axis Microbridge Junctions for HTS Single Flux Quantum Circuits

P.J.Hirst, J.S.Satchell, I.L.Atkin, M.J.Wooliscroft, R.G.Humphreys.
DERA, St Andrews Road, Malvern, Worcestershire, WR14 3PS, United Kingdom

Abstract— The two main factors affecting yield of HTS SFQ circuits are the junction reproducibility and the stray inductance of a circuit. The former is widely recognised but for HTS circuits it is equally important that the layout is designed to minimise stray inductances. The latest progress towards c-axis microbridge (CAM) junctions with the correct properties for SFQ logic applications is outlined. The connection between design rules and circuit yield has been studied by simulation.

I CAM TECHNOLOGY FOR SFQ LOGIC

This relatively novel junction geometry [2] utilises the anisotropic nature of the cuprate HTS materials in making a Likharev [1] type microbridge in the c-direction of the superconductor. The junction is simply a cylinder of superconductor joining two superconducting layers across which there is a coherent passage of vortices producing the Josephson effect. There is no intentional barrier in this structure although interfaces may play an important role in the nucleation and passage of vortices across the junction. The I-V characteristics of CAM junctions can be fitted by the RCSJ model at low currents (up to $2I_C$) with and without microwave radiation but deviations are observed at higher currents.

Figure 1 shows the two ways in which this structure can be manufactured either by the planarisation of a mesa [2] or by milling a hole (window) in an insulator [3]. The window type CAM junction J_c is very similar to that for the mesa type junctions ($Jc \approx 1.5 \times 10^5 Acm^{-2}$ at 70K) and I_c is proportional to the CAM area [3]. This critical current density suggests that a CAM diameter of 0.5μm is required for a target critical current of 500μA at 40 to 60K.

With target diameters of this size there is expected to be a problem with keeping the kinetic inductance of the junction low with CAM lengths ~300nm, as used in the standard mesa technology. We estimate that the CAM length must be of the order of 100nm to keep the junction kinetic inductance in the 0.3pH region. If such a thin insulator were used over the whole chip, the capacitance would be too large and the risk of pinholes would increase. For these reasons a new process has been designed for making sub-micron CAM junctions. The sub-micron bridge is situated on top of a larger (~3μm) mesa (using a combination of the processes shown in figure 1), so

Manuscript received April 30, 1999
pjhirst@dera.gov.uk
Work supported in part by ESPRIT Contract # 23429.

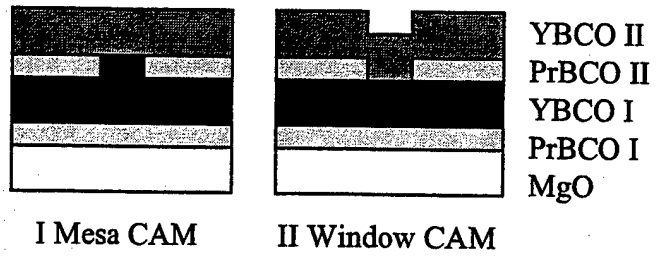

Figure 1: Two alternative processing routes for the production of CAM junctions I - formation of a mesa in the base superconductor and planarisation of an overgrown insulator to expose the top the mesa and II - the growth of the top superconductor into a patterned hole (window) in the insulator. Note the use of a PrBCO buffer layer on the MgO to prevent the formation of grain boundaries at steps in the substrate.

that the CAM length is controlled, but most of the isolation is achieved with a thicker insulator layer.

We have developed a trilayer carbon resist and electron beam lithography process for milling the sub-micron windows. This process involves evaporating carbon onto the thin PrBCO then depositing gold onto the carbon. Windows in the Au layer are patterned using electron beam lithography with PMMA resist and ion milling. This gold pattern is then transferred into the carbon using an anisotropic oxygen etch, producing the milling mask. Atomic force microscopy measurements have shown that this process produces windows with a standard deviation (σ) in area of 3.2% for a 0.6μm diameter window. Junctions of this type show promising reproducibility ($\sigma(I_c)$=13%) and high I_cR_n products (>1mV) at 60K for 0.6μm diameter windows [3].

Figure 2 shows a bright field cross-sectional TEM image of a 0.4μm diameter window junction. The sample was thinned using a focussed ion beam (FIB) thinning technique. The micrograph confirms the diameter of the sub-micron window is indeed *ca.*400nm. It also shows that the growth is epitaxial throughout, particularly into the window. An important factor in any HTS technology is the ability to grow over patterned slopes. Although PrBCO has a moderately high dielectric constant and a relatively low resistivity, it is isostructural with YBCO and high angle slopes can be grown over without the introduction of grain boundaries, although growth over slopes close to vertical is not reproducible [4]. This has important implications upon the design of SFQ circuits, which will become apparent in the next section.

It has now been realised that the process outlined above can be greatly simplified by eliminating the large mesa and reverting to a window process with thin insulator. If the

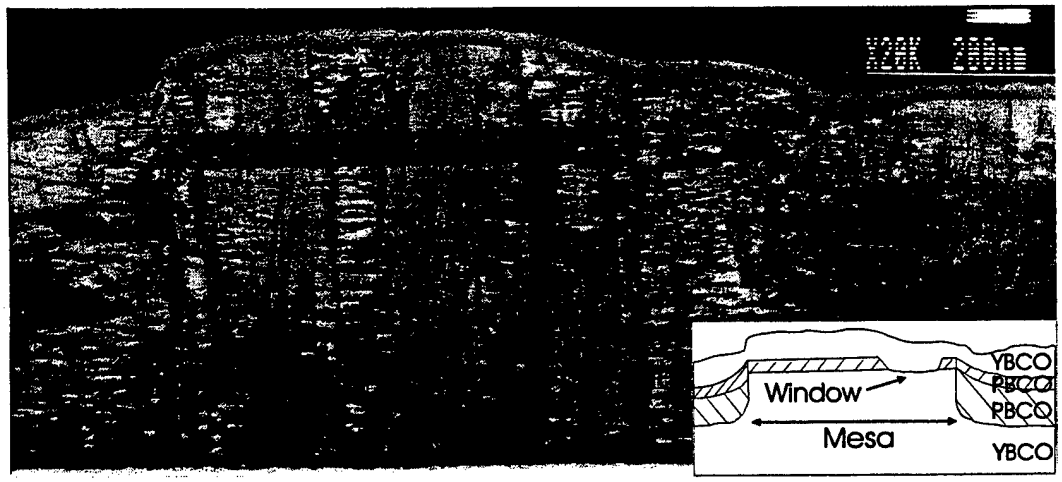

Figure 2: A bright field cross sectional TEM image through sub-micron (0.4μm diameter) window CAM on top of a mesa. The layer structure is shown schematically in the inset where the two PrBCO layers are shaded. This cross section was produced by a focussed ion beam (FIB) technique.

overlap area is minimised then the capacitance can be kept under control. It has been calculated that the maximum overlap area to keep the junctions non-hysteretic (β_c<1) with a 100nm insulator layer is 24μm^2 per junction. This should be readily achievable with the sub-micron CAM technology.

II CAM T-FLIP FLOP: EFFECT OF DESIGN RULES ON CIRCUIT YIELD

Figure 3 shows the layout and equivalent circuit for a T flip-flop incorporating a DC to SFQ input section. This subcircuit is one of the basic elements necessary for many useful SFQ circuits e.g. decimation filters in A/D converters. This circuit has good design margins but is particularly prone to stray inductances between the 4 junctions in the flip-flop loop (J1-J4 in fig 3). This is therefore an excellent circuit for the examination of the effect upon circuit yield of the proximity of junctions to track edges (g) and slot widths (s). To ensure good epitaxy over the base layer the edge of the track must be sloped. The edge of the track in the simulations is taken as the mid point of the actual edge slope. The steeper the slope, therefore, the smaller the parameters s and g.

can become. With the large mesa hybrid process the values are typically g=s=3μm, which can easily be reduced to g=s=2μm without the large mesa. Further tightening of tolerances will clearly stress the technology, and it is worth examining whether the benefits merit it.

The manufacturing yield is calculated using a Monte-Carlo method. This samples the circuit parameter distributions and calculates the number of circuits that pass and fail in an ensemble. The circuits are optimised separately for each technology before the yields are estimated. Yields are calculated at 60K to take into account errors due to thermal noise. A pass is defined as occurring after 100 correct successive retests of the circuit.

Figure 4a shows the simulated yields for sub-circuits optimised with and without a floating groundplane as a function of junction reproducibility. This shows that there is marked improvement in yield going from the large mesa hybrid process (g=s=3μm) to the simplified window process (g=s=2μm) without a groundplane. This is the equivalent of reducing the junction reproducibility required by around 6%.

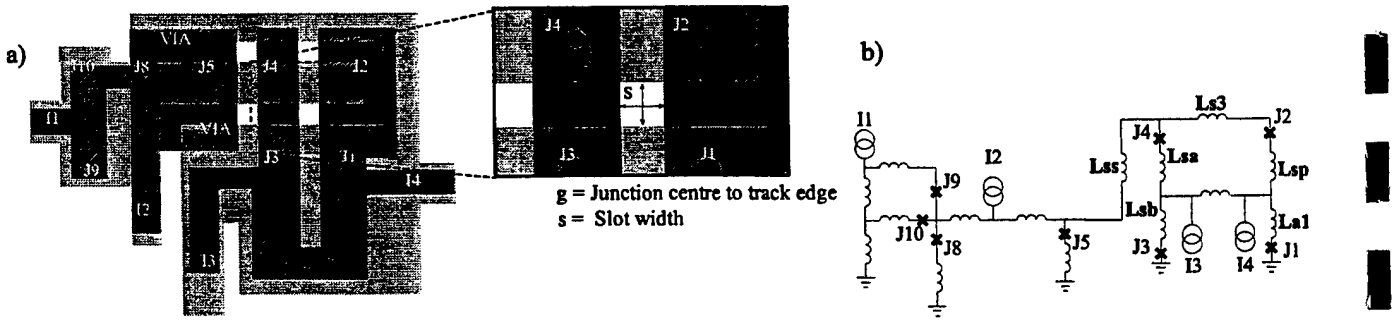

Figure 3: a) T flip-flop layout incorporating DC to SFQ converter. The base layer is dark and the top layer light. Inset shows the two parameters examined in this study, guard space (g) and slot width (s). b)equivalent circuit of the flip-flop showing the main strayinductances in the flip-flop loop (Lss, Ls3, Lsp, Lsb and La1)

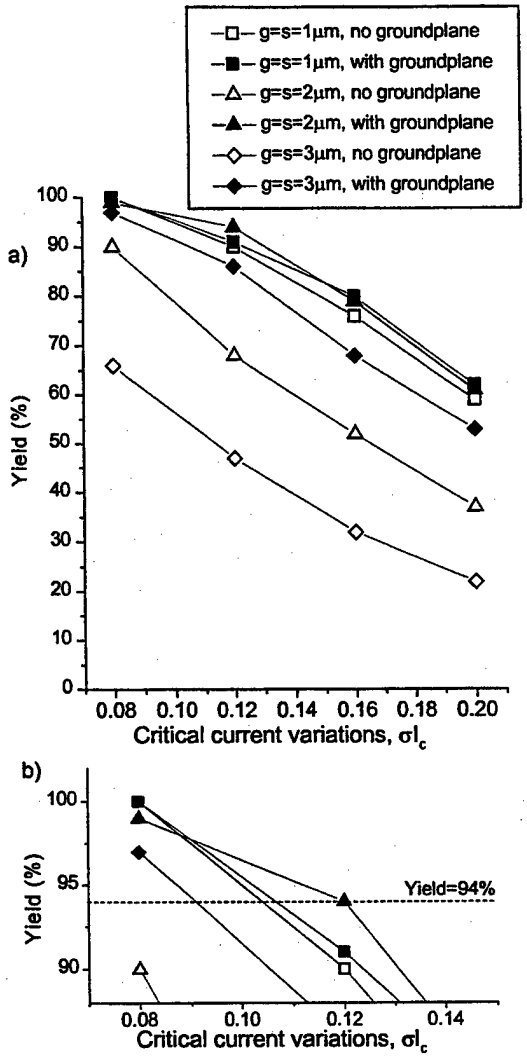

Figure 4: a) Optimised yield at 60K for different design rules; g, the guard space between junction and track edge and s, the slot width for the CAM technology. Yields are also shown for technologies with and without a floating groundplane. b) An expanded view of the higher yielding area of the plot, the dashed line indicates the yield necessary for a single T flip-flop if 10 such sub circuits are to be manufactured within a circuit with a fairly modest yield of 50%. N.B. Errors in the simulated yield are typically ±3%.

A further improvement results with a g=s=1μm design rule, which is probably at the limit achievable with conventional UV lithography and the steepest of base layer slope angles. The situation is improved markedly by using a groundplane and the difference between the different design rules is reduced. This shows that with a groundplane there is little point in pushing the technology this hard and the s=g=2μm design rule will be sufficient for the T flip flop with a 3 layer technology.

The yield of a single sub-circuit needs to be high if many such elements are to be used in single circuit. Figure 4b shows an expanded view of the yield plot along with the cut off point where a 10 T flip-flop circuit can be yielded at 50%, namely 94%.

CONCLUSIONS

The whole design, layout and optimisation cycle needs to be optimised for any particular technology to ascertain the relative importance of junction reproducibility and stray inductance. It is more advantageous, with the CAM technology, to add a groundplane than to tighten design rules further than can be presently achieved. It is predicted that a high yielding T-flip flop circuit can be made using a 3 layer CAM technology which operates at 60K.

REFERENCES

[1] K.K.Likharev. Sov. Phys. JETP, vol 34, pp 906, 1972

[2] S.W.Goodyear *et al.*, IEEE Trans. Superconductivity, Vol. 5. pp 3143-3146, June 1995.

[3] P.J.Hirst, T.G.Henrici, I.L. Atkin, J.S.Satchell, J.Moxey, N.J.Exon, M.J.Wooliscoft, T.J.Horton and R.G.Humphreys, Accepted for publication IEEE trans. Superconductivity. Proceedings of ASC '98, Palm Dessert, 1998.

[4] P.J.Hirst, M. Barnett, N.G.Chew, J.S.Abell, M.Aindow, R.G.Humphreys, Inst, Phys. Conf. Ser. No. 158, European Conference on Applied superconductivity, pp185, July 1997.

On the Characteristic Voltage of Highly Oxygenated YBCO Grain Boundary Junctions

Jason P. Sydow*, Michael Berninger and Robert A. Buhrman
Cornell University, Ithaca NY
*Presently at NIST, Boulder CO

Brian H. Moeckly
Conductus Inc. Sunnyvale CA

***Abstract*—Early in the study of cuprate grain boundary junctions (GBJs) it was observed that the junctions' characteristic voltage (I_cR_n) tended to scale, at least approximately, as $J_c^{1/2}$. To re-examine the cause of this effect we have measured I_cR_n as a function of the more complete GBJ oxygenation that can be achieved by ozone annealing and electromigration. While these enhanced oxidation techniques can increase J_c by up to a factor of 10, I_cR_n remains saturated at ~1.2 mV (at 4.2 K) for 24° GBJs on strontium titanate bicrystals. Only with oxygen *removal* through inert gas annealing is scaling observed. These results can be explained by a model where the GBJ consists of a thin barrier layer, created by the localized cation disorder, sandwiched between two interface layers of non-uniform YBCO of highly variable oxygen deficiency. The barrier layer is largely unaffected by the enhanced oxidation techniques leading to the plateau in I_cR_n. Inhomogeneities in oxygen content and order within the interface layers are dependent upon the quality of the grain boundary growth process and annealing history, and in turn are responsible for the variations in I_cR_n leading to the previously observed scaling. Ozone anneals and electromigration reduce the oxygen inhomogeneities within the interface region, facilitating the measurement of the intrinsic I_cR_n of the grain boundary barrier layer.**

I. Introduction

The enhanced partial pressure of atomic oxygen provided by ozone, and the local modification of oxygen content and order afforded by electromigration are used to achieve a greater level of oxygenation in crystallographically strained YBCO, than that which is routinely obtained through standard ~500°C, 1 atm. O_2, post fabrication anneals. As discussed below, by performing ozone anneals and electromigration experiments on HTSC GBJ structures we are able to observe the more intrinsic nature of the weak link present in a particular device architecture without the added complication of the oxygen disorder and loss which is often a secondary effect of fabrication procedures.

II. Ozone Annealing

GBJs were fabricated at Conductus Inc. The fabrication procedure is provided elsewhere [1]. Current-voltage (IV) characteristics were collected before and after various annealing treatments including ozone annealing and electromigration experiments. During anneals, samples were mounted with silver paste to a Haynes 214 alloy block which was heated by an enclosed halogen lamp. For O_2 and Ar anneals, the chamber was pumped down to ~5×10^{-6} Torr, and backfilled to slightly over 1 atm. For O_2/O_3 anneals, O_2 was flowed through a commercial ozone generator creating an O_2/O_3 mix with ~2% O_3, by weight. The O_2/O_3 mixture then flowed through the annealing chamber at slightly greater than 1 atm. Upon cool-down, the flow was maintained until the sample was near room.

III. Electromigration

In previous work it has been shown that electromigration (EM) can be used to significantly improve the basal plane oxygen content and order of well annealed YBCO microstructures [2]. Electromigration consists of the application of an electrical bias with a current density of 1-5 MA/cm^2 to a thin film microstructure. This process is conducted in 1 atm. of He and at room temperature, although there is some ohmic heating of the microstructure. The current bias induces long range migration of the positively charged oxygen vacancies towards the negative electrode. This is possible because the chain oxygen is relatively mobile, presumably due to the normally vacant off-chain or O(5) site in the a-axis direction of the crystal lattice. Once an oxygen atom is thermally excited to the O(5) site, the local electric field will bias it to diffuse towards a vacancy closer to the positive electrode. When such a bias is applied to a cuprate superconductor microstructure for a sufficient period of time, oxygen vacancies collect in the negative electrode. This resultant build up of oxygen vacancies is demonstrated by the more reflective, or whiter material which has the visual appearance of a plume shape at the end of a microstructure. The electric field and current densities decrease in the plume, resulting in the re-deposition of vacancies, similar to the re-deposition of silt in a river delta. In practice, EM experiments of this type are generally performed under constant current, while device resistance is monitored as a function of time.

IV. Modification Of Oxygen In Grain Boundary Junctions

The typical effect of ozone annealing on the IV characteristic for a GBJ at 4.2 K (5 μm wide, ~200 nm thick, misorientation angle ~24°) is demonstrated in Fig. 1. I_c increased from 0.80 mA to 1.78 mA while R_n decreased from 1.63 to 0.57 Ω for a net decrease in I_cR_n product from 1.31 to 1.02 mV. The general similarity of I_cR_n products in spite of the

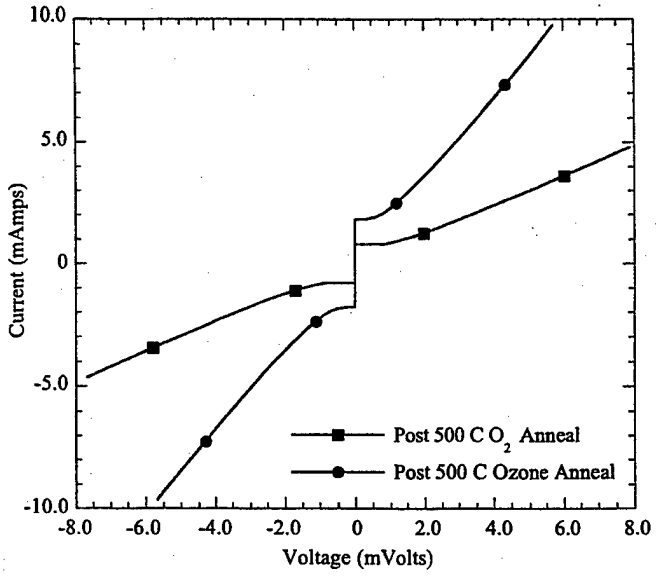

Fig. 1 IV characteristics at 4.2 K for a GBJ before and after ozone annealing at 500°C for 1.5 Hours.

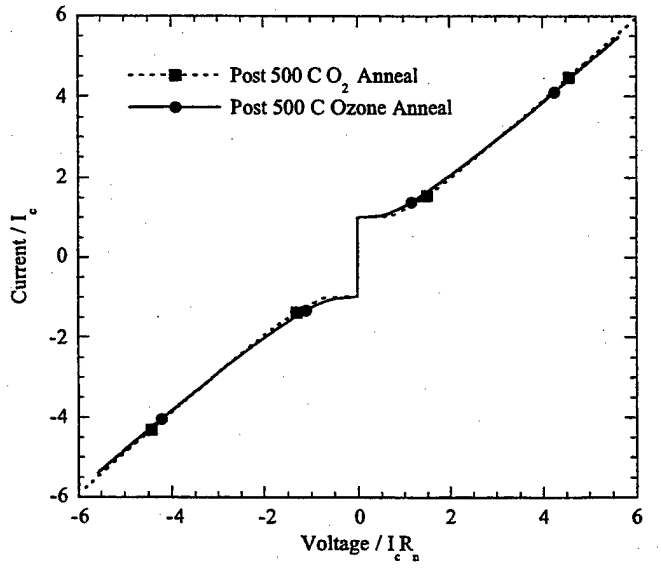

Fig. 2 Scaled IV characteristics at 4.2 K for the GBJ portrayed in Fig. 1.

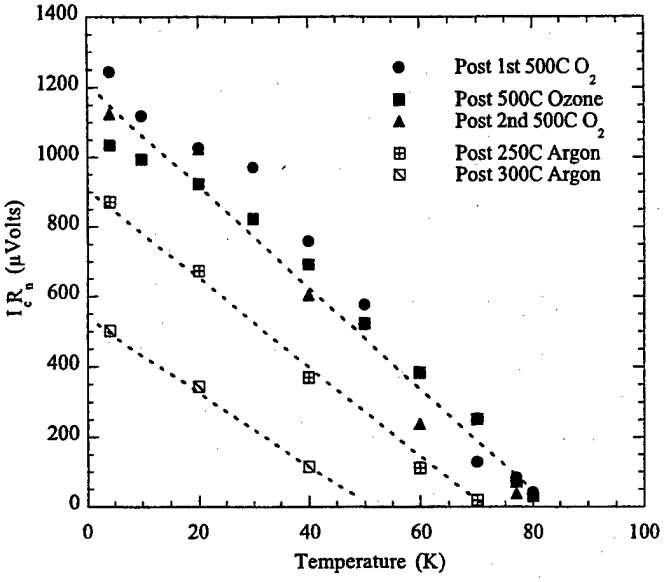

Fig. 3 I_cR_n versus temperature for a single GBJ following a series of anneals. O_2 and O_2/O_3 anneal were conducted for 1.5 Hours while Argon anneals were lengthened to 3 Hours.

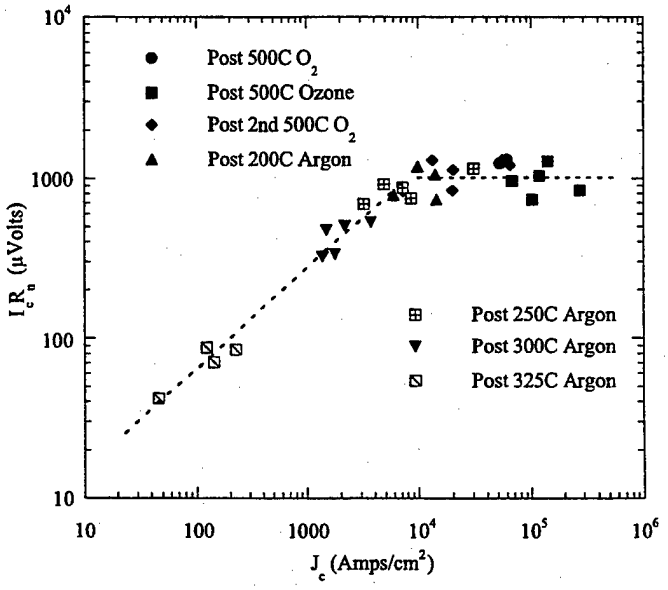

Fig. 4 I_cR_n versus J_c for five separate GBJs at 4.2 K.

more dramatic change in I_c and R_n is clarified in Fig. 2 which portrays scaled IV characteristics for the same data. The scaled data agree before and after ozone annealing. We attribute this to the fact that the GBJ consists of at least two components; a relatively immutable, thin barrier layer closely associated with the physical grain boundary, together with regions of inhomogenously de-oxygenated YBCO immediately on either side of the grain boundary. The barrier layer determines the "intrinsic" RSJ behavior of the junction, particularly I_cR_n, which is not substantially altered by ozone annealing. On the other hand the de-oxygenated electrodes can be substantially improved by ozone annealing, which impacts I_c and R_n through variation in the effective area of superconducting material that contacts the barrier, but does not alter I_cR_n of the grain boundary barrier. Consistent with this model is the fact that the temperature dependence of the characteristic voltage of the GBJ is not significantly affected by ozone annealing. This is demonstrated by Fig. 3 which portrays I_cR_n versus temperature after a series of anneals and which shows that I_cR_n is relatively constant across the entire temperature range before and after ozone annealing. I_cR_n only begins to decrease with the substantial amount of oxygen loss induced by the 250 and 300°C Ar anneals. Following these Ar anneals the I_c's have substantially decreased to 116 and 33 μA respectively.

The constancy of the I_cR_n product across a broad range of values for J_c is portrayed in Fig. 4 for a number of 24° GBJs. The scaling of I_cR_n with J_c in the lower J_c region, which we

obtain following with Ar annealing, has been observed in previous investigations, and has been attributed to a variety of mechanisms [1], [3-5]. The newly observed plateau behavior for I_cR_n in the case of nearly optimally and perhaps optimally oxygenated devices can be explained by the limiting effect of the intrinsic barrier in the immediate vicinity of the grain boundary, which is not altered by ozone annealing. The effect of ozone annealing is to increase the amount of completely oxygenated YBCO material adjacent to the grain boundary, and thus increase the effective junction area, which increases I_c and decreases R_n while holding I_cR_n constant. When the electrodes are progressively de-oxygenated with Ar anneals at progressively higher temperatures, first the area of fully oxygenated material adjacent to the grain boundary barrier diminishes. This reduces I_c and increases R_n while I_cR_n remains constant. When none of the YBCO material adjacent to the barrier is well oxygenated, the effective T_c and I_cR_n of the junction begin to decrease as the volume of oxygen deficient YBCO spreads outwardly from the grain boundary in a non-uniform manner.

It is important to note that 1-10 μm wide GBJs have shown similar plateau behavior when oxygenated by ozone annealing and electromigration. The independence of junction width on the plateau discounts explanations involving the wide junction limit and I_c suppression due to flux flow. Fig. 2 also demonstrates that there is only a marginal increase, if any, in excess current with ozone annealing.

Further evidence for the connection between oxygen microstructure in the vicinity of the crystallographic grain boundary and the power law scaling, and eventual plateau, of I_cR_n as a function of J_c is provided by the electromigration results presented in Fig. 5. IV characteristics were collected before and after a series of electromigration experiments with an applied current bias ranging from 0.33 to 1.33 MA/cm^2. As with ozone annealing, the primary observable effect of electromigration is to increase I_c and decrease R_n. Again we observe a plateau in the I_cR_n product, this time at ~1500 μV. The slightly greater plateau value may be attributed to the lower temperature range of the electromigration process compared to the thermal anneals. It is possible that a slightly greater level of localized oxygenation can be achieved immediately adjacent to the grain boundary barrier with the electromigration conducted at room temperature compared to what can be achieved with 500°C ozone anneals concluded with a non-equilibrium cooling step.

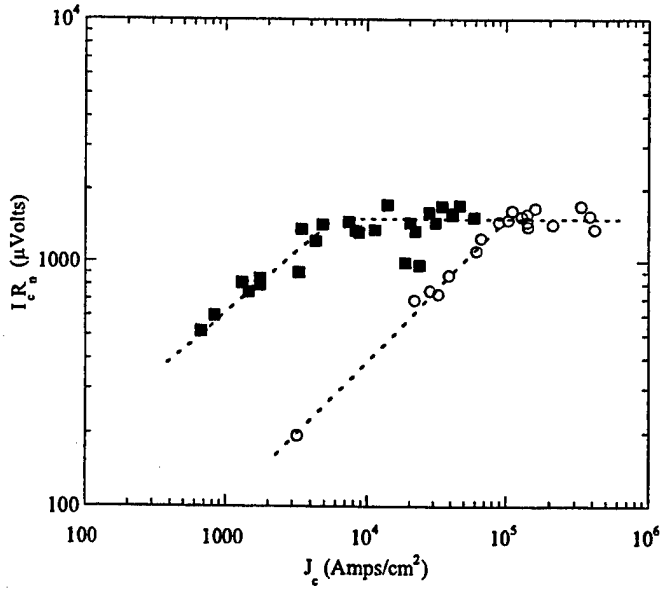

Fig. 5 I_cR_n versus J_c for eleven separate GBJs from two separate chips (filled squares and open circles) at 4.2 K following a series of room temperature electromigration experiments.

V Discussion And Conclusions

Two different techniques, thermal ozone anneals and electromigration, have been used to increase oxygen content and order within several sets of GBJs. Once optimally, or nearly optimally oxygenated, these devices continue to demonstrate RSJ like behavior. Access to this highly oxygenated regime enables the observation of more intrinsic GBJ behavior. The previously observed scaling of I_cR_n with J_c can now be accurately attributed to variations in oxygen content and order in the vicinity of the crystallographic grain boundary. In the highly oxygenated regime afforded by ozone annealing and electromigration I_cR_n remains constant as J_c increases. The consistency of the I_cR_n product is attributed to a model in which the *effective area* of the junction is increased as the oxygen content is increased. In this model, a greater number of optimally oxygenated regions of the YBCO electrodes make contact with an intrinsic barrier localized at the crystallographic grain boundary [6]. An increase in such filamentary contacts leads to a greater effective area, a greater value of J_c, but constant I_cR_n product.

The similarity of Figs. 4 and 5 despite the dissimilarity of the oxygenation techniques used to obtain these results provides further evidence for the importance of oxygen content and order in stressed YBCO systems, such as GBJs. Both techniques are useful tools for device development and intrinsic scientific investigation. Each approach provides access to a greatly extended portion of the oxygen phase diagram, allowing a more accurate understanding of the fundamental nature of HTS systems.

References

[1] R. Gross, P. Chaudhari, M. Kawasaki and A. Gupta, *Phys. Rev. B*, vol. 42, p. 10735, 1990
[2] B.H. Moeckly, R.A. Buhrman, and P.E. Sulewski, *Appl. Phys. Lett.*, vol. 64, p. 1427, 1994
[3] S.E. Russek, D.K. Lathrop, B.H. Moeckly, R.A. Buhrman, D.H. Shin and J. Silcox, *Appl. Phys. Lett.*, vol. 57, pp. 1155-57, 1990.
[4] H. Hilgenkamp and J. Mannhart, *Appl. Phys. Lett.*, vol. 73, p. 265, 1998
[5] R. Gross and B. Mayer, *Physica C*, vol. 180, p. 235, 1991
[6] N. D. Browning, H. O. Moltaji, J. P. Buban, *Phys. Rev. B*, vol. 58, p. 8289, 1998

Resonant tunneling and tunnel anomalies in YBCO-junctions

J. Halbritter
Forschungszentrum Karlsruhe
Institut für Materialforschung I
Postfach 3640, 76021 Karlsruhe
Germany

Nb-Nb_2O_{5-x}-tunnel junctions show large leakage currents $j_{bl}(\propto 1/R_{bl} \cong 1/R_{bn})$, noise and critical current degradation $j_{cJ}R_o \cong \pi\Delta(0)/2e(1 + R_{bl}/R_o)$, with the gap value Δ, the direct tunnel resistance R_o and R_{bl} due to resonant tunneling via oxygen vacancies (x). Up to date, YBCO-in-plane junctions show even stronger degradations of j_{cJ} and a leakage resistance $R_{bl} \approx R_{bn}$ being much smaller than R_o yielding $j_{cJ}\, R^2_{bn} \cong$ const. The present day atomistic and tunnel understanding of HTS junctions is analyzed in the light of recent proposals on $j_{cJ}(\theta)$-degradations with misorientation angle θ reaching from band bending to strain. Those approaches don't deal with the interface chemistry, interface relaxation, deoxygenation and disorder and, thus, are unable to explain, e.g., R_{bl} approaching the resistance R_{bn} above T_c. Following Nb_2O_{5-x} junction results, evidence is presented for disorder induced localized states at E_F being able to explain voltage and distance spectroscopy on YBCO/YBCO or YBCO/Ag or YBCO/STM-tip junctions. Aside of noise, the leakage current ($\sim 1/R_{bl}$) shows up most clearly in rf residual losses R_{res} scaling with $j_{cJ}R^2_{bl} \approx 10^{-11}$ $A\Omega^2cm^2$ proving over seven orders of magnitude for $j_{cJ} \leq 10^7$ A/cm² that $R_{bn} \approx R_{bl}$ holds and that R_{res} ($T < 0.8\ T_c$, f, H) can be explained quantitatively.

Homoepitaxial $YBa_2Cu_3O_{7-\delta}$ SNS Junctions with Normal Layers of Fe-doped YBCO and $Pr_{1+x}Ba_{2-x}Cu_3O_y$

Toshiyuki Usagawa, Jianguo Wen, Tadashi Utagawa, Satoshi Koyama, and Keiichi Tanabe
Superconductivity Research Laboratory, ISTEC, 10-13 Shinonome 1-chome Koto-ku Tokyo 135-0062, Japan

Abstract--We report on the first successful single crystal SNS junction based on (110) $YBa_2Cu_3O_{7-\delta}$ (YBCO)/$YBa_2(Cu_{1-x}Fe_x)_3O_{7-\delta}$ (YBCFeO:150 nm) /$YBa_2Cu_3O_{7-\delta}$ films grown on (110) YBCO single crystal substrates, which shows an anisotropic field dependence in large-junction behavior at 77 K. The field suppression of critical supercurrent Ic(T) is greater than 95% at 77 K and 9.0 K. Furthermore homoepitaxial c-axis oriented $YBa_2Cu_3O_{7-\delta}$ SNS Junctions with 90 nm thick normal layers of $YBa_2(Cu_{1-x}Fe_x)_3O_{7-\delta}$ shows a clear weak link characteristics with a normal Fraunhofer diffraction pattern. The 32 μm × 32 μm square junction shows a high value of IcRn product, 255 μV, at 6.71 K irrespective of low current density Jc= 28.3 A/cm^2.

I. INTRODUCTION

Since the discovery of $YBa_2Cu_3O_{7-\delta}$(YBCO) families with high Tc's beyond liquid nitrogen temperature (77K), a lot of efforts have been attempted to realize high quality Superconductor-Normal conductor (or Insulator)-Superconductor (SNS or SIS) Josephson junctions as was achieved by Nb/AlO_x-Al/Nb SIS junctions. However, it has not yet succeeded to obtain the same quality of junctions because of unexpected difficulty to control high quality NS interfaces without disorder or to be free from the influence of grain boundaries around NS interfaces. One of the methods to resolve such obstacles will be to realize single-crystallized SNS junctions. The preliminary good results of single-crystallized SNS junctions [1] have been reported by using (110) YBCO homoepitaxial technology [2]. Recently we have obtained large IcRn products irrespective of low critical supercurrent density Jc by c-axis oriented YBCO hohoepitaxial SNS junctions[3] grown on (001) YBCO single crystal substrates[4]. In this work we would like to introduce the present status of homoepitaxial YBCO SNS junctions.

II. EXPERIMENTAL

We have grown each layer by off-axis RF magnetron sputtering method under the same growth conditions with the previous YBCO homoepitaxial films [1-3]. The growth temperature Ts is 685 °C. The sample preparation of four-probe SNS or NS devices were carried out by two different methods: (1) direct Au wire bonding on the device area [1] with Focused Ion Beam (FIB) isolation, (2) standard photolithographic process [3].

A. (110) YBCO SNS Junctions

The (110) YBCO homoepitaxial films have been demonstrated to have excellent smooth surface morphology and reproducible high Tc's of 91.5-92.5 K [2]. In accordance with high resistivity of 1.2 GΩcm of $YBa_2Fe_3O_{8-\delta}$(YBFO) film [5] at 80 K, we have studied heavily Fe-doped YBCO films as possible candidates for N-layers of homoepitaxial SNS junctions. The SNS trilayer of YBCO(60 nm)/$YBa_2(Cu1-xFex)_3O_{7-\delta}$(YBCFeO; x=0.333; 150 nm)/YBCO(75 nm) was grown on the mechanically polished (110)YBCO single crystal substrates [4]. As was characterized by Transmission Electron Microscopy (TEM), Reflection High Energy Electron Diffraction (RHEED) and Scanning Electron Microscopy (SEM), the surface of SNS trilayers [1] are as smooth as the homoepitaxil films. The SNS device area, 170 μm x 76 μm, is patterned by FIB isolation, where the planar view is shown in the inset of Fig. 1. The field dependence of the critical supercurrent Ic(T=77K) for this sample shows anisotropic "large" junction behavior with normal Fraunhofer patterns (Fig. 1). The critical supercurrent density Jc(H=0) is 93 A/cm. The corresponding Josephson penetration depth, λ_J, is estimated as 17.0 μm and 7.2 μm for magnetic field parallel and perpendicular to the c-axis, if we assume the corresponding field penetration length to be λ_{ab}=0.15 μm and λ_c =1.2 μm [6].

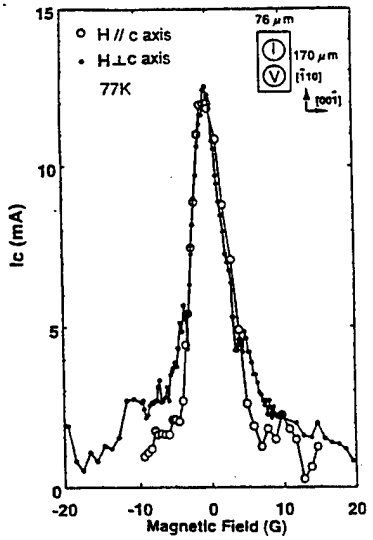

Fig. 1 Field dependence of Ic for the homo-epitaxial (110)YBCO/YBCFeO/YBCO SNS junction at 77 K.

The anisotropic "large" junction behavior is qualitatively understood by these parameters including the relation of

junction size L (denoted by the inset of Fig. 1)/$\lambda_J \approx 10$. The field suppression of Ic(T) is greater than 95% of Ic(H=0) as shown in Fig. 1. The Ic(H=0) of 99 mA is also suppressed to approximately 4 mA under a higher field of 97.3 Gauss at lower temperature of T=9.0 K (Fig. 2). The small excess supercurrent Ic even for large junction area, S= 1.29×10^{-4} cm^2, or low temperature is a direct evidence for the high quality of (110) homoepitaxial SNS structures.

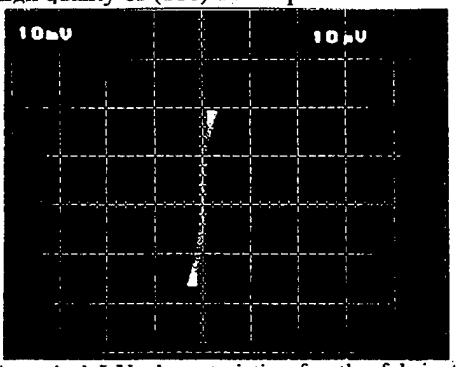

Fig. 2 A typical I-V characteristics for the fabricated four-probe homoepitaxial (110) YBCO/YBCFeO/YBCO SNS junction under magnetic field H=97.3 Gauss at 9.0 K. The Ic(T=9.0 k) is 99 mA without magnetic field. x-axis: voltage 10 μV/div.; y-axis: current 10 mA/div.

B. (110)$Pr_{1+x}Ba_{2-x}Cu_3O_y$/YBCO Bilayer

In the previous paper [7] about the superconductivity of (110)PBCO/YBCO bilayered diode grown on (110) YBCO single crystal substrates, we discussed the stoichiometric $Pr_{1+x}Ba_{2-x}Cu_3O_y$ (x=0) should show superconductivity. In order to test this hypothesis we have prepared non-stoichiometric (110) $Pr_{1+x}Ba_{2-x}Cu_3O_y$ (x=0.14; 180 nm)/YBCO bilayer grown on (110) YBCO single crystal substrates. The vertical four-probe resistivity measurements for the PBCO (x=0.14)/YBCO bi-layered diode, fabricated by FIB isolation [7], is shown in Fig. 3 under constant current I= 10 mA.

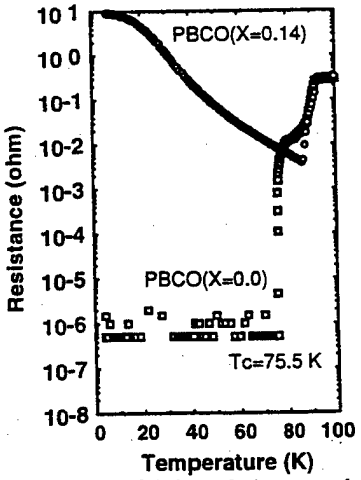

Fig.3 ρT curve for the fabricated 4-prove device for the PBCO(x=0.0; 220 nm)/YBCO(60 nm) and the PBCO (x=0.14; 180 nm)/YBCO(60 nm) bi-layered structures grown on the (110) YBCO single crystal substrates.

Expectedly the temperature dependence of electrical resistivity ρ shows a well-known semiconductor-like behavior in markedly contrast to that of stoichiometric (110)PBCO(x=0: 220 nm)/YBCO diode with two superconductivity transition steps associated with two different Tc's of 92.0 K of YBCO, 75.5 K for 220 nm thick PBCO. Each junction area for PBCO(x=0.14)/YBCO and PBCO(x=0.0)/YBCO bi-layered structures after FIB isolation is 3.6×10^{-4} cm^{-2} and 2.7×10^{-4} cm^{-2}. The film resistivity ρ at T= 30 K is 30 Ωcm, which is two order of magnitude smaller than that of bulk PBCO(x=0.14) single crystal [8]. This will come from the difference of measured current density due to non-linear I-V curve.

C. c-axis oriented Homoepitaxial YBCO SNS Junctions

As is well known, the non c-axis transport has been thought to be superior for SNS junctions due to large anisotropy of coherence length, $\xi_{ab} \sim 1.5$ nm and $\xi_c \sim 0.3$ nm, of YBCO. Only a few attention has been paid to c-axis oriented stacked YBCO SNS junctions. Furthermore, the stacked junctions themselves have been thought to have smaller IcRn products compared with ramp-edge type geometry. This is because the film inhomogeneity effects will prevent the stacked SNS junctions from realizing larger IcRn products by device shrinkage. In order to study the device characteristics, we have fixed the N-layer of Fe-doped YBCO as 90 nm and the Fe composition as 0.14 in expectation of less influence of grain boundary effects and low superconducting transition temperature Tc less than 4.2 K. The SNS trilayer [3] of YBCO(110 nm)/$YBa_2(Cu_{1-x}Fe_x)_3O_{7-\delta}$(YBCFeO; x=0.14; 90 nm)/YBCO (110 nm) was grown on the mechanically polished (001)YBCO single crystal substrates. The square-shaped 32 μm × 32 μm Fe-doped YBCO SNS junction shows RSJ(resistively shunted junction)-like weak link behavior as shown in Fig. 4 and a clear Shapiro step for f=20 GHz at T=6.65 K.

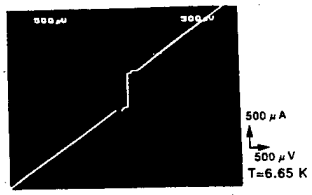

Fig. 4 Typical I-V characteristics for the fabricated Two connected 32 μm × 32 μm YBCO SNS junctions at T=6.65 K.

The corresponding magnetic field dependence of Ic shows an Fraunhofer pattern in Fig. 5 with excess current Ie of 140 μA. The field suppression of Ic(T) is about 67% of Ic(H=0). The period of Fraunhofer oscillation is about 3 Gauss for the first 3 periods. If we define the true Ic by the observed Ic–Ie, the critical current density Jc(H=0) is 28.3 A/cm^2 at T = 6.71 K.

The corresponding Josephson penetration depth, λ_J, is estimated as 68.7 μm if we assume the corresponding field penetration length as λ_L=0.15 μm [6].

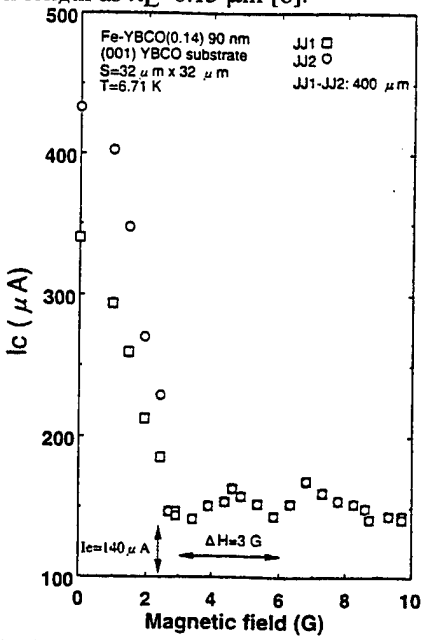

Fig. 5 Field dependence for Two Fe-doped SNS junctions (Fig. 4) connected in series, 400 μm separated each other on the YBCO substrate at T=6.71 K.

The device size L divided by λ_J, L/λ_J, is estimated as 0.466, which guarantees the small junction behavior. By using a formula of magnetic penetration length, $d= t + \lambda_L \tanh(t_1/2\lambda_L) + \lambda_L \tanh(t_2/2\lambda_L)$, for the thicknesses t, t_1, and t_2 of N-layer, upper and lower YBCO electrodes, we have estimated modulation period of $\Delta H= \Phi_0/Ld$ as 3.3 G as close as the observed period of 3 G. The temperature dependence of Ic and Rn for the single Fe-doped YBCO SNS junction with higher Ic of Fig. 4 is shown in Fig. 6.

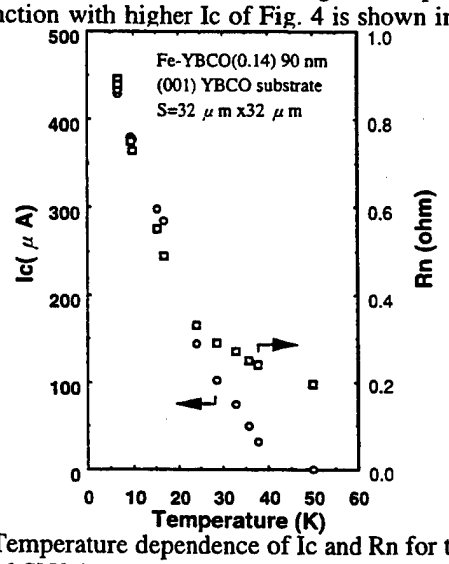

Fig. 6 Temperature dependence of Ic and Rn for the single Fe-doped SNS junction with higher Ic of Fig. 4.

The junction resistance Rn increases with decreasing temperature as is expected from the temperature dependence of resistivity ρ_c along c-axis for $YBa_2(Cu_{1-x}Fe_x)_3O_{7-\delta}$(x=0.065) single crystals [9]. If we neglect the contact resistance between YBCFeO and YBCO, the resistivity ρ is estimated to be 1.0 Ωcm at 6.71 K, which seems a reasonable value from the ρ_c of 235 mΩcm along c-axis for Fe-doped YBCO single crystals(x=0.065) [9]. The (Ic-Ie), Rn and (Ic-Ie)Rn products at 6.71 K are 290 μA, 0.88 Ω, and 255 μV, respectively. Furthermore, two connected junction (Fig. 4) in series shows about twice Rn of 1.38 Ω.

III. DISCUSSIONS AND CONCLUSIONS

We have demonstrated grain-free single crystallized SNS junctions for the first time by using (110) YBCO homoepitaxial technology. It clearly shows weak-link behavior even for thick N-layer of 150 nm although we do not have full understanding about its transport mechanism [1]. On the other hand as for the c-axis oriented YBCO homoepitaxial junctions, we have analyzed the data for IcRn products versus Jc around 4.2 K for the various stacked SNS junctions [3]. They suggest that the (001) stacked YBCO SNS junctions have a high potential to realize higher Rn, lower Ic and resultant higher IcRn products. If inhomogeneity of N-layers generates such high IcRn products irrespective low Jc, that is, the effective thickness of N-layer is much thinner than the nominated value, the observed agreement between theory and experiments seems not easy to explain. Furthermore, the equal first 3 periods of Fraunhofer pattern (Fig. 5) is another evidence for the current uniformity across the junction area.

As we think that the origin of Ie is related with the grain structure of (001) YBCO homoepitaxial film, the (001) stacked YBCO SNS junctions will become a challenging technology and an interesting target for device physics if the excellent surface morphology of each layer of SNS trilayers are realized from optimization of film growth.

This work was partly supported by New Energy and Industrial Technology Development Organization (NEDO).

REFERENCES

[1] T.Usagawa, J.G Wen, S.Koyama, T.Utagawa, and K.Enomoto, Jpn. J. Appl. Phys. 38, L436 (1999).
[2] T.Usagawa, Y.Ishimaru, J.G Wen, S.Koyama, and Y.Enomoto, Jpn. J. Appl. Phys. 36, L100 (1997).
[3] T.Usagawa, T.Utagawa, S.Koyama, K.Tanabe, and Y.Shiohara, submitted to Appl. Phys. Lett.
[4] Y.Namikawa, E.Egami, S.Koyama, and Y.Shiohara, J.Mater.Res. 11, 804 (1996).
[5] T.Usagawa, H.Unoki, I.Terasaki, J.G Wen, N.Koshizuka, Y.Enomoto, Jpn. J. Appl. Phys. 38, L370 (1999).
[6] J.Schutzmann, S.Tajima, S.Miyamoto and S.Tanaka, Phys. Rev. Lett. 73, 174 (1994).
[7] T.Usagawa, Y.Ishimaru, J.G Wen, T.Utagawa, S.Koyama, and Y.Enomoto, Jpn. J. Appl. Phys. 36, L1583 (1997).
[8] M.Tagami and Y.Shiohara, J. Crys. Growth 171, 409 (1997).
[9] Y.Eltsev and O.Rapp, Phys. Rev. B51, 9419 (1995).

Fabrication of natural-barrier ramp-edge Josephson junctions

M. Horibe, Y. Inagaki, G. Matsuda, N. Hayashi, K. Kawai, M. Maruyama, A. Fujimaki and H. Hayakawa
Department of Quantum Engineering, Nagoya University, Furo-cho, Chikusa-ku, Nagoya 464-8603, Japan

Abstract—We have studied the effect of process parameters on the natural-barrier ramp-edge Josephson junctions using $YBa_2Cu_3O_x$ electrodes, in order to improve uniformity and reproducibility of junctions. The natural-barrier is formed during an etching process and an annealing process. The junction properties are controlled by an annealing temperature and an annealing pressure. Also the junction characteristics depend on ramp-edge angle. After ramp structuring, the bulge of under-electrode is observed by AFM. The I_cR_n products of the junctions with the bulge of ramp surface reach 2mV at 4.2K. We speculate that the etching condition is very important parameter of the junction fabrication.

I. INTRODUCTION-

High temperature superconducting ramp-edge Josephson junctions are widely studied, because a variety of junction properties are obtained by selecting materials as an artificial barrier layer [1-2]. In fact, high performances have been achieved using a deposited $PrBa_2Gu_{2.85}Ga_{0.15}O_{7-x}$ barrier [1]. However, ramp-edge junctions with artificial barrier may have large spreads of junction properties due to deposition of barrier layer. If we take the realization of HTS SFQ circuits into account, the spreads of junction properties, such as junction resistance (R_n) and critical current (I_c), should be reduced to less than 10%. Several institutes and we try the non-artificial barrier junctions with High-T_c or Low-T_c superconductor [3-6]. We have already found that the junction properties depend on annealing pressures [5].

In this paper, we report the dependence of the natural-barrier junction properties on the ramp-angle and annealing temperature. Furthermore, we investigate the influence of the junction properties on the etching conditions.

II. FABRICATION PROCESS

We deposit a multilayer of $Au/PrGaO_3(PGO)/YBa_2Cu_3O_{7-x}$(YBCO) or $YBa_{1.95}La_{0.05}Cu_3O_{7-x}$(La-YBCO) on an MgO(100) substrate by an rf magnetron sputtering method. YBCO film is grown with c-axis normal to substrate surface. Typical transition temperatures of the YBCO films are 83-85K. The PGO film serve as an isolation layer in order to avoid electrical shorts between the superconducting electrodes in the overlapped area. Au is a passivation layer which protects the PGO surface form the pollution of photoresist during ramp-edge formation. The PGO template is obtained by an Ar ion beam etching using a photoresist mask. After removing photoresist, the ramp-edge is formed in an ECR plasma etcher using the PGO template as a mask. Ramp-angle (θ) is controlled from 2 to 40 degree to the substrate surface. After the etching, the sample is treated by an Ar plasma in the deposition chamber. Then, the sample is annealed at various annealing temperatures (T_{anl}) and pressures (P_{anl}) of an Ar+50%-O_2 mixture gas. The counter-YBCO electrode with 100nm thickness is deposited on annealed samples. After cooling down to room temperature in 2666Pa-oxygen atmosphere, a Au passivation layer is deposited. The desired junction structure is defined by the photolithographic patterning and the ion milling. The sample has 38 5μm –wide junctions with an SiO passivation layer.

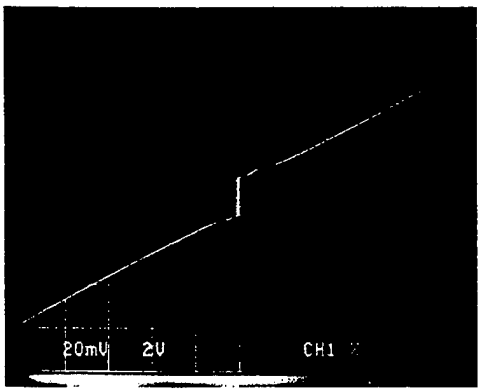

Figure 1 Typical current-voltage characteristics of a natural-barrier Josephson junction at 4.2K. The vertical scale is 200μA/div., and the horizontal scale is 200μV/div. The critical current is perfectly modulated by an applied magnetic field. The T_{anl}, P_{anl} and θ of this junction is 680°C, 1x10^{-5}Pa and 30°, respectively.

III. EXPERIMENTAL RESULTS AND DISCUSSION

A. *Current-Voltage Characteristics*

A typical current-voltage characteristic (*IV*Cs) at 4.2K is shown in Figure 1. The resistively-shunted-junction (RSJ) like *IV*Cs are observed at entire temperature range. For example, the characteristics at 4.2K for the junctions annealed at 680°C in about 1.0x10^{-5}Pa are; I_c=90μA, R_n=2Ω, I_cR_n=180μV. The junction resistances are independent of temperatures and voltages. Furthermore, the critical current is modulated by applied magnetic field. Sometimes the large excess currents are observed for a few junctions on a same chip.

Manuscript received April 30, 1999.

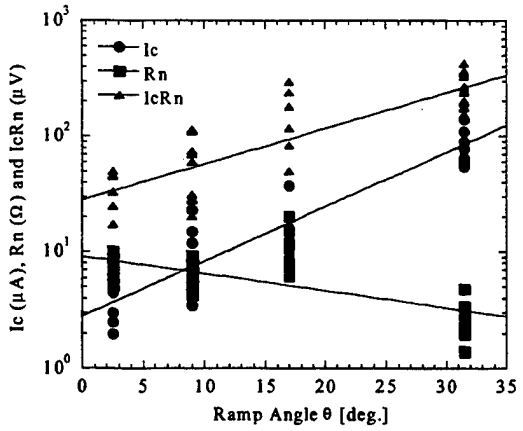

Figure 2. The ramp-angle dependence of junction properties, J_c, R_n, I_cR_n at 4.2K. T_{anl} and P_{anl} are 680°C and 1x10^{-5}Pa, respectively. I_cR_n product is decreased with narrowing ramp angles. Furthermore, the relationship between I_cR_n and J_c obays on scaling law.

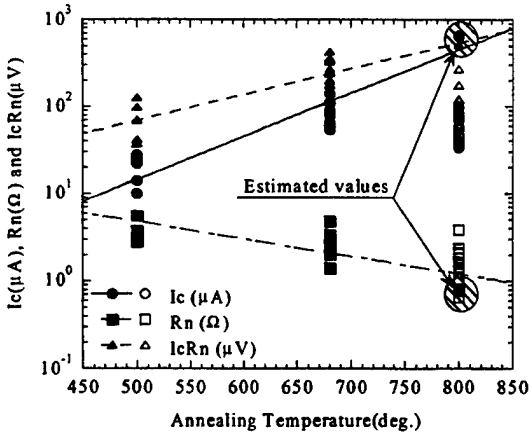

Figure 3. The junction properties as a function of annealing temperature (T_{anl}) at 4.2K. The circules, squares and triangulars are I_c, R_n and I_cR_n, respectively. The closed symbols are the data of the junctions with θ=30°. The open symbols are the data of the junctions with θ=10°. The data of junctions with T_{anl}=800°C and θ=30° are estimated from the data of junctions with T_{anl}=800°C and θ=10°. I_cR_n product is increased with T_{anl} rise.

B. *Ramp-Angle Dependence of Junction Properties*

We have fabricated the natural-barrier Josephson junctions with several ramp-edge angles. Here, the fabrication parameters of the junctions, such as etching conditions and annealing ones, are all the same except for a ramp-angle. Figure 2 shows the junction properties as a function of ramp-angle at 4.2k. The junction properties depend on the ramp-angle and the relationship between I_cR_n and J_c is similar to the scaling law. The junction properties can be controlled by the ramp-angle.

C. *The Annealing Temperature Dependence of Junction Properties*

Figure 3 shows the junction properties versus annealing temperature (T_{anl}) at 4.2K, for P_{anl}=1x10^{-5}Pa. The data of junctions with T_{anl}=800°C and θ=30° are estimated from the data for the junctions with T_{anl}=800°C and θ=10°. The I_c and I_cR_n increase with increasing T_{anl}. The I_cR_n is almost proportional to the square root of J_c. The junction properties can be roughly controlled by annealing temperature, however I_cR_n products are still small (less than 1mV at 4.2K). Furthermore junctions with T_{anl}=500°C have small yields and large spreads. We speculate that the natural-barrier formed by low temperature anneal is unstable on the thermodynamics, and then superconductivity of the ramp surface is unevenly restored during the upper-YBCO sputtering. As a result, the junction properties and yields go from bad to worse.

D. *The correlation Between Junction Properties and Ramp-Surface morphology*

Although we can control the properties of Josephson junctions with natural-barrier by changing the annealing pressure [5], then by annealing temperature in this study. However, the I_cR_n products are less than 0.4mV at 4.2K. We, thus, investigate the morphology of ramp surfaces and the electrical properties for many junctions formed by Ar ion beam etching with various etching conditions. The annealing conditions keep constant (T_{anl}=680°C, P_{anl}=1x10^{-5}Pa). The etching conditions of YBCO layer and junction properties are shown in Table I. We found from the AFM observation that the bulge of the edge surface was obtained only for Sample C as shown in Figure 4. We speculate that the bulges of La-YBCO surface correspond to a damaged layer formed during the etching. The junctions on Sample C showed excellent characteristics, while those on the other samples had poor properties as shown in Table I. The current-voltage characteristic of Sample A has been shown in Figure 1. All the junctions on Sample B have flux-flow-like *IV*Cs with critical current of 23.5mA at 4.2K. Figure 5(a) shows the

TABLE I

The etching conditions of YBCO layer by Ar ion beam etching and the junction properties

Sample name	Sample A	Sample B	Sample C	Sample D
Accelerating voltage	300V	200V	700V	300V
Microwave power	500W	200W	200W	500W
Ar	4.0sccm	4.0sccm	1.0sccm	1.0sccm
O_2	0.4sccm	0.4sccm	—	—
Etching Time	(on:10sec/off:30sec)x130	15min	9min	15min
Critical Current I_c	90μA	23.5mA	800μA	2mA
Junction Resistance R_n	2Ω	—	2.6Ω	1.1Ω
I_cR_n Product	180μV	—	2.08mV	2.2mV
Under electrodes	YBCO	La-YBCO	La-YBCO	La-YBCO

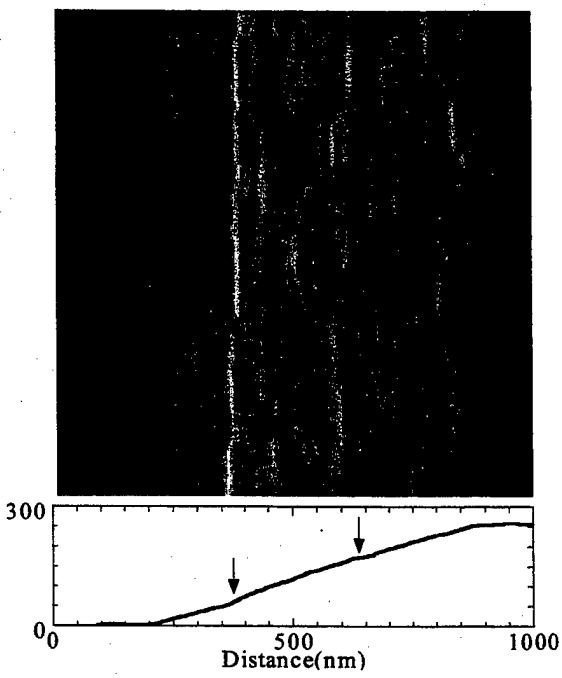

Figure 4. The AFM image (1μmx1μm) of a ramp surface and cross sectional view of ramp edge after ramp structuring using ion beam etching. The YBCO layer curves out slightly after etching with high accelerating voltage (700V). The arrows indicate a PGO/YBCO boundary and a YBCO/MgO substrate one, respectively.

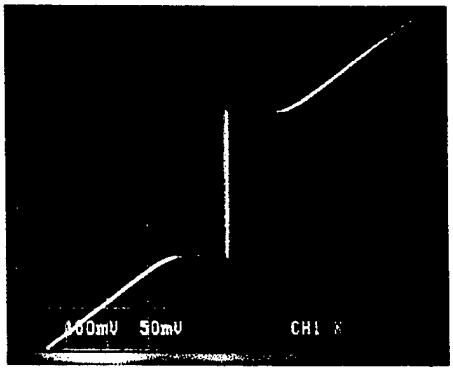

Figure 5(a) Typical current-voltage characteristics of natural-barrier Josephson junctions with the surface shown in Figure 4 at 4.2K. The vertical scale is 500μA/div., and the horizontal scale is 1mV/div. The hysterisis is observed below 30K. The T_{anl}, P_{anl} and θ of this junction is 680°C, 1x10^{-5}Pa and 20°, respectively.

RSJ-like *IV*Cs of Sample C at 4.2K. The electrical properties at 4.2K for Sample C are; I_c=800μA, R_n=2.6Ω and I_cR_n=2.08mV. The hysterisis vanishes at 30K. The critical current is perfectly suppressed by applied magnetic fields at 50K as shown in Figure 5(b). Only one junction in Sample D shows the RSJ-like current-voltage characteristics with I_c=2.2mA, R_n=1.1Ω and I_cR_n=2.2mV at 4.2K. The other junctions have large excess current of about 5mA at 4.2K. From these results, the accelerating voltage affects junction properties strongly. We specurlate that a moderate thickness of damaged layer is formed during the etching.

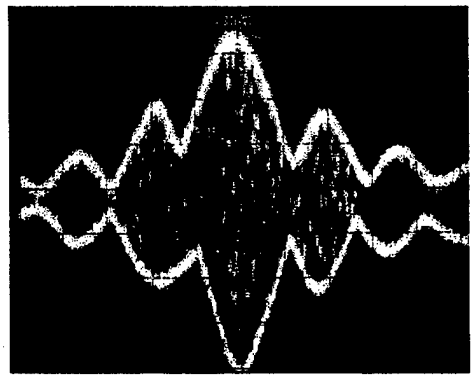

Figure 5(b) The critical current versus an applied magnetic field at 50K for the natural-barrier Josephson junctions. The vertical scale is 40μA/div., and the horizontal scale is 9x10^{-6}T/div. The critical current is perfectly modulated by an applied magnetic field.

IV. Conclusions

We have fabricated the natural-barrier Josephson junctions by ion beam etching and annealing. The junction properties are controlled by annealing pressure and enhanced by the improvement of etching condition. In fact, I_cR_n product reaches about 2mV at 4.2K for sample C. Improvement of the uniformity and reproducibility is the next subject.

Reference

[1] M. Horibe, K. Kawai, A. Fujimaki and H. Hayakawa, "Ramp-Edge Josephson Junctions Using Barriers of Various Resistivities," *IEICE Tarns. On Electronics*, vol. **E81-C**, pp. 1526-1531, 1998.

[2] M. A. J. Verhoeven, G. J. Geritsma, H. Rogalla and A. A. Golubov, "Ramp-type junction parameter control by Ga doping of $PBa_2Cu_3O_{7-\delta}$ barrier," *Appl. Phys. Lett.*, vol.**69**, pp.848-850, 1996.

[3] B. H. Moeckly and K. Char, "Properties of interface-engineered high T_c Josephson junctions," *Appl. Phys. Lett.*, vol.**71**, pp.2526-2528, 1997.

[4] T. Satoh, M. Hidaka and S. Tahara, "High-Temperature Superconducting Edge-Type Joesphson Junctions with Modified Interfaces," *IEEE. Trans. Appl. Supercond.*, in press.

[5] A. Fujimaki, K. Kawai, N. Hayashi, M. Horibe, M. Maruyama and H. Hayakawa, "Preparation of Ramp-Edge Josephson Junctions with Natural Barriers," *IEEE. Trans. Appl. Supercond.*, in press.

[6] H. Akaike, R. Oke, T. Aoyama, A. Fujimaki and H. Hayakawa, "Overdamped Niobium-nitride Junctions for 10K Operation," *IEEE. Trans. Appl. Supercond.*, in press.

3-D Intrinsic Josephson junctions using c-axis thin films and single crystals

Sang-Jae Kim, Yu. I. Latyshev and Tsutomu Yamashita
Research Institute of Electrical Communication, Tohoku University, Katahira, Aoba-ku, Sendai 980-8577, Japan
and CREST, Japan Science and Technology Corporation (JST)

Abstract — We report successful fabrication of 3-D intrinsic Josephson junctions (IJJs) using c-axis YBCO thin films of 800 nm thickness and Bi-2212 single crystal whiskers. The stacks of IJJs were equipped by lateral focused-ion-beam (FIB) etching method. A width depending on the required junction size and a full depth of film thickness were patterned in a micro area from the normal direction etching. By tilting of the sample stage up to 90° , two groove of the bridge were etched from lateral direction in accordance to the required junction size. The junctions did not show any degradation of critical current density (J_c) down to in-plane area of 0.5 μm^2.

I. Introduction

A number of fabrication methods based on high-resolution patterning have been applied to develop high-T_c superconducting (HTS) devices [1,2]. Particularly, such fine structures are needed in the fabrication of tunneling devices such as the intrinsic Josephson junction (IJJ) in layered high-T_c superconductors [3-5], because a perfect stacked structure with a very small lateral size compared with the Josephson penetration length is required, $\lambda_j (=\gamma d)$, where d is the interlayer spacing and $\gamma (=\lambda_c / \lambda_{ab})$ is the London penetration depth anisotropy ratio [6]. Perfect stacks are more often obtained in c-axis high quality thin films than in a-axis and single crystal whiskers. However, the IJJ fabrication process using c-axis thin films and single crystals need intricate process and limit the junction size like mesa structures [7].

Recently, we reported on the submicron IJJ fabrication by FIB etching method using single crystal whiskers as a base material [8,9]. Unfortunately, by using this procedure is difficult to adjust the process of thin film device fabrication because it needs turnover of the sample, even though the thin film process is very useful for integrated devices like superconducting memory and transistor, and need a few complicated process for single crystals. As an alternative approach, we present a 3-D IJJ fabrication method from c-axis thin films. The fabrication steps using c-axis single crystal is also simplified with in-situ process. Here, we report on the lateral FIB etching methods for fabrication of 3-D IJJ using 57 K-YBCO thin films and Bi-2212 single crystal whiskers as an example.

II. Experimental

We used commercial c-axis YBCO films with 800 nm thickness prepared by co-evaporation method from THEVA company. The samples were annealed at 450℃ for 3 hours in order to obtain the 60 K-YBCO phase deficient in oxygen. We used the Bi-2212 single crystal whiskers grown by Pb-free method and have been characterized by TEM as a very perfect crystalline object [10]. Four contacts were prepared with silver paste for the electrical measurements. For decreasing the contact resistance, the contacts were annealed in an oxygen flow at 450℃.

For the etching, we used a commercial FIB-machine, the SMI-9800 (SP) from Seiko Instruments Inc.. This apparatus uses a focused Ga^+ -ion beam with maximum energy of 30 keV and a probe current of 8 pA- 5 nA. For the smallest beam currents the beam can be focused down to 10 nm. We used an etching rate of 2500 $\mu m^3/(pA \cdot sec)$. From the results of a transport of ions in matter (TRIM) simulation [11] the maximum penetration depth of 30 keV Ga^+-ions along the c-axis of a YBCO thin film is 60 nm and the lateral scattering depth, including the beam spot size, is 40 nm. Therefore, the proportion of the fabricated junction affected by ion beam damage is not so large.

III. New Fabrication Methods

We devised two lateral etching methods by tilting the FIB sample stage [12]. The first lateral etching method is performed by using automatic sample stage tilting up to 90° and the other is by using a 60° tilting sample stage and a 30° slope support. We use the latter method in this experiment.

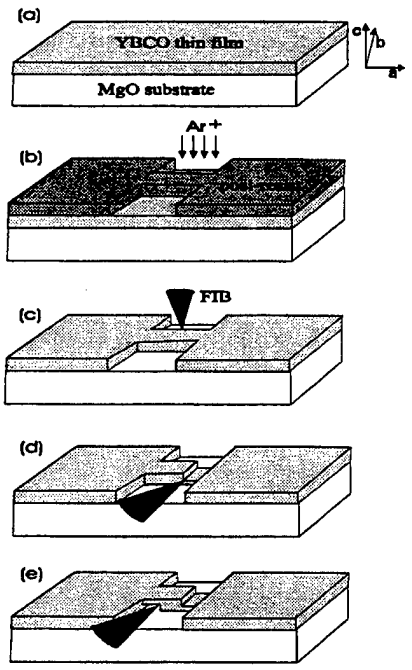

Fig. 1 Steps of the fabrication process using lateral FIB etching method.

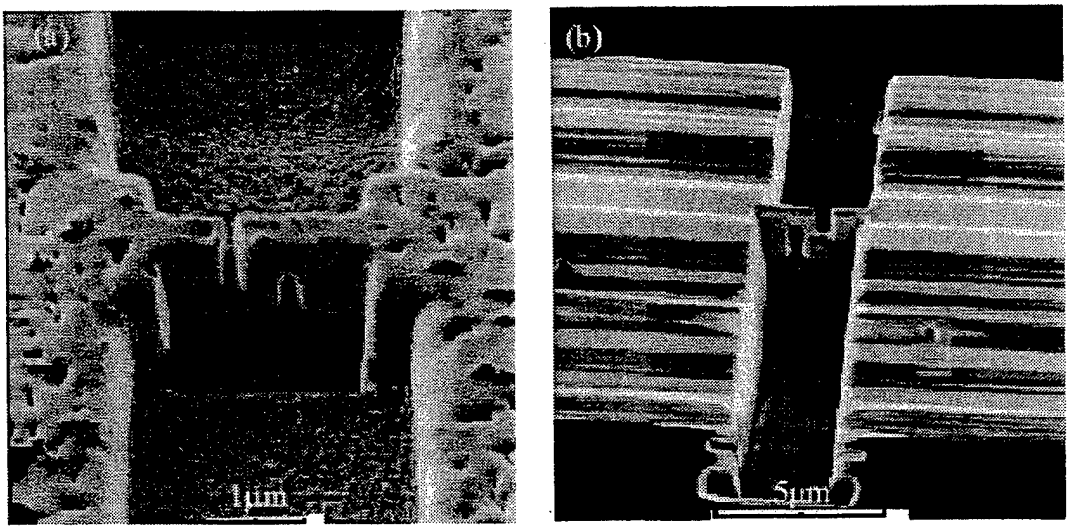

Fig. 2 SEM photographs of YBCO stack (a) and Bi-2212 stack (b) on MgO substrate fabricated by lateral FIB etching methods. Film thickness is 800 nm and whisker thickness is approximately 2 μm.

Thus, we patterned the bridge width from the top direction and the junction layers length from the lateral direction by tilting of the sample stage up to 90° . The exact stack size is etched by the scanning of the sample images from the top and lateral view.

The steps of the fabrication process of thin film using FIB etching are shown in Fig. 1 (a)-(e).

As the first step, the micro-bridges were patterned on YBCO film on MgO substrate using conventional photolithography and Ar ion milling method in Fig. 1 (a)-(b). Four contacts were prepared with silver paste. Next, the substrate was fixed to the sample holder of the FIB etching machine and a width (depending on the required stack size) and a full depth of film thickness were etched in the required stack area. (Fig. 1 (c)). After this, the substrate was turned over up to 90° by tilting of the sample stage. Then, two grooves of the similar depth were etched the whole length and the distance between grooves was offset according to the required junction size. A rectangular geometry of the stack in the ab-plane was formed, as can be seen in Fig. 1 (d)-(e). Using single crystal whiskers, only the procedure need in Fig. 1 (c)-(e). The in-plane area, S, of fabricated stacks is in the range of 0.5 μm^2 and 1 μm^2. The c-axis length of the stacks is approximately 0.1 μm. Fig. 2 shows the angular SEM view of the fabricated stacks on 800 nm YBCO thin film (a) and on Bi-2212 single crystal whisker (b). These methods offer the in-situ and simple fabrication processes for equipping micro S of stacks using anisotropic thin film and single crystals.

IV. Results

I-V characteristics of two fabricated YBCO stacks with S of 1 μm^2 and 0.5 μm^2 are shown in Fig. 3 (a) and (b), respectively. Those stacks are on the same film of a substrate. Critical temperature (T_c) of junctions is 57 K. 1 μm^2 stack show resistive shunted like I-V curves without any branch structure as shown in Fig.3 (a). With decreasing the stack size down to 0.5 μm^2, the junction shows hysteresistic I-V curves (Fig.3 (b)).

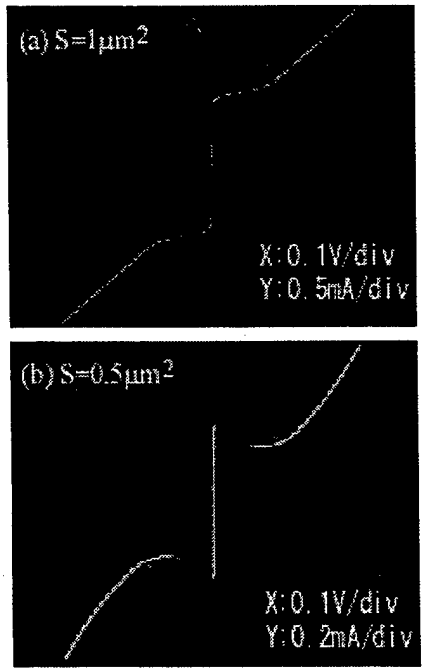

Fig. 3 Large scale I-V characteristics of IJJ fabricated by lateral etching method using 800 nm-YBCO thin film. In-plane areas of stack are 1 μm^2 (a) and 0.5 μm^2 (b).

Junction parameters of two samples are listed in Table I. Those samples show very high I_cR_n product of the junction indicating that the junction layers are well arrayed in series with constant I_c and increasing R_n equal to junction numbers. These critical current density (J_c) values didn't show any degradation down to 0.5 μm^2 due to fabrication methods. The J_c of 60 K-YBCO samples is in the range of $(5\text{-}10)\times 10^4$ A/cm^2 [13]. The I-V characteristic behavior of 1 μm^2 (#1) junction may be due to the shunted grain boundary effect, because the average grain boundary size is in the range of 0.1-0.2 μm. I-V curves of 0.5 μm^2 (#2) shows the switching behavior from zero voltage state to resistive state. The collective transition may be from the strong coupling between thin superconductive electrode and high J_c [14]. We believe that the hysteresis is caused by superconductive phase-lock switching of IJJ.

Fig. 4 shows the typical I-V characteristics with Bi-2212 stacked-junction area of 0.9 μm^2. A clear gap structure is seen in the I-V characteristics at V_g=1.5 V, which corresponds to a superconducting gap of N elementary junctions connected in series. The S-shaped I-V characteristics of the stack at $V \approx V_g$ is mainly from many stacked-junction layers of 85. The uniform distribution of critical current over the stack is shown in Fig. 4 (b).

The parameter of the fabricated stacked-junction of 0.9 μm^2 are shown in Table I. The critical current density (J_c) is not changed in the range 700 A/cm^2 means that the process don't give any damage from fabrication process.

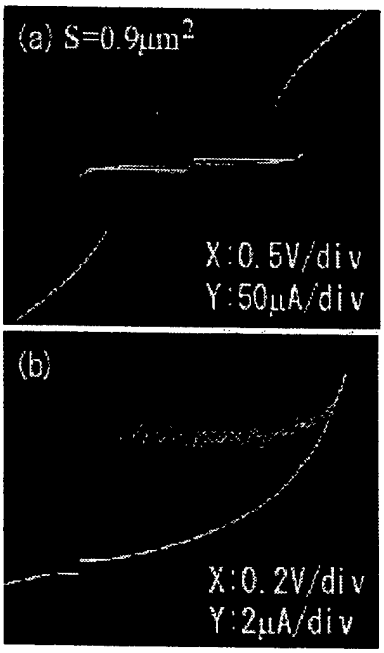

Fig. 4 Large scale I-V characteristics (a) of IJJ fabricated by lateral etching method using Bi-2212 single crystal whisker. The I-V characteristics in expanded scale are shown in (b) and (c). T=4.2 K. In-plane areas of stack are 0.9 μm^2.

TABLE I

PARAMETERS OF FABRICATED STACKS USING LATERAL FIB ETCHING METHOD

		S (μm^2)	I_c (μA)	R_n (Ω)	I_cR_n (mV)	J_c (A/cm^2)
60 K -YBCO	#1	1	800	240	192	8×10^4
	#2	0.5	360	400	144	7.2×10^4
Bi-2212 whisker	#3	0.9	7	12.5×10^3	88	7×10^2

The etching methods of stacks from lateral side show many advantages for IJJ fabrication using thin films and single crystals as follows; firstly, in-plane area and c-axis length of stacks is easily etched from scanning direction by monitoring of the lateral view. Secondly, simplify the fabrication process with in-situ processes without the changing of etching side in ref. 8. Thirdly, surface roughness of samples doesn't give any disturbance for fabrication process as shown in Fig. 2 (b).

V. SUMMARY

We demonstrated a fabrication method for equipping IJJs using lateral FIB etching method. The method was realized by tilting of sample stage up to 90° . The fabrication methods did not give any degradation of junction properties down to 0.5 μm^2. The stack number and area of IJJ were controlled easily by scanning and etching of ion beam. The lateral FIB etching method in this report is a very hopeful technique for fabricating those devices requiring minute tunneling junction layers.

The authors would like to thank Dr. K. Nakajima for valuable discussions.

REFERENCES

1) L. R. Harriott, P. A. Polakos, and C. E. Rice; Appl. Phys. Lett. 55, (1989) 495.
2) Q. Y. Ma, A. Wong, P. Dosanjh, J. F. Carolan, and W. N. Hardy; Appl. Phys. Lett. 65, (1994) 240.
3) F. X. Regi, J. Schneck, J. F. Palmier, and H. Savary, J. Appl. Phys. 76, (1994) 4426.
4) Yu. I. Latyshev and J. E. Nevelskaya, Physica C, 235-240, (1996) 2991.
5) A. Yurgens, D. Winkler, T. Claeson, and N. V. Zavaritsky, Appl. Phys. Lett. 70, (1997) 1760.
6) L. N. Bulaevskii, J. R. Clem, and L. I. Glazman, Phys. Rev. B 46, (1992) 350.
7) W. Prusseit, M. Rupp, K. Hirata, and T. Mochiku, Physica C 25, (1997) 174.
8) Yu. I. Latyshev, S.-J. Kim, and T. Yamashita, Pis'ma Zh. Eksp. Teor. Fiz. vol. 69 , 1999.
9) S.-J. Kim, Yu. I. Latyshev, and T. Yamashta: Appl. Phys. Lett. 74, (1999) 1156.
10) Yu. I. Latyshev, I. G. Gorlova, A. M. Nikitina, V. U. Antokhina, S. G. Zybtsev, N. P. Kukhta, and V. N. Timofeev, Physica C, 216, (1993) 471.
11) J. F. Ziegler, J. P. Biersack, and U. Littmark, "*The stopping and Range of Ions in Solids*", Pergamon Press, New York, (1996).
12) T. Yamashita and S. -J. Kim, Japan Patent 11-16491, (1999).
13) M. Rapp, A. Murk, R. Semerad, and W. Prusseit; Phys. Rev. Lett. 77, (1996) 928.
14) M. Sakai, A. Odagawa, H. Adachi, and K. Setsune: Physica C 299, (1997) 31.

Optimum Characteristics of High Temperature Josephson Junctions for "Lumped" Array Applications*

R.H. Ono and S.P. Benz
National Institute of Standards and Technology, Boulder, CO 80303, USA

Abstract– We present design criteria for arrays of Josephson junctions optimized for use in the Josephson digital-analog converter and for a THz oscillator. We will briefly analyze existing high temperature superconducting Josephson junction processes and describe possible implementation of a lumped array using electron-beam-damaged junctions and bilayer-SNS junctions.

I. Introduction

This paper reviews the desired characteristics for high temperature superconducting (HTS) Josephson junctions for use in arrays. We will analyze the case of "lumped" (as opposed to "distributed") systems where the circuit size is electrically small, that is, short compared to the wavelength of the radiation required.

Arrays of low-T_c Josephson junctions are the basis for a number of applications within superconducting electronics including Josephson voltage standards, millimeter-wave oscillators, and microwave frequency clocks [1]. For useful power or voltage output, large numbers of junctions are typically required with small spreads in individual characteristics. For most system applications, the broadest possible bandwidth is desirable, as is rapid and simple tunability. Of course, the higher the operating temperature of the Josephson circuit, the simpler and cheaper are the system insertions.

High temperature superconducting (HTS) junctions may permit arrays that can operate in a compact and inexpensive cryogenic system. However, existing HTS junction technologies are still in their infancy, in particular with regards to spreads in junction critical currents. The individual characteristics of many HTS junctions are in some cases ideal for lumped array designs, and we will discuss this and examine some particular approaches to junction fabrication.

II. Review of Junction Characteristics

HTS Josephson junctions typically are weak links that can be described by the Resistively-Shunted Junction (RSJ) model [2]. The important individual junction parameters are critical current I_C, normal resistance R_N, capacitance C_J, Josephson penetration depth λ_J, and the characteristic voltage $V_C=I_CR_N$. The spreads in these parameters over a large number of junctions should be small, as required by the operating margins of the array circuit. Practical issues of frequency source power and microwave or millimeter wave feed design must be taken into consideration. Operating temperature is a relatively unconstrained parameter, fundamentally related to thermal noise and stability of array operation. Higher temperature operation requires higher critical currents. In practice, these values are experimentally achieved in most HTS junction implementations. The following equations summarize the important junction and circuit characteristics:

$$V_J=\frac{h}{2e}f_0,\quad V_C=I_CR_N,\quad \Omega=\frac{f_0}{(2e/h)V_c},\quad \beta_C=\frac{2e}{\hbar}I_CR_N^2C_J.$$

The ac Josephson effect predicts that currents in the junction will oscillate at a frequency f_0 proportional to the time averaged voltage V_J; this is the basis for the types of applications we are considering. The characteristic voltage of the junction sets a voltage (and hence frequency) scale for operation. The ratio of f_0 to $(2e/h)V_C$ is the dimensionless reduced frequency Ω. The hysteresis parameter β_C should be much less than 1, requiring either a very small junction capacitance, external shunting to reduce junction resistance, or both. As we will see in the next section, I_C and R_N are chosen to maximize I_C and to set the product to approximately correspond to the frequency of interest.

III. Array Requirements

Given the above general constraints, we now discuss the particular requirements imposed by our applications of interest. These specifics are determined by the system into which the array is inserted, in particular impedance matching of sources and loads.

First, to ensure a tunable oscillator, resonances in the junctions and arrays should be avoided by having minimal inductive and capacitive parasitics. This rules out long junctions and complex multidimensional arrays. Two methods of external frequency control can be used. (1) Use an *external feedback* loop, which taps off some of the oscillator power, mixes it down to a much lower frequency,

* Contribution of the U.S. Government and not subject to copyright.
Support from the Office of Naval Research is acknowledged.

TABLE I

We present the design values for a 18 GHz digital-analog converter and a 2 THz oscillator. We assume that I_c is 10 mA for the above cases.

Device	f (GHz)	Z_L (Ω)	n	Ω	V_c (μV)	R (mΩ)	N
J-DAC	18	50	2	1	37	3.7	13,433
J-Oscillator	2000	75	1	2	2,068	206.8	363

TABLE II

This table shows the constraints on junction spacing due to different substrates with different dielectric constants.

Device	Dielectric	ε_{eff}	Λ/4 (μm)	Length/ JJ (nm)	Output
DAC	Si/Air	6.4	1647	123	1.00 V±
Oscillator	Quartz/Air	2.4	24	67	0.94 mW
Oscillator	Sapphire/Air	6.4	15	41	0.94 mW

compares it to an external reference, and adjusts the array bias. This method may require internal phase locking of the junctions or some form of high frequency feedback. In this method the array behaves as a variable frequency oscillator. The second method is to *subharmonically pump* the array at a lower frequency and bias the array so that it generates more than one quantized voltage pulse per drive cycle, i.e. f_0=nf. The lower frequency is tunable and locked to an external frequency reference. In this method the array behaves as a frequency multiplier. This method does *not* require internal phase locking of the array and may work better for arrays with significant junction nonuniformity.

The output power of an oscillator will be determined by the application and by the impedance of the load. Generally, higher output power is desirable. The output power will be highest when the ac Josephson current is highest. The ac Josephson current is proportional to the junction critical current, which is maximized by increasing the junction dimensions to $4\lambda_J$. In the case of HTS junctions, the usual square geometry of the tunnel junction [3] is not appropriate, and an inline geometry should be used to calculate λ_J [4].

The junction characteristic frequency $2e/hV_C$ should be chosen less than the desired operating frequency f_o to maximize the ac Josephson current in the fundamental frequency. However, phase locking will decrease as junction uniformity increases, in particular, as $f_o >> f_c$ [5]. Thus the operating frequency should be in the range $(1\text{-}3)f_c$. For example, a 1-2 THz oscillator with a load impedance of 75 Ω f_c = 1 THz and I_c = 10 mA, would have a junction resistance of about 200 mΩ. Similarly, a Josephson DAC driven at 18 GHz requires over 13,000 junctions. Some of these points are summarized in Table I.

The discussion to now has been a review of simple optimization concepts. We now turn to a brief discussion of the design criteria for lumped arrays fabricated on typical dielectrics. The following relationships are used in designing these electrically small arrays, and have been used to develop the values in Table II.

$$Z_{array} = NR_N \approx 50\Omega, \quad \Lambda = \frac{c}{f_0\sqrt{\varepsilon_R}}, \quad L_{Array} << \frac{1}{4}\Lambda.$$

The number of junctions N can now be chosen to match the array impedance to either a quasi-optical antenna or an on-chip detector. However, the maximum number of junctions is limited by requiring that the array remain a lumped element, that is, its total length is only 1/4 the length Λ corresponding to the maximum output frequency. Choosing an output frequency of 2 THz (150 μm) and a 75 Ω quasi-optical antenna, the array length is limited to about 12 μm for the necessary N= 375 junctions. Lumped arrays are preferred over distributed arrays for a number of reasons. Distributed arrays are intrinsically fixed frequency designs and their distributed nature increases the transmission line losses, which are particularly large at THz frequencies. Under the above assumptions, the junction spacing for the 375 junction lumped array is a challenging 32 nm. The array is tunable from 1-2 THz and delivers about 1 mW to the 75 Ω antenna at 2 THz. Smaller numbers of junctions (and output power) can be matched to antenna impedances as low as 25 Ω using junction spacings as large as 100 nm.

IV. HTS Josephson Junctions

In the past, we have explored several HTS junction technologies for arrays: SNS step-edge junctions, ramp-edge junctions, bicrystal junctions, and electron-beam irradiated

junctions. The e-beam junctions (EBJ) are excellent candidates because of their small size, allowing a large number of junctions to be placed in a small length [5]. Separations of 100 nm have been demonstrated, in the range discussed in the previous section. Because of this advantage, we are presently involved in a collaboration to develop electron-beam irradiated junction arrays. Figure 1(a) shows a schematic of the process and of a resulting lumped array.

Initial experiments in close spacing and in junction uniformity are presented in [5]. These results show promise for arrays numbering in the hundreds of junctions. Ultimately, very slow writing time may be the limiting factor in producing useful arrays by this technique. Long term stability must also be investigated.

A junction process that uses faster lithography than e-beam damage would be desirable for manufacturability.

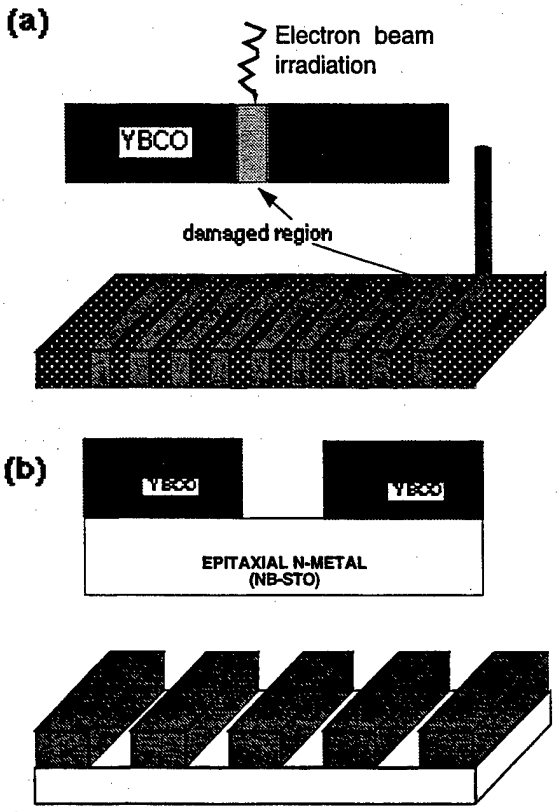

Fig.1 (a) Electron-beam irradiation damage forms a normal metal region in the YBCO. (b) E-beam lithography is used to form a bilayer microbridge SN-N-NS junction.

Resist-based e-beam lithography (EBL) will be investigated using epitaxial HTS/normal metal bilayers. As shown in Fig. 1(b), an epitaxial bilayer of YBCO on an oxide normal metal is patterned into a sequence of SNS microbridge structures. The etched pattern in the HTS layer is first formed by EBL and the resist pattern transferred by ion milling. A collaboration with the University of Colorado is presently underway to investigate Nb-doped $SrTiO_3$ (Nb-STO) as a normal metal. In this case, the important parameters we need to measure are the normal state properties of Nb-STO, in particular the normal metal coherence length over the temperature range of interest.

V. SUMMARY

We have briefly reviewed the various individual junction characteristics needed for electrically small arrays. These lumped arrays may find significant use as precision digital-analog converters and THz oscillators if the formidable fabrication challenges are overcome, either in low or in high temperature junction systems.

REFERENCES

1. M. Darula, T. Doderer, and S. Beuven, "Millimeter and sub-mm wavelength radiation sources based on discrete Josephson junction arrays," Supercond. Sci. Technol., vol. 12, pp R1-R25, 1999.
2. A. Barone and G. Paterno, *Physics and Applications of the Josephson Effects*, (Wiley, New York, 1982) chapter 3.
3. R.L. Kautz, " Shapiro steps in large-area metallic barrier Josephson junctions," J. Appl. Phys., vol. 28, pp.58115819, Nov. 1995
4. Sergey Tolpygo and Michael Gurvitch,, "Critical currents and Josephson penetration depth in planar thin-film high-Tc Josephson junctions," Appl. Phys. Lett, vol. 69, pp 3914-3916, Sept. 1996.
4. S.I. Borovitskii, A.M. Klushin, T.B. Korotina, A.E. Pariskii, S.K. Khorshev, and P.A. Shisharin, "Increasing the working voltage across chains of Josephson junctions," Sov. Tech. Phys. Lett., vol. 11, pp. 275-277, June 1985.
5. W.E.Booij, *Josephson Junctions and Devices Fabricated by Focused Electron Beam Irradiation*, (Ph.D. dissertation, Cambridge University, 1997).

Oral Session 6

Materials and Fabrication

Effects of Process Parameters on the Fabrication of Edge-Type YBCO Josephson Junctions by Interface Treatments

Jan-Klaas Heinsohn, Robert Hadfield, and Regina Dittmann
Research Center Jülich, Institute of Thin Film and Ion Technology, 52425 Jülich, Germany

Abstract—The preparation process of edge-type $YBa_2Cu_3O_7$ (YBCO) Josephson junctions by interface treatments is investigated in detail. By application of statistical methods in the design and analysis of the experiments we have investigated the dependence of the junction characteristics on the process parameters in a systematic way. By adjusting the process parameters, RSJ-like Josephson junctions as well as interconnects can be fabricated reproducibly. The annealing temperature and the deposition temperature of the counterelectrode have a significant influence on all junction parameters. Increasing the etching voltage, which is applied during the interface treatment, leads to higher modulations of the critical current. Many interaction effects are also significant. We discuss the influence of the process parameters and their interaction effects with respect to the formation of a nonsuperconducting barrier at the interface of the YBCO ramps.

I. Introduction

Josephson junctions in the ramp-edge geometry have been produced for almost a decade. Nevertheless, the problem of control of the growth of barrier material and counterelectrode on an atomic level still remains unsolved. The tendency of the rare earth barium cuprates to form facets when growing on a tilted area leads to inhomogeneities in the barrier thickness from several nanometers to tens of nanometers [1]. In consequence, the spatial distribution of the critical current becomes non-uniform, depending exponentially on the barrier thickness in SNS junctions [2], [3].

For this reason, efforts in fabricating superconducting weak links in the ramp-edge geometry without an artificial barrier have been made by several groups [4]-[8]. This is done by a subsequent treatment of the etched YBCO ramp before deposition of the counterelectrode. The additional treatment consists mainly of two parts: an additional milling step after etching of the ramp in order to damage the YBCO interface and a subsequent annealing step before deposition of the upper YBCO electrode in order to recrystallize the damaged interface, thereby forming the barrier.

In this paper, we show that the junction properties can be adjusted reproducibly by controlled variation of the process parameters. We employed statistical methods in the construction of the experiment (experimental design) and the analysis of the results (multiple regression). By this approach, the effects of process parameters and their interactions can be detected and quantified, leading to regression models of the junction properties.

Manuscript received April 30, 1999

II. Experimental Details

A. Junction Preparation

A detailed description of the preparation process will be given in another paper. In brief, first, a bilayer consisting of a 220 nm thick STO film and a 120 nm thick YBCO film are deposited *in situ* on a STO (100) substrate by on-axis pulsed laser deposition. The films are patterned by conventional photolithography and subsequently post-baked, which reflows the photoresist and ensures shallow edge angles. The ramp is fabricated by Ar-ion-beam milling using an ion-beam current density of 0.25 mA/cm^2 and an energy of 250 eV. The sample is tilted 30° to the substrate normal and rotates during the etching. At the end of the milling process, the sample is milled at a much higher voltage V_{mill} for a short time t_{mill} in order to produce an amorphous YBCO layer at the surface. Before deposition of the upper YBCO electrode, the sample is annealed in the deposition oxygen atmosphere of 60 Pa at a temperature T_{ann} which is held for a time t_{ann}. After deposition of a 180 nm thick YBCO film at a temperature T_{dep}, the junctions are structured by conventional photolithography and Ar-ion-beam milling. Finally, a 200 nm thick gold layer is evaporated and patterned by a lift-off process to provide electrical contacts.

B. Junction Characterization

In the statistical analysis of the experiments, the data from eight 4 µm wide junctions distributed over the whole chip were taken, providing good information about the on-chip spread of the measured quantities (the so-called *responses*). The junctions were measured in the standard four-point geometry at 77 K. From the current-voltage curves, the

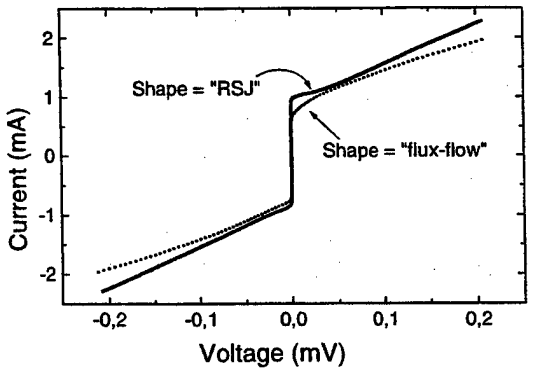

Fig. 1. *I-V* curves of junctions which are denoted "RSJ" or "flux-flow" like.

TABLE I. Factors and investigated regions used in the experimental design. The expression 5=1234 is the design generator (see [10] for details).

Factor	Name	Abbr.	Investigated Region
1	Milling Voltage	V_{mill}	600..900 V
2	Milling Time	t_{mill}	2..5 min
3	Annealing Time	t_{ann}	5..30 min
4	Deposition Temperature	T_{dep}	805..835°C
5 = 1234	Annealing Temperature	T_{ann}	500..805°C

normal resistance R_n and shape of the *I-V* curve (RSJ like, flux-flow like, intermediate) were determined (Fig. 1). The magnetic-field dependence of the critical current $I_c(B)$ was measured from which the following responses were determined: critical current I_c from the maximum of the $I_c(B)$ curve, modulation depth $\Delta I_c = (I_{c,max}(B) - I_{c,min}(B))/I_{c,max}(B)$, and resemblance to the Fraunhofer pattern (good, medium, none). Since we often observe trapped magnetic flux in our junctions, we determined the critical current from the maximum of the $I_c(B)$ curve. On three chips, all junctions were measured to verify the scaling behavior of I_c and R_n with the junction width.

C. Experimental Design

Details about the statistical background and terminology used in experimental design can be found e.g. in [9] or [10]. The factors investigated in a first 2_V^{5-1} fractional-factorial design are listed in Table I. According to this experimental design, 16 samples were produced under different process conditions. With these samples, all main effects and two-factor interaction effects are unconfounded, i.e. they can be estimated separately.

The first two factors, milling voltage V_m and time t_m, are believed to determine the strength of the damaging of the interface. The next two factors, annealing temperature T_a and time t_a, may determine the recrystallization of the material at the interface, and the fifth factor, deposition temperature T_d, influences the overgrowth of the upper YBCO layer and possibly also the deterioration of a previously formed barrier.

III. Results

A. Descriptive Statistics

Table II shows the correlation matrix of the measured responses before the calculation of the on-chip averages. As expected, the critical current and the normal resistance are strongly anti-correlated. Furthermore, the shape of the *I-V* curve, the modulation depth, and the Fraunhofer similarity are correlated significantly: The more RSJ-like and the more Fraunhofer-like, the higher is the modulation depth, and the RSJ-like junctions tend to have $I_c(B)$ curves more similar to the Fraunhofer pattern. What is striking, on the other hand, is the lack of correlation between the shape of the *I-V* curve and the critical current or normal resistance. Also the modulation depth and the Fraunhofer similarity are not significantly correlated with I_c or R_n.

TABLE II. Correlation matrix of the measured responses. Correlation coefficients above 0.20 are stronger than 5% significant.

	I-V Shape	Fraunhofer	Modul.	I_c	R_n
I-V Shape	1.00	-0.49	-0.63	0.20	-0.21
Fraunhofer	-0.49	1.00	0.61	0.12	-0.12
Modul.	-0.63	0.61	1.00	-0.14	0.13
I_c	0.20	0.12	-0.14	1.00	-0.73
R_n	-0.21	-0.12	0.13	-0.73	1.00

B. Multiple Regression Analysis

Calculation of the response averages on each chip yields further important responses, namely the standard deviations which are of great importance for applications, a test of the reliability of the process, and an indicator of the uniformity and stability of the barrier. With each of these responses, a multiple regression analysis was conducted, taking the factors as regressors and the responses as regressands. This yields the regression coefficients, which are directly related to the main and interaction effects of the factors [9].

As an example, we present the analysis of the critical current I_c. Fig. 2 shows the factor effects included in the regression model, which are all effects being stronger than 10% significant. The most significant effects are the interaction $T_{dep}\times T_{ann}$ of the deposition temperature with the annealing temperature and the two respective main effects T_{dep} and T_{ann}. The meaning of the interaction effect becomes clear in Fig. 3, where the response surface defined by the regression equation

$$I_c\,(\mu A) = 1181 - 365\,T_{ann}\times T_{dep} + 358\,T_{dep} - 228\,T_{ann} - 178\,V_{mill}\times t_{ann} + 167\,V_{mill}\times T_{ann} \quad (1)$$

is depicted in the (T_{dep}, T_{ann}) space. The annealing temperature has a large negative effect on the critical current only when the deposition temperature is on its high level of 835°. On the low level of 805°, it has a small positive effect, which is however not significant.

Interconnects with high critical currents and little Josephson behavior can be produced at T_{dep} = 835°C and T_{ann} = 500°C. Using a high annealing temperature of T_{ann} = 805°C obviously leads to a deterioration of the interface. Atomic

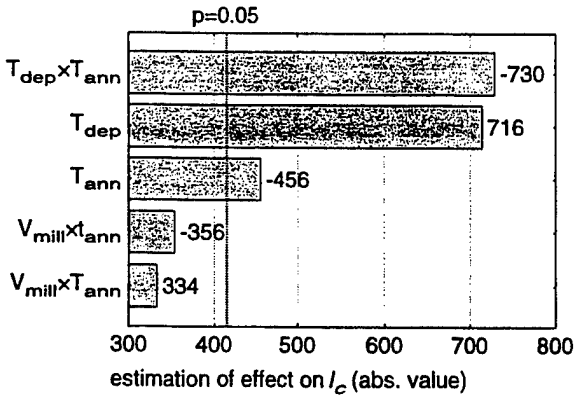

Fig. 2. Effects included in the regression model of the critical current. The dashed vertical line indicates the 5% significance level.

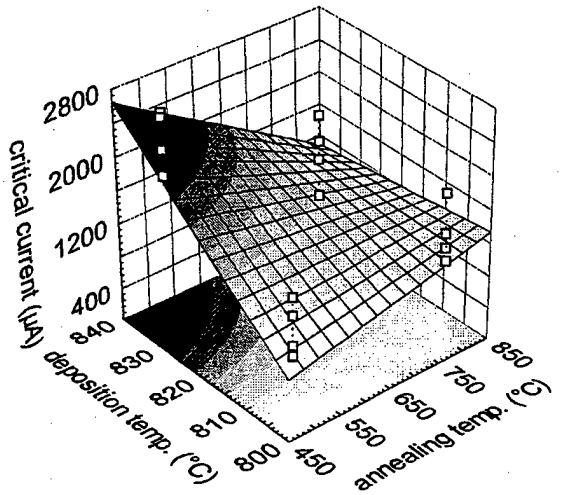

Fig. 3. Response surface of the critical current I_c in the (T_{dep}, T_{ann}) space. The squares indicate the on-chip averages of the measurements.

force microscopy studies show that the ramp region becomes strongly faceted when annealed at this temperature. On the other hand, the best RSJ-like Josephson junctions are produced at T_{dep} = 805°C and T_{ann} = 500°C. The small increase of I_c when annealed at 805°C can be explained by a higher mobility of the atoms in the interface region, possibly leading to a recrystallization of the superconducting orthorombic phase.

A summary of the multiple regression analysis is shown in Table III. Each row of the table contains a symbolic representation of the significance of the effects, which are represented by the columns. The significance level of an effect is represented by the color of the respective box. The quantitative order of an effect for each response is indicated by the number in the box. Only the main effects and the most important interaction effects are shown.

IV. Summary

The measured properties of the 16 samples can be modeled very nicely by regression equations, in which only the main and two-factor interaction effects are taken into account. Several additional samples fabricated under conditions belonging to factor settings in the center or the outside of the factor hypercube defined by Table 1 yield properties predicted by the regression models. Thus, we have shown that the properties of this kind of Josephson junctions can be reproducibly adjusted by the process conditions. The transition from RSJ-like Josephson junctions with I_c < 1 mA towards interconnects with high critical current densities above 10^6 A/cm^2 can be described by low-order regression models. This leads us to the conclusion that barriers with different strengths depending on the process conditions are formed.

Interpretation of the regression models with respect to the formation of a nonsuperconducting barrier is difficult, but the following conclusions can be drawn: R_n and I_c are not determined by the milling parameters, so the Josephson effect in our junctions probably is a surface effect, and no deeper damaging of the ramp takes place. The etching parameters have a significant influence on the modulation depth, the Fraunhofer similarity, and the RSJ-similarity of the *I-V* curves. Etching with higher voltages for a longer time leads to more homogeneous barriers. R_n cannot be well described by the investigated factors. The critical current is determined by the annealing temperature and deposition temperature of the upper electrode, so these parameters determine the recrystallization of damaged material at the interface. The spreads of I_c and R_n are predominantly determined by the annealing temperature. Higher annealing temperatures lead to a deterioration of the ramp, resulting in greater parameter spreads, which is consistent with the weaker Fraunhofer similarity and smaller modulation depths.

The junctions showing the most RSJ-like behavior are produced at V_{mill} = 1100 V, t_{mill} = 5 min, t_{ann} = 30 min, T_{ann} = 500°C, and T_{dep} = 805°C. These junctions exhibit critical currents in the range of 500 µA ± 40%, normal resistances of about 0.4 Ω ± 15%, and I_c modulation depths up to 70%.

TABLE III. Overview of significant effects. See the text for explanations.

	V_{mill}	t_{mill}	t_{ann}	T_{ann}	T_{dep}	$V_{mill} \times T_{dep}$	$t_{mill} \times T_{dep}$	$t_{ann} \times T_{dep}$	$T_{ann} \times T_{dep}$
I_c				3	2	5			1
$\sigma(I_c)$	5			1			4		3
R_n	3	4		6	2			1	
$\sigma(R_n)$				1	5	7	3	4	
Mod	3	5		1		4			2
Form	3	5		2	4	1			3
Fraunh	1	4	5	2				3	

significance level: n < 1% n < 5% n < 15%

References

[1] M. A. J. Verhoeven, R. Moerman, M. E. Bijlsma, A. J. H. M. Rijnders, D. H. A. Blank, G. J. Gerritsma, and H. Rogalla, "Nucleation and growth of PrBCO barrier layers on ion-beam etched ramps in DyBCO studied by AFM", *Appl. Phys. Lett.* 68, vol. 9, pp. 1276-1278 (1996).

[2] P. G. de Gennes, *Rev. Mod. Phys.* 36, 225 (1964).

[3] K.H. Likharev, *Sov. Tech. Phys. Lett.* 2, 12 (1976).

[4] B. H. Moeckly and K. Char, "Properties of interface-engineered high T_c Josephson junctions", *Appl. Phys. Lett.* 71, 2526 (1997).

[5] B. D. Hunt, Martin G. Forrester, J. Talvacchio, and R. M. Young, "High-resistance HTS edge junctions for digital circuits", *IEEE Trans. Appl. Supercond.*, in press.

[6] A. Fujimaki, K. Kawai, N. Hayashi, M. Horibe, M. Maruyama, and H. Hayakawa, "Preparation of ramp-edge Josephson junctions with natural barriers", *IEEE Trans. Appl. Supercond.*, in press.

[7] T. Satoh, M. Hidaka, and S. Tahara, "High-temperature superconducting edge-type Josephson junctions with modified interfaces", *IEEE Trans. Appl. Supercond.*, in press.

[8] R. Dittmann, J.-K. Heinsohn, and A. I. Braginski, "Fabrication of $YBa_2Cu_3O_7$ ramp-type junctions by interface treatments", *IEEE Trans. Appl. Supercond.*, in press.

[9] J.-K. Heinsohn, D. Reimer, A. Richter, K.-O. Subke, and M. Schilling, "Interaction of process parameters in the laser deposition of $YBa_2Cu_3O_7$ films", *Physica C* 299, pp. 99-112 (1998).

[10] G. E. P. Box, W. G. Hunter, and J. S. Hunter, *Statistics for Experimenters*, Wiley, New York, 1978.

Effect of Deposition Conditions and Annealing Process on Crystallinity and Superconducting Properties of High-T_c Multilayers

Yijie Li, T. Utagawa, and K. Tanabe
Superconductivity Research Laboratory, International Superconductivity Technology Center
10-13 Shinonome, 1-Chome, Koto-ku, Tokyo 135-0062, Japan

***Abstract*— On the basis of successful fabrications of multilayers based on $NdBa_2Cu_3O_{7-\delta}$ (NBCO) using Sr_2AlTaO_6 (SAT), Sr_2AlNbO_6 (SAN), and lanthanum doped SAT, $La_xSr_{2-x}AlTaO_6$ (LSAT) as insulators, we have systematically investigated the effect of deposition conditions and annealing process on crystallinity and superconducting properties of multilayers. It was found that the superconducting properties of bottom NBCO layers were dependent on both post annealing process and deposition conditions of multilayers. The insulator layers deposited at the same substrate temperature for growth of NBCO films had very good crystallinity. However, the bilayers showed relatively low T_{c0} (~80-85 K) even after annealing and rough surfaces. Since both the smooth surface and the epitaxial quality are the essential requirement for further epitaxial growth in multilayer technology, it is necessary to balance the crystallinity against surface and superconducting properties by optimizing deposition conditions. High-T_c multilayers with excellent superconductivity have been fabricated at a relatively low substrate temperature and high oxygen partial pressure.**

I. Introduction

In fabrications of high-T_c superconductor circuits, the issue of oxygen diffusion through insulator layers to bottom superconducting layers is a common problem for any practical applications. In developing new substrate materials for epitaxial growth of high-T_c superconducting thin films, a family of cubic perovskite oxides $A_2B'BO_6$ have recently become of interest because of their good lattice match with $YBa_2Cu_3O_{7-\delta}$ (YBCO) and excellent dielectric properties. Two representatives of this family are Sr_2AlTaO_6 (SAT) and Sr_2AlNbO_6 (SAN). SAT has been used as buffer layer for $Tl_2Ba_2CaCu_2O_8$ film deposition or insulator layer for multilayer high-T_c device applications [1]-[3] because of its good lattice match with high-T_c superconductors and relatively low dielectric constant. Although single crystal substrates of SAT and SAN have not been reported, they have been used as insulating layers in high-T_c multilayer technology and buffer layers for epitaxial growth of high-T_c thin films on the substrates with a relative large lattice mismatch. So far, lanthanum doped SAT single crystal substrates (LSAT) have been available. Single crystal LSAT has a cubic perovskite structure with a lattice constant of $a/2$=3.87 Å, quite good matching with that of YBCO and $NdBa_2Cu_3O_{7-\delta}$ (NBCO). It also has a quite small dielectric constant ε~22 and loss $\tan\delta=1.7\times10^{-4}$ (at 8.8 GHz, 77 K) comparing with those of $SrTiO_3$ (STO). Thus it is a superior substrate and insulator material for high-T_c thin film growth and device fabrication in the field of microwave and high frequency applications. A number of issues are critical in the insulator layer selection for applications. Besides the consideration of lattice match, chemical compatibility, the difference of thermal expansion coefficients, and dielectric properties, a favorable insulator should also have a sufficiently high oxygen diffusion rate at about 450 °C, permitting oxygen to diffuse through it and into the underlying high-T_c layer.

In this paper, we report on the fabrication of multilayers based on NBCO using SAT, SAN, and LSAT as insulators by pulsed laser deposition (PLD). To improve superconducting properties of bottom NBCO layers, the effect of deposition conditions and annealing process on crystallinity and superconducting properties of multilayers have been systematically investigated.

II. Experiment

Laser ablation (KrF, 248 nm) was used to deposit thin films of SAT, SAN, LSAT, and NBCO. The PLD growth system and details of deposition conditions were reported elsewhere [4], [5]. In this work, the dense, polycrystalline sintered SAT and SAN targets were prepared by the conventional solid reaction method at 1600 °C for 48 h in flowing oxygen atmosphere. For the deposition of LSAT and NBCO layers, both an LSAT and an NBCO single crystal targets were used. High-T_c bilayers and trilayers were grown *in-situ* on STO substrates. PLD was carried out at a repetition rate of 10 Hz. The laser energy density on NBCO and LSAT single crystal targets was 3 J/cm^2, while on the SAT and SAN sintered targets, it was 2 J/cm^2. NBCO layers were deposited at the substrate temperature of 780 °C and oxygen partial pressure of 300 mTorr. For the depositions of SAT, SAN, and LSAT layers in multilayer structures, the substrate temperature and oxygen partial pressure were changed in the range of 500-780 °C and 50-500 mTorr, respectively. The target-substrate distance for NBCO layer deposition was 7 cm. The distance for the growth of SAT, SAN, and LSAT insulator layers was 4-5 cm. After the deposition, the chamber was filled with oxygen to 700 Torr. The NBCO single layers were naturally cooled down to room temperature by switching off the heater power. However, after the depositions of the bilayers and trilayers, the samples were slowly cooled down to an annealing temperature in 10 min and then annealed at this temperature for 1-5 hours to fully oxygenate the bottom NBCO layer. The annealing

Manuscript received April 25, 1999.
This work was supported by the New Energy and Industrial Technology Development Organization (NEDO) for the R & D of Industrial Science and Technology Frontier Program.

Temperature was changed in the range of 400-550 °C to optimize the superconducting properties of bottom NBCO layers. The thickness of the NBCO and insulator layers was 200 nm. The structure and the orientation of each layer were analyzed by x-ray diffraction (XRD). The microstructure and interfaces of multilayers were observed with transmission electron microscopy (TEM). The surface morphology was observed by scanning electron microscope (SEM) and atomic force microscope (AFM). The superconducting properties were measured by a four probe method and a dc superconducting quantum interference device (SQUID) magnetometer (Quantum Design MPMS).

III. Results and Discussion

Fig. 1 shows a typical XRD 2θ–θ scan pattern for an NBCO film deposited on STO substrate. The exclusive (00*l*) peaks in the pattern indicate *c*-axis orientation of the film. The *c*-axis lattice parameter of the NBCO films is 11.71 Å, and no splitting is observed between the (003), (006), and (009) peaks from NBCO films and the peaks from the substrates. Typical critical temperature and critical current density are ~90 K and ~4×10^6 A/cm^2 at 77 K, as shown in Fig. 2.

The crystallinity and the lattice parameters of SAT, SAN, and LSAT films are sensitive to substrate temperature and oxygen pressure. The ω-scan rocking curve measurements show that the films have small FWHM values of <0.1° in the substrate temperature range of 650-800 °C. As the temperature increases, the rocking curve also becomes narrower. At the substrate temperature of ~800 °C, the value of FWHM is only around 0.05°. The *c*-axis constants of insulator films were found to be smaller than those of targets and dependent on the oxygen pressure. XRD patterns gave the lattice constant of a=7.774 Å for both SAT and SAN targets. The value of $a/2$ is slightly smaller than that of STO substrates (3.905 Å). The lattice parameter of LSAT single crystal target is 7.737 Å. However, the *c*-axis lattice constants of all SAT, SAN, and LSAT films were found to

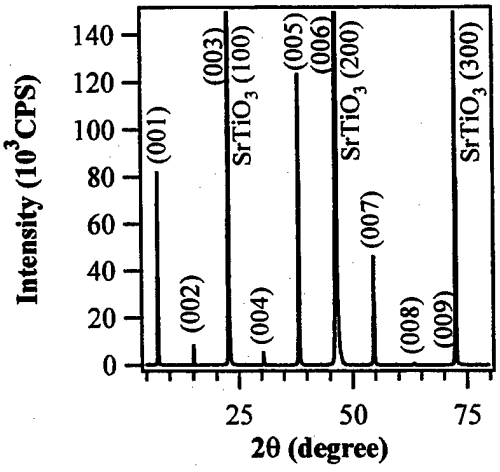

Fig. 1. The XRD pattern measured from an NBCO film deposited on STO substrate at 780 °C and 300 mTorr.

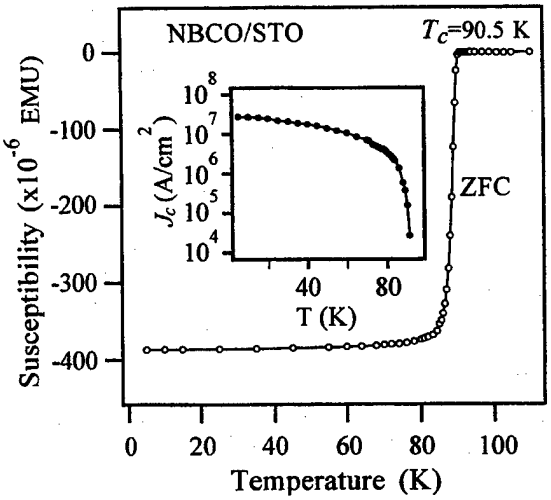

Fig. 2. Temperature dependence of magnetic susceptibility of an NBCO film deposited at 780 °C and 300 mTorr. The inset is the dependence of critical current density on temperature for a sample deposited under the same condition.

be lengthened, especially at low oxygen pressures. This may be caused by the cation compositional deviation in the deposited films. SEM and AFM observations demonstrated very smooth surface morphology of the insulator films. The calculated deposition rates derived from the satellite peaks in the XRD patterns using the Laue function were confirmed by the cross-section TEM observation. The temperature-dependent dielectric properties of 2000 Å thick SAT films were measured in the frequency range of 500 Hz to 1 MHz using the patterned structures on YBCO (001) single crystal substrates. At frequency of 0.1 MHz and 82 K, the dielectric constant ε_r and the loss value tanδ are 23.5 and <1×10^{-3}, respectively.

In order to investigate the effect of deposition conditions of insulator layers on crystallinity, compatibility and superconducting properties of bilayers, 200 nm thick insulator films were deposited in situ on NBCO films. It was found that the superconducting properties of bottom NBCO layers were dependent on both post annealing process and deposition conditions of multilayers. The insulator layers deposited on NBCO films at 750-800 °C had very good crystallinity proved by TEM observations. However, the bilayers showed relatively rough surfaces. Since both the smooth surface and the epitaxial quality are the essential requirements for further epitaxial growth in multilayer technology, it is necessary to balance the crystallinity against surface and superconducting properties by optimizing deposition conditions. Smooth insulator layers on NBCO films were deposited in an intermediate substrate temperature range of 650-700 °C.

The lattice parameters of SAT, SAN, and LSAT deposited on NBCO films are sensitive to oxygen pressure and the thickness of insulator layers due to the strain formed in epitaxial growth. Fig. 3 shows a series of XRD patterns of LSAT/NBCO bilayers grown on STO substrates. In these bilayers, NBCO films were deposited at the same conditions, but the LSAT layers were deposited at different oxygen

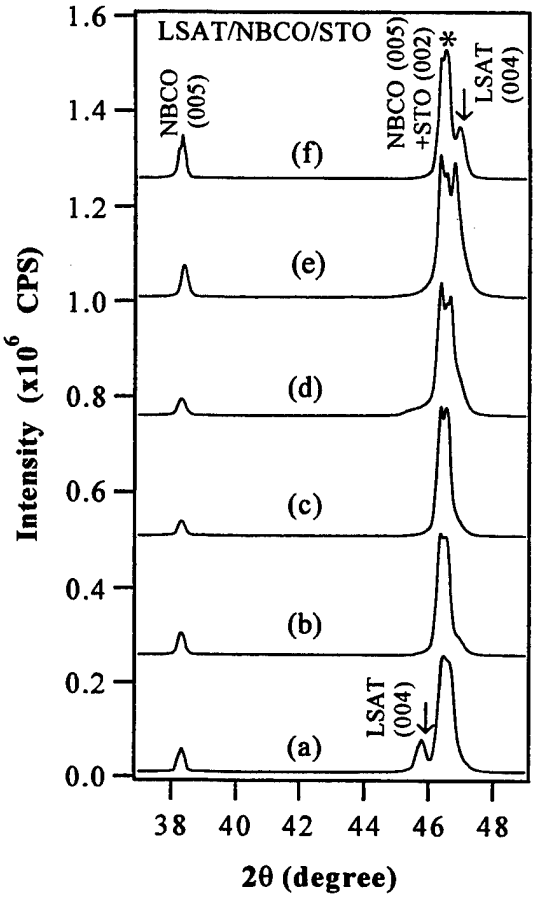

Fig. 3. XRD patterns for LSAT/NBCO bilayers deposited on STO substrates. The NBCO layers were deposited at 780 °C and 300 mTorr. The LSAT layers were grown at 700 °C and different oxygen pressures. (a) 50 mTorr, (b) 200 m Torr, (c) 300 mTorr, (d) 350 mTorr, (e) 400 mTorr, and (f) 500 mTorr.

pressures. The LSAT layers have only (00*l*) peaks at 700 °C in the oxygen pressure range of 100-500 mTorr. As oxygen pressure increases, the LSAT (004) peaks indicated by the arrows, gradually moves to large angle direction. The small splitting of the LSAT (004) from the NBCO (006) and STO (002) peaks denoted by the asterisk, which is seen in Fig. 3, is thought to arise from the cation compositional deviation. At 200-300 mTorr, the LSAT (004) and the NBCO (006) peaks overlap with the least lattice mismatches. Therefore, 300 mTorr oxygen pressure was selected to fabricate the trilayer structures.

Post annealing experiments for bilayers were carried out at different temperature and for different hours to optimize the superconducting properties of the bottom NBCO layers. There are much similarities in the crystal structures and dielectric properties of SAT, SAN, and LSAT. Because of the high stability and crystallinity of these insulator layers, oxygen diffusion through them into the bottom NBCO layers become difficult comparing with the other insulators. Thus post-annealing is necessary to improve the superconducting properties of bottom NBCO layers. In bilayers with the insulator layers deposited at high oxygen pressure (400-500 mTorr), it is easy to improve transition temperature, but deteriorated surface morphology was observed. Fig. 4 shows

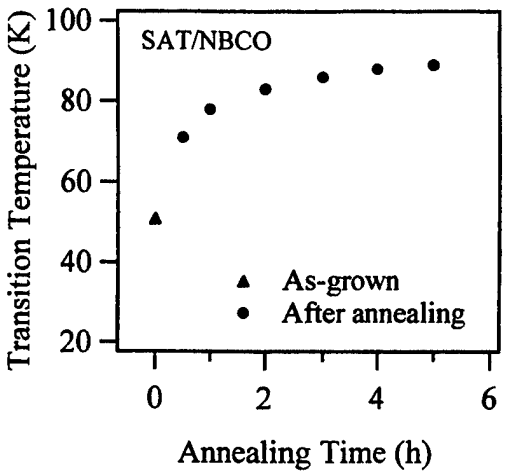

Fig. 4. Transition Temperature of SAT/NBCO bilayers as a function of annealing time in 700 Torr Oxygen at 450 °C.

the change in the superconducting transition temperature for SAT/NBCO/STO bilayers after annealing at 450 °C for different hours. The naturally cooled bilayer sample shows a quite low T_c of only ~50 K due to oxygen deficiency in the bottom NBCO layer. As shown in Fig. 4, the effect of post-annealing is appreciable. With an increase in the annealing time, the T_c also increases. The T_c for the sample annealed for 5 h is 87-90 K.

IV. Conclusion

High-T_c bilayers and trilayers based on NBCO films using SAT, SAN and LSAT as insulators have been grown *in situ* by PLD on STO substrates. The high stability and compatibility with sharp interfaces of these multilayers were demonstrated by TEM observations. Although as-grown bilayers show a lower T_c value of ~50 K, after annealing in O_2 at 450 °C, the top and bottom NBCO layers show a T_c of 87-90 K and J_c>1×10^6 A/cm^2 at 77 K.

Acknowledgment

The authors would like to thank X. Yao and S. Koyama for their assistance in preparing the NBCO single crystal target, and T. Sugano and J. G. Wen for their help in experiments. We also wish to acknowledge useful discussions with Y. Shiohara and T. Morishita.

References

[1] A. T. Findikoglu, C. Doughty, S. Bhattacharya, Q. Li, X. X. Xi, T. Venkatesan, R. E. Fahey, A. J. Strauss, and J. M. Phillips, *Appl. Phys. Lett.*, vol. 61, pp. 1718-1720, October 1992.

[2] Q. Y. Ying and C. Hilbert, *Appl. Phys. Lett.*, vol. 65, pp. 3005-3007, December 1994.

[3] Y. Q. Tang, K. Y. Chen, S. Afonso, X. L. Xu, Q. Xiong, G. Salamo, F. T. Chan, R. Guo, and A. Bhalla, *J. Appl. Phys.*, vol. 78, pp. 6846-6848, December 1995.

[4] Yijie Li and K. Tanabe, *J. Appl. Phys.*, vol. 83, pp. 7744-7752, June 1995.

[5] Yijie Li, Xin Yao, and K. Tanabe, *Physica C*, vol. 304, pp. 239-244, August 1998.

Source Optimization for Magnetron Sputter-Deposition of NbTiN Tuning Elements for SIS THz Detectors

N. N. Iosad, B. D. Jackson and F. Ferro
University of Groningen, Department of Applied Physics and Material Science Centre,
Nijenborgh 4.13, 9747 AG Groningen, The Netherlands

J .R. Gao
Space Research Organization of the Netherlands, PO Box 800, 9700 AV Groningen, The Netherlands

S. N. Polyakov
Institute of Nuclear Physics, Moscow State University, 119899, GSP, Moscow, Russia

P. N. Dmitriev
Institute of Radioelectronics Russian Academy of Sciences, Mokhovaya 11, 103907, GSP-3, Moscow, Russia

T. M. Klapwijk
Delft University of Technology, Department of Applied Physics (DIMES), Lorentzweg 1, 2628 CJ Delft, The Netherlands

Abstract— NbTiN is one of the most promising materials for use in the tuning circuits of Nb-based SIS mixers for operating frequencies above the gap frequency of Nb (≈ 700 GHz). Device development requires stable and reproducible film properties. In this manuscript we compare the properties of NbTiN films obtained with a sputtering source using balanced and unbalanced magnetic trap configurations. This experiment shows that reducing the effectiveness of the magnetic trap by changing the magnet configuration is equivalent to reducing the sputtering pressure. We also show that it is possible to optimize the configuration of the magnetron magnets to produce stable and reproducible NbTiN films under the same gas pressure and applied power throughout the target lifetime.

I. Introduction

Reactive magnetron sputtering is one of the most widely used methods for the deposition of nitrides. The spectrum of applications for nitrides obtained by this technique is very wide, including: NbN-based SIS tunnel junctions [1], [2], NbCN and NbTiN thin films for microwave applications [3]-[5], and TiN in low-barrier Schottky diodes and as a gate electrode in MOS transistors [6]. In general, the properties of these materials (NbN, TiN, NbTiN) show similar dependencies on the sputtering conditions. In particular, elevating the substrate temperature, sputtering at lower pressures, and applying a substrate bias each result in a reduction of the resistivity, a change in the texture from (111) to (100), and an increase in T_c [7]–[10]. This makes controlling the plasma heating of the substrate very important for these materials, because device development requires stable and reproducible film parameters.

For example, our recent research investigating the influence of target erosion on NbN film deposition showed considerable changes in the film properties though the target lifetime [10]. In this work, we compared the properties of films sputtered using two different targets (new and eroded) mounted in a sputtering source with a balanced and very effective magnetic trap (Fig. 1). It was found that as the target became grooved, the nitrogen injection had to be reduced by 30% in order to avoid T_c degradation. This was due to a reduction in the sputtering rate caused by a reduction in the effective power density in the erosion track of the grooved target. Furthermore, because sputtered particles have an initial velocity perpendicular to the cathode surface, the thermalization of the sputtering yield is more significant for the grooved target. This leads to a reduction in fast neutral bombardment and a corresponding reduction of the compressive stress in Nb films sputtered under the same Ar pressure and applied power through the target lifetime [10], [11]. Moreover, the reduction of the heat flux towards the substrate surface results in a 30% increase in the resistivity of the NbN films and a change in the basic crystal orientation. Films obtained from the fresh target have a ratio of (111) and (200) reflections equal to 0.4, while the films obtained from the eroded target have an intensity ratio of 0.2. This change in texture leads to a considerable change in the reactive ion etching rate of these films in a mixture of CF_4 and O_2, which further affects process repeatability. Similar changes in NbTi film properties as the target becomes grooved have been observed by C. D. Hawes et. al. [12].

The ultimate goal of this work is to develop SIS mixers for THz radiation detection by integrating NbTiN striplines with Nb/Al-AlO_x/Nb tunnel junctions. For this application we need reproducible NbTiN films with the lowest possible resistivity, the highest possible transition temperature (T_c), and intrinsic stress not exceeding 1 GPa in magnitude. In this paper, we examine the effect of the sputtering conditions on the properties of NbTiN films deposited using balanced and unbalanced magnetron sputtering sources. Additionally, as an extension of our previous work with NbN [10], we examine the effects of target erosion on NbTiN films deposited using the unbalanced source. From these results, we show that it is possible to optimize the sputtering conditions to produce stable and reproducible films under the

E-Mail: N.Iosad@phys.rug.nl
Manuscript received April 30, 1999
This work is supported in part by the Stichting voor Technische Wetenschappen, Nederlandse Organisatie voor Wetenschappelijk Onderzoek, European Space Agency (ESA) under contract No. 1653/95/NL/PB, the Russian SSP "Superconductivity", the INTAS project No. 97-1712.

same gas pressure and applied power throughout the target lifetime.

It has been shown previously [10] that, for the case of NbTiN deposition with an unbalanced source, grounding the substrate results in films with increased resistivities. This indicates that electron heating of the substrate has significantly less effect on the properties of the growing film than ion bombardment. For this reason, it is assumed in the sections that follow that the primary sources of energy for the film growth process are ion and fast neutral bombardment of the substrate and the energy of the sputtered particles themselves.

II. Experimental Procedure

Films of NbTiN are deposited by reactive magnetron sputtering in a Nordiko-2000 sputtering system with a base pressure of $4 \cdot 10^{-5}$ Pa. This sputtering machine is equipped with a cryopump and a throttling valve, which together determine the process pressure, while the injection of Ar and N_2 gases is controlled by flow-meters. In order to avoid the hysteretic sputtering regime, the pumping rate is fixed at a high value of 750 l/s for all experiments [13]. An alloy target with 30 at.% Ti and 70 at. % Nb is used. In order to maximize film uniformity, the substrate-target distance is set to the maximum for our sputtering system, 8 cm. Films are deposited on both glass and silicon substrates — the intrinsic stress in the deposited films is monitored by measuring the bending of thin glass wafers (160 μm) after deposition [9], while the films deposited on silicon wafers are used for resistivity and T_c measurements, and X-ray diffraction (XRD) analysis. The substrates are fixed to the copper chuck with diffusion pump oil to stabilize the thermodynamics of growth. Films sputtered without proper heat sinking are found to have a larger transition temperature width than those sputtered with heat sinking. All films are sputtered with 300 W DC power, resulting in a deposition rate of 80 ± 10 nm/min and a film thickness of 250 ± 25 nm. The residual resistance ratio is ≈ 1 for films with resistivities of 100 μΩ·cm, and gradually drops with increasing film resistivity to 0.9 for a resistivity of 300 μΩ·cm.

A homemade unbalanced magnetron sputtering source is used for the deposition of NbTiN (Fig. 2). The outer ring of a Leybold PK-75 magnet set is doubled to obtain an unbalanced magnetic trap and a magnetic lens is used to partially loop the magnetic field lines. This results in a flatter erosion zone and a corresponding improved stability in the sputtering rate relative to that observed previously for the sputtering source used for NbN deposition [10]. This reduces the correction to the nitrogen injection needed through the target lifetime (less than 10 %). A balanced version of this sputtering source is obtained by replacing the magnetic lens with an additional central magnet from the PK-75 magnet set.

III. Properties of NbTiN Films for Different Source Conditions

A. Comparison of balanced and unbalanced configurations

In order to evaluate the effectiveness of the balanced and unbalanced magnetic traps, we have compared the properties of the glow discharge for the two configurations at 6 mTorr Ar pressure. The self-bias of the floating substrate table is –19 V for the unbalanced configuration and –5 V for the balanced case. Furthermore, the ionic current measured with a –30 V biased substrate table is 60 mA for the unbalanced configuration and 7 mA for the balanced case. Finally, the grounding current is equal to the discharge current (≈ –1 A) for the unbalanced configuration, while it is equal to -10 mA for the balanced configuration. These results show that, as expected, the magnetic trap in the balanced configuration is much more effective than in the unbalanced configuration.

The properties of the NbTiN films obtained using the balanced and unbalanced magnetron configurations are shown in Fig. 3. All films are sputtered on a "floating" substrate table and the nitrogen flow rate is optimized to achieve the highest T_c for each total pressure. For both sources, reducing the total sputtering pressure leads to an increase in T_c and a decrease in resistivity.

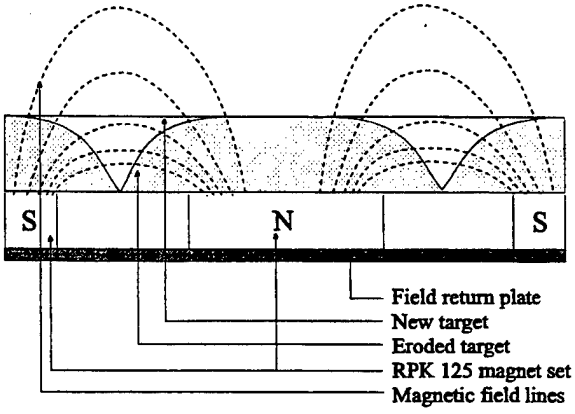

Fig 1. Cross-sectional view of the RPK-125 magnetron and magnetic field in the cases of the new and eroded targets. The eroded target profile is indicated by shading (modified from [10]).

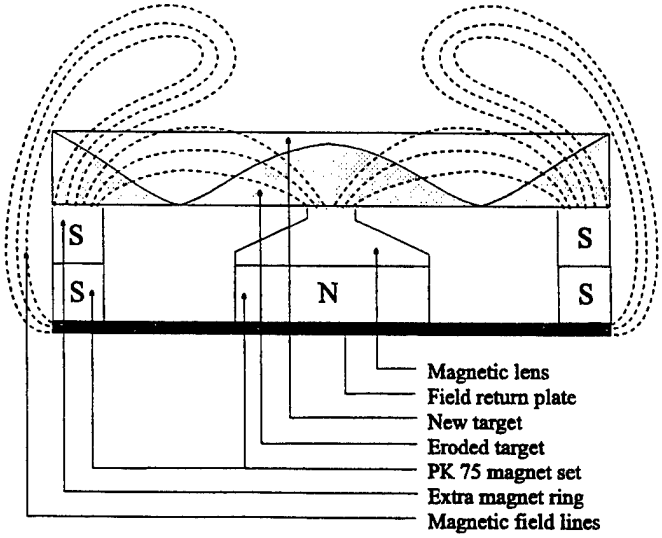

Fig 2. Cross-sectional view of the homemade unbalanced magnetron and magnetic field in the cases of the new and eroded targets. The eroded target profile is indicated by shading (modified from [9]).

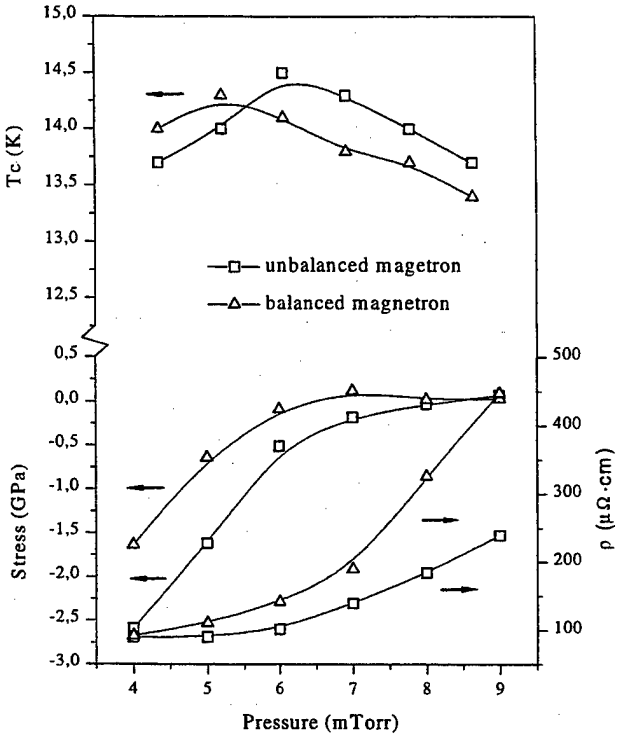

Fig. 3. Properties of the NbTiN films obtained from the balanced and unbalanced sputtering sources.

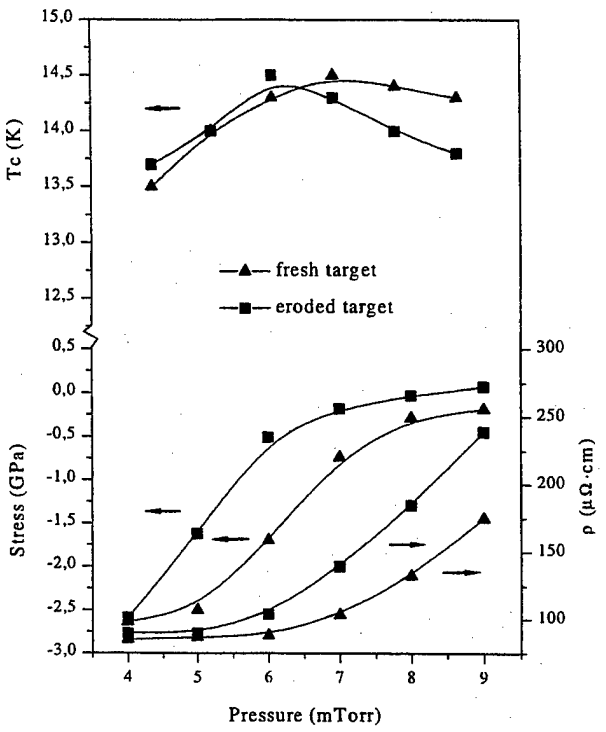

Fig. 4. Properties of the NbTiN films obtained from the fresh and eroded targets using the unbalanced sputtering source.

This is attributed to a reduced thermalization of the sputtering yield and increased film bombardment by fast neutrals. At the lowest pressures (4-5 mTorr), this bombardment becomes strong enough to damage the growing film, resulting in a saturation of the resistivity at ≈ 90 μΩ·cm and a degradation of T_c [6]. As is seen in Fig. 3, the properties of the NbTiN films obtained with the unbalanced configuration are similar to those of films obtained with the balanced configuration at lower total pressures. This indicates that the effect of the ion bombardment generated by the unbalanced source is similar to the effect of the increased fast neutral bombardment obtained by reducing the sputtering pressure.

B. Influence of target erosion on NbTiN film properties.

We have also examined the behavior of the unbalanced sputtering source versus target lifetime. The depth of the erosion track in the eroded target was ≈ 90 % of the target thickness. An examination of the properties of the glow discharge at 6 mTorr Ar pressure shows that the self–biasing of the substrate table is -19 V for the fresh target and –22 V for the grooved one. Additionally, the ionic current measured with a –30 V biased substrate table is 60 mA for the new target and 82 mA for the grooved one. These observations can be attributed to a decrease in the effectiveness of the magnetic trap through the target lifetime, due to the magnetic field produced by the outer ring becoming stronger as the target becomes grooved, making the magnetic trap more unbalanced. This explanation is supported by the fact that there is no considerable difference in the discharge voltage with and without the magnetic lens for the case of the eroded target. In contrast, using the magnetic lens in the case of the new target gives a 50 V reduction in the discharge voltage for a constant applied power.

The properties of the NbTiN films obtained from the fresh and eroded targets are illustrated in Fig. 4. From this figure, it is seen that there is a significant increase in the conductivity and intrinsic stress of NbTiN films deposited from the grooved target, relative to those deposited from a fresh target. Furthermore, at the lowest pressures (4-5 mTorr) the substrate bombardment actually becomes strong enough to cause a plastic flow of films sputtered from the grooved target (seen from the flattening of the stress curve in Fig. 4 [14]). These results are in direct contrast to the decrease in conductivity and intrinsic stress observed previously for NbN deposition using a balanced sputtering source [10]. This can be explained by a significant increase in the ion bombardment of the substrate due to the previously discussed reduction in the effectiveness of unbalanced magnetic trap. This effect is insufficiently compensated by the increased thermalization of the sputtering yield and reduced fast neutral bombardment expected to result from the target becoming grooved [10].

In order to suppress the contribution of ionic bombardment, we have repeated this experiment with a grounded substrate table. As is seen from a comparison of Fig. 4 and Fig. 5, this results in less-stressed films at low pressures. Furthermore, it is seen that it is possible to select an operating point at 5 mTorr, for which the film properties are roughly independent of the target erosion state. At this point, the films have a stress ≈ -1 GPa, T_C ≈ 14.3 K, and resistivity ≈ 100 μΩ·cm.

We have also analyzed our films using X-Ray diffraction analysis (XRD). The results of the θ-2θ pattern treatment are

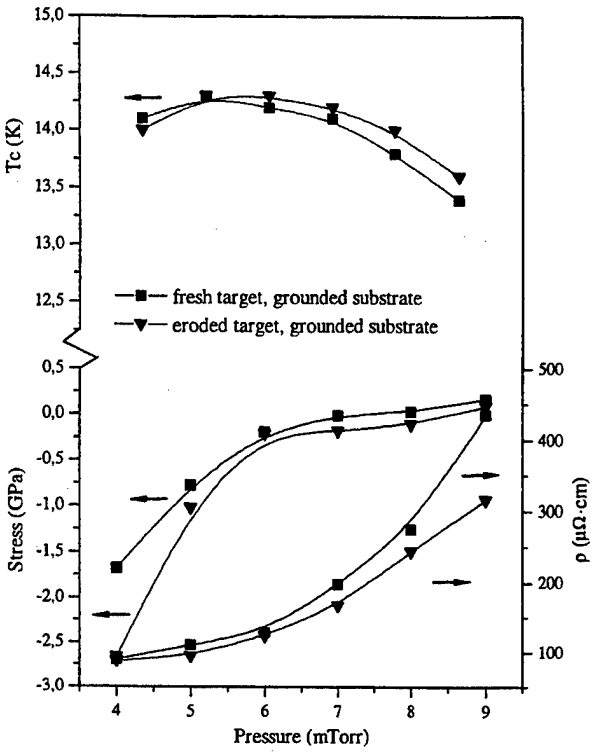

Fig. 5. Properties of the NbTiN films obtained from the fresh and eroded targets, using the unbalanced sputtering source and a grounded substrate.

illustrated in Table I. A reduction in pressure is seen to cause a change in texture from (111) to (100). In general, films sputtered from the fresh and eroded targets do not show considerable differences in the relative peak intensities, giving additional confirmation of the stability of the sputtering conditions with respect to target state.

IV. Conclusions

The sputtering pressure and the configuration of the sputtering source magnetic trap together determine the heat flux towards the substrate surface. This heat flux is not stable throughout the target lifetime. In particular, previous work [10] has shown that, for a balanced source, the effectiveness of the magnetic trap increases as the target becomes grooved. This results in a degradation of the film properties. In contrast, the unbalanced configuration shows the opposite behavior. In this case, the effectiveness of the magnetic trap decreases through the target lifetime, resulting in an improvement in film properties. Furthermore, using an unbalanced source together with a grounded substrate table, it is possible to choose deposition conditions which yield stable and reproducible NbTiN film properties throughout the target lifetime. In this case, the optimum films are obtained at sputtering pressure of 5 mTorr and have a stress ≈ −1 GPa, resistivity ≈ 100 μΩ·cm and T_C ≈ 14.3 K.

TABLE I. Results of the analysis of XRD patterns of NbTiN films sputtered from the fresh and eroded targets with a grounded substrate. The intrinsic stress, resistivity and T_c of these films are illustrated on the Fig. 5.

Target State	Total pressure, mTorr	Relative (111) peak intensity	Relative (200) peak intensity
Fresh	4	77	100
Eroded	4	70	100
Fresh	5	100	81
Eroded	5	100	83
Fresh	6	100	39
Eroded	6	100	35
Fresh	7	100	23
Eroded	7	100	18
Fresh	8	100	13
Eroded	8	100	12
Fresh	9	100	12
Eroded	9	100	12

Acknowledgment

We thank B. Wolfs, S. Bakker, E. K. Kov'ev, and V. P. Koshelets for helpful discussions and assistance in experimental work.

References

[1] N. N. Iosad, D. V. Balashov, M. Yu. Kupriyanov, S. N. Polyakov and V. V. Roddatis, "Characterization of NbN/AlN/NbN tunnel junctions fabricated without intentional heating," *IEEE Trans. Appl. Supercond.*, vol. 7, pp. 2805-2808, June 1997.

[2] Z. Wang, A. Kawakami, Y. Uzawa and B. Komiyama, "High critical current density NbN/AlN/NbN tunnel junctions fabricated on ambient temperature MgO substrates," *Appl. Phys. Lett.*, vol. 64, April 1994.

[3] S. Kohjiro, S. Kiryu and A. Shoji, "Surface resistance of epitaxial and polycrystalline NbCN films in submillimeter wave region," *IEEE Trans. Appl. Supercond.*, vol. 3, pp. 1765-1767, March 1997.

[4] B. D. Jackson, N. N. Iosad, B. Leone, J. R. Gao, T. M. Klapwijk, W. M. Laauwen, G. de Lange, H. van de Stadt, "DC and THz response in Nb SIS mixers with NbTiN striplines," *Proc. 10th Internat. Symp. on Space Terahertz Technology*, Charlottesville VA, March 1999, in press.

[5] J. A. Stern, B. Blumble, H. LeDuc, W. J. Kooi, J. Zmuidzinas, "Fabrication and dc-characterization of NbTiN based SIS mixers for use between 600 and 1200 GHz," *Proc. 9th Internat. Symp. on Space Terahertz Technology, CIT, PC*, p. 305, March 1997.

[6] M. Wittmer, "Properties and microelectronic applications of thin films of refractory metal nitrides," *J. Vac. Sci. Technol.*, vol. A3, pp. 1797-1803, July/August 1989.

[7] B. Window and G. L. Harding, "Ion-assisting magnetron sources: Principles and uses," *J. Vac. Sci. Technol.*, vol. A8, pp. 1277 1282, May/June 1990.

[8] N. Savvides and B. Window, "Electrical transport, optical properties, and structure of TiN films synthesized by low-energy ion assisted deposition", *J. Appl. Phys.*, vol. 64, pp. 225-234, July 1988.

[9] N. N. Iosad, B. D. Jackson, T. M. Klapwijk, S. N. Polyakov, P. N. Dmitriev and J. R. Gao, "Optimization of RF- and DC-Sputtered NbTiN Films for Integration with Nb-Based SIS Junctions," *IEEE Trans. Appl. Supercond.*, in press.

[10] N. N. Iosad, T. M. Klapwijk, S. N. Polyakov, V. V. Roddatis, E. K. Kov'ev, P. N. Dmitriev, "Properties of DC Magnetron Sputtered Nb and NbN films for Different Source Conditions," *IEEE Trans. Appl. Supercond.*, in press.

[11] R. S Amos, P. E. Breyer, H. H. Huang, A. W. Lichtenberger, "Stress and Source Conditions of dc Magnetron Sputtered Nb Films", *IEEE Trans. Appl. Supercond.*, vol. 5, p. 2326-2329, June 1995.

[12] C. D. Hawes, L. D. Cooley and D. C. Larbalestier, "Dependence of critical temperature and resistivity of Nb47wt%Ti on magnetron Sputtering Conditions," *IEEE Trans. Appl. Supercond.*, in press.

[13] K. L. Westra, M. J. Brett and J. F. Vaneldik, "Properties of reactively sputtered NbN films," *J. Vac. Sci. Technol.*, vol. A8, pp. 1288-1292, May/June 1990.

[14] B. Window, "Plastic flow and preferred orientation in molibdenium and zurconium films," *J. Vac. Sci. Technol.*, vol. A7, pp. 3036-3041, September/October 1989.

Nb-based single-electron devices fabricated with a planarized process

W. Chen, Daniel J. Flees, Jonathan R. Friedman, Vijay Patel, J. Mannik, J.E. Lukens
Department of Physics and Astronomy, State University of New York at Stony Brook, Stony Brook, NY 11794-3800

Abstract— Single-electron devices consisting of all-Nb electrodes have been fabricated from Nb/AlOx/Nb tri-layers. High-quality deep-sub-micron junctions are made using electron-beam lithography and a planarized process employing chemical-mechanical polishing. Single-electron charging effects, such as the modulation of the supercurrent with gate voltage and Coulomb blockade effects, have been observed.

I Introduction

Single-charge tunneling phenomena in small-capacitance Josephson junctions have been extensively investigated both experimentally and theoretically [1,2]. Nearly all experiments in this field have been done with Al/AlO_x/Al junctions, which can be easily fabricated by a shadow-evaporation technique [2]. However, it is advantageous to use niobium because compared to aluminum it has better stability under thermal cycling, a higher critical temperature and, concommitantly, a larger superconducting energy gap. This last fact is particularly attractive because unpaired electrons, which represent a significant obstacle to studying coherence in aluminum-based devices, should be strongly suppressed in niobium circuits at low temperatures.

There have been several reports on the fabrication of superconducting single-electron devices using Niobium. Among them, a modified shadow evaporation technique has been used to fabricate devices consisting of Nb as well as Al electrodes with Nb/AlO_x/Al junctions [3]. However, the energy gap of the Nb electrodes measured in these devices is much smaller than the bulk value due to limitations of the process. It has not been possible to make all-Nb devices with this method. All-Nb devices have been fabricated using other methods such as anodic oxidation and a self-aligned in-line technique [4] [5]. But the quality of the junctions is not as good as that of Al-based devices.

Niobium tri-layer technology has been shown to be a reliable method for making high-quality Nb junctions [6]. It has been used in the fabrication of analog and digital superconducting circuits [7] [8]. By employing electron-beam lithography and an erodible mask, high-quality Josephson junctions as small as 0.003 μm^2 have been fabricated from Nb tri-layers [9]. Single-electron effects have been observed in junctions made using Nb-tri-layer technology and a planarized process with chemical-mechanical polishing [10] or based on spin-on glass [11]. However, no supercurrent was observed in small devices where single-electron charging effects occur. In this paper, we report the fabrication of single-electron devices with deep-sub-micron junctions using electron-beam lithography and a planarized process employing chemical-mechanical polishing. Current-voltage characteristics with low leakage current and sharp gap features, typical of high quality Nb junctions with low critical-current density, have been obtained. The modulation of the supercurrent with gate voltage has been measured in these devices. Clear Coulomb-blockade gaps and modulation of the normal-state voltage with gate voltage have also been observed.

Manuscript received April 30, 1999.
This work is supported by AFOSR.

II Fabrication

Planarized all-refractory technology for low-Tc superconductivity (PARTS) has been successfully applied to the fabrication of analog and digital superconductor circuits [7] [8]. In this process chemical-mechanical polishing (CMP) is used to planarize the junctions defined in Nb/AlO_x/Nb tri-layers, ensuring good contact to the counter electrodes of the junctions. An extension of this PARTS process has been developed at Stony Brook for the fabrication of deep-sub-micron circuits [9]. The process was developed to include one step of electron-beam lithography (EBL) for the junction level and Josephson junctions as small as 0.003 μm^2 have been demonstrated [9]. In order to study the single-electron effects, the total capacitance of the junctions has to be very small so that the charging energy is larger than the thermal fluctuation at low temperatures. Therefore, it is necessary to reduce the dimensions, not only of the junctions, but of all levels. Recent improvements in fabrication technology allow us to pattern all levels using EBL.

The fabrication starts with the deposition of a Nb/AlO_x/Nb tri-layer on a 50 mm diameter oxidized Si wafer using DC magnetron sputtering. The Nb counter electrode (CE) and base electrode (BE) are 150 nm thick with ~ 8 nm of Al interlayer. The critical-current density of the junctions, J_c, is controlled by the oxygen exposure (pressure×time) during Al oxidation. All layers are patterned by EBL using (PMMA/P(MMA/MAA)) double layers as electron-beam resists. RF-sputtered quartz (SiO_2) films are lifted off and are used as etch masks for the CE and BE layers. The devices studied in this work have layouts typical of single-electron transistors, consisting of two Josephson junctions in series and a separate gate electrode, as shown in Fig. 1. The CE is defined first by reactive ion etching (RIE) in a SF_6 plasma with a lifted-off quartz mask. (The CE level can also be defined by a slightly different process where a negative resist is used to pattern large optical leads [10].) The Al layer acts as a natural etch-stop; however, precise end-point detection, which is essential for deep sub-micron junctions, is achieved

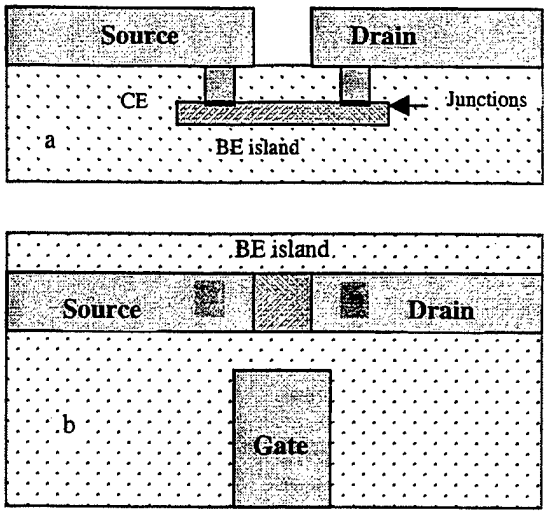

Fig. 1 Schematic of a Nb based single-electron transistor. a. cross-section view. b. top view.

by monitoring the intensity of certain fluorine lines. The Al layer is removed by a wet chemical etch performed in 15% phosphoric acid for 90 sec at 50°C before RIE of the Nb BE. Fig. 2 shows a SEM micrograph of a device after the CE etch. One can see that junctions smaller than 0.14 μm are clearly defined. Again, a lifted-off quartz mask is used as an etching mask for the BE definition. The two junctions of each device share the same BE of size 0.4 μm×1 μm, which forms the island of the single-electron transistor. After the BE definition, a 550-nm-thick layer of sputtered quartz is deposited as the dielectric, which is then planarized using chemical-mechanical polishing. The wiring-layer lift-off mask is defined by EBL using a double layer resist. Finally a 200-nm-thick Nb wiring layer is deposited and lifted off.

III Measurement Results

Many diagnostic devices were fabricated on the same wafer to characterize the process. Some of the chips consisted of many junctions of different sizes. From these diagnostic devices we could check the junction quality and extract the J_c of the tri-layer. At 4.2 K the I-V curves of the devices show characteristics typical of high-quality Nb junctions. The measured gap voltage is about 2.7 mV, close to the value of much larger Nb junctions. Also the leakage current is very low. The scaling from the large junctions was used to estimate the sizes of the deep-sub-micron junctions.

The single-electron devices were measured at 30 mK in a dilution refrigerator. The modulation of the normal-state voltage, when the superconductivity is suppressed by a magnetic field, is shown in Fig. 3a. The modulation is typical of a single-electron transistor with a modulation depth of about 17 μV. This modulation depth is much smaller than that expected based on the estimated junction size from the resistance scaling. As the specific capacitance of the junction is known (~43 fF/μm^2), the capacitance of the device is estimated from resistance scaling to be about 2.6 fF. But the capacitance obtained from the modulation depth is about 9.6 fF.

Extra overlap of different layers is required to ensure adequate interlevel alignment. The additional parasitic capacitance due to the overlap contributes to the total capacitance of the device. Assuming a parallel-plate-capacitor model, the capacitance due to the overlap is about

Fig. 2 SEM micrograph of a single-electron transistor after the counter electrode is defined by electron beam lithography and reactive ion etching.

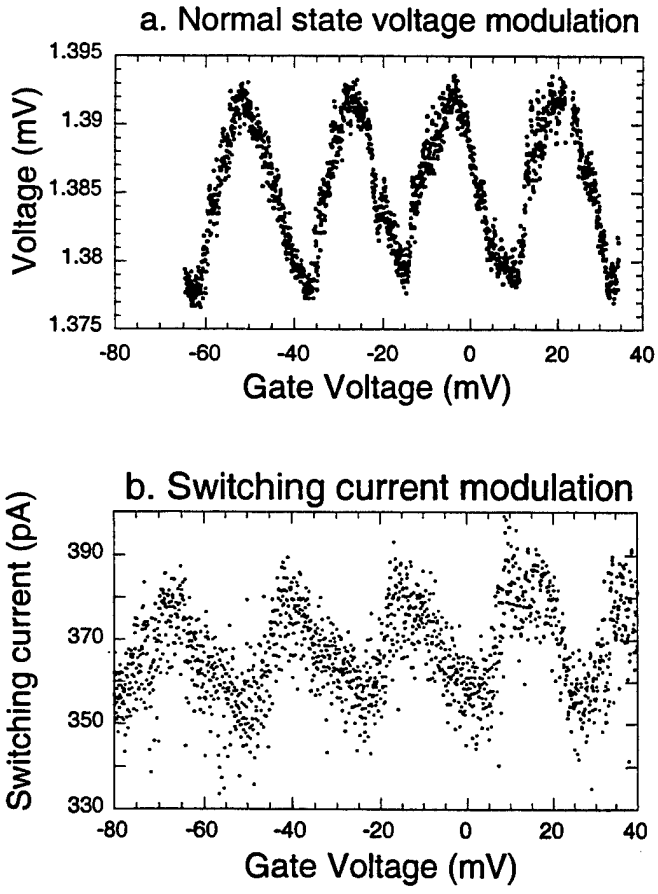

Fig. 3 Modulation of normal state voltage (a) and supercurrent by a gate voltage (b).

~0.24 fF/μm^2, where the dielectric constant of SiO_2 is $\varepsilon = 4$ and the thickness of the dielectrics is d = 150 nm. For the structure used in this experiment, this amounts to 0.04 fF. Even when the effects of fringing fields and the self-capacitance of the island are taken into account, the total parasitic capacitance is still too small to account for the discrepancy between the values obtained from resistance scaling and modulation depth. A number of devices with different size junctions, the smallest being 0.08 × 0.08 μm^2 (see Fig. 4), have been measured. The capacitances obtained from modulation depth are consistently several times larger than that deduced from resistance scaling. More experiments need to be done to clarify this discrepancy.

In the superconducting state, the critical current of a transistor can be modulated by the gate voltage. However the critical current cannot be easily measured. Instead, the switching current of the device, which is related to the critical current, is measured in this work. The switching current is obtained by ramping the bias current at a constant rate until the device switches to a finite-voltage state; the current at which this occurs is recorded. The gate voltage is independently ramped at a much slower rate so that the charge on the island is essentially constant during a switching cycle. Fig. 3b shows the modulation of the switching current with gate voltage. Comparing Fig. 3a and 3b, it can be seen that the periods of the modulations are almost identical, indicating that the modulation in the superconducting state is e-periodic. The $2e$-periodic modulation of critical current, the hallmark of superconducting single-electron transistors, has not been observed in this experiment, although it has been routinely observed in Al transistors measured in the same setup [12].

Normal-state charge noise was measured at 30 mK for the device with the smallest junction size (0.08 × 0.08 μm^2). As shown in Fig. 4 the measured charge noise at 10 Hz is about 2 × 10^{-3} e/Hz$^{1/2}$, about two orders of magnitude larger than high-quality Al/AlOx/Al single-electron transistors. This noise performance should still be acceptable for most basic-research applications. Even though the modulation depth in this device is relatively larger (~60 μV) than that shown in Fig. 3, it is still a few times smaller than what is expected from the junction-size estimate.

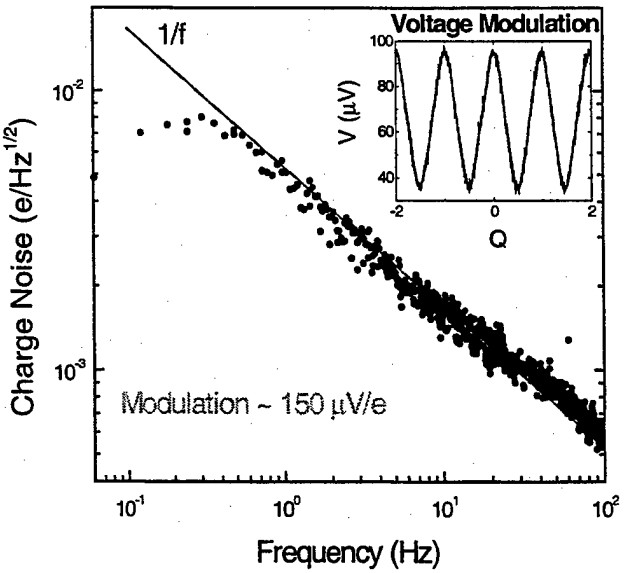

Fig. 4. Measured transistor charge noise with an applied 4 Tesla magnetic field to suppress superconductivity. The dashed line demonstrates a 1/f power spectrum. The modulation depth is about 60 μV (inset). Q is the charge on the island induced by the gate voltage.

IV Conclusions

In conclusion, all-Nb single-electron devices have been fabricated using Nb-tri-layer technology and a planarized process. Electron-beam lithography and erodible quartz masks are used to define all levels of the process. Junctions as small as 0.08×0.08 μm^2 have been fabricated. Current-voltage curves in the superconducting state show typical characteristics of low-J_c Nb junctions. Clear modulation of supercurrent with gate voltage and Coulomb blockade have been observed. However, capacitances obtained from modulation depths are significantly larger than those estimated from resistance scaling. This discrepancy requires further study.

References

[1] D.V. Averin and K.K. Likharev, "Coulomb blockade of single-electron tunneling, and coherent oscillations in small tunnel junctions," *J. Low Temp. Phys.* **62**, pp. 345-373, Feb1986.

[2] T.A. Fulton and G.J. Dolan, "Observation of single-electron charging effects in small tunnel-junctions," *Phys. Rev. Lett.* **59**, pp. 109-112 July 1987.

[3] Y. Harada, D.B. Haviland, P. Delsing, C.D. Chen, and T. Claeson, "Fabrication and measurement of a Nb based superconducting single-electron transistor," *Appl. Phys. Lett.* 65, 636, 1994.

[4] J. Shirakashi and K. Matsumoto, "298 K operation of Nb/Nb oxide-based single-electron transistors with reduced size of tunnel junctions by thermal oxidation," *J. Appl. Phys.* 84, pp. 5567, May 1998.

[5] K. Bluthner, M. Gotz, W. Krech, H. Muhlig, Th. Wagner, H.J. Fuchs, D. Schelle, L. Fritzsch, B. Nachtmann and A. Nowack, "Fabrication and characterization of single-electron transistors based on Al/AlOx/Al and Nb/AlOx/Nb tunnel junctions," *J. Phys.* IV 6, pp. 163-167 April 1996

[6] M. Gurvitch, W.A. Washington and H.A. Huggins, "High-quality refractory Josephson tunnel-junctions utilizing thin aluminum layers," *Appl. Phys. Lett.* **42**, pp. 472-474, 1983.

[7] M.B. Ketchen, "Design considerations for DC SQUIDs fabricated in deep sub-micron technology," *IEEE Trans. Magn.*, vol. 27, pp. 2916-2919, March 1991.

[8] W. Chen, A. V. Rylyakov, Vijay Patel, J. E. Lukens, and K. K. Likharev, "Superconductor digital frequency divider operating up to 750 Hz," *Appl. Phys. Lett.* **73**, pp. 2817-2819, Nov 1998.

[9] Z. Bao, M. Bhushan, Siyuan Han and J. E. Lukens, "Fabrication of high quality, deep-submicron Nb/AlOx/Nb Josephson junctions using chemical mechanical polishing," *IEEE Trans. Appl. Supercond.*, vol. 5, pp. 2731-2734, 1995.

[10] D.J. Flees, "Experimental studies of band-structure properties in Bloch transistors", Ph.D. Thesis, State University of New York at Stony Brook, 1998.

[11] A.B. Pavolotsky, T. Weimann, and H. Scherer, V. A. Krupenin, J. Niemeyer, and A.B. Zorin, "Multilayer technique for fabricating Nb junction circuits exhibiting charging effects," *J. Vac. Sci. Technol.* **B 17**, pp. 230-232 Jan-Feb 1999.

[12] D.J. Flees, Siyuan Han, J.E. Lukens, "Interband transitions and band gap measurements in Bloch transistors", Phys. Rev. Lett. 78, 4817, 1997.

Spin Injection Properties of $YBa_2Cu_3O_y$ Films

Kiejin Lee, Wan Wang and Ienari Iguchi
Department of Applied Physics, Tokyo Institute of Technology and CREST, Japan Science and Technology Corporation(JST), Oh-okayama, Meguro-ku, Tokyo 152-8551, Japan

Barry Friedman
Department of Physics, Sam Houston State University, Huntsville, Texas 77341, USA and Electrotechnical Laboratory, 1-1-4 Umezono, Tsukuba, 305-8568, Japan

Takayuki Ishibashi and Katsuaki Sato
Faculty of Technology, Tokyo Institute of Agriculture and Technology, 2-24-16 Nakacho, Koganei, Tokyo 184, Japan

Abstract—**We report the strong suppression of $YBa_2Cu_3O_y$ (YBCO) supercurrent by tunnel injection of spin-polarized quaiparticles using a cobalt ferromagnetic injector. The injection of spin-polarized quasiparticles generates a substantially larger nonequilibrium population as compared with that of an unpolarized injection current. The measurements of current gain for the directional-oriented spin-polarized quasiparticle injection on the [001] axis and the [110] surfaces of YBCO thin film show the anisotropic behavior according to the junction orientation.**

I. Introduction

The investigation of nonequilibrium superconductivity due to tunnel injection of spin-polarized quasiparticles(QP) provides useful information on the superconducting mechanism related to spin-dependent electronic properties[1] and may also lead to a new class of superconducting devices. The nonequilibrium state in a superconductor can be induced by injecting photons or phonons with energy greater than the superconducting energy gap or a tunnel current into it, so that the number of QP becomes greater than that in thermal equilibrium. One effective way to induce a strongly perturbed nonequilibrium state is tunnel injection of QP.[2] In this case, the suppression of superconducting properties such as critical current and energy gap is expected. Some results on the QP injection effect into a high T_c superconductor (HTSC) are reported previously.[3-5] However, as compared to a low temperature superconductor, the current gain of HTSC was considerably smaller and about unity. However, quite recently, it has been reported by many authors that the spin-polarized QP injection from either a colossal magnetoresistance (CMR) material[6,7] or a ferromagnetic material of permalloy[8] into a HTSC caused strong nonequilibrium effects. The experiments suggest that the high density of spin-polarized QP were injected into a superconductor and created a nonequilibrium state which was able to affect the electronic transport properties of the superconducting film. Recently, the directional dependence of QP tunnel injection in a YBCO superconductor has been reported.[4] The results showed the presence of strong anisotropic behavior, depending on the junction orientation and impedance.[9] The facts indicate that the tunnel injection properties due to unpolarized QP and spin-polarized QP are related to the tunnel direction.

In this paper, we report the Cooper-pair breaking effect in a HTSC superconductor due to the injection of spin polarized QP into a YBCO film from a cobalt(Co) film and compare it to that of unpolarized QP from a nonmagnetic metallic gate. We find that the spin-polarized QP injection suppressed the critical current of the superconductivity quite effectively showing the importance of the Cooper-pair breaking effect by spin-polarized carrier injection. The dependence of the current gain of YBCO/Au/Co (S/N/F) junctions on the thickness of Au interlayer (d_{Au}) and the tunnel injection direction have been studied.

II. Experiment

The YBCO films of 50-60 nm thick were prepared by pulsed-laser deposition technique on MgO (100) substrates

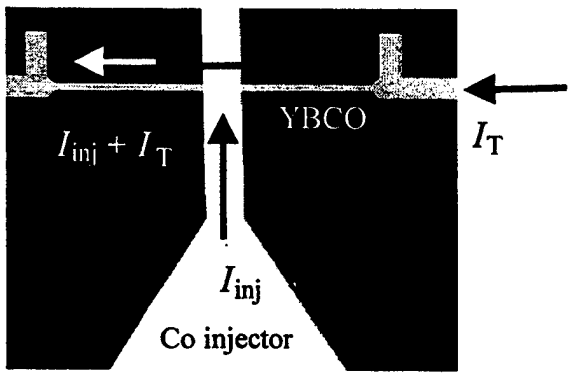

Fig. 1. Photograph of the $YBa_2Cu_3O_y$/Au/Co tunnel junction. Two currents were fed into a $YBa_2Cu_3O_y$ film; one is the injection current (I_{inj}) coming from the ferromagnetic Co film and the other is the transport current (I_T) through a YBCO film.

Manuscript received April 30, 1999.

and patterned into a stripline of 20 μm wide. Two type of samples with different counter electrodes were prepared in order to compare the tunnel injection effect of spin-polarized QP with that of unpolarized QP; one structure has a S/N/F structure and the other has a S/N structure. The effective junction area was 100x20 μm^2 for both junctions. The Au interlayer was evaporated by electron-beam technique. For S/N junctions, the thickness of the deposited Au layer was about 50 nm. For S/N/F junctions, we deposited an Au barrier film on the YBCO film to reduce the junction resistance and to avoid the formation of a spin glass phase

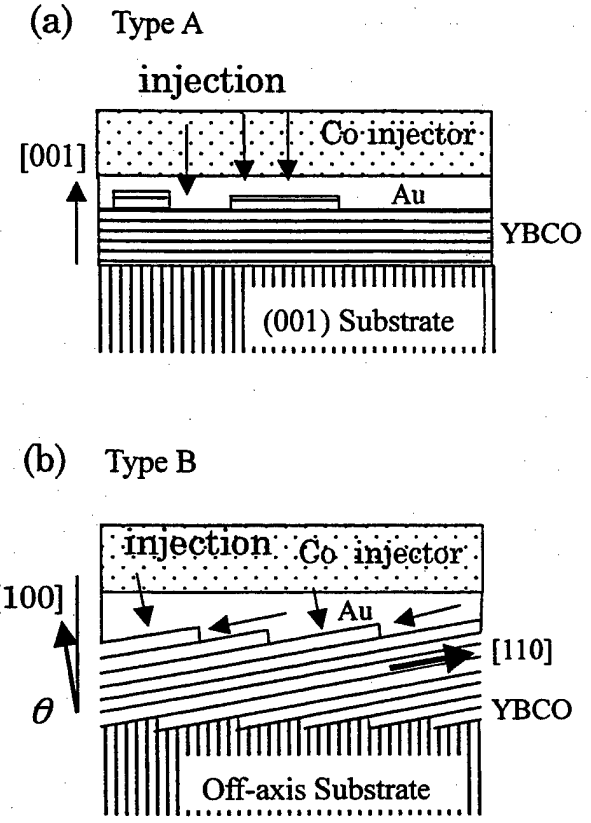

Fig. 2. Sample geometries with two tunnel injector junctions with c-axis injection geometry (type A) and [110] surface injection geometry (type B). The tunnel injection current flows in the [001] direction for type A and the [001] direction and [110] face for type B.

at the S/F interface.[9] The superconducting properties of YBCO films were always degraded when a Co layer was directly sputtered onto a YBCO film. The isolation effect of Au barrier at the S/F interface provided a noticeable change in superconductivity. With this sandwiched structure, the tunnel junction resistance changed about two orders of magnitude, nearly exponentially, with varying d_{Au} from zero to 10 nm. The deposition of a minimum 10 nm thickness of Au barrier layer was necessary to avoid the degradation of superconductivity of a YBCO film. The device geometry is depicted in Fig. 1. Two currents were fed into a YBCO film; one is the injection current (I_{inj}) and the other is the transport current (I_T) through a YBCO film. The I_{inj} goes from the ferromagnetic Co film to the YBCO film through an insulating tunnel barrier (I) formed at the S/I/N/F boundary.

In order to compare the direction-oriented tunnel injection effect of spin-polarized QP into a YBCO superconductor, two types of S/N/F samples with different YBCO crystal orientations were prepared: one corresponding to the tunnel injection mainly into the c axis and the other into both the c axis and the [110] plane. In Fig.2, type A junction is formed on a simple (100) MgO substrates and type B is formed on an off-axis (001) $LaAlO_3$ substrate. For the latter, the (001) $LaAlO_3$ substrate is tilted about 20° toward [110] $LaAlO_3$, with the steps and terraces aligned along a substrate [110] direction. The substrate tilt serves to break the symmetry of the surface, thereby leading to growth of [110] in-plane oriented YBCO films with T_c of 60 K phase. Therefore, the interface volume of [110] surface could be estimated from the tilted angle along the [11sin20°].

III. Results and Discussion

Fig. 3 shows the temperature dependence of the current gain for S/N and S/N/F junctions. The current gain is defined as the relation $\Delta I_c/\Delta I_{inj}$, where ΔI_c is the reduction of I_c and the criterion for I_c is taken to be the value 1μV appearing at the current-voltage characteristics. The current gain of the S/N/F junction, which decreases with increasing temperature, can be explained by the suppression of the order parameter of superconductor and the decrease of the spin polarization degree of the injected carrier with increasing temperature up to T_c. The current gain of a S/N/F junction was about 6 times larger than that of a S/N junction at 40 K. In the whole temperature range, the current gain of S/N/F junction is 5 to 10 times larger than that of the S/N junction. For S/N junctions, the current gain was about unity. Note that

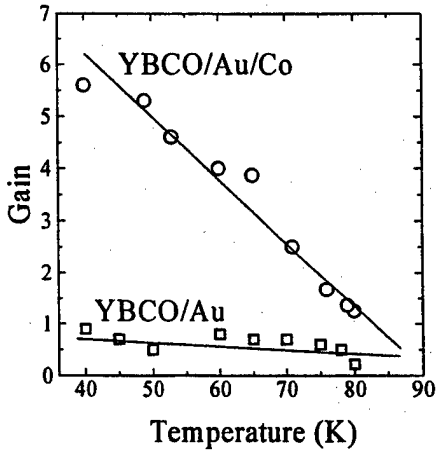

Fig. 3. Temperature dependence of current gain of $YBa_2Cu_3O_y$/Au/Co (d_{Au}=15 nm) and $YBa_2Cu_3O_y$/Au (d_{Au}=50 nm) tunnel junctions.

the current gain depended on the junction geometry and the QP injection direction into a HTSC.[4,5] However, for a simple cross-type tunnel junction structure, it was almost unity. Hence, the high current gain of a S/N/F junction may be attributed to an additional nonequilibrium effect due to the injection of spin-polarized QP into the superconductor

The dependence of the current gain of S/N/F junctions on the Au thickness was observed. It is known that the spin diffusion length was about ~1 μm for an Au film according to the measurement of the spin-injection-detection technique by Johnson, thus it would be nearly transparent for the spin-polarized QP passing through an Au interlayer.[11] However, we found that d_{Au} was directly related to the current gain and the tunnel conductance. As d_{Au} was increased, the spin-polarized injection effect might be weakened due to the effective boundary. According to the recent theory of spin transport properties between a ferromagnet material and an isotropic *d*-wave superconductor, one may expect that the Andreev reflection would be significantly disturbed.[12] This fact indicates that the directional-oriented spin-polarized QP tunnel injection current at the S/F interface has an important role to produce the nonequilibrium effect.

Fig. 4. shows the temperature dependence of the current gain of type A and type B junctions at higher injection energy range. For type A junction, all the tunnel injection current is expected to flow to the [001] direction of YBCO film. However, for type B, the tunnel current may be injected into both the c axis and the [110] face flowing the [11sin20°] direction of YBCO superconductor. In the previous report, we argued that the current gain due to spin-polarized QP tunnel injection was related to the junction orientation.[13] For type B, the observed current gain was slight larger than that of type A junction. The result reflects that the spin-polarized QP injection into a YBCO film may be related to the junction orientation.

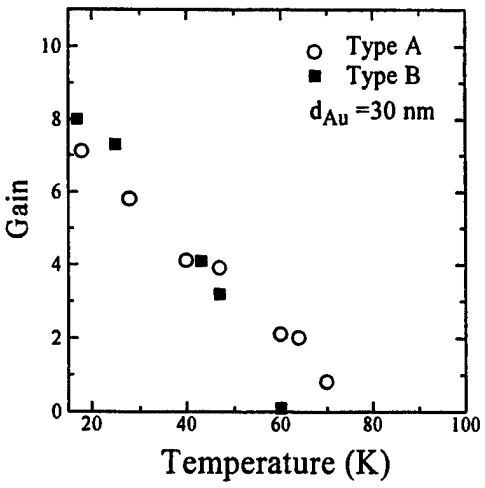

Fig. 4. Temperature dependence of current gain of $YBa_2Cu_3O_y$/Au/Co (d_{Au}=30 nm) junction for type A and Type B.

In summary, we have reported the suppression of the supercurrent of YBCO by injection of spin-polarized QP from a ferromagnetic injector, showing that the injection of spin-polarized QP generates a substantially large nonequilibrium population. The current gain of a YBCO/Au/Co junction was seems to be affected by the junction orientation. The observed results may be interpreted by the directional-oriented spin scattering processes in a ferromagnet/ d-wave superconductor tunnel junction.

Acknowledgment

We acknowledge the discussions and experimental support with H. Yamaguchi.

REFERENCES

[1] Q. Si, "Spin Conductivity and Spin-Charge Separation in the High-T_c Cuprates," Phys. Rev. Lett. 78, 1767-1770, 1997.

[2] K. E. Gray, Nonequilibrium Superconductivity, Phonon and Kapitza Boundaries, Plenum, New York, 1981.

[3] I. Iguchi, K. Nukui, and K. Lee, "Dynamic Cooper-Pair Breaking by Tunnel Injection of Quasiparticles in a High-T_c $YBa_2Cu_3O_y$ Superconductor," Phys. Rev. B 50, 457-460, 1994.

[4] K. Lee , H. Yamaguchi, W. Wang, H. Kume and I. Iguchi, "Directional-oriented quasiparticle injection and microwave emission in an $ErBa_2Cu_3O_y$ superconductor," Appl. Phys. Lett.74, 2375-2377, 1999.

[5] Yu. M. Boguslavskij, K. Joosse, A. G. Sivakov, F. J. G. Roesthuis, G. J. Gerritsma, and H. Rogalla, "Quasiparticle Injection Effects in Based Planar Structures at High Operating temperatures," Physica C 220, 195-202, 1994.

[6] V. A. Vas'ko, V. A. Larkin, P. A. Kraus, K. R. Nikolaev, D. E. Grupp, C. A. Nordman, and A. M. Goldman, "Critical current suppression in a superconductor by injection of spin-polarized carriers from a ferromagnet," Phys. Rev. Lett. 78, 1134-1137, 1997.

[7] Z. W. Dong, R. Ramesh, T. Venkatesan, M. Johnson, Z. Y. Chen, S. P. Pai, V. Talyansky, R. P. Sharma, R. Sheekala, C. J. Lobb, and R. L. Greene, "Spin-polarized Quasiparticle Injection Devices using Au/$YBa_2Cu_3O_7$/ $LaAlO_3$/ $Nd_{0.7}Sr_{0.3}MnO_3$ Heterostructures," Appl. Phys. Lett. 71, 1720-1722, 1997.

[8] D. B. Chrisey, M. S. Osofsky, J. S. Horwitz, R. J. Soulen, B. Woodfield, J. Byers, G. M. Daly, P.C. Dorsey, J. M. Pond, and M. Johnson, and R. C. Y. Auyeung, "Evidence for Modification of the Superconducting Order Parameter in $YBa_2Cu_3O_y$ Films by Injection of a Spin Polarized Current," IEEE Trans. on Appl. Supercond. 7, 2067-2070, 1997.

[9] J. Y. T. Wei, N.-C. Yeh, D. F. Garrigus, and M. Strasik, "Directional Ttunneling and Andreev Reflection on $YBa_2Cu_3O_y$ Single Crystals: Predominance of *d*-wave Pairing Symmetry Verified with the Generalized Blonder, Tinkham, and Klapwijk Theory," Phys. Rev. Lett. 81, 2542-2545, 1998.

[10] M. Rubinstein, P. Lubitz, W. E. Carolos, P. R. Broussard, D. B. Chrisey, J. Horwitz, and J. J. Krebs, "Properties of Superconductor-Ferromagnet Bilayers: $YBa_2Cu_3O_y$-Fe and $YBa_2Cu_3O_y$-Permalloy," Phys. Rev. B, 47, 15350-15353, 1993.

[11] M. Johnson, "Spin Accumulation in Gold Films," Phys. Rev. Lett. 70, 2142-2145, 1993.

[12] J.-X. Zhu, B. Friedman, and C. S. Ting, "Spin-Polarized Quasiparticle Transport in Ferromagnet-d-Wave Superconducting junction," to be published Phys. Rev.B.

[13] K. Lee, W. Wang, I. Iguchi, B. Friedman, T. Ishibashi, and K. Sato, "Spin-Polarized Quasiparticle Tunnel Injection in a YBCO/Au/Co junction," Appl. Phys. Lett., submitted.

Hybrid Ferromagnet-Nb Switch for Superconducting Nonvolatile Memory

T. W. Clinton, P. R. Broussard and Mark Johnson
Naval Research Laboratory, Washington D.C. 20375

In a simple bilayer geometry, a thin, microstructured ferromagnetic (F) film spans a superconducting (S) micro-strip. The magnetization of the F-film is rotated in the film plane to vary the magnitude of the magnetic fringe field locally applied to the superconductor from negligible (« H_c) to substantial values (> H_c). In the latter case, the *locally* strong magnetic fringe fields at the edge of the ferromagnet quench the superconductivity, creating a weak link and a corresponding suppression of the critical current. The strength of the weak link can be varied between on and off by controlling the orientation of the in-plane magnetization of the ferromagnet. A large modulation of the critical current is observed. The observation of Shapiro steps demonstrates the AC Josephson effect in the "quenched" state. In this switchable Josephson junction energy is required only to change states, which are thereafter maintained in thermodynamic equilibrium and are nonvolatile *even* above T_c. The effect is demonstrated in conventional low T_c superconductors Nb, Pb and Sn. The hybrid F-S switch has possible applications as a high speed switch and high density nonvolatile superconducting random access memory (RAM).

Thin film tunable dielectrics for HTS rf applications

B. H. Moeckly and Y. M. Zhang

Conductus, Inc., 969 W. Maude Ave., Sunnyvale, CA 94086

Thin-film tunable ferroelectrics such as $SrTiO_3$ are desirable for active tuning of high-Tc microwave filters. However, in order to preserve the high Q values of the filters, the properties of the $SrTiO_3$ films need to be dramatically improved. We desire films possessing both a significant electric-field tunability of their permittivity and a low loss tangent at an appropriate temperature (30 to 60 K). We will discuss our dielectric measurements of films whose growth protocols have been optimized to achieve these goals. We present evaluations of films grown on various substrates, with different buffer layers and interlayers, and with different dopings. In addition, we will discuss the tunability and loss obtainable for YBCO resonator structures incorporating the best available tunable dielectric films.

POSTER SESSION II

Group 1 - Digital

Superconducting flip-chip bonding method with a μm-scale gap

Masahiro Aoyagi, Hiroshi Nakagawa, Hiroshi Sato, Toru Taino*, and Hiroshi Akoh
Electrotechnical Laboratory (ETL), 1-1-4 Umezono, Tsukuba, Ibaraki 305-8568, Japan
*Kyushu University, 6-10-1 Hakozaki, Higashi-ku, Fukuoka 812-8581, Japan

Abstract—We have developed a new flip-chip bonding method for chip-to-chip or chip-to-substrate propagation of high-speed signals generated from superconducting Nb integrated circuits. A test chip that has 1-μm-high 150-μm-diameter superconducting Pb/In evaporated bumps and a test substrate that has 3-μm-high Pb/In bumps were successfully bonded by a flip-chip bonder with a narrow gap of 5 μm. The supercurrent and the shear strength was measured to be 1.8 - 1.9 A through the bump connections and 20 - 25 gf per bump, respectively.

I. Introduction

We are developing a superconducting Josephson sampling measurement system [1], in which a Josephson junction shows ps-width pulse generation and ps-level signal response. This sampling technique was used for only on-chip measurement. In order to measure an off-chip signal source, ultra-wideband chip-to-chip or chip-to-substrate interconnection technology should be developed. The flip-chip bonding method [2] is suitable for high-speed signal propagation because the connecting length can be made very short.

For superconducting integrated circuits, IBM has developed a superconducting flip-chip bonding method based on the so-called controlled-collapse-chip connection (C4) using In/Bi/Sn (having a melting point of 60 °C) solder bumps [3]. This method firstly realized a flip-chip bonding with very low temperature for Pb-alloy Josephson junctions. The bump shape was 25-μm-high 100-μm-diameter. The bump material was poor superconductor having Tc of about 6K. The bump inductance was measured to be 28 pH using a DC-SQUID [4].

ETL and Tanaka Denshi Kogyo have developed a flip-chip method based on the so-called stud bump technique using Pb/Sn solder wire [5,6]. The bonding process was performed at 100 °C. This method realized a flip-chip bonding with low temperature for Nb Josephson junctions. The stud bumps were formed using a wire-bonder. The bump shape was 25-μm-high 100-μm-diameter. The size of the bump was limited by the diameter of the wire.

These flip-chip technologies have a relatively large 20 – 30 pH bump inductance. Such inductance obstructs the high-speed signal propagation through the bump. The height of the bump must be sufficiently reduced to eliminate the effect of the inductance.

Reduced bump inductance is also needed to realize a high-speed coplanar waveguide chip-to-chip connection structure, which ETL and Technical University of Ilmenau proposed in ASC'98 [7].

In this paper, we propose a superconducting flip-chip method with a μm-level gap using thin evaporated Pb/In bumps with resist masks formed by photolithography. The flip-chip bonding procedure and the characteristics of the flip-chip bonded connection are discussed.

Manuscript received May 1, 1999.

II. Superconducting Flip-Chip Bonding Method

Superconducting Pb/In bumps were formed as shown in Fig. 1. The process of the bump formation is explained as follows. (a) The substrate having a superconducting integrated circuit structure except wiring is prepared. A 1-μm-thick resist pattern for wiring and pad is formed using an i-line stepper on a 500-nm-thick Nb film deposited by sputtering. Then, the Nb film is etched by reactive ion etching (RIE). (b) The resist mask is removed by immersing in solvent. (c) A 7-μm-thick SJR7540 resist pattern for bump is formed using the i-line stepper. 2.7-μm-thick Pb and 300-nm-thick In films are sequentially deposited by evaporation. (d) The Pb/In alloy film on the resist pattern is removed by the lift-off method. The Pb/In bumps are finally formed on the Nb pad.

Fig. 2 shows a SEM photograph of 3-μm-high 150-μm-diameter Pb/In bumps formed on 500-nm-thick Nb pads.

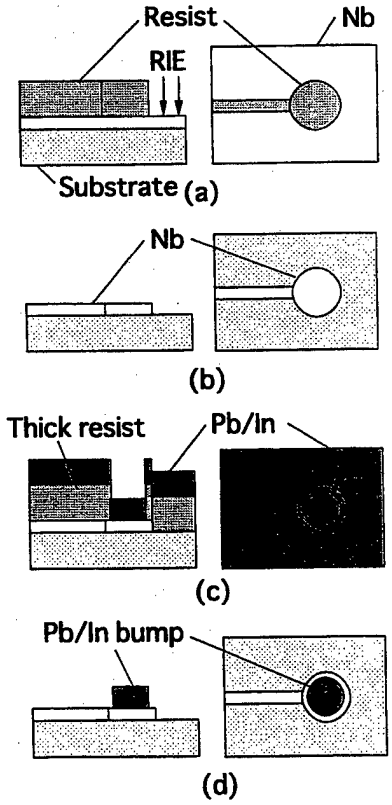

Fig. 1 Process flow of Pb/In bump formation.

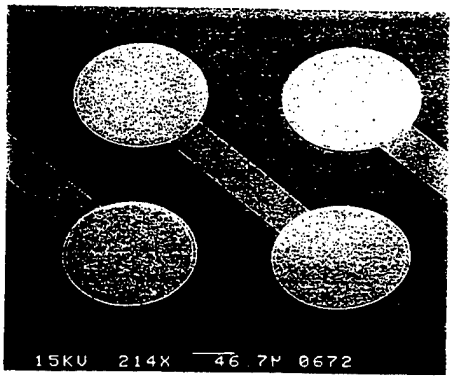

Fig. 2 SEM photograph of 150-μm-diameter Pb/In bumps on Nb pads and 50-μm-width Nb wires.

Test chips were prepared with the wiring layout pattern as shown in Fig. 3. The pattern has 2 daisy chains, 60 flip-chip bumps, and 8 large pads for wire bonding. For the flip-chip bonding test, two chips having the same wiring pattern were used. 5-mm-square chip was used for substrate side. 2.5-mm-square was used for chip side, where the 8 large pads were cut off. The height of the bump was 1 μm.

Flip-chip bonding was performed using a flip-chip aligner-bonder CB-1010Z [8], Misuzu FA Corp., where alignment accuracy was guaranteed to be ± 10 μm in 3σ even after bonding. The bonding condition was as follows. Both substrate and chip holders were constantly heated up to 100 °C. Bonding pressure was 250 gf per bump. Pressing duration was 15 min.

Fig. 4 shows the flip-chip bonding procedure. The process flow of the flip-chip bonding is explained as follows. (a) A substrate is fixed on the substrate holder with vacuum suction. A chip is picked up from a chip tray by the chip holder with vacuum suction. Alignment patterns located on the surfaces of the substrate and the chip are observed using two CCD cameras. The chip position is adjusted in the X-axis, Y-axis and rotation to overlap the alignment patterns. (b) The chip is moved down in Z-axis until it reaches the surface of the substrate. Then, the chip is pressed down with 250 gf per bump for more than 10 min.

III. Experimental Results

The cross-section of flip-chip bonded test chips was observed with magnification of 200 by a scanning electron beam microscope (SEM) system. Fig. 5 shows a SEM photograph of the bonded sample. The bottom was 5-mm-square chip having 3-μm-high bumps. The top was 2.5-mm-square chip having 1-μm-high bumps. The total bump height was 4 μm. Finally, the gap between the two chips was 5 μm including the Nb pads.

The cross-section of the flip-chip bonded Pb/In bump was observed with magnification of 5000 by a field emission (FE) SEM system after cross-sectional polishing. Fig. 6 shows a FE-SEM photograph of a bonded bump. The grain of Pb/In was emphasized by polishing. The narrow gap of 5 μm was confirmed successfully.

Electrical characteristics of the flip-chip connection were evaluated by four terminal measurement in liquid He at 4.2K. The supercurrent through Pb/In bumps in the two daisy chains and the electrical isolation between the two daisy chains were measured. For 5 samples of 7 measured samples, we observed supercurrent through all connections with complete isolation. The maximum supercurrent of 1.8 - 1.9 A was obtained through a daisy chain. It is estimated that the supercurrrent was limited by the 50-μm-wide wiring between Nb pads.

The shear strength was measured to be 20 - 25 gf per bump. This value did not changed after the cryogenic measurement.

The inductance of the bump should be reduced about 1/5 compared with the previous methods.

We plan to measure the high-speed signal propagation through the flip-chip connection using a superconducting Josephson sampling measurement system in the near future.

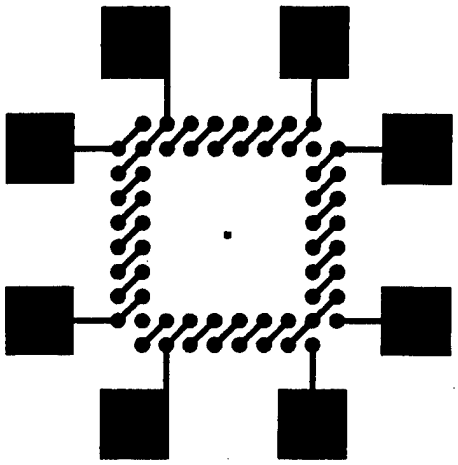

Fig.3 Layout pattern of the wiring layer for test chips.

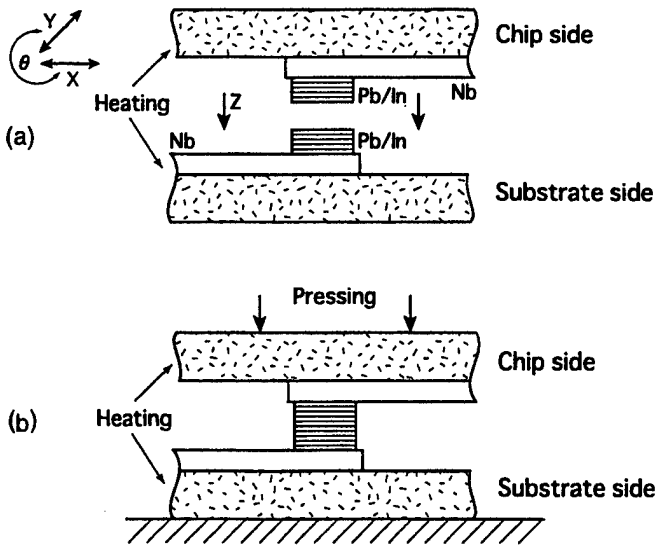

Fig. 4 Procedure of the flip-chip boning using Pb/In bumps.

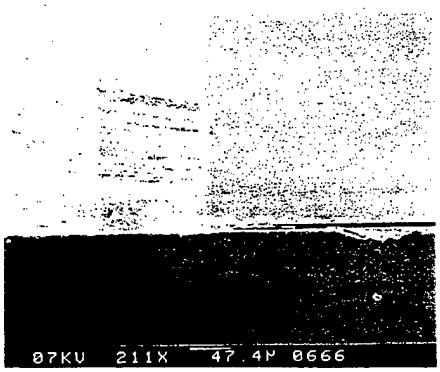

Fig. 5 Cross-sectional SEM photograph of flip-chip bonded test chips.

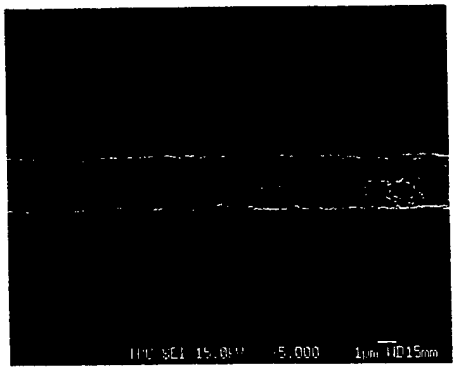

Fig. 6 Cross-sectional FE-SEM photograph of a flip-chip bonded bump.

IV. CONCLUSION

We have developed a new flip-chip bonding method with a μm-scale gap for high-speed superconducting Nb integrated circuits technology. A test chip that has 1-μm-high 150-μm-diameter superconducting Pb/In evaporated bumps and a test substrate that has 3-μm-high Pb/In bumps were successfully bonded by a flip-chip aligner-bonder with a narrow gap of 5 μm. The superconducting current and the shear strength was measured to be 1.8 - 1.9 A through the bump connections and 20 - 25 gf per bump, respectively. The inductance reduction of the bump should be reduced about 1/5 compared with the previous methods.

ACKNOWLEDGMENT

The authors would like to thank A. Esposito for his assistance with the sample fabrication. They also would like to thank T. Sakamoto for his encouragement and support during the course of this study.

REFERENCES

[1] M. Aoyagi, H. Sato, H. Nakagawa, and H. Akoh, "Digitizing Josephson Sampling System Using Nb/AlOx/Nb Junctions," *Extended Abstracts of 6th Inter. Superconductive Electronics Conf.*, Vol. 2, pp. 275-277, June 1997.

[2] P.A. Totta and T.C. Reiley, "Chip-to-Package Interconnections," in *Microelectronics Packaging Handbook*, part II, R.R. Tummala, E.J. Rymaszewski, and A.G. Klopfenstein, Eds. New York: Chapman & Hall, 1997, pp.129-283.

[3] C.Y. Ting, K. Grebe, and D. Waldman, "Controlled Collapse Reflow for Josephson Chip Bonding," *J.Electrochem. Soc.*, vol. 129, pp. 859-864, April 1982.

[4] H.C. Jones and D.J. Herrell, "The Characteristics of Chip-to-Chip Signal Propagation in a Package Suitable for Superconducting Circuits," *IBM J. Res. Develop.*, vol. 24, pp. 172-177, March 1980.

[5] T. Ogashiwa, H. Nakagawa, H. Akimoto, H. Shigyo, and S. Takada, "New Flip-Chip Bonding Technology for Superconducting IC," *Japanese J. Appl. Phys.*, vol. 31, pp. L36-L38, January 1992.

[6] T. Ogashiwa, H. Nakagawa, H. Akimoto, H. Shigyo, and S. Takada, "Flip-Chip Bonding Using Superconducting Solder Bump," *Japanese J. Appl. Phys.*, vol. 34, pp. 4043-4046, August 1995.

[7] H.Toepfer, T. Lingel, F.H. Uhlmann, and M. Aoyagi, "Numerical Studies of Interchip Pulse Transmission for Complex RSFQ Systems," *IEEE Trans. Appl. Supercond.*, vol. 9, June 1999, in press.

[8] K. Shindo, "Flip-Chip Bonder," *Electronic Parts and Materials (Denshi Zairyo)*, vol. 34, pp.83-85, April 1995 (in Japanese).

Design of an RSFQ Banyan Switching Node for Petaflops Computing

Dmitry Y. Zinoviev
Physics and Astronomy Department, SUNY, Stony Brook, NY 11794, USA

***Abstract*— Computing on the petaflops scale is one of the items at the top of the agenda of industrially developed nations for the beginning of the next millennium. However, the ultimate performance of a petaflops scale hypercomputer depends not only on fast and smart processing elements, but equally on reliable high-throughput low-latency interconnects. It is extremely important to pack the interconnecting network into the smallest possible volume to reduce communication latency and therefore the required level of the algorithmic parallelism. A switching network based on Rapid Single Flux Quantum (RSFQ) logic would be a natural choice, combining inherently high operating speed and low power dissipation. We propose a design of an RSFQ banyan switching network with internal buffering and contention resolution based on a backpressure mechanism. Our simulations show that the network can deliver more than 0.5 PBytes/sec of aggregate throughput with an average end-to-end latency of less than 18 ns. We present the design of a network switching node (successful operation of the data path has already been confirmed experimentally).**

I. Introduction

In our previous publications [1]–[3] we have presented the preliminary design of the RSFQ subsystem of the HTMT machine which would consist of 4,096 superconductor processing elements (SPELLs) and a self-routing multistage packet switching network (CNET). We have estimated the geometrical and timing properties of the network, such as system volume, the number of chips and multi-chip modules on which to place the circuitry and wiring, end-to-end packet propagation latency, and aggregate throughput [2], for two classes of networks: banyans and meshes. We based these estimations on the timing and real estate parameters of a single banyan switching node which was obtained using a very rough and sketchy model of the node [3]. In this paper, we present a more detailed study of the switching node structure and the way it affects the timing parameters of the node and of the entire network.

Manuscript received May 1, 1999.
This work was sponsored by the Defense Advanced Research Projects Agency (DARPA) and the National Security Agency (NSA) through an agreement with the National Aeronautics and Space Administration.

II. Switching Node Overview

The function of a 2×2 network switching node is to deliver network packets from the node's inputs to the node's outputs in accordance with the destination addresses and credits availability or to keep incoming packets in the internal buffers until their delivery becomes possible. For the sake of simplicity, we consider only the operation of a banyan node. The operation of a mesh node differs insignificantly in the address decoding stage.

Each node consists of FIFO buffers, address decoders, output line controllers, credit pools, and microstrip line interfaces — receivers and drivers (Fig. 1).

The operation of the node is organized in a pipelined manner. First, packets are received from input microstrip lines and placed into the first available W-bit-wide buffer in the corresponding FIFO queue (one queue per input). The queue is built as an elastic micropipeline [4] and will not be discussed here. Eventually, each packet reaches the head of the queue. At this point the destination address is decoded, and a routing request is sent to the corresponding output line controller. If a credit can be obtained from the credit pool [5], the controller sends at most one packet at a time to the output microstrip line driver.

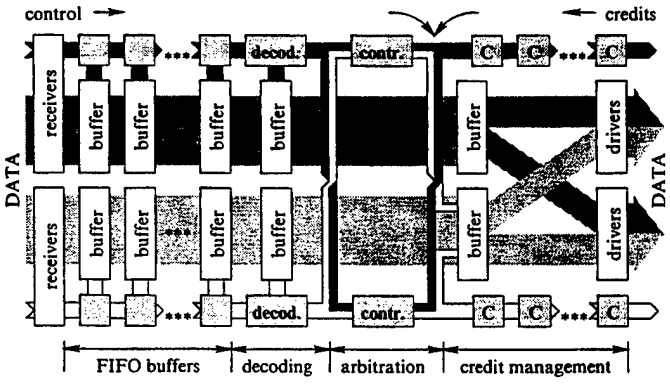

Fig. 1. Switching node pipeline.

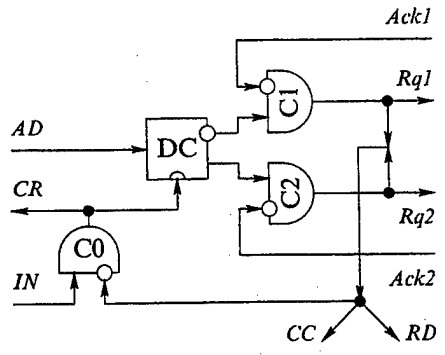

Fig. 2. Block-diagram of the address decoder.

III. Address Decoding

Address decoding in banyan networks is extremely simple. The switching node in the ith column of the network must examine only one (the ith) bit of the packet's destination address which is examined exactly once and does not have to be propagated to the next switching node. Depending on the value of that bit, the packet is forwarded to either the upper or lower output.

D flip-flop with complementary outputs DC comprises the core of the decoder (Fig. 2). The ith bit of the destination address AD is stored in the flip-flop. If the decoder is enabled (coincidence element C0 is set), indication bit IN toggles the flip-flop and produces acknowledgment CR and one of the routing requests. The request is further synchronized with the corresponding acknowledgment received from the arbiter Ack_i in the coincidence element Ci. The synchronized request propagates to the arbiter (as Rq_i), forwards the body of the package to the final stage of the data path (as RD), enables the decoder by setting C0, and sends credit CC back to the previous network node.

IV. Arbitration and Scheduling

In a system with input buffering, arbitration is necessary to determine which of the two input packets takes the priority if contending for the same output. In our case, the arbiter also serves as a packet scheduler, requesting credits from the credit pool (described in [3]) and forwarding packets to the correct output.

The line controller (Fig. 3) has two functional parts: the arbiter and the scheduler. The function of the arbiter is to separate incoming requests in time by synchronizing them with a high-frequency local clock. The function of the scheduler is to match those requests with credits.

Routing requests Rq_i from the decoders enter the synchronizer when the controller is enabled (coincidence elements Ci are set). The synchronizer consists of two D flip-flops, T flip-flop, and high-speed sampling clock generator G. It is described in detail in [6] and will not be discussed here. It is guaranteed that the time difference between the routing requests past the synchronizer is $> T_G/2$, where

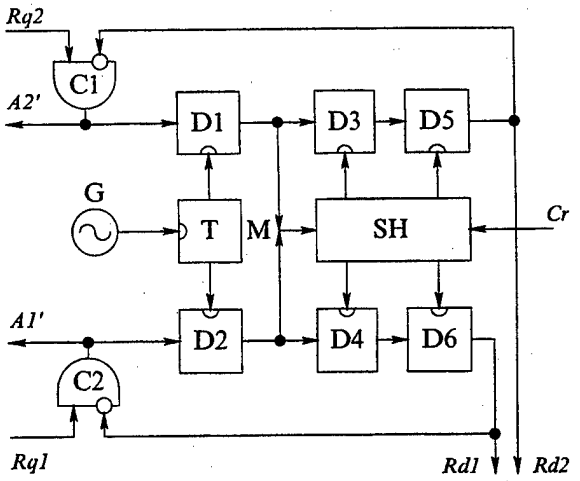

Fig. 3. Block-diagram of the output line controller.

T_G is the oscillation period of G. It is important to notice that since there are only two guard coincidence elements Ci, at most two requests can penetrate into the controller at a time.

A credit is indicated by the presence of an SFQ in loop J4-J3 (C1 in Fig. 4A).

Suppose request Rq1 is the first to enter the scheduler. The request is stored in D flip-flop D4. A copy of the request passes through merger M and switches Josephson junction J1. The inductance of superconductor loop J1-J2 is chosen in such a way that the loop does not trap a single-flux quantum unless another SFQ is trapped in the next loop J2-J3. So, the quantum switches Josephson junction J2, advances to the next superconductor loop and moves the original request from D4 to D6 (Fig. 4B). If a

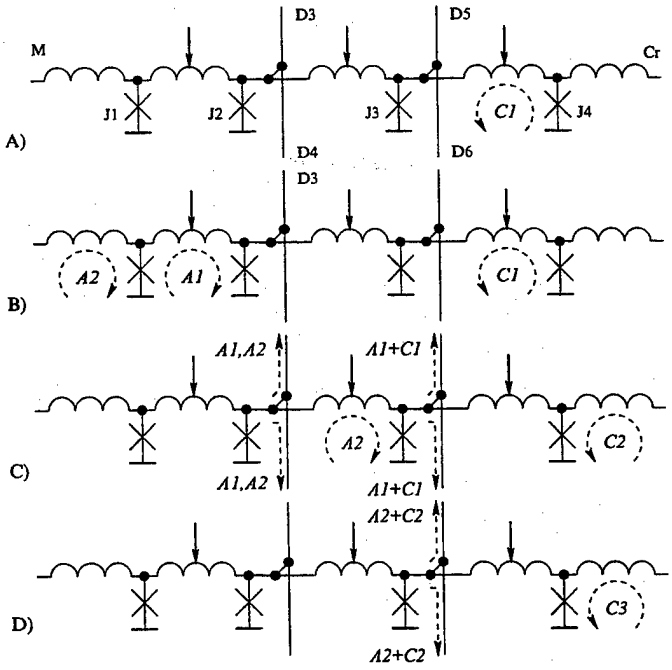

Fig. 4. Schematics and operating principles of the scheduler.

TABLE I
PERFORMACE PARAMETERS OF THE BANYAN SWITCHING NODE

Component	Θ, ps	L		T
		$N_c = 5$	$N_c = 50$	
Receiver		6	6	1/15
FIFO buffer		18×4	18×49	1/29
Decoder		30	30	1/48
Controller		48	48	1/55
Driver		7	7	1/15
Technology				
3.5μm	1.1	179 ps	1070 ps	16.5 Gw/sec
0.8μm	0.3	49 ps	292 ps	61 Gw/sec
0.4μm	0.165	27 ps	161 ps	110 Gw/sec

credit is available, the persistent current induced by A1 and C1 is large enough to switch Josephson junction J3. This will issue read-out signal Rd1 (Fig. 3) and enable the controller to accept yet another request from input Rq1 (Fig. 4C).

Now, suppose that request Rq2 follows Rq1, and no more credits are available in the credit pool (Fig. 4B). In this case, the second request will be stuck in loop J2-J3 and in flip-flop D5 until more credits are available (Fig. 4C,D).

Notice that because of the time separation introduced by the synchronizer, requests can only be stored in the diagonal pairs of flip-flops D3/D6 or D4/D5 (but not D3/D4 or D5/D6).

V. PERFORMANCE ESTIMATIONS

The most important performance parameters of the switching node are its latency L and its throughput T.

In a pipelined system,

$$T = \min_i T_i, \tag{1}$$

$$L = \sum_i L_i, \tag{2}$$

where T_i and L_i are throughputs and latencies of each pipeline component. The latency of the FIFO buffers depends on the number of credits N_c (less one credit — because one of the buffers belongs to the decoder). Some numerical results for $N_c = 5$ and $N_c = 50$ (and for various existing and perspective technologies) are summarized in Table I [1]. In general,

$$L = (73 + 18N_c)\,\Theta. \tag{3}$$

This differs significantly from the equation used in [2], where a latency of 7.6Θ per buffer was assumed.

In a distributed network (those with the switching nodes placed onto more than one chip), we come across a limitation on the chip-to-chip transfer rate T_r. Making an optimistic assumption of T_r =30 Gw/sec [2], we observe that the switching node cannot be utilized at its maximal throughput unless fabricated using the obsolete 3.5μm technology which is not suitable for the petaflops-scale project.

To obtain the formula for the number of credits, let us consider two identical switching nodes connected to each other, and calculate credit round-trip time (which depends on N_c). To make the mechanism of hiding the round-trip latency efficient, this time must be less than or equal to the number of credits times the distance in time between two consequent packets T_c ($T_c \geq T_r$) [5]. Substituting simulated values yields:

$$N_c = \lceil 0.8 + 0.025 T_f/\Theta \rceil, \tag{4}$$

where T_f is one-way flight time between the nodes. This equation does not take into account additional buffers (those not used for latency hiding). Otherwise, it is almost identical to the formula used in [2], and the value of throughput reported in [2] remains valid.

VI. CONCLUSION

We have carefully considered the internal structure of a 2 × 2 banyan network node. Based on the structural analysis and on physical-level simulations, we have been able to obtain reliable values of the timing parameters, such as service latency and throughput. These new results partially support and partially invalidate our previous estimations based on an approximate count of switching Josephson junctions. Further study of the timing parameters should take into account critical current density spread and thermal noises.

ACKNOWLEDGMENT

The author would like to thank K. Likharev, P. Bunyk, L. Wittie and G. Sazaklis for numerous helpful hints and fruitful discussions.

REFERENCES

[1] M. Dorojevets, P. Bunyk, D. Zinoviev, and K. Likharev, ""COOL-0": Design of an RSFQ subsystem for petaflops computing," *IEEE Trans. on Appl. Supercond.*, June 1999. In press.

[2] L. Wittie, D. Zinoviev, G. Sazaklis, and K. Likharev, "CNET: Design of an RSFQ switching network for petaflops-scale computing," *IEEE Trans. on Appl. Supercond.*, June 1999. In press.

[3] S. Yorozu and D. Zinoviev, "Design and implementation of an RSFQ switching node for petaflops networks," *IEEE Trans. on Appl. Supercond.*, June 1999. In press.

[4] K. Likharev and V. Semenov, "RSFQ logic/memory family: a new Josephson junction technology for sub-teraherz clock frequency digital systems," *IEEE Trans. on Appl. Supercond.*, vol. 1, pp. 3–28, Mar. 1991.

[5] D. Zinoviev and M. Maezawa, "Application of credit-based flow control to RSFQ micropipelines," *IEEE Trans. on Appl. Supercond.*, June 1999. In press.

[6] S. Yorozu, D. Zinoviev, and S. Tahara, "An asynchronous SFQ-pulse arbiter for high performance digital applications." Presented at ISEC'99, Berkeley, CA, June 1999.

[1] Notice that the results in the upper part of the Table are shown in dimensionless time units Θ.

Digital-to-Analog Converter Based on Digital Processing of SFQ Pulses (progress report)*

V.K. Semenov, Yu. A. Polyakov, SUNY at Stony Brook, NY USA

We would like to present new experimental results for digital-to-analog converter (DAC) based on processing of SFQ pulses. The structure of the device has been discussed at previous ASC conferences. The converters consist of a set of dc Voltage Multipliers (VM) each one with length (and hence gain) increasing by a factor of 8. The dc VMs are connected in series for dc output and independently controlled by a digital RSFQ circuit. This control is provided for each dc VM by the generation of a train of SFQ pulses with frequency (and hence average voltage) proportional to 3 corresponding bits of an input binary code. Due to different gains of VMs the total average output voltage is exactly proportional to an input code. The estimated parameters of the device are: margins for an output (load) current from +- 0.1 mA, the number of quantization levels 256,000, and a bandwidth over 1 MHz. The major goal of the project is to demonstrate the outstanding accuracy of the conversion, which is expected to be similar to one of the Josephson DC voltage standards.

*The work is supported in its parts by US DoC and HYPRES, Inc.

Experiments and Simulations of Picosecond Pulse Switching and Turn-on Delay Time in Y-Ba-Cu-O Josephson Junctions

Roman Adam, Carlo Williams, and Roman Sobolewski*
Department of Electrical and Computer Engineering and Laboratory for Laser Energetics
University of Rochester, Rochester, NY 14627-0231 USA

Oliver Harnack and Marian Darula
Institute for Thin Film and Ion Technology, Research Center Jülich, D-52425 Jülich, Germany

Abstract—We report our studies on single-picosecond electrical pulse switching of $YBa_2Cu_3O_{7-x}$ (YBCO) grain-boundary bicrystal Josephson junctions. The test structures consisted of coplanar strip (CPS) transmission lines that were patterned in 50-nm-thick YBCO films prepared on (100) MgO bicrystal substrates. Each CPS contained a 5-μm-wide and 10-μm-long microbridge and a 5-μm-wide grain-boundary Josephson junction. A train of 100-fs-wide optical pulses from a Ti:sapphire laser was used to excite the microbridge and generate ~2-ps-wide electrical pulses, which were then applied to switch the junction. The junction response was studied utilizing cryogenic electro-optic sampling system. We measured a 0.65-ps-wide single-flux-quantum (SFQ) pulse generated by the junction as well as a 0.7-ps junction turn-on delay time. Junction switching and turn-on delay time has been compared with JSPICE simulations.

I. Introduction

Josephson junction response to a picosecond input pulse has been studied both theoretically [1-4] and experimentally [5-6]. In [1], minimum input pulse duration τ_p necessary for junction switching was shown to be $\tau_p \sim \Phi_0/2I_CR_N$ where Φ_0 is magnetic flux quantum, I_C critical current and R_N junction normal-state resistance. Short junction-switching time τ is essential for proper performance of digital electronic circuits and can be expressed as $\tau = \tau_D + \tau_R$ where τ_D and τ_R are the junction-transient turn-on delay and rise time, respectively [2]. For small bias-current overdrive, δ, of the junction I_C ($\delta < 0.5\ I_C$), $\tau_D = \omega_p^{-1}\,\delta^{-1/2}$, where ω_p is the plasma frequency. For $\delta > 0.5I_C$, τ_D is negligible, thus $\tau \approx \tau_R$. From the resistively and capacitively shunted junction (RCSJ) model, $\tau_R = (4/\pi)(R_NC_J)(I_C/I_b)$ where C_J and I_b are the junction capacitance and the bias current, respectively [2].

For junctions with $\beta_C >> 1$ dynamic reduction of I_C may result in junction switching at $I_b < I_C$ [3]. In case of $YBa_2Cu_3O_{7-x}$ (YBCO) Josephson junctions, however, $\beta_C < 1$ due to small junction capacitance and the effect of I_C suppression can be neglected. When excited above I_C, a non-hysteretic junction generates a single flux quantum (SFQ) pulse of amplitude $2I_CR_N$ and pulse width $\Phi_0/2I_CR_N$ [4]. Direct measurement of SFQ pulse using electro-optic (EO) sampling technique has been reported in [5]. In the experiment, Nb-Si-Nb photodiode was excited with a 100-fs optical pulse and generated a few-ps-wide electrical transient, which was next shaped by the two resistively-shunted Nb tunnel junctions into a single SFQ pulse. The SFQ pulse was subsequently launched into a Nb microstrip transmission line and was directly measured using the EO sampler.

Recently, we observed a single-picosecond electrical response of a current-biased YBCO microbridge exposed to a femtosecond optical pulse [7], and in [8], we used a YBCO microbridge generated pulse to switch bicrystalline Josephson junction in a similar manner as in the Nb-tunnel junction experiment described above. In this paper, we present experiments and simulations of the YBCO junction switching triggered by a few-picosecond-long electrical pulses.

II. Experiment

The test structures, consisting of coplanar strip (CPS) transmission lines, were fabricated on (100) MgO bicrystal substrates, using a standard laser ablation technique and ion-beam etching. 50- to 100-nm-thick YBCO films were deposited at the substrate temperature 800 °C at the ambient oxygen pressure of 0.35 mbar. The deposition was followed by an annealing cycle in pure oxygen. Next, a 50-nm-thick gold layer was sputtered *in-situ* on top of YBCO thin film at room temperature at argon pressure of 0.05 mbar. The test structures were prepared in a two-step process. First, they were photolithographically defined and then etched with low current density (1 mA/cm^2) ion argon beam. In the second step, the Au layer was removed from the top of the junction and bridge areas, using the same low-intensity ion etching. As a result, 8-mm-long transmission-line structures, containing 10-μm×5-μm bridges and 5-μm-wide bicrystal Josephson junctions were fabricated. The long CPS was chosen to restrict the end-of-line reflections, assuring a 50-ps-long reflection-free measurement time-window.

The schematic of our test structure and the equivalent circuit are shown in Fig. 1. We note that the test structure is not a Josephson junction transmission line [4], but rather a high characteristic impedance (80 Ω) CPS line with the junction electrodes representing high inductance. Our optical system for the femtosecond pulse excitation and EO sampling detection is described in detail in [8]. Briefly, a mode-locked Ti:sapphire laser, operating at a repetition rate of 76 MHz was used to generate 100-fs pulses at a wavelength of 790 nm. To perform EO characterization, the laser beam was split into two paths: a frequency-doubled excitation beam was used for inducing the photoresponse response in the

Manuscript received May 1, 1999.
Email: adam@ece.rochester.edu
*Also at the Institute of Physics, Polish Academy of Sciences, PL 02668 Warsaw, Poland.
This research is supported by the Office of Naval Research grant N00014-98-1-0080. R. A. acknowledges support from the Frank Horton Graduate Fellowship Program.

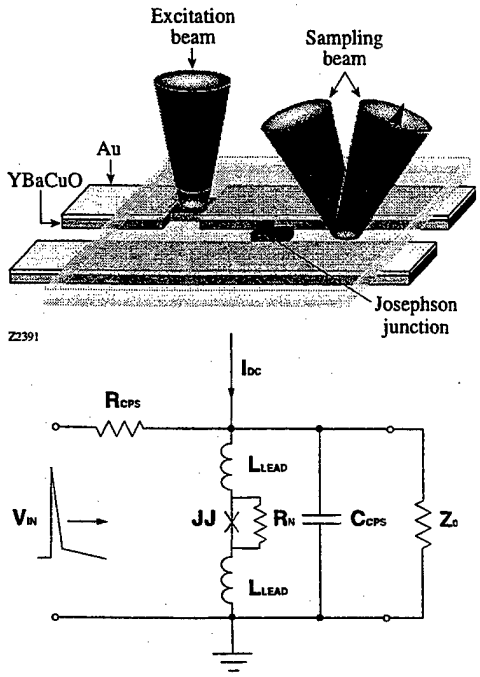

Fig 1. Experimental setup and equivalent circuit used in JSPICE simulations. $R_{CPS} = 80\ \Omega$, $Z_0 = 80\ \Omega$, $C_{CPS} = 12.5$ fF and $0 < L_{LEAD} < 10$ pH.

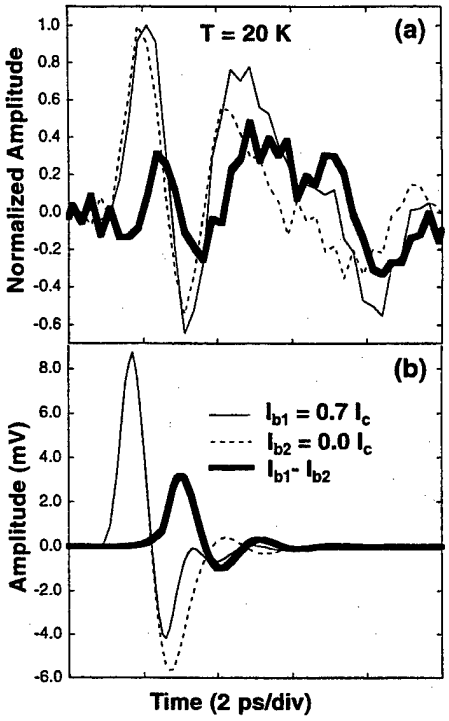

Fig 2. Experimentally measured response for 0 I_c and for 0.7 I_c junction bias (a) and JSPICE simulations for the same bias conditions (b).

bridge, while an 800-nm sampling beam monitored the electric field penetrating an EO ($LiTaO_3$) crystal during the electrical pulse propagation. The sampling beam was time delayed with respect to the excitation beam by a computer-controlled translation stage, directed in between the coplanar lines through the $LiTaO_3$ crystal less than 100 μm away from the junction, and reflected to the analyzer by a high reflectivity dielectric coating (see Fig.1). By varying the relative delay between photoresponse generation (excitation beam) and the signal probing (sampling beam), the whole time-domain waveform could be resolved.

The samples were mounted in a continuos-flow helium optical cryostat. All the experiments were carried out using current and voltage sources for the junction and the microbridge biasing.

III. Results and Discussion

The ~2 ps pulse with the amplitude equal to ~0.4 I_c, generated by microbridge photoexcitation, was applied to the junction and the resulting signal was EO detected approximately 50 μm after the junction (Fig 1). In order to elicit a junction response from the measured output, we biased our junction at zero I_c and +0.7 I_c and recorded the signal. Fig. 2(a) shows normalized transient responses from the junction at zero I_c (thin solid line), +0.7 I_c (dotted line) and the curve obtained as a subtraction of the zero I_c from the +0.7 I_c signal (thick solid line). We note that the initial, positive part of each response overlaps, while some differences are visible in the negative part.

Fig. 2(b) shows JSPICE simulations of the equivalent circuit (Fig. 1). The thin solid and dotted lines represent the circuit response for junction bias $I_b = 0.7\ I_c$ and for $I_b = 0\ I_c$, respectively. The thick solid curve has been obtained by subtracting the two above mentioned signals. Comparison of the experimental result with the simulation [Fig. 2(b)] shows that the experimental curve [Fig. 2(a)] obtained by signal subtraction indeed contains information about junction switching overlapped with response of the high-inductance junction leads. We note that at 20 K $I_cR_n \approx 2$mV, thus, the SFQ amplitude is expected to be ~ 4 mV, what leads to approx. 0.5-ps SFQ width, in good agreement with our observation.

Fig. 3 shows JSPICE simulations of the equivalent circuit for the zero lead inductance and for $L_{LEAD} = 2$ pH. $L_{LEAD} = 0$ pH case [Fig. 3(a)] illustrates an intrinsic response of the junction to the ~2 ps FWHM pulse, as well as junction turn-on delay dependence on the I_c overdrive. Junctions in all simulations were biased at 0.7 I_c. Fig. 3(b) shows response of the same junction connected to the circuit via 2 pH leads, for the similar values of I_c overdrive. Lead inductance is shown to cause substantial ringing as well as different dependence of the turn-on delay on the I_c overdrive (see also Fig. 4). For higher L_{LEAD}, junction turn-on delay changes only very little with I_c overdrive (Fig. 4); circuit response is dominated by junction-lead inductance.

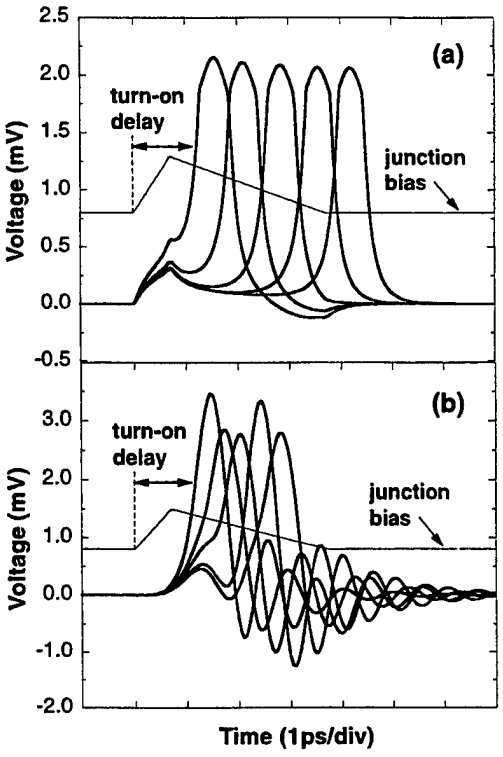

Fig 3. JSPICE simulations of the Josephson junction time-resolved response for L_{LEAD} = 0 pH (a) and for L_{LEAD} = 2 pH (b). In both cases junction I_C = 1 mA and current overdrive varied in 0.15 mA < δ < 0.4 mA range.

III. CONCLUSION

Picosecond electrical pulses, optically generated by voltage-biased YBCO microbridge, were used to switch a YBCO bicrystal Josephson junction placed in the superconducting coplanar transmission line. The measured transients (for 0.7 I_c junction bias) contained both junction response plus input signal due to the high lead inductances, but the junction response could be separated by subtracting the zero-bias signal from the 0.7 I_c signal. As a result, we were able to observe sub-picosecond switching of HTS Josephson junction, as well as to measure the junction turn-on delay time. Our results demonstrate that, by using EO sampling technique, it is possible to study in detail the characteristics of Josephson junction transient response. JSPICE simulations, based on the coplanar strip equivalent circuit, suggest the necessity for fabrication of structures with low-inductance Josephson junction leads for more direct observations of the junction dynamics.

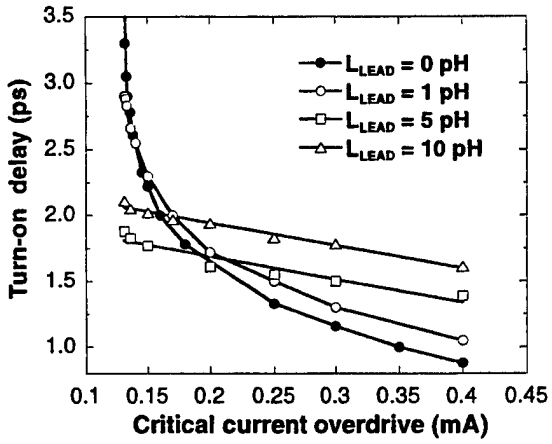

Fig 4. Josephson junction turn-on delay time as a function of junction critical current overdrive for different L_{LEAD}.

ACKNOWLEDGMENT

Authors thank Pavel Rott for junction lead inductance calculations.

REFERENCES

[1] S. H. Dong and T. Van Duzer, "Minimum-Width Control-Current Pulse for Josephson Logic Gates," *IEEE Trans. Electron. Dev.*, vol. ED-27, pp. 1965-1973, October 1980.

[2] D. G. McDonald, R. L. Peterson, C. A. Hamilton, R. E. Harris and R. L. Kautz, "Picosecond Application of Josephson Junctions," *IEEE Trans. Electron. Dev.*, vol. ED-27, pp. 1945-1965, October 1980.

[3] M. Darula and M. Kedro, "Dynamic Reduction of the critical current in a Josephson Junction," *J. Low Temp. Phys.*, vol. 78, May/June 1990.

[4] K. K. Likharev and V. K. Semenov RSFQ Logic/Memory family: "A new Josephson-Junction Technology for Sub-Terahertz-Clock-Frequency Digital Systems," *IEEE Trans. Appl. Supercon.*, vol. 1, pp. 3 - 28, March 1991.

[5] C.-C. Wang, M. Currie, D. Jacobs-Perkins, M. J. Feldman, R. Sobolewski, and T. Y. Hsiang, "Optoelectronic generation and detection of single-flux-quantum pulses," *Appl. Phys. Lett.*, vol. 66, pp. 3325-3327, June 1995.

[6] D. R. Dykaar, R. Sobolewski, T. Y. Hsiang, and G. A. Mourou, "Response of a Josephson junction to a stepped voltage pulse," *IEEE Trans. Appl. Magn.*, vol. MAG-23, pp. 767 - 770, March 1987.

[7] M. Lindgren, M. Currie, C. A. Williams, T. Y. Hsiang, P. M. Fauchet, R. Sobolewski, S. H. Moffat, R. A. Hughes, J. S. Preston and F. A. Hegmann, "$YBa_2Cu_3O_{7-\delta}$ Thin Film Picosecond Photoresponse in the Resistive State," *IEEE Trans. Appl. Supercon.*, vol. 7, pp. 3422-3425, June 1997.

[8] R. Adam, M. Curie, R. Sobolewski, O. Harnack, and M. Darula, "Picosecond response of optically driven Y-Ba-Cu-O microbridge and Josephson-junction integrated structures," *IEEE Trans. Appl. Supercon.*, in press.

Clock-Frequency and Temperature Margins of A High-Temperature Superconductor Delay-Line Memory

W. Hattori and S. Tahara
NEC Corp., 34 Miyukigaoka, Tsukuba, Ibaraki 305-8501, Japan

Abstract—We have developed a 10-GHz 32-bit delay-line memory, using a semiconductor crossbar switch and a $YBa_2Cu_3O_{7-\delta}$ coplanar delay line. For use in the high-speed (≥10 GHz) cell-buffer storage of large-throughput (≥1 Tbit/s) asynchronous transfer mode (ATM) switching systems, this memory must be fairly reliable. To evaluate the reliability of the operation, therefore, we measured the clock-frequency and temperature margins, and the temperature dependence of the bit-error rate. At 64 K, this memory has a capacity of 32 bits with a clock-frequency of 9.89±0.11 GHz. In general, clock-frequencies of communication systems are strictly managed so that the margins are less than 10^{-6}. Therefore, the frequency margin of this memory (~2×10^{-2}) is wide enough for use in communication systems. The temperature margin was 71.5±4.3 K at 10 GHz and 33 bits. This memory offered error-free operation (BER<10^{-13}) at 71.5±3.5 K. These temperature margins are wide enough to be controlled by a cryocooler. These results show that the memory offers reliability and that it can be applied to high-speed ATM cell-buffer storage.

I. Introduction

An asynchronous transfer mode (ATM) is a key technology for multimedia telecommunication networks. The rapid increase in telecommunication traffic demands large throughput over 1 Tbit/s for ATM switching systems by 2010 [1]. The maximum switching capacity reported to date for LSI-based ATM switching systems is 160 Gbit/s [2]. One limitation for expanding this switching capacity into Tbit/s order is the memory access speed of the semiconductor memory devices used in cell-buffer storage [3], [4]. Although the shift register is the fastest device in conventional semiconductor memory devices, the maximum clock frequency reported to date is no more than 3 GHz [4]. This is because the propagation delay time between the registers occupies the large part of the cycle time. Then, the shift registers operate several times slower than the single stage register used for retiming the data to the clock. On the other hand, combinational logic devices such as cross-point switching LSIs for routing ATM cells, operating with a clock frequency of 10 GHz, have already been reported [5].

Manuscript received April 30, 1999.

To overcome this speed restriction of the memory devices, we proposed using a superconductor delay-line memory as ATM cell-buffer storage [6]. This memory can store serial data in a storage loop consisting of a crossbar switch and a superconductor delay line. This memory has only a single register stage in a storage loop. Then, the loop delay is designed to produce the data length using analogue delay given by the superconductor delay line. Therefore, this memory can operate as fast as a single stage register and several times faster than the shift registers.

Recently, we have successfully developed a high-temperature superconductor delay-line memory [7]. This memory consisted of a 10-μm-wide 37-cm-long $YBa_2Cu_3O_{7-\delta}$ coplanar delay-line and a crossbar switch, which was discretely fabricated using 10-GHz GaAs MES-FET ICs. This memory operated as a 32-bit buffer memory with a clock-frequency of 10 GHz, with almost the same power dissipation as those of 4- or 5-bit shift registers. Accordingly, using this memory can break down the limitation of the memory access speed. Therefore, we have proposed using superconductor delay-line memories as high-speed ATM cell-buffer storage.

ATM switching systems, which handle large throughput over 1 Tbit/s, will be used in backbone network nodes. To apply them to the backbone network nodes, the ATM switching systems require fairy reliable operation. Then, the high-temperature superconductor delay-line memory also must be

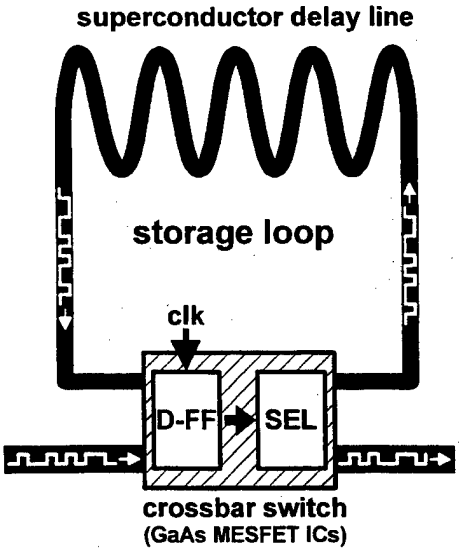

Figure 1 Superconductor delay-line memory.

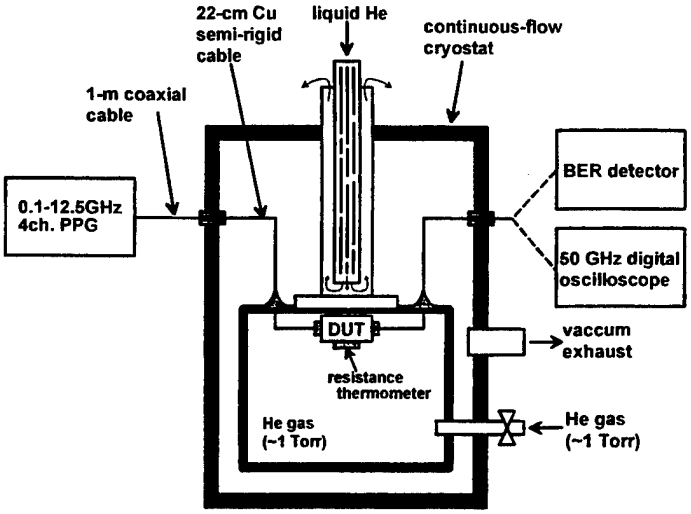

Figure 2 The measurement system.

reliable. To evaluate the reliability of the memory operation, we measured the frequency and temperature margins, and the temperature dependence of the bit-error rate (BER). In this report, we describe the experimental results of these measurements.

II. Origins of Clock-Frequency and Temperature Margins

The storage loop of the superconductor delay-line memory involves a single register (or delay flip-flop) stage for retiming the data to the clock, as shown in figure 1. This retiming operation quantizes the memory capacity. The tolerance of this quantization is decided by the phase margin of the register stage. If arrival timing of the data at the register is out of this phase margin after the circulation of the storage loop, the register falls into a meta-stable state and commits an error.

In this memory, the memory capacity is roughly given by the following equation.

(memory capacity)≈(loop delay)/(cycle time)
=(loop delay)×(clock frequency)

The delay time given by the delay line varies according to the temperature variation in the superconductor penetration depth. Then, the memory capacity varies depending on both the clock frequency and the operating temperature. The arrival timing of the data at the register also varies depending on both the clock frequency and the operating temperature. That is, the memory capacity has clock-frequency and temperature margins. Additionally, the bit-error rate of this memory also varies according to the variation of the operating temperature.

III. Results and Discuccion

The measurement system is illustrated in Figure 2. We used a liquid He continuous–flow cryostat, a 4-channel 0.1-12.5-GHz pulse pattern generator, a BER detector, a 50-GHz digital-sampling oscilloscope, and so on. While measuring the BER, we fixed the voltage threshold level to –0.45 V, which is a midpoint of the source-coupled FET logic level used in the GaAs ICs (V_H=0 V, V_L=-0.9~1.0 V). Temperature measurement was carried out using a resistance thermometer fixed on a outside wall of the package.

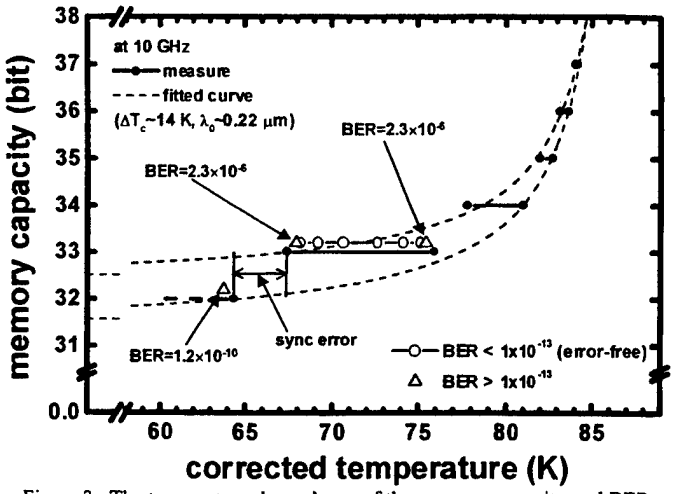

Figure 3 The temperature dependence of the memory capacity and BER.

A. Operating Temperature margin

The temperature dependence of the memory capacity is shown in Figure 3. Since the GaAs ICs inside the package heated up, the measured temperature was lower than the device temperature. Then, we corrected the measured temperature by fitting the temperature dependence of the memory capacity, according to the following equation,

$$\frac{C(T_2)}{C(T_1)} \approx \frac{\tau(T_1)}{\tau(T_2)} = \frac{v(T_1)}{v(T_2)} = \sqrt{\frac{L_{ex} + L_k(\lambda(T_2))}{L_{ex} + L_k(\lambda(T_1))}}$$

where C is memory capacity, T is temperature, τ is delay time, v is phase velocity, L_{ex} is external inductance, L_k is kinetic inductance, and λ is penetration depth. The same expression $L_k(\lambda)$ in reference [8] is used. The empirical temperature dependence of λ is used as follows: $\lambda(T)=\lambda_0/(1-(T/T_c)^2)^{1/2}$. The parameter λ_0 is 0.22 μm, and the temperature difference is 14 K. As shown in Fig. 3, the temperature range of the normal operation decreases as the temperature increases, according to the temperature dependence of the penetration depth. The temperature range with the memory capacity of 33 bits at 10 GHz is 71.5±4.3 K.

B. Temperature Dependence of BER

The GaAs ICs used in this memory offer error free operation (BER<1×10^{-13}) at room temperature. While the crossbar switch takes a parallel-connection state, this memory also offers error-

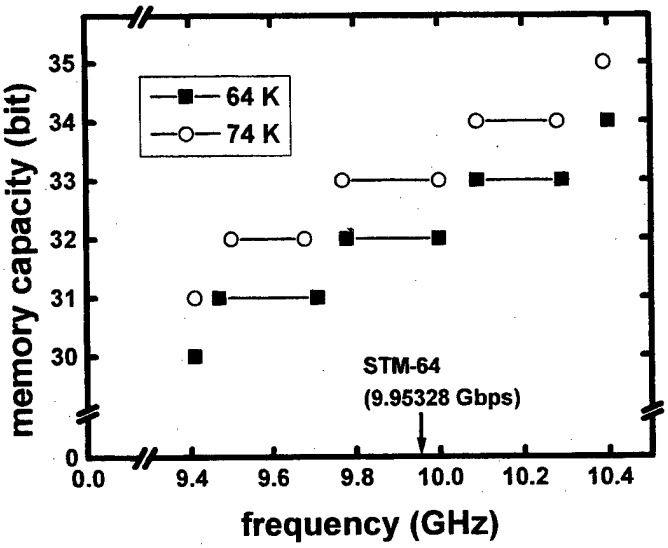

Figure 4 The clock-frequency dependence of the memory capacity.

free operation (BER<1×10^{-13}) at any measured temperature, i.e., at room temperature and between 50 and 100 K. This is because there is no superconductor delay line in the data path and the GaAs ICs are successfully implemented on the module. On the other hand, while the crossbar switch takes cross-connection state, the BER value shows temperature dependence as shown in Fig. 3. The BER could not measure without the operating temperature margins because it was out of synchronization. Additionally, the BER increased at the edges of the temperature margins. The error-free operation was still observed with the temperature of 71.5±3.5 K. This temperature margin is wide enough to be controllable by a cryocooler.

C. Clock-Frequency Margin

The clock-frequency dependence of the memory capacity is shown in Fig. 4. As the frequency increases, the memory capacity increases. At the temperature of 64 K, this memory has a capacity of 32 bits with a frequency of 9.89±0.11 GHz. In general, clock frequencies of communication systems are strictly managed so that the margins are less than 10^{-6}. For example, the clock frequency of 9.95328 GHz used in STM-64 indicated in Fig. 4 is pinpoint in comparison with the clock-frequency margin of this memory. Therefore, the frequency margin (~10^{-2}) of this memory is wide enough for use in communication systems. These results show that the superconductor delay-line memory offers reliable operation and that it can be applied to high-speed ATM cell-buffer storage.

IV. Conclusion

To evaluate the reliability of the high-temperature superconductor delay-line memory, we measured clock-frequency and temperature margins, and the temperature dependence of the BER. The memory capacity increased as the clock frequency increased and as the operating temperature increased. The temperature range with the memory capacity of 33 bits at the clock frequency of 10 GHz was 71.5±4.3 K. In this temperature range, we observed error-free operation (BER<1×10^{-13}) at 71.5±3.5 K. This temperature margin is wide enough to be controllable by a cryocooler. At 64 K, this memory had a capacity of 32 bits with a frequency of 9.89±0.11 GHz. This frequency margin (~10^{-2}) is also wide enough for use in real communication systems. These results show the reliable operation of the superconductor delay-line memory. We, therefore, confirm that the high-temperature superconductor delay-line memory can be applied to the high-speed ATM cell-buffer storage.

REFERENCES

[1] T. Koinuma, and N. Miyaho, "ATM in B-ISDN communication systems and VLSI realization," *IEEE J. Solid-State Circuits*, vol. 30, pp. 341-347, 1995.

[2] H. Yamada and Y. Doi, "A 160 Gb/s large capacity ATM switching system using dynamic link speed controlled switch architecture," *Globecom '93*, vol. 5, pp. 24-28, 1993.

[3] Y. Watanabe, Y. Nakashima, Y. Kato, K. Odani, and M. Abe, "A 9.6-Gb/s HEMT ATM switch LSI with event-controlled FIFO," *IEEE J. Solid-State Circuits*, vol. 28, pp. 935-940, 1993.

[4] H. Yamada, M. Tsunotani, F. Kaneyama, and S. Seki, "20.8 Gb/s GaAs LSI's self-routing switch for ATM switching systems," *IEEE J. Solid-State Circuits*, vol. 32, pp. 31-37, 1997.

[5] K. S. Lowe, "A GaAs HBT 16×16 10 Gb/s/channel crosspoint switch," *IEEE J. Solid-State Circuits*, vol. 32, pp. 1263-1268, 1997.

[6] W. Hattori, T. Yoshitake, and S. Tahara, "Fabrication of a 5-μm-wide YBCO coplanar delay line," in *Advances in Superconductivity IX*, S. Nakajima and M. Murakami, Eds. Tokyo: Springer-Verlag, 1997, pp.1319-1322.

[7] W. Hattori, T. Yoshitake, and S. Tahara, "A reentrant delay-line memory using a $YBa_2Cu_3O_{7-\delta}$ coplanar delay-line," *Proc. of the ASC' 98*, to be published in *IEEE Trans. Appl. Supercond.*

[8] W. Rauch, E. Gornik, G. Sölkner, A. A. Valenzuela, F. Fox, and H. Behner, "Microwave properties of $YBa_2Cu_3O_{7-x}$ thin films studied with coplanar transmission line resonators," J. Appl. Phys. Vol. 73, pp. 1866-1872, 1993.

Characteristic Analysis of Single Electron Transistor made by Double Unit Cell of $YBa_2Cu_3O_7$

J. Guo, J.F. Jiang and Q.Y. Cai

(Microelectronics Research Center, Shanghai Jiao Tong University, Shanghai, 200030, P.R.China.)

Abstract - It has been suggested that the planar crystal structure of high T_c materials may be utilized to fabricate single-electron devices. We calculate the quasiparticle tunneling conductance of junctions for single electron transistor made by double unit cell of $YBa_2Cu_3O_7$ (YBCO-SET). The source drain I-V characteristics and transfer I-V characteristics of YBCO-SET are obtained. We also discuss the operation voltage, speed and temperature of the proposed device.

I. Introduction

It is widely known that high T_c materials have stacking structures of strongly and weakly superconducting layers. In a previous work, Miller et al. suggested that such structure may naturally provide ultrasmall capacitors necessary for single electron tunneling. They measured the tunneling current as a function of applied voltage on $TlBa_2(Ca_{0.8}Y_{0.2})Cu_2O_7$ thin film at 10K and attributed the staircases in the observed I-V curves to single electron tunneling.[1][2] Later, it is suggested that the layered structure of $YBa_2Cu_3O_7$ may be used to fabricate single electron transistor. A rough estimation of junction parameters showed the feasibility of such device.[3]

In previous works, the tunneling resistance of junctions was approximated by the ohmic resistance of $R = \rho l/S$. In the present research, the resistance is calculated on the basis of a tunneling model. We consider only the quasiparticle tunneling current, neglecting the Josephson current, resonant tunneling of Copper pairs, Andreev reflection and cotunneling. We calculate the source drain I-V characteristics and transfer I-V characteristics of YBCO-SET. We also present the operation voltage, temperature and speed of the device, which are dependent on the junction area.

II. Basic Relations

The structure of YBCO-SET is shown schematically in Fig. 1. The two junctions of YBCO-SET are identical and formed

Manuscript received April 30,1999.

This work was supported by the National Natural Science Foundation of China and the R&D Foundation of Science and Technology of Shanghai..

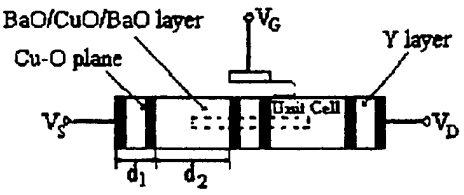

Fig. 1. The layered structure of $YBa_2Cu_3O_7$ may be used to fabricate single electron transistor. The c-axis unit cell dimension is 1.1673 nm and the inter-planar spacings are d_1=0.2843nm and d_2=0.883nm.

by tunneling between Cu-O planes through BaO/CuO/BaO layer. The junction capacitance of YBCO-SET is given by:

$$C = \frac{\varepsilon_0 \varepsilon_r S}{d} \tag{1}$$

where $\varepsilon_r = 5$ is the dielectric constant for BaO/CuO/BaO layer, S is the junction area and d is the tunneling barrier width.

To achieve a voltage gain of K_V, the gate capacitance should be[4]:

$$C_G = K_V C \tag{2}$$

So the total capacitance of the central island is:

$$C_T = (K_V + 2)C \tag{3}$$

The operation voltage between source and drain, which is twice the Coulomb blockade voltage of a junction, is given by

$$V_{op} = e/C_T + 2E_g/e = e/C_T + 4\Delta/e \tag{4}$$

where $E_g = 2\Delta$ is the superconducting energy gap.

To keep YBCO-SET works in the superconducting state and the thermal energy at least an order of magnitude lower than the charging energy, the maximum operation temperature is:

$$T_{max} = \min(T_C, 0.1\frac{e^2}{2k_B C_T}) \quad (5)$$

When the Josephson coupling energy, $E_J = \pi\hbar\Delta/2e^2R$, where Δ is the superconducting coupling energy, is smaller than kT, the Josephson current is negligible compared to the quasiparticle tunneling current. So the minimum operation temperature is expressed as:

$$T_{min} = \pi\hbar\Delta/2e^2Rk_B \quad (6)$$

The tunneling current in the junction is the function of voltage across the junction as follows:

$$I_{SS} = A\int_{-\infty}^{\infty} N_S(E-eV)N_S(E)[f(E-eV) - f(E)]dE \quad (7)$$

where $f(E)$ is the Fermi-Dirac function , A is a constant related to the nature of the junction and $N_S(E)$ is the superconducting density of states which is given by:

$$N_S(E) = \begin{cases} \frac{|E-E_F|}{\sqrt{(E-E_F)^2-\Delta^2}} D_0 & |E-E_F|>\Delta \\ 0 & |E-E_F|<\Delta \end{cases} \quad (8)$$

where E_F is the Fermi energy level and D_0 corresponds to a constant approximating the density of states for normal metal. Equation(7) can be expressed as:

$$I_{SS} = I_{NN}\left[(1+\frac{2\Delta}{eV})E(a) - 4\frac{\Delta(\Delta+eV)}{eV(2\Delta+eV)}K(a)\right] \quad (9)$$

where

$$E(a) = \int_0^1 \frac{(1-a^2t^2)^{1/2}}{(1-t^2)^{1/2}}dt$$

$$K(a) = \int_0^1 \frac{dt}{(1-t^2)^{1/2}(1-a^2t^2)^{1/2}}$$

$$a = \frac{eV-2\Delta}{eV+2\Delta}$$

and I_{NN} is the current in the corresponding normal state junction, which is derived by Simmons using WKB approximation[4][5]:

$$I_{NN} = \frac{Se}{2\pi hd^2}\{(\phi_0 - \frac{eV}{2})\exp[-A(\phi_0 - \frac{eV}{2})^{1/2}] - (\phi_0 + \frac{eV}{2})\exp[-A(\phi_0 + \frac{eV}{2})^{1/2}]\} \quad (10)$$

where

$$A = \frac{4\pi d(2m)^{1/2}}{h}$$

Here, m is the electron mass, h is the Planck' s constant

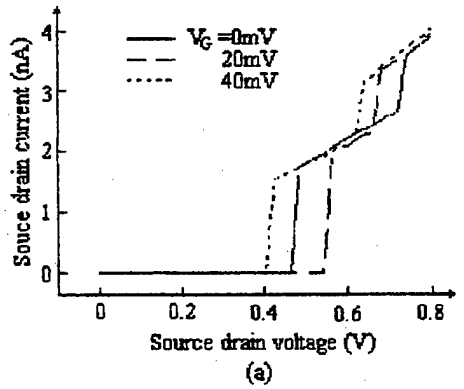

(a)

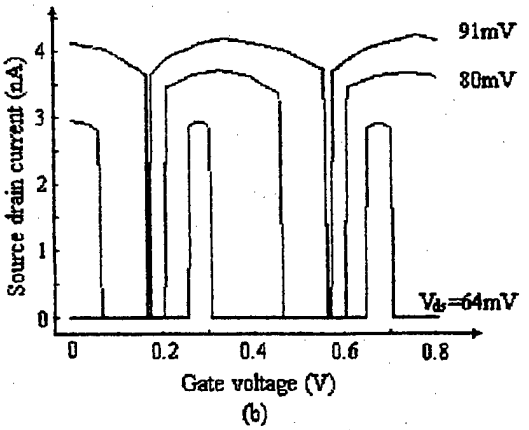

(b)

Fig. 2. The I-V curves of YBCO-SET for (a) the source drain characteristics (b) the transfer characteristics. Here, the background charge is Q_0=0, operation temperature is 18K, junction area is 25nm^2, E_g=30 meV is the superconducting energy gap for $YBa_2Cu_3O_7$ along C-axis and the tunneling barrier height is 0.8eV.

and ϕ_0 is the rectangular tunneling barrier height.

The junction conductance is obtained by differentiating (8) when the voltage across the junction is $V_{OP}/2$:

$$G = dI_{SS}/dV|_{V=Vop/2} \quad (11)$$

The maximum operation frequency is given by:

$$f_{max} = G/C \quad (12)$$

III. Simulation Results

The junction capacitance and conductance can be calculated from (1) and (11) after the junction area is given. The gate capacitance is found from (2) assuming $K_V = 2$. With these device parameters, I-V curves of YBCO-SET are obtained as shown in Fig. 2. using MOSES[6].

From topographical data collected by STM, the junction area ranges from 1 nm^2 to 100 nm^2, with the typical value of 25 nm^2.[2] The dependence of the operation voltage, temperature and the maximum operation frequency on the junction area can be found from (4)-(6), (12) and is shown in Fig. 3.

IV. Discussion

We have made following observations. Firstly, both the source drain I-V curves and the transfer I-V curves show several jumps, which are due to the superconducting energy gap. So the charge sensitivity of YBCO-SET can be much higher than similar SET made of normal metals. Secondly, reducing the junction area would improve the performance of YBCO-SET. For example, higher operation voltage, speed and temperature could be achieved. Thirdly, the layered high T_C materials can be used to fabricate other practical circuit devices based on single-electron tunneling, such as 1-D array, turnstile and trap.

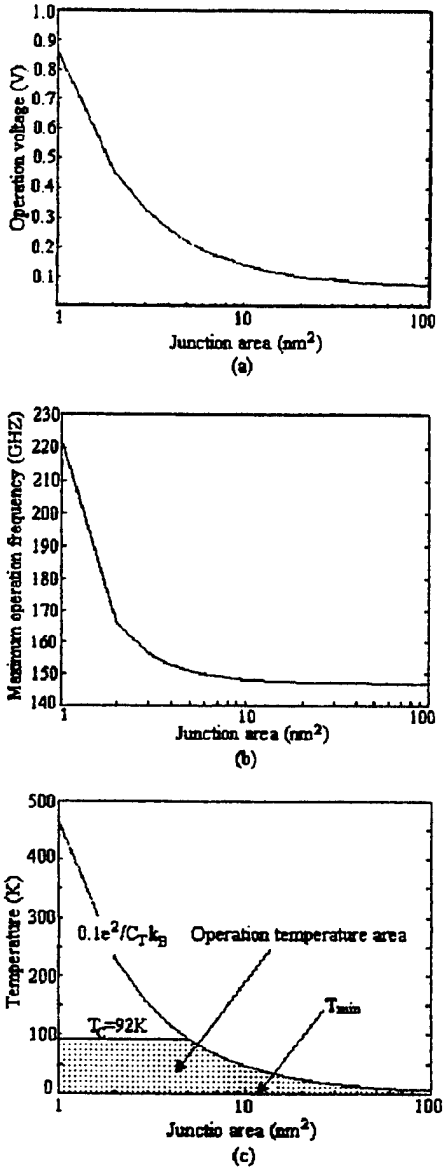

Fig. 3. (a) The operation voltage versus junction area (b) The maximum operation frequency versus junction area (c) The operation temperature versus junction area.

References

[1] T.G.Miller, R. Reifenberger and M. McElfrensh, "Single Electron Tunneling in $TlBa_2(Ca_{0.8}Y_{0.2})Cu_2O_7$ Thin Films at 10K," J. Low. Temp. Phys. vol. 94, pp. 239, 1994

[2] T.G.Miller and R. Reifenberger, "Three-tunnel-capacitor mode for single-electron tunneling in layered thin films," Phys. Rev. B , vol.50, no.5, pp.3342, 1994

[3] J.F.Jiang Q.Y.Cai B.Shen and M.Z.Tong, "Feasibility of a new type of Single Electron Tunneling Transistor (SETT) made of High T_c Superconductor," Physica C, vol. 282-287, pp. 2505-2506, 1997

[4] John. G. Simmons, "Generalized Formula for the Electric Tunnel Effect between Similar Electrodes Separated by a Thin Insulating Film," Journal of Applied Physics, vol. 34, no. 6, pp. 1793, 1963

[5] M.I.Lutwyche and Y.Wada, "Estimat of the ultimate performance of the single-electron transistor," J. Appl. Phys. vol. 75, no. 7, pp. 3654-3661, 1994

[6] MOSES, Monte Carlo Single-Electronics Simulator, 1995 available from R.Chen (rchen@fix.physics.sunysb.edu)

Reduction of Power Consumption of RSFQ Circuits by Inductance-Load-Biasing

Nobuyuki Yoshikawa and Yohsuke Kato
Division of Electrical and Computer Engineering, Yokohama National University
Tokiwadai 79-5, Hodogaya-ku, Yokohama, 240-8501, Japan

Abstract–We will propose an inductance-load-biasing method in order to reduce power consumption of Rapid Single Flux Quantum (RSFQ) logic circuits. The main idea is coming from the fact that a current source can be made of a large inductor accompanied with a large flux. In our proposal, the current source is composed of a large inductor L_b, a small resistor R_b and a small voltage source V_b. Computer simulations of inductance-load-biased Josephson transmission lines (JTL) show that an SFQ pulse propagates correctly when L_b is large enough even if R_b is very small. In order to implement the inductance-load-biased JTL, we have made two different layouts: one uses a large bias inductor L_b of a typical stripline structure on a ground plane which occupies rather large area, the other uses L_b in the shape of a coplanar stripline which costs smaller area.

I. Introduction

Rapid Single Flux Quantum (RSFQ) integrated circuit technologies have great potentialities as future VLSI key technologies in the area where the extreme performance is essential because of their high performance with clock frequency beyond hundreds of gigahertz and low power consumption [1]. Especially, extremely low-power consumption in the RSFQ circuits is very important because usually the power consumption per gate puts the upper limit on the number of the gate on a single chip. This high performance is due to the fact that the energy necessary for an SFQ pulse to propagate the Josephson transmission line (JTL) is only the order of 10^{-19} J per gate for the helium temperature operation.

At present, however, almost RSFQ circuits are usually driven by constant current sources which consist of an off-chip voltage source and bias resistors integrated on the chip. Typical power consumption at these biasing circuits is of the order of 10^{-7} W/gate for the helium temperature. Although this value is still small for the integrated circuits of small or medium scales, it might be problem in the RSFQ VLSI of large integration density containing more than 10^8 gates per chip.

In this study, we will propose an inductance-load-biasing method in order to reduce power consumption of RSFQ logic circuits. The main idea is coming from the fact that a current source can be made of a large inductor accompanied with a large flux. Based of this idea, the bias-resistor networks can be replaced by large bias-inductor networks accompanied with a superconducting current. The main problem in this circuit is the existence of large superconducting loops which might gain large magnetic flux trapping. In our proposal, the constant-current-biasing circuit is composed of a large inductor L_b, a small resistor R_b and a small voltage source V_b. Large superconducting loops are eliminated in our case.

We have investigated the propagation characteristics of an SFQ pulse on the inductance-load-biased JTLs, and considered the parameter conditions for the proper propagation. We have also laid-out the inductance-load-biased JTL by two manners and compared the cost of the area.

Manuscript received April 30, 1999.

II. Inductance-Load-Biased JTL

Figure 1a depicts a typical JTL circuit which is biased by a constant-current source composed of a bias resistor R_b and a voltage source V_b [1], [2]. Because a critical current I_c has to be larger than 100 μA for the helium-temperature operation in order to prevent thermal errors, the static power consumption on R_b is of the order of 10^{-7} W, assuming V_b is of the order of 1 mV. Further reduction of the value of V_b is impossible to maintain a constant-current source.

Figure 1b shows a JTL which is biased by a constant-current source proposed in this study. The circuit is composed of a large bias inductor L_b, a bias resistor R_b and a voltage source V_b. As will be shown later, V_b can be reduced further if L_b is large enough. Note that there is no

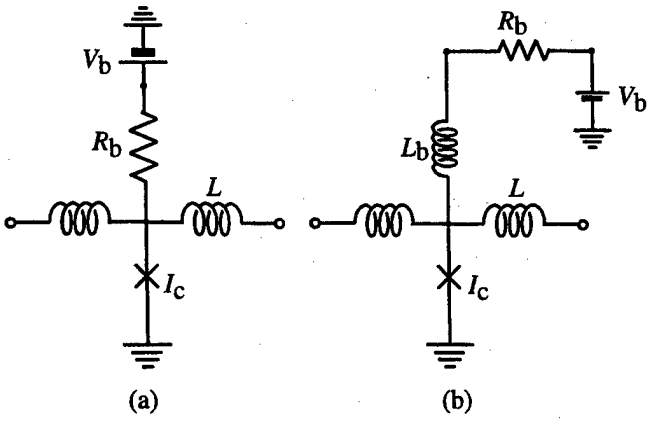

Fig. 1 (a) A resistance-load-biased JTL, and (b) an inductance-load-biased JTL.

superconducting loops at the biasing circuit because a small R_b of the order of V_b/I_C is included in the circuit.

Figure 2 shows SPICE simulations of an SFQ pulse propagating on the inductance-load-biased JTL for different bias-circuit parameters. In calculations, we assume that the JTL consists of fifty stages of two-junction-JTL cells. Plots show junction voltages at every five JTL cells. In these two examples, V_b and hence the power consumption are about one order smaller than those of the typical resistance-load-biased two-junction-JTL cells (2.5 mV and 0.875×10^{-6} W in our case). By observing two plots, one can see that pulse voltages are smaller and the propagation delay is larger for the JTL with a smaller L_b. The global dc bias margins of these JTLs are -32% ~ +42% for L_b = 10 pH and -50% ~ +42% for L_b = 500 pH, whereas that of the typical resistance-load-biased JTL is -48% ~ +42%.

Figure 3 shows the delay time and the voltage amplitude of an SFQ pulse propagating on the inductance-load-biased JTLs as a function of bias inductance L_b for various values of R_b. It can been seen that the delay time and the pulse amplitude are deteriorated considerably when L_b is lower than 20 pH if R_b is small.

This condition for L_b can be derived from the following simple consideration. Let's suppose the bias circuit shown in Fig. 1b. If the propagation time of the SFQ pulse through the Josephson junction is much smaller than the time constant L_b/R_b, the total current going through the inductor L_b during

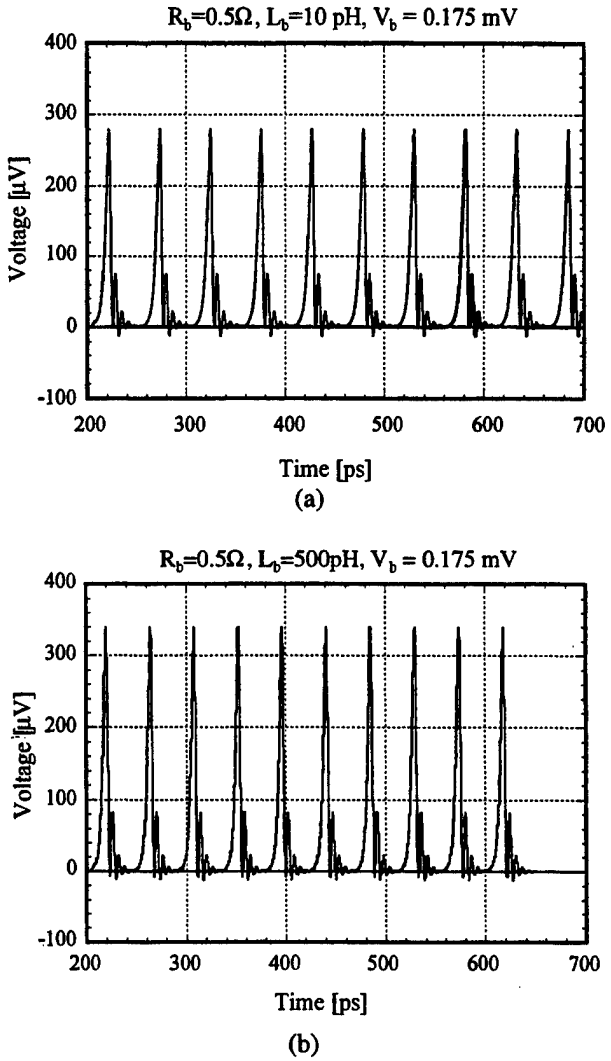

Fig. 2 Propagation of an SFQ pulse on the inductance-load-biased JTL. We assumed that a JTL is composed of fifty stages of two-junction JTL cells. In the figure, junction voltages at every five JTL cells are plotted. (a) R_b=0.5 Ω, L_b = 10 pH, V_b = 0.175 mV (b) R_b= 0.5 Ω, L_b = 500 pH, V_b = 0.175 mV. Circuit parameters of the JTL: I_C = 250 μA, L = 3.6 pH.

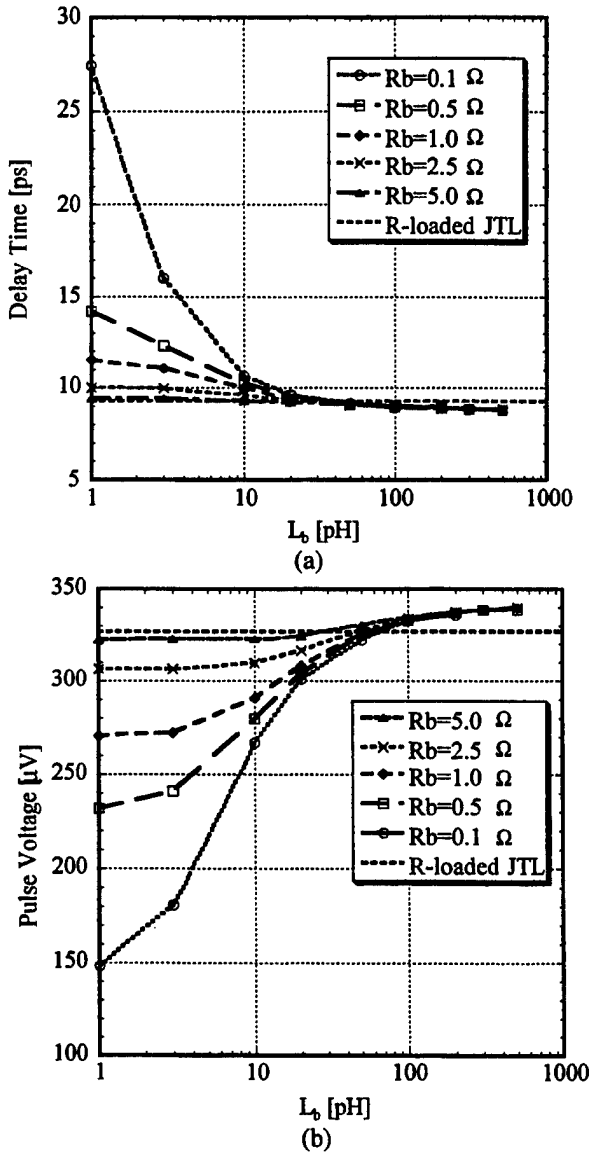

Fig. 3 (a) The delay time and (b) the pulse voltage of an SFQ pulse propagating on the inductance-load-biased JTL as a function of bias inductance L_b for various values of R_b. We assumed that a JTL are composed of fifty stages of two-junction-JTL cells. Broken lines indicates the delay time and the pulse voltage for the resistance-load-biased JTL.

the passage of an SFQ pulse is given by

$$i = (L_b)^{-1} \int v dt = (\Phi_0/L_b).$$

For the correct operation of the JTL, this current has to be much smaller than the critical current I_c,

$$(\Phi_0/L_b) << I_c.$$

Considering the typical condition for JTL parameters, $I_cL \approx \Phi_0/2$, we get the following condition for L_b:

$$L_b >> 2L.$$

For our parameters of the JTL, $2L_b$ equals to 7.2 pH.

III. Implementation of Inductance-Load-Biased JTL

We have laid-out the inductance-load-biased JTL in two manners assuming the HYPRES standard Nb process. Two examples of layout patterns for the two-junction-JTL cells are shown in Fig. 4. From the simulation results in Fig. 3, we chose L_b = 20 pH. The first layout uses a typical stripline structure on a ground plane to realize a large inductance (see Fig. 4a). The dimension of the cell is about 96 μm × 85 μm, which is somewhat larger than the resistance-load-biased JTL (70 μm × 85 μm in our case). The other layout uses a coplanar stripline as a inductance (see Fig. 4b), where we assume an inductance value per unit length is about 0.5 pH/μm [3]. In this case, the area of JTL is about 79 μm × 85 μm, which is almost same to that of the resistance-load-biased JTL.

IV. Conclusion

We have proposed an inductance-load-biasing method in order to reduce power consumption of RSFQ logic circuits. It was shown that static power consumption at the biasing circuit can be reduced by inserting a large bias inductance. The SPICE simulations showed that the propagation characteristics of the SFQ pulse are not degenerated if the bias inductance is large enough. We have also laid-out the inductance-load-biased JTL and shown that they can be implemented without reducing the integration density by using the coplanar type inductor.

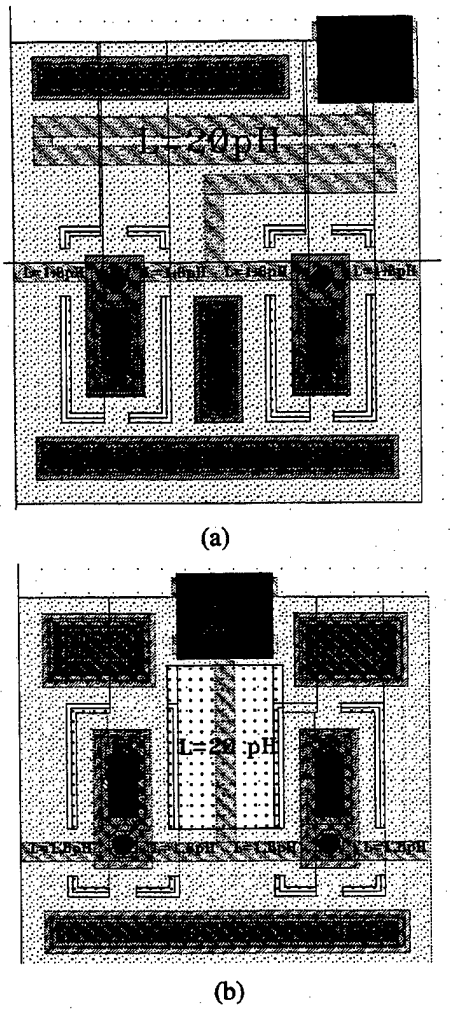

Fig. 4 Examples of mask layouts of the inductance-load-biased JTL. (a) A JTL loaded by an inductor L_b = 20 pH of a typical stripline structure. (b) A JTL loaded by an inductance L_b = 20 pH of a coplanar stripline structure.

References

[1] K. K. Likharev and V. K. Semenov, "RSFQ logic/memory family: A new Josephson-junction technology for sub-terahertz-clock frequency digital systems," IEEE Trans. Appl. Superconductivity, vol. 1, pp. 1-28, March, 1991.

[2] V. K. Kaplunenko, M. I. Khabipov, V. P. Koshelets, K. K. Likharev, O. A. Mukhanov, V. K. Semenov, I. L. Serpuchenko, and A. N. Vystavkin, "Experimental study of the RSFQ logic elements," IEEE Trans. Msagnetics, vol. 25, pp. 861-864, March, 1989.

[3] K. Yoshida. M. S. Hossain, T. Kisu, K. Enpuku and K. Yamafuji, "Modeling of Kinetic-Inductance Coplanar Stripline with NbN Thin Films," Jpn. J. Appl. Phys. vol. 31, pp.3844-3850, December, 1992.

Optimization of RSFQ Circuits Based on Monte Carlo Yield Analysis

Nobuyuki Yoshikawa and Kaolu Yoneyama
Division of Electrical and Computer Engineering, Yokohama National University
Tokiwadai 79-5, Hodogaya-ku, Yokohama 240-8501, Japan

Abstract--We have developed a parameter optimization tool for RSFQ circuits, MJSIM, based on Monte Carlo yield analysis. MJSIM can generate a number of net lists for JSIM, where all parameter values are varied randomly according to the Gaussian distribution function, so that the circuit yields are automatically calculated. MJSIM can also generate an improved parameter vector using the algorithm of the center-of-gravity method. In this algorithm, an improved parameter vector is derived by calculating the average of parameter vectors inside the operating region. For the speed up of the optimization process, we continuously increased the standard deviation in the parameter distribution during the calculation. As a case study, we have optimized circuit parameters of an RS flip-flop.

I. Introduction

Rapid single flux quantum (RSFQ) integrated circuits are being developed extensively because of their potentially high performance with high clock frequency and extremely low power consumption [1]. Although some degree of the integration scale of RSFQ circuits have been successfully implemented [2], for a further increase of the integration scale, development of circuit optimization tools is strongly required, because the circuit includes nonlinear circuit elements, Josephson junctions, whose gain is not so large.

So far, several methods for the optimization of the RSFQ circuits have been investigated [3]-[8]. The method by improving the critical margin while all other parameter are held at their nominal values are widely used because of its low computational cost [3], [4]. It was demonstrated that the method of inscribed hyperspheres [5] is effective for the small scale of RSFQ circuits as long as the shape of the operating region is convex. Above all, the design centering method based on Monte Carlo yield analysis [6] - [8] is thought to be most effective, because it can be used even if the operating region is not convex and the circuit scale is somewhat large.

In order to observe the properties of the operating region of the RSFQ circuits, we plot the operating region of an RS flip-flop [1] in a two-dimensional space as shown in Fig. 1, where two parameters in the circuit were changed randomly according to the Gaussian distribution function. Each point on the graph corresponds to a set of circuit parameters. Small dots indicate the circuit parameters for the correct operation, whereas large dots indicate those for the filed operation. Though this is a two dimensional case, one can observe that the shape of the operating and non-operating region is very complicated. This means that the optimization method by determining the edge of the operation margin might be difficult.

Manuscript received April 30, 1999.

We have developed a parameter optimization tool for RSFQ circuits, MJSIM, based on Monte Carlo yield analysis. MJSIM can generate a number of circuit parameter sets whose values are varied randomly according to the Gaussian distribution function, and calculates the circuit yields automatically. It also generate an improved circuit parameter set using the algorithm of the center-of-gravity method. As a case study, we will optimized the circuit parameters of the RS flip-flop.

II. Yield Analysis and Optimization Method

In order to simulate the theoretical yield of the RSFQ circuits, the MJSIM generates a number of net lists for JSIM [9], where all parameter values in the circuit, i.e. the critical current I_c, the resistance R and the inductance L, are varied randomly similar to the parameter variations due to the fabrication process. For each set of the circuit parameters, MJSIM determines whether a circuit operates correctly or not and calculates the theoretical circuit yield. In the calculation, we assume two kinds of parameter variations [7]; one is global spread and the other is local spread. The global spread reflects the wafer-to-wafer change of the parameters, where all the parameter values of the similar circuit elements are offset at the same time. The local spread represents the component-to-component change of the

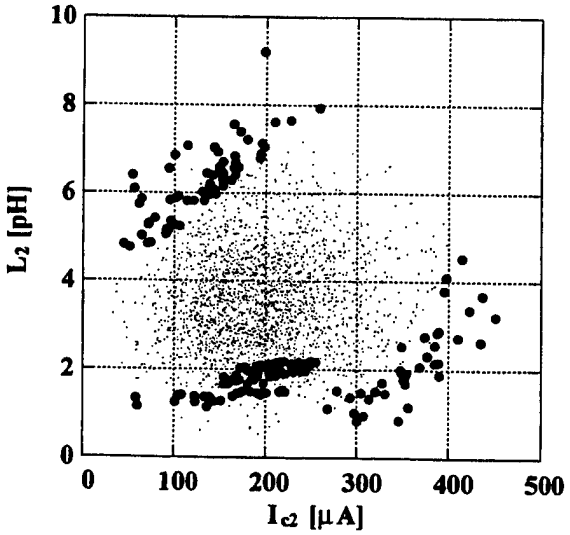

Fig. 1 The operating region of an RS flip-flop plotted in a two-dimensional space. Two circuits parameters (I_{c2} and L_2 in Fig. 3a) were changed randomly according to the Gaussian distribution function. Small dots indicate circuit parameters for the correct operation, whereas large dots indicate those for the filed circuit.

circuit parametersm, where all parameter values in the circuit are varied randomly.

We use the center-of-gravity method (CGM) [6] to improve the circuit yield. The optimization procedure in this method is depicted in Fig. 2 for two dimensional case. In the figure, $\mathbf{O}_M$ represents the nominal center of the circuit parameters at M-th iteration. A circle with center at $\mathbf{O}_M$ represents a 3σ-spread region for the parameter distribution. $\mathbf{G}_{PM}$ and $\mathbf{G}_{FM}$ are averaged vectors concerning with the passed and failed circuit parameter sets, respectively. According to the CGM, an improved parameter vector is given by

$$\mathbf{O}_{M+1} = \mathbf{O}_M + \lambda (\mathbf{G}_{PM} - \mathbf{G}_{FM}),$$

where $\lambda = 1 - N_P/N$. N_P and N are the number of passed circuits and the total number of the Monte-Carlo sampling, respectively.

III. Optimization of RS Flip-Flop

As a case study, we have optimized circuit parameters of an RS flip-flop using the MJSIM. The circuit diagram of the RS flip-flop is shown in Fig. 3a, which has set (S) and reset (R) inputs and an output (F). Though the circuit has nine parameters to be optimized, the critical current I_3 was fixed at the optimization process this time to prevent a global shift of the circuit parameters. Several stages of Josephson transmission lines were connected to the input and output terminals. Figure 3b shows a test pattern for the yield analysis where all the circuit functions were tested. Note that the MJSIM only checks the order of the SFQ pulses arriving at each terminal when judging the circuit operation.

Figure 4 shows development of the circuit yield and changes of circuit parameters during eighty optimization steps. In the yield analysis, 3σ parameter spreads are set to $3\sigma_{global} = 50\%$ and $3\sigma_{local} = 50\%$, and 500 Monte-Carlo samplings were performed to determine the circuit yield. It can be seen from fig. 4a that the circuit yield rapidly increases after a few initial optimization steps, and after that it gradually increases. Observation of fig. 4b-d shows that a few parameters still continue to change even after the yield and the other parameters are reached to their final value. After the eighty optimization steps, a global bias voltage margin has been increased from (-0% ~ +0%) to (-45% ~+34%).

The dependence of the final palameter values on the initial parameter values indicates that sufficiently large 3σ spread has to be used in order to obtained the consistent results for the different initial conditions. We also examined the dependence of the optimization process on the number of the Monte-Carlo sampling in the range from 50 to 1000, and found that optimization was correctly performed even for the 50 Monte-Carlo sampling, though the optimization speed is small and scattering in the yield analysis is large.

According to the theorem of the Monte-Carlo integration, the efficiency of the Monte-Carlo calculation is most effective when the yield is near 50% [8]. In order to increase the efficiency of the Monte-Carlo yield analysis, we continuously increased the 3σ spread by an increment of 5% so that the estimated yield always becomes lower than 60%. The dependence of the yield on the optimization steps is shown in Fig. 5, where the 3σ spreads are varied from 50% to 60% during optimization. Using this method we could obtained the final results after 25 optimization steps. After this optimization, a global bias voltage margin has been increased from (-0% ~ +0%) to (-44% ~+38%).

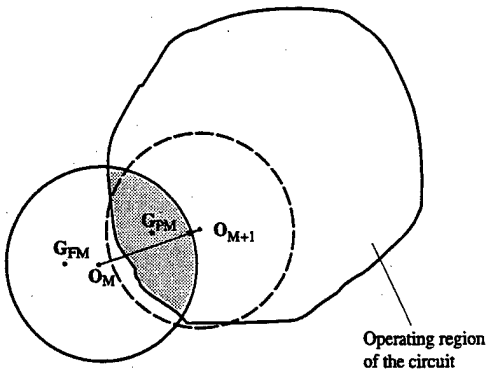

Fig. 2 The optimization procedure by the CGM.

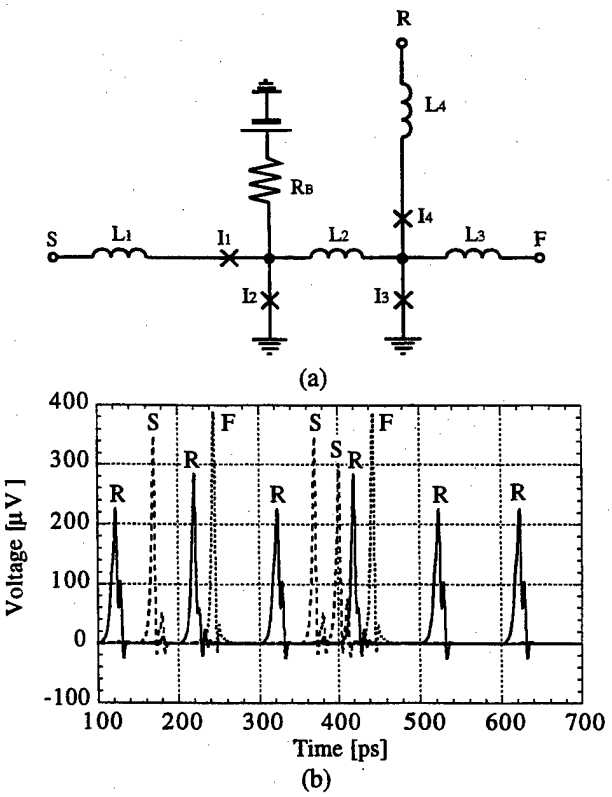

Fig. 3 (a) Schematic of an RS flip-flop and (b) a test pattern for the circuit optimization.

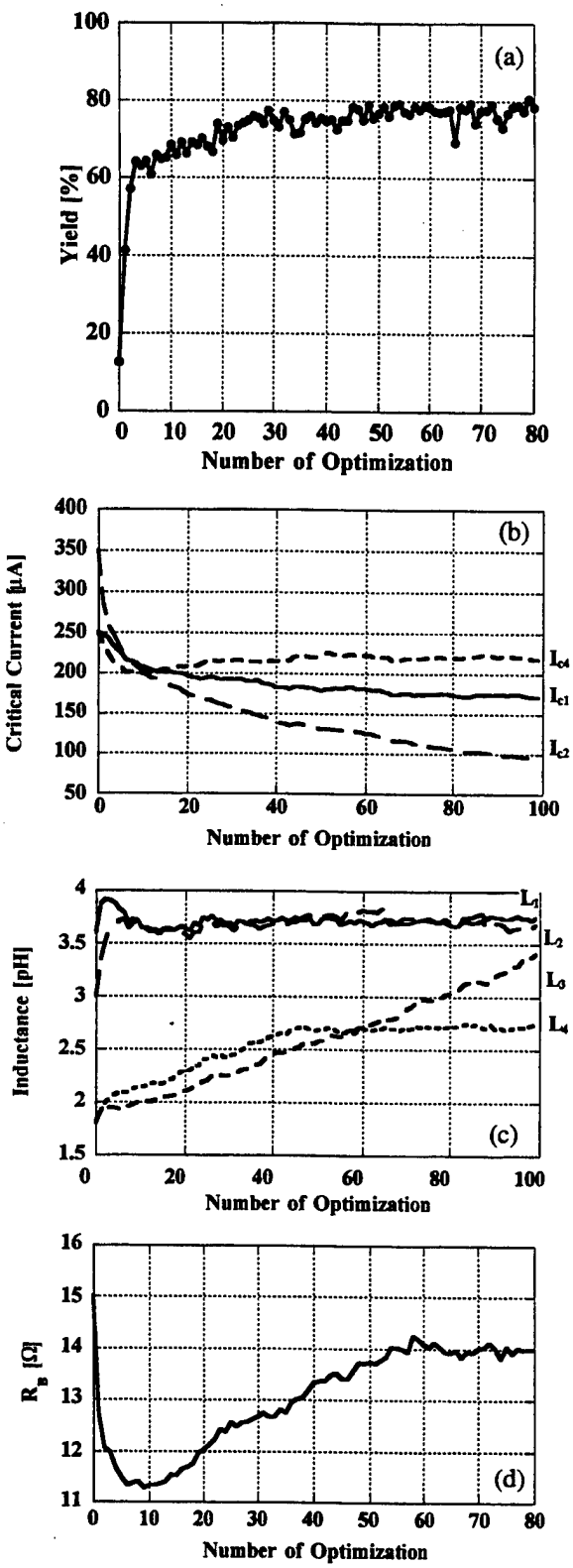

Fig. 4 Optimization of an RS flip-flop. Dependence of (a) the circuit yield, (b) critical currents, (c) inductances and (c) a bias resistance on the number of optimization steps. 3σ spreads of global and local parameter variations are set to $3\sigma_{global}$ = 50% and $3\sigma_{local}$ = 50%, respectively. The number of Monte-Carlo sampling is 500.

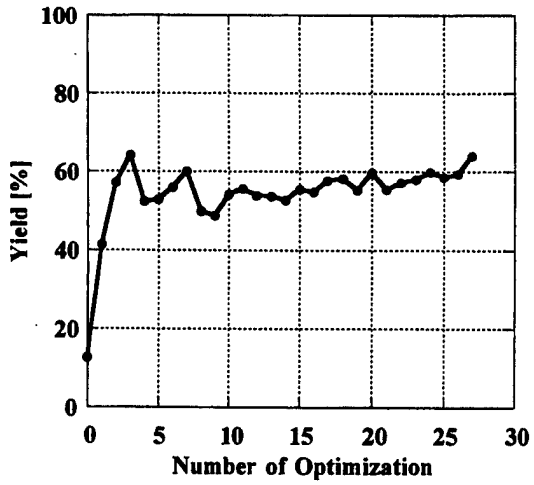

Fig. 5 Speed up of the optimization process. 3σ spreads of parameter variations $3\sigma_{global}$ and $3\sigma_{local}$ are increased by an increment of 5%, so that the yield always besoms lower than 60 %.

IV Conclusions

We have developed a parameter optimization tool for the RSFQ circuits, MJSIM, based on Monte Carlo yield analysis and the center-of-gravity method. It has shown that the Monte-Carlo yield optimization is effectively performed for the optimization of the RSFQ circuits. By using this optimization procedure, global dc bias margins have considerably improved. We also showed that the optimization speed can be improved by increasing the 3σ spread of the parameter distribution. Further consideration is required, however, for the existence of non-convergent properties in a few circuit parameters.

References

[1] K. K. Likharev and V. K. Semenov, "RSFQ logic/memory family: A new Josephson-junction technology for sub-terahertz-clock frequency digital systems," IEEE Trans. Appl. Superconductivity, vol. 1, pp. 1-28, March, 1991.

[2] J. C. Lin, V. K. Semenov and K. K. Likharev, "Design of SFQ-counting analog-to-digital converter", IEEE Trans. Appl. Superconductivity, vol. 5, pp. 2252-2259, March, 1995.

[3] C. A. Hamilton and K. C. Gilbert, "Margins and yields in single flux quantum logic", IEEE Trans. Appl. Superconductivity, vol. 1, pp. 157-163, December, 1991.

[4] S. V. Plolonsky, V. K. Semenov and A. F. Kirichenko, "Single flux quantum B flip-flop and its possible applications", IEEE Trans. Appl. Superconductivity, vol. 4, pp. 9-18, March, 1994.

[5] Q. O. Herr and M. J. Feldman, "Multiparameter optimization of RSFQ circuits using the method of inscribed Hyperspheres", IEEE Trans. Appl. Superconductivity, vol. 5, pp. 3337-3340, June, 1995.

[6] T. Harnisch, J. Kunert, H. Toepfer and H. F. Uhlmann, "Design centering methods for yield optimization of cryoelectronic circuits", IEEE Trans. Appl. Superconduct., vol. 7, pp.3434-3437, December 1997.

[7] M. Jeffry, W. Perold, W. Wang and T. Van Duzer, "Monte Carlo optimization of superconducting complementary output switching logic circuits", IEEE Trans. Appl. Superconductivity, vol. 8, pp.104-119, September 1998.

[8] M. W. Johnson, Q. P. Herr and J. W. Spargo, "Monte-Carlo yield analysis", presented at the 1998 Applied Superconductivity Conference, Palm Springs CA. To appear in IEEE Trans. Appl. Superconductivity.

[9] E. S. Fang and T. Van Duzer, "A Josephson integrated circuit simulator (JSIM) for superconductive electronics application", Extended Abstracts of 2nd International Superconductive Electronics Conference, Tokyo, Japan, 1989, pp. 407-410.

Inductance Calculation of 3D Superconducting Loop with Ground Plane

C. K. Teh, M. Kitagawa and Y. Okabe
Research Center for Advanced Science and Technology, The University of Tokyo
4-6-1 Komaba, Meguro-ku, Tokyo 153-8904, Japan

Abstract—An inductance calculation method, which is based on calculating the current distribution of a fluxoid-trapped superconducting loop by solving the expression of momentum and the Maxwell's equations simultaneously, is reconstructed to calculate those 3D structures which have ground plane (GP). The method of images is used to save computational resources by not calculating the current distribution of GP. However, since the penetration depth exists in GP, we demonstrate that the mirror plane is located just at the penetration depth below the boundary of GP. Calculations, that involve complex structures of superconductor system, such as tee junction and coupled superconducting loops, are also considered in this paper.

I. Introduction

The Josephson junction circuits especially the single flux quantum (SFQ) circuits are being investigated extensively for ultra-high speed digital devices. Since inductances play an important role in the threshold characteristics of the Josephson junction circuits, it is essential to determine the inductances of the circuits accurately. Recently, T.Nakazato et al. [1] of our laboratory formulated a numerical method to calculate inductances of 3D superconducting structures without GP. However, since most of the Josephson junction circuits today have GP, calculations including GP are needed. There is one main obstacle in doing so. As there exists an interaction of the magnetic field between the circuits and GP, arithmetic operations required to obtain the current distribution of the circuits and GP become $O(n^2)$ where n is calculations involved without GP. There are many papers using the method of images to overcome this problem [2][3][4]. However, to our knowledge all of them assume that the mirror plane is located at the boundary of GP. It is not true since the penetration depth λ exists in GP and the vector potential at the surface of GP is not zero. The accuracy of the method described in [2][3][4] is questionable since the thickness of the insulation in today fabrication process is not much greater than λ. We propose that, the mirror plane should be located at λ below the surface of GP in order to obtain the exact solution. The theoretical background is described in Sec.II. In Sec.III, a calculation method including GP is established by using T.Nakazato et al. method and the method of images. Sec.IV deals with calculations of inductance coefficients of complex structures such as tee junction. The optimization of the calculation speed is shown in Sec.V, and the relation between the calculation accuracy and the mesh-size is observed in Sec.VI.

Manuscript received April 30, 1999.
This study was performed through Special Coordination Funds for promoting Science and Technology of the Science and Technology Agency of the Japanese Government.

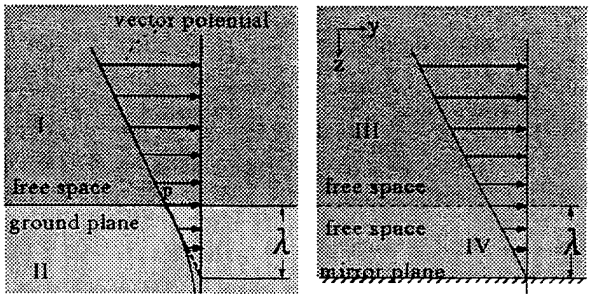

Fig.1: The method of images

II. Method of Images

Using the method of images, we can skip calculating the current distribution of GP, and arithmetic operations are reduced to $O(n)$ i.e. the same order to those without GP.

A. $d \gg \lambda$

Consider the thickness of GP d is much greater than the penetration depth λ, and the area of GP boundary is much greater than the superconducting loop. Using London equations, we can derive

$$\nabla^2 \mathbf{A} = \frac{1}{\lambda}\mathbf{A} \qquad (1)$$

where $\mathbf{A}$ is the vector potential. From Laplace equation and (1) we know that vector potential of arbitrary direction parallel to GP boundary decays linearly in the free space and decays exponentially in GP as shown in Fig. 1(left). Solving (1) we obtain

$$\mathbf{A} = -\lambda \frac{\partial \mathbf{A}}{\partial z} \qquad (2)$$

Since the vector potential is continuous and differentiable at the GP boundary, the intersection of the tangent of P and the perpendicular line, according to (2) is just λ below the boundary of GP. This indicates that we can substitute Fig.1(left) with the model shown in Fig.1(right), since the distribution of vector potential in region I and region III is the same, i.e. this fulfills the requirements of the method of images. Thus, the mirror plane should be set at λ below the boundary of GP, where $\mathbf{A}$ is zero.

B. $d \gtrsim \lambda$

In the case where d is not much greater than λ, it was predicted in London theory and proved empirically later [5]

that the effective penetration depth is

$$\lambda_{eff} = \lambda \coth\left(\frac{d}{\lambda}\right) \qquad (3)$$

Thus, we can choose our mirror plane to be at λ_{eff} below the upper boundary of GP.

III. Inductance Calculation

Considering a flux quantum Φ_0 trapped in the superconducting loop(Fig. 2), we can obtain the loop inductance L by

$$L = \frac{\Phi_0}{\iint_S \mathbf{J}_s(\mathbf{r})\, dS} \qquad (4)$$

where S is the cross section, $\mathbf{J}_s(\mathbf{r})$ is the current density of the loop at $\mathbf{r}$. The current distribution of the loop is obtained by solving the simultaneous linear equations which satisfy the expression of dynamical momentum (5) and the Maxwell's equations (6)

$$\frac{\hbar \nabla\theta(\mathbf{r})}{e^*} = \Lambda \mathbf{J}_s(\mathbf{r}) + \mathbf{A}(\mathbf{r}) \qquad (5)$$

$$\mathbf{A}(\mathbf{r}) = \mathbf{A}_f(\mathbf{r}) + \frac{\mu_0}{4\pi}\left[\int_{SC} \frac{\mathbf{J}_s(\mathbf{r}')\, dv'}{|\mathbf{r}-\mathbf{r}'|} + \int_{image} \frac{\mathbf{J}_i(\mathbf{r}'')\, dv''}{|\mathbf{r}-\mathbf{r}''|}\right] \qquad (6)$$

where $\theta(\mathbf{r})$ is the phase, $e^* = -2e$, $\Lambda = \mu_0\lambda^2$, $\mathbf{J}_i(\mathbf{r})$ is the current density of the image, and $\mathbf{A}(\mathbf{r})$ is the total vector potential made by the external vector potential $\mathbf{A}_f(\mathbf{r})$, the currents of the superconductor (SC) and the currents of its image.

We subdivide SC into small cubes, and assume that the current in each cube is uniformly distributed so that we can substitute the cubes by a current network such that the centers of adjacent cubes are interconnected by current paths. The smallest loop made by these paths is called a current mesh, and the hole of the SC is regarded as a hole-mesh. Thus, (5) and (6) are discretized as

$$|\mathbf{A}\rangle = -\Lambda |\mathbf{J}_s\rangle - \frac{\Phi_0}{2\pi a}|\phi\rangle \qquad (7)$$

$$|\mathbf{A}\rangle = |\mathbf{A}_f\rangle + \hat{\mathbf{M}}_s|\mathbf{J}_s\rangle + \hat{\mathbf{M}}_i|\mathbf{J}_i\rangle \qquad (8)$$

where $\langle i|\mathbf{A}\rangle$ is the vector potential of the i-th path of SC, a is the length of the path (which is called mesh-size), $\phi = a\cdot\nabla\theta$ is the phase difference between the ends of the path, and $\langle i|\hat{\mathbf{M}}_i|j\rangle$ is the vector potential of the i-th path due to a unit current at the image of j-th path. $\langle i|\hat{\mathbf{M}}_i|j\rangle$ and $\langle i|\hat{\mathbf{M}}_s|j\rangle$ have the same function, which is expressed as

$$\langle i|\hat{\mathbf{M}}|j\rangle = \frac{\mu_0}{4\pi V_i}\int_{V_i}\int_{V_j} \frac{dv\, dv'}{|\mathbf{r}_i - \mathbf{r}_j|} \qquad (9)$$

where V_i is the volume of the i-th cube, and the double integration is over the i-th cube region and over the j-th cube region respectively. Since the current of the i-th path and the current of its image have same magnitude but different direction, (8) can be rewritten as

$$|\mathbf{A}\rangle = |\mathbf{A}_f\rangle + \hat{\mathbf{M}}_s|\mathbf{J}_s\rangle - \hat{\mathbf{M}}_i|\mathbf{J}_s\rangle \qquad (10)$$

Substituting (7) in (10), we can derive

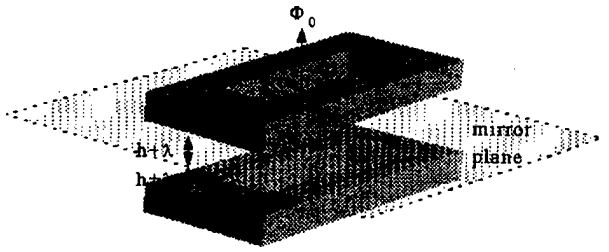

Fig.2: Superconducting loop with its image

$$'\hat{\mathbf{R}}(\Lambda\hat{\mathbf{I}} + \hat{\mathbf{M}}_s - \hat{\mathbf{M}}_i)\hat{\mathbf{R}}|\mathbf{J}_m\rangle = -'\hat{\mathbf{R}}|\mathbf{A}_f\rangle - \frac{\Phi_0}{2\pi a}|\phi_m\rangle \qquad (11)$$

where $\mathbf{J}_m$ is the mesh-current-density of SC, $\hat{\mathbf{I}}$ is an invariant operator, $\hat{\mathbf{R}}$ is an operator such that $|\mathbf{J}_s\rangle = \hat{\mathbf{R}}|\mathbf{J}_m\rangle$, $'\hat{\mathbf{R}}$ is an operator such that $\langle i|'\mathbf{R}|j\rangle = \langle j|\mathbf{R}|i\rangle$, $|\phi_m\rangle = {}'\hat{\mathbf{R}}|\phi\rangle$ is the phase change around the mesh such that $\langle i|\phi_m\rangle = -2n\pi\delta_{i,N_m}$ where $\{N_m\}$ is a set of the hole-meshes of SC. Equation (11) can be rewritten in matrix representation as

$$\mathbf{U}\cdot\mathbf{j}_m = \varphi \qquad (12)$$

where

$$\mathbf{U}_{ij} = \langle i|'\hat{\mathbf{R}}\,(\Lambda\hat{\mathbf{I}} + \hat{\mathbf{M}} - \hat{\mathbf{M}}')\,\hat{\mathbf{R}}|j\rangle$$
$$\varphi_i = -\langle i|'\hat{\mathbf{R}}|j\rangle\langle j|\mathbf{A}_f\rangle - \frac{\Phi_o}{a}\delta_{i,N_m} \qquad (13)$$

The current distribution therefore can be obtained by solving the system of linear equations in (12).

IV. Mutual Inductance

Consider there are two coupled superconducting loops over GP. Fluxoids trapped in the loops Φ_1, Φ_2 are related to the currents of the loops I_1, I_2 by

$$\begin{bmatrix}\Phi_1\\ \Phi_2\end{bmatrix} = \begin{bmatrix}L_{11} & L_{12}\\ L_{21} & L_{22}\end{bmatrix}\cdot\begin{bmatrix}I_1\\ I_2\end{bmatrix} \qquad (14)$$

where L_{11} is the self-inductance of the first loop, $L_{12} = L_{21}$ is the mutual inductance between the first loop and the second loop. The inductance matrix can be obtained by considering a fluxoid quantum trapped in the first loop with no fluxoid trapped in the second loop (15), and vice versa (16).

$$\begin{bmatrix}I_1\\ I_2\end{bmatrix} = \begin{bmatrix}L_1 & M\\ M & L_2\end{bmatrix}^{-1}\cdot\begin{bmatrix}\Phi_0\\ 0\end{bmatrix} \qquad (15)$$

$$\begin{bmatrix}I_1\\ I_2\end{bmatrix} = \begin{bmatrix}L_1 & M\\ M & L_2\end{bmatrix}^{-1}\cdot\begin{bmatrix}0\\ \Phi_0\end{bmatrix} \qquad (16)$$

The inductance coefficients of the n superconductor system are therefore can be calculated by using n combinations of fluxoid arrangements. Using this method, we can also obtain the inductances of the tee junction shown in Fig.3. Fluxoids are placed in the solid-line-shaded regions. The dotted-line regions are places far enough from the tee junction such that the mesh-currents aligned in the length direction can be treated as identical to reduce computations. See Sec.V(C).

V. Calculation Time

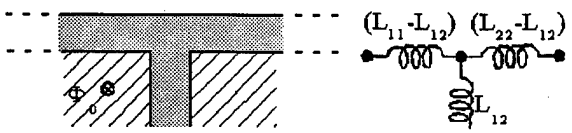

Fig.3: The inductance of tee junction

A typical calculation involves 40MB of the main memory and requires only 2 minute of CPU time on Intel PentiumII 400Mhz to obtain the accuracy of 0.001% error. The calculation can be divided into two parts, one is making the matrix **U**, and the other is solving $\mathbf{U}\cdot\mathbf{j}_m=\varphi$. Optimization is done especially by observing the property of **U**.

A. Tabulation of $\langle i|\hat{\mathbf{M}}|j\rangle$

The speed of making **U** depends very much on the speed of calculating $\langle i|\hat{\mathbf{M}}|j\rangle$ values in (9). Since the interaction between the vector potential and the current only depends on the distance between two paths involved, and since the distance is in discrete value only, $\langle i|\hat{\mathbf{M}}|j\rangle$ can be tabulated to speed up the algorithm. The tabulation of $\langle i|\hat{\mathbf{M}}|j\rangle$ offers 200 times faster than the ordinary method in a typical calculation, which involves a great number of meshes.

B. Conjugate Gradient (CG) method

Matrix **U** is a positive-definite symmetric matrix since $\langle i|\hat{\mathbf{M}}|j\rangle$ values are vector potential quantities. Therefore, we can apply the state-of-the-art CG method [6] to speed up the calculation of the simultaneous linear equations in (12). For n-by-n matrix, the calculation by CG method involves $O(n^2)$ operations. When the number of meshes is large, **U** become sparse matrix by assuming that no influence of the current to the vector potential of a point far away, e.g. 100 mesh-size away for the accuracy of 0.001% error. For sparse matrix, calculations by CG method involve only $O(n)$ operations.

C. Symmetry of Current Distribution

If a structure has n (anti-)symmetry planes with regard to the mesh-current distribution, (11) can be simplified to

$$ {}^t\hat{\mathbf{R}}\left\{\Lambda\hat{\mathbf{I}}+\sum_{k=0}^{n}\sigma_k\cdot\left(\hat{\mathbf{M}}_e^k-\hat{\mathbf{M}}_i^k\right)\right\}\hat{\mathbf{R}}|\mathbf{J}_m\rangle = -{}^t\hat{\mathbf{R}}|\mathbf{A}_t\rangle - \frac{\Phi_0}{2\pi a}|\phi_m\rangle \quad (17) $$

where σ_k is +1 for a symmetry plane and is -1 for an anti-symmetry plane, and $\langle i|\hat{\mathbf{M}}_s^k|j\rangle$ is the vector potential of the i-th path due to a unit current at the image of j-th path on k-th (anti-)symmetry plane. Calculations reduce exponentially by using this method.

VI. Accuracy and Mesh-Size

The calculation accuracy is expected to depend on the ratio of the smallest dimension of the structure to the mesh-size a. For optimization between the calculation time and the calculation accuracy, this relation is investigated by using Chang's formula [7] as our reference in a 2D stripline model such that t=20nm, h=2.5nm, w=700nm, λ=2.5nm, where t is the thickness of the superconducting stripline, h is the thickness of the insulation, w is the wide of the stripline, λ is the penetration depth of the stripline and GP. This model is purposely chosen to fulfill the requirement of Chang's formula, i.e. $w/h \gg 1$. The thickness of GP is considered much greater than λ. As shown in Fig.4, the error of calculation reduces to 0.3% when the ratio approaches 10. This indicates that the mesh-size should be set approximately tenth of the smallest dimension of the structure if we want our calculation accuracy to be under 1% error.

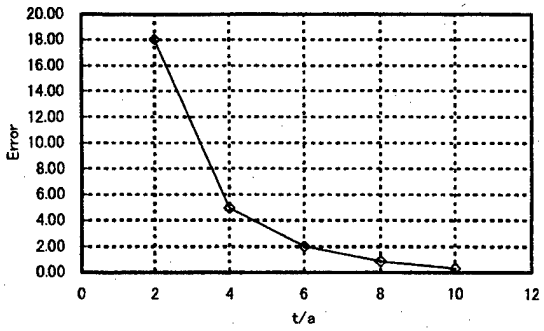

Fig.4: Accuracy and Mesh-Size relation

Acknowledgment

C.K.T is particularly indebted to Dr. Hiroki Kodaka and Mr. Tetsu Hosoki for numerous helpful discussion.

References

[1] T. Nakazato and Y. Okabe, "Inductance Computation of Microscopic Superconducting Loop," IEEE Trans. Appl. Supercond., vol. 7, pp. 3626-3629, Jun. 1997.

[2] L. E. Alsop, A. S. Goodman, F. G. Gustavson, W. L. Miranker, "A Numerical Solution of a Model for a Superconductor Field Problem," J. Comput. Phys., 31, 216, 1979

[3] M. Hosoya, E. Goto, N. Shimizu, N. Miyamoto, Y. Harada, "Inductance Calculation System for Superconducting Circuits", IEEE Trans. Magn., 25(2), 1111-1114, March 1989.

[4] B. Guan, M. J. Wengler, P. Rott, and M. J. Feldman, "Inductance Estimation for Complicated Superconducting Thin Film Structures with a Finite Segment Method," IEEE Trans. Appl. Supercond., pp. 2776-2779, vol. 7, Jun 1997.

[5] W. H. Henkels and C. J. Kircher, "Penetration Depth Measurements on Type II Superconducting Films," IEEE Trans. Magn., 13(1), 63-66, Jan. 1977.

[6] Anne Greenbaum, *Iterative Methods for Solving Linear Systems*, SIAM, 1997.

[7] W.H.Chang, "The Inductance of a Superconductor Strip Transmission Line," J. Appl. Phys., 50, 8129, 1979.

Behavior of vortex in Josephson junction network and its application on logic circuit

K. Hohkawa and K. Koh
Kanagawa Institute of Technology,
1030 Shimo-Ogino Atsugi, Kanagawa 243-0292, JAPAN
Tel. +81-462-91-3161, Fax. +81-462-42-8361,
E-mail ; hohkawa@ele.kanagawa-it. ac. jp

The vortex in Josephson junction network (JJ-net) has interesting features of soliton, and JJ-net is expected to apply on novel functional devices. We have proposed a vortex flow device consisting of JJ-net, in which multiple Josephson junctions are distributed two dimensionally and each junction is locally connected each other to form a lot of small loops. We have shown that it would be applicable to several devices, such as memory, signal transformer [1]. The key factor for the device to operate as a highly functional device is how to control motions of vortices in JJ-net. In this paper, the relation between the propagation characteristics of vortices, JJ-net structures and junction parameters were further studied. The conditions of regeneration of vortex by other vortices that are either on propagation or stored in local area in the JJ-net were investigated. The detail conditions of mutual interactions of vortices in JJ-net such pair annihilation, polarity inversion of vortices were investigated as well. Based on these results, we constructed basic logic circuit such as logic gate, flip flop, threshold logic gate, and discussed characteristics of these circuits. Further, we will propose functional circuit such as data selector, correlator using these basic logic circuits and the basic characteristics of functional circuit will be presented.

[1] K. Hohkawa and K. Koh; 6th ISEC Extended Abstract, Vol. 3, p. 168, 1997.

Can Superconductivity Become a Viable Electronic Technology?

M. Nisenoff
Nisenoff Associates
5605 Whitney Mill Way, Suite 302
North Bethesda MD 20852-3141 USA
- 1 – (301) 984 - 0833: - 1 – (301) 984 - 3325 FAX
m.nisenoff@ieee.org

Abstract: -- The superconducting state exhibits many unique properties that can be employed in fabricating electronic devices, components and subsystems. However, most of the applications of superconducting that have emerged from the research laboratory have utilized *only* the (near-) zero resistance property of the superconducting state. The other very unique and very intriguing properties of the superconducting state, such as magnetic flux exclusion (the Meissner Effect) and the quantum nature of the superconducting state, have only been used in a limited number of applications which, to date, have not emerged from the laboratory.

In this manuscript, the argument will be made that if superconductivity is to become a commercially viable electronic technology that is widely deployed outside the research laboratory, it must exploit not only zero-resistance but also the unique quantum-mechanical properties of the superconducting state. Electronic technologies based on *silicon* (or other semiconductors) and *copper* (or other low resistivity metals) are expanding so rapidly, superconductivity must employ all of its attributes if there is to be any chance for superconductivity to compete successfully with the more established (conventional) electronic technologies.

I INTRODUCTION

There has been much progress in the development of superconducting electronic technologies over the past thirty years employing low temperature superconducting (LTS) materials and, over the past twelve years, for those using high temperature superconductivity (HTS) materials. At the present time, the most commercially successful application of superconductivity has been high magnetic field magnets that are used for nuclear physics particle accelerators and in Magnetic Resonance Imagining (MRI) systems for medical diagnostics applications. These magnets were very attractive to those communities as they provide intense magnetic filed in a very small package with a very modest power supply compared to what would be required if either ferromagnetic materials or coils with very large power supplies were used to produce the desired magnetic field.

The advantages of superconducting magnets are that they can provide very intense magnetic field simultaneously with dramatic reduction in mass and input power compared to any other (conventional) magnetic technology.

These advantages in reduction in volume and electrical input power are so dramatic that this very exotic technology was eagerly accepted by these communities and incorporated into their equipment despite the need to periodically replenish liquid helium cryogens needed to maintain these magnets at their (cryogenic) operating temperature.

Another applications of potential commercial interest that has been developed in the laboratory and is currentty entering the market place, is HTS superconducting radio frequency and microwave filters for wireless telecommunications base stations. For these applications, reduction in system noise temperature and rejection of out-of-band interfering signal are crucial issues. Superconductivity can provide band pass filters with effective unloaded Q-values of greater than 10,000 (and approaching 50,000) which can simultaneously provide the desired frequency band-pass characteristics, out-of-band rejection and low in-band insertion losses. Comparable Q-values could also be obtained using dielectrically loaded three-dimensional (room temperature) cavity structures, but the weight and volume of a filter built using conventional (room temperature) technologies would be at least one or, maybe, two order of magnitude larger. The comparison between the volume of normal conducting/dielectric resonators and superconducting structures is shown in Figure 1. From this figure, it can be seen that for a given Q-value, the volume of the superconducting version can be about two orders of magnitude smaller in volume than the corresponding (conventional technologies. On the other hand, for a given volume, the superconducting structure would have a Q-value about a factor of 30 higher than the corresponding normal conducting technology.

If superconducting filters are used in the front-end sub-system for a wireless base station, which may consist of as many as twelve antennas and input amplifiers, the volume of the front end would be significantly smaller (even including the cryogenics) than if normal conducting/dielectric filters had been used. This reduction in weight and

Manuscript received 5 May 1999.
Work done while author was at the US Naval Research Laboratory, Washington DC 20375-5347 USA

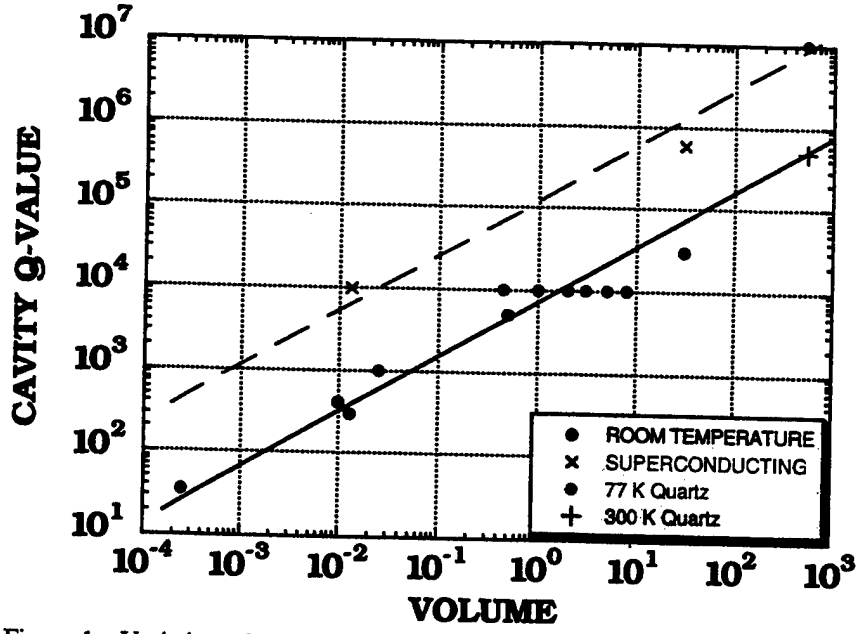

Figure 1. Variation of cavity Q-Value as function of cavity volume for normal conducting and superconducting filter technologies.

volume is especially important if this HTS front-end base station must be mounted at the top of a tower so as to reduce the cable length (and its associated attenuation) and thus improve system performance.

Superconducting filters can provide one to two orders of magnitude reduction in mass and volume compared to filters fabricated using conventional technologies. If the cryogenic packageand cryogenic refrigerator ares included the advantage of superconductivity is still, at least, a factor of two to five times smaller in mass and volume compared to conventional technologies.

However, the acceptance of other potential applications by the commercial world has been lest than enthusiastic. Clearly, one aspect of superconductivity that has been a major obstacle to wider acceptance outside the laboratory environment, has been the need for providing liquid cryogens to maintain these systems at the required cryogenic operating temperature. The recent development of improved, low cost, high reliability closed cycle mechanical cryogenic refrigerators ("cryocooler") should have a major impact on the acceptance of superconductivity into more commercial systems as it can mitigate the need for liquid cryogens and require only electrical input power to provide and maintain the cryogenic environment.

If one carefully examines the rationale for the use of superconducting materials in various applications, electronic as well as large scale, one realizes that the most successful commercial applications of superconductivity have taken advantage of the "zero resistance" of the superconducting state. Although the "zero" resistance property was the initial behavior that gave this phenomena its name and which remains the best known property of the superconducting state, there are other properties, such as magnetic flux exclusion (the Meissner Effect) and various quantum mechanical properties (such as superconducting Josephson tunneling), which have not yet been exploited in as many applications as has the zero resistance one. The objective of this paper is to call attention to these other properties and to encourage the superconducting technologist to exploit these very intriguing properties, in addition to the zero resistance property, in developing new electronic applications of superconductivity. ***It is the opinion of the author, that all of the very intriguing properties of the superconducting state mast be used to expedite the commercialization of superconducting electronic technology.***

II COMMECIAL APPLICATIONS

As was pointed out above, the most successful commercialization of superconductivity, albeit a large-scale applications, is that of high field magnets for nuclear accelerators and for Magnetic Resonance Imaging (MRI) systems that employ high field superconducting magnets that exploit the "zero" resistance property of the superconducting state that results in physically small sized magnets (since there is no need to extract heat from the magnet windings) and small power supplies (as the dissipation in the magnet are near zero and a small power supplies can be used to supply current at very low voltage). The use of these magnets over the past thirty years has generated a very large commercial market for superconducting technology.

The other applications of great potential commercial interest is the use of HTS superconducting radio frequency and microwave resonators for wireless telecommunications base stations applications. Again, in this instance, the very low surface resistance of superconductors can be used to fabricate very complex frequency-selective filters with dramatically lower mass and volume than filters fabricated using conventional (room temperature) filter technologies.

These two primary commercial applications of superconducting are both based on the "zero (or "near zero") resistance" of the superconducting state with no use of the other properties of the superconducting state such as magnetic flux exclusion or the quantum mechanical properties of the superconducting state.

Why have the only commercial applications of superconductivity employed only the zero resistance property? The quantum-mechanical properties, which make superconductivity very unique, have not yet resulted in any potential application that has been able to emerge from the research laboratory. Why?

III POTENTIAL NEW APPLICATIONS

Now let us assess the various established and emerging applications of superconductivity and attempt to determine which property(ies) of the superconducting state are exploited in each application. In Table I, the applications are presented in an order reflecting the "commercial" acceptance of the various applications. (Note: this ranking of "acceptance" of superconducting technologies is obviously quite subjective.) The larger number of "X" in a box implies that this property is more important in its potential application than if fewer "X" are shown. (Again, these rankings are obviously subjective and reflect the opinion of the author.)

APLLICATION	ZERO RESISTANCE	MEISSNER EFFECT	QUANTUM PROPERTIES
Magnets	XXX		
SIS Microwave Mixers			XXXX
DC Voltage Standard			XXXX
SQUID Magnetic Sensors		XX	XX
Wireless Telecommunications Filters	XXX		
Fault Current Limiter			XXX
NMR Coils	XX		
Digital Signal Processing	XX	XXX	XX

Table I A summary of superconducting applications and the properties of the superconductor state that are exploited in each application

According to the entries in Table I, the three most successful "commercial" applications of superconductivity are magnets, SIS Mixers and DC Voltage Standards. As was stated above, the operation and advantages of *superconducting magnets* rely on the zero resistance property of superconductivity. *Superconducting SIS mixers* which exploit quantum mechanical tunneling in superconducting tunnel junctions, is the detector of choice of the radio astronomy community for use as the detector of millimeter wave radiation with frequencies greater than 100 GHz, where conventional detector technologies degrade very dramatically. ***Superconducting SIS detectors are used when ultimate sensitivity is required but only when conventional technologies are not adequate for the desired application.***

The DC Josephson Voltage Standard has been adopted for the international voltage standard, but has created a very limited commercial market,. ***The performance of the superconducting Josephson voltage standard which based on the quantum-mechanical Josephson tunneling phenomena, is the ultimate standard since it is defined by fundamental constants***. No other voltage standard that has been proposed or used has been defined with this ultimate precision.

Hence the major commercial successes of superconductivity are high magnetic field magnets which relay on zero resistance while the other "success" of superconductivity, which are not particularly large markets, exploit the unique quantum mechanical properties of the superconducting state and do indeed provide "ultimate" performance but only in extremely small niche markets.

In the next category are those applications that have matured to a very advanced degree in the laboratory but have not yet been widely accepted by the commercial market. *SQUID magnetic sensors*, which employ both the Meissner Effect and the quantum Josephson Effect, are widely used in laboratory environments where measurements requiring the ultimate in magnetic field sensitivity at very low frequencies is required but their non-laboratory applications (such as medical diagnosis, Non-Destructive Evaluation, geophysical exploration, etc.) have not yet found a commercial acceptance.

SQUID magnetic sensors exhibit the ultimate in magnetic field sensitivity at low frequencies but there are few commercial applications for such sensors in the frequency regime in which they exhibit ultimate sensitivity compared to conventional magnetic sensing technologies.

The use of HTS filters and cryogenic cooled semiconductor Low Noise Amplifiers (LNAs) for *telecommunications base station* applications have been developed in many countries but the insertion of this technology into the market place has not yet occurred. Many field tests of this equipment have been conducted but the technical and economic advantages of HTS filter technology compared to conventional technologies for these applications has not yet been unequivocally demonstrated.

HTS filters for telecommunication base station applications exploit the (near) zero resistance property of the superconducting state.

Fault Current Limiters, which exploit the critical current behavior of the superconducting state, are under development for use in electrical utilities systems to limit current flow when there is an accidental fault or short in the system. The concept has been demonstrated in prototype systems but as yet this equipment has not been tested in operational power networks.

Fault current limiters which employ the critical current phenomena of superconductivity and are currently under development for insertion into electrical utility networks.

Superconducting input coils for Nuclear Magnetic Resonance (NMR) used for chemical analysis and for Magnetic Resonance Imaging (MRI) equipment for medical diagnostic applications have been developed and their commercialization is in progress but they have not yet impacted on the intended applications areas nor have they been commercialized. The lower resistance of superconducting coils relative to conventional coils reduces the noise figure of the system, which results in reduced data acquisition time, important factor for both of these applications.

MNR and MRI input coils, which take advantage of the zero resistance propert of superconductivityy, can reduce the data acquisition time for NMR, and MRI systems but their utility have not yet been demonstrated in the commercial market.

Finally, the last application considered is superconducting digital technology, which employs all of the attributes of the superconducting state, and has the potential to yield an extremely high speed (100 GHz and greater), low power dissipation (three orders of magnitude lower than semiconductor CMOS) digital technology.

Although superconducting digital technology is very impressive and does exploit all of the unique properties of the superconducting state, it is competing against the "silicon locomotive" which has tremendous momentum and huge financial resources and is not willing to be replaced.

IV. CONCLUSION

In this manuscript, the author has reviewed several current and potential commercial applications of superconductivity and has attempted to present the argument that most of these applications employ only the "zero resistance" property of the superconducting state. There are a few applications, which do employ the unique quantum-mechanical properties of the superconducting state, but these have either not left the research laboratory or, if they have matured sufficiently, their market niches are extremely limited.

Based on the observations outlined above, the superconductivity community must address the following question if superconductivity is to become a viable commercial electronic technology:

WHY HAS THE SUPERCONDUCTING COMMUNITY ONLY EXPLOITED THE ZERO RESISTANCE PROPERTY OF SUPERCONDUCTIVITY BUT HAVE NOT SUCCESSFULLY COMMERCIALIZIZING APPLICATIONS, WHICH EXPLOIT THE VERY UNIQUE QUANTUM MENCHANICAL PROPERITES OF THE SUPERCONDUCTING STATE? ? ?

It is the contention of the author that superconducting electronic technology will become a viable electronic technology, IF and only IF, all of the unique quantum-mechanical properties of the superconducting state are fully exploited, in addition to zero resistance, in conceiving, developing and marketing applications of superconducting electronic technology which can make an impact in the commercial marketplace.

A Superconductive High-Resolution Time-to-Digital Converter

Oleg A. Mukhanov and Alex F. Kirichenko
HYPRES, Inc., 175 Clearbrook Rd., Elmsford, NY 10523, USA

Abstract—We are developing an ultra-high resolution time-to-digital converter (TDC) based on a novel scheme combining a digital "coarse" TDC and analog "fine" TDC. The coarse TDC is derived from a previously reported RSFQ time digitizer based on binary counters. The fine TDC is based on an analog prescaler. A 31 GHz counter defines the coarse (~32 ps) time resolution, while the prescaler provides a fine time resolution by measuring time within a clock period with 4 ps resolution.

I. Introduction

We have been developing RSFQ (Rapid Single Flux Quantum) time-to-digital converters (TDCs) based on binary counters [1-3]. While these TDCs provide exceptional multi-hit time resolution, ultimately, their time resolution is limited to the level of a single clock period. Therefore, any increase in TDC performance can come only with an increase in the circuit clock frequency. We can project reaching a 12-ps resolution using 80-GHz counters; however, to go beyond the 10-ps mark would require using an enhanced circuit fabrication process.

Recently, a number of applications have been identified which require a sub-10 ps TDC. One of the high-profile applications is the Muon Cooling for the Muon Collider project – a novel particle accelerator concept for high-energy physics. In order to achieve the required TDC time resolution of 6 ps for this application, a novel TDC design must be devised. This TDC must be capable of resolving times shorter than the TDC clock period. This paper presents the design and the first test results of a high-resolution TDC which specifically addresses this challenge.

II. High Resolution TDC Design and Test

A. General Block Diagram

Fig. 1 shows a block-diagram of the proposed high-resolution TDC. The TDC design is based on a combination of our proven all-digital TDC (Coarse TDC) [1-3] and a novel analog prescaler (Fine TDC). The TDC resolution is set by the maximum counter speed divided by the number of channels or bins in the analog prescaler. For instance, a 31 GHz TDC with an 8-bin analog prescaler will be capable of measuring time intervals with 4 ps precision.

The digitized time stamps can be stored in a multi-hit buffer or first-in/first-out (FIFO) register integrated on the same IC. The multi-hit TDC resolution will still be limited by the time resolution of the Coarse TDC. The output of the superconductive TDC will be accessible via a parallel-to-serial converter and room-temperature interface, all run by a control module based on the VXI standard (VMEbus Extensions for Instrumentation).

Manuscript received May 7, 1999.
This work was supported in part by US Department of Energy under contract No. DE-FG02-98ER-82595.

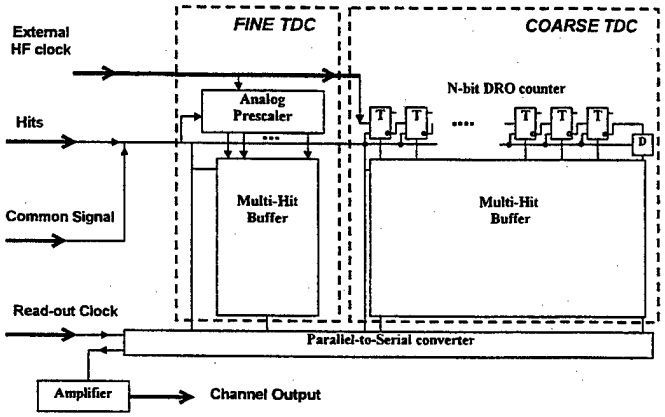

Fig. 1 Block diagram of the single channel high-resolution TDC with Coarse TDC and Fine analog prescaler TDC.

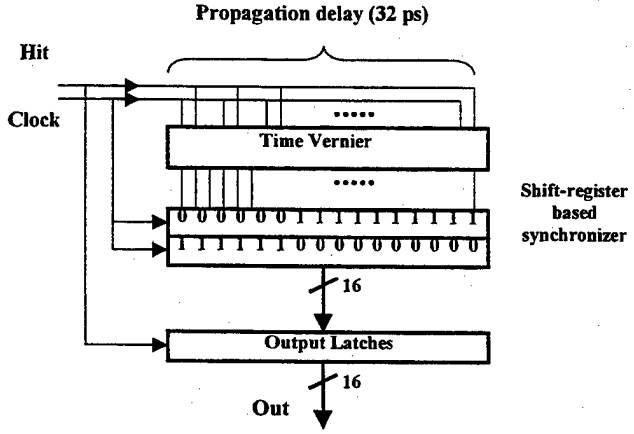

Fig. 2. Block diagram of the analog prescaler (Fine TDC) based on time vernier.

B. Analog Prescaler Based on Time Verniers

Fig. 2 shows a block diagram of the analog prescaler. The design of this circuit is similar to that of a multi-channel race arbiter (or synchronizer) employed in the HYPRES high-resolution ADC [4]. The prescaler consists of two parts: a time vernier and a two-phase synchronizer. The design of the time vernier is based on SFQ pulse propagation along a Josephson Transmission Line (JTL). The velocity of an SFQ pulse strictly depends on the dc bias current applied to the JTL. We exploit this dependence to tune and calibrate the time vernier. To detect the position where the two pulses meet (CLOCK and HIT), we use a series of 8 latches (for an 8-bin prescaler) distributed uniformly along delay lines. The

HIT line is connected to the inputs of these latches, while the CLOCK line triggers the latches and destructively reads out their data. Thus, after every HIT, we have two 8-bit words of ones and zeroes. In the first word a series of "ones" are followed by a series of "zeroes". The number of "ones" determines the position along the JTL, where a CLOCK pulse overrides the HIT pulse. A small logic block picks this first word, converts it into a serial format, and sends it to the output. Using this method, an 8-bin prescaler provides a 4 ps time resolution with a 31.3 GHz clock frequency.

We have designed and fabricated a test prescaler chip using the HYPRES 1.0 kA/cm^2 Nb fabrication process. In order to provide few-ps time delays, we integrated a JTL-based delay line on the same chip. Fig. 3 shows the low-speed test results of this circuit. All output bins were monitored with toggle-type monitors, thus switching of the output voltage state between 0 and ~0.2 mV indicates an output "one" in typical non-return to zero (NRZ) fashion.

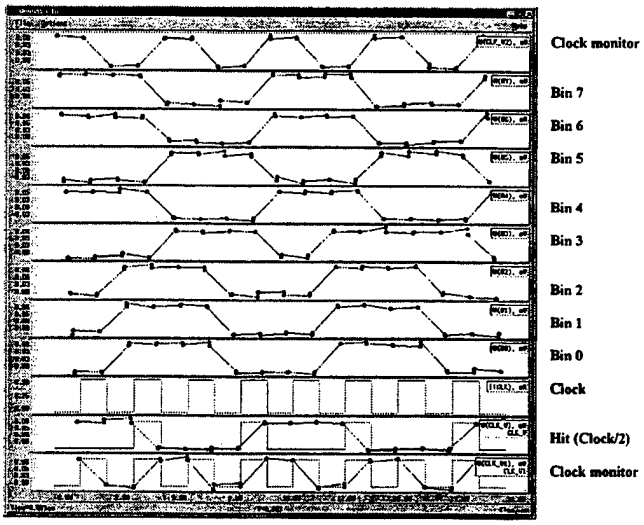

Fig. 3 Correct functionality of the time vernier based prescaler. Total time vernier delay is 50 ps. The preset value of the HIT-CLOCK delay is 20 ps. The output is 1110000, or 3/8 of 50 ps.

The preset value of the variable delay was 20 ps. At the first clock pulse, the outputs of bins 0 through 2 are "one", while the outputs of bins 3 through 7 are "zero". This indicates the delay between CLOCK and HIT pulses is 3/8 of 50 ps (18.75 ps). By changing the dc bias current on the variable delay JTL line, we have observed the expected response on the outputs of the prescaler. A computerized test setup allowed us to measure the operating margins of all critical parameters at different values of the dc bias current for the time vernier. As we mentioned above, the bias current of the time vernier changes the propagation time of the SFQ pulses, thus changing the resolution of the prescaler. In this experiment, we observed our prescaler fully operational at up to 30 ps propagation time, which corresponds to ~4 ps resolution (or 2 ps in case of 16 bins).

Fig. 4 shows the results of a similar experiment performed at a high clock frequency. A picture, taken of an oscilloscope shows the response of all 8 bins of the prescaler with a linear variation of the dc bias current of the variable delay line, i.e. the HIT-CLOCK delay time.

One can see all 8 bins consequently switching to "one", indicating the increase in delay. More importantly, there is no overlapping between bins. This means that internal noise does not affect the resolution of the prescaler at clock frequencies up to 17.5 GHz. We have also achieved successful interleaving above this frequency, with error-value of less than one LSB (least significant bit).

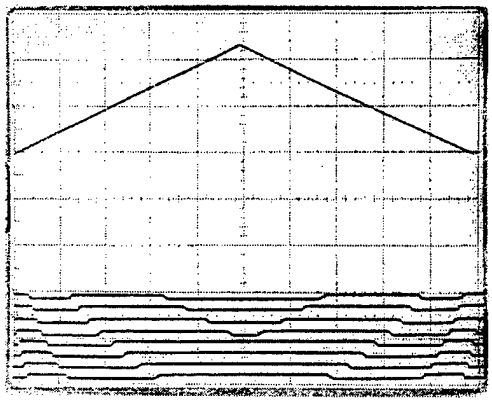

Fig. 4 High-speed operation of an 8-bin analog prescaler based on a time vernier at 17.5 GHz. Upper trace is a current, controlling the delay between CLOCK and HIT signals. Bottom traces are 8 output bins.

We have successfully measured a full transition width of 2 ps from dc to 15 GS/s and of 3 ps at up to 20 GS/s (Fig. 5). These results prove that the prescaler transition width is sharp enough to build a 16-bin prescaler, i.e. to interleave the individual bins without superposition of their transitions.

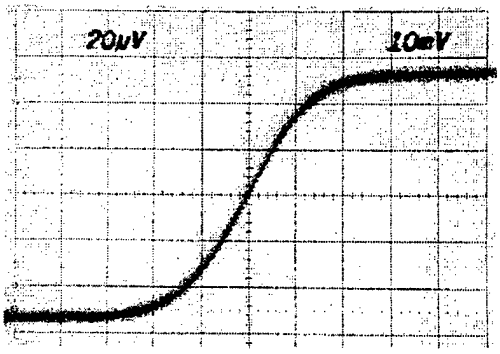

Fig. 5 Measured discrimination curve (1 ps/div).

There are, however, a few drawbacks of the time vernier. It leads to a cumbersome design, sophisticated post-processing electronics, and requires complicated tune-up and calibration processes.

C. Analog Prescaler Based on Dynamic AND-Elements

To avoid the drawbacks mentioned above, a novel design for an analog prescaler based on dynamic AND-elements has also been proposed. This novel design will allow us to increase the sharpness of the transitions seen in Fig. 4, enabling us to interleave 16 bins of prescalers. This new design also allows us to substantially simplify the peripheral logic. Fig. 6 shows a schematic of this new prescaler. It is

based on a novel dynamic AND gate. This gate produces an output when the delay between input pulses is less than a particular threshold value.

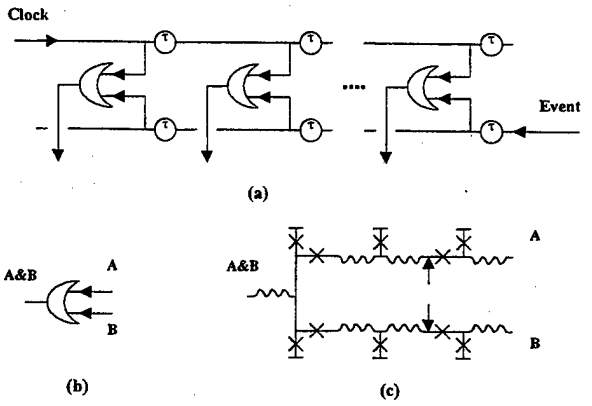

Fig. 6 An analog prescaler based on dynamic AND-elements: (a) block diagram; (b) notation, and (c) schematic of the dynamic AND-element.

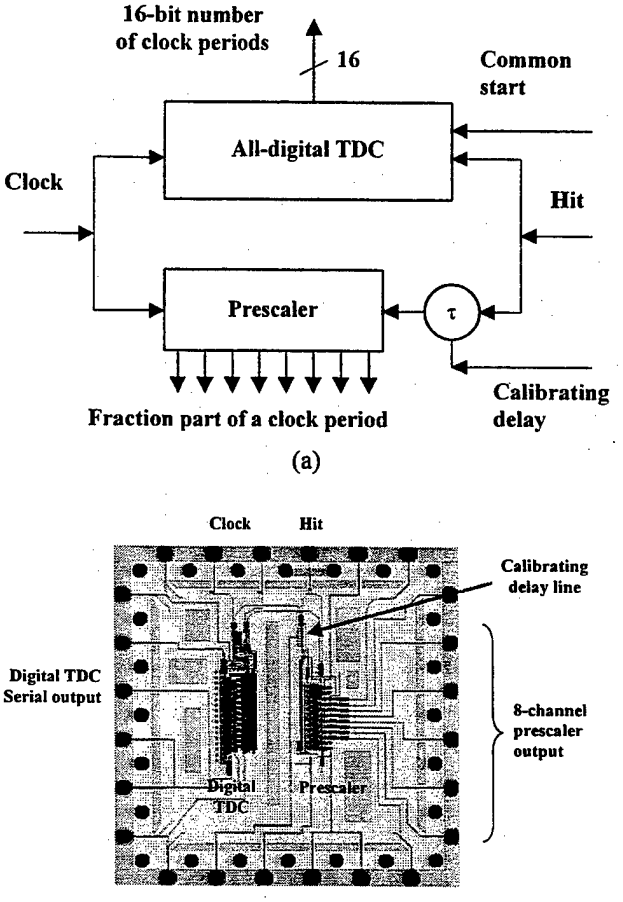

Fig. 7. A 4 ps single-hit TDC using an 8-bin Fine TDC and a 14-bit Coarse TDC: (a) block-diagram and (b) chip layout.

In this design, the CLOCK and HIT pulses are moving toward each other from opposite ends of the two delay lines. These delay lines are connected with dynamic AND gates. The delay between two AND gates (τ) is 2 to 6 ps. The dynamic AND gate has an internal cycle time, which is set to 1.5 τ. If and only if two pulses arrive at the input terminals of the gate within this time interval, the gate will produce an output pulse. In this way, we can detect the position along the delay line where the HIT and CLOCK pulses meet.

The delay element τ is a segment of a Josephson transmission line (JTL). The delay time of this element can be tuned by changing the bias current of the transmission line, allowing one to adjust the prescaler to other clock frequencies. A 16-bin version of this prescaler with a 31 GHz clock frequency will result in a time resolution of ~2 ps.

D. High-Resolution TDC Chip

Fig. 7 shows a block diagram and chip layout of the integrated TDC chip. The TDC consists of two parts, – a digital Coarse TDC (counting clock periods) and an 8-bin Fine TDC (measuring a 1/8 fraction of the clock period). The digital part counts the number of clock periods between COMMON START and HIT signals. The analog part (the 8-bin prescaler) gives the position of HIT pulse corresponding to CLOCK pulse in 1/8's of a clock period. This provides a time resolution of up to 2 ps. Both analog and digital parts share the same CLOCK and HIT terminals. To remove any induced delay between signals arriving at the digital TDC and prescaler, we use a calibrated delay line. The calibration process for this line is simple. By applying the same signal to both CLOCK and HIT terminals, the user sets the reading of the prescaler to exactly zero.

III. Conclusion

We are developing a TDC based on the combination of the fine-resolution analog prescaler and a coarse digital TDC, which will provide a substantial performance improvement over both existing as well as prospective TDCs based on other technologies. We have successfully demonstrated 6 ps performance and have shown the feasibility of 2 ps time resolution.

Acknowledgment

We thank D. Brock, A. Bross, S. Rylov, and J. M. Vogt for helpful discussions and assistance.

References

[1] O. A. Mukhanov, A. F. Kirichenko, and J. M. Vogt, and M. S. Pambianchi, "A superconductive multi-hit time digitizer," *IEEE Trans. Appl. Supercond.*, vol. 9, 1999. (in press).

[2] O. A. Mukhanov and S. R. Rylov, "Time-to-digital converters based on RSFQ digital counters," *IEEE Trans. Appl. Supercond.*, vol. 7, pp. 2669-2672, Jun. 1997.

[3]A. F. Kirichenko, O. A. Mukhanov, and S. V. Rylov, "Superconductive time-to-digital converters", in: *Extended Abstracts of ISEC'97*, Berlin, Germany, vol. 1, pp. 34-37, Jun. 1997.

[4] S. V. Rylov, L. A. Bunz, D. V. Gaidarenko, M. A. Fisher, R. P. Robertazzi, and O. A. Mukhanov, "High resolution ADC system," *IEEE Trans. Appl. Supercond.*, vol. 7, pp. 2649-2652, Jun. 1997.

Multiple Bit-Rate Clock Recovery Circuit: Theory

Vsevolod Kaplunenko
Conductus, Inc., 969 West Maude Ave., Sunnyvale, CA 94086

Abstract—The multiple bit rate clock recovery circuit has been recently proposed as a part of the communication packet switch. All packets must be the same length and be preceded with the frequency header, which is a number of consecutive ones (return-to-zero mode). The header is compared with the internal clock, and result is used to set output clock frequency. The clock rate is defined by a number of fluxons propagating in ring oscillator, which is a close circular Josephson transmission line. The theory gives a bit rate bandwidth as a function of internal clock frequency, header length, and silence time (maximum number of consecutive zero's in the packet.)

I. Introduction

The most severe bottleneck in high-speed packet-switched networks is the limited synchronization speed of semiconductor electronics. Different receive packets can have different bit-clock alignment and different clock frequencies (bit-rates), thus requiring the receiver system to perform a new clock recovery for each data packet. The clock recovery, or phase locking of the clock to incoming data, must be completed in a small fraction of the packet duration to minimize wastage in transmission capacity. Although advanced GaAs circuits and silicon technology can operate at 40 Gb/s [1-3], the synchronization circuits are limited too much lower speed and long locking time. Recently the instantaneous single bit-rate clock recovery circuit [4] with a locking time of 1-bit has been reported to operate at 35 Gb/s [5]. The next step is taking an advantage of superconductivity to build a circuit that accepts digital signal with different bit-rates. This paper shows the background theory of the relatively simple multiple bit-rate clock recovery (*MBRCR*) architecture (see also [4].) One of the main parts of the circuit is an adjustable bit-rate oscillator, which is discussed in section II. Section III describes how to obtain desired bit-rate bandwidth and section IV be about the possible error treatment.

II. Adjustable Bit-Rate Clock Recovery Circuit

The heart of the *MBRCR* circuit is an adjustable bit-rate clock recovery cell (*ABRCR*) shown in Fig.1. It has one output and three inputs: "set phase" (sp), "set frequency" (sf), and "reset" (r). The Non destructive readout circuit (*NDRO*) is a switch for fluxons coming from Josephson transmission line *JTL3*. Input "s" sets and input "r" resets the state of the *NDRO*. If the *NDRO* is in the "set" state, fluxons are passed to *JTL4*; otherwise they escape. Thus *JTL2-JTL3-NDRO-JTL4* forms a closed *JTL* loop (or ring oscillator *RO*) in the first case, and just *JTL* with open ends, in the second case. A ring oscillator used in the single bit-rate clock recovery circuit (*SBRCR*) is described in [4]. The *ABRCR* cell differs from *SBRCR* cell by addition of the *NDRO*, Josephson junction J_2, and input "sf" (*JTL5*). A fluxon coming from *JTL5* will switch junction J_2, and starts circulating within the ring oscillator if the *NDRO* is set. The more fluxons are sent to "*sf*" input the higher clock frequency will be at the output [6]. The *SBRCR* has a superconducting transformer instead, which can set only the fixed number of fluxons in the ring oscillator [4]. Generally, fluxons, which arrive to the set frequency input might not be equally time spaced. This means that if n fluxons are sent to "*sf*" input, the same number of n equally time spaced fluxons should be sent to the set phase input (after set frequency process is completed.) During this process there is need to prevent backward fluxons from the output to the input of *NDRO* cell, which requires the fluxon time propagation in *JTL2* and *JTL4* to be larger than the propagation time in *JTL3*. Only one fluxon has to be sent to the reset input of *NDRO* cell to remove all fluxons from the ring oscillator. The typical time required for that is a time, which a fluxon needs to make one turn in the ring oscillator. The maximum number of fluxons n_{max}, which can be written into the ring oscillator, is defined by the fluxon interaction during their propagation within the *JTL* [7]. If there is no such interaction, each fluxon added to the ring oscillator increases output frequency proportionally.

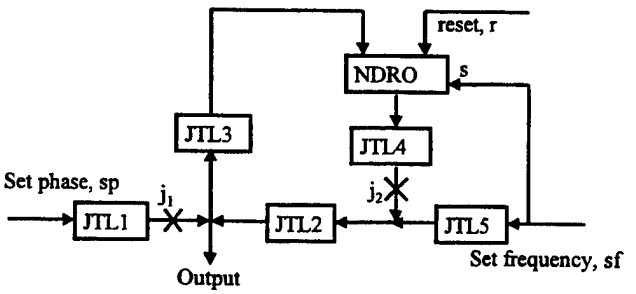

Fig. 1 Block diagram of the adjustable bit-rate clock recovery cell (*ABRCR*). Crosses are Josephson junctions, *JTL* - Josephson transmission lines, *NDRO* - non-destructive readout cell.

Manuscript received April 30, 1999.
This work was supported in part by the U.S. SBIR Grant No. DASG60-98-M-128

III. Multiple Bit-Rate Clock Recovery Circuit

The circuit in Fig.2 separates the frequency header from the packet, and routes it to the *ABRCR*. The initial state of the *MBRCR* is set by reset fluxon, which can be sent either by *counter2* or externally upon the error occurrence. The fluxon resets *ABRCR*, *counter1*, *counter2*, closes *NDRO2*, and sets *latch1*. One of the key elements of the circuit is a single bit-rate clock recovery (*SBRCR*), which is a synchronized internal clock with locking time of one bit. It generates fluxons at frequency f_c, which is a little higher than the maximum frequency f_{max} of the *ABRCR*. The first incoming bit is extracted by the *latch1*. It synchronizes internal clock [4] and opens *NDRO1*. *Counter1* starts calculation of the fluxons arriving from the internal clock. On the counting completion *NDRO1* is closed, and this stops the frequency header sampling by *latch2* (*latch2* is set with the speed of the incoming data, and it is reset by the synchronized *SBRCR*.) Sampling time is defined by speed of the internal clock and by the size of the *counter1*. Input data frequency f_{in}, is less than f_c, thus only part of the frequency header will be written into the set frequency input of *ABRCR*. The written number of fluxons, n, may vary from 1 to n_{max}. Time delay *d1* provides *latch2* inputs synchronization (see discussion below). Time delay *d2* should be larger than the setting frequency time n_{max}/f_c to prevent any phase change during the writing fluxons into *ABRCR* cell. The first bit of the packet is delayed by *d2*, opens *NDRO2*, and *counter2* starts calculation of the packet length just after frequency is set in *ABRCR*. Such a connection provides a good margin for time delay *d2* - it can be as large as the time distance between the packets. The whole header is also passed to the set phase input of the *ABRCR* and sets right phases for all fluxons in the ring oscillator. Time delay *d3* matches the data with the recovered clock. As a result of normal operation the *counter2* sets circuit to the initial state, which is the one when it is ready to accept an incoming packet. Fig. 3 shows the result of simulation of the circuit in the Fig. 2 obtained for the packets with the four bits frequency header length.

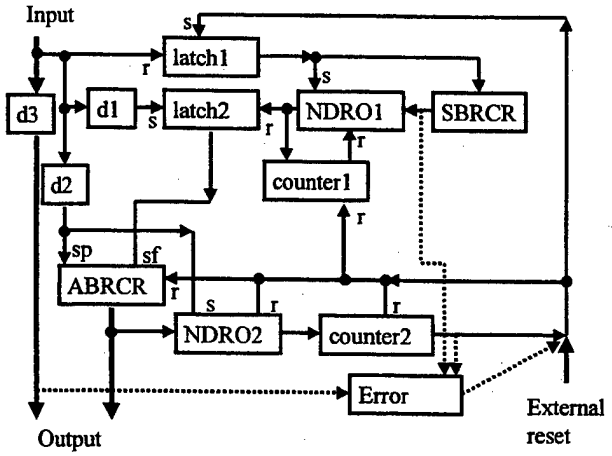

Fig.2 Block diagram of the circuit recovering phase and frequency.

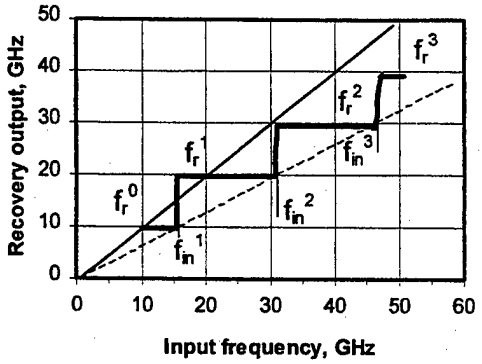

Fig. 3. Output frequency produced by 22 junctions ring oscillator as a function of the four-bit header frequency. Maximum frequency of the ABRCR f_{max}=39.3 GHz. Curves calculated for *SBRCR* frequency f_c=46.5 GHz. Clock recovery operation area ($f_{in}>f_{max}$) is under the thin solid line. Horizontal distance between this and a dashed line shows possible bandwidth for each harmonic. f_r^k- recovery output frequencies at different number of written fluxons $n=k+1$. f_{in}^k - input frequencies at which number of written fluxons is changed.

Fig. 4 shows time diagram at the inputs of the *latch2* cell in Fig. 2. The data proceed via delay *d1* to the set input of *latch2*, and the synchronized *SBRCR* sends four fluxons to its reset input (*counter1* in Fig.2 has only two stages). Having this synchronization and varying *d1*, one can adjust the first set bit arriving to the *latch2* just before the first reset bit from *SBRCR*. The small time delay is required to enable *latch2* to transmit first bit to its output. In a case of the clock frequency of the data, f_{in} is equal or higher than the *SBRCR* frequency f_c, all input bits proceed to the *latch2* output (Fig. 4a). For the smaller values of the input clock frequency only the first three bits (Fig. 4b) or the first two bits (Fig. 4c) will be sent to *ABRCR*.

From Fig. 4 relatively easy to find number of fluxon n which will be written into the *ABRCR* cell:

$$n = 1 + \mathrm{int}(t_c(n_{\max} - 1)/t_{in}) \quad (1)$$

$$n = 1 + \mathrm{int}(f_{in}(n_{\max} - 1)/f_c) \quad (2)$$

where int() means integer or whole part of the expression. Thus the clock recovery output frequency f_r^k (Fig. 3) can be written as:

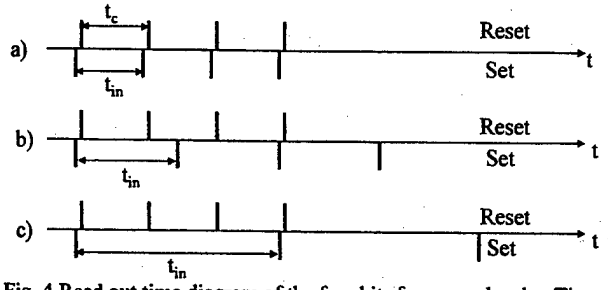

Fig. 4 Read out time diagram of the four bits frequency header. Time period t_c corresponds to the frequency f_c of the *SBRCR*, and t_{in} to the input frequency f_{in}.

$$f_r^k = \frac{n \bullet f_{\max}}{n_{\max}} = \frac{f_{\max}}{n_{\max}}(1+\mathrm{int}(\frac{f_{in}}{f_c}(n_{\max}-1))) = \frac{f_{\max}}{n_{\max}}(1+k) \quad (3)$$

From equition (3) we can find input frequency f_{in}^k at which *ABRCR* changes frequency (Fig. 3):

$$\frac{f_{in}^k}{f_c}(n_{\max}-1) = k, \text{ and } f_{in}^k = f_c \frac{k}{n_{\max}-1} \quad (4)$$

where k is integer which may change from k_{min} to n_{max}-1, and k_{min} - specifies the low frequency limit of wide band clock recovery circuit. For each frequency must be $f_{in}>f_r$, but the most critical requrement for wide band circuit, which covers a few adjusent *ABRCR* frequencies, is $f_{in}^k \geq f_r^k$ (top corners in Fig. 3). Thus combining this with (3) and (4) one can obtain:

$$f_{in}^k = f_c \frac{k}{n_{\max}-1} \geq f_r = \frac{f_{\max}}{n_{\max}}(1+k), \text{ or}$$

$$f_c \geq f_{\max} \frac{k+1}{k} \frac{n_{\max}-1}{n_{\max}}. \quad (5)$$

This ratio should be valid for all k, but it is most critical for the low frequency limit, at which $k=k_{min}$:

$$f_c \geq f_{\max} \frac{k_{\min}+1}{k_{\min}} \frac{n_{\max}-1}{n_{\max}}. \quad (6)$$

Another ratio is seen from Fig. 3. It is coming from the dependence of the bandwidth versus silence time (in bits) t_S [3]:

$$\frac{f_{in}^k - f_r^{k-1}}{f_r^{k-1}} < \frac{1}{t_s} \quad (7)$$

By combining equitions (3), (4), and (7) one can receive:

$$f_c < f_{\max} \frac{(n_{\max}-1)}{n_{\max}}(1+\frac{1}{t_s}) \quad (8)$$

It is easy to obtain simple relation by eliminating f_C from (6) and (8):

$$k_{\min} \geq t_s. \quad (9)$$

Keeping from (6) the smallest single bit rate clock frequency f_C, and having in mind (9), we can calculate optimum value for this frequency:

$$f_c = f_{\max} \frac{t_s+1}{t_s} \frac{n_{\max}-1}{n_{\max}}. \quad (10)$$

Now, by having $k_{min}=t_S$ from (9) and use (4) and (10), we can find the low band frequency f_{LO}:

$$f_{LO} = \frac{f_{\max}(k_{\min}+1)}{n_{\max}} = \frac{f_{\max}(t_s+1)}{n_{\max}} \quad (11)$$

By replacing an input frequency in (7) with the high band freqiency f_{HI}: and a ring frequency with f_{max} one can obtain:

$$f_{HI} = f_{\max}(1+\frac{1}{t_s}) \quad (12)$$

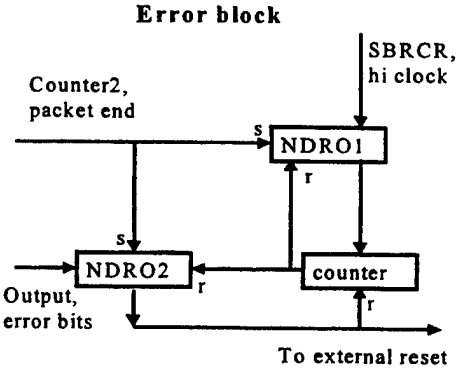

Fig. 5 Block diagram of the error block. See also Fig.2.

Equitions (11) and (12) shows that only n_{max}=16 heading bits of the packet are required to establish its clock frequency in a range from 22.5 to 45 Gb/s, and heaving f_c=42.2 Gb/s, t_S=8, f_{max}=40Gb/s.

IV. Error Treatment

Fig. 5 shows the structure of *Error* cell in Fig.2. There is an assumption that the transfer protocol implies definite minimum time interval between the consecutive packets. The error block watches the input for that time, and if any extra bits arrive, it resets *MBRCR* and resets itself. When *counter2* (see Fig. 2) resets *MBRCR*, it also sends bit to the error block, as shown in Fig.2. This bit opens *NDRO1*and *NDRO2*. Thus the high -speed clock from *SBRCR* (see Fig. 2) is proceeded to the *counter* in Fig. 5. The counter calculates required number of clocks and closes both *NDROs*, which makes circuit ready to accept new packet.

References

[1] H. Suzuki, K. Watanabe, K. Ishikawa, H. Masuda, K. Oichi, T. Tanoue, and R. Takeyari, "Very-High-Speed InP/InGaAs HBT IC's for optical Transmission Systems," IEEE Journal of solid-state circuits, vol. 33, No. 9, pp. 1313-1319, September 1998.

[2] T. Otsuji, K. Murata, T. Enoki, Y. Umeda, "An 80-Gbit/s Multiplexer IC Using InAlAs/InGaAs/InP HEMT's," IEEE Journal of solid-state circuits, vol. 33, No. 9, pp. 1321-1327, September 1998.

[3] Stefano Bregni, Cefriel, "A Historical Perspective on Telecommunications Network Synchronization," IEEE Communications Magazine, vol. 36, pp. 158-166, June 1998.

[4] V. K. Kaplunenko, V.V. Borzenets, N. B. Dubash and T. Van Duzer, "Superconducting Single Flux Quantum 20 Gb/s Clock Recovery Circuit," *Applied Physics Letters*, vol. 71 (1), pp. 128-130, July 1997.

[5] V. K. Kaplunenko, V.V. Borzenets, S. J. Berkowitz, and N. B. Dubash, "Single Flux Quantum Components for Telecommunication Switches," to be published in proceedings of Applied Superconductivity Conference (ASC'98) *IEEE Transactions on Applied Superconductivity1999.*

[6] E. B. Goldobin, V.M. Golomidov, V. K. Kaplunenko, M. I. Khabipov, D. Yu. Khokhlov, A. Yu. Kidiyarova-Shevchenko, "Direct determination of the ultimate performance of the RSFQ digital devices and Single Flux Quantum Voltage amplifiers", IEEE Trans. Supercond. Vol. 3, no 1, pp. 2641-2644, March 1993.

[7] V. K. Kaplunenko, "Fluxon interaction in an overdamped Josephson transmission line", Appl. Phys. Lett. vol. 66 No 24, pp. 3365-3367, June 1995.June 1995.

A Feasibility Study on a High-end Digital Communication System Based on SFQ Technology

Shinichi Yorozu, and Shuichi Tahara

Fundamental Research Laboratories, NEC Corporation, 34 Miyukigaoka, Tsukuba, Ibaraki 305-8501, Japan

Abstract— High-end telecommunication systems will have to have an over 5 Tbps-level switching capacity on the nationwide layer network in the next few decades. Optical fiber data transmission technologies will be able to realize such performance using wavelength division multiplexing (WDM) technologies. However, semiconductor technology which has supported the switching capability increase up to present-day, will may not be able to maintain such a high throughput data switching function from the point of power consumption and operating speed. Superconducting RSFQ technology is a promising alternative, which should be able to overcome such problems.

Based on RSFQ technology, we report on the results of feasibility studies on an over 5 Tbps RSFQ switch fabric and a possible architecture of an optical-electrical-RSFQ hybrid future communication system.

I. Introduction

Broadband networks are evolving rapidly, with constant user demand for improved features, such as larger switching capacities, higher link rates, larger buffer capacities, and better provision of quality-of-service (QoS) guarantees. Some manufacturer have proposed terabit routers, however, these routers have fatal disadvantages of poor QoS, hardware power and volume, so the effective performance of a network equipped with such a router would be strongly limited because of the propagation delay in the router itself. "Real" high-end digital systems will have many unknown solutions in its construction by the device processing performance and its packaging technology, although CMOS is clearly dominant commodity circuit technology today and in future. Superconducting RSFQ technology has very advanced characteristics for digital signal processing. In this paper, we will report on some proposals and considerations for Tbps communication systems.

II. Next-generation communication system

Consider the transmission capacity of Japan in around 2010 as a starting point for the discussion. It's estimated that the information transmitted to each home consisting of many multi-media data from voice to high-definition TV images would be over 100 Mbps. The total traffic in the nation's backbone network would therefore be about 400 Tbps and transmission capacity would be over 5 Tbps [1]. This means that a switching system with a capacity of over 5 Tbps will be required. We regard this value as a lower limit in the future communication system. Optical fiber transmission with compound semiconductor driver/receiver interface system to supply such a capacity is way for transmission. For switching, it is very difficult. Si CMOS technology will be able to operate at several giga-herz ranges in the future [2], so it can play an important role only in future access and subscriber network switching systems. For the future backbone network however, although some compound semiconductors are possible candidates, it is still unknown whether they will ever be capable of such tremendous speeds.

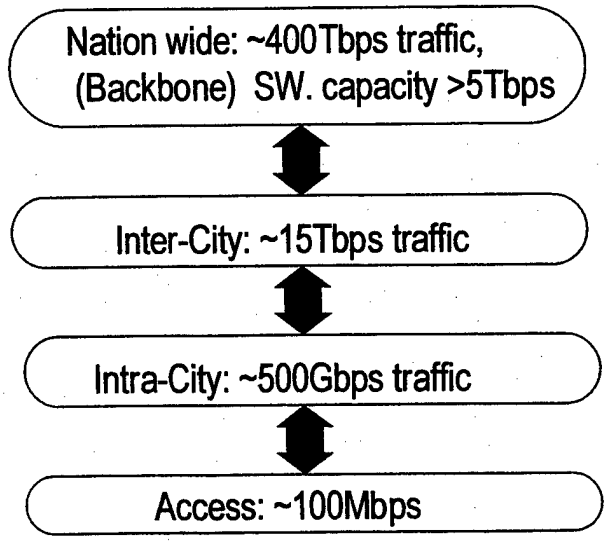

Fig. 1. Predicted hierarchical transmission capacity in Japan in 2010

III. Consideration of switching system with RSFQ

A. Architectural issues

Asynchronous transfer mode (ATM) switching and other forms of packet switching such as IP routing, are emerging as key to the implementation of future high-capacity and multi-function networks. ATM switching techniques, combined

Manuscript received April 30, 1999.
This work was performed through Special Coordination Funds for promoting Science and Technology of the Science and Technology Agency of the Japanese Government.

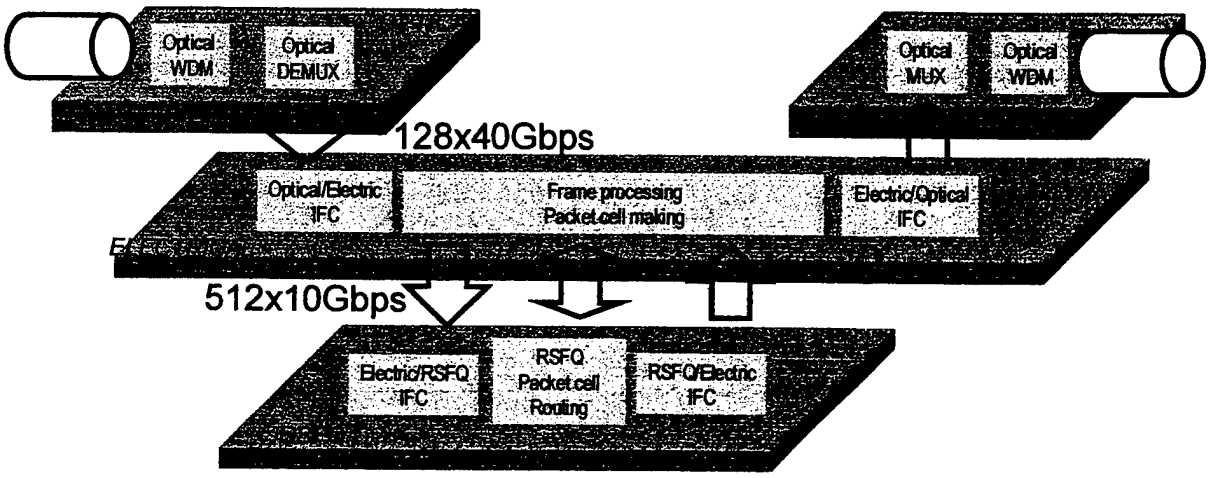

Fig. 2. Optical/Electrical/RSFQ hybrid telecommunication switch unit

with the SDH/SONET standard, provide a flexible transmission. Meanwhile, IP routing and switching is emerging as a key to future expansion of data and other internet-related services. Both techniques need a high performance packet switch. In this report, we focus on a packet switching system that has no specialized switching techniques. There are many complex processing parts in a packet switching system, and the integration scale of RSFQ is smaller than that of conventional semiconductor logic. As a result, we propose hybrid system approach in which the switching system is separated into two functions. The first is a packet routing function which requires non-blocking high-performance packet switch, and other one is a control function which requires complex operations to be performed at relatively moderate speeds like high-performance CMOS.

Fig. 2 shows a proposed optical/electrical/RSFQ hybrid communication unit. Optical WDM signal is optically demultiplexed and converted to an electrical signal. The electrical signals are first processed in a semiconductor processor. In this electrical processor, a simple packet including only the destination address and data creating, packet frame processing, packet header conversion, and other control signal processing are done. After the electrical processor procedure has been completed, the packets are sent to the RSFQ part for packet switching. RSFQ circuit can be operated at over 40 GHz, so we can develop a packet compression to increase the input speed in RSFQ packet switch to 40 Gbps when the incoming packet speed is below 40 Gbps.

This approach is expandable in hierarchical switching systems. For example, ATM switch has many different QoS classes. So if we switch data directly, we need complex circuits that limit effective performance. In this case, we propose that switching procedure itself should be divided hierarchically. Fig. 3 shows the hybrid-hierarchical switching system. There are two kinds of switches with control logic. Inserted packets are pre-processed for two stage switching. Stage 1 involves relatively complex processing, and stage 2 involves simple high-speed routing.

B. Performance needs of RSFQ switching fabric

Fig. 4 shows performance results of switching LSI chip [3-5]. The performance of CMOS and compound semiconductors may be limited to around 160 Gbps/chip by heating or pin-neck. The performance of a 2x2 superconducting crossbar switch is estimated at below 20 ps using 0.8 μm technology [6]. We can therefore assume 25 ps or 40 GHz operation in the RSFQ switching fabric. So we can aim more attractive throughput target than semiconductor fabric. TARGET A in Fig. 4 has a 40 Gbps in/out interface speed. In this case an improved interface, optical/RSFQ/optical direct interface will have to be developed. TARGET B in Fig. 4 is for 10 Gbps port speed versions. In the 10 GHz domain, the reliability of the

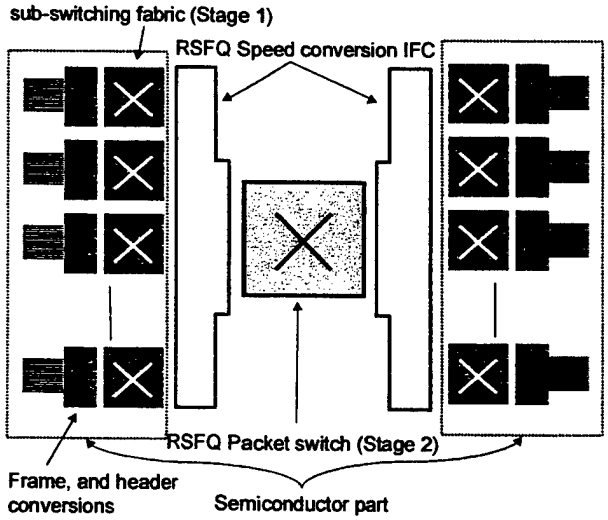

Fig. 3. Block diagram of a hierarchical switch

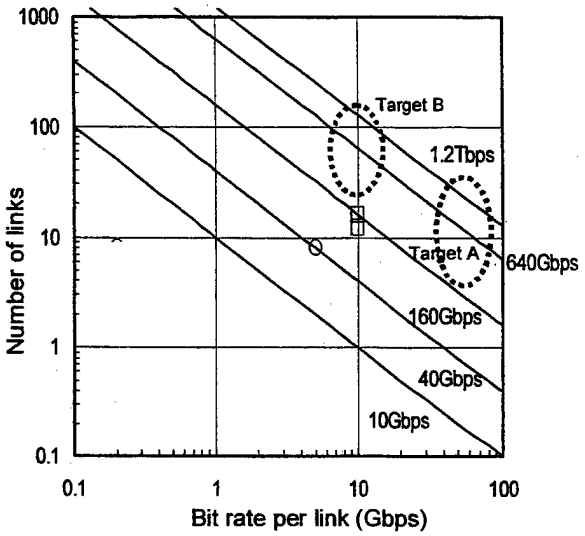

Fig. 4. Reported results of performance of switching LSI. The open circles show the results of CMOS; Open rectangles show the results for compound semiconductors.

interface circuit will be better than in the 40 GHz domain. Although the number of I/O pins has to be increased, it looks like TARGET B may be more possible way from the consideration the state of the art of RSFQ interface technology. For example of the case TARGET B, a 5 Tbps optical WDM signal switching unit can be created from 128-40 Gbps optical signals and converted 512-10 Gbps electrical and RSFQ signals as shown in Fig. 2.

The switch fabric's topology is also a significant component of the communication systems hardware design. For superconducting devices, the criteria for fabric selection are; the total throughput, latency, and hardware complexity (number of JJ, power dissipation, and area). Space division type is better than time division type because time division type requires many high-speed memories. A Banyan network is constructed from 2x2 switching elements with a single path between any input and output pair. The Banyan network's complexity of paths and switching elements is of order N logN, which means that it uses less hardware than other types of switches, such as crosspoint switches. This makes it much more suitable than the crossbar structures for the construction of large switch fabrics. According to the estimation of SUNY's group and one of authors [6,7], it is possible to have a throughput of several hundred Tbps, if one employ an RSFQ Banyan network. Therefore, we will be able to make an RSFQ space division packet switch for the system.

IV Open issues

From the above discussion, consider the technology that will be needed. Interface technology is the most important problem. For chip-to-chip communication, high speed MCM with solder bonding will be needed. For an interface between 4.2 K to room temperature is also a problem. As far as we use metal wiring, we don't need special interface technology for signal conversion, but the many wires and huge amount of incoming heat associated with the wiring and limits its bandwidth about 10GHz digital signal. If we use an optical interface case, we can drastically change our system. We can reduce hardware quantity, the number of cables and heat load, but we have to develop a special I/O interface between the signals. In large-scale superconducting systems which include outer processing systems, the latency between 4.2 K and room temperature should be restricted to a reasonable length, even if we take latency-hide architecture. This means we should make cable length as short as possible. From a refrigeration point of view, we should continue to develop optical interface technology. Fabrication technology is also important. In our optimistic estimate, it will be possible to have 1.0 μm-10 MJJ/cm^2 with 1 %σ technology. We should demonstrate a proof of concept system until the fabrication technology will be ready.

V. Conclusion

We report on a feasibility study on a future optical-electrical-RSFQ hybrid telecommunication system. We propose separating system into two functions; a packet routing function, which requires a non-blocking high performance packet switch, and a control functions which requires complex operations to be performed at relatively moderate speed. This approach has the advantage that the RSFQ part can route packets without complex processing.

Acknowledgment

We would like to express our gratitude thanks to Dr. D. Zinoviev, Dr. H. Terai and Dr. K. Matsuoka for their useful discussions.

References

[1] K. Hirahara, T. Fujii, K. Ishida, and S. Ishihara, "Optical Communications Technology Roadmap," *IEICE TRANS. ELECTRON.*, vol. E81-C, No.8, 1998.

[2] Semiconductor Industry Association, "National Technology Roadmap for Semiconductors," 1997 Edition.

[3] Y. Ohmoto, et al., "A 40-Gb/s 8x8 ATM Switch LSI Using 0.25-μm CMOS/SIMOX," *IEICE TRANS. ELECTRON.*, vol. E81-C, No. 5, 1998.

[4] K. Lowe, "A GaAs HBT 16x16 10-Gb/s/Channel Crosspoint Switch," *IEEE J. of SOLID-STATE CIRCUITS*, vol. 32, No. 8, 1997.

[5] A. Metzger, et al., "A 10Gb/s 12x12 Cross-Point Switch Implemented with AlGaAs/GaAs Heterojunction Bipolar Transistors," Tech. Dig. 1997 GaAs IC Symp., pp. 109-112, 1997.

[6] S. Yorozu, and D. Zinoviev, "Design and Implementation of an RSFQ Switching Node for Petaflops Networks," to be published in *IEEE TRANS. APPLIED SUPERCONDUCTIVITY*, 1999

[7] L. Wittie, D. Zinoviev, G. Sazaklis, and K. Likharev, "CNET: RSFQ Switching Network for Petaflops-Scale Computing," to be published in *IEEE TRANS. APPLIED SUPERCONDUCTIVITY*, 1999

Towards a 16 Kilobit, Sub-Nanosecond Josephson RAM

Quentin P. Herr and Larry Eaton
TRW, Space & Electronics Group, Redondo Beach, CA 90278

***Abstract*—A critical component of ultra high speed Josephson logic systems is compatible memory. We are developing a fast Josephson memory that could be used as a small memory or first-level cache. Performance goals include sub-ns access and cycle time, 16 kb/cm^2 integration scale, low power consumption, and appreciable yield. Initial test results on circuits fabricated in TRW's standard Nb integrated circuit process, indicate that all these goals may be achieved. A 5-bit parallel decoder and 1 kb memory array have been tested at 0.5 GHz. The maximum operating frequency of the memory array was limited by the test equipment. Circuit density is consistent with 16 kb/cm^2. The top-level architecture has been chosen to achieve high throughput and low skew. The architecture is word-organized, multi-ported, and interleaved.**

I. Introduction

RECENT ADVANCES in Josephson single-flux-quantum (SFQ) analog-to-digital converters and digital signal processing logic circuits have been dramatic [1], [2], [3]. There is now renewed interest in Josephson logic for general computing applications, such as the Hybrid-Technology, Multi-Threaded (HTMT) supercomputer project [4], [5], [6]. Such a system requires Josephson random-access memory (RAM) to serve as a high-bandwidth, low-latency, first-level cache. We report progress in the development of a Josephson RAM. Project goals include sub-ns access time, high bandwidth, low power, and 16 kb/cm^2 density. This density, achievable using TRW's conservative but stable 2.5 μm, 2 kA/cm^2 Nb foundry process [7], is hardly within sight of semiconductor SRAM. Nevertheless, it does scale to meet HTMT requirements given the development of a 0.8 μm, 20 kA/cm^2 process [8].

Two sources of information have proven invaluable to the present project. The first is the 4 kb Josephson RAM developed at NEC [9], [10], which has achieved favorable gate density and yield. The second is development of a 16 × 16 crossbar switch operating at 3 Gb/s [11]. This bears directly on the problem of high-speed signal propagation in the memory gate array. We discuss RAM design in terms of three orthogonal fields: architecture, decoder design, and memory array design, which includes address line amplifiers and sense amplifiers.

II. Architecture

To maximize speed and bandwidth, the RAM organization we propose is multi-ported, interleaved, and low skew. Low skew is especially important for Josephson RAM as it is relatively fast and sparse; access time may be dominated by time-of-flight rather than gate delay. A top-level schematic of our RAM organization is shown in Fig. 1. The RAM consists of two independent RAM blocks each with its own input and output ports. The blocks are 64 × 128, as appropriate to achieve 16 kb capacity. The blocks are word-organized; each row stores a 64-bit word. The proximity of all bits in the word minimizes skew. This differs from the H-tree architecture reported in [10], in which each bit of the word is stored in a different block. Decoding is required only for the rows. *Two* row decoders are shown for each block; this is because two bits of information must be supplied to each row. Together, these two bits indicate whether the row is selected and whether the operation is a read or a write. Decoders are not needed on the columns. However, address line amplifiers are needed for both columns and rows as shown. Finally, sense amplifiers are required to detect ouput of the read operation.

Manuscript received May 1, 1999.

This effort was funded by the Department of Defense's Microelectronics Activity (DMEA) under contract F04606-95-D-0069-0015.

III. Decoder

The decoder logic takes an N-bit input address and converts it to a 1-of-2^N output. The most critcal considerations for decoder design are power and footprint. As drawn in Fig. 1. the linear dimension of one output bit of decoder logic must not exceed that of the memory cell itself in order to achieve maximum density. Decoder power can dominate the total power budget, as all decode logic must be powered continuously. By contrast, only one row of the memory array need be powered at any given time. Total real estate and delay of the decoder is generally small compared to the size and delay of the memory array itself; this relationship holds as the architecture is scaled to larger capacity.

Various possibilities exist for implementation of the decode logic, such as an SFQ gate array, a tree decoder using latching squids at each node, and the latching decoder described in [12], which achieves a delicate balance between junction count, speed, and power. Here we report a decoder design which marries features of the squid-based tree decoder with the resistively shunted, self-resetting junctions and dc power commonly

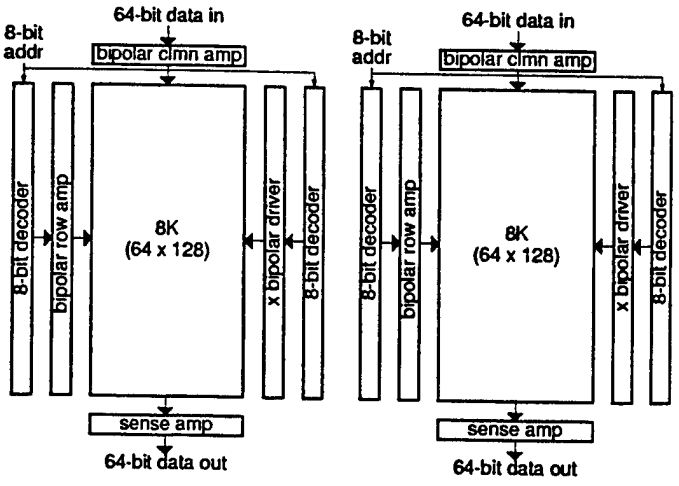

Fig. 1. Schematic of 16 kb RAM, showing memory array, decoders, address amplifiers, and sense amplifiers. One word is stored in each row of the array. Organization is multi-ported, interleaved, and low skew.

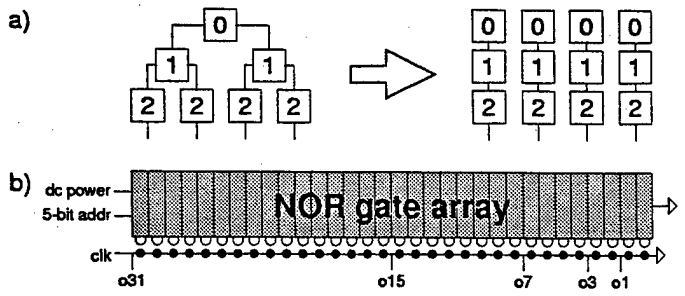

Fig. 2. Schematic of 5-bit parallel decoder. a) Tree decoder configuration, with fanout of two (left) can be reconfigured as a NOR gate array with fanout of one (right). b). The decoder as tested includes latching squids at each output (dark dots). These are arranged in a series.

associated with SFQ logic. Signal levels are an order of magnitude less than that of latching logic and fanout is limited. Fanout of one is all that is required if redundant gates are used to pad out the tree decoder configuration, as shown in Fig. 2a. Each column in the figure represents a NOR gate. The NOR-gate array is dc-powered in series; this obviates the need for isolation resistors between each gate and the power bus. Current and power requirements are both kept to a minimum. The dc power requirement is 5 μW and 0.6 mA. Address signal levels are 0.2 mA at 2.8 mV contributing a heat load of about 1 μW.

A stand-alone 5-bit decoder has been fabricated and tested using TRW's standard Nb process [7]. The width of each NOR gate is 44 μm; total dimensions are 1.5×0.3 mm^2. A schematic of the decoder is shown in Fig. 2b. A series stack of 32 latching squids, inductively coupled to the NOR gate array, serve to amplify the output level. Several but not all of these squids were wired up, as indicated. The circuit was tested using an HP 80000 data generator and a Tektronix sampling oscilloscope. A gradual

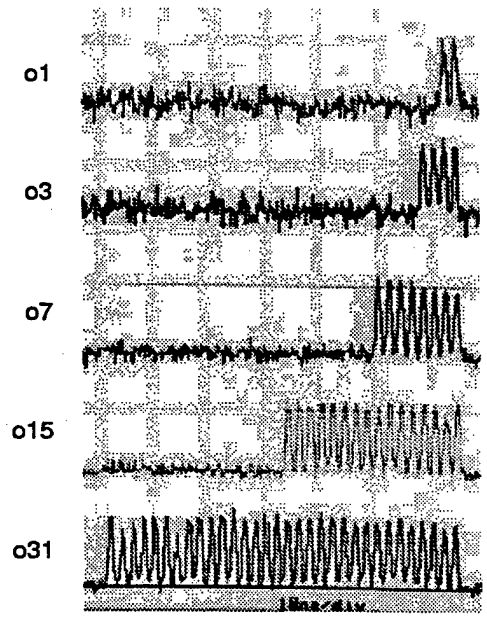

Fig. 3. Output of the 5-bit decoder at 0.5 GHz indicating correct operation. The address input counts sequentially from the high (o31) to low (o0). This is reflected in the output read from the latching squid stack.

cool down through the superconductor transistion temperature was accomplished using a flow-controlled, variable temperature cryostat. Output indicating that the decoder is fully functional, at a clock rate of 0.5 GHz, is shown in Fig. 3. Correct output was observed up to 0.9 GHz. Speed was most likely limited by resonance in the series stack of squids at the output, rather than by the internal dynamics of the NOR gate array. In simulation, the NOR gate logic is limited by the fall time in the coupling to the latching squid ouput, but this fall time is on the order of 0.1 ns. If so, operating frequency will be dramatically improved by powering the output squids in parallel.

IV. Memory Array

Josephson memory cells are similar in complexity to semiconductor SRAM, but are unique in that they feature zero power dissipation in the hold state. With appropriate design, power is only consumed by cells which are actively read or written. Integration scale and speed are the two most critical design issues. Integration scale is predicated on the size of the unit memory cell. Speed typically has little to do with the dynamics of the individual cell, but depends upon the speed of signal propagation through the array; the address line amplifier, memory array, and sense amplifier must be considered as a unit. In the worst case, signal propagation is limited by the time constants present in the circuit; is the inductance of the address line in the memory array, is determined by the current and voltage levels generated in the address line amplifier. In the best case, the address line may be modeled as constant impedance microstrip, impedance matched to the address line amplifier. In this case signal propagation may approach the speed of light.

We have developed a memory cell similar to the vortex-transistional (VT) memory cell developed by NEC. The VT memory cell features wide operating margins, SFQ storage, compact layout, bipolar row and column address levels, and bit addressing. These last two features have direct implications for the architecture of Fig. 1. While a read operation can be effected in a single clock cycle, the write operation requires that "zeros" are explicitly written to each bit of the word during the first clock cycle, using a certain polarity on the row address line, and that "ones" are written to the appropriate bits during the second clock cycle, using the opposite polarity on the row address line. A weakness of the VT cell is that the stored SFQ is inductively coupled to the read squid. A specialized fabrication process is required to achieve the unusually high coupling effeciency necessary to realize robust operation [13]. We have implemented a cell with improved read-out.

A 1 kb RAM block, complete with address line amplifiers and sense amplifiers, has been fabricated and tested. The block is arranged as a 32×32 array, as shown in Fig. 4. Cell dimensions are 44×44 μm^2. The address line amplifiers and sense amplifiers are all arranged as 32-high latching squid stacks. The circuit was tested using the same room-temperature electronics listed above. In all, 6 rows and 6 columns within the array were wired. All 36 memory cells thus accessable were fully functional at low speed. This speaks to good process control. Fig. 5 shows correct output of a single cell at 0.5 GHz. Speed was limited by the 1 ns minimum pulse width of the data generator. It is expected that the operating frequency is ultimately limited by

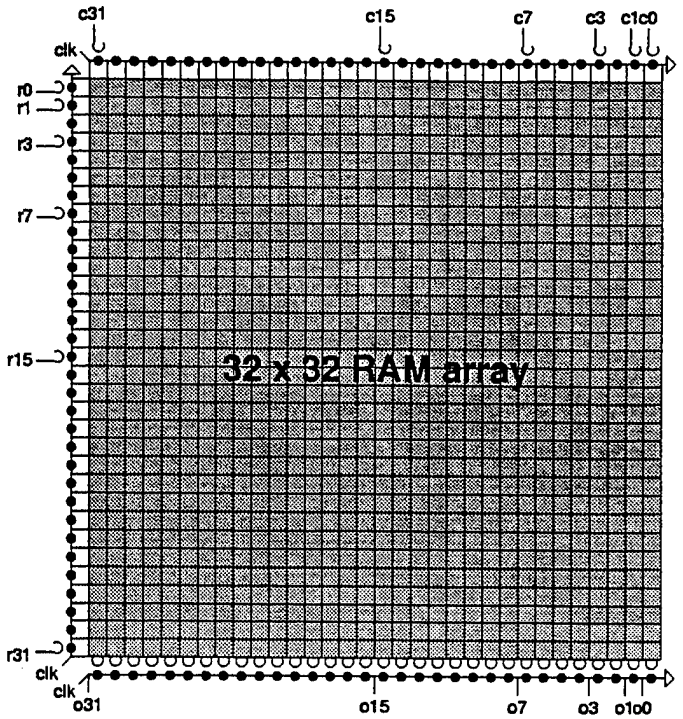

Fig. 4. Schematic of 1 kb RAM array, complete with address line amplifiers and sense amplifiers. The amplifiers (dark dots) are latching squids arranged in series stacks. Six column and six row input lines, and six output lines were wired up, as indicated.

signal propagation during the read operation. Data on maximum frequency has been gleened by measuring the width of the timing window on the sense-amplifier clock. The timing window of 0.66 ns within the 1 ns pulse width suggests a maximum clock frequency well above 1 GHz.

Stacking of the column address amplfiers as shown in Fig. 4 allows individual cells to be accessed with minimum power. However, this configuration is not consistent with the architecture of Fig. 1, in which data is stored with each RAM block as words, not individual bits. The data shown in Fig. 5 corresponds to the cell in the lower left-hand corner of the array, which is the row and column furthest from ground. Other cells in the same column also operated at 0.5 GHz. Cells in lower columns, however, suffered speed limitations; the lower the column, the lower the maximum operating frequency. Detailed circuit simulations of the entire memory array indicate that this is attributable to the parasitic capacitance-to-ground of the memory array; when the column address line amplifier nearest ground latches, the entire memory array must be charged to that voltage level. This problem is easily solved by powering the amplifiers in parallel, which also yields a configuration consistent with the top-level architecture.

V. Conclusion

We are pursuing an architecture for a multi-ported, interleaved, low skew Josephson RAM. Initial estimates and circuit demonstrations indicate 16 kb/cm^2 density and sub-nanosecond access and cycle time are achievable using TRW's standard 2 kA/cm^2 Nb fabrication technology. Capacity scales to HTMT

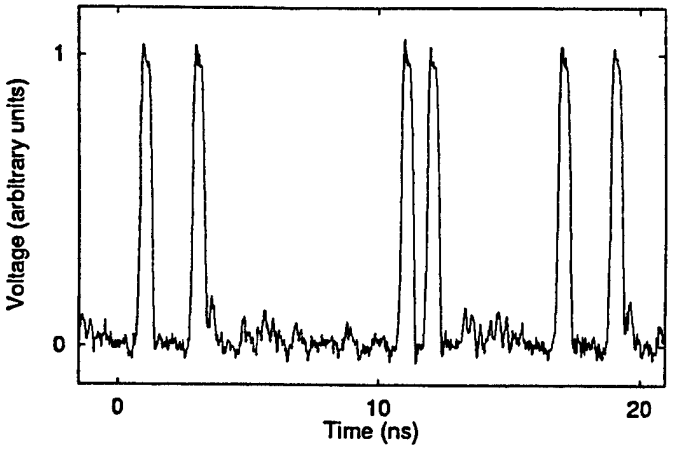

Fig. 5. Output of one cell within 1 kb memory array at 0.5 GHz indicating correct operation. Input wavefrom includes half-select conditions for the cell. Output amplitude is approximately 2.8 mV. No averaging or smoothing is used.

requirements given advanced design rules. Decoder and memory circuits have been demonstrated which feature critically-damped, self-resetting junctions for all logic operations; latching squids are used only for signal amplification.

Acknowledgment

The authors thank Mike Leung, Lynn Abelson, John Spargo, Dave Feld, and Doc Bedard for invaluable discussions and review of the work.

References

[1] M. W. Johnson, D. Durand, L. Eaton, M. Leung, A. Spooner, and T. Tighe, "NbN Circuits and Packaging for 10 Kelvin IR Focal Plane Array Sensor Signal Processing," *IEEE Trans. Appl. Supercond.*, in press.

[2] S. V. Rylov, D. K. Brock, D. V. Gaidarenko, A. F. Kirichenko, and J. M. Vogt, "High Resolution ADC Using Phase Modualtion-Demodulation Architecture," *IEEE Trans. Appl. Supercond.*, in press.

[3] Q. P. Herr, et. al., "Design and Low Speed Testing of a Four-Bit RSFQ Multiplier-Accumulator," *IEEE Trans. Appl. Supercond.*, vol. 7, pp. 3168-3171, June 1997.

[4] J. Cohen, "Mix of technologies spurs future supercomputer," *Insights*, pp. 2-11, July 1998.

[5] T. Sterling, "In pursuit of a quadrillion operations per second," *Insights*, pp. 8-11, April 1998.

[6] M. Dorojevets, P. Bunyk, Dmitri Zinoviev, and K. K. Likharev, "Petaflops RSFQ System Design," *IEEE Trans. Appl. Supercond.*, in press.

[7] L. Abelson, "Superconductive process technologies," *Ext. Abstr. 6th Int'l Supercond. Elec. Conf.*, pp. 1-4, June 1997.

[8] L. A. Abelson, Q. P. Herr, G. L. Kerber, M. Leung, and T. Tighe, "Manufacturability of Superconductor Electronics for a Petaflops-Scale Computer," *IEEE Trans. Appl. Supercond.*, in press.

[9] S. Nagasawa, Y. Hashimoto, H. Numata, and S. Tahara, "A 380 ps, 9.5 mW Josephson 4-Kbit RAM Operated at High Bit Yield," *IEEE Trans. Appl. Supercond.*, vol. 5, pp. 2447-2450, June 1995.

[10] S. Nagasawa, Y. Hashimoto, H. Numata, and S. Tahara, "High-frequency Clock Operation of Josephson RAMs," *Ext. Abstr. 6th Int'l Supercond. Elec. Conf.*, pp. 290-292, June 1997.

[11] R. D. Sandell, J. W. Spargo, M. Leung, and S. R. Whiteley, "High Data Rate Switch with Amplifier Chip," *IEEE Trans. Appl. Supercond.*, in press.

[12] D. A. Feld, *A 2 Gigabit/s 5-32 Bit-Serial-Decoder for Application in a Crossbar Switch.* PhD thesis, University of California at Berkeley, Berkeley, CA, 1993.

[13] S. Nagasawa, S. Tahara, H. Numata, and S. Tsuchida, "Miniaturized Vortex Transitional Josephson Memory Cell by a Vertically Integrated Device Structure," *IEEE Trans. Appl. Supercond.*, vol. 4, pp. 19-24, March 1994.

Design of a 16-Kbit Superconducting Latching/SFQ Hybrid RAM

Shuichi Nagasawa, Haruhiro Hasegawa, Tatsunori Hashimoto, Hideo Suzuki, Kazunori Miyahara, and Youichi Enomoto
Superconductivity Research Laboratory, ISTEC, 2-1200 Musaigakuendai, Inzai 270-1382, Japan

Abstract— We have designed a 16-Kbit superconducting latching/SFQ hybrid (Slash) RAM, which enables high-frequency clock operation up to 10 GHz. The 16-Kbit Slash RAM consists of four 4×4-matrix arrays of 256-bit RAM blocks, block decoders, latching block drivers, latching block senses, impedance matched lines, and the powering circuits. The 256-bit RAM block is composed of a 16×16-matrix array of vortex transitional memory cells, latching drivers, SFQ NOR decoders, and latching sense circuits. We have also designed and implemented an SFQ NOR decoder that is composed of magnetically coupled multi-input OR gates and RSFQ inverters.

I. Introduction

Several Josephson RAMs have been developed using ac-powered latching devices [1]-[3]. However, the maximum clock frequency of these RAMs is only about 1 GHz. Moreover, high-frequency ac-powering for Josephson RAMs is difficult due to the extremely low impedance of their power bus. Recently, much attention has been focused on single flux quantum (SFQ) devices. These devices have low power dissipation, are capable of high-speed operation up to several hundred GHz, and are remarkably suitable for a deep pipeline architecture. However, SFQ devices lack a large fan-out, making it difficult to construct a RAM having a two-dimensional matrix array of memory cells. On the other hand, the ac-powered latching devices have the advantage of large drivability. Therefore, we have combined the advantages of both the latching devices and the SFQ devices, and designed a 16-Kbit superconducting latching/SFQ hybrid (Slash) RAM that enables high-frequency clock operation up to 10 GHz.

II. Slash RAM Concept

Fig. 1 is a block diagram of the 16-Kbit Slash RAM. The 16-Kbit Slash RAM consists of four 4×4-matrix arrays of 256-bit RAM blocks, block decoders, latching block drivers, latching block senses, impedance-matched lines, and powering circuits. The 256-bit RAM block, as shown in Fig. 2, is composed of a 16×16-matrix array of vortex transitional memory cells [1], latching drivers, SFQ NOR decoders, and latching sense circuits. The main features of the design are as follows. First, latching devices are used to drive a large inductance load such as the word lines of the memory-cell array. Second, impedance-matched lines and latching devices are used for long signal propagation between the 256-bit RAM blocks. Third, SFQ devices are used for the decoder to reduce the power dissipation. Fourth, we introduced the four-stage pipeline architecture shown in Fig. 3. The decoding of the block address and the signal propagation to the 256-bit RAM blocks are carried out in the first stage. The decoding of the internal address in each 256-bit RAM block is done in the second stage. The memory cells are accessed by the latching drivers and the stored information is transferred to the latching senses of each 256-bit RAM block in the third stage. Output signals from the 256-bit RAM blocks are transferred to the latching block senses through the impedance-matched lines in the last stage. We have confirmed by computer simulation that the 16-Kbit Slash RAM functions at a clock frequency of 10 GHz.

Fig. 4 shows an equivalent circuit of an SFQ/latch converter. It consists of a dc-powered over-damping junction

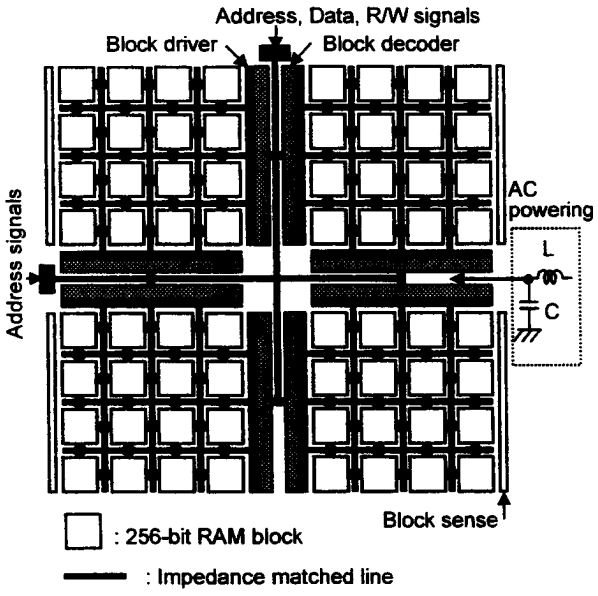

Fig. 1. Block diagram of a 16-Kbit Slash RAM.

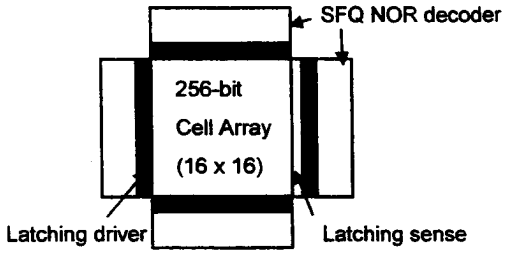

Fig. 2. Block diagram of a 256-bit RAM block.

Manuscript received April 30, 1999.
This work was supported by Special Coordination Funds (Research on Innovative Information Processing using Single Flux Quantum) of the Science and Technology Agency of the Japanese Government.

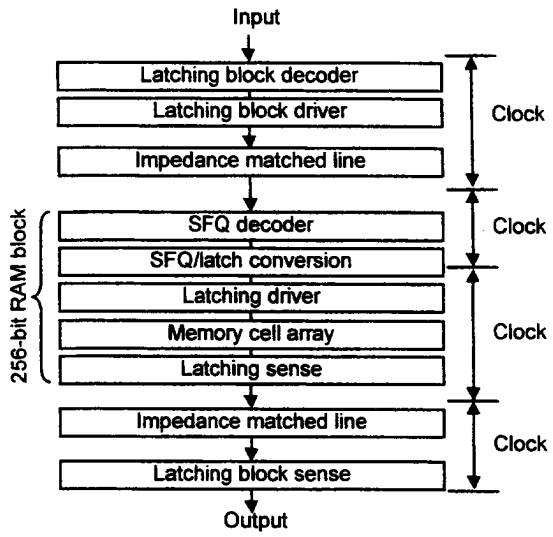

Fig. 3. Four-stage pipeline of the 16-Kbit Slash RAM.

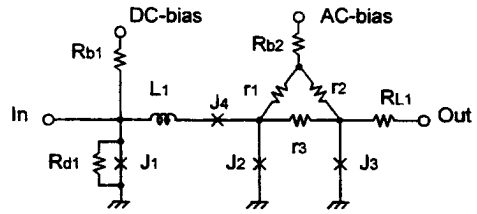

Fig. 4. Equivalent circuit of an SFQ/latch converter. (J_1=0.25 mA, J_2=0.15 mA, J_3=0.15 mA, J_4=0.18 mA, L_1=4 pH, R_{b1}=14 Ω, R_{b2}=46 Ω, R_{d1}=1.5 Ω, R_{L1}=10 Ω, r_1=r_2=r_3=0.5 Ω)

(J_1), and ac-powered under-damping junctions (J_2 to J_4). The critical current of junction J_4 is designed to be higher than those of junctions J_2 and J_3. This condition maximizes the operating margin for the SFQ/latch converter. The simulated ac-bias margin was ± 33%. This circuit enables conversion of an SFQ pulse signal into a latching signal of about 2.8 mV.

III. SFQ NOR DECODER

The SFQ decoder is a main component of the 16-Kbit Slash RAM. The multi-input SFQ NOR circuit, shown in Fig. 5, is a basic element of the SFQ decoder. The multi-input SFQ NOR circuit consists of a multi-input OR gate and an RFSQ inverter. The OR gate is composed of serially connected SQUIDs, each including under-damping junctions (J_{s1} and J_{s2}). The inverter circuit is almost the same as a previously reported one [4], but the circuit parameters were adjusted to obtain a larger operating margin in this NOR circuit. To enable operation of the OR gate with dc power, it is designed to function with a self-resetting mode, determined by the value of resister R_{L1}. As a result, the OR gate outputs a multi-flux quantum (MFQ) signal. However, the MFQ signal is converted to an SFQ signal in the inverter, because the inverter circuit ignores subsequent pulses after the arrival of the initial SFQ pulse in the MFQ pulse. An inverted output SFQ signal is then generated on the arrival of the clock signal.

Fig. 6 shows simulated waveforms of the multi-input SFQ NOR circuit at a clock frequency of 10 GHz. In this figure, "In 1, In 2, In 3, and In 4" are input signals. "OR out" is an output signal from the OR gate. "Clock" is a clock signal for the inverter. "Out" is an output signal from the inverter. When more than one input signal are applied, the OR gate switches into the voltage state, and generates an MFQ output signal, shown as "OR out". The inverter correctly generates an SFQ signal on the arrival of the clock signal, as shown in "Out", only when there is no MFQ signal. This correct NOR function was obtained with parameter margins of more than ± 30%.

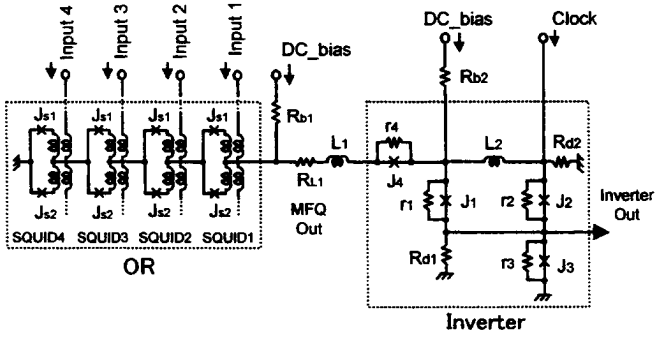

Fig. 5. Equivalent circuits of a multi-input SFQ NOR circuit. J_{s1}= J_{s2}= 0.125 mA, J_1= 0.28 mA, J_2= 0.23 mA, J_3=0.3 mA, J_4=0.18 mA, L_1=10 pH, R_{L1}= 1 Ω, R_{b1}= 57.5 Ω, R_{b2}= 11.5 Ω, R_{d1}= 0.5 Ω, R_{d2}= 0.5 Ω, r_1= 1.4 Ω, r_2= 1.5 Ω, r_3= 1.2 Ω, r_4= 2.0 Ω.

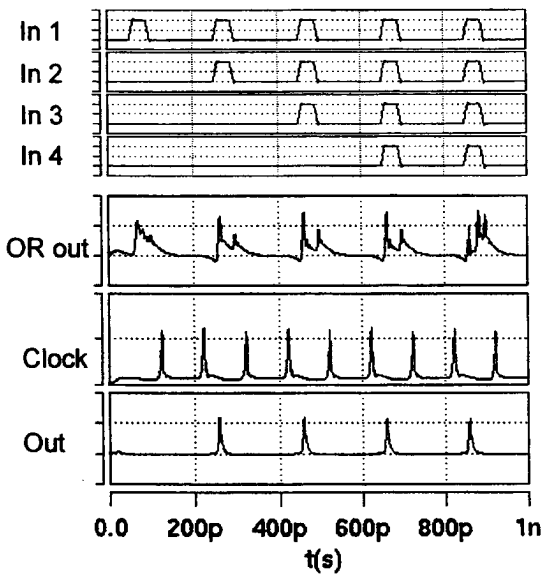

Fig. 6. Simulated waveforms of a multi-input SFQ NOR circuit at a 10-GHz clock frequency. The dc-bias current margin was ± 30%.

Fig. 7 shows half of the equivalent circuit of the SFQ NOR decoder, which outputs 16-bit decoded signals from the input of 4-bit address signals. It consists of 16 multi-input SFQ NOR circuits and a clock-signal-distribution circuit. The address signals are generated by the latching drivers, and are applied magnetically to the multi-input OR gates. The decoder circuit can be easily constructed through the design layout of the magnetically coupled control lines of the OR gates. A clock signal is injected simultaneously to the 16 inverters by the clock-signal-distribution circuit. This circuit has a binary-tree structure that consists of splitters and JTLs. The 16-bit decoded signals are generated at the corresponding output terminals (Out 1 to Out 16) after the clock signal is injected to the inverters.

Fig. 8 shows the layout pattern of the SFQ NOR decoder. 16 NOR circuits are laid out with a 50-μm pitch, which corresponds to the circuit size of the vortex transitional memory cell [3]. The total dc-bias current is 40 mA, and the ac-bias current, which is biased to the latching drivers, is 4.5 mA. This ac-bias current is to about 1/10 that of the previous latching decoder [3]. This layout pattern was designed under the design rule of NEC's Nb standard process [1], where the critical current density of the junction is 2500 A/cm^2, minimum line width is 1.5 μm, and sheet resistance is 1.2 Ω/□.

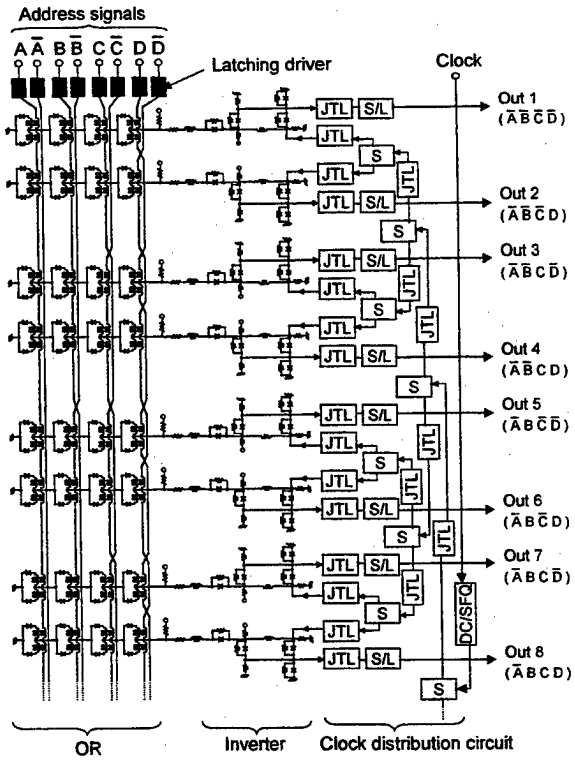

Fig. 7. Half of the equivalent circuit of the SFQ NOR decoder. S: splitter, S/L: SFQ/latch converter.

IV. Conclusion

We have effectively applied the advantages of both latching devices and SFQ devices to design a 16-Kbit Slash RAM that enables high-frequency clock operation up to 10 GHz. AC-powered latching devices are used to drive a large inductance load such as the word lines of the memory cell array or the long impedance-matched lines between the 256-bit RAM blocks. DC-powered SFQ devices are used for the decoder to reduce power dissipation, and are used in the latch circuit of the four-stage pipeline architecture. We designed a new SFQ decoder composed of multi-input SFQ NOR circuits, and confirmed by computer simulation that the SFQ decoder functions correctly with parameter margins of more than ± 30%.

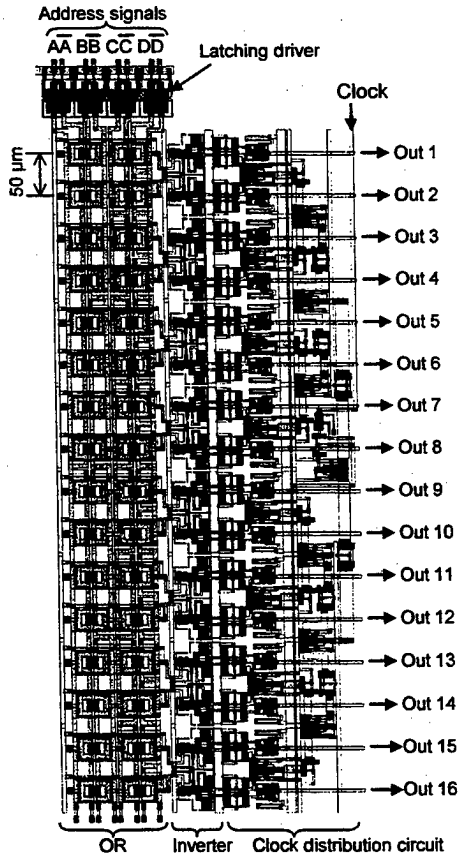

Fig. 8. Layout pattern of the SFQ NOR decoder. Circuit size: 885 μm × 350 μm, Junctions: 489

References

[1] S. Nagasawa, Y. Hashimoto, H. Numata, and S. Tahara, "A 380ps, 9.5mW Josephson 4-Kbit RAM operated at a high bit yield," IEEE Trans. on Applied Superconductivity, vol. 5, no. 2, pp. 2447-2452, Jun. 1995.

[2] S. Nagasawa, H. Numata, Y. Hashimoto, and S. Tahara, "High-frequency clock operation of Josephson memories," ISEC'97 Extended Abstracts, D31, pp. 290-292, 1997.

[3] S. Nagasawa, H. Numata, Y. Hashimoto, and S. Tahara, "High-frequency clock operation of Josephson 256-word × 16-bit RAMs," IEEE Trans. on Applied Superconductivity, to be published in Jun. 1999.

[4] S. Polonsky, V. K. Semenov, P. I. Bunyk, A. F. Kirichenko, A. Yu. Kidiyarova-Shevchenko, O. A. Mukhanov, P. N. Shevchenko, D. F. Schneider, D. Yu. Zinoviev, and K. K. Likharev, "New RSFQ circuits," IEEE Trans. on Applied Superconductivity, vol. 3, no. 1, pp.2566-2577, Mar. 1993.

POSTER SESSION II

Group 2 - SQUIDs

LTS Gradiometers Based-on Superconducting Imaging Surface Design

Andrei N. Matlashov, Robert H. Kraus, Jr., Michelle A. Espy
Los Alamos National Laboratory, Los Alamos NM, 87545 USA

Abstract—Gradiometer-like devices can be built using a superconducting imaging surface design. Such devices behave similarly to conventional wire-wound gradiometers for nearby magnetic sources. A large gradiometer array can be built by placing SQUID magnetometers close to the surface of a large superconducting plane. The most attractive advantage of such a gradiometer array is the ability to change a baseline for all channels simultaneously by mechanically moving the superconducting imaging surface relative to the sensor array. This can easily be accomplished even when the gradiometer array is cold. We built, experimentally tested, and simulated both first- and second-order gradiometer-like devices with adjustable baseline using the superconducting imaging surface design. First-order radial gradiometer sensors were made by placing planar magnetometers parallel to and near the superconducting imaging surface. A second-order electronic gradiometer was realized by subtracting the output from two of the first-order gradiometers described above.

I. Introduction

The superconducting imaging surface (SIS) design is based on the Meissner effect. A magnetic source placed near an infinite superconducting planar surface produces image currents on the surface of the superconductor. This nulls the orthogonal magnetic field component on the surface. The magnetic field at a SQUID magnetometer placed near the superconducting surface is a superposition of both the source and its image. The resulting signal is equivalent to the signal that would result from a radial gradiometer without the SIS. The equivalent baseline is equal to twice the distance from the magnetometer to the superconducting imaging surface. This is true for finite imaging planes where the separation between both SQUID magnetometer and sources and the imaging plane are much smaller than the distance to the edge of the imaging surface. The theoretical basis for the superconducting imaging surface technique for both planar and spherical surfaces is presented in [1]. In this paper we consider only a planar superconducting imaging surface.

Using a sufficiently large superconducting imaging surface with a magnetometer sensor, one can build a device that behaves very similarly to a conventional wire-wound gradiometer for nearby magnetic sources. The gradiometric baseline of such a system can readily be changed by varying the distance between the superconducting surface and the magnetometer. This technique provides a method for building large gradiometer arrays with adjustable baselines (for all channels simultaneously). Adjusting the gradiometer array baseline allows the sensitivity to nearby magnetic sources to be tuned for specific situations. Furthermore, signals recorded with several different baselines can be used to separate sources placed at different distances from the array.

Manuscript received April 30, 1999
This work was supported by the US Department of Energy

II. Separation of Buried Magnetic Sources

Fig. 1 shows two conventional wire-wound gradiometers with different baselines connected in a scheme that can be used to separate magnetic dipoles placed at different depths, D. Assume that there is just one magnetic dipole M, that is placed close to a sample surface. The output gradiometer voltages, V_1 and V_2, are different as a result of the different baselines. The output voltage V_1 is scaled by amplifier SA, and then routed to a differential amplifier, DA, along with V_2. The scale amplifier gain is adjusted to null the output voltage of the differential amplifier, V_{OUT}. In our case, the two-gradiometer system is adjusted to minimize sensitivity to the magnetic field generated by very shallow dipoles in the sample. The output signal for deeper magnetic dipole sources

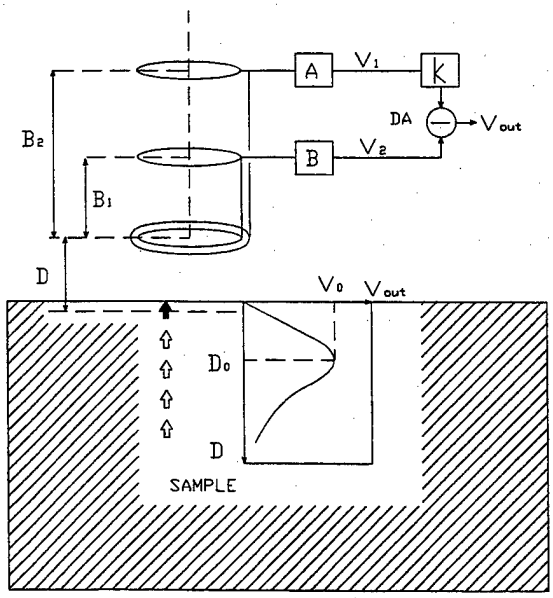

Fig. 1. Separation of buried magnetic dipoles using two gradiometers with different baselines. The gradiometers have output voltage V_1 and V_2 as a response on a shallow dipole M (black bold arrow). V_1 compensates V_2 in the output of a differential amplifier DA. Moving M in deeper areas (white arrows) generates the output voltage V_{OUT}. D_0 is the depth at which the system has the highest sensitivity.

increases and reaches a maximum at some depth D_0 that depends on gradiometer baselines B_1 and B_2. This behavior is qualitatively shown in Fig.1. It means that such a two-gradiometer system has the highest sensitivity to magnetic sources placed at around depth D_0. Changing gradiometer baselines B_1 and B_2 enables the experimenter to adjust the depth at which the sensitivity curve is maximal, D_0, up or down. Data recorded for different D_0 allows separation of magnetic dipole sources at different depths.

This method of separating sources was realized using gradiometer-like devices based on superconducting imaging surface. Of course, such systems do not allow simultaneous detection of signals with a variety of baselines. Such a system can be constructed, in principle, by using an array of sensors at varying distances from the imaging surface. Nevertheless, multiple measurements can be made with different baselines and digital subtraction of these data sets to construct the depth sensitivity plots.

III. Experimental Setup

We placed two planar niobium thin-film SQUID magnetometers under a 240 mm diameter lead disc to create two first-order gradiometers based on the superconducting imaging surface design. The magnetometers have 8×8 mm^2 pick-up loop and 0.83 nT/Φ_0 field sensitivity [2]. The distance between magnetometer pick-up loop centers along the x-axis was 38 mm. The magnetometers were placed parallel to and at minimum distance of 22 mm from the lead disc. This distance could be increased up to about 90 mm using three fiberglass rods, that extend from a room-temperature dewar flange into the helium bath. Each rod length could be precisely adjusted using 120 mm stainless steel pivot with 8-36 thread. Both of the planar magnetometers and the lead disc were horizontal and parallel to the dewar flat bottom.

A magnetic source, together with its image from the superconducting imaging surface, produces a field at the planar magnetometers equivalent to the first-order axial gradient $\Delta B_Z/\Delta z$ ("Δ" is used in place of the traditional "δ" to emphasize that these sensors are "differencing" sensors, not true gradiometers). Two output signals from such gradiometers were input to scale amplifiers and then to a differential amplifier to form the tangential electronic gradiometer. The power line ambient noise was used to balance the tangential gradiometers by adjusting the scale amplifier gains. This procedure reduced both 60 Hz and 180 Hz harmonic output from the differential amplifier by factors of more than 100. The $\Delta B_Z/\Delta x$ sensitivity of the planar gradiometer, combined with the superconducting imaging surface, yields a $\Delta^2 B_Z/\Delta x \Delta z$ sensitivity.

The test magnetic field was generated by a straight 220 mm wire placed in parallel to the lead disc and magnetometer lops. The wire was moved down from the magnetometers at a distance from about 26 mm to 180 mm. The ends of the test

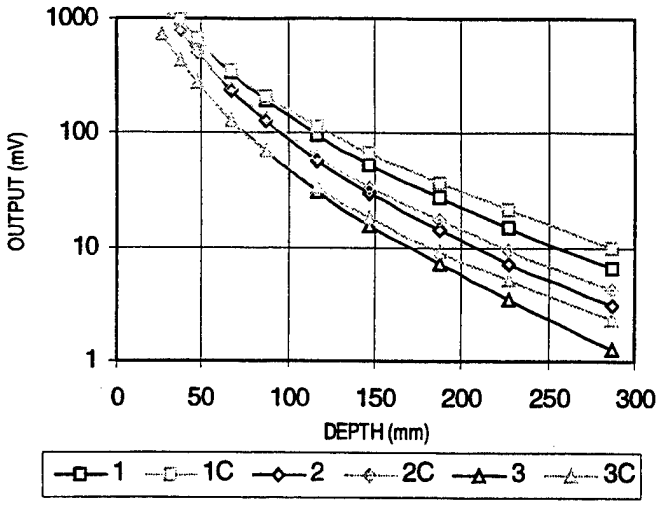

Fig. 2. Output signals vs. depth: 1 – gradiometer output signal at 90 mm distance to the SIS, 2 and 3 – gradiometer and magnetometer output signals at 22 mm to the SIS respectively, 1C, 2C and 3C – calculated values. The field sensitivity is 0.6 V/nT.

signal wire were connected to two vertical wires, that went vertically down and then horizontally to complete the test signal loop. The lower horizontal part of the test loop was at 470 mm below the magnetometers. The test current was 2 mA peak-to-peak at 134 Hz frequency. The test wire was precisely oriented to equalize signal amplitudes (with opposite phase) from the two magnetometers. The experimental setup was placed inside a one-layer magnetically shielded room [3].

III. Experimental and Calculated Results

We experimentally investigated the dependence of the magnetometer and electronic gradiometer output signals as a function of distance from the test signal wire to the SQUID magnetometers. We acquired data for three different distances from the lead disc to the magnetometers, equivalent to three different baselines along the z-axis (the equivalent baseline is twice the sensor-to-imaging plane separation). Signal amplitudes were also calculated for these arrangements. The calculated signal amplitudes took into consideration both the "primary" source wire as well as the return wire, assuming both wires were infinite length. Fig. 2 shows both the experimental and calculated results for 22 mm and 90 mm distances between the sensors and the SIS. We found very good agreement between experimental and calculated data for the source distances up to about 120 mm.

We tested the method, described above, to separate signals from sources buried at different depths using digital manipulation of recorded data. We subtracted the magnetometer data (output from the magnetometers, $\Delta B_Z/\Delta z$, as a function of source distance) for two different z-baselines. Prior to subtraction, the data at the two different baselines were normalized at the first wire position (first data point). The normalization was performed to compensate for the effect of baseline on absolute magnitude of the "gradient" data. The same procedure was repeated for the electronic gradiometer

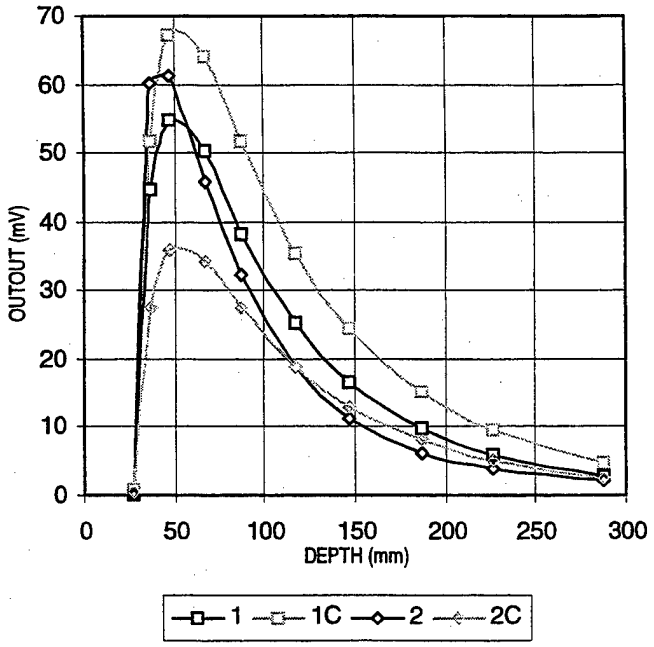

Fig. 3. Differences between signals recorded with different distances to the SIS (22 mm and 90 mm, e.g. z-baseline), one signal was scaled to null the sensitivity to the closest test wire position (D=26mm): 1 – gradiometer , 2 – magnetometer, 1C and 2C – calculated results. The field sensitivity is 0.6 V/nT.

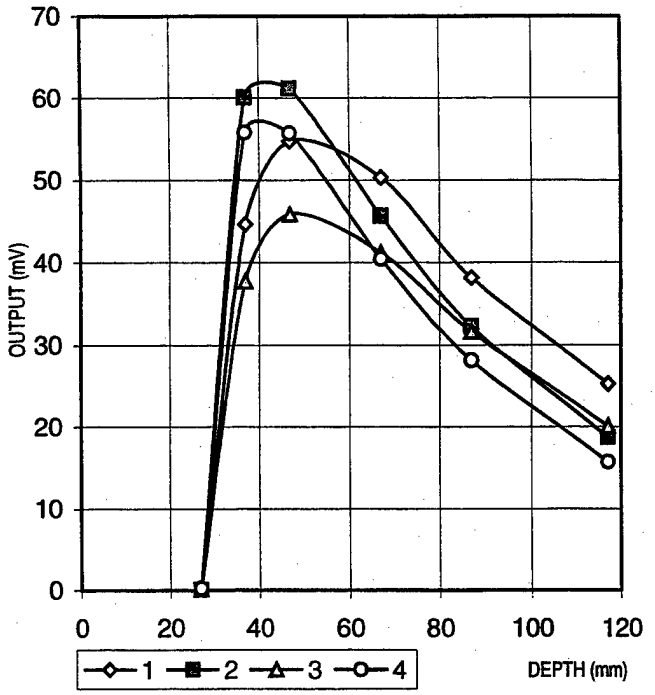

Fig. 4. Differences between signals recorded with three different distances to the SIS (22 mm, 55 mm and 90 mm). Signals, which correspond to 22 mm distance were scaled to null the sensitivity to the closest test wire position (D=26mm): 1 and 2 – gradiometer and magnetometer outputs respectively for the signal difference at 22 mm and 90 mm distances, 3 and 4 – gradiometer and magnetometer outputs respectively for the signal difference at 22 mm and 55 mm distances.

($\Delta^2 B_Z/\Delta x \Delta z$) data. The result of this procedure is shown in Fig. 3 and Fig. 4. Curves 1 and 1C in Fig. 3 show the difference of the experimental and calculated gradiometer data, respectively. Curves 2 and 2C plot the difference of the experimental and calculated magnetometer data, respectively.

As one can see from the Fig. 3, curve 2 has sharper extrema than curve 1 in both experimental and calculated results. This extrema is placed at around 40 mm distance from the sensors position. The second curve has a broader extrema centered at around 50 mm depth. Using a magnetometer array and a movable SIS, it will be possible to change both the position and shape of the extrema of the sensitivity distribution as a function of the source depth.

IV. Conclusion

We have investigated first- and second- order gradiometer-like devices that are based on the superconducting imaging surface technique. We have tested a new concept in variable baseline gradiometry based on this technique. Adjusting baselines is made possible by movement of the SIS and enables analysis of data that provide enhanced information about the spatial distribution of sources. This technique provides the potential to build devices that have an enhanced sensitivity to sources "buried" at specific depths below sample surfaces. This may be very attractive for non-destructive evaluation applications and possibly for biomagnetic applications, as well.

The superconducting imaging surface technique can be used to build LTS or HTS gradiometer arrays with simultaneously adjustable baselines. In the present paper we used LTS materials, however the SIS technique has also been demonstrated using HTS materials [4]. In the case of HTS, this technique provides the only easily constructed radial gradiometers.

References

[1] D. R. van Hulsteyn, A. G. Petschek, E. R. Flynn, W. C. Overton, "Superconductor Imaging Surface Magnetometry", *Rev. Sci. Instrum.*, 66 (7), 1995, pp. 3777-3784

[2] R. Cantor, "DC SQUIDs: Design, Optimization and Practical Applications." In *SQUID Sensors: Fundamentals, Fabrication and Applications*, H. Weinstok, Ed. Boston, London: Kluwer Academic Publishers, 1996, pp. 179-233.

[3] G. W. Sullivan, P. S. Lewis, J. S. George, E. R. Flynn, "A Magnetic Shielded Room Designed for Magnetoencephalography", *Rev. Sci. Instrum.*, 60 (4), 1989, pp. 765-770.

[4] M. A. Espy, A. N. Matlashov, R. H. Kraus, "Experimental Investigation of High Temperature Superconducting Imaging Surface Magnetometry", ISEC'99, Extended abstracts, Berkeley, June 21-25, 1999

Experimental Investigation of High Temperature Superconducting Imaging Surface Magnetometry

Michelle A. Espy, Andrei N. Matlashov, and Robert H. Kraus, Jr.
Los Alamos National Laboratory, Los Alamos, NM. 87545

Abstract—The behavior of high temperature superconducting quantum interference devices (SQUIDs) in the presence of high temperature superconducting surfaces has been investigated. When current sources are placed close to a superconducting imaging surface (SIS) an image current is produced due to the Meissner effect. When a SQUID magnetometer is placed near such a surface it will perform in a gradiometric fashion provided the SQUID and source distances to the SIS are much less than the size of the SIS. We present the first ever experimental verification of this effect for a high temperature SIS. Results are presented for two SQUID-SIS configurations, using a 100 mm diameter $YBa_2Cu_3O_{7-\delta}$ disc as the SIS. These results indicate that when the current source and sensor coil (SQUID) are close to the SIS, the behavior is that of a first-order gradiometer. The results are compared to analytic solutions as well as the theoretical predictions of a finite element model.

I. Introduction

The theoretical basis of superconducting imaging surface (SIS) magnetometry was introduced by van Hulsteyn *et al.* in [1]. The primary concept is that a single coil detector located in the vicinity of a superconducting surface can be made to act like a first-order gradiometer. Conceptually, one can think of the SIS as acting as a mirror to the magnetic sources in its vicinity. A single coil detector (i.e. SQUID) placed close to the SIS would see a signal from both the source and the image of the source. This leads to "gradiometer-like" behavior.

It is important to note, however, that unless the SIS is infinite it cannot mirror all the flux lines from the source to create a complete image. For any finite-sized SIS the device is not a true gradiometer. Thus, uniform magnetic fields (or fields from very far placed sources) are not completely canceled out. However, when the sensor coil and current source distances to the SIS are much less than the size of the SIS, the behavior is essentially that of a gradiometer.

Manuscript received April 30, 1999.

Two biomagnetic systems using low temperature SQUIDs and lead surfaces have been developed at Los Alamos National Laboratory. These systems take advantage of the built-in shielding and easily adjustable baseline provided by the SIS. One system uses a flat 25 cm diameter lead plate and 12 SQUID magnetometers. The other is a magnetoencephalography system using 155 SQUID magnetometers and a lead hemispherical SIS of radius 11 cm. Tests of these systems indicated that when the SQUIDs were near the center of the SIS they did behave primarily as gradiometers [2].

This paper presents the first results investigating SIS magnetometry with high temperature superconducting (HTS) materials. A $\mathring{A}2000$ thick Planar $YBa_2Cu_3O_{7-\delta}$ disc was used as the SIS. Although the SIS magnetometry theory is not specific to superconductor type, our investigation of the use of HTS material was motivated for two reasons. First, because it was not clear that HTS material could be obtained of sufficient quality to perform as an SIS. Second, to investigate whether the SIS technique would provide a useful alternative to HTS SQUID gradiometry. The SIS technique has the advantage of a very easily adjustable baseline (move the disc) which could be appealing when building HTS SQUID gradiometer arrays.

We designed two experiments to explore the behavior of magnetic field sources near a 100 mm diameter YBCO surface. HTS SQUID magnetometers were used as the magnetic sensing coil. The second section of this paper presents the results for the case with a current loop as the source and the SQUID normal oriented orthogonally to the disc. Magnetometer data (no disc) were also taken. These data are compared to analytic solutions as well as the theoretical predictions of a finite element model [3]. The third section of this paper presents the shielding factor for the disc. The fourth section presents the results of an experiment with a long straight wire as the field source and the SQUID normal oriented tangentially to the disc. These data are presented and compared to the finite element model.

II. Measurements With A Current Loop

Our first experiment used a 3-turn 2.5 mm radius coil as the source. The current to the loop was provided by a func-

tion generator at 70 Hz. The loop produced a magnetic dipole that was oriented parallel to the z-axis. The normal of the YBCO disc was also along this axis. A SQUID magnetometer was located between the current loop and the disc and oriented orthogonally, to measure the z component of the magnetic field. The SQUID was a bare Conductus Mr. SQUID^{TM}, with 70 μm $\times$ 70 μm area and 700 nT/Φ_0, positioned such that the distance from the SQUID to the plate was about 2.2 mm. The baseline of the "gradiometer" is twice this distance. The disc consisted of a 100 mm diameter substrate with a YBCO layer Å2000 thick. The SQUID remained fixed above the YBCO disc while the current loop was moved upward along the z-axis.

The upper panel of Fig. 1 shows the results for both the magnetometer (triangles) without the YBCO disc, and gradiometer (diamonds) with the YBCO disc. The magnetometer data were fit (solid line) to the analytic form

$$Bz = \frac{\alpha a^2}{(a^2 + (z+\beta)^2)^{\frac{3}{2}}} \tag{1}$$

where the terms allowed to vary were α, a normalization factor, and β, which allowed for any error in z. The best fit to the magnetometer data was with α=76877.2 a.u.mm and β=0.01 mm. The dashed line is the result the finite element model. The gradiometer data were fit (solid line) to the analytic form

$$Bz = \frac{\alpha a^2}{(a^2 + (z+\beta)^2)^{\frac{3}{2}}} - \frac{\alpha a^2}{(a^2 + (b+z+\beta)^2)^{\frac{3}{2}}} \tag{2}$$

where α and β were constrained to the values for the magnetometer fit and the baseline b was allowed to vary. The best fit to the gradiometer data was with b=2.06 mm. The dashed line is the prediction of the finite element model, where b was taken to be 2.15 mm.

The lower panel of Fig. 1 shows the ratio of the magnetometer to gradiometer data (diamonds). The solid line is a best fit to the ratio of equation 2 to equation 1

$$\frac{Bz(grad)}{Bz(mag)} = 1 - \frac{(a^2 + (z+\beta)^2)^{\frac{3}{2}}}{(a^2 + (b+z+\beta)^2)^{\frac{3}{2}}} \tag{3}$$

where β was constrained to the value from the magnetometer fit but baseline b was allowed to vary. The best fit the the ratio was found to be b=2.23 mm and is shown as a solid line. The dashed line is the ratio of the values from the finite element models. Both models are in excellent agreement with the data for all z values. The disc is large enough that it is a good approximation to an infinite disc and the gradiometry is nearly exact.

III. Shielding Factor

The SIS is not a true gradiometer. For example, magnetic fields from very distant sources are not completely canceled out. However, the SIS does provide some magnetic shielding. To test this we placed the SQUID sensor in a uniform magnetic field from a Helmholtz coil both with and without the YBCO disc. The ratio of the value with the disc to that without the disc is what we call the shielding factor.

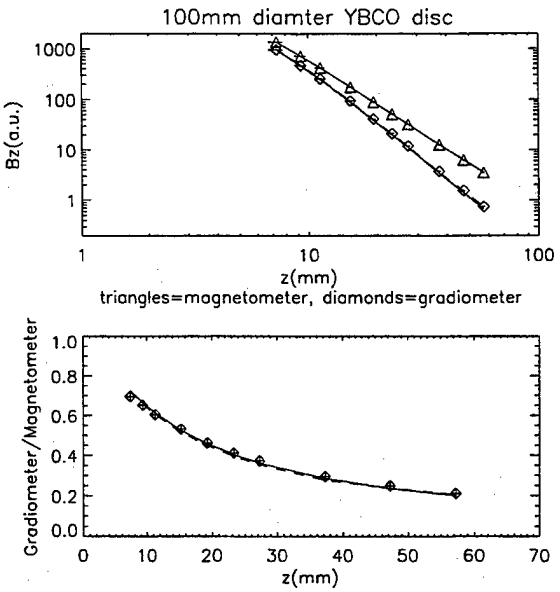

Figure 1: Upper panel: Magnetometer (triangles) and gradiometer (diamonds) data. Lower panel: Ratio of the magnetometer to gradiometer data (diamonds). The solid lines are a fit to the analytic forms (see text). The dashed lines are from the finite element models.

Fig. 2 presents shielding factor, S, as a function of the distance, b, from the YBCO disc to the SQUID sensor. The solid line shows a fit to the function

$$S = k\left(\frac{R}{b}\right)^p \approx \frac{R}{b} \tag{4}$$

where k is a normalization factor, R is the radius of the disc, b is the distance from SQUID-to-disc, and p is the exponential power. The best fit values were k=0.90 and p=0.92.

IV. Measurements With A Long Wire

These experiments used a long straight wire that ran parallel to the surface of the 100 mm diameter YBCO disc, along the x-axis. The normal of the YBCO disc was along the z-axis and the SQUID was tangentially oriented to detect the y component of the magnetic field. The wire was 100 mm in length and the current was provided by a function generator at 70 Hz. The same SQUID was used as with the current loop experiments. The wire was moved both along the y-axis as well as the z-axis.

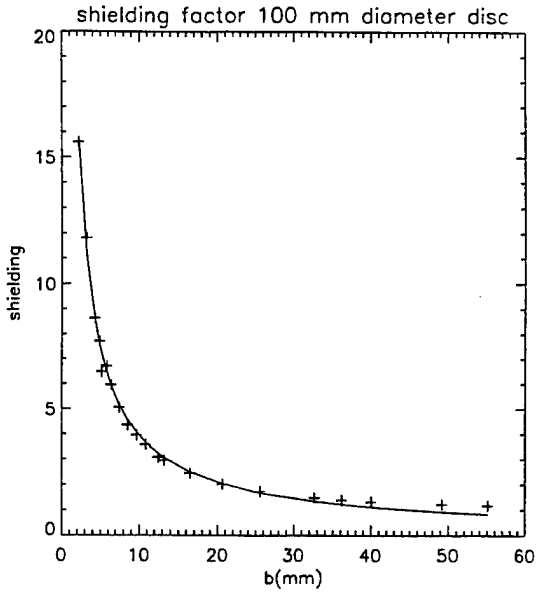

Figure 2: Shielding factor vs. distance.

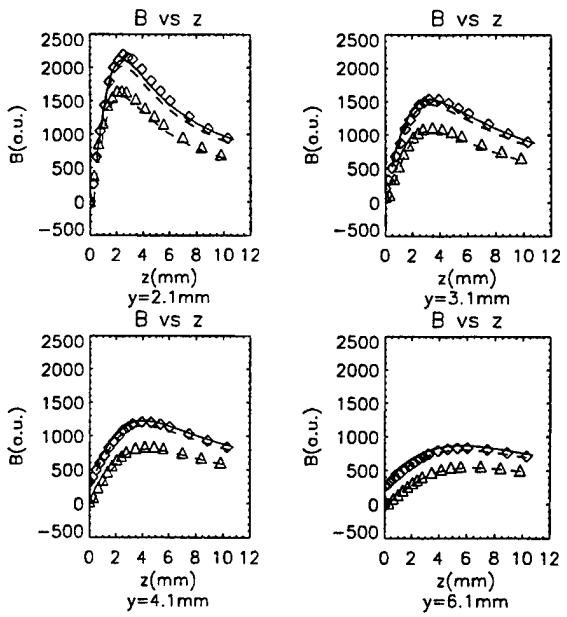

Figure 3: Magnetic field plotted vs. z for for both the magnetometer (triangles) and gradiometer (diamonds), for various wire positions along the y axis. The dashed and solid lines are the result of finite element models (see text).

Figure 3 shows the y component of the magnetic field B plotted as a function of z for for both the magnetometer (triangles) and gradiometer (diamonds), for various wire positions along the y axis. The dashed lines are the result of the finite element model. For the magnetometer, the model was of a single long wire. For the gradiometer, the model was of a single long wire and a superconducting disc of 100 mm radius. The solid line fit to the gradiometer data was the result of the finite element code using two long wires with currents in the opposite direction as source and its magnetic image. The finite element data was normalized to fit the data.

The single wire model is in good agreement with the magnetometer data. For the gradiometer data, both the wire-and-disc model and the two-wires model are similar. Neither of these models takes into account the finite wire length or the return leads. We have to note that the gradiometer values are actually *larger* than the magnetometer values. This is because when the SQUID is located between the source wire and its image, as in our case, the y component of the magnetic fields have the same sign and are summed. Thus, the plate does not produce the equivalent of a gradiometer, but rather simulates the case of two coils wound in the same direction.

V. Discussion

A 100 mm diameter $\mathring{A}2000$ YBCO disc was used as a superconducting imaging surface. A HTS SQUID magnetometer placed close to the disc acted as a first-order gradiometer orthogonally when the source was a current loop. When the SQUID was oriented tangentially and the source was a long straight wire, the SIS produced the effect of two coils wound in the same direction. Either behavior was true as long as the SQUID and source current were at distances from the disc much less than the disc's radius. The shielding factor in a uniform magnetic field was about 16 when the SQUID was 2 mm from the disc. HTS SIS gradiometry could prove a useful alternative to other HTS gradiometry techniques, particularly in cases where an easily adjustable baseline is desired.

Acknowledgment

The Authors wish to thank Conductus, Inc. for the YBCO superconducting surface used in this work.

References

[1] D. B. van Hulsteyn, A. G. Petschek, and E. R. Flynn, Rev. Sci. Instrum. **66** (7), (1995) pp. 3777-3784

[2] R. H. Kraus, Jr. *et al.*, "First Results for a Novel Superconducting Imaging-Surface Gradiometer Array", IEEE Trans. Appl. Superconductivity (*in press*)

[3] Vector Fields Inc., 1700 North Farnsworth Avenue Aurora, Il 60505, USA

Planar Single Layer HTSC-SQUID Gradiometers with high Balance

L.Dörrer, S.Wunderlich, F.Schmidl, and P.Seidel
Institut für Festkörperphysik, Friedrich-Schiller-Universtät Jena, Helmholtzweg 5, D-07743 Jena, Germany

Abstract — The development of single layer HTSC-SQUID gradiometers was forced in the last few years. Usually a parallel direct (also called galvanometric) coupled scheme is used for single layer gradiometers. The performance of such sensors is enhanced and different applications are demonstrated, typically with sensors on bicrystal substrates. Unfortunately there are two disadvantages of this scheme. The first one, the small ratio of effective area to geometric size is inherent due to the inductance mismatch between antenna and SQUID. The second one, the small balance, is caused by the sensitivity to homogeneous magnetic fields of the SQUID itself. This is ordinary described with the effective area of the galvanometer SQUID, which is a parasitic area for the gradiometer. The balance of the gradiometer is equal to the quotient of the parasitic area to the effective area. Some different methods to enhance the balance of planar gradiometers are described in literature (e.g. unsymmetric antennas, multilayer structures with vias and crossovers or superconducting shield-layer). Based on our investigations to enhance the performance of planar single layer gradiometers we present a new layout with only one superconducting layer and a high balance.

I. Introduction

HTSC-SQUID based sensors were developed and applied by many scientific groups around the world ([1] to [4]). Especially the simple direct (also called galvanometric) coupled scheme is used for applications [3,5]. For this scheme only one superconducting layer is necessary. Unfortunately this type of sensor has two main disadvantages. At first the mismatch between the antenna and the SQUID leads to a small coupling coefficient and thats why to a small ratio between effective area A_{eff} and geometric area A_{geo}. The second disadvantage of the direct coupled scheme is the sensitivity of the SQUID itself to the external magnetic field. This galvanometer-SQUID has an effective area $A_{eff,SQ} = \Phi_{SQ} / B_{ext}$. In this contex and due to the fact that antennas and SQUID are sensitive in the same field direction one can see that the balance of a planar direct coupled gradiometer is limited by the ratio of $A_{eff,SQ} / A_{eff}$.

There are different possibilities to enhance this balance. To realize the first one, the shielding of the galvanometer SQUID with an additional superconducting layer, a stable multilayer technology is necessary. But if one likes to use this technology, one should realize coupling schemes with a better ratio between geometrical and effective area. Additionally the shielding of a HTSC-film have a poor shielding factor (e.g. for $YBa_2Cu_3O_{7-x}$ (YBCO) film thickness d = 200 nm and London penetration depth λ_L = 220 nm only 50 % shielding [6]).

A second possibility to enhance the balance of a planar gradiometer is to create an asymmetric antenna layout. The calculation and realization of such an „compensation" is very difficult due to the strong influence of λ_L on the inductance of structures with film thickness in the same range.

A third variant is a flip-chip arrangement. In this case it's possible to adjust the two chips to minimize the sensitivity to homogeneous fields and so to enhance the balance. A combination of the second and third variant is shown in [7]. This may be a solution for a general demonstration but not for a commercial sensor.

An other variant and may be the best way to increase the balance of a planar gradiometer intrinsically is to use a galvanometer-SQUID with a gradiometric structure. This article shows a possible design for a galvanometer-SQUID with a minimum sensitivity for homogeneous magnetic fields and with only one superconducting layer.

II. Standard Planar Gradiometers

In planar parallel gradiometers the difference of the magnetic flux penetrating two antennas is converted into a current. This current is injected directly in a SQUID which is acting as a galvanometer. If the antennas are equal in geometry the magnetic flux that is measured by the galvanometer-SQUID is proportional to the spatial difference of the magnetic field. By this way the described sensor measures the gradient of the magnetic field (if the source is not to close). The gradient resolution $\sqrt{S_G}$ is determined by the baselength b, the flux noise of the SQUID $\sqrt{S_\Phi}$, and the effective area A_{eff} of the gradiometer:

$$\sqrt{S_G} = \frac{\sqrt{S_\Phi}}{b\, A_{eff}}. \qquad (1)$$

In the case of planar gradiometer the effective area is given by

$$A_{eff} = \frac{1}{b} \frac{\partial \Phi_{SQ}}{\partial \left[\frac{\Delta B_z}{\Delta x} \right]} \cong A_w \frac{L_M}{L_A} = E\, L_M, \qquad (2)$$

were A_w and L_A are the effective area and the inductance of one antenna [8]. L_M the coupling inductance of the galvanometer SQUID and E the efficiency which depends on

Manuscript received April 30, 1999.
This work was supported in part by the German BMBF within contract Nos. 13N6864 and 13N6644.

the geometry of the antenna. Additionally to this sensitivity to magnetic field gradients the typically used galvanometer-SQUID represents a magnetometer with an effectiv area of

$$A_{eff,SQ} = \frac{\partial \Phi_{SQ}}{\partial B_z} \quad . \tag{3}$$

Thats why the magnetic flux inside the galvanometer-SQUID is given by:

$$\Phi_{SQ} = A_{eff}\ b\ \frac{\Delta B_z}{\Delta x} + A_{eff,SQ}\ B_z \quad . \tag{4}$$

The balance of the gradiometer is limited by the quotient of $A_{eff,SQ} / A_{eff}$.

More details for principles and layout of the planar parallel single layer direct coupled gradiometer are reported elsewhere [2, 3, 8].

III. GALVANOMETER-SQUID

In a typically used galvanometer-SQUID layout the SQUID hole has a strong rectangular shape due to the minimization of the effective area of the SQUID itself. Nevertheless the $A_{eff,SQ}$ of this layout is in the order of 1000 μm^2 [3], so that the balance of a planar single layer gradiometer on 5 * 10 mm^2 substrate with an effective area of 0,2 mm^2 is not better than 0,5 %.

Much better balance is possible due to a gradiometric galvanometer SQUID. A principle circuit of such a device is shown in Fig.1. The terminal A represents the bias and signal connector while terminals B and C are used to apply the measurement current. For an ideal structure with equal inductances $L_1 = L_{11} + L_{12} = L_2$ and equal effective areas $A_1 = A_2$ the sensitivity for an homogeneous field is zero and therefor the galvanometer SQUID does not limit the balance of the gradiometer.

The SQUID inductance is given by

$$L_{SQ} = L_3 + \frac{L_1\, L_2}{L_1 + L_2} . \tag{5}$$

The flux quantization $\Phi_1 + \Phi_2 = n\ \Phi_0$ allows to calculate the flux inside the SQUID due to a current I_m between terminal B and C

$$\Phi_{SQ} = \left[\left(I_M \frac{L_2}{L_1 + L_2}\right) L_1\right] - \left[-\left(I_M \frac{L_1}{L_1 + L_2}\right) L_2\right] = I_M \frac{2 L_1 L_2}{L_1 + L_2} = I_M L_M \quad . \tag{6}$$

Due to comparison of equation (5) and (6) one finds that it is possible to design a structure with a larger coupling inductance L_M than SQUID inductance L_{SQ}!

IV. REALIZATION

One important point for realization of a gradiometric galvanometer SQUID structure is to connect the inner part of the structure without an additional superconducting layer. We use metallic connections in 4-point arrangement to minimize the influence of the contact resistance. Another design problem is connected with the fixed position of the grain boundary in the case of bicrystal substrates.

We developed designs for step-edge- (a) and bicrystal (b) Josephson junctions which are shown in Fig.2 without metallic connections. This metallic connections, marked as ground in Fig.1, are necessary for bias. The position of the step and the grain boundary is marked by a dashed line.

Because of some technological reasons we had no success with the realization till now. The first 2 samples with 3 each galvanometer SQUIDs are made with step-edge junctions as it shown in Fig.3. In this layout both ramps (up to down and vice versa) are used for the preparation of Josephson junctions. The quality of the ramps is strongly different. That's why in the tested samples in maximum one Josephson junction per SQUID was acting, so that the SQUIDs are not working.

In preparing further experiments with bicrystal Josephson junctions we have made some inductance calculations with the programme SCIM [9]. Following parameters were fixed: London penetration depth λ_L = 250 nm, film thickness d = 100 nm, line width around the loop 10 µm, line width of

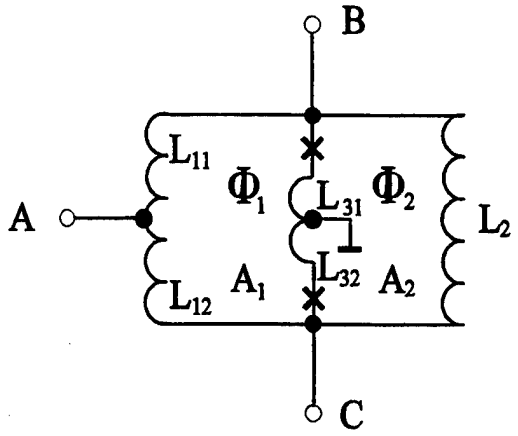

Fig.1 Equivalent circuit of a gradiometric galvanometer SQUID

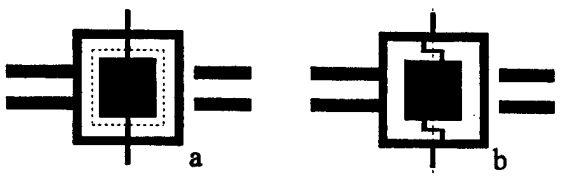

Fig.2 Principle sketch of gradiometric galvanometer SQUIDs for step-edge (a) and bicrystal (b) Josephson junctions

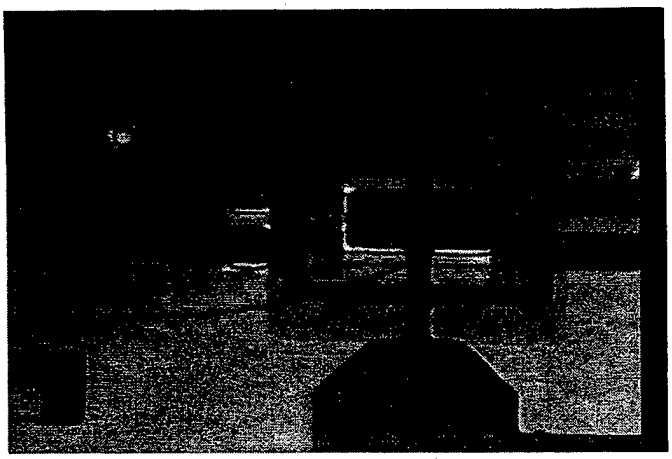

Fig3 Micriscopic picture of a gradiometric galvanometer SQUID with step-edge Josephson junctions without metallic contacts, 300 x 220 μm²

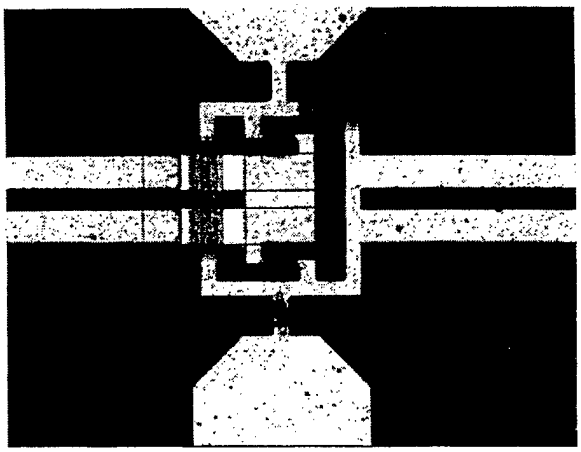

Fig.4 Microscopic picture of a gradiometric galvanometer SQUID with bicrystal Josephson junctions, with metallic contacts, picture size equal to 350 x 260 μm²

the current leads 20 μm and the width of the Josephson junctions 5 μm. The calculated inductances are shown in table I for the parameters: outer dimensions of the SQUID in vertical (a) and horizontal (b) direction with respect to Fig. 2b. Additionally we have calculated the effective area of the left and right loop of the gradiometric SQUID to 4730 μm² and 4590 μm². The real effective area of the SQUID is equal to the difference of both $A_{eff, SQ}$ = 140 μm². This is nearly 10 times lower than in usually used galvanometer SQUIDs.

The microscopic picture of a galvanometer SQUID with bicrystal Josephson junctions is shown in Fig.4. The insulation between superconductor and metallic connection for bias are not acting up to now because of pinholes in the isolation layer. In this experiment we have used cold deposited amorphous YBCO as it is described in [10].
Further experiments are in progress.

V. Conclusions

We developed designs for a galvanometer-SQUID with a minimum sensitivity to homogeneous magnetic fields and with only one superconducting layer for step-edge as well as bicrystal Josephson junctions. As calculated the effective area of the SQUID itself is approximately 10 times lower than in usually used galvanometer-SQUIDs for high sensitive gradiometers with one superconducting layer. Samples which should demonstrate the performance of this gradiometric galvanometer SQUIDs using in planar gradiometers are in progress.

We would like to thank J. Schulz, U.Hübner, and G. Hildebrandt for technical assistance.

TABLE I

Calculated inductances of three different gradiometric galvanometer SQUIDs with bicrystal Josephson junctions a and b are the total dimension in horizontal and vertical direction

No.	a	b	L_1	L_2	L_3	L_{SQ}	L_M
	[μm]		[pH]				
I	100	200	182	184	49	140.5	183
II	100	160	151	155	44.5	121	153
III	85	165	140	143	46	116.5	141.5

References

[1] S. Knappe, D. Drung, T. Schurig, H. Koch, M. Klinger, J. Hinken, „A planar gradiometer at 77K", *Cryogenics* **132**, pp.881-884, 1992

[2] V. Zakosarenko, F. Schmidl, H. Schneidewind, L. Dörrer, and P.Seidel, „Thin film dc SQUID gradiometer using a single $YBa_2Cu_3O_{7-x}$ layer", *Appl. Phys. Lett.* **65**, 6, pp. 779-780, 1994

[3] S. Wunderlich, F. Schmidl, H. Specht, L. Dörrer, H. Schneidewind, U. Hübner, and P. Seidel, „Planar gradiometers with high-T_c DC SQUIDs for non-destructive testing", *Supercond. Sci. Technol.* 11, pp.315-321, 1998

[4] A.I. Braginski, „Application of High.Temperature SQUID Magnetometers to Nondestructive Evaluation and Geomagnetic Exploration", accepted for *Poc. 11th ISS*, Fukuoka, 1998

[5] P. Seidel, F. Schmidl, S. Wunderlich, L. Dörrer, T. Voigt, H. Schneidewind, R. Weidl, S. Lösche, U. Leder, O. Solbrig, H. Nowak, „High.Tc SQUID System for Practical Use", accepted for *IEEE Trans. Appl. Supercond.*, 1998

[6] H. Töpfer, Modellierung, numerische Simulation und Unterstützung des Entwurfs von dc-SQUID-Strukturen", PhD thesis, Shaker Verlag 1996

[7] E. Dansker, O.M. Fröhlich, S. Tanaka, K. Kouznetsov, J. Clarke, Z. Lu. V. Matijasevic, and K. Char, „High-Tc superconducting gradiometer with a long baseline asymmetric flux transformer", *Appl. Phys. Lett.* **71**, 2, pp. 1712-1714, 1997

[8] L. Dörrer, S. Wunderlich, F. Schmidl, H. Schneidewind, U. Hübner, and P. Seidel, „Development of planar thin film HTSC-SQUID gradiometers for different applications", accepted for *Applied. Superconductivity*, 1998

[9] G. Hildebrand, F.H. Uhlmann, „Inductance calculation for integrated superconducting structures by minimizing free energy", *IEEE Trans. on Appl. Supercond.* **5**, 2, pp.2766-2769, 1995

[10] H.Schneidewind, S.Wunderlich, F.Schmidl, L. Dörrer, and P. Seidel, „Application of ion-beam etching to investigate the electrical behaviour of Josephson junctions", *Physics and Materials Science of High Temperature Superconductors, IV*, Eds. R. Kossowsky, M. Jelinek, and J. Novak, Kluver Academic Publishers, pp.311-322, 1997

Characteristics of the planar second-order high-Tc SQUID gradiometer

Soon-Gul Lee
Korea University, Jochiwon, Chungnam 339-800, Republic of Korea

Yunseok Hwang
Korea University, Sungbuk-ku, Seoul 136-701, Repubic of Korea

Jin-Tae Kim and Yong Ki Park
Korea Research Institute of Standards and Science, Taedok Science Town, Taejon 305-600, Republic of Korea

Abstract—We have studied the planar-type single-layer second-order high Tc SQUID gradiometer that detects the transverse field gradient, d^2B_z/dx^2. The gradiometer consists of 3 parallel-connected rectangular pickup loops that are directly coupled to SQUID. The pickup loops are designed in such a way that SQUID measures the difference in the differential screening currents of neighboring pickup loops. The SQUID has either step-edge or bicrystal Josephson junctions. The gradiometer was made from a single layer of $YBa_2Cu_3O_7$ film on a 1 cm x 1 cm chip. The response of the gradiometer was tested in various flux distributions generated by three identical multi-turn film coils patterned on the same chip in parallel with each pickup loop. The balanced gradiometer responded sensitively only to the second-order field gradient. Reduction of the inductive coupling between loops improved the intrinsic balance.

I. Introduction

SQUID is so sensitive to faint magnetic signals, such as those emanating from brain activity or from metallic corrosion, and thus applicable to various testing areas from biomagnetism to nondestructive tests. The extremely high sensitivity of SQUID makes it vulnerable to noises as well. For this reason most of the SQUID measurement is performed in a shielded room. However, some applications, such as nondestructive tests, require measurement in unshielded environments. SQUID gradiometers are advantageous in such cases, for they are much less sensitive to noise whose sources are usually located relatively remote.

The first SQUID gradiometer based on multilayer thin-film process was developed two decades ago [1]. The first high T_c SQUID gradiometer was developed also by multilayer technique [2]. However, since the results of multilayer process are not reproducible for high T_c oxides, most high T_c devices are made from single layers. Directly coupled first-order SQUID gradiometers [3], [4] and 3 SQUID gradiometer [5] were developed from single layers of $YBa_2Cu_3O_7$. Asymmetric first-order SQUID gradiometer with a flip-chip coupling was developed [6]. Electronic second-order gradiometers composed of independent sets of SQUID magnetometers have been developed [7]. Planar 2nd-order gradiometer with flip-chip coupling has been developed recently [8]. We have reported the first single-layer 2nd-order SQUID gradiometer on a single chip very recently [9].

In this work we studied design, fabrication, and field response of the single-layer second-order $YBa_2Cu_3O_7$ SQUID gradiometer.

II. Design

The schematic of the directly coupled second-order SQUID gradiometer is shown in Fig. 1. The balancing condition in a uniform field is [9]:

$$\frac{A_C}{A}\frac{L}{L_C} = \frac{\alpha_L + \alpha_R}{\alpha_C} = \frac{2\alpha}{\alpha_C}. \quad (1)$$

Where α_L and α_R are the coupling coefficients of the left and the right loops, respectively. For a symmetric design $\alpha=\alpha_L=\alpha_R$. Since $\alpha_C \cong 2\alpha$, the balancing condition is $A_C/L_C \cong A/L$.

For the first order gradient of field, the flux coupled to the SQUID by the three loops is zero for a symmetric design, and thus the device is automatically balanced.

In the presence of the second-order gradient, the net flux coupled to the SQUID by the pickup loop is [9]:

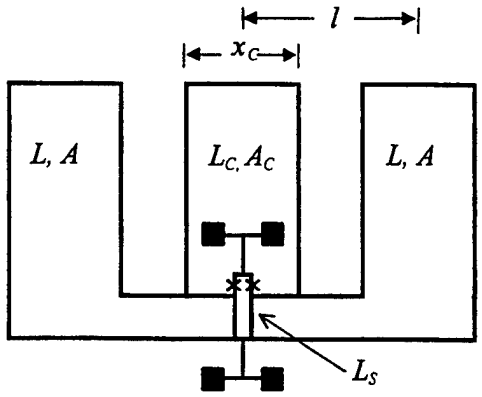

Fig. 1. Schematic of the second-order SQUID gradiometer. The region near the SQUID is exaggerated.

Manuscript received April 30, 1999
This work was supported by the Ministry of Science and Technology, Republic of Korea.

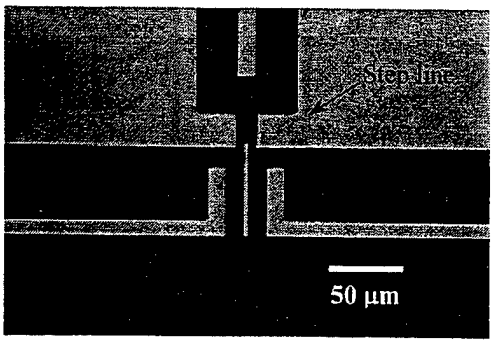

Fig. 2. Optical micrograph of the SQUID area of the gradiometer.

$$\Phi = \frac{1}{3}\alpha_c\left(\frac{\partial^2 B}{\partial x^2}\right)\frac{x_C^2}{4}\left(4l^2 + x_C l\right)A\,\frac{L_S}{L} \qquad (2)$$

l is the distance from the center of the center loop to that of the left or right loop, and x_C is the geometric mean width of each loop. Sensitivity of the gradiometer is [9]:

$$\left(\frac{\partial^2 B}{\partial x^2}\right)_n = \frac{1}{\alpha_C A_C}\frac{L_C}{L_S}\frac{\phi_n}{l^2}\frac{1}{1+\kappa}, \qquad \kappa \equiv \frac{1}{3}\left(1-\frac{x_C}{l}\right). \qquad (3)$$

ϕ_n is the SQUID noise. For $l = x_C = 3$ mm with $\alpha_C = 0.8$, $A_C = 6$ mm^2, $L_C = 5$ nH, $L_S = 40$ pH, and $\phi_n = 1\times10^{-5}\ \phi_o/\mathrm{Hz}^{1/2}$, the gradient sensitivity will be $(\partial^2 B/\partial x^2)_n \cong 6.0\times10^{-8}$ G/cm^2/Hz$^{1/2}$.

III. Experimental Results

The gradiometer was made from single layer of $YBa_2Cu_3O_7$ film by using a standard pulsed laser deposition method and photolithography with argon ion milling technique. An optical micrograph of the SQUID area is shown in Fig. 2. The size of each pickup loop is 1.8 mm × 3.5 mm. The width of all the lines of the pickup loops is 0.4 mm except the 50-μm-wide detour lines. Effective inductance is calculated to be about 5.7 nH for the left or right loop and 4.6 nH for the center loop. SQUID of the gradiometer contains two step-edge or bicrystal junctions. The step height is about 2,000 Å and the film thickness is 1,500 Å. The junction width is 3 μm and the hole size of the SQUID is 3 μm × 54 μm. The total inductance of the SQUID including the kinetic part is estimated to be about 39 pH.

Current-voltage curve of the SQUID is shown in Fig. 3. The data were collected without a magnetic shield in ambient field. In Fig. 3, the curve is rounded near the critical current due partly to thermal fluctuations and partly to external noise. Most of the SQUIDs with low critical currents showed a similar behavior. The critical current of the SQUID is about 20 μA. The normal state resistance of the junction is 6 Ω. I_cR_n product is about 120 μV.

We tested the response of the gradiometer to various flux distributions generated by using three identical test coils patterned from the $YBa_2Cu_3O_7$ film on the same chip. Each coil was coupled inductively to each loop in the same way. We generated different flux distributions by applying current in the serially connected three test coils in different polarity combinations. Since all three loops of the pickup coil have the same area, the ratio of the modulation period of the side loops to that of the center loop is twice of the inductance ratio (1).

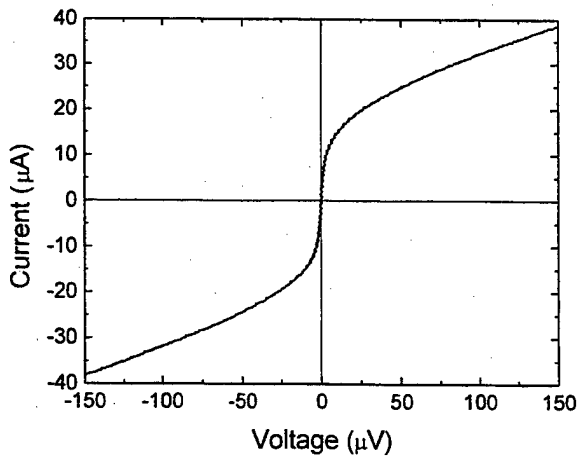

Fig. 3. Current-voltage curve measured in ambient field without a shield at 77 K.

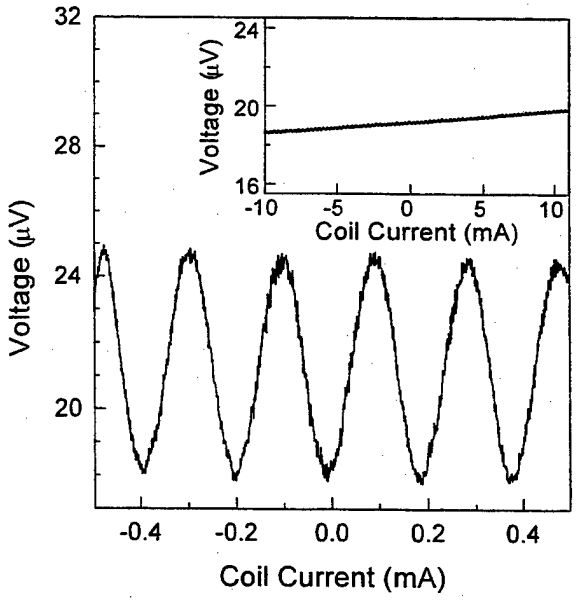

Fig. 4. Modulation signal for the flux distribution corresponding to the second order field gradient. The period is about 0.19 mA. The inset is the signal for the first order gradient. The estimated period for the first order gradient is of the order of 1 A.

The ratio of the period of the side loops to twice of that of the center loop was measured to be 1.65, which is larger than the inductance ratio by about 30 %. The discrepancy in the ratio is believed due partly to that the portion of the SQUID inductance coupled to the center loop is slightly larger than twice of that coupled to the side loop. Another possible source of the discrepancy is the error in the estimation of the inductance and the effective area of the loops due to rather complicated structure of the device. We could compensate the coupling imbalance by placing a small chip of $YBa_2Cu_3O_7$ bulk in the center loop. The final balancing was achieved by trial and error by chipping off the $YBa_2Cu_3O_7$ bulk in the center loop.

The modulation data of the balanced gradiometer in response to the second order field gradient are shown in Fig. 4. The applied flux distribution corresponding to the second order gradient was such that the center loop flux had the same magnitude but opposite polarity compared with those of the side loops. The period of the modulation is about 190 μA in coil current. On the other hand, the response to the first order gradient was extremely small. As shown in the inset of Fig. 4, the data show almost no change in a much wider current range. The estimated period was of the order of 1 A, which is 5,000 times larger than the period of the second-order signal. Thus, the error due to the first-order imbalance is about 2×10^{-4}. Identical pattern and coupling of the flux coils are believed to have reduced the balancing error to such a small value. The balancing in a uniform field was much more tedious. It was done by trial and error by nipping the $YBa_2Cu_3O_7$ bulk in the center loop. The error due to uniform fields was less than a percent. The intrinsic balance will be much improved by optimizing the center loop inductance in the design.

IV. SUMMARY

We have designed and fabricated a planar type direct-coupled second-order SQUID gradiometer from a single $YBa_2Cu_3O_7$ film. We tested the response of the device to various flux distributions generated by 3 identical patterned film coils. The device responded sensitively only to the second-order gradient of the magnetic field. The new type of device will be useful for SQUID measurements in unshielded environments, such as nondestructive tests.

REFERENCES

[1] M. B. Ketchen, W. M. Goubau, J. Clarke, and G. B. Donaldson, "Superconducting thin-film gradiometer," *J. Appl. Phys.*, vol. 49, pp. 4111-4116, July 1978.

[2] W. Eidelloth, B. Oh, R. P. Robertazzi, W. J. Gallagher, and R. H. Koch, "$YBa_2Cu_3O_{7-\delta}$ thin-film gradiometers: Fabrication and performance," *Appl. Phys. Lett.*, vol. 59, pp. 3473-3475, December 1991.

[3] S. Knappe, D. Drung, T. Schurig, H. Koch, M. Klinger, and J. Hinken, "A planar $YBa_2Cu_3O_7$ gradiometer at 77 K," *Cryogenics.*, vol. 32, pp. 881-884, October 1992.

[4] V. Zakosarenko, F. Schmidl, H. Schneidewind, L. Dörrer, and P. Seidel, "Thin-film dc SQUID gradiometer using a single $YBa_2Cu_3O_{7-x}$ layer," *Appl. Phys. Lett.*, vol. 65, pp. 779-780, August 1994.

[5] R. H. Koch, J. R. Rozen, J. Z. Sun, and W. J. Gallagher, "Three SQUID gradiometer," *Appl. Phys. Lett.*, vol. 63, pp. 403-405, July 1993.

[6] E. Dantsker, S. Tanaka, O. Froehlich, K. Kouznetzov, and J. Clarke, "High-T_c SQUIDs with slots and holes and a long-baseline asymmetric gradiometer," *Extended Abstracts of ISEC'97*, vol. 1, H. Koch and S. Knappe, Eds. Berlin, Germany, June 1997, pp. 60-62.

[7] Y. Tarvin, Y. Zhang, W.. Wolf and A. I. Braginski, "A second-order SQUID gradiometer operating at 77 K," *Supercond. Sci. Technol.*, vol. 7, pp. 265-268, March 1994.

[8] A. Kittel, K. A. Kouznetsov, R. McDermott, B. Oh, and John Clarke, "High T_c Superconducting second-order gradiometer," *Appl. Phys. Lett.* vol. 73, pp. 2197-2199, October 1998.

[9] S. G. Lee, Y. Hwang, and B. C. Nam, "Direct-coupled second-order superconducting quantum interference device gradiometer from single layer of high temperature superconductor," *Appl. Phys. Lett.* vol. 73, pp. 2345-2347, October 1988.

Low T_c magnetometer used for active shielding in the frequency range DC-500Hz in biomagnetic measurements

D. Platzek
Biomagnetic Center, Dep. of Neurology, University Hospital Jena, Philosophenweg 3, 07740 Jena, Germany

H. Nowak
JENASENSORIK, Am Planetarium 5, 07743 Jena, Germany

Abstract — Ultra low noise DC-SQUIDs have been used to detect disturbances in biomagnetic measurements and to feed an active shielding system that compensates these disturbances.
This work describes some properties of the used SQUIDs and the principle of active shielding that has been improved for frequencies from DC to 500 Hz.
So far an attenuation of up to 50 dB for DC-near and about 25 dB for 50 Hz magnetic disturbances has been achieved.

I. INTRODUCTION

Biomagnetic fields caused by electrical activity (ion currents in cells or neuronal activity) of the brain, heart or muscles are in the order of magnitude from fT to pT whereas external magnetic fields (caused, e.g., by running cars, trains or by power lines) are with flux densities of nT to μT several orders of magnitude stronger (Fig. I). Hence biomagnetic measurements are disturbed in spite of expensive shieldings like passive shields of Mumetall, eddy current shields or gradiometers due to the decreasing shielding factor at low frequencies and the increasing external noise at these frequencies [1,2]. Because higher frequency disturbances are shielded sufficiently by eddy current shields, so far active shielding has been used only to improve the DC near signal/noise ratio [3,4]. Indeed technical frequencies like 16 $^2/_3$, 50 or 60 Hz cause much higher magnetic disturbances than surroundings and the biomagnetic signals (see Fig. I), so that usually they must have been filtered and biomagnetic measurements at these frequencies have been rather difficult or impossible.

We developed an active shielding system that attenuates DC near disturbances as well as disturbances of higher or technical frequencies like 16 $^2/_3$, 50 or 60 Hz and tested it inside magnetically shielded rooms (amuneal and Vacuumschmelze) with two layers of Mumetal and one layer of Aluminum as eddy current shield.

Manuscript received April 26, 1999.
This work was supported by the Thuringia Ministery of Science Research and Culture under Grant No. B301-96053

FIGURE I

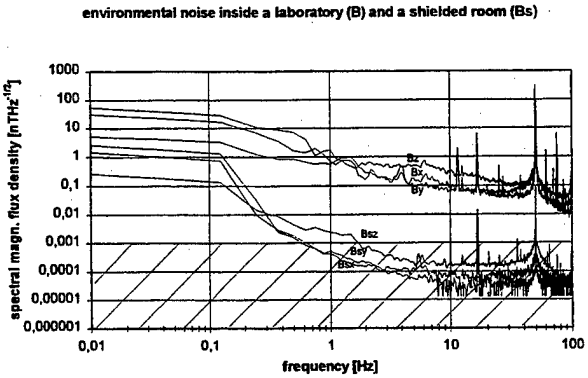

Spectral magnetic flux density of the environmental magnetic noise in a laboratory of the hospital (upper curves) and inside a magnetically shielded room (amuneal, two layers of Mumetal and one layer of Aluminum, lower curves). The noise increases at low, but also at technical frequencies about some orders of magnitude. The hatching marks the range of biomagnetic signals.

II. EQUIPMENT AND METHOD

The active shielding consists of a Low T_c SQUID vectormagnetometer, a PID (Proportional-Integral-Differential) controller system and Helmholtz-like coils in 3 orthogonal directions. The vectormagnetometer consists of 3 magnetometers oriented orthogonally to each other and connected to a DC SQUID each. The magnetic flux sensors, developed at the Physics Department of the University of Jena, are 8 loop thin film (9 layers, planar construction) DC SQUIDs (UJ111/UJ111Tr) [5] in gradiometer configuration with Nb-NbO_x-Pb/In/Au window-type Josephson tunnel junctions. These junctions are shunted by strips of AgIn with a resistance of 1.5 - 3 Ω. The inductance provided by the input transformer (two coils, 18 turns each) is about 0.8μH. The overall size of the printed circuit board with SQUID is 8mm x 16mm. The intrinsic magnetic flux noise of the SQUID system of 2 $\mu\phi_0 Hz^{-1/2}$ corresponds to a noise limited sensitivity of 0.7 $fTHz^{-1/2}$ [6]. Every SQUID is shielded with a Nb tube and connected with a 20mm diameter magnetometer coil of Nb-wire as antenna.

The dewar with these reference magnetometers is placed in the vicinity of the biomagnetic measuring system so that only disturbances and not the biomagnetic signal is measured.
The signals of the LT_c SQUID magnetometers are used as reference signal and fed into the PID controller that generates a current into the Helmholtz-like coils. Thus an antiphasic magnetic field is provided and the disturbing field is compensated. The principle is shown in Fig. II. Since the reference sensor and the biomagnetic measuring system cannot be at the same position, a residual field remains.

So far it has been unusual to mount the Helmholtz-like coils inside the magnetically shielded room due to antenna effects. But not only the shielding factor of the Mumetal/Al walls is strongly frequency dependent, but also the phase shift of the residual penetrating magnetic fields, of course of the compensating field too. At low frequencies (DC-1Hz) it does not play a role, but to compensate disturbing magnetic fields of technical frequencies we had to elude this problem. Consequently we mounted a second Helmholtz-like coil system inside the shielded room. With combined controllers and filters both coil systems can be driven.
The current through the Helmholtz-coils is monitored and continuously recorded and can additionally be compared with the biomagnetic data, whether a biomagnetic signal is disturbed.

FIGURE II

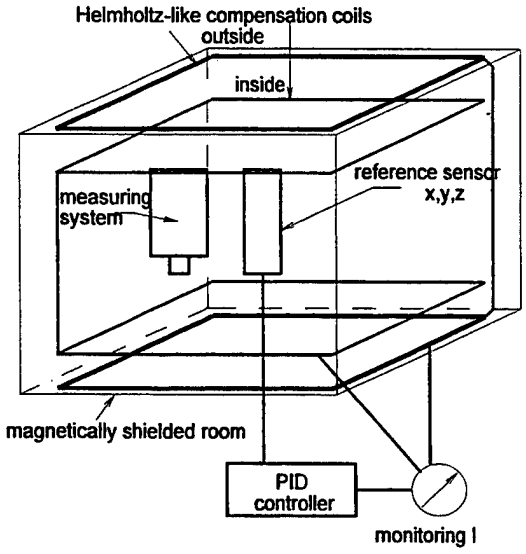

Principle of the active shielding. The signal of a reference detector is proportional to the flux density of the disturbances and is fed into a PID controller, that generates a current into Helmholtz-like coils to provide an antiphasic magnetic field. A second coil system inside the shielded room provides a higher frequency antiphasic magnetic field.

To estimate the functionality and the attenuation caused by the active shielding, data were measured and compared without and with ongoing active shielding. Therefore, the signal of an additional magnetometer with the same sort of SQUIDs, placed next to the reference system described above, has been measured with a HP3562 spectrum analyzer during working hours with normal public traffic in the hospital area.

III. RESULTS AND DISCUSSION

In contrast to the values for good SQUID charges of 2 $\mu\phi_0 Hz^{-1/2}$ measured in [6], the noise of the used SQUIDs has been determined with a HP3562 spectrum analyzer to about 5 $\mu\phi_0 Hz^{-1/2}$ (see Fig. III) with the SQUID inside a superconductive shielded Nb-tube.

FIGURE III

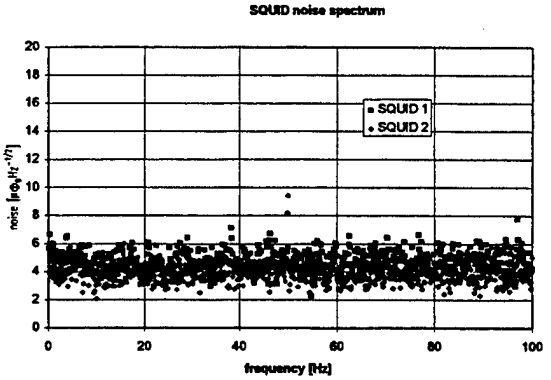

Noise spectrum of two of the used SQUIDs. The intrinsic noise has been determined to 5 $\mu\phi_0 Hz^{-1/2}$ corresponding to a field noise of about 2 fT.

For the active shielding system and the measuring system the SQUIDs have been connected with a Nb coil of 20 mm diameter as antenna for the magnetometer.

In Fig. IV the the spectral magnetic flux density B inside the shielded room without active shielding is compared with B with ongoing active shielding for the direction perpendicular to the ground (z-direction).
The signals show the environmental noise from 0 to 500 Hz originated mainly by power lines or machines respectively, with maxima at 16 $^2/_3$ Hz (caused by the tram and railway), or 50 Hz and harmonics from the power supply system. The upper line represents B without active shielding, whereas the dashed line below stands for B with ongoing active shielding. The hatching marks again the range where biomagnetic signals usually occur. This active shielding reduces the disturbing fields but at 50 Hz the signals still are rather strong. One has to consider that especially at this frequency the noise is not only caused by magnetic fields but also by stray fields directly into the electronics.

FIGURE IV

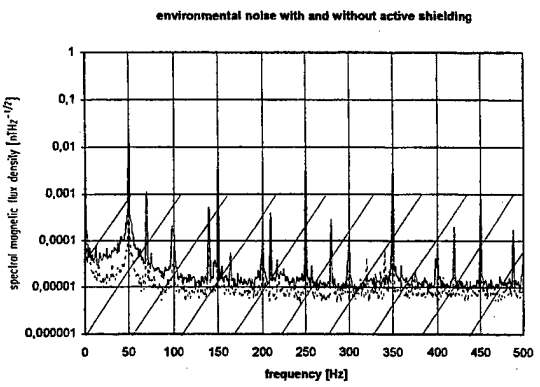

Environmental noise from 0 to 500 Hz originated mainly by power lines or machines respectively, with maxima at 16 $^2/_3$ Hz, or 50 Hz and harmonics. The upper line is without active shielding, whereas the dashed line below stands for B with ongoing active shielding. The hatching marks the range of biomagnetic signals.

It should also to be pointed out that this results have been achieved by measurements with magnetometers not with gradiometers, so the noise can be still in the range of biomagnetic signals (hatching).
To clarify the effect of the active shielding, the data obtained with active shielding are divided by the data obtained without active shielding, yielding the attenuation. The result is shown in Fig.V for frequencies up to 500 Hz. The peak at 4 Hz is caused by an interaction of the not yet completely optimized controllers with the active filters; this bug will be solved in next future.

FIGURE V

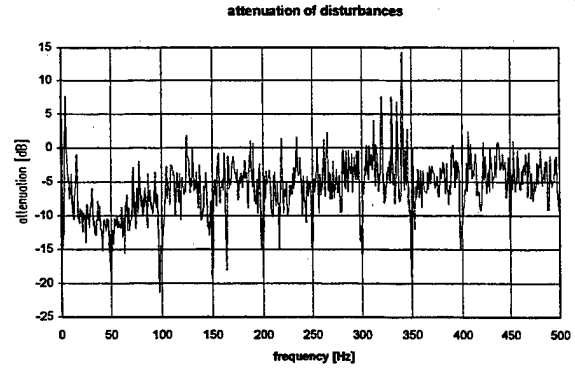

Attenuation of disturbances in the frequency range up to 500 Hz.

As shown in Fig. VI on a logarithmic scale, low frequency magnetic disturbances can be shielded more sufficient than higher frequency noise. The upper line in Fig. VI shows the spectral magnetic flux density B in a shielded room in the frequency range up to 20 Hz for a measurement without, the lower line with ongoing active shielding.
At frequencies of some 10mHz the environmental noise is on the order of some hundred pT, however with ongoing active shielding the noise is reduced to lower than 1 pT.

FIGURE VI

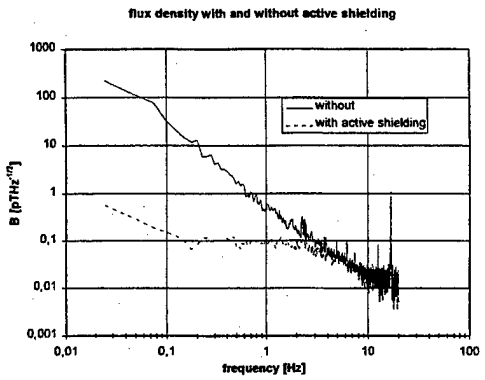

Frequency spectra of magnetometer signals inside a magnetically shielded room without (upper line) and with ongoing active shielding (dashed line below). The reduction of the low frequency noise is more than the factor 100.

IV. CONCLUSIONS

We developed an active shielding system that attenuates magnetic field disturbances for the range DC up to 500 Hz.
So far, the attenuation of low frequency disturbances is about 50 dB, the attenuation of higher frequencies up to 25 dB.
Best results have been achieved with two controllers, one PI controller for the DC-near frequencies with Helmholtz-coils outside, and one PD controller for the higher frequencies with the coil inside the shielded room. To avoid disturbances caused by an interaction between the separated controllers, the signal to the inner coil is filtered with an active high pass.

ACKNOWLEDGMENTS

Thanks to U. Schulze for continuous support and T. Fieseler, F. Gießler, J. Haueisen, R. Huonker for fruitful discussions.

REFERENCES

[1] J. Vrba: SQUID Gradiometers in Real Environment; in SQUID Sensors: Fundamentals, Fabrication and Applications; H. Weinstock (ed.), Kluwer Academic Publishers (1996) 117-178.
[2] H. Nowak: Biomagnetic Instrumentation; in Magnetism in Medicine - A Handbook; W. Andrä and H. Nowak eds.; Wiley-VCH (1998) 87-135.
[3] D.Platzek, H.Nowak, F.Gießler, J.Röther, M.Eiselt:Active Shielding to Reduce Low Frequency Disturbances in DC near Biomagnetic Measurements; Rev. Sci. Instrum. 70 (5) (1999).
[4] H.J.M. ter Brake, R. Huonker and H. Rogalla: New Results in Active Noise Compensation for Magnetically Shielded Rooms; Meas. Sci. Technol. 4 (1993) 1370-1375.
[5] F.Dettmann, W.Richter, G.Albrecht and W.Zahn:A monolithic thin film DC SQUID; Phys. Stat. Sol. A 51 (1979) 185.
[6] W. Vodel and K. Mäkiniemi: An ultra low noise DC SQUID system for biomagnetic research; Meas. Sci. Technol. 3 (1992) 1155.

Noise Characteristics of Double Relaxation Oscillation Superconducting Quantum Interference Devices with Reference Junction

Yong-Ho Lee, Hyukchan Kwon, Jin-Mok Kim, Yong-Ki Park and Jong-Chul Park

Korea Research Institute of Standards and Science, P.O.Box 102, Yusong, Taejon, 305-600, Republic of Korea

Abstract—**We fabricated double relaxation oscillation SQUIDs (DROSs) with a reference junction and investigated its noise characteristics. Due to the large flux-to-voltage transfer of 1~3 mV/Φ_0, the room-temperature dc preamplifier could readout the SQUID output voltage directly and the contribution of the preamplifier input noise to the total system noise was negligible. The flux noise of the DROS planar gradiometer is about 4 $\mu\Phi_0/\sqrt{\text{Hz}}$ at 100 Hz, corresponding to the field gradient noise of 1 fT/cm$\sqrt{\text{Hz}}$, when operated inside a moderately shielded room. Due to the large modulation voltage of about 100 μV, stable flux-locked-loop operation was possible against drift in the input offset voltage.**

I. INTRODUCTION

Low-temperature dc superconducting quantum interference devices (SQUIDs) are the most sensitive low-frequency magnetic field sensors and are widely used for measuring magnetic fields from human brain and heart, etc [1],[2]. For the SQUIDs to be useful in a biomagnetic multichannel system, the flux-to-voltage transfer of the SQUID should be large enough, such that direct readout of the SQUID output voltage can be done [3].

DROS provides large modulation voltage and large flux-to-voltage transfer and simple electronics were used for flux-locked-loop (FLL) operation [4]. For the DROS to be more suitable as a multichannel sensor, the reference SQUID should be replaced by a reference junction [5].

In this report, we fabricated DROSs with a reference junction and analyzed its noise characteristics. To find the optimum operation condition, dependence of the DROS noise characteristics on the bias current and on the offset flux was investigated.

Manuscript received April 27, 1999.
This work was supported by the Ministry of Science and Technology, Korea.

II. DESIGN OF THE DROS

The DROS consists of a hysteretic dc SQUID (the signal SQUID) and a reference junction in series, shunted by a relaxation circuit of an inductor and a resistor [4]. The schematic circuit drawing of the DROS is shown in Fig. 1. In order to reduce the number of wires between the SQUID and the room-temperature electronics, and to reduce the possibility of flux trapping by the reference SQUID, we used a reference junction instead of the reference SQUID [6]. The DROS functions as a comparator of two critical currents ; the signal current and the reference current, resulting in a very large flux-to-voltage transfer $dV/d\Phi$ when the two critical currents are equal.

The signal SQUID is designed to be a gradiometric type with two 100 μm x 100 μm square holes connected in parallel and has an inductance of 113 pH. The size of each Josephson junction in the signal SQUID is 4 μm x 4 μm. The reference junction has size of 5 μm x 5 μm, so that its critical current is 78 % of the maximum critical current of the signal SQUID.

The input coil consists of two series-connected coils, 15-turns each, integrated on each SQUID loop and its inductance is calculated to be 87 nH. The pickup coil is a first-order gradiometer with two planar 12 mm x 12 mm coils connected in series. The linewidth of the pickup coil is 0.5 mm and the baseline is 40 mm. To remove various resonances in the SQUID, several damping circuits ; R_d, R_w and (R_x-C_x), have been connected, as shown in Fig. 1.

The SQUIDs were integrated on Si wafers by a simple 4-level process based on Nb/AlO_x/Nb junction technology. The Josephson junctions were defined by reactive ion etching and the insulation between metal layers was made by SiO_2 film

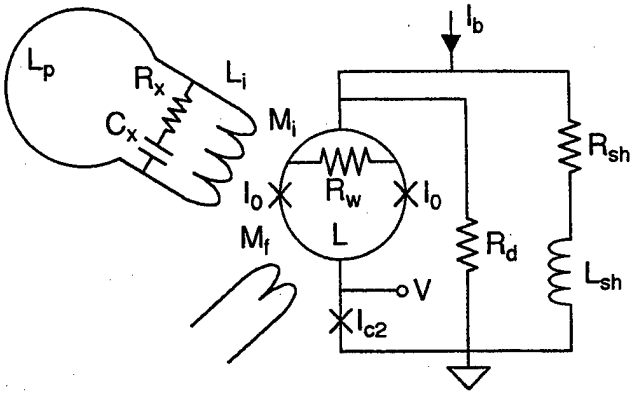

Fig. 1. Schematic circuit drawing of the DROS with a reference junction. The voltage output is measured across the reference junction. Various damping circuits were added.

deposited by plasma-enhanced chemical vapor deposition. The resistor is a reliable thin film of Pd. The overall size of the planar gradiometer is 12 mm x 52 mm and 4 devices were fabricated on each 3-inch wafer.

III. CHARACTERISTICS OF THE DROSs

The fabricated sensors were characterized inside a moderately shielded room. The DROSs have reference critical currents in the range of 10~20 μA and maximum modulation voltages of up to 120 μV. The flux-voltage curves of DROSs showed almost a step function of the applied field. The maximum $dV/d\Phi$ is 1~3 mV/Φ_0, which is about 10 times larger than the $dV/d\Phi$ of dc SQUIDs. Due to the large transfer, the DROS output could be connected directly to a room-temperature dc preamplifier without an impedance matching circuit. The FLL circuits have a dc bias current, without using flux modulation. The preamplifier is an instrumentation amplifier made of LT1028 op-amps. and has an input noise of about 1.7 $nV/\sqrt{Hz}$ at 100 Hz. With a typical $dV/d\Phi$ value of 2 mV/Φ_0, the preamplifier contributes an equivalent flux noise of 0.85 $\mu\Phi_0/\sqrt{Hz}$ at 100 Hz.

Fig. 2(a) shows the $dV/d\Phi$, the total flux noise in FLL $\Phi_{n,FLL}$ and the intrinsic flux noise $\Phi_{n,int}$ of a DROS versus the bias current. The intrinsic flux noise was measured in an open loop and determined after subtracting the preamplifier noise. The flux noise is minimum at a bias current of 25 μA, and except for the peak around 22.5 μA, the flux noise is below 5 $\mu\Phi_0/\sqrt{Hz}$ in the bias

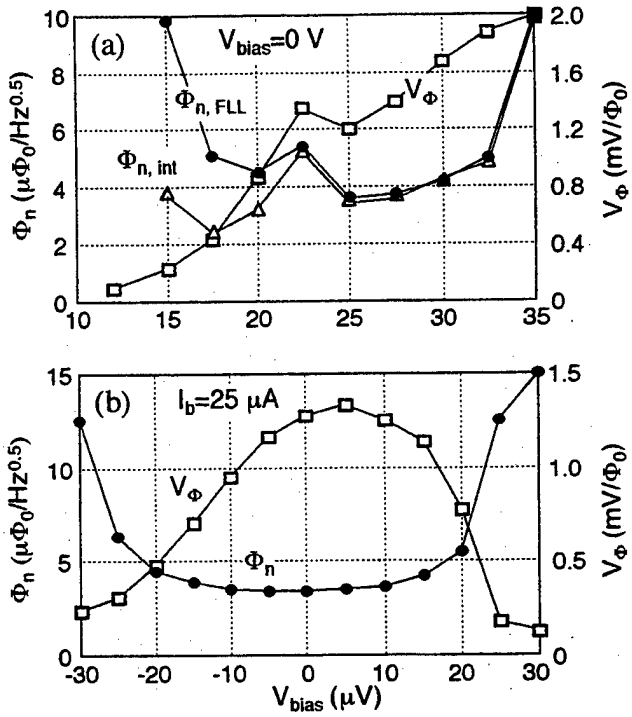

Fig. 2. Flux-to-voltage transfer and flux noises of a DROS versus the bias current (a) and the bias voltage.

current range of 18~32 μA. For bias currents larger than 22.5 μA, the total flux noise is nearly equal to the intrinsic flux noise, meaning that the preamplifier noise contribution is negligible. However, below this bias currents, the preamplifier contribution increases with decreasing bias current due to the decrease of $dV/d\Phi$. From the critical current of the reference junction (= 12 μA) and the effective McCumber parameter (≈0.12), the maximum bias current is given as 35 μA. But, in the current-voltage curve, modulation appears for bias currents up to 42 μA.

At the bias current of 25 μA, the dependence of the flux noise on the working point of the flux-voltage curve was measured. Fig. 2(b) shows the flux noise and $dV/d\Phi$ versus the bias voltage, here the center of the voltage swing is defined as zero voltage and the positive polarity means the working point is above the center of the voltage swing. Within a bias voltage range of $\pm$15 μV around the center of the voltage swing, the flux noise is minimal, meaning that the DROS is quite stable against the offset voltage drift of the preamplifier. This operation margin for the offset drift is about 3 times larger than the dc SQUID with additional positive feedback [7].

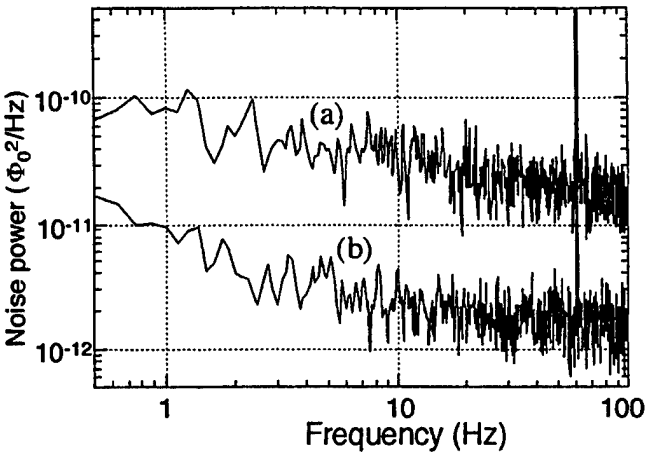

Fig. 3. Total noise power of the DROS (a) and equivalent noise power of the preamplifier (b).

Fig. 3 shows the flux noise power of the SQUID system (a) and the preamplifier (b), respectively. Here the equivalent preamplifier noise is determined by the preamplifier input noise divided by $dV/d\Phi$. In the frequency range of 1~100 Hz, the preamplifier noise contribution is about 10 % of the total SQUID noise.

Fig. 4 shows the flux noise and gradient noise spectrum of a DROS gradiometer, measured inside a magnetically shielded room without using a superconducting tube. Here the DROS was operated at the bias current of 25 μA and zero bias voltage. The flux noise is about 4 $\mu\Phi_0/\sqrt{\text{Hz}}$ at 100 Hz, increasing to 8 $\mu\Phi_0/\sqrt{\text{Hz}}$ at 1 Hz. These correspond to the field gradient noise of 1 and 2 fT/cm$\sqrt{\text{Hz}}$, respectively. Multiplied by the baseline, the corresponding field noise is 4 and 8 fT/$\sqrt{\text{Hz}}$, at 100 and 1 Hz, respectively.

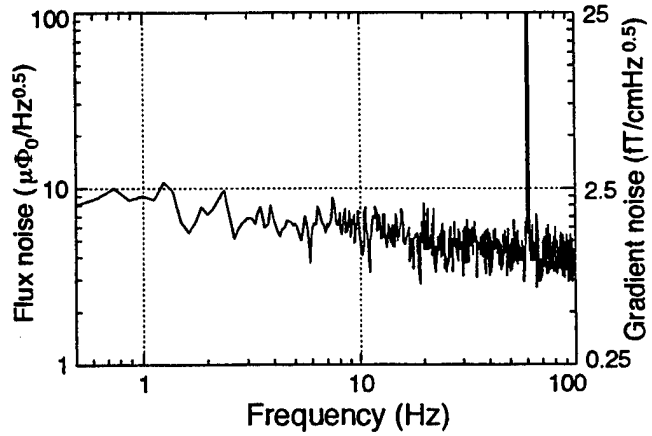

Fig. 4. Flux noise and field gradient noise spectrum of the DROS planar gradiometer.

IV. CONCLUSION

DROSs with a reference junction were fabricated and its noise characteristics were analyzed for use in biomagnetic measurements. Due to the large flux-to-voltage transfer, the flux-locked-loop could be made simple, and the noise contribution of the room-temperature preamplifier is negligible. Due to the large modulation voltage, the DROS have stable operation margin against the drift in the preamplifier offset voltage, and the noise characteristics is not critical on the working point of the flux-voltage curve.

The DROS gradiometer system has a flux noise of around 4 $\mu\Phi_0/\sqrt{\text{Hz}}$ at 100 Hz, corresponding to a field gradient noise of 1 fT/cm$\sqrt{\text{Hz}}$, which is low enough for the measurements of neuromagnetic fields.

REFERENCES

[1] J.P. Wikswo, Jr., "SQUID magnetometers for biomagnetism and nondestructive testing: important questions and initial answers", *IEEE Trans. Appl. Supercond.*, vol. 5, pp.74-120, June 1995.

[2] D. Drung, "Recent low temperature SQUID developments," *IEEE Trans. Appl. Supercond.*, vol. 4, pp.121-127, Sept. 1994.

[3] D. Drung, "Advanced SQUID read-out electronics," in *SQUID Sensors : Fundamentals, Fabrication and Applications*, ed. H. Weinstock, Kluwer Academic Pub. Dordrecht, 1996. pp.63-116.

[4] D.J. Adelerhof, H. Nijstad, J. Flokstra, and H. Rogalla, "(Double) relaxation oscillation SQUIDs with high flux-to-voltage transfer : Simulations and experiments," *J. Appl. Phys.*, vol. 76, pp.3875-3886, Sept. 1994.

[5] D.J. Adelerhof, M. van Duuren, J. Flokstra, and H. Rogalla, "Second generation dc SQUID sensors : ROS with frequency readout and DROS with voltage readout," in *Superconductive Devices and Circuits, SPIE*, vol.2160, pp. 142-153, Jan. 1994.

[6] Y.H. Lee, H.C. Kwon, J.M. Kim, Y.K. Park, and J.C. Park, "Double relaxation oscillation SQUID with reference junction for biomagnetic multichannel applications," *Applied Superconductivity*, vol. 5, pp. 413-418, 1998.

[7] T. Ryhänen, R. Cantor, D. Drung and H. Koch, "Practical low-noise integrated dc superconducting quantum interference device magnetometer with additional positive feedback", *Appl. Phys. Lett.* vol. 59, pp. 228-230, July 1991.

Design and Construction of an HTS DC SQUID Electronic Gradiometer NDE system

J. Y. Kim, S. G. Han, and J. H. Kang
Department of Physics, University of Inchon, Inchon 402-749, Republic of Korea

E. H. Lee, I. H. Song, and J. H. Gohng
Material and Device Sector, Samsung Advanced Institute of Technology, P. O. Box 111, Suwon 440-600, Republic of Korea

Abstract— We designed and constructed a non-destructive evaluation system using an HTS DC SQUID electronic gradiometer. Our DC SQUID electronic gradiometer is composed of two DC SQUID magnetometers. The system included a non-magnetic stainless steel cryostat and a set of coaxial exciting coils, which were used to induce an eddy current in the test piece. We also have calculated the eddy current density produced by an exciting coil in any direction of the testing object. We could compute the eddy current density distribution in 3D. The SQUIDs were computer controlled and the output data from the electronic gradiometer was obtained by using a Labview software.

I. INTRODUCTION

Applying the SQUIDs to a NDE system, however, usually requires operating the SQUIDs in a magnetically noisy environment exposed to the earth's magnetic field and other noise sources. Therefore, when designing a SQUID NDE system, it is crucial to design the system so that it may properly operate under the ambient or noisy magnetic field environment. In general, unlike a magnetometer, a gradiometer has the advantage of being easily operated under an ambient or noisy magnetic field [1]. The main goal of this work was to construct a gradiometer system by combining two DC SQUIDs in electronic means, forming an electronic gradiometer and to construct an exciting coil to maximize the sensitivity of the gradiometer to the defects in test pieces.

II. EXPERIMENTS

We fabricated the two DC SQUID magnetometers, on the basis of a single layer YBCO film as follows. The c-axis YBCO film of 200nm thick was deposited on a $SrTiO_3$ bi-crystal substrate using a pulsed laser deposition method. General photo-lithography with ion etching technique was used to form SQUID patterns on YBCO films. The Junction width and the length were 3um and 6um, respectively.

Manuscript received April 30, 1999.
The work at University of Inchon was supported in part by the Basic Science Institute Program, Ministry of Education, South Korea.

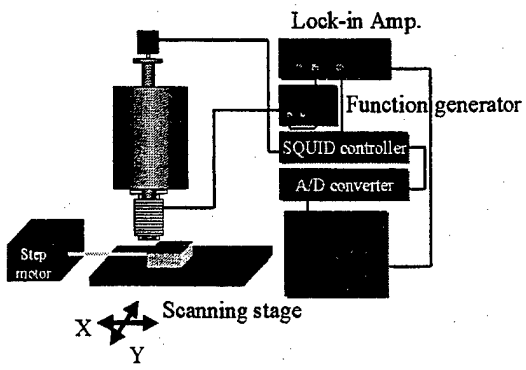

Fig. 1. Diagram of the SQUID NDE system.

The SQUIDs were operated in a non-magnetic stainless steel dewar. Figure 1 shows the diagram of our NDE system which is composed of two SQUIDs and their control electronics [2]. In this work, we have focused to fabricate an electronic gradiometer using two dc magnetometers. Since fabricating an HTS gradiometer with a good balance is difficult, Our approach was to make an electronic gradiometer where two dc SQUID magnetometers are used and an external electronics are used to get a good balance. Figure 2 shows a block diagram of an electronic gradiometer, consisted of two individual SQUID magnetometers and to be used in an ambient field environment [3].

A PCB board was designed and used to mount two SQUIDs on it to work as an electronic gradiometer[4]. And then the board was placed on a probe to be inserted into a non-magnetic liquid nitrogen dewar. To achieve this, we have designed an exciting coil to use in our non-destructive

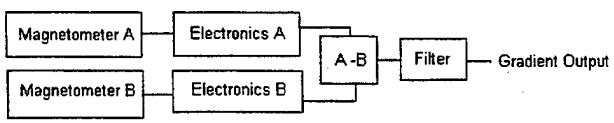

Fig. 2. A block diagram of an electronic gradiometer composed of two SQUID magnetometers.

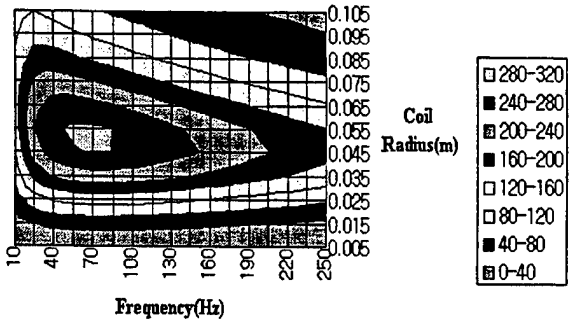

Fig 3. Eddy current distributions on the 2cm thick finite plate. It shows the contour plots of the eddy current density on the frequency and the coil radius plane.

evaluation device. Our cryostat, with a tail made of stainless steel, served as a weak magnetic shield and is a little better in reducing the noise than a plastic one. The coil frame was designed in such a way that the inner and the outer coil radii were 2cm and 4cm, respectively. The wire radius was 0.01mm and the values of each resistance of the inner and the outer coils were 200ohms each.

We also calculated the eddy current density produced by an exciting coil in any direction of the testing object. We could compute the eddy current density distribution in 3D. Each SQUID receives separate control signals and send the data through separate channels. The sample motion stage and the SQUIDs were computer controlled and the output data from the electronic gradiometer was obtained by using a Labview software.

III. Results and Discussion

To optimize the exciting coil design, we calculated the eddy current distribution generated by a circular coil on a finite plate by using the following formular[5];

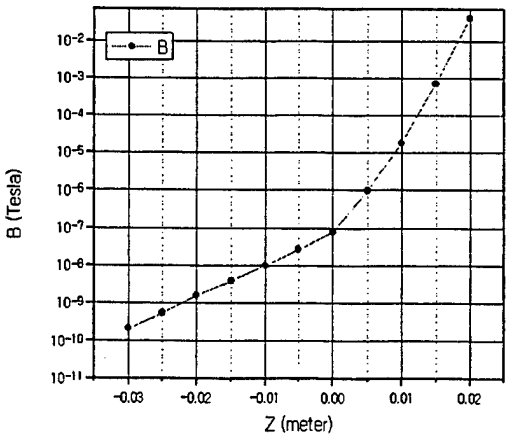

Fig 4. Magnetic field distribution along the z axis.

$$J_{2,\theta}(r,z) = -\frac{ip^2 I}{a^2}\int_0^\infty \{\exp(-kb/a)\}J_1(k)J_1(kr/a)\cdot \frac{(k\mu_r+q)\exp\{q(c-z')/a\}-(k\mu_r-q)\exp\{-q(c-z')/a\}}{(k\mu_r+q)^2\exp(qc/a)-(k\mu_r-q)^2\exp(-qc/a)}\,kdk$$

where $q=(k^2+ip^2)^{1/2}, p=\sqrt{\mu\omega\sigma a^2}$. $\mu=\mu_0\mu_r\cdot\mu_r$ and k are the relative permeability of the medium and the constant of separation, respectively. Results of this calculation are shown in Fig. 3. In this figure, the contour plots of the eddy current density on the frequency and the coil radius plane are shown. In the calculation, we used 10mA as the current flowing in the coil and a 2cm thick finite plate as the test piece where eddy currents are induced. From Fig. 3, we could find that we get the maximum eddy current induced on the plate if we use about 70Hz and the coils with about 5cm in radius.

We also calculated the magnetic field produced by an exciting coil. We placed an 1 inch thick plate under an exciting coil and calculated the magnetic field distribution. This is shown in Fig. 4 where the vertical distance, Z, was measured from the top surface of the plate. From this figure we can see that reducing the distance between the exciting coil and the plate is quite important.

To test our gradiometer we used a Conductus PC-1000 SQUID controller to control our SQUIDs and a Labview software to get a good balance. First, we did put a Mu-metal shield around the dewar tail to reduce the ambient field noise and tested the gradiometer. We first obtained the output data from the SQUID controller and fed the data to the Labview sortware to balance the data from the two different channels. The results are shown in Fig. 5. Ch1 denotes the signal from one SQUID and Ch2 from the other SQUID. Ch1-Ch2 is the balanced signal. Spectrum analysis of the balanced output signal, shown in Fig. 6, shows that 60Hz noise is the main source of the noise and the noise floor is about $10^{-7}\,\Phi_0$.

We also performed the same experiment without Mu-metal shield and the results are shown in Fig. 7. Spectrum analysis of the balanced output signal, shown in Fig. 8, shows that our gradiometer is noisier without shield and the noise floor is

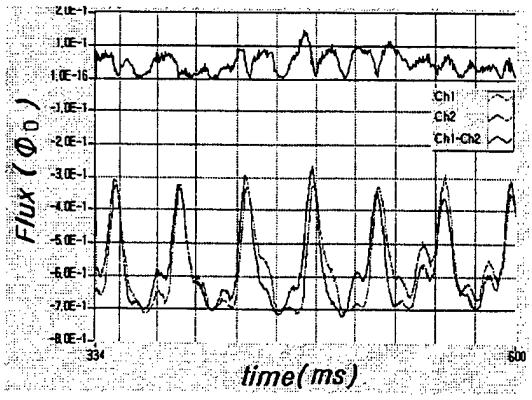

Fig 5. Measurement data of each SQUID channels and the resulting gradiometer output (Ch1-Ch2) at a Mu-metal shielding environment.

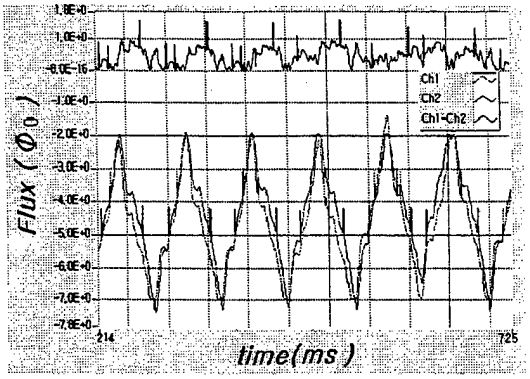

Fig 6. Measurement data of each SQUID channels and the resulting gradiometer output (Ch1-Ch2) at an unshielded environment.

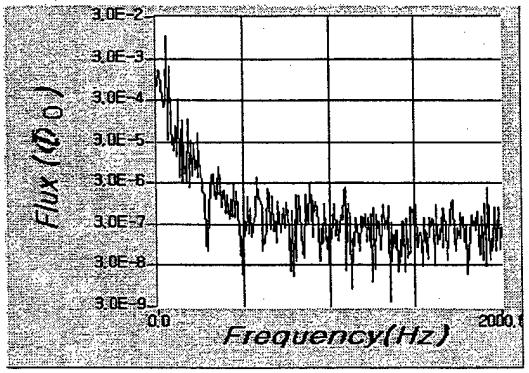

Fig 7. Spectrum analysis of the electronic gradiometer output under a shielded environment.

about 10^{-4} Φ_0 which is about 3 orders of magnitude higher than without shield.

As a preliminary test of our NDE system, we used a weak magnet as a test piece. When we placed a Gaussmeter 2cm above the test piece we observed 1.5 Gauss. We pulled the test piece at the speed of 6cm/s. The vertical distance between the gradiometer and the test piece was 2cm. Part of the resultant output signal is shown is Fig. 9. 15 Hz low pass filter was used to the output signal in Fig. 9.

IV. Conclusion

In this work, an electronic gradiometer system has been constructed from two independent channels of YBCO DC SQUIDs. We have fabricated and tested electronic gradiometers of being scanned test magnet in a magnetically noisy environment. The result is a working NDE system that can be operated in a relatively noisy ambient field environment.

ACKNOWLEDGMENT

J.H.K. acknowledges the support by the Korea Ministry of Science and Technology. The work at University of Inchon was partially supported by the Korea Science and Engineering Foundation through the Multimedia Research Center at University of Inchon.

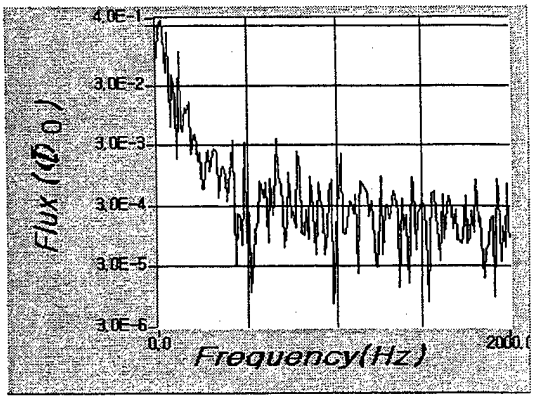

Fig 8. Spectrum analysis of the electronic gradiometer output under an unshielded environment.

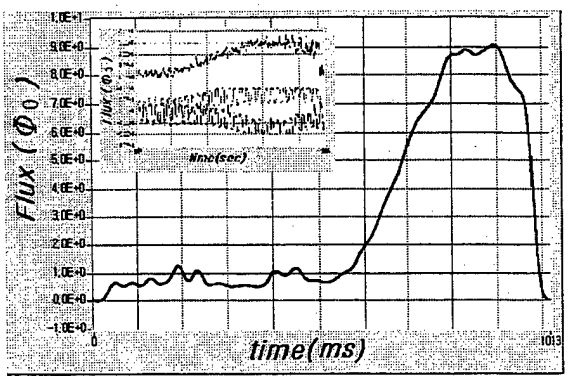

Fig 9. Gradiometer output signal when a magnetic test piece was passed under the gradiometer. Inset shows the raw data of Ch1, Ch2, and Ch1-ch2.

REFERENCES

[1] V. Schultze, R. Stolz, and V. Zakosarenko "High T_c SQUIDs for Unshielded Measuring in Disturbed Environments" JOURNAL DE PHYSIQUE IV, vol 6, C3-367, 1996.

[2] N. Kasai, N. Ishikawa and H. Yamakawa "Non-destructive Detection of Dislocations in steel Using a SQUID Gradiometer" IEEE Transaction on Appl. Supercond. Vol. 7, pp. 2315-2318, 1997.

[3] F. Schmid, S. Wunderlich and H. Specht "HTSC-dc-SQUID Gradiometer for a nondestructive testing system", Inst. Phys. Conf. No158, pp. 651-654, 1997.

[4] J. Y. Kim, J. H. Kang, E. H. Lee, I. H. Song, J. H. Gohng , and T. S. Hahn, "Construction and Measurements of HTS DC SQUID Electronic Gradiometer to be used in NDE Systems," IEEE Transaction on Appl. Supercond, accepted for publication in June, 1999

[5] J.A. Tegopoulos, E.E.Kriezis, "Eddy current in linear conducting media," 1985.

Optimization of field homogeneity of Helmholtz-like coils for measuring the balance of planar gradiometers

M. A. Nordahn[†*], T. Holst, and Y. Q. Shen

NKT Research Center, Priorparken 878, DK-2605 Brøndby, Denmark.
[*]Department of Physics, Technical University of Denmark, DK-2800 Lyngby, Denmark.
[†]Department of Clinical Neurophysiology, Rigshospitalet, Blegdamsvej 9, DK-2100 København, Denmark.

Abstract—Measuring the balance of planar SQUID gradiometers using a relatively small Helmholtz-like coil system requires a careful design of the coils in order to have a high degree of field uniformity along the radial direction. The level to which planar gradiometers can be balanced will be affected by any misalignment of the gradiometer relative to the ideal central position. Therefore, the maximum degree of balancing possible is calculated numerically for the Helmholtz geometry under various perturbations, including misalignment of the gradiometer along the cylindrical and the radial axis, and angular tilting relative to the normal plane. Furthermore, if the ratio between the coil separation and coil radius is chosen to be less than unity, calculations show that the expected radial uniformity of the field can be improved considerably compared to the traditional Helmholtz geometry. The optimized coil geometry is compared to the Helmholtz geometry and is found to yield up to an order of magnitude improvement of the worst case error signal within a volume spanned by the uncertainty in the alignment.

I. Introduction

The well-known Helmholtz coil configuration with two circular coaxial current loops separated by a distance, s, which equals the coil radius, a, has often been used to characterize the degree of balance in axial gradiometers due to the very homogeneous field distribution midway between the coils [1], [2], [3]. Normally, such coil systems tend to be quite large (~ meter size). Furthermore, if planar thin film gradiometers are characterized, the field homogeneity in the radial direction becomes important and the Helmholtz geometry turns out to no longer be optimal. The signal measured by a planar gradiometer in a nearly homogeneous field involves contributions from the intrinsic gradiometer imbalance as well as contributions from the inevitable misalignment errors of the gradiometer. Our aim is to calculate the worst case errors due to the misalignment of the gradiometer, so we can discriminate this type of error from the intrinsic gradiometer imbalance. Assuming that the dominant source of magnetic field gradients

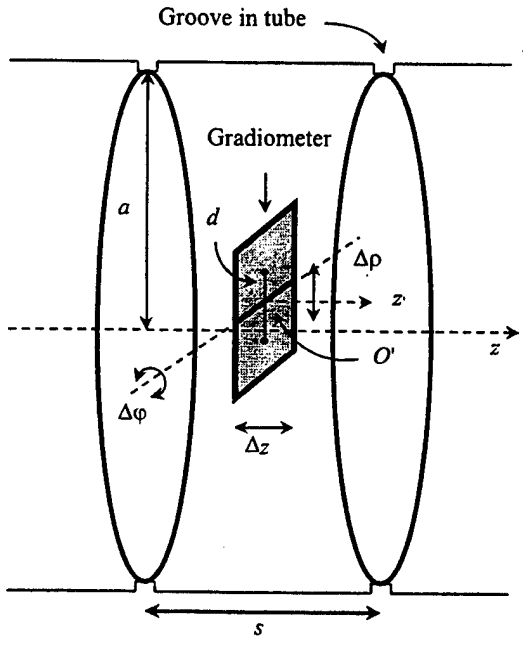

Figure 1: The geometry of the coil system with the planar gradiometer (with baseline d) placed around the ideal central position. Misalignment of the gradiometer is characterized by axial and radial tolerances Δz and $\Delta\rho$, respectively. The misalignment error in angular tilt is denoted $\Delta\varphi$. The gradiometer investigated in the simulations is modelled by two adjoined rectangles each with an area of 9 mm × 9 mm. The central point of the gradiometer is labelled O', while the z'-axis runs through O' and is parallel to the z-direction.

in an unshielded SQUID gradiometer system comes from the power lines, the gradient-to-field ratio can be approximated by $2d/R$ requiring a balancing level of 3,000-10,000 ppm (parts-per-million), where d is the gradiometer baseline (≈ 1 cm for a typical HTS planar gradiometer) and R (2-7 m used here) is the distance from the power lines [4]. Therefore, the intrinsic SQUID gradiometer imbalance should be better than 1,000 ppm, while the coil characterization system should be even better, e.g. reaching the 100 ppm level.

II. METHODS

A. Physical Setup.

Circular coaxial coils of small dimensions, e.g. with a diameter < 20 cm, are comfortably constructed by winding the current loops in machined grooves on a tube, thus allowing us to assume perfect parallelism and negligible off-axis errors. The geometry of the system is depicted in Fig. 1. The actual positioning of the gradiometer relative to the ideal central position is important, since it affects the error signal seen by the gradiometer mostly due to the field inhomogeneity in the radial direction. A rather conservative estimate of the misalignment tolerances is given in Table 1. These absolute values span a volume within which we are sure that the gradiometer is located, here assumed to be independent of the coil geometry.

TABLE I

UNCERTAINTIES IN ALIGNMENT OF GRADIOMETER

Δz	$\Delta\rho$	$\Delta\varphi$
± 1 mm	± 2 mm	± 5 °

Here Δz is the misalignment along the cylindrical axis, $\Delta\rho$ the misalignment along the radial direction, and $\Delta\varphi$ is the angular tilt about one of the gradiometer axes, refer to Fig. 1.

B. Optimization of the Helmholtz system.

In Fig. 2 is shown the z-component of the magnetic field as a function of radial distance from the center both for the traditional Helmholtz geometry ($s = a$) and for two perturbed geometries $s = 0.96a$ and $s = 1.04a$. In general, two local maxima are created around $\rho = 0$ for s < a. Since a planar gradiometer spans a finite fraction of the coil diameter, the precise location of these field maxima (depending on the s/a ratio) will affect the effective field homogeneity seen by the gradiometer. An important point of these qualitative observations is that the relative error signal is expected to increase dramatically as the s/a ratio becomes *larger* than unity. Remember that the Helmholtz geometry is optimized for best field homogeneity at the center *point* $\rho = 0$ and not for finite span in the radial direction.

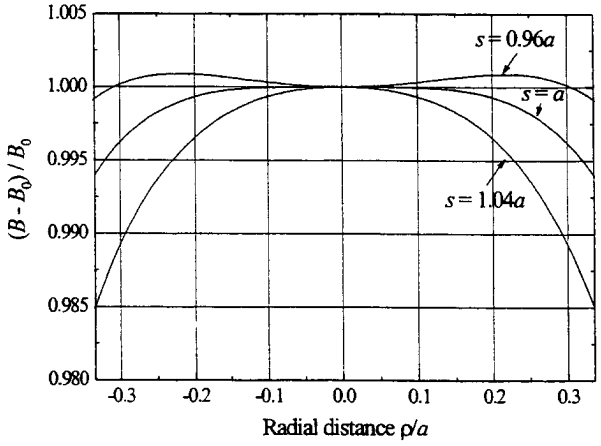

Figure 2: The radial deviation of the z-component of the magnetic field normalized to $B_0(\rho=0)$ midway between the two coil loops. The field homogeneity in the radial direction is affected if the s/a ratio is changed.

C. The Numerical Calculations.

The law of Biot and Savart is used to calculate the z-component of the magnetic field anywhere in space. The planar gradiometer is modelled with two adjoined rectangular areas, which are located in the same plane, see Fig. 1. The relative error signal seen by the gradiometer is calculated as the flux difference between the two gradiometer areas, normalized to the normal component of the field in the center of the gradiometer. Besides the idealization of the gradiometer, we also assume the absence of any field coming from the wiring to and from the coil loops and the absence of any magnetically conductive material in the vicinity of the coil system. Preliminary computer simulations indicate that the effect of a finite coil winding cross section area is a negligible perturbation of the relative error signal. In order to get information about the worst case error signal, calculations are performed for several locations and orientations of the idealized gradiometer within the volume spanned by the misalignment errors Δz, $\Delta\rho$, and $\Delta\varphi$. Rotation and tilting are performed by the successive application of rotation matrices. The volume of misalignment errors is scanned for maximum error signal in the following way: first the gradiometer center O' is positioned at z and ρ within the ranges $\pm\Delta z$ and $\pm\Delta\rho$, respectively, and then it is tilted a certain angle φ (within the range $\pm\Delta\varphi$) around the axis which runs through O', is perpendicular to the baseline, and lies the plane of the gradiometer (see Fig. 1). Finally, the gradiometer is rotated 180° around the z'-axis. Angular misalignment tilt around the baseline axis is neglected, since the relative error signal in general is small due to field symmetry considerations. We note that it is not intuitively clear, where in the misalignment volume the relative error signal is maximum in a perturbed Helmholtz coil system.

III. RESULTS

Inspired by the above-mentioned observations, the calculations are now extended to include a gradiometer. The coil radius chosen is $a = 25$ mm, while the two areas of the

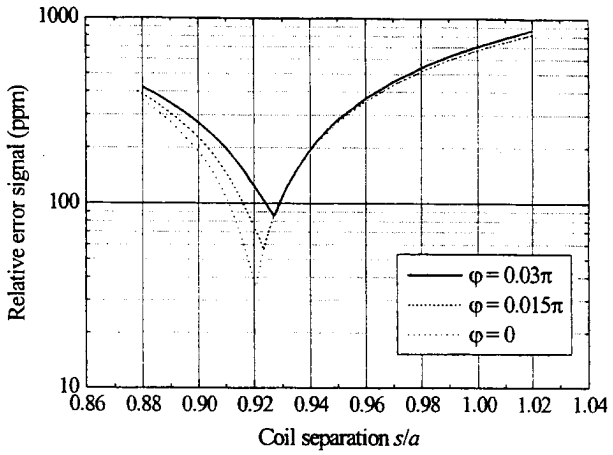

Figure 3 The relative error signal is plotted for a = 25 mm as a function of the coil separation. The gradiometer under consideration is scanned in the volume defined by the misalignment tolerances listed in Table 1. Curves are shown for three different angles of the misalignment tilt. Here, maximum tilt angle corresponds to the worst case situation.

gradiometer have the dimensions 9 mm × 9 mm. We emphasize that the actual values of the presented results are specific to these choices of coil diameter, gradiometer size,and misalignment tolerances. Fig. 3 shows the relative error signal within our misalignment volume for a range of different coil separations. The relative angle of the misalignment tilt, φ, of the gradiometer has a significant effect on the degree of balancing possible. As can be clearly observed, the curves show a distinct minimum for a certain value of separation. It is seen that the maximum relative error signal for the Helmholtz system is ≈ 700 ppm, whereas it would be ≈ 85 ppm if the s/a ratio is chosen to be $s = 0.927a \approx 23.2$ mm. In a mechanical fabrication process, this suggested coil separation can be clearly distinguished from $s = a = 25$ mm. The degree of balancing possible in the suggested coil system should be improved by a factor of approx. eight.

Other Geometries.

We have calculated the optimal coil separation for a range of radii (keeping the two gradiometer areas and misalignment volume constant). Fig. 4 shows this result together with the maximum relative error signal for the Helmholtz geometry and the optimized geometry. The improvement factor of approx. eight seems to be valid over the investigated range of radii (20 to 75 mm). As expected, the value of the optimal s/a ratio approaches unity for large radii (Helmholtz geometry), since the gradiometer now spans a relatively smaller fraction of the coil diameter.

IV. SUMMARY

Using numerical simulations of the magnetic field induced by two circular coaxial coils, we have calculated the expected maximum relative error signal seen by an idealized 9 mm × 18 mm gradiometer under various perturbations of the gradiometer position. Even with a coil diameter of only 5 cm it is possible to reach balancing levels down to 100 ppm. This should be sufficient for most applications. Such a small coil system is advantageous if it is used inside a high permeability shield, where the proximity of the shield can perturb the homogeneity of the magnetic field produced by the coil system. Small coil dimensions also mean that the coil system and sample holder can be machined from a single piece of material and immersed in liquid nitrogen. This gives a good opportunity to have a well-defined and mechanically stable gradiometer position relative to the coils, which also minimizes part of the vibration induced noise. If we take 300 μA for ampere × windings, the gradient signal from the coils should be ~ 1 pT/cm, which is easily measured with a HTS planar gradiometer. In conclusion, we have shown that it should be possible to construct small-sized and inexpensive coil systems for measuring the balance of planar gradiometers.

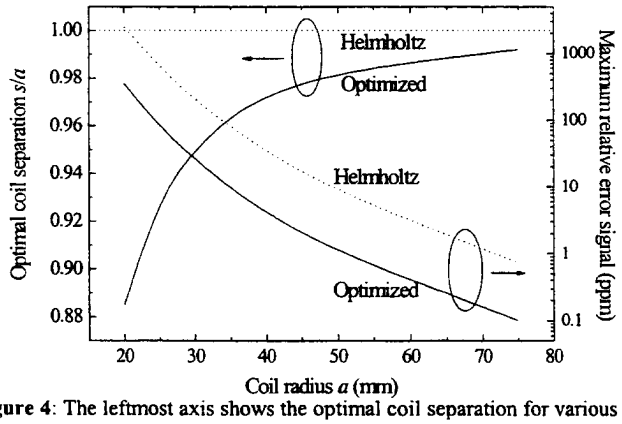

Figure 4: The leftmost axis shows the optimal coil separation for various radii (refer to Fig. 2 for more details). The corresponding maximum relative error signals are plotted on the rightmost axis.

REFERENCES

[1] J.R. Reitz, F.J. Milford, and R.W. Christy, "Foundations of electromagnetic theory", 3rd ed., pp. 168-172, 1979.

[2] A. Chwala, F. Bauer, V. Schultze, R. Stolz and H.-G. Meyer, "Helmholtz coil systems for the characterization of SQUID sensor heads", *Applied Superconductivity, Proceedings of EUCAS*, vol. 1, no 158, pp. 739-742, 1997.

[3] R. Merritt, G. Purcell and G. Stroink, "Uniform magnetic field produced by three, four, and five square coils", *Rev. Sci. Instrum.*, vol. 54, no. 7, pp. 879-892, 1983.

[4] J. Vrba, "SQUID gradiometers in real environments", *SQUID Sensors: Fundamentals, Fabrication and Applications*, pp. 117-178, Kluwer Academic Publishers, 1996.

Comparison of Calibration Methods for SQUID Gradiometers

P. H. Ornelas, A. C. Bruno and C. H. Barbosa
Pontifícia Universidade Católica do Rio de Janeiro, Rua Marquês de São Vicente, 225, Rio de Janeiro, RJ 22453-900, Brazil

***Abstract*—The accuracy of three distinct experimental procedures for calibrating axial SQUID gradiometers have been compared, for the same gradiometer design and experimental setup. Each procedure employs a different field source, and a non-linear least squares algorithm is used to fit the measured data to the simulated field, thus determining Tesla/Volt calibration factors. We also studied the effect of gradiometer imbalance on the accuracy of each method.**

I. Introduction

SQUIDs (Superconducting Quantum Interference Devices) are the utmost magnetic flux sensing transducers, establishing a linear relation between an input magnetic flux detected inside a cryogenic Dewar, and an output voltage measured at room temperature. Such devices are usually coupled to sets of coils wound in differential configurations, known as gradiometers, in order to discriminate the field of interest against magnetic noise. Nevertheless, to use them as quantitative measurement instruments, it is extremely important to have them properly calibrated.

Along the last decade several methods for calibrating SQUID gradiometers have been proposed, with accuracy ranging from tenths of percent to a few percent [1]-[3]. However, each calibration method was performed under different experimental conditions and setups, and also with distinct SQUID systems, making it difficult to compare the accuracy of the various methods.

In the present work we use a calibration method previously developed [4] but with three different experimental procedures, all of them using the same gradiometer and setup. We used a LTS SQUID coupled to a second-order axial gradiometer with 1.5 cm diameter coils and 4 cm baseline, shown schematically in Fig.1.

II. Methods

The general procedure used to establish the flux/voltage calibration factor of SQUID gradiometers consists on measuring a known magnetic field and then comparing the simulated and experimental values [3]. However, the calibration factor is usually stated as *field*/voltage. This can be done by dividing the gradiometer net flux by the effective area of the pickup coil. Clearly, this is an approximation, since it is assumed a uniform magnetic field over the pick-up coil area, and also no magnetic field coupling to the other coils.

Manuscript received April 30, 1999.
This work was partially supported by CNPq, FAPERJ and FINEP.

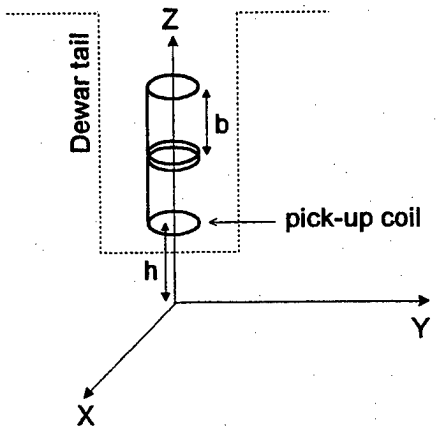

Fig. 1. Schematic drawing of second order gradiometer (baseline b, standoff distance h) inside the Dewar, and coordinate system used for the simulated calculations.

Even though the field/voltage calibration factor is an approximation, the importance of its accurate determination is more critical in the case of multichannel systems used to locate biomagnetic sources. For instance, an inaccuracy of a few percent can lead to errors of several millimeters in the source location [1].

A. First Source: Long Wire

The first procedure used consists of displacing a current-carrying wire, a few centimeters below the dewar tail, along the direction perpendicular to the wire. Using the Law of Biot-Savart, the vertical component of the magnetic field, B_z, generated by a wire with length l and current I, at a point (x, y, z) is given by

$$B_z(x,y,z) = \frac{\mu_0 I y}{4\pi}\left[\frac{\left(x+\frac{l}{2}\right)}{\left(y^2+z^2\right)\sqrt{\left(x+\frac{l}{2}\right)^2+y^2+z^2}} - \frac{\left(x-\frac{l}{2}\right)}{\left(y^2+z^2\right)\sqrt{\left(x-\frac{l}{2}\right)^2+y^2+z^2}}\right]. \quad (1)$$

Equation (1) combined with a numerical method to integrate the magnetic field over coils area [5] was used to compute the flux over each gradiometer coil. After summing each flux, regarding the winding directions, we obtain the simulated net flux due to a finite length wire.

The main drawback in this procedure is the need to accurately know the gradiometer vertical position inside the Dewar. To circumvent this problem we first normalize both the simulated flux and experimental voltage values. After that

a least-squares optimization algorithm is used to find the standoff distance that best matches the normalized curves.

Once the optimum standoff value is found, the signals are denormalized and the calibration factor, C, is calculated by means of another least-squares algorithm, aiming to minimize the error function given by

$$\mathcal{E} = B_{exp} \cdot C + K - B_{sim} \ , \qquad (2)$$

where K is a factor that accounts for differences between the dc values of both fields.

B. Second Source: Small Coil

In the second procedure used, we displace a small current carrying coil with radius R, a few centimeters under the SQUID system for several positions in a grid pattern. Using again the Law of Biot-Savart, the vertical component of the magnetic field, B_z, at a point (x, y, z) is given by

$$B_z(x,y,z) = \frac{\mu_0 I}{4\pi} \int_0^{2\pi} \frac{(R - x\cos\theta - y\sin\theta) R \, d\theta}{\left[(x - R\cos\theta)^2 + (y - R\sin\theta)^2 + z^2\right]^{\frac{3}{2}}} \ . \qquad (2)$$

In this case it is necessary to use a numerical integration algorithm to calculate the magnetic field, since (2) does not have a closed form. The gradiometer net flux is then calculated as in section A. This procedure has the same drawback as before, that is, the lack of precision of the relative positions between the small coil and the gradiometer coils inside the cryogenic Dewar. The same process described earlier is used to overcome this difficulty.

C. Third Source: Large Coil

In the last procedure we move a large current carrying coil, encircling the Dewar, along the gradiometer axis. We measure the SQUID output for several positions of the large coil. Again, using the Law of Biot-Savart we express the z component of the magnetic field as

$$B_z(x = 0, y = 0, z) = \frac{\mu_0 I r^2}{2\left(r^2 + z^2\right)^{3/2}} \ . \qquad (3)$$

Because such large coil has about 20 times the size of the gradiometer coils, we assume an uniform field over the gradiometer coil areas. It should be noticed that in this procedure there is no need to find the vertical position of the gradiometer inside the Dewar by optimization methods. The center of the gradiometer is located at the position where the experimental signal reaches its maximum value.

III. Experimental Results

Examples of fitting results for the three procedures are shown in the following figures. In Fig. 2 it can be seen the simulated (solid line) and experimental (crosses) signals for the first calibration procedure. After performing 7 sets of measurements, we found an average calibration factor of 1.95×10^{-8} T/V with a standard deviation of 0.02×10^{-8} T/V.

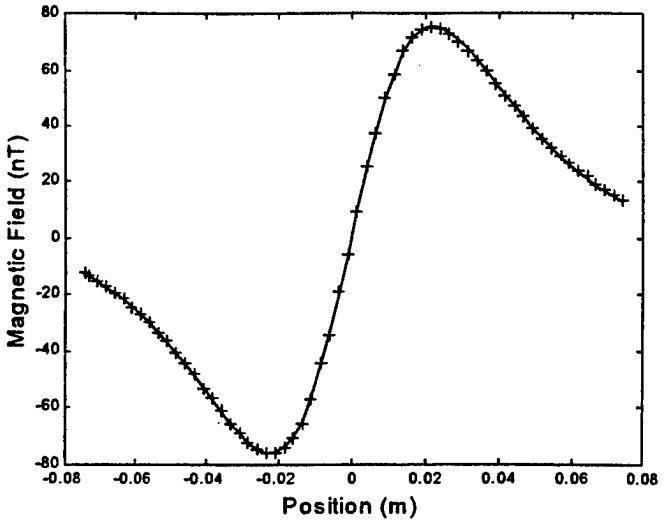

Fig. 2. Simulated (solid line) and experimental (crosses) field values due to a long (60 cm) calibration wire scanned under the gradiometer. We used a dc current of 50 mA at a standoff distance 3.14 cm.

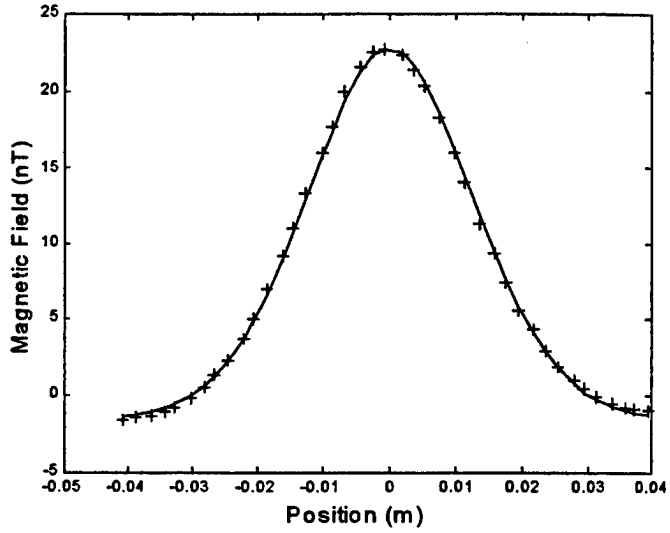

Fig. 3. Simulated (solid line) and experimental (crosses) field values due to a small coil (5 mm diameter) scanned under the gradiometer. We used a dc current of 100 mA at a standoff distance 3.91 cm.

The results for one set of measurements using the second procedure (small coil) can be seen in Fig. 3. The average calibration factor obtained was 1.92×10^{-8} T/V with a standard deviation of 0.13×10^{-8} T/V, using 10 sets of measurements.

In both cases we observed a variability on the optimized standoff distance, due to noise in the experimental signal. Such variability plays a considerable role in the variations of the calibration factor. To reduce this problem, we averaged the standoff distance over all sets of measurements, and used this average value on the second optimization. For the small coil this procedure decreased the standard deviation to 0.01×10^{-8} T/V and the average value is now 1.94×10^{-8} T/V.

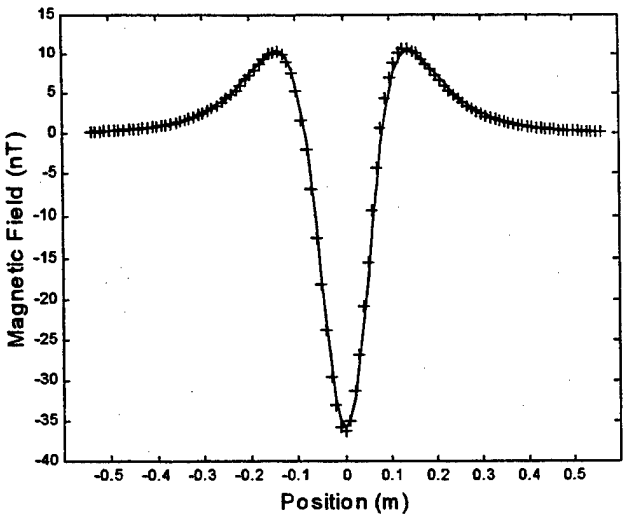

Fig. 4. Simulated (solid line) and experimental (crosses) field values due to a large coil (32 cm diameter) moved along the gradiometer axis. We used a dc current of 52 mA.

The result of the third method (large coil) is shown in Fig. 4. The solid line is the simulated field and the crosses are the experimental values. The calibration factor found with this procedure was 2.00×10^{-8} T/V.

IV. Imbalance Effect

In order to study the effect of gradiometer imbalance on the calibration procedure we fed the calibration algorithm with the simulated instead of the experimental data. Obviously, the calibration factor found in this case was 1.0. Then, we introduced an imbalance on the gradiometer area, ranging from 10^{-4} to 10^{-2}. Depending on the amount of imbalance, each method will be affected differently

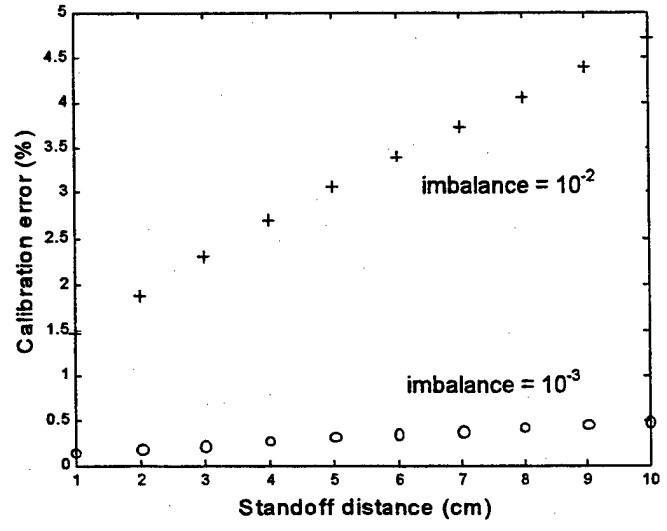

Fig. 5. Calibration error as a function of imbalance and standoff distance for the wire calibration method. An imbalance of 10^{-2} is shown by the crosses and an imbalance of 10^{-3} is shown by the circles.

For the third procedure (large coil), when the imbalance is severe (10^{-2}), the largest error is 13 %, and when it is low (10^{-4}) its gives about 0.1 % error. For the two first procedures, the effect depends on the standoff distance, as depicted in Fig. 5, for 10^{-2} and 10^{-3} imbalaces on the wire case. As it can be seen, the combination of imbalance and large standoff can lead to a 5 % error. If the gradiometer imbalance is 10^{-4} the error drops below 0.1 %. The small coil procedure leads to an error about two times smaller.

V. Conclusion

Three different procedures for calibrating a second order SQUID gradiometer were tested. The calibration found using the wire method was 1.95×10^{-8} T/V, using a small coil 1.94×10^{-8} T/V and a large coil 2.00×10^{-8} T/V. We simulated also the imbalance effect on the calibration result, we found out that for high imbalances, the procedure most affected is the one that uses the large calibration coil. Regarding the other two methods, it is better to place the calibrating source as close as possible to the Dewar tail, in order to avoid imbalance errors. To have a negligible effect on the calibration result the imbalance in the area must be as low as 10^{-4}. We believe that our second order gradiometer imbalance is between 10^{-2} and 10^{-3} and since, for experimental reasons, we could not place the calibration source closer than 3 cm, the differences on the calibration factors found using the three procedures could be explained by our gradiometer imbalance.

Acknowledgment

We would like to thank Eduardo Andrade Lima for valuable discussions.

References

[1] P. Costa Ribeiro, S. J. Williamson and L. Kaufman, "SQUID arrays for simultaneous magnetic measurements: calibration and source localization performance", IEEE Trans. on Biomed. Eng., vol. 35, pp. 551-560, July 1988

[2] D. S. Buchanan and D. N. Paulson, "Neuromagnetometer calibration using an array os small coils", in *Advances in Biomagnetism*, S. J. Williamson et al, Eds. New York: Plenum, 1989, pp. 705-708.

[3] A. C. Bruno and P. Costa Ribeiro, "Spatial Fourier calibration method for multichannel SQUID magnetometers", *Rev. Sci. Instrum.*, vol. 62, pp. 1005-1009, November 1991.

[4] C. Hall Barbosa, E. Andrade Lima and A. C. Bruno, "Fluxvoltage calibration of axial SQUID gradiometers using an optimization procedure", *IEEE Trans. Appl. Supercon.*, in press.

[5] B.J. Roth and S. Sato, "Accurate and efficient formulas for averaging the magnetic field over a circular coil", in *Biomagnetism: Clinical Aspects*. M.Hoke et al., Eds. Elsevier Publishers B.V., 1992, pp. 797-800.

PII2.11

Two-dimensional spatial frequency response of SQUID planar gradiometers

E. Andrade Lima, A. C. Bruno and J. Szczupak

Pontifícia Universidade Católica do Rio de Janeiro, Department of Physics and Department of Electrical Engineering
Rua Marquês de São Vicente 225, Rio de Janeiro, RJ 22453-900, Brazil

Abstract— Planar gradiometers can be modeled as two-dimensional spatial filters, taking into account area, baseline and shape of the coils. We associate a spatial frequency response to each configuration studied and show that planar gradiometers behave as band-pass spatial filters. Also, in order to determine a spatial frequency range for typical magnetic field sources, we calculate the two-dimensional Fourier transform of the field due to a current dipole for several liftoffs. Important issues such as gradiometer spatial cutoff frequencies, bandwidth and symmetry are discussed.

I. Introduction

A one-dimensional spatial frequency model has been previously developed to analyze SQUID (Superconducting Quantum Interference Device) gradiometers, where it was assumed that each gradiometer coil had a negligible area [1][2]. Later on, another model was developed in which magnetometer coils with non-negligible areas were modeled by two-dimensional spatial filters [3][4]. By combining both techniques it is possible to model realistic planar gradiometers as two-dimensional spatial filters.

In this context, signal processing methods provide a useful framework to characterize and compare the performance of such devices. Since the model is not dependent on any particular field source, it can be used as a powerful tool for designing planar gradiometers.

Next section describes how to obtain the spatial frequency response for two gradiometer configurations: planar and planar concentric. In the subsequent section the spatial frequency range of the magnetic field due to a current dipole is obtained for several liftoffs. Section IV presents the spatial frequency response for the two gradiometers configurations studied with typical dimensions. In the last section, the gradiometer spatial filtering characteristics are discussed.

II. Gradiometer Modeling

The magnetic flux through a single gradiometer coil, parallel to the x-y plane, can be expressed as the convolution of the magnetic field with a step function:

$$\Phi(x,y,z) = \iint_S \vec{B}\cdot\hat{n}\,da = \int_{-\infty}^{+\infty}\int_{-\infty}^{+\infty} B_z(x',y',z)F(x-x',y-y') \times dx'\,dy' = B_z(x,y,z) * F(x,y). \quad (1)$$

This step function accounts for geometrical characteristics of the coil such as size, shape and number of turns. Taking the two-dimensional (2-D) Fourier transform on (1) and using the convolution property, we get

$$\varphi(\kappa_x,\kappa_y,z) = b_z(\kappa_x,\kappa_y,z)\cdot f(\kappa_x,\kappa_y), \quad (2)$$

where $\varphi(\cdot)$, $b_z(\cdot)$ and $f(\cdot)$ stand for the Fourier transforms of $\Phi(x,y,z)$, $B_z(x,y,z)$ and $F(x,y)$, respectively.

Equation (2) shows that the Fourier transform of the flux is related to the magnetic field transform by means of a (complex-valued) scaling function. This function can then be interpreted as the frequency response of a spatial filter. The input of such filter is the magnetic field on the measuring plane and the output is the flux through the gradiometer coil. It should be noticed that the frequency response, which defines how the magnetic field is filtered, is related exclusively to geometrical characteristics of the coil.

A. Planar Gradiometer

Consider now two identical coils connected in series, constituting a first-order planar gradiometer (Fig. 1) with a baseline of length d in the x direction. The center of the gradiometer is defined as the midpoint between the two coils. Consequently, the net flux of the gradiometer can be expressed as

$$\Phi_G(x,y,z) = \Phi(x+d/2,y,z) - \Phi(x-d/2,y,z), \quad (3)$$

where $\Phi(\cdot)$ is the magnetic flux through one of the coils. In the spatial frequency domain this is equivalent to

$$\varphi_G(\kappa_x,\kappa_y,z) = \varphi(\kappa_x,\kappa_y,z)\cdot\left[e^{i\kappa_x d/2} - e^{-i\kappa_x d/2}\right]. \quad (4)$$

The combination of (4) and (2) leads to

$$\varphi_G(\kappa_x,\kappa_y,z) = b_z(\kappa_x,\kappa_y,z)\cdot f_G(\kappa_x,\kappa_y), \quad (5)$$

where the gradiometer frequency response, $f_G(\cdot)$, is given by

$$f_G(\kappa_x,\kappa_y) = 2i\sin(\kappa_x d/2)\cdot f(\kappa_x,\kappa_y). \quad (6)$$

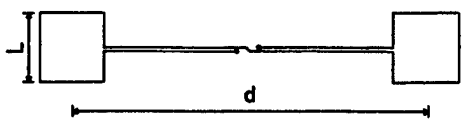

Fig. 1: Schematics of a first-order planar gradiometer.

Manuscript received April 30, 1999.
This work was supported in part by CNPq, FAPERJ, FINEP and PADCT.

For a square coil with sides of length L, made up of N turns and parallel to the x-y plane, we have

$$F(x,y)=\begin{cases} N, & |x|\le L/2 \text{ and } |y|\le L/2 \\ 0, & \text{otherwise} \end{cases}, \tag{7}$$

and so the 2-D Fourier transform is given by

$$f(\kappa_x,\kappa_y)=4N\left[\frac{\sin(\kappa_x L/2)}{\kappa_x}\cdot\frac{\sin(\kappa_y L/2)}{\kappa_y}\right]. \tag{8}$$

Consequently, for a planar gradiometer with square coils the frequency response becomes

$$f_G(\kappa_x,\kappa_y)=8i\,N\sin(\kappa_x d/2)\left[\frac{\sin(\kappa_x L/2)}{\kappa_x}\cdot\frac{\sin(\kappa_y L/2)}{\kappa_y}\right]. \tag{9}$$

It is worthwhile noting such response is separable, which means that (9) can be decomposed into the product of two functions of a single frequency variable (i.e. the cascading of two 1-D filters) [5]:

$$f_G(\kappa_x,\kappa_y)=f_1(\kappa_x)\cdot f_2(\kappa_y). \tag{10}$$

Hence, we can analyze the gradiometer response by investigating the behavior of these two functions separately.

B. Planar Concentric Gradiometer

A planar concentric gradiometer comprised of two coils with different sizes but coincident centers (Fig. 2) has a net flux as follows:

$$\Phi_G(x,y,z)=\Phi_i(x,y,z)-\Phi_o(x,y,z), \tag{11}$$

where $\Phi_i(\cdot)$ and $\Phi_o(\cdot)$ stand for the flux in the inner and outer coils, respectively. Then, combining (11) and (2) yields

$$\varphi_G(\kappa_x,\kappa_y,z)=b_z(\kappa_x,\kappa_y,z)\cdot f_G(\kappa_x,\kappa_y). \tag{12}$$

In this case, the gradiometer frequency response, $f_G(\cdot)$, is given by

$$f_G(\kappa_x,\kappa_y)=f_i(\kappa_x,\kappa_y)-f_o(\kappa_x,\kappa_y). \tag{13}$$

The step function for a circular coil of radius a, parallel to the x-y plane and made up of N turns, is given by

$$F(x,y)=F(r)=\begin{cases} N, & r\le a \\ 0, & \text{otherwise} \end{cases}, \tag{14}$$

where $r=\sqrt{x^2+y^2}$.

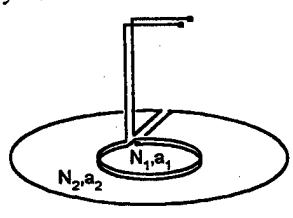

Fig. 2 Schematics of first-order planar concentric gradiometer.

Because $F(x,y)$ has circular symmetry, we can use the zero-order Hankel transform [6] to calculate the frequency response (also circularly symmetrical). That is,

$$f(\kappa_x,\kappa_y)=f(\kappa)=\int_{-\infty}^{+\infty}\int_{-\infty}^{+\infty}F(x,y)\,e^{-i(\kappa_x x+\kappa_y y)}dxdy= \\ =2\pi\int_{-\infty}^{+\infty}rF(r)J_0(r\kappa)dr, \tag{15}$$

where $\kappa=\sqrt{\kappa_x^2+\kappa_y^2}$ and $J_0(\cdot)$ is the Bessel function of the first kind and zero order. Then we have

$$f(\kappa_x,\kappa_y)=2\pi N a\frac{J_1\left(a\sqrt{\kappa_x^2+\kappa_y^2}\right)}{\sqrt{\kappa_x^2+\kappa_y^2}}. \tag{16}$$

Thus, for a concentric gradiometer consisting of two circular coils with radius a_1 (inner coil) and a_2 (outer coil), made up of N_1 and N_2 turns, respectively, we have

$$f_G(\kappa_x,\kappa_y)=\frac{2\pi N_1 a_1}{\sqrt{\kappa_x^2+\kappa_y^2}}\left[J_1\left(a_1\sqrt{\kappa_x^2+\kappa_y^2}\right)- \right. \\ \left. -J_1\left(\alpha\cdot a_1\sqrt{\kappa_x^2+\kappa_y^2}\right)\Big/\alpha\right], \tag{17}$$

where the condition $N_1/N_2=(a_2/a_1)^2$ must be satisfied in order to make null the flux for spatially constant fields, and $\alpha=a_2/a_1$.

III. Spatial Frequency Range of Magnetic Fields

To compare the performance and characteristics of the gradiometers we have used as typical magnetic fields the ones generated by current dipoles. In particular, we are interested in determining the spatial frequency range of these fields. Since their spectrum in fact extends towards infinity, we consider that the maximum spatial frequencies are the ones associated to 95% of the total field energy, being the same in both directions.

For a current dipole in the x direction placed at the origin, the z component of the magnetic field is given by

$$B_z(x,y,z)=\frac{\mu_0 I}{4\pi}\cdot\frac{y}{\left(x^2+y^2+z^2\right)^{3/2}}, \tag{18}$$

and its 2-D Fourier transform is

$$b_z(\kappa_x,\kappa_y,z)=\begin{cases} -i\mu_0 I\dfrac{\kappa_y\,e^{-z\sqrt{\kappa_x^2+\kappa_y^2}}}{2\sqrt{\kappa_x^2+\kappa_y^2}}, & \text{for } \kappa_x\neq 0,\ \kappa_y\neq 0. \\ 0, & \text{otherwise.} \end{cases} \tag{19}$$

The calculation of the maximum spatial frequencies can be done by first computing the total field energy, by means of the Parseval's theorem [5],

$$\mathcal{E} = \frac{\mu_0 I}{64\pi z^2}, \tag{20}$$

and then by solving (21) below numerically, obtaining the maximum spatial frequencies κ_{max}:

$$\int_0^{\kappa_{max}} \int_0^{\kappa_{max}} \left| b_z(\kappa_x, \kappa_y, z) \right|^2 d\kappa_x d\kappa_y = \frac{1}{4} \cdot 4\pi^2 \cdot 95\% \cdot \mathcal{E} \ . \tag{21}$$

By the repetition of this procedure for several standoff distances a least-squares fitting was done, resulting in the following relationship

$$\kappa_{max} = 0.3487 \cdot h^{-1}, \tag{22}$$

where h is the standoff distance in meters and κ_{max} is expressed in m^{-1}. Table I shows the maximum spatial frequencies for several standoff distances.

IV. Results

In this section we analyze two typical first-order planar gradiometer designs. The first one is a planar gradiometer with 5 mm single turn square coils and 5 mm baseline. The other one is a planar concentric gradiometer with circular coils. The inner coil has 4 turns and 5 mm diameter while the outer coil has a single turn and 10 mm diameter.

Fig. 3a shows the magnitude of the spatial frequency response for the first design. It should be noticed the lack of symmetry in the frequency response, resulting in different filtering along distinct directions. In Figs. 3b and 3c it is shown the normalized spatial frequency responses, expressed in decibels, for the one-dimensional filters $f_1(\kappa_x)$ and $f_2(\kappa_y)$.

For practical purposes, a typical field spectrum ranges from dc up to a few hundred m^{-1} for very near sources (Table I). Therefore, because only the main lobes of the frequency response need to be considered, the gradiometer can be interpreted as a band-pass (BP) filter in the baseline direction (Fig. 3b) and as a low-pass (LP) filter in the other direction (Fig. 3c). It can be observed that for frequencies below the lower 3 dB cutoff frequency, the band-pass filter response has a slope of –20 dB/decade.

TABLE I

MAXIMUM SPATIAL FREQUENCIES FOR SEVERAL STANDOFFS

Standoff distance	Maximum spatial frequencies
1 mm	348.7 m^{-1}
2 mm	232.5 m^{-1}
5 mm	69.7 m^{-1}
10 mm	34.9 m^{-1}
50 mm	7.0 m^{-1}
100 mm	3.5 m^{-1}

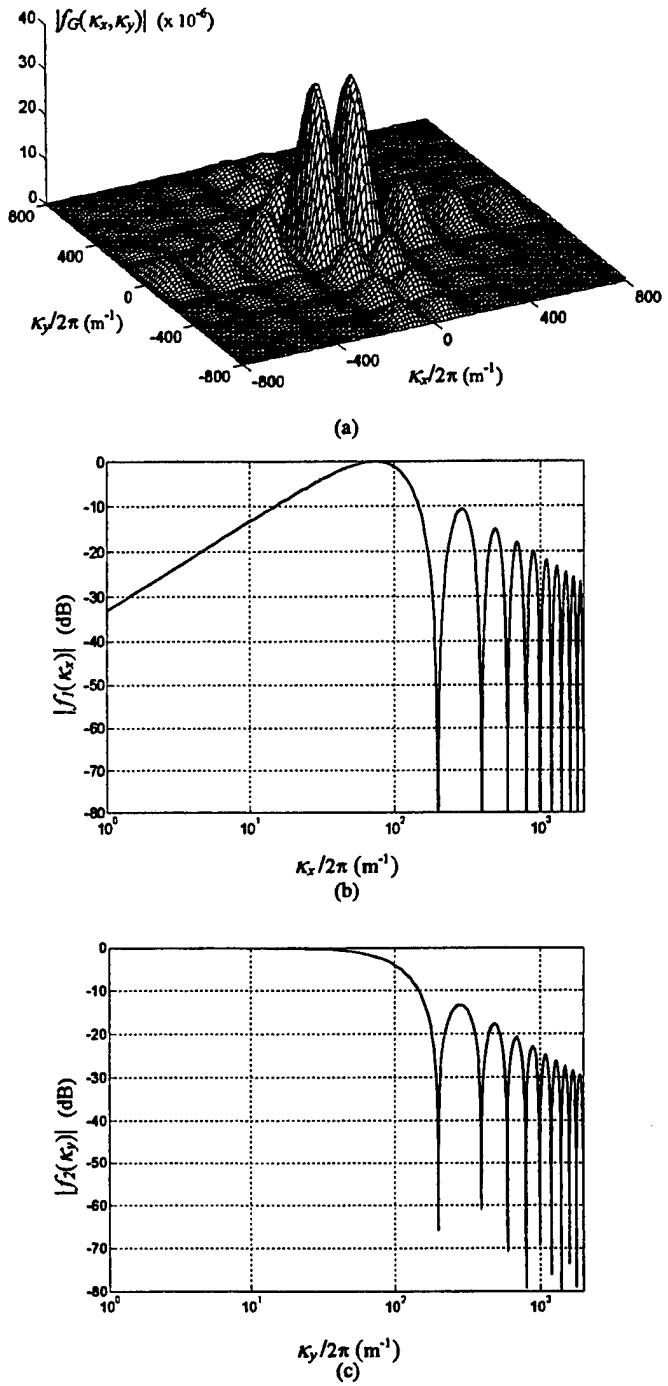

Fig. 3 (a) Magnitude of the 2-D spatial frequency response. (b) and (c) Normalized magnitude of the 1-D spatial frequency responses in the x and y directions.

The magnitude of the frequency response for the second design is presented in Fig. 4a. Due to the circular symmetry the filtering is the same in all directions. Again, only the main lobe needs to be considered and in this case the gradiometer behaves also as a band-pass filter. For frequencies below the lower 3 dB cutoff frequency, the filter response has a slope of –40 dB/decade (Fig. 4b). Table II summarizes the relevant filter parameters for both gradiometer designs.

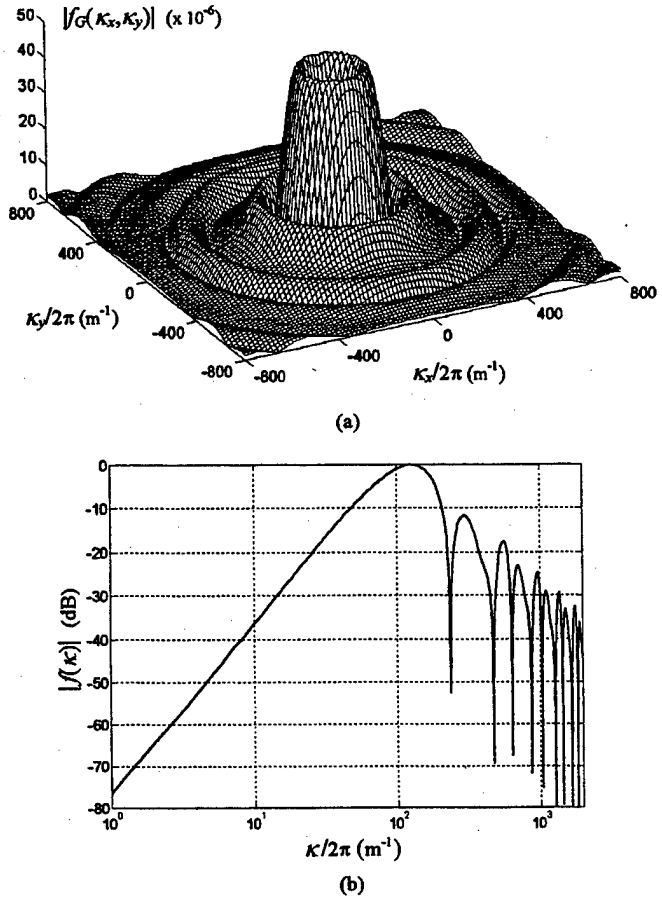

Fig. 4 (a) Magnitude of the 2-D spatial frequency response. (b) Normalized magnitude of the 1-D spatial frequency response in an arbitrary direction.

V. Discussion

We will focus our discussion only on the subjects related to the spatial filtering properties of the gradiometers. Ideally, a first-order planar gradiometer should behave as a perfect high-pass filter with lower cutoff frequency at 0 m^{-1}, nulling exclusively the spatial constant (dc) component of the magnetic field while preserving the rest of the spatial frequency spectrum. In practice, however, typical gradiometer configurations deviate hugely from such ideal filter, as it can be seen in Figs. 3a and 4a. Furthermore, non-concentric planar gradiometers do not remove the spatial dc component in the y (orthogonal) direction, as can be noticed from Fig. 3c.

Hence, to minimize distortion and loss of information we must assure that the field spectrum of interest lies as much as possible within the filter passband. Specifically, we should never allow the spectrum to reach the first non-dc zero, imposing an upper limit to the gradiometer coil size. On the other hand, decreasing coil size also lowers the gain, thereby reducing sensitivity. Thus, we should design gradiometer coils as large as possible while keeping the location of the first non-dc zero beyond the maximum frequency of the field.

TABLE II

FILTER PARAMETERS FOR THE TWO GRADIOMETER DESIGNS

Design	Filter	1st zero	2nd zero	Lower 3dB cutoff	Upper 3dB cutoff
Planar	BP	0 m^{-1}	200 m^{-1}	36 m^{-1}	116 m^{-1}
	LP	200 m^{-1}	400 m^{-1}	—	88 m^{-1}
Pl.Conc.	BP	0 m^{-1}	235.5 m^{-1}	81.5 m^{-1}	175 m^{-1}

The influence of the baseline on the frequency response is also of great importance. By increasing the distance between the two coils, we make the first sinusoidal term in (9) oscillate more rapidly. Consequently, the zeroes due to this term are shifted to lower frequencies, decreasing the upper and lower 3dB cutoff frequencies of the 1-D band-bass filter. The low-pass filter remains unaltered in this case, leading to an increased asymmetry in the 2-D spatial frequency response. Alternatively, if we enlarge the coils the effect on the band-pass filter is similar, except that the upper 3dB cutoff frequency of the low-pass filter is also reduced.

In the case of planar concentric gradiometers, the baseline (in the conventional sense) is not defined, because there is no separation between coils. However, by changing the ratio $\alpha = a_2 / a_1$ we can modify the 2-D spatial frequency response. If we keep the inner coil size fixed and increase α then we enlarge the filter passband as well as the overall gain, and also slightly shift the first non-dc zero.

The material presented in this paper provides a framework both for design of planar gradiometers (aiming to minimize distortion), and for realistic modeling of such devices, a vital issue in the development of deconvolution algorithms.

Acknowledgment

We would like to thank Carlos Hall for valuable discussions.

References

[1] A. C. Bruno, P. Costa Ribeiro, J. P. von der Weid and O. G. Symko, "Discrete spatial filtering with SQUID gradiometers in Biomagnetism," *J. Appl. Phys.*, vol. 59, pp. 2584-2589, 1986.

[2] A. C. Bruno and P. Costa Ribeiro, "Digital filter design approach for SQUID gradiometers," *J. Appl. Phys.*, vol. 63, pp. 2820-2823, 1988.

[3] B. J. Roth, N. G. Sepulveda and J. P. Wikswo Jr, "Using a magnetometer to image a two-dimensional current distribution," *J. Appl. Phys.*, vol. 65, pp. 361-372, 1989.

[4] B. J. Roth and J. P. Wikswo Jr, "Apodized pickup coils for improved spatial resolution of SQUID magnetometers," *Rev. Sci. Instrum.*, vol. 61, pp. 2439-2448, 1990.

[5] J. S. Lim, *Two - dimensional Signal and Image Processing*, Englewood Cliffs, NJ: Prentice-Hall, 1990.

[6] R. N. Bracewell, *The Fourier Transform and its Applications*, 2nd ed., New York: McGraw-Hill, 1986.

LTS SQUID Gradiometer System for *in vivo* Magnetorelaxometry

L. Warzemann, J. Schambach and P. Weber
Friedrich-Schiller-Universität Jena, Max-Wien-Platz 1, D-07743 Jena, Germany

W. Weitschies and R. Kötitz
Institut für Dignostikforschung GmbH Berlin, Spandauer Damm 130, D-14050 Berlin, Germany

Abstract—A system for the spatially resolved magnetorelaxometry (MRX) in spatially expanded objects (e.g. for *in vivo* investigations) in a disturbed environment is presented. The system is based on a LTS SQUID gradiometer with a field gradient sensitivity of 30 fT/cmHz$^{1/2}$ and an intrinsic balance of some 10^{-5}. A Helmholtz coil of 80 cm diameter allows the magnetization of the samples with fields up to 7 mT. A nonmagnetic x-y stage (driven by step motors) covers a scanning area of 40 cm × 25 cm. We present spatially resolved measurements of the Néel relaxation of samples (dried ferrofluid) and compare them with model calculations. The data acquisition and monitoring as well as the filtering and fit procedure are discussed.

I. Introduction

Magnetorelaxometry (MRX) is the measurement of the relaxation of the magnetization of magnetic nanoparticles after switching off a magnetizing field H_{mag}. The relaxation of such single domain ferro- or ferrimagnetic particles is either due to the movement of whole particles (Brownian relaxation) or due to the rotation of the magnetization vector inside the particle (Néel relaxation) [1]. Due to the different relaxation times (Brownian relaxation about 10^{-5} s and Néel relaxation in the order of 10^{-2} ... 10 s for particles with about 20 nm diameter) it is possible to distinguish between the signals of moveable and immoveable (only Néel relaxing) particles.

Many medical and biological investigations are based on the detection of labeled substances with different techniques (e.g. fluorescence or enzymatic reactions). Such methods usually require additional separation and cleaning steps in order to eliminate unbound labels. The detection of magnetic nanoparticles (used to label substances) with MRX allows the discrimination of the signals of bound and unbound particles without further separation steps only due to the different relaxation times, which simplifies the procedure considerably [2],[3].

For medical and biological investigations it is interesting to obtain information about the spatial distribution of labeled substances in organisms. A MRX system for such investigations requires the magnetization of large volumes with magnetic fields up to some mT. Therefore it can not be operated inside a magnetically shielded room.

Manuscript received April 27, 1999.
This work was supported by the German BMBF under Grant No. 13N7005/1.

Due to their stable operation in disturbed environment and their high sensitivity to magnetic fields LTS SQUID gradiometers are suitable to measure the time-dependent magnetization of a sample. Such a system for MRX has recently been introduced [4]. Here we present experiments with samples of dried ferrofluid and discuss the filtering and fit procedure.

II. Measurement System

In the following the measurement principle and the components of the realized system are described.

A. Measurement Principle

A relaxation measurement consists of the following steps:

1. x-y positioning of the sample,
2. magnetization of the sample for a time t_{mag} with H_{mag},
3. data acquisition (measuring of the time dependent gradient $\partial B_z/\partial x$ caused by the sample magnetization),
4. data filtering and fitting.

Therefore a system for *in vivo* magnetorelaxometry requires the following main components:

- a nonmagnetic positioning system for the sample,
- coils to generate a homogeneous field up to some mT and an electronic unit to switch off that field very fast,
- a detector to measure the time-dependent magnetization,
- a data acquisition and system control unit.

For unshielded magnetorelaxometry measurements in a disturbed environment SQUID gradiometers as detectors are preferable because of their high sensitivity to magnetic fields and their ability to suppress disturbances from remote sources. We have arranged a SQUID gradiometer, the sample and the magnetizing coils in a configuration shown in Fig. 1. The sample is magnetized in the x-direction, whereas the planar SQUID gradiometer measures the $\partial B_z/\partial x$ component. So the magnetizing field doesn't couple flux into the gradiometer antenna (neglecting contributions by parasitic areas).

B. Realized System

According to the measurement principle and the requirements described above we realized a complete measurement system [4]. It is based on integrated planar LTS SQUID gradiometers of the transformer and multiloop type, which were designed, fabricated (in Nb-NbO_x-Pb/In/Au-technology)

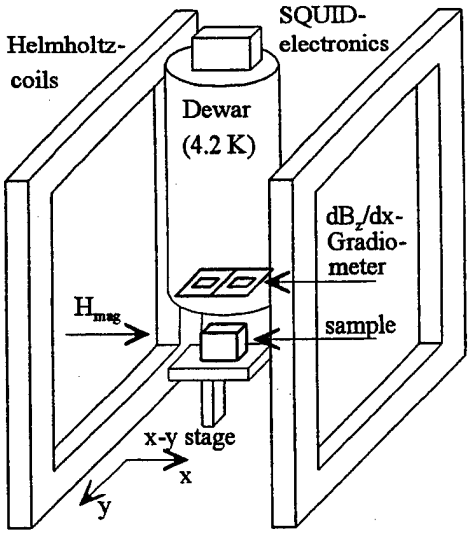

Fig. 1. Principle sketch of the measurement system.

and characterized at the Friedrich-Schiller-University Jena [5],[6]. With a field gradient sensitivity of 30 fT/cmHz$^{1/2}$ and an intrinsic balance of some 10^{-5} these sensors are suitable for measurements in disturbed environment.

The homogeneous magnetizing field is generated by Helmholtz coils (80 cm × 80 cm). A 1.3 kW power supply unit provides the current for magnetizing fields up to 7 mT. To switch off the magnetizing current a power electronics is used, which allows a fast decrease of the field (a magnetizing field of 1 mT decreases to 10 nT in less than 5 ms).

For sample positioning and scanning a nonmagnetic x-y stage was implemented. The stage is driven by stepper motors and the positioning is controlled by the host computer. The stage covers an area of 40 cm × 25 cm with a resolution better than 0.5 mm. Additionally a manual vertical adjustment up to 10 cm is possible.

The whole measurement system is controlled by a host computer (200 MHz Pentium) by means of a LabView program. For data acquisition the PC was equipped with a multifunction PC card (16 bit, 20 kHz). The LabView program supports either full automatic x-y scan measurements or manually controlled measurements.

III. Measurements

In this chapter we describe at first the data acquisition, filtering and fitting for a solitary MRX measurement. Subsequently spatially resolved measurements are discussed.

A. Data Aquisition, Filtering and Fitting

After switching off the magnetizing field H_{mag} and a delay time of 10 ms the SQUID gradiometer measures a time-dependent gradient signal $(\partial B_z/\partial x)(t)$, which is caused by the sample magnetization. For our MRX measurements we use a 1 kHz antialiasing filter and a sampling rate of 2000 Hz.

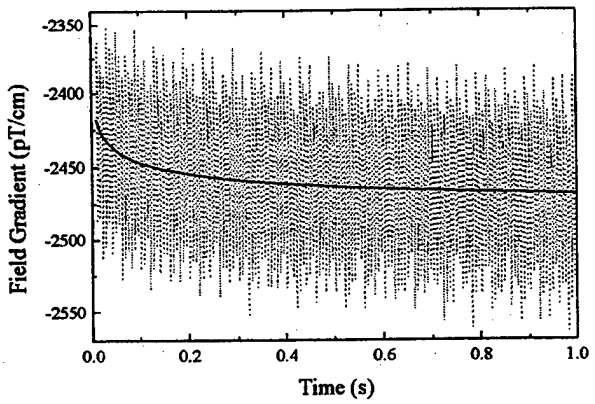

Fig. 2. Measured (dotted line) and fitted (solid line) MRX signal $(\partial B_z/\partial x)(t)$ of a sample with dried ferrofluid containing 3×10^{-8} mol (1.7 µg) iron.

A typical relaxation signal $(\partial B_z/\partial x)(t)$ is shown in Fig. 2. It was performed with a sample of dried ferrofluid (so only pure Néel relaxation can be observed). The sample with 1.7 µg iron is located 16 mm beneath the SQUID and was magnetized with a field of 1 mT for 1 s. To suppress the influence of power line frequencies 50 Hz and 100 Hz filters were used.

Because of the unshielded operation in disturbed environment the MRX signal is strongly superposed by interference sources such as power lines (50 Hz and its harmonics) and computer monitors (75 Hz) as well as random events like switching effects, driving cars near the building and the equipment in other laboratories in the same building (e.g. laser systems). These disturbances cause different effects on the measured signal $(\partial B_z/\partial x)(t)$ like steps, peaks or a shift.

The decay of the sample magnetization with time M(t) due to the Néel relaxation can be described by [7]

$$M(t) = M_0 \ln(1 + t_c/t) , \qquad (1)$$

where t_c is a characteristic time proportional to the magnetization time t_{mag}. M_0 is the sample magnetization at $t = t_c/(e-1)$. Accordingly the measured field gradient can be fitted by

$$\frac{\partial B_z}{\partial x}(t) = \left(\frac{\partial B_z}{\partial x}\right)_{offset} + \left(\frac{\partial B_z}{\partial x}\right)_0 \ln\left(1 + \frac{t_c}{t}\right) , \qquad (2)$$

where the offset term is arbitrary, since SQUID systems do not supply absolute values. In the fit procedure we set $t_c = t_{mag}$.

Furthermore we implemented a diagnostic program to detect signal steps and a signal drift. It compares the low pass filtered (40 Hz) MRX signal and the MRX fit of this filtered signal. The standard deviation of the difference between these two signals must not exceed a defined value. Another diagnostic programm detects particular peaks in the signal curves. Only relaxation signals, which fulfil all the defined conditions were used for the further analysis. Every relaxation measurement was repeated until seven usable MRX signals were collected. Subsequently the mean value of the corresponding fit parameters $(\partial B_z/\partial x)_0$ were determined.

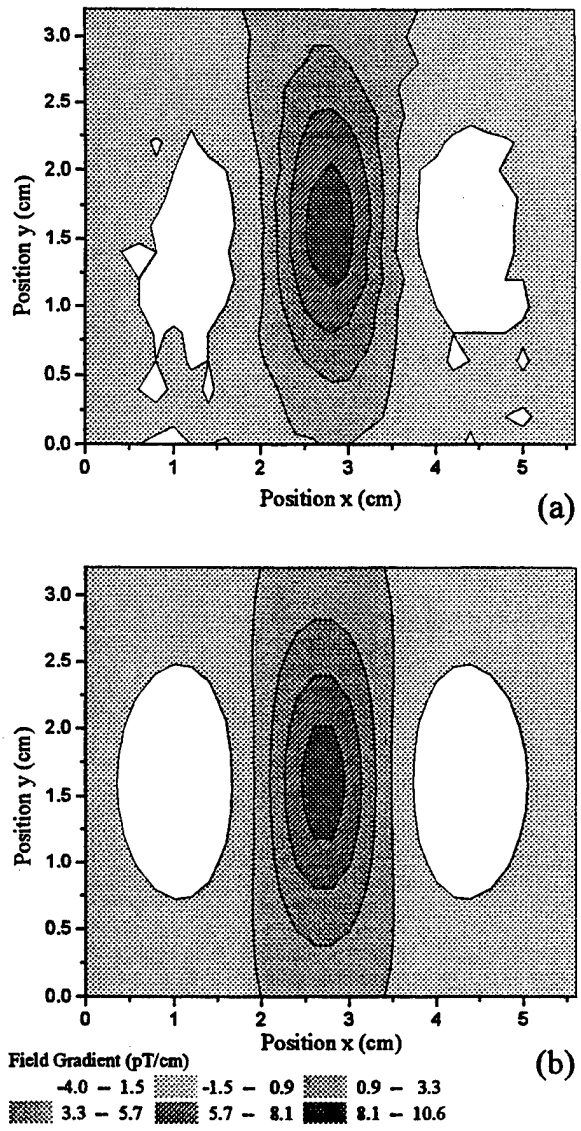

Fig. 3. Measured (a) and calculated (b) results of x-y scanning of a sample with dried ferrofluid containing 1.7 µg iron.

B. Spatially Resolved Relaxation Measurements

For spatially resolved MRX measurements the complete measuring procedure described above (data acquisation, filtering, fitting, signal test on disturbances and averaging) was repeated for each grid point of a x-y scan to obtain the value of $(\partial B_z/\partial x)_0$ as a function of the sample position. In Fig. 3(a) such a x-y scan of a sample (7 mm × 7 mm × 7 mm) of dried ferrofluid containing 3×10^{-8} mol (1.7 µg) iron 16 mm beneath the SQUID is shown. The whole x-y scan is based on 3451 particular relaxation measurements as shown in Fig. 2 (29 steps in x- and 17 steps in y-direction, 7 measurements per position).

For comparison in Fig. 3(b) the corresponding calculated data are plotted. The calculation is based on the model of a point dipol, whereas the sample is divided into 125 (5×5×5) seperate dipol elements. The integral magnetic field gradient $\partial B_z/\partial x$ is caused by the sum of the signals of all point dipoles (aligned in x-direction). Measurement and calculation are in good agreement.

IV. Conclusion

We have presented a SQUID gradiometer based measurement system which is suitable for the spatially resolved determination of magnetic nanoparticles due to the detection of their Néel relaxation. The system is able to detect relaxation signals automatically in a x-y scan in disturbed environment. Features to improve the sensitivity of the system and a signal diagnostic program were implemented. The spatially resolved detection of a sample with dried ferrofluid is in good agreement with calculations.

Acknowledgment

We thank St. Prass for the assistance on the realization of the system and the measurements and Th. Rheinländer for the sample preparation.

References

[1] R. Kötitz, P.C. Fanning, L. Trahms, "Time domain study of Brownian and Néel relaxation in ferrofluids," *J. Mag. Magn. Mat.* 149: 42 1995.

[2] W. Weitschies, R. Kötitz, T. Bunte and L. Trahms, "Determination of relaxing or remanent nanoparticle magnetization provides a novel binding-specific technique for the evaluation of immunoassays," *Pharm. Pharmacol. Lett.* 7 pp. 1-7, 1997.

[3] R. Kötitz, H. Matz, L. Trahms, H. Koch, W. Weitschies, T. Reinländer, W. Semmler and T. Bunte, "SQUID based remanence measurements for immunoassays," *IEEE Trans. Appl. Supercond.*, vol. AS-7, 1997.

[4] J. Schambach, L. Warzemann, P. Weber, "SQUID gradiometer measurement System for Magnetorelaxometry in a disturbed emvironment", *IEEE Trans. Appl. Supercond.*, in press.

[5] P. Weber, V.M. Zakosarenko, K.-H. Berthel, K. Blüthner, J. Schambach, L. Warzemann, G. Kirsch., T. Döhler and R. Stolz, "Integrated LTS gradiometer SQUID system for measuring the magnetic field distributions in an unshielded emvironments," *IEEE Trans. Appl. Supercond.* S-5, pp. 2493-2496, 1995.

[6] V.M. Zakosarenko, L. Warzemann, J. Schambach, K. Blüthner, K.-H. Berthel, G. Kirsch., P. Weber and R. Stolz, "Integrated LTS gradiometer SQUID system for unshielded measurements in a disturbed emvironment," *Supercond. Sci. Technol.* 9, A112-A115, 1996.

[7] R. W. Chantrell, S.R. Hoon, B.K. Tanner, "Time dependent magnetization in fine particle ferromagnetic systems," *J. Mag. Magn. Mater.* 38, pp. 133, 1983.

Magnetic Nanoparticle Relaxation Measured by a Low Tc SQUID System

A. Haller, S. Hartwig, H. Matz, Th. Rheinländer, R. Kötitz, W. Weitschies and L. Trahms
Physikalisch-Technische Bundesanstalt , Berlin, Germany,
Institut für Diagnostikforschung, Berlin, Germany

Abstract— A low-Tc SQUID system was developed for measuring magnetic relaxation of polymer-coated magnetic nanoparticles (MNP) in a liquid carrier (e.g. water). The system consists of two low-Tc SQUIDs which are electronically combined to form an axial gradiometer using high-bandwidth directly-coupled FLL electronics. The system is operated in a magnetically shielded room.The magnetic relaxation of the investigated MNPs in a liquid carrier is dominated by Brownian motion. In a solid phase, when the MNPs are immobilized, the magnetization of the sample decays via the Néel mechanism. A similar situation occurs when the mobility of the MNPs is reduced by a biochemical binding reaction. This effect is used for identifying biological reactions for purposes of medical diagnostics, e.g. immunoassays. By investigating the magnetic relaxation of dried samples, quantities as small as 1 nmol Fe of γ-Fe_2O_3 were detected. In first agglomeration assay the binding reaction of the biochemical model complexes biotin avidin can be clearly identified down to concentrations of < 1µg avidin in a volume of 150 µl of human blood.

I. Introduction

Magnetic nanoparticles (MNPs) in colloidal suspension – called ferrofluids – are well established tools in medical diagnostics, e.g. in MRI as contrast agent [1,2]. A new application in medical laboratory diagnostics has been proposed and demonstrated: a magnetically labeled immunoassay ("MARIA") [3,4]. In this application, MNPs are coupled to antibodies, which serve as magnetic tracers in highly specific biochemical reactions to antigens. Reaction products are quantified by the magnetic moment originating from the bound MNPs. Particularly the magnetic relaxation signal, i.e. the decay of the net magnetic moment of samples after magnetization, can be used to differentiate between bound magnetic tracers and surplus labels. The temporal dependence of the magnetic relaxation signal of MNPs in a liquid carrier is significantly changed, when the rotational diffusion of particles is impeded by binding to antigens. MNPs of magnetic anisotropic material of sufficient core size have a remnant moment, whose magnetization vector is oriented at some angle to the easy axis.

After removing external magnetizing fields, Brownian motion causes the aligned particles to reorientate in a random manner with exponential time dependence. The time constant τ is described by [5]

$$\tau = 3\eta V / kT \qquad (1),$$

where η is the viscosity of the liquid, V the hydrodynamic volume of a spherical particle and kT the thermal energy.

If the rotation of particles is hindered by increased hydrodynamic volume due to the bound antigens the relaxation process is slowed down. When MNPs are bound to solid phase the magnetization takes place by changing the internal magnetization vectors of the MNP relatively to their easy axis. The relaxation process is then described by the Néel mechanism, resulting in an approximate logarithmic time dependence [6].

Using SQUIDs as sensors to record the relaxation of magnetic nanoparticles, low concentrations of labeled antigens in common sample volumes of 100 – 150 µl are detectable. In order to resolve the relaxation process, the flux locked loop has to provide high bandwidth, since typical time constants involved range from 20 µs to 1s.

II. Experimental Setup

The measurement system consists of an electronic gradiometer, which is formed by two magnetometers using low temperature DC-SQUIDs (PTB-type W7A) [7]. The axial gradiometer has a baseline of 160 mm and is operated inside a magnetically shielded room (BMSR). The electronics was designed to have high bandwidth of 3.5 MHz. The two magnetometers are mounted inside a low-noise fibre glass dewar . The total system noise in white noise region (> 7 Hz) is 4.5 fT/ $Hz^{1/2}$, dominated by dewar noise (see [8] for details). Samples are placed at a distance of approximately 8 mm from the lower magnetometer SQUID and are magnetized inside a twin coil. In a typical experiment samples of ferrofluids are exposed to magnetization fields from 0.1 to 1.2 kA/m for 1s. After switching off the magnetizing field the flux locked loop is put into operation with a defined time delay to reduce the signal slew rate and to allow fast transients to die out. A delay time of 250 µs was chosen, compromising for maximum stability of the FLL to lock within < 10 µs and minimum residual signal from the magnetizing coils.

Manuscript received April 30, 1999.
This work was supported by the German Ministry of Education and Research under Grant No. 13N7005/1.

III. Results & Discussion

Using this setup, it is possible to observe Brownian relaxation of MNPs in the time domain. In fig. 1 the relaxation signal of a water-based ferrofluid is shown after switching off a magnetizing field of 1.2 kA/m. The deviation of the measured signal from an exponential decay, shown in fig. 1, clearly indicates that the particles exhibit a broad size distribution resulting in a superposition of different relaxation time constants. As a rough estimate of the mean size, the average time constant of the fit (607 µs) yields a hydrodynamic diameter of 60 nm using (1) with $\eta = 10^{-3}$ Pas for water at a temperature T= 293 K.

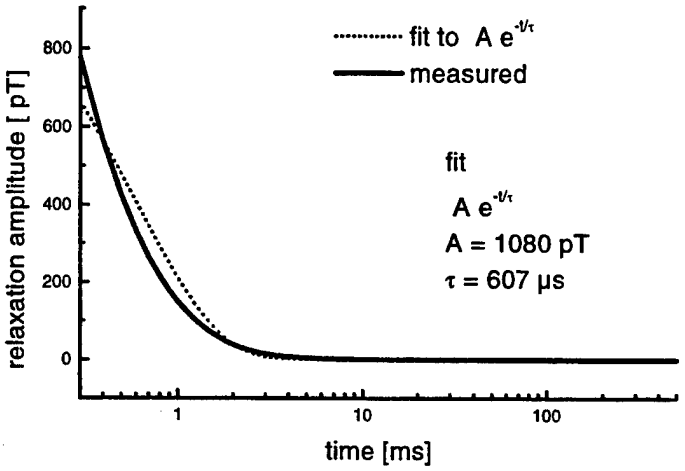

Fig.1 Brownian relaxation signal of a water-based ferrofluid of γ-Fe_2O_3, corresponding to 1.5 µmol Fe. The best fit to a single exponential decay is indicated for comparison.

A dilution series of water-based ferrofluids was investigated to verify that the magnetic relaxation amplitude is proportional to the amount of magnetic material within the sample.
The relaxation amplitude was defined as the total measured change in magnetic field from 400 µs to 500 ms after switching off magnetizing field and measured for samples of decreasing concentrations. This quantity provides a simple measure to account for all relaxation processes within the measurement time window. As illustrated in fig. 2 the relaxation amplitude was found to be proportional to the amount of Fe, determined by optical emission spectroscopy, within the measurement error of the determination of the concentration and the relaxation measurement. The minimum detectable amount of Fe was approximately 4.5 nmol. Assuming a size of the magnetic core of the MNP from 15 to 20 nm this corresponds to approximately 10^8 to 10^{10} MNPs.
When samples were dried, the MNPs showed relaxation signals with approximate logarithmic time dependence corresponding to the Néel relaxation, as has been reported previously [9]. Evaluating again the relaxation amplitude from 400 µs to 500 ms, the detection limit was estimated to be 1 nmol, which differs only slightly from the liquid samples.

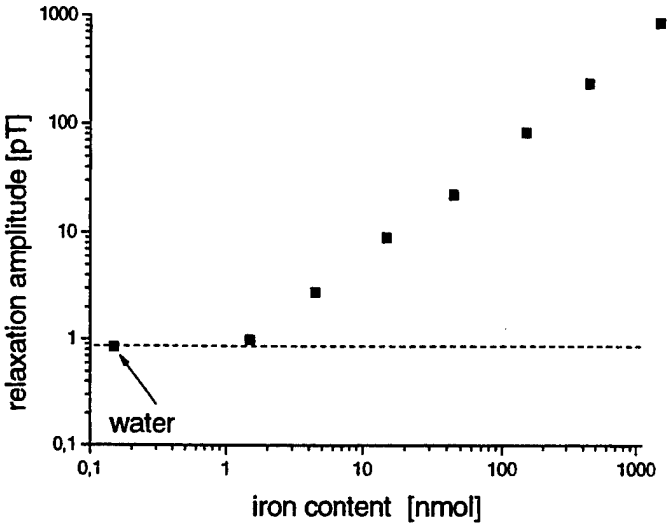

Fig 2. Relaxation amplitudes of a dilution series of ferrofluid samples , relaxation amplitude for a water sample is shown for comparison

Yet a more application-oriented magneto-relaxometric experiment was performed to demonstrate the sensitivity of our experimental setup. Compared to a similar investigation [9], agglomeration was detected in the presence of human blood. Concentrations < 1 µg avidin in a volume of 150 µl human blood could be detected.

Conclusion

Using a dedicated low Tc SQUID system, magnetic relaxation measurements of ferrofluids have been performed to estimate its detection sensitivity for magnetic nanoparticles. The lowest amount of MNP expressed for ferrites (γ-Fe_2O_3) in amount of iron is 1 nmol Fe for dried samples and 4.5 nmol Fe for liquid samples. Improvement by further signal processing is possible. Relaxation signals are recorded as early as 250 µs after switching off the magnetizing field. At these early times Brownian relaxation can be directly observed in the time domain. In first agglomeration assay the binding reaction of the biochemical model complexes biotin avidin can be clearly identified down to concentrations of < 1µg avidin in a volume of 150 µl of human blood.

ACKNOWLEGDMENT

We are grateful for the technical help of H. J. Scheer, D. Gutkelch and L. Blume.

REFERENCES

[l] R. Weissleder, G. Elizondo, J. Wittenberg, C.A. Rabito, H.H. Bengele, and L. Josephson, "Ultrasmall superparamagnetic iron oxide: characterization of a new class of contrast agents for MR Imaging," Radiology 175, 489-493 (1990).

[2] Proceedings of the Second International Conference on Scientific and Clinical Applications of Magnetic Carriers (SCAMC2), J. Mag. Magn. Mat. 194 (1999).

[3] W. Weitschies, R. Kötitz, T. Bunte, L. Trahms: "Determination of relaxing or remanent nanoparticle magnetization provides a novel binding-specific technique for the evaluation of immunoassays", Pharm. Pharmacol. Lett. 7, 1-4 (1997).

[4] W. Weitschies et. al Patent WO 9623227.

[5] P. Debye: Polar molecules, Chemical Cataloge Company, New York, (1929).

[6] R.W. Chantrell, S.R. Hoon, B.K. Tanner: Time-Dependent Magnetization in Fine-Particle Ferromagnetic Systems, J. Mag. Magn. Mat. 38, 133-141 (1983).

[7] D. Drung, H. Koch: An integrated dc SQUID magnetometer with variable additional positive feedback, Supercond. Sci. Technol. 7, 242-245 (1994)

[8] H. Matz, D. Drung S. Hartwig, H. Groß, R. Kötitz, W. Müller, A. Vass, W. Weitschies, L. Trahms: "A SQUID Measurement System for Immunoassays", IEEE- ASC, in press.

[9] R. Kötitz, W. Weitschies, L. Trahms, W. Brewer, W. Semmler, "Direct determination of a biological binding reaction by relaxation measurements of magnetic nanoparticles", J. Mag. Magn. Mat. 194 (1999).

PII2.14

A Cryocooled Helmet-shaped MEG Measurement System

K. Sata, T. Yoshida, S. Fujimoto, S. Miyahara, and Y. M. Kang
MEC Laboratory, DAIKIN INDUSTRIES, LTD.,3 Miyukigaoka, Tsukuba 3050841, Japan

Abstract—We developed a cryocooled helmet-shaped magnetoencephalographic (MEG) measurement system. We determined the sources of white noise that contribute to the total white noise of this system, and determined the source of cyclic noise generated by the Gifford-McMahon/Joule-Thomson (GM/JT) cryocooler. Design modifications based on these results will reduce the white noise of our future cryocooled systems to 5fT/√Hz at the cyclic noise to 1pT.

I. Introduction

Biomagnetic measurement is the most common application for SQUID devices. Many SQUID-based biomagnetic measurement systems are already used in clinical applications. However, such systems are usually cooled by liquid helium, which requires special handling techniques. We therefore have been developing cryocooled SQUID systems that are user friendly for people who are not familiar with cryogenic techniques [1]. We have already constructed three of these systems, which are cooled by Gifford-McMahon/Joule-Thomson (GM/JT) cryocoolers [2]-[5].

In this paper, we describe our recently developed cryocooled system that has a helmet-shaped cryostat for magnetoencephalographic (MEG) measurement. We also describe our evaluation of the system components that contribute to the white noise level. Because the cyclic noise from the cryocooler limits the system performance, we discuss the mechanism of the cyclic noise generated by a GM/JT cryocooler and describe how we will reduce that noise in our future cryocooled systems.

II. System

In our latest cryocooled system (Fig. 1), both the cryostat with a GM/JT cryocooler suspended on a nonmagnetic gantry and a nonmagnetic bed are set inside a magnetically shielded room (MSR). A valve motor unit and a compressor unit of the cryocooler are set outside the MSR to shield the cryostat from electromagnetic noise. Similarly, except for the preamplifier unit, all of the electronics are also set outside the MSR. The gantry and the bed were designed to reduce the burden on the subject during the MEG measurement. The subject lies on the bed and places his or her head into the helmet-shaped cavity of the cryostat.

The shape of this cavity was designed by using data collected for most of the body sizes of Japanese [6].

Manuscript received April 30, 1999.

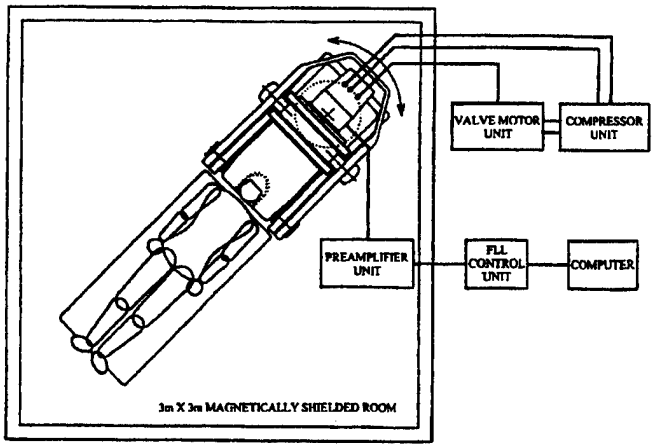

Fig.1 Block diagram of the system

Based on that data, we calculated an average head-shape of Japanese (males and females) between 18 and 30 years old, and designed the dimension of the cavity to accommodate a head that was 10% larger than this calculated average.

The cryostat (cross-section shown in Fig. 2) has 119 channels of detection coils arranged on a helmet-shaped plastic holder inside the cryostat. These detection coils are first-order axial gradiometers, each with a diameter of 18 mm and a base length of 60 mm. Nine channels of other detection coils can be used for reference-signal detection to reduce the ambient magnetic noise by processing with a computer. Super insulator (SI, a kind of multi-layered thermal insulator) is wrapped around the radiation shield to control the thermal radiation from the vacuum chamber.

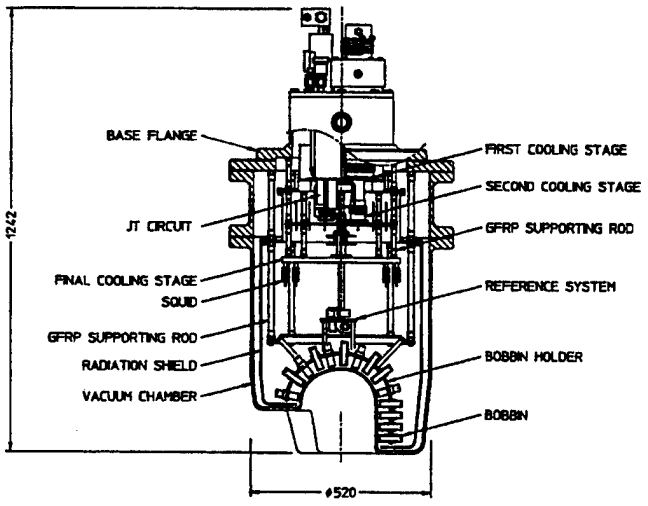

Fig.2 Cross-section of the cryostat

Most components of the cryostat, not including the cryocooler, are made from nonmagnetic materials, such as Glass-Fiber-Reinforced Plastic (GFRP), copper, copper alloy, and titanium alloy. Resin-coated copper wires are used to maintain thermal conduction pathways between the final cooling stage of the cryocooler and the bobbins of the detection coils. To isolate the mechanical vibration of the GM cryocooler, the final cooling stage and the helmet-shaped plastic holder containing the bobbins of the detection coils are supported by GFRP rods connected directly to the base flange of the cryostat. To absorb the vibration transmitted via the JT circuitry tubing from the first and second cooling stages of the GM cryocooler, the tubing connected to the final cooling stage is wound in a 50-mm-radius loop. Ferromagnetic parts in the displacer of the GM cryocooler were replaced by parts made of nonmagnetic materials. To reduce the amount of heat conducted through the wiring in the cryostat, we used Flexible Printed Circuit (FPC) wiring so that the cross-section area of the conductor of the FPC can be controlled.

III. Noise

A. White Noise

The white noise level of a SQUID system depends on the characteristics of the SQUID device, detection coil, and preamplifier of the FLL circuit. In the FLL circuit in our system, the noise of the preamplifier was 0.59 nV/$\sqrt{}$Hz. Using parameters for the SQUID with a detection coil used in our helmet-shaped system (Table 1), we calculated the noise of sources that contribute to the white noise level of our helmet-shaped system and of a conventional system cooled by liquid helium. To measure the thermal noise of the thermal anchor, we used liquid helium to cool the same detection coil, bobbin, and thermal anchor used in our cryocooled system. The results (Table II) show that our system can achieve a white noise level as low as 5fT/$\sqrt{}$Hz. If even less noise is required, possible modifications include the use of a superconducting shielding for the wiring between the input coil and detection coil.

B. Cyclic Noises

Despite the replacement of ferromagnetic parts in the cryostat, the level of cyclic noise in our cryocooled systems was still 10~50% of the level seen in a system that uses a conventional GM/JT cryocooler. This means that this remaining noise is not caused by ferromagnetic material. This noise was in synch with the operating frequency of the GM cryocooler, implying that the GM cryocooler of the GM/JT cryocooler induces cyclic noise. To confirm this source, we measured the distribution of the 2Hz component of the cyclic noise by using a flux gate magnetometer. The results (Fig. 3) suggest that the strongest noise occurred at the top of the second cylinder of the GM cryocooler; this cylinder is made from an austenitic stainless steel (SUS316).

By using a 32-channel cryocooled system [3], we also measured the cyclic noise of a GM cryocooler at various times (and therefore temperature) until the GM cryocooler completely cooled down after we pushed the start button of the GM cryocooler. The results (Fig. 4) show that the cyclic noise increased as temperature decreased, and peaked when the temperature exceeded that of the GM cryocooler during its cool-down. The same temperature dependency was observed for the magnetic susceptibility of austenitic stainless steel [7]. These results suggest that the cyclic noise was generated from the stainless-steel cylinder of the GM cryocooler that was stressed by the pressure of the refrigerant helium gas that pulsated at a 2Hz cycle. In general, reciprocating cryocoolers made from austenitic stainless steels therefore generate cyclic magnetic noise. To eliminate such noise in our cryocooled systems, we are currently making a GM cryocooler from other nonmagnetic materials, such as titanium, copper, aluminum, and their alloys.

TABLE I

PARAMETERS OF THE SQUID

Parameter	Value
damping resistance of SQUID ring	12 Ω
shunt resistance for Josephson Junction	6 Ω
damping resistance of input coil	100 Ω
self-inductance of SQUID ring	134 pH
output voltage per a flux quantum	≦170 μV/Φ_0
mutual inductance between SQUID ring and feedback coil	213 pH
mutual inductance between SQUID ring and input coil	9.28 nH
mutual inductance between feedback coil and input coil	8.72 nH
self-inductance of input coil	574.8 nH

TABLE II

WHITE NOISE SOURCES

Source	White noise level at 1kHz
damping & shunt resistance in the SQUID	0.35 fT/$\sqrt{}$Hz
damping resistance of input coil	1.78 fT/$\sqrt{}$Hz
preamplifier	1.77 fT/$\sqrt{}$Hz
S.I. of helium cryostat (measured)	2.55 fT/$\sqrt{}$Hz
S.I. of cryocooled cryostat (assumption)	~3 fT/$\sqrt{}$Hz
thermal anchor (measured)	3~4 fT/$\sqrt{}$Hz
total noise of liquid helium cooled system (measured)	3.57 fT/$\sqrt{}$Hz
total noise of cryocooled system (calculated)	4.94~5.61 fT/$\sqrt{}$Hz

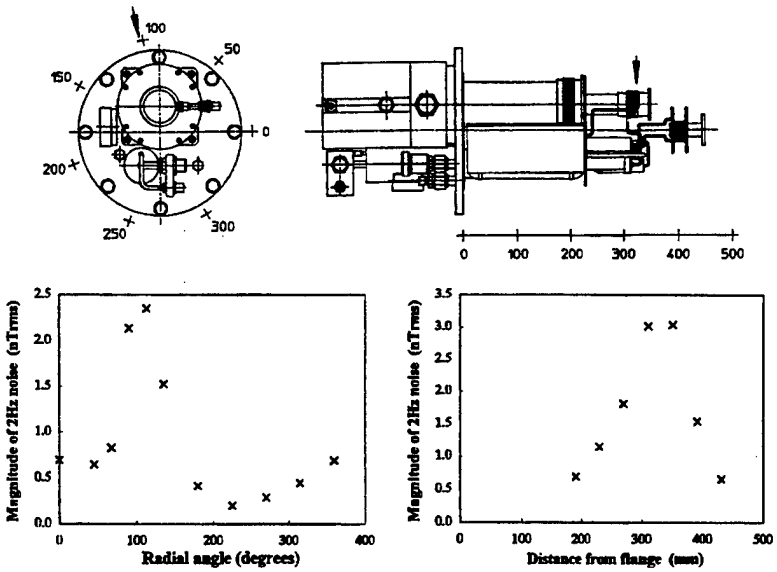

Fig.3 Distribution of the cyclic noise in the GM/JT cryocooler

IV. Conclusion

We designed a helmet-shaped MEG measurement system that is cooled by a GM/JT cryocooler. The design modifications of the cryostat in our system reduced the electromagnetic noise level by 50~90%, compared with the level seen in a system that uses a conventional GM/JT cryocooler. Although noise still remains, our system can measure the faint magnetic fields from a human brain by using custom-made software to remove the cyclic noise [4], [5]. By determining the sources of white noise and by determining how the cyclic noise is generated in our cryocooled systems, we can now improve the cryocooler to be more electromagnetically silent. Design modifications based on these results will help our future cryocooled systems achieve a white noise level of less than 5fT and cyclic noise of less than 1pT.

References

[1] K. Sata, T. Ueda, N. Fukui, T. Yoshida, Y. M. Kang, and K. Nishiguchi, "Biomagnetic measurements with a SQUID cooled by a GM/JT cryocooler," *Book of Abstracts*, 8th International Conference on Biomagnetism, pp.131-132, 1991.

[2] N. Fukui, K. Sata, S. Fujimoto, and Y. M. Kang, "A cryocooled SQUID system with minimal clearance between the pick-up coil and specimen," *Proc. Biomag 96*, in press.

[3] S. Fujimoto, K. Sata, N. Fukui, E. Haraguchi, T. Kido, K. Nishiguchi, and Y. M. Kang, "A 32-channel MCG system cooled by a GM/JT cryocooler," *Proc. Biomag 96*, in press.

[4] K. Sata, S. Fujimoto, N. Fukui, E. Haraguchi, T. Kido, K. Nishiguchi, and Y. M. Kang, "Development of a 61-channel MEG system cooled by a GM/JT cryocooler," *Proc. Biomag 96*, in press.

[5] K. Sata, S. Fujimoto, N. Fukui, E. Haraguchi, T. Kido, K. Nishiguchi, and Y. M. Kang, "A 61-channel SQUID system for MEG measurement cooled by a GM/JT cryocooler," *IEEE Trans. Appl. Supercond.*, Vol.7, No.2, pp.2526-2529, 1997.

[6] M. Kouchi, K. Yokoyama, J. Yamashita, T. Yokoi, H. Ogi, M. Yoshioka, "Human body dimensions data for ergonomic design," *Research Report*, National Institute of Bioscience and Human-Technology, Agency of Industrial Science and Technology , Vol.2, No.1, 1994.

[7] E. W. Collings, R. L. Cappelletti , "Mictomagnetism in austenitic stainless steels," *Cryogenics*, Vol.25, pp.713-718, December1994.

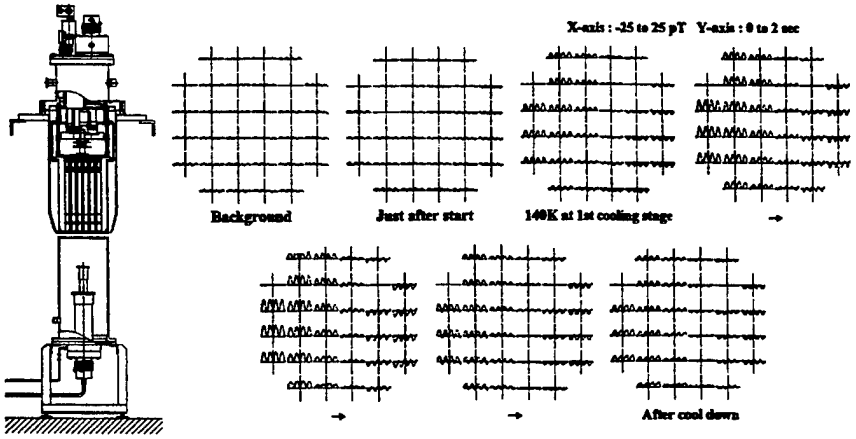

Fig.4 Temperature dependency of the cyclic noise

Magnetocardiographic application of directly-coupled high T_c dc SQUID magnetometer with bicrystal junctions of high junction resistance

Hyukchan Kwon, In-Seon Kim, Yong-Ho Lee, Jin-Mok Kim, Yong Ki Park, and Jong-Chul Park
Korea Research Institute of Standards and Science, P.O.Box 102, Yusong-gu, Taejon, 305-600, Republic of Korea

Abstract—A low-noise high T_c SQUID magnetometer with directly-coupled pickup coil was fabricated for magnetocardiogram (MCG). The magnetometer was made from single layer of laser-deposited $YBa_2Cu_3O_{7-\delta}$ thin film on $SrTiO_3$ bicrystal substrate with 30° misorientation angle. The junction parameters were characterized to ensure the high quality of the junctions. Due to the high resistance of the junctions, the voltage modulation depth and flux-to-voltage transfer were 65 μV and 250 μV/Φ_o, respectively. The best magnetic field noise was around 100 fT/√Hz down to 4 Hz, measured inside a magnetically shielded room. The magnetometers were used to measure magnetocardiographic fields in real time and showed signal-to-noise ratio of around 50 for the R-peak.

I. Introduction

During the past couple of years, the magnetic field noise level of high T_c dc superconducting quantum interference device (SQUID) magnetometers has improved remarkably, enabling measurements of weak magnetic signals from the heart (magnetocardiogram : MCG) [1]-[3]. Directly-coupled SQUID magnetometers with bicrystal junctions are widely used for this purpose, since it can be fabricated from single layer films by a simple fabrication process and provides a high fabrication yield. In addition, it is desirable to make a device on a small substrate for multichannel systems.

In order to reduce the magnetic field noise, we need to reduce the flux noise or increase the effective flux capture area A_{eff}. In a directly-coupled magnetometer, it is difficult to enhance the A_{eff} due to the poor coupling. Although the increase of SQUID inductance L_s ensures large A_{eff}, the voltage modulation depth ΔV is degraded considerably with the thermal noise flux [4]. According to numerical simulation results on the inductance dependence of flux noise power S_Φ, the parameter $R_o S_\Phi / L_s^2$ of a high T_c SQUID is weakly dependent on SQUID inductance for L_s<100 pH and increases rapidly with inductance for L_s>150 pH, where R_o is the junction resistance. This indicates that the field noise $S_B^{1/2} \propto S_\Phi^{1/2} / L_s$ weakly depends on L_s in a directly-coupled magnetometer for L_s<100 pH and decreases with $1/\sqrt{R_o}$. It is also recommended that R_o should be as high as 10 Ω with $I_o R_o$ product of larger than 150 μV. Recently, it has been shown that above requirement can be easily satisfied by a conventional process using 30 ° bicrysyal junction, and a voltage modulation of 39 μV and a white noise of 32 fT/√Hz with L_s of 100 pH was obtained [5]. The results suggest the utility of 30 ° bicrystal junction in the development of low noise SQUID magnetometers.

In the following, we describe the fabrication and the behavior of directly-coupled high-T_c SQUID magnetometers fabricated on $SrTiO_3$ bicrystal substrates with 30 ° misorientation angle. The performance of the magnetometer is demonstrated by measuring the high quality magnetocardiogram signals inside a magnetically shielded room

Manuscript received April 30, 1999.
This work was supported by the Ministry of Science and Technology, Republic of Korea.

II. Fabrications

The devices were fabricated from a single layer of a high-T_c superconducting thin film. C-axis oriented $YBa_2Cu_3O_{7-\delta}$ thin films, around 140 nm thick, were deposited on 10 mm x 10 mm $SrTiO_3$ bicrystal substrates with 30° misorientation angle by pulsed laser ablation as descibed elsewhere [6]. Prior to deposition, the substrates were annealed at 1000 °C for 10 h to provide an atomic-flat surface. The unpatterned films showed a critical temperature of $T_c \geq 90$ K and a critical current density of $j_c = 4.6 \times 10^6$ A/cm^2 at 77 K. The films were patterned by conventional photolithography (photoresist : AZ5214E) and Ar ion milling.

The SQUID loop has a line width of 8 μm and inner area of 4 μm x 106 μm. The 6 μm long, 2 μm wide bicrystal junctions are located at the ends of the slit. We calculated the slit inductance from the geometry of the SQUID loop, including the kinetic inductance contribution for a film thickness of 140 nm and a London penetration depth of 250 nm. Assuming the parasitic inductance associated with the junctions to be 10 pH, L_s has the total value of 90 pH. The SQUID loop is coupled to a square washer pickup loop with inner and outer dimensions of 3 mm and 9 mm, respectively. Then we calculate A_{eff} = 0.38 mm^2. The SQUID was cooled by immersing in a fiberglass liquid nitrogen dewar. The characterizations and noise measurements were performed inside a magnetically shielded room (MSR).

III. Results

We investigated four magnetometers with 30 ° misorientation angles. The devices exhibited high junction resistance of up to 10 Ω. Since it is difficult to determine the noise-free critical current I_o in the I-V curve due to the thermal noise rounding, we estimate I_o from the bias current [1]. Fig. 1 shows the correlation between the critical current and the junction resistance. For comparison, the measured data with

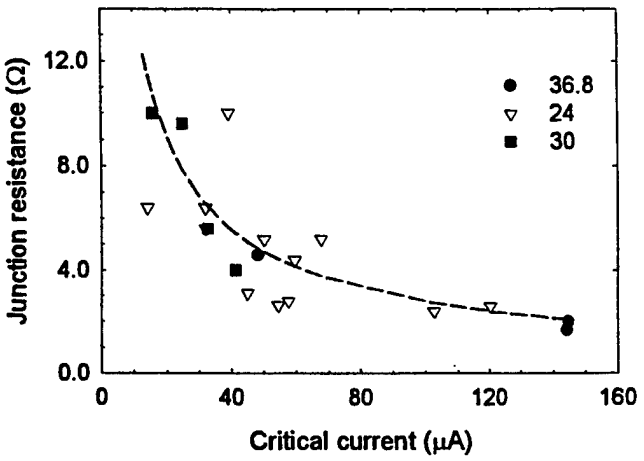

Fig. 1. Correlation between the critical current and the junction resistance of bicrystal junctions. The dashed line shows the relation calculated from (1).

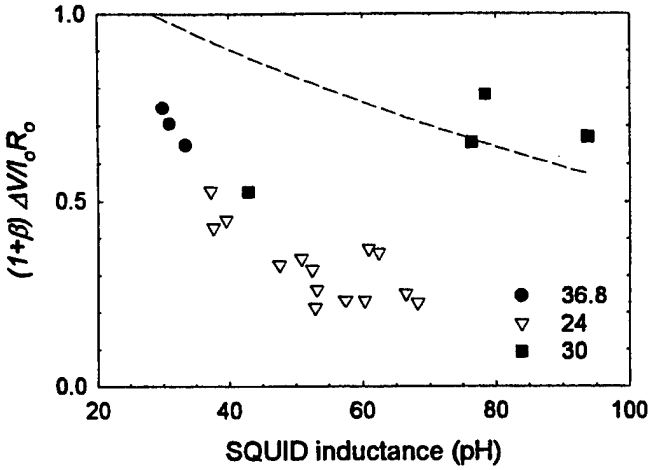

Fig. 3. Dependance of the normalized modulation voltage on the inductance. The dashed line is calculated from (2)

different misorientation angles (24 ° and 36.8 °) were shown together. For the grain boundary junctions, the analytical relation between I_o and the junction conductance $G = 1/R_o$ has been obtained as

$$G = 1/R_o = AI_o + B\sqrt{I_o}, \qquad (1)$$

where the parameters A and B were experimentally determined to be 2100 S/A and 15 S/A$^{1/2}$ [7]. In Fig. 1 the dashed line represents the above relation and shows a good agreement with our data. We have also investigated the dependence of critical current fluctuation $S_{Io}^{1/2}$ on the junction conductance. Since the low frequency noise due to the fluctuation of critical current can be considerably suppressed by bias reversal scheme, the value of $S_{Io}^{1/2}$ can be estimated from the reduction of the flux noise with ac-bias method. As can be seen in Fig. 2, the value of $S_{Io}^{1/2}$ becomes very small due to high resistance. Here, the dashed line shows the experimental results obtained in [7].

The measured values of modulation voltage ΔV are plotted as a function of the SQUID inductance in Fig. 3. Here, y-axis represents normalized ΔV and the dashed line shows the theoretical prediction given by

$$\Delta V = 4(I_o R_o)\exp(-3.5\pi^2 k_B TL_s/\Phi_o^2)/\pi(1+\beta) \qquad (2)$$

As shown in Fig. 3, two samples with a large value of I_oR_o product (250 μV,184 μV) show rather large modulation depth of 65 μV, 31 μV, respectively, and it may be explained by the strip line resonance occurring in the SQUID inductance [8].

To operate the magnetometer, we used conventional flux-locked loop electronics using 100 kHz flux modulation with an additional 1.5 kHz bias reversal scheme. The noise spectra for the best magnetometer inside an MSR are shown in Fig. 4. With a static bias current, the noise scales approximately as $1/f^{1/2}$ for frequencies below 100 Hz and becomes

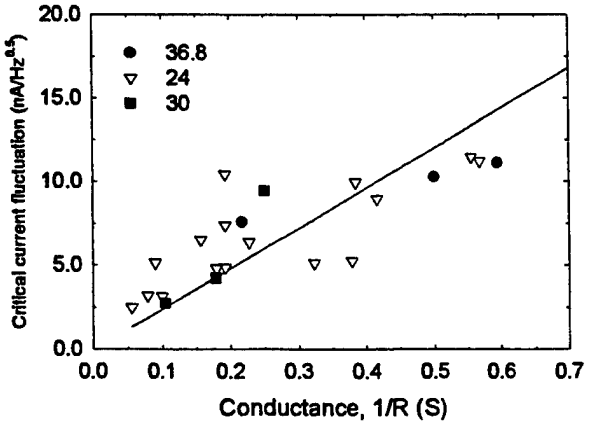

Fig. 2. Dependence of the critical current fluctuation on the conductance. The dashed line shows the experimental results ($S_{Io}^{1/2}$=2.4x10^{-8}/R) obtained in [7].

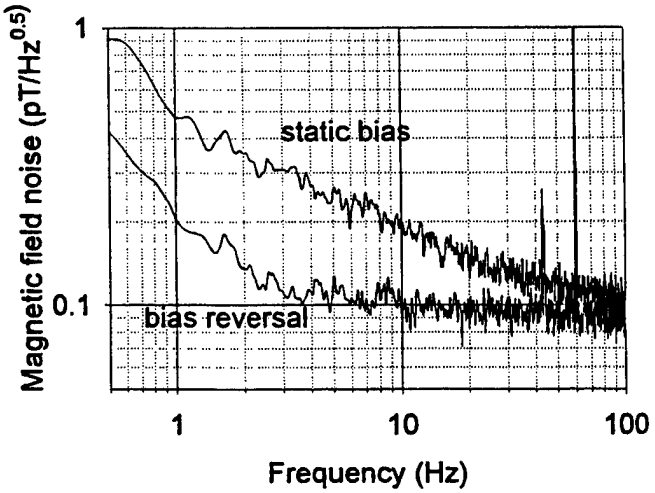

Fig. 4. Magnetic field noise of the best magnetometer, measured inside a magnetically shielded room.

nearly white at 1 kHz with a flux noise of 12 $\mu\Phi_o/\sqrt{Hz}$. With a magnetic field sensitivity of 6.3 nT/Φ_o, this corresponds to a field noise of 74 $fT/\sqrt{Hz}$. The use of bias reversal reduced the $1/f$ noise to a nearly frequency-independent value of 16 $\mu\Phi_o/\sqrt{Hz}$ down to 4 Hz, corresponding to 100 $fT/\sqrt{Hz}$. This indicates that the low frequency noise is mainly caused by ctitical current fluctuations of the junctions. The specific fluctuations of the ctitical current $S_{Io}^{1/2}/I_o$ of 1.1 x 10^{-4} /Hz is consistent with the typical values obtained for high T_c junctions. We believe that the noise levels of our magnetometers are suitable for MCG measurements.

IV. MCG MEASUREMENTS

In order to demonstrate the noise performance of our magnetometer, MCG signals were recorded at a position of approximately maximum peak intensity inside an MSR. The distance between the magnetometer plane and the chest surface was approximately 13 mm. The measurement bandwidth was 1.4-50 Hz and a 60 Hz notch filter was applied. Fig. 5 shows a realtime trace of the MCG signal recorded from a healthy male volunteer. Comparing with a QRS peak of about 110 pT, the low noise level of less than 2 pT_{pp} demonstrates a good signal-to-noise ratio of around 50. The result of averaging 100 heartbeats, shown in the inset, is comparable to a high quality electrocardiogram. The high quality of these MCG data demonstrates that our magnetometers have sufficiently high sensitivities for biomagnetic applications.

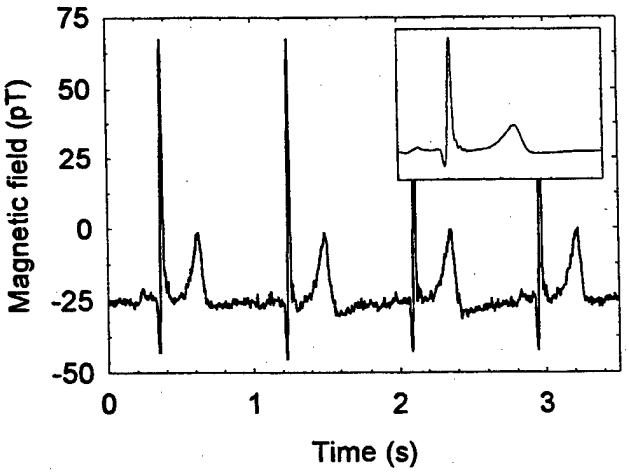

Fig. 5. A realtime trace of a magnetocardiogram. In the inset, the averaged data of 100 heartbeats is shown.

SUMMARY

We have fabricated and characterized low-noise directly-coupled dc SQUID magnetometers on 10 mm x 10 mm bicrystal substrates with 30 ° misorientation angle. High quality junction with high junction resistance and large voltage modulation depth have been obtained by a conventional fabrication process. Using conventional flux-locked loop electronics with a bias reversal scheme, we obtained the magnetic field noise of 74 $fT/\sqrt{Hz}$ at 1 kHz and around 100 V. $fT/\sqrt{Hz}$ down to 4 Hz. The high quality of MCG signals demonstrate the suitability of our magnetometers for biomagnetic applications.

ACKNOWLEDGMENT

The authors would like to thank Mr. S. K. Lee for his assistance with sample preparation.

REFERENCES

[1] D. Drung, F. Ludwig, W. Miler, U. Steinhoff, L. Trahms, H. Koch, Y. Q. Shen, M. B. Jensen, P. Vase, T. Holst, T. Freltoft, and G. Curio, "Integrated $Yba_2Cu_3O_{7-x}$ magnetometer for biomagnetic measurements," *Appl. Phys. Lett.*, vol. 68, pp. 1421-1423, 1996.

[2] H. J. M. ter Brake, R. Karunanithi, H. J. Holland, J. Flokstra, D. Veldhuis, L. Vargas, J. W. Hilgenkamp, W. Jaszczuk, N. Janssen, F. J. G. Roesthuis, and H. Rogalla, "A seven-channel high-T_c SQUID-based heart scanner," *Meas. Sci. Technol.*, Vol. 8, pp. 927-931, 1997.

[3] M. S. Dilorio, K-Y. Yang, and S. Yoshizumi,"Biomagnetic measurements using low-noise integrated SQUID magnetometers operating in liquid nitrogen," *Appl. Phys. Lett.*, vol. 67, pp. 1926-1928, 1995.

[4] K. Enpuku, Y. Shimomura, and T. Kisu,"Effect of thermal noise on the characteristics of a high T_c superconducting quantum interference device," J. Appl. Phys., vol. 73, pp. 7927-7934, 1993.

[5] J. Beyer, D. Drung, F. Ludwig, T. Minotani, and K. Enpuku,"Low noise single layer dc SQUID magnetometer based on bicrystal junctions with 30° misorientation angle," Appl. Phys. Lett., vol. 72, pp. 203-205, 1998.

[6] Hyukchan Kwon, In-Seon Kim, Yong-Ho Lee, Jin-Mok Kim, Yong-Ki Park, and Jong-Chul Park,"Low Noise Directly-Coupled High Tc dc Superconducting Quantum Interference Device Magnetometers for Magnetocardiogram," *Jpn. J. Appl. Phys.*, vol. 37, pp. L1308-L1311, 1998

[7] K. Enpuku, T. Minotani, F. Shiraishi, and A. Kandori,"Relationship between Critical Current Fluctuation of Superconducting Bicrystal Junction and Junction Parameters," *Jpn. J. Appl. Phys.*, vol. 38, pp. L433-L435, 1999.

[8] K. Enpuku, T. Minotani, A. Kandori, F. Shiraishi, and J. Beyer, "Direct-Coupled High T_c Superconducting Quantum Interference Device Magnetometers on $SrTiO_3$ Substrate:Theoretical Description and Comparison with Experiment," *Jpn. J. Appl. Phys.*, vol. 37, pp. 4769-4773, 1998.

Simulation of a SQUID Transformer with Moats

G. Benz and W. Jutzi
Institut für Elektrotechnische Grundlagen der Informatik, University of Karlsruhe, Hertzstrasse 16, D-76187 Karlsruhe, Germany

D. Drung
Physikalisch-Technische Bundesanstalt, Abbestrasse 2-12, D-10587 Berlin, Germany

Abstract—The self and mutual inductances of Nb washers with and without moats for flux pinning has been numerically evaluated. Neither the inductances nor the measured 1/f noise of the investigated Nb gradiometer are changed significantly by moats.

I. Introduction

As the integration level of superconducting digital circuits increases, flux trapping may become a serious problem. Ground plane holes and moats have been used as pinning centers for trapped flux [1]. In general, the larger and more numerous the ground plane holes are, the better the protection from flux trapping. Large moats, even though they were placed a distance away from the circuitry, are the most effective ones [2]. The influence of moats on the distribution of flux lines has been directly observed with a SQUID microscope. A few long moats protect digital circuits more effectively from trapped flux than a large number of small holes in the same configuration [3].

Flux trapping may also be a serious problem when high-T_c SQUIDs are cooled in a large magnetic field. Strong low-frequency noise is reported for field-cooled high-T_c SQUIDs, e. g. in [4]. The excess low-frequency noise is due to thermally activated hopping of flux vortices or flux lines. These vortices are generated spontaneously as the film is cooled through T_c. The low-frequency noise of dc SQUIDs can be dramatically lowered by reducing the largest linewidth. If one reduces the outer dimensions of the washer so that the inner hole is surrounded by a strip of film width w, it is energetically unfavourable for flux to enter the superconducting film below a threshold field of $B_0 = \pi\Phi_0/4w^2$. Thus, no increase of the low-frequency noise due to vortex motion is expected for fields below this threshold value [5]. Slots or holes in dc $YBa_2Cu_3O_{7-x}$ SQUIDs cooled in an static magnetic field perpendicular to the washer reduce the magnitude of the low-frequency noise dramatically [6]. The field distribution around a slotted washer SQUID of a Niobium gradiometer with moats is presented in [7]. Jansman et al. [8] calculated the current distribution and the effective area of a slotted high-T_c washer SQUID.

In this paper, the self and mutual inductances of a SQUID transformer consisting of a washer with moats and an input coil are calculated. Misalignements of the coil with respect to the moats are taken into account. 1/*f*-noise measurements of Niobium gradiometers with unslotted and slotted SQUID transformers are compared.

This work was supported by the Deutsche Forschungsgemeinschaft (DFG).

II. Simulation Techniques

The self inductance of some simple superconducting structures such as microstrip lines [9] and square washers [10] can be estimated by analytical expressions. The inductance of complicated superconducting structures may be calculated efficiently with SPICE after a transformation into a equivalent network [11].

Single Flux Quantum circuits, e. g. reported in [12], [13], require an accurate evaluation of inductances and magnetic fields. Especially for conductor thicknesses in the order of the London penetration depth, the kinetic energy must be taken into account. The superconducting circuit is transformed in a current network according to the SCM (Surface Current Method) [14]. Each current satisfies both, London's and Maxwell's equations. In a preprocessing step each structure has to be transformed into a current network. Inductances of complex geometry may be calculated in minimizing the free energy [9]. This method has also been applied to three dimensional structures with an automatic discretisation [15].

A more efficient and conceptually simpler way to calculate three dimensional superconducting structures is chosen here. As described in [16] the close relationship between Maxwell's and London's differential equation is used. The static currents in a superconductor are simulated by ac currents in normal conductor of conductivity σ_n at a frequency f_s where the skin penetration depth is equal to the London penetration depth λ_L. The static currents in a superconductor are simulated by ac currents in normal conductor of conductivity σ_n at a frequency f_s where the skin penetration depth is equal to the London penetration depth λ_L. Thus, the simulation frequency f_s is:

$$f_s = \frac{1}{\pi\mu_0\sigma_n\lambda_L^2}. \qquad (1)$$

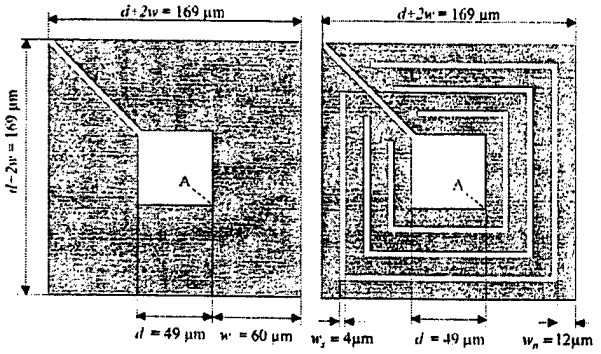

Fig. 1. Design of the unslotted and slotted washer. The thickness of the film is $t = 0.3$ µm. The threshold field $B_0 = \pi\Phi_0/4w^2$ increases from $B_{0U} = 0.45$ µT for the unslotted to $B_{0S} = 11$ µT for the slotted structure.

The conductivity σ_n is chosen sufficiently high that the wave length at the simulation frequency is larger than the largest dimension ($d+2w$). There is a difference in the field distributions of the superconducting and normal conducting structures due to the kinetic inductance of the superconductor. This is taken into account by a factor r_i which is defined as the ratio of the magnetic energy inside a superconductor to that inside a normal conductor of the same geometry. If the smallest superconducting dimension is more than 4 times the London penetration depth λ_L the factor is $r_i = 0.5$ and may be used to calculate Niobium structures with $\lambda_L = 86$nm and dimensions $t = 0.3\mu$m. The total inductance L of the superconducting structure is calculated with

$$\frac{1}{2}LI^2 = \frac{1}{2}\int_{\text{outside the conductor}} \mathbf{B}\cdot\mathbf{H}^* dv + \frac{1}{2}\mu_0\lambda_L^2 \sum_i \left[\int_{\text{inside the conductor}} \mathbf{J}\cdot\mathbf{J}^* dv\right]_i \times r_i \quad (2)$$

where I is the current source. The magnetic fields **B**, **H** and current density **J** are simulated with a normal metal field solver. The conjugate complex fields are marked with a star. Inductances calculated according to Eq. (2) yield good agreement with measurements [16].

The magnetic coupling of a SQUID transformer is $k = M/\sqrt{L_1 L_2}$, where the washer inductance L_1 and the input coil inductance L_2 are evaluated with (2) and the mutual inductance M is calculated with

$$M = \frac{\int_{s_2} \mathbf{E}\,ds}{j2\pi f_s I_1}. \quad (3)$$

where are f_s the frequency and s_2 the integration path over the input coil L_2. The current in the washer is I_1.

The magnetic field and current densities in Eq. (2) are simulated with the solver MAFIA (Maxwell Finite Integration Algorithm) [17]. Since this program takes into account the displacement currents, i. e. the capacitances, the simulation has been performed for $\lambda_L = 86$ nm and $f_s =$ 50 MHz where the capacitive reactances can still be neglected.

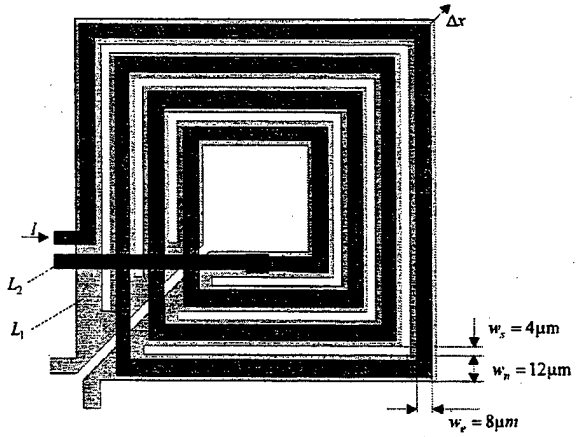

Fig. 2. SQUID transformer with moats. The dimensions of the washer are given in Fig. 1. The input coil L_2 is placed 0.3 μm above the washer L_1.

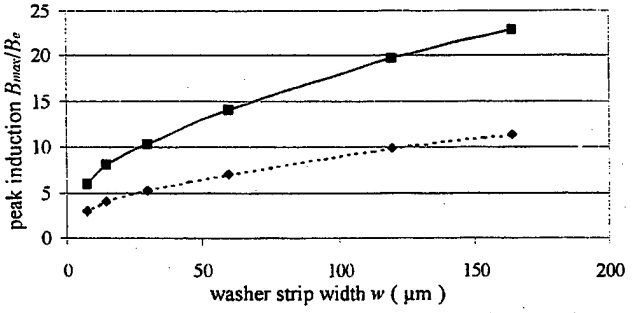

Fig. 3. Maxima of the absolute value of the magnetic field vector **B** at the edges (A in Fig. 1) of the washer hole without (+) and with (6) moats normalized to the applied field B_e. The dimensions of the washer are given in Fig. 1. The ratios w/d = 1.22, $w_n/w = 0.2$ and $w_n/w_s = 3$ are kept constant.

III. Simulation Results

The field destribution around the washer coil L_1 according to Fig. 1 i.e without input coil L_2 was calculated. The peak magnetic inductions or fields in the washer hole at the marked position A with and without slots are $B_{max} = 7 \cdot B_e$ and $14 \cdot B_e$, respectively. The peak inductivity as a function of washer strip width is given in Fig. 3. Since flux penetrates the slots the corresponding maximum field B_{max} is reduced, by about a factor 2.

The inductances L_1, L_2 and the coupling coefficient k of the SQUID transformer in Fig. 2, are calculated and compared in Table I. The washer inductance L_1 without moats in Table I practically coincides with the approximations for the hole and slot inductances [18].

Because of the different current distribution in the SQUID transformer with slots compared to the unslotted case, the inductance of the washer L_1 increases by 5% and the coupling coefficient k decreases by 7%. The inductance L_2 of the input coil has approximately the same value with and without slotted washer. The coupling coefficient k has a first maximum, when the strips of the input coil are properly aligned in the middle of the stems of the washer coil as shown in Fig. 2 for Δx=0. Shifting the input coil in the diagonal direction by Δx with respect to the washer changes the coupling coefficient as shown in Fig. 4.

TABLE I

Simulated inductances and coupling coefficients of the SQUID transformers without and with moats. The geometry is given in Fig. 2.

Structures L_1	L_2	Inductances L_1	L_2	Coupling coefficient k
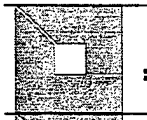		107 *pH*	1.454 *nH*	0.94
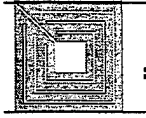		112 *pH*	1.543 *nH*	0.88

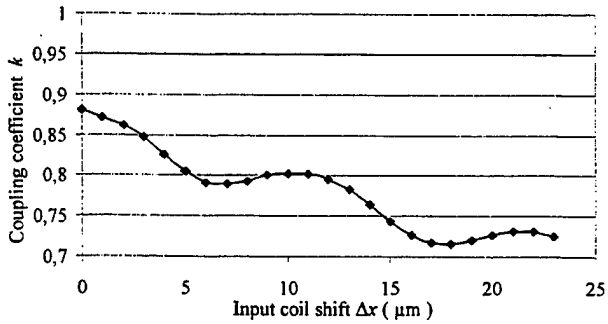

Fig. 4. Calculated coupling coefficient k between slotted washer L_1 and input coil L_2 with a misalignement of the input coil by Δx as marked in Fig. 2.

The second maximum at $\Delta x = 8 \cdot \sqrt{2}$ μm occurs if most of the input coil strips are on top of the washer slots. It is smaller than the first one since the centers of washer and input coil do not coincide.

IV. Measurement

To test the influence of slots, planar thin-film gradiometers designed for the $Nb/Al_2O_x/Nb$ technology have been used with and without the slots in the transformers. The gradiometer design is described in [19],[7]. Briefly, the devices consist of two 1.85 mm 2.3 mm pickup coils with a center-to-center distance (baseline) of 3.7 mm connected to the input coil of the SQUID inductivity of four transformers of the typ in Sec. II and III in parallel. The noise of the gradiometer has been measured with a direct-coupled flux-locked loop electronics developed at the PTB Berlin, type HS1/0497 in Ref. [20]. The gradiometers were cooled down in an open flux-locked loop. After cool down they have been operated with a closed flux-locked loop. Without magnetic shielding in the Earth field, the measured noise is $\sqrt{S_\Phi}(0.1\text{Hz}) = 382\ \mu\Phi_0/\sqrt{Hz}$ without and $\sqrt{S_\Phi}(0.1\text{Hz}) = 395\ \mu\Phi_0/\sqrt{Hz}$ with slots. Unfortunately, the measured noise is dominated by environmental noise. Therefore, influence of slots could not be observed although the Earth field is larger than the threshold field $B_{0U} = 11\ \mu T$. After magnetic screening by a factor 100 the gradiometer is exposed to $B \approx 50\ \mu T/100 \approx B_{0S} = 0.45\ \mu T << B_{0U}$, so that the expected noise of slotted washers should be extremely small. The shielded $1/f$-noise values $\sqrt{S_\Phi}(0.1\text{Hz}) = 4.8\ \mu\Phi_0/\sqrt{Hz}$ for the unslotted and $5.2\ \mu\Phi_0/\sqrt{Hz}$ for the slotted washer in a closed flux-locked loop are not significantly different. The white noise of both gradiometers at 4 kHz is $0.9\ \mu\Phi_0/\sqrt{Hz}$. Measurements with open flux-locked loops may reveal an influence of slots, but have not yet been tried.

V. Summary

The magnetic field at the edges of the described square washer hole is reduced by moats. The investigated slots increase the washer self inductance by 5% and decrease the coupling coefficient by 7% if the input coil is properly aligned. If the input coil is misaligned on top of the slotted washer the coupling coefficient may drop k=0.88 to k=0.72.

Until now the Nb gradiometers measured in a flux locked loop did not reveal a significant influence of slots at a sensitivity level of $\sqrt{S_\Phi}(0.1\text{Hz}) \approx 5\ \mu\Phi_0/\sqrt{Hz}$.

References

[1] S. Bermon and T. Gheewala, "Moat-guarded Josephson squids," *IEEE Trans. Magn.*, vol. 19, pp. 1160-1164, 1983.

[2] S. V. Rylov and R. P. Robertazzi, "Superconducting high-resolution A/D converter based on phase modulation and multichannel timing arbitration," *IEEE Trans. Appl. Superconductivity*, vol. 5, pp. 2260-2263, 1995.

[3] M. Jeffery, T. van Duzer, J. R. Kirtley, and M. B. Ketchen, "Magnetic imaging of moat-guarded superconducting electronic circuits," *Appl. Phys. Lett.*, vol. 67, 1995, pp. 1769-1771.

[4] A. H. Miklich et al., "Low-frequency excess noise in $YBa_2Cu_3O_{7-x}$ dc superconducting quantum interference devices cooled in static magnetic fields," *Appl. Phys. Lett.*, vol. 64, pp. 3494-3496, 1994.

[5] E. Dantsker, S. Tanaka, P. Nilsson, R. Kleiner, and J. Clarke, "Reduction of 1/f noise in high-T_c dc superconducting quantum interference devices cooled in an ambient magnetic field," *Appl. Phys. Lett.*, vol. 69, pp. 4099-4101, 1996.

[6] E. Dantsker, S. Tanaka, and J. Clarke, "High-T_c superconducting quantum interference devices with slots or holes: Low 1/f noise in ambient magnetic fields," *Appl. Phys. Lett.*, vol. 70, pp. 2037-2039, 1997.

[7] B. de Turckheim, "Auslegung eines Gradiometers 1. Ordnung in der Nb-Technologie mit digitalem Ausgang," Diplomarbeit, IEGI, University of Karlsruhe, 1.11.95-31.5.96. G. Benz, B. de Turckheim and W. Jutzi, "Simulation und Layout eines Gradiometers mit Flußgräben," Tagungsband Kryoelektronische Bauelemente, Se25, pp. 42, 1997.

[8] A. B. M. Jansman, M. Izquierdo, A. Eiguren, J. Flokstra and H. Rogalla, "Effective area in slotted high Tc dc washer superconducting quantum interference devices," *Appl. Phys. Lett.*, vol. 72, pp. 3515-3517, 1998.

[9] W. H. Chang, "The inductance of superconducting strip transmission line," *J. Appl. Phys.*, vol. 32, pp. 461-469, 1979.

[10] M. B. Ketchen, W. J. Gallagher, A. W. Kleinsasser, S. Murphy and J. R. Clem, "DC SQUID focuser," *in SQUID'85*, pp. 865-871. Walter de Gruyter and Co., Berlin, New York, 1985.

[11] T. V. Dinh, B. Cabon, N. Daoud, and J. Chilo, "Electromagnetic modelling of conductive or superconductive microstrip lines using spice as electromagnetic solver," *J. Phys. III France*, vol. 2, pp. 2165-2174, 1992.

[12] K. K. Likharev, "Ultrafast superconducting digital electronics: RSFQ technology road map," *Czechoslovak Journal of Physics*, vol. 46, pp. 3331-3338, 1996.

[13] R. Koch, P. Ostertag, E. Crocoll, M. Götz, M. Neuhaus, T. Scherer, M. Winter and W. Jutzi, "A NRZ - Output Amplifier for RSFQ Circuits," ASC '98, EID-05, 1998.

[14] M. Hosoya, E. Goto, N. Shimizu, N. Miyamoto, and Y. Harada, "Inductance calculation system for superconducting circuits," *IEEE Trans. Magn.*, vol. 25, pp. 1111-1114, 1989.

[15] G. Hildebrandt and F. H. Uhlmann, "Inductance calculation for integrated superconducting structures by minimizing free energy," *IEEE Trans. Appl. Superconductivity*, vol. 5, pp. 2766 - 2769, 1995.

[16] Z. Du, S. R. Whiteley, and T. Van Duzer, "Inductance calculation of 3D superconducting structures," *Proc. of the ISEC 97 Berlin*, vol. 3, pp. M293-M295, 1997.

[17] T. Weiland, "Zur numerischen Lösung des Eigenwellenproblems längshomogener Wellenleiter beliebiger Randkontur und transversal inhomogener Füllung," Darmstädter Dissertation D 17, 1977. CST GmbH, Lauteschlägerstr. 38, D64285 Darmstadt, http://www.cst.de.

[18] B. Ketchen, "Integrated thin-film d.c. SQUID sensors," *IEEE Trans. on Magnetics*, vol. mag-23, no. 2, 1987.

[19] D. Drung, E. Crocoll, R. Herwig, A. Knuettel, M. Neuhaus and W. Jutzi, "Experimental Gradiometer with a Digital Feedback Loop," *Proc. of the ISEC 87 Tokyo*, pp. 21-24, 1987.

[20] D. Drung, "Improved dc SQUID read-out electronics," *Proc. of the ISEC 97 Berlin*, vol. 1, pp. 72-75, 1997.

POSTER SESSION II

Group 3 - Analog

Experimental Observation of Subharmonic Gap Structures in Long Josephson Junctions

M. A. Nordahn, M. H. Manscher, and J. Mygind
Department of Physics, Technical University of Denmark, B309, DK-2800 Lyngby, Denmark

L. V. Filippenko
Institute of Radio Engineering and Electronics RAS, Mokhovaya 11, Moscow 103907, Russia

Abstract—Subharmonic gap structure (SGS) in long overlap Nb-AlO$_x$-Nb Josephson tunnel junctions has been investigated. The experimental results show peaks in the differential conductance at both odd and even integer fractions of the gap voltage, V_G. Furthermore, the conductance peak at $V_G/2$ has been observed to split into two peaks with different characteristics. At high magnetic fields, the I-V characteristic approaches a single curve, while retaining the SGS conductance peaks. The gap structure and the SGS show the same temperature dependence. The SGS can be explained by Josephson self-coupling effect or multiple Andreev reflections. The results are important for the development of the flux flow oscillator used as local oscillator in integrated all-superconducting 200-800 GHz receivers.

I. Introduction

Considerable research efforts are presently being devoted to the development of the *flux flow oscillator* (FFO), based on the dc bias current and magnetic field driven unidirectional flow of magnetic flux quanta (fluxons) in long Josephson junctions with relatively high damping [1,2]. The functionality of the FFO depends critically on the damping [3], which strongly influences both the dc I-V curve and the linewidth of the radiation emitted from the FFO. In this paper we focus on the dominant damping mechanism, the quasiparticle excitations which manifest themselves in the dc I-V curve as the so-called *subharmonic gap structure* (SGS). SGS is observed as strong onsets of current, i.e. an increasing conductance, at integer fractions of the gap voltage V_G. Previously SGS has been observed in a variety of Josephson structures, such as microbridges, SNS junctions, and small tunnel junctions. Here we report on SGS in long overlap low-T_c tunnel junctions (physical length larger than the Josephson penetration length, λ_J).

Several explanations have been proposed for the SGS, two of which seem more likely. Both apply to short tunnel junctions. The first explanation, *Josephson self-coupling* (JSC), was published by Werthamer in 1966 [4]. The other, *multiple Andreev reflections* (MAR), was published in 1983 by Klapwijk, Blonder and Tinkham [5], based on the work from 1964 by Andreev [6]. Both theories explain the odd-numbered SGS, but MAR appears to be the more likely explanation, as this theory can also explain the even subharmonics.

Manuscript received April 30, 1999.
The work was supported in part by the Danish Natural Science Council, and INTAS contract 97-1712.

II. Theory

A. Josephson Self-Coupling

The JSC theory is based on two well-known effects in Josephson junctions. One is the *ac Josephson effect*, which is the appearance of an oscillating supercurrent I_s when the junction is biased at a dc voltage V^{DC}

$$I_S(t) = I_C \sin(2\pi ft), \quad f = (1/\Phi_0)V^{dc} \qquad (1)$$

where I_C is the critical current and $\Phi_0 = \frac{h}{2e}$ is the flux quantum.

Furthermore, *photon assisted tunneling* (PAT) is the absorption of microwave quanta by quasiparticles in the superconducting electrodes. It manifests itself in the dc I-V curve as an increased quasiparticle tunneling, and thus a higher conductance, at the voltages V^{dc} where the extra energy provided by p photons corresponds to eV_G:

$$eV^{dc} + phf = eV_G = 2\Delta \Leftrightarrow V^{dc} = V_G - p\frac{hf}{e} \qquad (2)$$

In JSC [4], microwave quanta generated internally by the ac Josephson effect are absorbed by the quasiparticles in a PAT process:

$$\begin{aligned} eV^{dc} + phf &= eV^{dc} + ph\frac{V^{dc}}{\Phi_0} \\ &= eV^{dc} + 2peV^{dc} = eV_G \Rightarrow V^{dc} = \frac{V_G}{1+2p} \end{aligned} \qquad (3)$$

As it is seen from (33), the self-coupling should result in strong onsets of tunneling, at odd integer fractions of V_G. However, Werthamer [4], suggested that JSC could also give rise to structures at even fractions through coupling to higher harmonics. We will use the symbol n to denote the fraction; thus $n = 1+2p$.

B. Multiple Andreev Reflections

MAR [5,6] is a process in which a quasiparticle transferred across the barrier causes the coherent reflection of a quasihole. This in turn causes the reflection of a quasiparticle etc., until finally after n-1 such reflections, a particle (quasiparticle/quasihole) enters an available state in one of the superconductors.

Since the individual Andreev reflections are energetically symmetric around the Fermi energy, MAR should give rise to an onset of current at V_G/n, where a new 'tunneling path' for the reflections is opened. The even-numbered MAR

correspond to the transfer of a number of superelectron pairs, whereas the odd-numbered include the transfer of a single quasiparticle. This means that even for MAR, the odd and even series may be different [7]. This contrasts JSC, which in the basic theory gives only odd integer fractions.

III. Experimental Setup

For clarity we only present measurements done on three Nb-AlO_x-Nb samples, all fabricated at the Institute of Radio Engineering and Electronics (IREE), Moscow, similar geometry and production parameters. Production details and design considerations are documented elsewhere [2]. The length L is 400 μm, with a 50 μm unbiased overlap extension [2,3]. The width W is 5 μm. The critical current density j_c is 6-8 kA/cm^2, which corresponds to a Josephson penetration depth $\lambda_J \approx$ 6-7 μm, and a specific resistance $R_N LW \approx$ 30-35 Ω·μm^2. This gives a normalized length $\ell = L/\lambda_J \approx 60$. The barrier thickness t is about 1 nm, which is oxidized from the top of a 7 nm Al layer, leaving a 6 nm Al normal metal layer.

We used a simple dipstick-type cryoprobe with built-in, low-noise amplifiers and filters for the measurements. The samples were mounted inside a μ-metal can to suppress external noise. The magnetic field was applied by a control current I_{CL} in an overlying line formed by the top electrode of the FFO. A computer controls the biasing, recording and storage of the dc I-V curves .

IV. Results

Fig. 1 shows a set of I-V curves, each recorded for a fixed I_{CL}. The bias current I is increased in 30 μA steps from 0 to 25 mA, and returned to zero with the same steps. Between successive curves, I_{CL} is increased by ΔI_{CL} = 0.5 mA. Apart from the increase in the differential conductance $G_D = dI/dV$ at approx. 0.9 mV $\approx V_G/3$, one can also see structures at other integer fractions of V_G. At low magnetic fields, the structures at V_G/n, $n > 3$, are obscured by the presence of high-order Fiske steps. For high magnetic fields, the curves seem to converge towards a limiting curve, at which the junction dynamics become insensitive to magnetic field.

Fig. 2 demonstrates the technique we devised to extract the common features of all the I-V curves in Fig. 1. The graph shows the density of sample points in small, discrete voltage intervals ΔV (here 7 μV) along the voltage axis. This means that the method favors features that are constant in voltage. The method utilizes the fact that the sample points (I,V) are equally spaced in bias current, and thus a higher slope gives a higher density, which is similar to showing G_D. The dotted curve in Fig. 2 shows the result of using only the curves recorded at high magnetic fields. Consequently the Fiske Steps are suppressed, and curves with discontinuities are excluded.

Experiments confirmed that the measured temperature dependence of V_G was in agreement with the BCS theory. The narrow peak in the density plot (Fig. 2) is at $V \approx V_G/3$.

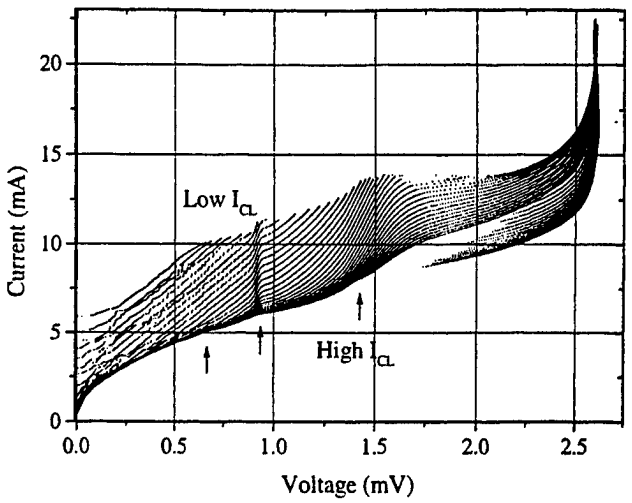

Fig. 1: Typical set of dc I-V curves for sample 14#6. Each curve is recorded with a fixed control line current, I_{CL}. The curves have been recorded for (top to bottom) -3 mA < I_{CL} < 20 mA in steps of ΔI_{CL} = 0.5 mA (47 curves). T = 4.6 K, $V_G \approx$ 2.67 mV. Arrows indicate the SGS.

Experiments showed that this ratio is independent on temperature from 4.2 to 7.0 K. This strongly supports the conclusion that the structure at $V_G/3$ is SGS. The much broader structure also observed at a voltage close to $V_G/2$ is examined below.

Fig. 3 shows G_D as a function of voltage around $V_G/2$ for a range of values of magnetic field. G_D was determined from the (I,V) sample points using a simple difference quotient method, and subsequently smoothened in order to improve the visualization.

Fig. 3 includes results for three samples with similar configuration. These results are representative for all samples investigated. The relatively broad peak at I_{CL} = 10 mA splits into two peaks, A and B, with different properties. The plot shows that the peak voltages seem to depend on magnetic field, in disagreement with either theories presented above. The dotted lines in Fig. 3 indicate the variation of the peaks with increasing magnetic field.

For relatively small values of I_{CL}, peak A is entirely

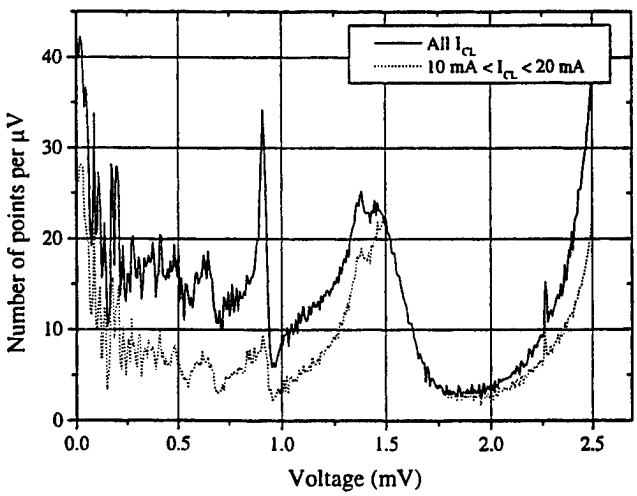

Fig. 2: A density plot of sample 14#6 derived from the data in Fig. 1. The full line shows the density from all 47 curves (full line); the dotted curve is the density of curves recorded for a control line current between 10 mA and 20 mA (dotted). ΔV for this plot is 7 μV.

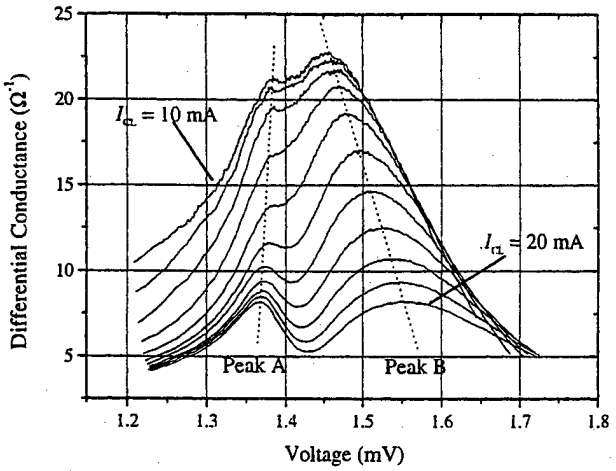

Fig. 3: The differential conductance G_D as function of voltage for different values of magnetic field at $T = 4.6$ K. The top curve is recorded for a control line current I_{CL} of 10 mA, while the bottom curve is for 20 mA.

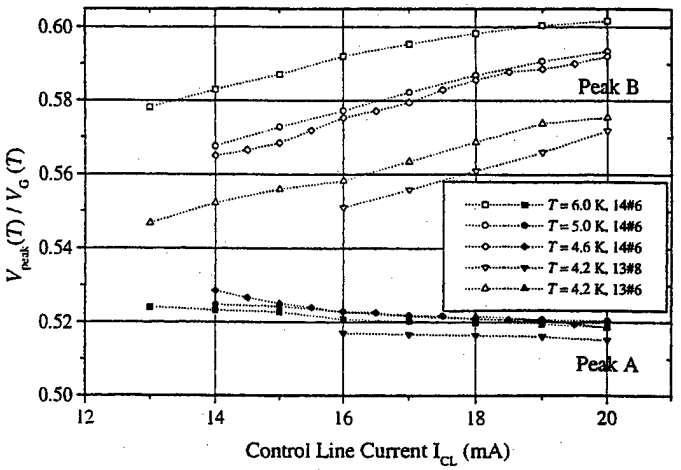

Fig. 4: The locations of the two peaks (A and B) near $V_G/2$ as a function of control line current. The voltage is normalized to V_G at the particular temperature.

contained in peak B, which at this point dominates at $V_G/2$. As the magnetic field is increased, peak B is shifted. Its amplitude decreases, while the width of the peak increases (corresponding to an increasing linewidth of the emitted FFO signal). At a certain field, the narrower peak A becomes visible. Its position is almost independent on magnetic field, and like peak B the amplitude decreases with magnetic field.

In order to further examine the behavior of the structure at $V_G/2$, Fig. 4 shows the locations of the two peaks relative to V_G as a function of I_{CL} for three samples at various temperatures. The two peaks have distinct differences. Peak B seems to increase almost linearly in voltage, with a slope that is independent of sample and temperature, while the offset increases with temperature. Peak A, on the other hand, seems to converge towards $V_G/2$. In conclusion, peak A is the usual SGS, while peak B is not.

IV. Conclusion

We have investigated SGS in long one-dimensional Josephson junctions. The I-V curves approach a limiting curve at high magnetic fields, where the junction dynamics become so linear due to the dense packing of the fluxons that its behavior can be explained using a model with many short junctions in parallel.

It has been shown earlier [2] that the damping increases dramatically at the SGS found at $V_G/3$. This leads us to believe that there is also an increase at $V_G/2$. FFO linewidth measurements to confirm this are in progress.

The theoretical prediction that long tunnel junctions should show SGS is confirmed by the experimental results, which show that the position of the structures remain at an integer fraction of V_G at all temperatures. Furthermore, an additional structure has been observed close to $V_G/2$, which did not scale with V_G. This structure may be a resonance in the system or a new kind of splitting of the SGS at $V_G/2$. This property is highly dependent on the magnetic field.

Although multiple Andreev reflections are most prominent in SNS junctions [5], this may still be the explanation for the observed structures. Since our insulating layer is only 1 nm thick, oxidized onto a 7 nm layer of normal Al metal, there may very well be local SNS pinholes in the insulating layer. Regardless of the explanation, we observe a significant increase in the FFO damping at the SGS.

Acknowledgment

We thank Jørn Bindslev Hansen, Valery P. Koshelets and Mogens R. Samuelsen for useful discussions.

References

[1] V.P. Koshelets, S.V. Shitov, A.V. Shchukin, L.V. Filippenko, P.N. Dmitriev, V.L. Vaks, J. Mygind, A.M. Baryshev, W. Luinge and H. Golstein, "Flux Flow Oscillators for Sub-mm Wave Integrated Receivers", *IEEE Trans. on Appl. Supercond.*, 1999, *ASC'98*, in press.

[2] V.P. Koshelets, S.V. Shitov, A.V. Shchukin, L.V. Filippenko, J. Mygind and A.V. Ustinov, "Self-pumping effects and radiation linewidth of Josephson flux-flow oscillators", *Phys. Rev. B*, vol. 56, pp. 5572-77, 1997.

[3] Yongming Zhang: *Dynamics and Applications of Long Josephson Junctions*. Ph.D. thesis, Chalmers University of Technology, 1993.

[4] N.R. Werthamer, "Nonlinear Self-Coupling of Josephson Radiation in Superconducting Tunnel Junctions", *Phys. Rev.*, vol. 147, pp. 255-63, 1966.

[5] M. Octavio, M. Tinkham, G.E. Blonder, T.M. Klapwijk, "Subharmonic energy-gap structure in superconducting constrictions", *Phys. Rev. B*, vol. 27, pp. 6739-46, 1983.

[6] A.F. Andreev, *Zh. Eksp. Teor. Fiz.*, vol. 46, pp. 1823-, 1964 (Sov. Phys. - JETP, vol. 19, pp. 1228-, 1964).

[7] J. Kutchinsky, R. Taboryski, O. Kuhn, C. B. Sørensen, P. E. Lindelof, A. Kristensen, J. Bindslev Hansen, C. Schelde Jacobsen and J. L. Skov, "Coherent diffusive transport mediated by Andreev reflections at $V=\Delta/e$ in a mesoscopic superconductor/semiconductor/superconductor junction", *Phys. Rev. B*, vol. 56, pp. R2932-35, 1997.

Forward and Backward Wave in Cherenkov Flux-Flow Oscillators

Andrey M. Baryshev
Groningen Space Research Laboratory and Materials Science Center, P.O. Box 800, 9700 AV Groningen, The Netherlands

Alexey V. Yulin, Vladislav V. Kurin,
Institute for Physics of Microstructures, Russian Academy of Science, GSP-105, 603600 Nizhny Novgorod, Russia

Valery P. Koshelets, Pavel N. Dmitriev, Lyudmila V. Filippenko,
Institute of Radio Engineering and Electronics Russian Academy of Science, Mokhovaya 11, 103907 Moscow, Russia

***Abstract*—Josephson Flux-Flow Oscillators (FFO) have been used as an on chip local oscillator at frequencies up to 650 GHz. An autonomous FFO linewidth of about 1 MHz was measured in the resonant regime at $V_b < 950$ μV for niobium – aluminum oxide – niobium tunnel junctions, while considerably larger values were reported at higher voltages. To overcome this fundamental linewidth broadening we propose an on chip Cherenkov radiation flux-flow oscillator (CRFFO). It consists of a long Josephson junction and a superconducting slow wave transmission line that modifies essentially the junction dispersion relation. Two superconductor insulator-superconductor junction detectors are connected both to the long Josephson junction and the slow wave line to determine the available microwave power. The power is measured at different CRFFO biasing conditions. Both a forward wave and a backward wave oscillation regime are observed. A FFO and a CRFFO with the same junction parameters are compared.**

A FFO has been used as a local oscillator at frequencies up to 650 GHz. An Integrated Receiver including an SIS mixer and a FFO as LO has shown a receiver noise temperature below 100 K in the 500 GHz band [1]. The FFO linewidth has been carefully investigated [2]. It was shown that with a free running FFO a linewidth below 1 MHz could be achieved in the resonant regime [2]. The possibility to decrease the FFO linewidth by an external phase lock system (PLL) has been demonstrated recently [4]. The free running FFO linewidth should be small enough in order to reduce the linewidth by means of a PLL. At bias points above the boundary voltage $V_b = 950$ μV for $NbAlO_xNb$ junctions it is observed that both R_d and linewidth increase. This can be explained by the increase of the rf loss in a long Josephson junction (LJJ) due to the self-pumping effect [2], [3].

The FFO performance could be improved if the mutual interaction between vortices and waves takes place in the whole junction. To achieve this the velocities of the vortices and the excited wave must be the same. The maximum vortex velocity never exceeds the linear waves velocity in the plain FFO and a resonant interaction is impossible. The dispersion characteristic of the waves in a LJJ can be modified by the addition of an external system. The resonant Cherenkov radiation conditions can be met if there are waves with low phase velocity. Then the interaction between vortices and waves occurs in whole junction and can significantly increase the output power of the flux-flow device. This effect has been discussed in theoretical papers [5]-[9] as well as in experimental ones [10]-[12].

The other advantage of devices based on Cherenkov radiation effect is the possibility to make the radiation spectrum narrower. The linewidth ΔF is proportional to R_d^2 in a conventional FFO. Cherenkov radiation has a resonant nature and it would lead to a decrease in R_d and a narrower radiation spectrum.

A modification of I-V characteristics has been observed by the authors for half annular junctions embedded with slow wave structure. [12]

In this work measurement results for a long linear junction with the same slow wave structure as in [12] and a modified design of detector circuits are presented. A clear indication of backward and forward wave is found from an experimental data.

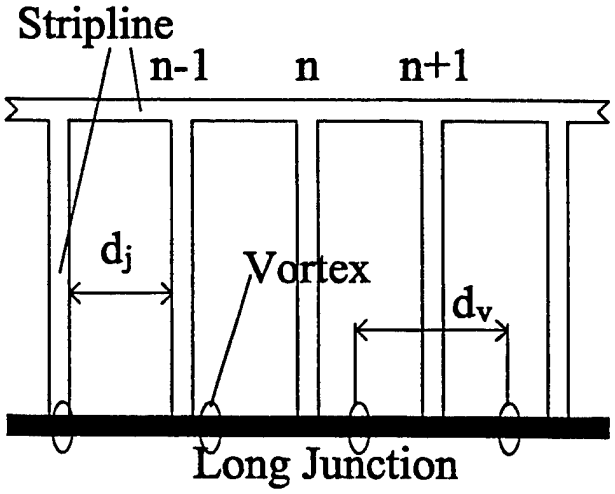

Fig. 1. Operation principle schematics.

Manuscript received May 5, 1999.
This work was supported in part by the by Russian Ministry of Science and Tecnology under Grants No. 95042 (Physics of Superconductivity) and No. 4.7 (Physics of Microwaves); by INTAS project 97-1712 and ESA TRP contract No. 11653/95/NL/PB/SC/CCN4.
Email: andrey@sron.rug.nl

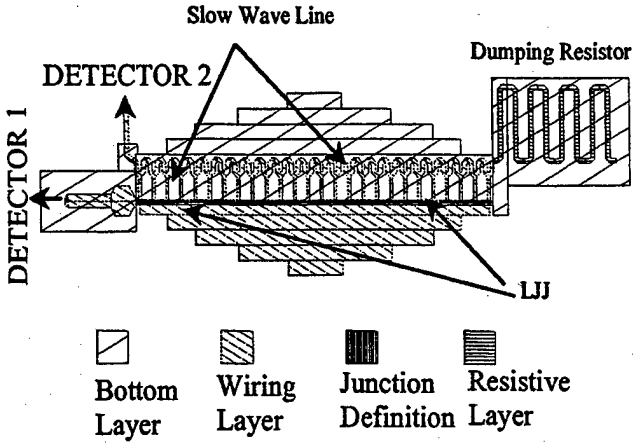

Fig. 2. CRFFO Layout.

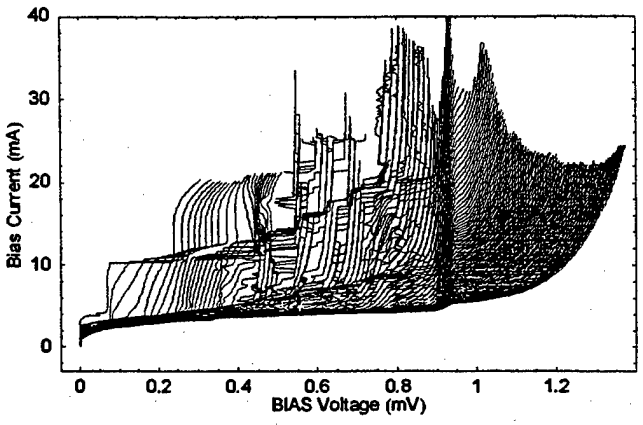

Fig. 3. Set of I-V curves for a LLJ without slow wave structure. Curves were recorded with the magnetic field across LLJ as parameter.

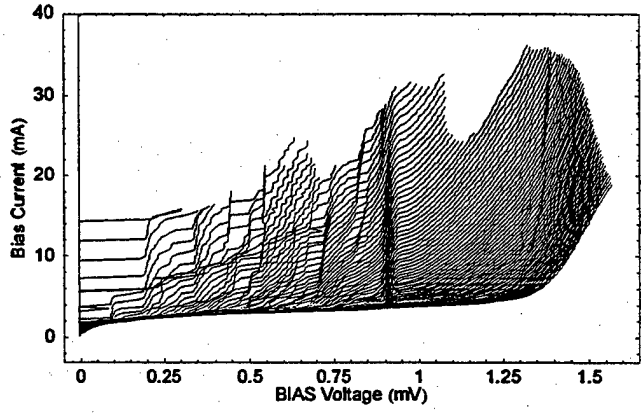

Fig. 4. Set of CRFFO I-V Characteristics recorded with the magnetic field control line current as parameter.

The LJJ is connected to the periodical stripline structure shown in Fig. 1. Radiation appears when vortices move along the junction and scatter on the all strip line ends. Let the vortex scatter on n-th node of the system at time $t = t_n$ and the radiation enters the strip line. The same vortex scatters on $n+1$ -th node at a time $t_{n+1} = t + \tau$ where $\tau = \frac{d_j}{v_v}$ is the delay time needed for the vortex to run from n-th to $n+1$ -th node, d_j is the junction length between nodes, v_v is vortex velocity. The waves emitted due to the vortex scattering on the different nodes should be added with proper phase. In order to get effective wave excitation the following condition must be satisfied $kd_l \pm \omega(k)\tau = 2\pi l$ where k is wave number, $\omega(k)$ is dispersion of waves in strip line, l is any integer. The frequency of the radiation of a single vortex can be found from last equation.

In case of a moving vortex chain the radiation from all vortices should be added in phase. To achieve it the condition $kd_v = 2\pi m$ where d_v is the distance between vortices and m is an integer must be satisfied. This condition could be achieved in practice by changing the distance between fluxons varying the magnetic field across the LJJ. It is possible to excite a strong wave by a large number of vortices scattering on the strip line ends using one with small dissipation. The radiation amplitude can be controlled by adjusting the fluxons density.

The layout of the experimental chip is shown in Fig. 2. The CRFFO consists of a 510 μm long and 3.5 μm wide LJJ and the periodical slow wave line. The period of the line along the LJJ is 20 μm. The $\frac{\lambda}{4}$ length of the parts of the slow wave system, perpendicular to the LJJ, has been chosen in order to provide a good impedance match between the 20 Ω impedance line and the low impedance ($\approx 0.5\ \Omega$) of the LJJ at around 450 GHz. The needed delay in the line is realized by additional sections along the LJJ. The external magnetic fileld has been applied to the LJJ by means of the integrated magnetic field control line in the top electrode of the LJJ. Most of the *dc* control line current follows the low-inductance part on top of the LJJ. The LJJ critical current density was $\approx 8\ kA/cm^2$. A normal metal stripline load is connected to the end of the slow wave line to prevent possible reflection.

Two detector chains are attached to the experimental structure as shown in Fig. 2. Detector 2 is connected to the slow wave line and detector 1 is connected directly to the LJJ. Each detector has a band pass filter and *dc*-breaks. A twin SIS junction circuit is used as the wide band microwave detector. The operating range of this circuit is 300-650 GHz. The detector chain design is described in detail in [2].

LLJ of the same size and with the same detector 1 chain has also been made for comparison.

The experiment has been carried out on a dipstick at 4.2 K physical temperature. The power from both detectors has been measured simultaneously with the I-V characteristics of the LLJ. Each detector junction has a normal resistance of 14 Ω. The microwave power is estimated by measuring the increase of the SIS junction bias current at a fixed bias voltage in the first photon step. This current is propotional to the absorbed rf power in the range of experimental parameters.

The measured I-V characteristics of LLJ without slow

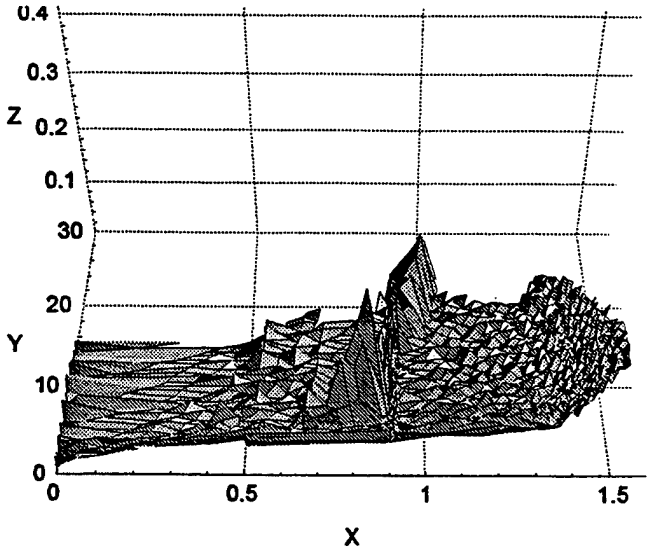

Fig. 5. Set of CRFFO I-V characteristics with detector 2 output signal shown in Z coordinate. Flux-flow is directed towards detector 2. X coordinate is CRFFO bias voltage in mV. Y-coordinate is CRFFO bias current in mA. Z-coordinate is detector power a.u.

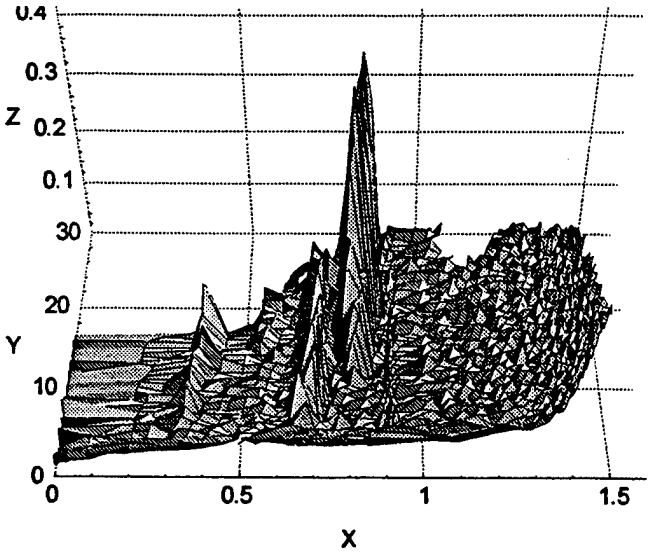

Fig. 6. Set of CRFFO I-V characteristics with detector 2 output signal shown in Z coordinate. Flux-flow is directed from detector 2. X coordinate is CRFFO bias voltage in mV. Y-coordinate is CRFFO bias current in mA. Z-coordinate is detector power a.u.

wave structure is presented in Fig. 3. Fiske steps are clearly visible at voltages below 0.95 mV. The measured I-V characteristics of the CRFFO are presented in Fig. 4. It shows the set of resonances around 0.8 mV bias voltage at different bias currents and magnetic fields. These resonances correspond to the different modes of operation of the CRFFO and confirmes that R_d of the LJJ can be reduced by the slow wave line. It is possible to tune the voltage of the resonances by adjusting the external magnetic field, while the position of Fiske steps in Fig. 3 is fixed.

The CRFFO I-V characteristics with power received by the detector 2 are presented in Fig. 5, 6. In Fig. 5 fluxons are moving towards detector 2. The peak of output power in this figure reperesents a forward wave mode of operation. In Fig. 6 fluxons are moving from detector 2 and a backward wave mode of operation is shown. Both modes can be continuously tuned by changing the bias current and the external magnetic field across the structure. The power scale for both figures is the same.

We conclude that the Cherenkov Flux-Flow Oscillator with microstrip loops type slow wave system has been designed fabricated and measured. The measurement shows induced resonances on the CRFFOs I-V curves with tunable frequency. The positions of resonances and it's magnetic field dependance comfirm the Cherenkov mode of interaction between vortices and electromagnetic waves in the system. Both forward and backward wave type of resonances have been observed by changing the direction of flux-flow. The microwave power of order 0.8 μW has been measured both in the LJJ and in the slow wave system.

Authors would like to thank Willem Luinge, Nick Whyborn, Teun Klapwijk and Sergey Shitov for useful comments and stimulating discussions.

References

[1] S.V. Shitov, A.B. Ermakov, L.V. Filippenko, V.P. Koshelets, A.M. Baryshev, W. Luinge, Jian-Rong Gao, Superconducting Chip Receiver for Imaging Applications, ASC'98 conference, report EMA-09, in press.

[2] V.P. Koshelets, S.V. Shitov, A.V. Shchukin, and L.V. Filippenko, J Mygind, A.V. Ustinov, Self-Pumping Effects and Radiation Linewidth of Josephson Flux-Flow Oscillators,Phys. Rev. B, **56**, 9, p. 5572-5577, (1997).

[3] V.Yu.Belitsky and E.L. Kollberg, Superconducter-insulator-superconductor tunnel strip line: Features and applications, J.Appl.Phys.,**80** (8), 4741-4748, (1996).

[4] V.P. Koshelets, S.V. Shitov, A.V. Shchukin, L.V. Filippenko, P.N. Dmitriev, V.L. Vaks, J. Mygind, A.M. Baryshev, W. Luinge, H. Golstein, Flux-Flow Oscillators for Submm vawe Integrated Receivers, ASC'98 conference, report EQB-04, in press.

[5] Yu.S. Kivshar, B.A. Malomed, Dynamics of fluxons in a system of coupled Josephson junctions, Phys. Rev. B, **37**, 9325-9330, (1988)

[6] R.G. Mints and I.B. Snapiro, Josephson-vortex Cherenkov radiation, Phys. Rev. B, **52**, 9691-9696, (1995)

[7] V.V. Kurin, A.V. Yulin, Radiation of linear waves by solitons in a Josephson transmission line with dispersion, Phis. Rev. B, **55**, 11659-11669, (1997)

[8] S.N. Artemenko, S.V. Remisov, Excitation of plasma waves by moving Josephson vortices in layered superconductors, Sov. Pis'ma v ZhETPh, 66, 12, p. 811, (1997) in russian

[9] V.V. Kurin, A.V. Yulin, I.A. Shereshevsky, N.K. Vdovicheva, Cherenkov radiation of vortices in a two-dimensional annular Josephson junction, Phys. Rev. Lett, **80**, 3372-3375, (1998)

[10] H.S.J. van der Zant and T.P. Orlando, Sh. Watanabe and H. Strognatz, Hirling Modes and Parametric Instabilities in the Discrete Sine-Gordon Equation: Experimental Tests in Josephson Rings, Phys. Rev. Lett., **74**, 379-382, (1995).

[11] E. Goldobin, A. Wallraff, N. Thyssen, A.V. Ustinov, Cherenkov radiation in coupled long Josephson junctions, Phys. Rev. B, **57**, 130-133, (1998)

[12] A.M. Baryshev, A.V. Yulin, V.V. Kurin, V. P. Koshelets, S. V. Shitov, A.V. Shchukin, P.N. Dmitriev, L.V. Filippenko, Design and Fabrication of Cherenkov Flux-Flow Oscillator, ASC'98 conference, in press.

Numerical Simulations of the Current Gain of Fluxonic Josephson Transistors

S. Weiss, J. Schuler, T. Bauch, D. Koelle, R. Gross
II. Physikalisches Institut, Lehrstuhl für Angewandte Physik, Universität zu Köln, Zülpicher Str. 77, 50937 Köln, Germany

Abstract—We used a numerical iteration method for the calculation of the magnetic field dependence of the maximum Josephson current of different types of Josephson vortex flow transistors (JVFT), including Josephson fluxon-antifluxon transistors (JFAT). The method is based on the maximization of the critical current I_c of a parallel array of Josephson junctions as a function of the applied magnetic flux and the bias current configuration in a self consistent way. The slope of the I_c versus applied flux dependence determines the current gain of the JVFTs and therefore yields important information on their performance. We have calculated the current gain as a function of the number of coupled junctions, the inductance of the array loops and the configuration of the gate line. In addition we show experimental results obtained for JVFTs and JFATs based on YBCO grain boundary Josephson junctions which qualitatively confirm our calculations. In addition, fitting the experimental data allows us to derive the magnetic coupling constant, which is the only free parameter.

I. Introduction

The availability of a superconducting transistor is expected to significantly expand the application range of superconducting electronics. This has stimulated considerable activities towards the development of three-terminal devices based on high transition temperature superconductors. Among the various types which have been investigated, the Josephson vortex flow transistor (JVFT) shows probably the most promising performance [1]-[3]. In JVFTs the density of Josephson vortices in either a long Josephson junction or an array of small junctions is controlled by applying a magnetic field via a control current flowing through a gate line, which is inductively coupled to the junction(s). Hence, the critical current I_c or the voltage V across the junction(s), if biased at $I_b > I_c$, is controlled by the gate current I_g. A figure of merit is the current gain g, which by definition is given by the slope of the resulting $I_c(I_g)$ characteristics in its steepest point. To maximize the gain, various designs have been developed which basically differ in

1. the *type of Josephson junctions*, i.e. whether a parallel array of N short junctions which are coupled by N-1 loops of inductance L [Fig.1(a)] or a single long junction [Fig.1(b)] is used,
2. the *junction geometry*, which determines self-field effects from the bias current I_b, e.g. in the symmetric overlap geometry [Fig.1(b)] or in an asymmetric inline geometry [Fig.1(a)] and
3. the *gate line geometry*, which determines how the gate line is positioned and oriented with respect to the Josephson junction(s).

In particular with respect to point 3 the design of the Josephson fluxon antifluxon transistor (JFAT) [4],[5], as schematically shown in Fig.1(b), has not yet been investigated in detail. In contrast to the JFAT, where the gate current generates fluxons of opposite polarity in the Josephson junction, the device with the "conventional" gate line configuration, as shown in Fig.1(a), is denoted as JVFT.

Optimization of the performance of these transistors requires to predict their $I_c(I_g)$ characteristics. Among the variety of different approaches to solve this problem most techniques are based on directly solving the underlying differential equations by numerical simulation. In very simple cases this can even be done analytically. But as soon as the influence of the self-fields of the bias current has to be taken into account, most of these methods fail, as the solution of the problem essentially determines the boundary conditions.

In contrast to the techniques mentioned above the work presented here uses a more physical approach [6]. We developed an iterative algorithm to numerically calculate the $I_c(I_g)$ characteristics for any type of devices including the JFAT and JVFT gate line configuration. Based on this algorithm we performed simulations on arrays with both JVFT and JFAT gate line configuration to compare the performance of both device concepts for a wide range of parameters. For comparison with our simulation results we

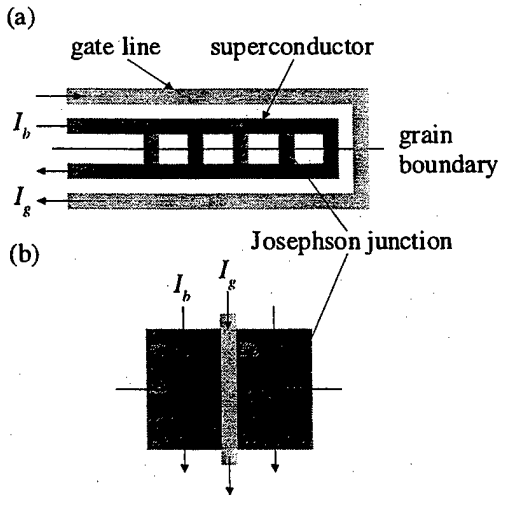

Fig.1: Basic design principles of Josephson vortex flow transistors using bicrystal grain boundary Josephson junctions. (a) asymmetric inline-type array of short Josephson junctions with a JVFT gate line configuration, (b) symmetric overlap-type long junction with a JFAT gate line configuration.

Manuscript received April 30, 1999.
This work was supported by the BMBF (project no. 13N6999).

investigated vortex flow transistors based on $YBa_2Cu_3O_{7-x}$ (YBCO) bicrystal grain boundary junctions which were designed to allow operation in JFAT *and* JVFT geometry.

II. ALGORITHM

Our algorithm calculates the maximum supercurrent, i.e. the critical current I_c, through a network as the one depicted in Fig.2 for N=5 Josephson junctions. Each junction is described by the first Josephson equation

$$I_j(n) = I_c^J \cdot \sin \varphi(n) , \qquad (1)$$

where n = 1, ..., N is the index of the junction, I_c^J is the critical current of a single junction and $\varphi(n)$ is the gauge-invariant phase difference across junction n. As the algorithm is not designed to simulate the behavior of a vortex flow transistor at a finite voltage drop, the junctions do not have to be modeled in terms of an RCSJ-model. The phase differences are determined by the magnetic flux penetrating the loops of the network according to

$$\varphi(n) - \varphi(n+1) = 2\pi \Phi / \Phi_0 , \qquad (2)$$

where Φ is the magnetic flux penetrating the loop between the two neighboring junctions n and $n+1$ and Φ_0 is the magnetic flux quantum.

The magnetic flux penetrating each loop of the array is composed of two contributions, the externally applied flux Φ_{ext} and the flux of the self-fields Φ_{self} created by the currents flowing through the array

$$\Phi = \Phi_{ext} + \Phi_{self} . \qquad (3)$$

Here, only the transverse currents $I_t(n)$ directly above and below the n-th loop and the junction currents $I_j(n)$ and $I_j(n+1)$ are assumed to contribute to Φ_{self} and couple magnetic flux into this loop.

The final boundary condition is the current conservation, which applies to each node and which simply states, that

$$I_b(n) = I_t(n) - I_t(n-1) + I_j(n) . \qquad (4)$$

Starting with an initial distribution of the junction currents, the algorithm iteratively calculates the transverse current distribution $I_t(n)$ using (4), the phase differences $\varphi(n)$ using (2), where Φ is calculated from $I_t(n)$ and $I_j(n)$, and finally a new distribution of the junction currents $I_j(n)$, which is used in the next step of the iteration. If at the end of an iteration step the difference between the newly calculated and the junction current distribution of the previous step does not differ (within a given margin), the iteration will be stopped. The final $I_j(n)$-distribution is then a self-consistent solution corresponding to a total supercurrent flowing through the array, which is equal to the sum of all N junction currents. The value of this supercurrent may depend on the choice of the phase difference across an arbitrarily chosen reference junction $\varphi(r)$ in the network, which has to be kept fixed during the iteration process. To find the particular current distribution which gives the maximum value of the supercurrent of the whole array, i.e. the critical current, the iteration process has to be repeated for values of $\varphi(r)$ ranging from 0 to 2π in as small steps as possible.

This algorithm can be applied to both array structures and long Josephson junctions. In the latter case the long junction has to be divided into a sufficiently large number of segments, each segment being typically $10^{-2}\lambda_j$ long (λ_j is the Josephson penetration depth).

The flux induced by the gate current can be taken into account by two possible approaches. On the one hand the magnetic field created by the gate line can be described in terms of the external magnetic flux Φ_{ext}, or on the other hand by using the image current model introduced in [4]. The first approach, which we denote as "direct coupling method", is obvious and can be implemented in the algorithm simply by introducing an effective mutual inductance L_M, which takes into account the interaction of the superconductor and the magnetic field of the gate line (focussing of magnetic flux), and expressing the external magnetic flux as $\Phi_{ext} = L_M \cdot I_g$. However, this method is restricted to fairly simple designs, where the distribution of the magnetic flux is easily calculated. This is the case for the JVFT gate line configuration, where the externally coupled magnetic flux is essentially equal for all loops in an array, or is homogeneously distributed over the entire length of a long junction. In this case the effective mutual inductance L_M is independent of the position n.

The other alternative is based on the Meissner effect. If a superconductor is subjected to a magnetic field, the magnetic flux is (partially) expelled by induced currents. If, as depicted in Fig.3, a gate line is positioned right above a superconducting plate, the induced currents "mirror" the gate

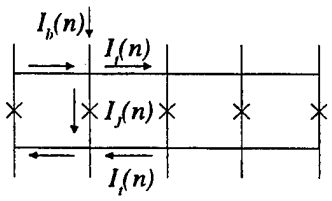

Fig.2: Sketch of Josephson junction network used for the numerical algorithm together with the relevant currents flowing in the network. The crosses mark the Josephson junctions.

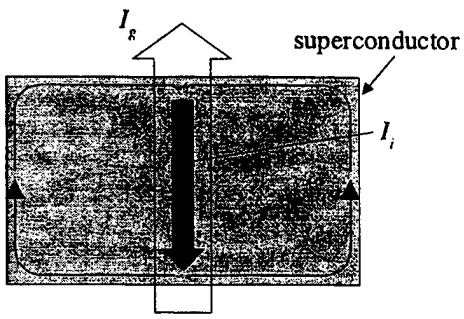

Fig.3: Schematic view of the image current model.

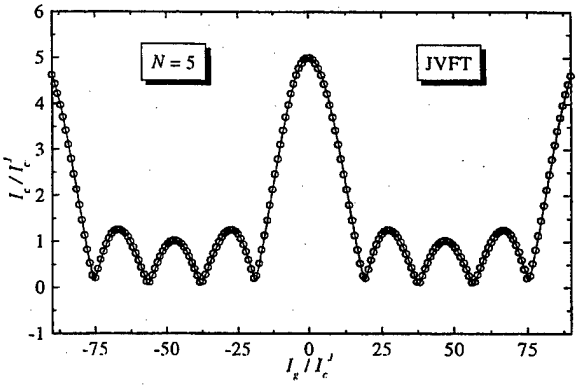

Fig.4: Calculated $I_c(I_g)$ characteristics using the direct coupling method (line) and the image current method (open circles) for an overlap-type JVFT ($k_i = 1$).

current I_g, creating an image current I_i, which is opposite to the gate current, but in most cases smaller in magnitude. Generally the image current satisfies the relation

$$I_i = - k_i \cdot I_g \qquad (5)$$

with a coupling constant k_i ($0 \leq k_i \leq 1$). The image current model can also easily be incorporated into the algorithm presented here.

As the JVFT configuration can be simulated with both, the direct coupling method and the image current method, the validity of the image current method can be verified for this type of device. Our analysis shows, that both methods yield exactly the same results as shown by Fig.4.

Due to the position of the gate line in the JFAT configuration and the interaction of the superconductor with the magnetic field of the gate line the magnetic flux distribution is by far not trivial, so that the method of direct coupling cannot be used for the JFAT gate line configuration.

III. Comparison with Experimental Data

Fig.5 shows a comparison of simulated and measured $I_c(I_g)$ characteristics of an array with three Josephson junctions. This device was fabricated with a cross-type gate line, which allows operation as both, a JFAT [Fig. 5(a)] and a JVFT [Fig. 5(b)]. The device was operated at a temperature of 77K and yields a current gain of g = 0.39 when operated as a JVFT, and of g = 0.64 when operated as a JFAT. Fig. 5 shows that there is good qualitative agreement between the experimental and simulation data demonstrating that the numerical algorithm can be applied to evaluate the performance of fluxonic Josephson transistors with various designs. By fitting the simulated to the experimental data, we can derive the coupling constant k_i. For the JFAT-mode of operation we obtain a coupling constant k_i = 0.49 and for the JVFT-mode a coupling constant of 0.33. We observed for all devices that could be operated in both gate line configurations, that the coupling constant k_i of the JFAT-mode is generally higher than that of the JVFT-mode.

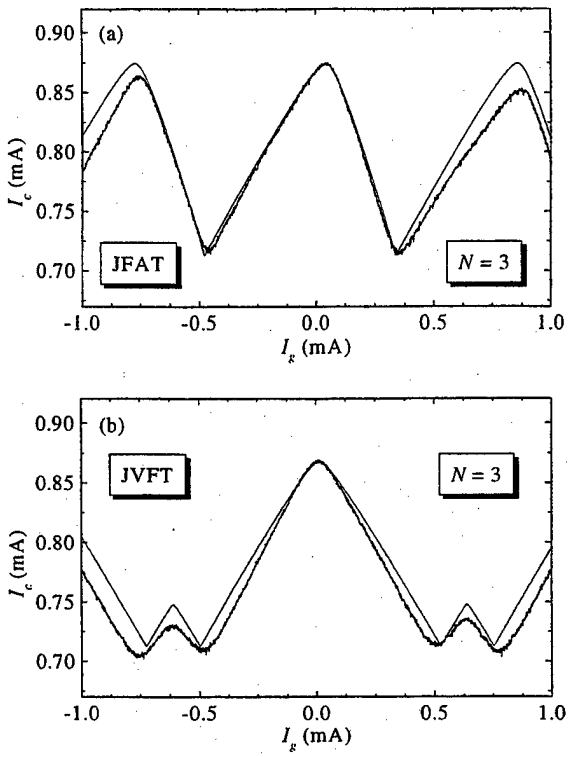

Fig.5: Comparison of calculated and measured $I_c(I_g)$ characteristics at 77K of a JFAT (a) and a JVFT (b).

References

[1] R. Gross, R. Gerdemann, L. Alff, T. Bauch, A. Beck, O.M. Froehlich, D. Koelle and A. Marx, "Physics and performance of high temperature superconducting vortex flow transistors," *Applied Superconductivity*, vol. 3, pp. 443-462, July—October 1995.

[2] D. Koelle, R. Gross, L. Alff, T. Bauch, H. Haensel, A. Marx, S. Weiss, „Physics and performance of high temperature superconducting transistors," in *Extended Abstracts of 6th Int. Superconductive Electronics Conference (ISEC'97)*, H. Koch and S. Knappe, Eds., PTB Berlin 1997, vol. 1, pp.137-139.

[3] R. Gerdemann, T. Bauch, O. M. Froehlich, L. Alff, A. Beck, D. Koelle, and R. Gross, "Asymmetric high temperature superconducting Josephson vortex flow transistors with high current gain", *Appl. Phys. Lett.*, vol. 67, pp. 1010-1012, August 1995.

[4] E.Terzioglu, M. R. Beasley, Y. M. Zhang and S. J. Berkowitz, "Theory of operation of high temperature Josephson fluxon-antifluxon transistor," *J. Appl. Phys.*, vol. 80, pp.5483-5488, November 1996.

[5] S.J. Berkowitz, Y.M. Zhang, W.H. Mallison, K. Char, E. Terzioglu, and M.R. Beasley, "High-temperature superconducting Josephson fluxon-antifluxon transistors," *Appl. Phys. Lett.*, vol. 69, pp. 3257-3259, November 1996.

[6] J. Mannhart, J. Bosch, R. Gross, and R. P. Huebener, "Calculation of the Josephson current distribution in two-dimensional tunnel junctions", *Phys. Lett. A 121*, pp. 241-246 (1987).

Plasma Nature of Superconductor Transition

N. P. Netesova
M.V.Lomonosov Moscow State University. Department of Physics. Russia.

Abstract — A relation between the plasma modes, the forbidden gap, the superconducting gap, and the critical temperature is proved for high temperature superconductor by the electron anharmonic oscillator model.

I. Introduction

In the microscopic theory of Bardeen-Cooper-Schrieffer, the presence of a net attractive interaction between conduction electrons, which would normall repeal each other because of their like electrical charges, is essential to the occurrence of superconductivity. In conventional superconductors this attraction originates in the dynamic motion of the crystal lattice, which leads to an attractive "electron-phonon-electron" interaction. But the appearance of superconductivity in a class of materials quite different from the conventional superconductors, and with extremely high transition temperatures as well, has led physicists [1] to explore a very wide spectrum of possible new pairing mechanisms involving, for example, spin fluctuations, acoustic plasmons, and excitonic processes. There have been several experimental, as well as theoretical studies on plasmons of cuprate superconductors [2-5]. It has largely been accepted that the phonon exchange mechanism, which can yield the transition temperature Tc~30 K within the conventional BCS framework, can not be responsible for superconductivity at and above 90 K in copper oxide materials. It is shown that only the plasmons play a dominat role in producing high superconucting transition temperatures in cuprate superconductors.

In this paper the connection of the plasma modes with the forbidden gap, the superconducting gap, and the phase transition temperature is considered by the electron anharmonic oscillator model. The role of the plasma oscillations in the process of the phase transition has been proved.

II. Anharmonic oscillator model

At temperatures below T_c , a superconductor consists of paired as well as unpaired electrons which can be described in terms of a two-fluid model within the Fermi-liquid hypothesis. The superconducting state is characterised principally by three energetic parameters. Those parameters are the superconducting energy gap at zero temperature $E_d(0)$, the plasma energy E_{ms} , and the critical temperature T_c. This theoretical approach allows to propose the diagram of plasma energy – temperature for superconductor. The phase superconducting transition curve indicates the dependence electron density of the critical temperature. The plasma modes are determined by the effective electron density. The Fermy energy E_f is the temperature oscillator energy in the phase transition point

$$E_f = 1.5\, kT_c \ ,$$

$$E_f = [(3\pi^2)^{2/3} / 2](\hbar^2/m)\, N_e^{2/3},$$

$$\log N_e = 15.835 + 1.5 \log T_c \ ,$$

$$\log E_{ms} = 0.75 \log T_c - 2.513, \qquad (1)$$

where, m, N_e are electronic mass and density, $\hbar$ is Planck constant, k is Boltzmann constant. The connection between the plasma energy and the transition temperature is accounted for the electron oscillator model.

In case of the polyoscillator model the equations of complex dielectric function ε are assumed

$$\varepsilon = 1 + \sum_k \omega_{pk}^2 / (\omega_{ck}^2 - \omega^2 + 2\imath\gamma_k\omega), \qquad (2)$$

$$\omega_{pk}^2 = (4\pi e_k^2 / m_k)\, N_{ek}\, (f_k / \theta_k),$$

where e_k , m_k , N_{ek} , f_k , θ_k , γ_k , ω_{ck} , ω_{pk} are electronic charge, mass and density, oscillation force, the interaction parameter, the radiant friction coefficient, effective natural and plasma frequencies of the k oscillator mode. The summation is produced with respect over all k values. Each effective frequency is consistent with its absorption band near by which the absorption coefficient shows anomalous variations. For anharmonic bioscillator model, dielectric function (2) is given by

$$\omega_{p1}^2 / [\omega_{c1}^2 - 4\gamma_1^2] + \omega_{p2}^2 / [\omega_{c2}^2 - 4\gamma_2^2] = C_- / (T_c - T), \qquad (3)$$

where $T<T_c$, C_- is constant in the vicinity of a superconducting transition temperature point T_c , ω_{p1} , ω_{c1} are the superconducting plasma and coupling frequencies, ω_{p2} , ω_{c2} are effective natural and plasma frequencies of the forbidden gap oscillator mode, γ_1 , γ_2 are the radiant friction coefficients of the superconducting and forbidden gaps, accordingly. Let us consider the mode being responsible for the superconducting band $E_d = \hbar\omega_d$,

$$[\omega_{c1}^2 - 4\gamma_1^2] / \omega_{p1}^2 = (1 - T/T_c) / [b^2 - z^2(1 - T/T_c)], \qquad (4)$$

where are $z^2 = \omega_{p2}^2 / [\omega_{c2}^2 - 4\gamma_2^2]$, $b^2 = C_- / T_c$.

For $T=T_c$, (4) is $\omega_{c1}=2\gamma_1$, for $T=0$, (4) is given by

$$[\omega_{c1}^2-4\gamma_1^2]=\omega_{p1}^2/[b^2-z^2]. \quad (5)$$

The superconducting gap ratio is

$$\hbar\omega_d/kT_c=\hbar\omega_{ms}/[kT_c(b_m^2-z^2)^{1/2}], \quad (6)$$

where b_m is parameter.

For one oscillator anharmonic model, dielectric function is given by

$$\omega_{p1}^2/[\omega_{c1}^2-4\gamma_1^2]=C_-/(T_c-T), \quad (7)$$

The superconducting gap ratio is

$$\hbar\omega_d/kT_c=\hbar\omega_{ms}/[b_m kT_c]. \quad (8)$$

It is necessary to investigate the conditions for $T>T_c$

$$\omega_{p1}^2/[\omega_{c1}^2-4\gamma_1^2]+\omega_{p2}^2/[\omega_{c2}^2-4\gamma_2^2]=C_+/(T-T_c), \quad (9)$$

$$\omega_{p1}^2/[\omega_{c1}^2-4\gamma_1^2]=C_+/T-\omega_{p2}^2/[\omega_{c2}^2-4\gamma_2^2]+(C_+/T)T_c/T, \quad (10)$$

$$\omega_{p1}^2/[\omega_{c1}^2-4\gamma_1^2]=\delta^2+2(T_c/T), \quad (11)$$

$$\delta^2=C_+/T-\omega_{p2}^2/[\omega_{c2}^2-4\gamma_2^2],$$

where C_+ is parameter, T =constant$>T_c$, $\hbar\omega_{c1}$ is electron classical liquid bond energy.

For $T>T_c$, the forbidden gap ω_{g+} is given by

$$[\omega_{c2}^2-\omega_{g+}^2]/\omega_{p2}^2=(T/T_c-1)/[2b^2-z_1^2(T/T_c-1)], \quad (12)$$

$$\omega_{g+}^2=\omega_{c2}^2-\omega_{p2}^2[T/T_c-1]/[2b^2-z_1^2(T/T_c-1)], \quad (13)$$

where are $z_1^2=\omega_{p1}^2/[\omega_{c1}^2-\omega_g^2]$, $2b^2=C_+/T_c$.

For $T<T_c$ the forbidden gap ω_{g-} is given by

$$\omega_{g-}^2=\omega_{c2}^2-\omega_{p2}^2[1-T/T_c]/[b^2-z_1^2(1-T/T_c)]. \quad (14)$$

For $T=T_c$, the forbidden gap is

$$\omega_{g+}^2=\omega_{g-}^2=\omega_{c2}^2.$$

For $T=0$, the difference between (13) and (14) is

$$\omega_{g+}^2-\omega_{g-}^2=3b^2\omega_{p2}^2/[(2b^2+z_1^2)(b^2-z_1^2)],$$

$$\omega_{g+}^2-\omega_{g-}^2\approx 1.5\,\omega_{p2}^2/b^2. \quad (15)$$

With the decrease of temperature, the forbidden gap is increased. Below the transition temperature, the devitation from straight takes place.

III. Results and Discussion

There have traditionally been two direct methods for measuring the energy gap in superconductors: tunneling and infrared techniques. Tunneling spectroscopy has been important to the study of superconductivity, providing a direct measurement of the superconducting energy gap [6]. It is necessary to compare the superconducting energy ratios with the direct tunneling measurements for Hg and other high-T_c cuprates. The superconducting energy ratio results are given in table I. The plasma energies E_{ms} are counted up (1). Tunneling measurements showed the superconducting energy gaps in the range $E_d/kT_c\approx 7.6\div 13$ [6] and a factor 2 larger than the infrared measurements [7]. The differences are explained by the different measuring fields.

TABLE I
THE SUPERCONDUCTING RATIOS FOR HIGH-T_c CUPRATES

	[6]		Our calculations			
HTSCs	T_c	E_d/kT_c	kT_c	E_{ms}	E_{ms}/kT_c	$b_m^2-z^2$
HgBaCaCuO -1223	135	13	0.0116	0.1215	10.5	0.6
HgBaCaCuO -1212	123	9.5	0.0106	0.1134	10.7	1.2
HgBaCaCuO - 1201	97	7.9	0.0084	0.0949	11.3	2.0
YBaCuO -1237	88.56	7.6	0.0076	0.0886	11.7	2.3
BiSrCaCuO -22128	86.36	8.6	0.0074	0.0869	11.7	2.0

The differences between the infrared measurements on the thin film and polycrystalline samples [8] are explained by the different local coefficients b.

The dielectric function is tensor. Then the superconducting energy gap, the plasma energy are tensor functions. The superconducting energy gap depends on symmetry, anisotropy, stoihiometry, impurites, and the measuring conditions.

The electron anharmonic oscillator model is described the cases of weak and strong bonds. The plasma frequency ω_{pv} is calculated by

$$\omega_{pv}^2=(4\pi e^2/m)Ns,$$

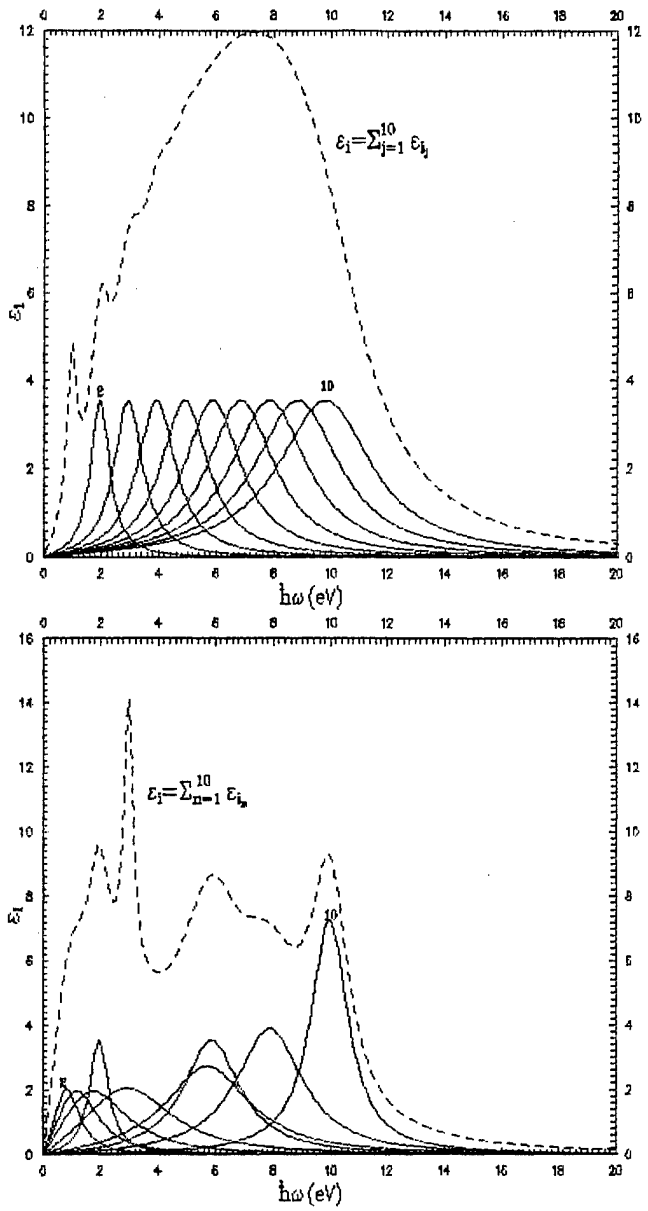

Fig. 1. The imaginary part of dielectric function for ten oscillator model for different bonds.

where N is molecular density, s is valency electron number per molecule .The plasma frequency ω_L is determined by the electron loss function L, and corrected one ω_m is determined by the corrected electron loss function E·L

$$L = \mathrm{Im}(-1/\varepsilon) = \varepsilon_i / [\varepsilon_r^2 + \varepsilon_i^2].$$

The electron bond strength (fig.1) is equal ω_m^2 / ω_L^2. In table II the electron loss results for superconductors are given . The parameter z^2 depends on ω_m^2 / ω_L^2.

TABLE II
OSCILLATOR PARAMETERS OF SUPERCONDUCTORS

SC	T_c(K)	ω_L(eV)	ω_m(eV)	ω_m^2 / ω_L^2
Al	1.14	15.8	15.8	1
$YBa_2Cu_3O_7$	89	16.0	27.5	3.0
$YBa_2Cu_4O_8$	74	16.6	26.8	2.6

Among the most debatable questions on HTSCs, there is the question about the so called pseudogap which is experimentally observed in normal state samples with lowered carrier density. The charge transfer gap is observed in $YBa_2Cu_3O_6$ near 1.7 eV, while in $YBa_2Cu_3O_7$ it is not clear whether this gap still exists [9]. The superconducting gap and the normal state gap are in fact of different nature [10]. The forbidden gap decreases with rising temperature from 2.1 eV (0K) to 1.7 eV for T=293 K . It is accorded with the electron anharmonic oscillator model.

As follows from (11), the transition temperature increases for T=const>T_c with the plasma frequency for superconductors. These conclusions are completely borne out by measurements [4] the plasma reflectivity spectra of YBaCuO-123y for various oxygen content y and the room temperature.

REFERENCES

[1] V.Daniel Hunt. *Superconductivity. Sourcebook.* N-Y.1989.

[2] Ivan Bozovic, "Plasmons in cuprate superconductors," *Physical Review B*, Vol. 42, N.4, pp. 1969-1984, 1990.

[3] A.C.Sharma, Ina Kulshrestha, "Plasmons below T_c in cuprate superconductors," *Physica C*, Vol. 228, pp. 254-258, 1994.

[4] S. Tajima, T. Nakchashi, S. Uchida, S.Tanaka,"Correlation between plasma frequency and superconducting transition temperature," *Physica C*, vol. 156, N.1, pp. 90-96, 1988.

[5] M. Knupfer, G. Roth, J. Fink, J. Karpinski, E. Kaldis, "Plasmon dispersion and the dielectric function in $YBa_2Cu_4O_8$ single crystals," *Physica C*, Vol. 230, N. 1-2, pp. 121-127, 1994.

[6] J.Y.T.Wei,C.C.Tsuei, P.J.M.Van Bentum, Q.Xiong,C.W.Chu,M.K. Wu, "Quasiparticle tunneling spectra of the high-T_c mercury cuprates:Implications of the d-wave two-dimensional Van Hove scenario," *Physical Review B*, Vol. 57, N.6, pp. 3650-3662, 1998.

[7] J.R.Kirtley, R.T.Collins, Z.Schlesinger, W.J.Gallagher, R.L.Sandstrom, T.R.Dinger, D.A.Chance, "Tunneling and infrared measurements of the energy gap in the high-critical-temperature superconductor Y-Ba-Cu-O," *Physical Review B*, Vol. 35, N.16, pp. 8846-8849, 1987.

[8] R.T.Collins, Z.Schlesinger, R.H.Koch, R.B.Laibowitz, T.S.Plaskett, P.Freitas, W.J.Gallagher, R.L.Sandstrom, T.R.Dinger,"Comparative study of superconducting energy gaps in oriented films and polycrystalline bulk samples of Y-Ba-Cu-O," *Physical Review Letters*, Vol.59, N. 6, pp.704-707, 1987.

[9] H.Romberg, N.Nucker, J.Fink, Th.Wolf, X.X.Xi, B.Koch, H.P.Geserich, M.Durrler, W.Assmus, B.Gegenheimer, "Dielectric function of $YBa_2Cu_3O_{7-\delta}$ between 50 meV and 50 eV,"*Z.Phys.B.*,Vol.78, N.3, pp.367-380, 1990.

[10] G.J.Kaye, "Interpretation of the ARPES normal state gap in cuprate superconductors from a mixed boson-fermion model," *Physica C*, Vol. 296, pp. 281-297, 1998.

Dynamic Properties of Asymmetric Discrete Vortex-flow Transistors

B. A. Davidson, V. Granata, E. Sarnelli and S. Pagano
Istituto di Cibernetica - CNR, via Toiano 6, 80072 Arco Felice (NA), Italy

Abstract—The dynamic properties of discrete vortex-flow transistors (DVFTs) comprised of a parallel array of 10 Josephson junctions with asymmetric bias-current configurations have been studied numerically. Using parameters typical of high-temperature superconductor junctions at liquid-nitrogen temperatures, we show explicitly that the asymmetric-inline geometry, while it has the advantage of large (low-frequency) current gain (of order 50) and peak transresistance (of order 10 Ω), is inherently limited by slow vortex transit times (of order 100 ps) which result from the absence of Lorentz forces on vortices moving in the structure. We also explain the extremely small dynamic range of the high-gain regime seen in the simulations here and observed experimentally in the literature. As the device symmetry is increased, faster transit times and a significant increase in dynamic range are observed. These results have direct impact on the feasibility of these devices as high-frequency amplifiers.

I. Introduction

Vortex-flow transistors (VFTs) fabricated in the high-temperature superconductors (HTS) have attracted attention as potential high-frequency amplifying devices, for example, in all-superconducting microwave circuits. Devices fabricated in low-temperature superconductors have used continuous long junctions ($L/\lambda_J > 4$, with L the junction length and λ_J the Josephson penetration depth) (for a review, see [1]). VFTs can also be based on discrete junctions constructed of a parallel array of (short) junctions joined by an inductance L_s and characterized by a penetration length per cell $\Lambda_J = \sqrt{L_J / L_s} \leq 1$ (with $L_J = \phi_0 / 2\pi I_{cJ}$ the junction inductance, ϕ_0 the flux quantum and I_{cJ} the junction critical current) [2]. One possible advantage of discrete structures is increased device output voltage $\overline{V}$, transresistance $r_m \equiv \partial \overline{V} / \partial I_g$ (with I_g the gate current) and output resistance $r_o \equiv \partial \overline{V} / \partial I$ (with I the bias current). The low-frequency characteristics of a symmetric-bias, four-terminal device using 0.5 KA/cm^2 Nb junctions showed a current gain $G \equiv \partial I_c / \partial I_g \approx 1.2$ (with I_c the device critical current), maximum output voltage $\overline{V}_{\max} \approx 150\,\mu\text{V}$, $r_m \approx 0.4\ \Omega$, and $r_o \approx 0.55\ \Omega$ at 4.2 K [2] and a model was presented to accurately describe the device behavior. Device characteristics improve as the individual junction critical voltage $V_{cJ} \equiv I_{cJ} R_{nJ}$ increases (with R_{nJ} the normal resistance).

Early implementations of continuous and discrete VFTs in HTS with symmetric bias geometries showed $G \leq 2$ and peak $r_m \leq 5\ \Omega$ [3]. Subsequently, attempts to increase G by asymmetric biasing resulted in values of G and peak r_m up to 30 and several Ohms, respectively, for discrete devices between 60-70 K [4], [5] and 5-8 and 5 Ω for continuous devices at 4 K [6]. One significant drawback of discrete asymmetric devices has been the small dynamic range which invariably characterized the high-gain regime (typically $\Delta I_g \leq 10\,\mu\text{A}$ and $\overline{V}_{\max} \leq 25\,\mu\text{V}$) [4], [7]. For example, this seriously limits fan-out capability [8]. These low-frequency measurements gave no information about high-frequency response, origin of the limited dynamic range and whether this limit was fundamentally related to the device geometry.

In this article we explain the origin of the small dynamic range and small output voltage in asymmetric-inline DVFTs through a study of vortex dynamics in the high-gain regime. Using a three-terminal implementation of the inline geometry in which the degree of bias asymmetry is systematically varied, the volt-ampere [$\overline{V}(I)$] curves were calculated in the high-gain regime, yielding the trans- and output resistances and maximum output voltage. Then the vortex dynamics were identified which explain the change in device characteristics as the asymmetry is varied. We find that, for asymmetric bias, high gain (a static property) is intrinsically related to a small dynamic range via two dynamic mechanisms: first, a slow vortex transit time across the structure, and second, impeded vortex nucleation at the array edge until the previous vortex has exited the structure. The former is due to the lack of the Lorentz force on vortices in the unbiased part of the array, while the latter is a consequence of the stability of the static vortex configuration.

Manuscript received May 17, 1999.
This work was supported in part by NSF/NATO grant DGE-9710678.
Email: davidson@fisica.cib.na.cnr.it

As the bias symmetry is increased, the vortex transit time decreases and multiple vortices can be in transit simultaneously, significantly increasing the dynamic range, output resistance and output voltage. This highlights the trade-off between gain on one hand and dynamic range and response time on the other that limits DVFT performance.

II. Device Geometry and Numerical Results

The three-terminal device studied here is constructed from an $N=10$ junction transmission line, shown schematically in Figs. 1(a)-(b). All individual junctions have identical I_{cJ}, R_{nJ} and $C=0$ and follow the RSJ model [9]. The device normal resistance $r_{eq} \equiv r_{nJ}/N$ is the parallel equivalent resistance of the junctions. The holes are represented by a loop inductance L_s. The bias current symmetry is determined by the number of junctions biased, starting at one edge. One resistor yields a distribution corresponding to the standard asymmetric-inline geometry, while 10 resistors corresponds to the overlap (symmetric) geometry. The gate current is injected along the lower electrode. In this study the discreteness parameter $\Lambda_J \equiv 0.6$, its optimized value for the symmetric geometry [2], [4].

To illustrate the nature of the vortex dynamics studied here, Fig. 1(c)-(d) show the different vortex "flows" for the asymmetric and symmetric geometries biased in their high-gain regimes (defined below). In the simulations, a vortex is observed as a 2π phase shift around a loop; monitoring the phase differences of all loops in time allows tracking of

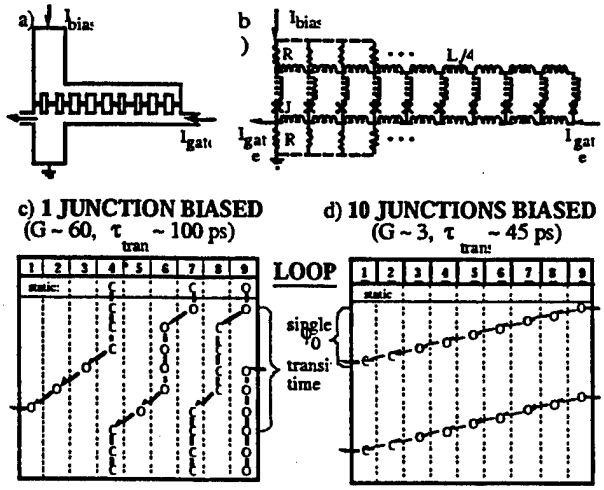

Fig. 1 Davidson et a

Fig. 1.(a) Physical layout of the planar 3-terminal DVFT with 2 junctions biased, and (b) equivalent circuit; resistors $R >> R_{nJ}$ distribute the bias current as desired. (c)-(d) Vortex dynamics in the high-gain regime for 1 and 10 junctions biased, showing transit of single vortices.

vortices in the array. Biased slightly above I_c, the simulations show that the device's instantaneous voltage consists of distinctly separated pulses [10]. The time integral of each voltage pulse equals one ϕ_0, representing the passage of one vortex. The pulse width can be correlated to the vortex transit time τ_{trans}, and the pulse period T is determined by the time between vortex nucleation. The time-averaged voltage is then $\overline{V} = \phi_0 / T$. For asymmetric bias (Fig. 1(c)), the static vortex configuration (just below I_c) consists of three antivortices in the array; slightly above I_c, the pulse corresponds to the entrance of one vortex which eventually expels another at the opposite side. For typical high-T_c junction parameters (discussed below) this time ≈ 100 ps. For symmetric bias (Fig. 1(d)), the pulse results from the nucleation and transit of a single vortex in half the time (≈ 45 ps). Monitoring the instantaneous voltage in time, we see that an increase in average voltage (by increasing bias or gate currents) is due only to an increase in the nucleation rate, i.e., τ_{trans} is constant for a given bias geometry.

The behavior of I_c as a function of I_g [$I_c(I_g)$] is shown in Fig. 2(a)-(d) (insets) for various degrees of bias asymmetry. The currents have been normalized to the single junction critical current I_{cJ} (the maximum device $I_c = 10 I_{cJ}$ occurs for uniform bias). The derivative of $I_c(I_g)$ is the current gain G. The high-G region is defined as the steepest part of the main lobe. For asymmetric bias the maximum $G \approx 60$, decreasing to $G \approx 3$ for symmetric bias. The normalized zero-temperature $\overline{V}(I)$ curves in the high-G regime are also given in Fig. 2. In the asymmetric case, the $\overline{V}(I)$ curves are not RSJ in shape (region B of Fig. 2(a)), with the most striking feature being the restriction of the output voltage to small values $\overline{V}_{\max} \sim 0.05\, V_{cJ}$. As bias symmetry increases, the $\overline{V}(I)$ curves approach RSJ model and $\overline{V}_{\max}$ increases an order of magnitude ($\overline{V}_{\max} \sim 0.5\, V_{cJ}$, Fig. 2(d)). Because the $\overline{V}(I)$ curves obey the RSJ model, the analysis of Ref. [2] describes well the symmetric device's behavior (e.g., $G \propto N/\Lambda_J$ and $r_m \approx G r_o/2$ for $I_c << I_c^{\max}$).

To understand possible correlations between G and r_m for asymmetric bias, these are plotted together as a function of I_g in Fig. 3. In the asymmetric-inline geometry G is not constant in the high-gain region (instead it increases linearly), while the symmetric case has a large range of nearly constant G. In contrast, for both geometries r_m peaks

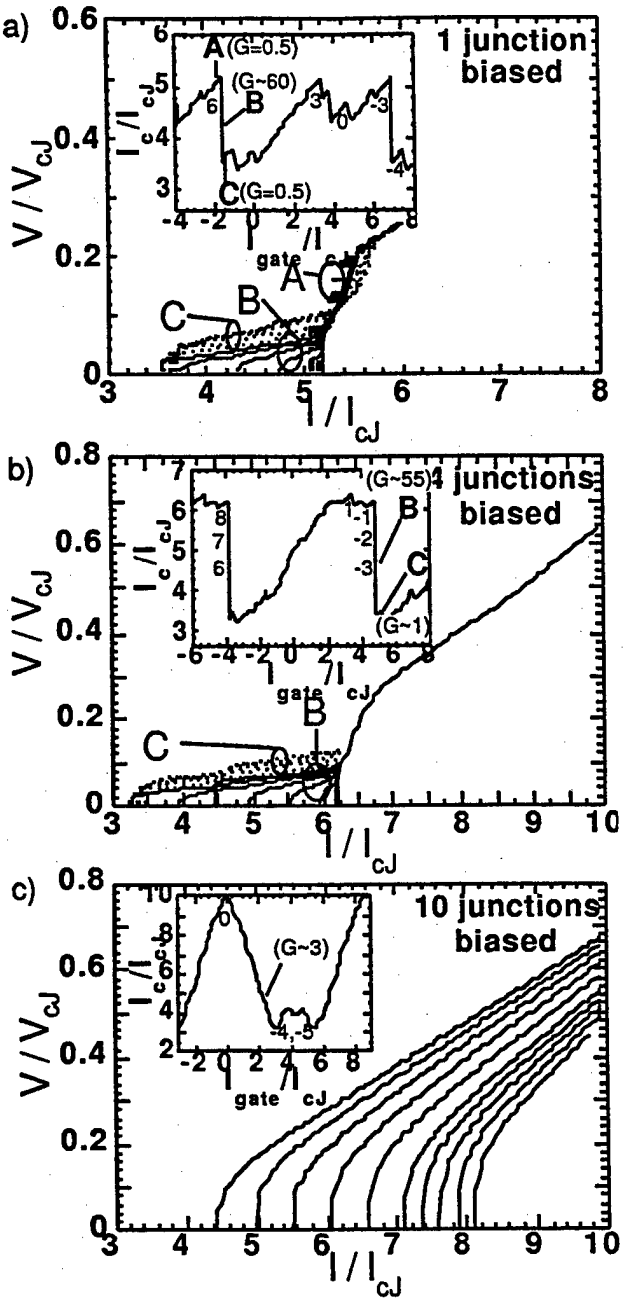

Fig. 2.(a)-(c) Device $\bar{V}(I)$ characteristics for differing bias asymmetries (1, 4, and 10 junctions biased) in the high-G regime. Insets show $I_c(I_g)$, indicating the number of vortices stably trapped in the array below I_c.

sharply, then quickly approaches r_{eq}. This peak ($r_m / r_{nJ} \approx 10$) is a consequence of the divergence of $\partial\bar{V}/\partial I$ at I_c and is nearly identical for the high- and low-gain sides of the $I_c(I_g)$ lobes, regardless of the bias asymmetry or G. Using individual junction parameters typical of high-J_c junctions at 77 K ($I_{cJ} \approx 200\,\mu A$, $R_{nJ} \approx 1\,\Omega$), this peak

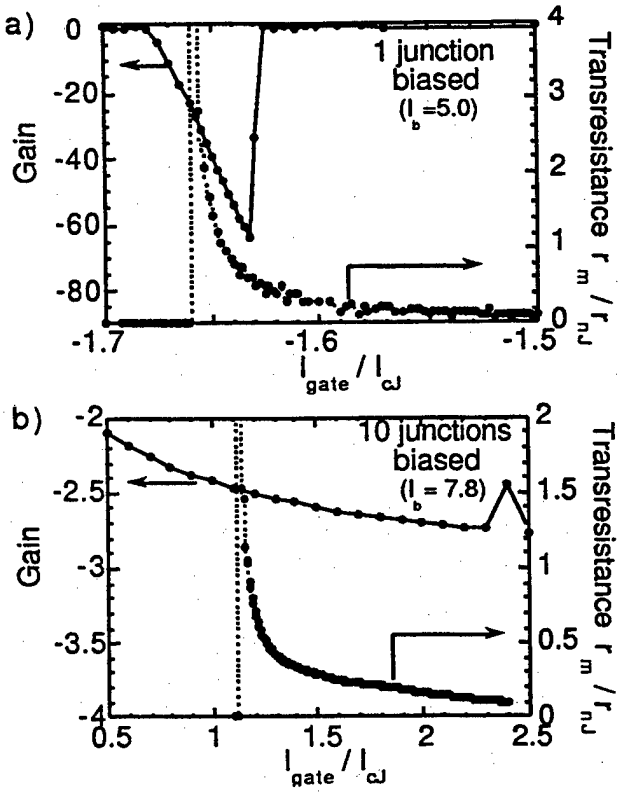

Fig. 3. Gain and normalized transresistance (biased at $I = 0.95 I_c^{max}$) around the high-gain regime for (a) 1 and (b) 10 junctions biased.

width is $\Delta I_g \leq 5\,\mu A$ FWHM. The position of the peak can be located in the highest-G region (adjusting the bias), but it is highly nonlinear and the resulting dynamic range is small. Realistically, a usable dynamic range can be defined as the range of I_g over which G and r_m are constant, for example, to within $\pm 15\%$. This gives a range $\Delta I_g \approx 2\mu A$ (asymmetric) and $100\mu A$ (symmetric case).

Because the behavior of r_m is independent of gain and bias asymmetry, from the definitions of r_m and G it follows that the product $\bar{V}_{max} \cdot G \approx$ constant (to within a factor of ~3). Thus increasing the gain with asymmetric bias results in a corresponding decrease in $\bar{V}_{max}$. To understand the origin of this relationship, the dynamic behavior of vortices studied in the high-G region. Fixing the bias current at $0.95 I_c^{max}$, the transit time τ_{trans} and nucleation period T corresponding to single-ϕ_0 pulses were measured as a function of I_g and are plotted in Fig. 4. The simulations show that the transit time is constant for each geometry, decreasing from $\sim 65\, t_J$ (asymmetric) to $\sim 30\, t_J$ (symmetric case). Here $t_J \equiv \phi_0 / 2\pi V_{cJ}$ is the junction relaxation time [11], typically $t_J \approx 1.6$ ps for $V_{cJ} = 200\,\mu V$.

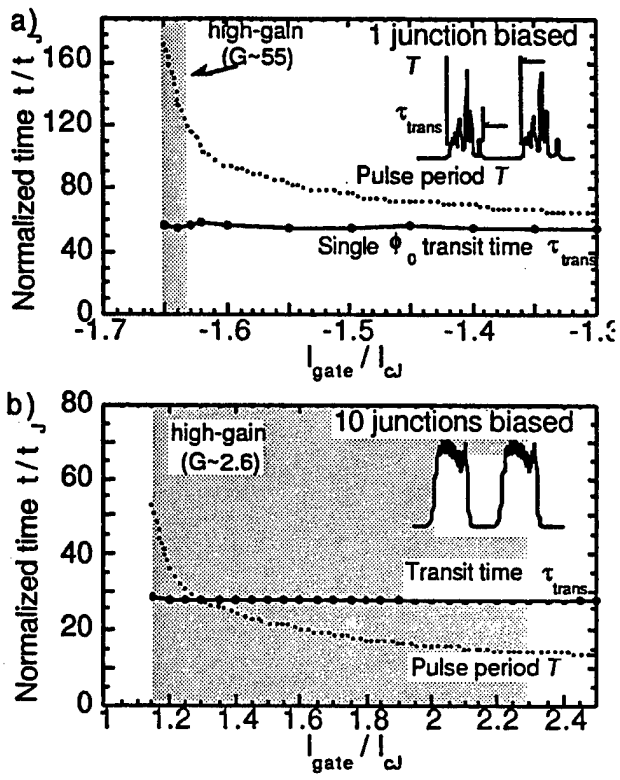

Fig. 4. Single-ϕ_0 transit time τ_{trans} and period T between vortex nucleation events as a function of I_g for (a) 1 and (b) 10 junctions biased.

For sufficiently asymmetric bias, we observe that $\tau_{trans} < T$ in the high-G regime (i.e., single-ϕ_0 pulses do not overlap). In contrast, with increasing bias symmetry, additional vortices can enter while others are in transit ($T < \tau_{trans}$). For 10 junctions biased, up to $2.2\phi_0$ (on average) can be propagating in the array. We note that the time between vortex nucleation observed here for uniform bias is quantitatively consistent with the minimum time that separates two vortices propagating on a discrete overdamped Josephson transmission line which is limited by mutual vortex repulsion [12]. Vortex motion under asymmetric bias is driven by both the bias current on the left part of the array and vortex repulsion on the right. The simulations show that the resulting maximum (average) voltage is limited in this case because 1) vortex motion from repulsive forces is inherently slow and 2) only one additional vortex (beyond the static configuration) can be present in the array at any given time. Thus, for asymmetric bias the nucleation period has a lower limit of τ_{trans}, determining $\bar{V}_{max} \approx \phi_0/105$ ps $\approx 20\,\mu$V ($\bar{V}_{max}$ in the high-G region is half this value). For symmetric bias, the additional Lorentz force and superposition of vortices give $\bar{V}_{max} \approx 2.2\phi_0/45$ ps $\approx 95\,\mu$V.

The above discussion highlights a fundamental limitation of the use of vortex flow in these structures for amplification: it is the *period* of the voltage pulses that is modulated by the gate current, thus the amplification is parametric in nature [11]. For asymmetric geometries, the limiting "response" time of the device should then be the pulse period, not the transit time, since r_m depends on the time-averaged $\bar{V}$ generated by the passage of single vortices. As seen in Fig. 4(a), in the high-G region of the asymmetric device, the small voltage corresponds to a long period (≈ 200 ps). Furthermore, because this device functions as a current-controlled voltage source, r_m is the crucial device parameter (not necessarily G) since in the small-signal model the available power gain is proportional to $r_m^2/r_o r_i$, with r_i the circuit input resistance [13]. Increasing G by asymmetric bias not only reduces $\bar{V}_{max}$ and the dynamic range but also slows the response time, leaving r_m basically unchanged.

We have shown that asymmetric-inline DVFTs are limited to response times ≥ 100 ps and output voltages $\approx 10-20\mu$V when implemented with typical high-J_c HTS junctions near 77 K. Increases in operation frequency, dynamic range and output voltage are observed as bias symmetry increases.

REFERENCES

[1]. J. E. Nordman, Super. Sci. Tech. **8**, 681 (1995).

[2]. D. Berman, H. S. J. van der Zant, T. P. Orlando, and K. Delin, IEEE Trans.Appl. Supercon. **4**, 161 (1994).

[3]. Y. M. Zhang, D. Winkler, P. A. Nilsson, and T. Claeson, Appl. Phys. Lett. **64**, 1153 (1993); J. S. Satchell et al, IEEE Trans. Appl. Supercon. **3**, 2273 (1993).

[4]. R. Gross, R. Gerdemann, L. Alff, T. Bauch, A. Beck, O. M. Froelich, D. Koelle and A. Marx, Appl. Supercon. **2**, 443 (1995), and references therein; D. Koelle et al, Appl. Phys. Lett. **66**, 640 (1995).

[5]. J.-C. Villagier et al, IEEE Trans. Appl. Supercon. **7**, 2390 (1997).

[6]. H. R. Yi, D. Winkler and T. Claeson, IEEE Trans. Appl. Supercon. **7**, 2623 (1997); S. P. Isaac, E. J. Tarte, A. Moya and M. G. Blamire, Applied Superconductivity, The Netherlands, 30 June - 3 July 1997 (Inst. Phys. Conf. Ser. No. 158), 453.

[7]. T. Bauch et al, IEEE Trans. Appl. Supercon. **7**, 3605 (1997).

[8]. T. Nguyen et al, presented at the Applied Superconductivity Conference, Sept. 9-16, 1998, Palm Springs, CA.

[9]. A. Barone and G. Paterno, *Physics and Applications of the Josephson Effect*, (1982).

[10]. The exact shape of the pulse depends on the voltage probe location; pulses shown in Fig. 4 use the average voltages across all junctions.

[11]. K. K. Likharev, *Dynamics of Josephson Junctions and Circuits* (Gordon and Breach, New York, 1986).

[12]. V. K. Kaplunenko, Appl. Phys. Lett. **66**, 3365 (1995).

[13]. G. K. G. Hohenwarter, J. S. Martens, J. H. Thompson, J. B. Beyer, and J. E. Nordman, IEEE Trans. Mag. **27**, 3297 (1991).

States in the structure of two rings

I.N.Zhilyaev, S.G.Boronin
Institute of Microelectronics Technology, The Russian Academy of Sciences, Chernogolovka, Moscow Region 142432, Russia

Abstract –Jump-like oscillations have been detected in the structure resistance with the variation of magnetic field in the region of superconducting transition. The oscillation period corresponds to a magnetic flux quantum through the ring square. Moreover, a hysteresis is observed, depending on the magnetic field. These observations are supposed to be connected with the redistribution of vortices in the structure. The vortices are located separately in the rings at magnetic fields close to the one corresponding to the flux quantum through the ring square. At other fields they are not located.

I. Introduction

In recent years attempts are being made to create computers on the basis of superconducting structures. To this end, several promising physical phenomena in superconducting structures are studied in order to find an acceptable base. This paper deals with investigations of one of these new phenomena.

II. Experimental

Films under study were evaporated thermally onto a silicon substrate. Ring structures with lines approximately 200 nm wide were patterned by e-beam lithography. Weak links (Al-Al tunnel junctions) were fabricated by oxidation of aluminum in a single vacuum cycle, using a two-angle deposition-oxidation-deposition cycle [1]: the first layer 50 nm thick was evaporated, then tunnel junctions were formed by oxidation and, finally, the second 80 nm thick layer was evaporated at a different angle. The time of oxidation was 6 minutes at the pressure 0.1 mbar. A SEM picture of one of the structures is shown in Fig.1. The measurements were carried out on several structures with identical geometry, prepared in the same conditions, in a helium cryostat with the evacuation of He4. Typical resistances of the structure were approximately a few tens of kilohms. We present here the results of measurements of one typical structure.

III. Results

Fig. 2 presents the measurements of resistance R vs temperature for the structure whose SEM micrograph and drawing are given in Fig.1. The resistance is seen to increase as the temperature decreases in the region of superconducting transition in aluminum. This nonusual dependence can be explaned by the coulomb blockade arising in a structure consisting of several succesive tunnel junctions and passing to the superconducting state (see the discussion in [2]). The coulomb blockade mechanism must operate in our structure because the capacity of tunnel junctions is of the same order as in those studied in [2] where the coulomb blockade was distinctly observed. We

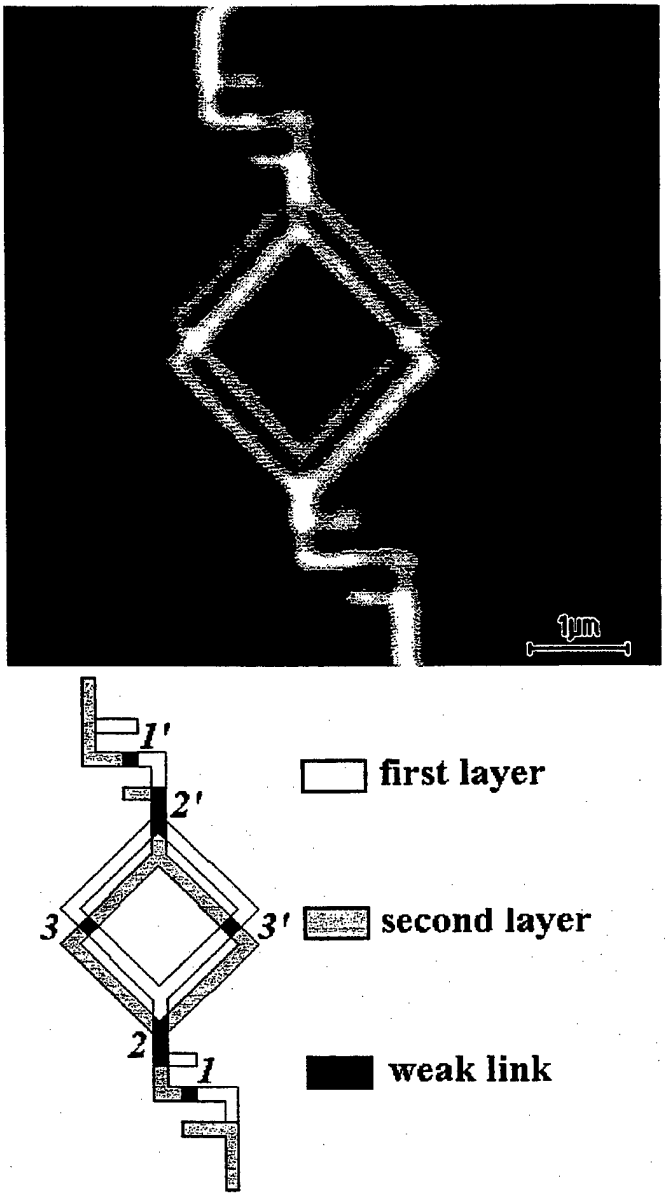

Fig.1 The SEM micrograph of the structure and its schematic drawing.

Manuscript received April 30, 1999.
This work was supported by the Russian Program "Physics of Solid State Nanostructures".

prepared a control structure of the same geometry in the same cycle but without tunnel junctions. The temperature dependence of resistance in this control structure is also displayed in Fig.2. We consider this dependence to be as the start of superconducting transition which is shifted to lower temperatures. All this suggests that our structure with tunnel junctions was measured in the region of superconducting transition.

At the lowest temperatures obtainable in our equipment we detected resistance-dependent jumplike oscillations vs magnetic field H applied perpendicular to the structure (Fig.3). Measurements at negative fields are not shown, but R(H) was found to be a symmetrical function of H, if we do not take into account noise which was 20 nV. It is seen that the resistance of the structure jumps to a higher value with an increase in the magnetic field, then returns to the previous value and so on. The oscillations period corresponds to the superconducting flux quantum Φ_0=hc/2e through the square of each ring. The amplitude decreases with the magnetic field. The oscillation amplitude does not depend on current for currents of the order of 1 nA through the structure, decreases when current increases and disappears at currents around 10 nA. The amplitude deceases very quickly with temperature. When magnetic field decreases a hysteresis is observed. Fig.4 shows the hysteresis for the first two jumps up and down. The jump takes place in the range of H which is not broader than 0.03 Oe at least (this is the magnetic field which our measuring system resolves). The dependence is not connected with the rate of changing of the applied magnetic field. However, the magnetic field at which the jump takes place slightly varied in the experiment. This is casual value and can differ from a certain mean value by 0.2 - 0.3 Oe approximately.

IV. Discussion

We assume that the observations can be explained by the penetration of vortices into the structure of two rings and their redistribution between the rings depending on the applied magnetic field. Now let consider this assumption in greater detail. Suppose the vortices penetrate into the structure as into a box. Junctions 1 and 1' (Fig.1) play the role of walls of the box. In the box, there are two stable and approximately equal positions for vortices: in one ring and in the other. When Φ is close to Φ_0, the vortices in the rings are separated, whereas at $\Phi \neq \Phi_0$ the vortices are connected to form a whole. So, we have two electron states and observe jumps between them. The jumps occur because the configuration of the electron system depends on magnetic field. Let assume the following mechanism of changes of the configuration. The potential energy of a vortex in one and the other rings can be tentatively described as shown in Fig.5. The depths of the pits differ because the thickness of the first (first ring) and the second layer (second ring) differ from each other. In this case tunneling of vortices can occur between the rings owing to the presence of weak links between them (Fig.5a). The situation changes when the value of magnetic field is close to that at which the magnetic flux through each ring is close to Φ_0 =hc/2e. Energy states of the vortices are narrow and do not overlap, which hampers tunneling (Fig.5b). At $\Phi \neq \Phi_0$ our situation is similar to that in a magnetic system in which broadening of the energy level takes places because of the precession of the magnetic moment in applied magnetic field.

We assume that the effect of these states on the resistance of the two- ring structure is analogous to the Little-Parks

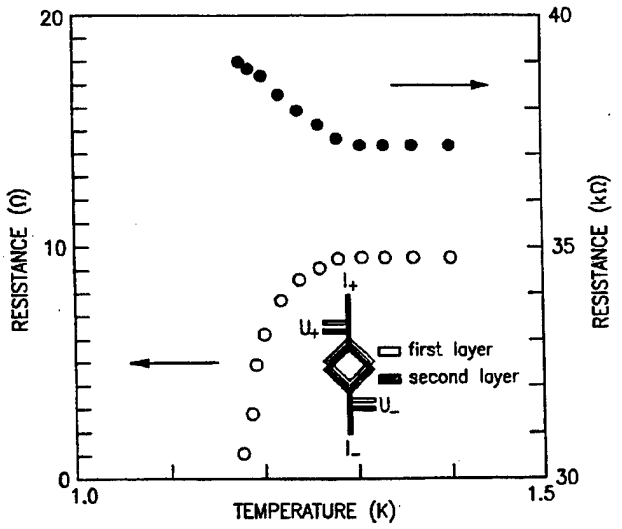

Fig.2 Measured resistance vs temperature in the superconducting region of the structure studied in the present work (upper dependence) and of the control structure of the same size (lower dependence).

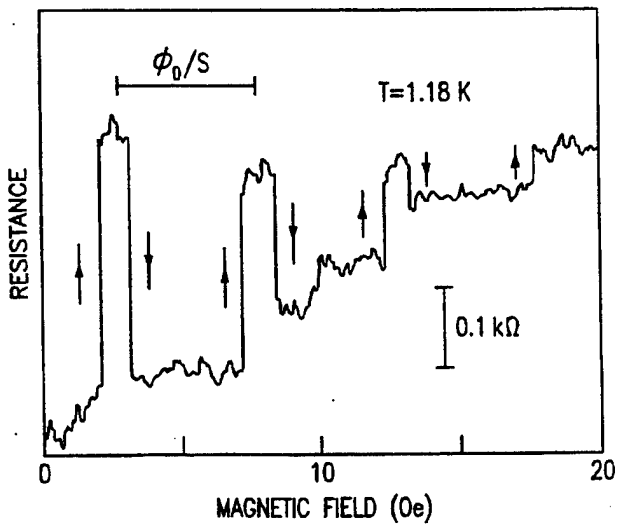

Fig.3 The magnetic field dependence of structure resistance measured at T=1.18K. The current through the structure is 1 nA. Vertical arrows show the directions of jumps (as we suppose) when the magnetic field increases. S is the square of each ring.

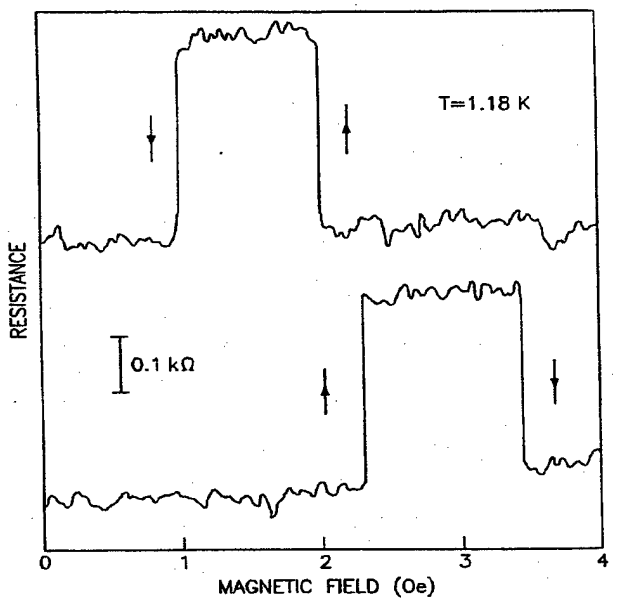

Fig.4. The resistance dependence upon an increased and a decreased magnetic fields (hysteresis) at T = 1.18K.

effect: when a structure is in the $\Phi \neq \Phi_0$ state, its critical temperature is lower than in a state with Φ close to Φ_0.

A large resistance oscillation amplitude is evidently due to the nonlocality effect: oscillations of the structure order parameter influence the state (and resistance) of tunnel junctions [3]. Now, let roughly estimate the maximum amplitude on the basis of the proposed model. The closest to the rings are junctions 2,2'.3,3'. Let their resistances change, while the resistances of junctions 1 and 1' remain unchanged because they are far away from the rings. Take the resistance of junction 1 and 1' equal to r. The structure can be represented as a chain of resistances: resistances 1, 1' are connected succesive by with parallel resistances 2, 2', 3, 3' (Fig.6). The total resistance of this chain is (2+1/8)r. Changing resistances 2, 2', 3, 3' by a value comparable with their values (result of jump) we find a change in the total resistance 1/16. At the total resistance 39 kohm, the maximum changes is 2.2 kohm. This value is approximately 5 times more than the observed one (Fig.3,4). However, this rough estimate is only an estimate of the maximum value. It can be changed by the compensation effect caused by the coulomb blockade whose mechanism gives jumps of the opposite sign.

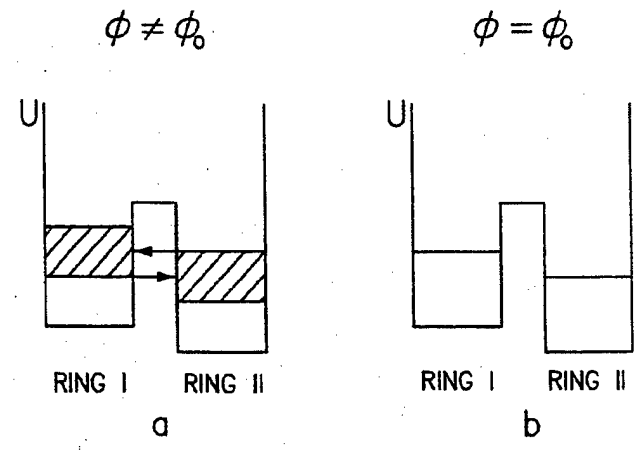

Fig.5. Schematic drawings for the explanation of the effect observed. Ring I - the first layer; ring II - the second layer.

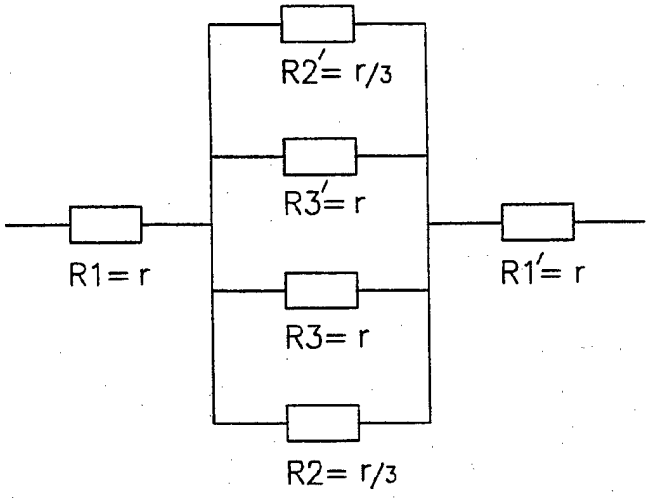

Fig.6. The equivalent resistance scheme of the structure.

V. Conclusion

The investigation of this new phenomenon is of interest from the viewpoint of its application in digital electronic circuits.

Acknowledgment

We are grateful to S. V. Dubonos and L. G. Maistrenko for the assistance in preparing the structures. I.Z. thanks Y. M. Galperin, V. A. Marchenko, A. V. Nikulov and V. A. Tulin for useful discussions of the results.

References

[1] G. Y. Dolan, "Offset masks for lift-off photoprocessing", Appl.Phys.Lett., vol. 31, pp. 337-339, September 1977.

[2] P. Delsing, K. K. Likharev, L. S. Kuzmin and T. Claeson, "Time-correlated single-electron tunneling in one-dimensional arrays of ultrasmall tunnel junctions", Phys.Rev.Lett., vol. 63, pp. 1861-1984, October 1989.

[3] I. N. Zhilyaev, S. G. Boronin, "Fabrication and characterization of a ring-tunnel junction quantum electron interferometer", Japan. J. Appl. Phys., vol. 37, pp. 1574-1575, March 1998.

Analysis of Propagation Power Dependence of Attenuation of Superconducting Stripline using TDGL Equation

Shigeru Yoshimori, Akira Kobayashi and Mitsuo Kawamura
Takushoku University, 815-1, Tatemachi, Hachioji-shi, Tokyo 193-8585 Japan

Abstract—Using two dimensional Time-Dependent-Ginzburg-Landau equation, we analyzed the relationships between the propagation powers and the attenuations of Nb-SiO_2-Nb and Nb-AlN-Nb structure superconducting striplines. Analytical solution was derived by the iteration method under the assumptions that the propagation mode was the TEM mode and that the vector potential exponentially decayed in the superconductor.

I. Introduction

Superconducting stripline is the key component of superconducting electronics application in the microwave field. Recently, application of high Tc cuprate superconductors to the analog filter in the mobile communication system has been remarkably progressed [1].

In this paper, we analyzed the relationships between the propagation powers and the attenuations of the superconducting stripline. We applied two dimensional Time-Dependent-Ginzburg-Landau equation (TDGL) to the superconducting stripline with assumptions that the propagation mode was the TEM mode and that the vector potential exponentially decayed in the superconductor region. The time-space distribution of the order parameter was derived by the iteration method. The attenuation of the superconducting stripline was expressed by using the solution of the TDGL equation.

II. Solution of TDGL Equation

The time-dependent-Ginzburg-Landau (TDGL) equation is expressed as follows,

$$\xi^2(\nabla - i\frac{2e}{\hbar}A)^2\Delta + (1-|\frac{\Delta}{\Delta_0}|^2)\Delta = \tau(\frac{\partial}{\partial t} - i\frac{2e}{\hbar}V)\Delta \qquad (1)$$

where ξ, e, $\hbar$, A, Δ, Δ_0, τ and V are the coherence length of the superconductor, the absolute value of the electron's charge, $h/2\pi$ (h : Plank's constant), the vector potential, the order parameter, the order parameter of bulk superconductor (therefore, a constant), the relaxation time of the Cooper pair and the scalar potential, respectively [2],[3].

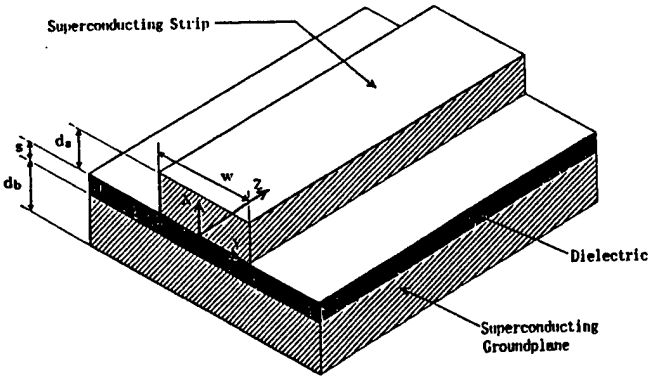

Fig.1. Superconducting stripline and coordinate system used for analysis of two dimensional TDGL equation.

Figure 1 shows the coordinate system used for the analysis of TDGL equation, where da, db, s and W denote thickness of the stripline, thickness of the ground plane, thickness of the dielectric layer and width of the stripline, respectively. In this coordinate system, the order parameter does not vary along the y axis. So we deal with two dimensional problem of the TDGL equation.

Following assumptions are made in order to derive the solution of two dimensional TDGL equation.

(1) Propagating mode through the strip line is the TEM mode even though the true propagating mode is the TE and TM hybrid mode. This assumption is reasonable when W>>s.

(2) Superconducting and normal currents which flow inside the superconducting regions satisfy the equations of current continuation, that is,

$$\mathbf{div}J_s = 0 \qquad (2)$$

$$\mathbf{div}J_n = 0 \qquad (3)$$

Here J_s and J_n are the supercurrent density and the normal current density, respectively.

(3) The order parameter $\Delta(x,z,t)$ satisfies the following boundary condition.

$$\frac{\partial}{\partial x}\Delta(x,z,t)\,|_{x=0} = 0 \qquad (4)$$

Manuscript received April 30, 1999.

This work was supported in part by the Takushoku University research fund.

Inside the superconductor, the vector potential is thought to depend on the x axis as $\exp(-x/\lambda)$, where λ is the magnetic penetration depth of superconductor. So we set the vector potential A in (1) as follows.

$$A = (\mathbf{A}(x,z,t),\ 0,\ 0) = (A_0 \exp(-x/\lambda)\sin(\omega t - \frac{\omega}{c}z),\ 0,\ 0) \quad (5)$$

By substituting $\Delta(x,z,t)=\Delta_0\Psi(x,z,t)\exp(i\phi(x,z,t))$ into (1), we obtain the fundamental equation from real part of (1) as follows.

$$\tau\frac{\partial}{\partial t}\Psi(x,z,t) = \xi^2(\frac{\partial^2}{\partial x^2}+\frac{\partial^2}{\partial z^2})\Psi(x,z,t) - [\Psi(x,z,t)^2 + \{\frac{2e}{\hbar}\xi A(x,z,t)\}^2 + \{\xi\frac{\partial}{\partial x}\phi(x,z,t)\}^2 + \{\xi\frac{\partial}{\partial z}\phi(x,z,t)\}^2 - \frac{2e}{\hbar}\xi^2 A(x,z,t)\frac{\partial}{\partial x}\phi(x,z,t) - 1]\Psi(x,z,t) \quad (6)$$

Since the TDGL equation is valid in the frequency range $\tau\omega < 1$, all terms including $\phi(x,z,t)$ and the magnitude of order parameter variation along the z axis are much less than $\xi^2\partial^2\Psi/\partial x^2$ and negligible. Thus, the following equation is derived.

$$\xi^2\frac{\partial^2}{\partial x^2}\Psi(x,z,t) = [\{\frac{2e}{\hbar}\xi A(x,z,t)\}^2 - 1]\Psi(x,z,t) + \Psi(x,z,t)^3 + \tau\frac{\partial}{\partial t}\Psi(x,z,t) \quad (7)$$

The solution of (7) can be obtained by the iteration method as follows,

$$\Psi(x,z,t) = 1 - \frac{\kappa}{2\sqrt{2}(2-\kappa^2)}(\frac{2e\,c\,\mu_0\xi H_0}{\hbar\omega})^2 \times [\exp(-\frac{\sqrt{2}}{\xi}x) - \frac{\kappa}{\sqrt{2}}\exp(-\frac{2}{\lambda}x)] \times \{1 - \frac{\sin(2\omega t - \frac{2}{c}\omega z + \arctan\frac{1}{\tau\omega})}{\{(\tau\omega)^2+1\}^{1/2}}\}. \quad (8)$$

where $\kappa=\lambda/\xi$ and $H_0 = A_0\omega/c\mu_0$ are the GL parameter and the magnetic field amplitude, respectively.

III. Attenuation of Superconducting Stripline

The attenuation of the superconducting stripline, α [dB/m], is given by (subscripts a and b denote the stripline and the ground plane, respectively)

$$\alpha = (20\log_{10}e)\times \frac{\mu_0^{\frac{3}{2}}\varepsilon_r^{\frac{1}{2}}\varepsilon_0^{\frac{1}{2}}}{4\,s}\omega^2[1+\frac{\lambda_a}{s}coth(\frac{d_a}{\lambda_a})+\frac{\lambda_b}{s}coth(\frac{d_b}{s})]^{-\frac{1}{2}}\times \{\sigma_{1a}\lambda_a^3[\frac{\lambda_a}{s}coth(\frac{d_a}{\lambda_a})+\frac{d_a/\lambda_a}{\sinh^2(d_a/\lambda_a)}] + \sigma_{1b}\lambda_b^3[\frac{\lambda_b}{s}coth(\frac{d_b}{\lambda_b})+\frac{d_b/\lambda_b}{\sinh^2(d_b/\lambda_b)}]\}. \quad (9)$$

Here σ_1 is the real part of the complex conductivity of the superconductor, $\sigma=\sigma_1-i\sigma_2$ and is corresponding to the conduction related with thermally excited electrons. σ_1 is also a function of the superconductor's energy gap and the frequency [4].

As seen in (8), the energy gap of the superconductor used in the superconducting stripline is a function of the time-space coordinates and the frequency. Here we define the conductivity σ_1 averaged respect to the time-space coordinates as,

$$\overline{\sigma}_{1a,b} = \frac{2\sigma_{Na,b}}{\hbar\omega}\frac{1}{(cT)^2}\frac{1}{d_{a,b}}\int_0^T dt\int_0^{cT} dz\int_0^{d_{a,b}} dx\int_{\Delta_{a,b}}^{\infty} dE \times [f(E)-f(E+\hbar\omega)]\frac{E^2+\Delta_{a,b}^2+\hbar\omega E}{(E^2-\Delta_{a,b}^2)^{1/2}[(E+\hbar\omega)^2-\Delta_{a,b}^2]^{1/2}}. \quad (10)$$

Here $T \equiv 2\pi/\omega$ and $f(E)$ is the Fermi-Dirac distribution function, $f(E) = [1+\exp(E/k_BT_{abs})]^{-1}$, where E, k_B and T_{abs} are energy relative to the Fermi energy, Boltzmann's constant and absolute temperature, respectively. $\sigma_{Na,b}$ is assumed to be independent of the temperature.

IV. Results and Discussions

Figures 2 and 3 show the relationships between the propagation powers and the attenuations at 4.2K for Nb-SiO_2-Nb and Nb-AlN-Nb superconducting striplines, respectively. In these analyses, we design the striplines so that the characteristic impedance of the stripline, in which the fringe field factor is taken into account, is equal to 50 Ω [5]. We assume Nb as the superconducting material so that our TDGL model is valid in the frequency range less than 750GHz at 4.2K.

In Fig.2, da, db, s and W are 3000nm, 6000nm, 3500nm and 3000nm, respectively. Relative dielectric constant of SiO_2 is 4.1 [6].

In Fig.3, da, db, s and W are 3000nm, 10000nm, 8000nm and 3000nm, respectively. Relative dielectric constant of AlN is 8.8 [7].

According to Kautz's theory, the attenuation of the superconducting stripline is independent of the propagating power [4]. As seen in Fig.2 and 3, however, the attenuations are dependent of the propagating power according to our TDGL model. When the power increases 20dB, the attenuation increases about 50% at frequencies greater than 300GHz. On the other hand, the attenuation is almost independent of the power at frequencies less than 100GHz.

We think that the increase of the attenuation is due to the increase of thermally excited electrons in the superconductor.

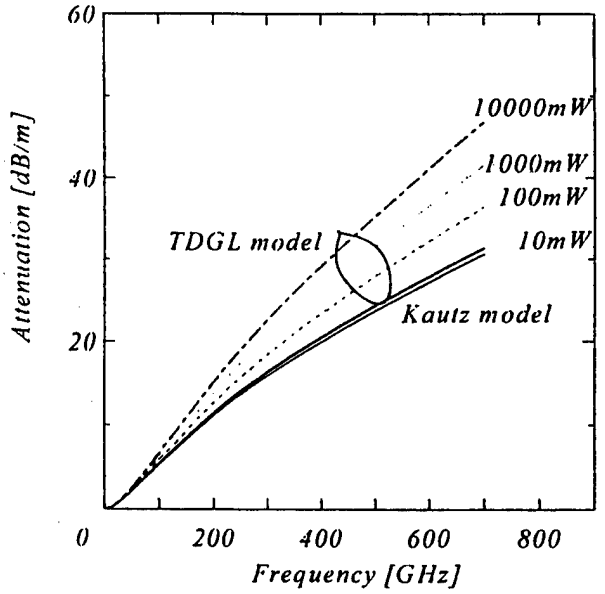

Fig. 2. Attenuation as a function of frequency for the superconducting strip line at 4.2K. Ground plane : 6000nm thick Nb thin film, Stripline : 3000nm thick and 3000nm wide Nb thin film, Dielectric layer:3500nm thick SiO_2 thin film.

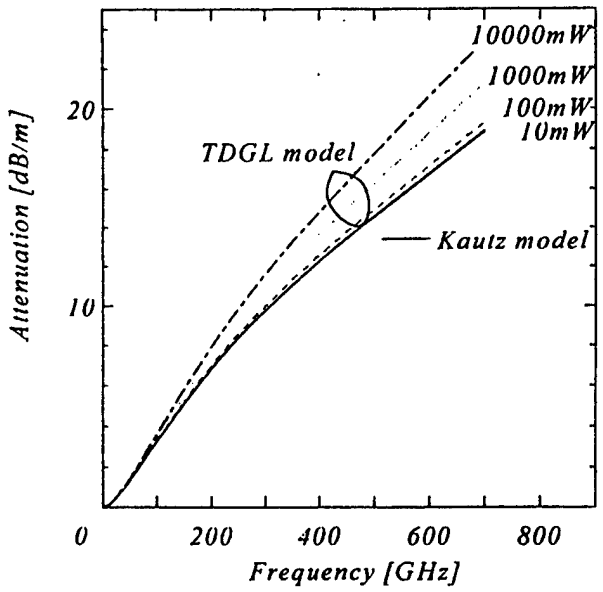

Fig. 3. Attenuation as a function of frequency for the superconducting microstrip line at 4.2K. Ground plane : 10000nm thick Nb thin film, Strip line : 3000nm thick and 3000nm wide Nb thin film, Dielectric layer : 8000nm thick AlN thin film.

V. Conclusions

We analyzed the relationships between the propagation power and the attenuation of the superconducting striplines by applying two dimensional Time-Dependent-Ginzburg-Landau equation with assumptions that the propagation mode was the TEM mode and that the vector potential exponentially decayed in the superconductor region. The time-space distribution of the order parameter was derived by the iteration method. The attenuation of the superconducting stripline was expressed by using the solution of the TDGL equation. We found that the attenuation increased about 50% at 4.2K when the power increased 20dB at frequencies greater than 300GHz. At low frequency region, the attenuation was almost independent of the propagating power.

References

[1] Z. Ma, H. Wu, P.Polakos, P. Mankiewich, D. Zhang, G. Liang, A. Anderson, P. Kerney, B. Andeen and R. Ono, "Superconducting front-ends for PCS basestation application," *Extended Abstracts of 6th Int. Supercond. Electron. Conf. Berlin*, vol. 1, pp.128-130, June 1997.

[2] L. P. Gor'kov and G. M. Eliashberg, "Superconducting alloys in a strong alternating field," *Soviet Physics JETP*, vol. 29, pp.698-700, October 1969.

[3] S. Yoshimori, T. Terashima and M. Kawamura, "Responsivity analysis of the series-connected Josephson array in the submillimeter wave region using the time-dependent-Ginzburg-Landau equation," *Infrared Physics & Technology*, vol. 39, pp.41-45, January 1998.

[4] R. L. Kautz, "Picosecond pulses on superconducting striplines," *J. Appl. Phys.*, vol. 49, pp.308-314, January 1978.

[5] W. H. Chang, "The inductance of a superconducting strip transmission line," *J. Appl. Phys.*, pp.8129-8134, December 1979.

[6] A. Kawakami, Z. Wang and B. Komiyama, "Evaluation of microstripline for mm wave range using Josephson effect," *Technical Report of IEICE*, vol. SCE92-43, pp.37-42, October 1992.

[7] S. Yoshimori, K. Mizushima, A. Kobayashi, S. Takei, Y. Uchida and M. Kawamura, "Synthesis and AES analysis of Nb(NbN)-AlN multilayers by off-axial DC magnetron sputtering," *Physica C*, vol. 305, pp. 281-284, September 1998.

Phase-Locked Josephson-Junction Arrays with Distributed Coupling Circuits

Victor K. Kornev, Alexey V. Arzumanov, and Nikita A. Shcherbakov
Department of Physics, Moscow State University, Moscow, 119899, Russia

Abstract—Two Josephson junction arrays with distributed coupling circuits have been studied by numerical simulation technique. It has been shown that an additional significant reduction in phase-locked oscillation linewidth can be provided by impact of the standing electromagnetic waves excited in the coupling circuits. Despite the fact that Josephson junctions are included into dc superconducting loops, the phase-locked oscillation state in-phase can be provided by strong interaction of the junctions with the standing waves regardless to applied magnetic field. The possible designs of both low-T_c and high-T_c Josephson-junction arrays with the distributed coupling circuits are discussed.

I. Introduction

There are reasons to considere one- and two-dimensional Josephson junction arrays as promising systems for submillimeter wave generators and receivers. The main requirement for the multijunction structures is a strong Josephson-junction interaction, which should provide both (i) high-frequency coherent state within wide critical current margins and (ii) oscillation linewidth reduction with number N of the junctions. It has been shown that the purpose may be achieved by means of either passive or active coupling circuits, which provide strong nonlocal interaction between Josephson junctions [1]. Such systems are able to provide the linewidth reduction proportional to the number N of Josephson junctions or unit cells [2], [3]. However, it has been recently shown that the reduction is always limited by a finite value of the coupling radius. In other words, a "saturation" effect for the linewidth reduction takes place, and the linewidth does not decrease with number N, if the system size exceeds the coupling radius [3], [4]. Therefore, the factor of the linewidth reduction is unlikely to exceed 100 for multijunstion arrays with lumped coupling circuits.

An additional significant linewidth reduction may by achieved by means of distributed coupling circuits via the excited standing wave impact on the Josephson-junction oscillations [4].

The goal of the research was investigation of two promising multijunction systems with distributed coupling circuits. We used numerical simulation technique [5] and both RCSJ and Wirthamer models of Josephson junctions.

Manuscript received April 30, 1999.

This work was supported in part by INTAS under Grant No. INTAS-OPEN-97, Russian State Program of Condensed Matter Physics under Grant No. 96051, and Russian Ministry of Education under Grant No. 97-8.3-58.

II. The Arrays with Distributed Coupling Curcuits

The first to be investigated was a parallel array of Josephson junctions inserted into the superconducting microstrip line with matched terminations (Fig. 1, *a*). Each section of the line between neighboring Josephson junctions had the same length and was modeled by LC-chain of 10...20 elements. The experimental system me by easy fabricated on the base of low-T_c superconductor (niobium) technology of tunnel Josephson junctions and microstrip lines [6].

The second system was an array of biased in parallel Josephson junctions which were connected in series for high frequency signal and coupled by the superconducting distributed circuits described by LC-chains of $N = N_1 + N_2$ elements each (Fig. 1, *b*). High frequency losses in the LC-chains were taken into account by means of a set of resistors connected in parallel to each capacitor C (the resistors are not shown in Fig. 1). The system may by fabricated on the base of low-T_c as well as high-T_c Josephson-junction technologies. Both types of the distributed circuits provide as dc coupling via superconducting interferometer loops, so also high frequency coupling through the standing electromagnetic waves exited in the coupling circuits.

In the first system (Fig. 1, *a*) the high-frequency Josephson-junction interaction is most pronounced when Josephson-junction microwave impedance Z is less then the characteristic wave impedance ρ of the microstrip line. The condition, which is fulfilled well at small values of normal Josephson-junction resistance R_n and large values of its intrinsic capacitance C, provides high wave reflectivity and hence the high standing wave amplitude [4], [6]. The decrease of Z gives the sharp resonance peaks on I-V curves of the junctions. It should be stressed that it is just the standing waves of voltage that impact on Josephson junctions in this system.

In contrast, the second system (Fig, 1, *b*) is characterized by the impact of the current standing waves on Josephson junctions. By this is meant that the most wave impact corresponds to the junction positions at the points of the maximum current-wave amplitudes. The output high-frequency voltage of the array V_{out} (between points 1 and 2) is a sum of the voltages across Josephson junctions $(V_J)_i$ and the values V_i of the standing voltage waves at the points where the junctions are inserted. At high amplitudes of the waves the output voltage is practically the sum of V_i. Since the peaks of the voltage standing wave coincide with zero points of the current wave, there is an optimal junction

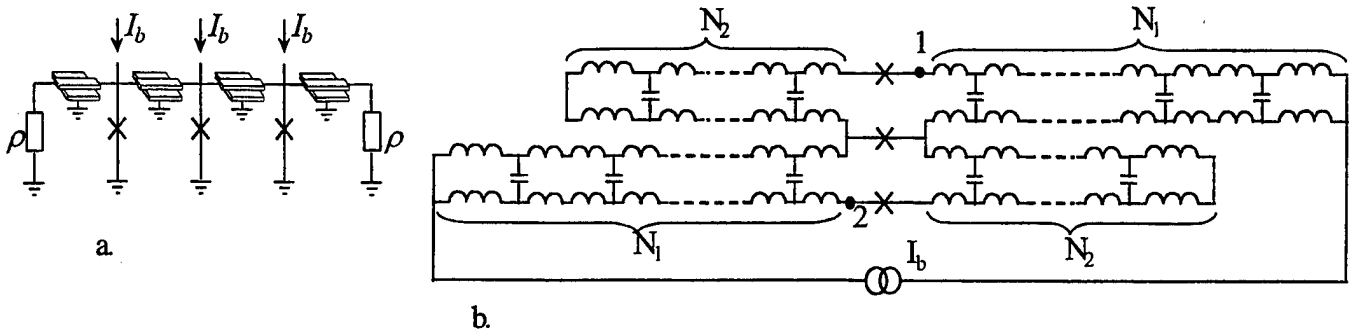

Fig. 1. Two Josephson junction arrays with distributed coupling circuits.

position that provide the maximum output voltage amplitude (see Fig. 2). It is particularly remarkable that no standing waves are exited if Josephson junctions are placed at the points that correspond to the peaks of the voltage wave amplitude. This is also seen from Fig. 3 where a set of I-V curves for Josephson junctions at different junction positions is shown. At $N_1 \approx N_2$ the resonance peculiarity which corresponds to the main mode of the standing wave is absent, and the next mode excitation is seen.

III. Resonance peculiarity on I-V curves

Resonance peculiarities on I-V curves of Josephson junctions in the both arrays can correspond to series as well as parallel resonances depending upon the junction impedance Z [4]. Double-peaked peculiarities on the I-V curves in Fig. 3 correspond to an intermediate case. The standing wave amplitude dependence on bias current for the case of parallel resonance is shown in Fig. 4. Figure 5 presents the output voltage amplitude dependence on bias current within the double-peaked peculiarity. One can say that the two peaks correspond to the different resonances that merge together in the middle of the peculiarity.

As Josephson-junction microwave impedance Z is decreased, resonance peaks on I-V curves become sharper for both systems presented in Fig. 1. Wave reflectivity in the process increases for the first system and decreases for the second one. In the letter case the resonance frequency is defined only by the total length of the coupling circuit at small Z. By contrast, at high values of Z the junctions divide the coupling circuit in to several sections (resonators) that are under strong nonlinear interaction. This results in progressive modifying of the resonance mode structure and resonance frequency within the same resonance peculiarity. Therefore, despite the high wave amplitude, the resonance peculiarity is not so sharp at high values of Z, as it is at smaller Z in comparison with ρ.

IV. Oscillation linewidth reduction

Figure 4 shows both the standing wave amplitude and the oscillation linewidth as functions of the bias current within the resonance peculiarity on I-V curve for the first array (Fig. 1, a). of two Josephson junctions. It is seen that the oscillation linewidth decreases approximately by 100 times. Outside of the resonance peak the linewidth is two times less than for a single junction because of mutual phase-locking of the junctions via dc superconducting loop. Therefore the total factor of the linewidth reduction is about 200. Despite

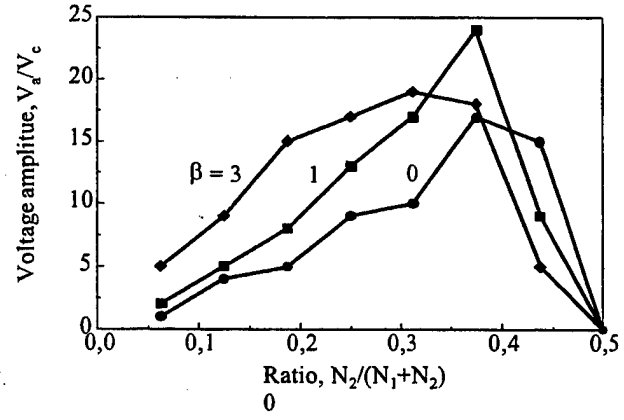

Fig. 2. Output voltage amplitude V_a for the array shown in Fig. 1, b (between the points 1 and 2) at different values of McCumber parameter $\beta = (2e/\hbar)I_c(R_n)^2C$ as a function of the ratio $N_2/(N_1+N_2)$ which characterizes Josephson-junction position within the distributed coupling circuit. Coefficient of high frequency losses $\alpha = 10^{-3}$.

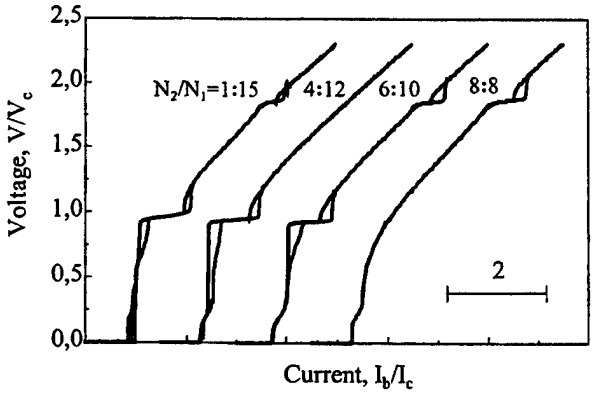

Fig. 3. A set of I-V curves for Josephson junctions of the system which is shown in Fig. 1, b at the different junction positions within the coupling circuit. McCumber parameter $\beta = 1$, coefficient of high frequency losses $\alpha = 10^{-3}$.

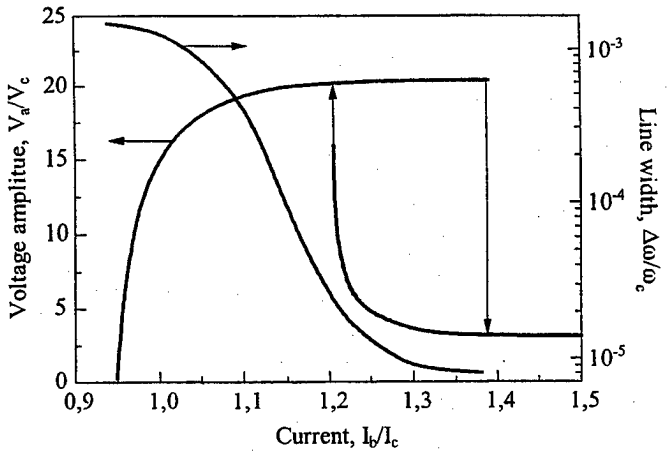

Fig. 4. Standing wave amplitude and Josephson-oscillation linewidth dependences on bias current within parallel resonance peak on I-V curve for two-junction array shown in Fig. 1, *a* at $\beta = 10$ and $\rho/R_n = 6.3$.

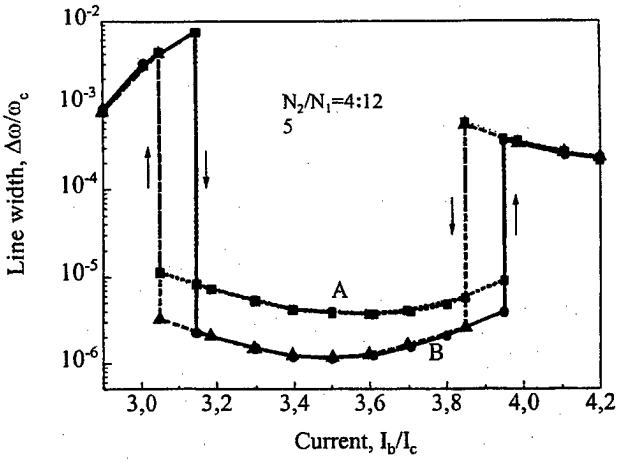

Fig. 6. Oscillation linewidth dependence on bias current within resonance peak on I-V curve for the array shown in Fig. 1, *b* at $\beta = 1$, $\rho/R_n = 10$, and $\alpha = 10^{-3}$. A – for Josephson junction oscillations, B – for output signal V_{out}.

the fact that Josephson junctions are connected into the superconducting loop, the coherent oscillation state in-phase is steady regardless to applied magnetic field.

Pertinent curves for the array, which is shown in Fig. 1, *b*, are presented in Fig. 5 and 6. It should be pointed that the linewidth for the output signal V_{out} is several time less then the one for Josephson junction oscillations within resonance peak. It has been also found that crucial role of high-frequency losses takes place when coefficient of losses $\alpha \geq 10^{-2}$ (the coefficient means that wave amplitude decreases by factor e^{α} on each element of LC-chain). Therefore the low surface resistance losses as well as the low radiation losses in the distributed coupling circuits are the properties of great importance for both low- and high-Tc Josephson junction arrays [7].

Nevertheless, there is very reason to assume that it is the arrays based on distributed coupling circuits that are able to provide the factor *k* of Josephson oscillation linewidth reduction up to 10^3 and higher at frequencies up to 1 THz and above.

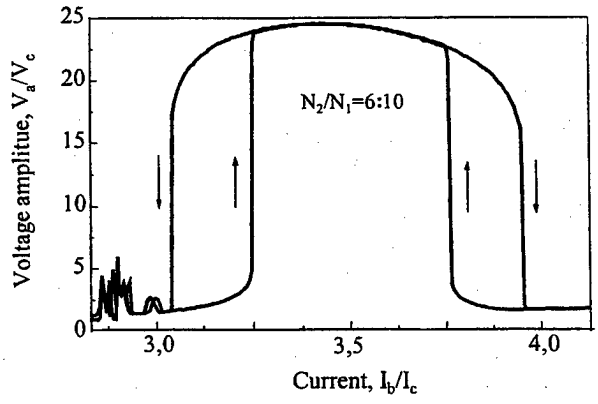

Fig. 5. Output voltage amplitude dependence on bias current within 1 resonance peak on I-V curve for Josephson junctions in the array shown in Fig. 1, *b* at $\beta = 1$, $\rho/R_n = 10$, and $\alpha = 10^{-3}$.

REFERENCES

[1] V. K. Kornev, A. V. Arzumanov, A. D. Mashtakov, G. A. Ovsyannikov, "Phase-locked one- and two-dimensional Josephson-junction arrays as millimeter and submillimeter wave generators", *IEEE Trans. on Appl. Superconductivity*, vol. 7, No. 2, pp. 3111–3114, 1997.

[2] V. K. Kornev and A. V. Arzumanov, "Oscillation linewidth for phase-locked Josephson-junction arrays", *Extended Abstracts of 6th Int. Superconductive Electronics Conf. (ISEC'97)*, Berlin, Germany, June 25-28, 1997, vol. 3, pp. 183-185.

[3] V. K. Kornev, A. V. Arzumanov, "Josephson-junction oscillation spectral linewidth for some phase-locked multijunction systems", *Journal de Physique IV, France*, vol. 8, p. Pr3-279 – Pr3-282, 1998.

[4] V. K. Kornev, A. V. Arzumanov, "Oscillation spectral linewidth for some phase-locked Josephson-junction arrays", *IEEE Trans. on Appl. Superconductivity*, 1999, in press.

[5] V. K. Kornev and A. V. Arzumanov, "Numerical Simulation of Josephson-Junction System Dynamics in the Presence of Thermal Noise", *Inst. Physics Conf. Ser. No 158*, IOP Publishing Ltd, pp. 627 – 630, 1997.

[6] V. K. Kaplunenko, B. H. Larsen, J. Mygind, and N. F. Pedersen, "600 GHz Resonant Mode ina Parallel Array of Josephson Tunnel Junctions Connected by Superconducting Microstrip Lines", *IEEE Trans. on Appl. Superconductivity*, vol. 5, No. 2, pp. 2711–2714, June 1995.

[7] K. Lee, I. Iguchi, "Millimeter-wave self-radiation from high-Tc Josephson junction arrays", *IEEE Trans. Appl. Supercond.*,vol. 7, pp. 1443-1446, June 1997.

Design and Preparation of Single Chip HTS Coplanar Waveguide Bandpass Filters

Haruichi Kanaya, Takuhiro Nakamura, Kazumi Sashiyama and Keiji Yoshida
Department of Electronic Device Engineering, Graduate School of Information Science and Electrical Engineering, Kyushu University, Fukuoka 812-8581, JAPAN

Tetsuji Uchiyama, Hisashi Shimakage and Zhen Wang
KARC Communications Research Laboratory, Kobe-shi, 651-2401, JAPAN

Abstract— An extremely low-loss, sharp cut-off and single chip high-temperature superconducting (HTS) Coplanar waveguide (CPW) bandpass filter (BPF) was designed and prepared, which are practically useful for the future telecommunication systems. 9-pole CPW BPF which has a center frequency (f_0) = 10GHz and fractional bandwidth = 1.5% (whose chip size is less than 10mm square) was designed, and confirmed by a computer simulation (HP-Momentum). In order to realize fully 2-dimentional HTS filters, we make use of meanderline geometry and interdigital capacitance coupling. In order to make BPF compact, we clarify the cross coupling between meanderlines and modeling of the corner bend of the transmission lines. Experiments of a prototype miniaturized CPW BPF (3-pole) on 10mm square YBCO film was also presented.

I. Introduction

Microwave applications (for example, mobile and satellite telecommunications) of high-temperature superconductors (HTS) are very promising because of their extremely low loss at the microwave frequencies [1]. Coplanar waveguide (CPW) is one of the simplest examples of planar transmission lines and is particularly well suited to high temperature superconductor (HTS) films because only one side of the substrate needs to be coated before patterning [2]. Besides, since the size of the CPW device can be reduced in scale without changing its characteristic impedance, it is easy to miniaturize toward "single chip" HTS bandpass filter (BPF) and make it compatible with the monolithic microwave integrated circuits (MMICs). In this paper, we design 9-pole CPW Chebyshev BPF which has a center frequency (f_0) =10GHz, fractional bandwidth =1.5% and design ripple (L_{Ar}) =0.2dB, and also make experiments on a prototype BPF. In order to realize fully 2-dimentional single chip CPW BPF, we make use of meanderline geometry and interdigital capacitance coupling. Furthermore, in order to make BPF compact, we clarify the cross coupling between meanderlines and modeling of the corner bend of the transmission lines.

Manuscript received April 30, 1999.
This work was supported in part by the Grant-in-Aid for Encouragement of Young Scientists from the Ministry of Education, Science, Culture and Sports.

II. Design and Simulated Performance of CPW Filter

A. Design Theory

BPFs at microwave frequencies can be realized by open-ended resonators connected with J inverters composed of parallel inductance and capacitance of the resonator [3]. In order to realize the J inverter using by CPW structure, interdigital gaps are adopted in the signal line of CPW as shown in Fig. 1. The electrical length ϕ and J value are given by [4][5],

$$\phi = -\tan^{-1}\left(\frac{2B_b}{Y_0}+\frac{B_a}{Y_0}\right)-\tan^{-1}\left(\frac{B_a}{Y_0}\right) \quad (1)$$

$$\frac{J}{Y_0} = \left|\tan\left\{\frac{\phi}{2}+\tan\left(\frac{B_a}{Y_0}\right)\right\}\right| \quad (2)$$

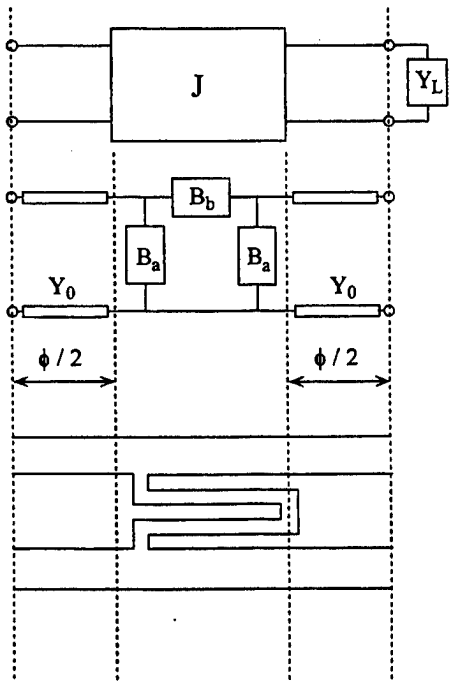

Fig. 1. Schematic diagram of J inverter.

where Y_0 is the characteristic admittance, B_a and B_b are susceptance calculated form the parallel and series capacitance in the interdigital gap.

B. Design of the Meander Structure

When pole number increases, the straight-line filter becomes longer. In order to make filter compact, the transmission line must be bent. So we first carried out the design of the corner bend structure. Figure 2 shows the typical filter pattern of the designed 9-pole meander CPW BPF. This filter size is less than 10mm square. We assume that the HTS is placed on a MgO single crystal substrate with the thickness of 0.5mm and relative dielectric constant ε_r=9.6. The characteristic impedance of CPW is 50Ω.

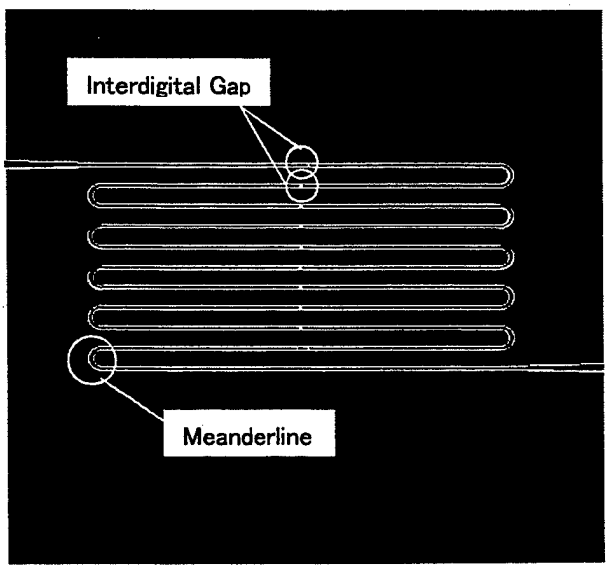

Fig. 2. Pattern of the designed 9-pole meander CPW BPF (Size of the substrate: 10mm×10mm, Filter size: 0.4mm×10mm).

An electromagnetic field simulator HP-Momentum obtains the transmission characteristics of BPF. In order to clarify the overlapping of the electromagnetic fields between the transmission lines, we simulated the *s/d* dependence of the transmission characteristics, where *s* and *d* are the length between the center of the transmission lines and gap width between ground conductors, respectively (see Fig. 3).

Figure 4 shows the *s/d* dependence of the transmission parameter S_{21}, where *d* is 70μm constant. In the figure, S_{21} of the straight line BPF is also plotted. As shown in Fig. 4, when *s/d* decreases, the attenuation in off-band increases and the transmission characteristic reaches the straight type BPF. Because the center conductors leave each other, the electromagnetic fields of transmission lines do not disturb each other. So the transmission characteristic reaches that of the straight line BPF.

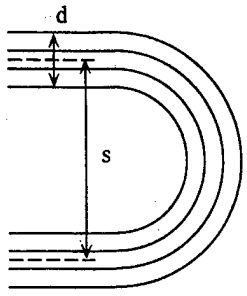

Fig.3. Configurations of meanderline.

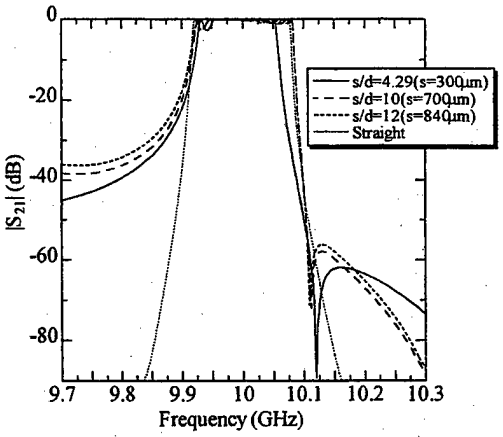

Fig. 4. Simulated frequency responses of the transmission coefficient (*d*=70μm).

Figure 5 shows the *s/d* dependence of the transmission parameter S_{21}, where *s* is fixed to be 300μm constant. In the figure, S_{21} of the straight line BPF is also plotted. As shown in Fig. 5, when bending radii are constant, the attenuation in off-band also increases as the *d* decreases. As the "relative" width between the signal lines increases, the transmission characteristic approaches that of the straight type BPF.

IV. Experiment of a Prototype CPW BPF

YBCO thin films used in this experiment were prepared by pulsed laser ablation method on MgO (100) single crystal substrates. Figure 6 shows the mask patterns of the prototype CPW BPFs. The size of the MgO substrate is $10 \times 10 \times 0.5\text{mm}^3$. These BPF have a center frequency f_0=10GHz, fractional bandwidth =1.5% and L_{Ar} = 0.2dB. The pole number of their BPFs is 3, and *s* is 350mm and 150mm, respectively. These BPFs were placed in a vacuum chamber with refrigerator cooling system. Microprocessor-Based Digital Temperature Indicators / Controllers (9650: Scientific Instrument) from 300K to 17K controlled their temperature. Vector network analyzer (HP-8722C) measured S parameter by using

Cascade-Microtech coplanar waveguide probes (GSG150).

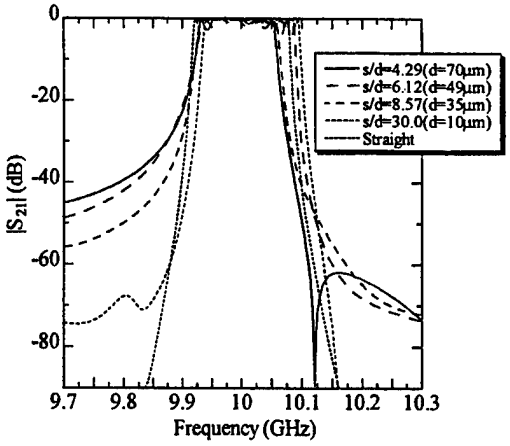

Fig. 5. Simulated frequency responses of the transmission coefficient (s=300μm).

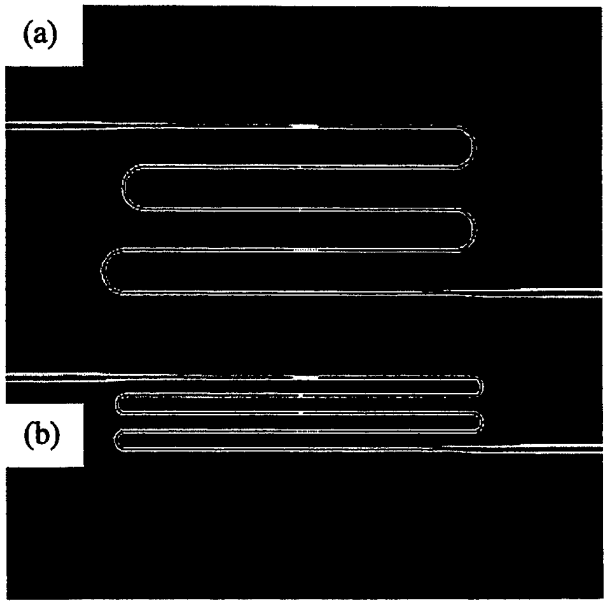

Fig. 6. Mask patterns of prototype CPW BPFs. (a):s=350μm, (b):s=150μm.

V. CONCLUSION

Design of CPW BPF using YBCO high temperature superconducting films have been presented, and the modeling of gap parameters and the corner bends of the meanderline strucutures has been made using an electromagnetic-field simulator. The designs of miniaturized CPW BPF are presented. Experiments on a prototype YBCO CPW BPF have also been made, and now measuring the microwave characteristics at low temperature.

REFERENCES

[1] Special Issue on the Microwave and Millimeter Wave Applications of High Temperature Superconductivity. *IEEE Trans. Microwave Theo. Tech.*, MTT-44, July 1996.

[2] H. How, R. G. Seed, C. Vittoria, D. B. Chrisey, J. S. Horwitz, C. Carosalla and V. Folen, "Microwave characteristics of high T_c superconducting coplanar waveguide resonator," *IEEE Trans. Microwave Theory & Tech.*, vol. 40, pp. 1668-1673, 1992.

[3] G. Matthaei, L. Young and E. M. T. Jones, *Microwave Filters, Impedance-Matching Networks, and Coupling Structures*, McGraw-Hill, New York, 1964.

[4] D. F. Williams and S. E. Schwarz, "Design and Performance of Coplanar Waveguide Bandpass Filters," *IEEE Trans. Microwave Theory & Tech.*, MTT-31, pp. 558-566, 1992.

[5] K.Yoshida, K. Sashiyama, S. Nishioka, H. Shimakage and Z. Wang, "Desing and Performance of Miniaturized Superconducting Coplanar Waveguide Filters", *IEEE Trans. Appl. Supercond.*, Vol.9, 1999 (in press).

Fabrication and Characterization of Electrically Tunable High-T_c Superconducting Resonators Incorporating Barium Strontium Titanate as a Tuning Material

Eun-Hong Lee, Junghyun Sok, Sang-Jin Park, Jeong-Soon Lee, I-Hun Song, Junesik Kwak,[a)]
Ku-Rak Jung,[b)] Jin-Young Kim,[b)] and Seok-Yeol Yoon

Microelectronics Laboratory, Samsung Advanced Institute of Technology, P.O. Box 111, Suwon 440-600, Korea

Duk Young Jeon

Department of Materials Science & Engineering, KAIST, Taejon, Korea

Abstract— We have made the electrically tunable microstrip resonators by using both high-T_c superconducting and dielectric films. The 2-pole resonators employ a dielectric barium strontium titanate film on their center in the form of flip chip. The superconducting $YBa_2Cu_3O_y$ (YBCO) and dielectric $Ba_{0.1}Sr_{0.9}TiO_3$ were deposited on the CeO_2-buffered sapphire substrate and $LaAlO_3$ substrate, respectively, by a pulsed laser deposition technique. Variations of the relative permittivity, ε_r, and dielectric loss tangent, tan δ, of the $Ba_{0.1}Sr_{0.9}TiO_3$ were studied as a function of the applied dc-bias at the liquid nitrogen temperature. The tunability, defined as $C_{(0V)}$ / $C_{(100V)}$, and loss tangent of the resonators were measured to be ~1.9 and 1.5x10^{-2} (at 100 V), respectively.

I. INTRODUCTION

Dielectrics such as $SrTiO_3$ (STO) and $Ba_xSr_{1-x}TiO_3$ (BSTO) exhibit the dielectric nonlinearity with regard to electric field, i.e., their dielectric constant is dependent on applied electric field. This nonlinear property can be used to make frequency (or phase agile) tunable microwave devices, such as resonators, delay lines, and phase shifters. The integration of the dielectric films and microwave frequency devices makes their characteristics to be tuned in real time varying externally applied electric field. In general, STO and BSTO have a large nonlinearity and a low dielectric loss at cryogenic temperatures and around room temperature, respectively. Recently, the BSTO is now being studied extensively as a dielectric material for tunable devices, because their flexible dielectric properties can be obtained easily by changing the mixing ratio of $BaTiO_3$ and STO. For microwave applications, it is necessary to have structures with high relative permittivity, ε_r, and low loss tangent, tan δ. As it is not easy to obtain high tunability and low loss tangent simultaneously, compromises are needed between them in order to optimize the reasonable tunability and loss tangent of the BSTO capacitors operating at cryogenic temperature.

Manuscript received April 30, 1999.

[a)] Also at the Dept. of Physics, Hanyang Univ. Seoul, Korea.
[b)] Also at the Dept. of Physics, Inchon Univ. Inchon, Korea.

Considering the ferroelectric to paraelectric phase transition temperature (Curie temperature, T_C) of the capacitors and the operating temperature (77 K) of the tunable devices, the $Ba_{0.1}Sr_{0.9}TiO_3$ is chosen as the composition for capacitors in this experiment.

We describe high crystallinity $Ba_{0.1}Sr_{0.9}TiO_3$ films as well as YBCO films by pulsed laser deposition (PLD). Fabrication details and electrical measurements of the resonator as a trial to get high tunability and low loss tangent are described using the $Ba_{0.1}Sr_{0.9}TiO_3$ capacitors.

II. EXPERIMENTAL

PLD was used to deposit YBCO and CeO_2 as well as $Ba_{0.1}Sr_{0.9}TiO_3$ thin films using a KrF excimer laser (λ = 248 nm, pulse duration = 25 ns, Lambda Physik, LPX 305i). Repetition rate of 5~10 Hz and fluence of 1~2 J/cm^2 were used for film preparation. The laser beam was focused to about 1x4.5 mm^2 size onto stoichiometric YBCO, CeO_2, and $Ba_{0.1}Sr_{0.9}TiO_3$ targets. Commercially available single-crystal $LaAlO_3$ (LAO) and Al_2O_3 wafers were used as the substrates. Substrates, mounted on the heater (US Thin Film Inc.) by silver paste, were placed in front of the target at the distance of 40~70 mm. The target pellets were rotated during irradiation to minimize surface degradation [1]. The depositions were done at a substrate temperature (T_s) of 750~800°C and an oxygen pressure of 400 mTorr for YBCO but 200 mTorr for CeO_2. In case of $Ba_{0.1}Sr_{0.9}TiO_3$ films, T_s of 650~780 °C and oxygen pressure of 10~200 mTorr were used. The typical thicknesses of the YBCO, CeO_2, and $Ba_{0.1}Sr_{0.9}TiO_3$ thin films were 500, and 30, and 1,000 nm, respectively. More detailed experimental setup and procedures have been reported previously [2].

The structural properties of the films were characterized by x-ray diffraction (XRD) using θ-2θ scan, ω-rocking curve, and Φ-scan. The capacitance and loss tangent were measured from 10 to 500 kHz using a HP 4284A Precision LCR meter at room temperature. Great attention was paid to secure the accuracy of the dielectric loss measurement. A HP 8510C network analyzer and a cryogenic system were used to measure the microwave properties of the resonator.

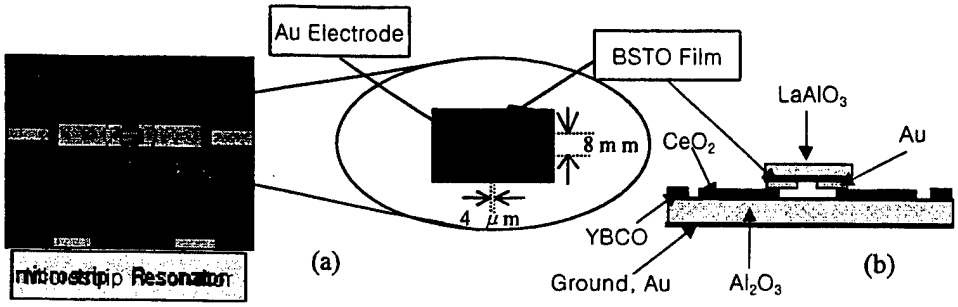

Fig. 1 Schematic of the tunable microstrip resonator employing dielectric films on its center. (a) Top view, (b) Front view.

III. Results and Discussion

Fig. 1 shows the schematic of the resonator, consisting of a microstrip resonator and a flip-chip. The size of the resonator and the chip capacitor are 28 x 30 mm^2 and 2 x 3 mm^2.

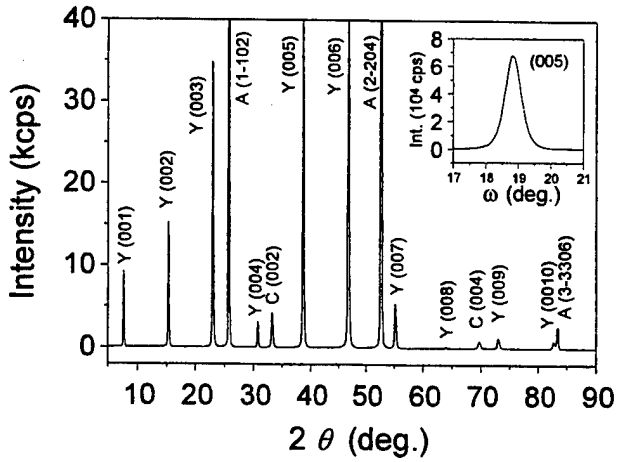

Fig. 2. XRD θ-2θ scan and ω-rocking curve of the YBCO/CeO_2 films on a r-plane (1$\bar{1}$02) Al_2O_3 substrate.

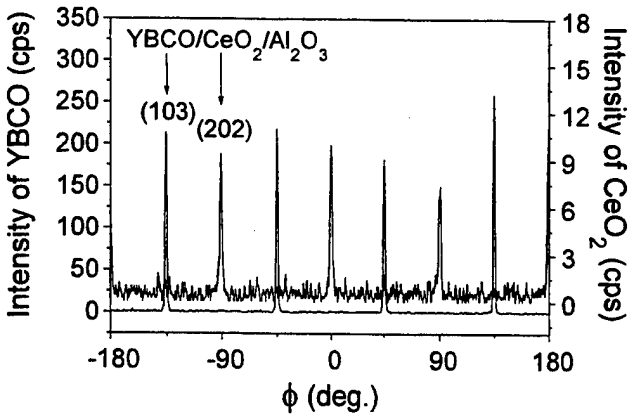

Fig. 3. XRD Φ-scans on (103) YBCO and (202) CeO_2 films. The YBCO peaks are shifted by 45° with respect to the CeO_2 peaks, which leads to YBCO [110] ∥ CeO_2 [100].

Fig. 2 shows the XRD θ-2θ scan and ω-rocking curve of the YBCO/CeO_2 films on a r-plane (1$\bar{1}$02) Al_2O_3 substrate. Except the peaks of the substrate, as seen in the figure, only (00l) peaks of the YBCO and CeO_2 films appear. No peaks of either a-axis oriented YBCO grain or foreign phases could be detected within the resolution of the experiment, indicating these films are well-oriented with respect to the substrate plane. The inset in Fig. 2 shows a ω-rocking curve on (005) of the YBCO films. The full width at half maximum (FWHM) is around 0.53°, denoting high-quality mosaic spread of the YBCO film with the c-axis perpendicular to the substrate plane. This value is comparable with the results reported by the others in YBCO/CeO_2/Al_2O_3 multi-layer structure [3].

Fig. 3 shows the XRD Φ-scan on (103) YBCO and (202) CeO_2 films. As can be seen in this figure, only 4 peaks of the respective films appear at every 90° and there is a 45° rotation between the basal plane of the YBCO and that of the CeO_2. Taking into account the fourfold symmetry with a high peak to background ratio of the Φ-scan, it can be found that the films have a high grade of in-plane orientation. In addition, 45° shift in the peak position denotes the epitaxial relationships YBCO [100] (001) is parallel to CeO_2 [110] (001). The FWHM of (103) YBCO peak ($\Delta\Phi$) in the Φ-scan mode was measured to be 1.44°. The above results indicate that the YBCO and CeO_2 films grow epitaxially on (1$\bar{1}$02) Al_2O_3 substrate.

Fig. 4 shows the XRD Φ-scan on (211) $Ba_{0.1}Sr_{0.9}TiO_3$ on a $LaAlO_3$ substrate. As the Φ-scan on YBCO and CeO_2 films, the fourfold symmetry and reasonably good peak to background ratio can be observed. Also, the $Ba_{0.1}Sr_{0.9}TiO_3$ films were confirmed to be single phase c-axis oriented normal to the substrate from the measurement of the XRD θ-2θ scan.

Prior to the fabrication of the resonator, simulation of transmission response was performed using a commercial simulator. From the simulation results, several designs of the HTS microstrip resonator with resonant frequency of around 6 GHz were obtained. The resonator was designed to achieve a movable mode, which depends on the capacitance value of

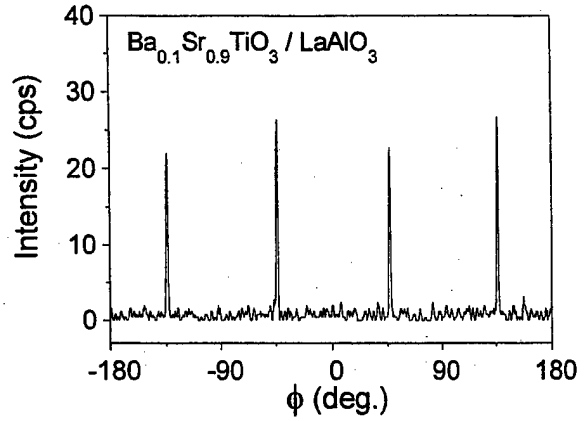

Fig. 4. XRD ϕ-scans on (211) $Ba_{0.1}Sr_{0.9}TiO_3$ on a $LaAlO_3$ substrate.

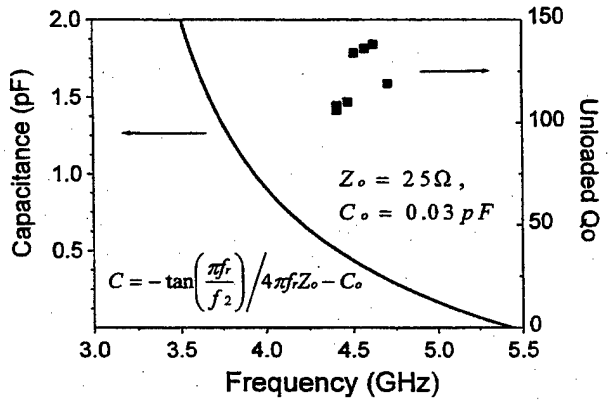

Fig. 5. Fitting curve for capacitance–frequency and unloaded qualtiy factors.

the gap at the center of the resonator, and an immovable mode at 5.8 GHz. The movable mode shifted toward lower frequency with increasing the capacitance.

The HTS microstrip resonator was fabricated using a simulated design and the insertion loss, S_{21}, of the resonator was measured at 77 K without a planar capacitor on the gap. The immovable peak has –0.9 dB at 5.53 GHz and the movable peak is located at 5.45 GHz. The noticeable difference between the simulated results and measured one is the loss of the movable modes, this resulted from the fact that the dielectric films acting as a capacitor is not taken into consideration in the simulation.

As is stated above, the movable peak depends on the gap capacitance, C, according to the following equations [4],

$$C = -\frac{\tan\varphi}{2Z_o\omega_r} - C_o, \quad \varphi = \pi\frac{\omega_r}{\omega_2} \qquad (1)$$

where ω_r and ω_2 are angular frequency of the movable and immovable modes, resepctively; φ is the electrical length of the microstrip line of the resonator; Z_o and C_o are the characteristic impedance and the parasitic capacitance of the microstrip line, respectively. C_o is the temperature and bias voltage independent capacitance due to the electric field in the substrates of both capacitor and microstrip line. We determined the Z_o and C_o, as reported earlier [5], fitting the C vs. movable frequencies which, in turn, were derived from the frequency dependences of the S_{21} of a resonator with various standard capacitors having different capacitance. These frequency dependences are measured from the microwave measurement of the resonance frequency and the low-frequency (10 kHz) measurements of the capacitance of the standard capacitors. The values of the Z_o and C_o as fitting parameters were obtained as 25 Ω and 0.03 pF. The fitting curve and the unloaded quality factor, Q_O, are shown in Fig. 5.

Taking the non-dispersion of the substrates, LAO and α-Al_2O_3, into consideration in this frequency range, it is possible to determine the high-frequency capacitance values of the dielectric BSTO capacitors from the measurements of the resonance frequency. As a result, the fitted curve can be used for the BSTO capacitor as a conversion curve between the capacitance and resonance frequency.

Fig. 6 shows the applied bias dependencies of the movable frequencies and the derived capacitances of a resonator using the BSTO capacitor with a electrode dimension of 4 μm (gap) x 8 mm (width). The movable frequency appears at 3.73 GHz at zero bias. As the bias increases, the movable frequency increases to higher frequency, resulting from the decrease of the gap capacitance. The corresponding capacitance values, derived from the fitted curve, are shown in the figure, also.

The measurement of the movable resonance frequency using the standard capacitor, also, give the unloaded quality factor, Q_O, which is used to calculate the loss tangent, tan δ, of the BSTO capacitor using the following equations (2):

$$\tan\delta = \xi^{-1}(Q_u^{-1} - Q_O^{-1})$$

$$\xi = \frac{2}{1 - \frac{2\varphi}{\sin 2\varphi}} \qquad \varphi = \pi\frac{\omega_r}{\omega_2} \qquad (2)$$

where Q_u is the unloaded quality factor of the resonator with the BSTO capacitor and Q_O is that of the resonator with a capacitor without the dielectric BSTO films (standard capacitor). The average value of the Q_O is determined to be as 120 from the Fig. 5. The inclusion factor, $\xi = W_C/(W_l - W_C)$, is the main parameter that characterizes the influence of the capacitor on the Q factor and on the frequency controllability of the resonator. W_l and W_C are the electrical energy stored in the microstrip part of the resonator and in the capacitor, respectively. Fig. 7 shows the bias dependences of the relative permittivity, ε_r, and the loss tangent, tan δ. The estimated ε_r values are obtained using the following modified formulae(3):[6]

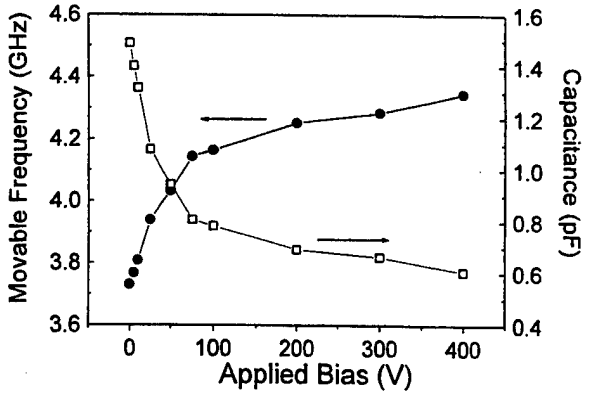

Fig. 6. Applied bias dependences of the movable frequency and the capacitance.

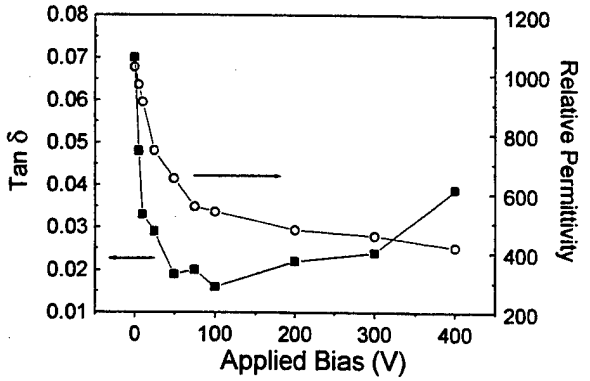

Fig. 7. Applied bias dependences of the loss tangent and the relative permitivity.

$$\varepsilon_r = 4C\,(ln\,2 + \pi\,L/4H)/\pi\;\varepsilon_o W \qquad (3)$$

where W and L are the width and the gap size, respectively, and H is the dielectric film thickness. For the BSTO films quoted in this paper was approximately 1 μm. The loss tangent of the BSTO capacitor at the zero bias was measured to be 7 x 10^{-2} and decreased rapidly showing minimum of 1.5 x10^{-2} at 100 V. The variation of loss tangent is closely related to the loaded quality factor, Q_O. Comparing the loss tangent of the BSTO with that of the $SrTiO_3$ under the same condition, 2.7 (100V) to 4.3 (0 V) times larger values are obtained. Because the Curie temperature of the $Ba_{0.1}Sr_{0.9}TiO_3$ is closer to the liquid nitrogen temperature than that of the STO, the higher capacitance value of the BSTO affected to the higher values of loss tangent. On the other hand, the tunability, defined as C (77 K, 0 V) / C (77 K, 100V), of 2 is obtained, denoting superior controllability of the BSTO capacitors to STO capacitors.

IV. SUMMARY

The electrically tunable HTS YBCO microstrip resonators employing a dielectric $Ba_{0.1}Sr_{0.9}TiO_3$ film have been fabricated. The resonators and the dielectrics having a good crystallinity have been made by the PLD technique on the CeO_2-buffered Al_2O_3 and $LaAlO_3$ substrates, respectively. The resonators have been designed to achieve a movable mode, which depends on the capacitance value of the gap, and an immovable mode at 6 GHz. The transmission response, S_{21}, of the YBCO resonator exhibits the insertion loss of 0.9 dB at resonant frequency. We have determined the critical parameters, Z_o and C_o, by fitting the C vs. movable frequencies. Applying the movable resonant frequency of the resonators to the fitted curve, corresponding capacitance values have been obtained. Variations of the relative permittivity, ε_r, and dielectric loss tangent, tan δ, of the $Ba_{0.1}Sr_{0.9}TiO_3$ have been studied as a function of the applied dc bias at the liquid nitrogen temperature. The tunability, defined as $C_{(0\ V)}/C_{(100\ V)}$, and loss tangent of the resonators have been measured to be ~1.9 and 1.5x10^{-2} (at 100 V), respectively.

ACKNOWLEDGMENT

We would like to thank Dr. Kookrin Char of Seoul National Univ. for helpful discussions on this work.

REFERENCES

[1] C. Doughty, A. T. Findikoglu, and T. Venkatesan, "Steady state pulsed laser deposition target scanning for improved plume stability and reduced particle density," *Appl. Phys. Lett.* vol 66 (10), pp. 1276-1278, March 1995.

[2] E.-H. Lee, S.-J. Park,I.-H. Song, I. Song, J. Gohng, J. Sok, J.-W. Lee, D. Y. Jeon, and C. Y. Dosquet, IEEE Transact. Appl. Supercond. 7, pp.1193-1196, 1997.

[3] M. Lorenz, H. Hochmuth, D. Natusch, H. Börner, T. Thärigen, D. G. Partikarakos, J. Frey, K. Kreher, IEEE Transact. Appl. Supercond. 7, pp.1240-1243, 1997; B. F. Cole, G.-C. Lian, N. Newman, K. Char, and G. Zaharchuk, Appl. Phys. Lett. 60, pp.1727, 1992; M. Maul and B. Schulte, J. Appl. Phys. 74, pp.2942, 1993.

[4] E. K. Hollmann, A. V. Ivanov, A. B.Kozyrev, V. E. Loginov, P. K. Petrov, O. I. Soldatenkov, A. V. Tumarkin, and O. G. Vendik, Proceeding of NATO Advanced Research Workshop, Bulgaria, Sep. 30 1996; D. Galt, J. C. Price, J. A. Beall, and R. H. Ono, Appl. Phys. Lett. 63 pp. 3078, 1993.

[5] J. Sok, J. S. Lee, and E. H. Lee, Supercond. Sci. Technol., vol.11, pp. 875-879, 1998.

[6] S. F. karmanenko, A. I. Dedyk, V. T. Barchenki, R. A. Chakalov, A. V. Lunev, A. A. Semenov, and L. T. Ter-Martirosyan, Supercond. Sci. Technol., vol.11, pp. 284-287 1998; O. G. Vendik, L. T. Ter-Martirosyan, A. I. Dedyk, S. F. Karmanenko, and R. A. Chakalov, Ferroelectrics 144 pp. 33, 1993.

POSTER SESSION II

Group 4 - Detectors and Mixers

Normal Metal Hot-Electron Microbolometer with On-Chip Protection by Tunnel Junctions

Denis Chouvaev, Leonid Kuzmin, and Michael Tarasov
Department of Microelectronics and Nanoscience, Chalmers University of Technology, S-412 96 Gothenburg, Sweden

Abstract— We describe recent development in a fully on-chip integrated antenna-coupled bolometer for astrophysical applications at millimeter and submillimeter wavelengths. We develop a normal metal hot-electron microbolometer (NHEB) with Andreev mirrors for thermal protection of the absorber and coupling to antenna In previous experiments we could not operate the sensor at temperatures below 300 mK presumably because of the high external noise load. Our latest results with absorber protected by tunnel junctions show how this problem can be solved experimentally. We have achieved noise performance mostly limited by the amplifier, which corresponds to expected detector NEP on the order of $1.5 \cdot 10^{-17}$ W/Hz$^{1/2}$ at 100 mK.

I. Introduction

Cryogenic bolometers are the most sensitive direct detectors of infrared and millimeter waves radiation and are widely used for astronomical observations. Most common bolometers used in radio-astronomy are made with a suspended absorber, being heated by incident radiation, and a semiconducting thermistor or superconducting bolometers, where the sensor is a suspended chip with a superconducting structure [1,2]. One disadvantage with the existing bolometers is that they compromise sensitivity and speed – to reach NEP < 10^{-17} W/Hz$^{1/2}$ one needs to make the absorbing area large, thus getting also large thermal capacity C and, consequently, longer reaction time $\tau=C/G$, where G is thermal conductance between the absorber and environment. Another problem is that suspended structures are often fragile, and it is difficult to combine many of them into a 2D-detector array.

The normal metal hot-electron microbolometer (NHEB) with Andreev mirrors proposed in [3] and later partly implemented [4] can be a promising choice. This is a planar microfabricated bolometer using an antenna to receive a signal (fig. 1). In an antenna-coupled bolometer the sensor itself can be miniaturized, minimizing the thermal conductance. A microwave signal received by the antenna will induce current in a normal-metal resistor (absorber) and heat the resistor. This heat will be delivered first to the electron gas in the resistor. At temperatures below 0.5 K, the thermal coupling between electrons and phonons is very low, and the electrons will establish their own equilibrium at a temperature above the phonon temperature (hot electron effect). In this sense, the electron gas in the resistor can be seen as a power absorber, and the thermal conductance to the environment is then limited by the energy exchange between the electrons and the phonons. Thus, one does not need to suspend the absorber to thermally isolate it. Furthermore, the thermal capacity of the electrons is much less than the thermal capacity of the whole structure, and this makes the sensor very fast.

Manuscript received April 30, 1999.
This work was supported in part by the Swedish SSF foundation.

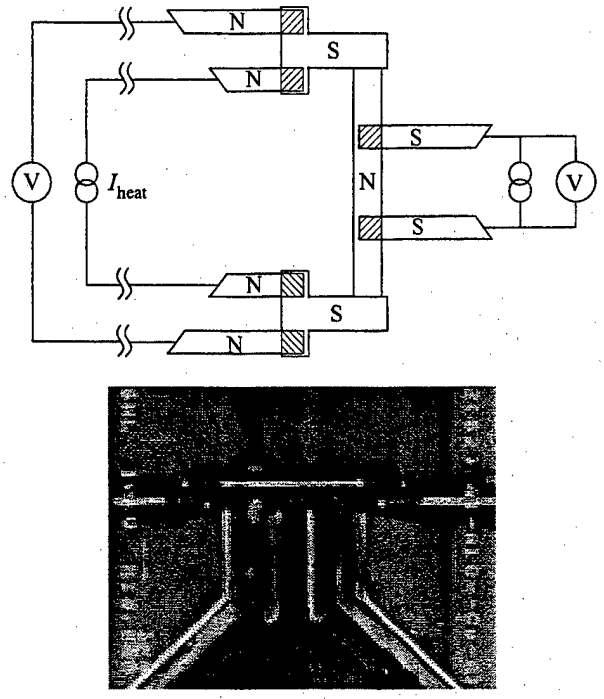

FIG. 1. The bolometer schematic with additional NIS tunnel junctions in the absorber bias circuit for protection. Two NIS junctions in measurement circuit are used to increase the response dV/dT. SEM-image shows a central part of the bolometer.

To prevent escape of heated electrons back to the antenna, a very elegant decision has been suggested by authors of Ref. 3 to use Andreev reflection [5] for thermal protection of the absorber but keeping good electrical conductivity between the absorber and superconducting antenna.

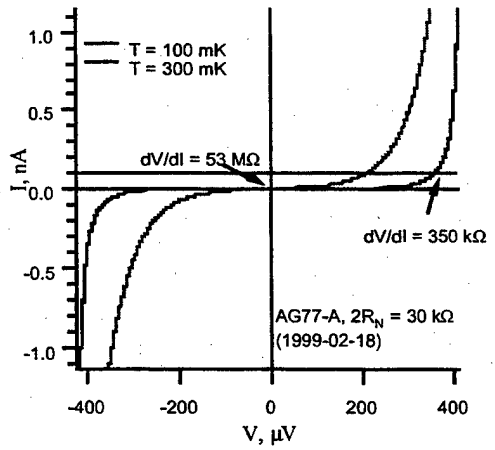

FIG. 2. Principle of measuring electron temperature by means of two NIS tunnel junctions biased with constant current.

Finally, a small signal power results in a substantial rise of the electron temperature in the absorber. The temperature rise is converted to voltage response using one or two normal metal/insulator/superconductor (NIS) tunnel junctions, where the normal electrode is the absorber. When the junction is biased by fixed current, the voltage depends on the electron temperature in the N-electrode (fig. 2). The power responsivity of this sensor depends on temperature responsivity (dV/dT) and heat conductance ($G = dP/dT$):

$$S = \frac{dV}{dP} = \left|\frac{dV}{dT}\right| \cdot \left|\frac{dP}{dT}\right|^{-1} \qquad (1)$$

The temperature responsivity of the tunnel junctions is nearly constant almost in the whole range of operating temperatures (typically $dV/dT \approx 3\text{-}5\cdot10^{-4}$ V/K). The heat conductance depends mostly on properties of the absorber and can be estimated from the energy exchange rate between electrons and phonons in equilibrium at different temperatures:

$$P = \Sigma\Omega(T_e^5 - T_p^5) \quad \rightarrow \frac{dP}{dT} = 5\Sigma\Omega T_e^4 , \qquad (2)$$

where Ω is the absorber volume and Σ - a material parameter.

II. DEVICE FABRICATION AND MEASUREMENT SETUP

The microbolometer has been fabricated by e-beam lithography and shadow evaporation techniques. Three metal layers are used – a superconductor for NIS tunnel junctions (aluminum film, 36-38 nm), a normal metal for the absorber (copper, 58 nm), and a superconducting layer the antenna (aluminum, 70 nm). The tunnel junctions are formed by oxidizing the first superconducting layer ($P(O_2)$ = 0.3-0.4 mbar and t = 0.5-2 min) resulting in the junction normal resistance of 5-15 kΩ for area about 0.1 μm^2. The Andreev contacts between the absorber and the second superconductor can be done either by a two lithography process and ion beam cleaning in-between, or by our new single-step process with tilting a sample in two perpendicular planes is employed (fig. 3). The dimensions of the copper absorber are 4.5×0.25 μm^2, thickness - 58 nm, and resistance is about 20 Ω.

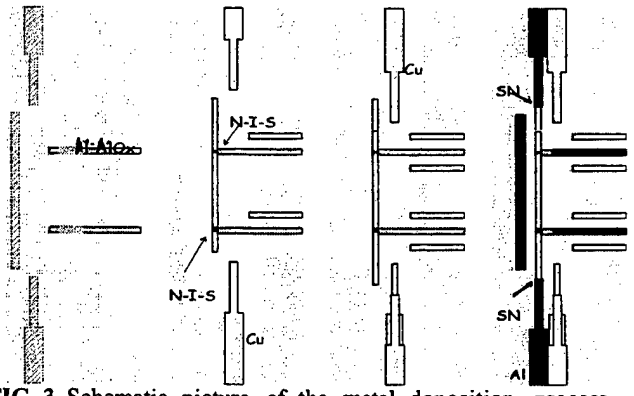

FIG. 3. Schematic picture of the metal deposition process. A double PMMA-copolymer resist is used to make a suspended mask. In the leftmost picture both resist layers are shown by slightly darker areas, on the three others – only the underlying copolymer mask. By tilting the sample in different planes the metal structures are shifted in respect to the original openings in the PMMA-mask, providing necessary overlaps between subsequently deposited metal layers.

For dc-measurements we have used a current bias for heating the absorber in a dilution refrigerator. The current sources for the NIS junctions and the absorber are made of a symmetric voltage sources and two high-Ohmic (10 or 100 MΩ) resistors in series at room temperature. Johnson noise in those resistors is the main source of bias noise. For calibration measurements the voltage response from the tunnel junctions at the working bias is studied as a function of the bath temperature. IV-curves of the tunnel junctions at different bath temperatures are registered to determine the choice of the working point. Then the sensor is tested by driving current through the absorber and measuring the response at a fixed cryostat temperature. Finally, noise spectra at different measurement conditions can be taken.

3. EXPERIMENTAL RESULTS

When we started our experiments, we obtained good power responsivity (at the predicted level) at relatively high electron temperatures above 300 mK but not in the temperature range 100-300 mK where it was most expected. The reason for this was saturation of the response V(T) of the tunnel junctions, apparently seen in the calibration curves (fig. 4).

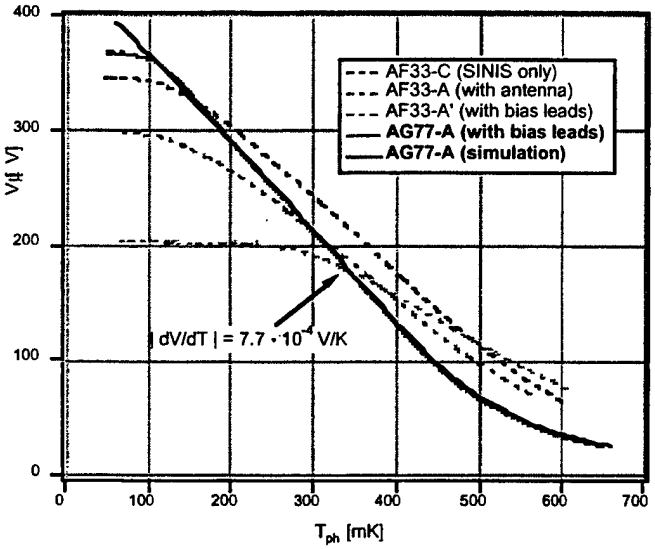

FIG. 4. Comparison of V(T) dependencies for different structures of non-protected sample AF33 (dashed curves) and the same dependence for sample AG77, where additional tunnel junctions in the absorber bias leads have been used (the thick curve). A strong saturation can be seen for the structure with long bias leads on the sample AF33. Saturation is present even for the sample AG77, but only below 130 mK. The thin curve is a theoretical fit for this sample's V(T).

Yet worse, the measured noise level used to be an order of magnitude higher then the noise of our amplifier, which had modest 30 nV/Hz$^{1/2}$ at 10 Hz. It has taken a while to realize that those phenomena must have had the same cause, namely intensive interference coupled to the absorber and heating the electrons sometimes above +300 mK. The main clue convinced us in the validity of this hypothesis was a comparison of the voltage noise and the gain (=power responsivity) of the device. Both dependencies had very similar shapes, which must indicate that the noise is present already as fluctuations of electron temperature in the absorber.

Once being convinced about the presence of external heating we tried to identify how the noise comes in. Pick-up in the circuit connected for heating the absorber was one suggestion; a microwave "leakage" into the sample cavity was another one. Eliminating the second being a more difficult task, we started by breaking the absorber bias circuit by high-resistive elements close to the absorber. We hoped that the voltage induced in that low-ohmic (R_{abs} = 20 Ω) circuit would drop on those high-resistive links, thus not being able to generate any noticeable current. We have chosen NIS tunnel junctions on both sides of the absorber as such protecting links, since they have very high intrinsic resistance in the sub-gap region, and they are very easy to fabricate simultaneously with other junctions (fig. 1).

This measure has given surprisingly good results, bringing the V(T) saturation down to 100-130 mK (fig. 4) and the noise level almost to the amplifier level. However, if we look at the noise spectra (fig. 5), we may notice that connecting wires to the absorber and closing this circuit result in additional noise contributions, thus indicating that even this strong protection is not perfect. Furthermore, even the noise associated with an isolated "absorber" island (7-10 nV/Hz$^{1/2}$) is clearly higher then what is expected from the thermometry noise (3 nV/Hz$^{1/2}$). We think that some high-frequency leak still exists and is responsible for this additional noise.

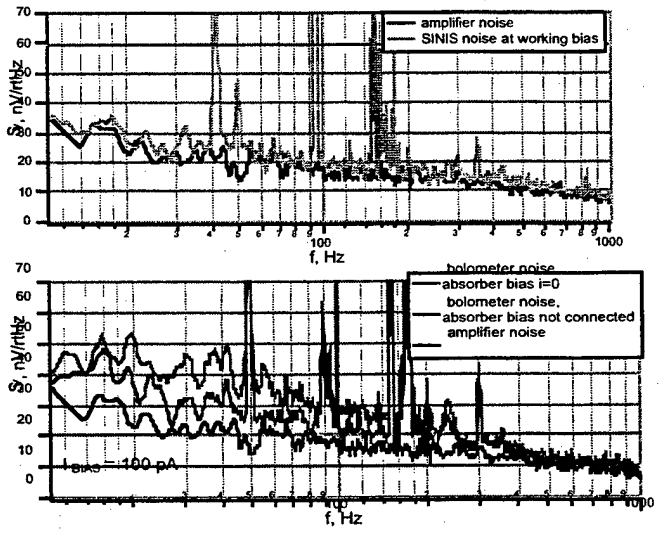

FIG. 5. Noise spectra for a) simple SINIS structure, i.e. without superconducting electrodes connected to the absorber and b) complete microcalorimeter structure equiped with protection NIS junctions and connected to long leads for biasing; the higher noise curve corresponds to leads terminated by a current source. The lowest curve in the both graphs is the amplifier noise.

The protection by tunnel junctions, however, distorted completely the heating power calibration at $I_{absorber} > 0$. Earlier we could assume that the dissipated power was $P=P_J=R_{absorber} \times I^2_{absorber}$. Now, as soon as $I_{bias}>0$ high-energy electrons are injected into the superconducting electrode of the protecting NIS-junction as quasiparticles, and further to the absorber, where their energy apparently dissipates, giving $P>>P_J$. This effect is similar to the electronic cooling by NIS tunnel junctions described elsewhere [7], but now our object is on the "warm" side of the Peltier cooler. This is the reason why we could not measure directly the value of the power responsivity S at low temperature. We could only estimate S for the sample AG77 using formulas (1) and (2). For $dV/dT \approx 3\times10^{-4}$ V/K (fig. 4), $\Sigma \approx 3\times10^{-9}$ W μm^{-3} K^{-5} and $\Omega = 0.065$ μm^3 one can get thermal conductance G = 1x10^{-13} W/K and power responsivity S = 3x10^9 V/W at 100 mK. Using this power responsivity and the measured output noise 45 nV/Hz$^{1/2}$ at 10 Hz (fig. 5) we can estimate the noise equivalent power NEP ≈ 1.5x10^{-17} W/Hz$^{1/2}$.

Further modification of the bolometer scheme includes reversing the NIS protecting junctions and thus setting the N-part at the absorber side to solve the problem of overheating. An additional NS-interface between the superconducting electrodes going to the absorber and the N-side of the protecting junctions would interrupt the unwanted energy flow due to the Andreev reflection. Another simple (but probably not as elegant) solution is to use small external resistors bonded to the chip wiring.

The new results show that there are no severe problems with the sensor itself. If we manage to couple the absorber efficiently to an integrated antenna, and place the device in an enclosure with well-controlled input of high-frequency radiation, we expect it to function properly. Disregarding the input noise, the performance of the detector will be limited by thermal fluctuations in the absorber and the noise introduced by the electron temperature readout. The level of thermal fluctuations at a given operating temperature depends on volume and material of the absorber.

IV. Conclusion

We have demonstrated a reasonable performance of the power sensor in an integrated antenna-coupled bolometer. We could operate it at temperatures down to 100 mK, where the responsivity of the sensor is much higher than in our earlier results (at 300 mK). The measured noise level corresponds to NEP = 1.5·10^{-17} W/Hz$^{1/2}$, and it is dominated by the input noise external to the sensor itself and the amplifier noise. Some refinement of the experiment is still needed to make a fully calibrated characterization of the device.

References

[1] P.L. Richards, J. Appl. Phys. **76** (1), 1 (1994).
[2] A.T. Lee, S-F. Lee, J.M. Gildemeister, and P.L. Richards, Proc. of the 7th Int. workshop on Low Temperature Detectors, Munich, July-Aug 1997, pp 123-125.
[3] M. Nahum, P.L. Richards, and C.A. Mears, IEEE Trans. Appl. Supercond. **3**, 2124 (1993).
[4] M. Nahum and J. Martinis, Appl. Phys. Lett. **63**(22), 3075 (1993).
[5] A.F. Andreev, Sov. Phys. JETP, **19**, 1228 (1964).
[6] D.Chouvaev , L.Kuzmin , M.Tarasov, P. Sundquist, M. Willander, T.Claeson. Proc. of the 9th Int. Symposium on Space Terahertz Technology, Pasadena, p. 331, March 1998.
[7] M.Nahum, J.M.Martinis, Appl. Phys. Lett., v. 65, N 23, 3123 (1994).

NbN Hot Electron Bolometric Mixers at Frequencies Between 0.7 and 3.1 THz

Pavel Yagoubov, Matthias Kroug, Harald Merkel, Erik Kollberg
Chalmers University of Technology, S-412 96 Gothenburg, Sweden

Josef Schubert, Heinz -Wilhelm Hübers
DLR Institute of Space Sensor Technology, D-12489 Berlin, Germany

Abstract-The performance of NbN based phonon-cooled Hot Electron Bolometric (HEB) quasioptical mixers is investigated in the 0.7-3.1 THz frequency range. The devices are made from a 3.5-4 nm thick NbN film on high resistivity Si and integrated with a planar spiral antenna on the same substrate. The length of the bolometer microbridge is 0.1-0.2 μm, the width is 1-2 μm. The best results of the DSB receiver noise temperature measured at 1.5 GHz intermediate frequency are: 800 K at 0.7 THz, 1100 K at 1.6 THz, 2000 K at 2.5 THz and 4200 K at 3.1 THz. The measurements were performed with a far infrared laser as the local oscillator (LO) source. The estimated LO power requirement is less than 500 nW at the receiver input. First results on spiral antenna polarization measurements are reported.

I. Introduction

In the past years, several research groups have been working on the development of low noise broadband receivers for detection of THz radiation. They are needed for atmospheric observation and radio astronomical applications. Only Schottky diode mixers are now used as receivers at frequencies beyond 1 THz. The prime advantage of this mixer technology is the possibility to operate at room temperature. However, Schottky diodes have rather poor sensitivity which makes it difficult to detect weak signals. In addition, the local oscillator (LO) power requirement for these mixers is very high. Due to the few available powerful laser lines in the THz frequency range, this is an important issue.

The concept of superconducting HEB mixers for receivers at submillimeter wavelengths has been suggested in [1]. They have already been shown to be competitive with SIS mixers at frequencies around 1 THz [2-4] and represent a very attractive candidate at higher frequencies [5-7]. The development has now reached a stage where they are successfully used for astronomical observation [8]. HEB mixers can in principle operate up to at least 30 THz without degradation in performance. An intermediate frequency (IF) bandwidth of several GHz has been achieved for both phonon-cooled [9-11] and diffusion-cooled [12,13] HEB mixers in experiments below 1 THz. Another attractive feature of HEB mixer technology is a very low power required from the LO source. In our experiments the measured power absorbed in the bolometer element is about 100 nW. Taking into account the estimated optical losses of 3-5 dB we end up with less than 500 nW needed from the LO source at the input of the receiver. This is 3-4 orders of magnitude lower than that of Schottky diode mixers.

II. Mixer Fabrication and Design

The devices are made from a 3.5-4 nm NbN film sputtered on a high resistivity, double side polished, silicon substrate. The film is patterned by e-beam lithography to form a 0.1-0.2 μm long and 1-2 μm wide strip across the center gap of an Au spiral antenna, see Fig. 1. Details of the fabrication process can be found in [14]. The normal state resistance of the bolometer measured at 20 K ambient temperature is 250-450 Ohm depending on the geometry and film thickness. The critical current density at 4.5 K is about $4x10^6$ A/cm^2. The antenna is an equiangular spiral with a 90° arm width yielding a self-complementary design. This implies that the antenna impedance is purely real and equal to 75 Ohm for the antenna on a Si substrate. The spiral structure of the antennas extends 1.5 turns and the spiral expansion rate is 3.2 per turn. Three different designs have been used: spiral "A", "B" and "C". The spiral "A" antenna is the largest one, spirals "B" and "C" are the products of scaling down spiral "A".

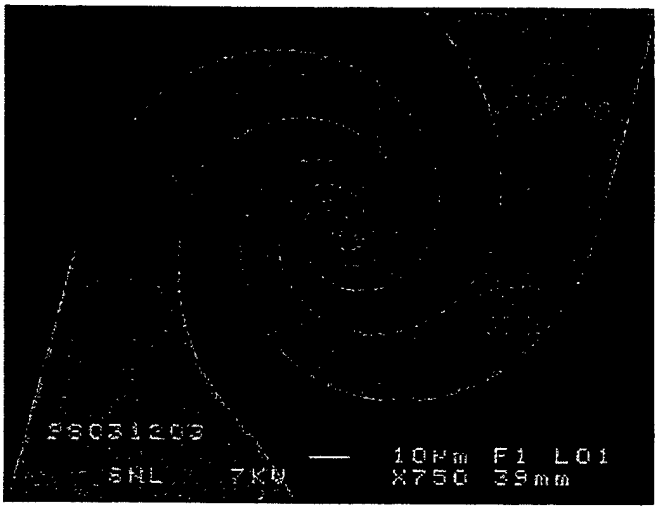

Fig.1. SEM micrograph of the spiral antenna integrated HEB mixer. The antenna design is spiral "B".

Manuscript received April 30, 1999
This work has been supported in part by ESA (ESTEC/No.11738/95/NL/MV), Swedish Research Council for Engineering Sciences, and Swedish National Space Board.

III. MEASUREMENT SETUP AND TECHNIQUE

The setup for heterodyne measurements at frequencies between 0.7 THz and 3.1 THz is shown in Fig. 2. The local oscillator (LO) source is a far infrared (FIR) laser which is optically pumped by a CO_2 laser. The LO and the signal are combined by a thin 6 μm Mylar beamsplitter with almost no transmission losses for the signal. The LO power is adjusted by a rotatable wire grid. The mixer chip is mounted onto a copper block which is placed in a liquid helium vacuum cryostat equipped with a high-density polyethylene window. The rf radiation is coupled to the mixer by 12 mm diameter elliptical lens. IR radiation is blocked by a 380 μm Zitex G115 filter. The device output is connected through a bias-T to a 1.3-1.7 GHz cooled HEMT amplifier with a noise temperature of ≈5 K. The output of the HEMT amplifier is filtered with a 1.5±0.02 GHz bandpass, further amplified and detected with a power meter.

The receiver noise temperature is measured using the traditional Y-factor technique by alternatively placing a hot/cold (295/77 K) load in the signal path of the receiver.

For polarization measurements we use two rotatable grids in the LO path as shown in Fig. 2. The Mylar beamsplitter is replaced by a metal mirror in order to avoid a polarization modification by reflection from the dielectric film. By changing the orientation of both grids (polarizer and analyzer) and measuring the coupling efficiency one can determine the polarization of the receiver antenna. The radiation coupling to the bolometer is obtained from the pump level of the IV curve which is a measure of the power absorbed in the bolometer. Details of the absorbed power measurement technique can be found elsewhere [3].

V. NOISE TEMPERATURE

The results presented here are obtained with 4 devices from two different batches, named "V" and "W". The full information about the devices' geometry, dc parameters and noise temperature data are summarized in Table 1. The device dc parameters (resistance and critical current) scale well with the geometry of the bolometer element. This fact indicates the spatial uniformity of the film and the reproducibility of the fabrication process.

The noise temperature data shown in the table is the total DSB receiver noise temperature, not corrected to any losses. It is derived from the measured Y-factor with 77/295 K loads at the input of the receiver. All devices measured in this work show very similar performance. The best results of the DSB receiver noise temperature obtained at 4.2 K ambient temperature are: 800 K at 0.7 THz, 1100 K at 1.6 THz, 2100 K at 2.5 THz and 4200 K at 3.1 THz. Lowering the device ambient temperature gives a slight improvement of the noise temperature. For instance, 2200 K at 2.5 THz measured for device W47 at 4.2 K drops to 2000 K at 3 K. The reason for the strong rise in the noise temperature to 4200 K at 3.1 THz is not clear yet. We believe that it could be due to increase of optical losses (cryostat window, Zitex filter, etc.) and the strong water absorption in the atmosphere at this frequency. The degradation of the sensitivity of the device W47 at 0.7 THz is because this frequency is well below the lower cutoff frequency of antenna "C", see next chapter for details.

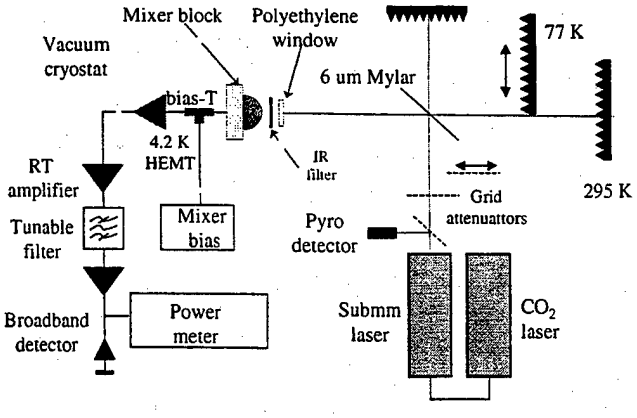

Fig.2. Setup for noise temperature measurements.

VI. ANTENNA POLARIZATION

As mentioned before we have used three antenna designs, spiral "A", "B", and "C". Spiral "A" has inner and outer radii of 10 and 100 μm, respectively. The spirals "B" and "C" are downscaled versions (factors of 2 and 4) of spiral "A".

The total antenna arm length of spiral "A", calculated from its radii and the expansion rate of 3.2 per turn, is about 300 μm. Setting this equal to a maximum effective wavelength yields a lower cutoff frequency of the antenna of 300 GHz in free space. The cutoff of spiral "B" and "C" is 600 GHz and 1.2 THz. This explains the deterioration of the noise temperature performance of the mixer W47 (with spiral "C") at 700 GHz.

The higher cutoff frequency of the antenna is defined [16] as the frequency at which the antenna polarization changes from circular to elliptical with an axial ratio of 2 to 1. This

TABLE 1. DEVICE PARAMETERS AND RESULTS OF NOISE TEMPERATURE MEASUREMENTS.

Device number	**V14**	**V24**	**W24**	**W47**
R_{300K}, Ω	160	160	100	190
R_{20K}, Ω	350	320	230	430
Antenna design	A	B	B	C
Bol. length, μm	0.2	0.15	≤0.1	≤0.1
width, μm	2	2	2	1
I_c, μA (at 4.2 K)	290	285	280	145
Bias current, μA	45	45	60	30
voltage, mV	1.2	0.8	1.1	1.0
DSB NT, K				
0.7 THz	800	800	1100	1900
1.4 THz	1500	1100	1300	1700
1.6 THz	1300	1100	1300	1700
2.5 THz	2300	2100	2300	2000*
3.1 THz	not meas	not meas	4200	4200

*measured at 3 K ambient temperature. The NT measured at 4.2 K is 2200 K.

frequency depends on the construction precision of the antenna feed. Since the spiral arms naturally converge to a point, one has to terminate the center in a tapered section, see Fig.1. According to [16] the cutoff frequency occurs when the total length of the tapered section becomes effectively a half-wavelength. This length is roughly 20 μm, 10 μm, and 5 μm for spirals "A", "B", and "C" setting the upper frequency limit to 2.2 THz, 4.4 THz, and 8.8 THz, respectively.

The axial ratio of elliptical polarization increases towards higher frequencies. Notice, however, that since there are no marked changes in pattern shape of the antenna at these frequencies [16], the antenna can still work efficiently although the polarization might not be circular.

The antenna polarization measurements have been performed at 2.5 THz with a device based on spiral "C". The polarization is elliptical with the ellipse axial ratio of about 3 to 1. The last number is within ± 50% error due to the uncertainty of the absorbed power measurement technique. This technique is based on the assumption that the resistance of the bolometer is equally affected by dc and rf power. The limited accuracy of this technique causes an error for determining the coupling efficiency and hence the ellipse axial ratio. The long axis of the ellipse coincides with the direction of the tapered section in the antenna center, Fig. 1.

The obtained result on the antenna polarization does not agree well with that reported in [16]. In that paper the change of polarization from circular to elliptical with a ratio of 2 to 1 was found at a frequency when the tapered section is equal to the effective half-wavelength. At higher frequencies the ellipse axial ratio increases further. In our case the length of the tapered portion is only 1/7 of the effective wavelength but the axial ratio is already larger than 2 to 1. One possible reason is that not only the length but also the shape of the tapered section is important. The design of the antenna terminal region used in ref. [16] is quite different from our one and may be more advantageous in terms of the polarization property. Another explanation could be that by other reasons (high resistivity of the Au, mismatch between bolometer and antenna impedance, etc) the field decays faster along the antenna arms making the influence of the antenna center larger. To understand this better, further investigation (testing different antenna designs at different frequencies) is needed.

ACKNOWLEDGMENT

The authors are thankful to Gregory Gol'tsman for numerous fruitful discussions and Boris Voronov for fabrication of NbN films.

REFERENCES

[1] E. M. Gershenzon, G. N. Gol'tsman, I. G. Gogidze, Y.P. Gusev, A. I. Elant'ev, B. S. Karasik and A. D. Semenov, "Millimeter and submillimeter range mixer based on electronic heating of superconducting films in the resistive state", *Sov. Phys. Superconductivity*, 3, 1582, 1990.

[2] P. Yagoubov, M. Kroug, H. Merkel, E. Kollberg, G. Gol'tsman, A. Lipatov, S. Svechnikov and E. Gershenzon, "Quasioptical NbN phonon cooled hot electron bolometric mixers with low optimal local oscillator power", *Proc. 9th Int. Symp. on Space Terahertz Technology*, Pasadena, CA, 131, 1998.

[3] P. Yagoubov, M. Kroug, H. Merkel, E. Kollberg, G. Gol'tsman, S. Svechnikov and E. Gershenzon, "Noise temperature and local oscillator power requirement of NbN phonon-cooled hot electron bolometric mixers at Terahertz frequencies", *Appl. Phys. Lett.*, 73, 2814, 1998.

[4] A. Skalare, W.R. McGrath, B. Bumble and H. G. LeDuc, "Noise and RF bandwidth measurements of a 1.2 THz HEB heterodyne receiver", *Proc. 8th Int. Symp. on Space Terahertz Technology*, Cambrige, MA, 47, 1997.

[5] B. S. Karasik, M. Gaidis, W.R. McGrath, B. Bumble and H. G. LeDuc, "Low noise in a diffusion-cooled hot-electron mixer at 2.5 THz", *Appl. Phys. Lett.* 71, 1567, 1997.

[6] E. Gerecht, C.F. Musante, Y. Zhuang, K.S. Yngvesson, T. Goyette, J. Dickinson, J. Waldman, P.A. Yagoubov, G.N. Gol'tsman, B.M. Voronov, and E.M. Gershenzon, "NbN Hot Electron Bolometric Mixers – A New technology for Low Noise THz Receivers," Presented at the 10th Int. Symp. on Space Terahertz Technology, Charlottesville, VA, March 1999, in press.

[7] P. Yagoubov, M. Kroug, H. Merkel, E. Kollberg, J. Schubert, H.-W. Hübers, G. Schwaab, G. Gol'tsman, and E. Gershenzon, "Heterodyne Measurements of a NbN Superconducting Hot Electron Mixer at Terahertz Frequencies", Presented at the *Applied Superconductivity Conference*, Palm Springs, 13-18 September, 1998.

[8] J. Kawamura, C.Y.E. Tong, R. Blundell, G. Gol'tsman, S. Cherednichenko, B. Voronov, G. Gershenzon, "NbN Phonon-cooled Hot-electron Mixer Receivers at 800 GHz", Presented at the *Applied Superconductivity Conference*, Palm Springs, 13-18 September, 1998.

[9] P. Yagoubov, G. Gol'tsman, B. Voronov, L. Seidman, V. Siomash, S. Cherednichenko, and E. Gershenzon. "The Bandwidth of HEB Mixers Employing Ultrathin NbN films on Sapphire Substrate", *Proc. 7th Int. Symp. on Space Terahertz Technology*, Charlottesville, VA, 290, 1996.

[10] S. Cherednichenko, P. Yagoubov, K. Il'in, G. Gol'tsman and E. Gershenzon, "Large bandwidth of NbN phonon cooled hot-electron bolometer mixers on supphire substrates", *Proc. 8th Int. Symp. on Space Terahertz Technology*, Cambrige, MA, 245, 1997.

[11] H. Ekström, E. Kollberg, P. Yagoubov, G. Gol'tsman, E. Gershenzon and S. Yngvesson, "Gain and noise bandwidth of NbN hot-electron bolometric mixers", *Appl. Phys. Lett.* 70, 3296, 1997.

[12] D.Prober. "Superconducting Terahertz Mixer using a Transion Edge microbolometer", *Appl. Phys. Lett.* 62(17), 2119, 26 April, 1993.

[13] B.S. Karasik, A. Skalare, W.R. McGrath, B. Bumble, H.G. LeDuc, J.B. Barner, A.W. Kleinsasser, P.J. Burke, R.J. Schoelkopf and D. Prober, "Low noise and wide band hot-electron superconductive mixer for THz frequencies", Presented at the *4th Int. Conf. On MM & CMM Waves and Applications*, San Diego, 20-23 July, 1998.

[14] M. Kroug, P. Yagoubov, G. Gol'tsman and E. Kollberg, "NbN quasioptical phonon cooled hot electron bolometric mixers at THz frequencies", *Proc. the 3rd. European Conference on Applied Superconductivity*, Veldhoven, Netherlands, 1997, (Inst. Phys. Conf. Ser. No 158, p.405).

[15] A. R. Kerr, M.J. Feldman, and S.-K. Pan, "Receiver Noise Temperature, the Quantum Noise Limit, and the Role of the Zero-Point Fluctuations", *Proc. 8th Int. Symp. on Space Terahertz Technology*, Cambrige, MA, 101, 1997.

[16] J. D. Dyson, IRE Trans. Ant. Prop. AP-7, 181, 1959.

NbN phonon-cooled hot-electron bolometers prepared on MgO substrates

Shigehito Miki and Nobuyuki Kaya
Graduate School of Science and Technology, Kobe University, 1-1 Rokkodai-cho, Nada-ku, Kobe 657-8501, Japan

Yoshinori Uzawa, Akira Kawakami, and Zhen Wang
Kansai Advanced Research Center, Communications Research Laboratory, 582-2 Iwaoka, Iwaoka-cho, Nishi-ku, Kobe, 651-2401, Japan

Abstract— We report on fabricating and testing hot electron bolometers with an ultrathin NbN film as heterodyne receivers operating at the terahertz frequencies. The NbN thin films were deposited on single-crystal MgO substrates by dc-magnetron sputtering at room temperature. The NbN films with an ultrathin thickness of 2.8 nm demonstrated good superconductivity with a high T_C of 9.8 K and a low resistivity of 185 μΩ cm at 20 K. The film structures, which were investigated by electron diffraction patterns and transmission electron micrographs, showed a single crystal structure with a (100) orientation. Hot-electron bolometers were constituted of 3-nm-thick NbN strip lines and Au contact pads to test the intermediate frequency (IF) bandwidth. The mixer IF bandwidth was estimated to be 2.3 GHz at the 15 GHz band.

I. Introduction

Superconducting hot-electron bolometric (HEB) mixers are expected to replace supercondutor-insulator-superconductor (SIS) mixers as low-noise heterodyne receivers at the terahertz (THz) frequencies. However, a fundamental problem in the HEB is that the intermediate frequency (IF) bandwidth is narrower than a few GHz. In the phonon-cooled HEB, the IF bandwidth is restricted by elctron-phonon relaxation time $\tau_{e\text{-}ph}$ [1] and the phonon escape time from film to substrate [2]. In order to achieve a wide bandwidth in the phonon-cooled HEB, one must use a superconducting material with a short $\tau_{e\text{-}ph}$, such as NbN, and also must improve epitaxial growth of the superconductor thin films on the substrate to reduce the thermal resistance in the interface of the film and substrate [2]. Therefore, single-crystal NbN ultrathin films with high T_C must be available for constituting NbN phonon-cooled HEB mixers.

In this work, we used (100) single-crystal MgO substrates to promote the epitaxial growth of the NbN thin films. The MgO substrate is also useful for phonon-cooling, because the thermal conductivity of MgO is the same as diamonds around the temperature of liquid He. We describe the development of high-quality ultrathin NbN films with excellent superconducting properties and fine crystal structures and present results of IF bandwidth measurements.

Manuscript received April 30, 1999.

II. Fabrication

NbN films were deposited by reactive dc-magnetron sputtering in a mixture of Ar and N_2. A direct-current power supply was used in order to stabilize the discharge state [3]. The background pressure was $8 \cdot 10^{-8}$ Torr, and the total pressure was set at 2 mTorr to elevate the sputtering energy. The relative amounts of argon and nitrogen introduced for sputtering were carefully controlled to 5:1 by mass flow controllers. The target was 99.99% pure niobium and the target size was 6 in. in diameter. The substrates were not heated intentionally.

The HEB devices were constituted of NbN strip lines and Au contact pads. NbN strip lines were defined by using photolithography and reactive ion etching. Au contact pads were fabricated by vacuum deposition and a lift-off process. The final dimensions of the strip lines were 2.0 μm long by 2.0 μm wide. The number of strip lines were four. In order to control the impedance of HEB devices, strip lines were trimmed by fluorine radical etching and the variation of device resistance *in situ* was monitored.

III. Experiments and Discussion

A. Superconducting Properties of NbN Films

In reactive dc-magnetron sputtering, $\Delta U = U - U_{Ar}$, where U_{Ar} is the discharge voltage in pure argon for a stavilized current and U is the discharge voltage in a gas mixture for the same current, serves as an index which shows nitrogen partial pressure in the discharge [3]. We have carefully investigated the relation of the ΔU and the superconducting properties of NbN films. Figure 1 shows the superconducting transition temperature T_C and resistivity ρ_{20} as a function of the ΔU. The thickness of the films were about 150 nm. The transition temperature T_C and resistivity ρ_{20} varies in the range from 15 to 16 K and from 62 to 90 μΩ cm when the ΔU varies from 30 V to 63 V. The prepared NbN films had best superconducting properties: a maximum T_C of 16 K and minimum ρ_{20} of 60 μΩ cm at ΔU = 40 V. The films with maximum T_C and minimum ρ_{20} had a lattice parameter of 0.447 nm which agree with our reported NbN films fabricated by rf sputtering [4].

Figure 2 shows the transition temperature and resistivity as a function of the film thickness. The thickness of films thicker than 10 nm were measured directly by a TENCOR

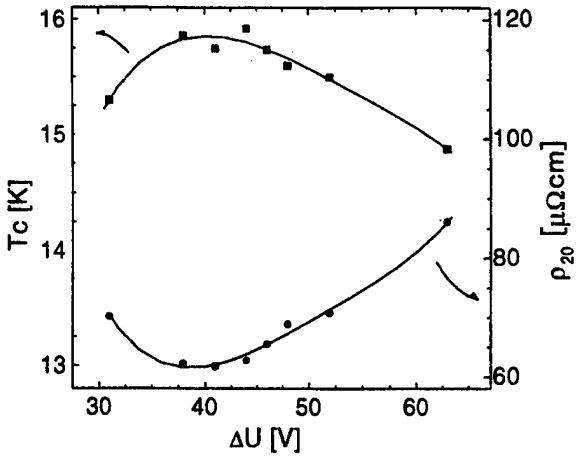

Fig. 1. Transition temperature T_C and resistivity ρ_{20} as a function of ΔU (=U-U_{Ar}, where U_{Ar} is the discharge voltage in pure argon for a stavilized current and U is the discharge voltage in a gas mixture for the same current).

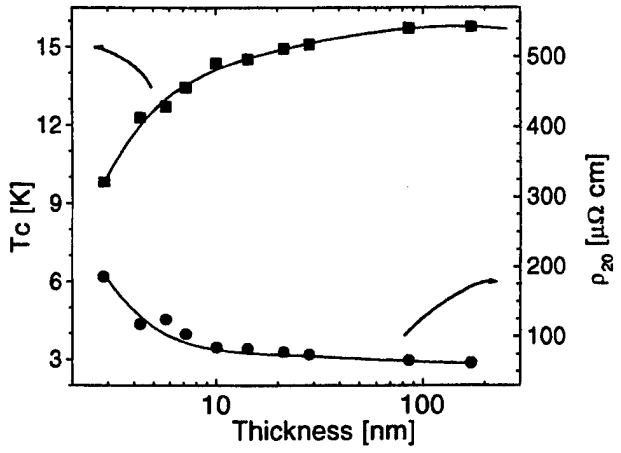

Fig. 2. Transition temparature T_C and resistivity ρ_{20} as a function of film thickness.

ALPHA-STEP 500 thickness monitor. The thickness of films less than 10 nm were estimated from the deposition rate and time. A 2.8-nm-thick ultrathin film had excellent superconducting properties with a T_C of 9.7 K and a resistivity of 185 μΩ cm.In reactive dc magnetron sputtering, $\Delta U=U-U_{Ar}$(U_{Ar} is the discharge voltage in pure argon for a stavilized current, and U is the discharge voltage in a gas mixture for the same current) serves as index which knows nitrogen partial pressure in the discharge[3].

B. Crystal Structures of NbN Films

The film structures were also studied by a transmission electron microscope for the cross-sectional observations. Figure 3 (a) shows a typical selected-area electron diffraction pattern of the NbN films. The electron diffraction pattern showed clear electron-diffraction lattice spots ranging in cubic distributions from the NbN films. The concentric circular distribution from (111) and other orientations were not observed in the diffraction patterns, indicating a single-phase orientation in the NbN films. The cross-sectional TEM micrograph of NbN films on MgO substrates is shown in Fig. 3 (b). The MgO substrates were single-crystal with the (100) plane parallel to the substrate and to the surface, and the deposited NbN films were epitaxially grown in single crystalline with its (100) plane parallel to the substrate. It is evident that the single-crystal NbN films grew straight on the MgO substrates without any initial amourphous layers. The lattice matrix is arranged in a good order, and no columnar structures were observed in the TEM observation region at a few micrometers.

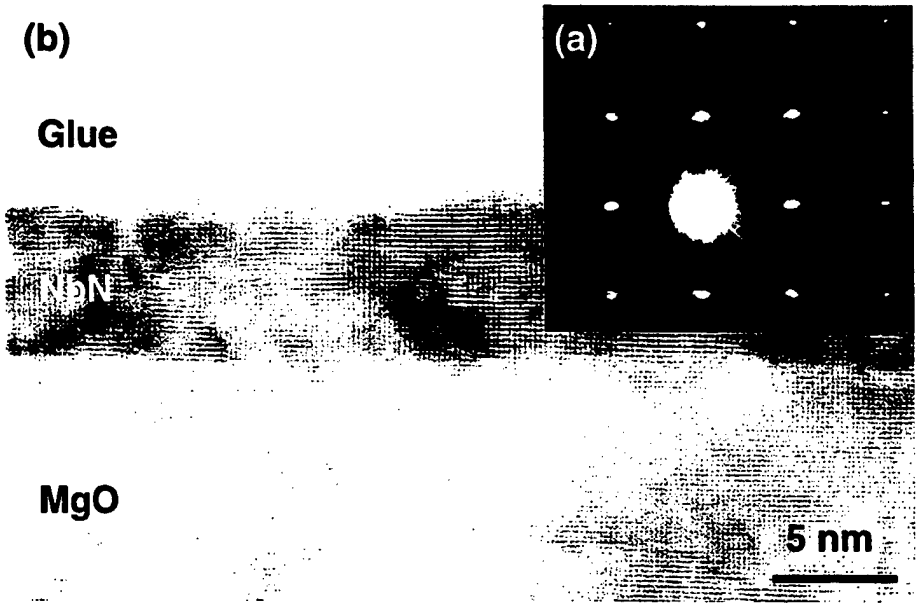

Fig. 3. (a) Selected-area electron diffraction pattern of the NbN films (b) cross-sectional TEM micrograph of NbN films.

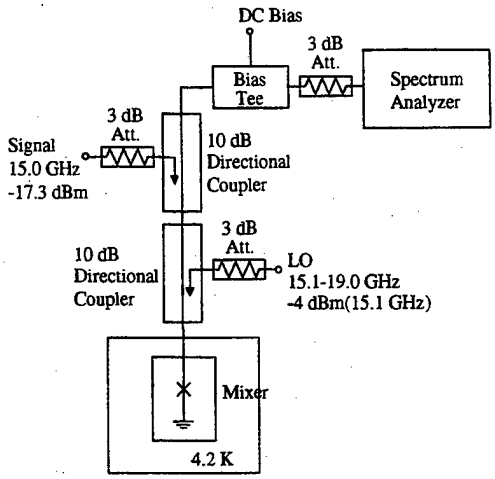

Fig. 4. Set up for the IF bandwidth measurements.

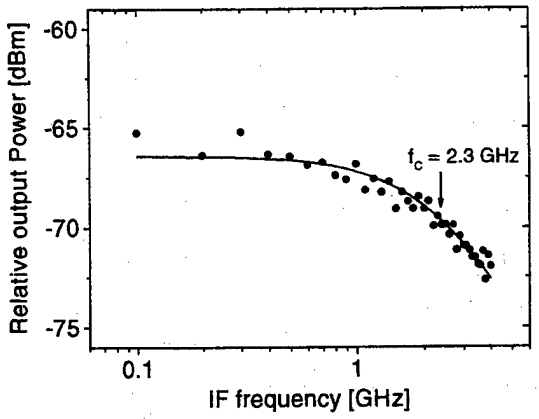

Fig. 5. IF output power as a function of the IF frequency.

C. Measurements of IF Bandwidth

The setup used for bandwidth measurements is shown in Fig. 4. The mixer block with the sample was located in a liquid helium cryostat. The local oscillator (LO) and the signal were weakly coupled by directional couplers and attenuators. The signal frequency and power were fixed to 15 GHz and a constant value. The frequency of LO was varied from 15.1 GHz to 19.0 GHz and the power was set to the same operating point at each LO frequency. The IF signal was observed by the spectrum analyzer.

The IF output power as a function of the IF frequency is shown in Fig. 5. The line was fitted from the expected frequency dependence $[1+(f/f_C)^2]^{-1}$ [5], where f_C is the IF frequency at which the IF output power dropped by 3 dB. The roll-off occurred at 2.3 GHz, indicating a 2.3-GHz bandwidth in the mixer.

IV. Conclusion

We have fabricated high-quality NbN thin films on an single-crystal MgO substrate to apply phonon-cooled HEB mixers. The films had excellent superconducting properties and a single crystal structure. The best films with an ultrathin thickness of 2.5 nm had a T_C of 9.8 K and ρ_{20} of 185 μΩ cm. The HEB mixers with the NbN films were fabricated and the IF bandwidth was measured at microwave bands. The –3-dB IF response extends to 2.3 GHz, a reasonable value for the mixing test in the high-frequency region.

Acknowledgment

We would like to thank Dr. Y. Yabuuchi of Matsushita Technoresearch Inc. for the TEM observations.

References

[1] Yu. P. Gousev, G. N. Gol'tsman, A. D. Semenov, E. M. Gershenzon, R. S. Nebosis, M. A. Heusinger, and K. F. Renk, "Broadband Ultrafast Superconducting NbN Detector for Electromagnetic Radiation", *J. Appl. Phys.*, 75 (7), pp. 3695-3697, 1 April 1994.

[2] G. N. Gol'tsman, A. D. Semenov, Y. P. Gousev, M. A. Zorin, I. G. Gogidze, E. M. Gershenzon, P. T. Lang, W. J. Knott, and K. F. Renk, "Sensitive picosecond NbN detector for radiation from millimetre wavelengths to visible light", *Supercond. Sci. Technol.*, 4, pp. 453-456, 1991.

[3] P. Yagoubov, G. Gol'tsman, B. Voronov, L. Seidman, V. Siomash, S. Cherednichenko, and E. Gershenzon, "The Bandwidth of HEB mixers employing ultrathin NbN films on sapphire substrate", Proc. of the 7th Int. Symp. on Space Terahertz Tech., Charlottesville, VA, pp. 290-302, 1996.

[4] Zhen Wang, Akira Kawakami, Yoshonori Uzawa, and Bokuji Komiyama, "Superconducting properties and crystal structure of single-crystal niobium nitride thin films deposited at ambient substrate temperature", *J. Appl. Phys.*, 79 (10), pp. 7837-7842, 1996.

[5] P. J. Burku, R. J. Schoelkopf, D. E. Prober, A. Skalare, W. R. McGrath, B. Bumble, and H. G. LeDuc, "Length scaling of bandwidth and noise in hot-electron superconducting mixers", *Appl. Phys. Lett.*, 68 (23), pp. 3344-3346, 1996.

Characteristics of Superconducting Tunnel Junction with a Microstrip Coil for X-ray Detector

H.Nakagawa, M.Aoyagi and H.Akoh
Electrotechnical Laboratory (ETL), 1-1-4 Umezono, Tsukuba, Ibaraki, 305-8568 Japan

T.Taino, K.Maehata and K.Ishibashi
Department of Nuclear Engineering, Kyusyu University, 6-10-1 Hakozaki, Higashi-ku, Fukuoka, Japan

H.Sato, T.Ikeda, T.Oku, C.Otani, W.Ootani, H.Kato, K.Kawai, H.Miyasaka, H.M.Shimizu, Y.Takizawa, and H.Watanabe
The Institute of Physical and Chemical Research (RIKEN), 2-1 Hirosawa, Wako, Saitama, 351-0198, Japan

Abstract—We have proposed and demonstrated a superconducting tunnel junction (STJ) with a microstrip coil for X-ray detectors. The microstrip coil consists of multiple superconducting microstrip lines, and applies a magnetic field into the STJ to suppress a dc-Josephson current. The STJ devices were fabricated by a Nb/Al/AlOx/Nb integration technology using a 2 μm design rule. The magnetic field dependence of the dc-Josephson current and the current-voltage characteristics were measured at 4.2 K applying the magnetic field by the microstrip coil and by a conventional external electromagnet. We confirmed that a magnetic field of 13 mT was applied at a 200 μm square STJ by applying a current of 60 mA into the microstrip coil, under which condition Josephson current was sufficiently suppressed.

I. Introduction

Superconducting tunnel junctions (STJs) have been intensively investigated as X-ray detectors because of their high intrinsic energy resolution, high speed counting, and wide energy range [1]-[6]. The energy resolution for a 5.9 keV X-ray has already achieved 29 eV for a Nb-based STJ [1] and 22 eV for a Ta-based STJ [2], respectively. Due to the fast pulse decay time, the STJ detectors also have the advantage of a high counting rate. A counting rate of more than 10,000 cps was achieved with an energy resolution below 10 eV for a 277 eV X-ray [6]. While this method was being investigated, development of Josephson IC technology based on the Nb-based STJ held the potential to provide high-speed signal processing circuits [7]-[9]. By combining these Josephson signal processing circuits and the STJ detectors, a high performance detector system can be expected, particularly in the case of array detectors. However, the Josephson device utilizes a dc-Josephson current, which should be suppressed during use with the STJ detectors. A superconducting quantum interference device (SQUID) had already been introduced in the STJ detector system as an ultra-low noise readout amplifier for the X-ray signal [1]. In this system, an electromagnet of relatively large size is utilized near the STJ chip to apply a magnetic field. The SQUID readout of the Josephson circuit was in a magnetic shield isolated from the STJ, which resulted in a large system size.

In the resuls of our investigation, a superconducting tunnel junction (STJ) with a microstrip coil, which can suppress the dc-Josephson current without an external electromagnet, allowed a small size detector system with a combination of STJs and Josephson circuits.

II. Microstrip Coil

For recent X-ray detection experiments, the magnetic fields at the STJ which can sufficiently suppress the Josephson current have been reported in a range of 7 – 10 mT to suppress the Josephson current [1], [2], [4], [6]. Based on these magnetic fields we designed the microstrip coil to apply a magnetic field of 10 mT at the STJ.

When a magnetic field B is generated by a flowing current I in a superconducting microstrip line of width W located at a distance h above a superconducting ground plane, B can be estimated by $\mu_0 I/W$, where μ_0 is the permeability of the free space. The line width is assumed to be larger than the distance or thickness of the microstrip line, and also to neglect the fringing effect. The magnetic field at the STJ that is inserted between the microstrip line and the superconducting ground plane can also be estimated by the above relation. We calculated the current density I/W of a microstrip line to be 8 mA/mm for generating a magnetic field of 10 mT. This result indicates that, in the case of 200 μm square STJ, a current of 1.6 A is needed for the microstrip

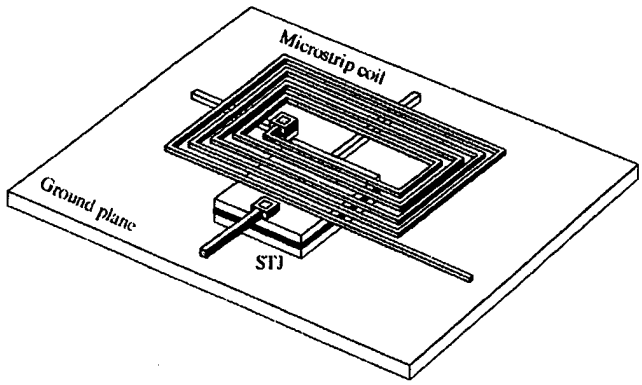

Fig.1. Schematic illustration of the STJ with a microstrip coil.

Manuscript received April 30, 1999.

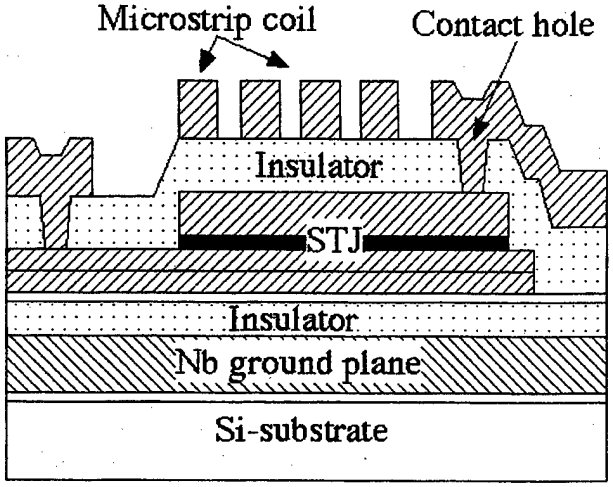

Fig.2. Schematic cross section of the STJ with a microstrip coil.

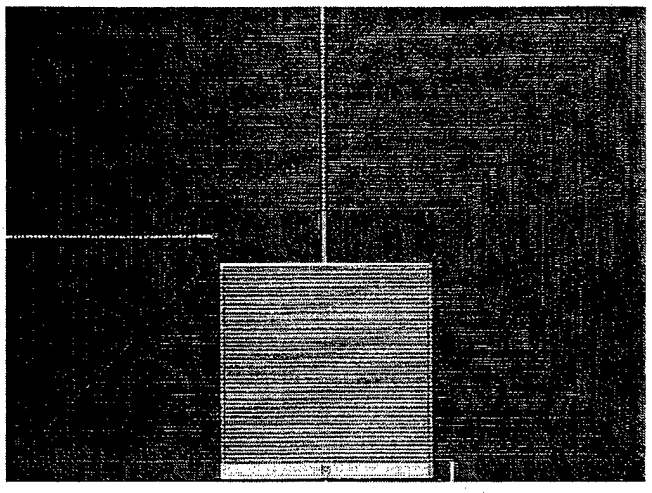

Fig.3. A photograph of the STJ with a microstrip coil

line. It is difficult to handle this large a current level in the STJ-IC chip. In order to decrease the necessary current level, the microstrip line is divided in multiple microstrip lines and each line is serially connected in a planar spiral microstrip coil. A schematic illustration of this STJ with the microstrip coil is shown in Fig.1. Utilizing a line and space design rule of 2 μm, the microstrip line can be divided into 47 microstrip lines for the 200 μm square STJ. The current level of the microstrip coil is calculated to be 34 mA. A critical current of a Nb thin film line 2 μm wide and 500 nm thick was reported to be 90 mA [10], and sufficiently guarantees the above necessary coil current. Other STJs can be put under the microstrip coil, as can be seen in Fig. 1, which indicates an array configuration realized by extending the coil.

III. FABRICATION

In order to confirm the above consideration, a STJ with a microstrip coil was manufactured by the following fabrication process. A cross-section of the STJ device is shown in Fig. 2. A 20 nm thick MgO film was first deposited by thermal evaporation on a 3 inch {100}Si wafer. A Nb ground plane (400 nm) was deposited by dc-magnetron sputtering and was patterned by a photolithography technique and a reactive ion etching (RIE) process in CF_4 gas. The MgO film was utilized as an etching stopper in the RIE process. The ground plane was isolated by depositing a sputtered SiO_2 film (200 nm) and a 20 nm thick MgO film. A 150 nm Nb underlayer was deposited and etched into a base electrode pattern in order to reduce internal stress in the following STJ sandwich structure. Each layer of the Nb (50 nm) / Al (10 nm) / AlOx/ Nb (200 nm) sandwich structure was sequentially formed on the underlayer without any vacuum breaking. The AlOx tunnel barrier was made by thermally oxidizing the Al film surface in 2.6 kPa O_2 gas for 30 min. The STJ sandwich was etched to define the base electrode pattern and the counter electrode was subsequently etched for the junction area. A 350 nm SiO_2 layer was sputter-deposited for isolation between the base and counter electrodes. A contact hole was made by the RIE process on junctions and base electrodes. Finally, the Nb wiring layer (600 nm) was deposited and patterned for making the connection lines of the STJ and the superconducting microstrip coil.

IV. EXPERIMENTAL RESULTS AND DISCUSSIONS

A photograph of a 200 μm square STJ with a microstrip coil fabricated by the above process is shown in Fig.3. The whole 47-turn microstrip coil is 635 μm x 430 μm, which is located on the ground plane. A portion of the coil is overlapped on the STJ area except where the contact hole of 4 μm square is exposed for wiring.

The current-voltage (I-V) characteristics of the STJs were measured at 4.2K. The fabricated STJs exhibited a Josephson critical current density Jc of 180 A/cm^2, a subgap voltage Vg of 2.9 mV, and a quality parameter Vm of about 80 mV.

Fig.4 (a) shows the microstrip coil current dependence of the dc-Josephson current of the 200 μm square STJ. The Fraunhofer characteristics in Fig.4(b) was also measured by using external electromagnet to calibrate the magnetic field of the microstrip coil. The same feature was observed on both characteristics, which indicate that the magnetic field at the STJ by using the microstrip coil acts as a parallel magnetic field of the external electromagnet. This magnetic field can be calculated based on the Fraunhofer characteristics to be 0.22 mT/mA. The applied value is 24% lower than the predicted one, and difference may be caused primarily by the fringing effect of the 2 μm width microstrip lines. Fig.5 shows I-V characteristics under condition of feeding a current of 20 mA into the microstrip coil. The microstrip coil current was limited to be 60 mA. This current can sufficiently suppress dc-Josephson current. In fact, neither dc-Josephson current or

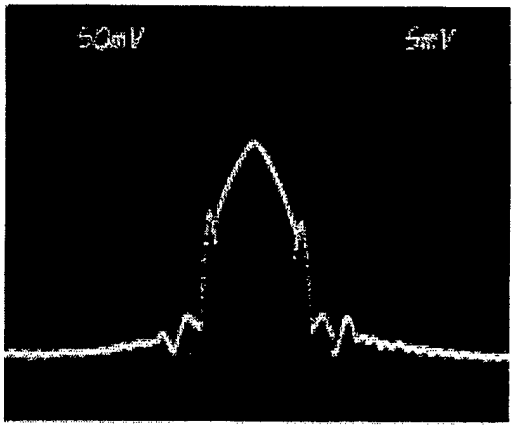

Scales: Vertical: 5 mA/div. Horizontal: 0.5 mA/div

(a)

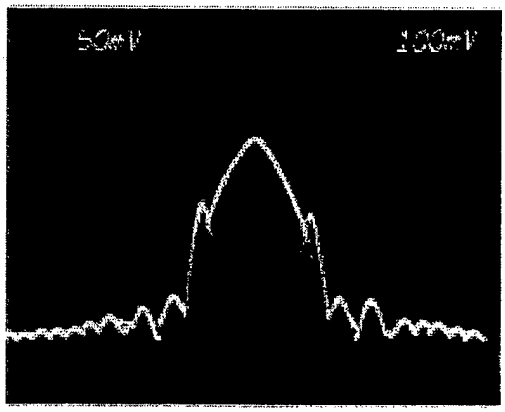

Scales: Vertical: 5 mA/div. Horizontal: 0.22 mT/div.

(b)

Fig.4. Magnetic field dependence of the dc-Josephson current for the 200 μm square STJ, to which the magnetic field was applied by (a) microstrip coil and (b) an external electromagnet.

iske step were observed at a coil current of more than 10 mA, which value corresponds to 2.2 mT.

In summary, we have proposed and demonstrated a superconducting tunnel junction (STJ) with a microstrip coil comprised of multiple superconducting microstrip lines for use as an X-ray detectors. The dc-Josephson current of the STJ was sufficiently suppressed by feeding an appropriate current into the microstrip coil. The use of an external electromagnet in the STJ detector system is expected to coalesce the STJ detector and the Josephson signal processing circuits at the chip level.

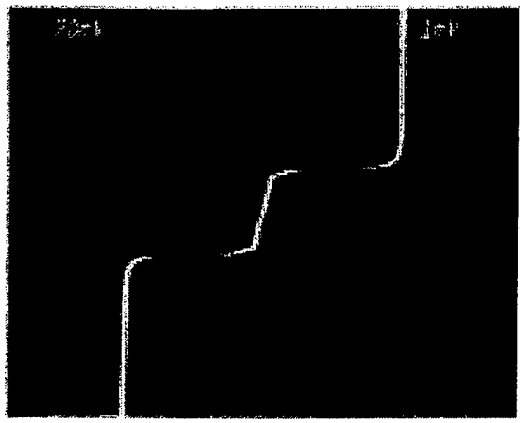

Scales: Vertical: 2 mA/div. Horizontal: 1 mV/div

Fig.5. I-V characteristics of the 200 μm square STJ under condition of feeding a microstrip coil current of 20 mA.

ACKNOWLEDGMENT

The authors wish to thank Tsunenori Sakamoto for his encouragement and also thank Hiroshi Sato and Susumu Takada of Saitama University for valuable discussions.

REFERENCES

[1]M.Frank, C.A.Mears, S.E.Labov, F.Azgui, M.A.Lindeman, L.J.Hiller, H.Netel, A.Barfknecht, "High-resolution X-ray detectors with high-speed SQUID readout of superconducting tunnel junction," *Nucl. Instrum.*

[2]P.Verhoeve, N.Rando, A.Peacock, A. van Dordrecht, B.G.Taylor, D.J.Goldie, "High-resolution x-ray spectra measured using tantalum superconducting tunnel junctions," *Appl. Phys. Lett.*, vol. 72, no. 25, pp. 3359-3361, June 1998.

[3]M.P.Bruijn, F.B.Kiewiet, M.L. van den Berg, O.J.Luiten, and P.A.J.de Korte, "Superconducting tunnel junctions on Nb- and Ta-single crystal substrates for X-ray spectrometry," *IEEE Trans. Appl. Supercond.*, vol. 7, no.2, pp. 3387-3390, June 1997.

[4] K.Maehata, K.Ishibashi, H.Nakagawa, H.Akoh, K.Joosse, S.Takada, M.Katagiri, "Characteristics of large Nb-Based tunnel junction for X-ray detection," *IEEE Trans. Appl. Supercond.*, vol. 7, pp. 3371-3374, June 1997.

[5] S.Frienrich, K.Segall, M.C.Gaidis, C.M.Wilson, D.E.Prober, P.J.Kindlmann, A.E.Szymkowiak and S.H.Moseley, "Single photon imaging X-ray spectrometers using low noise current preamplifiers with dc voltage bias," *IEEE Trans. Appl. Supercond.*, vol. 7, no.2, pp. 3383-3386, June 1997.

[6] M.Frank, L.J.Hiller, J.B.Le Grand, C.A.Mears, S.E.Labov, M.A.Lindeman, H.Netel D.Chow, A.T.Barfknevht, "Energy resolution and high count rate performance of superconducting tunnel junction x-ray spectrometers," *Rev. Sci. Instrum.*, vol. 69, no. 1, pp. 25-31, January 1998.

[7]S.V.Rylov, L.A.Bunz, D.V.Gaidarenko, M.A.Fisher, R.P.Robertazzi and O.A.Mukhanov, "High resolution ADC system," *IEEE Trans. Appl. Supercond.*, vol. 7, no.2, pp. 2649-2652, June 1997.

[8] H.Nakagawa, I.Kurosawa, M.Aoyagi, S.Kosaka, Y.Hamazaki, Y.Okada and S.Takada, "A 4-bit Josephson computer ETL-JC1," *IEEE Trans. Appl. Supercond.*, vol. 1, no. 1, pp. 37-47, March 1991.

[9]S.Nagasawa, H.Numata, Y.Hashimoto, S.Tahara, "High-frequency clock operation of Josephson RAMs,"*ISEC'97, Extended Abstracts*, vol. 2, pp. 290-292, June 1997.

[10]T.Imamura, S.Ohara, S.Hasuo, "Bias-sputterd Nb for wirings in Josephson circuits," *IEICE Tech. Report.*, vol. SCE90-14, pp. 31-36, 1990 (in Japanese).

Characteristics of Nb/Al/AlO_x/Al/Nb Superconducting Tunnel Junction with a Al_2O_3 Buffer Layer for X-ray Detectors

H.M.Shimizu, T.Ikeda, H.Kato, K.Kawai, H.Miyasaka, T.Oku, W.Ootani, C.Otani, H.Sato, Y.Takizawa, H.Watanabe, H.Nakagawa*, M.Aoyagi* and H.Akoh*

The Institute of Physical and Chemical Research (RIKEN),
2-1 Hirosawa, Wako, Saitama 351-0198, Japan
*Electrotechnical Laboratory (ETL),
1-1-4 Umezono, Tsukuba, Ibaraki, 305-8568 Japan
Phone: +81-48-467-9720, Fax: +81-48-467-9721
e-mail: shimizu@riken.go.jp

Abstract

We have studied the characteristics of superconducting tunnel junction (STJ) with an aluminum quasiparticle trapping layer (Nb/Al/AlO_x/Al/Nb) fabricated on a silicon substrate with Al_2O_3 buffer layer for phonon suppression. The phonon signals induced by X-rays absorbed in the silicon substrate were suppressed by choosing the thickness of Al_2O_3 buffer layer. Details of junction design, fabrication and response to X-rays will be presented.

RF Responses of Double-Junction SQUID Models

Yoshinao Mizugaki, Jian Chen, Kensuke Nakajima
Research Institute of Electrical Communication, Tohoku University, Sendai 980-8577, Japan,
and CREST, Japan Science and Technology Corporation, Japan

Tsutomu Yamashita
New Industry Creation Hatchery Center, Tohoku University, Sendai 980-8579, Japan,
and CREST, Japan Science and Technology Corporation, Japan

Abstract — We present numerical investigation on the RF properties of a double-junction SQUID model, which is referred as an RF-Field-Driven double-junction SQUID (RFDS). The RFDS utilizes the RF circulating current in the SQUID loop. It has an interesting dependence on an external DC field. If no DC field is applied, the even-order steps (including the supercurrent) appear and the odd-order steps are suppressed. On the other hand, if the external flux of 0.5 Φ_0 (Φ_0 is a flux quantum) is applied, the even-order steps are suppressed and the odd-order steps appear. We numerically investigate the frequency dependence of the step height. The results indicate that the RFDS is applicable as a wide-band RF detector.

I. Introduction

Detection of RF electromagnetic wave is one of most prospective applications of Josephson devices, because of their high sensitivity and ultimate response frequency expected from the superconducting energy gaps. We have published both experimental and numerical results on terahertz (THz) responses of high-T_c Josephson junctions [1]–[4]. Recently, we have also found interesting features of THz response enhanced by an external magnetic field, and explained this phenomena by introducing an "RF-Field-Driven double-junction SQUID (RFDS)" [5].

In this paper, we present the numerical results for the RFDS, especially on the frequency dependence of the step height.

II. RF-Field-Driven double-junction SQUID (RFDS)

Fig. 1(a) shows the schematic concept of the RFDS. The RFDS is a double-junction SQUID activated by RF-field. The RF-field generates the RF circulating current in the SQUID loop. This alternatively circulating current produces the voltage steps, of which behavior is quite different from that of a single junction.

Manuscript received April 30, 1999.

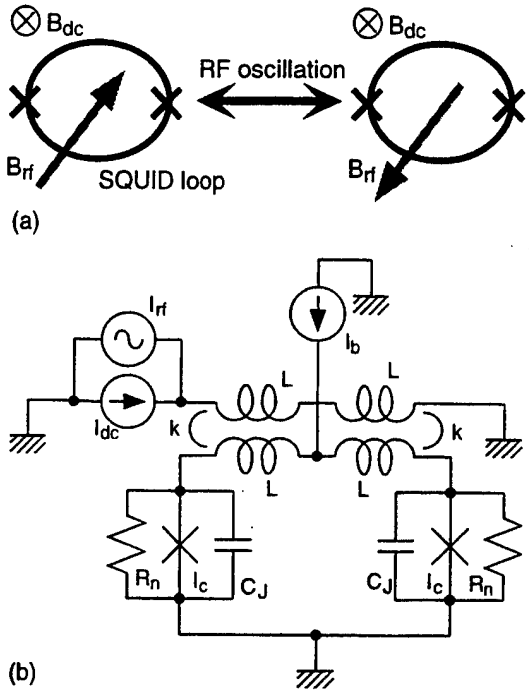

Fig. 1. RF-Field-Driven double-junction SQUID (RFDS). (a) Schematic concept. (b) Simulated circuit. The device parameters are I_c=0.10mA, R_n=16Ω, C_J=12.9fF, L=10.3pH, and k=1.0.

We simulated the current-voltage (I-V) characteristics of the RFDS by using the Josephson circuit simulator "JSIM" [6]. The simulated equivalent circuit is shown in Fig. 1(b). I_{dc} and I_{rf} are for generating the external flux of B_{dc} and B_{rf}, respectively. The JSIM can be used to simulate the time-dependent voltage, as it stands. To obtain the DC I-V characteristics, we accumulated the phase difference in steady state for a certain time (typically 1ns) and calculated the average voltage according to the AC Josephson relation. In the simulation, we assumed the following junction parameters; The I_cR_n product and the McCumber parameter $\beta_c = 2eI_cC_JR_n/\hbar$ were 1.6mV and 1.0 respectively, where I_c, R_n, e, C_J, and $\hbar$ were the critical current, the normal resistance, the electron charge, the junction capacitance, and Planck's constant (h) divided by 2π. The applied frequency f was set from 50GHz to 3.86THz.

To expand the calculated results to a general case, we

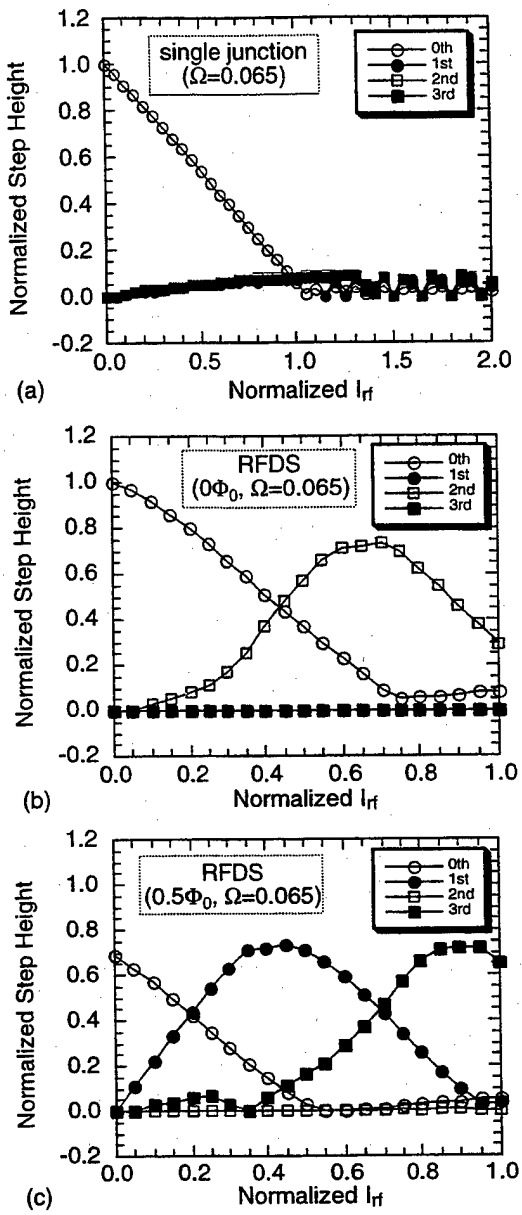

Fig. 2. I_{rf} dependence of the voltage steps for low frequency (Ω = 0.065). (a) For a single junction. (b) For the RFDS with $B_{dc} = 0$. (c) For the RFDS with $B_{dc} = 0.5\Phi_0$. I_{rf} and the step height are normalized by $2I_c$ in (b) and (c).

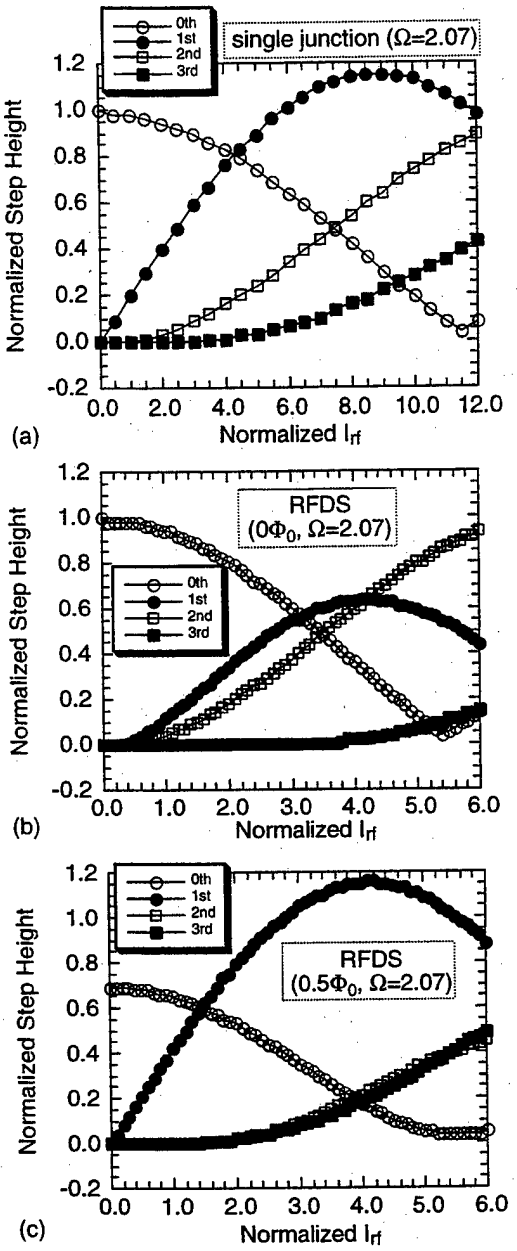

Fig. 3. I_{rf} dependence of the voltage steps for high frequency (Ω = 2.07). (a) For a single junction. (b) For the RFDS with B_{dc} = 0. (c) For the RFDS with $B_{dc} = 0.5\Phi_0$. I_{rf} and the step height are normalized by $2I_c$ in (b) and (c).

use the normalized parameters in the following sections; that is, we use the normalized I_{rf}, the normalized step height, and normalized frequency Ω ($=hf/2eI_cR_n$).

III. Results

Figs. 2 and 3 are the normalized I_{rf} dependence of the voltage steps (especially called as Shapiro steps for a single junction) with low (Ω = 0.065) and high (Ω = 2.07) frequency signals, respectively. In both figures, the results for (a) a single junction, (b) the RFDS with B_{dc} = 0, and (c) the RFDS with $B_{dc} = 0.5\Phi_0$ are included.

For a single junction, it is well known that the height of Shapiro steps strongly depends on the applied frequency [7]. In the case that the normalized frequency is much less than unity, large steps cannot be produced by a single junction, as shown in Fig. 2(a), even if large I_{rf} is applied. But the RFDS can produce big steps for such low frequency signals (Figs. 2(b) and (c)). Furthermore, only the even-order steps are enhanced if $B_{dc} = 0$, while

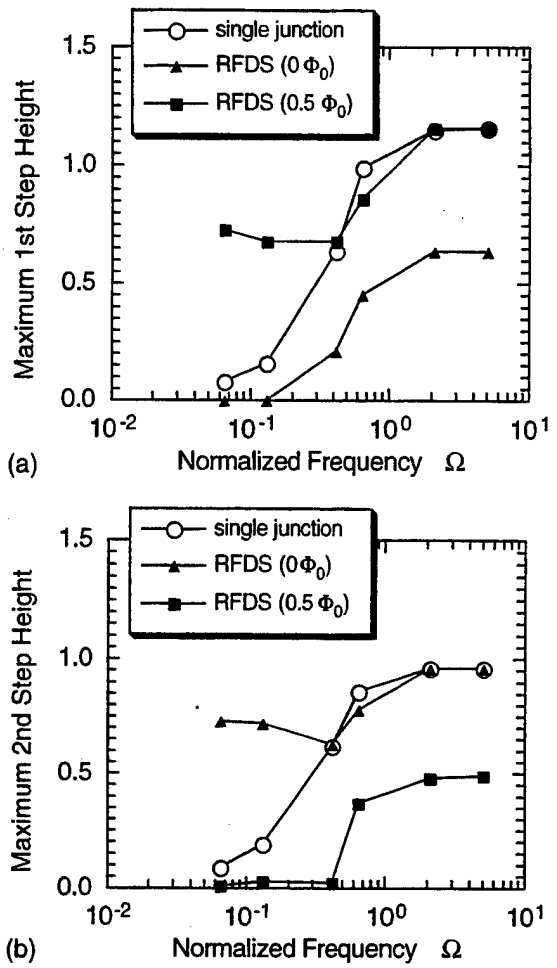

Fig. 4. Frequency dependence of the maximum step height. (a) 1st voltage step. (b) 2nd voltage step.

only the odd-order steps are enhanced if $B_{dc} = 0.5\Phi_0$. In these case, the steps appear at the bias current below $2I_c$ and can be explained by introducing the transition between the quantum states [8].

The same enhancement phenomena can been observed in the case of high frequency (Fig. 3). But in this case, the steps appear at the bias current above $2I_c$, and the explanation using the quantum transition is not applicable. The qualitative explanation for the enhancement was given by introducing the phase relation between the two junctions [5].

Figs. 4(a) and (b) show the frequency dependence of the maximum step height for the 1st and 2nd voltage steps, respectively. For the single junction, both the 1st and 2nd step height increases with the frequency. This is a general feature for a single junction, and the same feature can be observed for the RFDS. The RFDS can generate the voltage steps as large as a single junction if B_{dc} is properly set. Furthermore, the RFDS can produce the large steps even if the frequency is lower than unity. For example, as shown in Fig. 4(a), the RFDS with $B_{dc} = 0.5\Phi_0$ can generate the 1st step about nine times larger than that of a single junction for $\Omega = 0.065$. That is, the RFDS can work as a high-performance RF detector for wide frequency region.

IV. Conclusion

We presented the numerical results of the RF response of the RFDS. The RFDS utilizes the RF circulating current in the SQUID loop. It has an interesting dependence on an external DC field. If no DC field is applied, the even-order steps appear and the odd-order steps are suppressed. On the other hand, if the external flux of 0.5 Φ_0 is applied, the even-order steps are suppressed and the odd-order steps appear. We also investigated the frequency dependence of the step height by simulation. The RFDS can generate large voltage steps in the normalized frequency range between 0.065 and 5.0. Especially, it is remarkable that the step height of the RFDS is nine times larger than that of a single junction for $\Omega = 0.065$. Hence, the results indicate that the RFDS is applicable as a wide-band RF detector.

Acknowledgment

The authors would like to thank E. Kobayashi and T. Endo for fruitful discussions.

References

[1] K. Nakajima, J. Chen, H. Myoren, T. Yamashita, and P. H. Wu, "Terahertz response for bicrystal YBCO Josephson junctions," *IEEE Trans. Appl. Superconduct.*, vol. 7, pp. 2607–2610, June 1997.

[2] J. Chen, H. Myoren, K. Nakajima, T. Yamashita, and P. H. Wu, "Mixing at terahertz frequency band using $YBa_2Cu_3O_{7-\delta}$ bicrystal Josephson junctions," *Appl. Phys. Lett.*, vol. 71, pp. 707–709, Aug. 1997.

[3] J. Chen, E. Kobayashi, K. Nakajima, T. Yamashita, S. Linzen, F. Schmidl, and P. Seidel, "Response properties at 2.525 terahertz using high-T_c Josephson junctions on silicon bicrystal substrates," unpublished.

[4] Y. Mizugaki, J. Chen, K. Nakajima, and T. Yamashita, "Numerical evaluation for the high-frequency response of Josephson junctions having finite capacitance," *Jpn. J. Appl. Phys.*, vol. 37, part 1, pp. 5971–5972, Nov. 1998.

[5] Y. Mizugaki, J. Chen, K. Nakajima, and T. Yamashita, "Terahertz response of Josephson devices enhanced by a magnetic field," unpublished.

[6] E. S. Fang and T. Van Duzer, "A Josephson integrated circuit simulator (JSIM) for superconductive electronics application," *Ext. Abstr. 1989 Int. Superconductivity Electronics Conf.*, (Tokyo, 1989) pp.407-410.

[7] P. Russer, "Influence of microwave radiation on current-voltage characteristic of superconducting weak links," *J. Appl. Phys.*, vol. 43, pp. 2008–2010, Apr. 1972.

[8] G. S. Lee, H. L. Ko, R. C. Ruby, and A. T. Barfknecht, "Large RF-controlled voltage steps in DC SQUIDs applicable to voltage standards and sources," *IEEE Trans. Appl. Superconduct.*, vol. 3, pp. 2740–2743, Mar. 1993.

Detection of Emitted Radiation Spectra from a Quasiparticle-Injected high T_c $YBa_2Cu_3O_{7-y}$ Superconductor

Eiji Kume, Hirokazu Takahashi and Ienari Iguchi
Department of Applied Physics and CREST, Tokyo Institute of Technology,
2-12-1 Oh-okayama, Meguro-ku, Tokyo 152-8551, Japan

Abstract—We present the new spectroscopic measurements of electromagnetic wave emission from a $YBa_2Cu_3O_{7-y}$ superconductor due to quasiparticle injection using a Josephson Junction fabricated on the same sample chip as a detector. The observed electromagnetic spectrum has a broad peak near 1THz and extends up to 2.5THz.

I Introduction

The electromagnetic wave radiation from a high T_c superconductor is a very attractive subject for basic understanding of the high T_c superconductive mechanism as well as the possible application to mixers and filters, etc. It is well known that electromagnetic waves are emitted from the superconductor in terms of the Josephson self-radiation. Recently, it has been also reported that the THz electromagnetic waves are emitted by photoexcitation of a high T_c superconducting film irradiated by a femtosecond laser [1].

Quite recently, we have reported a novel method for the generation of microwave by biasing an Au/ insulating barrier/ $YBa_2Cu_3O_{7-y}$ (YBCO) thin film tunnel junction at certain injection currents [2]. The microwave power detected by a superheterodyne mixer technique increased with injection current approximately linearly up to a certain value, above which it exhibited saturated behavior. For further increase of injection current, the injector characteristic exhibited a sharp transition, probably to the normal state, and the emitted power decreased abruptly. The microwave power decreased when the temperature was raised from 4.2K to near T_c . The results suggest that this electromagnetic wave radiation originates from superconducting state. The emitted power increased with the increase of the receiver frequency in contrast to the Josephson self-radiation, suggesting the existence of a broad band spectrum extending to the terahertz region. It has been recently shown that the phenomenon is closely related to the Josephson plasma emission.

Manuscript received April 28,1999.

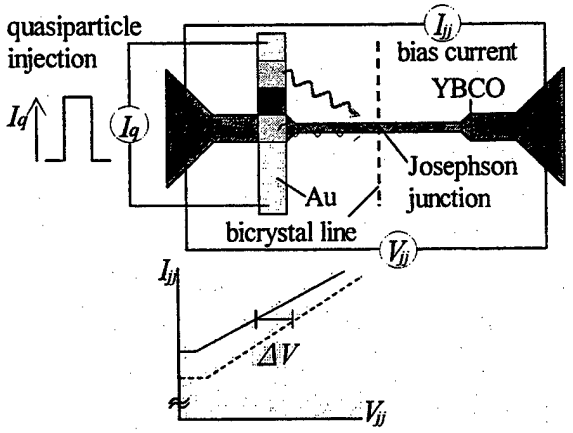

Fig. 1. Method of measurement: The voltage difference of a detector Josephson junction with and without injection current.

We here present the spectroscopic measurements on this electromagnetic radiation in the terahertz region using a high T_c Josephson bicrystal junction fabricated on the same sample chip as a detector. The Josephson junction detector is highly sensitive [3], and the energy gap of about 10meV for high T_c superconductors enables us to detect radiation in the terahertz region.

II Experimental

The c-axis oriented YBCO films were deposited by PLD method on a MgO bicrystal substrate. The films were patterned by a photolithography method and the tunnel junction structure was formed by Au evaporation and lift-off technique. The spectroscopic data were taken by measuring the voltage difference of a detector Josephson junction with and without injection current (Fig.1). The voltage difference $\Delta V(V)$ is related to the spectral density $S(u)$ by an inverse Hilbert transformation according to

$$S(u) \sim \frac{1}{\pi}\int_{-\infty}^{+\infty}\frac{g(V)}{V-u}dV \qquad (1)$$

where

$$g(V) = \frac{8}{\pi}I(V)V\Delta I(V) \sim \frac{8}{\pi}I(V)V\frac{\Delta V(V)}{R_d} \qquad (2)$$

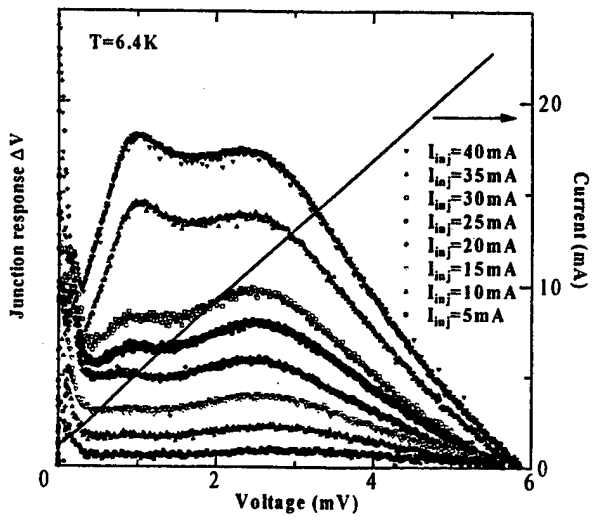

Fig. 2. The observed voltage signal as a function of Josephson junction voltage at $T = 6.4$K.

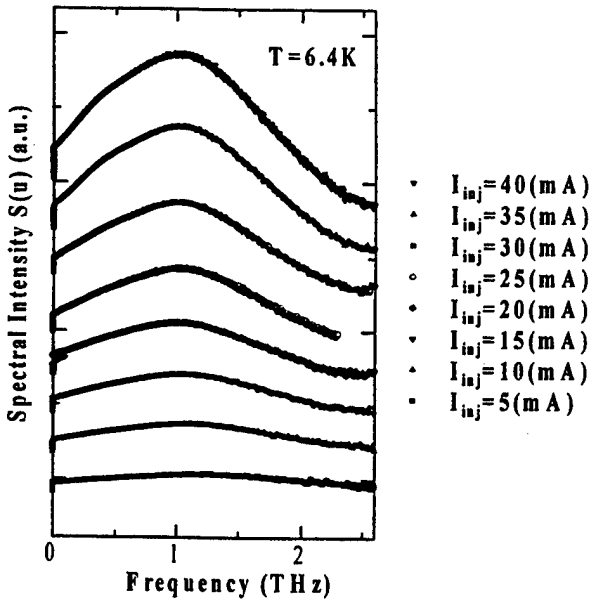

Fig. 3. Calculated spectral density of electromagnetic waves($T = 6.4$K).

and V is the Josephson junction voltage, I is the junction current, u is the voltage related to the frequency by Josephson voltage-frequency relation ($f = 2eu/h$), R_d is the dynamic resistance [4]-[6]. The Cauchy principal value is taken for the integral. The inverse discrete Hilbert transformation can be calculated using discrete Fourier transform (DFT) routines.

III Results and Discussions

Fig. 2 shows the results of the measured response ΔV as a function of Josephson junction voltage at $T = 6.4$K together with the $I - V$ curve without electromagnetic radiation. The response increased with the increase of the injection current. At a fixed injection current, it increased with increasing Josephson junction voltage and it formed a peak-like structure, then decreased to become zero at about 6mV.

Fig. 3 shows the calculated spectral density of electromagnetic waves using the inverse Hilbert transformation. The results indicate that broad band electromagnetic waves are emitted in the range 0 - 2.5THz with the maximum intensity at about 1THz.

Recently, it has been shown that Josephson plasma emission by quasiparticle injection may have a spectral peak at a half-gap frequency [7]. If we assume the gap $\Delta \simeq 10$meV,

$$0.5\Delta \rightarrow 0.2418(\text{THz/meV}) \times 5(\text{meV}) \simeq 1.2(\text{THz}) \quad (3)$$

This value almost agrees with the experimental result, hence the electromagnetic radiation by the quasiparticle injection seems to originate from the Josephson plasma phenomenon.

Fig. 4 shows the measured voltage response at $T = 20$K, and Fig. 5 shows the calculated electromagnetic wave spectrum using the inverse Hilbert transformation. It is understood that the spectrum has a broad peak near 1THz and extends up to 2.5THz, similar to $T = 6.4$K case, but the intensity at $T = 20$K is smaller than that at $T = 6.4$K. It is expected that the peak of the electromagnetic wave spectrum shifts toward the lower frequency, when the effective system temperature is raised. In fact, this tendency is observable as the injection current increases.

IV Conclusions

In conclusion, we have reported the observation of broadband spectrum of electromagnetic radiation in terahertz range emitted from a YBCO superconductor under quasiparticle injection using a Josephson junction fabricated on the same sample chip as a detector. The observed electromagnetic spectrum had a broad peak around 1THz and extends up to 2.5THz. The results agree with theoretical calculation value of the possible Josephson plasma emission by quasiparticle injection. Since the electromagnetic radiation by quasiparticle injection is possible by supplying a dc bias current, it may apply to terahertz electromagnetic wave electronic devices.

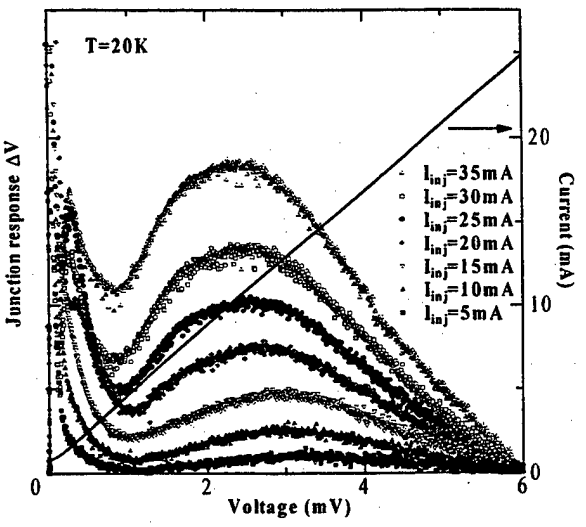

Fig. 4. The observed voltage signal as a function of Josephson junction voltage at $T = 20$K.

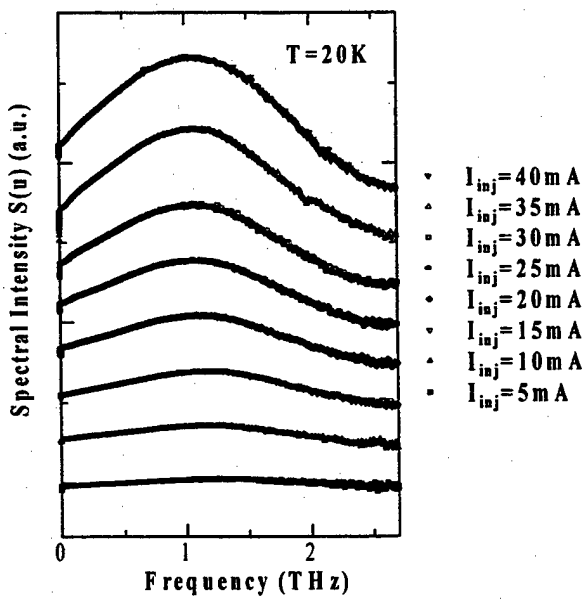

Fig. 5. Calculated spectral density of electromagnetic waves($T = 20$K).

REFERENCES

[1] M. Hangyo, S. Tomozawa, Y. Murakami, M. Tonouchi, M. Tani, Z. Wang, K. Sakai and N. Wada, "Novel terahertz radiation from flux-trapped $YBa_2Cu_3O_{7-\delta}$ thin films excited by femtosecond laser pulses," *Jpn. J. Appl. Phys.*, Vol. 36, pp. L93-L95, 1997.

[2] K. Lee, I. Iguchi, H. Arie and E. Kume, "Nonequiliblium microwave emission from dc-biased high T_c $YBa_2Cu_3O_{7-y}$ junctions," *Jpn. J. Appl. Phys.*, Vol. 37, p. 278, 1998; K. Lee, H. Yamaguchi, W. Wang, E. Kume and I. Iguchi, "Direction-oriented quasiparticle injection and microwave emission in an $ErBa_2Cu_3O_y$ superconductor," *Appl. Phys. Lett.*, Vol. 74, No. 16, p. 2375, 1999.

[3] K. Lee and I. Iguchi, "Josephson effects in $YBa_2Cu_3O_y$ grain boundary junctions on (100)MgO bicrystal substrates," *Appl. Phys. Lett.*, Vol. 66, No. 6, p. 769, 1995.

[4] Yu. Ya. Divin, O. Yu. Polyanski and A. Ya. Shul'man, "Incoherent radiation spectroscopy based on ac Josephson effect," *IEEE Trans.*, Vol. MAG-19, No. 3, pp. 613-615, 1983.

[5] U. Stumper, J. H. Hinken, W. Richter, D. Schiel and L. Grimm, "Experimental investigation of a new spectrometer comprising a Josephson junction," *Electron. Lett.*, Vol. 20, No. 13, pp. 540-541, 1984.

[6] Yu. Ya. Divin and N. A. Mordovets, "Width of the Josephson-generation line in the far-IR region," *Sov. Tech. Phys. Lett.*, Vol. 9, No. 2, p. 108, 1983.

[7] S. E. Shafranjuk and M. Tachiki, "Emission of plasmons caused by quasiparticle injection to a high T_c superconductor," *Phys.Rev.*, B(June 1 issue),1999.

POSTER SESSION II

Group 5 - Junctions and Fabrication

Coplanar Transmission Lines with Meandering Center Conductors in Y-Ba-Cu-O/Au Bilayers

C. Weber,* R. Ono, J. C. Booth, L. Vale, and S. Benz
National Institute of Standards and Technology, Boulder, CO 80303, USA

A. M. Klushin, and H. Kohlstedt
Research Center Jülich, 52425 Jülich, Germany

R. Semerad
Department of Physics at the Technische Universität München, 85747 Garching, Germany

Abstract—We have investigated both conventional and meandering coplanar microwave transmission lines patterned in Y-Ba-Cu-O/Au bilayers on yttria-stabilized zirconia and sapphire substrates. Within the meandering waveguides, the center conductor was deformed from a straight line to a meander. Such a layout could be useful for metrological High-T_c Superconductor arrays, which are based on series arrays of shunted YBCO bicrystral junctions. The microwave properties of the lines were measured in the range 0 – 40 GHz at 76 K, using on-chip through-reflect-line calibrations. We discuss the measured attenuation in terms of conductor losses in the bilayers and show to what extent the disturbance of the line geometry affects the microwave properties.

I. Introduction

Shunted Y-Ba-Cu-O (YBCO) bicrystal junctions on yttria-stabilized zirconia (YSZ) substrates may be suitable for metrological applications because of their small spreads in critical current I_c and normal resistance R_n. In particular, they provide a large I_cR_n product at temperatures unattainable by low-T_c junctions [1]. However, the demand of placing all junctions in the form of a meander along the straight grain boundary is a strong restriction on the array design. A homogeneous microwave power distribution, which is crucial to the phase locking of the array, is difficult to achieve under these circumstances.

As an alternative to the High-T_c Superconductor (HTS) arrays that have been realized so far, we have developed a new concept with a meander line being the center conductor of a coplanar waveguide (CPW). Such a layout would be close to already existing layouts in low-T_c voltage standards and has the advantage of fewer patterning steps.

In this work we focus on the extent that the microwave properties are influenced by the disturbance of the ideal straight CPW geometry. To be close to the metrological application mentioned above, we realized our test structures in YBCO/Au bilayers on single crystal substrates of YSZ and sapphire.

Manuscript submitted on April 30, 1999.
This work is a contribution of the U.S. Government and not subject to U.S. copyright.
*on leave of the Research Center Jülich, 52425 Jülich, Germany (supported by the German Academic Exchange Service).

II. Description of the Transmission Lines

Four different variations of CPWs with meandering center conductor were designed. Each of these four types was investigated using a set of lines with an increasing number of meander turns per length, ranging from an undisturbed CPW to a CPW with a center conductor having a maximum number of turns. As an example, Fig. 1 shows three CPWs from the set of type 1 and three from the set of type 2. Within one set, all CPW dimensions were kept constant. The distance d between the turns is used to distinguish the lines within one set (see Fig. 1).

Among the four types, two characteristics were varied: The shape of the meander and the CPW center and gap dimensions. These parameters are characterized in Table I.

Characteristic of type 1 is the rectangular meander (crossing the center vertically). It is also the type with the smallest dimensions, a 6 μm wide center conductor and a 10 μm gap between the center and the grounds. Within types 2, 3, and 4, the center conductor turns are more slightly sloped (45°) and the width is 12 μm. Except for type 3, the inner edges of the grounds were formed to follow the center conductor to maintain the gap distance. In case of type 1, this adjustment of the grounds was only possible to a certain distance between the meander turns (compare the second and third image of type 1 in Fig. 1).

All four sets were equipped with their own lines needed for the through-reflect-line (TRL) calibration. Details of this multiline method are described in [2]. The TRL lines had the same lateral dimensions as the CPWs of each set and were not meandered. The straight CPWs of each set were part of the TRL lines. All microwave properties of the CPWs were calibrated in respect to the TRL structures of the same set.

Fig. 1 also contains images of the end pieces of two CPWs, showing the launching pads for the microprobes and the exponential transitions connecting the pads to the CPWs.

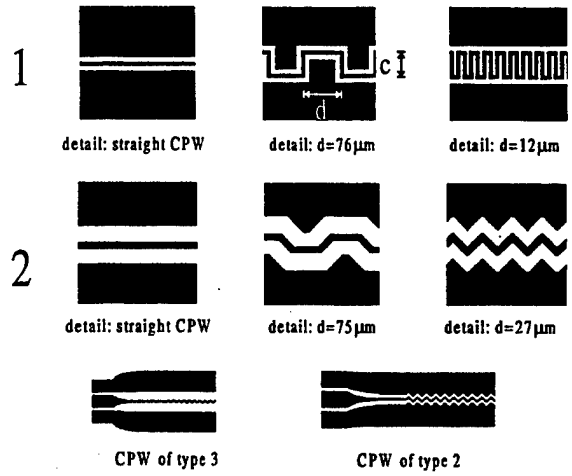

Fig. 1: Diagrams of some of the CPWs of types 1, 2, and 3. The meander detail pictures do not show the grounds in complete width. Values for the lateral extension of the meander, span c, are given in Table I.

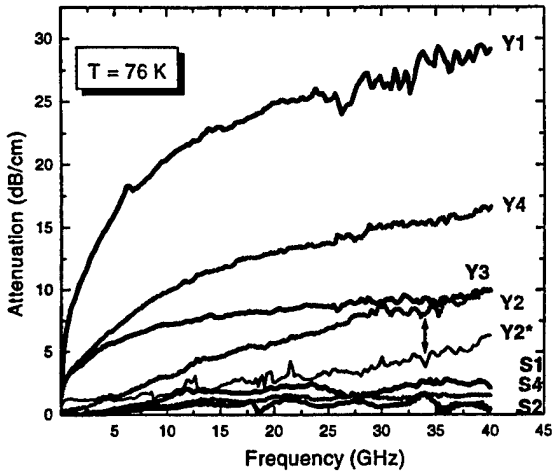

Fig. 2: Attenuation data for the undisturbed CPWs on YSZ and sapphire.

Each set of CPWs was patterned in YBCO/Au bilayers on YSZ by means of standard ultraviolet lithography and Ar-ion milling, resulting in the four samples Y1 to Y4. The bilayers consisted of 300 nm YBCO (by pulsed-laser deposition) and an *ex situ* sputtered 100 nm Au cap layer. Another three samples were fabricated on sapphire, with 330 nm thermal coevaporated YBCO (buffered with 10 nm CeO_2) followed by 300 nm *in situ* sputtered Au. These samples are called S1, S2, and S4 (the set of type 3 was skipped). All substrates were 10 mm x 10 mm. Resistive T_c measurements showed a transition temperature of 88-89 K for films on both substrates.

Due to the different layouts, the characteristic impedances of the four types ranged from 40 Ω to70 Ω on YSZ and 60 Ω to 110 Ω on sapphire (calculated for the undisturbed CPWs using the standard models for coplanar lines).

III. Attenuation of the Undisturbed CPW-Lines

Fig. 2 displays the attenuation versus frequency data obtained from the TRL calibration at 76 K. The straight CPWs on YSZ show much higher attenuation than their counterparts on sapphire. In addition, the four types are more widely separated, and the shape of the curves is square-root like. Sample Y2 was measured a second time, after removal of the Au-layer by ion milling, shown as Y2*. Removal of the normal metal reduced the attenuation considerably.

Longitudinal loss components must be considered to qualitatively explain the loss data. The square-root like shape of the YSZ samples differs from the quadratic dependence usually obtained for superconducting transmission lines [3]. In [3] the quadratic dependence was caused by the conductor losses of the superconductor, which is a longitudinal loss component. The reduced loss after removal of the Au layer in Y2* suggests that the normal metal dominates the conductor loss in the YSZ sample.

Using a program for the calculation of the conductor losses [3], we simulated the losses for the YBCO and the Au separately. We used a 300 nm thick, pure YBCO CPW on YSZ and a 100 nm thick, pure Au CPW on YSZ. The results obtained for the normal metal alone closely reproduced the measured results for the samples on YSZ. Simulations also confirmed a strong decrease in attenuation for an increase of the Au thickness up to 300 nm. Since the normal metal appears to dominate the bilayer attenuation, the lower loss in the sapphire specimen is partially due to the three times thicker Au compared to the YSZ samples. We also removed the Au from S2, S2* being roughly 2 times smaller in attenuation. So even without Au, a comparison between S2* and Y2* shows a considerably lower attenuation for sapphire. This difference is probably due to smaller longitudinal losses in the sapphire films (10 % thicker films than on YSZ and possibly different film quality). The attenuation component due to dielectric losses of the substrates ($\tan\delta > 6 \cdot 10^{-4}$ (YSZ), $\tan\delta = 10^{-8}$ (sapphire) at 10 GHz, [4]) was calculated to be much smaller than the observed attenuation values.

TABLE I

THE FOUR DIFFERENT TYPES OF TRANSMISSION LINES

Type	Dimensions (μm) (center, gap, span c)	Slope of Crossings	Shape of Grounds
1	6, 10, 44	vertical	Follow/Straight
2	12, 32, 25	45°	Follow
3	12, 94, 25	45°	Straight
4	12, 14, 25	45°	Follow

IV. Comparison with the Disturbed CPW-Lines

To evaluate the effect of the meandering on the microwave propagation, we measured the scattering parameters of all CPWs. For each sample the S parameters were determined by referring to the line impedance obtained for the straight CPWs by the TRL multiline method.

Fig. 3(a) displays the S_{12} parameters for all CPWs of set 2 on YSZ and sapphire. The CPWs on YSZ show a strong decrease in transmission as the turn density increases. The lines on sapphire show a better transmission and only small dependence on the turn density.

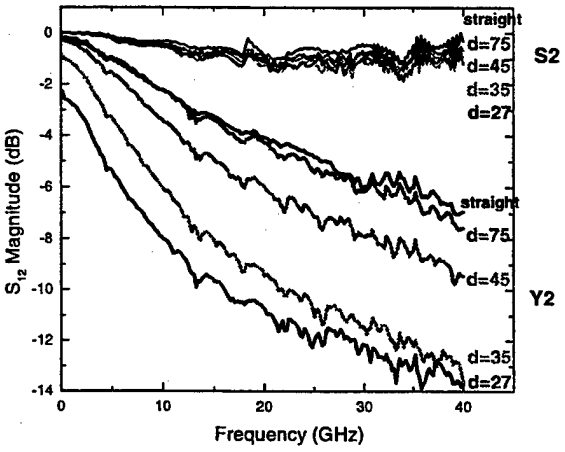

Fig.3(a): Comparison of all CPWs of type 2 on YSZ and sapphire (d in μm). The S parameters refer to the line impedance determined for the straight lines using the TRL multiline method.

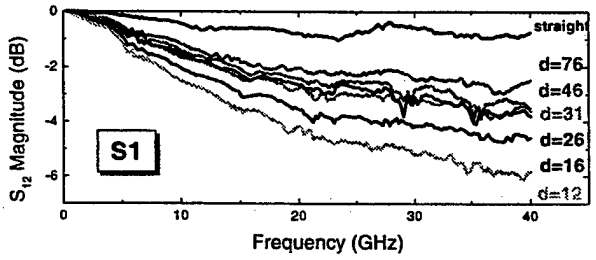

Fig. 3(b): On sapphire, even the worst design, type1, gives considerable results (d in μm).

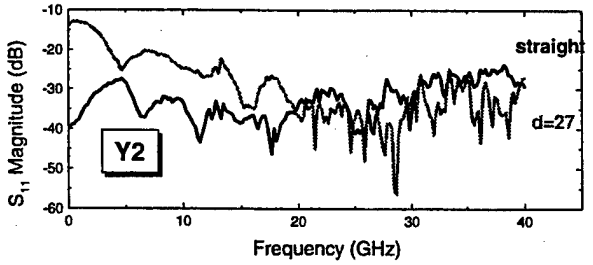

Fig. 3(c): Comparison of the most strongly disturbed CPW and thestraight one of type 2 on YSZ (d in μm).

In accordance with the strong increase of attenuation from type 2 to type 4 to type 1, which was obtained for the straight CPWs on YSZ (Fig. 2), the transmission data get also worse and the dependence on the turn density increases for type 4 and type 1. The three sapphire samples show the same behavior, but less extensively. Even for the worst design, type 1, the transmission values are considerable, as can be seen in Fig. 3(b).

Looking at the reflection of the CPWs, we found no larger mismatch between the undisturbed lines and the disturbed CPWs, showing that the meanders do not change the characteristics of the lines significantly. As an example, Fig. 3(c) displays the S_{11} parameters of the straight and the most disturbed CPW of Y2.

V. Conclusion

The microwave properties of our lines are ruled mainly by the normal metal losses. The disturbance of the CPW geometry by a change of the center conductor into a meander does not strongly influence the microwave characteristics, as could be seen on the sapphire samples. However, the increased length of the meander resulted in significant higher losses on YSZ because of the high longitudinal losses there. An improvement of the attenuation data seems possible by either removing the Au layer, or by thickening it. The latter approach would be of double advantage for metrological applications: It would improve the shunting of the junctions (suppression of R_n spread) and reduce the junctions resistance, an additional source of attenuation.

The considerable difference between the losses on sapphire and YSZ suggests differences in the film quality.

Acknowledgment

We thank D. C. DeGroot for helpful discussions. This work was supported by the German Academic Exchange Service (DAAD).

References

[1] A. M. Klushin, C. Weber, R. K. Starodubrovskii, R. Semerad, A. Lauer, I. Wolff, H. Kohlstedt, *IEEE Trans. Appl. Supercond.*, in press.

[2] R. B. Marks, *IEEE Trans. Microwave Theory and Technol.*, vol. 39, no. 7, July 1991, pp.1205-1215.

[3] J. C. Booth, and C. L. Holloway, *IEEE Trans. Microwave Theory and Technol.*, in press.

[4] E. K. Hollmann, O. G. Vendik, A. G. Zaitsev, and B. T. Melekh, *Supercond. Science & Techn.*, vol. 7, 1994, pp. 609-622.

Fabrication of YBCO/CeO_2/YBCO crossover and via structures for digital circuit and integrated SQUID applications

A. Tsukamoto, T. Fukazawa, Y. Soutome, Y. Tarutani and K. Takagi

Hitachi, Ltd. Advanced Research Laboratory, Kokubunji, TOKYO 185-8601, JAPAN

Abstract—We have developed a multilayer process for fabricating crossover and via structures. A crossover structure with T_c > 85 K was fabricated by using a $SrTiO_3$ buffer layer to repair the $SrTiO_3$ surface damaged during etching. The interlayer resistance of a 10 μm x 50 μm crossover area was 150 kΩ. Via contacts fabricated under various process conditions all showed residual resistance with reduced T_c, indicating the formation of damaged layers at the contact interfaces. The I_c measured through the via contacts was high enough for digital circuits that operate at 30-40 K, but I_c at 77 K was not acceptable for liquid-nitrogen-cooled applications like SQUIDs.

I. Introduction

Multilayer structures including crossovers and via contacts will be needed for advanced high-temperature superconductive electronics. For digital circuit application, a multilayer structure in which Josephson junctions and other components are formed on a superconducting ground plane will be necessary to reduce the circuit inductances. For superconducting quantum interference device (SQUID) application, the largest effective area will be achieved by integrating a multi-turn input coil on a washer SQUID by using multilayer structures.

In this study, we have investigated multilayer structures with CeO_2 as an insulation layer. CeO_2 is widely used as a buffer layer for Si and sapphire substrates and is also used as an insulation layer in multilayer structures [1]-[3]. Although CeO_2 has a fluorite structure, it has good crystallographic compatibility with $YBa_2Cu_3O_y$ (YBCO)[1],[3].

We roughly estimated the required properties for the multilayer structure as follows.

(1) The T_c and J_c of the superconducting layers must be above 85 K and $1x10^6$ A/cm^2 at 77 K. These are our criteria for the desired quality of the superconducting thin films and are not critical factors.

(2) The interlayer sheet resistance in the crossover must be higher than 2.5 Ωcm^2. This criterion corresponds to 1-kΩ isolation for a 500 μm x 500 μm crossover, which should be adequate for most superconducting circuits [4].

(3) The I_c through the via contact must be larger than 3 mA at working temperatures: 30-40 K for a digital circuit and 77 K for a SQUID.

Manuscript received April 30, 1999.

This work was supported by New Energy and Industrial Technology Development Organization (NEDO) through ISTEC.

II. Multilayer Structure Fabrication Process

A. Growth conditions for the multilayer film

The growth conditions for the YBCO/CeO_2/YBCO multilayer films were optimized through the analysis of samples prepared by a metal-mask process. The YBCO and CeO_2 films were deposited on $SrTiO_3$(100) substrates by pulsed laser deposition. After deposition, the samples were cooled in 300 mTorr of oxygen. The metal-mask, which was a 0.1 mm-thick stainless-steel plate with desired shape holes, was exchanged *ex situ* after the deposition of each layer. The samples were annealed in an electric furnace at 450-500°C in a 1 atm oxygen flow after final film deposition to form the fully oxidized YBCO structure.

We confirmed that the c-axis oriented YBCO layers and the a-axis oriented CeO_2 layers were epitaxially grown on each other although the CeO_2 layer contained a small amount of (111) orientation. The percentage of (111) oriented grains was lower when the oxygen pressure during the CeO_2 deposition was lower. However, the T_c of the bottom YBCO layer also fell with a decreasing oxygen pressure even though the T_c of the top YBCO layer remained about 85 K (Fig. 1). This suggested that a high-quality CeO_2 film without irregular

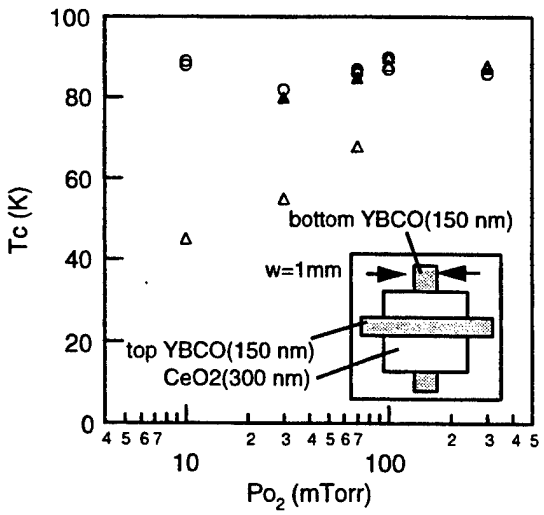

Fig. 1 The dependence of T_c of the YBCO layers in the multilayer film on the oxygen pressure during the growth of the CeO_2 insulating layer. Open circles represent the data for the top YBCO layers, and open and solid triangles represent the data for the bottom YBCO layers annealed at 450°C and 500°C, respectively. The inset shows a schematic drawing of the measured samples fabricated using the metal-mask process.

Table I
THE GROWTH CONDITIONS FOR THE YBCO, CeO_2 AND $SrTiO_3$ THIN FILMS

	YBCO	CeO_2	$SrTiO_3$
Target	$YBa_2Cu_3O_y$ polycrystal	CeO_2 polycrystal	$SrTiO_3$ single crystal
Substrate Temp.[a]	760°C	<—	<—
Oxygen pressure	300 mTorr	70 mTorr	10 mTorr
Laser power[b]	65 mJ	<—	<—
Energy density	1.5 J/cm^3	<—	<—
Repetition	2 Hz	4 Hz	2 Hz
Growth rate	0.05 nm/s	0.04 nm/s	0.04 nm/s
Thickness	150 nm	300-350 nm	20 nm
Cooling condition[c]	300 mTorr O_2	<—	<—

[a]Sample holder temperature on which the $SrTiO_3$(100) substrates was fixed using Ag paste.
[b]A KrF eximer laser (λ=248 nm) was used.
[c]After final layer deposition all samples were annealed with a 1atm O_2 flow in an electric furnace at 500°C

orientation prevented oxygen from diffusing into the bottom YBCO layer. We increased the annealing temperature from 450°C, which was enough to oxidize the single-layer YBCO thin films, to 500°C in order to accelerate the diffusion of oxygen through the CeO_2 layer. This considerably increased the T_c in the bottom YBCO layer (Fig.1). Thus, we could obtain a YBCO/CeO_2/YBCO trilayer film with T_c > 85 K under the growth conditions listed in Table I.

B. Micropatterning process

Samples for characterizing the properties of crossovers and contacts were prepared using a microscopic patterning process in which electron-beam lithography and ion-beam etching were used. In this process, some parts of films necessarily grow on a surface damaged during the ion-beam etching. Figure 2 shows the strange surface morphology (rough with an apparent waven pattern) of a top YBCO layer deposited on a CeO_2 layer formed on a $SrTiO_3$ surface that was damaged when the bottom YBCO layer was removed by etching. We found from x-ray diffraction and TEM analysis that the top YBCO layer shown in Fig. 2 contained (103) oriented grains and had degraded superconducting properties (T_c=77K, J_c(10K)=3x10^{5}A/cm^2). Although the morphology shown in Fig. 2 is similar to that of a CeO_2 film grown on R-plane sapphire [3], the surface of the underlying CeO_2 layer grown on the damaged $SrTiO_3$ did not show a peculiar morphology. Since the cause of the (103) growth of the top YBCO layer seems to be the damaged $SrTiO_3$ surface, it may be necessary to use less powerful etching or to repair the damaged surface. We inserted a $SrTiO_3$ buffer layer just before CeO_2 deposition to repair the damaged $SrTiO_3$ surface. The growth conditions for the $SrTiO_3$ buffer layer are included in Table I. Consequently, a crossover structure with a c-axis oriented top YBCO layer was successfully obtained.

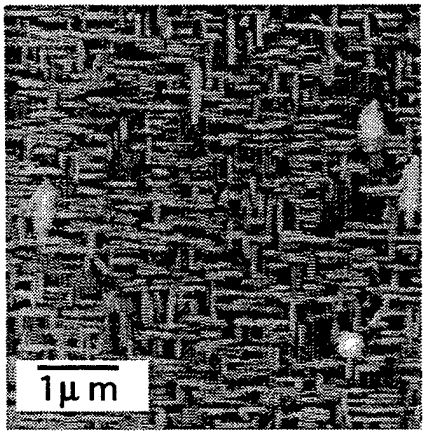

Fig. 2 AFM image of the top YBCO layer in YBCO/CeO_2/etched $SrTiO_3$ substrate.

III. ELECTRICAL PROPERTIES OF MULTILAYER STRUCTURES

A. Crossovers

A schematic drawing of a crossover is shown in the inset of Fig. 3. A 20-nm-thick $SrTiO_3$ layer was inserted between the bottom YBCO and CeO_2 layers. The T_c of both YBCO layers in the crossover were 87 K (Fig. 3). The J_c of the bottom YBCO layer was 1.7x10^6 A/cm^2 at 77 K, which is close to that of our single-layer YBCO film, however the J_c of the top YBCO layer was only 3x10^{5}A/cm^2 at 77 K despite T_c of 87 K. The top YBCO layer may have extended over the steps at the edge of the bottom YBCO pattern whose angle was about 40-45°. We speculate that the J_c of the top YBCO layer decreased at the inclination point formed on the edge of the bottom YBCO pattern [5].

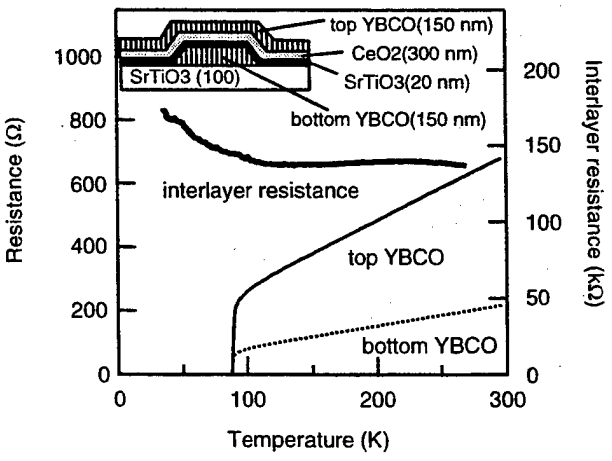

Fig. 3 Temperature dependence of the resistance of the top and bottom YBCO layers (left axis) and interlayer resistance (right axis) in the crossover structure shown in the inset. The crossover area was 10 μm x 50 μm.

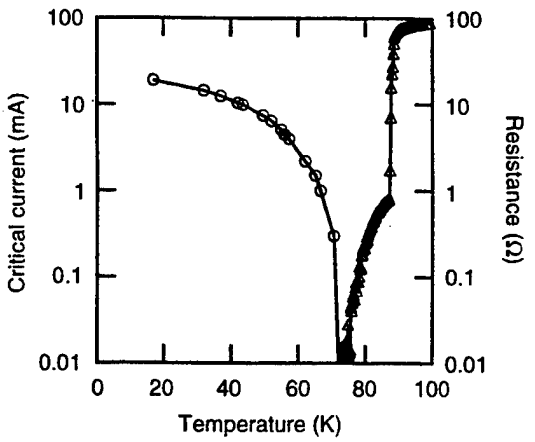

Fig. 4. Temperature dependence of critical current (circles) and resistance (triangles) measured through the via hole of 10 μm x 10 μm. The vertical axes are logarithmic.

The interlayer isolation resistance increased slightly at low temperatures and was about 150 kΩ (Fig.3). The crossover area was 10 μm x 50 μm. Therefore, the sheet resistance between the top and bottom YBCO layers was about 0.75 Ωcm^2. The observed sheet resistance was several orders of magnitude smaller than that obtained from the multilayer films prepared using only the metal-mask process. This suggested that the interlayer isolation would be reduced at the steps formed on the edge of the underlying patterns. Although this value was smaller than our criterion by a factor of 3, it is sufficient for small size circuits.

B. Via contacts

We tested various process conditions for fabricating the via contacts to obtain a higher superconducting current. We found that the contact properties strongly depended on the etching conditions. The best result was obtained by using the following process. The contact hole was first patterned using a resist mask that was reflowed at 200°C to obtain a gentle slope at the sidewall of the contact hole. The etching of the CeO_2 layer was stopped just above the CeO_2/bottom YBCO interface. After the resist was removed using 2-butanon the contact hole was further etched using the CeO_2 pattern as a mask. The thickness of the bottom YBCO layer at the bottom of the holes was about 1/3 of the original thickness. This etching process was performed using Ar at $1x10^{-4}$ Torr and an acceleration voltage of 500 V. The surface was then further etched to obtain a clean surface layer using an Ar +O_2 mixed gas at $1x10^{-4}$ Torr and an acceleration voltage of 500V for 3 min, 300 V for 3 min, and 150 V for 10 min. Contacts prepared by etching using the Ar + O_2 mixed gas showed a higher I_c than when only Ar was used. The slope of the sidewall of the contact hole was about 10-15°. Finally, the top YBCO layer was deposited *ex situ* and patterned to form the counter electrode.

We measured the resistance through the contact interface and observed a slight residual resistance near the film T_c as shown in Fig. 4, indicating that the damaged layer with reduced T_c was formed. Although the I_c at 77 K was almost zero because of the reduced T_c, the I_c at temperatures below 40 K, the range in which the high-temperature superconductive digital circuit will operate, exceeded our criterion of 3 mA.

IV. Conclusions

We have developed a multilayer process for fabricating YBCO/CeO_2/YBCO crossovers and via structures. A crossover structure with $T_c > 85$ K was successfully fabricated by using a $SrTiO_3$ buffer layer between the CeO_2 layer and bottom YBCO layer. The interlayer resistance of a 10 μm x 50 μm crossover area was 150 kΩ. All the via contacts fabricated under various process conditions showed residual resistance with a reduced T_c, indicating the formation of damaged layers at the contact interfaces. Although the I_c measured through the via contacts was high enough for digital circuits that operate below 40 K, that at 77 K was not acceptable for liquid-nitrogen-cooled applications like SQUIDs.

References

[1] M. A. A. A. van Wijck, M. A. Verhoeven, E. M. C. M. Reuvekamp, G. M. Gerritsma, D. H. A. Blank, and H. Rogalla, "CeO_2 as insulation layer in high T_c superconducting multilayer and crossover structures," Appl. Phys. Lett., vol. 68, pp. 553-55, January 1996.

[2] H. Sato, R. Miyakawa, N. Nakamura, S. R. Gjoen, H. Akoh, and S. Tanaka, "$YBa_2Cu_3O_y$ crossover structures using CeO_2 film as insulating layer," Jpn. J. Appl. Phys., vol. 35, pp. L311-L313, March 1996.

[3] O. Michikami, A. Yokosawa, H. Wakana, and Y. Kashiwaba, "$EuBa_2Cu_3O_{7-\delta}$ thin films grown on sapphires with epitaxial CeO_2 buffer layers," Jpn. J. Appl. Phys., vol. 36, pp. 2646-2651, May 1997.

[4] K. P. Daly, J. M. Murduck, C. L. Pettiette-Hall, and M. Sergant, "Integration of step-edge grain boundary Josephson junctions with YBCO multilayers for electronics applications," IEEE Trans. Appl. Supercond., vol. 5, pp. 3131-3134, June 1995.

[5] C. L. Pettiette-Hall, J. Murduck, J. F. Burch, M. Sergant, R. Hu, J. Cordrump, M. Luong, and R. K. Ellis, "Characterization and Improvement of a YBCO multilayer film process for HTS circuit applications," IEEE Trans. Appl. Supercond., vol. 7, pp. 2057-2062, June 1997.

Inferring $YBa_2Cu_3O_{7-\delta}$ Grain Boundary T_c Microstructure from Critical Current Temperature Dependence

Jerome A. Luine
TRW Space and Electronics Group, Redondo Beach, CA

Alexander M. Klushin
Forschungszentrum Jülich GmbH, Institut für Schicht-und Ionentechnik, Jülich, Germany

Vladimir Z. Kresin
Lawrence Berkeley Laboratory, Berkeley, CA

Abstract— The measured temperature dependence of $YBa_2Cu_3O_{7-\delta(x)}$ (YBCO) grain boundary junction (GBJ) maximum critical current $I_c(T)$ is used to infer grain boundary YBCO local transition temperature $T_c(x)$ where x is the distance from the grain boundary center. The conversion of $I_c(T)$ to $T_c(x)$ is made using an S_α-S_β-I-S_β-S_α tunneling/proximity-effect model previously developed by one of us, where S_α and S_β are superconducting layers with transition temperatures $T_{c\alpha}$ and $T_{c\beta} < T_{c\alpha}$ respectively, and I is a tunneling barrier. The use of this model is motivated by the fact that different YBCO electrical properties within a GBJ result from inhomogeneous oxygen deficiency $\delta(x)$ within the grain boundary region. Since the transition temperature T_c of YBCO depends, in part, on oxygen content, it follows that at a given GBJ temperature, T_{GBJ}, the S_β regions adjacent to the I-layer have transition temperature $T_{c\beta} < T_{GBJ}$. At a distance $\pm x(T_{GBJ})$ from the I-layer the local T_c exceeds T_{GBJ} to form the S_β-S_α boundaries (proximity contacts). Beyond the S_β-S_α boundaries $T_{c\alpha} > T_{GBJ}$ thereby forming the S_α regions. Thus, inhomogeneous oxygen content results in a S_α-S_β-I-S_β-S_α proximity effect structure wherein the locations $\pm x(T_{GBJ})$ of the S_α-S_β proximity contacts vary with T_{GBJ} while $T_{c\beta} = (1-\varepsilon)T_{GBJ}$ and $T_{c\alpha} = (1+\varepsilon)T_{GBJ}$ at the contacts. In this paper we use our S_α-S_β-I-S_β-S_α model with measured $\eta(T)$ to infer grain boundary $T_c(x)$ profiles with nanometer resolution for both step-edge and bicrystal GBJs. We find distinctly different $T_c(x)$ profiles for step-edge junctions, bicrystal junctions with 19° misorientation angle, and bicrystal junctions with 36.8° misorientation angle.

I. Introduction

There is great interest in understanding the details of high T_c superconductor (HTS) grain boundaries since HTS macroscopic conduction properties are strongly influenced by grain boundary electrical transport. It is well established that electrical transport through a $YBa_2Cu_3O_{7-\delta}$ (YBCO) grain boundary is affected not only by the coupling across the crystal discontinuity [1] but also by the electrical properties of the material surrounding the discontinuity [2]. Among the various physical properties that determine electrical transport, oxygen deficiency δ stands out as a particularly important variable because of its significant effect on transition temperature ($T_c \sim 92$ K for $\delta \sim 0$ and $T_c \sim 0$ K for $\delta \sim 0.5$ [3]) combined with high oxygen mobility in the a-b plane [4], [2]. Near a crystal orientation discontinuity, charge imbalance caused by lattice distortion and disorder sets up local electric fields that can displace the loosely bound plane and chain oxygen ions [5]. Thus, near the discontinuity δ is inhomogeneous giving rise to a spatially varying local T_c.

Several techniques for analyzing grain boundary microstructure are being pursued [5]. We propose a new technique to obtain grain boundary local T_c spatial profiles with nanometer resolution.

In cases where the superconductor order parameter coupling across the grain boundary is severely weakened, a Josephson junction results and the region is called a "grain boundary junction" or GBJ. The GBJ critical current density J_c depends on the nature of the crystal orientation discontinuity and on the electrical transport properties of the surrounding oxygen-deficient material. In this paper we treat the sharp discontinuity simply as an insulating tunneling barrier [1] (the I-layer) whose length and barrier height are temperature-independent. The region surrounding the I-layer is treated as superconductor with spatially varying T_c monotonically increasing with distance from the I-layer. At a distance $\pm x(T_{GBJ})$ from the I-layer the local T_c exceeds the GBJ temperature T_{GBJ} to form the S_β-S_α boundaries (proximity contacts). Beyond the S_β-S_α boundaries $T_{c\alpha} > T_{GBJ}$ thereby forming the S_α regions. Thus, inhomogeneous oxygen content results in a S_α-S_β-I-S_β-S_α proximity effect structure wherein the locations $\pm x(T_{GBJ})$ of the S_α-S_β proximity contacts vary with T_{GBJ} while $T_{c\beta} = (1-\varepsilon)T_{GBJ}$ and $T_{c\alpha} = (1+\varepsilon)T_{GBJ}$ at the contacts. The proximity contact positions $\pm x(T_{GBJ})$ as a function of temperature are extracted by solving the transcendental equation $\eta_{theory}(x(T_{GBJ})) - \eta_{measured}(T_{GBJ}) = 0$, where $\eta = I_c(T_{GBJ})/I_c(0)$ and I_c is GBJ critical current. Finally, $T_c(x)$ is obtained from the inversion of $x(T_{GBJ})$.

II. Numerical Analysis

The theoretical expressions for GBJ critical current used in this study were originally derived by one of us [6] and are similar to those used in our previous study on step-edge grain boundary junctions (SEJs) [7]. In order to treat the case where $T_{c\beta} \neq 0$, the expression for GBJ critical current in [7] is replaced by one with the additional parameter ϕ, the solution to a transcendental equation, as shown in Table I.

Manuscript received April 30, 1999

TABLE Ia

VARIABLE DEFINITIONS AND VALUES FOR S_α-S_β-I-S_β-S_α CRITICAL CURRENT

Parameter	Definition or Value
$\eta_{theory}(x,T)$	Normalized Critical Current = $\dfrac{I_c(x,T)}{I_c(x,0)}$
x	Distance from I-layer where local $T_c = T$
T	GBJ temperature
$I_c(x,T)$	$\dfrac{2\pi kT}{q_e R}\sum_{n=0}^{\infty}\dfrac{[f(X_n)+\phi F(X_n)]^2}{X_n^2[1+F(X_n)]^2+[f(X_n)+\phi F(X_n)]^2}$
$I_c(x,0)$	$\dfrac{\Delta_{o\alpha}}{q_e R}\int_0^{\infty}\dfrac{[f(X)+\phi F(X)]^2}{X^2[1+F(X)]^2+[f(X)+\phi F(X)]^2}dX$
$\phi = \phi(T_{c\alpha}, T_{c\beta}, T)$	$\phi - \dfrac{\Lambda_\beta}{1+\Lambda_\beta}\dfrac{\pi kT}{\Delta_\alpha}\sum_{n=0}^{\infty}\dfrac{f(X_n)+\phi F(X_n)}{\sqrt{X_n^2[1+F(X_n)]^2+[f(X_n)+\phi F(X_n)]^2}} f(X_n) = 0$

TABLE Ib

VARIABLE DEFINITIONS AND VALUES FOR S_α-S_β-I-S_β-S_α CRITICAL CURRENT (CONTINUED)

$f(X)$	$\dfrac{A^2}{A^2+X^2}$
$F(X)$	$a\sqrt{X^2+f^2(X)}$
$X_n = X_n(T_{c\alpha}, T)$	$(2n+1)\pi kT/\Delta_\alpha(T)$
$A = A(T_{c\alpha}, T)$	$\Omega_o/\Delta_\alpha(T)$
$\Lambda_\beta = \Lambda_\beta(T_{c\beta})$	$\left[\ln(\Omega_o/(kT_{c\beta}))\right]^{-1}$
Δ_o	$T = 0$ Gap energy = $3.5kT_c$
Ω_o	Characteristic phonon energy = 25 meV
$\Delta_\alpha(T)$	Gap energy = $\Delta_{o\alpha}\Delta_{HTS}(T/T_{c\alpha})$
$\Delta_{HTS}(T/T_{c\alpha})$	Normalized HTS gap temperature dependence; See [7]
a	$\dfrac{L_\beta\Delta_{o\alpha}B}{\hbar v_F\sigma}$
L_β	S_β-layer thickness = distance x from the I-layer to the S_β-S_α boundary
B	related to electron scattering mean free path, ~2 in the clean limit
v_F	Fermi velocity = 10^5 m/sec
σ	S_β-S_α boundary transparency ~1 since S_β-S_α boundary is a smooth transition defined by $T_{c\beta} < T < T_{c\alpha}$
R	GBJ normal resistance; Not needed since $\eta \sim R/R$
$T_{c\alpha}$	S_α-layer transition temperature = (1+0.15)T
$T_{c\alpha}$	S_β-layer transition temperature = (1-0.15)T

Since the theory is strictly valid only for piecewise homogeneous systems, we approximate the continuously varying T_c system by the piecewise homogeneous model as shown in Fig. 1. Thus, for a given GBJ temperature, the grain boundary is treated as if it consists of an S_β region of uniform $T_{c\beta}$ in proximity contact with an S_α region of uniform $T_{c\alpha}$ where $T_{c\beta} = (1-\varepsilon)T_{GBJ}$ and $T_{c\alpha} = (1+\varepsilon)T_{GBJ}$ ($\varepsilon = 0.15$).

Measurements of GBJ critical current versus temperature are normalized by the T = 0 K value obtained from extrapolation as shown in Fig.2. Each of the normalized critical current values $\eta_{meas}(T)$ are then inserted into the following transcendental equation which is solved for $x(T)$,

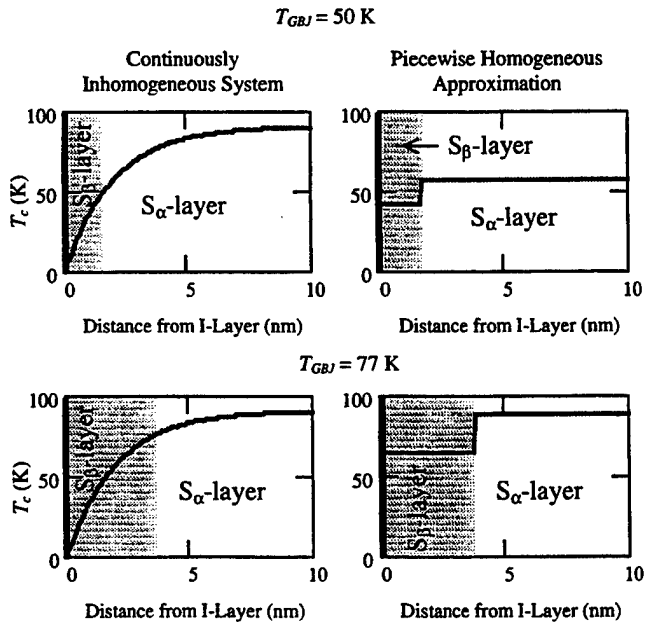

Fig. 1 Piecewise homogeneous approximation to the continuously-varying T_c system. Our S_α-S_β-I-S_β-S_α theory is strictly valid only in the piecewise homogeneous limit.

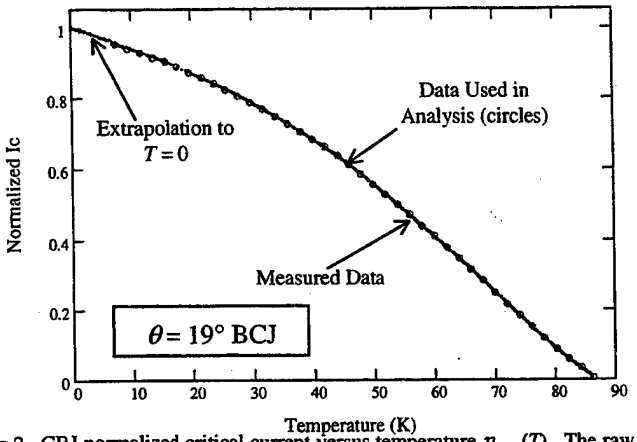

Fig 2. GBJ normalized critical current versus temperature $\eta_{meas}(T)$. The raw $I_c(T)$ data is extrapolated to $T = 0$ K to find the value of $I_c(0)$ which is then used to normalize the data. To reduce the computational time required to extract $T_c(x)$, 40 representative data points are selected for the analysis.

the distance between the I-layer and S_β-S_α contact:

$$\eta_{meas}(T) - \eta_{theory}(x,T) = 0 \qquad (1)$$

Since the T_cs of the S_α- and S_β-layers are ~ T at the S_β-S_α contact, x represents the position where the local T_c has a value T.

III. GBJ Fabrication

Details of SEJ and bicrystal junction (BCJ) fabrication are discussed in [7] and [8] respectively.

IV. Results and Discussion

Figs. 3 and 4 show the inferred local T_c versus position x relative to the I-layer for SEJs and BCJs, respectively. For $x > 1$ nm, step-edge junction $T_c(x)$ is well described by

$$T_c(x) = (82.4\pm0.4)\exp[-x/(1.40\pm0.14\text{ nm})]\text{ K} \qquad (2)$$

These junctions have 20 K<T_c<30 K at the I-layer. BCJs with θ = 19° misorientation angle exhibit steep T_c gradients for 1 nm < x < 2 nm while 10 K<T_c<20 K at the I-layer. BCJs with θ = 36.8° exhibit T_c gradients of intermediate steepness with T_c~0 K for x < 5 nm. Compared to the θ = 19° BCJs, the θ = 36.8° BCJs have a significantly greater oxygen deficiency near the I-layer with δ apparently falling below 0.5 for x < 5 nm. This is consistent with the larger misorientation angle resulting in greater crystal distortion and oxygen disorder.

In conclusion, while independent measurements are required to validate our analyses, this method for obtaining grain boundary T_c microstructure appears to be a valuable tool for understanding HTS grain boundary physics.

References

[1] H. Hilgenkamp and J. Mannhart, "Superconducting and normal-state properties of $YBa_2Cu_3O_{7-\delta}$-bicrystal grain boundary junctions in thin films," *Appl. Phys. Lett.*, vol. 73, pp. 265-267, July 1998

[2] B. H. Moeckly, D. K. Lathrop, and R. A. Buhrman, "Electromigration study of oxygen disorder and grain-boundary effects in $YBa_2Cu_3O_{7-\delta}$ thin films," *Phy. Rev. B*, vol. 47, pp. 400-417, January 1993

[3] J. D. Jorgensen, H. Shaked, D. G. Hinks, B. Dabrowski, B. W. Veal, A. P. Paulikas, L. J. Nowicki, G. W. Crabtree, W. L. Kwok, L. H. Nunez, and H. Claus, "Oxygen vacancy ordering and superconductivity in $YBa_2Cu_3O_{7-x}$," *Physica C*, vol. 153-155, p. 578, 1988

[4] S. J. Rothman, J. L. Routbort, and J. E. Baker, "Tracer diffusion of oxygen in $YBa_2Cu_3O_{7-\delta}$," *Phys. Rev. B*, vol. 40, pp. 8852-8860, November 1989

[5] N. D. Browning, H. O. Moltaji, and J. P. Buban, "Investigation of three-dimensional grain-boundary structures in oxides through multiple-scattering analysis of spatially resolved electron-energy-loss spectra," *Phys. Rev. B*, vol. 58, pp. 8289-8300, October 1998

[6] V. Z. Kresin, "Josephson tunneling and the proximity effect," *Phys. Rev. B*, vol. 28, pp. 1294-1303, August 1983

[7] J. A. Luine and V. Z. Kresin, "Critical current in high T_c grain boundary junctions," *J. Appl. Phys.*, vol. 84, pp. 3972-3979, October 1998

[8] A. M. Klushin, W. Prusseit, E. Sodtke, S. I. Borovitskii, L. Amatuni, and H. Kohlstedt, "Shunted bicrystal Josephson junctions arrays for voltage standard", *Appl. Phys. Lett.*, vol. 69, pp. 1634-1637, Sept. 1996

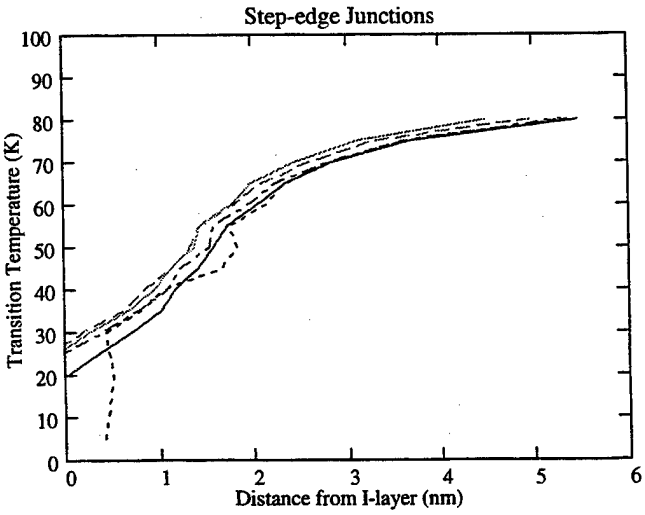

Fig. 3 Inferred grain boundary critical current as a function of distance from the crystal discontinuity (I-layer) for step-edge junctions.

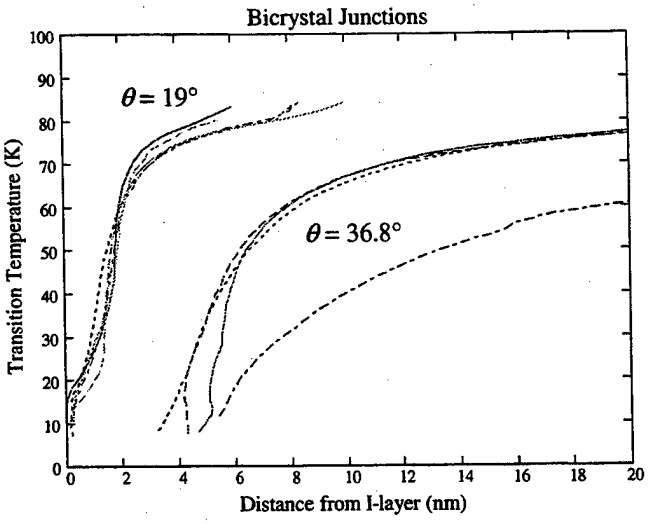

Fig. 4 Inferred grain boundary critical current as a function of distance from the crystal discontinuity (I-layer) for bicrystal junctions with 19° and 36.8° misorientation angles.

Flux-flow Resonant Current Steps in Intrinsic Josephson Junctions on $Bi_2Sr_2CaCu_2O_8$ Single Crystal

H. B. Wang[1,3], T. Tachiki[1], Y. Aruga[1], Y. Mizugaki[1,3], J. Chen[1,3], K. Nakajima[1,3], T. Yamashita[2,3], and P. H. Wu[2,4]

[1]Research Institute of Electrical Communication, Tohoku University, Sendai 980-8577, Japan
[2]New Industry Creation Hatchery Center, Tohoku University, Sendai, Japan
[3]CREST, Japan Science & Technology Cooperation, Japan
[4]Department of Electronic Science & Engineering, University of Nanjing, Nanjing 210093, China

Abstract—A mesa with *a-b* plane dimensions of 12 μm×12 μm was patterned on $Bi_2Sr_2CaCu_2O_8$ single crystal, after which two separate electrical contacts were carefully fabricated on the top of the mesa to ensure a standard four-probe arrangement. With contact resistance excluded, the measured current-voltage (*I-V*) curves featured high voltage resolution. Voltage jumps up to 20 mV and remarkable hysteresis at 4.2 K indicated typical SIS (superconductor-insulator-superconductor) properties. A few sharp current steps started to manifest themselves clearly when a magnetic field of about 10 KOe was applied parallel to the *a-b* plane. Carefully studied were the dependences of the current steps on the magnetic fields and the operating temperatures. We attributed the field-induced steps to the flux-flow resonances, and the multi-steps implied different modes existing in the stacked intrinsic junctions. The voltage region at which the steps occurred was in the order of millivolts, indicating possible high frequency applications at mm and sub-mm wavebands.

I. Introduction

It is well known that single long Josephson junction, operated in flux-flow regime, can be used as tunable high frequency oscillator over a wide range. In addition, by phase-locking many junctions in an array, the performance as an oscillator can be greatly improved, giving rise to higher output power and lower phase noise. So far Josephson junction arrays have been fabricated either in the form of artificially stacked Nb junctions or in the form of intrinsic junctions in oxide superconductors such as $Bi_2Sr_2CaCu_2O_8$ (BSCCO), and theoretical studies have been successfully carried out.

Thyssen et al [1]. observed pronounced resonant modes with large and regular voltage spacing in a 7-layer stacked Nb/Al-AlO_x/Nb long Josephson junction array, where the junctions were magnetically coupled by the screen currents in the common superconducting electrodes thinner than the London penetration depth. Arrays made of intrinsic Josephson junctions in BSCCO, where the superconducting layers are roughly 3Å thick, were also carefully looked at in recent years. Kleiner [2] predicted that vortices motion could be triggered by two-dimensional resonances of the stacked Josephson junctions. Lee et al. [3] examined the vortex flow resistivity and velocity in the displaced linear branch of current-voltage (*I-V*) curve. G. Hechtfischer et al. [4] observed typical flux-flow branch and explained it in terms of vortex motion with the lowest collective-mode velocity of the system. Very interesting non-Josephson emission in the BSCCO intrinsic junctions was observed by the same group [5], who believed that the vortex motion with higher mode velocities could be excited in the case of dense vortex lattice. And quite recently, Ustinov et al. [6] performed numerical simulations of stacked Josephson junctions using experimentally feasible parameters for niobium tunneling junctions, and proposed high-power radiation sources for the terahertz range using BSCCO. Indeed, high frequency resonances in BSCCO stacks have been attractive hot topics from both the theoretical and the practical points of view.

In this paper, we report our new experimental data on the flux-flow resonances in BSCCO intrinsic junctions with magnetic field parallel to an a-*b* plane. At fields of a few tesla we observed a series of current steps in the *I-V* curves of 12 μm×12 μm samples. Such experimental observations were made possible by modifying the fabrication of BSCCO mesa structure to ensure standard four-probe measurements. After discussing how these current steps depend on the magnetic field and operating temperature, possible explanations of them are also suggested here.

II. Device Fabrication

Although the fabrication of our samples was quite similar to that for a conventional mesa structure which was reported elsewhere [7], some steps were modified to realize four-probe arrangement. We began our process from sputtering a 1000 Å thick gold layer onto the surface of a cleaved BSCCO single crystal with T_c of about 90 K. Annealing the sample under flowing oxygen at 500°C to 600 °C for 10 minutes, we could usually get a metallic contact between the gold layer and the BSCCO single crystal. Then a conventional photolithography was used to define the sizes of a mesa structure in the *a-b* plane, 12 μm×12 μm for the sample reported below. By using Ar ion milling, the sample was etched down to a certain depth along *c*-axis; and a second photolithography and ion milling was carried out to define two counter electro-

Manuscript received April 30, 1999.

des on the top of mesa. Carefully adjusting the etching time, we were able to precisely control the number of junctions in one mesa. After the second etching, SiO layer was evaporated into the sample to be an insulator. The photo resist as well as the SiO above it remaining on the top of the mesa were removed in a lift-off procedure. Noticeably, since the two counter electrodes were put just within the mesa area, we were able to prevent any leakage or short between the mesa and SiO film which happened in many of our previous experiments and were disastrous. For measurements to follow, another gold layer was sputtered to contact the exposed top gold electrodes on the mesa, and then was separated photolithographically again by ion milling. A typical sample is shown in Fig. 1.

All samples were measured in a Physical Property Measurement System (PPMS) manufactured by Quantum Design which can supply magnetic fields up to 7 T. The fields were applied to the samples along the *a-b* plane perpendicular to the longer side of the counter electrodes (see Fig.1) so that the bias current was as uniform as possible along the vortices moving direction.

III. Experimental Results

Shown in Fig. 2 is the typical *I-V* curve for one mesa, where only the zero-voltage critical current branch and the first resistive branch is indicated, from which a voltage jump of about 20 mV is observed. We ramped a bias current up and down repeatedly and measured typical multi-branch *I-V* curves, from which about 30 branches could be clearly identified, in good agreement with the number estimated from the height of this stack.

With the magnetic field oriented along the *a-b* plane, the *I-V* characteristics at various fields were measured (Fig. 3). When we increased the magnetic fields gradually but kept them low, the zero-voltage branch of the *I-V* characteristics exhibited field-dependent flux-flow branches which were already well studied. At 11.0 KOe, however, we observed current steps at ±5.0 mV. Further increase of the field to 24.1 KOe, resulted in more current steps manifesting themselves clearly. Obviously both the voltage positions, at which these current steps appeared, and the heights of the steps were strongly magnetic field-dependent. Reversing the direction of the magnetic fields, we got the same results. At 29.0 KOe, less steps were visible although very sharp ones were clearly seen at ±6.1 mV and ±7.0 mV. Measurements of the temperature dependence of the step structures revealed that they were rather stable within a considerably large temperature region, which will be reported elsewhere.

IX Discussion and Conclusion

The observed experimental results might be attributed to the collective motion of vortices in the multi-junction stack. In contrast to the single Swihart velocity in a single junction, N different mode velocities exist in the stack [8]. For a 10 micron sample it was estimated that at around 1.4 KOe flux quantum would penetrate into a junction [4]. In our case, given the estimated Josephson penetration depth λ_j of around 1 μm, the vortices penetrated under high magnetic fields were in dense state when the current steps appeared. At low fields, the vortices in different layers could move collectively and couple to the lowest mode. With increase of the magnetic fields, the dense vortices had more chances to attract others in neighboring junctions; in addition, at high velocities vortices of the same polarity in different layers tended to attract each other. Thereby the vortices motion could couple to higher modes in the stack. At sufficiently high velocity, it was possible to achieve remarkable in-phase oscillation [9]. In the case of our experiments, we observed a set of steps,

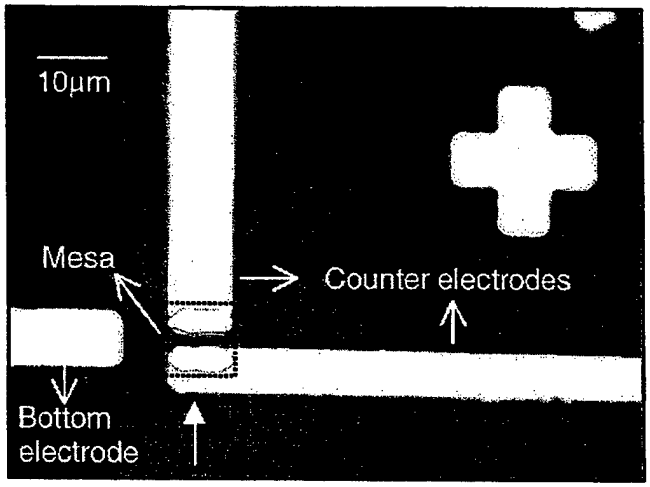

Fig. 1. Microscope image of a *c*-axis mesa structure fabricated on a $Bi_2Sr_2CaCu_2O_8$ single crystal. Note two counter electrodes are separately prepared on the mesa marked with dashed line.

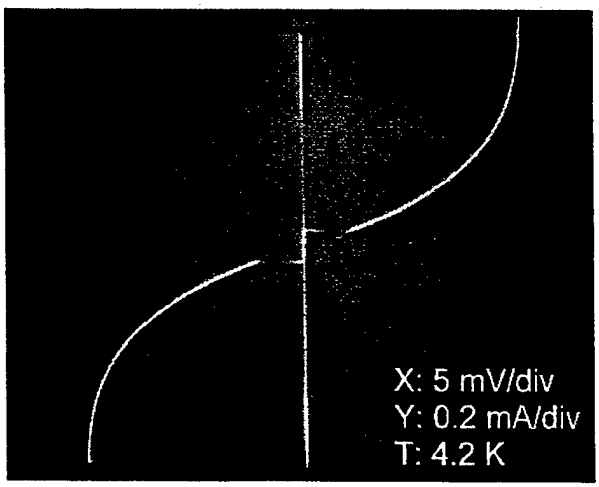

Fig. 2. Zero-voltage branch and the first resistive branch of the current-voltage curves for a BSCCO mesa structure with a-b plane sizes of 12×12 μm^2, where a standard four-probe arrangement is used.

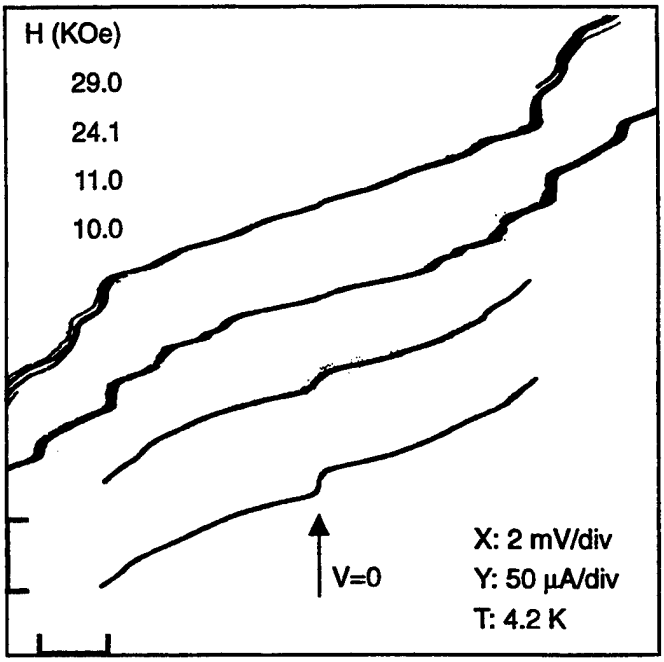

Fig. 3. Typical *I-V* curves for the BSCCO stack under various magnetic fields. Note the curves are vertically offset for each field.

which became larger and sharper at higher fields and bias current region, implying high order collective modes were stimulated in the stack especially at high bias current. With up to 30 junctions, it was difficult for us to precisely describe the vortices dynamics in our stack. Nevertheless, our results resembled those predicted theoretically [2], [6] and observed experimentally for Nb/Al-AlO$_x$/Nb junction stacks [1], supplying evidence for possible high frequency resonances in BSCCO intrinsic Josephson junctions.

To conclude, with standard four-probe arrangement, we measured the *I-V* characteristics for a BSCCO intrinsic junction stack with the *a-b* plane sizes of 12 μm×12 μm under magnetic fields up to 30 KOe. Current steps manifested themselves on the *I-V* curves above 10 KOe, which we attributed to the vortices motion at higher velocity modes rather than the lowest one in the stack. Fabricated have been stacks with only a few junctions for quantitative studies, and stacks with uniform properties for possible high frequency applications.

REFERENCES

[1] N. Thyssen, H. Kohlstedt, and A. V. Utsinov, "Experimental study of flux flow and resonant modes in multi-junction stacks", *IEEE Trans. on Appl. Supercond.*, Vol. 7, pp2901-2904, June 1997.

[2] R. Kleiner, "Two-dimensional resonant modes in stacked Josephson junctions", *Phys. Rev. B*, Vol. 50, pp6919-6922, September 1994.

[3] Ji Ung Lee, James E. Nordman, and Gert Hohenwarter, "Josephson vortex flow in superconducting single-crystal $Bi_2Sr_2CaCu_2O_x$", *Appl. Phys. Lett.*, Vol. 67, pp1471-1473, September 1995.

[4] G. Hechtfischer, R. Kleiner, K. Schlenga, W. Walkenhorst, and P. Müller, "Collective motion of Josephson vortices in intrinsic Josephson junctions in $Bi_2Sr_2CaCu_2O_{8+y}$", *Phys. Rev. B*, Vol. 55, pp14638-14644, June 1997.

[5] G. Hechtfischer, R. Kleiner, A. V. Ustinov, and P. Müller, "Non-Josephson emission from intrinsic junctions in $Bi_2Sr_2CaCu_2O_{8+y}$: Cherenkov radiation by Josephson vortices", *Phys. Rev. lett.*, Vol. 79, pp1365-1368, August 1997.

[6] A. V. Ustinov, and S. Sakai, "Submillimeter-band high-power generation using multilayered Josephson junctions", Appl. Phys. Lett., Vol 73, pp686-688, August 1998.

[7] H. B. Wang, Y. Aruga, T. Tachiki, Y. Mizugaki, J. Chen, K. Nakajima, T. Yamashita, and P. H. Wu, "Microwave-induced Current Steps in Intrinsic Josephson Junctions Patterned on $Bi_2Sr_2CaCu_2O_x$ Single Crystal", Appl. Phys. Lett., in press.

[8] S. Sakai, A. V. Ustinov, H. Kohlstedt, A. Petraglia, and N. F. Pedersen, "Theory and experiment on electromagnetic-wave-propagation velocities in stacked superconducting tunnel structures", Phys. Rev. B, Vol. 50, pp12905-12914, November 1994.

[9] Alexey V. Ustinov and Hermann Kohlstedt, "Interlayer fluxon interaction in Josephson stacks", Phys. Rev. B, Vol. 54, pp6111-6114, September 1996.

$YBa_2Cu_3O_{7-x}$ Josephson Junctions and dc SQUIDs based on 45° a-axis tilt and twist Grain Boundaries: atomically clean interfaces for applications

F. Tafuri*, F. Carillo, F. Lombardi, F. Miletto Granozio and U. Scotti di Uccio
INFM-Dipartimento di Scienze Fisiche dell'Università di Napoli "Federico II", 80125, Napoli (ITALY)
*Dipartimento di Ingegneria dell'Informazione, Seconda Università di Napoli, 81031, Aversa (CE) (ITALY)

G. Testa and E. Sarnelli
Istituto di Cibernetica del CNR, Via Toiano 6, 80072 Arco Felice (NA), (ITALY) - also INFM

K. Verbist and G. Van Tendeloo
EMAT, University of Antwerp, Antwerp, BELGIUM

Abstract- **$YBa_2Cu_3O_{7-x}$ (YBCO) artificial grain boundary Josephson junctions have been fabricated, employing a recently implemented biepitaxial technique. The grain boundaries can be obtained by controlling the orientation of the MgO seed layer and are characterized by a misalignment of the c-axes (45° a-axis tilt or 45° a-axis twist). These types of grain boundaries are still mostly unexplored. We carried out a complete characterization of their transport properties and microstructure. Junctions and dc SQUIDs associated with these grain boundaries exhibit an excellent Josephson phenomenology, high values of the I_CR_N product and of the magnetic flux-to-voltage transfer parameter respectively. Remarkable differences in the transport parameters of tilt and twist junctions have been observed, which can be of interest for several applications. A maximum speed of Josephson vortices as calculated from the voltage step values, of the order of 2 10^6 m/sec is obtained. These devices could also have some impact on experiments designed to study the symmetry of the order parameter. High resolution electron microscopy showed the presence of perfect basal plane faced boundaries in the cross sections of tilt boundaries.**

I. Introduction And Main Concepts

The biepitaxial technique has been used to obtain 45° a-axis tilt and twist grain boundaries (GBs) [1], whose structure is shown in Fig. 1. In the tilt case, the current through the boundary plane flows in the a-b plane in the (001) YBCO and with a component along the c-axis in the (103) YBCO. In the twist case the current through the boundary plane flows parallel to the YBCO a-b plane in both the electrodes. These types of GBs are still mostly unexplored and their nature and potential applications are not completely understood. The phenomenology of these junctions presents remarkable differences from the one typical of traditional biepitaxial junctions [2],[3], in which a 45° tilt in-plane grain boundary (GB) is usually determined.

The proposed structures employs a (110) MgO film as seed layer to modify the crystal orientation of $YBa_2Cu_3O_{7-x}$ (YBCO) on (110) $SrTiO_3$. YBCO grows along the (001) direction on the MgO seed layer [1] and along the (103)/(013) direction on the bare (100) $SrTiO_3$ substrate respectively. Besides being extremely flexible in designing circuits, the Josephson structure we realized seems to be very promising also for devices in which anisotropic characteristics could be fruitfully used, such as some types of three terminal devices and RF SQUIDs. This is also encouraged by the good quality and excellent reproducibility of the junctions and by the high values of the I_CR_N product of the order of 2 mV at T=4.2 K and 50-100 μV at T =77 K (I_C is the critical current and R_N is the normal state resistance respectively).

In this work, YBCO junctions and dc Superconducting Quantum Interference Devices (SQUIDs) based on 45° a-axis tilt and twist GBs, have been realized and fully characterized in terms of transport properties. These are among the first

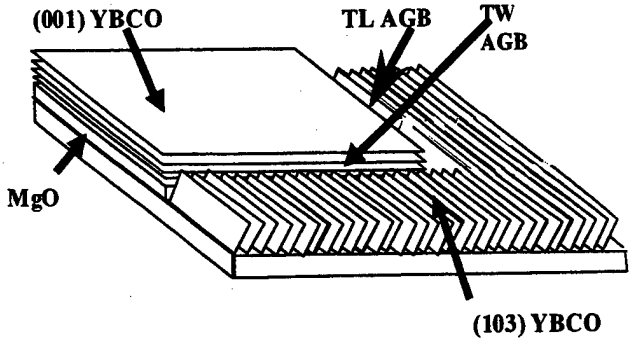

FIG. 1. A schematic representation of the junction structure with a (001) $YBa_2Cu_3O_{7-x}$ growth on the (110) MgO seed layer and (103) on the bare (110) $SrTiO_3$ substrate. The twist (TW) and tilt (TL) grain boundaries can be clearly distinguished.

Partially supported by the Istituto Nazionale di Fisica della Materia (INFM) under the projects PRA "High Temperature Superconductor Devices" and "Analisi non distruttive con correnti parassite tramite dispositivi superconduttori"

SQUIDs which employ these types of GB. Such devices could also have some impact on experiments designed to study the symmetry of the order parameter [1].

II. Experimental Results

The fabrication process is described in detail elsewhere[1],[4]. MgO thin films of thickness of 20-30 nm are deposited by 100 W RF magnetron sputtering from a stoichiometric oxide target on (110) $SrTiO_3$ substrates, kept at a temperature of 600 °C. Part of the MgO is removed by employing standard ion milling procedures. $YBa_2Cu_3O_{7-x}$ films of thickness of 120 nm were finally deposited by inverted cylindrical magnetron sputtering in Ar/O_2 atmosphere (PO_2=PAr=50 Pa) usually at a temperature of 780°C. The obtained grain boundaries were investigated in detail by using High Resolution Electron Microscopy [1],[5]. The presence of perfect basal plane faced boundaries in the cross sections of tilt boundaries has been demonstrated, as shown in Fig.2. A discussion of the implications of these kinds of interfaces on the uniformity of Josephson properties has been carried out elsewhere [1].

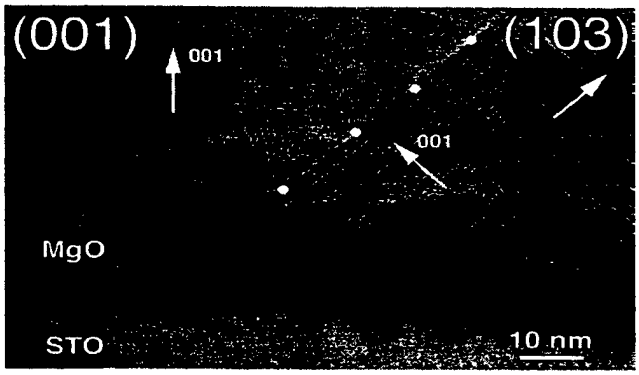

FIG. 2. High magnification cross section TEM image of a 45° tilt. The atomically flat artificial grain boundary interface, following the basal plane face of the (103) film, is marked by dots.

From the typical I-V characteristics at T= 4.2 K of a *twist* and a *tilt* junction, shown in Fig. 3, one can clearly distinguish two different regimes in terms of the critical current densities J_C and the normal state specific conductances σ_N, corresponding to the two types of GBs. In both cases the maximum working temperature T_C of the devices is typically higher than 77 K. *Twist* GB junctions typically have J_C values in the range 0.1-4.0 $\times 10^5 (A/cm^2)$ and σ_N values in the range 20-120 $(\mu\Omega cm^2)^{-1}$ at T = 4.2 K. *Tilt* AGB junctions have lower J_C and lower σ_N values, in the ranges 0.5-10 $\times 10^3 (A/cm^2)$ and 1-10 $(\mu\Omega cm^2)^{-1}$ respectively. J_C and σ_N values fall in the ranges typical for in plane GB Josephson junctions, usually fabricated using bicrystal or conventional biepitaxial techniques. The I_CR_N values are high in both cases, of the order of 1-2 mV at T = 4.2 K. They are larger for the corresponding J_C values than those provided by conventional biepitaxials and are of the same order of magnitude as in bicrystal and step edge junctions.

The Josephson nature of the junctions has been verified by applying an external magnetic field H. A typical $I_C(H)$ pattern measured at T = 4.2 K is shown in Fig. 4, where I-V curves are plotted as a function of H. A Fraunhofer-like dependence of I_C on H is evident, as well as slight deviations manifested in the fact that I_C does not modulate down to zero. The pattern is symmetric around zero magnetic field, and in all samples the absolute maximum of I_C occurs at zero magnetic field. The implications of such behavior within the debate on the symmetry of the order parameter have been discussed elesewhere [1].

From the presence of steps at finite voltages, which resemble Fiske steps [6] in ordinary tunnel junctions, we obtain the value for the barrier thickness, t, to the relative dielectric constant, ε_r, of the order of 0.3 Å, and a Swihart velocity, which is the maximum speed of the Josephson vortices, of the order of 3 10^6 m/sec. This corresponds to a transit frequency of 1 THz for a device having a 2-μm wide drain-source channel.

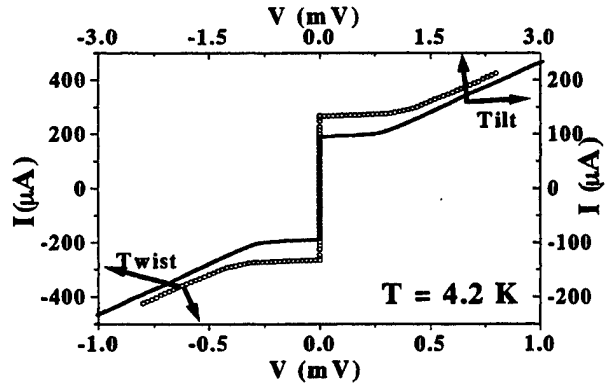

FIG. 3. Typical I-V characteristics of a 45° twist and a 45° tilt junction, measured at T= 4.2 K.

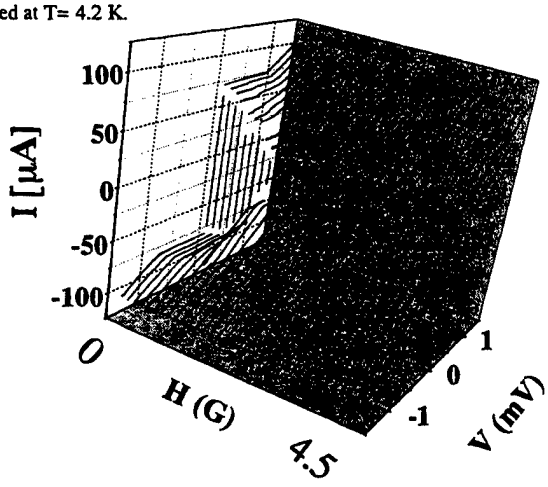

FIG. 4. I-V curves are shown as a function of an externally applied magnetic field at T = 4.2 K. A typical Fraunhofer-like dependence is evident. The absolute maximum is observed for zero field.

SQUIDs with hole and washer–like geometry and different inductance have been realized [7],[8]. In Fig.5, the maximum voltage dependence on the external magnetic field at different temperatures is reported for a washer-like geometry with an inductance of 67 pH [7]. A large number of modulation periods can be observed without any significant influence due to the field sensed by the junction. Maximum values of the voltage modulation ΔV of the order of 15-20 μV at T = 77 K and 100 μV at T=4.2 K were measured respectively. Typical values of of the transfer coefficient $h = \partial V/\partial \Phi = 30\ \mu V/\Phi_0$ at T = 77 K and h =280 $\mu V/\Phi_0$ at T= 20 K were also measured respectively. Preliminary noise measurements give evidence of better performances when compared with those of traditional biepitaxial and will be presented elsewhere.

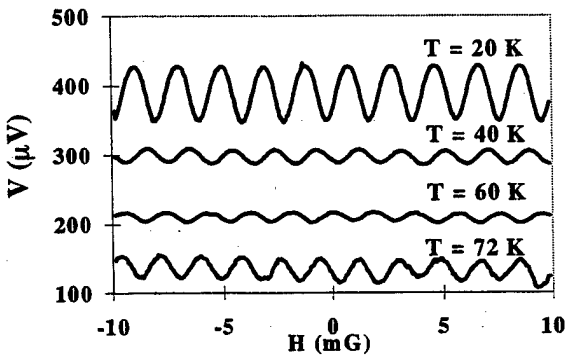

FIG. 5 Maximum d.c. voltage modulations of a 45° tilt grain boundary junctions vs applied magnetic fields at different temperatures (T=20 K, 40 K, 60 K and 72 K). The modulation at 72 K is enlarged by a factor of 10.

III. CONCLUSIONS

Biepitaxial $YBa_2Cu_3O_{7-x}$ junctions and dc-SQUIDs based on 45° a-axis tilt and twist grain boundaries have been fabricated and characterized. These devices present a phenomenology different from traditional biepitaxial Josephson junctions and, due to their microstructure and intrinsic nature, represent an interesting tool for investigating on the pairing symmetry of HTS materials. Within the framework of the d-wave order parameter symmetry, the order parameter orientations do not produce an additional π phase shift along our junction in contrast with the 45° tilt bicrystal junctions [1]. We can argue that no unquantized magnetic flux would be expected in our junctions. The realized SQUIDs are among the first which employ such grain boundaries. High values of the I_CR_N quality factor and of the magnetic flux-to-voltage transfer parameter were obtained. Low frequency 1/f noise lower than in the asymmetric in plane 45° (001) tilt bicrystal and biepitaxial junctions has been measured. Moreover dc-SQUID behavior and dielectric properties are promising for using these devices in applications as discrete flux flow transistors.

REFERENCES

[1] F. Tafuri, F. Miletto Granozio, F. Carillo, A. Di Chiara, K. Verbist and G. Van Tendeloo "Microstructural investigation and Josephson phenomenology in 45° c-axis tilt and twist YBCO artificial grain boundaries", *Phys. Rev. B* 59, pp11523-11531, 1999.

[2] K.Char, M.S.Colclough, S.M.Garrison, N. Newman and G. Zaharchuk,"Bi-epitaxial grain boundary junctions in YBCO", *Appl. Phys. Lett.*, vol 59, pp. 733-735 ,1991.

[3] H. Hilgenkamp, J. Mannhart and B. Mayer, " Implications of d symmetry and faceting for the transport properties of grain boundaries in high Tc superconductors", *Phys. Rev. B* vol.53, 14586-14593, 1996.

[4] A. Di Chiara, F. Lombardi, F. Miletto Granozio, G. Pepe,U. Scotti di Uccio, F. Tafuri and M. Valentino, "A new type of biepitaxial c-axis tilt YBCO Josephson junction", *J. Supercond.*, vol. 9, pp. 245-251, 1996.

[5] K. Verbist, O. Lebedev, G. van Tendeloo, F. Tafuri, F. Miletto Granozio and A. Di Chiara, *Appl. Phys. Lett.* vol. 74, 1024-1026 (1999)

[6] F. Tafuri, B. Nadgorny, S. Shokhor, M.Gurvitch, F. Lombardi, F. Carillo, A. Di Chiara and E. Sarnelli " A study of barrier properties in $Y_1Ba_2Cu_3O_{7-x}$ grain boundary Josephson junctions using electron beam irradiation " , *Phys. Rev. B* vol. 57, pp.R14076-R14079, 1998.

[7] F. Tafuri, F. Carillo, L. De Nunzio, F. Lombardi, F. Miletto Granozio, A. Di Chiara, G. Testa, A . Monaco and E. Sarnelli, "Fabrication and Characrterization of 45° a –axis tilt grain boundary YbaCuO Josephson junctions and dc SQUIDs", to be published in *IEEE Trans. on Applied Supercond.* (1999)

[8] E. Sarnelli, C. Camerlingo, M. Russo, G. Torrioli, and M. G. Castellano "Low 1/f noise in sputtered $Yba_2Cu_3O_{7-\delta}$ bicrystal dc-superconducting quantum interference devices", *J. Appl. Phys.*vol. 82, pp.3922-3927, 1997.

Tunneling Characteristics of Nd-Ba-Cu-O/Pr-Ba-Cu-O/Nd-Ba-Cu-O Planar and Ramp-edge Junctions

G. A. Alvarez, M. Sato, T. Utagawa, T. Morishita, Y. Enomoto, and K. Tanabe
Superconductivity Research Laboratory, ISTEC, Tokyo, 135 Japan

K. Toma and U. Kawabe
*Chiba Institute Of Tech., Tsudanuma, Narashino-shi, Chiba 274-0016, Japan

Abstract—We report on planar junctions fabricated from a- and c-axis quasi-homoepitaxial $NdBa_2Cu_3O_{7-\delta}/PrBa_2(Cu, Co)_3O_{7-\delta}/NdBa_2Cu_3O_{7-\delta}$ (NBCO/PBCO/NBCO) multilayers. Investigations of the dependence of the maximum Josephson supercurrent on the external applied magnetic fields made evident spatial variations of the critical current due to nonuniformities assumed to be localized in the PBCO barrier layer. Well developed Shapiro steps were observed. C-axis tunneling spectroscopy investigations provide evidence of quasiparticle tunneling that is commonly observed for superconductor/insulator/ superconductor (SIS) junctions. Furthermore, it was confirmed that NBCO layers could be incorporated in a multilayer structure without substantial degradation.

I. INTRODUCTION

The future of high-T_c superconducting electronics depends on the understanding of many technological issues in thin film growth and device fabrication, i.e. the reliability and reproducibility of Josephson junctions. For the fabrication of high T_c superconducting tunnel junctions, very high quality thin films with atomically flat surfaces and interfaces are required. To date, there is no good method of fabricating all high T_c superconductor/insulator/superconductor (SIS) structures, although tunneling properties in the case of planar $NdBa_2Cu_3O_{7-\delta}/PrBa_2Cu_3O_{7-\delta}/NdBa_2Cu_3O_{7-\delta}$ (NBCO/PBCO/NBCO) quasi-homostructures [1] have been observed and reported. The majority of work has been focused on the fabrication of SNS (N-normal metal) Josephson junctions, or weak links with electrical performance consistent with the resistively shunted junction (RSJ) model. Some groups have focused on the fabrication of ramp edge type devices using high T_c superconductive oxide electrodes and normal metal layers [2]-[4]. In this paper we present results obtained from planar and ramp-edge type junctions fabricated from well characterized a- and c-axis quasi-homoepitaxial NBCO/PBCO/NBCO multilayers. X-ray diffraction (XRD) and Rutherford backscattering spectrometry (RBS) analyses provide evidence of a well-equilibrated and relaxed crystal.

Manuscript received April 30, 1999.
This work was supported by the New Energy and Industrial Technology Development Organization for the R&D of Industrial Science and Technology Frontier Program of Japan.

With the availability of these high quality NBCO/PBCO/NBCO multilayer structures both the reproducibility and the quality of the tunneling experiments have improved considerably.

II. EXPERIMENTAL RESULTS AND DISCUSSION

In the fabrication of junctions based on the use of artificial N barriers, one has to deal with extrinsic interfaces between the HTS electrodes and the barrier material. The controllability in the fabrication process is difficult for HTS and requires the most advanced fabrication technology. One of the most important aspects in the junction fabrication process is the possibility of growing epitaxial SIS and SNS trilayer structures using c-axis thin films while retaining the Josephson coupling along the ab-plane.

The high quality a- and c-axis NBCO/PBCO/NBCO multilayers used in this study were fabricated by hybrid plasma sputtering in on-axis configuration and pulsed laser deposition (PLD) respectively. Single thin film deposition is described elsewhere [5], [6]. The crystal structure of the NBCO/PBCO multilayers was analyzed by using a X-ray diffractometer (XRD) and Rutherford backscattering spectrometer (RBS). Atomic force microscopy (AFM) studies of the multilayers showed a very smooth surface morphology [5], [6].

High quality planar junctions with widths varying from 5 to 20 μm were fabricated from these a- and c-axis-oriented NBCO/PBCOO/NBCO multilayers by using standard photolithographic and ion milling techniques [7]. All the devices were contacted with Au bonding pads.

Investigations of the magnetic field dependence of I_c for a-axis junction [8] made evident spatial variations of the critical current due to nonuniformities assumed to be localized in the PBCO barrier layer (Fig. 1). The results are compared with numerical calculations of I_c (H) patterns corresponding to a current density profile in which nonuniformities of the current density are localized at the two edges of the junction [9].

Through ac measurements we studied the properties of the NBCO/PBCO/NBCO multilayer junctions. We found stable Shapiro steps. (Fig. 2). Our junctions in an external microwave field of 7-20 GHz show Shapiro steps that appear at voltages $Vk=h/10ekf$, k=0, 1, 2,... .

The I and dI/dV curves of the c-axis NBCO/PBCO/NBCO multilayer junction measured at 4.2K is shown in Fig. 3. At bias currents above I_c the CVC becomes single valued and resembles the I-V characteristics of standard SIS Josephson

junctions. At high voltages the CVC exhibit a tunneling like quasiparticle curve.

The tunneling conductance dI/dV vs V of the junctions under high fields are found to be complex. Figure 4 shows the tunneling conductance for various values of H for a 16x16 μm^2 c-axis NBCO/PBCO/NBCO trilayer junction with a PBCO barrier thickness of 40 nm. In zero field the usual SIS tunneling characteristic is obtained. When H is greater than 3 T, the peaks in the dI/dV are noticeably broadened. As H increases this broadening develops into three peaks. These peaks reveal a splitting of the quasiparticle density of states. The positions of these peaks as a function of H. clearly exhibit a linear field dependance [10].

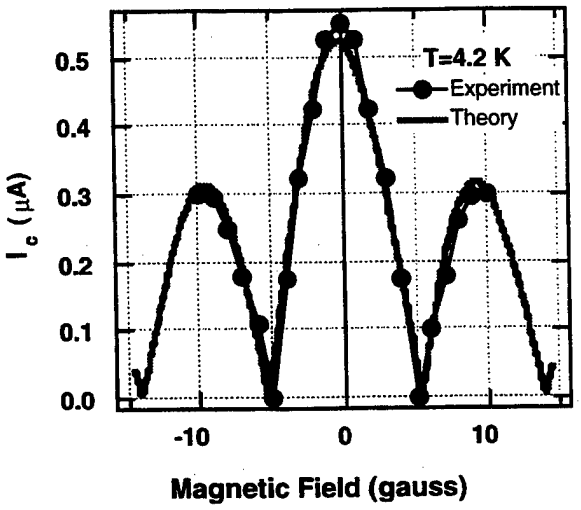

Fig. 1. Magnetic field dependence of I_c for 5x5 μm^2 a-axis NBCO/PBCO/ NBCO junction

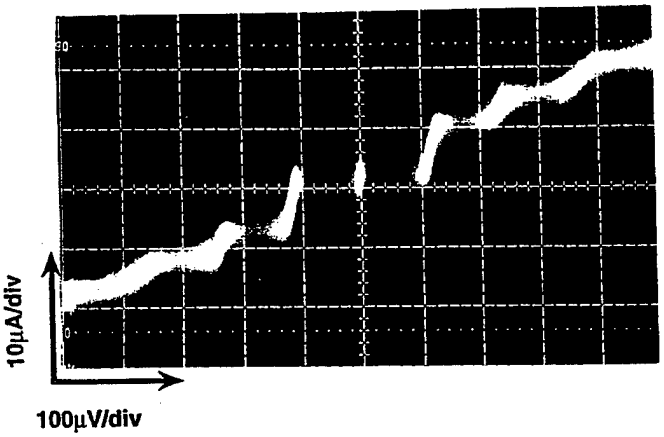

Fig. 2. CVC of a 8x14 μm^2 c-axis NBCO/PBCO/ NBCO multilayer junction at 4.2 K showing 9.8 Ghz microwave induced steps at multiples of h/10ekf, k=0, 1, 2,... ..

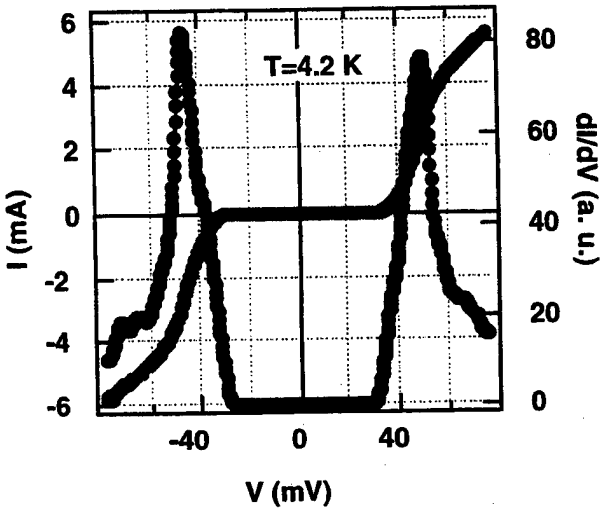

Fig. 3. I-V and dI/dV characteristics of a NBCO/PBCO/NBCO trilayer junction (16x16 μm^2). The PBCO thickness is 40 nm. A 2Δ value of 45±3 meV was obtained.

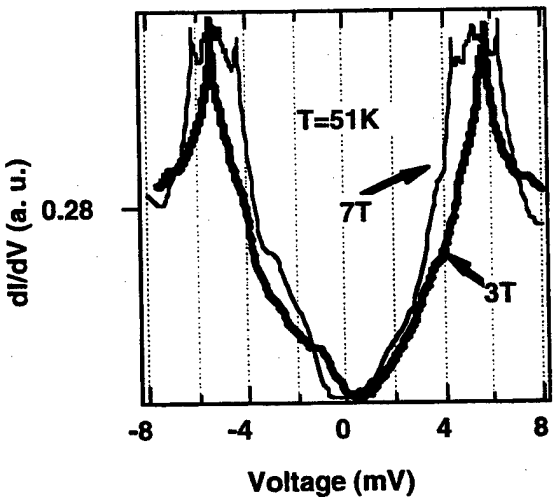

Fig. 4. Tunneling conductance curve for NBCO/PBCO/NBCO trilayer junction (16x16 mm^2) in 3 and 7 T fields respectively. The curve corresponding to 7 T reveals the spin-split superconducting density of states. The NBCO and PBCO thicknesses are 70 and 40 nm respectively.

Furthermore we fabricated high T_c NBCO ramp edge junctions with a PBCO barrier by PLD. Fig. 5 shows the I-V characteristics at 4.7 K. A I_cR_n product of about 1.5 mV was obtained. These I-V characteristics exhibited RSJ-like behavior. Fig. 6 shows the I-V characteristics at 5.3 K for five 5-μm-wide junctions on the same chip. The I-V characteristics exhibited flux-flow type behavior.

Most present digital circuits are based on rapid single flux quantum (RSFQ) logic with typical designs requiring groundplanes in order to satisfy the inductance constraints. We have started the fabrication of high-T_c SNS weak links in an edge geometry with integrated ground planes and insulators using a process which incorporates five epitaxial layers including the PBCO normal metal interlayer. The process was discussed elsewhere [11].

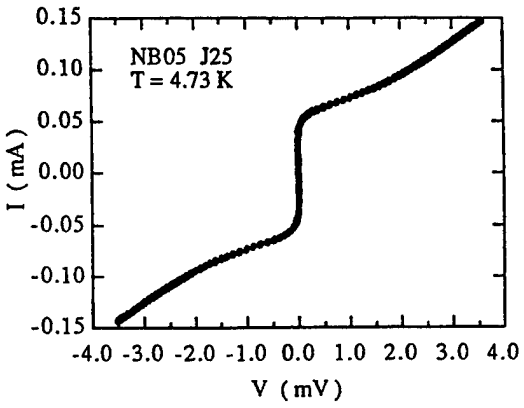

Fig. 5. I-V curve at 4.7 K for a NBCO/PBCO/NBCO ramp-edge junction. A I_cR_n product of about 1.5 mV was obtained.

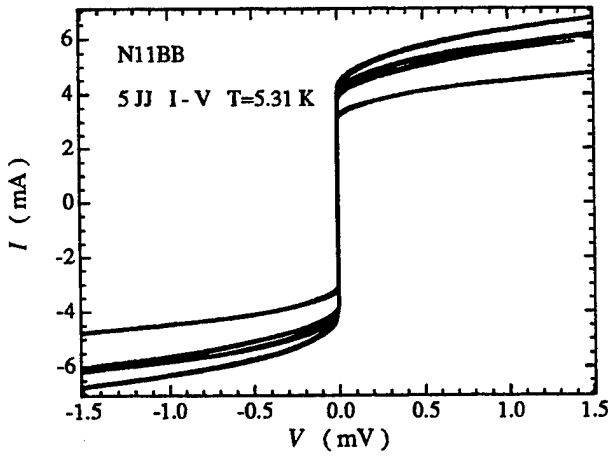

Fig. 6. I-V curves of five NBCO/PBCO/NBCO ramp-edge junctions on the same chip.

IV SUMMARY

We have successfully fabricated high quality a- and c-axis oriented NBCO/PBCO/NBCO multilayer junctions. The a-axis oriented trilayers showed a well defined Shapiro steps corresponding to the 7-20 Ghz microwave irradiation. The dependence of the maximum Josephson supercurrent on the external applied magnetic fields made evident spatial variations of the critical current due to nonuniformities assumed to be distributed over the PBCO barrier layer. An increase in the ratio between the heigtht of the secondary maxima and the central maximum with respect to its value in a Fraunhoffer-like pattern (0.217) indicates an enhancement of the current at the edges of the junction. The tunneling conductance dI/dV of the c-axis junctions in parallel magnetic field reveals an anomalous Zeeman splitting of the superconducting quasiparticle density of states. The magnitude of the splitting was found to be proportional to $\mu_B H$ and may be related to the magnetic moment of the quasiparticles. The ramp-edge junctions results represent clear engineering steps in the right direction and significant advances in multilayer oriented junction work. We find it very promising that the NBCO layers could be incorporated in the multilayer structure without substantial degradation. We expect in the near future ramp-edge junctions with reasonable I_C spread and reproducible characteristics both on and off of groundplanes.

REFERENCES

[1] G. Alvarez, T. Utagawa and Y. Enomoto, " c-axis tunneling in multilayers $NdBa_2Cu_3O_{7-\delta}$ junctions with $PrBa_2Cu_3O_{7-\delta}$ barriers," Appl. Phys. Lett. vol. 69, pp. 2473-2475, Oct. 1996.

[2] E. Polturak, G. Koren, D. Cohen, D. Aharoni, *Phys. Rev. Lett.* vol. 67, pp. 3038-3041, 1991.

[3] M. A. J. Verhoeven, G. J. Gerritsma, H. Rogalla, *IEEE Trans. Appl. Supercon.* vol. 5, pp. 2095-2098, 1995.

[4] G. A. Alvarez, M. Kuroda, M. Matsuda, K. Miyamoto, N. Kasai, T. Nemoto, and M. Koyanagi, "Fabrication and characterization of ramp edge-type junction and SQUIDs," *IEEE Trans. Appl. Superconduct.*, vol. 5, pp. 2755-2758, June 1995.

[5] G. A. Alvarez, J. G. Wen, F. Wang and Y. Enomoto, "Growth and properties of Nd-Ba-Cu-O/ Pr-Ba-Cu-O quasi-homoepitaxial multilayers", *Jpn. J. Appl. Phys*, vol. 35, pp. L1050-L1052, Aug. 1996.

[6] M. Sato, G. A. Alvarez, F. Wang, T. Utagawa, K. Tanabe, and K. Tanabe, "Preparation and Characterization of a-axis oriented NBCO/PBCCO/NBCO trilayers," *Advances in SuperconductivityXI*, 1999, unpublished.

[7] M. Konishi and Y. Enomoto, " Fabrication of Josephson junction on (001) $YBa_2Cu_3O_7$ single crystal substrate, "*Jpn. J. Appl. Phys.*, vol. 34, pp. L1271-L1273, Oct. 1995.

[8] M. Sato, G. A. Alvarez (unpublished work).

[9] A. Barone, G. Paterno, M. Riso, and R. Vaglio, Phys. Stat. Sol. (a) 41, pp. 393-401, 1977.

[10] G. A. Alvarez, T. Utagawa, K. Tanabe, and Y. Enomoto "Magnetic Field Splitting of the Quasiparticle States in Nd-Ba-Cu-O/Pr-Ba-Cu-O/Nd-Ba-Cu-O Planar Junctions," IEEE Transactions on Applied Superconductivity (unpublished).

[11] G. A. Alvarez, M. Becht, T. Utagawa, K. Toma, U. Kawabe, F. Wang, Y. Li, F. Saba, M. Sato and K. Tanabe,"Fabrication and Properties of Nd-Ba-Cu-O/Pr-Ba-Cu-O/Nd-Ba-Cu-O Ramp-Edge Junctions,". IEEE Transactions on Applied Superconductivity (unpublished).

Nature of the Interface Engineered High-T_c Josephson Junctions

S.S. Tinchev
Institute of Electronics, Bulgarian Academy of Sciences, Tzarigradsko Chausse 72, Sofia 1784, Bulgaria

Abstract— The mechanism of operation of the interface engineered high-T_c Josephson junctions with ion modified barrier has been discussed. An analysis is performed for YBaCuO base electrode modified by Ar^+- and O^+- ions. Using the diffusion coefficients of each YBaCuO component it is shown that at the counter electrode deposition temperature (about 780° C) the O and Cu defects annealed out and the Ba and Y sublattice disorder remains the only factor to play an important role in YBaCuO interface modification.

I. Introduction

Ramp - type Josephson junctions fabricated without any deposited interlayer and in which the barrier is created by a interface modification attracted a great attention recently [1]-[4]. In this method of fabrication an YBaCuO ramp (the base electrode) is treated with Ar^+ or O^+ ions and subsequently annealed prior to the deposition of the top electrode. These devices appear to be reproducible and with I-V characteristics well described by the resistive shunted junction (RSJ) - model. The modulation of the critical current with an external magnetic field indicates the formation of a homogeneous barrier layer at the interface. The temperature dependence of the critical current and of the normal resistance suggests the existence of a non-superconducting barrier. However, the nature of the barrier is still under debate and the mechanism of operation of these junctions is unclear.

Recently [5] we have made an attempt to shed light on the nature of the interface - engineered junctions. We supposed that these devices can be described as S-N-S devices, where the normal region is created by ion modification similarly to our e-beam modified or oxygen-ion modified weak links [6]-[10]. The thickness of the modified region in the layer was calculated for a typical experimental ion energy of 500 eV and it was found to be only 2 - 3 nm. Obviously the plasma treatment creates a barrier region, only a few of the YBaCuO units cell thick. This extremely thin layer determines actually the length of the created weak link and is responsible for the excellent properties of these junctions. Such a barrier thickness is consistent with the recent observation [11] by transmission electron microscopy of a 2 - 3 nm thin region at the YBCO interface with a different structure.

Manuscript received April 30, 1999.
This work was supported by the National Science Fund of Bulgaria under Grant No. F-561.

However, there is a problem that has to be solved precisely. During the deposition of the top YBaCuO layer a thermal annealing occurs at a temperature of about 780°C. We suggested [5] that the displacement of oxygen ions alone is important for the depressing of T_c and during the high-temperature treatment a significant part, but not all of the induced oxygen defects will be annealed out. A rough estimation using the value of the activation energy for oxygen diffusion was made there [5] leading to a reasonable agreement with the experimental data. However, recently some strong indications have been given that not the oxygen sublattice disorder, but rather the cation disorder is probably the primary cause of the Josephson effect in these devices [11]. The authors stated that these junctions are stable under high temperature oxygen anneals for several hours, which means that the oxygen diffusion at 780°C probably can not play the larger role in these devices. In this paper we try to present a more accurate analysis of this still open question, taking into account also the created cation defects.

II. Analysis

The well known Monte Carlo code TRIM [12] can be used for this purpose, similarly to our previsious work [5], [13]. The profiles of the total ion energy loss together with the energy absorbed by each YBaCuO component are plotted in Fig.1 in a case of 500 eV argon ion modification. The YBaCuO critical temperature reduction is related to the total energy losses of the ions, as it was already shown by Summers [14]. As seen in Fig. 1 about one half of these defects are oxygen defects. They probably annealed out almost completely [15] already at 500°C. However, after such a treatment the critical temperature does not recover to its original value [15]. This fact shows that not only oxygen defects, but also the cation sublattice disorder has an important effect on the T_c degradation. The suggestion that the cation sublattice disorder is responsible for the operation of the interface engineered junctions has been expressed already [2], [11].

All curves shown in Fig.1 can be fitted quite well with a Gaussian function

$$F(x) = y_0 + \frac{A}{\sqrt{2\pi}\sigma}\exp\left[\frac{-(x-x_0)^2}{2\sigma^2}\right] \qquad (1)$$

Here y_0 is the baseline offset, A is the total area under the curve, x_c is the center of the peak and σ is the standard deviation.

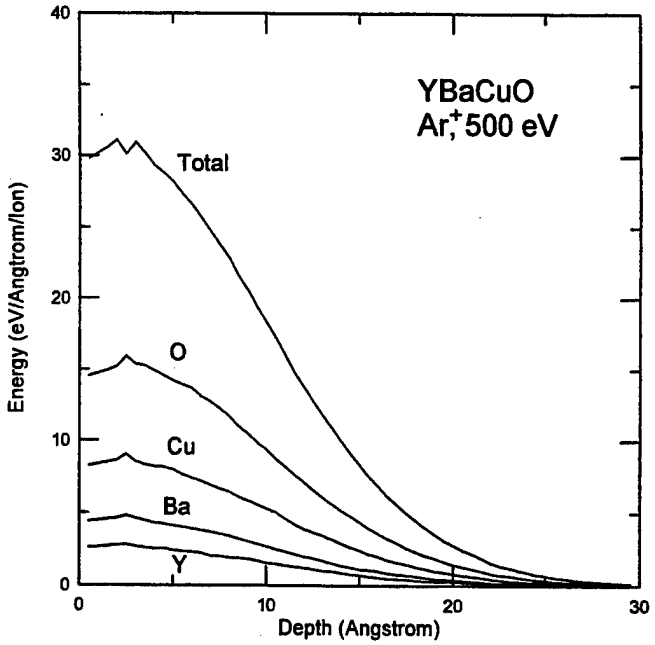

Fig. 1. Calculated total energy losses and energy losses for each component in YBaCuO film for modification by argon ions with energy of 500 eV.

During the thermal treatment of the base electrode and during the deposition of the counter electrode a thermal diffusion occurs. For a Gaussian distribution the analytical solution of the diffusion equation is:

$$F_a(x) = \frac{A}{\sqrt{1+\frac{2Dt}{\sigma^2}}} \exp\left[\frac{-(x-x_0)^2}{2\sigma^2+4Dt}\right], \qquad (2)$$

where D is the diffusion coefficient and t is the annealing time. Obviously an annealing takes place when $Dt \geq \sigma^2$. For ions with energy of 500 eV the standard deviation σ for all curves from Fig.1 is about 1.1 nm for oxygen ions and about 0.8 nm for argon ions. Using $t \sim 10^3$ s as a typical time for the counter electrode deposition, one obtains that the diffusion coefficient has to be greater then 10^{-17}cm^2/s in order created defects to anneal out completely.

Table I summarized the diffusion coefficients found in the literature [16]-[18] for O and Cu [19] at temperature T ≅ 780 °C. The data for Ba and Y available in the literature [20] at temperatures different from 780 °C, were extrapolated for the same temperature using the Arrenius relation.

TABLE I

DIFFUSION COEFFICIENTS OF THE YBaCuO COMPONENTS

	D (cm^2/s) at 780°C	Reference
O	10^{-8} - 10^{-10}	16 - 18
Cu	10^{-13}	19
Ba	10^{-20}	20
Y	10^{-33}	20

Obviously at 780 °C for oxygen and cooper $Dt >> \sigma^2$ and the ion induced defects will be almost completely annealed out. Since the heat treatment at this temperature and for the same deposition time is not sufficient to cause changes in the disordered Ba and Cu sublattices, their amount is likely to be the factor controlling for YBaCuO interface modification.

III. Conclusion

On the basis of this result, we can conclude that the remained Ba and Y sublattice displacements, which can not be removed during the counter electrode deposition at 780°C are responsible for the suppression of T_c and thus for the Josephson effect observed in these junctions. They can be misinterpreted in TEM investigations as a new (cubic) phase [2], [11] of YBaCuO or as an a - axis oriented YBaCuO [21]. Similar is probably the mechanism of operation of the sandwich junctions YBCO/PBCO/YBCO [22] made by planarization of the base electrode by Ar-ion beam at 700 eV.

Acknowledgment

I thank Dr. A. Veneva for providing the papers [19, 20], with data for Cu, Ba and Y diffusion coefficients.

References

[1] B.H. Moeckly and K. Char, "Properties of interface-engineered high-T_c Josephson junctions", *Appl. Phys. Lett.* , vol. 71, pp. 2526-2528, October 1997.

[2]B.H. Moeckly, K. Char,Y. Huang and K. Merkle, "Interface-engineered YBCO edge junctions", preprint Applied Superconductivity Conference 1998, in press.

[3] B.D. Hunt, M.G. Forrester, J. Talvacchio and R. M. Young, "High-resistance HTS edge junctions for digital circuits", preprint Applied Superconductivity Conference 1998, in press.

[4] R. Dittmann, J.K. Heinsohn, A.I. Braginski and C.I. Jia, "Fabrication of $YBa_2Cu_3O_7$ ramp-type junctions by interface treatments", preprint Applied Superconductivity Conference 1998, in press.

[5] S.S. Tinchev and S. Alexandrova, "Comment on properties of interface-engineered high-T_c Josephson junctions", *Appl. Phys. Lett.* vol. 73, pp.1745-1546, September 1998.

[6] S.S. Tinchev, "Investigation of RF SQUIDs made from epitaxial YBCO films", *Supercond. Sci. Technol.* vol. 3, pp. 500 -503, 1990.

[7] S.S. Tinchev, "High-T_c-SQUIDs with local oxygen-ion irradiated weak links", *IEEE Trans. Appl. Supercond.*, vol. 3, pp. 28 32, 1993.

[8] S.S. Tinchev, "Current-phase relation in high-T_c-weak links made by oxygen-ion irradiation", *Physica C*, vol. 222), pp. 173-176. 1994.

[9] S.S. Tinchev, "High-T_c SQUIDs made by oxygen-ion irradiation - technology, properties and applications", in

Proceedings of the Seventh International Symposium on Weak Superconductivity, Smolenice Castle, Slovak Republic, p. 312-323,. 1994

[10] S.S. Tinchev, "Properties of YBCO weak links prepared by local oxygen-ion induced modification", *Physica C*, vol. 256, pp. 191-198, 1996.

[11] B.H. Moeckly and K. Char, "Response to comment on properties of interface-engineered high Tc Josephson junctions", *Appl. Phys. Lett.*, vol. 73, p. 1747, September 1998.

[12] J. Ziegler and P. Biersack, *The stopping and range of ions in solids*, Pergamon Press, New York, 1985.

[13] S.S. Tinchev, "Modeling of $YBa_2Cu_3O_{7-\delta}$ weak links produced by oxygen-ion modification", *J. Appl. Phys.*, vol. 78, pp. 5851 -5853, 1995.

[14] G.P. Summers, E.A. Burke, D.B. Chrisey, M. Nastasi, and J.R. Tesmer, "Effect of particle-induced displacement on the critical temperature of $YBa_2Cu_3O_{7-\delta}$ ", *Appl. Phys. Lett*, vol. 55, pp. 1469-1471, 1989.

[15] F. Kahlmann, Ph.D. Thesis, Koln University, 1998.

[16] S.H. Lee, S.C. Bae, J.K. Ku, H.J. Shin, "Oxygen diffusion in epitaxial $YBa_2Cu_3O_{7-x}$ thin films" , *Phys. Rev. B,* vol. 46, pp. 9142-9146, 1992.

[17] Y. Li, J.A. Kilner, T.J. Tate, M.J. Lee, R.J. Chater, H. Fox, R.A. De Souza, P.G. Quincey, "Secondary-ion-mass-spectroscopy study of oxygen tracer diffusion in c-axis-oriented $YBa_2Cu_3O_{7-\delta}$ film", *Phys. Rev. B*, vol. 51, pp. 8498-8502, 1995.

[18] A. Michaelis, E.A. Irene, O. Auciello and A.R. Krauss, "A study of oxygen diffusion in and out of $YBa_2Cu_3O_{7-\delta}$ thin films", *J. Appl. Phys.*, vol. 83, pp. 7736-7743, 1998.

[19] J.L. Routbort, S.J. Rothman, N. Chen, J.N. Mundy and J.E. Baker, "Site selectivity and cation diffusion in $YBa_2Cu_3O_{7-\delta}$", *Phys. Rev. B,* vol. 43, 5489-5497, 1991.

[20] N. Chen, S.J. Rothman, J.I. Routbort and K.C. Goretta, " Tracer diffusion in $YBa_2Cu_3O_{7-x}$", *J. Mater. Res.*, vol. 7, pp. 2308-2316, 1992.

[21] Y. Li, S. Linsen, F. Machalet, F. Schmidl and P. Seidel, "Recovery of superconductivity and recrystalization of ion damaged $YBa_2Cu_3O_{7-x}$ films after thermal annealing treatment", *Physica C*, vol. 243, pp. 294-302, 1995.

[22] M. Maruyama, K. Yoshida, M. Horibe, A. Fujimaki, H. Hayakawa, Improvement of the sandwich junction properties by planarization of YBCO films, preprint Applied Superconductivity Conference 1998, in press.

Intrinsic Josephson effects in submicrometer Bi2212 mesas fabricated by using focussed ion beam etching

Dag Winkler[†], Niklas Mros, August Yurgens, and Vladimir M. Krasnov
Department of Microelectronics and Nanoscience, Chalmers University of Technology and Göteborg University, SE-412 96 Göteborg, Sweden

Edward J. Tarte, David T. Foord, Wilfred E. Booij, and Mark G. Blamire
IRC in Superconductivity, University of Cambridge, Madingley Rd, Cambridge, CB3 0HE, UK

Abstract—We have investigated the current-voltage (I-V) characteristics of sub-μm sized mesas made on the surface of $Bi_2Sr_2CaCu_2O_8$ (Bi2212) single crystals. The mesas were fabricated using focussed ion beam etching (FIB). The samples showed excellent I-V characteristics and their conductance-voltage (G-V) curves were measured from above the transition temperature down to 4.2 K. New ways of making annular mesas with diameters down to 0.5 μm were also investigated.

I. Introduction

The intrinsic Josephson effect in anisotropic high-T_c materials is now well established [1]-[6]. In the Bi2212 single crystal the structure is composed of stacked layers of CuO double planes separated by SrO and BiO layers. The CuO double planes form superconducting electrodes, while the intermediate layers (SrO and BiO) form tunnel barriers across which the weak superconducting coupling gives rise to the Josephson effects. The space periodicity of stacked Josephson junctions is 15 Å, and across a single crystal of thickness ~100 μm there are thousands of junctions in series. In order to produce a reduced set of junctions with smaller area, standard photolithography together with dry or chemical etching has been used to fabricate small mesas on top of single crystal Bi2212 [4]. However, the resolution of this method makes it difficult to reduce the dimensions to below the Josephson penetration depth (~1 μm). Recently, focussed ion beam (FIB) has been used on Bi2212 whiskers [7]. Here, we will report on the fabrication of submicrometer sized Bi2212 stacked junctions produced by using FIB-etching on the surfaces of single crystal Bi2212.

Manuscript received April 30, 1999.
This work was supported by the Swedish Research Council for Engineering Sciences (TFR), the British Council and UK Engineering and Physical Sciences Research Council.

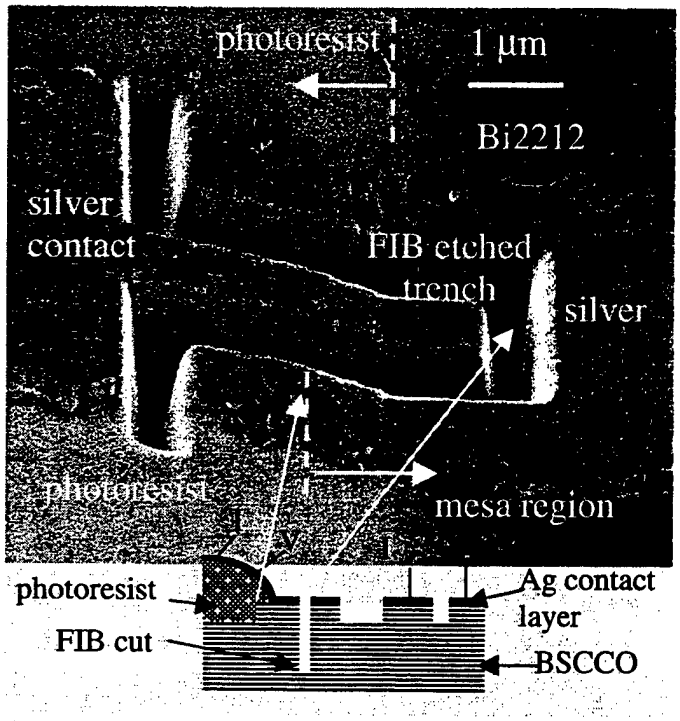

Fig. 1. FIB image of a region where FIB was used to reduce the size of the stacked junctions mesa to the edge of a contact.

II. Experimental

All of the micro machining of these devices was carried out in an FEI FIB200 focussed ion beam system. In this, a 30 keV Ga focussed ion beam was used for machining and imaging of the specimens, with secondary electrons emitted by the specimen during the scanning of the beam being detected to provide the image. The Bi2212 single crystals (about 1 x 1 x 0,01 mm^3) were mounted on 5 x 5 mm^2 sapphire substrates using Stycast epoxy. The crystal was cleaved with adhesive tape after mounting and immediately placed in a vacuum system where a layer of gold was evaporated onto the fresh Bi2212 surface.

[†] Now with the IMEGO Institute, Aschebergsgatan 46, Building 11 SE-411 33 Götbeorg, Sweden

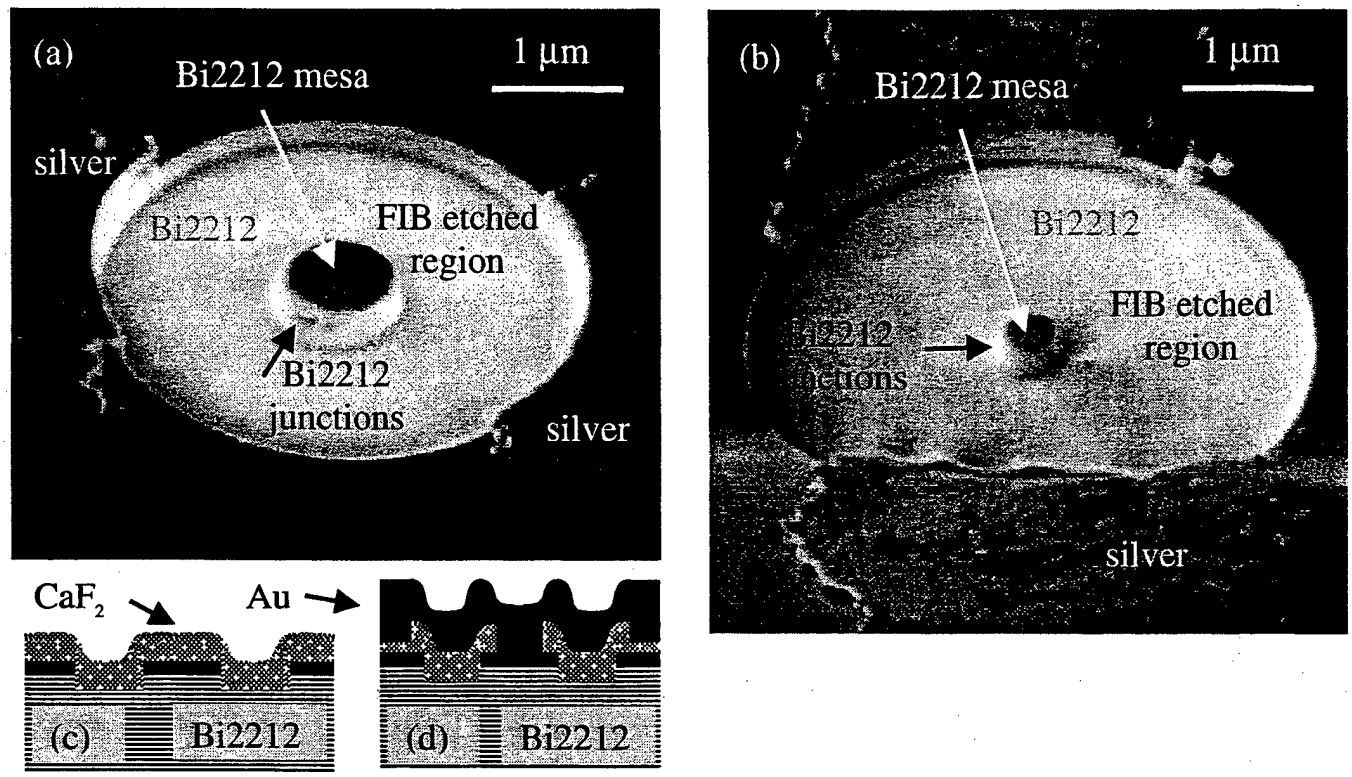

Fig. 2. FIB image of FIB etched circular mesa (a) 1 μm and (b) 0.5 μm diameter. The following fabrications steps are indicated in (c) CaF_2 isolation and (d) FIB etched via to the mesa and gold contact deposition.

In one set of samples, 10 x 20 μm^2 large mesas were etched by using an EDTA solution. The height of the mesas defined the number of junctions in series. Hard baked photoresist was used as an insulation layer and for planarization.

In this case, the electrical connections were formed by strips of silver, which extended from contact pads on the substrate across the Stycast and photoresist isolation layers to terminate on top of the mesa. In order to reduce the active area of the device, the FIB was used to mill a trench in the silver strip close to the point where it left the crystal surface and began to climb over the photoresist isolation. The shape of this structure was a rectangular Ω shape, as shown in Fig. 1. Care was taken to ensure that the depth of the milling was definitely below the level of the foot of the mesa even when cutting the photoresist, see the schematic diagram of the device structure also in Fig. 1. This process enabled the width of the device to be reduced to 0.5 microns but its other dimension could not be well controlled because it was fixed by the overlap of the photoresist isolation and the edge of the mesa which we estimate was typically a few microns (~2-4 μm).

In order to alleviate this problem, a second design of device was prepared. In this case, circular mesas were defined by milling an annular trench in the BSCCO crystal, which was covered with coatings of silver and gold. The height of the FIB defined mesa fixed the number of layers and this was chosen by measuring the etch rate of the multilayered structure and using this to set the milling time. In order to obtain the optimum milling resolution, the minimum beam current possible was used (<20 pA). However, since these specimens tended to charge, it was sometimes necessary to use much larger beam currents (70 pA) in order to reduce the etching time and avoid excessive beam drift. Examples of circular mesas are shown in Fig. 2 (a) and (b). Isolation for these samples was provided by thermally evaporating a 100 nm thick layer of CaF_2 over the whole sample (see Fig. 2 (c)) followed by a gold layer to minimize charging during the final FIB step. This involved using the Ga beam to open via holes in the center of the circular mesas. This required the milling process to be stopped accurately after the last of the CaF_2 had been removed from the via and before penetrating the metal layers on the top of mesa. This process would have been extremely difficult without the built in end-point detection facility of the FIB200, which utilizes the current induced in the sample and flowing to ground. The magnitude of this current depends on the electrical properties of the material being milled and so it was possible to determine when the top gold and CaF_2 layers had been removed independently. Here the beam current was chosen so that to remove the required volume of material to be removed took a reasonable amount of time (about 5 minutes). After the vias were opened, the sample was coated with more gold that was then patterned into electrodes (see Fig. 2 (d)).

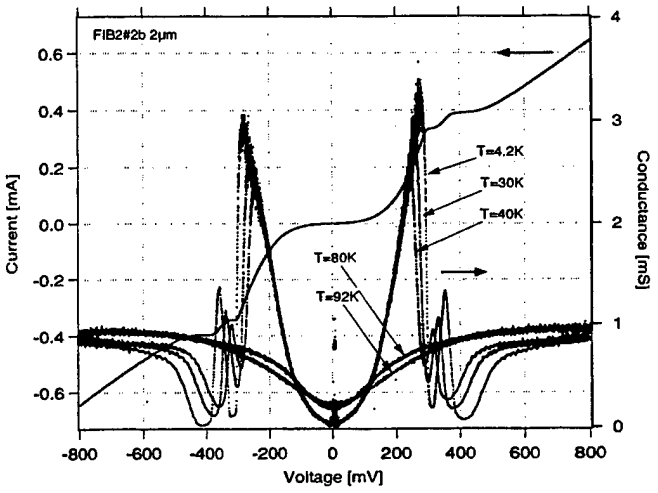

Fig. 3. I-V and G-V characteristics of a 2 μm wide mesa.

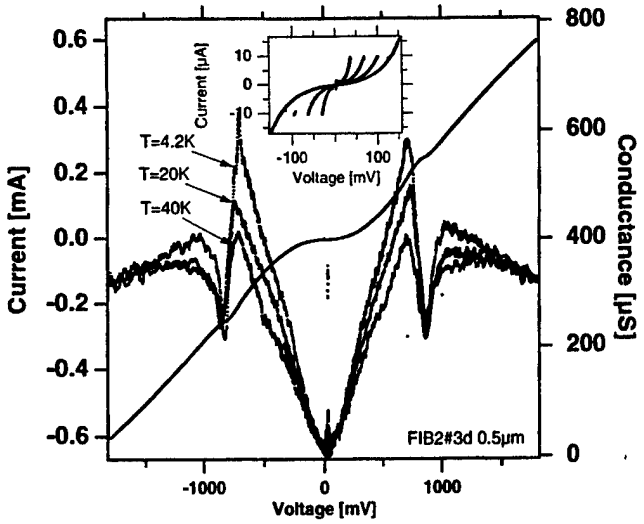

Fig. 4. . I-V and G-V characteristics of a 0.5 μm wide mesa.

III. Results

The I-V curves from the first set of FIB samples (e.g. Fig . 1) showed excellent tunneling characteristics with well-defined quasiparticle branches, see Fig. 3 and 4. Conductance-voltage curves were traced from well above the transition temperature (T_c~90 K) down to 4.2 K. The normal-state tunneling parts of the I-V curves can be clearly seen in Fig. 3 and 4. There are additional features (peaks) beyond the main gap-edge, which possibly reflect another characteristic superconducting gap for the c-axis tunneling. A pseudogap [8, 9] (see Fig. 3) above T_c develops into the superconducting gap when passing T_c. Measurements were also done on a reduced set of annular junctions, and a fairly large series resistance at the mesas made it difficult to characterize them in detail.

References

[1] R. Kleiner, F. Steinmeyer, G. Kunkel, and P. Müller, "Intrinsic Josephson effects in $Bi_2Sr_2CaCu_2O_8$ single crystals," *Phys. Rev. Lett.*, vol. 68, pp. 2394-2397, 1992.

[2] R. Kleiner and P. Müller, "Intrinsic Josephson effects in high-T_c superconductors," *Phys. Rev. B*, vol. 49, pp. 1327-1341, 1994.

[3] A. Yurgens, D. Winkler, Y. M. Zhang, N. Zavaritsky, and T. Claeson, "Intrinsic Josephson tunnel junctions fabricated on the surfaces of Bi2212 single crystals by photolithography," *Physica C*, vol. 235-240, pp. 3269-3270, 1994.

[4] A. Yurgens, D. Winkler, N. V. Zavaritsky, and T. Claeson, "In situ controlled fabrication of stacks of high-T_c intrinsic Josephson junctions," *Appl. Phys. Lett.*, vol. 70, pp. 1760-1762, 1997.

[5] N. Mros, V. M. Krasnov, A. Yurgens, D. Winkler, and T. Claeson, "Multiple valued c-axis critical current and phase-locking in $Bi_2Sr_2CaCu_2O_{8+x}$ single crystals," *Phys. Rev. B Rapid Communications*, vol. B57, pp. pp. R8135-8138, 1998.

[6] V. M. Krasnov, N. Mros, A. Yurgens, and D. Winkler, "Fiske steps in intrinsic $Bi_2Sr_2CaCu_2O_{8+x}$ stacked Josephson junctions," *Phys. Rev.*, vol. B 59, pp. 8463-8466, 1999.

[7] Y. I. Latyshev, S.-J. Kim, and T. Yamashita, "Experimental evidence for Coulomb charging effects in submicron Bi-2212 stacks," *JETP Lett.*, vol. 69, pp. 84, 1999.

[8] M. Suzuki, S. Karimoto, and K. Namekawa, *J. Phys. Soc. Jpn.*, vol. 67, pp. 732, 1998.

[9] I. F. G. Parker, C. E. Gough, M. Endres, P. J. Thomas, G. Yang and A. Yurgens, "Observation of normal and superconducting state energy gap features from intrinsic c-axis interlayer tunneling in $Bi_2Sr_2CaCu_2O_8$ crystals," in *Conference on Superlattices II: Native and Artificial*, vol. SPIE Vol. 3480, I. Bozovic and D. Pavuna, Eds.: SPIE, Bellingham, WA, 1998, pp. 11-20.

Fabrication of Trilayer Junctions using YBCO Surface Treatment

Michitaka Maruyama, Toshiki Furutani, Kazuhiro Yoshida, Masahiro Horibe, Akira Fujimaki, and Hisao Hayakawa
Department of Quantum Engineering, Nagoya University, Furo-cho, Chikusa-ku, Nagoya, 464-8603, Japan

Abstract—We have successfully fabricated c-axis-oriented YBCO/PBCO/YBCO trilayer junctions using surface treatment. The junctions, in which the surface of the base YBCO film was annealed prior to the deposition of 20-nm-thick PBCO barrier, showed almost uniform Josephson currents and little excess currents. The characteristic voltage is 1.4 mV at 4.2 K. From the microscopic observation of several samples, we found a correlation between the surface morphology and the junction properties. We consider that the surface treatment promotes more uniform growth of the barriers.

I. Introduction

To realize digital applications using high temperature superconductors (HTSs), much effort on fabrication of high quality Josephson junctions has been made. Some attempts to demonstrate digital circuits using HTS junctions have succeeded [1]-[3]. In these circuits, however, the number of employed junctions is several tens at most. For larger scale integrated circuits, the junction quality including parameter spread is not sufficient yet. Further development in the fabrication technology of the junctions is required.

One of the most important matters in fabrication of Josephson junctions is barrier uniformity. Poor uniformity of the barriers causes either large spread of the junction parameters by dispersed current flow or degradation of the junction quality by leakage currents. Though trilayer junctions are very attractive in design of digital circuits because of many structural advantages for integration, poor uniformity of the barriers is more remarkable than other types of junctions. Therefore, the barrier thickness cannot be thin enough and is usually more than several tens nm. Tsuchiya et al. fabricated a-axis-oriented trilayer junctions with 2.4-nm-thick $PrGaO_3$ (PGO) barriers by atomic scale control for epitaxy [4]. The junctions showed large I_cR_n values up to 5.8 mV and demonstrate a possibility that thin and uniform barriers realize high performance.

In circuit applications, the need for using c-axis-oriented films is strong even in the trilayer junctions. However, the quality of most trilayer junctions using c-axis-oriented films is lower than that of the junctions using a-axis-oriented films. It is true that superconductivity along c direction is weaker than ab direction because of anisotropy of HTSs. But it seems that the junction properties are limited by the fabrication technology rather than by the anisotropy at present. In junctions we previously fabricated, the nominal barrier thickness below which the electrical shorts are observable is around 20 nm, though this value seems to be very thick for tunnel junctions [5]. More thin and uniform barriers are required to improve junction quality. It seems that the condition of the interface between superconductor and barrier is important to the uniform growth of the barrier.

In this paper, we report the effect of the anneal in the $YBa_2Cu_3O_{7-x}$ (YBCO)/$PrBa_2Cu_3O_{7-y}$ (PBCO) interfaces on the properties of c-axis-oriented trilayer junctions.

Manuscript received April 30, 1999.

II. Fabrication Process

The multilayers are deposited on MgO (100) substrates by using an RF magnetron sputtering method. The deposition conditions are 720°C, 40 Pa of 50%-O_2/Ar. The nominal thicknesses of YBCO and PBCO are 120 nm and 20 nm, respectively. The surfaces of base YBCO and/or PBCO are annealed for 10 minutes in the intervals between the depositions of YBCO and PBCO. The annealing conditions are the same as the deposition. This means that the lower and/or upper interfaces are treated at 720°C, 40 Pa. We prepared three types of junction as shown in Fig. 1. Type A is treated in both interfaces. Type B and C are treated only in the upper and lower interfaces, respectively. After the deposition of the YBCO/PBCO/YBCO trilayer, the sample is cooled to room temperature in an atmosphere of O_2/Ar at 3×10^3 Pa. Then, an 80-nm-thick Au film, which acts as a passivation layer and contact pads, is in-situ sputtered.

After the sample is taken out from a vacuum chamber, junctions are defined by etching the multilayer in an ECR plasma etcher. Following the evaporation of a SiO film for insulation, contact holes are made by lift-off process. Finally, a Ag film is evaporated and patterned to wiring pads. The samples are measured in a four-terminal configuration. The junction sizes are 10 μm × 10 μm.

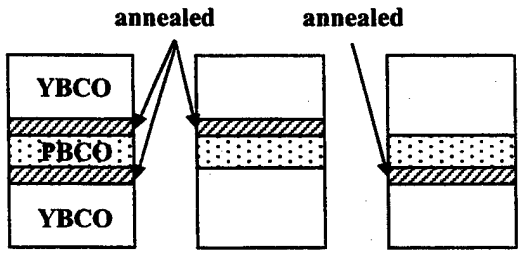

Fig. 1. The schematic cross sections in three types of the fabricated junctions.

III. Results and Discussions

A. Junctions Treated in Both Interfaces (Type A)

First, we tried to fabricate the junctions by treating both upper and lower interfaces. Typical current-voltage (*I-V*) curve is shown in Fig. 2 (a). The junctions can be described by using resistively shunted junction (RSJ) model with excess current. Hystereses are observed at the temperatures below 20 K. The magnetic field dependence of the critical current (*Ic*) is shown in Fig. 2 (b). The junction current is confirmed to include Josephson current. The modulation depth is about 60% at 4.2 K. The critical current density (*Jc*), which represents only Josephson current, the normalized junction resistance (*RnA*) and the characteristic voltage (*Vc*) are 40 A/cm^2, 1.5 × 10^{-5} Ωcm^2 and 0.38 mV, respectively.

Since the junctions without the surface treatment cause electrical shorts in the case of using 20-nm-thick PBCO barriers, it is considered that 20-nm-thick PBCO layer is usually not uniform and has many pinholes. It can be said that the surface treatment in the upper and/or lower interface contributes to the reduction of pinholes in barriers. We then performed further experiments to clarify the effects of the treatment in each interface as follows.

B. Junctions Treated in Upper Interface (Type B)

The junctions with the upper interface treated did not show RSJ-like but flux-flow-like characteristics as shown in Fig. 3. *Jc* is 6.4 × 10^4 A/cm^2 at 4.2 K, which is larger than that of Type A by three orders. Moreover, the junction current is not suppressed by external magnetic field at all. In the junctions, electrical shorts occur between superconducting electrodes, which is the same behavior as the junctions without surface treatment.

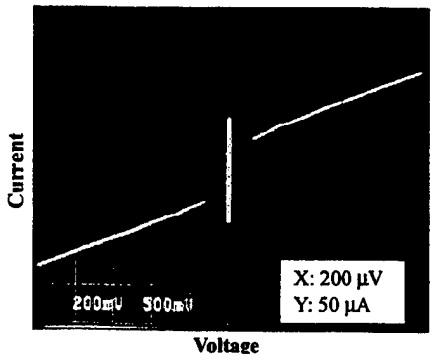

(a) *I-V* curve

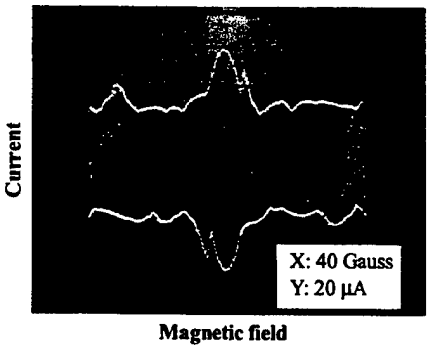

(b) Magnetic field dependence of *Ic*

Fig. 2. Typical characteristics of Type A junctions at 4.2 K.

C. Junctions Treated in Lower Interface (Type C)

Fig. 4 (a) is typical *I-V* curve of the junctions in which the surface of the base YBCO is treated. The junctions showed RSJ-like characteristics at the temperatures below 70 K. Clear hystereses are observed below 40 K. The junction current contains little excess current even at 4.2 K. *Jc*, *RnA* and *Vc* is 3.6 × 10^2 A/cm^2, 3.8 × 10^{-6} Ωcm^2 and 1.4 mV, respectively. Fig. 4 (b) shows the magnetic field modulation of *Ic*. A Fraunhofer pattern is observed. The modulation depth is more than 90% at 4.2 K.

From these results, it can be said that the treatment in the lower surface suppresses the formation of pinholes in barriers. The concrete role of the surface treatment has not cleared yet, but there are two different possibilities as discussed bellow. One is the uniform growth of the PBCO layer, and the other is the formation of some interface layer that covers pinholes in the PBCO layer. However, the results on Type B junctions exclude the latter possibility because the Type B junctions are also expected to have Josephson currents if the interface layer is formed by the treatment. We then support the former possibility at present. The crystallinity of the YBCO surface might be improved by the anneal, promoting more uniform and pinhole-free growth of the PBCO layer.

D. Comparison of Surface Morphology

We observed the surfaces of the YBCO/PBCO/YBCO multilayers by an optical microscope. Fig. 5 shows the micrographs in Type A, B and C. The surfaces of the multilayers are covered with Au layers. A clear difference between Type A, B and C can be seen in the surface morphology. By relating the micrograph of each type to its electrical properties, we can find a correlation between the

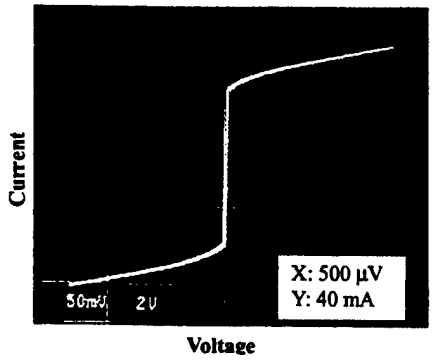

Fig. 3. Typical *I-V* characteristics of Type B junctions at 4.2 K.

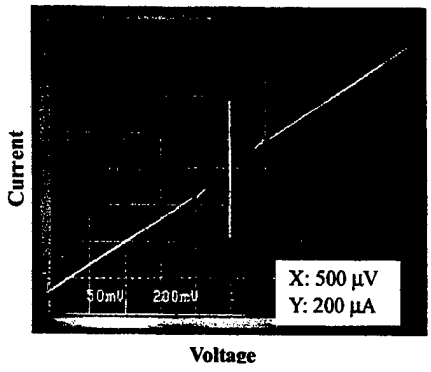

(a) *I-V* curve

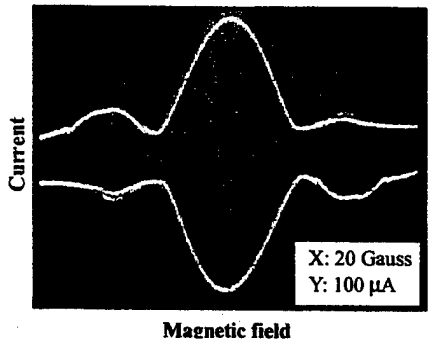

(b) Magnetic field dependence of *Ic*

Fig. 4. Typical characteristics of Type C junctions at 4.2 K.

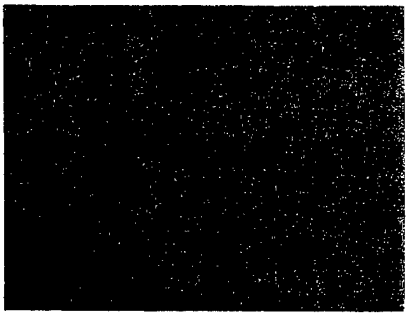

(a) Type A

(b) Type B

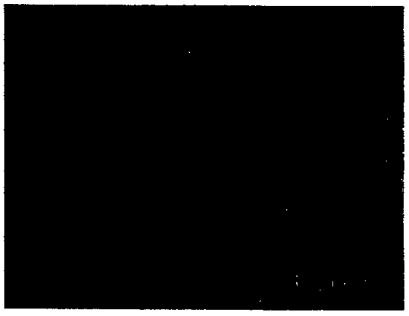

(c) Type C

Fig. 5. The surfaces of the YBCO/PBCO/YBCO/Au multilayers observed by an optical microscope.

surface morphology and the junction properties. Type C junctions have a smooth surface showing relatively uniform Josephson currents, and Type B junctions have a rough surface showing electrical shorts. Type A junctions have a somewhat rough surface showing Josephson currents with excess currents. The rough surfaces in Type A and B consist of many depressions. It seems that the junctions with many depressions have many pinholes in the barriers. These results from the microscopic observations agree with the idea that the surface treatment of the base YBCO reduces pinholes in barriers, though the surface treatment of the PBCO expands the area and/or number of pinholes.

IV. Summary

We have investigated the effects of the anneal in the YBCO/PBCO interfaces on the properties of c-axis-oriented trilayer junctions. The junctions treated on the surface of the base YBCO showed RSJ-like characteristics having high characteristic voltages and little excess currents. It was found that the surface morphology changed by the method of the treatment, relating to the junction properties. From these results, we consider that the anneal on the base-YBCO surface promotes more uniform growth of the PBCO barrier. The crystallinity of the YBCO surface might be improved by the anneal.

References

[1] B. Oelze, B. Ruck, E. Sodtke, A. F. Kirichenko, and M. Yu. Kupriyanov, Appl. Phys. Lett. **70**, 658 (1997)
[2] M. Hidaka, T. Satoh, H. Terai, and S. Tahara, IEICE Trans. Electron. Vol. E80-C, 1226 (1997)
[3] A. G. Sun, D. J. Durand, J. M. Murduck, S. V. Rylov,M. G. Forrester, and B. D. Hunt, 1998 Applied Superconductivity Conference, ENA-04 (1998)
[4] R. Tsuchiya, M. Kawasaki, H. Kubota, J. Nishino, H. Sato, H. Akoh, and H. Koinuma, Appl. Phys. Lett. **71**, 1570 (1997)
[5] M. Maruyama, A. Fujimaki, and H. Hayakawa, 10th International Symposium on Superconductivity, DAP-21 (1997)

Fabrication of Ramp-Type Junctions Using a Two Angle Ion Beam Etching Process

U. Schoop, M. Schonecke, S. Schymon, T. Bauch, A. Marx, B. Wiedenhorst, L. Alff†, and R. Gross
II. Physikalisches Institut, Universität zu Köln, Zülpicher Str. 77, D-50937 Köln, Germany

Abstract— The development of tunnel junctions consisting of high-T_c superconductors (HTS) and other perovskite transition metal oxides offers the possibility of creating a variety of new functional devices. The fabrication of such devices represents a challenge with respect to both thin film technology and the clarification of the underlying physics of charge transport across the involved barriers and interfaces. In particular, the use of manganite/HTS junctions allows the study of spin-polarized charge injection into HTS and the interaction between superconducting and ferromagnetic materials. Here, we present recent advances in the fabrication of ramp-type junctions using *in-situ* surface cleaning by low-energy oxygen ions and Two Angle Ion Beam Etching (TA-IBE). The latter process prevents the formation of redeposit and allows the fabrication of flat surfaces in the ramp region. In our fabrication process the interfaces and surfaces between the different process steps have been characterized by Atomic Force Microscopy (AFM) and Transmission Electron Microscopy (TEM). The fabricated junctions have been characterized by standard electrical measurements.

I. Introduction

Ramp-type geometries have been used in fabrication of Josephson junctions of high-T_c superconductors since about a decade. Most of the related work is dedicated to the fabrication of Josephson junctions with reproducible and high I_cR_n products. In a recent approach the tunneling barrier was obtained by a controlled treatment of the ramp surface instead of the deposition of an artificial barrier. This is believed to enhance the possibility of tuning the superconducting junction properties [1]. However, this approach cannot be used if one is interested in the investigation of specific heterostructures such as e.g. superconductor - ferromagnet - superconductor junctions. Such structures are interesting not only for possible device applications but also to study the physics of the electrode and barrier materials in tunneling experiments. It has become clear over the recent years that in order to fabricate ramp-type junctions with artificial barriers, the ramp etching process and epitaxial growth of the counter electrode and barrier has to be controlled on atomic length scales [2–4]. In this paper, we focus on the recent progress in the ramp etching process using *in-situ* oxygen ion beam cleaning of the ramp surface and Two Angle Ion Beam Etching (TA-IBE).

II. Junction Fabrication

A. Process overview

The standard junction fabrication process is sketched in Fig. 1. First we deposit a bilayer of *c*-axis oriented $YBa_2Cu_3O_{7-\delta}$ and $SrTiO_3$ (STO) using pulsed laser deposition (PLD). The $SrTiO_3$ layer provides insulation in *c*-axis direction between the junction electrodes. The base electrode has typically critical temperatures $T_c \approx 89-90$ K, critical current densities $J_c(77\,\mathrm{K}) \approx 2-4\times10^6$ A/cm^2, and FWHM of rocking curves of the (005) $YBa_2Cu_3O_{7-\delta}$ peak of 0.1-0.2°. In order to obtain a flat ramp, a smooth surface of the bilayer is required. Our bilayers have rms roughnesses ranging between 2-4 nm. In the next fabrication step it is necessary to achieve a sharp edge of a photo resist mask. We use the standard resist AZ5214E, which is spun with 4000 rpm for 40 sec and baked at 110°C for 1 min. The height of the resist stencil is 1.4 μm. Following a standard exposure process, the resulting edge is steeper than 80°. For the fabrication of the ramp we use the TA-IBE process which is described in detail below. The ion energies during etching are reduced from 500 eV initially to 100 eV at the end of the etching process in order to keep the damaged surface layer thin [5]. As shown in detail in the next section even a thin layer of amorphous material disturbs the epitaxy of the subsequently deposited barrier and counter electrode. After the IBE process the photo resist is stripped in acetone. The sample with the freshly milled ramp is then mounted in a sputtering system. Of course, during this step the ramp surface is exposed to ambient atmosphere. In the sputtering system an oxygen ion beam cleaning step is used to remove the surface contamination and the layer of amorphous material on the ramp. For the cleaning process a low-energy oxygen ion beam of 50 eV is used to prevent the formation of an oxygen depleted surface layer [6]. During the cleaning process the sample is heated in oxygen atmosphere to the deposition temperature of 795°C and subsequently barrier layer and counter electrode are deposited *in-situ* by off-axis magnetron sputtering. Typically, for the counter electrode we obtain $T_c \approx 90-91$ K and $J_c(77\,\mathrm{K}) \approx 4-6\times10^6$ A/cm^2. X-ray diffraction shows a high degree of epitaxy. Typically, the FWHM of the rocking curve of the (005) $YBa_2Cu_3O_{7-\delta}$ peak is less than 0.3°. Finally, in a single IBE step the sample structure used for electrical transport measurements in the active area of the junction (i.e. the ramp interface) is defined and the layers on top of the base electrode are removed to allow the evaporation of silver pads. Wiring is done by ultrasonic bonding.

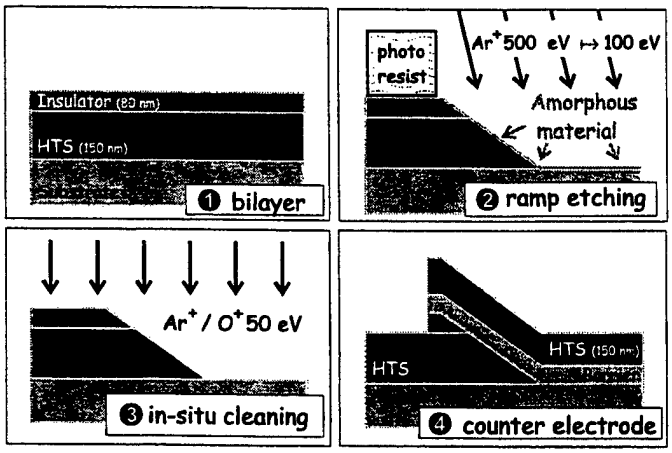

Fig. 1 Basic steps of the fabrication process of HTS ramp-type junctions with artificial barriers.

Manuscript received April 30, 1999.
†e-mail: alff@ph2.uni-koeln.de.
This work was supported by the Deutsche Forschungsgemeinschaft.

B. *Two angle ion beam etching (TA-IBE) system*

Before discussing the details of the TA-IBE process we briefly describe the realization of the TA-IBE system which represents an extension of a previously described setup [7]. We use a 3 cm Kaufmann ion source. The maximum energy of the Ar-ions used in our experiments is 500 eV with a beam current of 12 mA. This gives an ion current density of $\leq 0.4\,\mathrm{mA/cm^2}$ at the sample. To prevent sample heating resulting in oxygen loss an effective cooling system has to be provided. In our system, the sample is mounted onto a copper block that can be cooled down to well below room temperature by using liquid N_2. To allow the rotation of the sample holder by a vacuum stepper motor, the copper block is connected to the liquid nitrogen part by flexible copper braids that effectively remove the heat from the sample holder. The temperature of the sample is monitored and constantly kept below 180 K during the process.

As shown in Fig. 3 the sample holder can be installed with its axis of rotation in any angle α to the incident ion beam. Regarding the sample rotation, the ion beam travels on the surface of a cone with the *opening angle* α. By using a wedge shaped sample plate with an angle β, the sample normal is tilted with an *offset angle* β to the axis of rotation i.e. the axis of the cone. Both angles are adjustable between 0 and 90°.

C. *Effect of redeposit on the ramp surface*

In an IBE process using a standard photo resist mask with a thickness of about 1 μm and an inclined incidence of the ion beam with respect to the surface, there is always a nonvanishing area that is not exposed to the ion beam. In this region, etched material forms an amorphous redeposit of undefined stoichiometry (see Fig. 3a). Surface topography profiles of a sample that was etched with a fixed angle of 70° are shown in Fig. 2. The line scans were obtained using Atomic Force Microscopy (AFM). The width of the redeposit region (about 4 μm) is indicated by the hatched area and is determined by the resist thickness and the angle of incidence of the ion beam. The measured width is in good agreement with the expected value. Note, that AFM always generates an image of the AFM tip and the sample. Therefore, the resist edge appears to have a slope of about 55°. This slope, however, is caused by the AFM tip and not the real resist edge. Line (2) in Fig. 2 indicates the real, about 80-90° steep edge of the resist stencil. The measured slope of the ramp etched into the HTS/STO bilayer is only about 6°. This angle is surprisingly small but consistent with the result of our simulation (see next section) which includes the higher etching rate for the resist as compared to the HTS/STO bilayer. During heating the sample to $T = 795$°C, required for the deposition of the barrier and the counter electrode, large outgrowths are formed by recrystallization of the redeposit. The size of the outgrowths is comparable to the film thickness. Such ramp surfaces are very rough, impeding the deposition of a smooth barrier and counter electrode.

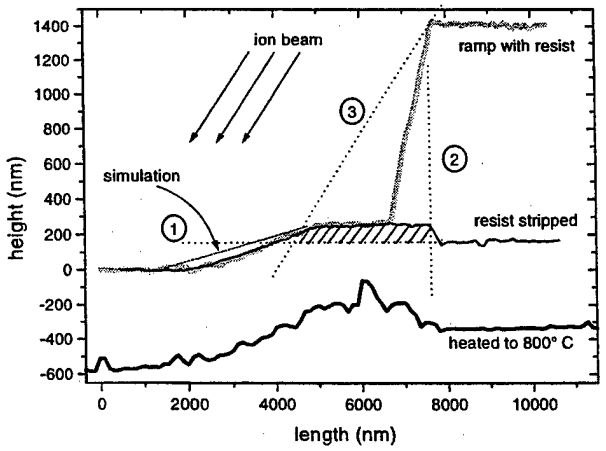

Fig. 2 AFM line scans showing the topography of a ramp etched at a fixed angle of 70°. The grey line shows the profile with the photoresist, the black line after stripping the resist. The hatched area indicates redeposited material piling up in the shade of the resist. The thin black line is the result of our simulation. Also shown is the AFM line scan obtained after heating up the sample, which is displaced for clarity.

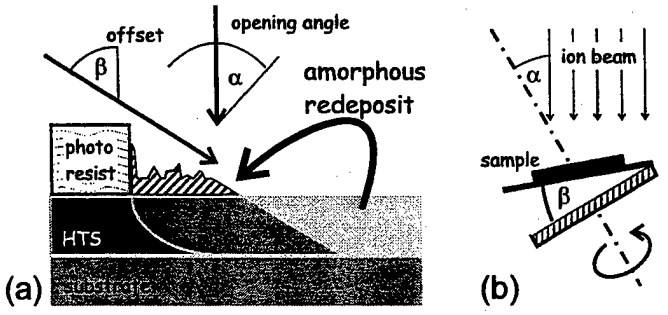

Fig. 3 (a) Schematic view of the etching process with the definition of the *opening angle* α and the *offset angle* β. (b) TA-IBE setup showing the relative orientation of the ion beam, the sample surface and the rotation axis of the sample holder.

To avoid the recrystallization of the amorphous redeposit layer the IBE process has to be modified to get rid of the redeposit. This is achieved in a TA-IBE process introduced in the following. A fixed offset angle of 70° and a zero opening angle were used for the sample shown in Fig. 2. Here, the freshly etched ramp is smooth and the slope well defined. However, at high temperatures the redeposit forms large outgrowths on the ramp surface, as shown in Fig. 2. In the case of a zero offset angle and a large opening angle a strongly rounded ramp surface is obtained with the disadvantage of an undefined slope of the ramp as indicated in Fig. 3 by the black profile. A suitable combination of the two angles allows for an almost linear ramp profile and vanishing redeposit.

D. *Simulation of the etching process*

To find the optimum values for the opening and offset angle, a simple model simulation was used. The two-dimensional model accounts for the selectivity of the ion beam etching, i.e. the larger etching rate of the resist, as well as the redeposition of sputtered material on all involved surfaces. In this simple model we do not account for the dependence of the etching rate on the angle of incidence. Of course, for a more detailed model this dependence can no longer be ignored.

In the simulation the angle of incidence of the ion beam varies periodically from the steepest angle $(\beta - \alpha)$ to the lowest angle $(\beta + \alpha)$. For each angle a certain layer thickness is removed in those regions exposed to the ion beam. Before the next angle is calculated, the simulation accounts for redeposition in the shaded area and the faster milling of the photo resist. Some crucial parameters for the model, such as the ratio of etching rates for photo resist and the different sample materials (e.g. ≈ 2 in the case of $YBa_2Cu_3O_{7-\delta}$) or the rate of redeposition, were obtained experimentally and implemented in the model.

The goal of the simulation was to obtain a constant ramp slope of about 25 - 30° and no redeposit. Evidently, large values for the offset angle lead to a large area of redeposition

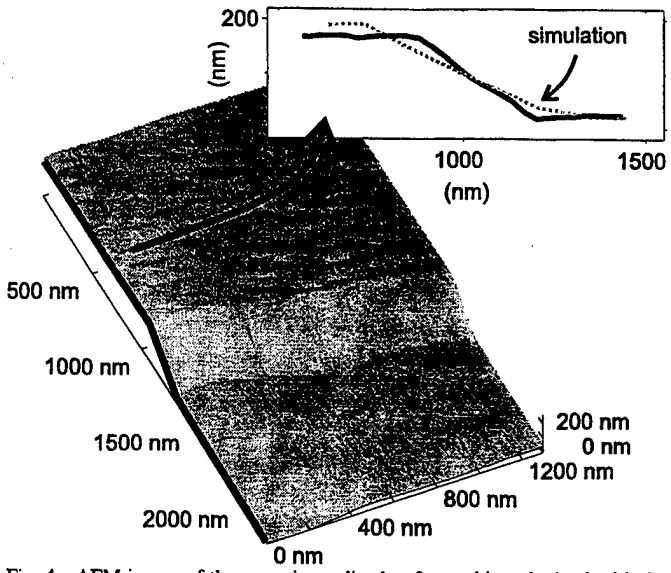

Fig. 4 AFM image of the ramp immediately after etching obtained with the optimum angles as determined from the simulation. The inset shows the line scans of the simulated and the measured ramp profile.

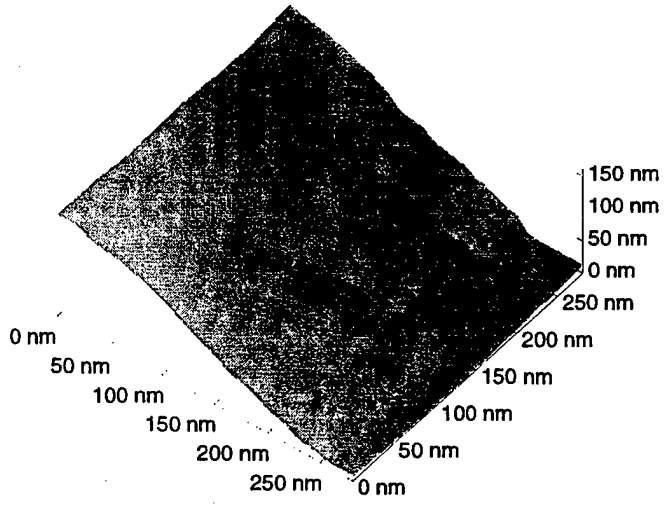

Fig. 5 AFM image of the ramp surface after the standard process treatment before barrier deposition. After the cleaning step the sample was heated up to the deposition temperature (795 °C) and then cooled in the sputter atmosphere to get the AFM image.

and low ramp slopes, whereas large values for the cone angle reduce the redeposit and yield steep and less straight ramps. From the simulation, we obtained best results for an offset angle of 11° and an opening angle of 10°. We note that this result is not intuitive showing the importance of the simulation of the etching process. An AFM image of an optimized ramp is shown in Fig. 4. Also shown is the comparison of the measured and the simulated ramp profile. The simulated ramp angle of about 20° slightly deviates from the measured ramp angle of 25°. This deviation most likely is due to the neglected dependence of the etching rate on the angle of incidence of the ion beam.

III. Improved Interface Morphology

We now compare results from fixed angle etching as shown in Fig. 2 to the results of the TA-IBE process with respect to the achievable surface roughness. It is evident from Fig. 5 that a smooth ramp surface can be obtained by the TA-IBE process. The rms surface roughness in this case is less than 3 nm. It can also be seen from Fig. 5 that small outgrowths due to residual amorphous material tend to form at the bottom of the ramp. Without these regions the rms surface roughness is even smaller (about 1 nm). The effect of the residual outgrowths on the barrier can be minimized by etching into the substrate and thus shifting the region with outgrowths at the bottom of the ramp below the interface of the completed junction.

High resolution Transmission Electron Microscopy (TEM) analysis was used for analyzing the epitaxy of the multilayers used for the ramp-type junctions. The *in-situ* grown interface in the bilayer of $YBa_2Cu_3O_{7-\delta}$ and $SrTiO_3$ is of high quality and relaxes within less than 4 nm. We also studied an *ex-situ* treated interface. Here, $SrTiO_3$ was exposed to air, photoresist, and acetone during the process. Before growing $YBa_2Cu_3O_{7-\delta}$ on top of it, we applied the above described oxygen ion beam cleaning process to the contaminated surface. TEM analysis revealed that the quality of the *in-situ* cleaned interface between $SrTiO_3$ and the top $YBa_2Cu_3O_{7-\delta}$ layer is almost the same as for the *in-situ* grown interface.

As a first test, junctions without an artificial barrier were made in order to determine the superconducting transport properties of the interfaces in junctions without any barrier. Test junctions showed flux flow behavior with no reduction of T_c and high J_c values. Typically, the junctions without artificial barrier have $J_c(77\,\mathrm{K}) \approx 5 \times 10^5\,\mathrm{A/cm^2}$.

IV. Conclusions

The ramp-type geometry for tunnel junctions offers the possibility to combine different perovskite type oxides along their *ab*-plane. We used standard photo resist masks and established an ion beam etching process with two angles (TA-IBE). The obtained ramps are straight, free of redeposit, and have a well defined angle of about $\approx 25°$. Prior to barrier deposition we expose the contaminated ramp surface to a low energy oxygen ion beam for cleaning purposes. We showed that such surfaces have a rms roughness of less than 3 nm after being heated to deposition temperature. The TEM analysis shows good epitaxial growth and high quality of the *c*-axis interfaces between both electrodes and the insulator. $YBa_2Cu_3O_{7-\delta}$ junctions without barrier show flux flow behavior with full T_c and high J_c values. Our process is promising for the fabrication of tunnel junctions with new artificial barrier materials such as manganites allowing the study of interactions between ferromagnetic and superconducting materials.

References

[1] B. H. Moeckly and K. Char, *Appl. Phys. Lett.* vol. 71, pp. 2526-2528, October 1997.

[2] D. H. A. Blank and H. Rogalla, *J. Mater. Res.* vol. 12, pp. 2952-2957, November 1997.

[3] D. H. A. Blank, G. J. M. Rijnders, R. M. H. Bergs, M. A. J. Verhoeven, and H. Rogalla, *IEEE Trans. Appl. Supercond.* , vol. 5, pp. 3323-3326, June 1997.

[4] C. Horstmann, P. Leinenbach, A. Engelhardt, R. Gerber, J. L. Jia, R. Dittmann, U. Memmert, U. Hartmann, and A. I. Braginski, *Physica C*, vol. 302, pp.176-182, 1998.

[5] C. L. Jia, M. I. Faley, U. Poppe, and K. Urban, *Appl. Phys. Lett.* , vol. 67, pp. 3635-3637, December 1995.

[6] L. Alff, U. Schoop, R. Gross, R. Gerber, and A. Beck, *Physica C*, vol. 271, 339-348, 1996.

[7] L. Alff, G. M. Fischer, R. Gross, F. Kober, A. Beck, K. D. Husemann, T. Nissel, F. Schmidl, and C. Burckhardt, *Physica C*, vol. 200. pp. 277-286, 1992.

Proposal of New PLD "Eclipse-Aurora Method" and its application to NiO/YBCO Josephson Junction Formation Suitable for Low-Noise SQUID

T. Kobayashi, M. Tachiki and C. Cai
Graduate School of Engineering Science, Osaka University
1-3 Machikaneyama-cho, Toyonaka, Osaka 560-8531, Japan

Abstract- We have proposed a new PLD method in which we can manipulate the plume activation, to very large extent, during particle transportation in the chamber under the magnetic field application. By placing a permanent magnet at the backside of the substrate holder, particles got sufficient ionization near the substrate. In the eclipse-aurora method, we obtained the deposition rate 2.6 times as high as that without applying magnetic field. Moreover, NiO layer grew epitaxially on both (100)MgO anf (001)YBCO surface even at the room temperature. Some characterization was done for NiO/YBCO step-edge junction thus made.

I. INTRODUCTION

NiO is an antiferromagnetic and insulator as long as no doping is done. From the microscopic view point, the magnetic interaction of antiferromagnetic NiO and vortex is of much interest. When we intentionally disperse Ni precipitation inside the NiO matrix, the magnetic interaction of Ni precipitation and vortex is interesting, too. Both are expected to enhance pinning force for vortex at the junction consisting of NiO/YBCO bi-layer.

The problem arising from NiO/YBCO structure is the inter-diffusion of constituent atoms at the heterointerface. This is due, particularly, to low energy of Ni-O bond. Because of this, Ni atoms are thought to easily dissociate and out-diffuse into YBCO layer during the film growth at the elevated temperatures. As a result, the superconducting properties of NiO/YBCO step-edge junctions significantly degraded, inspite of addition of NiO-layer. To overcome this kind of diffusion problem and bring out superior talent of NiO layer, the growth temperature of NiO should be lowered as low as possible.

In the present work, we propose a new PLD method named "Eclipse-Aurora PLD method". This method is characterized by application of the magnetic field between the target and substrate in the Eclipse PLD system, as shown in Fig.1. Owing

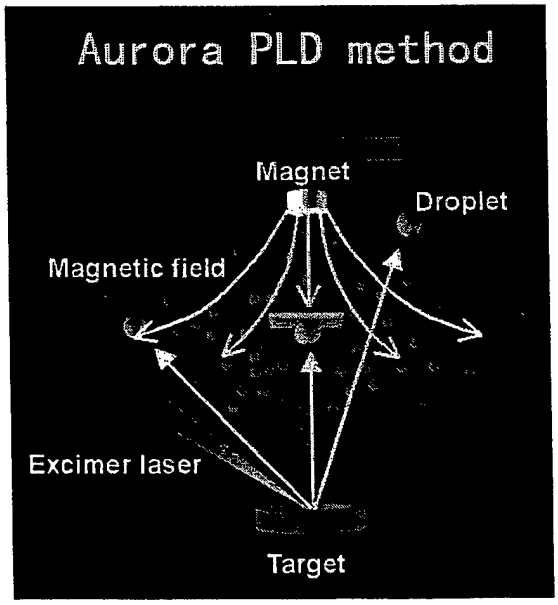

Fig.1 Schematic drawing of Eclipse-Aurora PLD.

to the magnetic field effect, extremely enhanced ionization of ablated particles near the substrate location was obtained. The deposition rate of NiO

film was increased 2.6 times as high as that without magnetic field (conventional eclipse PLD[1]).[2] Furthermore, NiO film was grown epitaxially on both (100)MgO and (001)YBCO surface at room temperature.

Some preliminally experiments were done on NiO/YBCO step-edge josephson junctions. The junction worked well at 77K, and noise spectrum was examined.

II. PROPERTIES OF ECLIPSE-AURORA PLD

Outstanging feature of the aurora PLD is its plume shape varying with time. In Fig.2, high-speed camera observation results of developing plume pattern are given. In this figure, we showed the conventional PLD results (without applying magnetic field) as a reference. In this experiment, the $SrTiO_3$ was ablated by the ArF-excimer laser in O_2 ambient of 0.01 Torr.

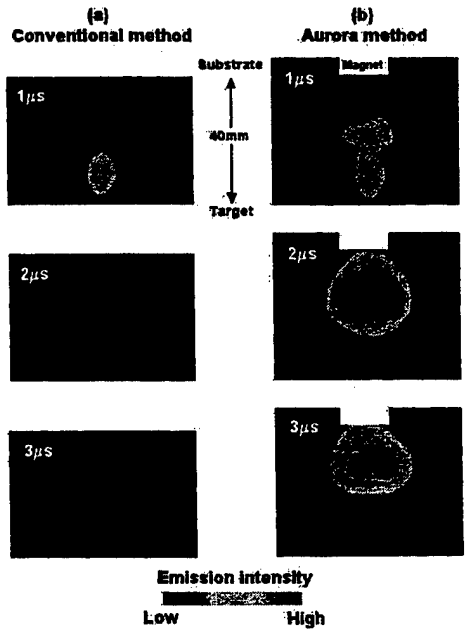

Fig.2. Plume patterns observed by the high speed camera. Permanent magnet was placed at the substrate position (Surface magnetic field about 5000 gauss).

As clearly seen in this figure, the plume is shining more and more when the plume is approaching to the substrate. Surprisingly, brightness of the plume is much better at the time of 2 μs than that of the initial one. According to the precise spectrum measurement, emission from Sr-ion at the substrate position is about 20 times stronger than that at the target position (Fig.3), and about 100 times brighter than that without magnetic field application at the substrate position.

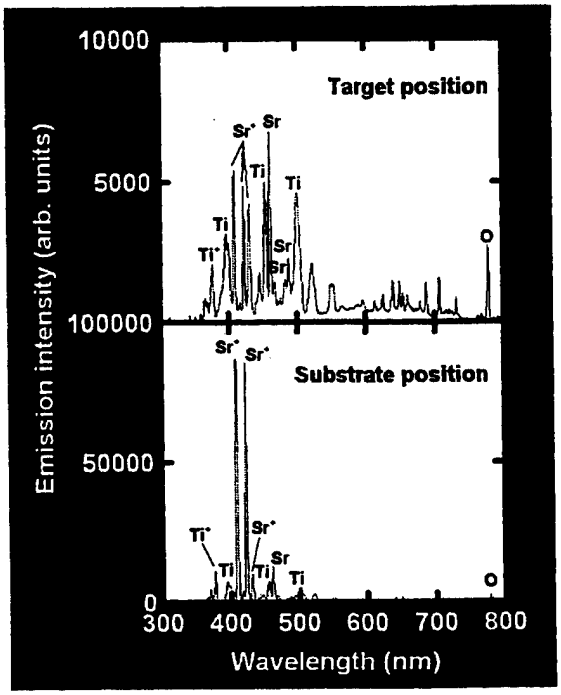

Fig.3. Spectra of plumes at the target and substrate positions in aurora PLD.

Enhanced emission of plume in the aurora PLD was coming from increased Sr-ion multiplied inside the magnetic field region. In addition to the above specrum measurement, we did camera observation using the interference-filters with the center wavelengths matched with Sr, Sr-ion and O-radical. This supplemental experiment also revealed selective increase of emission from Sr-ions. Increase in plasma density under magnetic field application can be well understood by an analogy of magnetron excitation of the plasma. However, the reason why only Sr+ is selectively multiplied still remained unsolved. More intensive studies are necessary.

An advantage of the aurora technique can be seen in Fig.4, where the RHEED patterns taken from NiO films grown on (100)MgO substrates by the eclipse-aurora PLD and conventional PLD at room temperature. Though there is no sign of lattice ordering for the conventional one, the RHEED pattern taken from the film grown by eclipse-aurora method clearly shows the epitaxial ordering. Room temperature growth of epitaxial NiO films was also obtained on (001)YBCO film surface by the eclipse-aurora method.

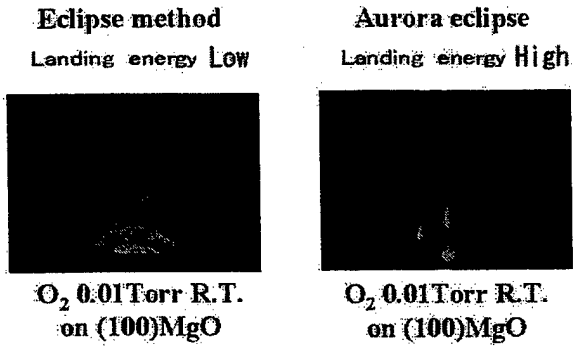

Fig.4. RHEED patterns of NiO films. (Right) Eclipse-Aurora PLD, (Left) conventional eclipse PLD.

Another characteristic feature of the eclipse-aurora method is the increased growth rate of NiO films. Namely, the growth rate increased 2.6 times higher than that of the conventional eclipse method.

III. JOSEPHSON JUNCTION PROPERTIES

A step-edge Josephson junction was prepared using NiO/YBCO bi-layer on (199)MgO substrate. The junction structure and current-voltage curve are shown in Fig.5. The junction width was about 10 μm. The test junction was mounted on TO-5 transistor header and four-terminal connection was made by Au wire-bonding. As seen in Fig.5, sufficient dc Josephson current was obtained at 77 K, and the junction worked at around 85 K without any obstacle.

Using the same junction, we measured the noise spectrum at 77 K. The results are plotted in Fig.6, showing clearly an appearance of 1/f noise property at low frequency range. Unfortunately, however, absolute noise power was not obtained yet.

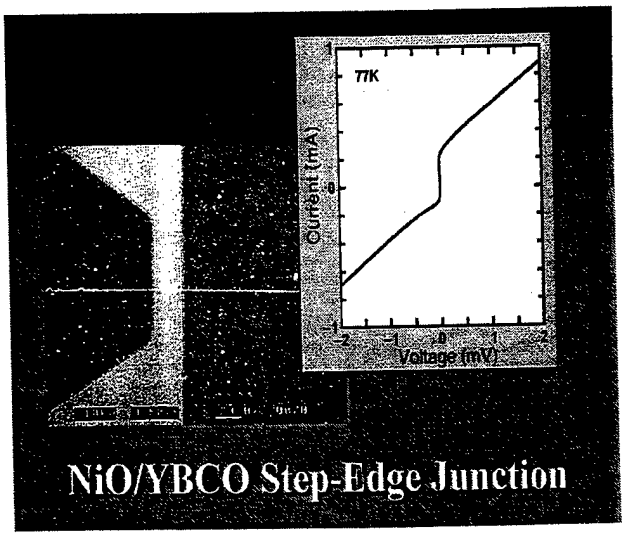

Fig.5. NiO/YBCO step-edge Josephson junction.

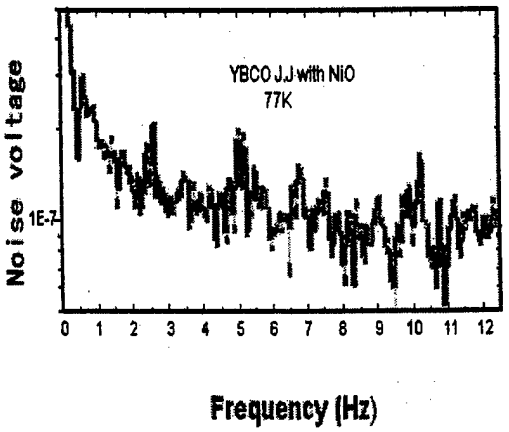

Fig.6. An example of noise spectrum of NiO/YBCO Josephson junction at 77K.

REFERENCES

1) M.Tachiki and T.Kobayashi: Jpn. J. Appl. Phys. Vol.38, No.6 (1999) (in press).
2) K.Kinoshita, H.Ishibashi and T.Kobayashi: Jpn. J. Appl. Phys. **33** (1994) L417.

PII5.12

Fabrication and Transport Properties of Asymmetric High-T_C *d*-wave $YBa_2Cu_3O_{7-y}$ Josephson Junctions

Hiroyuki Arie, Kyounei Yasuda, Hirokazu Kobayashi and Ienari Iguchi
Department of Applied Physics and CREST, Tokyo Institute of Technology, 2-12-1 Oh-okayama, Meguro-ku, Tokyo, 152-8551, Japan

Abstract—We report the measurements on the Josephson junctions with the different ab-plane orientation electrodes. We have fabricated ramp-edge type junctions having relatively tilted ab-plane electrodes using a CeO_2 seed layer on a MgO substrate. The junction characteristics were RSJ type, and the I_CR_N product was around 0.14mV. In the temperature dependence of I_C, the phenomenon characteristic of the d-wave superconductor was observed, indicating the possibility of the new type superconductive device when several of these junctions are connected in parallel.

I. Introduction

The symmetry of the wave function of Cooper pair of oxide high-T_C superconductor has been attracted considerable attention between many researchers. It is very important and interesting to clarify this in order to understand the high-T_C oxide superconductor. According to the conventional BCS theory, the superconductivity has been interpreted as forming Cooper pair between electrons by the attractive force due to mediating phonon and these Cooper pairs being condensed in one energy state. If the force which acts between electrons in the vicinity of Fermi surface is isotropic, it is called the isotropic superconductor, and in this case the gap has the s-wave symmetry.

On the other hand, the gap may have the anisotropic $d_{x^2-y^2}$-wave symmetry in the k space in case of the oxide high-T_C superconductors. By a series of experiments in recent years, it has been clarified that the pairing symmetry of the high-T_C oxide superconductor has an anisotropic d-wave symmetry[1]-[4]. In one of the experiments testing the symmetry, a method using the Josephson tunneling junction has been reported. Wollman et al. demonstrated the d-wave symmetry of high-T_C superconductors from the magnetic field dependence pattern of the maximum Josephson current which flows between Pb of the s-wave superconductor and $YBa_2Cu_3O_{7-y}$(YBCO)[1],[2]. And, Ishimaru et al. carried out the measurements on the Josephson current using asymmetric bicrystal junctions. They showed the evidence of the d-wave superconductor from the magnetic field dependence pattern of the maximum Josephson current[5].

Manuscript received April 28, 1999.

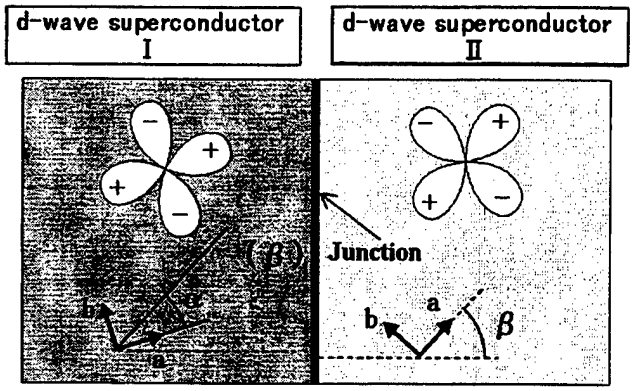

Fig.1. The definition of the angle α and β in the d-wave Josephson junction.

When the d-wave symmetry is considered, the phenomena in the high-T_C Josephson junction are different from the conventional s-wave superconductor. It would be strongly dependent on the angle which the crystal of superconductor and boundary interface makes. For example, the Josephson current is closely related to the crystal orientation angles α and β as shown in Fig. 1. Here, α is the relative angle of the crystal lattice, and β is the angle between the crystal orientation and the direction normal to the boundary interface. According to the theory by Sigrist and Rice, the maximum Josephson current depends on the angles α and β in the following way[6],[7].

$$I_C = A \cos 2(\alpha-\beta) \cos 2\beta \qquad (1)$$

This relational expression is well established, if the conductivity of the quasiparticles in the junction approaches zero[8]. In particular, this angle dependence will remarkably appear, when the junction resistance becomes larger. With this equation, it is shown that the maximum Josephson current value also differs, if α and β are different. In a parallel series of these junctions, the whole maximum Josephson current value takes zero or a finite value according as their combination. Hence, it is possible to develop a multiple input digital device with a new architecture.

However, there is almost no report that Josephson

current depends on shape and angle of the junction. Here, we present the fabrication of such junctions of which the in-plane orientation angle differ in two electrodes obtained by using a seed layer technieque, and the results on their transport properties.

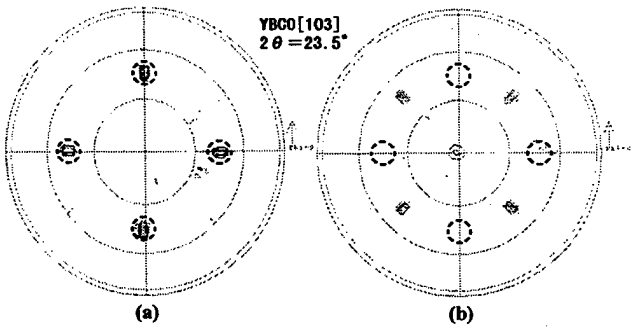

Fig. 2. XRD pole figure. (a) YBCO/MgO (b) YBCO/CeO_2/MgO (The YBCO[103] peak appears in the dotted line circle, when MgO and YBCO are cube on cube.)

II. Experiment

The thin films were grown using a PLD method. The fabricated junctions were ramp-edge type. The detailed fabrication processes of the samples are as follows. To begin with, a multilayer film CeO_2(200nm)/YBCO(200nm)/ CeO_2(20nm) was grown in-situ on a MgO(100) substrate. The bottom CeO_2 layer is the seed layer for rotating the in-plane orientation of YBCO crystal. Next, the process forming pattern was done by photolithography and Ar ion milling of 250eV beam voltage. In this process, an ion gun and a substrate were relatively leaned toward 45 degrees, and the ramp-edge structure was thus formed. The edge surface was cleaned by 150eV ion milling after photoresist was removed, then a bilayer film YBCO(200nm) /PBCO(10nm) was deposited in-situ, where, $PrBa_2Cu_3O_{7-y}$ (PBCO) served as a barrier layer. Thereafter, again by photolithography and Ar ion milling technique, the pattern

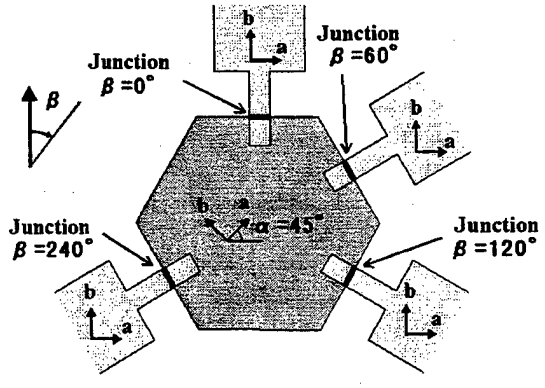

Fig. 3. The geometry of the fabricated junction with different β angles.

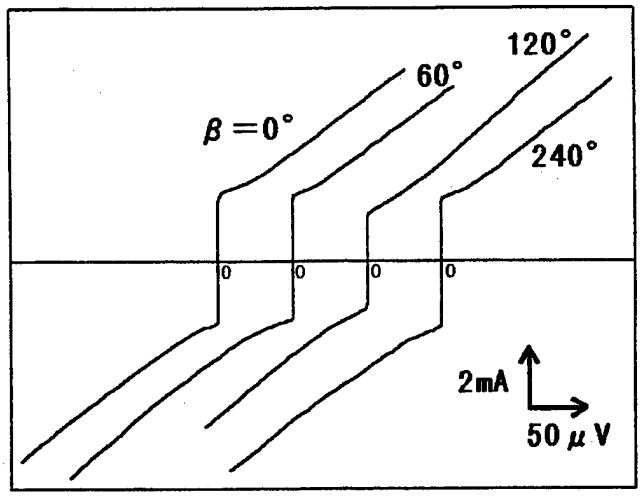

Fig. 4. Current-Voltage characteristics of the Josephson junctions given in Fig. 3 at 4.2K. (β=0°, 60°, 120° and 240°)

of the counter electrode was formed. The junction width was 20 μm.

For the two electrodes YBCO/MgO and YBCO/CeO_2 /MgO fabricated in this way, the in-plane orientation of two YBCO films relatively rotated 45 degree. In fact, it is clearly seen in the result of the XRD pole figure (Fig. 2). The measurements on the current-voltage characteristics and the magnetic field properties for the fabricated junctions were performed in liquid He.

III. Result and Discussions

For the fabricated samples, T_C of a YBCO thin film itself was 80 - 85K, and the critical current density J_C was 1×10^7A/cm^2 at 4.2K, irrespective of the existence of the CeO_2 seed layer. However, T_C of the junction after microfabrication was about 60K. The inhomogeneity of the junction barrier may be attributed to this. The typical observed *I-V* characteristics at 4.2K corresponding to the junction geometry in Fig. 3 are shown in Fig. 4. In this geometry, β differs in each junction and is given by 0°, 60°, 120°and 240°. The *I-V* characteristics exhibited RSJ type behavior, and I_C was 1.4 - 2.0mA, and the I_CR_N product was 0.12 - 0.14mV. The maximum Josephson current was modulated by an external magnetic field applied parallel to the substrate surface, and the observed period was about 250G, three to four times larger value as compared with the estimated period.

The difference in the Josephson characteristics for the junctions with different angle β was, however, not clearly observed. For β=0°, 60°, 120°and 240°, the normalized I_C value deduced from (1) is 0, 0.433, 0.433 and 0.433, respectively. For β=0°, we anticipate that there is no I_C. However, we find from Fig. 4 that I_C was 1.9mA, the same

order of magnitude of I_C as for the other angles. We explain this in the following. It is found that the junction resistance R_N was small and 0.1 Ω or less for all junctions. When the junction conductivity is significantly high, however, it is difficult to observe the effects of angles α and β[8],[9]. In this case, a finite value of I_C may be observed even at β=0 degree.

The temperature dependence of the maximum Josephson current is shown in Fig. 5, where β is 120° and 240°. Near T_C, it is found that I_C slowly changes. This is the general tendency common to high-T_C Josephson junctions. It is pointed out that I_C became saturated or decreasing near 10-20K, as bath temperature was reduced. Under the condition for satisfying (1), it has been theoretically shown that the temperature dependence of I_C is given by the dotted line of Fig. 5 [8],[9]. The experimental results in Fig. 5 suggest that they might have some tendency to this characteristics. In the present samples, the expected phenomenon did not appear clearly because the junction resistance was small. It is instructive to study this phenomenon in detail by fabricating the samples with larger junction resistance.

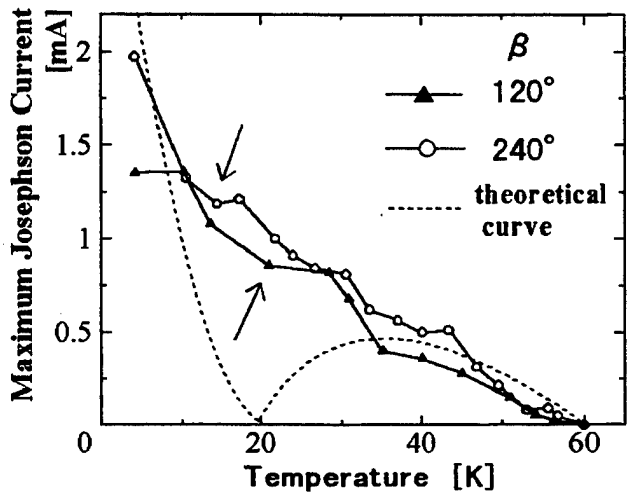

Fig. 5. Temperature dependence of the maximum Josephson current for the junctions with different β angles (β=120° and 240°). The dotted curve is the theoretical one calculated assuming the d-wave symmetry.

IV. CONCLUSION

We have reported the fabrication of the asymmetric Josephson junctions in which the in-plane orientation of two electrode crystals is different. It was confirmed that the in-plane orientation relatively rotated 45 degrees for the YBCO film on the CeO_2 seed layer and that on the substrate as judged from the XRD pole figure. The fabricated Josephson junctions exhibited RSJ type behavior. The junction resistance was, however, small and the I_CR_N product was 0.12 - 0.14mV. The observed temperature dependence of I_C indicates the possibility of the d-wave superconductivity.

ACKNOWLEDGMENT

We are very thankful to Prof. Y. Tanaka for helpful discussions and providing the theoretical calculation data.

REFERENCES

[1] D. A. Wollman, D. J. van Harlingen, J. Giapinntzakis and D. M. Ginsberg, "Evidence for $d_{x^2-y^2}$ pairing from the magnetic field modulation of $YBa_2Cu_3O_7$-Pb Josephson junctions," Phys. Rev. Lett. 74, 795 (1995).
[2] D. A. Wollman, D. J. van Harlingen, W. C. Lee, D. M. Ginsberg and A. J. Leggett, "Experimental determination of the superconducting pairing state in YBCO from the phase coherence of YBCO-Pb dc SQUIDs," Phys. Rev. Lett. 71, 2134 (1993).
[3] I. Iguchi and Z. Wen, "Experimental evidence for a d-wave pairing state in $YBa_2Cu_3O_{7-y}$ from a study of $YBa_2Cu_3O_{7-y}$/insulator/Pb Josephson tunnel junctions," Phys. Rev. B49, 12388 (1994).
[4] C. C. Tsuei and J. R. Kirtley, "Phase-sensitive tests of pairing symmetry in cuprate superconductors," Physica C 282-287, 4-11 (1997).
[5] Y. Ishimaru, T. Utagawa and Y. Enomoto, "Properties of Josephson junction using asymmetrical bicrystal substrate," Technical Report of IEICE SCE97-19, 13 (1997).
[6] M. Sigrist and T. M. Rice, "Paramagnetic effect in High T_C superconductors —A hint for d-wave superconductivity," J. Phys. Soc. Jpn. 61, 4283 (1992).
[7] P. Chaudhari and Shawn-Yu Lin, "Symmetry of the superconducting order parameter in $YBa_2Cu_3O_{7-\delta}$ epitaxial films, " Phys. Rev. Lett. 72, 1084 (1994).
[8] Y. Tanaka, "Theory of Josephson effects in anisotropic superconductors," Phys. Rev. B 56, 892 (1997).
[9] Y.Tanaka and S.Kashiwaya, "Theory of the josephson effect in d-wave superconductors," Phys. Rev. B 53, R11957 (1996).

Fabrication of C-Axis Oriented YBaCuO Trilayer Junctions

Hiroshi Akoh and Hiroshi Sato
Electrotechnical Laboratory, 1-1-4 Umezono, Tsukuba, Ibaraki 305-8568, Japan

Atsushi Kaneko and Kohji Hohkawa
Kanagawa Institute of Technology, 1030 Shimoogino, Atsugi, Kanagawa 243-0203, Japan

Abstract—We have fabricated *c*-axis oriented YBaCuO/PrBaCuO/YBaCuO trilayer junctions on an LSAT single crystal as a new substrate. The junctions showed RSJ-like current-voltage characteristics with hysteresis, and modulation of the critical current by the external magnetic field. The typical junction with a dimension of 4×4 μm² and a PrBaCuO barrier thickness of 20nm had a critical current I_c of 14μA, junction resistance R_n of 118Ω, and an I_cR_n product of 1.4mV. By changing the thickness of PrBaCuO barrier ranging from 10nm to 35nm, it is found that J_c is exponentially decreased as the barrier thickness is increased. The decay length value of J_c is estimated to be 5.3nm. This value is less than that of (103) oriented YBaCuO trilayer junctions, which may be due to the shorter coherence length of *c*-axis oriented junctions, compared to (103) oriented junctions.

I. Introduction

All high-T_c superconducting Josephson junctions have attracted extensive attention from electronic applications, since they can be operated at high temperatures and can be expected to have a high operating speed. One of the key elements in high-T_c superconducting integrated circuits is the Josephson junction with well reproducibility and controllability of the junction properties. Among the high-T_c Josephson junctions, trilayer [1]-[6] and ramp-edge [7]-[9] Josephson junctions are especially attractive for integrated circuits, because the junctions can be fabricated at any desired location and with device properties determined by the requirements of the application. Very recently, a small spread of the critical current I_c with 1σ=8% has been reported in the YBaCuO ramp-edge junctions which have the modified interface of YBaCuO film as a junction barrier [10].

For the trilyer junctions, we have already reported an improvement of parameter spread for (103) oriented YBaCuO trilayer junctions with PrBaCuO barriers [4]. The 1σ spread of critical current density J_c was obtained to be 34% for 88 trilayer junctions with various dimensions on the 15×15mm² substrate. In order to demonstrate integrated circuits using high-T_c trilayer junctions, the fabrication of insulating films is a key issue, since superconducting circuits require superconducting wiring layers and superconducting ground planes to achieve the required value of the various device parameters. We have attempted to demonstrate (103) oriented YBaCuO trilayer junctions with *c*-axis oriented YBaCuO wiring layers, using CeO_2 insulating films [11] with MgO buffer layer on (110) $SrTiO_3$ substrates [12]. However, there are some technological problems to be considered; such as the contact between (103) oriented junctions and *c*-axis oriented wiring, the control of suitable orientation of the insulating films, and so on. From the point of view of digital circuit, therefore, it is very important to realize *c*-axis oriented trilayer junctions at this moment.

In this paper, we report the fabrication process of *c*-axis oriented YBaCuO/PrBaCuO/YBaCuO trilayer junctions. We have introduced a $(LaAlO_3)_{0.3}(SrAl_{0.5}Ta_{0.5}O_3)_{0.7}$ single crystal (an LSAT single crystal) as a substrate of junctions, since LSAT has a good lattice matching to YBaCuO, no crystalline phase transition, and a relatively small dielectric constant of 20, which is suitable to the transmission of a high-speed signal. In addition, the basic properties of *c*-axis oriented junctions are discussed, comparing with those of (103) oriented junctions.

II. C-Axis Oriented Film on LSAT Substrate

First, we have characterized *c*-axis oriented YBaCuO films on LSAT substrates, since the quality of base-electrode films of trilayer junctions, such as the surface roughness, density of precipitated particles, crystalline properties, and superconductivity, affects strongly the junction properties.

YBaCuO films with *c*-axis orientation were fabricated on (100) LSAT substrates by using a reactive coevaporation

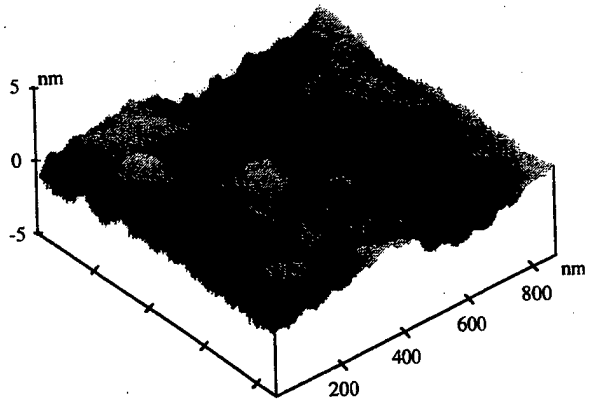

Fig. 1. AFM image of *c*-axis oriented YBaCuO film on LSAT substrate.

Manuscript received April 30, 1999.

method with pure ozone vapor. The deposition rates and compositions of YBaCuO films were precisely controlled by using computer-operated electron-beam guns. The composition ratio of films was set to be Y:Ba:Cu=1:1.8:2.5 to reduce the precipitated particles on the surface of films. In order to ensure the uniform substrate temperature, in addition, a backing plate consisting of Al(15μm)/Cu(50μm)/Al(15μm) stacked foils was inserted between the substrate and the sample holder. The substrate temperature was fixed at 710°C. The pure ozone vapor was supplied during the deposition with a typical pressure of 1×10^{-4} Pa.

Conventional θ-2θ X-ray measurement revealed that YBaCuO films on LSAT substrates showed the *c*-axis orientation. YBaCuO films on LSAT substrates had smooth surface with a very low density of precipitated particles from the observation of a scanning electron microscope. The observations of the surface morphology of the film were carried out by using an atomic force microscope (AFM). Figure 1 shows an AFM image of the film surface. It is found that there are no obvious screw dislocations to be observed on the films. The values of root-mean-square and peak-to-valley are estimated to be 1.4nm and 4.3nm, respectively. Note that the *c*-axis oriented films on LSAT substrate have the smoother surface by one order of magnitude than (103) oriented films on (110) $SrTiO_3$ substrates. The films had a T_c of above 85K, which was almost the same value of the films on $SrTiO_3$ substrates.

III. Fabrication Of C-axis Trilayer Junction

Figure 2 shows a schematic cross section of the fabricated trilayer junction. The details of our junction fabrication were almost the same as that of (103) oriented YBaCuO trilayer junctions, which has already been reported in the previous paper [4]. In brief, YBaCuO/PrBaCuO/YBaCuO trilayer films with *c*-axis orientations were *in-situ* fabricated on whole (100) LSAT substrates using the reactive co-evaporation method with pure ozone vapor. Thicknesses of YBaCuO base- and counter-electrodes were fixed at 150 and 75nm, respectively. The thickness of the PrBaCuO barrier was changed from 10nm to 35nm. After trilayer deposition, a protective layer of Au film (100nm) was deposited *in-situ* to prevent chemical reactions during the junction fabrication process. The formations of the junction base-electrode and the junction isolation were carried out by using a dry etching method with an electron-cyclotron-resonance plasma of Ar gas, in which film samples were cooled by liquid nitrogen to reduce etching damage [13]. A stacked film consisting of SiO (600nm) and MgO (20nm) was deposited as an insulation layer to isolate the junction edges from wiring layers. A film of Au (900nm) was deposited as a wiring layer. Finally, in order to prevent the degradation of junction properties due to moisture, junctions were covered by a negative photoresist.

A $15\times15mm^2$ substrate contains nine test chips of the junctions. Each chip has 45 trilayer junctions with various dimensions ranging from $2\times2\mu m^2$ to $50\times50\mu m^2$ and from $3\mu m\phi$ to $50\mu m\phi$.

IV. Properties Of C-axis Trilayer Junction

Figure 3 shows a typical *I–V* characteristic at 4.2K for a junction with a dimension of $4\times4\mu m^2$ and a barrier thickness of 20nm. The junction shows the RSJ (resistively shunted junction)–like characteristic, and also showed a Fraunhofer-like interference pattern as a function of the magnetic field. In order to characterize the junction properties more precisely, the Josephson critical current I_c is defined as the value of subtracting the excess current I_e observed by applying the magnetic field from the total critical current I_0. According to these definitions, the junction in Fig. 4 has I_0=25μA, I_c=14μA, and I_e=11μA. The I_cR_n product is estimated to be 1.4mV from the observed junction resistance R_n of 118Ω. The values of a critical current density J_c and normalized

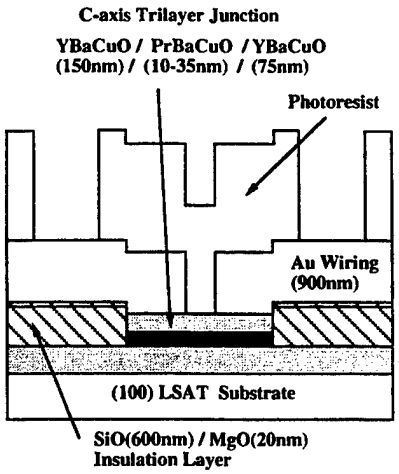

Fig. 2. Schematic configuration of *c*-axis oriented YBaCuO/PrBaCuO/YBaCuO trilayer junction.

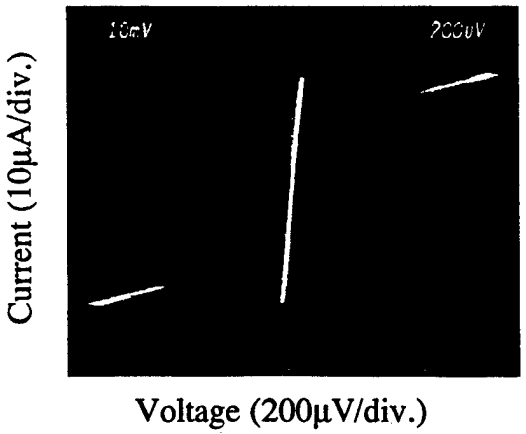

Fig. 3. *I–V* characteristic at 4.2K for *c*-axis oriented YBaCuO trilayer junction with a PrBaCuO barrier of 20nm.

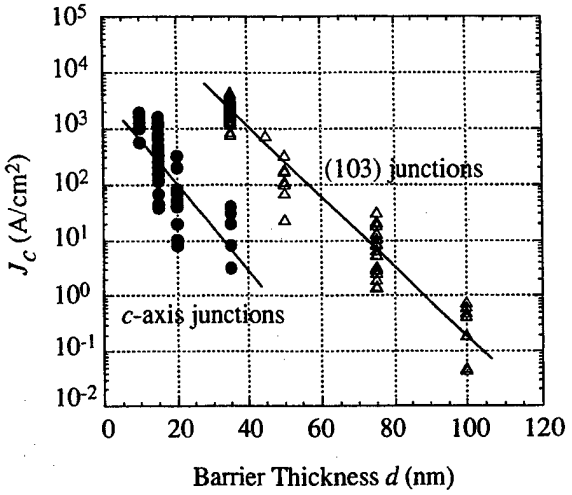

Fig.4. Barrier thickness d dependence of J_c for YBaCuO trilayer junction with PrBaCuO barrier.

junction resistance R_nA are estimated to be 72A/cm^2 and 1.9×10^{-5} Ωcm^2, respectively. The modulation ratio of the critical current, defined as I_c/I_0, is estimated to be 57%.

In order to study the basic properties of c-axis oriented junctions, we have changed the PrBaCuO barrier thickness d ranging from 10nm to 35nm. The junctions with d of 35nm and a junction area of $<5\times5\mu m^2$ had a very small I_c and sometimes showed no I_c to be observed. A rather large number of junctions with d of 10nm and a junction area of $>10\times10\mu m^2$, on the other hand, showed a flux-flow type I-V characteristics. Figure 4 shows the barrier thickness d dependence of J_c for c-axis oriented junctions at 4.2K. In this figure, the results [4], [14] of (103) oriented junctions (indicated by open triangles) are also plotted, in comparison to the behaviors of c-axis oriented junctions (indicated by closed circles). Though the results of c-axis oriented junctions have scatters to some extent at the present, there is a large different behavior between c-axis and (103) oriented junctions as can be seen in this figure. For instance, c-axis oriented junctions have above two order of magnitude smaller J_c than (103) oriented junctions with the same barrier thickness of 35nm. Note that R_nA of c-axis oriented junctions with d=35nm was by about two order of magnitude larger than that of (103) oriented junction with d=35nm. With decreasing the barrier thickness d, we observe an exponential increase of J_c for both c-axis and (103) oriented junctions. J_c can be fitted with an exponential relation of $J_c \propto \exp(-d/a)$, where a is defined as a decay length of the Cooper pair. While the (103) oriented junction has the estimated value of a=7nm, the c-axis oriented junction has a smaller value of a=5nm. These facts indicate that the properties of c-axis oriented junctions are more sensitive to the barrier thickness than those of (103) oriented junctions. It might be reflected by the shorter coherence length of c-axis oriented junction, compared to (103) oriented junction.

ACKNOWLEDGMENT

The authors would like to acknowledge helpful discussions with Dr. H. Nakagawa and Dr. M. They also would like to thank Dr. T. Sakamoto and Dr. H. Shimizu for continuous support and encouragement.

REFERENCES

[1] J. B. Barner, C. T. Rogers, A. Inam, R. Ramesh, and S. Bersey, "All a-axis oriented $YBa_2Cu_3O_{7-y}$-$PrBa_2Cu_3O_{7-z}$-$YBa_2Cu_3O_{7-y}$ Josephson devices operating at 80 K, " *Appl. Phys. Lett.*, vol. 59, pp. 742-744, August 1991.

[2] T. Hashimoto, M. Sagoi, Y. Mizutani, J. Yoshida, and K. Mizushima, "Josephson characteristics in a-axis oriented $YBa_2Cu_3O_{7-\delta}$/$PrBa_2Cu_3O_{7-\delta}$/$YBa_2Cu_3O_{7-\delta}$ junctions, " *Appl. Phys. Lett.*, vol. 60, pp. 1756-1758, April 1992.

[3] H. Sato, H. Akoh, and S. Takada, "Anisotropic Josephson effect in all (103)-oriented $YBa_2Cu_3O_{7-\delta}$/$PrBa_2Cu_3O_{7-\delta}$/$YBa_2Cu_3O_{7-\delta}$ junctions, " *Appl. Phys. Lett.*, vol. 64, pp. 1286-1288, March 1994.

[4] H. Sato, N. Nakamura, S. R. Gjøen, and H. Akoh, "Improvement in parameter spread of YBaCuO/PrBaCuO/YBaCuO trilayer junctions, " *Jpn. J. Appl. Phys.*, vol. 35, pp. L1411-1414, November 1996.

[5] R. Tsuchiya, M. Kawasaki, H. Kubota, J. Nishino, H. Sato, H. Akoh, and H. Koinuma, "$YBa_2Cu_3O_{7-\delta}$ trilayer junctions with nm-thick $PrGaO_3$ barrier, " *Appl. Phys. Lett.*, vol. 71, pp. 1570-1572, September 1997.

[6] M. Maruyama, K. Yoshida, M. Horibe, A. Fujimaki, and H. Hayakawa, "Improvement of the sandwich junction properties by planarization of YBCO films," *IEEE Trans. Appl. Supercon.*, 1999, in press.

[7] M.A.J. Verhoeven, G.J.Gerritsma, H. Rogalla, and A.A. Golubov, "Ramp-type junctions parameter control by Ga doping of $PrBa_2Cu_3O_{7-d}$." *Appl. Phys. Lett.*, vol. 69, pp. 848-850, August 1996.

[8] B.D. Hunt, M.G. Forrester, J. Talvacchio, R.M. Young, and J.D. McCambridge, "High-T_c SNS edge junctions with integrated $YBa_2Cu_3O_\delta$ groundplanes," *IEEE Trans. Appl. Supercon.*, vol. 7, pp. 2936-2939, June 1997.

[9] B.H. Moeckly and K. Char, "Properties of interface-engineered high-T_c Josephson junctions," *Appl. Phys. Lett*, vol. 71, pp. 2526-2528, October 1997.

[10] T. Satoh, M. Hidaka, and S. Tahara, "High-temperature superconducting edge-type Josephson junctions with modified interfaces, " *IEEE Trans. Appl. Supercon.*, 1999, in press.

[11] H. Sato, R. Miyakawa, N. Nakamura, S. R. Gjøen, H. Akoh, and S. Takada, "$YBa_2Cu_3O_x$ Crossover structures using CeO_2 film as insulating layer, " *Jpn. J. Appl. Phys.*, vol. 35, pp. L311-313, March 1996.

[12] H. Sato, H. Akoh, T. Onizawa, K. Hohkawa, A. Tomioka, and U. Kawabe, "Fabrication of YBaCuO wiring for YBaCuO trilayer junctions," *IEEE Trans. Appl. Supercon.*, 1999, in press.

[13] H. Sato, H. Akoh, K. Nishihara, M. Aoyagi, and S. Takada, "Liquid-Nitrogen-Cooled Dry Etching of YBaCuO thin films," *Jpn. J. Appl. Phys.*, vol. 31, pp. L1044-1046, August 1992.

[14] H. Akoh, H. Sato, M. Aoyagi, and S. Takada, "YBaCuO trilayer Josephson junctions," in *Extended Abstracts of 13th Symposium of Future Electron Devices*, Tokyo, Japan, pp. 130-134, October 1994.

Fabrication of $HgBa_2CaCu_2O_y$ Grain Boundary Junctions with Cation Exchange Method

Yang Yu, S.L.Yan, L.Fang, Y.Y.Xie, J.Z.Wu and Siyuan Han,
University of Kansas, Lawrence, KS 66045, USA

H.Shimakage and Zhen Wang,
Kansai Advanced Research Center, Communications Research Laboratory, 588-2 Iwaoka Kobe, 651-24 Japan.

Abstract—Grain boundary Josephson junctions have been fabricated using high quality epitaxial Hg-1212 HTS films grown on bicrystal $SrTiO_3$ substrates with a 24° misorientation angle. The films are prepared by the cation exchange method, with T_c between 120 K and 124 K. I-V characteristics of the junctions show typical RSJ behavior. Critical current density obtained from junctions with different widths is uniform over a few micrometer length scale and reproducible. The relatively high I_cR_n product at 77 K and 100 K and stability against thermal cycles show that the Hg-1212 junctions are promising for operations at temperatures higher than 77 K.

I. Introduction

Although operation of Josephson junctions at 77 K is considered adequate for a number of applications involving SQUIDs and microwave devices, higher temperature operation is highly desirable in case where liquid nitrogen cooling is difficult or inconvenient to implement. Since Hg-based superconductors have the highest critical temperature [1], [2] they are attractive candidates for developing Josephson junctions that can operate at temperatures above 100 K. However, due to high volatility and toxicity of Hg and Hg-based compounds, the synthesis of good Hg-based HTS films is extremely difficult. For example, the conventional process of making Hg-based HTS films involves two steps: a deposition of precursor films followed by annealing in a Hg vapor environment. Since the Hg vapor pressure cannot be precisely controlled the resulting films often have rather poor superconducting properties and reproducibility. This has seriously impeded progress on the effort to develop useful Hg-based HTS Josephson junctions. As a consequence, previous efforts of fabricating junctions and SQUIDs with Hg-based HTS films have produced less than satisfactory result [3]. Although the situation has improved recently as Tsukamoto et al. showed that good quality bicrystal grain boundary junctions (GBJ) and SQUIDs can be fabricated using $(HgRe)Ba_2CaCu_2O_y$ films [4] success in fabricating quality Hg-based HTS junctions is still sparse. In this work, we describe a new method of fabricating GBJs using single-phase eptaxial Hg-1212 thin films. Our data show that this process can produce junctions with nearly ideal RSJ I-V characteristics and quite uniform and reproducible critical current density. In addition, the property of the junctions is stable after many thermal cycles.

Manuscript received May 17, 1999.
This work is supported in part by NSF, AFOSR and the State of Kansas.

II. Junction Fabrication

The grain boundary junctions are fabricated with Hg-1212 films prepared on bicrystal $SrTiO_3$ substrates with 24-degree misorientation angle using the recently developed cation exchange method described in detail elsewhere [5], [6]. The 200-nm Tl-1212 films were prepared by dc-magnetron sputtering and post annealing process on 10 mm × 5 mm × 0.5 mm bicrystal substrates. The Tl-1212 thin films were superconducting with T_c about 90 K. X-ray diffraction (XRD) θ-2θ scans, Φ scans, and rocking curves proved that the Tl-1212 films were strongly textured with the c-axis perpendicular to the substrate surface and epitaxially grown on the $SrTiO_3$ substrate. The Tl-1212 films were then sealed in vacuumed quartz tubes together with Hg-Ba-Ca-Cu-O/Ba-Ca-Cu-O pellets. The sealed tubes were annealed in a furnace at temperature of 750°C for 3 hours. The Hg-1212 films were then annealed in flowing oxygen at about 300°C for 1 hour to improve the superconductivity. The as made films are epitaxial and their superconducting properties such as T_c and J_c are reproducible. The superconducting transition temperature of the Hg-1212 films was in the range of 120-124 K. The zero field critical current J_c is in the range of 3-5×10^6 A/cm^2 at 77 K. The critical current decreased by only about a factor of two at 100 K and was 7.8×10^5 A/cm^2 at 110 K. Therefore, Hg-1212 film made by the cation exchange process is promising for fabricating junctions operating at 100 K.

The micro-bridges were patterned across the grain boundaries using standard photolithography techniques and ion beam etching. The micro-bridges were 2.5-4 μm wide to minimize flux trapping [7]. All junctions had contact pads arranged in a four-probe configuration. The pads were metallized with evaporated silver in order to minimize contact resistance. For ac Josephson effect measurements, an open-end coaxial antenna was placed about 1 cm from the junctions.

III. Characteristics of Junction

Five bicrystal grain boundary junctions were fabricated in two separate runs and have been tested extensively to determine various properties. The dc current-voltage characteristics (IVC) of the junctions were measured using battery operated current source and preamplifiers to minimize the effects of noise. Between 4.2 K and 110 K all junctions exhibited non- hysteretic resistively shunted junction (RSJ)

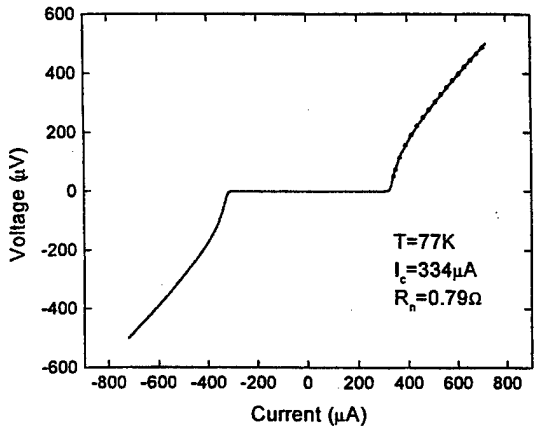

Fig. 1. Current-voltage characteristic of a junction at 77 K. The dot line is fitted by RSJ mode.

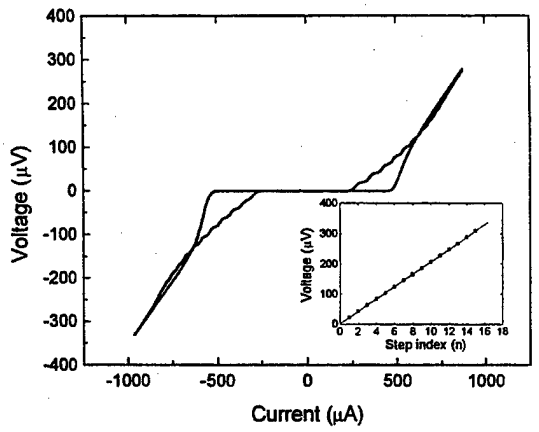

Fig.3. I-V curve of a Hg-1212 GBJ with 9.96 GHz microwave radiation at 77 K. The I-V curve without microwave radiation is presented for comparison. The inset is the voltage of Shapiro steps vs. the step index.

type IVC. Fig. 1 shows the IVC of a 2.5 μm wide junction measured at 77 K and the corresponding fit to the zero capacitance RSJ model. The good agreement between the measured and calculated IVC indicates that there are very few barrier defects which often leads to noticeable excess current and thus non-RSJ characteristics. The stability of the junctions has been tested by subjecting them to many thermal cycles between the room and cryogenic temperatures. The characteristics of junctions stayed virtually unchanged.

Since for most applications a uniform J_c is desirable for reliable device performance and ease of circuit design we also investigated the critical current as a function of junction width. Using the measured junction widths and critical currents and the nominal film thickness of 200 nm an average critical current density of 66 kA/cm^2 is obtained. The linear dependence of the critical current on junction width shown in Fig. 2 indicates that the superconducting properties of the Hg-1212 HTS electrodes and the thin interfacial layer between the grains are uniform when averaged over a scale of several micrometers. We emphasize that this result is preliminary and

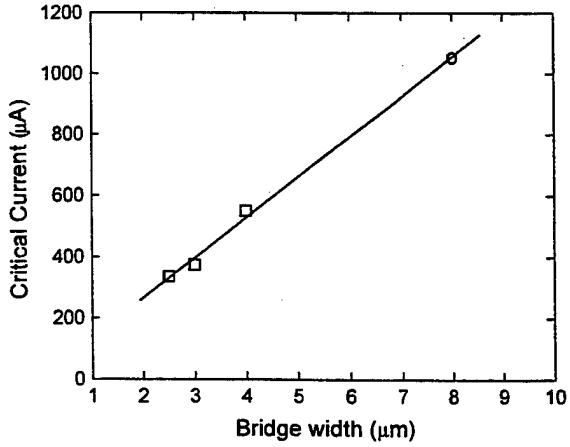

Fig.2. The critical current of five junctions vs. the junction width. The circle is the I_c of two 4-μm wide junctions in parallel.

further study is required to confirm our initial finding. However, as a magnetic field perpendicular to the plane of the film was applied to the junctions irregular field-dependent critical currents, similar to that reported in [4], was observed. The critical currents usually decreased from their maximum value at zero field to their minimum value, which is about 25% of $I_c(0)$, at fields between 1 to 2 mT (depends on the junction width). Efforts were made to eliminate flux trapping but have shown no significant effect on the observed $I_c(B)$. The lack of regular Fraunhofer pattern indicates that the critical current density is quite non-uniform within each junction, which could be the consequence of a high density of localized states in the barrier [8]. Further study is obviously needed to clarify the issue.

One of the important figure of merits of a Josephson junction is the I_cR_n product which determines the performance of the junction for high frequency applications. In general, junctions with larger value of I_cR_n can operate at higher frequencies. At 77 K, all junctions we tested have I_cR_n values greater than 0.20 mV. The largest I_cR_n product is 0.45 mV at 77 K which compares favorably to the best previously published result [4]. Therefore, Hg-1212 grain boundary junctions are attractive candidates for applications at temperatures above 77 K.

The ac Josephson effect was clearly demonstrated by applying a 9.96 GHz microwave to the junctions which produced Shapiro steps in the I-V curves. Fig. 3 shows the voltages at the middle of each step V_n vs. the step index n at 77 K. The steps were rounded due to strong thermal fluctuations. By varying microwave power as many as 15 steps had been observed at 77 K. The observed linear relationship between V_n and n and the slope of the line confirm that these GBJs are genuine Josephson junctions.

IV. SUMMARY

In summary, Hg-1212 grain boundary Josephson junctions were made on bicrystal STO substrates with 24-degree misorientation angle. The 200 nm Hg-1212 thin films were

grown using a novel cation exchange process which produced high quality films with stable and reproducible properties. The current-voltage characteristics of the junctions show typical RSJ behavior with little excess current. The critical current density of the junctions is reproducible. The linear relationship between the critical current and width of junctions indicates that the electronic properties of the films and interfacial barrier layers were uniform over a scale of few microns but the irregular field-dependent critical current implies highly non-uniform barrier on a much smaller length scale. Despite the rather constant critical current density among all junctions tested the I_cR_n product of the junctions had a much larger range with the highest value of 0.45 mV at 77 K. Work is in progress to investigate and to understand the relation between J_c and I_cR_n product. In addition, clear ac Josephson effect was observed. Our work also shows that the Hg-1212 junctions made from films grown by the cation exchange method are stable after many thermal cycles. These results indicate that the Hg-based superconductors are promising for use in the development of Josephson junction based devices and circuits operating at 77 K and above.

REFERENCE

[1] A. Schiling, M. Cantoni, J. D. Guo, and H. R. Ott, "Superconductivity above 130 K in the Hg-Ba-Ca-Cu-O system," *Nature*, vol. 363, pp. 56-59, 1993.

[2] A. Fukuoka, A. Tokiwa-Yamamoto, M. Itoh, R. Usami, S. Adachi, and K Tanabe, "Dependence of T_c and transport properties on the Cu valence in $HgBa_2Ca_{n-1}Cu_nO_{2(n+1)+\delta}$ (n = 2,3) superconductors," *Phys. Rev. B*, vol. 55, pp. 6612-6620, 1997.

[3] A. Gupta, J. Z. Sun, and C. C. Tsuei, "Mercury-based cuprate high-transition temperature grain-boundary junctions and SQUIDs operating above 110 Kelvin," *Science*, vol. 265, pp. 1075-1077, 1994.

[4] A. Tsukamoto, K. Takagi, Y. Moriwaki, T. Sugano, S. Adachi, and K. Tanabe, "High-performance $(Hg,Re)Ba_2CaCu_2O_y$ grain-boundary Josephson junctions and dc superconducting quantum interference devices," *Appl. Phys. Lett.*, vol. 73, pp. 990-992, 1998.

[5] S. L. Yang, Y. Y. Xie, J.. Z. Wu, T. Aytug, A. A. Gapud, B. W. Kang, L. Fang, M. He, S. C. Tidrow, K. W. Kirchner, J. R. Liu and W. K Chu, "High critical current density in epitaxial $HgBa_2CaCu_2O_x$ thin films," *Appl. Phys. Lett.*, vol. 73, pp. 2989-2991, 1998.

[6] J. Z. Wu, S. L. Yan, Y. Y. Xie, "Cation exchange: A scheme for synthesis of mercury-based high-temperature superconducting epitaxial thin films," *Appl. Phys. Lett.*, vol. 74, pp. 1469-1471, 1999.

[7] E. Dantsker, S. Tanaka, P. A. Nilsson, R. Kleiner, and John Clarke, "Low excess flux noise in $YBa_2Cu_3O_{7-x}$ dc SQUIDs cooled in static magnetic fields," *IEEE Trans. Appl. Supercon.*, vol. 7, pp. 2772-2775, 1997.

[8] O. M. Froehlich, F. Richter, A. Beck, D. Koelle, and R. Gross, "Barrier Properties of Grain Boundary Junctions in High-T_c Superconductors," *IEEE Trans. Appl. Supercon.*, vol. 7, pp. 3189-3192, 1997.

In-situ Monitoring of the Growth of Oxide Thin Films at High Oxygen Pressure

J. Klein, C. Höfener, L. Alff†, and R. Gross
II. Physikalisches Institut, Universität zu Köln, Zülpicher Str. 77, D-50937 Köln, Germany

Abstract—Pulsed Laser Deposition (PLD) is a well established deposition technique for oxide thin films and heterostructures. The knowledge and control of the growth processes of oxide materials is important for the fabrication of high quality epitaxial and heteroepitaxial thin film structures. Due to the high oxygen pressure during the growth process standard reflection high energy electron diffraction (RHEED) analysis is not possible. To overcome this problem we have used a two stage differential pumping system [1]. In this way, the electron path in the high pressure oxygen atmosphere within the deposition chamber has been reduced considerably. The specular beam intensity of the RHEED system was sufficiently high to allow the observation of intensity oscillations during the growth of oxide materials such as $SrTiO_3$ and $La_{2/3}Ca_{1/3}MnO_3$. In addition to the RHEED investigation the surface morphology of the deposited films has been characterized *in-situ* by ultra high vacuum atomic force microscopy (UHV-AFM).

I. Introduction

Epitaxial thin films and heterostructures of complex oxide materials are required for a large number of devices showing interesting properties both with respect to applications and basic physics. Typical examples are Josephson junctions made from cuprate high-temperature superconductors [2] or magnetic tunnel junctions based on doped manganites [3, 4]. In order to control the epitaxial growth, the interface properties, and the layer thickness in heterostructures RHEED represents a powerful tool. In the thin film growth of metallic or semiconducting materials under UHV conditions RHEED is a well established method (for an overview see [5, 6]). However, the high oxygen pressure (a few 100 mTorr) used during the growth of oxide materials prevents the use of standard RHEED systems due to the small mean free path of the beam electrons. One way to overcome this problem is the reduction of oxygen pressure during film deposition. In order to achieve a similar oxidation potential atomic oxygen or ozone instead of molecular oxygen has to be used [7]. The molecular oxygen pressure also can be reduced to below 1 Pa in a standard PLD process [8]. However, these modified fabrication processes have the common problem that the oxygen partial pressure is far from the typically used optimum values. Moreover, in a typical PLD process the shape of the laser plume is strongly changed by the reduced oxygen pressure what significantly affects the epitaxial growth process. Therefore, in our setup we use a two stage differential pumping system similar to that proposed by Rijnders *et al.* [1]. In this article we show how the modified RHEED system can be used for the *in-situ* control of the growth process of the colossal magnetoresistance (CMR) materials $La_{1/3}D_{2/3}MnO_3$ with D = Ca and Ba.

Manuscript received April 30, 1999.
†e-mail: alff@ph2.uni-koeln.de.
This work is supported by the Deutsche Forschungsgemeinschaft.

II. Experimental Setup

A schematic view of our high-pressure RHEED system is shown in Fig. 1. In the deposition chamber the oxygen pressure can be as large as 0.3 mbar. A double differential pumping system decreases the pressure between the two coaxial tubes to below 10^{-3} mbar and at the filament of the RHEED gun and inside the inner tube to below 10^{-5} mbar. Along their path from the filament to the substrate the beam electrons have to

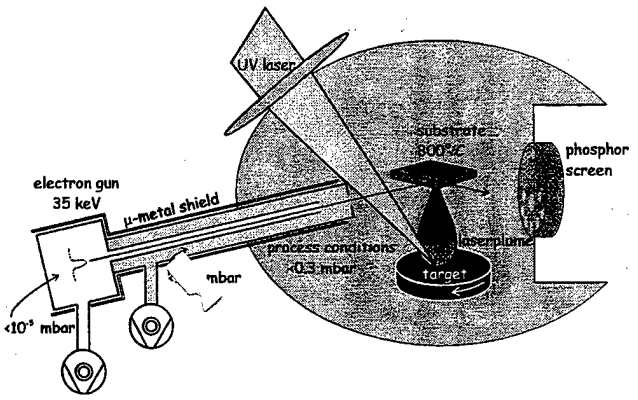

Fig. 1 Schematic view of the high-pressure RHEED system.

pass two apertures at the front end of the tubes with a diameter of 500 μm. Stray magnetic fields result in a deflection of the electron beam making it difficult to pass the beam through the apertures. Therefore, a proper magnetic shielding is crucial in our setup.

In the high vacuum regime (pressure $p < 10^{-5}$ mbar) between the RHEED filament and the first aperture the scattering probability for the beam electrons is vanishingly small. However, in the high pressure regime inside the deposition chamber, the small mean free path of the beam electrons results in a decrease of the specular beam intensity. The mean free path ℓ of the electrons is given by

$$\ell = \frac{1}{\sigma_{O_2} n} = \frac{k_B T}{\sigma_{O_2} p}.$$

Here, n is the oxygen molecular number density and ℓ depends on p and the energy dependent scattering cross section σ_{O_2} of oxygen. With $p = 0.1$ mbar and $\sigma_{O_2} \approx 10^{-20}\,\mathrm{m}^2$ the mean free path is estimated to about 5 cm. In our setup the actual path length of the beam electrons in the high pressure regime is about 20 cm. A further reduction of the path length was not required in order to have still enough reflected intensity to be able to monitor RHEED oscillations.

III. Growth Oscillations for Oxide Films

The oxide thin films ($La_{2/3}Ba_{1/3}MnO_3$, $La_{2/3}Ca_{1/3}MnO_3$) were fabricated on $SrTiO_3$ substrates using PLD. The substrate

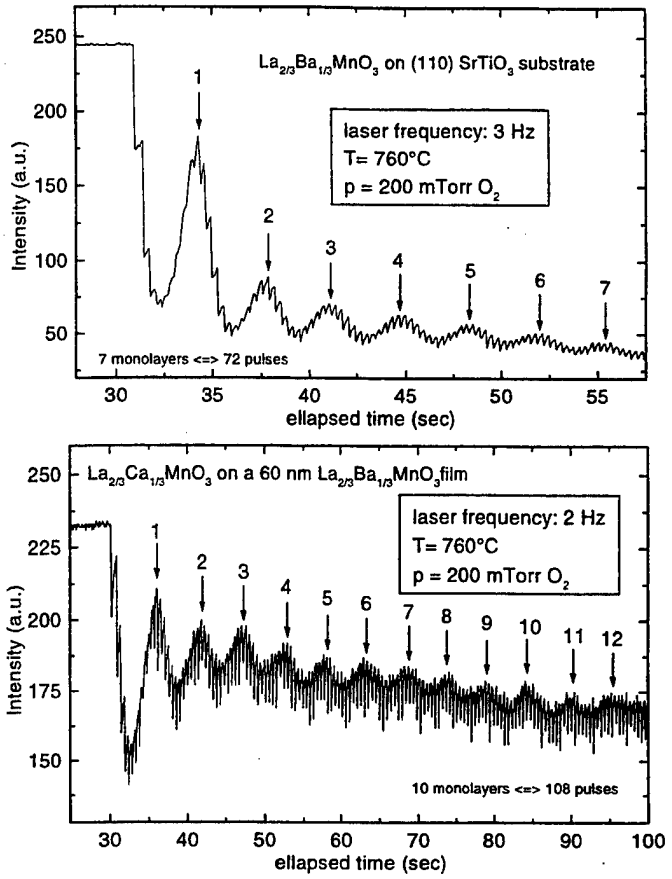

Fig. 2 RHEED oscillations observed during the growth of $La_{2/3}Ba_{1/3}MnO_3$ on $SrTiO_3$ (top) and $La_{2/3}Ca_{1/3}MnO_3$ on a 60 nm thick epitaxial $La_{2/3}Ba_{1/3}MnO_3$ film (bottom).

temperature was 760°C and the films were deposited at an oxygen pressure of 200 mTorr using a 248 nm KrF-eximer laser with a pulse energy of 450 mJ. During the growth of the films the intensity of the specular beam was monitored. Oscillations in the intensity have been clearly observed. Each intensity oscillation corresponds to the growth of a single monolayer [9–11]. Fig. 2 (top) shows the RHEED intensity oscillations during the growth of a $La_{2/3}Ba_{1/3}MnO_3$ film on $SrTiO_3$. The angle of incidence and the energy of the electron beam was 2° and 15 kV, respectively. Seven maxima with decreasing intensity as indicated by the arrows can be seen corresponding to the deposition of seven monolayers of $La_{2/3}Ba_{1/3}MnO_3$. Note that the spikes superimposed on the RHEED oscillations are caused by the laser pulses. About 10 pulses are required for a single monolayer. The occurrence of RHEED oscillations during the layer by layer growth of a thin film is intuitively understandable: During the growth of a single monolayer the surface morphology changes from smooth over rough to smooth. For a completed layer the surface is smooth because of the absence of steps, thus, the specular beam intensity will be maximum. After the deposition of half a monolayer the number density of surface steps will be maximum enhancing diffuse scattering at the step edges. As a result the intensity becomes minimum. We note, however, that in spite of the comprehensibility of the step density model a more detailed description of RHEED oscillations and even the applicability of the step density model itself is still under discussion [12, 13].

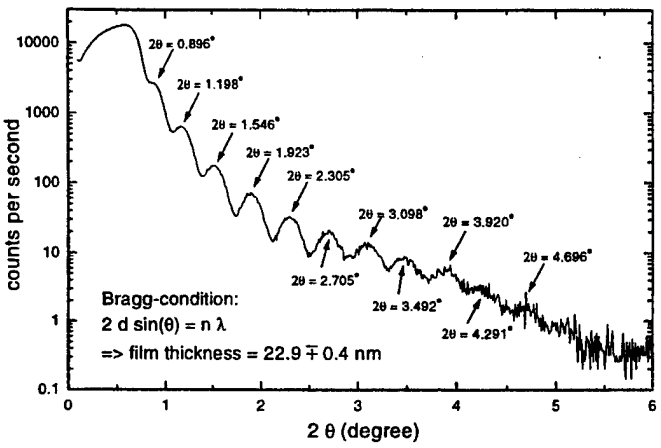

Fig. 3 X-ray diffraction pattern of a 23 nm thick LBMO film obtained at grazing incidence.

A. *Film and Surface Characterization*

Counting the number of RHEED oscillations during growth immediately allows the determination of the film thickness d. For example, for a $La_{2/3}Ba_{1/3}MnO_3$ film grown on $SrTiO_3$ using 600 laser pulses according to the number of RHEED oscillations we expect $d = 22.7$ nm. Another precise measurement method for the film thickness is X-ray diffraction at grazing angles of incidence. In Fig. 3 a typical result is shown. Here, by using the Bragg condition we determine the film thickness to be 22.9 ± 0.4 nm. This is in good agreement with the result of the RHEED analysis. We also note that the observation of a large number of reflected X-ray intensity maxima and the weak decay with increasing angle of incidence give clear evidence for a well defined interface between substrate and film as well as a very low roughness of the film [14].

A well established technique for measuring the surface roughness is AFM. In our deposition system, the sample can *in-situ* be transferred to an UHV-AFM system. This allows the investigation of interface morphology in heterostructures by interrupting the film growth between two subsequent layers for AFM analysis. In Fig. 4 the surface topology of a 20 nm thick heterostructure of 4 manganite layers is shown. The root

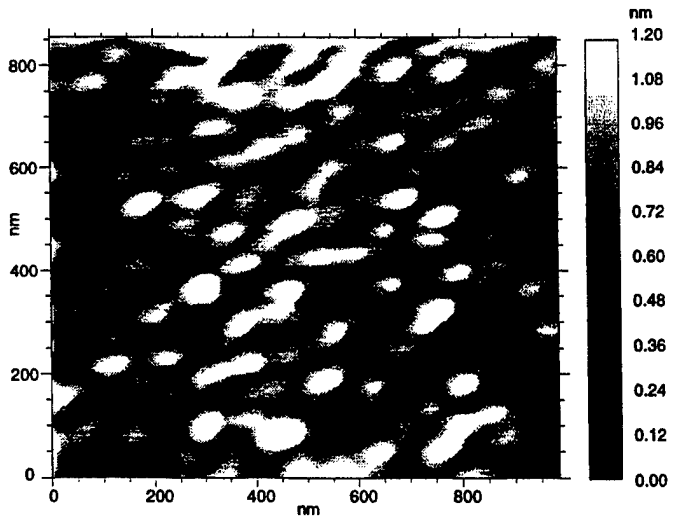

Fig. 4 AFM image showing the surface topology of a 20 nm thick LCMO/LBMO/LCMO/LBMO heterostructure.

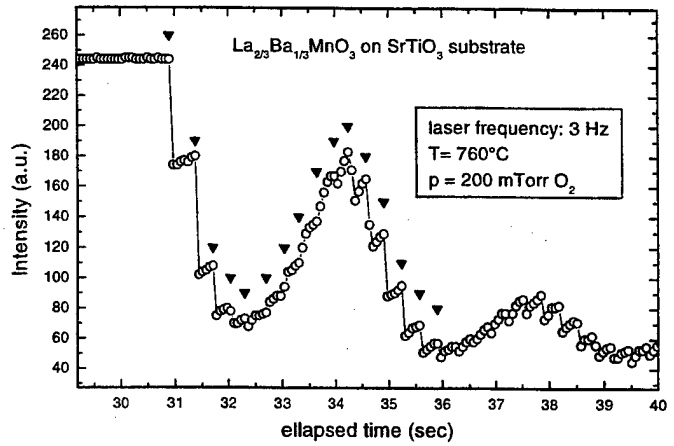

Fig. 5 Detailed view of the specular beam intensity during the first RHEED oscillation for the growth of LBMO on STO. The triangles mark the instant of the laser pulse.

mean square roughness of the surface is about 0.4 nm confirming the results of the RHEED and X-ray analysis. Note that the grazing incidence x-ray analysis and the AFM study give complementary information. Whereas AFM gives spatially resolved information on a small, freely selectable part of the surface (typically 1 μm^2), the X-ray analysis provides a spatially averaged value of a several 100 μm^2 large area. We believe that for the further development of oxide thin film processing the *in-situ* combination of these methods is highly desirable.

B. RHEED Study of Manganite Heterostructures

For the fabrication of multilayer devices the control of interfaces between subsequently grown layers of different materials is crucial. For example, in tunnel junctions using the CMR materials (e.g. $La_{2/3}Ca_{1/3}MnO_3$-$SrTiO_3$-$La_{2/3}Ca_{1/3}MnO_3$ junctions) the growth properties and precise thickness of the insulator, as well as the interfaces between the different layers have to be known and optimized. In Fig. 2 (bottom) the RHEED oscillations observed for the growth of $La_{2/3}Ca_{1/3}MnO_3$ on a 60 nm thick $La_{2/3}Ba_{1/3}MnO_3$ film are shown. In order to be able to measure a clear RHEED intensity modulation, the surface of the completed $La_{2/3}Ba_{1/3}MnO_3$ structure was annealed for about 20 min in the deposition system allowing the material to form a smooth surface layer. Also, the beam intensity was increased by a factor of three compared to the top figure. Twelve oscillations corresponding to the deposition of 12 monolayers can be clearly distinguished in Fig. 2. The completed film structure also was studied by X-ray diffraction. The $\theta - 2\theta$-scan showed only (00l) peaks and the FWHM of the rocking curve of the $La_{2/3}Ca_{1/3}MnO_3$ (002) peak was 0.018°. Note that the mosaic spread of the film in this case already is limited by the quality of the $SrTiO_3$ substrate [15]. Due to the almost perfect lattice match between $La_{2/3}Ba_{1/3}MnO_3$ and $SrTiO_3$ the $La_{2/3}Ba_{1/3}MnO_3$ peaks are completely superimposed by the substrate peaks. However, it is evident that the $La_{2/3}Ba_{1/3}MnO_3$ layer serving as the substrate for the subsequent $La_{2/3}Ca_{1/3}MnO_3$ layer is expected to have a similarly small mosaic spread.

C. Detailed Study of the Film Growth

In this subsection we show how the RHEED analysis can be used to reveal more detailed information on the growth process. As an example we choose the growth of the first monolayer of a $La_{2/3}Ba_{1/3}MnO_3$ film on $SrTiO_3$ as shown in Fig. 5. We first consider the behavior of the intensity measured between the start of the deposition process and the first minimum. Evidently, after each laser pulse the intensity sharply drops due to the amount of material deposited on the surface leading to diffuse scattering. Then, the material starts to rearrange on the surface forming mostly two-dimensional islands. This causes a reduction of the number of steps, and, thus, an increase of the RHEED intensity until the next laser pulse. Now, we consider the intensity measured between the first minimum and the following maximum. Here, immediately after the laser pulse the intensity increases without any initial drop. Within the step edge model, this indicates that the deposited material moves right into the holes between growth islands in the half completed monolayer thereby enhancing the surface smoothness and the specular beam intensity. The described behavior is periodically repeated. In order to prove the validity of our interpretation within the step density model, still a clear correlation with AFM surface morphology images have to be provided.

IV. Conclusions

We have developed a high pressure RHEED system suitable for the typical deposition conditions used for the fabrication of oxide materials. Intensity oscillations due to the layer by layer growth of epitaxial thin films and heterostructures have been observed for the manganites. By independent complementary measurement methods such as X-ray diffraction at grazing incidence and *in-situ* AFM surface morphology studies consistent information of the high quality of the epitaxy was obtained. In particular, the rms surface roughness was well below 1 nm and the mosaic spread of the the manganite films was found to be limited by the substrate quality. In summary, we have shown that high pressure RHEED supplemented by other techniques such as X-ray diffraction and *in-situ* AFM analysis represents a powerful tool in the advanced processing of complex oxide materials.

References

[1] G. J. H. M. Rijnders, G. Koster, D. H. A. Blank, and H. Rogalla, *Appl. Phys. Lett.* **70**, 1888 (1997).
[2] R. Gross, L. Alff, A. Beck, O. M. Fröhlich, D. Kölle, and A. Marx, IEEE Trans. Appl. Supercond. **7**, 2929 (1997).
[3] J. Z. Sun, W. J. Gallagher, P. R. Duncombe, L. Krusin-Elbaum, R. A. Altman, A. Gupta, Yu Lu, G. Q. Gong, and Gang Xiao, *Appl. Phys. Lett.* **69**, 3266 (1996).
[4] T. Obata, T. Manako, Y. Shimakawa, and Y. Kubo, *Appl. Phys. Lett.* **74**, 290 (1999).
[5] M. G. Lagally and D. E. Savage, *MRS Bulletin* **XVIII**(1), 24 (1993).
[6] I. Bozovic and J. N. Eckstein, *MRS Bulletin* **20**, 32 (1995).
[7] T. Terashima, Y. Bando, K. Iijima, K. Yamamoto, K. Hirata, K. Hayashi, K. Kamigaki, and H. Terauchi, *Phys. Rev. Lett.* **65**, 2684 (1990).
[8] H. Karl and B. Stritzker, *Phys. Rev. Lett.* **69**, 2939 (1992).
[9] J. J. Harris, B. A. Joyce, and P. J. Dobson, *Surf. Sci.* **103**, L90 (1981).
[10] J. H. Neave, B. A. Joyce, P. J. Dobson, and N. Norton, *Appl. Phys.* A 31, 1 (1983).
[11] M. G. Lagally, D. E. Savage, and M. C. Tringides, in *Reflection High Energy Electron Diffraction and Reflection Electron Imaging of Surfaces*, P. K. Larsen and P. J. Dobson eds (Plenum, London 1989) pp. 139-174.
[12] U. Korte and P. A. Maksym, *Phys. Rev. Lett.* **78**, 2381 (1997).
[13] Z. Mitura, S. L. Dudarev, and M. J. Whelan, *Surf. Rev. Lett.* **5**, 701 (1998).
[14] S. K. Sinha *Jour. de Phys.* III **4**, 1543 (1994).
[15] B. Wiedenhorst, C. Höfener, Yafeng Lu, J. Klein, L. Alff, R. Gross, B. H. Freitag, and W. Mader, to appear in *Appl. Phys. Lett.* (1999).

Effects of Sputtered SiO_2 Passivation Layers on YBCO Microbridges and Step-edge Junctions

J. Du, K. E. Leslie, C. P. Foley, G. L. Harding, B. Sankrithyan and D.L. Tilbrook
CSIRO Telecommunications & Industrial Physics, West Lindfield, NSW 2070, AUSTRALIA

Abstract — High-temperature superconducting $YBa_2Cu_3O_{7-\delta}$ (YBCO) microbridges and step-edge junctions (SEJ) were coated with SiO_2 thin film by an rf magnetron sputtering technique. The effect of the coating on critical temperature T_c and critical current I_c was studied. It was found that the T_c and I_c of microbridges increased as a result of the coating, by up to 3K for T_c and up to 23% for I_c . We believe this is due to the oxygen in the plasma penetrating into $YBa_2Cu_3O_{7-\delta}$ resulting in an increase in oxygen content and restoration of the degraded microbridge edges. The I_c of the SEJ, however, was found to decrease by 20-30 % after deposition of SiO_2 films despite no degradation in T_c. The results of accelerated aging tests showed that SiO_2 film forms a good passivation layer protecting $YBa_2Cu_3O_{7-\delta}$ film from reacting with water.

INTRODUCTION

Since the discovery of high-temperature superconductors (HTS) a decade ago, great effort has been devoted to the fabrication of HTS thin films with high critical current density J_c. $YBa_2Cu_3O_{7-x}$ (YBCO) thin film has received considerable attention because of its high J_c. A major drawback of this material, however, is its chemical instability. YBCO reacts with water, which leads to the degradation of the material properties even if only exposed to the ambient environment [1, 2]. One way to overcome this problem is to coat the YBCO film with a passivation layer. A number of coating materials, such as polyimide, PMMA, polyfluorocarbon, Nb_2O_5, Al_2O_3, amorphous YBCO and SiO_2 [2-7] have been studied. Most of these passivation layers degrade the film T_c and J_c due to the factors such as heating [2] and interdiffusion between the overcoated films and the HTS films [4]. Müller et al [5] have shown that, in-situ deposition of an amorphous YBCO (α-YBCO) layer immediately after YBCO deposition, is an effective passivation technique. However, they have also shown that ex-situ deposition of α-YBCO to be less effective. The technique of applying a thin film of SiO_2 over YBCO has been trialed on HTS microstrip line resonators [6] and focused ion beam (FIB) damaged junctions [7]. Measurements of resonant frequency and unloaded Q factor showed that the application of a SiO_2 passivation layer did not degrade the microstrip device performance, while providing good protection from water ingress. Good protection was also shown for FIB junctions, however a decrease of over 30% in the junction I_c was observed. The effect of passivation on the material T_c and J_c was not reported in either of these two publications.

As any changes in a HTS device's T_c or J_c, due to the application of a passivation layer, may degrade the device performance, we examined changes in these parameters after passivating two different types of the test structures — YBCO microbridges and step-edge junctions (SEJ) via rf sputtering of SiO_2. We also studied the passivation effect of the SiO_2 thin films on YBCO by accelerating aging tests in water. The SiO_2 thin films were chosen as they are chemically stable, resistant to water and most chemical solutions, and have been extensively used for passivation of semiconductor devices and circuits. They are potentially good candidates for passivating HTS materials and devices.

EXPERIMENTAL PROCEDURE

YBCO films were deposited on 10×10 mm^2 MgO (100) substrates by magnetron sputtering from a sintered target of the stoichiometric YBCO followed by in-situ annealing [8]. The film thickness varied between 250-300 nm with a film J_c between 1-3 MA/cm^2. The SEJ junctions were fabricated using the techniques described in Refs. 9 and 10. The step angles and heights are 35-40° and 400-500 nm respectively. Both microbridges and SEJ junctions were patterned by standard photolithography and LN_2 cooled substrate IBE techniques. Gold contact pads were sputtered on the samples for characterisation of electrical properties.

The SiO_2 passivation layer was deposited on the test structures by an rf magnetron sputtering technique, with a silicon target reacting in a mixture of oxygen and argon gases. The deposition rate and the physical properties of the film can be adjusted by altering the rf power, the ratio of oxygen and argon, the gas flowing pressure and the distance between target and sample. As the substrate was not heated, the deposited SiO_2 films were amorphous. The films used in these experiments were ~ 300 nm thick.

All microbridges and junctions were characterised by a standard four-point I-V measurement technique. T_c and I_c (77K) were determined from the R-T and I-V (77K) curves measured before and after the deposition of SiO_2 films. The accelerating aging tests were carried out on the coated and

uncoated microbridges by immersing the samples in water at room temperature.

RESULTS AND DISCUSSION

The properties of YBCO microbridges after deposition of SiO_2 films are summarised in Table 1. It is noted that both T_c and I_c of all microbridges increased as a result of the coating, by up to 3K for T_c and up to 23 % for I_c. T_c depends on the quality of the film and will change with changes in oxygen content. The I_c of microbridges depends on both film J_c and the width of the bridges. Normally, the oxygen content of the film would be under the ideal stoichiometric value, especially near the surface and the edges of the microbridges due to oxygen out-diffusion while in storage and during lithography processing. The degraded edges of the microbridges would also reduce the effective width of these bridges and lower the I_c values. In our SiO_2 deposition technique, a high ratio (5:4) of oxygen to argon gases was used. During the sputtering, the energy of activated oxygen in the plasma is quite high, enabling oxygen to penetrate into the YBCO film, resulting in an increase in the films' oxygen content. Consequently, it was anticipated that the film T_c and J_c should an increase after deposition of the SiO_2 passivation layer. The large percentage increase in I_c of the narrow bridges indicates that oxygen depleted edges are being restored which increases the effective width of the bridges.

TABLE 1
Summary of the properties of YBCO microbridges after deposition of SiO_2 film.

Bridge	d (μm)	T_{co} (K)	ΔT_{co} (K)	$\Delta I_c/I_c$ (%)
A	97	87.0	+3	+9
B	97	-	-	+5
C	97	-	-	+5
D	6	85.6	+1.4	+7
E	6.5	-	-	+17
F	7	85.0	+2.5	+23
G	7	-	-	+20
H	7	-	-	+18

d is the width of the microbridge, I_c is the critical current at T=77K, and T_{co} is the critical temperature at zero resistance.

Four SEJ junctions were characterised before and after deposition of SiO_2 thin films. Measurements of T_c and I_c are shown in Table 2. The T_c of the measured junction did not degrade at all. However, the I_c of all junctions was found to have decreased by 20-30% after deposition of SiO_2. Preliminary results showed that the I_cR_n products remained constant. The junction I_c is determined by the weak-coupling of grain boundary. This result indicates that the overcoating makes the junction coupling become weaker, which could be related to the stress of the overcoating on the step-edge. Altering the deposition conditions may reduce the effect. It is possible that oxygen out-diffusion may occur during rf sputtering deposition, causing a reduction of the I_c. More work is currently being undertaken to clarify the mechanisms of the I_c reduction and to improve the SiO_2 overcoating.

TABLE 2
Summary of the properties of YBCO SEJ junctions after deposition of SiO_2 film.

SEJ	d (μm)	T_{co} (K)	ΔT_{co} (K)	$\Delta I_c/I_c$ (%)
A	10	-	-	-21
B	5	-	-	-22
C	5	86.8	+0.2	-30
D	2	-	-	~ -30

Accelerated aging tests were carried out on both coated and uncoated YBCO microbridges. Fig.1 shows that the I_c of three uncoated 97 μm wide microbridges decreased rapidly due to immersion in water. Examination with an optical microscope showed that the YBCO films were completely decomposed after being in water for 14 days. The I_c and T_c of the SiO_2 coated YBCO narrow (7μm) microbridges, on the contrary, showed little variation after 21 days in water, as shown in Fig.2. This indicates that the SiO_2 thin films efficiently protect the YBCO films from water attack and is a suitable passivation material.

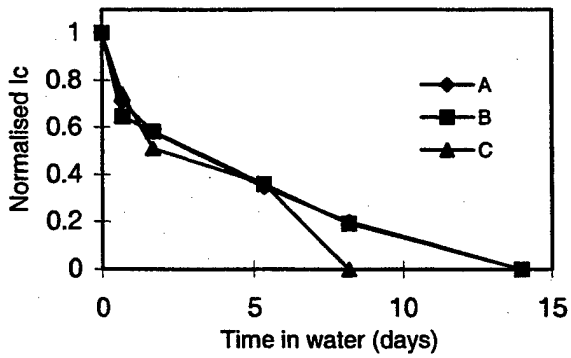

Fig. 1 Normalised I_c of three uncoated 97μm wide YBCO microbridges against the time in water

We applied the SiO_2 passivation layer to a YBCO flux focuser which was flip-chip coupled to an rf SQUID. The noise spectrum of the SQUID was measured before and after application of SiO_2 to the flux focuser. As shown in Fig. 3, the noise performance of the SQUID did not degrade but slightly improved after deposition of the SiO_2 thin film on the coupled flux focuser. This is consistent with the microbridge results described above.

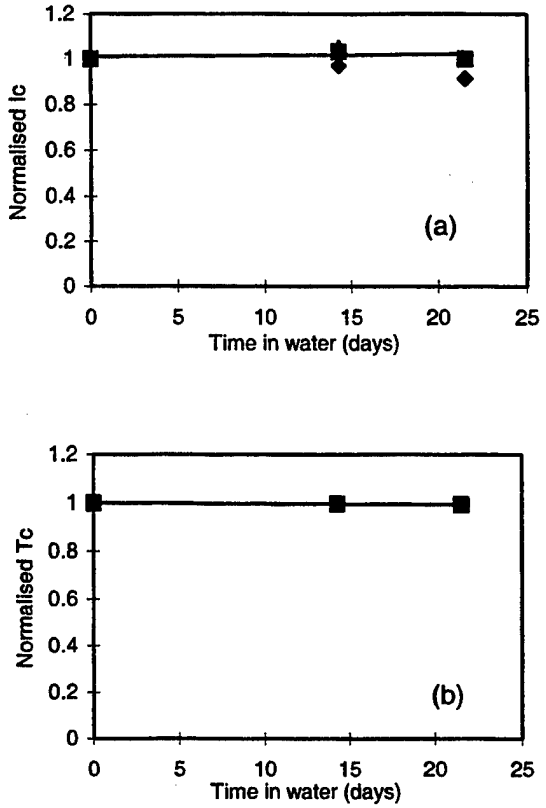

Fig. 2 Normalised I_c (a) and normalised T_c (b) of the SiO_2 coated 7μm wide YBCO microbridges against the time in water.

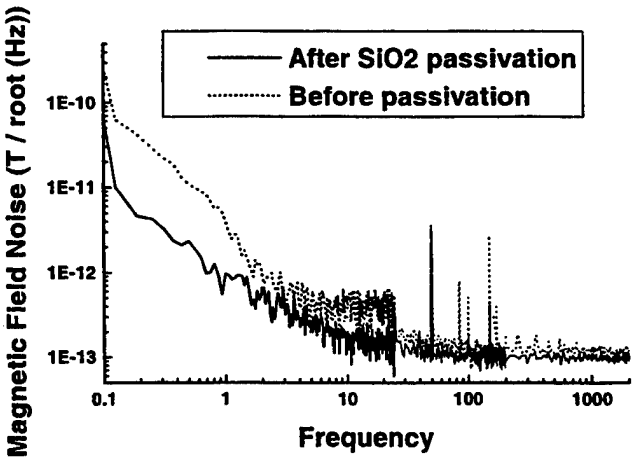

Fig. 3 A comparison of SQUID noise performance before and after coating flux focuser with a SiO_2 passivation layer.

CONCLUSIONS

The effectiveness of rf sputtered SiO_2 thin films as a passivation layer on YBCO microbridges and SEJ junctions have been studied. The T_c and I_c of the microbridges were found to increase as a result of the overcoating, indicating an improvement of the film quality. This is attributed to activated oxygen in plasma penetrating into the YBCO and restoring the oxygen content in the film, particularly at the film surface and the microbridge edges. The I_c of SEJ junctions, however, decreased by 20-30% after deposition of SiO_2. The reduction of junction I_c could be related to the stress of the overcoating changes the weak-link coupling. Changing deposition conditions may lead to improvement of the overcoating on SEJ. Aging tests showed that SiO_2 film is an excellent passivation material for preventing YBCO from reacting with water. Application of this passivation technique to a SQUID flux focuser proved successful. The work has important implications for the passivation of high-T_c superconductor microwave devices, SQUIDs and other junction based devices.

REFERENCES

[1] M.F. Yan, R.L. Barns, H.M. O'Bryan, Jr., P.K. Gallagher, R.C. Sherwood and S. Jin, Appl. Phys. Lett. 51 (1987) 532.

[2] C.F. Foley, R. Driver, S.K. Lam, Y. Wilson, B.Sankrithyan and E.E. Mitchell, Proc. EUCAS 1997, The Netherlands, vol. 1, p507, 1995

[3] K. Sato, S. Omae, K. Kojima, T. Hashimoto and H. Koinuma, Jap. J. Appl. Phys. 27 (1988) L2088.

[4] Y. Ichikawa, H. Adachi, T. Mitsuyu and K. Wasa, Jap. J. Appl. Phys. 27 (1988) L381.

[5] O. Müller, J. Schubert, W. Zander and B. Stritzker, Physica C 191 (1992) 103.

[6] M. Ban, K. Suzuki and Y. Enomoto, Physica C 290 (1997) 345.

[7] S. Tokunaga, Y. Ohkawa, K. Suzuki and Y. Enomoto, Physica C 306 (1998) 107.

[8] N. Savvides and K. Katsaros, J. Appl. Phys., 62 (1993) 528.

[9] S. Lam and C.F. Foley, Proc. 5th ISEC'95, Nagoya, Japan, 1995, p120.

[10] C. P. Foley , E.E. Mitchell, S.K.H. Lam, B. Sankrithyan, Y.M. Wilson, D.L. Tilbrook and S.J. Morris, To be published in IEEE Trans. Appl. Supercon. (1999).

Superconducting NbN films grown using pulsed laser deposition for potential application in internally shunted Josephson junctions

Anupama Bhat, Xiaofan Meng, A. Wong, and Theodore Van Duzer
Department of Electrical Engineering and Computer Sciences and the Electronics Research Laboratory
University of California, Berkeley, CA 94720-1770

Abstract--We have grown superconducting NbN films using a pulsed KrF laser for potential use as superconducting electrodes in SNS Josephson junctions being developed for nonlatching logic applications. The NbN films show a superconducting transition of 16 K using an Nb target in background N_2 gas. The T_c dependence on N_2 pressure in the range of 50-80 mTorr was investigated at a growth temperature of 600 °C. The NbN films were grown on MgO (100) and amorphous SiN_x/Si substrates. In the latter case, the films had a lower T_c, and appeared amorphous from x-ray diffraction measurements, while those on the MgO (100) substrates were strongly textured. AFM measurements reveal RMS surface roughness as low as 1 nm, over a 5 μm x 5 μm area, indicating that these films appear suitable for SNS junctions.

I. Introduction

Materials that exhibit superconducting transitions well above 10 K are technologically important for electronic applications, due to the availability of compact closed cycle refrigerators in this temperature range, which is an important consideration for promoting the commercial use of superconductor electronics. One material that meets this requirement is niobium nitride. Besides having a bulk T_c of ~ 16 K, NbN is mechanically and chemically stable, has an excellent thermal cyclability, which is important for the formation of robust integrated circuits and is relatively easy to process. This avoids some of the reasons for which the high T_c materials have had little success in their application to complex integrated circuits.

Niobium nitride thin films for Josephson junctions have commonly been prepared using sputtering [1, 2] where the standard barrier material is a thin insulating MgO layer. These well characterized sputtered films are used to make tunnel junctions which produce the hysteretic I-V characteristic necessary for latching logic applications [3], [4]. For the inherently faster nonlatching logic applications, however, such as Rapid Single Flux Quantum (RSFQ), it is necessary to overdamp the tunnel junctions with an external shunt [5]. An internal shunt has several advantages so there is growing interest in developing internally shunted junctions for use in ultra high speed RSFQ technology. Although SNS Josephson junctions exhibit nonhysteretic I-V characteristics, a feature of overdamped junctions, to date there are no appropriate metal barrier materials with parameters suitable for circuit applications. These have typically been too conductive, resulting in impedance matching problems, in addition to low I_cR_n values and hence lower circuit speeds.

Presently, we are exploring junctions with a wide variety of barrier materials and NbN superconducting electrodes for nonlatching logic applications using pulsed laser deposition. PLD is ideally suited for this investigation as a wide variety of materials can be evaluated with relative ease, the target cost is low and the target stoichometry can be transferred easily (compared to sputtering) [6].

The focus of this paper is to discuss the growth conditions necessary to produce niobium nitride films with high transition temperature using PLD, which will serve as base- and counterelectrodes for the junctions. These films have been grown on MgO (100) and SiN_x/Si substrates. Aside from the fact that it is also a nitride, SiN_x was chosen because of its stability at high temperatures when compared to SiO_x where oxygen may diffuse into the growing nitride film, degrading its superconducting properties [7]. After growth, the films were characterized using T_c and x-ray diffraction measurements. Also, although there has been prior work on the PLD of NbN [8 - 10], we have analysed these films from the point of view of device applications by presenting AFM data to evaluate their surface roughness.

II. Deposition Procedure

The PLD system is equipped with a cryopump and the base presssure is normally ~ 3 x 10^{-7} Torr. The 1/2 inch diameter targets are housed in a rotating carousel which can hold up to 10 targets, as shown in Fig. 1. The substrates, after being washed in ethanol, are mounted onto a 2-inch diameter heater block using silver paste. The heater block is capable of reaching 850°C, and the temperature during deposition is set with a temperature controller and measured using a thermocouple inserted into the heater block where the

Manuscript received April 30, 1999. This work was supported in part by the University Research Initiative Grant No. (ONR) N000014-92-J-1835.

substrates are mounted. The gases available during deposition are Ar, N_2, and O_2 which come into the chamber as shown in Fig. 1; a capacitance manometer is used to measure the flow rate of the incoming gases. The KrF laser (λ = 248 nm, τ = 38 ns) hits the target surface at approximately 45 degrees, after passing through a rotating lens, as shown in Fig. 1. A shutter is placed between the target and substrate and a few hundred shots are used to clean the target surface prior to deposition. After deposition, the gate valve is opened and the samples are cooled in vacuum.

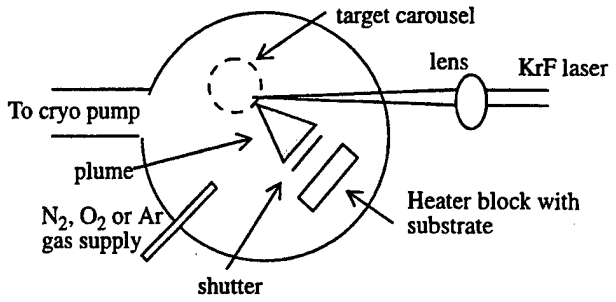

Figure 1. A schematic of the PLD chamber.

III. Film Growth and Characterization

Films were grown at a laser fluence of ~ 6 J/cm^2 and at various nitrogen pressures. Typical film thicknesses were 200 nm after about 6000 shots at a substrate temperature of 600°C. The substrate-to-target distance was about 5 cm, while the N_2 flow rate was maintained at 80 sccm. After the films were grown on MgO (100) and SiN_x/Si substrates the T_c was measured using the 4-point method, where the vapor above the liquid He was used for cooling. The temperature was measured with a Si diode which is mounted in the block on which the sample is mounted.

A typical R-T characteristic is shown in Fig. 2, where the film growth temperature was 600°C, and the N_2 pressure was 60 mT, similar to the conditions used in [8]. The T_c of this film on MgO (100) is ~16 K while it is 11 K for NbN on SiN_x/Si; the transition width on MgO (100) is less than 0.4 K, while it is about 1 K for NbN on SiN_x/Si. As shown in Fig. 2, the resistivity of the films was very temperature insensitive down to T_c which is typical of the transition metal nitrides [7]. The residual resistivity ratio (R_{300K}/R_{20K}) of the films in this case was greater than 1, though it is common to find a RRR less than 1 in these films, which is indicative of a granular or coloumnar void structure [2, 7]. These films were grown using an Nb target though an NbN target was also attempted. In the latter case, however, with a laser fluence of ~ 4 J/cm^2, substrate temperatures ranging from 300°C to 700°C, and in the presence or absence of background N_2, the T_c under all these conditions was less than 12 K and exhibited a transition width greater than 1 K with a RRR less than one.

The T_c of the films was sensitive to the N_2 pressure as shown in Fig. 3 for films deposited at 600°C. In this case, the N_2 pressure ranged from 50 mT to 80 mT; there was a gradual increase in T_c with N_2 pressure, then a decrease after 60 mT for NbN on MgO, while the peak occurred at 70 mT for NbN on SiN_x/Si. This type of T_c dependence on N_2 pressure has been commonly observed in other superconducting transition metal nitrides using other deposition techniques [11].

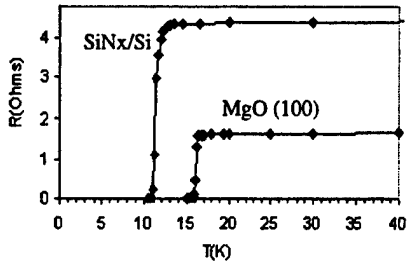

Fig. 2. The R-T characteristic of NbN films grown at 60 mT and 600 C.

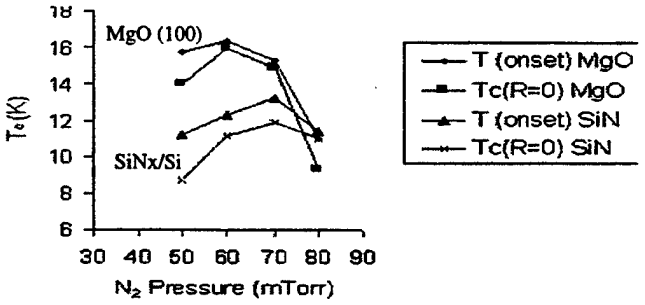

Fig. 3. The T_c dependence on N_2 pressure for NbN on MgO and SiN_x/Si substrates.

The films have also been analysed using x-ray diffraction. The x-ray diffraction data revealed that the films on SiN_x/Si were amorphous while those grown on MgO substrates were strongly (100) textured. Treece et al. found (100) and (300) peaks which is inconsistent with the commonly known FCC or rock salt structure for NbN and they determined this to be the PC structure [8]. The (100) and (300) peaks are also evident in our θ–2θ scan for the film grown at 60 mT and 600 °C, as shown in Fig. 4. Our measurements resulted in a lattice constant of 0.4439 nm which is consistent with the data reported in [8]; this is larger than the bulk value for the B1 structure.

As our intent is to use these films for the fabrication of SNS Josephson junctions, the need to analyse the film surface characteristics using the AFM should be apparent. Fig. 5 shows an AFM image of NbN films grown at 60 mT N_2 pressure and 600°C on a) MgO and b) SiN_x/Si substrates. These data indicate that the surfaces are fairly

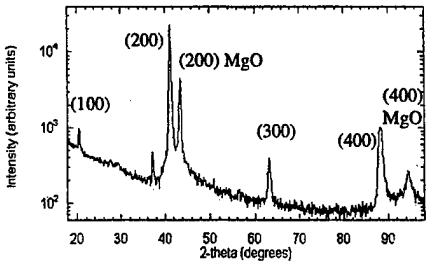

Fig. 4. x-ray diffraction data for NbN on MgO (100)

smooth, both on MgO (100) and SiN_x/Si substrates with a typical rms roughness of 1 nm. In one case however, the base pressure was higher and the surface roughness increased to ~ 3 nm on MgO, though a more in-depth study is necessary to confirm this correlation. In general, barriers in SNS junctions are much thicker than those in tunnel junctions so thickness sensitivity is much smaller and electrode smoothness should be less critical. Surface roughness data indicate that these films are adequate for SNS device applications.

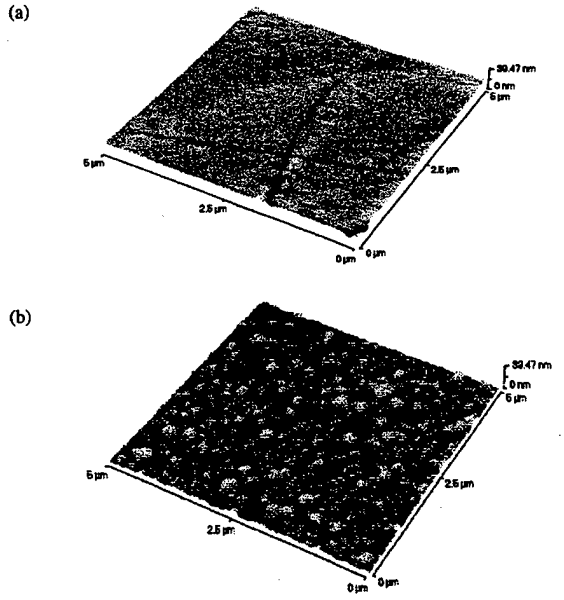

Fig. 5. AFM data for NbN films on (a) MgO and (b) SiN_x/Si.

IV. CONCLUSIONS

We have grown NbN on MgO (100) substrates using pulsed laser deposition at a substrate temperature of 600 °C. The maximum T_c of 16 K was observed at 60 mT N_2 pressure in the case of MgO (100) substrates while on SiN_x/Si substrates, the maximum T_c of 12 K occured at a slightly higher N_2 pressure. X-ray diffraction data indicate the films are strongly textured on MgO substrates and appear to be amorphous on SiN_x/Si substrates. The AFM measurements reveal RMS surface roughness of ~ 1 nm on MgO which is comparable to the RMS roughness values on SiN_x/Si. In conclusion, the films appear smooth enough for the formation of SNS Josephson junctions for nonlatching logic applications.

REFERENCES

[1] A. Shoji, M. Aoyagi, S. Kosaka, F. Shinoki, and H. Hayakawa, "Niobium nitride Josephson tunnel junctions with magnesium oxide barriers," *Appl. Phys. Lett.*, vol. 46, pp. 1098-1100, June 1985.

[2] Z. Wang, A. Kawakami, Y. Uzawa, and B. Komiyama, "Superconducting properties and crystal structures of single-crystal niobium nitride thin films deposited at ambient substrate temperature," *J. Appl. Phys.*, vol. 79, no. 10, pp. 7837-7842, May 1996.

[3] S. Thomasson, A. Moopen, R. Elmadjian, J. Murduck, J. Spargo, L. Abelson, and H. Chan, "All refractory NbN integrated circuit process," *IEEE Trans. Appl. Superconduct.*, vol. 3, pp. 2058-2061, Mar. 1993.

[4] M. Radparvar, L. Yu-Jahnes, and R. Hunt, "All niobium nitride Josephson tunnel junctions with thermally oxidized magnesium barrier," *IEEE Trans. Appl. Superconduct.*, vol. 3, pp. 2050-2053, Mar. 1993.

[5] K. K. Likharev and V. K.. Semenov, "RSFQ logic/memory family: a new Josephson junction technology for sub-teraherz clock frequency digital systems," *IEEE Trans. Appl. Superconduct.*, vol. 1, pp. 3-28, Mar. 1991.

[6] D. Chrisey and G. Hubler (Eds.), *Pulsed Laser Deposition of Thin Films*, Wiley, New York, 1994.

[7] L. E. Toth, in "Transition Metal Carbides and Nitrides", (J. Margrave, Ed.), *Refractory Materials*, vol. 7, Academic Press, New York, 1971.

[8] R. Treece, J Horwitz, S. Quadri, E. Skelton, E. Donovan, and D. Chrisey, "Metastable nitride synthesis by pulsed laser deposition: A new phase in the NbNx system," *J. Solid State Chem.*, vol. 117, pp. 294-299, 1995.

[9] R. Treece, M. Osofsky, E. Skelton, S. Qadri, J. Horwitz, and D. Chrisey, "New phase of superconducting NbN stabilized by heteroepitaxial film growth," *Phys. Rev. B*, vol. 51, pp. 9356-9359, April 1995.

[10] V. Boffa, U. Gambardella, V. Marotta, A. Morone, F. Murtas, S. Orlando, G. Parisi, "NbN superconducting thin films grown by pulsed laser ablation," *Appl. Surf. Sci.*, vol. 106, pp. 361-364, Oct. 1996.

[11] T. Chen, X Yang, P Sourivong, K. Kamimura, A Viescas, C. Chen, J. Curley, D. Phares, H. Hall, P. Dayton, C. Hart, and J. Wang, "Fabrication, superconducting T_c and charge transfer of VNx, NbNx and TaNx foils," *Phys. Lett. A*, vol. 217, pp. 167-175, July 1996.

Oral Session 7

Mixers and Detectors

Superconducting Transition Edge Sensor Microcalorimeters for X-ray Microanalysis

John M. Martinis, D. A. Wollman, G. C. Hilton, K. D. Irwin, N. F. Bergren, and D. A. Rudman
NIST, 325 Broadway, Boulder, Co 80303

Abstract—We have developed a high-resolution x-ray energy-dispersive spectrometer (EDS) based on cryogenic microcalorimeter x-ray detectors for use in x-ray microanalysis. With an energy resolution of 3 eV at 1.5 keV, count rate of ~500 s^{-1}, and an effective collection area of ~5 mm^2 (using polycapillary x-ray optics), microcalorimeter EDS combines the favorable qualities of commercially-available wavelength dispersive spectrometers (WDS) and semiconductor EDS. After describing the spectrometer system, we present several applications of microcalorimeter EDS to important microanalysis problems, including the analysis of contaminant particles in the semiconductor industry.

I. Introduction

We have recently developed a high-energy-resolution x-ray microcalorimeter energy-dispersive spectrometer[1] (EDS) for use in x-ray microanalysis. X-ray microanalysis is a sensitive, nondestructive analytical technique that provides spatially resolved qualitative and quantitative microchemical analysis. The combination of high-energy-resolution x-ray spectrometers with high-spatial-resolution scanning electron microscopes (SEM) has provided powerful microanalysis instruments which are widely used in both industry and academia. In these instruments, a finely focused electron beam is used to excite x rays in a small region of a sample under analysis. The x rays are then analyzed using a commercially-available wavelength-dispersive spectrometer (WDS) or semiconductor energy-dispersive spectrometer (EDS) to obtain an x-ray spectrum. Comparing the integrated characteristic x-ray intensities produced by the sample and elemental standards yields qualitative and quantitative compositional information on a micrometer or even a nanometer length scale.

Unfortunately, neither semiconductor EDS nor WDS fully satisfy the microanalysis requirements facing many technology-intensive industries. In a semiconductor EDS detector, x rays are absorbed in a voltage-biased intrinsic semiconductor to create electron-hole pairs, which separate under the applied electric field to yield a collected charge proportional to the x-ray energy. Semiconductor EDS is used in over 90% of installed x-ray microanalysis systems because it is easy to use, inexpensive to operate, and offers both rapid qualitative evaluation of chemical composition and accurate quantitative analysis. However, it is limited by an energy resolution on the order of 100 eV, which is insufficient to resolve many important overlapping x-ray peaks in materials of industrial interest, such as the Si Kα and W Mα peak overlap in WSi_2. In contrast, WDS uses Bragg reflection from curved diffracting crystals to achieve the excellent resolution (typically 2 eV to 10 eV) needed to resolve most peak overlaps. However, qualitative WDS analysis is severely limited by the long time needed to serially scan over the entire energy range using multiple diffraction crystals.

There is a need for a new generation of x-ray spectrometer that combines the excellent energy resolution of WDS with the ease of use and the parallel energy detection capability of semiconductor EDS. One such next-generation x-ray spectrometer is microcalorimeter EDS. In this paper, we review the prototype microcalorimeter EDS system[1] developed at NIST, and examine several applications of microcalorimeter EDS to important microanalysis problems. Portions of the research described here have been published previously; in particular, Ref. 1 provides a more detailed overview of the microcalorimeter EDS system.

II. Detector and Instrumentaton

An x-ray microcalorimeter consists of an x-ray absorber in thermal contact with a thermometer. When an x-ray photon of energy E interacts with the absorber, the deposited energy is thermalized and measured as a temperature rise $\Delta T = E/C$, where C is the heat capacity of the detector. The temperature of the microcalorimeter returns to the equilibrium temperature with a $1/e$ time constant $\tau = C/G$, where G is the thermal conductance between the absorber and the heat bath. The energy resolution ΔE of a microcalorimeter is limited by thermodynamic temperature fluctuations, such that $\Delta E \propto \sqrt{k_B T^2 C}$, where k_B is Boltzmann's constant and T is the operating temperature of the detector. Microcalorimeters are typically operated at low temperatures ($T \sim 0.1$ K) where materials have low heat capacity (leading to a large temperature rise), thermal and electrical noise sources are reduced, and sensitive thermometers are available. The first x-ray microcalorimeters used semiconductor-thermistor thermometers[2-4] read out using field effect transistors. While these devices obtain energy resolutions sufficient for many microanalysis problems (~ 8 eV at 6 keV), their intrinsically slow response times (typically $\tau \geq 1$ ms) limit widespread application.

The microcalorimeter EDS developed at NIST uses a new type of microcalorimeter[5] with a superconducting transition-edge sensor (TES) thermometer, which is a superconducting film biased in temperature within its narrow resistive transition from the normal to the superconducting state. The TES is biased with a voltage V, and the current flowing through the film is measured with a low-noise

superconducting quantum interference device (SQUID) amplifier. The heat bath is then cooled to well below the transition temperature of the film, typically chosen to be ~100 mK. As the TES cools, its resistance R drops and the Joule heating (V^2/R) in the film increases. A stable equilibrium is established when the resistance is reduced to the point where the Joule heating equals the heat flowing to the heat bath. The TES thus self-regulates in temperature within its transition, an effect referred to as negative electrothermal feedback.[5]

When an x ray deposits its energy in the absorber, the temperature and resistance of the TES increase, leading to a decrease in the current and thus the dissipation of Joule power in the TES, while the heat flowing to the heat bath remains approximately constant. Thus, the x-ray energy is primarily removed by a reduction in Joule heating, which can lead to a thermal response time more than a hundred times faster than the natural relaxation time τ.[5] This faster time constant significantly increases the output count rate of TES microcalorimeters (to ~500 s^{-1}, at present), making these new microcalorimeters very attractive for microanalysis applications.

Figure 1 shows a cross-sectional view of a microcalorimeter including the physical layout and the external electrical connections. Using electron-beam evaporation through shadow masks, the TES, Bi absorber, and electrical contacts are deposited on a 0.5 μm thick freely suspended silicon nitride membrane supported by a micromachined silicon substrate. The thin membrane reduces the thermal conductance from the detector to the bath, prevents the loss of absorbed x-ray energy via high energy phonons escaping into the substrate, and eliminates x-ray absorption in the substrate.[6] Additionally, the electrical contacts to the TES are made with superconducting aluminum lines, which have very small thermal conductivity. The TES itself is 400 μm by 400 μm in lateral area and consists of a 300 nm thick Ag/Al bilayer. Proximity coupling between the normal metal Ag and the superconducting Al provides sharp and reproducible superconducting transitions at temperatures in the range 50 mK to 1 K. The thicknesses of the two metals are chosen to obtain a suitable transition temperature, typically near 100 mK. A 2 μm Bi film deposited on top of the TES bilayer is used as an x-ray absorber. A 350 μm diameter circular Pt aperture is used to collimate incoming x rays so that they are incident only on the absorber.

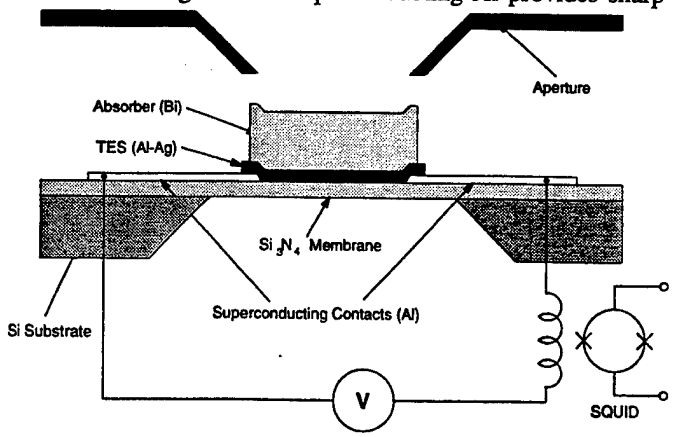

Figure 1. Cross-sectional view of the TES microcalorimeter. An x ray passes through an aperture and is absorbed in the Bi film. The resulting thermal energy pulse raises the temperature of the TES, causing an increase in resistance of the TES, and a pulse of decreased current at the SQUID input.

The use of a superconducting transition as a thermal sensor provides the detector with many of the advantages typically associated with superconducting circuits. Due to their low normal-state resistance (R_n ~ 30 mΩ), TES microcalorimeters are far less susceptible to microphonic pickup than high-impedance semiconductor thermistor microcalorimeters. Their low impedance also allows efficient coupling to low-noise, low-power SQUID amplifiers. Because the detector's electrical bandwidth is limited by the L/R_n time constant of the SQUID input circuit (L is the sum of the stray and SQUID input inductances), improved speed and stability are obtained by mounting a first-stage SQUID at 0.1 K close to the detector chip, thus minimizing stray inductance. The output of this SQUID is amplified by a series-array SQUID[7] operating at 4 K. The large output voltage (5 mV) and high output impedance (100 Ω) of the series-array SQUID allows the use of simple room temperature amplifiers for read out. At this stage, signal pulses resulting from discrete x-ray photon events are shaped for real-time peak height analysis using a commercially available EDS multichannel analyzer. In addition, pulse pileup rejection circuitry is used to veto x-ray pulses that are coincident in time.

For microcalorimeter EDS to be practical and useful to industry, a convenient and simple refrigeration system is required to reach operating temperatures of less than 100 mK. The refrigerator must be compact enough to be mounted on an SEM, have low vibration, and be very simple to operate. To satisfy these requirements, we have used an adiabatic demagnetization refrigerator[8] (ADR) installed in a commercial two-cryogen (liquid helium and liquid nitrogen) cryostat to provide cooling from the liquid helium reservoir at 4 K to the detector stage at 100 mK. The ADR consists of two paramagnetic "pills" constructed of ferric ammonium alum (FAA) and gadolinium gallium garnet (GGG) which are supported in the bore of 4 T superconducting magnet by a low thermal conductance mechanical support. A mechanical heat switch is used to thermally ground both pills to 4 K during magnetization. Demagnetization causes the FAA pill to cool to 50 mK and the GGG pill to 1 K. The GGG pill is used as an intermediate heat intercept between 50 mK and 4 K, reducing thermal leakage to the FAA pill, thus increasing the hold-time of the FAA pill. The detector is mounted on a Cu rod which is in thermal contact with the FAA pill. A detector operating temperature of 70 mK can be held for over 12 hours, after which the ADR requires a magnetic "recharge" cycle that takes less than 45 minutes to complete. A cross-sectional view of the ADR cryostat is shown in Fig 2.

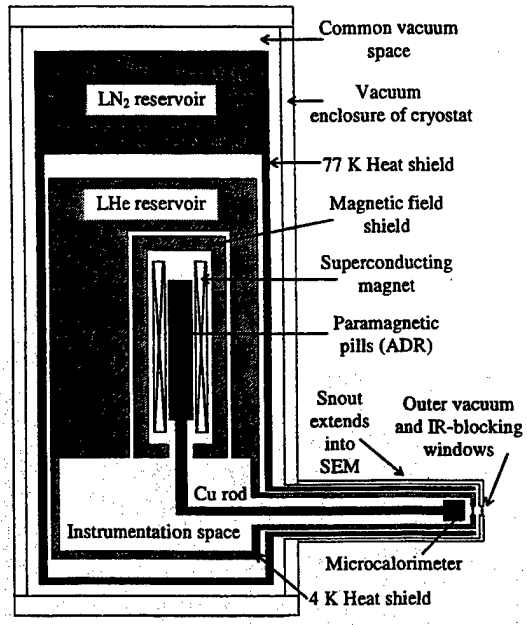

Figure 2. Cross-sectional drawing of the ADR cryostat (not to scale) from Ref. 1. The microcalorimeter is mounted at the end of a Cu rod that extends into the sample chamber of the SEM.

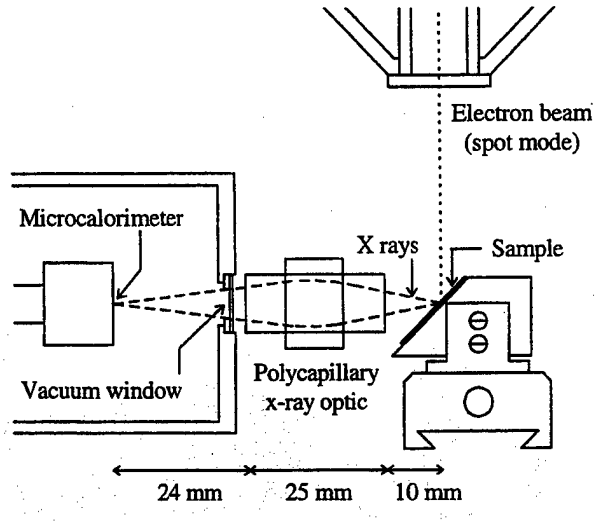

Figure 3. Diagram (approximately to scale) of microcalorimeter, polycapillary x-ray optic, and sample inside the SEM chamber, adapted from Ref. 1. By mechanically positioning the optic, the input and output focal spots of the optic are aligned with the sample and the microcalorimeter. For clarity, translation stages, heat shields and infrared-blocking Al filters are not shown.

To increase the fraction of x rays collected from the sample, the TES microcalorimeter is placed at the end of a long Cu rod which is surrounded by heat and vacuum shields that protrude from the cryostat and extend into the SEM. A commercial vacuum-tight x-ray window placed at the end of the snout permits x-ray illumination of the detector. Within the snout, two free-standing Al-coated polymer membranes at 4 K are positioned between the x-ray window and the detector, reducing the infrared heat load on the detector. This arrangement allows us to place the detector less than 30 mm from the SEM sample stage.

Although our microcalorimeters have a small collection area (~0.1 mm^2), we have dramatically increased the effective detector area using polycapillary x-ray optics.[1,9,10] These optics utilize high-efficiency grazing-angle x-ray reflections to deflect x rays over a wide angle. A polycapillary optic consisting of tens of thousands of fused glass capillaries can collect x rays from a point x-ray source and focus the x rays onto the small area absorber of our detector, as shown in Fig 3. This technique increases the effective area of the microcalorimeter to ~5 mm^2 (relative to an effective sample-detector distance of 25 mm) over a broad range of x-ray energies (200 eV to 10 keV).

III. Microcalorimeter Performance and Applications

Microcalorimeter EDS must show significant performance increases over currently available techniques to be of practical value to the microanalysis community. The current performance of microcalorimeter EDS approaches that of high-resolution semiconductor EDS in terms of solid angle (~7 msr (millisteradians) using a polycapillary optic x-ray lens) and maximum count rate (~500 s^{-1}), while providing improved energy resolution comparable to that of a wavelength-dispersive spectrometer (WDS). The excellent energy resolution of our "general purpose" microcalorimeter EDS (~10 eV FWHM over the energy range 0 keV to ~10 keV) allows straightforward identification of closely spaced x-ray peaks in complicated spectra, including overlapping peaks in important materials (such as TiN and WSi_2) which cannot be resolved by semiconductor EDS. Recently, we have developed a TES microcalorimeter[11] with an instrument-response energy resolution of 3.1 eV ± 0.1 eV FWHM (digital processing) and ~4 eV FWHM (analog processing) over the energy range 0 keV to ~2 keV. The ability to resolve severe peak overlaps using this detector is clearly observed in Fig. 4, in which we show an x-ray spectrum of TiN acquired in real time with our microcalorimeter EDS mounted on a SEM. The impressive increase in resolution over semiconductor EDS,

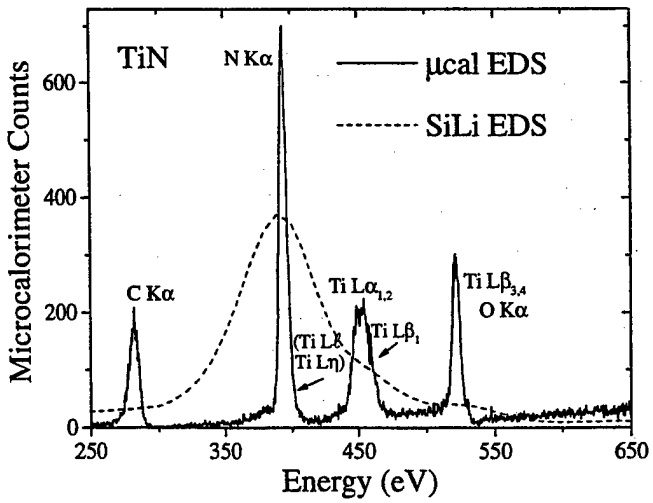

Figure 4. Microcalorimeter (μcal) and semiconductor (SiLi) EDS x-ray spectra of TiN, from Ref. 12.

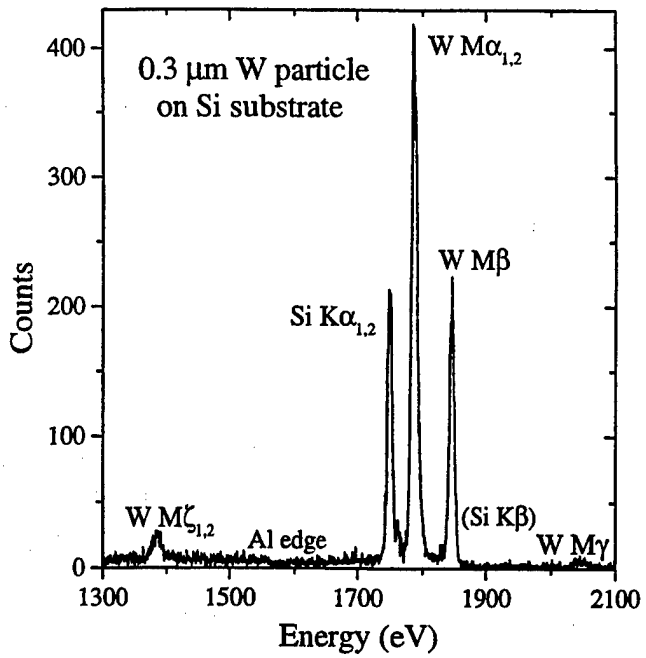

Figure 5. Microcalorimeter EDS x-ray spectrum of a 0.3 μm diameter W particle on a Si substrate (from Ref. 12), acquired under the following conditions: 5 keV beam energy, 50 pA beam current, 63 s^{-1} input count rate, 60 s^{-1} output count rate, 5% dead time, 400 s live time, and a 45° x-ray takeoff angle.

coupled with reasonable output count rates and solid angle, demonstrates the usefulness of microcalorimeter EDS for x-ray microanalysis.

IV. Particle Analysis in the Semiconductor Industry

A difficult microanalysis challenge facing the semiconductor industry is the chemical identification of the small particles and defects that occur in the manufacture of integrated circuits.[12] As circuit dimensions continue to shrink, it becomes impossible to perform this task efficiently with either EDS or WDS systems. To obtain x-ray spectra of a small particle, the electron-beam energy must be substantially reduced so that the majority of x rays originate from the particle and not the underlying substrate. The low energy electron-beam greatly reduces the x-ray flux per unit beam current, while increasing the likelihood of unresolvable peak overlaps. Because of this, both high energy resolution and efficiency are required, so that neither WDS nor semiconductor EDS are good detector choices. Additionally, the small x-ray flux imposes only modest requirements on detector count rate, making the microcalorimeter EDS very attractive in this analytical situation.

In Fig. 5 we show a microcalorimeter EDS spectrum of a 0.3 μm diameter W particle on Si. Such particles cannot be analyzed using semiconductor EDS due to the severe peak over-laps between the Si-K and W-M x-ray lines. The ability of microcalorimeter to analyze small Al oxide particles has also been investigated. In Fig. 6 we show microcalorimeter EDS spectra of Al oxide particles as small as 0.1 μm in diameter. In all cases, peaks from the Al oxide particles are clearly observable and are a significant fraction of the Si substrate peaks. In the case of the smallest particles (0.1 μm and 0.14 μm) the electron beam diameter was larger than the particle, leading to increased substrate peaks. This problem can be alleviated in the future through the use of a high-spatial-resolution field-emission SEM.

V. Chemical Shift Measurements

Chemical shifts result from changes in electron binding energies with the chemical environment of atoms. Measurements of chemical shifts in analytical techniques such as x-ray photoemission spectroscopy (XPS) and Auger electron spectroscopy (AES) have been demonstrated to provide valuable chemical bonding state information.[13] For example, the ability to identify particle composition by distinguishing different oxidation states (for example, Al and Al_2O_3) using AES has been demonstrated to be useful in determining sources of contamination in semiconductor processing tools.[14]

While chemical shift measurements are not as well established in x-ray spectroscopy, chemical shifts have been observed in WDS x-ray spectra as changes in x-ray peak positions, relative peak intensities, and peak shapes.[15] These chemical shift effects can be significant (with x-ray peak shifts on the order of 1 eV), particularly for x-ray lines

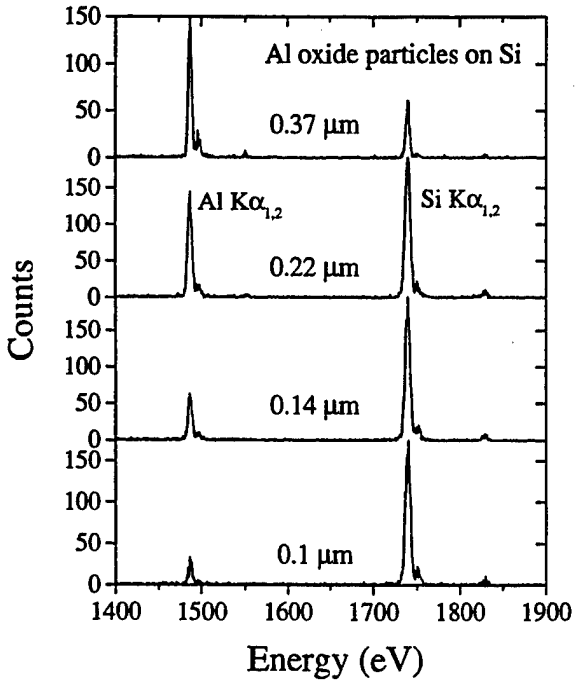

Figure 6. Microcalorimeter EDS x-ray spectra of several sized Al_2O_3 particles on a Si substrate (from Ref. 12), acquired under similar conditions as the spectrum in Fig. 5. The average diameter of each particle is displayed directly above its spectra. The electron beam diameter was estimated to be larger than the diameters of the two smallest particles.

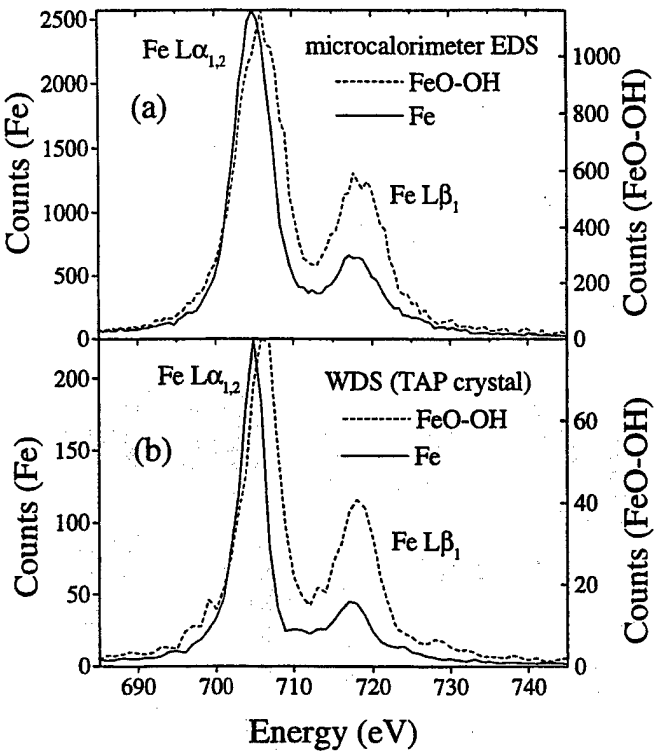

Figure 7. (a) Microcalorimeter EDS spectra and (b) WDS spectra of Fe (solid line) and FeO-OH (dashed line), from Ref. 17. The observed changes in the Fe-L peak positions and intensities result from chemical bonding effects. Good agreement is observed between microcalorimeter EDS and WDS spectra.

resulting from transitions involving valence electrons of light elements[16] such as C. However, chemical shift measurements are not routinely performed in WDS analysis due to the extreme time penalty of scanning.

The improvement in energy resolution of our most recent TES microcalorimeter now allows microcalorimeter EDS measurements of chemical shifts[17] in x-ray spectra, as shown in Fig. 7 for Fe and FeO-OH. The EDS operation of the microcalorimeter ensures that all peak shapes and integrated peak intensities are readily accessible. With further improvements in the energy resolution of microcalorimeter EDS, analysis using x-ray peak shapes and positions may become practical and provide valuable chemical bonding state information for particle analysis and other applications.

VI. Conclusion

Microcalorimeter EDS is a next-generation spectrometer for x-ray microanalysis with the energy resolution of a WDS and the parallel energy detection of an EDS. The excellent energy resolution of microcalorimeter EDS will allow many new applications to important microanalysis problems, including the analysis of contaminant particles on semiconductor surfaces and chemical shift measurements. With commercialization and further development, microcalorimeter EDS will help to meet the analytical requirements for x-ray microanalysis in the future.

References

[1] Wollman, D. A., Irwin, K. D., Hilton, G. C., Dulcie, L. L., Newbury, D. E., and Martinis, J. M., J. Microscopy, vol. 188 (1997) 196–223.

[2] Moseley, S. H., Mather, J. C., and McCammon, D., J. Appl. Phys., vol. 56 (1984) 1257-62.

[3] McCammon, D., Cui, W., Juda, M., Plucinsky, P., Zhang, J., Kelley, R. L., Holt, S. S., Madejski, G. M., Moseley, S. H., and Szymkowiak, A. E., Nucl. Phys. A, vol. 527 (1991) 821c-824c.

[4] Silver, E., LeGros, M., Madden, N., Beeman, J., and Haller, E., X-ray Spectrometry, vol. 25 (1996) 115–112.

[5] Irwin, K. D., Appl. Phys. Lett., vol. 66 (1995) 1998-2000; Irwin, K. D., Hilton, G. C., Wollman, D. A., and Martinis, J. M., Appl. Phys. Lett., vol. 69 (1996) 1945–1947.

[6] Nahum, M., and Martinis, J. M., Appl. Phys. Lett., vol. 66 (1995) 3203–3205.

[7] Welty, R. P., and Martinis, J. M., IEEE Trans. Magn., vol. 27 (1991) 2924–2926.

[8] Hagmann, C., and Richards, P. L., Cryogenics, vol. 34 (1994) 221–6.

[9] Kumakhov, M. A., and Komarov, F. F., Phys. Rep., vol. 191 (1990) 289–350.

[10] Wollman, D. A., Jezewski, C., Hilton, G. C., Xiao, Q.-F., Dulcie, L. L., and Martinis, J. M., Microsc. and Microanal., vol. 3 (Supp. 2) (1997) 1075–76.

[11] Martinis, J. M., Irwin, K. D., Wollman, D. A., Hilton, G. C., Dulcie, L. L., and Bergren, N. F., Microsc. Microanal., vol. 4 (Suppl. 2) (1998) 172-173.

[12] Wollman, D. A., Hilton, G. C., Irwin, K. D., Dulcie, L. L., Bergren, N. F., Newbury, D. E., Woo, K.-S., Liu, B. Y., Diebold, A. C., and Martinis, J. M., Characterization and Metrology for ULSI Technology: 1998 International Conference (1998) 799-804.

[13] Briggs, D. and Riviere, J. C., Practical Surface Analysis, Vol. 1: Auger and X-ray Photoelectron Spectroscopy, New York: John Wiley and Sons (1990) 85-141; Waddington, S. D., ibid., 587-594.

[14] Brundle, D., Uritsky, Y., and Pan, J. T., Micro, vol. 13 (1995) 43–56.

[15] Fabian, D. F., Watson, L. M., and Marshall, C. A. W., Rep. Prog. Phys. Vol. 34 (1971) 601-696.

[16] Holliday, J. E., J. Appl. Phys., vol. 38 (1967) 4720-4730.

[17] Wollman, D. A., Newbury, D. E., Hilton, G. C., Irwin, K. D., Dulcie, L. L., and Martinis, J. M., Microsc. Microanal., vol. 4 (Suppl. 2) (1998) 196-197.

A Hot-Electron Direct Detector for Radioastronomy

Boris S. Karasik, William R. McGrath, and Henry G. LeDuc
Jet Propulsion Laboratory, California Institute of Technology, Pasadena, CA 91109

Michael E. Gershenson
Dept. of Physics & Astronomy, Rutgers University, Piscataway, NJ 08854

Abstract — A hot-electron transition-edge superconducting bolometer with adjustable thermal relaxation speed is proposed. The bolometer contacts are made from a superconductor with high critical temperature which blocks the thermal diffusion of hot carriers into the contacts. Thus electron-phonon interaction is the only mechanism for heat removal. The speed of thermal relaxation for hot electrons in a nanometer-size superconducting bolometer with T_c = 100-300 mK is controlled by the elastic electron mean free path l. The relaxation rate behaves as $T^4 l$ at subkelvin temperatures and can be reduced by a factor of 10-100 by decreasing l. Then an antenna- or waveguide-coupled bolometer with a time constant ~ 10^{-3} to 10^{-4} s will exhibit photon-noise limited performance at millimeter and submillimeter wavelengths. The bolometer will have a figure-of-merit NEP$\sqrt{\tau}$ = 10^{-22}-10^{-21} W/$\sqrt{\text{Hz}}$ at 100 mK which is 10^3 to 10^4 times better (ie: smaller) than that of a state-of-the-art bolometer. A tremendous increase in speed and sensitivity will have a significant impact for observational mapping applications.

I. Introduction

Future submillimeter radioastronomy missions will require significant improvement of the sensitivity of radiation detectors. Use of the space interferometers with cooled telescopes will reduce the background-limited noise-equivalent power (NEP) down to 10^{-19} W/$\sqrt{\text{Hz}}$ [1]. Better detectors will be needed to take advantage of these new telescopes. Bolometers are most the promising candidates to meet these future needs. Currently, state-of-the-art bolometers offer the NEP of the order of 10^{-17} W/$\sqrt{\text{Hz}}$ at 0.1 K along with a ~1 ms time constant [2]. The high sensitivity of these bolometers is achieved using carefully-engineered mechanical suspensions which provide high thermal isolation of the absorber and the thermometer from the heat sink. Specially-designed spider-web suspensions also play the role of radiation absorber at the same time. For even higher sensitivity, the thermal conductance between the device and the heat sink should be reduced. In general, this slows down the bolometer response which, in turn, increases the 1/f-noise contribution and limits the rate of data flow from the instrument.

We propose a new approach for improving the sensitivity of bolometers for use at millimeter to far-infrared wavelengths. The innovative idea is to use an antenna-coupled hot-electron transition-edge sensor (TES) with *impurity-controlled* electron-phonon relaxation time. The small heat capacity of a micron or even submicron size microbridge, high thermal resistance of superconducting leads, and finally, properly adjusted electron-phonon relaxation time at ultra-low temperatures provides the high sensitivity of this novel detector. It is noteworthy that the electron-phonon relaxation time is sensitive to the inelastic electron scattering by vibrating impurities and to the modification of the phonon spectrum in thin films. This allows one to regulate the characteristic time constant and to avoid losses of sensitivity because of the excessively large bolometer speed. These detectors will have a figure-of-merit, $NEP\sqrt{\tau}$, up to four orders of magnitude better (ie: smaller) than that for conventional bolometers. We expect that an antenna- or waveguide-coupled bolometer with a time constant τ ~ 10^{-3} - 10^{-4} s at T = 0.1-0.3 K will exhibit photon-noise limited performance in millimeter, submillimeter and infrared wavelengths. Alternatively, the proposed bolometer could operate at higher temperatures with still superior sensitivity. This device can significantly increase the science return and reduce the cost of the future radioastronomy missions.

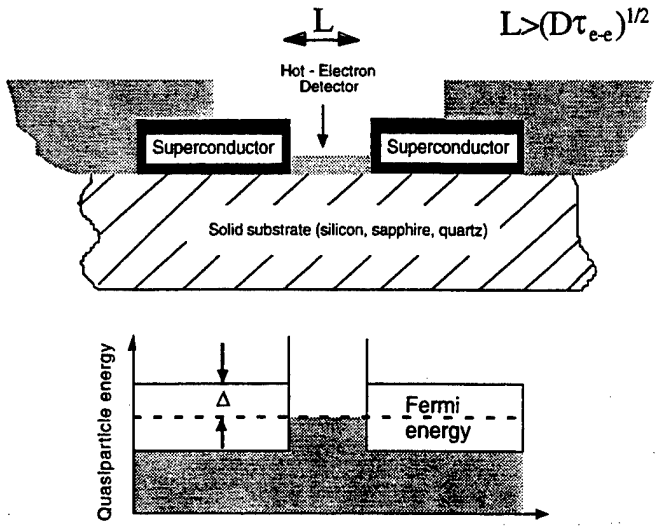

Fig. 1. Schematic diagram of the detector design. The TES is surrounded by superconducting "Andreev mirrors" which prevent the leakage of the thermal energy into the contacts. The energy gap in the TES is suppressed while in the contacts it is fully open. The size of superconducting contacts is small to avoid undesirable rf loss at high frequencies.

II. Device Concept

The hot-electron bolometer may be viewed as the limiting case of a conventional bolometer when the thermal

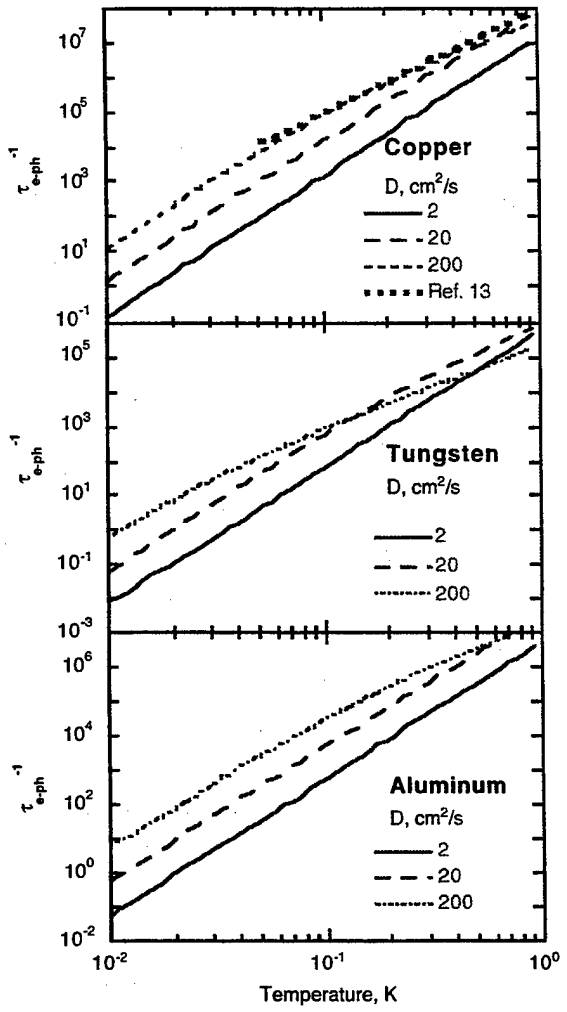

Fig 2. The electron-phonon relaxation rate, $\tau_{e\text{-}ph}^{-1}$, in some metals. The experimental data for Cu were obtained for the diffusivity $D = 200$ cm²/s.

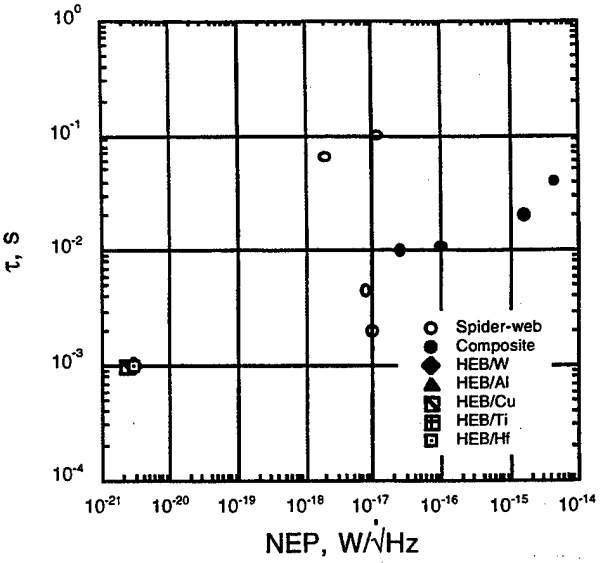

Fig. 3. Comparison of the performance of the state-of-the-art bolometers (circles) and that for HEB detectors of 0.5x0.2x0.01 μm³ volume. It is assumed that the time constant for HEBs can be adjusted to 1 ms at 0.1 K. The NEP data for HEB fall very close to each other so the symbols overlap.

conductance due to the electron-phonon coupling is much smaller than those for the phonon escape from the film to the substrate and for the heat transfer between the substrate and the environment. At subkelvin temperatures this is especially easily to achieve if the device is fabricated on a highly-thermal-conductive bulk substrate. For 10-30 nm thick films, the phonon escape time is < 1 ns and the electron-phonon relaxation is the slowest process which governs the energy relaxation.

A practical implementation of the hot-electron mechanism at subkelvin temperatures requires special design of the contact areas (Fig. 1). The leads should be made from a superconductor with a high critical temperature than the bolometer material. A large superconducting gap, Δ, creates a barrier for the energy leakage of the electrons energy from the detector. The bias and rf currents will flow freely through the structure, whereas the outdiffusion of hot electrons with energies $\varepsilon < \Delta$ will be blocked by the Andreev reflection. A similar design for the contacts was proposed for a normal-insulator-superconductor (NIS) HEB sensor [3]. We prefer to use a superconducting TES because of its higher responsivity, and lack of undesirable shot-noise effects. The TES plays the role of both absorber and temperature sensor, and in the vicinity of the superconducting transition, the bolometer is in a mixed state and represents a simple resistive load for incoming radiation.

As in the case of a conventional bolometer, the sensitivity limit of a HEB detector is given by thermodynamic fluctuations and the corresponding NEP is:

$$NEP = \sqrt{4k_B T^2 G_{e-ph}} = \sqrt{4k_B T^3 \gamma V / \tau_{e-ph}}\,. \qquad (1)$$

where $G_{e\text{-}ph} = C_e/\tau_{e\text{-}ph}$ is the effective thermal conductance for the heat transfer between electrons and phonons; and $C_e = \gamma TV$ is the electron heat capacity, γ is the Sommerfeld constant, V is the film volume. In contrast to the case of conventional bolometers, where the thermal conductance depends on the mechanical design of the bolometer suspension, the NEP of an HEB depends on volume.

It is common to characterize the performance of bolometers by the figure-of-merit $NEP\sqrt{\tau}$; that is, the minimum energy that can be detected by a bolometer. In the case of hot-electron detectors, this figure depends only on the specific heat of electrons, whereas for conventional bolometers there is an additional large contribution due to the specific heat of phonons in the whole device (the absorber, the sensing element, and the thermometer). Thus, in principle, the hot-electron detectors offer the maximum possible sensitivity among all types of bolometers with the *same* time constant.

The time constant τ of the hot-electron detector is determined by the inelastic electron-phonon relaxation time

$\tau_{e\text{-}ph}$ [4] (for a conventional bolometer, τ is determined by the ratio of the total heat capacity to the design-dependent thermal conductance). At $T = 4.2$ K, the electron-phonon time can be as small as 10^{-10} s; for this reason, the *NbN* devices of this type are used as terahertz mixers with the intermediate frequency response up to 3-4 GHz [5]. On the other hand, the time constant τ required for direct detection applications is typically of the order of 10^{-3} s. Thus, to minimize the *NEP*, one has to adjust the electron-phonon time $\tau_{e\text{-}ph}$ to the required $\tau \sim 10^{-3}$ s.

The use of a TES instead of a normal metal bolometer with an NIS-junction [3] allows to explore the electro-thermal feedback (ETF) [6]. The NEP of a bolometer is not affected by the ETF [7], therefore for a hot-electron TES, one can attain both sensitivite and fast performance in two steps: first, *increasing* the intrinsic response time (≡ increasing the sensitivity) by adjusting the disorder in the film, and, second, *decreasing* the response time again employing the ETF.

III. Electron-Phonon Interaction in Disordered Metals

The electron-phonon interaction in impure metals depends on the material disorder. This fact has not been appreciated by the bolometric community yet, though there is an extensive literature on this subject (see [8,9] for a review). The crucial parameter driving $\tau_{e\text{-}ph}$ is $q\ell$ (q is the phonon wavevector). In very clean metals ($q\ell >> 1$), $\tau_{e\text{-}ph} \sim T^{-3}$. However, at subkelvin temperatures, the opposite limit $q\ell < 1$ takes place even in clean thin films because of the diffusive scattering of electrons at the film surface. In the latter case, $\tau_{e\text{-}ph} \sim T^{-4}l^{-1}$ [10]. In the intermediate range $ql \sim 1$, the temperature dependence is weaker and the disorder dependence is less pronounced [8,11]. Theory [10] agrees well with the most of experimental data (see [8]). Some predictions of the theory are shown in Fig. 2 (more detailed comparison between the theory and experiments can be found in [8,12]). For instance, $\tau_{e\text{-}ph}$ is of the order of 1×10^{-5} s at $T = 0.1$ K in clean Cu films [13]. By introducing disorder, $\tau_{e\text{-}ph}$ can be easily decreased by two orders of magnitude. Similar effects are expected for the other metals, e.g. W and Al (see Fig. 2), which can be interesting for HEB detectors (see below). The control of the electron mean free path can be achieved by making films thinner or/and by irradiating films with high-energy ions [12]. The theory predictions obtained for $\tau_{e\text{-}ph}$ in normal metals, apply to the electron-phonon interaction in the resistive state of a superconducting film due to a large concentration of quasiparticles.

IV. Performance Discussion

Figure 3 shows the performance of HEBs fabricated from superconductors with the critical temperature T_c around 0.1 K (*W, Hf)* as well as for *Al, Ti* and *Cu*, which can be used for fabrication of proximity bi-layers with adjustable T_c [14]. Although the parameters of bi-layer structures (γ and $\tau_{e\text{-}ph}$) are not well known, one can expect that the specific heat would be somewhere in between of those for a normal metal and a superconductor. In principle, the materials with smaller γ offer better sensitivity (see Eq. 1). In this sense, the best materials are semimetals (Bi, Sb) offering an NEP as low as ~ 10^{-22} W√Hz. However, it is clear that even for conventional materials, the controllable adjustment of the electron-phonon time to the required time constant will allow to reach the *NEP* by three to four orders of magnitude lower than the *NEP* of existing ultra-sensitive conventional bolometers.

Conclusion

We have proposed a new type of direct detector based on a hot-electron TES where the electron-phonon relaxation time is adjusted by proper control of the film disorder. It results in a very low NEP which will allow for photon-noise limited performance of the detector from millimeter to infrared wavelengths. A number of superconducting materials are potentially suitable for fabrication of the TES. Tests of new devices will begin soon.

Acknowledgment

Fruitful discussions with A. Kozhevnikov L. Kuzmin, K. Likharev, D. Prober, R. Schoelkopf, and A. Sergeev are greatly appreciated.

References

[1] J.C. Mather, S.H. Moseley, Jr., D. Leisawitz, E. Dwek, P. Hacking, M. Harwit, L.G. Mundy, R.F. Mushotzky, D. Neufeld, D. Spergel, and E.L. Wright, *http://xxx.lanl.gov/abs/astro-ph/9812454*
[2] J.J. Bock, J. Glenn, S.M. Grannan, K.D. Irwin, A.E. Lange, H.G. LeDuc, and A.D. Turner, *SPIE* **3357**, 297 (1998).
[3] M. Nahum and J.M. Martinis, *Appl. Phys. Lett.* **63**, 3075 (1993); A. Vystavkin, D. Chouvaev, L. Kuzmin, M. Tarasov, E. Anderstedt, M. Willander, and T. Claeson, *SPIE* **3465**, 441 (1998).
[4] E.M. Gershenson, M.E. Gershenzon, G.N. Gol'tsman, A.D. Semenov, and A.V. Sergeev, *Sov. Phys.-JETP Lett.* **36**, 297 (1982); *Sov.Phys.-JETP* **59**, 442 (1984); *Solid State Commun.* **50**, 207 (1984).
[5] S. Svechnikov, G. Gol'tsman, B. Voronov, P. Yagoubov, S. Cherednichenko, E. Gershenzon, V. Belitsky, H. Ekström, E. Kollberg, A. Semenov, Yu. Gousev, and K. Renk, *IEEE Trans. Appl. Supercond.* **7**, 3395 (1997).
[6] A.T. Lee, P.L. Richards, S.W. Nam, B. Cabrera, and K.D. Irwin, *Appl. Phys. Lett.* **69**, 1801 (1996).
[7] W.A. Mels, M.P. Bruijn, H.F.C. Hoevers, M. Frericks, F.B. Kiewiet, A.C. Bento, and P.A.J. de Korte, *Proc. SPIE* **3445**, 255 (1998).
[8] N.G. Ptitsina, G.M. Chulkova, K.S. Il'in, A.V. Sergeev, F.S. Pochinkov, E.M. Gershenzon, and M.E. Gershenzon, *Phys. Rev. B* **56**, 10089 (1997).
[9] B.I. Betevtsev, Yu.F. Komnik, and E.Yu. Beliayev, *Phys. Rev. B* **58**, 8079 (1998).
[10] M.Yu. Reizer and A.V. Sergeev, *Sov. Phys. - JETP* **63**, 616 (1986).
[11] B.S. Karasik and A.V. Sergeev, *unpublished.*
[12] K.S. Il'in, N.G. Ptitsina, G.N. Gol'tsman, E.M. Gershenzon, B.S. Karasik, E.V. Pechen and S.I. Krasnosvobodtsev, *Phys. Rev. B* **57**, 23 (1998).
[13] M.L. Roukes, M.R. Freeman, R.S. Germain, R.C. Richardson, and M.B. Ketchen, *Phys. Rev. Lett.* **55**, 422 (1985).
[14] H. Hoevers, *http://www.sron.nl/divisions/srt/*

Noise Temperature of a NbN Hot-Electron Bolometric Mixer at Frequencies from 0.7 THz to 5.2 THz

J. Schubert[1], A. Semenov[2], G. Gol'tsman[2], H.-W. Hübers[1], G. Schwaab[3], B. Voronov[2], E. Gershenzon[2],

[1] DLR Institute of Space Sensor Technology, Rudower Chaussee 5, 12489 Berlin, Germany

[2] Physical Department, State Pedagogical University, 119435 Moscow, Russia

[3] Physical Chemistry Department II, Ruhr University Bochum, 44801 Bochum, Germany

Abstract — We report on noise temperature measurements of a NbN phonon-cooled hot-electron bolometric mixer in the terahertz frequency range. The devices were 3 nm thick films with in-plane dimensions 1.7×0.2 μm² and 0.9×0.2 μm² integrated in a complementary logarithmic spiral antenna. Measurements were performed at seven frequencies ranging from 0.7 THz up to 5.2 THz. The measured DSB noise temperatures are 1500 K (0.7 THz), 2200 K (1.4 THz), 2600 K (1.6 THz), 2900 K (2.5 THz), 4000 K (3.1 THz) 5600 K (4.3 THz) and 8800 K (5.2 THz).

1. Introduction

So far Schottky diodes have commonly been used as mixers in heterodyne receivers at frequencies above 1 THz. The achieved double side-band (DSB) receiver noise temperatures range from 2500 K at 1 THz to about 70000 K at 4.75 THz [1,2]. These numbers are far beyond the quantum noise limit. However, many research and observation goals require a receiver noise temperature close to the quantum limit. Superconducting hot-electron bolometric (HEB) mixers represent a new class of heterodyne detectors that seems to be very prospective in satisfying the above requirements. Here we report an improved design of spiral antenna for HEB mixers and the results of noise temperature measurements performed at seven frequencies from 0.7 THz to 5.2 THz.

II. Mixer Design and Experimental Setup

Devices were fabricated from a 3 nm thick superconducting NbN film; they typically had a transition temperature of about 9.3 K and 870 μΩ·cm resistivity at room temperature. Films were deposited by dc reactive magnetron sputtering of Nb in N_2 atmosphere onto a 350 μm thick high resistivity (5 kΩ·cm) Si substrates. The details of the process are described elsewhere [3].

A planar two-arm logarithmic-spiral antenna is used to couple both the signal and the local oscillator (LO) radiation with the bolometer. The central part of the antenna was patterned using electron beam lithography while the outer part was defined by conventional UV photolithography (for details see Ref. [4]). We developed two types of HEB (A and B) with different sizes of both the NbN bridge and the central part of the antenna (Fig. 1). The circle, inside which the antenna arms formed inner terminals and seized to represent a spiral, has 2.2 μm diameter for type A and 1.3 μm diameter for type B. The diameter of the circle that circumscribed the spiral structure was 130 μm for both types of devices. Between these circles, the antenna arms make 2.15 turns for devices of the type A and 2.45 turns for devices of the type B. The spiral structure terminated a coplanar line with an impedance of 50 Ω, which was lithographed on the same substrate. According to an estimate [5], such an antenna should have rf impedance of about 75 Ω when suspended in free space. We expect an even smaller value for our antenna since it is supported by the semi-infinite dielectric half-space simulated by the substrate with the thickness much larger than the wavelength.

The substrate carrying the HEB and the planar antenna was glued onto the flat side of an extended hyperhemispheric lens. The lens was cut off from an optically polished 6 mm diameter sphere that was made from high resistivity (>10 kΩ cm) silicon. The extension of the lens together with the substrate yields a total extension length of 1.2 mm. This is very close to the optimal extension length for which the beam pattern of the hybrid antenna is diffraction limited.

The lens and the HEB were mounted in a copper holder which in turn was directly screwed to the 4.2 K cold plate of

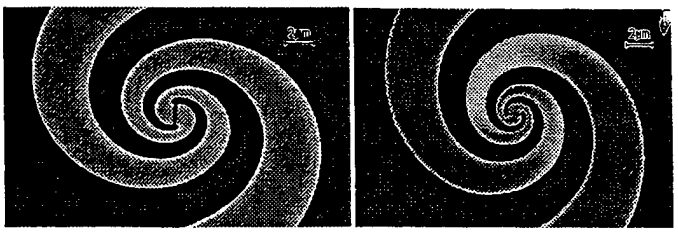

Fig. 1. SEM images of the device A (left panel) and B (right panel).

an Infrared Labs HD-3 LHe cryostat. The cryostat had a wedged 1.5 mm thick TPX pressure window. A 1.2 mm thick quartz window with an antireflection coating was mounted on the 77 K shield. This filter has a cut-off frequency exceeding 6 THz. The intermediate frequency (IF) signal was guided out of the HEB via a 50 Ω flexible coplanar line, which was soldered to SMA connector. A bias tee followed by an isolator was used to feed the bias to the mixer and to transmit the IF signal to a low noise (< 3 K) 1.2 - 1.8 GHz HEMT amplifier (36 dB gain at 1.5 GHz). Bias tee, isolator, and amplifier were also mounted on the cold plate of the cryostat. The output of the amplifier was filtered at 1.5 GHz with a bandwidth of 75 MHz, further amplified, and rectified with a crystal detector.

The noise temperature was measured at seven different frequencies from 0.7 THz to 5.2 THz. As a local oscillator we used an optically pumped FIR ring laser [6] or transversely excited FIR laser [7] for frequencies from 0.7 THz to 2.5 THz and between 2.5 THz and 5.2 THz, respectively. It should be mentioned that the noise temperature measured at 2.52 THz was the same independently on which laser system was used.

Double side-band (DSB) receiver noise temperatures were determined by the Y-factor method. Ecosorb was used as the hot and cold load at temperatures 293 K and 77 K, respectively. At all frequencies above 1 THz we used the general form of the dissipation-fluctuation theorem (Callen and Welton, [8]) for deriving the receiver noise temperature from the measured Y-factor.

III. Noise Temperature

Noise temperatures reported in this paper were measured for a HEB mixer of the type A. Mixers of the type B will be tested soon and the results will be reported at the conference.

Fig. 2 shows current-voltage (I-V) characteristics of the mixer at a temperature of 4.2 K. The device was pumped by the local oscillator operated at 2.52 THz.

The series resistance in the superconducting state is about 3 Ω. There is a first plateau in the unpumped I-V-characteristic at a current of 45 μA that is followed by a second almost linear increase corresponding to a resistance of 40 Ω. Another plateau develops at a current of 55 μA. After the third linear increase, which corresponds to a resistance of 80 Ω, the maximum critical current of 90 μA is reached. The normal resistance of the HEB at the operation temperature was practically the same as at room temperature. This behavior is likely due to the existence of three patches in the superconducting film each with a different critical current. We speculate that two of them are situated under the contact pads. The critical current in those parts is reduced due to the proximity effect between NbN and gold. A tail seen in the resistive transition of the device below the critical temperature likely supports this tentative explanation. Low noise temperatures were usually found at a moderate bias voltage (around 1.8 mV and 22 μA, region 1) corresponding to an almost linear part of the pumped I-V-characteristic. The power of the local oscillator absorbed in the HEB was evaluated from the pumped and unpumped I-V characteristics. We used the isothermal method described elsewhere [9]. In the region 1 an absorbed LO power of about 100 nW was determined at all frequencies.

In Fig. 3 the DSB receiver noise temperature is shown as a function of the LO frequency between 0.7 THz and 5.2 THz. Also shown is the noise temperature corrected for the losses in the optical elements as given in the Table. In this latter case the increase of the noise temperature with frequency is linear and follows closely the 10 hν/k line. The result suggests that the hybrid antenna of the type A is frequency independent from 0.7 THz up to 5.2 THz.

According to the Table the quartz filter and the Si lens make together the major contributions to the total losses. Using a Zitex filter instead of the quartz filter could reduce the noise temperature by about 0.6– 1.4 dB in the frequency range from 0.7 THz to 2.5 THz. Thus, for example, a DSB noise temperature of about 2400 K at 2.5 THz (loss of

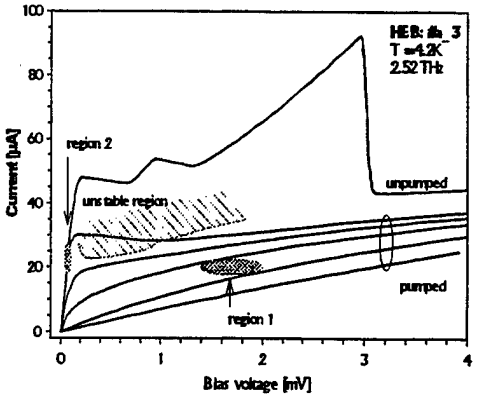

Fig. 2. Current-Voltage characteristics of the mixer at 4.2 K recorded at different powers of the local oscillator.

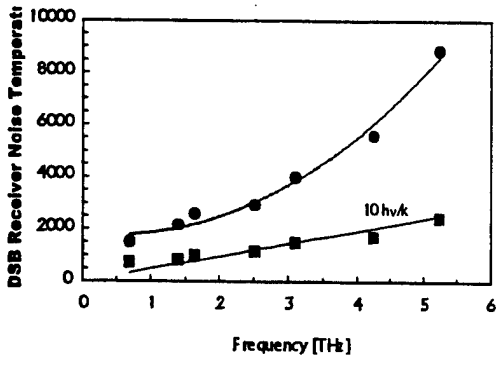

Fig. 3 Noise temperatures calculated via measured Y-factor (upper curve) and corrected for optical losses (lover curve).

LOSSES IN THE OPTICS (DATA FOR THE BEAMSPLITTER ARE CALCULATED, DATA FOR THE TPX WINDOW AND THE QUARTZ FILTER ARE FROM THE TRANSMISSION CURVES AS GIVEN BY THE MANUFACTURER, DATA FOR THE SI LENS ARE ESTIMATED)

	Losses (dB)						
Frequency	0.7 THz	1.4 THz	1.6 THz	2.5 THz	3.1 THz	4.3 THz	5.2 THz
Beamsplitter	0.1	0.2	0.3	0.6	0.7	1.2	1.2
TPX window	0.4	0.4	0.5	0.6	0.6	0.8	0.9
Quartz filter	1.1	1.8	1.9	1.2	1.3	1.5	1.9
Si lens (refl.)	1.5	1.5	1.5	1.5	1.5	1.5	1.5
Si lens (absorp.)	0.1	0.1	0.1	0.1	0.1	0.1	0.1

ZITEX filter ≤0.5 dB [9]) could be achieved. This is comparable with other phonon cooled HEB mixers [10,11] as well as with Nb diffusion cooled HEB mixers [12]. Above this frequency a quartz filter has an advantage. For the reduction of the loss in the Si lens no straightforward solution is available. A way to reduce reflection by use of grooves and separation on the lens surface is discussed in Ref. 13.

IV. Conclusion

We have measured the noise temperature and fluctuation sensitivity of a phonon-cooled hot-electron bolometric mixer operated in the frequency range from 0.7 THz to 5.2 THz. We demonstrated that the superlinear increase of the DSB noise temperature with frequency resulted from frequency dependent losses in coupling optics. When corrected for losses, the noise temperature of the mixer increased linearly with frequency with the slope 10 hν/k, thus suggesting that the hybrid antenna was frequency independent in the specified frequency range.

Acknowledgment

We would like to thank U. Bartels for assistance during measurements and with the mounting of devices.

References

[1] H. P. Röser, H.-W. Hübers, T. W. Crowe, W. C. B. Peatman, *Infrared Phys. Technol.* **35**, 451 (1994).

[2] A. L. Betz, R. T. Boreiko, *Proc. of the 7th Int. Symp. on Space Terahertz Technology,* 503 (1996).

[3] S. Cherednichenko, P Yagoubov, K. Il'in, G. Gol'tsman, E. Gershenzon, *Proc. of the 8th Int. Symp. on Space Terahertz Technology,* 245 (1997).

[4] S. Svechnikov, A. Verevkin, B. Voronov, E. Menschikov, E. Gershenzon, G. Gol'tsman, *Proc. of the 9th Int. Symp. on Space Terahertz Technology,* 45 (1998).

[5] J. D. Kraus, *Antennas*, McGraw-Hill, Inc., (1988).

[6] H.-W. Hübers, G. W. Schwaab, H. P. Röser, *Proc. 30th ESLAB Symp. „Submillimetre and Far-Infrared Space Instrumentation"*, ESA SP-388, 159 (1996).

[7] H.-W. Hübers, L. Töben, H. P. Röser, *Rev. Sci. Instr.* **69**, 290 (1998).

[8] A. R. Kerr, M. J. Feldman, S. K. Pan, *Proc. of the 8th Int. Symp. on Space Terahertz Technology,* 101 (1997).

[9] B. Karasik, M. Gaidis, W. R. McGrath, B. Bumble, H. G. LeDuc, *Proc. of the 8th Int. Symp. on Space Terahertz Technology,* 55 (1997).

[10] P. Yagoubov, M. Kroug, H. Merkel, E. Kollberg, H.-W. Hübers, J. Schubert, G. Gol'tsman, E. Gershenzon, G. Schwaab, *Proc. of the 9th Int. Symp. on Space Terahertz Technology,* Charlottesville, USA (1999).

[11] P. Yagoubov, M. Kroug, H. Merkel, E. Kollberg, J. Schubert, H.-W. Hübers, G. Schwaab, G. Gol'tsman, E. Gershenzon, to appear in *IEEE Trans. on Appl. Superconductivity* (1999).

[12] B. Karasik, M. Gaidis, W. R. McGrath, B. Bumble, H. G. LeDuc, *Appl. Phys. Lett.* **71**, 1567 (1997).

[13] G. Schwaab, H.-W. Hübers, J. Schubert, G. Gol'tsman, A. Semenov, A. Verevkin, S. Cherednichenko, E. Gershenzon, *Proc. of the 9th Int. Symp. on Space Terahertz Technology,* Charlottesville, USA (1999).

Cryogenic Performance of Semiconducting Y-Ba-Cu-O for Infrared Detection

Mahmoud Almasri, Donald P. Butler, and Zeynep Çelik-Butler
Southern Methodist University, Dallas, Texas 75275

Roman Adam and Roman Sobolewski
University of Rochester, Rochester, New York 14627

Abstract–Semiconducting Y-Ba-Cu-O (YBCO) has been demonstrated to be attractive for uncooled infrared (IR) detection acting as either a bolometer or pyroelectric detector. At room temperature, YBCO possesses a relatively high temperature coefficient of resistance -3.5%/K and a high pyroelectric coefficient, up to 20 μC/cm^{2}K. In this work, we report on the cryogenic characterization of semiconducting Y-Ba-Cu-O thin films on substrate in response to 100-fs optical pulses at 810 nm and suspended thin film pixels in response to chopped broadband infrared radiation. The temperature dependence of the zero-bias pyroelectric response of the detectors is reported.

I. Introduction

Semiconducting Y-Ba-Cu-O (YBCO) has been demonstrated to be attractive as a thermal infrared detector operating both as a bolometer[1] and pyroelectric detector [2][3]. In this paper, the pyroelectric behavior of YBCO is investigated at cryogenic temperatures in response to femtosecond optical pulses and chopped broadband infrared radiation.

The thermoelectric behavior of crystalline metallic (x~1) and semiconducting (oxygen deficient, x≤0.5) $YBa_2Cu_3O_{6+x}$ (YBCO) and similar compounds in the normal state [4,5,6,7,8,9,10,11,12,13,14,15], has been studied extensively in recent years. Very recently, thermoelectric behavior has been investigated in amorphous, semiconducting YBCO thin films [16]. The latter studies were motivated by the application of YBCO as an uncooled thermal detector for infrared and other radiation or solar cells. The thermoelectric behavior has been attributed to the pyroelectric effect [5],[16],[17], Seebeck effect [6] and photovoltaic effect [18] in Y-Ba-Cu-O. In addition, piezoelectricity has been reported in Y-Ba-Cu-O. Although, pyroelectricity and piezoelectricity should be forbidden due to the centrosymmetric crystal structure of Y-Ba-Cu-O, Mihailovic and Foster [17] postulated the symmetry to be broken by the coupling of the hole to the apex oxygen of a CuO_2 plane.

II. Background

The pyroelectric effect refers to the temperature dependence of the spontaneous electric polarization resulting in the variation of the surface charge and the associated flow of a pyroelectric current [19]. A voltage results from the pyroelectric current flowing through the equivalent impedance of the detector and amplifier recording the signal.

In the case of chopped or a sinusoidal optical intensity, the voltage responsivity R_v is given by [19]:

$$R_v = \frac{\eta}{C_{th}} \frac{pA}{C} \frac{\omega\tau_e}{\sqrt{1+\omega^2\tau_e^2}} \frac{\tau_{th}}{\sqrt{1+\omega^2\tau_{th}^2}} \qquad (1)$$

where p is the pyroelectric coefficient of the detector material, A is the area of the detector sampling the change in the surface charge, η is the absorptivity, ω is the modulation frequency of the light, τ_e (=RC), is the electrical time constant determined by the equivalent circuit of the detector and preamplifier, and τ_{th} is the thermal time constant of the detector (τ_{th} = C_{th}/G_{th} with thermal mass C_{th} and thermal conductance G_{th} to the substrate). Under pulsed laser illumination with the optical pulse duration much less than both the electrical and thermal time constants, the optical pulse can be approximated as an impulse, yielding the time varying voltage [15]:

$$v_A(t) = \frac{K\tau_e}{\tau_{th}-\tau_e}\left[\exp\left(\frac{-t}{\tau_e}\right) - \exp\left(\frac{-t}{\tau_{th}}\right)\right] \qquad (2)$$

where K = pAηΦ/C_{th}C with Φ as the incident optical power.

III. Experimental Details and Results

The Y-Ba-Cu-O thin films used in these experiments were fabricated by rf magnetron sputtering at ambient temperature. Films deposited in this manner are polycrystalline to amorphous with a typical stoichiometry of 1:0.5:2.2:4.6, as determined by wavelength dispersive electron probe. As deposited, the films exhibit semiconductor-like resistance versus temperature characteristics with a temperature coefficient of resistance of -3 to -4 %K^{-1} and resistivity of 5 to 10 Ωcm.

The pulsed laser experiments employed 200nm thick films deposited on oxidized silicon wafers. Silver (Ag) electrodes were fabricated onto the YBCO film in a microstrip transmission line geometry (100 μm wide) to allow for the propagation of high-speed electrical signals. A 20-μm-wide gap was patterned in the Ag microstrip to allow for optical illumination of the YBCO and form a "photoconductive switch" geometry. However, no bias was used during the measurements. The sample was mounted on a substrate holder providing the conducting ground plane for the microstrip. Aluminum (Al) wires were ultrasonically bonded

Manuscript received 7 May, 1999.
This material is based in part upon work supported by the NSF ECS-9800062 and ARO-38673PH (SMU) and ONR-N00014-98-1-0080 (UR).

to the silver microstrips to provide electrical contact. The substrate holder was mounted on a cold finger in an evacuated cryostat. The voltage response was measured directly with a 400 MHz bandwidth oscilloscope. The sample was illuminated by 100-fs optical pulses at 810 nm with a pulse repetition rate of 1 kHz. The optical intensity was varied with neutral density filters. The optical spot size is estimated to be 20 μm at the sample.

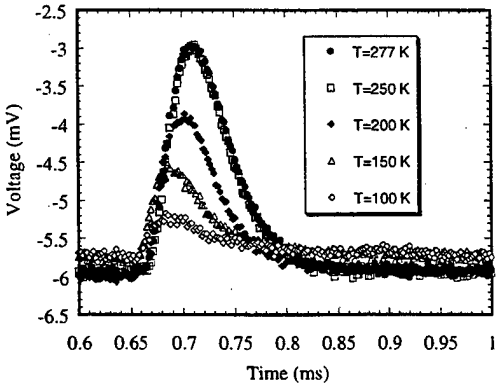

Fig. 1 Unbiased voltage response of YBCO thin film illuminated by 100 fs, 810 nm laser pulses at different temperatures.

Typical unbiased voltage responses from the pulsed laser illumination are shown in Fig. 1. The voltage signal corresponds to the change in voltage across the gap in the microstrip. In this geometry, the Ag microstrips sample the change in the surface charge due to the temperature dependence of the spontaneous polarization. The nature of the voltage response was relatively independent of the location of the excitation. The polarity and general shape of the voltage signal did not depend upon whether the gap was illuminated directly, the silver electrodes were illuminated or the beam was positioned about 100 μm beside the gap and silver microstrips. However, the magnitude of the voltage signal depended upon the position of illumination. We believe that this indicates that the voltage response was thermal in origin, resulting from the heating by the optical pulse. The data was fitted to (2), yielding distinct time constants for the fall and rise of the voltage signal. The rise time-constant was observed to decrease with decreasing temperature while the fall time-constant increased with decreasing temperature. The rise time-constant is interpreted to be the electrical time constant τ_e of the system while the fall time constant is interpreted as the thermal time constant τ_{th}. The temperature dependence of τ_e is observed to obey an Arrhenious relationship $\tau=\tau_o\exp(-E_A/k_BT)$ where E_A=0.025 eV is the activation energy, τ_o is a constant and k_B is Boltzmann's constant. Although, τ_e and τ_{th} had similar magnitudes near room temperature, their magnitudes differed by more than an order of magnitude at 100K. The different temperature dependence indicated that the time constants correspond to intrinsically different processes.

Curiously, in some cases, the fall time constant was observed to change significantly when the sample was also illuminated by a continuous wave incandescent lamp during the laser pulse excitation. As shown in Fig. 2, the relaxation, when illuminated by the lamp, was at least one order of magnitude shorter than when the sample was dark. The dependence of the relaxation rate upon illumination was not present in most samples. The amplitude of the voltage response also displayed a corresponding dependence upon continuous wave illumination as well as the value of the baseline voltage present between pulse excitations. At this time, the mechanism for the reduction in the relaxation time with continuous illumination is not well understood.

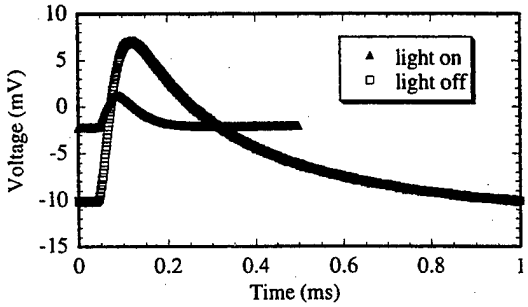

Fig. 2 Voltage response of YBCO at 300 K when illuminated with and without illumination by cw light in addition to 100 fs laser pulses. The average power of the laser pulses was 200 μW.

The energy (power) dependence of the voltage response was also investigated. The time constants were found to be independent of the laser pulse energy. The amplitude of the voltage response depended directly upon the laser pulse energy, increasing with increased energy. The voltage response was observed to saturate in amplitude at large pulse energies (0.6 μJ). The strength of the laser illumination was sufficient to write a visible pattern in the YBCO film. The amplitude of the voltage response diminished over time from continued laser illumination. Illumination by the laser light altered the YBCO film properties.

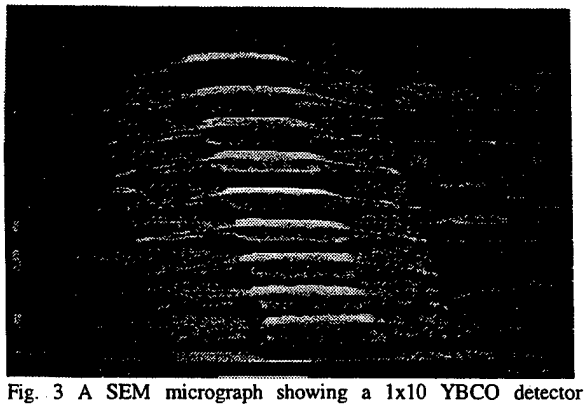

Fig. 3 A SEM micrograph showing a 1x10 YBCO detector array suspended above the substrate. The pixel size is 40 mm x 40 mm.

The YBCO were fabricated into thermal isolation structures by employing silicon (Si) micromachining techniques. Suspending the detector above the substrate, decreases the thermal conductance G, thereby increases the responsivity as predicted by (1). 1×10-detector arrays with

pixels measuring 40 μm × 40 μm were produced. A scanning electron micrograph of the detector array is shown in Fig. 3.

The detectors were fabricated by depositing and patterning Al mirrors on the substrate. The Al mirrors form a resonant cavity with the pixel to enhance optical absorption. A 1.7-μm-thick polyimide mesa was patterned as a sacrificial layer upon which the pixels were fabricated above the Al mirrors. The detector pixels were formed by sequential depositing 400 nm of YBCO and 100 nm of niobium (Nb). The Nb electrodes were patterned by dry etching. The YBCO pixels were patterned by etching with Al-etch 1:20 concentration. The pixels were over-etched removing the YBCO from under the Nb electrode arms. The polyimide was then ashed in an oxygen plasma to remove it from under the pixels and suspend the YBCO film above the substrate.

The completed detectors were wire bonded into a package and mounted in a cryostat for characterization. The detectors were illuminated with chopped broadband infrared radiation covering the spectrum of 0.6 to 12 μm. The voltage response was measured using a PAR 113 amplifier and signal analyzer to determine the corresponding voltage signal and noise levels. The responsivity was calibrated with an Oriel pyroelectric detector.

The unbiased responsivity and detectivity of the YBCO detector is plotted versus temperature in Fig. 4. The chopper frequency was 330 Hz, corresponding to a rate where the responsivity was relatively constant with respect to chopper frequency. The detectivity ($D^*=R_V(A\Delta f)^{1/2}/V_n$) is determined by the area normalized signal-to-noise-ratio where Δf is the bandwidth and V_n is the noise voltage. The data displays relatively constant behavior with decreasing temperature from room temperature to approximately 200 K. From 200 K to 100 K, the detectivity and responsivity decrease dramatically. The responsivity and detectivity appear to level off below 100 K. The decrease in the YBCO detector responsivity can be attributed to an increase in the thermal conductivity of the supporting Nb electrode arms with decreasing temperature and an apparent decrease in the pyroelectric coefficient with decreasing temperature. The latter can also explain the decrease in the voltage amplitude observed in the pulsed laser experiments. Although, the detectivity is near 10^8 $cmHz^{1/2}W^{-1}$ at room temperature, the detectivity falls to 10^6 $cmHz^{1/2}W^{-1}$ at 50 K.

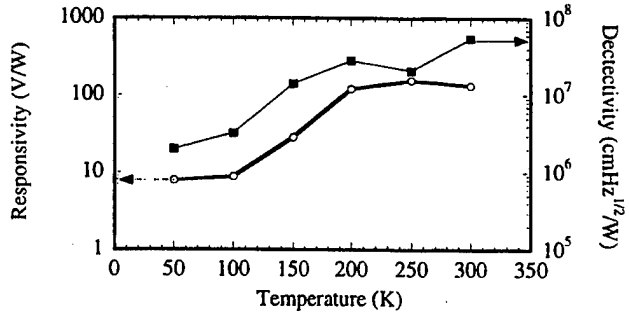

Fig. 4 Temperature dependence of unbiased YBCO responsivity and detectivity in response to broadband IR radiation chopped at 330 Hz.

IV. Discussion and Conclusions

This investigation has demonstrated the semiconducting Y-Ba-Cu-O thin films deposited at ambient temperatures continue to exhibit thermoelectric behavior at cryogenic temperature. The behavior is believed to be pyroelectric in origin [15]. The magnitude of the effect decreases with decreasing temperature. Since the YBCO films were strain poled as deposited, the decrease in responsivity may be attributed to the strain associated with cooling. Other factors such as moving further away from the Curie temperature and changes in thermal conductivity may also be factors. Poling the samples with the application of an electric field may maintain the magnitude of the pyroelectric behavior at low temperatures. The observation of a dependence of the voltage relaxation strongly suggests an electronic role in the thermoelectric behavior of semiconducting YBCO.

Acknowledgment

The authors would like to thank Carlo Williams for his assistance in the laser illumination experiments.

References

[1] A. Jahanzeb, C. M. Travers, Z. Çelik-Butler, D. P. Butler, and S. G. Tan, *IEEE Trans. on Electron Devices* **ED-44**, 1795 (1997).
[2] A. Jahanzeb, C.M. Travers, D.P. Butler, Z. Çelik-Butler, and J.E. Gray, *Appl. Phys. Lett.* **70**, 3495 (1997).
[3] D. P. Butler, Z. Çelik-Butler, A. Jahanzeb, J. E. Gray, and C. M. Travers, *J. of Appl. Phys.* **84**, 1680 (1998).
[4] C. L. Chang, A. Kleinhammers, W. G. Moulton, and L. R. Testardi, *Phys. Rev. B* **41**, 11564 (1990).
[5] D. Mihailovic and A.J. Heeger, *Solid State Commun.* **75**, 319 (1990).
[6] H. Lengfellner, G. Kremb, A. Schnellbögl, J. Betz, K. F. Renk, and W. Prettl, *Appl. Phys. Lett.* **60**, 501 (1992).
[7] D. Mihailovic and I. Poberaj, *Physica C* **185-189**, 781 (1991).
[8] I. Poberaj and D. Mihailovic, *Ferroelectrics* **128**, 197 (1992).
[9] S. Zeuner, W. Prettl, and H. Lengfellner, *Appl. Phys. Lett.* **66**, 1833 (1995).
[10] H. S. Kwok, J. P. Zheng, and S. Y. Dong, *Phys. Rev. B* **43**, 6270 (1991).
[11] A. Palti, V. Svetchnikov, V. Pan, and A. Snarski*J. Appl. Phys.* **77**, 2814 (1995).
[12] A.I. Grachev, I.V. Pleshakov, A.P. Paugurt, and S.G. Shul'man, *Phys. Solid State* **38**, 1598 (1996).
[13] A.I. Grachev and I.V. Pleshakov, *Solid State Commun.* **101**, 507 (1997).
[14] D. Mihailovic, I. Poberaj, and A. Mertelj, *Phys. Rev. B* **48**, 16634 (1993).
[15] D.P. Butler, Z. Celik-Butler, R. Adam, and R. Sobolewski, *J. Appl. Phys.* **85**, 1075 (1999).
[16] J.E. Gray, Z. Celik-Butler, D.P. Butler, and a. Jahanzeb, *Ferroelectrics* **209**, 517 (1998).
[17] D. Mihailovic and C.M. Foster, *Solid State Commun.* **74**, 753 (1990).
[18] J.F. Scott, *Appl. Phys. Lett.* 56, 1914 (1990).
[19] C.M. Hanson, in *Semiconductors and Semimetals* **47**, 123 (1997). Ed. D. Skatrud and P. W. Kruse, Academic Press.

Infrared Hot-Electron NbN Superconducting Photodetectors for Imaging Applications

K. S. Il'in,[1] A. A. Verevkin,[1] G. N. Gol'tsman,[1,2] and Roman Sobolewski[2,*]
[1]Department of Physics, Moscow State Pedagogical University, Moscow 119435, Russia
[2]Department of Electrical and Computer Engineering and Laboratory for Laser Energetics
University of Rochester, Rochester, NY 14627-0231

Abstract—We report on effective quantum efficiency of 340, responsivity >200 A/W (>10^4 V/W), and response time of 27±5 ps at temperatures close to the superconducting transition for NbN superconducting hot-electron photodetectors (HEP's) in the near-infrared and optical range. Our studies were performed on a few-nm-thick NbN films deposited on sapphire substrates and patterned into μm-size multi-bridge detector structures, incorporated into a coplanar transmission line. The time-resolved photoresponse was studied by means of subpicosecond electro-optic sampling with 100-fs-wide laser pulses. The quantum efficiency and responsivity studies of our photodetectors were conducted using an amplitude-modulated infrared beam, fiber-optically coupled to the device. The observed picosecond response time and the very high efficiency and sensitivity of the NbN HEP's, make them an excellent choice for infrared imaging photodetectors and input optical-to-electrical transducers for superconducting digital circuits.

I. Introduction

The quantum efficiency N, responsivity η, and the response time constant τ are the main performance parameters, used for characterizing optical receivers. For modern semiconducting photodetectors, in the visible and near infrared wavelengths, all these parameters can independently (i.e., for different devices) reach the following values: $N = 1$ [1], or up to 100 for avalanche photodiodes [2], $\eta \sim 1$ A/W [1], and $\tau < 0.9$ ps [3]. As the radiation wavelength increases, however, it is becoming progressively more difficult to implement these ultimate characteristics, especially N and η, for semiconducting technology, since the photon energy, even for narrow-gap semiconductors, becomes smaller than the gap itself. For that reason, there are practically no semiconducting photodetectors for a significant and technologically important very-far-infrared (THz) part of the radiation spectrum.

In this work, we report our studies on the optical response of NbN superconducting hot-electron photodetectors (HEP's). We have measured both the electron energy relaxation time and the response sensitivity of high quality 3.5-nm-thick NbN films at the near-infrared and optical wavelengths. The quantum efficiency $N \approx 340$, responsivity $\eta \approx 200$ A/W, and the response time constant $\tau \approx 30$ ps were obtained using the results of our measurements.

Manuscript received May 1, 1999.
*Also at the Institute of Physics, Polish Academy of Sciences, PL-02904 Warsaw, Poland.
This research was supported by the U. S. Office of Naval Research grant N00014-97-1-0696 and the NATO Linkage Grant CRG.LG974662.

II. Experimental

NbN films with a 3.5-nm thickness were deposited on sapphire substrates by reactive dc magnetron sputtering in the Ar+N_2 gas mixture [4]. The largest values of both the critical current density j_c and the transition temperature T_c were achieved at the discharge current of 300 mA, the partial N_2 pressure of 1.1×10^{-4} mbar, and the substrate temperature 850 °C.

The films were patterned into 4-mm-long coplanar waveguide (CPW) structures with a 30-μm-wide central line, separated by 6-μm-wide gaps from the ground planes. The tested HEP's consisted of several parallel, μm-wide strips, located in the middle of the CPW, between the central line and the grounds. Vanadium strips terminated both ends of the CPW to assure 50-Ω output impedance of our device. Typically, after processing, the device exhibited the midpoint of the superconducting transition (definition of T_c) at 10.3 K to 11.7 K range, with <1 K transition width, and $j_c = (1.6–2)\times10^6$ A/cm^2 at 4.2 K. The sheet resistance in the normal state was $R_s \approx 200$ Ω/cm.

The devices were mounted on a copper cold finger inside an exchange-gas, liquid-helium dewar, with optical access through a pair of fused-silica windows. To facilitate electro-optic (EO) measurements the entire waveguide structure was overlaid with an electro-optic $LiTaO_3$ crystal. EO-sampling experimental set-up and the method of transient response measurements of our NbN films are described in detail in [5]. On the other hand, the measurement system, we used to study the response sensitivity of NbN samples to near-infrared radiation ($\lambda = 0.79$ μm), including the signal-detection circuitry, laser-diode bias, fiber-optic beam delivery, and the NbN HEP is presented in [6].

III. Results and Discussion

A. Characterization time determination

A typical response of our HEP, consisting of 25 parallel, 2-μm-wide stripes, measured with the EO-sampling

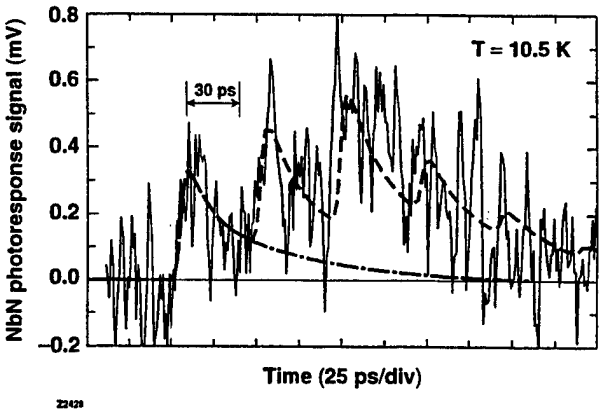

Fig. 1. Time-resolved response of a NbN HEP to a 100-fs optical excitation pulse. Temperature was 10.5 K.

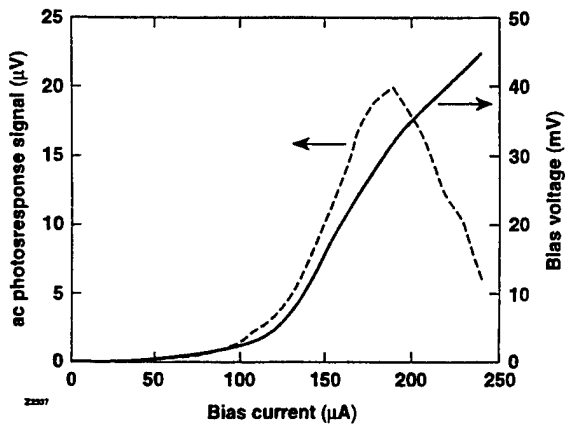

Fig. 2. Photoresponse (dashed line) and *I–V* characteristics (solid line) of a NbN HEP exposed to an ac-modulated 0.79-μm-wavelength radiation. Temperature was 11.4 K.

technique is presented in Fig. 1. We note that the signal (thin solid line) contains a large amount of noise, but it was acquired at low bias current, 175 μA, and at temperature of 10.5 K, just at the superconducting-resistive transition. The dashed-dotted line represents the response of the sample for the single-pulse input, calculated based on the two-temperature (2-T) model [7]. Since the reflection-free time window for our experiments, due to limited length of the CPW and large signal propagation velocity on sapphire, was only about 40 ps, the reflections from the CPW ends contributed to the response measured by the EO sampling and had to be included in simulations. The dashed line in Fig. 1 shows the result of our 2-T model calculations that considered those reflections. The fit allowed us to determine the 30-ps (27±5 ps) effective decay time for NbN HEP, which is given by the time that elapses from the pulse arrival until the magnitude of the response decreases down to $1/e$ from its maximum value (see Fig. 1). We also obtained from the 2-T equations, the inelastic electron-phonon interaction time $\tau_{e\text{-}ph}$ = 10±2 ps. The $\tau_{e\text{-}ph}$ represents the intrinsic response time of the NbN HEP. In [7], we indicated several possible ways to reduce the current experimental 30-ps device response time to the intrinsic 10 ps value.

B. Efficiency and responsivity determination

Figure 2 shows the dependence of the ac measured photoresponse signal on the bias current, $\Delta U(I)$, overlaid with the current–voltage ($I-V$) curve. The device was irradiated with the ac modulated cw light from an infrared (λ = 0.79 μm) laser diode and kept at T = 11.4 K, what corresponded to the superconducting transition, near the maximum value of the dR/dT curve. The data presented in Fig. 2 are for the HEP that consisted of 5 parallel stripes, 6-μm long and 0.6-μm wide. The dependence $\Delta U(I)$ shows that the maximum value of the photoresponse ΔU_{max} = 20 μV is for I = 190 μA, which corresponds to the resistive nonlinear part of the HEP $I-V$ characteristics with differential resistance R_{opt} = 168 Ω. Simultaneously, we have verified that ΔU_{max} also corresponded to the maximum of the dR/dT curve (approximately 250 Ω/K at 11.4 K), calculated from the R vs. T dependence, obtained with the 190 μA current bias.

The power of laser radiation absorbed by the film P_{abs} was estimated according to the following relation:

$$P_{abs} = 4P_1(S_d/S_1)(R_s/Z_0)/[(R_s/Z_0)(n+1)+1]^2, \quad (1)$$

where n is the index of refraction, S_d is the area of the HEP, S_1 is the area of the radiation spot, and Z_0 = 377 Ω is the free-space impedance. Using (1), we can estimate that for P_1 = 0.3 mW incident on the sample, whose response is presented in Fig. 2, $P_{abs} \approx 5.3\times10^{-10}$ W. The absorbed power allowed us to calculate at ΔU_{max}, both the voltage $R = \Delta U_{max}/P_{abs}$ (V/W) and current $\eta = (\Delta U_{max}/R_{opt})/P_{abs}$ (A/W) responsivities, which are $R \approx 4\times10^4$ V/W and $\eta \approx$ 220 A/W, respectively. Please note that the latter value is over two magnitudes higher than the best A/W responsivity obtained by any semiconductor photodetector.

The HEP quantum efficiency can be explained within the simple model of relaxation processes in a thin superconducting film, schematically illustrated in Fig. 3. For the superconducting strip in the resistive state, we observe a viscous vortex flow; thus, we have in the film both the normal (vortex cores) and superconducting (the remaining area) regions. Within the latter, the superconductivity is substantially suppressed, as at T close to T_c the energy gap is very small. Upon absorption of a light quantum by either a normal electron or a Cooper pair, the highly excited electron, with an energy close to the incident photon energy is created (due to the large physical size of a Cooper pair, only one electron absorbs a photon, while the second one becomes a low-energy quasiparticle). Next, this excited (very hot) electron rapidly (on <0.1 ps time scale, according to optical pump–probe experiments [8]) starts to lose its energy via electron–electron scattering and creation of secondary excited electrons. At energies of the order of 0.1 eV (near Debye temperature) the most efficient mechanism for redistribution of energy within the electron subsystem becomes emission of Debye phonons by

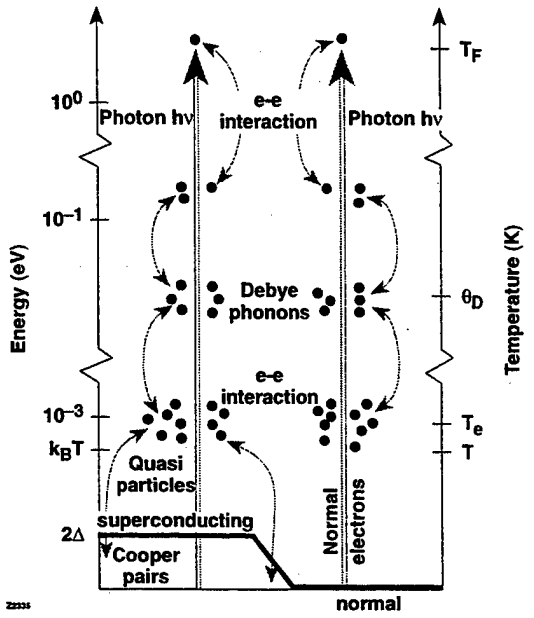

Fig. 3. Schematics of the energy thermalization/relaxation process in a superconducting film in the flux-flow state exposed to optical photons.

electrons. The mean-free path of those phonons is very small, and they efficiently excite additional electrons (break additional Cooper pairs). As the average energy of the electrons in the avalanche decreases to approximately 1 meV ($T \approx 10$ K), their further multiplication due to absorption of phonons is replaced by multiplication due to electron-electron collisions, either in the quasiparticle-quasiparticle, or quasiparticle-Cooper-pair form. At the time moment of the relaxation that corresponds to the thermalization time [$\tau_{et} \sim$ 7 ps for NbN (Ref. 9)] the global T_e, is established somewhat above the sample lattice temperature. Further cooling of the electron subsystem toward the lattice temperature occurs via the electron–phonon interaction by emitting thermal phonons, for which the film is transparent.

Since for ultrathin NbN films the characteristic escape time of nonequilibrium phonons from the film to the substrate τ_{es} is longer than τ_{et} and, simultaneously, is shorter than the time of their reabsorption by electrons $\tau_{ph\text{-}e}$, the whole energy of the light quantum $h\nu$ remains in the electron subsystem, redistributing within it, and contributing to the elevated T_e. Thus, in this case, the multiplication rate of the electrons may reach the low-temperature value $N_q = h\nu/\Delta(0)$, which for the NbN HEP excited with 0.79 μm radiation is $N_q \approx 250$. On the other hand, if we estimate the number of excessive quasiparticles and the quantum efficiency of our samples according to the formula used for semiconductor devices: $N_q = (\Delta N_{max}/R_{opt})h\nu/eP_{abs}$, where e is the electron charge, we get a value of ~340 for the sample shown in Fig. 2. The fact that the latter N_q value exceeds the former value is a simple consequence of the fact that at our operating temperature Δ is substantially suppressed [much smaller than $\Delta(0)$].

IV. Conclusion

In this work, we have demonstrated that NbN HEP's exhibit device responsivity $R \approx 4\times10^4$ V/W or $\eta \approx 220$ A/W, much higher than that for semiconductor photodetectors. Simultaneously, the quantum efficiency reaches 340, demonstrating a very large intrinsic gain of the device. The above parameters show that the NbN HEP's should be able to detect single quanta of far-infrared radiation and successfully compete as single-photon detectors with SIS-tunnel devices. One can also use HEP's as picosecond optoelectronic input transducers for feeding optically coded information into superconducting integrated digital circuits based on the rapid-single-flux-quantum (RSFQ) logic [10]. Thin-film HEP elements, manufactured as planar, microbridge-type structures are only several μm in size and can be easily impedance matched with the input of the RSFQ circuit, as well as coupled to standard, single-mode fibers. Finally, the manufacturing methods of the HEP single-layer-film element are well established [4] and are much less involved than those for multilayer SIS elements.

References

[1] F. E. Ejeckam, C. L. Chua, Z. H. Zhu, Y. H. Lo, M. Hong, and R. Bhat, *Appl. Phys. Lett.*, **67**, 3936, 1995.
[2] D. F. Levine, *J. Appl. Phys.*, **74**, R1, 1993; T. Ikegami, *Proc. of IEEE*, **80**, 411, 1992.
[3] S. Y. Chou, Y. Liu, W. Khalil, T. Y. Hsiang, and S. Alexandrou, *Appl. Phys. Lett.*, **61**, 819, 1992.
[4] P. Yagoubov, G. Gol'tsman, B. Voronov, L. Seidman, V. Siomash, S. Cherednichenko, and E. Gershenzon, Proc. of the 7th Int. Symp. on Space Terahertz Technology, 290, 1996.
[5] M. Lindgren, M. Currie, C. Williams, T. Y. Hsiang, P. M. Fauchet, R. Sobolewski, S. H. Moffat, R. A. Hughes, J. S. Preston, F. A. Hegmann, *IEEE J. Sel. Top. Quantum Electron.* **2**, 668, 1996.
[6] K. S. Il'in, I. I. Milostnaya, A. A. Verevkin, G. N. Gol'tsman, E. M. Gershenzon, R. Sobolewski, *Appl. Phys. Lett.* **73**, 3938, 1998.
[7] A. D. Semenov, R. S. Nebosis, Yu. P. Gousev, M. A. Heusinger, K. F. Renk, *Phys. Rev. B* **52**, 581, 1995.
[8] T. Gong, L. X. Zheng, W. Xiong, W. Kula, Y. Kostoulas, R. Sobolewski, and P. M. Fauchet, *Phys. Rev. B* **47**, 14495, 1993.
[9] K. S. Il'in, M. Lindgren, M. Currie, R. Sobolewski, S. I. Cherednichenko, G. N. Gol'tsman, and E. M. Gershenzon, *Appl. Phys. Lett.* (to be published).
[10] K. K. Likharev and V. K. Semenov, *IEEE Trans. Appl. Supercon.*, **1**, 3, 1991.

Oral Session 8

SQUIDs I

A Radio Frequency Amplifier Based on a Niobium dc SQUID with Microstrip Input Coupling

Michael Mück, Marc-Olivier André and John Clarke
Department of Physics, University of California, Berkeley, CA 94720

Christian Hagmann
MS 414, Lawrence Livermore National Laboratory, Livermore, CA 94550

Jost Gail and Christoph Heiden
Institut für Angewandte Physik der Justus-Liebig-Universität Gießen, 35392 Gießen, Germany

Abstract—We have developed a high frequency amplifier using a dc SQUID in a new configuration in which the input coil of the SQUID is used as a microstrip resonator. By using a coil with an appropriate length, resonant frequencies of 200 MHz to 1 GHz and gains of about 20 dB have been obtained. We measured a minimum noise temperature of 0.12 ± 0.10 K for a frequency of 438 MHz and a bath temperature of 0.5 K. By loading the otherwise open end of the microstrip resonator with a varactor, we were able to reduce the frequency at which the maximum gain occurred by nearly 50 %.

I. Introduction

Certain experiments in fundamental physics, such as axion detectors [1], require preamplifiers with ever-increasing sensitivity. DC SQUIDs are promising sensors to meet these demands. For these devices, the noise temperature continues to decrease linearly with the bath temperature as it is lowered to about 0.1 K [2].

The conventional dc SQUID amplifier consists of two resistively shunted Josephson junctions incorporated into a square washer of inductance L over which is deposited an n-turn superconducting input coil with inductance $L_i \approx n^2 L$. The SQUID is current- and flux-biased so that the flux to voltage transfer function $V_\Phi = \partial V/\partial \Phi$ is close to a maximum. A signal current I_i in the input coil generates a flux $M_i I_i$ in the SQUID and an output voltage $V_0 \approx M_i I_i V_\Phi$ across it; M_i is the mutual inductance between the input coil and the SQUID. We note that in this kind of operation, the amplitude of the input signal is limited to currents which produce flux changes in the SQUID of less than $\Phi_0/4$.

Using a SQUID amplifier with an input circuit tuned to 93 MHz, Hilbert and Clarke [3] achieved a gain of about 18 dB and a noise temperature of about 1.5 K for a bath temperature of 4.2 K. Above 100 MHz, however, parasitic capacitance C_p between the input coil of inductance L_i and the SQUID produced self-resonances and severely reduced the gain.

Manuscript received April 30, 1999. This work is supported by the NSF under Grant No. FD96-00014.

The L_iC_p-parallel resonance can be shifted to higher frequencies by reducing the number of turns, decreasing their width or increasing the thickness of the insulating layer separating the coil from the SQUID. However, reducing the number of turns may reduce the mutual inductance between the coil and the SQUID to a value that is too small to produce a satisfactory gain.

II. A SQUID Amplifier with Microstrip Input Coupling

Recently, we described a new configuration in which the input coil is used as a microstrip resonator [4]. The input signal is no longer coupled to the two ends of the input coil, but rather between one end of the coil and the SQUID loop, which acts as a ground plane for the coil. The microstrip resonator is thus formed by the inductance of the input coil and its ground plane and the capacitance between them. In this configuration, the parasitic capacitance no longer prevents currents from flowing through the coil. The microstrip resonator is analogous to a parallel tuned circuit and, neglecting losses in the microstrip and the SQUID, one calculates a quality factor $Q = \pi Z_{in}/2Z_0$. Here, Z_{in} and Z_0 are the impedance of the source and stripline, respectively. At the resonant frequency the current fed into the resonator is amplified by Q. One selects the resonant frequency by choosing the length of the coil appropriately.

We have fabricated and tested a number of such SQUID amplifiers. We used conventional square-washer SQUIDs in our experiments, with inner and outer dimensions of 0.2 mm × 0.2 mm and 1 mm × 1 mm; the individual turns of the input coil had a width of 5 μm. The SQUID loop and input coil were fabricated from niobium films and separated by a SiO_x film with a thickness $d \approx 400$ nm. The estimated inductance of the SQUID was 320 pH. The critical current and shunt resistance per junction were typically 5 μA and 10 Ω, and the maximum value of V_Φ was about 60 $\mu V/\Phi_0$.

To measure the gain of such amplifiers, we supplied the necessary current and flux biases by batteries that could be floated relative to the system ground. The bias flux was generated by a copper coil. It was necessary to use a cold attenu-

ator of about 20 dB to prevent noise produced by the room temperature signal generator from saturating the SQUID. The attenuator also presented an impedance of 50 Ω to both the input coaxial line and the microstrip. This impedance matching largely eliminated standing waves on the coaxial line, and also helped to minimize errors in the measured gain due to impedance mismatch. For the same reasons, a cold 4 dB attenuator coupled the output of the SQUID to a low noise (80 K) preamplifier at room temperature. The gain of the system excluding the SQUID was calibrated by disconnecting the SQUID and connecting together the input and output attenuators. All measurements of the gain of the SQUID amplifier were referred to the baseline so obtained.

Since the conventional washer SQUID is an asymmetric device (the two Josephson junctions are situated close together rather than on opposite sides of the SQUID loop), one can either ground the washer or ground the counter electrode close to the Josephson junctions. Using the washer as ground plane for the input coil suggests one should ground the washer. However, it is also possible to ground the counter electrode and have the washer at output potential. In this case, depending on the sign of V_Φ, one can obtain either a negative or positive feedback from the output to the input. This is shown in Fig. 1, where we plot the measured gain of a SQUID amplifier with a 6-turn input coil as a function of frequency. The input signal was connected between the innermost turn of the coil and ground. When we grounded the washer, we measured a gain of about 14 dB at 635 MHz, with a Q of about 10. On the other hand, when we grounded the counter electrode of the junctions and allowed the square washer to float at output potential, for the sign of the transfer function which we denote as V_Φ^+, the gain increased to 18 dB at 620 MHz and the Q increased to about 31. Conversely, for the other sign of the transfer function, V_Φ^-, the gain is greatly diminished with no evidence of a resonance.

To achieve the maximum possible gain, we mostly operated our SQUID amplifiers with the counter electrode grounded and the washer at output potential. When we measured the gain as a function of frequency, for SQUIDs with 31-turn coils with a total length of 71 mm we obtained a resonant frequency of about 200 MHz. To achieve higher resonant frequencies, we used SQUIDs with shorter coils (see Fig. 2).

We measured the noise temperature T_N of the SQUID amplifier by connecting a 64 Ω resistor to the input of the SQUID. We could raise the temperature of this resistor by passing a current through a manganin wire wound tightly around it. By comparing the noise powers at the output of the SQUID with the input resistor at 4.2 K and at 10 K we could estimate T_N. At 4.2 K the noise temperatures of such amplifiers ranged from 0.5 ± 0.3 K at 80 MHz to 1.6 ± 1.2 K at 1 GHz; in the latter case, a postamplifier contribution of

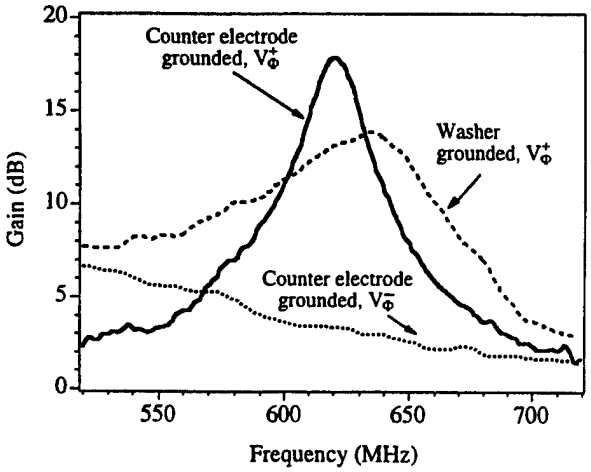

FIG. 1 Gain of a SQUID amplifier with a 6-turn input coil as a function of frequency. The input signal was connected between the innermost turn of the coil and ground.

2.5 ± 1.5 K has been subtracted. Since, at least for low frequencies, it has been shown that the noise temperature continues to decrease linearly as the bath temperature is lowered to 0.1 K [2], one expects the noise temperature of these amplifiers to decrease as well for bath temperatures lower than 4.2 K.

In order to reduce the contribution of the semiconductor postamplifier to the system noise, we built a single-stage cryogenic amplifier using a heterostructure field effect transistor (HFET). The noise temperature of these HFET postamplifiers was about 4 K at 90 MHz and 15 K at 440 MHz. When we cooled our SQUID amplifiers to 1.8 K and used the HFET postamplifier, we achieved a system noise temperature of 0.30 ± 0.05 K for a SQUID amplifier at 250 MHz, and 0.28 ± 0.06 K for another one at 365 MHz.

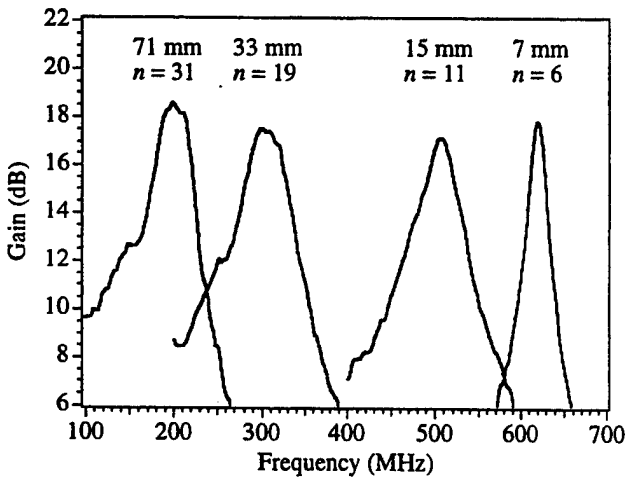

FIG. 2 Gain vs. frequency for four different coil lengths, with signal applied to the innermost turn. Data are for counter electrode grounded and V_Φ^+.

To achieve an even lower noise temperature, we cooled the SQUIDs to 0.4 - 0.5 K using a closed-cycle ^{3}He cryostat. The HFET postamplifier was mounted on the 1 K pot of the system and kept to about 1.8 K during the measurements. In this configuration, it was no longer possible to use a resistor at different temperatures as a noise source as in the previous experiments. Instead, we measured the signal-to-noise ratio of the system with a precisely calibrated signal power (–134 dBm) applied to the input of the SQUID. To compensate for possible errors introduced by the detector and the IF filter of the spectrum analyser, we calibrated the system using several semiconductor amplifiers with accurately measured noise temperatures.

The noise temperature of 0.10 ± 0.02 K measured at 90 MHz contained a noise contribution from the HFET postamplifier of about 0.04 K. In the case of a 438 MHz SQUID, the contribution by the postamplifier (0.38 ± 0.07 K) was subtracted from the measured system noise (0.50 ± 0.07 K) to obtain an intrinsic noise temperature for the SQUID of 0.12 ± 0.10 K.

III. Increasing the Bandwidth of a SQUID Amplifier by Varactor Tuning

The high gain and low noise temperature make the SQUID amplifier attractive for a number of applications. However, the limited bandwidth of the device may be somewhat disadvantageous. Although for a given device the bandwidth over which the gain exceeds a certain value, say 15 dB, is typically 50 MHz to 100 MHz, the gain falls off rapidly outside this range.

The resonant frequency of a transmission line resonator can be changed by terminating the normally open end by a reactive load, for example a capacitor. By making the capacitance variable, in principle, one can reduce the resonant frequency with zero capacitance to one-half its value (infinite capacitance). It is convenient to use a varactor or capacitance diode as the variable capacitor. The capacitance is determined by the depletion layer, the thickness of which can be changed by varying the reverse voltage of the diode. Since the diode has to be close to the SQUID and thus at its operating temperature, one has to use a GaAs, rather than an Si device. In Fig. 3 we plot the gain of a SQUID amplifier vs frequency for different static voltages applied to a varactor at one end of the microstrip resonator. The frequency at which the amplifier has maximum gain can be tuned from 195 MHz down to 117 MHz. The resonant frequency without the varactor was about 205 MHz. Over this tuning range, the gain varies by no more than 1 dB. We have made noise measurements at 4.2 K with and without the varactor, but have found no noticable difference in the noise temperature of the amplifier.

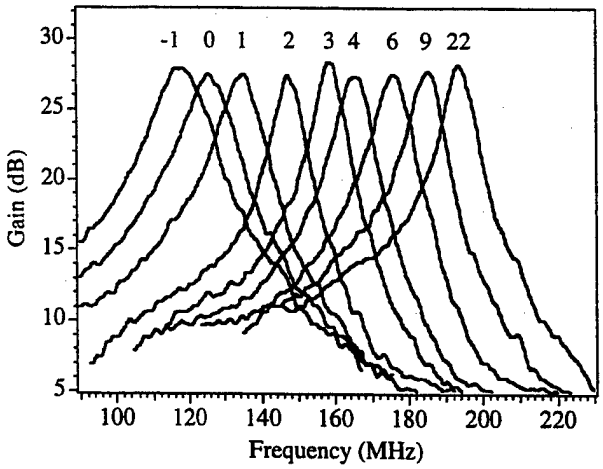

FIG. 3 Gain of a SQUID amplifier vs frequency for different static voltages applied to a varactor at one end of the microstrip resonator.

IV. Conclusion

We have demonstrated a novel SQUID amplifier in which the signal is coupled via a microstrip resonator. For a bath temperature of 4.2 K and a room temperature postamplifier, we achieved gains of about 20 dB and amplifier noise temperatures of between 0.5 K and 1.6 K for resonant frequencies of 100 MHz to 1000 MHz, respectively. For a bath temperature of 0.4 – 0.5 K and a cooled postamplifier, the noise temperature was reduced to about 0.1 K. The resonant frequency of these amplifiers could be varied substantially by terminating the otherwise open end of the microstrip resonator with a varactor diode. There was no noticable contribution of the varactor at least at operating temperatures of 4.2 K. Finally, we anticipate that these SQUID amplifiers operated at dilution refrigerator temperatures with a second SQUID as a postamplifier will be quantum limited.

Acknowledgments

The authors are indebted to L. Rosenberg and K. van Bibber for their ongoing encouragement, and to X. Meng for technical support. This work was supported by the National Science Foundation under grant number FD96-00014.

References

[1] C. Hagmann, D. Kinion, W. Stoeffl, K. van Bibber, E. Daw, H. Peng, L. J. Rosenberg, J. La Veigne, P. Sikivie, N. S. Sullivan, D. B. Tanner, F. Nezrick, M. S. Turner, D. M. Moltz, J. Powell, and N. A. Golubev, Phys. Rev. Lett. **80**, 2043 (1998).

[2] F. C. Wellstood, C. Urbina, and J. Clarke, Phys. Rev. B **49**, 5942 (1994).

[3] C. Hilbert and J. Clarke, J. Low Temp. Phys. **61**, 237 (1985).

[4] M. Mück, M.-O. André, John Clarke, J. Gail, and C. Heiden, Appl. Phys. Lett. **72**, 2885 (1998).

A Radiofrequency dc SQUID Amplifier with a Microstrip Input Coil: Simulations and Experiment

Michael A. Tarasov
Institute of Radio Engineering and Electronics, Russian Academy of Sciences, 103907 Moscow, Russia

Alexey S. Kalabukhov, Oleg. V. Snigirev
Department of Physics Moscow State University, 119899 Moscow, Russia

Sergey I. Krasnosvobodtsev
Lebedev Institute of Physics, Russian Academy of Sciences, 117924 Moscow, Russia

Evgueni A. Stepantsov
Institute of Crystallography, Russian Academy of Sciences, 117333 Moscow, Russia

Abstract — A radiofrequency amplifier based on a HTS dc SQUID with a microstrip-type input coil has been studied. A realistic model provided reasonable fit to known experimental results has been developed. The possibility to realize amplifier in well-established bicrystal dc SQUID technology has been demonstrated. Together with a thin film HTS input filter such an amplifier can be used in the base stations of the mobile communication systems, in the RSFQ circuits, and as a low-noise intermediate frequency amplifier in the microwave cryogenic heterodyne receivers.

I. Introduction

An effective matching of the microwave signal to a SQUID loop is one of the main problems arising in the design and implementation of the HTS dc SQUID rf amplifier. The several approaches are known to couple a low-inductance, low size SQUID loop with the relatively high 50 Ω convention impedance of the signal source.

One of the first approaches was realized [1] in the low -Tc (LTS) dc SQUIDs fabricated in so called Ketchen-Jaycox topology [2] where a multi-turn input coil was placed above the wide washer-type SQUID loop. Another matching method is to use a multi-turn loop which consists of several sections connected in parallel [3].

Both methods have strong frequency limitation due to the large capacity between the input coil and the SQUID loop and, besides, they require a complicated multilayer technology with many vias and interlayer connections that is difficult to realize with HTS.

An elegant method was suggested and realized recently in [4] where the input coil was used as a microstrip resonator. The input signal was applied not to the two ends of the spiral coil fabricated above the LTS dc SQUID washer, but between the one end of the coil and the SQUID washer, which became the groundplane in this case. Contrary to the Ketchen-Jaycox layout the spiral coil in such device can be even open-circuit at one end, that strongly simplifies fabrication technology and gives a possibility to realize the radiofrequency amplifier based on the HTS dc SQUID.

Using the approach developed in [4] we try to extend it on the HTS material basis and to investigate the signal coupling mechanism, not absolutely clear till present. The first results obtained in this work are presented in the report.

II. Circuit Layout and Model

The layout of the designed dc SQUID with integrated microstrip input coil (MISQUID) was determined by the compatibility with the conventional bicrystal HTS dc SQUID technology (see Fig. 1). The square washer of the SQUID had 300×300 μm^2 and 60×60 μm^2 outer and inner dimensions. The slot in the washer had 130 μm length and 10 μm width. The Josephson junctions had 2 - 4 μm width and were formed on the bicrystal boundary of the symmetric YSZ substrate with a misorientation angle equal to 32° or 36°. Film of Y-ZrO_2 with thickness $d \approx 150$ nm was used as an insulator between the YBCO washer and the input coil.

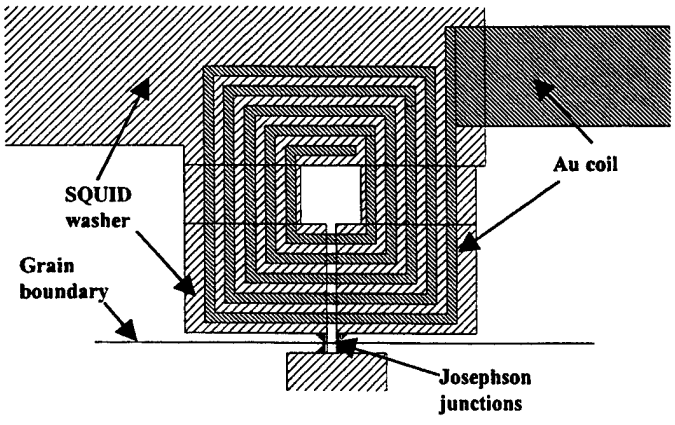

Fig. 1. Layout of the MISQUID with input spiral planar coil that is fed in microstrip mode.

Manuscript received April 30, 1999. This work was supported in part by the INTAS foundation under grants No. 97-731 and No. 96-268, the Russian Scientific Council on Superconductivity under grant "*Signal*".

The 4 - 9-turn input coils were included in design and can be patterned in Au layer with thickness $t \approx 150$ nm and a width $w \approx 10$ μm. Two amplifiers can be placed on 5×5 mm^2 substrate.

For signal frequency of our interest 1- 2 GHz the details of the coupling can be studied using an equivalent lumped circuit shown in Fig. 2. The origin of such circuit follows from the next. The each turn of the microstrip line contents two parts. The first is a regular one over the washer and the second, peculiar, is part over the slot.

The regular part of microstrip line with specific inductance L_O and capacitance C_O per unit length is presented in Fig. 2 by inductance L_R and capacitance C_R in each turn-section. In the region over the slot a mirror-reflected return current in the ground plane have to split in the two parallel paths. The first part of the current flows around the SQUID central hole with the path inductance of the order of the SQUID inductance L. The second flowing around the slot passes two Josephson junctions in series. As a result, the slot inductance L_S connected in series with resistor R equal to $2R_n$ appears in parallel to the inductance L. Here R_n is the Josephson junction resistance. To complete the equivalent circuit it is necessary to add to the right end the resistor representing the free-space impedance R_O. Of cause, the inductance and capacitance change from section to section but in this paper we neglect this circumstance and the corresponding effect.

We can estimate the specific parameters to be $L_O \approx \mu_0 \times (\lambda + d + t)/w \approx 100$ nH/m and $C_O \approx \varepsilon\varepsilon_0 w/d \approx 4$ nF/m; here, $\lambda \approx 170$ nm is the penetration depth of YBCO at 77 K and $\varepsilon \approx 6$ the dielectric constant of amorphous Y - ZrO_2 film [5]. The estimated inductance of the SQUID loop including the inductance of a slot was about 170 pH. All other parameters of the equivalent circuit can be easily determined from the amplifier layout.

The results of numerical calculation for $n = 4$ turn input coil are presented in Fig. 3. One can find high enough real part of the impedance of about 50 Ω at the signal frequencies of interest, so the amplifier can be directly connected to the usual signal source or cable. The positive imaginary part allows to estimate the maximum input inductance of the coil at level close to $2n(L_R + L)$.

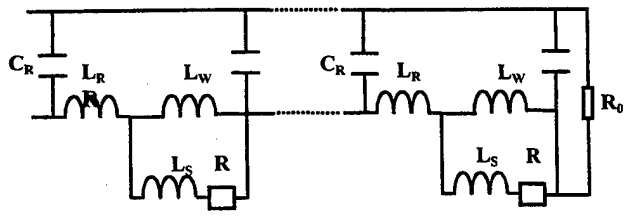

Fig. 2. The equivalent circuit of the MISQUID input coil. The inductance L_R and capacitance C_R represent the regular part of the microstrip line in the chosen turn, L is about the hole-part of the SQUID inductance, L_S is inductance of a piece of slot line, R is resistance of the two JJ connected in series, resistor R_O to the right represents a free-space impedance.

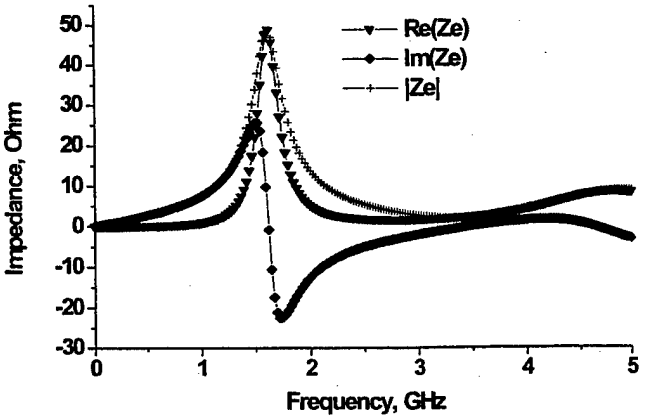

Fig. 3. Real part, imaginary part and total impedance of designed transformer calculated for 4 turn input coil, 200 nm insulator thickness.

The main feature of the equivalent circuit - the current decrease versus turn's number beginning the input allows to estimate mutual inductance between input coil and SQUID as $nL/2$.

III. Experimental

High-Tc SQUIDs were made on 5×5 mm^2 (100) bicrystal YSZ substrates with 32° and 36° misorientation angles. All substrates were tested using atomic-force microscope (AFM) and X-ray methods. Typical AFM image of YSZ substrate with YBCO film is shown in Fig. 4. This technique lets us to control both surface roughness and bicrystal boundary quality of the substrates.

The 200 nm thick $YBa_2Cu_3O_{7-\delta}$ films were grown by the conventional pulsed laser deposition technique.

Electromagnetic properties of HTC films were examined by measurements of temperature dependencies of magnetic susceptibility and electrical conductivity, which revealed high critical temperatures equal to 90 K. X-ray analysis showed that films had predominantly c-axis orientation with less than 0.5% a,b-axis component. A standard photolithography method with consequence wet-etching in 0.1% HNO_3 was used to pattern the SQUIDs. Bicrystal single junctions of 4 μm width revealed high I_cRn products about 90÷150 μV at 77 K. Critical current exists up to 87÷89 K.

The integrated input spiral microstrip coil was made from gold. 100÷200 nm thick amorphous Y-ZrO_2 film was used as an isolator between the input coil and the SQUID washer. The insulation layer was deposited by pulsed laser ablation at room temperature and 0.1÷0.2 mbar oxygen pressure. A lot of work was dedicated to avoid the shorts in circuits and the degradation of the YBCO film.

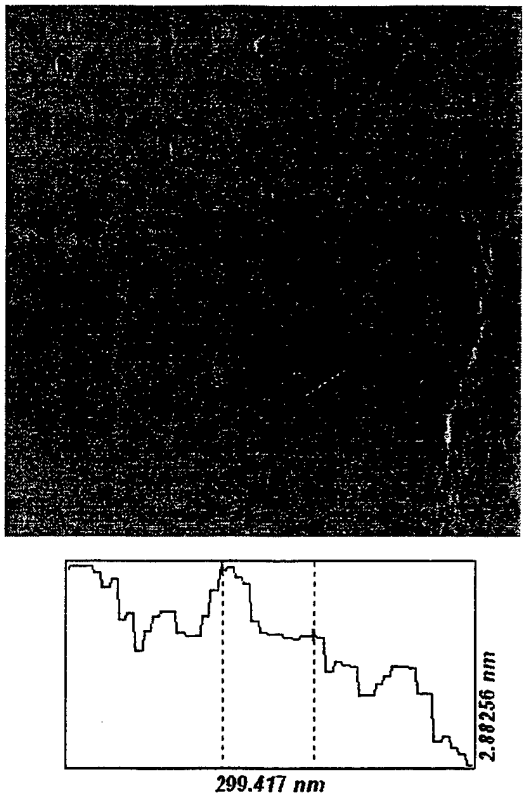

Fig. 4. The AFM image of YSZ bicrystal substrate after patterning of SQUID structure (upper picture) and cross section of the local area (at bottom).

The dc SQUIDs made on 36° bicrystal substrates had critical current *Ic*, normal resistance *Rn* and modulation depth ΔV in the ranges of 15÷30 μA, 1.5÷3 Ohm and 20÷25 μV at 77 K, respectively. Noise measurements performed for the dc SQUIDs on 36° substrates revealed flux noise level of 1.5÷2 $\mu\Phi_0/Hz^{1/2}$ at 1 kHz.

The SQUIDs fabricated on 32° YSZ substrates had high values of *IcRn* product (up to 150 μV), but very low modulation depth (less than 5 μV).

DISCUSSION

We have presented a model of microstrip input circuit coupling for radiofrequency amplifier based on a dc SQUID. In the simplest version developed model gives the good fit to the experimental results found in [4] and allows to explain experimentally measured parameters.

To perform the additional check of the equivalent circuit we made 100:1 scale model that was made using two-side copper plated 0.2 mm thick fiberglass sheet. The 5×5 cm^2 scaled circuit corresponds to 100 times enlarged 500×500 μm^2 device. The difference was in the dielectric that was 1000 times thick instead of 100 compared to our 200 nm isolating layer. The calculated resonance frequency was found close to measured, but Q-factor differ 3-5 times.

The concept of microstrip input coil brings possibility to realize dc SQUID rf amplifier with nonsophisticated available HTS technology based on laser ablation deposition on bicrystal substrates. Natural for buffer layer ZrO2 insulator and Au input spiral coil does not degrade the SQUID parameters and allow to achieve required amplifier parameters, e.g. frequency, bandwidth, gain. Such amplifier can have various areas of application. The HTS SQUID amplifier together with HTS input filter can be used as a single-channel input amplifier at base station for mobile communications, significantly increasing the area covered by such station.

The MISQUID both HTS and LTS can be used as interface between RSFQ circuit and external circuits. Besides MISQUID can be promising candidate as IF amplifier in HTS heterodyne receivers. In all these applications the cryogenic cooling is already presented and cold SQUID amplifier is natural element to improve performance margins of these devices.

ACKNOWLEDGMENT

The authors are thankful to I.A. Yaminsky and S.N. Polyakov for AFM and X-ray tests. .

REFERENCES

[1] C. Hilbert and J. Clarke, "DC SQUIDs as Radiofrequency Amplifiers", *Journal of Low Temp. Phys.*, vol. 61, Nos. 3/4, 1985.

[2] M.B.Ketchen, J.M.Jaycox, "Ultra-low-noise tunnel junction dc SQUID with tightly coupled planar input coil", *Appl. Phys. Lett.*, vol. 40, N 8, pp.736-738, 1982.

[3] M.W. Cromar, P. Carelli, " ", Appl. Phys. Lett., vol. 38, pp. 723 –725, (1981)

[4] M.Mueck, M-O. Andre, J. Clarke, J. Gail, C. Heiden, "Radiofrequency amplifier based on a niobium dc SQUID with microstrip input coupling",*Appl. Phys. Lett.*, vol. 72, pp. 2885 - 2887, June 1998.

[5] Yu.A. Boikov, Ioffe Physical-Technical Institute, St. Petersburg, Personal communication, 1998.

A new family of low-T_c multiloop SQUIDs

D. Drung, S. Knappe, C. Aßmann, M. Peters, K. Wenzel, and Th. Schurig
Physikalisch-Technische Bundesanstalt, D-10587 Berlin, Germany

Recently, we have developed a new theoretical description for magnetic coupling, effective area, and inductance of SQUID sensors. This theoretical basis was used to design a family of improved low-T_c multiloop SQUIDs with outer pickup coil dimensions of 1.5 mm to 7 mm, effective areas of 0.2 mm^2 to 4.5 mm^2, and SQUID inductances of 100 pH to 420 pH, respectively. Each SQUID contains an integrated feedback coil, additional positive feedback (APF) coil, bias current feedback (BCF) coil, various damping resistors, and filter capacitors. Two of the devices are realized with an integrated 0.47 μH or 1.1 μH input coil „wound" around the pickup coil in order to minimize the capacitance between input coil and SQUID. Good agreement between theoretical prediction and experiment is obtained, e.g., deviations of typically below 1 % for the effective areas and the input coil mutual inductances, and of a few % for the feedback coil mutual inductances were found. At T = 4.2 K, white noise levels down to 9 fT/√Hz, 3 fT/√Hz, and 1 fT/√Hz have been achieved for 1.6 mm, 3.4 mm, and 7 mm pickup coils, respectively, including read-out electronics noise. For the devices with input coil, *coupled* energy sensitivities below 200 h (h = Planck´s constant) have been measured. The 1/f noise corner typically occurs at a few Hz. Our new devices are intended for use in a biomagnetic 304-channel system, nondestructive semiconductor wafer inspection, magnetic relaxation immuno assay, and nuclear magnetic resonance (NMR) experiments.

*Partially supported by the Commission of the European Communities under grant No. SMT4-CT95-2014.

Direct read out flux locked loop circuit with automatic tuning of bias current and bias flux for high Tc SQUID

Tetsuya Hirano, Tatsuoki Nagaishi, and Hideo Itozaki
Itami Research Laboratories, Sumitomo Electric Industries, Ltd.
1-1, Koya-kita 1-chome, Itami, 664-0016 Japan

Abstract—Measurement of high frequency magnetic signals has been required from some SQUID applications. We fabricated a high Tc SQUID magnetic sensor system that can treat high frequency signals. This system is composed of a SQUID, a preamplifier circuit, a flux locked loop circuit with I/O and a personal computer and a PC card. We used the FLL circuit with no-modulation to treat the high frequency signal and to simplify the circuit. This system can treat a signal from DC to 1MHz. All the sequence from tuning the SQUID to data acquisition can be done by personal computer. This system successfully realized easy operation of SQUID measurement.

I. Introduction

The progress of development in high Tc SQUID applications indicates the feasibility of the variety of fields such as nondestructive evaluation, biomagnetism and geographical exploration. The direct readout FLL circuit was developed by Drung et al. [1] It has the advantages of simplify of circuit and the high frequency response. This kind of circuit is attractive for the industrial applications such as diagnosis of electric cable insulation [2] and inspection of integrated circuit. [3] We developed a direct readout FLL circuit with automatic adjustment of circuit parameters for the high Tc SQUIDs. This system can also acquire the data and analyze it by the personal computer. Easy operation is essential for the non-professional use of the SQUID and it will encourage the spread of SQUID applications.

II. FLL Circuit

A FLL circuit with no-modulation was used in our system to treat high frequency signals, and simplify the electronics unit. Fig. 1. shows the over view of the FFL circuit. An additional positive feedback (APF) coil and a resistance Ra is connected to the SQUID.[1] A small change of the magnetic flux in the SQUID produces the change of voltage, and the voltage produce the additional flux by the current through the APF coil, so that the flux-to-voltage transfer coefficient increases. For FFL circuit with no-modulation, increasing the flux-to-voltage transfer coefficient makes the system noise decrease and the sensitivity increase. Since SQUID output current to the preamplifier is so weak as noise comes in, a preamplifier was separated from the main electronics in order to minimize the cable length between SQUID and preamplifier. The signal that amplified by preamprifier is connected to main amplifier a integrator, and fed to feedback coil, so flux in the SQUID is kept zero. This circuit has a bias current supplier, and an oscillator for tuning the SQUID. These elements are controlled by the computer. And we used the step edge type SQUID made from $HoBa_2Cu_3O_{7-X}$ on a $SrTiO_3$ substrate. The washer size is 5x5mm. Table. 1. shows the performance of the SQUID. The SQUID was mounted on the chip carrier made from epoxy resin. The chip carrier includes feedback coil and additional positive feed back circuit. Fig. 2. shows the view of the SQUID on the chip carrier. We used an APF circuit to increase the flux-to-voltage transfer coefficient to increase the sensitivity. The APF circuit is consist of coil and resistance. The APF coil is settled under the SQUID chip. We used a 11mm×11mm spiral coil of 50 turn.

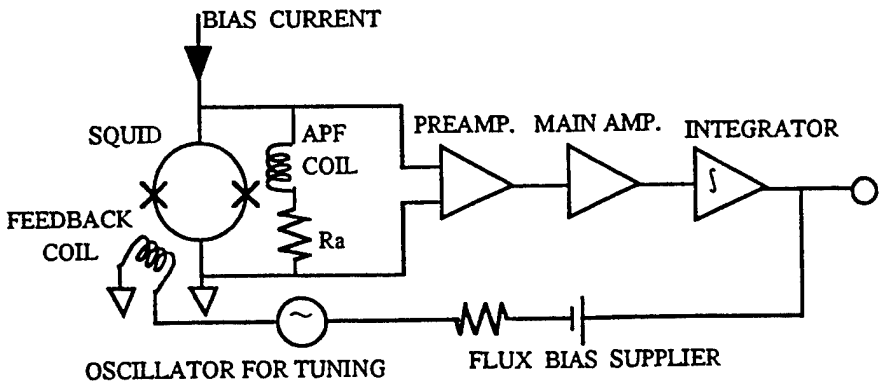

Fig. 1. FFL circuit without modulation

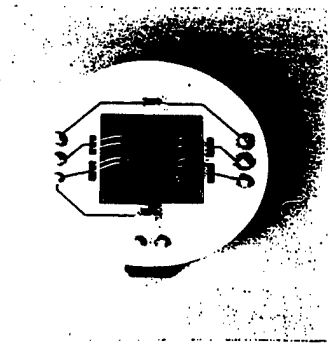

Fig. 2. The overview of SQUID on the chipcarrier

Table 1. SQUID Preparation

Material	$HoBa_2Cu_3O_{7-X}$
Washer size	5x5mm
Hole size	5x100um
Josephson junction	step edge type
Effective area	$0.08mm^2$
Magnetic field resolution	400 $fT/Hz^{1/2}$ (1kHz)

III. Tuning Sequence

The FLL circuit was fully controlled by personal computer. The bias current was determined to maximize the output voltage of the SQUID. Fig. 3(a). shows the sequence for bias current sequence. The flux that applied by the oscillator is $\phi_0/2$, where $\phi_0 = 2\times10^{-15}$ Wb. The frequency of the oscillator for tuning is 1kHz, and voltage output signal is connected to filter that only 1kHz and 2kHz signals can pass. Under such a condition, the frequency elements of voltage signal of the SQUID is flux frequency and its double. The bias current is controlled to maximize the filtered signal. Then flux bias is controlled to find the point of the highest flux-to-voltage transfer coefficient in the flux-voltage curve. The sequence is showed in Fig. 3(b). The frequency of oscillator for tuning is 1kHz, and the voltage output signal is connected to the filter that only 1kHz signals can pass. The flux bias is controlled to maximize the filtered signal. After these process, the tuning of SQUID is finished and we can measure the magnetic signals. If we use the FLL circuit with modulation, the circuit and the sequence are more complicate.

IV. Results

At first we optimize the APF circuit to obtain the largest flux-to-voltage transfer coefficient. The current at the APF coil is controlled by the APF resistance Ra. The flux-to-voltage transfer coefficient gets higher as the APF current increases. But as Ra decrease to increase the APF current, output voltage of the SQUID decrease. So that maximum point of the flux-to-voltage transfer coefficient had to find. Fig. 4. shows the change of flux-voltage curve by using the APF circuit. Fig. 5. shows the flux-to-voltage transfer coefficient for each APF resistance. In the case of our SQUID, Ra=5 Ω shows best performance.

A notebooktype personal computer and an A/D PC card was used for control, display and acquire the magnetic signals. The software includes analysis of the signals, such as FFT, digital filtering. We achieved SQUID sequence and data processing by one personal computer. Fig. 6. shows the frequency performance for high frequency magnetic signal. The high frequency response of the FLL circuit with 40kHz modulation was below 1kHz, but this system can measure 1MHz magnetic signal in analog output. Table. 2 shows the performance of the system. Easy operation and high frequency measurement realized.

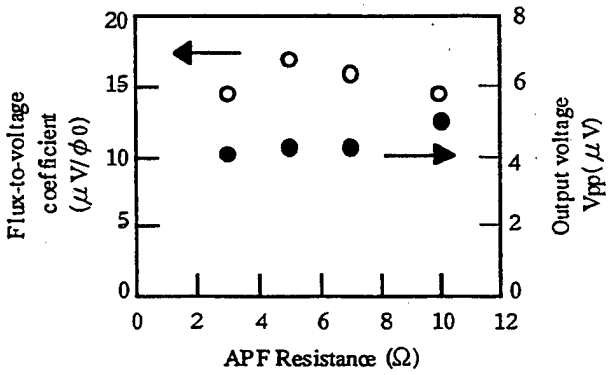

Fig. 5. Flux-to-voltage coefficient and SQUID output voltage for change of APF resistance

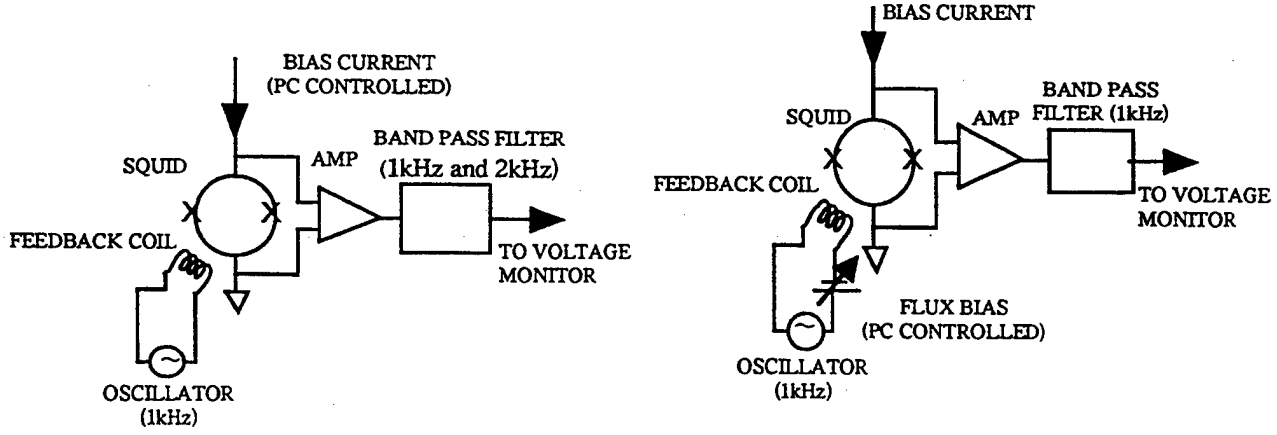

(a) Bias current tuning (b) Flux bias tuning

Fig. 3. Sequence of tuning of bias current and flux bias

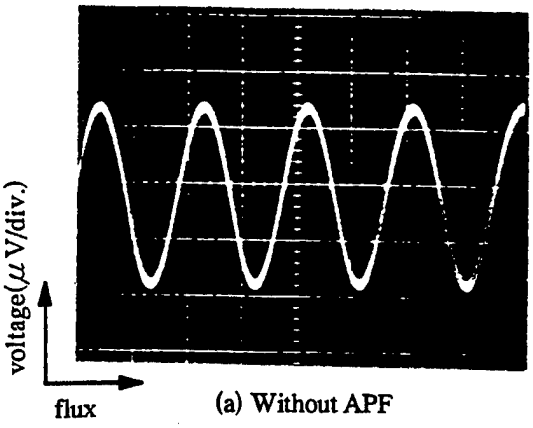

(a) Without APF

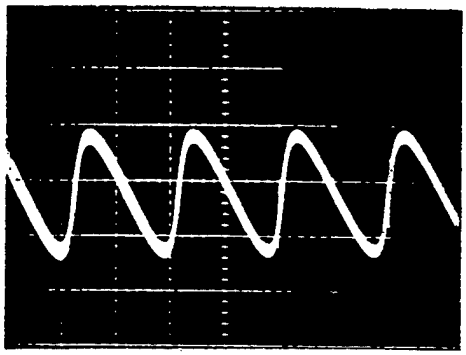

(b) Ra=5Ω

Fig. 4. Change of flux-voltage curve of SQUID

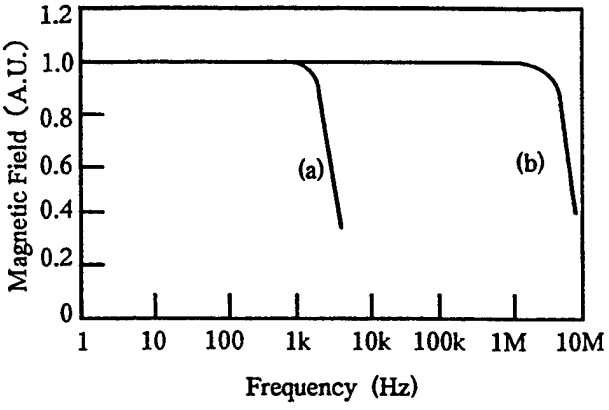

Fig. 6. Frequency response of the system
(a) FLL circuit with 40kHz modulation
(b) FLL circuit with no-modulation

Table 2. Performance of the system

Magnetic field resolution	400 fT/Hz$^{1/2}$ (1kHz)
Dynamic range	1pT~5nT
Frequency performance	DC~1MHz(analog output) DC~100kHz (computer processing)
Soft ware	Automatical tuning Real time signal display Data acquisition (text file) FFT analysis Digital filtering

V. Conclusion

We discussed about a direct readout FLL circuit and an APF circuit to obtain wide frequency performance, and measurements of magnetic signal 1MHz. Using PC sequence of the bias current and flux bias is automatically tuned, and data acquisition and analysis could done. In this system, we can use SQUID without an oscilloscope or a recorder for tuning and data acquisition.

The system works successfully and easy operation of SQUID measurement has been realized. Such a system is attractive for industries and encourage the spread of SQUID applications.

Acknowledgment

The authors would like thank T. Mizoguchi for his assistance in the experiments.

References

[1] D. Drug, D Dancer, F. Ludwig, H. Koch, R. Kleiner, J. Clarke, S. Krey, D. Reimer, B. David, and O. Doessel, "Low noise $YBa_2Cu_3O_{7-x}$ SQUID magnetometers operated with additional positive feedback", Appl. Phys. Lett. 68 (13), 25 pp.1856.

[2] S. Tanaka and K. Inadomi, "Diagnosis of electric cable insulation by High Tc SQUID", to be published in IEEE Transactions on Applied Superconductivity in 1999.

[3] A. Braginski, "Application of High-Tc SQUID Magnetometers to Nondestructive Evaluation and Geomagnetic Exploration", to be published in Proc. 11th ISS, Fukuoka, Japan.

High-Frequency Characterization of DC SQUID Series Array Amplifiers Incorporating Intracoil Damping

Patricia A. Neil, Robert G. Benson, Deborah A. Burns, Alan M. Corey, Christopher S. Flynn, and Martin E. Huber
University of Colorado at Denver, Denver, CO 80217 USA

Abstract—We report on high-frequency (1 – 100 MHz) characteristics of 100-element dc SQUID (Superconducting Quantum Interference Device) Series Array Amplifiers incorporating intracoil damping. Each SQUID is individually modulated by an eight-turn signal coil and a single-turn feedback coil. The signal coils are connected together in series, as are the feedback coils, in order to modulate all SQUIDs in the array simultaneously. With 0.25 Ω/turn intracoil damping on the signal coil, the voltage-flux transfer characteristics are free of significant resonance distortions. Use of PdAu resistors allows operation at temperatures as low as 50 mK. The total input inductance of the array is 160 nH. At the optimal operating point, these devices have a transresistance of 200 V/A, equivalent current noise as low as 3 pA/√Hz at 4 K, and a 30 MHz bandwidth. S-parameter measurements are presented for a range of operating points; the bandwidth is limited by a resonance at 33 MHz, which is present under all operating conditions.

I. Introduction

We have fabricated a 100-element dc SQUID (Superconducting Quantum Interference Device) series array amplifier (SSAA) with negligible distortions in its current-to-voltage transfer function. The transfer function is also stable and reproducible over multiple cooling cycles. This SSAA has an equivalent input current sensitivity of 3 pA/√Hz, a 30 MHz bandwidth, and operates down to 50 mK. Taken together, these properties make the SSAA ideal for use as a high-speed, low-noise preamplifier in multi-channel microcalorimetric particle and/or photon detectors [1]-[3]. In part, these characteristics have been obtained through the use of intracoil damping [4], [5], implemented by placing a resistive damping element across each turn of the signal coil. Here, we describe in detail the features of this device, as well as others of similar design.

II. Design and Fabrication

As originally developed by Welty & Martinis [6], SSAAs consisted of a tightly coupled array of dc SQUIDs surrounded by a common flux-focusing washer and a common coupling coil. We use a number of new features to improve the device characteristics, motivated by the assumption that the distortions in the transfer function are caused by rf resonances (as proposed by [7] for individual SQUIDs). These features include use of an individual washer, signal coil, and feedback coil for each SQUID, intracoil damping, and electrically isolated washers.

We use SQUIDs with individual washers and coupling coils to reduce coupling of high-frequency Josephson currents between adjacent SQUIDs; each of these elements is connected in series with like elements of other SQUIDs (Fig. 1). We also use 0.25 Ω/turn intracoil damping on the 8-turn input, or signal, coil. Our feedback coil consists of a single turn and is damped with a single 1.25 Ω resistor. We use the notation of Fig. 1b as a simplified schematic representation of the SSAAs. In individual SQUIDs, the washer is electrically isolated from the SQUID body. Although this design does result in slightly reduced coupling efficiency, it also results in a significantly improved transfer function. The junction shunt resistance is 1.5 Ω. The inductance of each SQUID L_{sq} = 18 pH, and the design values for β_L [= $2I_0L/\Phi_0$, where I_0 is the junction critical current and $\Phi_0 = h/2e$ is the flux quantum] and β_c [= $2\pi I_0R^2C/\Phi_0$, where R = 1.5 Ω and C ≈ 1 pF are the junction resistance and capacitance] are 0.8 and 0.2, respectively. The maximum critical current of each SQUID is 90 μA. The total (array) self inductance of our signal coil is 160 nH and the mutual inductance between the signal coil and the SQUID is 80 pH.

The devices are fabricated using Nb/AlO_x/Nb trilayer Josephson junctions, PdAu resistors, SiO_2 interlayers, and Nb

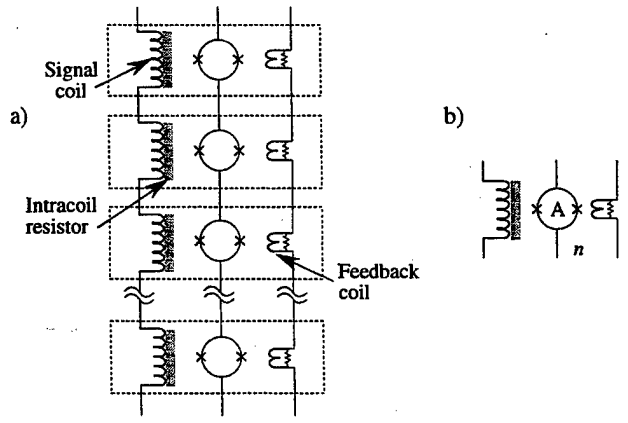

Fig.1 a) Schematic of dc SQUID Series Array Amplifier. The shaded bar in contact with the signal coil represents the intracoil damping resistors. b) Simplified notation to represent a series array amplifier without the need for multiple, individual SQUIDs. The "A" distinguishes the array from a single SQUID, and the "n" is the number of SQUIDs in the array.

Manuscript received April 30, 1999
This work was supported in part by the US Office of Naval Research under Grant No. N00014-97-1-0143.

wiring in a process described in detail in [8]. PdAu resistors, unlike Mo resistors, do not become superconducting at low temperatures; hence, operation at temperatures as low as 50 mK has been achieved [9].

For all measurements, the die containing the array is mounted in a flip-chip printed circuit board. Different configurations are used depending on the measurement.

III. DC Properties

In this section, we present current-to-voltage transfer functions of our devices, demonstrating the effect of the intracoil damping described above. Individual SQUIDs are essentially ideal with intracoil damping (not shown) and manifest only slight distortions in devices without intracoil damping (Fig. 2a). However, the transfer function of an array of 100 dc SQUIDs is highly distorted and hysteretic without damping (Fig. 2b). The transfer function is greatly improved with intracoil damping of 0.25 ohms/turn (Fig. 2c). In the device with optimum transfer function, there is only a 12% variation in amplitude over a range of approximately 35 periods, indicating a high degree of uniformity among the SQUIDs. The total amplitude is 90% of that expected from an ideal 100-SQUID array.

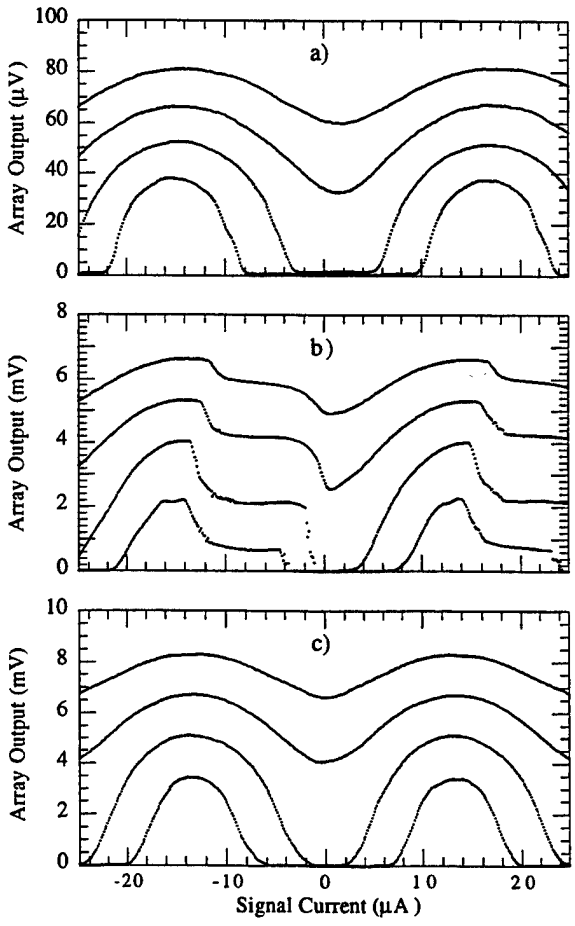

Fig. 2. SQUID transfer functions. a) The undamped single SQUID is relatively ideal but still exhibits minor resonances. b) The undamped 100 series array is seriously distorted. c) The 100 series array, with intracoil damping, is greatly improved. Note that the shape of c) is the same as that of a), indicating nearly ideal operation.

IV. Noise Properties

The device noise was measured in the range 1 – 100 kHz using the configuration shown in Fig. 3. The noise at 10 kHz was measured for various bias conditions (Fig. 4a). The noise peaks noticeably at bias points with residual resonances. A plot of the minimum spectral density of the equivalent input current noise is shown (Fig. 4b). The noise is greater for

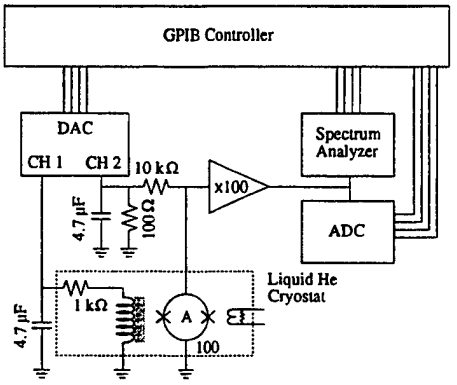

Fig. 3. Noise measurement schematic. A two channel Digital to Analog Converter (DAC) supplies the biasing currents for the SQUID array and the signal coil. The output of the array is amplified by a X100 pre-amplifier before being read by both a spectrum analyzer and Analog to Digital Converter (ADC). Capacitors filter the DAC output to reduce noise.

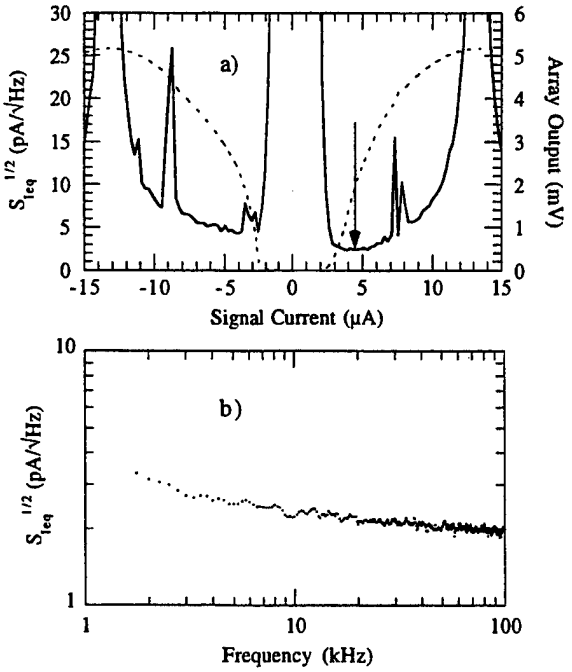

Fig. 4. a) Spectral Density of Equivalent Input Noise (S_{Ieq}) measurements of 100 series array, overlayed by array's current to voltage transfer function. Spikes in the noise are due to residual resonances, causing a slight variation in transresistance. b) Noise measurements over 1 to 100 kHz range, biased at point of lowest noise, noted by arrow above.

devices with greater damping (lower intracoil resistance), but the dependence is not yet quantified.

V. Frequency Response

The frequency response of the arrays was measured using a network analyzer with S-parameter capability over the range 1 – 100 MHz (Fig. 5). With no applied bias current, there is a resonance in transmission (S_{21}) at 33 MHz (Fig. 6a) for signals input both to the signal coil and to the SQUID bias (output) line. The resonant frequency changes only minimally with the number of SQUIDs in the array, and is present for all bias points in its operating state. We also measured the frequency response at various points along the dc transfer function. Two points of interest are also shown, from regions of opposite slope on the dc transfer function. One is chosen at a value of bias conditions to emphasize an additional resonance at 16 MHz (Fig. 6b), which we presume is due to positive voltage-current feedback [7]; however, we have not yet modeled this behavior. The other point of interest is the point of maximum transresistance (Fig. 6c), which would typically be used as the operating point. At the point of maximum transresistance, the resonance appears as a dip in gain of approximately 4 dB. Beyond 33 MHz, the transmission rises slightly (~2 dB) and does not cut off by 100 MHz.

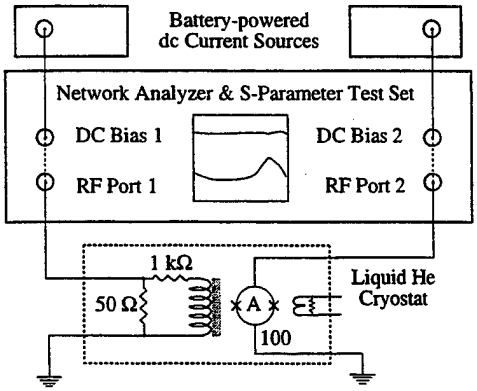

Fig. 5. High Frequency Measurement Setup. Two battery powered dc current sources supply biasing currents through the two DC Bias Ports of the Network Analyzer. The signal coil and SQUID bias line are connected to the RF Ports 1 and 2, respectively, which are 50 Ω terminations.

V. Summary

We are able to fabricate SSAAs free of significant resonance distortions through de-coupling of the washer from the SQUID body, use of intracoil damping, and appropriate device spacing. We find that the device sensitivity is lowest for the lightly dampedcoils, with an equivalent input current

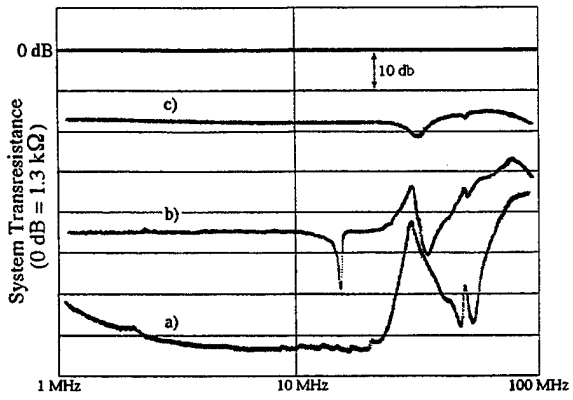

Fig. 6. Trasmission parameter S_{21} of 100 element SSAA. a) With no bias current to either port. b) Biased at a point of positive voltage-current feedback to emphasize resonance at 16 MHz [not a point of maximum transresistance] c) Biased at the point of maximum transresistance. The curves have *not* been offset.

noise of 3 pA/√Hz. The device bandwidth is limited by resonances at 33 MHz. We are in the process of modeling the system to understandthese resonances.

Acknowledgment

The authors thank John M. Martinis and Gene C. Hilton (NIST, Boulder)for useful discussions regardingthis work.

References

[1] R. W. Schnee, D. S. Akerib, P. D. Barnes Jr., D. A. Bauer, P. L. Brink, B. Cabrera, D. O. Caldwell, R. M. Clarke, P. Colling, M. B. Crisler, A. Da Silva, A. K. Davies, B. L. Doughetry, S. Eichblatt, K. D. Irwin, R. J. Gaitskell, S. R. Golwala, E. E. Haller, J. Jochum, W. B. Knowlton, V. Kuzminov, S. W. Nam, V. Novikov, M. J. Penn, T. A. Perera, R. R. Ross, B. Sadoulet, T. Schutt, A. Smith, A. H. Sonnenschein, A. L. Spadafora, W. K. Stockwell, S. Yellin, and B. A. Young, "Results and status of the cryogenic dark matter search (CDMS)," *Physics Reports*, vol. 307, pp. 283-290, 1998.

[2] D. A. Wollman, K. D. Irwin, G. C. Hilton, L. L. Dulcie, D. E. Newbury, and J. M. Martinis, " High-resolution, energy-dispersive microcalorimeter spectrometer for x-ray microanalysis," *J. Microscopy*, vol. 188, pp. 196-223, 1997.

[3] J. A. Chervenak, K. D. Irwin, E. N. Grossman, J. M. Martinis, C. D. Reintsema, and M. E. Huber, "Superconducting multiplexer for large format arrays of transition edge sensors," unpublished.

[4] R. H. Ono, J. A. Koch, A. Steinbach, M. E. Huber, and M. W. Cromar, "Tightly coupled dc SQUIDs with resonance damping," *IEEE Trans. Appl. Supercond.*, vol. 7, pp. 2538-2541, 1997.

[5] M. E. Huber, A. M. Corey, K. L. Lumpkins, F. N. Nafe, J. O. Rantschler, G. C Hilton, J. M. Martinis, and A. H. Steinbach, "DC SQUID series arrays with intracoil damping to reduce resonance distortions," *Applied Superconductivity*, vol. 5, pp. 425-429, 1998.

[6] R. P. Welty and J. M. Martinis, "A series array of DC SQUIDs," *IEEE Trans. Magn.*, vol. 27, pp. 2924-2926, 1991.

[7] K. Enpuku, T. Maruo, and T. Minotani, " Resonant characteristics of high T_c DC SQUID caused by large dielectric constant of $SrTiO_3$," *IEEE Trans. Appl. Supercond.*, vol. 7, pp. 3355-3358, 1997.

[8] J. E. Sauvageau, C. J. Burroughs, P. A. A. Booi, M. W. Cromar, S. P. Benz, and J. A. Koch, "Superconducting integrated circuit fabrication with low temperature ECR-based PECVD SiO_2 dielectric films," *IEEE Trans. Appl. Supercond.*, vol. 5, pp. 2303-2309, 1995.

[9] K. D. Irwin, National Institute of Standards and Technology, Boulder, CO, private communication

Shapiro-Step SQUIDs — Theory and Experiments

Boris Chesca [+,▽], Stefan Weiss[*], Knut Barthel[+], Dieter Koelle[*,+], A.I. Braginski[+], and R. Gross[*]
[+]Forschungszentrum Jülich, Institut für Schicht- und Ionentechnik, D-52425 Jülich, Germany,
[▽]Exp. Phys. VI, Center for Electronic Correlations and Magnetism, University of Augsburg, D-86135 Augsburg, Germany
[*] II. Physikalisches Institut, Universität zu Köln, Zülpicher Str. 77, D-50937, Germany

Abstract—The effect of thermal noise on the I-V curves of a microwave irradiated dc SQUID is analyzed in detail in the frame of an analytical approach based on the 2D Fokker-Planck equation. As an application of the present analysis a new type of SQUID is introduced, in the following denoted as the Shapiro-step SQUID. In contrast to all other known types of SQUIDs, the Shapiro-step SQUID operation is based on simultaneous ac and dc current biasing resulting in the appearance of Shapiro steps in the I-V curves of a dc SQUID. The preliminary experimental results performed on high T_c bicrystal junction Shapiro-step SQUIDs confirm some of the theoretical predictions.

I. Introduction

In [1] on the basis of a 2 D Fokker-Planck equation the I-V curves (IVCs) of a microwave (MW) irradiated dc SQUID operating under the influence of thermal fluctuations has been obtained in the form:

$$i^* = v^* + \frac{\theta^2}{4} e^{-\alpha} \sum_{n=-\infty}^{\infty} \frac{J_n^2(i_1)(n+v^*)}{(\alpha\rho)^2+(n+v^*)^2} \times\left[\left(e^{-\alpha}+S_{nv-}\right)\cos 2\phi_x + \left(e^{\alpha}-S_{nv+}\right)\right] \quad (1a)$$

with

$$S_{nv\pm}(\alpha,\rho,v^*) = \sum_{m=0}^{\infty} \frac{(\pm\alpha)^m}{m!} \frac{\alpha(\alpha+m+1)\rho^2-(n+v^*)^2}{(\alpha+m+1)^2\rho^2+(n+v^*)^2}. \quad (1b)$$

Here, $V = v^*\Phi_0\omega/2\pi$ is the average dc voltage developed across the SQUID, $i^* = \theta I/2I_c$, I is the dc bias current, $\theta = \omega_c/\omega$, $\omega_c = 2\pi RI_c/\Phi_0$ is the characteristic frequency of the two Josephson junctions (with I_c and R the critical current and the shunt resistance of the junctions, respectively, and Φ_0 the flux quanta), ω is the MW frequency, $\rho = 2R/\omega L$, $\alpha = L/4L_F$, L is the SQUID inductance, $L_F = (\Phi_0/2\pi)^2/k_BT$ is the so-called fluctuation threshold inductance (with k_B the Boltzmann constant and T the absolute temperature; L_F= 100 pH at T=77 K), $i_1 = \theta I_1/2I_c$ (I_1 is the amplitude of the MW current), $\phi_x = \pi\Phi_x/\Phi_0$ (Φ_x is the low frequency applied flux to be measured), and J_n are the Bessel functions of the first kind.

In the absence of MW radiation (i_1=0) we have $J_n(i_1)$=0 for all n≠0 and J_0 (i_1)=1. Then, by elementary calculations (1) allow us to obtain all the important dc SQUID characteristics, namely the IVCs, the dynamic resistance $R_{dyn} = \partial V/\partial I$, the transfer function $\partial V/\partial\Phi_x$, and the energy sensitivity $\varepsilon = 2k_BTR/L(\partial V/\partial\Phi_x)^2$, even for large values of the noise parameter $\Gamma = 2\pi k_BT/I_c\Phi_0$, i.e. Γ>1. As shown in Sec. II, in the presence of MW radiation similar calculations (for details see [1]) can be performed to characterize the operation of a new type of SQUID denoted as the Shapiro-step SQUID.

II. Shapiro-step SQUIDs

A. Theory

It is well known that constant-voltage Shapiro steps due to the ac Josephson effect appear in the IVCs, when a MW current I_1 is applied to a dc SQUID biased with a dc current I. The Shapiro steps appear at voltages given by $V_n = n\Phi_0\omega/2\pi$, where n is an integer indexing the step number. Equations (1) give us the analytical expression for the IVCs in the presence of thermal fluctuations for the non-adiabatic regime (namely for $\omega \geq \omega_c$) and for all SQUID inductances of practical interest. This includes values of L comparable to the fluctuation threshold inductance L_F =100 pH at 77 K. In the absence of thermal fluctuations (Γ=0), this case has been theoretically considered by means of numerical simulations in [2].

Recently, the impact of an increase of the SQUID inductance up to or even above the fluctuation threshold inductance on the non-linearity of the system due to the dc Josephson effect has been investigated in detail (see [3] for rf SQUIDs and [4]-[8] for dc SQUIDs). In those papers it has been found that the non-linearity of both types of SQUIDs is strongly suppressed, if L/L_F is increased well above unity. Therefore, it is important to explore conceptually new SQUID configurations and to clarify whether or not the performance of such SQUIDs at larger inductances is improved compared to traditional systems. Such an attempt is presented in the following, where a dc SQUID is MW irradiated. It is shown that the presence of MW irradiation changes the dynamics of the system substantially because of the appearance of the Shapiro steps. For that reason the new

Manuscript received April 30, 1999.
This work was supported in part by the Deutsche Forschungsgemeinschaft and the BMBF (project no. 13N6918/1).
[▽] Present address.

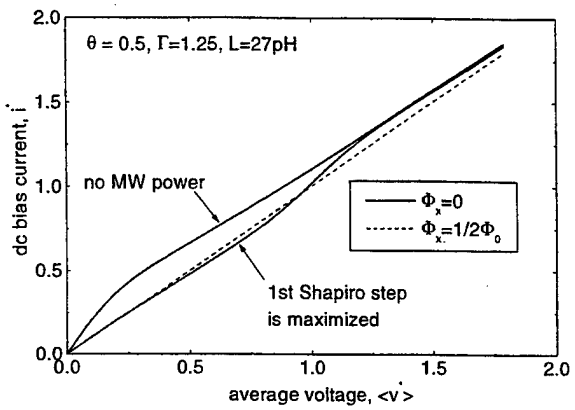

Fig.1(a) Calculated IVCs (in normalized units) of a dc SQUID in the absence of MW power and for a MW power level that maximizes the first Shapiro step. The IVCs for $\Phi_x=\Phi_0/2$ (dashed line) do not depend on MW power.

type of SQUID is denoted as the Shapiro-step SQUID.

The IVCs given by (1) in the presence or absence of MW power and for two particular values of the applied magnetic flux are shown in Fig.1(a). Differentiating (1a) yields the dynamic resistance $R_{dyn} = \partial V / \partial I = R / 2(\partial i^* / \partial v^*)$. In Fig.1(b), R_{dyn} (normalized to R/2) is plotted versus the dc bias current for two different values of the applied magnetic flux. In Fig.1(c) the dynamic resistance is shown as a function of the applied MW current amplitude again for two different values of the applied flux. The curves have been calculated for two different values of the normalized dc bias current $i^*=0$ and $i^*=1$.

It is evident that the Shapiro step is modulated by the applied magnetic flux in the same way as the non-linearity due to the dc Josephson effect of the IVC of a dc SQUID which is obtained without MW irradiation. That is, in the presence of MW irradiation the dc output voltage of the SQUID is also sensitive to flux changes, if the SQUID is dc current biased just on a Shapiro step. For that reason the

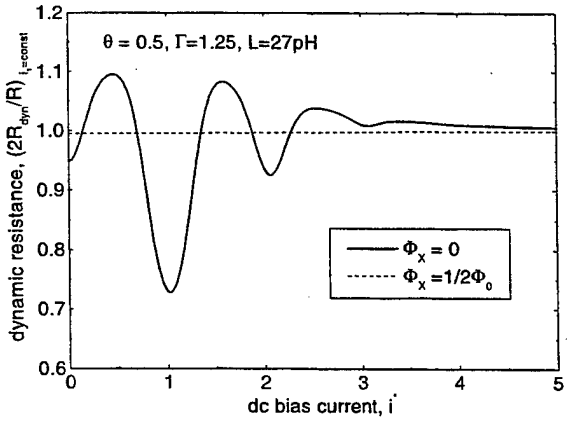

Fig.1(b) Calculated normalized dynamic resistance vs. dc bias current for a dc SQUID irradiated with a MW power that maximizes the 1st Shapiro step.

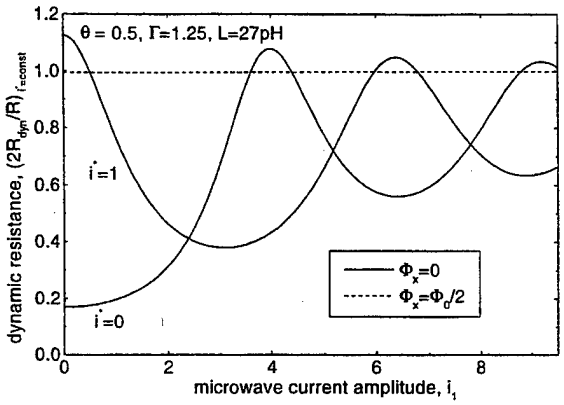

Fig.1(c) Calculated normalized dynamic resistance vs. MW current amplitude of a Shapiro-step SQUID for two different values of bias current i*. The curves for $\Phi_x=\Phi_0/2$ (dashed line) do not depend on i*.

SQUID biased simultaneously by a dc and MW current is denoted as Shapiro-step SQUID. By an optimal choice of the relevant parameters (dc bias current, MW power, SQUID inductance, etc.) it can easily be shown on the basis of (1)that a Shapiro-step SQUID may have sufficiently high values for the transfer function in order to be used as a sensitive device for magnetic flux measurements. However, one can conclude from (1) that all non-linearities in the IVCs that occur at specific values of the dc bias current and voltage (at integers in units of $i^*=\theta I/2I_c$ and $v^*=\theta V/I_cR$), i.e. which are related to Shapiro steps can be regarded as smaller copies of the non-linearity obtained in the absence of MW power. For that reason, a Shapiro-step SQUID operated in the usual mode of a dc SQUID is expected to have a worse magnetic flux sensitivity than a dc SQUID with the same characteristic parameters. However, Shapiro-step SQUIDs show some new interesting features as compared to a dc SQUID, which may find interesting applications in the field of MW devices. We note, e.g., that a Shapiro-step SQUID can preserve a relatively high transfer function which may be controlled by two new parameters, namely the MW current amplitude and the MW frequency.

B. Experiment

Measurements have been performed on a MW irradiated $YBa_2Cu_3O_{7-x}$ bicrystal junction dc SQUID which confirm some of the theoretical predictions. The experimental setup was designed to maximize the coupling of MW current across the Josephson junctions and to minimize the coupling of MW flux into the SQUID loop by placing the Josephson junctions of the SQUID close to the shorted end of a coplanar waveguide. Experimental details will be reported elsewhere.

Fig. 2(a) ($f=\omega/2\pi$ is the MW frequency) provides the experimental confirmation that the Shapiro-step SQUID operates in a proper way. In particular, modulation of the output voltage as a function of applied magnetic flux is observed, confirming that the device can be characterized by

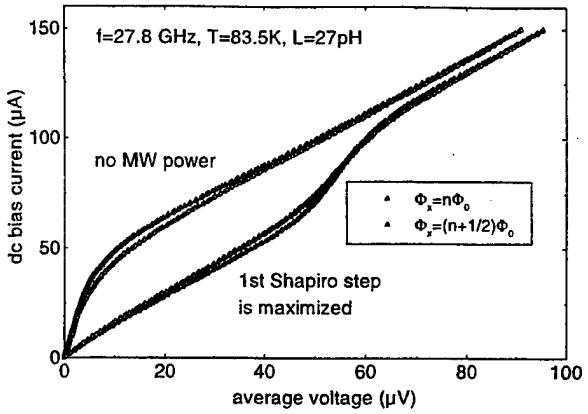

Fig.2(a) Measured IVCs of a dc SQUID in the absence of MW power and for a MW power level that maximizes the first Shapiro step. Solid lines are for applied flux of integer of flux quanta. Triangles are for applied flux of half integer of flux quanta.

a transfer function although the flux modulation is less than the theoretical expectation.

In the case of integer flux quanta in the SQUID loop there is good agreement between the theoretical predictions and experimental data with respect to the dynamic resistance as a function of bias current [see Fig. 2(b) and Fig. 1(b)] or the applied MW current amplitude [see Fig. 2(c) and Fig. 1(c)].

In the case of half integer flux quanta the discrepancy between theory and experiment is evident. However, we note that this discrepancy is not a particular property of the Shapiro-step SQUID, since it is also present in the case of no applied MW power as shown in Fig. 1(a).

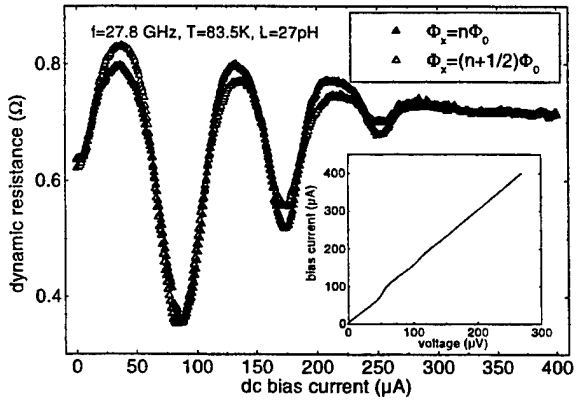

Fig.2(b) Measured dynamic resistance vs. dc bias current for a dc SQUID irradiated with a MW power that maximizes the first Shapiro step. The inset shows the corresponding IVC.

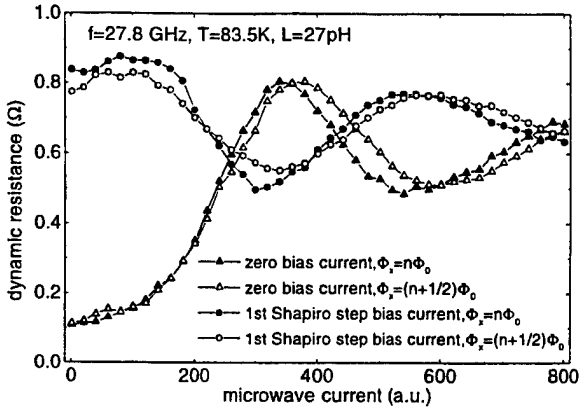

Fig.2(c) Measured dynamic resistance of a Shapiro-step SQUID as a function of applied MW current amplitude for two different bias currents and two values of the applied magnetic flux.

REFERENCES

[1] B. Chesca, "The Effect of thermal noise on the I-V curves of high inductance dc SQUIDs in the presence of microwave radiation", *J.Low.Temp.Phys*, in press.

[2] E. Heinz and P. Seidel, *J.Low.Temp.Phys.* vol. 106, p. 233 (1997).

[3] B.Chesca, *J.Low.Temp.Phys.* vol. 110, pp. 963-1001, March 1998.

[4] K. Enpuku, G. Tokita, T. Maruo, and T. Minotani, *J.Appl.Phys.*, vol. 78, p. 3498 (1995).

[5] B.Chesca, *J.Low.Temp.Phys.* vol. 112, p. 165, July 1998.

[6] B.Chesca, The effect of thermal fluctuations on the operation of dc SQUIDs at 77 K - a fundamental analytical approach, *IEEE Trans. Appl. Supercond.*, vol. 9, (1999); in press.

[7] K.Barthel, D.Koelle, B.Chesca, A.I. Braginski, A.Marx, R.Gross, and R.Kleiner, *Appl. Phys. Lett.*, vol. 74, pp. 2209–2211, April 1999.

[8] D. Koelle, R. Kleiner, F. Ludwig, E. Dantsker, and John Clarke, High transition temperature superconducting quantum interference devices, *Rev.Mod.Phys.71*, pp.631-686, April 1999.

64-Channel whole-head SQUID systemin a superconducting magnetic shield

H. Ohta [1,2], M. Aono[2], T. Matsui[1], Y. Uchikawa[3], K. Kobayashi[3], K. Tanabe[3], S. Takeuchi[3]
[4]K. Narasaki, [4]S. Tsunematsu, [4]Y. Koyabu, [4]Y. Kamekawa, [5]K. Nakayama, [5]T. Shimizu
[6]Koike, K. [6]Hoshino, [6]H. Kotaka, [6]E. Sudoh, [6]H. Takahara, [8]Y. Yoshida,
[7]K. Shinada, [7]M. Takahata, [7]Y. Yamada and [9]K. Kamijo

[1]Communications Research Laboratory, Ministry of Posts and Telecommunication, Nukuikitamachi 4-2-1, Koganei, Tokyo 184, Japan
[2]The Institute of Physical and Chemical Research (RIKEN), Hirosawa 2-1,Wako-shi,Saitama 351-01, Japan;
[3]Tokyo Denki University, Oaza-Ishizaka, Hatoyama-cho, Hiki-gun, Saitama 350-03, Japan; [4]Sumitomo Heavy Industry, Soukai-cho 5-2, Niihama-shi, Ehime 792-8588, Japan; [5]Nihonkeiki Corporation, Goshogaoka 4-3-5, Moriyacho, Kitasoma-gun, Ibaragi 302-0119, Japan; [6]Mitsui Mining & Smelting Co, Ltd., Corporate R&D Center, Haraichi 1333-2, Ageo, Saitama 362, Japan; [7]Shimadzu Corporation, Keihanna Research Laboratory, Inuidani-Sunagatani, Seika-cho, Soraku-gun, Kyoto 619-02, Japan; [8]National Research Institute of Metals, Tsukuba, Ibaragi 305-0047, Japan and [9]NEC Fundamental Research Laboratory, Tsukuba, Ibaragi 273-2310, Japan

Abstract — **A superconducting magnetic shield of high-Tc superconductor Bi(Pb)-Sr-Ca-Cu-Ox has been constructed whose diameter is 65 cm and length is 160 cm respectively. We have successfully observed magnetic fields coming out from somatosensory-evoked human brains in the superconducting magnetic shield stimulating the median nerves of patients by current pulses. We made a 64-channel whole-head SQUID magnetometer of SNS (Superconductor/ Normal metal / Superconductor) junctions which does not low-frequency telegraph noise. The sensitivities of the dc-SQUID of mesoscopic SNS junctions are around 5 even in rather unfavorable surroundings. The magnetic shield can reduce a magnetic field to around - 80 dB or 10^{-4} even at as low a frequency as 0.05 Hz. Therefore SQUID's of SNS junctions and a superconducting magnetic shield are a good combination.**

I. Introduction

We spent a few weeks in 1987 doing neuromagnetic SQUID experiments in a large magnetically shielded room of Permalloy. We have wanted to have a less expensive and more effective shield room since then. When we confirmed a YBCO vessel can reduce an external magnetic field to -100 dB or 10^{-5}, we proposed the application of superconducting magnetic shields to neuromagnetic SQUID [2] . We have successfully detected magnetic fields emitted from human brains with a 64-channel whole-head SQUID magnetometer in the superconducting magnetic shield of high-Tc superconductor. We describe characteristics of the superconducting magnetic shield , a 64-channel whole-head SQUID of SNS junctions, neuromagnetic SQUID measurements and topographies of magnetic fields above human.

II. Superconducting Magnetic Shield

We have already published details about fabrication method and basic properties of superconducting magnetic shield. We started with a palm-top superconducting cup of BSCCO to confirm that a superconducting magnetic shield of high-Tc superconductors has the same shielding factor as that of a conventional metal superconductor has.

Manuscript received , March 1 , 1999 .

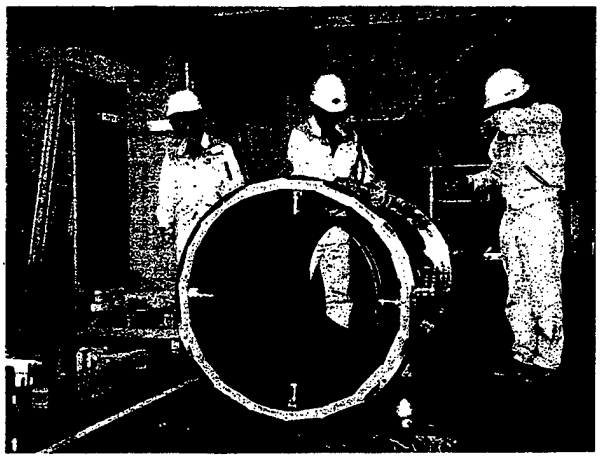

Fig.1 A body-size magnetic shield of thick-film high – Tc Superconductor BSCCO

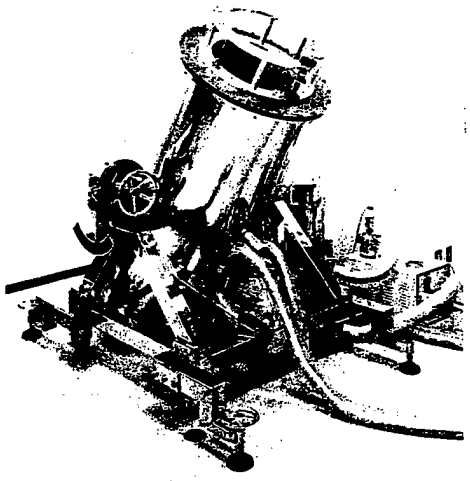

Fig.2 In the cryostat, the nickel cylinder coated with thick BSCCO film is cooled by helium gas from a closed-cycle helium refrigerator.

The magnetic field inside the superconduting shield is theoretically given by

$$H_{axial} = H^{(0)}_{axial} \exp\left(-6.76\frac{L}{D}\right) \qquad (1)$$

and

$$H_{transversal} = H^{(0)}_{transversal} \exp\left(-3.68\frac{L}{D}\right) \qquad (2)$$

when one side of the superconcuting shield is closed.
We have experimentally confirmed the depth L dependence and the diameter D dependence inside several samples measuring the shielding factor S define by

$$S = \frac{H^{(0)}}{H} \qquad (3)$$

The unbalance between the axial and transversial magnetic fields are compensated by something like magnetic caps of permalloy near inlet of the superconducting magnetic shield.

Palm-top superconducting cups are still important although we have constracted a whole-body size superconducting magnetic shield. Generally speaking it is not easy to mesure a shilding factor of body-size magnetic shields exactly because they requires a costly huge Hermholtz coil to prepare a homogeneous magnetic field of several meter diameter.

We also made a helmet-size superconducting shield of bulk BSCCO measuring somatosesary evoked magnetic field from human brains successfully. In order to make a body-size magnetic shield, we switched from heavy bulk superconductors to thik-film superconductors on a nickel cylinder. Figure 1 shows that the inside wall of the nickel cylinder is covered with thick film of BSCCO which is spray-coated by high-temperature plasma in the atomospher.

The high-temperature plasma spray-coating guarantees the best adheesion between the superconductiong thick film and nickel.

In the cryostat , the nickel cylinder coated with thick BSCCO film is cooled by helium gas from a closed-cycle helium refrigatator. You can see in the Fig. 2 the flexible double layer tubes between the cryostat and a closed-cycle helium refrigatator.

Because we wanted this cryostat to be tilted in any angle, we use a closed-cycle refrigerator instead of liquid nitrogen above whose liquid level the temperature of the superconductor goes up. We used high-Tc-phase $Bi(Pb)_2Sr_2Ca_2Cu_3O$ instead of low-Tc-phase $Bi_2Sr_2Ca_1Cu_2O$ worrying about power of the refrigerator connected with the cryoostst by the 10-meter flexible stainless tubes which cut mechanical vibrations. It turned out to take about one day to cool the cylinder from room temperature down to lower than liquid nitrogen temperature. It was a risky gamble because we circulated helium gas instead to liquid nitrogen. In other words the 2-meter tall cryostat is a part of the refrigarator.

The coaxial Permalloy cylinders prerared a-few-milligauss surroundings during cooling to minimize trapped magnetic fields.

The cryostat is a little shorter than 2 meters. The top of the cryostat does not hit the ceiling because the height of the ceiling of typical Japanese houses is 255 cm. You can take off transfer tubes for liquid helium when you make it tilted a little.

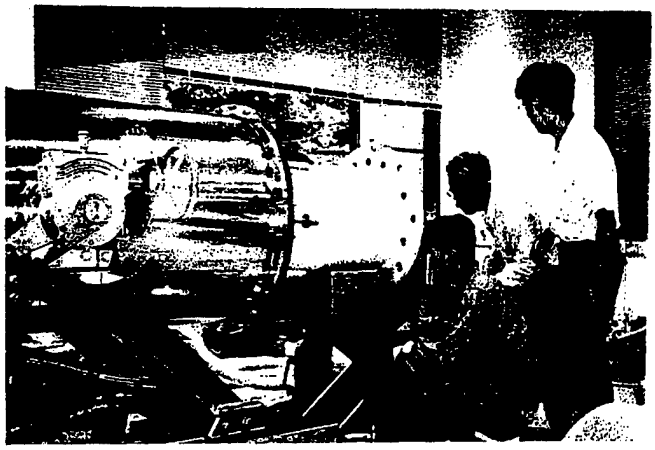

Fig. 3 We insert the FRP dewar for the SQUID into the magnetic shield holizontally

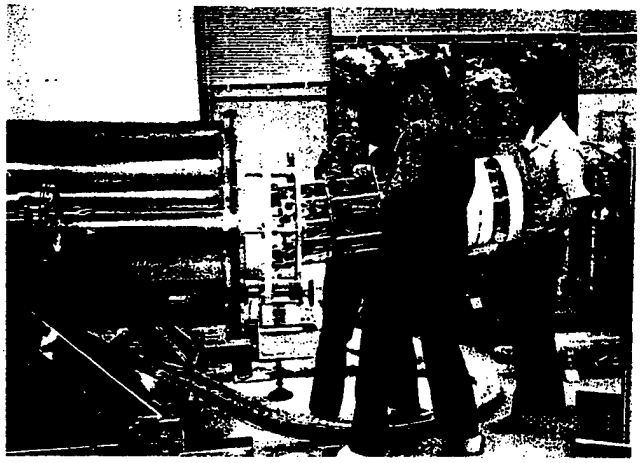

Fig. 4 We insert the SQUID cryostat into the magnetic shield holizontally.

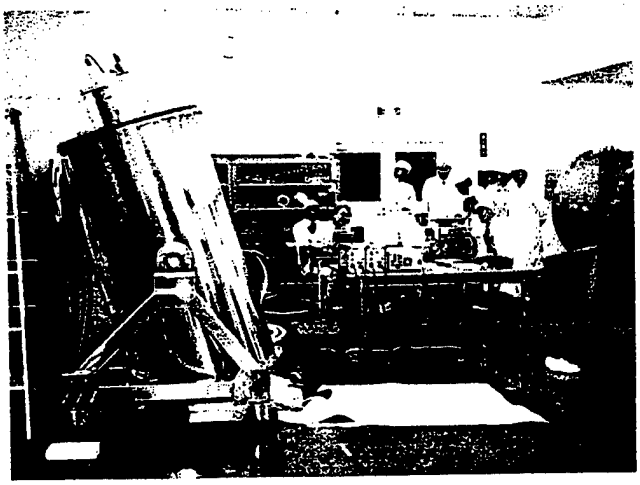

Fig. 5 Neoromagnetic SQUID measurement in the superconducting magnetic shield.

We insert both the FRP dewar and the SQUID cryostat into the magnetic shield horizontally as shown in Fig. 3 and

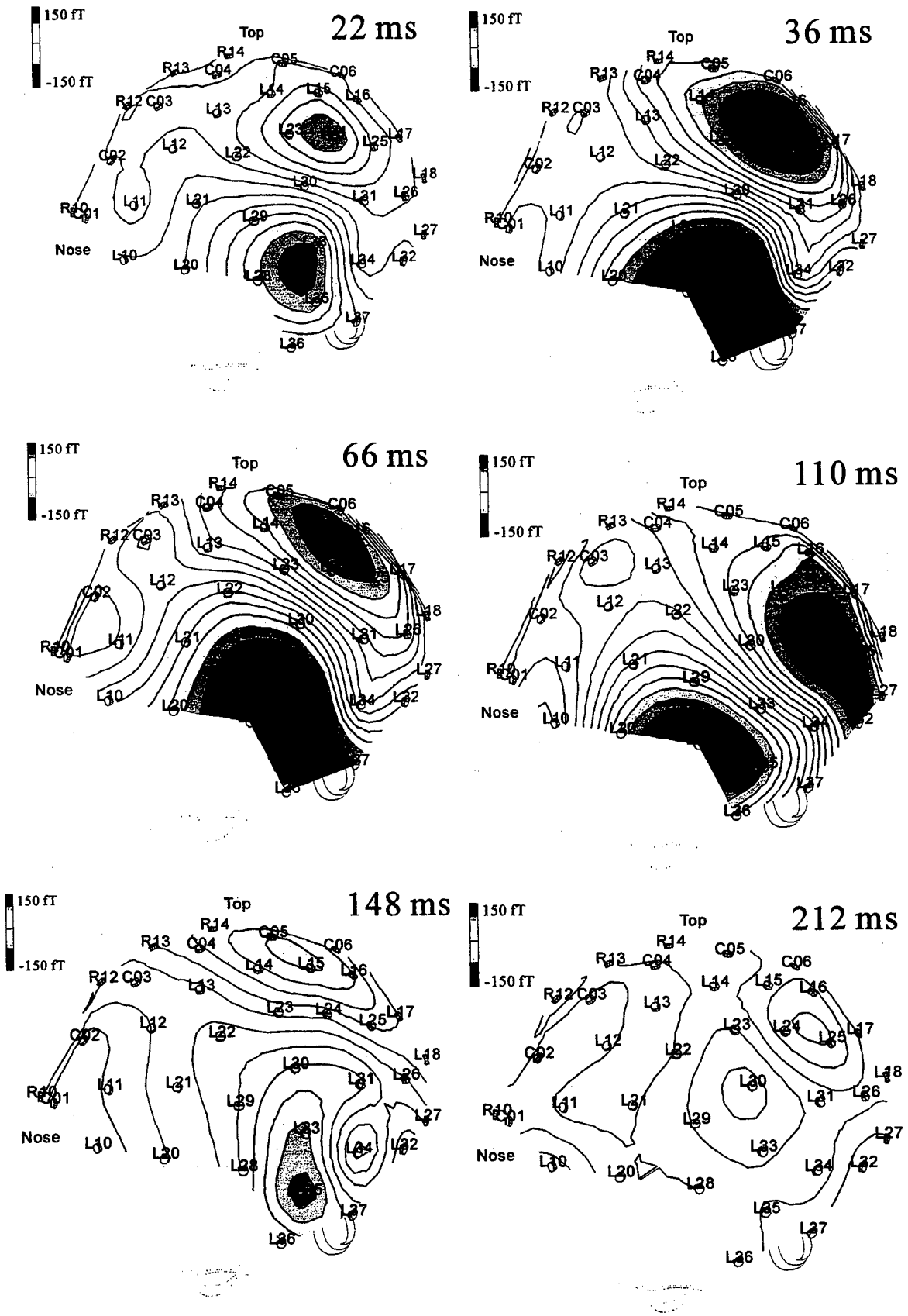

Fig.6 Topographies of magnetic fields correspond to the data in Fig.7

Fig. 4 respectively without using any lifting machine on the ceiling.

III. 64 Channel SQUID of SNS Junction

Somatosensory evoked magnetic field was measured by a 64-channel whole-head SQUID magnetometer of SNS junctions.

A typical junction sensitivity s is 5 $fT/\sqrt{Hz}$.

The bandwidth Δf is wider than several hundred Herz.

We average about one hundred events (N). Therefore the system sensitivity S is around

$$S = s\sqrt{\frac{\Delta f}{N}} \approx 5\,[fT] \quad .$$

The data show that the N20 peaks of 50 fT have a good Signal-to-Noise ratio.

The neuromagnetic measurement has been done in the superconducting magnetic shield.

The data indicate that mesoscopic SNS junction are important not only theoretically but also practically.[3]

IV. Neuromagnetic SQUID Measurement in the Superconducting Magnetic Shield

You can see the two legs of the patient in the superconducting magnetic shield as shown in Fig. 5

A median nerve in the right wrist was stimulated by current pulses. The N20 peaks of 50 fT from the radial current dipole in the 3a field or the 1 field of the human brain are reproducibly observed in Figs. 6 and 7 .

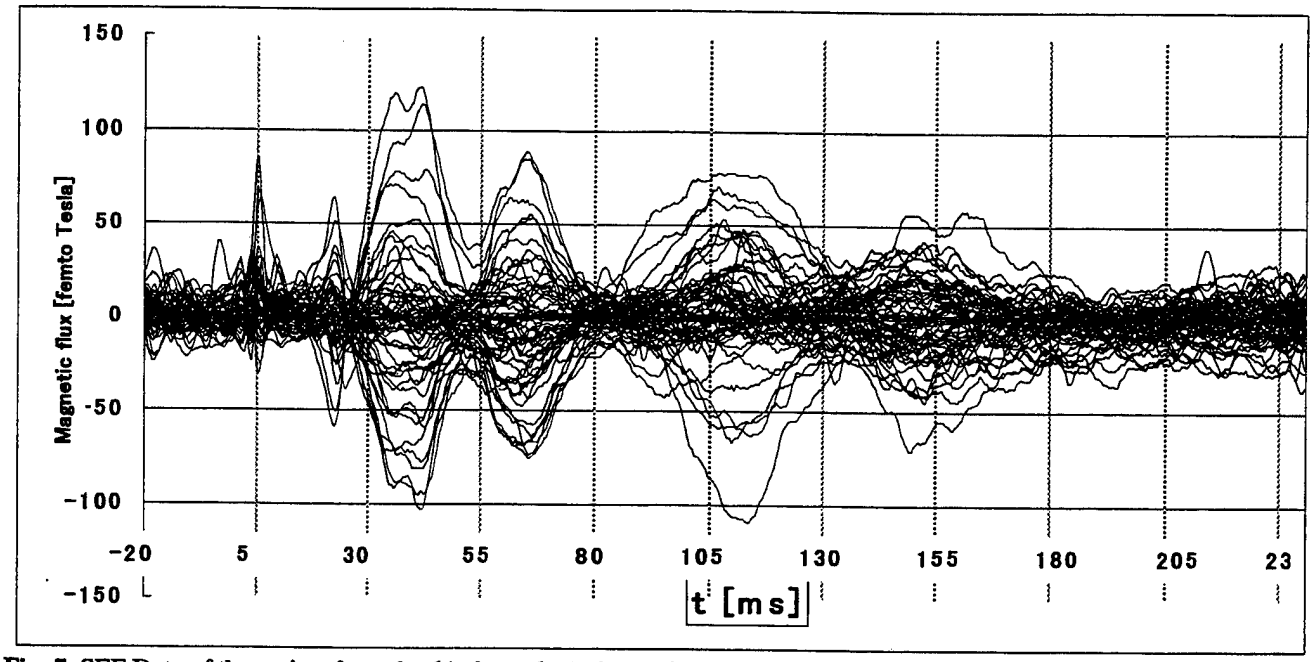

Fig. 7 SEF Data of the patient from the 64-channel whole-head SQUID system in the superconducting magnetic shield. Vertical : Magnetic flux [fT], Horizontal: Time [ms]

The current dipole for the N20 peaks of 50 fT is confirmed to rotate at a frequency of about 10 Hz.

The SQUID is also cooled by a vibration-free closed-cycle helium refrigerator. The system need neither liquid helium nor liquid nitrogen. Then this system could be a candidate for a mobile mental clinic in the future.

V. Conclusion

Our whole-head SQUID system has a system sensitivity of 5 fT although our site is only 10 m far from both an elevator and a power transformer bank. When we started making this SQUID system with a superconducting magnetic shield about 10 years ago, we had too many unknown factors to be sure about any coming results. It would be safe now to say that a SQUID system with a superconducting magnetic shield is very promising.

References

[1] H. Ohta, A. Koike, K. Hoshino, H. Kotaka, E. Sudoh, K. Kato, H. Takahara, Y. Uchikawa, K. Shinada, M. Takahata, Y. Yamada and T. Matsui, " Neuromagnetic SQUID Measurements in a Helmet-type Superconducting Shield of BSCCO ", *IEEE Trans. Applied Superconductivity*, vol. 3, pp.1953 - 1956, March, 1993.

[2] H. Ohta, T. Matsui, K. Shinada and Y. Yamada, "Reduction of Telegraph Noise in Superconducting Short Weak Links", *IEEE Trans. Applied Superconductivity*, vol. 5, pp.3098 - 3101, June, 1995.

[3] H. Ohta and T. Matsui , "Semiclassical Picture of Mesoscopic SNS Junctions ", *Physics and Applications of Mesoscopic Josephson Junctions* ed. By H. Ohta and C. Ishii , the Physical Society of Japan, Tokyo, 1999

Oral Session 9

SQUIDs II

Low-Frequency Noise in YBCO dc SQUIDs and Vortex Imaging by Low-Temperature Scanning Electron Microscopy

D. Koelle and R. Gross
II. Physikalisches Institut, Lehrstuhl für Angewandte Physik, Universität zu Köln, Germany

S. Keil, R. Straub, M. Fischer, M. Peschka and R.P. Huebener
Physikalisches Institut, Lehrstuhl für Experimentalphysik II, Universität Tübingen, Germany

K. Barthel
Institut für Schicht- und Ionentechnik (ISI), Forschungszentrum Jülich, Germany

Abstract—We present a technique for direct imaging of Abrikosov vortices trapped in YBCO washer dc SQUIDs and in a Ketchen-type integrated high-T_c magnetometer. Simultaneously we are able to measure the low-frequency noise of our devices under test, which allows correlation of the local distribution of vortices with low-frequency noise in the SQUIDs. The vortex imaging and noise measurements are performed with the SQUIDs operated in a standard flux-locked loop and mounted on a liquid nitrogen cooled cryostage of a scanning electron microscope for investigation at variable temperature ($77K<T<T_c$) and in controllable magnetic fields up to several hundred μT. Our imaging technique, which yields a spatial resolution of about 1μm, is based on the electron-beam-induced local displacement Δr of vortices, which is detected as a flux change $\Delta\Phi = \Delta r(\delta\Phi/\delta r)$ in the SQUID loop. Hence, the signal amplitude provides direct information on the coupling strength $\delta\Phi/\delta r$. Since $\delta\Phi/\delta r$ determines the amount of flux noise which a fluctuating vortex induces in the SQUID, we obtain valuable information on possible low-frequency noise sources in the SQUIDs. We investigated washer SQUIDs with regular arrays of micron-sized holes (antidots) to image the competing formation of multiquanta trapped in antidots versus the formation of interstitial vortices. In most cases the interstitial vortices are pinned reproducibly at the same locations. These pinning sites do not correlate with the surface morphology of the films.

I. Introduction

Impressive progress towards the development of sensitive superconducting quantum interference devices (SQUIDs) based on high transition temperature (T_c) superconductors (HTS) and high-T_c SQUID based magnetometers [1] yielded a white noise level around $10fT/Hz^{-1/2}$ at 77K for the best devices made so far from epitaxially grown thin films of $YBa_2Cu_3O_7$ (YBCO). More typical values for the magnetic field resolution are some tens of $fT/Hz^{-1/2}$. If such a low noise level could be obtained down to low frequencies of a few Hz or less, the performance of high-T_c SQUIDs would be very adequate for more applications.

Manuscript received April 30, 1999.
This work was supported by the Deutsche Forschungsgemeinschaft

A major problem, however, which still has to be resolved, is low-frequency $1/f$ noise from thermally activated vortex motion in the HTS films. This problem becomes even more serious for devices operated in a magnetically unshielded environment and cooled in the earth's magnetic field, which can lead to an increased density of fluctuating vortices present in the superconducting films. Optimization with respect to low-frequency flux noise will require either to avoid the presence of vortices or to provide efficient pinning. To avoid vortex entry, SQUIDs with small maximum linewidth w have been used. It has been shown that for the cooling field B_0 a threshold value B_T exists, above which $1/f$ noise starts to increase with B_0, indicating that vortices enter the film [2]. A second approach to reduce $1/f$ noise from vortex motion is based on the idea to efficiently pin vortices in micropatterned holes (antidots). Matching of the vortex lattice with the antidot lattice in fields far below the earth's magnetic field has been shown to reduce the $1/f$ noise in HTS rf SQUIDs [3]. For operation in higher fields, the competing formation of multiquanta pinned in antidots versus formation of interstitial vortices between the andtidots and its implications on noise have still to be clarified.

Evidently, the $1/f$ noise is correlated with the quality of the HTS films [4], which in turn is affected by the presence of a variety of defects in these films. A detailed understanding of the interplay between microstructure and noise properties of HTS films, however, is still lacking, which hinders further improvement of the low-frequency performance of HTS SQUIDs and magnetometers. Furthermore, the geometry of the micropatterned devices and the patterning process itself may significantly affect their noise properties. Hence, a number of specific locations within a device may represent possible noise sources.

Obviously, the low-frequency noise properties of high-T_c SQUIDs and magnetometers depend on *local properties* (defects, geometry). Noise measurements, however, give only spatially integrated information on the device properties, which makes it difficult to *locate* noise sources. In this work we present a technique for visualization of vortices and for obtaining local information on noise sources in SQUIDs. This technique is based on low-temperature scanning electron microscopy (LTSEM), which has been used previously for

imaging the local distribution of T_c or critical current density j_c in superconducting thin films and Josephson junctions and of Josephson vortices in long junctions [5]. In contrast, the LTSEM technique presented here exploits the high sensitivity of SQUIDs to magnetic flux directly. That is, we detect electron-beam-induced changes $\Delta\Phi$ of the magnetic flux coupled into the SQUID hole, where the SQUID itself is the device under test. This opens up the possibility to obtain both images of the local distribution of vortices *and* local information on noise properties of the devices under investigation.

II. Experimental Setup and Device Characteristics

A. Cryostage for Scanning Electron Microscope

All measurements presented here were performed in a liquid nitrogen (LN_2) cooled cryostage of an SEM which was described in more detail in [6,7]. In brief, the cryostage consists of a LN_2 bath cryostat which is connected to a small LN_2 tank placed inside the SEM. The sample is mounted on top of a cold finger which allows one to scan its surface with the electron beam (e-beam) while the temperature is adjusted and well stabilized within approximately 77K-130K. A combination of magnetic shielding and field coils provides a low-noise environment with well-defined magnetic fields up to a few hundred μT.

B. Measurement Technique

The investigated dc SQUIDs are read out using 100kHz flux modulation and a flux-locked loop (FLL), with both a static current bias (dc bias) and a 3.125kHz bias reversal scheme to eliminate $1/f$ noise due to I_c-fluctuations in the Josephson junctions. The SQUID electronics typically provides an output signal of $1V/\Phi_0$ with a bandwidth of 20-30kHz. Typical levels of flux noise of the investigated SQUIDs range between $10\text{-}20\mu\Phi_0/Hz^{1/2}$ in the white noise limit.

For the spatially resolved measurements, the e-beam can be used to cause a local perturbation, $\Delta T(x\text{-}x_0,y\text{-}y_0)$, on the sample surface in the vicinity of the beam spot at position (x_0,y_0). The maximum ΔT is typically about 0.5 K × I_{el} [nA], where I_{el} [nA] is the beam current in units of nA. The length scale for the spatial decay of ΔT is set by the beam-electron range $R \approx$ 500nm for a typical beam voltage V_{el}=10kV [5]. Images are obtained by recording the e-beam-induced flux change $\Delta\Phi(x,y)$ as a function of the beam coordinates (x,y). The experimental set-up is shown in Fig.1. The detected output signal from the SQUID electronics is further amplified and then used to control the brightness of a video screen. Additionally, the time trace or the power spectrum of that signal can be recorded by a signal analyzer. For imaging we use a beam-blanking unit operating at typically 3kHz, and the signal from the SQUID electronics is lock-in detected.

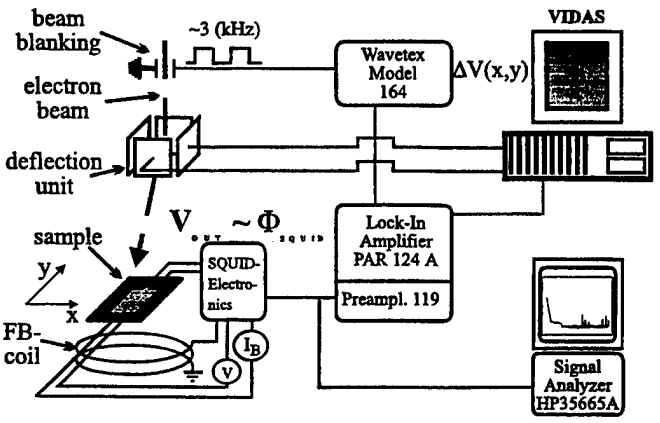

Fig.1 Experimental set-up for LTSEM on dc SQUIDs

C. Samples

All devices presented here were fabricated by pulsed laser deposition of YBCO and $SrTiO_3$ (STO) films on 24° bicrystal STO substrates. Patterning was performed by optical lithography and Ar ion beam etching and/or chemical wet etching. The investigated devices are (1) *single layer washer dc SQUIDs* with arrays of 1-5μm diameter holes (antidots), with 10-19μm lattice spacing, and (2) an *integrated Ketchen-type magnetometer* [8] based on a YBCO/STO/YBCO multilayer structure with the dc SQUID washer in the bottom YBCO film and a YBCO spiral input coil (8 turns) in the top YBCO film with one superconducting interconnect (via) at the innermost turn of the input coil.

III. Vortex Imaging – Singal Generation

We observed a variety of e-beam-induced changes in the output of the SQUIDs which have been described in more detail in [9]. The mechanism which is responsible for imaging of vortices is briefly described as follows: The e-beam-induced change in temperature ΔT within a radius set by the beam-electron range R causes a local increase in the London penetration depth λ. If the beam spot is within a distance R of a vortex, the circulating currents flowing around the vortex core are spatially extended due to the local increase in λ. If the e-beam hits the center of an interstitial vortex, ΔT will simply increase the size of the vortex, however no change of flux will be coupled to the SQUID hole. In contrast, if the beam spot is slightly displaced (within ~R) from the center of the vortex, the deformation of the screening currents comes along with an apparent displacement of the vortex towards the position of the beam spot. In the same way, a vortex pinned in an antidot will experience a local displacement when the beam hits the edge of the antidot. Hence, if the electron beam is scanned across a vortex, this vortex will be dragged along with the beam, if

the beam is within the radial distance R from the vortex. The beam-induced displacement Δr of the vortex will be on the order of the change in λ and this will couple a positive (negative) flux change $\Delta\Phi$ to the SQUID if the vortex is moved away from (towards) the SQUID hole. This is shown in the $\Delta\Phi$ image in Fig.2(b) where the vortices appear as pairs of positive (bright) and negative (dark) signals. For comparison the same section of the central part of the scanned washer is shown in the secondary electron image in Fig.2(a), with the SQUID hole as a vertical slit and the antidots with 19μm lattice spacing. The positive signal along the SQUID slit in Fig.2(b) is due to an e-beam-induced change in the effective area of the SQUID washer [9].

The e-beam-induced flux change for vortex imaging is given by $\Delta\Phi=(\partial\Phi/\partial r)\Delta r$. The coupling strength $\phi_r\equiv(\partial\Phi/\partial r)(r)$ can be calculated from (2) in [10], which gives the flux $\Phi(r)$ that is coupled into the SQUID by a single vortex placed at a distance r from the center of a circular washer with hole size $2a$ and washer diameter $2c$ [see inset of Fig.3(a)]. The calculated flux change $\Delta\Phi(r)$ is plotted in Fig.3(a), together with the measured signals from antidot vortices taken from a single flux image. We get reasonable agreement between theory and experiment if we assume a beam-induced displacement of Δr=22nm. Evidently, the magnitude of the signal decreases rapidly with increasing distance r from the center of the SQUID hole. This means, only vortices within a few tens of μm away from the slit are imaged. We note that for a fixed value of Δr the magnitude of the signal $\Delta\Phi$ is a direct measure of the coupling strength ϕ_r of an imaged vortex. The contribution of a fluctuating vortex to the flux noise of the SQUID is also given by ϕ_r and by the spectral density $S_r(f)$ for motion of the vortex. Hence, our signal generation mechanism exactly mimics the mechanism which is responsible for the generation of flux noise. This is certainly a striking advantage of our imaging technique over other techniques which detect the spatial distribution of flux density, like e.g. scanning hall microscopy. Measuring ϕ_r directly gives important information on possible noise sources in the investigated devices. This is particularly important for more complex structures, which may have no radial symmetry, so that calculation of ϕ_r is not straightforward (see Sec.VI.). The e-beam induced vortex displacement Δr is expected to be proportional to $(\partial\lambda/\partial T)\Delta T$.

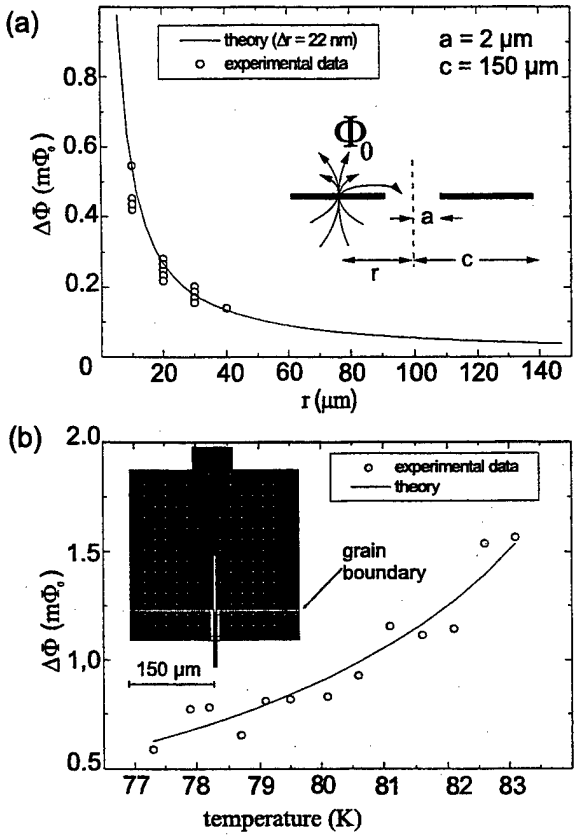

Fig.3: (a) Beam-induced flux change in the SQUID $\Delta\Phi$ vs. r due to radial displacement Δr of a vortex located at radial distance r from the center of a SQUID washer (see inset with schematic cross section of the washer). The line is calculated for Δr=22nm as only adjustable parameter. (b) $\Delta\Phi$ vs. T for irradiation of a vortex at fixed position. The line is calculated using the BCS expression of $\lambda(T)$ (with T_c=91K, ΔT=1.2K, λ_0=250nm). The inset shows the SQUID washer geometry.

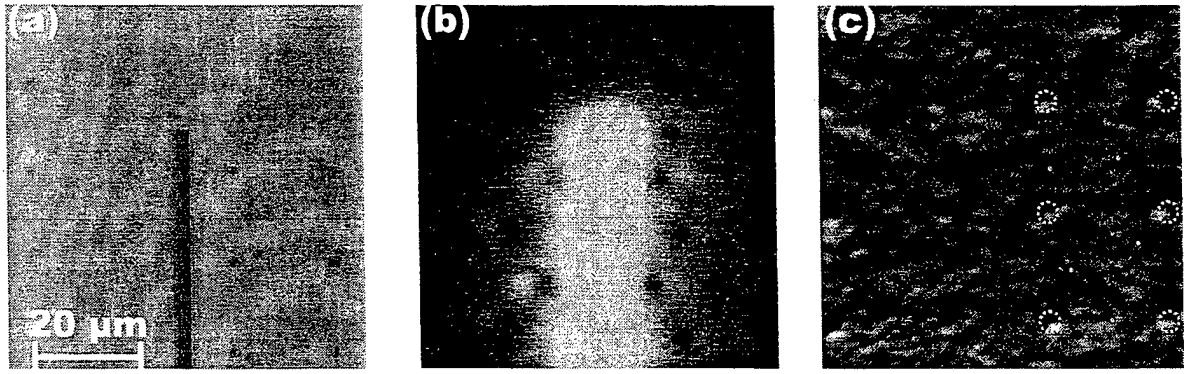

Fig.2: Comparison of (a) SEM image (b) $\Delta\Phi$ image (T=77 K; B_0=60 μT) and (c) scanning laser microscopy image (white dashed circles and white dots at the right indicate the position of antidots and pinning sites, respectively).

Hence the vortex signal depends on operating temperature, since $(\partial \lambda/\partial T)$ depends on T. This is shown in Fig.3(b), with good agreement with the theoretical prediction taking $\lambda(T)=\lambda_0(1-(T/T_c)^2)^{-1/2}$.

IV. Vortex Distribution in Washer SQUIDs

As shown in Fig.2(b), which was taken at a cooling field B_0=60μT, vortices are pinned in antidots as well as between the antidots (interstitial vortices). Careful examination of the location of interstitial vortices for repeated temperature cycles through T_c revealed that the interstitial vortices are essentially always pinned at the same locations. SEM and AFM analysis of the surface morphology showed that there is no correlation of the vortex positions with the local distribution of precipitates in the films. Hence the local distribution of pinning sites seems to be determined by either the vortex-vortex interaction or by the interaction between a vortex and the microstructure of the film or by a combination of both. It has been demonstrated recently that room temperature laser scanning microscopy (LSM) is a useful tool for visualization of low angle tilt grain boundaries in c-axis oriented YBCO films [11]. The thermoelectric voltage response ΔV due to laser irradiation shows a change in polarity if the laser beam is scanned across such a grain boundary. We used this technique [12] to produce room temperature $\Delta V(x,y)$ images from the same section of the SQUID washer [Fig.2(c)] which had been examined by LTSEM. The bipolar voltage signals detected at the antidots [see Fig.2(c)] are possibly due to laser-induced local thermoelectric currents in film areas with a non-zero angle between the surface normal and the c-axis of the YBCO film. We note that the film itself produces a distinct thermoelectric voltage contrast with a rich structure, which however is not correlated with the surface morphology as imaged by SEM and AFM or with the distribution of pinning sites for interstitial vortices as imaged by LTSEM.

V. Multiquanta in Antidot Washer SQUIDs

In cooling fields above the first matching field $B_{M1}=\Phi_0/a^2$ for a given array of antidots with lattice parameter a there exists a competing formation of multiquanta in antidots versus the occupation of vortices at interstitial sites. To obtain low $1/f$ noise in the SQUIDs it appears favorable to avoid the pinning of vortices at interstitial sites where they may fluctuate due to thermal activation. Since the saturation number n_s (the maximum number of flux quanta per antidot [13]) depends on the antidot diameter d, we examined SQUIDs which were patterned to have antidots with d =1—5μm. Fig.4 shows $\Delta\Phi$ images of such a SQUID with fixed d for horizontal rows of antidots, while d changed from row to row. Obviously, for

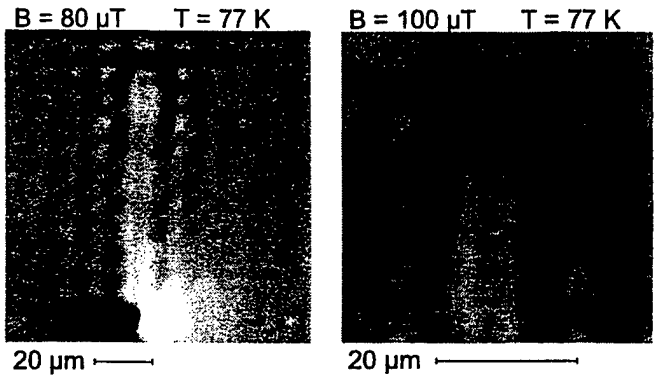

Fig.4: $\Delta\Phi$ images of washer SQUID with 2D-array of antidots with variable diameter d. (a) Overview — d is fixed within horizontal rows of antidots (d=4μm,4μm,1μm,2 - 5μm [in 0.5μm-steps] from top to bottom) (b) expanded view of (a) at the upper end of the vertical SQUID slit.

fixed r the amplitude of the e-beam-induced flux change at antidots varies significantly, which indicates the presence of multiquanta. Furthermore we observe interstitial vortices only at rows with small d. To give a more quantitative picture we plot in Fig. 5 the signal amplitude $\Delta\Phi$ for antidot vortices vs. d obtained within a series of measurements in cooling fields ranging from 40—150μT. To a first approximation one expects $\Delta\Phi \propto n\Phi_0$ with n being the number of flux quanta per antidot. Obviously the scatter in Fig.5 is quite significant. However we still observe a tendency towards three distinct signal levels which could be attributed to the occupation of n=1, 2 and 3 vortices in one antidot. Taking this interpretation we find occupation of all three levels only in the highest cooling field (B_0=150μT), n=1 and 2 for the intermediate fields and n=1 for the lowest fields. We note that we observed a tendency towards increasing beam-induced flux change with increasing antidot diameter at an average value of k=0.14mΦ_0/μm. This effect has been subtracted in Fig.5. Its origin has not been clarified yet.

In principle is should be straightforward to examine now the correlation between the presence of multiquanta and/or

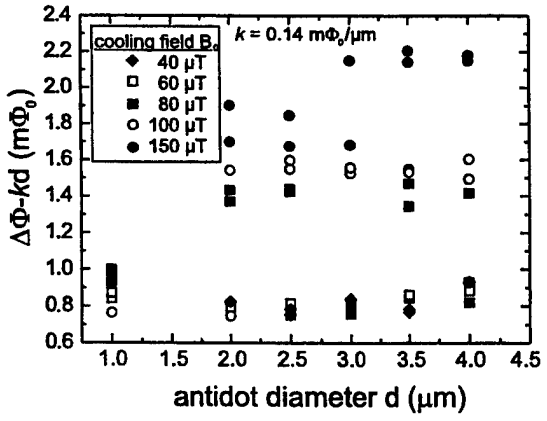

Fig.5: LTSEM signal $\Delta\Phi$ vs. antidot diameter (T=77 K).

interstitial vortices with low frequency noise data. Unfortunately we cannot draw clear conclusions from the noise data we obtained so far on our devices with a geometry as shown in the inset of Fig.3(b). This is due to the presence of Josephson vortices in the grain boundary intersecting the washer over its entire width. These Josephson vortices, which are e.g. visible at the right and left bottom part of Fig.4(a) can also move and induce flux noise. Hence it is not clear yet, whether features like distinct peaks in S_Φ(1Hz) vs. B which we observed at T=77K are caused by flux noise from vortices in the grain boundary or from (interstitial) vortices close to the SQUID slit.

VI. Activation of Random Telegraph Signals

Beyond the imaging of vortices, a full characterization of local noise sources requires the detection of $S_r(f)$, or equivalently, of amplitude and frequency of their spatial fluctuations. The e-beam as a local perturbation may change these properties, for example by changing the shape of a double well pinning potential, which will affect the hopping process between two pinning sites. Alternatively the e-beam will induce hopping between two such pinning sites which may be detected as a random telegraph signal (RTS) at the output of the SQUIDs. An example for such a process is shown in Fig.6 where we plotted the time trace and the flux noise spectrum of a SQUID which had a vortex pinned a few μm apart from one of the two Josephson junctions. Irradiation of this particular spot produced an RTS signal as shown in the time trace of the SQUID output in Fig.6(a). In the frequency domain this switching process produces a Lorentzian noise spectrum with a roll-off frequency around 10Hz. For comparison the time trace and noise spectrum obtained without e-beam irradiation are also shown. We were able to turn this RTS signal reproducibly on and off with the e-beam. The switching amplitudes, $6m\Phi_0$ and $16m\Phi_0$, correspond to an estimated hopping distance of a few tens of nm, given the fact that the vortex was only a few μm away from the junctions. Such a small hopping distance does not allow to visualize the hopping process directly by LTSEM, since our spatial resolution is limited to approximately 1μm.

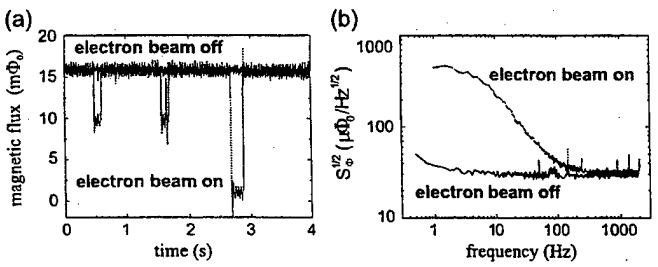

Fig.6: (a) time trace of SQUID output; (b) rms flux noise $S_\Phi^{1/2}$ vs frequency with (I_r=3 nA) and without e-beam irradiation.

VII. Integrated Magneotmeter

Multilayer high-T_c dc SQUIDs tend to show higher $1/f$ noise than single layer devices due to possible degradation from ex-situ film growth and additional patterning steps involved [1]. Cooling such structures in the ambient field is expected to lead to a further increase in low frequency noise, although no systematic studies on this issue have been presented yet. We investigated a Ketchen-type magnetometer with a spiral input coil on top of a dc SQUID washer with the geometry shown in the SEM picture of Fig.7(a). This device has been fabricated at UC Berkeley [8]. Previous studies of the local transport properties of this particular device by means of LTSEM has e.g. revealed that the input coil has reduced j_c at the locations where it crosses over the slit in the underlying washer [14]. We operated this device now in a flux-locked loop mode to produce $\Delta\Phi$-images as the ones shown in Fig.7(b) and Fig.8(b). Both Figures show SEM images (at the left) and $\Delta\Phi$-images (at the right) of the central part of the magnetometer which had its pick-up loop cut open to allow direct injection of a current. We find that most vortices are located *between* the turns of the input coil, and hence are only penetrating the lower YBCO film. This observation implies that the 8μm wide input coil is at least up to the maximum applied field of 40μT narrow enough to prevent entry of most vortices. An important observation is the presence of vortices at the via at the innermost turn of the input coil, which is shown more clearly in Fig.8 at higher magnification. Note that the $\Delta\Phi$-image in Fig.8(b) was taken at higher cooling field (B_0=40μT) as in Fig.7. The via was fabricated such that the bottom YBCO and STO layer was entirely milled away before deposition of the top YBCO layer. Hence, the contact of the two superconducting layers is only along the rectangular shaped via edges, which is indicated by the black lines in Fig.8(a). Evidently, the vortices are exactly located at these edges. It has been shown

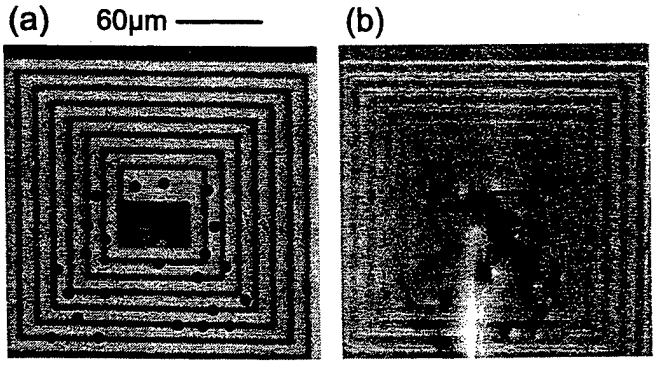

Fig.7: (a) SEM image of central part of integrated magnetometer with 8-turn input coil patterned in top YBCO film which is separated by an STO layer from the square washer in the bottom YBCO film with a vertical slit as SQUID hole (running from center to bottom). The via at the innermost turn connects both YBCO layers. (b) ΔΦ image at B_a≈20μT, T=77K showing various pinned vortices which are schematically drawn as dark dots in (a).

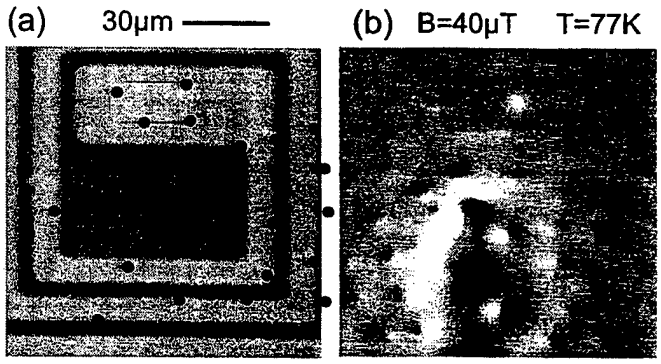

Fig.8: (a) SEM image of central part of integrated magnetometer showing the innermost turns of the input coil (light grey) on top of the washer (dark grey) in the bottom YBCO layer with the vertical slit (black) forming the SQUID hole. The via edges are indicated by black lines (b) $\Delta\Phi$ image showing various pinned vortices which are schematically drawn as dark dots in (a).

in [14] that the upper YBCO has a higher T_c than the bottom YBCO and that inside the via T_c is higher than in the input coil. This fact may play an important role upon cooling the device through T_c. The possibly degraded film quality at the via edges may be another important issue. A minimum in the pinning potential along these edges could explain the presence of vortices as we observed by LTSEM. The vortices may move rather easily along the via edge. This is expected to have particular impact on the low-frequency flux noise properties of the device, which we have not measured so far. Further investigation of low-frequency noise and vortex distribution in variable magnetic field will shed more light on these issues.

VIII. Conclusions

We demonstrated that LTSEM provides useful information on the local distribution of flux lines pinned in high-T_c SQUIDs and magnetometers based on either single layer or multilayer structures. The combination of vortex visualization with low frequency noise measurements in variable magnetic field is expected to give new insights into the mechanisms which are responsible for generation of the frequently observed high levels of flux noise in high-T_c SQUID magnetometers.

Acknowledgment

We would like to thank John Clarke and Greg Nichols for providing detailed layouts of their SQUID-readout electronics. The integrated magnetometer presented in this work was fabricated at UC Berkeley. We gratefully acknowledge the collaboration with F. Ludwig, E. Dantsker, R. Kleiner, A. H. Miklich , D. T. Nemeth and John Clarke who provided this device.

References

[1] D. Koelle, R. Kleiner, F. Ludwig, E. Dantsker, and J. Clarke, "High-transition temperature superconducting quantum interference devices," *Rev. Mod. Phys.* vol. 71, pp. 631-686, April 1999.

[2] E. Dantsker, S. Tanaka, and J. Clarke, "High-Tc SQUIDs with slots or holes: low 1/f noise in ambient magnetic fields," *Appl. Phys. Lett.*, vol. 70, pp. 2037-2079, April 1997.

[3] P. Selders, M. Vaupel, R. Wördenweber, G. Ockenfuß, A. v. d. Hart, and K. Keck, "Observation of and noise reduction by vortex lattice matching in $YBa_2Cu_3O_7$ thin films and rf SQUIDs with regular arrays of antidots", *Appl. Supercond.*, in press.

[4] M. J. Ferrari, M. Johnson, F. C. Wellstood, J. J. Kingston, T. J. Shaw, and J. Clarke, "Magnetic flux noise in copper oxide superconductors," *J. Low Temp. Phys.*, vol. 94, pp.15, 1994.

[5] R. Gross, and D. Koelle, "Low temperature scanning electron microscopy of superconducting thin films and Josephson junctions," *Rep. Prog. Phys.*, vol. 57, pp. 651-741, July 1994.

[6] R. Gerber, T. Nissel, H.-G. Wener, A. Willmann, R. P. Huebener, D. Koelle, and R. Gross, "Liquid nitrogen cooled sample stage for scanning electron microscopy," *Cryogenics*, vol. 37, pp. 21-25, January 1997.

[7] R. Gerber, T. Nissel, H.-G. Wener, A. Willmann, S. Keil, H. Hänsel, R. P. Huebener, D. Koelle, and R. Gross, "Low-temperature scanning electron microscopy for low noise studies of high-T_c superconductors," *IEEE Trans. Appl. Supercond.*, vol. 7, pp. 3231-3234, June 1997.

[8] F. Ludwig, E. Dantsker, D. Koelle, R. Kleiner, A.H. Miklich, D.T. Nemeth, J. Clarke, D. Drung, S. Knappe, and H. Koch, "High-T_c Multilayer Magnetometers with Improved Noise, " *IEEE Trans. Appl. Supercond.*, vol. 5, pp. 2919-2922, June 1995.

[9] S. Keil, R. Straub, R. Gerber, R. P. Huebener, D. Koelle, R. Gross, K. Barthel, "Imaging of vortices and 1/f-noise sources in YBCO dc SQUIDs using low-temperature scanning electron microscopy," *IEEE Trans. Appl. Supercond.*, vol.9, 1999; in press.

[10] M. J. Ferrari, J. J. Kingston, F. C. Wellstood, and J. Clarke, "Flux noise from superconducting $YBa_2Cu_3O_{7-x}$ flux transformers," *Appl. Phys. Lett.*, vol. 58, pp. 1106 - 1108, March 1991.

[11] P.M. Shadrin, Y.Y. Divin, S. Keil, J. Martin, and R.P. Huebener, "Comparative study of electron and laser beam scanning for local electrical characterization of high-T_c thin films and junctions, " *IEEE Trans. Appl. Supercond.*, vol. 9, 1999; in press.

[12] M. Peschka, Dissertation, Universität Tübingen, 1999.

[13] G.S. Mkrtchyan and V.V. Schmidt, *Sov. Phys. JETP*, vol. 34, pp.195, 1972.

[14] R. Gerber, D. Koelle, R. Gross, R. P. Huebener, F. Ludwig, E. Dantsker, R. Kleiner, and J. Clarke, "Low temperature scanning electron microscopy study of $YBa_2Cu_3O_{7-x}$ multilayer dc SQUID magnetometers," *Appl. Phys. Lett.*, vol. 68, pp. 1555-1557, March 1996.

Improved Direct-Coupled High-T_c SQUID Magnetometers for Operation in Magnetically Unshielded Environment

Frank Ludwig, Dietmar Drung, Sylke Bechstein, Jörn Beyer, and Thomas Schurig
Physikalisch-Technische Bundesanstalt, Section Cryosensors, D-10587 Berlin, Germany

Abstract — We have developed direct-coupled SQUID magnetometers based on 30° bicrystal junctions that can be cooled in static magnetic fields of 60 μT and exposed to ac magnetic fields with peak-to-peak amplitudes of at least 5 μT without increasing the noise at 1 Hz. The improved magnetometers are composed of a 100 pH SQUID loop with a linewidth of 4 μm and a pickup coil consisting of 16 parallel, 50 μm wide loops. Each of these loops crosses the bicrystal line, thus forming a flux dam with a critical current of about 1 mA. The best noise at 1 Hz of such a direct-coupled magnetometer cooled in 64 μT was 65 fTHz$^{-1/2}$.

I. Introduction

For various applications of high-T_c SQUIDs, systems are required that can be operated in magnetically unshielded environment. Here, the SQUID sensors are exposed to the static magnetic field of the earth (≈ 50 μT) as well as to time-varying magnetic fields, e.g., power line interferences with peak-to-peak amplitudes of up to about 1 μT. Even higher magnetic field variations in time occur in mobile SQUID systems, e.g., for the detection of mines. On the one hand, this requires the availability of highly balanced gradiometers, either hardware, electronic or software; on the other hand, the intrinsic noise of the sensors must not be increased by the environmental fields.

As published in [1,2], utilizing the superior properties of our 30° $SrTiO_3$ bicrystal junctions, we are able to fabricate direct-coupled SQUID magnetometers with system noise levels down to 24 fTHz$^{-1/2}$ and typical 1/f corners of 4 Hz when operated in a magnetically well shielded environment. However, we also found that these devices exhibit low-frequency excess noise when exposed to ac magnetic fields with peak-to-peak amplitudes of a few 100 nT [2]. In addition, for $B_{pp} > 500$ nT flux jumps occured with amplitudes corresponding to a change of magnetic flux in the pickup loop of 1 Φ_0. Replacing the wide pickup loop by a slotted one, consisting of 150 parallel lines with 10 μm linewidth, reduced the sensitivity to ac fields by at least one order of magnitude, but often low-frequency excess noise was observed even if operated in well shielded environment. We attribute this to the increased area of patterned edges which may exhibit sites of weaker pinning.

Manuscript received April 30, 1999.
This work was supported in part by the German BMBF under contract no. 13N7326.

In this paper, we present an improved direct-coupled SQUID magnetometer that is based on our own results and on recent work at Berkeley [3], IBM [4,5] and Magnesensors [6]. As will be shown the new SQUID magnetometers can be cooled in static magnetic fields as large as 80 μT and be operated in ac magnetic fields with peak-to-peak amplitudes at least up to 5 μT without increasing the noise at 1 Hz.

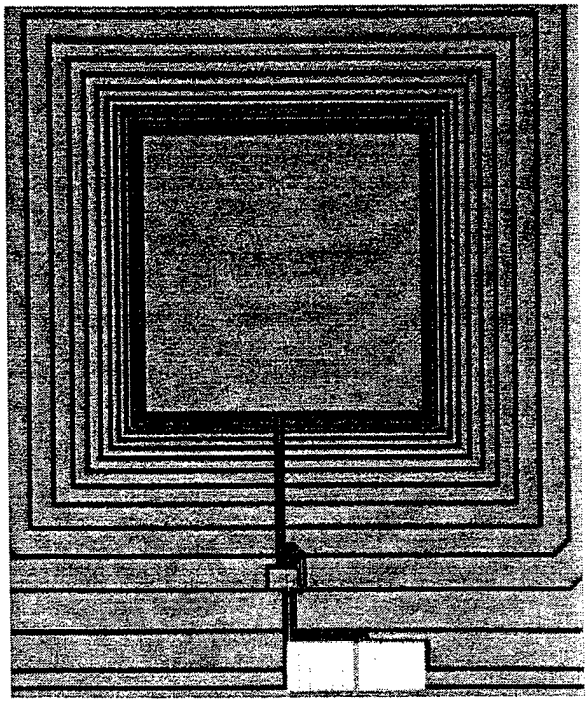

Fig. 1. Photograph of the SQUID region and part of the pickup loop of improved direct-coupled SQUID magnetometer. The bright areas at the lower edge are bond pads. The outermost pickup loop lines can only be seen at the lower edge of the photograph.

II. SQUID Magnetometers

A. Design

The SQUID inductance of the direct-coupled SQUID magnetometers discussed in this paper is 100 pH, the bicrystal junctions are 1.5 μm wide and 6 μm long. Compared to our previous design [2], the new one contains two basic modifications. First, the linewidth of the SQUID loop is reduced to 4 μm and the minimum separation of the SQUID to the pickup loop is increased to 100 μm. Second,

the originally 3 mm wide pickup loop is replaced by 16 parallel loops, each 50 μm wide. A photograph of part of a completed SQUID magnetometer is depicted in Fig. 1. As can be seen, in contrast to other approaches to replace a washer-like structure by several narrow parallel lines [2,6,7], the parallel loops are not equidistant but arranged to reproduce the current distribution of a wide, solid pickup loop. Consequently, although drastically reducing the area of superconducting thin film, the area A_p and inductance L_p of the pickup structure and thus the effective area of the magnetometer should remain almost unchanged. Furthermore, the screening current induced in each of the individual lines is expected to be about the same. All 16 loops cross the grain boundary, thus containing flux dams. With a critical current density of about 1×10^4 Acm^{-2}, which is a typical value for 30° grain boundary junctions, this provides a critical current of about 1 mA for each loop. Using the estimated inductance and area of the pickup loop, this results in a threshold field of about 4 μT (corresponding to an ac field peak-to-peak amplitude of $B_{pp} \approx 8$ μT) above which all flux dams should simultaneously open.

B. Fabrication

The SQUID magnetometers were fabricated from typically 200 nm thick $YBa_2Cu_3O_{7-x}$ (YBCO) films deposited by hollow cathode discharge sputtering on 10 mm x 10 mm $SrTiO_3$ bicrystals with 30° misorientation angle. The patterning is done by conventional photolithography and Ar ion beam etching. Details of the fabrication process are given in [8].

C. Housing

To prevent the YBCO films from moisture and to allow one to heat them above T_c, the SQUID chips are hermetically encapsulated in a ceramic housing with integrated thick-film heater. Compared to our previous encapsulation [2] where a heating power of about 7 W was necessary to warm the sample completely above T_c, in our current version a power of around 1 W is sufficient to thermally cycle the sensor. This improvement is mainly due to the better thermal decoupling of the SQUID and heater from the LN_2 bath.

D. Read-out Electronics and Measurement Setup

All sensors were operated with a direct-coupled flux-locked loop (FLL) electronics with 100 kHz bias reversal in the Berlin magnetically shielded room (BMSR). Details of the FLL electronics are comprehensively discussed in [9].

To characterize the sensors when exposed to external magnetic fields, we built a probe stick with an integrated gradiometrically wound Cu coil. This type of coil arrangement allows us to simultaneously characterize two SQUID magnetometers. The encapsulated SQUID sensors are placed in the center of the two 100-turn coils with a coil constant of 3.4 μT/mA. To measure the intrinsic magnetic field noise of the SQUID magnetometers cooled in a large static magnetic field, we developed a low-noise current source consisting of two 9 V-battery blocks buffered by operational amplifiers. For static fields of the order of the earth's magnetic field, the normalized white noise level of this current source is about 2.2×10^{-10} Hz$^{-1/2}$ with a 1/f corner around 1 Hz, i.e., for a field as high as 80 μT the noise level is only 17 fTHz$^{-1/2}$ at 1 kHz and 24 fTHz$^{-1/2}$ at 1 Hz, respectively. Note that the noise of the current source remains unchanged if the static field is set to zero (i.e., for grounded buffer amplifier input).

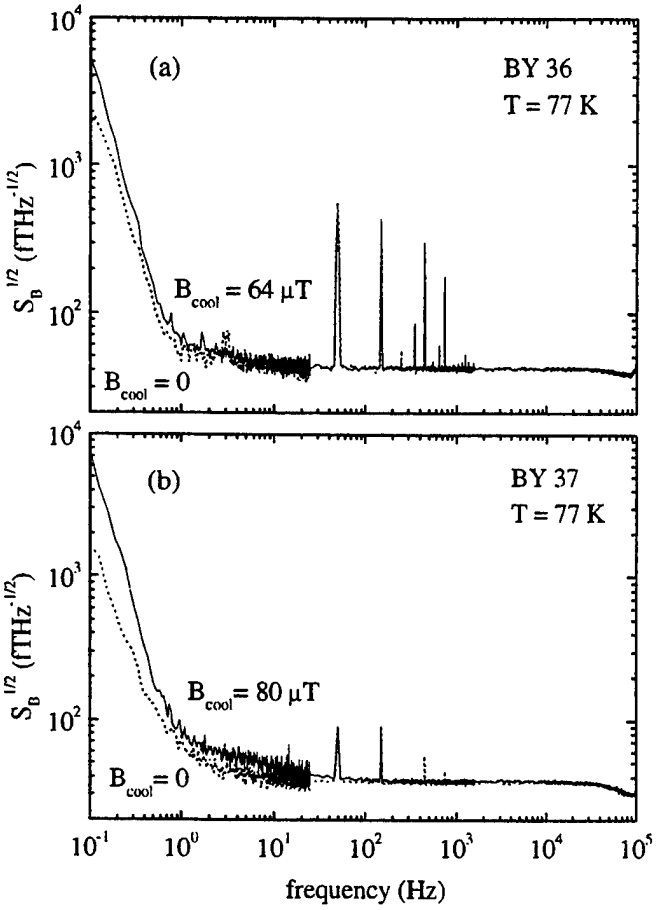

Fig. 2. Magnetic field noise spectra of two direct-coupled SQUID magnetometers cooled in zero magnetic field (dotted lines) and in a static magnetic field of (a) B_{cool} = 64 μT and (b) 80 μT (solid lines), respectively. Measurement were performed in BMSR with 100 kHz bias reversal FLL electronics. The noise includes the noise contribution from the direct-coupled preamplifier and the noise from the current source driving the field coil.

III. Sensor Performance

The magnetic field noise of two direct-coupled SQUID magnetometers with 16 parallel pickup loop lines measured in the BMSR with 100 kHz bias reversal is shown as dotted lines in Fig. 2. The total white noise of BY 36 (Fig. 2(a)), amounts to about 42 fTHz$^{-1/2}$ increasing to 54 fTHz$^{-1/2}$ at 1 Hz. The maximum peak-to-peak modulation voltage of this

device was 41 μV at a bias current of 52 μA. The field sensitivity of the magnetometers, measured with a Helmholtz coil, was 5.2 nT/Φ_0 which, within the usual 7% scatter from run to run, agrees with the calculation for a device with a solid, 3 mm wide pickup loop

A. Noise when Cooled in Static Magnetic Fields

To measure the noise when cooled in a static magnetic field, the SQUID is cycled above T_c by means of the integrated heater after the static magnetic field was switched on and has stabilized. Fig. 2(a) shows the magnetic field noise versus frequency of the SQUID magnetometer BY 36 cooled in nominally zero magnetic field and in a static magnetic field of $B_{cool} = 64$ μT, respectively. As can be seen, the magnetic field noise is about the same down to about 1 Hz. The magnetic field noise $S_B^{1/2}$ (1 Hz) = 65 fTHz$^{-1/2}$ is to our knowledge the lowest value reported for a high-T_c SQUID magnetometer cooled in a static magnetic field higher than that of the earth. The higher noise at 0.1 Hz in the field-cooling case is presumably caused by thermal fluctuations which will be subject of further investigations. Device BY 37 could be cooled without significantly increasing the 1 Hz noise in a static magnetic field of 80 μT (Fig. 2(b)). Here, the noise at 1 Hz was about 80 fTHz$^{-1/2}$. Note that the low-frequency spectrum in the field-cooling case was recorded over about 20 min.

B. Noise in ac Magnetic Fields

To investigate the influence of ac magnetic fields on the SQUID noise, a sinusoidal signal with frequency 5.3 Hz was applied to the coil while the SQUID was in the reset, i.e., unlocked mode. In this case, the ac field induces shielding currents in the closed superconducting loop, formed by the pickup loop and the SQUID shunt inductance, in contrast to the FLL mode, where the feedback coil should compensate all external field changes and the SQUID sensor should ideally remain field-free. After the generator was disconnected from the field coil, the FLL was closed and the noise was measured. When the generator voltage was gradually increased, peak-to-peak amplitudes of at least 5 μT could be applied without increasing the noise of the SQUID. However, when the maximum field amplitude was turned on abruptly or when a square-wave signal with an amplitude of a few 100 nT was applied, flux jumps with amplitudes of typically 1.2 mΦ_0 were observed. This amplitude just corresponds to a flux jump of 1 Φ_0 across a single pickup loop line. Note that in between these jumps the SQUID low-frequency noise was unchanged indicating that the induced shielding currents did not drive vortices into the superconducting films.

The same experiment was also performed for the field-cooling case. In contrast to the zero-field cooling case, we found that peak-to-peak amplitudes of a few 100 nT were sufficient to produce flux jumps in the pickup structure. This might be caused by the reduced critical current of the flux dams, representing long junctions, when cooled in a static magnetic field [10].

IV. Conclusions

We have developed high-T_c direct-coupled SQUID magnetometers that can be cooled in a static magnetic field exceeding that of the earth without increasing the noise at 1 Hz. The lowest noise at 1 Hz of a magnetometer cooled in $B_{cool} = 64$ μT was about 65 fTHz$^{-1/2}$. Measurements of the noise when the SQUID magnetometer was exposed to ac magnetic fields indicated that the device can stand fields with peak-to-peak amplitudes of at least 5 μT as long as there are no transients.

Transient signals, even with field amplitudes below 1 μT, resulted in flux jumps with amplitudes of 1.2 mΦ_0, corresponding to a jump of 1 Φ_0 across an individual line of the pickup structure. Importantly, there were no flux vortices driven into the superconducting films. However, since a peak-to-peak amplitude of 1 μT corresponds to about 200 Φ_0 in the SQUID loop, a saturation of the occurence of such flux jumps was usually not observed until about 30 min after the ac generator was disconnected. This problem could be solved by using flux dams with smaller critical currents [6].

References

[1] J. Beyer, D. Drung, F. Ludwig, and Th. Schurig, *Appl. Phys. Lett.*, vol. 72, pp. 203-205, 1998.

[2] F. Ludwig, J. Beyer, D. Drung, S. Bechstein, and Th. Schurig, *IEEE Trans. Appl. Supercond.*, in press.

[3] E. Dantsker, S. Tanaka, P.-A. Nilsson, R. Kleiner, and J. Clarke, *Appl. Phys. Lett.*, vol. 69, pp. 4099-4101, 1996.

[4] R. H. Koch, J. Z. Sun, V. Foglietti, and W. J. Gallagher, *Appl. Phys. Lett.*, vol. 67, pp. 709-711, 1995.

[5] F. P. Milliken, S. L. Brown, and R. H. Koch, *Appl. Phys. Lett.*, vol. 71, pp. 1857-1859, 1997.

[6] M. S. DiIorio, K.-Y. Yang, S. Yoshizumi, S. G. Haupt, D. Haran, R. H. Koch, F. P. Milliken, J. R. Rozen, D. K. Lathrop, S. Kumar, and H. S. Trammell III, *IEEE Trans. Appl. Supercond.*, in press.

[7] E. Dantsker, S. Tanaka, and J. Clarke, *Appl. Phys. Lett.*, vol. 70, pp. 2037-2039, 1997.

[8] F. Ludwig, J. Beyer, D. Drung, S. Bechstein, and Th. Schurig, *Appl. Supercond.*, vol. 5, pp. 345-352, 1998.

[9] D. Drung, *Rev. Sci. Instrum.*, vol. 68, pp. 4066-4074, 1998.

[10] B. Mayer, S. Schuster, A. Beck, L. Alff, and R. Gross, *Appl. Phys. Lett.*, vol. 62, pp. 783-785, 1993.

A HTS Gradiometer for Unshielded Operation from Moving Platforms.

Mark N. Keene, Nick J. Exon, Tom Horton, Richard G. Humphreys, Julian S. Satchell
DERA, St. Andrews Rd., Malvern, Worcs., WR14 3PS, U.K.

Abstract— We describe a configuration for a HTS SQUID-based gradiometer that may allow high sensitivity to be maintained from unshielded moving platforms in the earth's field. To operate with sufficient dynamic range, the gradiometer is located within a 'global' coil set which operates in a feedback loop in three orthogonal directions to maintain the field nearly constant. This loop is controlled by three or more orthogonal SQUID magnetometers with feedback to the global coil sets. Gradiometers are then configured from discrete magnetometers within the global coil sets. To obtain accurate gradient measurements, the mis-scaling, misalignment and misorientation between the sensors must be compensated for as well as additional effects due to the noise and non-homogeneity of the global feedback fields. Each of these difficulties belong to a class of problems which may be overcome with an adaptive signal processing algorithm based on the linearly constrained least squares method. We have made a single-axis gradiometer of this type using an array of four HTS SQUID magnetometers and initial results from it are presented.

I. INTRODUCTION

For SQUID sensors to operate well in unfavorable magnetic field environments, they must be configured into systems that reject the effects of their environment whilst remaining sensitive to the wanted signals. For example, in biomagnetic measurement systems the SQUIDs are often configured into gradiometers that are insensitive to uniform fields and distant magnetic sources, but remain highly sensitive to small nearby sources. In addition, the instruments are usually operated within magnetically shielded rooms that considerably help in rejecting interference from distant sources. There are a number of other applications (e.g. geomagnetic prospecting, magnetic anomaly detection, non-destructive evaluation etc.) where distant magnetic sources require measurement from platforms that are in motion. For these, magnetic shielding is not convenient and the motion of the sensor in the comparatively massive field of the earth presents great difficulty.

The main problems with operating SQUIDs from moving unshielded platforms are in achieving high levels of balance and low hysteresis in the gradiometers. Balance – the extent to which a uniform field is rejected – is mostly dependent upon the accuracy of the scaling, alignment, orientation and linearity of two remote field measurements. For thin film 'intrinsic' gradiometers where gradiometric flux transformers are employed, the linearity, alignment and orientation are usually very good and the scaling is the most problematical – requiring accurate matching of the two pickup coils of the flux transformer. In the 'configured' gradiometer schemes, such as Koch's 'Three SQUID Gradiometer (TSG)' [1], all the requirements for good balance are hard to achieve. However, with configured gradiometers there is scope to adjust the balance with external electronics or software whereas intrinsic gradiometers require mechanical adjustments.

The problem of hysteresis arises if flux enters or moves within the superconducting structures. Apart from hysteresis in the gradiometer output, this can substantially increase the low frequency noise. Hysteresis is more problematical for HTS gradiometers [2] than LTS, although attempts have been made to reduce the amount of flux trapping in HTS devices [3]. Configured gradiometers are far less affected by hysteresis because the feedback arrangements tend to maintain the local field at the SQUIDs largely constant irrespective of the external field.

In this abstract we present a scheme by which it may be possible to operate a SQUID gradiometer instrument for the measurement of remote dipoles whilst in motion within the earth's field. In section II we describe the gradiometer and in section III the balancing algorithm is discussed. Initial results from the gradiometer are presented in section IV.

II. THE GRADIOMETER

For simplicity we shall initially describe the gradiometer concept [4] based on two SQUIDs although this is not sufficient for a practical device. The SQUIDs operate in individual flux-locked loops (FLLs) to behave as separate linear magnetometers as shown in Fig. 1. The outputs are summed to form an estimation of the mean field between them and this is fed back via an integrating current source to a global coil set acting in the sensitive direction of the

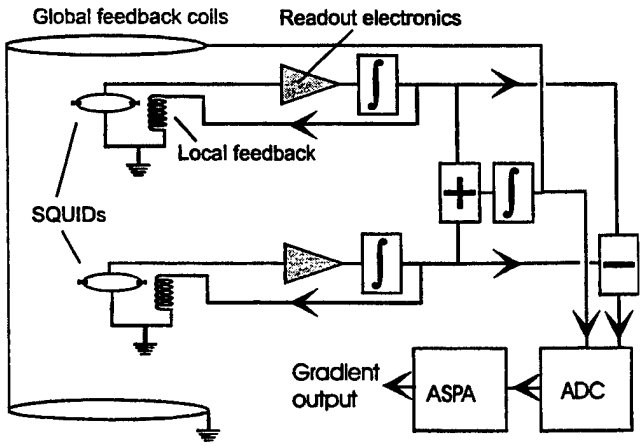

Figure 1. Schematic of the principles of the gradiometer. The sum and difference are digitised (ADC) before signal processing (ASPA).

SQUIDs. The dynamics of the feedback electronics for this outer loop are set to have enough output range and slew rate to cope with the expected motions of the platform in the earth's field. However, to do this the field noise within the gradiometer, caused by the outer feedback loop electronics, will be higher than the equivalent SQUID noise. The requirement on the dynamic range of the inner FLLs is to be sufficient to track this field noise whilst being SQUID noise limited. Because this field noise from the outer feedback loop is common to all SQUIDs in the instrument, the balance requirement for the gradiometer is that it should cancel the electronics induced field noise rather than the external field.

This description applies to most configured gradiometer schemes like the TSG and similar [1] but there are important advantages to using global feedback as opposed to the localized second feedback of previous schemes in mobile systems. The global feedback can be applied in three orthogonal directions provided one has sensors interrogating those directions. This is illustrated in Fig. 2 and represents the configuration to measure a single gradient accurately. The risk of flux trapping is reduced because all components of the external field are nulled over the entire gradiometer and the feedback field over the area of the SQUIDs is far more uniform than with localized feedback. With global feedback the effects of mis-orientation of the SQUIDs can also be more easily corrected. Although four SQUIDs are required to measure a single gradient, each additional gradient requires the addition of only one extra SQUID.

In Fig. 2 the output of the SQUIDs from which the gradient is derived, Z1 and Z2, are subtracted with an analogue circuit. The output of this contains the scaling, alignment and orientation errors of the SQUIDs and should be regarded as an estimate of the gradient. (Imperfect subtraction from this circuit tends to compound the scaling error but does not introduce new types of error.) Its main function is to allow 16 bit analogue-to-digital conversion (ADC) without loss of precision. The direct outputs of the X and Y SQUIDs are used in software to correct for the errors and lower precision is required for this function.

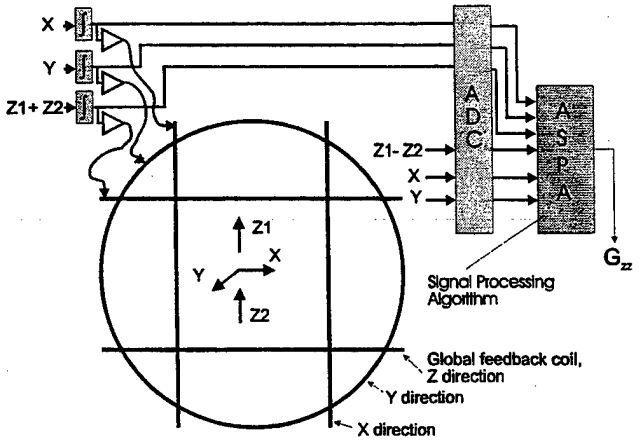

Figure 2. Schematic of the configuration for a single axis gradiometer that could operate unshielded whilst in motion.

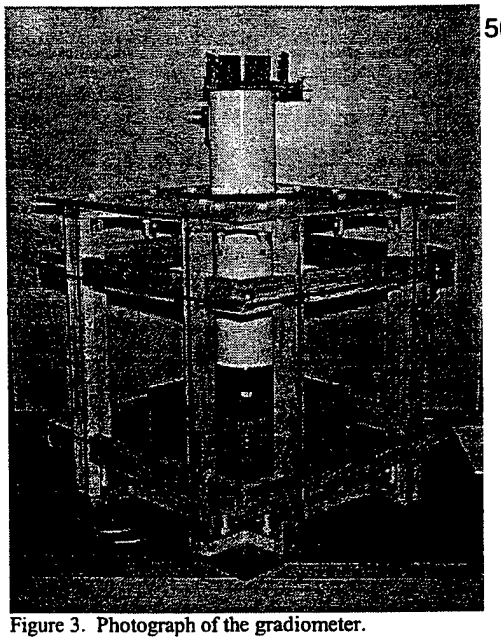

Figure 3. Photograph of the gradiometer.

III. Adaptive Balancing

The adaptive processing technique to balance the gradiometer is known as the 'linearly constrained least-squares method' [5]. This is used extensively in phased array radar and sonar systems but we have modified it for use for magnetic sensor arrays [6]. Our algorithm called ASPA, functions by minimising the energy of all inputs from the sensors subject to a constraint that forces the best estimate of the required field gradient. The cost function we used is,

$$E(N) = \sum_{n=1}^{N} \left(\beta^{(N-n)} \underline{\mathbf{x}}^T(n)\, \underline{\omega}\right)^2 \qquad (1)$$

where $\underline{\mathbf{x}}(n)$ is the input data set at time n, $\underline{\omega}$ is a vector of weights and β ($0<<\beta<1$) discounts older data. *E(N)* is thus minimised with an appropriate constraint on $\underline{\omega}$ to yield the required gradient, then the output is the single value,

$$y(n) = \underline{\mathbf{x}}^T(n)\, \underline{\omega}\,. \qquad (2)$$

The selection of β is important because if it is too small the adaptation becomes rapid and the wanted signals may be 'adapted out'. If it is too large then the adaptation time may be inconveniently long. β can be adjusted in real time to suit the conditions. The ASPA outputs a single gradient estimation defined by the constraint on $\underline{\omega}$, so for multiple gradient measurements several algorithms with different constraints are operated in parallel. All algorithms share the same input data.

There are several important advantages of this technique over mechanical and electronic balancing. The orientation and alignment of the sensors do not require careful setting up and the mechanical rigidity of the baseline need not be as great as a non-adaptive gradiometer. Another important advantage is there is no requirement on measuring and correcting the imbalance in a low gradient environment.

These considerably reduce the cost of making and setting up a gradiometer as well as servicing.

IV. Apparatus

A single axis gradiometer has been constructed, comprising four SQUID magnetometers configured as illustrated in Fig. 2. The SQUIDs are encapsulated and mounted on a Tufnol former in the bottom of a cylindrical biomagnetism dewar containing liquid nitrogen. The SQUID readout electronics are mounted on the top plate, and a single ribbon cable connects them to a controller box and power supply. A direct readout scheme similar to that developed by Drung [7] was adopted. The dewar is rigidly mounted within a 3-axis coil set comprising three orthogonal pairs of square coils as shown in Fig. 3. The coils are all 0.5 m on each side and each pair is separated by 0.545 times the side length for maximum uniformity of the internal field.

The dewar is initially cooled in a state of zero field that is maintained within the global coil set. This is accomplished by using a three-axis fluxgate in the control loop. Once the SQUIDs are cooled and operating, control is switched over to them and the fluxgates are removed. This procedure ensures the SQUIDs are zero-field cooled and maintained near zero whilst the gradiometer is in operation irrespective of its motion. The SQUID outputs are passed to a computer that performs the data processing and storage operations

IV. Initial results

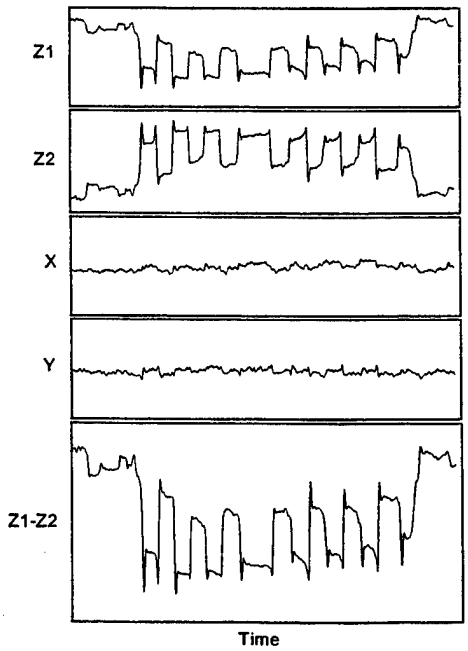

Figure 4. Outputs of the four magnetometers and the analogue difference of Z1 and Z2 when influenced by a small remote dipole that is rocking. Vertical scales are identical.

Initial testing has been conducted within an electrostatically shielding room, but no magnetic shielding was used. With the SQUIDs controlling the global feedback coils, the outputs of the four magnetometers and the electronically differenced Z1-Z2 pair are shown in Fig. 4. Here, a magnetic dipole was rocked to-and-fro several times to influence the gradiometer. The Z1 and Z2 outputs are largely equal and opposite to one another. This is because the global feedback in the Z direction is subtracting the mean field between Z1 and Z2. The difference between the Z1 and Z2 traces is shown in the lower trace and represents an approximation to the gradient that includes the errors discussed in Section II. The outputs of the X and Y sensors are largely independent of the applied field from the dipole, as expected because the current in the X and Y global coils reflects the applied fields. (A weak influence on the X and Y outputs can be seen in Fig. 4, which is believed to be due to non-orthogonality of the sensors or mis-alignment between the sensors and the global coils. These errors are expected to be adapted out in the ASPA.)

This gradiometer has not yet been integrated with the ASPA so the noise performance and motion characteristics are not yet known. The ASPA has, however, been extensively tested with gradiometers based on fluxgates [6] and proved advantageous over mechanical and electronic balancing for this type of sensor.

Summary

We have devised a gradiometer concept designed to allow high sensitivity operation of SQUID gradiometers from moving platforms in the earth's field. A system of global feedback coils has been shown to cancel the uniform field on the gradiometer whilst allowing the gradient field to be measured. An adaptive balancing algorithm, that has proved successful in balancing fluxgate gradiometer systems, has not yet been incorporated.

References

[1] R. H. Koch, J. R. Rozen, J. Z. Sun, W. J. Gallagher, *Appl. Phys. Lett.*, vol. 63, pp 403, 1993.

[2] M. N. Keene, N. J. Exon, R. G. Humphreys, N. G. Chew, *J. Appl. Phys.*, vol. 79, (11), pp8783-8791, June 1996.

[3] E. Dantsker, T. Tanaka, J. Clarke, *Appl. Phys. Lett.*, vol. 70, pp2037, 1997.

[4] M. N. Keene, J. S. Satchell, Patent GB 9705348.2, 1997.

[5] R. A. Monzingo, T. W. Miller, *Introduction to Adaptive Arrays*, John Wiley and Sons.

[6] M. N. Keene, S. Takel, J. Morrison, N. J. Exon, J. S. Satchell, (1999 Maritime Electromagnetics Conference) unpublished.

[7] D. Drung, *Appl. Phys. Lett.* vol. 67, (10), pp1474-1476, Sept. 1995.

A High Tc Superconducting Magnetic Gradiometer for Mobile Operation

Ted R. Clem, David J. Overway, John W. Purpura, George I. Allen, and John T. Bono
Coastal Systems Station, Panama City, FL 32407, USA

Roger H. Koch, James R. Rozen, and George A. Keefe,
IBM T.J. Watson Research Center, Yorktown Heights, NY 1059, USA

Abstract • High Tc SQUID magnetic sensors cooled by liquid nitrogen offer new opportunities for magnetic anomaly detection in mobile applications. The prototype for a high-Tc SQUID-based magnetic gradiometer cooled by liquid nitrogen has been developed and is being evaluated for such applications. Sensor design and experimental procedures for the evaluation are described. The results of experiments with the sensor operating unshielded stationary and in motion are reported.

I. Introduction

Passive magnetic sensors provide one means to conduct mobile area surveys and search operations for the detection of magnetic anomaly targets, especially for underwater detection. A helium-cooled SQUID-based magnetic-field gradiometer incorporating niobium bulk and wire superconducting components was developed in the 1980's and has been successfully demonstrated for such applications [1], [2]. A nitrogen-cooled sensor can have the following advantages compared to its helium-cooled counterpart: (1) significant reduction in dewar size for systems with significant space constraints and (2) reduction of cryogen logistics and support requirements. Current limitations in high-Tc fabrication technology (available in 1999) do not permit the development of high-sensitivity gradiometers following approaches pursued with niobium technology in which counterwound wire or thin-film loops can be adapted appropriately. The concept of a three-sensor gradiometer (TSG) provides one means to circumvent these limitations [3]-[5]. In this approach a gradiometer is synthesized by differencing two independent SQUID magnetometers. A third reference sensor is used to null out the ambient Earth background field at the position of the two primary magnetometers, providing common-mode rejection critical for mobile operation. The prototype for a nitrogen-cooled High-Tc SQUID Gradiometer (HTSG) based on the TSG concept has been developed and is being evaluated for mobile operation. The TSG concept has also been explored for man-portable operation using fluxgate magnetometers [5], [6]. Sensitivity on the order of 300 pT/m-$Hz^{1/2}$ at 0.1 Hz has been obtained in motion for the fluxgate sensor. The high-Tc version described here is being explored to attain higher sensitivity and correspondingly longer detection ranges.

Manuscript received April 30, 1999.
This work is being supported by the U.S. Office of Naval Research (Code 322GG).

II. Sensor Design

The HTSG prototype consists of cryogenic electronics, room temperature electronics and a dewar. The cryogenic electronics, including SQUID magnetometers and copper-wire coils for field nulling, are mounted on a single-crystal silicon rod (Fig. 1). Three SQUID magnetometers are mounted orthogonally on three faces on each of two cubes. The cubes are mounted within the silicon rod midway down center bores transverse to the rod's axis and are separated by a distance of 0.3 m along the cylinder's axis. The SQUID magnetometers are $YBa_2Cu_3O_{7-x}$ devices with the magnetometer loops directly-coupled to dc SQUIDs with bicrystal junctions, manufactured by Conductus, Inc. [7].

For each cube, three sets of orthogonal Helmholtz-like coil pairs, controlled by a triad of fluxgate magnetometers, null out the Earth's magnetic field at the position of the SQUID magnetometers. One coil pair is oriented with its axis normal to the plane of each magnetometer in the cube. The nulling coils are connected in series for common mode rejection of the external field components in the gradient signals synthesized by magnetometer subtraction.

16-MHz Flux-Locked Loop (FLL) electronics, developed previously for low-Tc thin film sensors, are also being utilized for the HTSG to provide large bandwidth for electromagnetic interference immunity [8]. Bias-reversal circuits have been added in the high Tc case for 1/f noise suppression. A liquid helium dewar developed previously for high performance in mobile operation is being used to cool the high-Tc electronics with liquid nitrogen and to evaluate sensor performance in motion [9].

In a conventional low-Tc gradiometer with counterwound loops, the gradiometer channels cannot be perfectly balanced. In other words, they are not immune to field changes when rotated in a uniform magnetic field because of limitations in manufacturing precision and the presence of magnetic material close to the loop. Balance for a TSG is complicated by three factors: (1) the complexity in mechanically aligning independent SQUID and fluxgate magnetometers and nulling coils; (2) electronic balance of electronic gains and phases, and (3) noise introduced into the magnetometers from the coils. For this HTSG prototype, several initial balance steps are implemented to maintain resolution for proper signal digitization. First, care is taken in the mechanical alignment of the sensors and field nulling is optimized for maximum balance. In addition, analog signal subtraction after the SQUID electronics is used to synthesize gradient signals and thus minimize signal dynamic range in digitization. Magnetometer signals are electronically summed with the

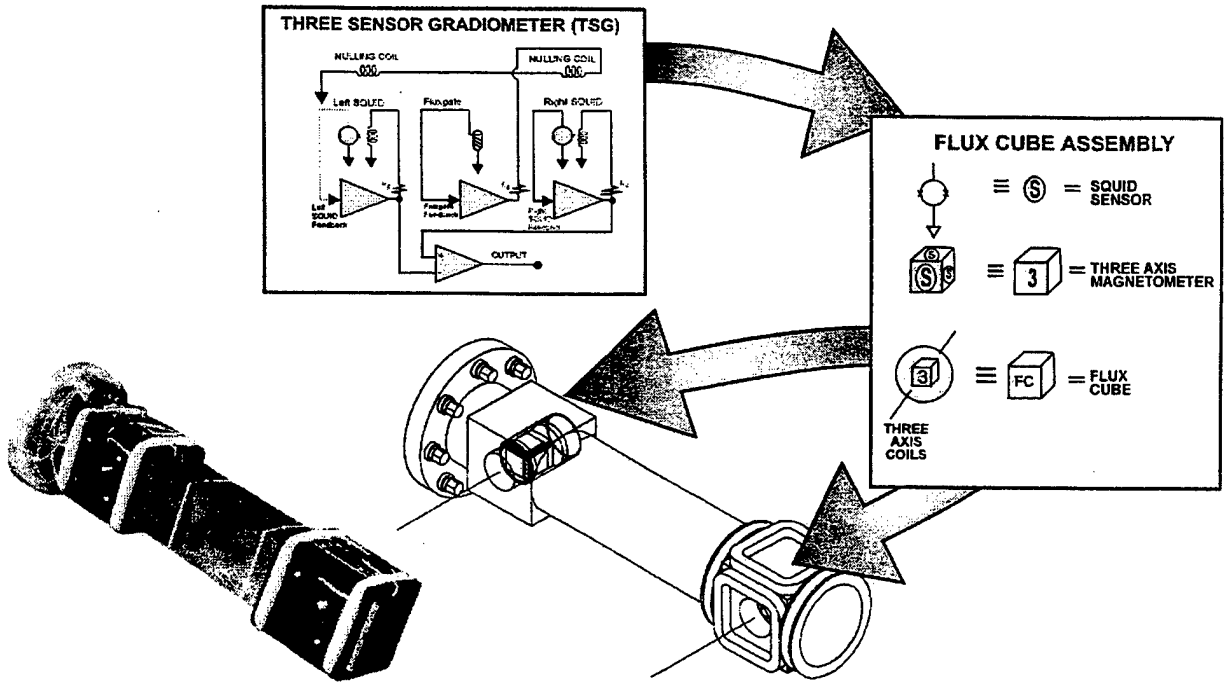

Figure 1. Concept of three-sensor gradiometer implemened in high Tc superconducting gradiometer and photograph of prototype under evaluation.

synthesized gradiometers prior to the digitization to further reduce residual imbalance signals. Frequency-dependent signal processing provides balance correction and also eddy-current compensation. In this study, the gradiometer channels are compensated using the 3 orthogonal fluxgate magnetometers and 3 orthogonal SQUID magnetometers. The autospectral densities, appropriate cross-spectral densities and corresponding transfer functions for gradiometer and magnetometer channels are calculated. Each compensated gradiometer spectral density is then calculated by subtracting the 6 correlated magnetometer contributions from the raw gradiometer autospectral density.

III. Experimental Results and Discussion

HTSG performance stationary and in motion is summarized below. *In totally unshielded field operation stationary*, a white noise floor of 0.8 pT/m-Hz$^{1/2}$ at 1 Hz and 4 pT/m-Hz$^{1/2}$ at 0.1 Hz have been demonstrated (Fig. 2(a)). The magnetometer white noise, assumed to be equally divided between the two differenced magnetometers, is 0.1 pT/Hz$^{1/2}$, consistent with noise figures of 0.08 pT/Hz$^{1/2}$ reported by the manufacturer. This noise amplitude at 0.1 Hz is 30 times smaller than the initial results obtained with the cryogenic electronics immersed directly in liquid nitrogen inside a metallic dewar [10]. The following factors are significant in explaining this improvement. Operation in an exchange-gas environment lowered the noise amplitude at 0.1 Hz by a factor of 3. The exchange-gas environment apparently eliminated noise from nitrogen boiling when the SQUIDs were immersed in cryogen. Once this noise source was eliminated, the impact of field nulling was unmasked. The sensitivity at 0.1 Hz was reduced by another factor of 3 by nulling. This noise reduction is attributed to reduction in the magnitude of flux trapped at cooldown and the affiliated reduction in thermally activated flux motion. Operation in a composite-material dewar further reduced the low-frequency noise power obtained in initial measurements using metallic dewars from a 1/f^2 law down to a 1/f law to provide the noise level of 3 pT/m-Hz$^{1/2}$ at 0.1 Hz in Fig 2(a). This reduction is attributed to elimination of eddy currents generated in a metal dewar from geomagnetic field fluctuations even in a stationary condition.

The HTSG has been operated in a test facility isolated from magnetic, electrical, and RFI noise typical of building, vehicular and personnel activity. This isolation provides one means to measure sensor-intrinsic noise at frequencies less than 1 Hz. The test facility has a nonmagnetic design as required for motion testing. The motion testing is conducted with the sensor mounted on a platform that generates yaw, pitch and roll rotations. Rotations on the order of one degree and corresponding field fluctuations on the order of 1000 nT/Hz$^{1/2}$ are generated at sub-Hertz frequencies to simulate conditions of interest for mobile operations.

When the sensor is operated in motion, the noise power is substantially elevated and follows a 1/f^2 law at lower frequencies. The sensitivity at 0.1 Hz is 100 pT/m-Hz$^{1/2}$, a factor of 30 above its performance stationary (Fig. 3(b)). It is a factor of 16 above the motion performance displayed for the low Tc gradiometer obtained from an at-sea demonstration to locate unexploded ordnance. As discussed below, flux motion induced by field change has been identified as one major source for this excess noise.

We are currently attaining balance on the order of 3 parts in 10^5, primarily through frequency-dependent signal processing. Balance of the SQUID magnetometers at levels of several parts per 100 is expected from the precise

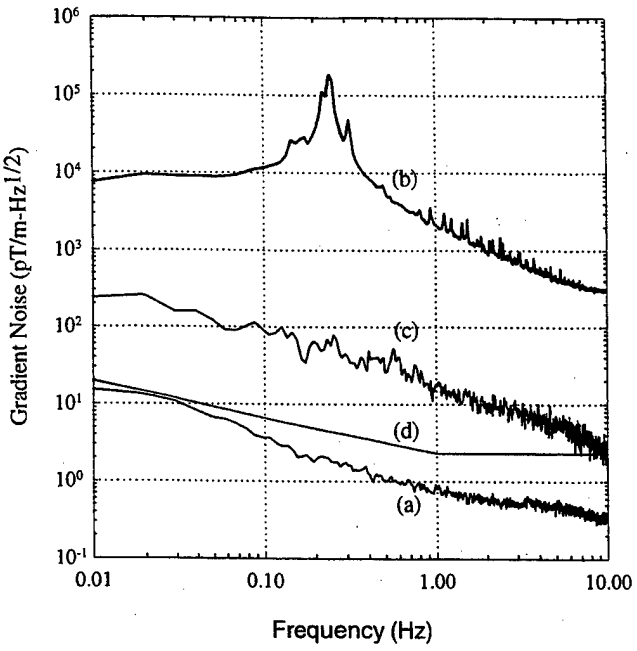

Figure 2. Performance of high Tc superconducting gradiometer operating inside composite-material dewar with SQUID sensors cooled in exchange-gas environment and maintained in a low-field environment established by nulling coils: (a) stationary spectrum, (b) uncompensated spectrum in motion, and (c) compensated spectrum in motion. The performance of the low Tc gradiometer in at-sea demonstration to locate unexploded ordnance is depicted in (d).

mechanical alignment in fabrication. The balance components as measured in motion studies with the field-coil gains optimally set are on the order of 1 part in 100. This represents a factor of 10 improvement over original results.

Originally large quadrature imbalance signals were observed that could not be effectively removed using the analog balance trim electronics. The quadrature signals were identified with phase shifts in the nulling-coil electronics. Based on results of field ramping experiments, threshold field changes on the order of 100 nT are sufficient to generate appreciable nonlinear, hysteretic behavior in these SQUID magnetometers. Hence anomalous signals were excited from the 300-nT signals imposed on the SQUIDs. Modification to the nulling-coil electronics to eliminate the phase shifts has reduced this noise effect.

In addition to field-induced flux motion, temperature stability and acceleration-induced substrate flexure have been identified as potential sources of anomalous noise. SQUID susceptibility to temperature change on the order of 100 mK/K-$Hz^{1/2}$ is projected for this class of SQUID sensors. Dewar thermal stability is critical to mitigate this susceptibility. The convectively cooled dewar used for the low-Tc gradiometer mentioned in Section I has demonstrated temperature fluctuations on the order of 30-100 mK/$Hz^{1/2}$ when filled with liquid nitrogen and subjected to motions typical of this study. In contrast, the temperature stability for the exchange-gas dewar used in this study when filled with liquid nitrogen has been measured to be less than 1 mK/$Hz^{1/2}$ in the for frequencies greater than 0.1 Hz. Hence temperature-induced effects are not considered to be a limiting factor at current sensitivity levels. Based on estimates of elastic bending, dynamic balance fluctuations arising from substrate flexure is predicted not to limit performance at current sensitivity levels. Experiments using accelerometers to measure balance stability will be conducted to validate this factor.

IV. Summary and Future Plans

The prototype for a high-Tc superconducting gradiometer for use in mobile operation has been assembled and its evaluation is in progress. Its sensitivity stationary has been demonstrated at a level of 0.8 pT/m-$Hz^{1/2}$ at 1 Hz and 4.0 pT/m-$Hz^{1/2}$ at 0.1 Hz, performance better than its low Tc counterpart in motion. Promising results have been attained from initial motion testing of the high Tc sensor, with a performance of 3 pT/m-$Hz^{1/2}$ at 10 Hz. Investigations continue to understand and reduce elevated noise at lower frequencies, reaching a level of 100 pT/m-$Hz^{1/2}$ at 0.1 Hz. Future plans include upgrade of room-temperature electronics from benchtop to field-deployable version and an at-sea demonstration of the sensor against a test field of ferrous targets.

References

[1] T. Clem, "Superconducting magnetic sensors operating from a moving platform," IEEE Trans. Appl. Sup., vol. 5(2), p. 2124, 1995.

[2] T.R. Clem, G.J. KeKelis, J.D. Lathrop, D.J. Overway, and W.M. Wynn, "Superconducting magnetic gradiometers for mobile applications with an emphasis on ordnance detection," in *SQUID Sensors: Fundamentals, Fabrication and Applications*, H. Weinstock, Ed., Kluwer Academic Publishers, p. 517, 1996.

[3] R.H.Koch, "Gradiometer having a magnetometer which cancels background magnetic field from other magnetometers," U.S. Patent No. 5,122,744, 1992.

[4] R.H. Koch, J.R. Rozen, J.Z. Sun, and W.J. Gallagher, "A three sensor gradiometer," Appl. Phys. Lett., vol. 63(3), p. 403, 1993.

[5] G.I. Allen, R.H. Koch, and G. Keefe, "Unique man-portable 5 element fluxgate gradiometer system, in *Detection Technologies for Mines and Minelike Targets*, A. C. Dubey, I. Cindrich, M. Ralston, and K. Rigano, eds., the International Society for Optical Engineering, Proc. SPIE 2496, p. 384, 1995.

[6] R.H. Koch , G.A. Keefe, and G. Allen, "Room temperature three sensor magnetic field gradiometer," Rev. Sci. Instrum. 67(1), p. 230, 1996.

[7] R. Cantor, L.P. Lee, M. Teepe, V. Vinetskiy, and J. Longo, "Low Noise, Single-Layer $YBa_2Cu_3O_{7-x}$ DC SQUID Magnetometers at 77K," IEEE Trans. Appl. Sup., vol. 5(2), p. 2927, 1995.

[8] R.H. Koch, J.R. Rozen, P. Woltgens, T. Picunko, W.J. Goss, D. Gambrel, D. Lathrop, D. Overway and R.F. Wiegert, "High Performance SQUID Feedback Electronics," Rev. Sci. Instrum., vol. 67(8), p. 2968, 1996.

[9] J.H. Eraker, "Sensor temperature stability performance of the Advanced Liquid Helium Dewar," in *Advances in Cryogenic Engineering*, vol. 41.

[10] R.H. Koch, F.P. Milliken, G.A. Keefe, J.R. Rozen, S.L. Brown, and S. Haupt, "Motion-Capable High T_c SQUID Gradiometer," presented at the 3rd European Conference on Applied Superconductivity, July 1997, unpublished.

Long Baseline HTS Flipchip Gradiometer

K. A. Kouznetsov, J. Borgmann, R. McDermott and John Clarke
University of California, Berkeley and Materials Sciences Division, LBNL, Berkeley, CA 94720

R. H. Koch
IBM T. J. Watson Research Center, Yorktown Heights, NY 10598

C. Soble, V. Matijasevic
Conductus Inc., Sunnyvale, CA 94086

Abstract—We have fabricated and tested a thin film, first-derivative gradiometer in which a planar flux transformer deposited on a sapphire substrate is permanently bonded to a directly coupled magnetometer deposited on a $SrTiO_3$ bicrystal. The asymmetric flux transformer has a baseline of 48mm. The two substrates are bonded together with a layer of epoxy 10μm thick. Rejection of the out-of-plane component of the uniform magnetic field is achieved by trimming the pickup loop; the best values of out-of-plane balance are about 1 part in 2000. The balance with respect to the two in-plane components of the uniform magnetic field are 1 part in 150 and 1 part in 1050.

I. Introduction

For many years, Superconducting Quantum Interference Devices (SQUIDs) have been successfully used in biomagnetic applications such as magnetocardiography (MCG) and magnetoencephalography (MEG). Because the magnetic signals are weaker than the background noise, it is essential to reduce the ambient noise by means of spatial gradiometry or magnetic shielding or often a combination of both [1]. In the case of low-T_c SQUIDs, the most commonly used first-order gradiometer is axial and consists of two loops of superconducting wire wound in opposition with a baseline of 40-100 mm. In the case of high-T_c SQUIDs, where suitable wire is not available, only planar hardware gradiometers have been demonstrated [2]. The baselines of these devices are limited to the size of the substrate, typically 10 mm, and are not suitable for biomagnetic measurements. An alternative technique is to form gradiometers electronically by subtracting signals from two or more flux-locked magnetometers [3].

II. Principles of Operation

In previous publications, we described planar gradiometers [4] fabricated from a thin film of $YBa_2Cu_3O_{7-x}$ (YBCO) that measures off-diagonal gradients. Both a first-order gradiometer with a baseline of 48mm and a second-order gradiometer with a baseline of 31mm have been demonstrated.

The principle of the first-order gradiometer is shown in Fig. 1(a). The asymmetric flux transformer consists of a pickup loop of area A_p and inductance L_p and an input coil of area A_i and inductance L_i. The input coil is inductively coupled to a directly coupled magnetometer of area A_m and inductance L_m via a mutual inductance M_i. Using flux conservation in the magnetometer and the transformer, we find

$$B_0 A_m - L_m J_m - M_i J_i = 0 \qquad (1)$$

$$B_0 (A_1 + A_i) - (L_1 + L_i) J_t - M_i J_m = 0, \qquad (2)$$

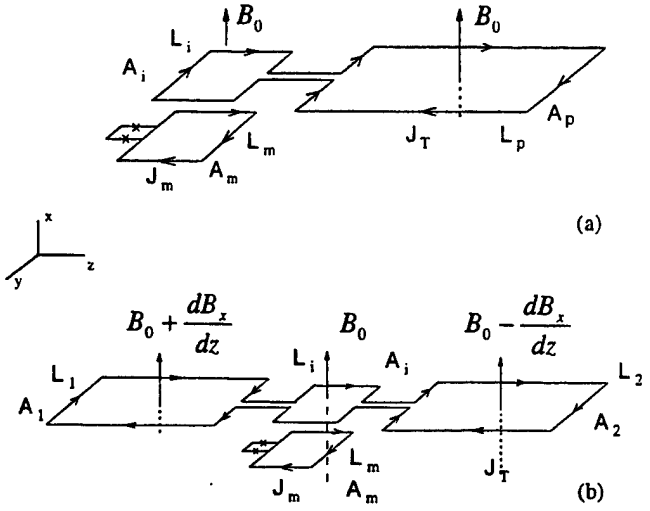

FIG. 1 Schematic diagrams of (a) first-order and (b) second-order gradiometers.

Manuscript received April 30, 1999. This work was supported by the Director, Office of Energy Research, Office of Basic Energy Sciences, Materials Sciences Division of the U.S. Department of Energy under Contract No. DE-AC03-76SF00098.

where J_m and J_t are the screening supercurrents in the magnetometer and transformer, respectively. To achieve the balance condition $J_m=0$, we find the value of the mutual inductance that satisfies the balance condition:

$$M_i = [A_m/(A_1 + A_i)](L_1 + L_i). \quad (3)$$

In the second order gradiometer, shown in Fig. 1(b), there are two identical pickup loops of areas $A_1=A_2$ and inductances $L_1=L_2$ placed symmetrically on either side of the input coil. Any first-order gradient dB_x/dz is rejected by the symmetry of the flux transformer. Rejection of uniform fields is achieved by choosing the appropriate value of the mutual inductance between the magnetometer and the input coil:

$$M_i = [A_m/(A_1 + A_2 + A_i)](L_1 + L_2 + L_i). \quad (4)$$

In our previous work [4], we varied the position of the magnetometer with respect to the flux transformer by means of a mechanical screw to achieve the optimal value of the mutual inductance. Although this sufficed to demonstrate the principles of the gradiometers, a device with mechanical adjustment is obviously not a viable option for practical biomagnetic systems. Any practical solution must involve a permanently assembled hardware gradiometer with an intrinsic balance better than 1 part in 100.

III. FLIPCHIP GRADIOMETER

We describe a hardware first-order gradiometer in which the magnetometer is permanently bonded to the flux transformer in a flipchip configuration. The single-layer, directly coupled magnetometer was patterned in a 150nm thick film of YBCO that was laser deposited a $SrTiO_3$ bicrystal. We estimate $A_m=20mm^2$ and $L_m=4nH$. The flux transformer was patterned in a 260nm thick YBCO film that had been coevaporated onto a 100mm diameter r-plane sapphire wafer with a CeO_2 buffer. The baseline of the gradiometer, given by the distance between the centers of two pickup loops, is 48mm. For the flux transformer, we estimate $A_1=213mm^2$, $L_1=23nH$, $A_i=49mm^2$, $L_i=9nH$.

The two substrates were bonded together with a two component, 24 hour epoxy. The epoxy was approximately 10μm thick. We aligned the substrates in-plane using a high power microscope, with an accuracy of approximately 20μm. The separation between the substrates was chosen to yield a mutual inductance higher than the optimal value given by Eq. (3).

We cooled the gradiometer to 77K and applied a 12Hz uniform magnetic field perpendicularly to its plane by means of a Helmholtz pair; there was no magnetic shielding. The output of the flux-locked loop was measured with a lock-in detector to determine the degree of imbalance. We then brought the device back to room temperature and trimmed the outside edge of the pickup loop. The effect of trimming is to increase the inductance of the pickup loop L_1 so that the balance condition Eq. (3) is satisfied for a fixed valued of M_i. Using this technique, we could adjust the balance of the gradiometer with respect to out-of-plane fields to between 1 part in 400 and 1 part in 2000 in 2 or 3 iterations. We also determined the in-plane balance by applying a uniform field along the y- and z-directions, and found typical values of 1 part in 1050 and 1 part in 150, respectively. These values are determined by the degree to which we can adjust the two substrates to be parallel, and possibly by any non-planarity of the flux transformer. We made no attempt to improve on the in-plane response.

After trimming the out-of-plane balance, we measured the response of the gradiometer to magnetic fields and higher order field gradients. Two parallel wires arranged beneath the Dewar in the plane of the gradiometer were used as a source of field and field gradient. An alternating current was passed through one wire and back through the other in order to create a first-order gradient that falls off as $1/x^3$ in the far field limit; here x is the distance between the centerline of two wires and the center of the baseline of the gradiometer. The results of these measurements are shown in Fig. 2 on a log-log plot. A least-squares fit yields an exponent of -3.1, which differs slightly from the far field value of –3. This departure is as calculated for the finite separation of the two wires and the gradiometer.

Eddy currents induced in nearby conducting bodies can limit the degree of gradiometer balance that can be achieved [1]. Eddy currents produce a quadrature response (phase shifted by 90°) in the gradiometer signal that can be difficult to correct with reference magnetometers and gradiometers.

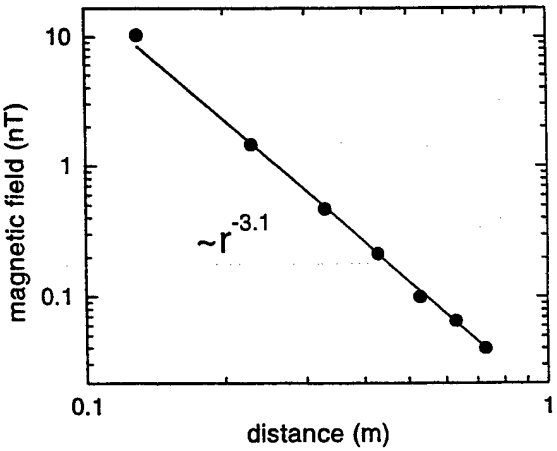

FIG. 2 Gradiometer signal vs distance from two parallel wires.

To characterize these eddy currents generated by the system and its environment, we measured the frequency dependence of the gradiometer response to a uniform field of 75.5nT applied in the out-of-plane direction by the Helmholtz pair. The results are shown in Fig. 3 where the out-of-plane balance at 12Hz is 1 part in 2000. The observed phase shift varies from 1° at 10Hz to –4.7° at 100Hz. These measurements indicate that in our environment, eddy currents may limit the overall balance to 9 ppm and 40 ppm at 10 and 100Hz, respectively, unless one can use software with a frequency dependent phase-shift [1].

We have built a system with two first-order gradiometers and three-orthogonal magnetometers for operation in an unshielded environment. The balance achieved electronically and measurements of magnetic signals from the human heart will be reported.

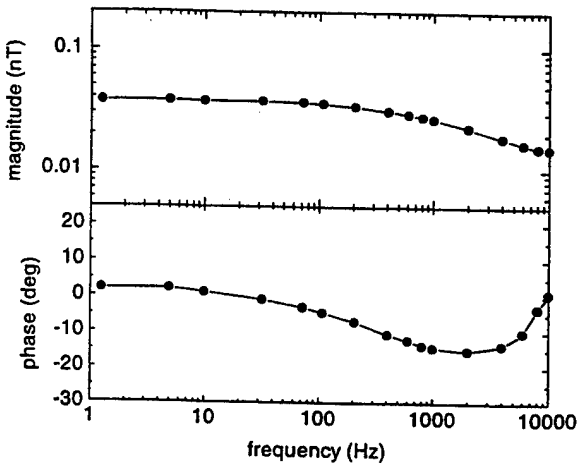

FIG. 3 Frequency dependence of the gradiometer response to a uniform field of 75.5 nT applied perpendicular to the plane of the device.

REFERENCES

[1] For a review, see J. Vrba, in "SQUID Sensors: Fundamentals, Fabrication and Applications", *NATO ASI Series, ed. H. Weinstock, (Kluwer Academic, Dordrecht 1996).*

[2] For example: W. Eidelloth, B. Oh, R.P. Robertazzi, W.J. Gallagher, and R.H. Koch, *Appl. Phys. Lett. 59, 3473 (1991)*; V. Zakosarenko, F. Schmidl, H. Schneidewind, L. Dorrer, P. Seidel, *ibid. 65, 770 (1994)*; V. Schultze, R. Stolz, R. Ijsselsteijn, V. Zakosarenko, L. Fritzsch, F. Thurm, E. Il'ichev, and H.-G. Meyer, IEEE Trans. Appl. Supercond. 7, 3473 (1997); M.I. Faley, U. Poppe, K. Uran, H.-J. Krause, H. Soltner, R. Hohmann, D. Lomparski, R. Kutzner, R. Wordenweber, H. Bousack, A.I. Braginski, V.Y. Slobodchikov, A.V. Gapelyuk, V.V. Khanin, and Y.V. Maslennikov, *ibid. 7, 3702 (1997)*; G.M. Daalmans, Appl. Supercond. *3, 399 (1995).*

[3] For example, D. Drung, *IEEE Trans. Appl. Supercond. 5, 2112 (1995)*; R.H. Koch, J.R. Rozen J.Z. Sun, and W.J. Gallagher, *Appl. Phys. Lett. 63, 403 (1993)*; Y. Tarvin, Y. Zhang, M. Muck, A.I. Braginski, and C. Heiden, *Appl. Phys. Lett. 62, 1824 (1993)*; H.J.M. ter Brake, W.A.M. Aarnink, P.J. van den Bosch, H.J. Holland, J. Flokstra, O. Dossel, and H. Rogalla, *Proceedings of the 2nd workshop on HTS Application and New Material, University of Twente, Enshede, The Netherlands, May 8--10, 1995, p.154*; B.O. David. O. Dossel, V. Doorman, R. Eckhart, W. Hoppe, J. Kruger, H. Landau, and G. Rabe, *IEEE Trans. Appl. Supercond. 7, 3267 (1997).*

[4] E. Dantsker, O.M. Froehlich, S. Tanaka, K.A. Kouznetsov, J. Clarke, Z. Lu, V. Matijasevic, and K. Char, *Appl. Phys. Lett. 71, 1712 (1997)*; A. Kittel, K.A. Kouznetsov, R. McDermott, B. Oh, John Clarke, C. Soble, V. Matijasevic, *ibid. 73, 2197 (1998).*

High Temperature Single Layer SQUID Gradiometers with Long Baseline and Parasitic Effective Area Compensation

C.M. Pegrum, A. Eulenburg, E.J. Romans, C. Carr, A.J. Millar and G.B. Donaldson
Department of Physics and Applied Physics, University of Strathclyde, Glasgow G4 0NG, UK

Abstract— First order HTS SQUID gradiometers were fabricated on 30 × 10mm² bicrystal substrates. These devices have baseline of 13mm, intrinsic balance levels of ~1/700 and typical gradient sensitivity at 1kHz of 79 fT/(cm√Hz). A two-SQUID coupling scheme is discussed that further enhances the device's ability to reject uniform fields.

I. Introduction

First order gradiometers based on high temperature superconducting quantum interference devices (HTS SQUIDs) are convenient sensors for measuring small, localised magnetic fields in unshielded environments. There are two main techniques for forming such an HTS SQUID gradiometer.

The first approach is that of electronic gradiometry where two separate SQUID magnetometers are utilised and their ouput signals are subtracted. The advantage of these systems is that they can have large baselines and a high degree of balance [1]. However, the electronic subtraction imposes stringent requirements on the system linearity, slew rate and the synchronisation of the multichannel electronics [2], [3], making the operation of the gradiometer somewhat complicated.

The second approach is to form a planar gradiometer by coupling two symmetric pickup loops to a SQUID. Such devices can be made simply from a single layer of HTS thin film with the pickup loops directly coupled to the SQUID. However, the size of such single layer gradiometers (SLGs) demonstrated to date [4], [5] is restricted by the common use of 10 × 10mm² substrates, limiting the baseline to typically 4mm and the area of the two pickup loops to small values resulting in low gradient sensitivities. An additional disadvantage of these SLGs is that the SQUID in the centre of the structure acts as a sensor of uniform fields, giving rise to a parasitic effective area of the order ~500μm² which corresponds to a balance of ~1/300 [6]. An alternative to the SLG is to couple a large flip-chip flux transformer to a single layer magnetometer [7] or gradiometer [8]. This greatly enhances the gradient sensitivity but requires very accurate manual alignment.

Here we present a device that combines the above two approaches. In order to achieve a longer baseline and larger pickup loops we have fabricated directly coupled first order SLGs on 30 × 10mm² substrates. We can compensate for the device's intrinsic parasitic effective area using a novel two-SQUID coupling scheme for which we employ simple electronic gradiometry. As the two individual SQUIDs have much smaller effective areas than large SQUID magnetometers used in conventional electronic gradiometry, the requirements on the SQUID electronics are much less demanding.

This work was supported by the UK EPSRC.

II. Concept, Design and Fabrication

The gradiometer is shown in Fig. 1. It consists of two symmetric and approximately rectangular pickup loops to which four identical SQUIDs are directly coupled. The estimated inductance of one pickup loop is $L_{loop} \sim 15$nH. The SQUIDs are arranged in two pairs and one pair is shown in greater detail in Fig. 2. The layout results in a baseline, $b = 13$mm. Following the work of Dantsker *et al* [9], the linewidth of the SQUIDs was restricted to 4μm to prevent magnetic flux penetration when the device is operated unshielded. The width of the junctions was 3μm and the SQUID slit had a length of 108μm and width of 4μm giving an estimated SQUID inductance, $L_{SQ} \sim$ 100pH.

In the ideal case of perfectly symmetric pickup loops, the output signal of each SQUID is a combination of the gradiometric response of the pickup loops and the magnetometric response of the SQUID itself. It can be seen from Fig. 2 that the two SQUIDs in each pair are coupled in opposite senses to the pickup loops, so that for any given combination of uniform and first order fields, the gradiometric and magnetometric signals add for one SQUID, while they substract for the other SQUID. If the SQUIDs are identical then adding the two outputs yields perfect balance, since the magnetometric responses cancel out. In practice, the effective areas of the two SQUIDs, A_{SQ1} and A_{SQ2}, will be slightly different. In addition, imperfections in the pickup loops mean that they will give

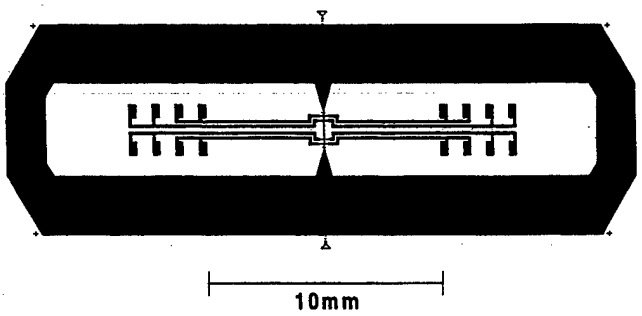

Fig. 1. Layout of the single layer gradiometer with a baseline of 13mm and two pairs of SQUIDs in the centre of the structure.

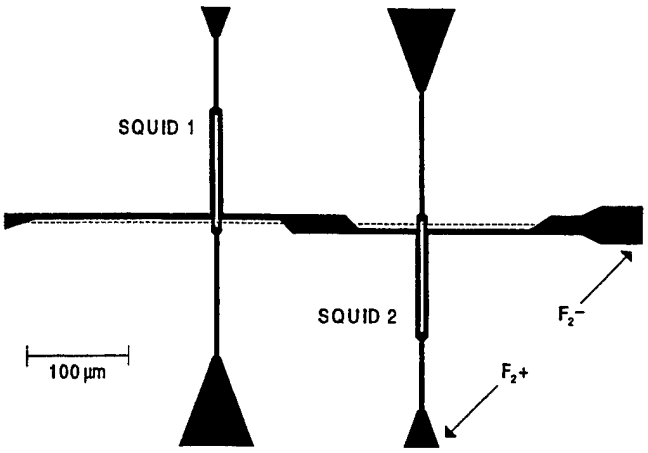

Fig. 2. The arrangement of a pair of SQUIDs with antiparallel coupling to the gradiometer loops. The dashed line indicates the position of the bicrystal grain boundary and the two arrows labelled F_2+ and F_2- point towards the feedback connections of SQUID2.

a small magnetometric response represented by an additional parasitic effective area, $A_{\rm loop}$. In this case, if we take a linear combination of the output voltages from the two SQUIDs in a pair, $V = V_{\rm SQ1} + \lambda V_{\rm SQ2}$, where λ is an adjustable factor (in practice close to unity) we find

$$V \propto (A_{\rm SQ1} + A_{\rm loop})B + A_{\rm grad}\frac{\partial B}{\partial z} + \lambda[(-A_{\rm SQ2} + A_{\rm loop})B + A_{\rm grad}\frac{\partial B}{\partial z}] \quad (1)$$

where $A_{\rm grad}$ is the gradient effective area. To cancel out the magnetometric response we require

$$A_{\rm SQ1} + A_{\rm loop} + \lambda[-A_{\rm SQ2} + A_{\rm loop}] = 0$$

$$\Rightarrow \quad \lambda = \frac{A_{\rm SQ1} + A_{\rm loop}}{A_{\rm SQ2} - A_{\rm loop}}. \quad (2)$$

This balancing condition allows us to remove simultaneously the magnetometric response of the SQUIDs and the pickup loops. Note that in the above analysis we have ignored small differences in the coupling between each SQUID and the pickup loops (*i.e.* different values of $L_{\rm SQ}$ leading to different values of $A_{\rm loop}$ and $A_{\rm grad}$). However, in practice such differences will be small and can be compensated for as λ may be found experimentally.

The gradiometers were fabricated on $30 \times 10{\rm mm}^2$ 24° $SrTiO_3$ (STO) bicrystal substrates from $YBa_2Cu_3O_7$ (YBCO) thin films deposited by pulsed laser deposition at a substrate temperature of 820°C, an oxygen pressure of 0.15mbar, a laser energy density of $1.2{\rm Jcm}^{-2}$ and a target-substrate distance of 68mm with 6000 laser pulses. We achieve a good degree of film homogeneity along the 30mm long substrate by focusing the laser beam to a narrow spot to a horizontal dimension of ~10mm and a vertical dimension of ~0.5mm at the target. This results in a plume that expands little in the horizontal direction but significantly in the vertical direction, parallel to which we align the longer side of the substrate during deposition. For YBCO grown on $30 \times 10{\rm mm}^2$ substrates, a film with a thickness of 200nm and $T_c = 90$K at the centre had a thickness of 180nm and $T_c = 89$K at the ends of the substrate. Devices were patterned using standard photolithography and argon ion milling. The contact pads were fabricated from a sputtered gold film. After fabrication the devices were wire bonded and then encapsulated on double-sided chip carriers. Device testing was performed in liquid nitrogen in a flux locked loop (FLL) with DC-bias using Conductus electronics. Magnetically shielded testing was carried out inside two layers of mumetal shielding. The device's effective area was measured in the open laboratory using a calibrated pair of Helmholtz coils. A 320Hz test current was passed through the coils and the resulting SQUID response was lock-in detected.

III. Results and Discussion

Initial device characterisation was performed in single channel experiments. We measured the effective area, $A_{\rm eff}$, of a few gradiometers using several of the SQUIDs in each device and obtained values in the range 838–$1160\mu{\rm m}^2$ with an estimated uncertainty in each measurement of $\sim\pm10\mu{\rm m}^2$. The effective areas are of the order we might expect for the SQUID alone as predicted by Ketchen *et al* [10] (though strictly for a square washer) of $A_{\rm eff} \sim \sqrt{A_{\rm w}A_{\rm h}} = 775\mu{\rm m}^2$, where $A_{\rm h}$ and $A_{\rm w}$ are

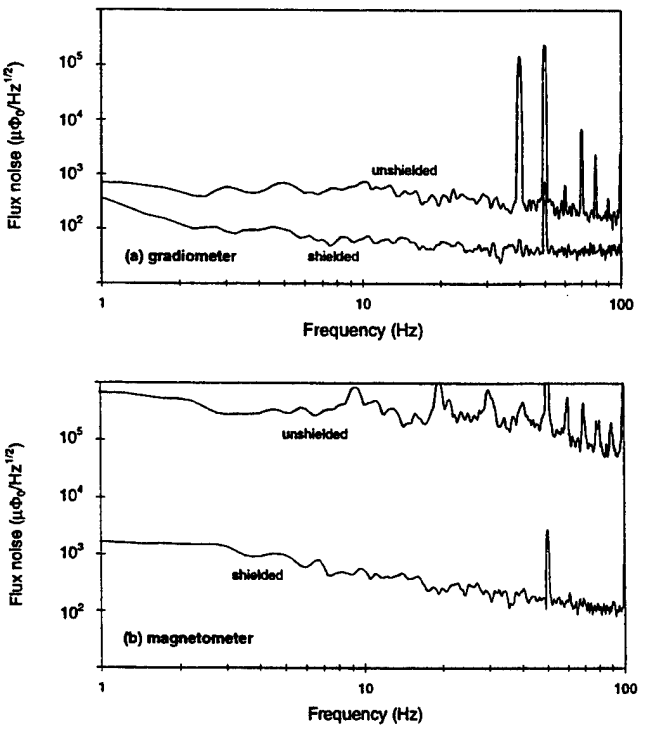

Fig. 3. Closed loop noise spectra measured shielded and unshielded with DC-bias at 77K for (a) the gradiometer and (b) the magnetometer (gradiometer with one loop cut).

the areas of SQUID slit and washer. Simple estimates show that the measured spread in effective area is consistent with the linewidth tolerances in our fabrication process ($\sim \pm 0.5\mu$m) and that we expect contributions of the same order from the individual spreads in A_{SQ} and A_{loop}. Further measurements (*e.g.* with the removal of both pick-up loops) would enable these two contributions to be separated. To assess the device's balance we measured the effective area of a device on which one of the pickup loops had been deliberately cut and obtained a value of $A_{mag} = 0.73\text{mm}^2$. This compares well with the order of magnitude expected from the product of the inductance mismatch between the SQUID and pickup loop ($L_{SQ}/L_{loop} \sim 1/150$) and the actual effective area of the pickup loop (enhanced by the flux focussing effect of the cut loop). Defining the gradiometer balance as A_{eff}/A_{mag}, we obtain balance levels in the range 1/866 – 1/626 which are approximately two times better than the typical values we measured previously on a smaller SLG incorporating a 50pH SQUID [6].

The flux noise of one of the SQUID gradiometers inside magnetic shielding is shown in Fig. 3(a). The critical current (taking noise rounding into account) and normal state resistance per junction were 8μA and 5.7Ω respectively and the peak-to-peak voltage modulation was 4μV. At 1Hz, the flux noise was $340\mu\Phi_0/\sqrt{\text{Hz}}$ which reduces to $36\mu\Phi_0/\sqrt{\text{Hz}}$ at 1kHz (not shown). The high level of low frequency noise is related to critical current fluctuations in the junctions which are not fully surpressed by our use of DC-bias. These levels of flux noise correspond to gradient sensitivities $S_g^{1/2} = S_\Phi^{1/2}/(bA_{mag})$ of $746\,\text{fT}/(\text{cm}\sqrt{\text{Hz}})$ at 1Hz and $79\,\text{fT}/(\text{cm}\sqrt{\text{Hz}})$ at 1kHz. To our knowledge, the latter is the best magnetic field gradient sensitivity reported to date for an HTS SLG in the white noise region. This also compares well with that of $73\,\text{fT}/(\text{cm}\sqrt{\text{Hz}})$ recently reported by Tian *et al* [8] for an SLG to which a large flux transformer with $b = 14.7$mm was flip-chip coupled. With the removal of the mumetal shielding, magnetic interference in our laboratory causes an approximately two- to five-fold increase in the device's flux noise level in the range 0–100Hz. For comparison, the flux noise level of the cut gradiometer (operating as a magnetometer) increases by a factor of ~400 in the same frequency range as shown in Fig. 3(b).

We investigated the optimum configuration for simultaneous operation of a SQUID pair (SQUID1 and SQUID2 of Fig. 2). The voltage and bias connections of SQUID1 and SQUID2 were connected to two synchronised FLL channels (FLL1 and FLL2). We coupled the flux modulation of FLL1 via an external coil to one of the gradiometer loops via which FLL1 modulates both SQUIDs; the flux modulation of FLL2 was not used. The flux feedback of FLL1 was connected to the same external coil so that it feeds back any signal measured by SQUID1 to both SQUIDs. The flux feedback of FLL2 was directly coupled to SQUID2 (via the two connections F_2+ and F_2- in Fig. 2) so that the feedback directly couples to half of the inductance of SQUID2 while the coupling to SQUID1 is negligible. The direct feedback coupling did not raise the flux noise level of SQUID2. Using this coupling scheme with correct polarity such that flux measured by the gradiometer loops yields voltages with the same polarity in FLL1 and FLL2, we achieve stable operation of both FLLs. The achievable balance using this coupling scheme is currently under investigation and detailed results will be published elsewhere.

IV. Summary

SLGs have been fabricated and characterised on 30 × 10mm^2 bicrystal susbtrates. The devices have a baseline of 13mm, intrinsic balance levels of ~1/700 and the gradient sensitivity at 1kHz for the best device was $79\,\text{fT}/(\text{cm}\sqrt{\text{Hz}})$. The effective rejection of magnetic interfence was demonstrated by operating the devices unshielded which caused an increase in flux noise by a factor of less than five compared to 400 for a magnetometer of identical dimensions. A novel two-SQUID coupling scheme was introduced that further enhances the device's ability to reject uniform fields.

References

[1] J. Borgmann, P. David, G. Ockenfuss, R. Otto, J. Schubert, W. Zander and A.I. Braginski, *"Electronic high-temperature radio frequency superconducting quantum interference device gradiometers for unshielded environment"*, Rev. Sci. Instrum. 68, pp. 2730-2734, 1997.

[2] F. Ludwig, J. Beyer, D. Drung, S. Bechstein and T. Schurig, *"High-performance high-T_c SQUID sensors for multichannel systems in magnetically disturbed environment"*, to be published in IEEE Trans. Appl. Supercond.

[3] M.A. Espy, R.H. Kraus, E.R. Flynn and A. Matlashov, *"Two methods for a first order hardware gradiometer using two high temperature superconducting quantum interference devices"*, Rev. Sci. Instrum. 69, pp. 123-129,1998.

[4] S. Knappe, D. Drung, T. Schurig, H. Koch, M. Klinger and J. Hinken, *"A planar $YBa_2Cu_3O_7$ gradiometer at 77K"*, Cryogenics 32, pp. 881-885, 1992.

[5] S. Wunderlich, F. Schmidl, H. Specht, L. Dörrer, H. Schneidewind, U. Hübner and P. Seidel, *"Planar gradiometers with high-T_c DC SQUIDs for non-destructive testing"*, Supercond. Sci. Technol. 11, pp. 315-321, 1998.

[6] C. Carr, A. Eulenburg, E.J. Romans, C.M. Pegrum and G.B. Donalsdon, *"High-temperature superconducting YBCO DC SQUID gradiometers fabricated on STO bicrystal substrates"*, Supercond. Sci. Technol. 11, pp. 1317-1322, 1998.

[7] E. Dantsker, O. Froehlich, S. Tanaka, K. Kouznetsov, J. Clarke, Z. Lu, V. Matijasevic and K. Char, *"High-T_c superconducting gradiometer with a long baseline asymmetric flux transformer"*, Appl. Phys. Lett. 71, pp. 1712-1714, 1997.

[8] Y.J. Tian, S. Linzen, F. Schmidl, L. Dörrer, R. Weidl and P. Seidl, *"High-T_c directly coupled direct current SQUID gradiometer with flip-chip flux transformer"*, Appl. Phys. Lett. 74, pp. 1302-1304, 1999.

[9] E. Dantsker, S. Tanaka and J. Clarke, *"High-T_c superconducting quantum interference devices with slots or holes: low 1/f noise in ambient magnetic fields"*, Appl. Phys. Lett. 70, p. 2037, 1997.

[10] M.B. Ketchen, W.J. Gallagher, A.W. Kleinsasser, S. Murphy and J.R. Clem, *"DC SQUID flux focuser"*, SQUID '85, pp. 865-871, 1985.

Different Applications of High-T_C SQUID Sensors

P.Seidel, F.Schmidl, S.Wunderlich, L.Dörrer, R.Weidl, T.Vogt, and S.Linzen

Institut für Festkörperphysik, Friedrich-Schiller-Universität Jena, Helmholtzweg 5, D-07743 Jena, Germany

Abstract - We use planar dc-SQUID sensors with a single film of $YBa_2Cu_3O_{7-x}$ (YBCO) for different applications. For a galvanically coupled gradiometer layout with 4 mm standard baselength we achieve a field gradient resolution of 340 fT/(cm√Hz) (white noise level) and 2.6 pT/(cm√Hz) at 1 Hz measured in unshielded environment. This enables such sensors for investigations of cardiac infarction by MCG measurements in a hospital. The effect of a large effective area antenna in flip-chip configuration is discussed as well as the application of dc-SQUIDs for the determination of the hardening depth in non-destructive testing.

I. Introduction

The development of high-T_C dc-SQUID sensors with increasing sensitivity even achieved at 77 K offers the application of this type of magnetic field sensors in different fields like biomagnetism [1] or non-destructive testing [2]. For investigation of weak signals the use of a gradiometric scheme is necessary in order to aviod the influence of environmental disturbances like the earths magnetic field [3]. In addition to the choise of a suitable layout of the SQUID sensor other methods like accumulation of data and an active background compensation offer the improvement of the signal to noise ratio as well as a higher sensitivity of the sensor, respectively.

II. Applied DC-SQUID Sensors

For the applications our group is working in we use dc-SQUID sensors on $SrTiO_3$ bicrystal substrates with 24° and 30° misorientation angle. On these substrates we prepare $YBa_2Cu_3O_{7-x}$ (YBCO) films with 150 nm typical film thickness by laser deposition. The gradiometers realize the concept of a galvanically coupled dc-SQUID in the inner part of the gradiometer. With an U-like dc-SQUID layout [4] mutual inductances between antenna and dc-SQUID of 150 up to 200 pH and 30 up to 100 pH are realized for our biomagnetic and non-destructive testing systems, respectively. For the transfer of the layout of the dc-SQUID sensors an ion beam etching technique on the basis of a photolithographic mask is used with additional deposition of a passivation layer of amorphous YBCO [5].

In our investigations we focus on both to realize a sensitive dc-SQUID in the inner part of the gradiometer and a high efficiency $E= A_{ant}/L_{ant}$ of the gradiometer antenna. A_{ant} and L_{ant} are the antenna area in the magnetic field and antenna inductance, respectively. Considering the layout of the gradiometer antennas we commonly use dc-SQUID gradiometers with baselength a= 4 mm on 10×10 mm² substrates shown in Fig.1. In Fig.1a an array of four gradiometers for non-destructive testing (NDT) is presented. The efficiency of the antenna of 1.13 mm²/nH results with a typical mutual inductance M= 45 pH in an effective area $A_{eff}=M\times E$ of one gradiometer antenna of 0.05 mm². Althought the value of A_{eff} is small a high sensitivity of the gradiometer device is reached by means of transfer functions up to 180 $\mu V/\Phi_0$. A field gradient resolution in the white noise level of 340 fT/(cm√Hz) was achieved even measured unshielded in highly disturbed industrial environment. At 1 Hz the noise level deteriorates to 830 fT/(cm√Hz) in magnetically shielded and 10 pT/(cm√Hz) in unshielded environment.

For biomagnetic measurements on the humans heart the antenna layout in Fig.1b is realized. With considerably higher mutual inductances the effective area is increased to values between 0.2 mm² and 0.3 mm² exhibiting a sufficiently high

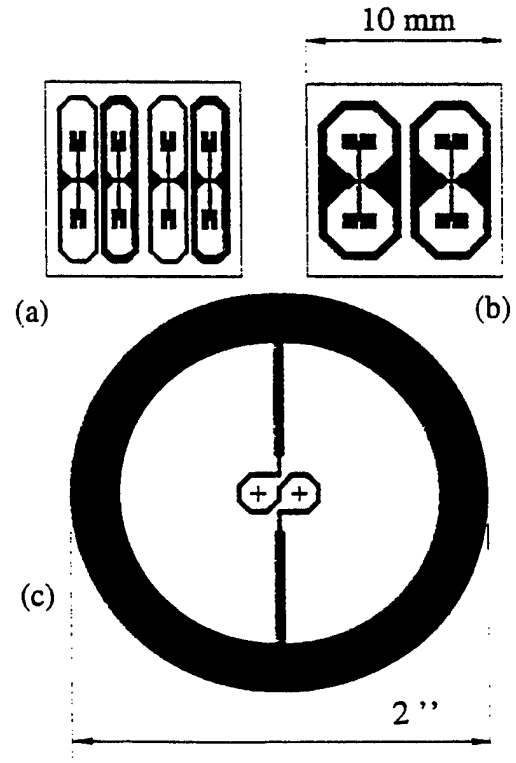

Fig.1 Layout of planar galvanically coupled dc-SQUID gradiometers for non-destructive testing (a) and biomagnetics (b) and antenna on a 2" silicon substrate for flip-chip measurements (c), not in same scale

Manuscript received 30April, 1999
This work was partially supported by the German BMBF under contract no. 13 N 6644.

transfer function of the device. This enables clinical research in unshielded environment. The achieved white noise level is comparable to NDT sensors but at 1 Hz the noise level is improved reaching 2.6 pT/(cm√Hz) in unshielded environment. For further increase of the gradiometer sensitivity especially for biomagnetic research a flip-chip configuration was tested. In this case a gradiometer antenna on a buffered 2" silicon substrate [6], see Fig.1c, transforms the measured magnetic signals on a conventional gradiometer, see Fig.1b. The gradient sensitivity $1/(a \times A_{eff})$ was with 2.6 nT/(cm Φ_0) six times higher compared to the pure gradiometer.

III. Magnetocardiography

The planar gradiometers introduced in Fig.1b are the basis for biomagnetic measurements at the hospital in unshielded environment recording the MCG (magnetocardiogram)[7]. The new system is a two channel system consisting of two planar gradiometer sensors in a glass fibre reinforced liquid nitrogen dewar. In Fig.2 the curves (b) and (c) show the measured magnetic field gradient of these two channels. The average of these two signals delivers an improved signal to noise ratio, see curve (d) in Fig 2. By additional operation of a single dc-SQUID as a reference sensor (placed 6 cm from the bottom of the cryostat) the influence of homogeneous disturbances at the intensive-care unit in the hospital can be further reduced leading to curve (e) in Fig.2. For comparison curve (a) in Fig.2 shows the patients ECG as a reference.

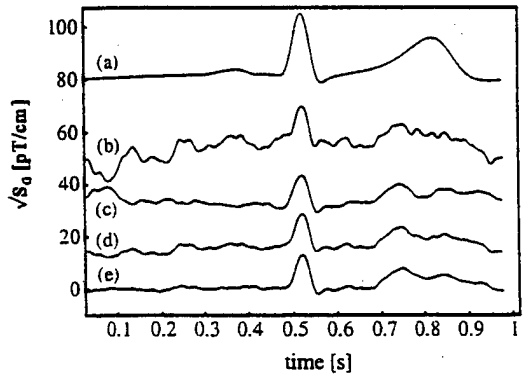

Fig.2 MCG measurements of the humans heart: (a) reference ECG, (b) gradiometer channel ch1, (c) gradiometer channel ch2, (d) averaged signal from ch1 and ch2, (e) SNR reduction by additional use of a reference SQUID

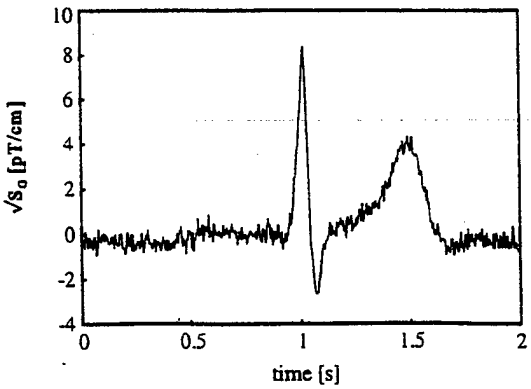

Fig.3 MCG measured with a flip-chip configuration on a buffered 2" silicon substrate with enlarged effective area

Applying the described flip-chip configuration in Fig.1c the MCG of the human heart was recorded in shielded environment. In Fig.3 there this signal is displayed after 320 averages triggered by a simultaneously recorded ECG.

We also measured MCG on a nonmagnetic cold head of a pulse tube refrigerator [8] producing disturbances far below the values of recorded MCG's.

IV. Non-destructive testing

We investigated hardened parts in steel samples. In formula (1) the skin depth s is dependent on the frequency f, conductivity σ and relative permeability μ_r of the material,

$$s = \frac{1}{\sqrt{\pi f \sigma \mu_0 \mu_r}} \quad . \qquad (1)$$

By the hardening process this permeability is changed. On the basis of this effect we detected the hardening depth with an eddy current technique applying dc-SQUIDs. In Fig.4 there the experimental setup for our investigations is shown. The steel plates are moved in the x-y-plane under a liquid nitrogen filled dewar with the dc-SQUID [9]. The maximum scan area is 600×400 mm² with a scan speed of 30 mm/s enabling a further application for industrial NDT. In the case of hardened steel plates a high remanent magnetic field of the sample strongly influences the SQUID operation in the detection of the magnetic fields of the eddy currents. That is why a compensation method of this 'offset' is used. In Fig.4 the signal of the dc-SQUID electronics is processed by a compensation electronics. This electronics filters the signal with a low pass filter and controls the compensation coil via a power amplifier by delivering accurate phase and amplitude of the feedback signal. For inducing the eddy currents a small coil is placed under the dewar directly over the steel sample with 4 cm distance between coil and dc-SQUID. The coil is fed by a power amplifier with an ac-current of 1.5 A at frequencies between 270 Hz and 1270 Hz. The position of this

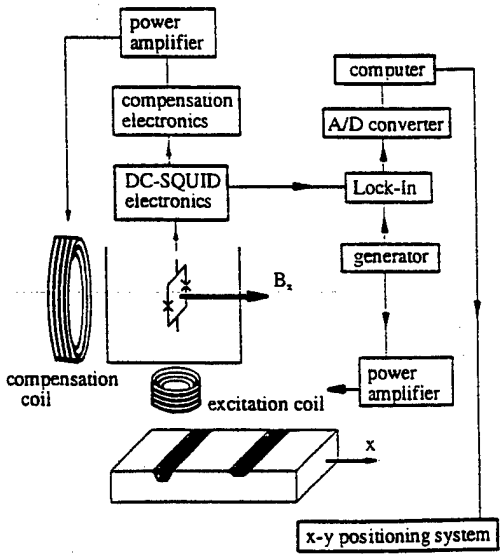

Fig.4 Experimental setup for NDT measurements

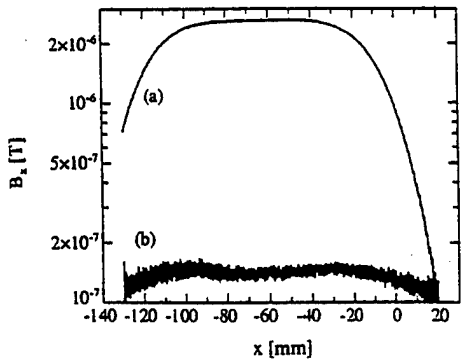

Fig.5 Measured remanent magnetic field of the steel plate without (a) and with (b) additional compensation

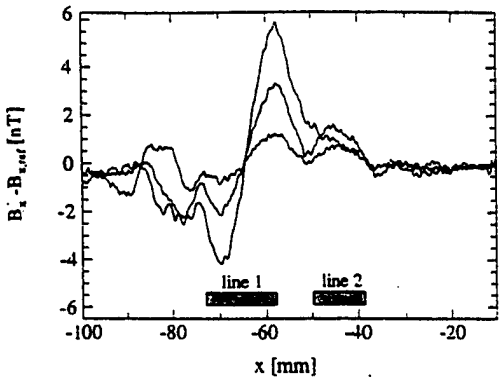

Fig.7 Scan of 3 steel plates with different hardening depth on line 1

coil is chosen in a way that the SQUID doesn't detect the excitation field of this coil but the response of the steel sample. For the evaluation of the ac-signal on the output of the dc-SQUID electronics a Lock-In amplifier is used. In Fig.5 there the remanent magnetic field of the steel sample was measured. The initial values of the magnetic field were with 2 μT too high for in depth investigation of the steel plates. With an additional compensation these magnetic field amplitudes are suppressed by a factor 72 gaining 2 orders of magnitude with corresponding higher sensitivity of the dc-SQUID device.

Fig.6 shows a scan of one steel plate. From -10 to -110 mm the sensor is moved over this plate. There are two lines on the plate hardened by an electron beam. Line 2 is a reference line with the same hardening depth (1.5 mm) and on line 1 different hardening depths between 0.4 mm and 1.5 mm were realized on different samples. In Fig.6 there the measured magnitude of the ac field is displayed. Furthermore, a method is introduced by which the signal to noise ratio (SNR) can be improved. A single scan like curve (c) was done 6 times and all these scans, summarized in the curve (b) were averaged. By this accumulation we obtained curve (a) exhibiting an improved SNR. In this figure it is hard to distinguish between the influence of the sample geometry and the effect of the hardened lines. That is why we have taken the sample with the smallest hardening depth in line 1 (0.4 mm) as the reference. In Fig.7 the difference between the signals of the samples with the other hardening depths (0.7 mm, 1.1 mm, 1.5 mm) and the reference sample (0.4 mm) is displayed. Without the geometry effects the different signals on line 1 can be clearly identified with the highest magnitude detected for the sample with the deepest hardening in that order. For further investigations the use of dc-SQUID gradiometers promises an increase of the sensitivity by more than two orders of magnitude for the detection of deeper hardened materials.

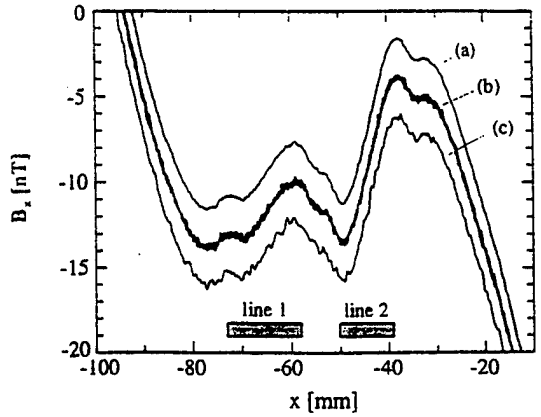

Fig.6 Improvement of the SNR in the investigation of hardened steel plates by accumulation of scans described in the text (curves are vertically shifted)

V. Summary

We produced planar dc-SQUID gradiometers on 10×10 mm² substrates with a field gradient resolution of 2.6 pT/(cm√Hz) at 1 Hz. On the basis of that type of gradiometer sensor the MCG in clinical environment was recorded delivering additional information about cardiac electrophysical properties. By applying a flip-chip configuration the gradient sensitivity for MCG measurements was six times higher. A method for the determination of the hardening depth in steel plates using an eddy current technique with single dc-SQUIDs and compensation of remanent background was also introduced.

References

[1] S.N.Erné and J.Lehmann: "Magnetocardiography - an introduction". H.Weinstock (ed.), SQUID sensors: *Fundamentals, Fabrication and Applications* (Proc.NATO-ASI, June 18-30, 1995), Kluwer Acad.Publ., Dordrecht, 395-412

[2] J.P.Wikswo: "SQUID magnetometers for biomagnetism and non-destructive testing: Important questions and initial answers.", *IEEE Trans.Appl.Supercond.*, vol.5, no.2, 74-120 (1995)

[3] J.Vrba: "SQUID gradiometers in real environments". H.Weinstock (ed.), SQUID sensors: *Fundamentals, Fabrication and Applications*(Proc. NATO-ASI, June 18-30, 1995), Kluwer Acad.Publ., Dordrecht, 117-178

[4] E.Il'ichev, L.Dörrer, F.Schmidl, V.Zakosarenko, and P.Seidel, "Current resolution, noise, and inductance measurements on high-T_c dc SQUID galvanometers", *Appl.Phys.Lett.*, vol.68, 708-710 (1996)

[5] H.Schneidewind, F.Schmidl, S.Linzen and P.Seidel: "The possibilities and limitations of ion-beam etching of $YBa_2Cu_3O_{7-x}$ thin films and microbridges", *Physica C*, vol.250, 191-201 (1995)

[6] Y.J.Tian, S.Linzen, F.Schmidl, L.Dörrer, R.Weidl, and P.Seidel: "High-T_c directly coupled direct current SQUID gradiometer with flip-chip flux transformer", *Appl.Phys.Lett.*, vol.74, 1302-1304 (1999)

[7] R.Weidl, S.Brabetz, F.Schmidl, F.Klemm, S.Wunderlich, and P.Seidel: "Heart monitoring system with high-T_c DC SQUID gradiometers in unshielded environment", *Supercond.Sci.Technol.*, vol.10, 95-99 (1997)

[8] J.Gerster, G.Kaiser, L.Reißig, M.Thürk, and P.Seidel: "Low noise cold head of a four-valve pulse tube refrigerator", *Adv.Cryo.Eng.*, vol.43, 2077-2084 (1998) (P.Kittel (ed.), Plenum Press, New York)

[9] S.Wunderlich, F.Schmidl, H.Specht, L.Dörrer, H.Schneidewind,U.Hübner and P.Seidel: "Planar gradiometers with high-T_c DC SQUIDs for non-destructive testing", *Supercond.Sci.Technol.*, vol.11, 315-321 (1998)

Oral Session 10

Analog Instruments and Novel Coolers

Low-field NMR and MRI of room temperature samples detected with a high-T_c SQUID

Robert McDermott, Klaus Schlenga, and John Clarke
Department of Physics, UC Berkeley and LBNL

Ricardo E. de Souza, Annjoe Wong-Foy, and Alexander Pines
Department of Chemistry, UC Berkeley and LBNL

Abstract—We have constructed a high-transition temperature Superconducting QUantum Interference Device (high-T_c SQUID) spectrometer to detect pulsed nuclear magnetic resonance (NMR) signals from samples at room temperature in magnetic fields as low as 0.059 mT. The multiloop SQUID magnetometer is operated in vacuum at 77 K, and is separated from the sample, which is less than 1.5 mm away, by a sapphire window. We have detected NMR spectra of protons and flourine nuclei in thermal equilibrium, as well as of hyperpolarized, isotopically-enriched ^{129}Xe nuclei. In a magnetic field comparable to that of the Earth, we can resolve the proton spin echo produced by 1 ml of mineral oil at 2.5 kHz after 2000 averages. When the field is increased to 2 mT we can detect the proton spin echo at 86 kHz in a single shot. In addition we have obtained two-dimensional proton magnetic resonance images (MRI) of mineral oil filled phantoms at room temperature. The spatial resolution of these images is approximately 0.8 mm.

I. INTRODUCTION

In a conventional NMR experiment with a Faraday detector, the signal is proportional to the product of the sample magnetization M and the Larmor frequency ω [1]. Since both magnetization and precession frequency scale with magnetic field strength, the NMR signal is greatly enhanced as the magnetic field is increased. However, the high fields that are typical of conventional NMR experiments can introduce several complications. For example, in polycrystalline or amorphous materials, the random orientation of individual molecules with respect to the applied field leads to local variations of the Larmor frequency; therefore, the spectra display a characteristic "powder pattern" [2]. Similarly, spatial variations in the magnetic susceptibility of a sample cause uncontrolled variations of the local magnetic field which can severely distort magnetic resonance images taken at high field [3].

Manuscript received April 30, 1999
This work was supported by the Director, Office of Energy Research, Office of Basic Energy Sciences, Materials Sciences Division of the US Department of Energy under Contract No. DE-AC03-76SF00098; the Deutsche Forschungsgemeinschaft; and the Brazilian Agency for Research CNPq.

The complications associated with high-field NMR can be circumvented by using low fields with a SQUID as the NMR detector. While conventional pickup coils measure the time derivative of a magnetic flux, the SQUID measures magnetic flux directly. Therefore the signal scales with ω ; for this reason the SQUID is far more sensitive than conventional detectors at low frequencies. In the past, low transition temperature (low-T_c) SQUIDs have been used extensively to detect NMR and nuclear quadrupole resonance (NQR) signals [4]-[12]. More recently, Kumar *et al.* were the first to use a high-T_c SQUID to detect NMR spectra in fields as low as 23 mT [13].

In this abstract we describe a newly constructed high-T_c SQUID spectrometer which detects spatially resolved NMR signals from samples at room temperature. The field sensitivity of our detector allows us to obtain proton NMR spectra in fields as low as 0.059 mT, which is comparable to the Earth's field. In addition, we have implemented a system of magnetic field gradient coils which allows us to perform MRI at 2 mT. We present two-dimensional proton magnetic resonance images obtained from phantoms filled with mineral oil and solid objects.

II. EXPERIMENTAL CONFIGURATION

The spectrometer is based on a $YBa_2Cu_3O_{7-x}$ integrated multiloop magnetometer operated in a flux-locked loop. In the relevant frequency range the system flux noise is 25 $\mu\Phi_0/Hz^{1/2}$, where $\Phi_0 = h/2e$ is the flux quantum. The effective area of the magnetometer is 1.8 mm^2; this corresponds to a magnetic field noise of 30 fT/Hz$^{1/2}$. The magnetometer is operated without a tuned input circuit, and the system bandwidth is 1.1 MHz. The voltage across the SQUID is fed directly into a low noise preamplifier at room temperature. The signal is further amplified, integrated, and fed back via a single turn coil of copper wire inductively coupled to the magnetometer. The voltage across the feedback resistor is amplified, filtered, and sent to a computer which performs data digitization and storage.

Fig. 1 shows a simplified drawing of the dewar and coils. The magnetometer is operated in vacuum and separated from the sample, which is less than 1.5 mm away, by a sapphire window. A sapphire cold finger anchored to the liquid nitrogen

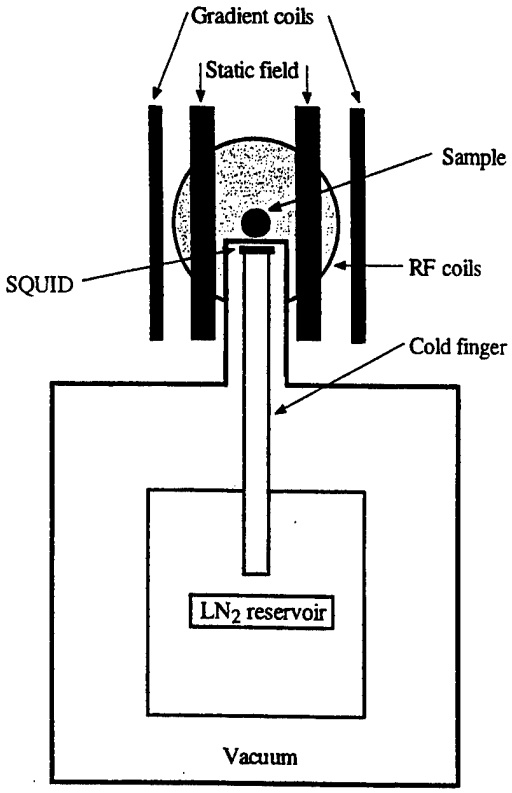

Fig. 1 Liquid nitrogen dewar, magnetometer, and coils.

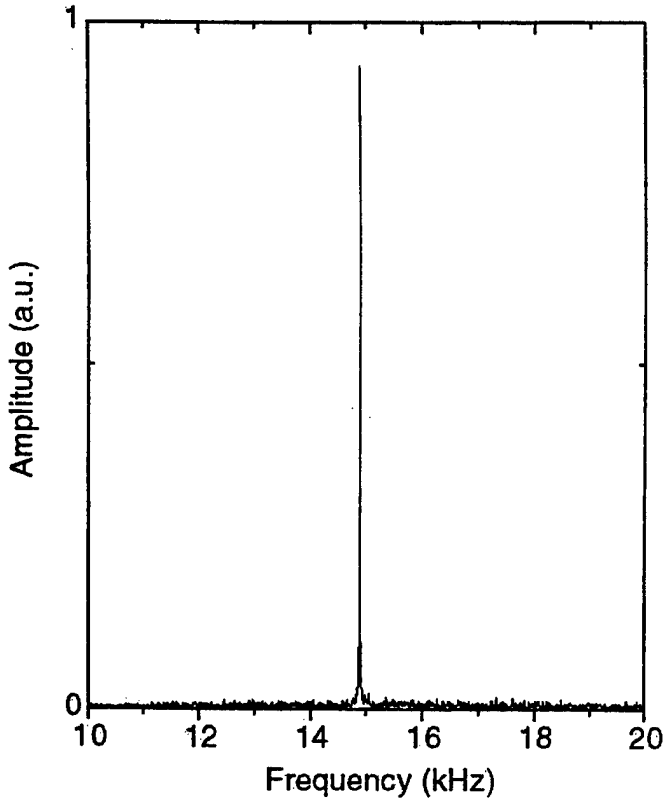

Fig. 2 NMR signal from hyperpolarized ^{129}Xe gas obtained in a magnetic field of 1.27 mT without averaging.

can provides efficient cooling. The dewar is similar to that described in detail in [14]. A static magnetic field B_0 in the z-direction is produced by a pair of Helmholtz coils. A second Helmholtz pair oriented perpendicular to the first is used to apply a pulsed alternating magnetic field B_1. A gradient field G in the z-direction is applied by a Maxwell pair situated outside the static field coils. Both the dewar and coils are enclosed in a three-layer mu-metal shield, and all experiments are carried out in an electromagnetically shielded room.

III. RESULTS

A. Spectroscopy

Our first experiments were performed on samples with either a high density of nuclear spins, or on isotopically enriched hyperpolarized ^{129}Xe. Our ^{129}Xe nuclei had a polarization of about 2×10^{-2}, an enhancement of roughly seven orders of magnitude over the equilibrium polarization at room temperature. We measured the free induction decay (FID) of ^{129}Xe in a sample tube 14 mm long with a 5 mm inner diameter after a single $\pi/2$ pulse without averaging. We obtain a S/N ratio of approximately 100 (Fig. 2) [15].

For our proton samples we chose mineral oil because of its relatively short spin-lattice relaxation time T_1 and its relatively long spin-spin relaxation time T_2. In 2 mT and without an applied gradient, we are able to detect the proton NMR signal of 1 ml of mineral oil in a single shot [15]. With 10,000 averages we are able to detect the proton NMR signal of 1 ml of mineral oil in 0.059 mT, a field comparable to that of the Earth.

B. Imaging

The high field sensitivity of our multiloop magnetometer has enabled us to obtain proton magnetic resonance images in a static field B_0 of 2 mT. As phantoms for these experiments we chose cylindrical containers with solid objects immersed in mineral oil. Because our SQUID magnetometer does not enclose the sample, but rather acts as a surface coil, the intensity of the NMR signal from a given part of the sample depends on its position with respect to the magnetometer. Therefore, to minimize possible distortion due to "position encoding" of the spins in our sample, we chose our phantom cross section to match roughly the dimensions of the magnetometer (7 mm diameter). For our mineral oil phantoms in a static field of 2 mT and without an applied gradient, the linewidth of the proton NMR signal is approximately 70 Hz; this linewidth is dominated by the inhomogeneity of our static field, which we calculate to be 7×10^{-4} over a 1000 mm^3 volume at the center of the static field coils. Therefore, with

an applied gradient G = 2 mT/m, we obtain a spatial resolution of $\delta z \approx 2\pi\delta f/\gamma G \approx 0.8$ mm, where γ is the proton gyromagnetic ratio.

For our two-dimensional imaging experiments we used the projection-reconstruction method [16]. The phantom was centered on the sapphire window above the magnetometer and rotated in steps of 15° about its vertical axis; for each orientation we averaged 30,000 FIDs. The excitation pulse was adjusted to provide a tipping angle of 54° (Ernst angle); this gave the maximum S/N ratio for a given averaging time. By rotating the sample through the half-circle from 0° to 180° we should, in principle, recover all the information necessary to reconstruct the sample's image. However, in order to correct for any asymmetry in the sensing area of the magnetometer, we took 24 projections, covering the full circle from 0° to 360°. Finally, the image of the sample was reconstructed using filtered back-projection with a generalized Hamming filter [16]. An example is shown in Fig. 3.

We are currently extending our experiments by using three-dimensional pulsed gradients for improved two-dimensional imaging. In addition, we plan to eliminate the noise contribution of the preamplifier by using additional positive feedback [17]. This should improve the magnetic field sensitivity of our spectrometer by about a factor of two.

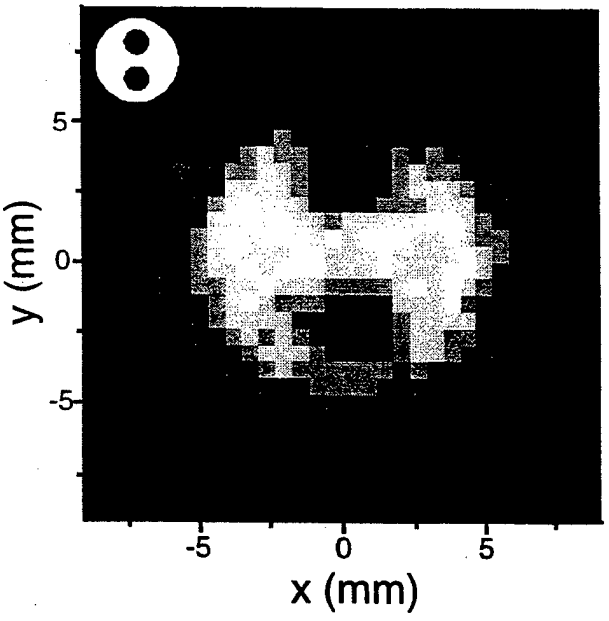

Fig. 3 Two-dimensional NMR image of a phantom consisting of two glass rods immersed in mineral oil (shown schematically in inset). The image is reconstructed from 24 one-dimensional projections taken at angular steps of 15° in a static field of 2 mT.

ACKNOWLEDGMENTS

We thank Michael Mück for valuable advice. The integrated multiloop magnetometer was fabricated in 1994 by Frank Ludwig.

REFERENCES

[1] A. Abragam, *The Principles of Nuclear Magnetism.* Oxford: Oxford University Press, 1961.

[2] R.K. Harris, *Nuclear Magnetic Resonance Spectroscopy.* Harlow: Longman Scientific & Technical, 1986.

[3] C.H. Tseng, G.P. Wong, V.R. Pomeroy, R.W. Mair, D.P. Hinton, D. Hoffman, R.E. Stoner, F.W. Hersman, D.G. Cory, and R.L. Wallsworth, "Low-field MRI of laser polarized noble gas," *Phys. Rev. Lett.*, vol. 81, pp. 3785-3788, October 1998.

[4] C. Hilbert, J. Clarke, T. Sleator, and E. Hahn, "Nuclear quadrupole resonance detected at 30 MHz with a dc superconducting quantum interference device," *Appl. Phys. Lett.*, vol. 47, pp. 637-639, September 1985.

[5] N.Q. Fan and J. Clarke, "Low-frequency nuclear magnetic resonance and nuclear quadrupole resonance spectrometer based on a dc superconducting quantum interference device," *Rev. Sci. Instrum.*, vol. 62, pp. 1453-1459, June 1991.

[6] B. Black, G. Majer, and A. Pines, "SQUID-NMR study of methyl quantum tunneling in a series of carboxylic acids," *Chem. Phys. Lett.*, vol. 201, pp. 550-554, January 1993.

[7] D.M. TonThat and J. Clarke, "Direct current superconducting quantum interference device spectrometer for pulsed nuclear magnetic resonance and nuclear quadrupole resonance at frequencies up to 5 MHz," *Rev. Sci. Instrum.*, vol. 67, pp. 2890-2893, August 1996.

[8] D.M. TonThat, M. Ziegeweid, Y.-Q. Song, E.J. Munson, S. Appelt, A. Pines, and J. Clarke, "SQUID detected NMR of laser-polarized xenon at 4.2 K and at frequencies down to 200 Hz," *Chem. Phys. Lett.*, vol. 272, pp. 245-249, June 1997.

[9] H.C. Seton, D.M. Bussell, J.M.S. Hutchison, I. Nicholson, and D.J. Lurie, "DC SQUID-based NMR detection from room temperature samples," *Phys. Med. Biol.*, vol. 37, pp. 2133-2138, November 1992.

[10] S. Kumar, B.D. Thorson, and W.F. Avrin, "Broadband SQUID NMR with room-temperature samples," *J. Magn. Reson. Series B*, vol. 107, pp. 252-259, November 1995.

[11] S. Kumar, W.F. Avrin, and B.R. Whitecotton, "NMR of room temperature samples with a flux-locked dc SQUID," *IEEE Trans. Magnetics*, vol. 32, pp. 5261-5264, November 1996.

[12] Ya.S. Greenberg, "Application of superconducting quantum interference devices to nuclear magnetic resonance," *Rev. Mod. Phys.*, vol. 70, pp. 175-222, January 1998.

[13] S. Kumar, R. Matthews, S.G. Haupt, D.K. Lathrop, M. Takigawa, J.R. Rosen, S.L. Brown, and R.H. Koch, "Nuclear magnetic resonance using a high temperature superconducting quantum interference device," *Appl. Phys. Lett.*, vol. 70, pp. 1037-1039, February 1997.

[14] T.S. Lee, E. Dantsker, and J. Clarke, "High-transition temperature superconducting quantum interference device microscope," *Rev. Sci. Instrum.*, vol. 67, pp. 4208-4215, December 1996.

[15] R.E. de Souza, K. Schlenga, A. Wong-Foy, R. McDermott, A. Pines, and J. Clarke, "NMR and MRI obtained with high transition temperature dc SQUIDs," *Journal of the Brazilian Chemical Society*, in press.

[16] A.K. Jain, *Fundamentals of Digital Image Processing.* New Jersey: Prentice-Hall, 1989.

[17] D. Drung, R. Cantor, M. Peters, H.J. Scheer, and H. Koch, "Low-noise high-speed dc superconducting quantum interference device magnetometer with simplified feedback electronics," *Appl. Phys. Lett.*, vol. 57, pp. 406-408, July 1990.

RF Measurements of High-Temperature-Superconducting Resonators at 25 T

William Brey, Richard Withers, Clifford Soble, and Victoria Soghomonian

Conductus, Inc., 969 W. Maude Ave., Sunnyvale, CA 94086

The National High Magnetic Field Laboratory (NHMFL) is developing for high-resolution NMR a 21.1-T magnet, equivalent to a 900-MHz proton resonance. In addition to the wide spectral dispersion and the possibility of exploiting dipolar ordering in liquids, the 21.1-T magnet will yield a sensitivity that has been exceeded only by 500 and 600 MHz spectrometers using superconductive probes. To take full advantage of the potential sensitivity of the instrument will require a superconductive RF probe. While high-sensitivity NMR probes based on the high-temperature superconductive (HTS) material $YBa_2Cu_3O_{7-\delta}$ (YBCO) have been demonstrated at proton frequencies up to 600 MHz, it was not clear that the material would have favorable RF properties at higher fields. To answer this question, we have recently performed RF tests of YBCO in a resistive magnet at the NHMFL at up to 25 T (corresponding to a proton frequency of 1.065 GHz) to determine if this material will be appropriate to use in superconductive RF probes for the next generation of high-field NMR magnets.

To prepare for the test, thin films of the HTS material YBCO were deposited on dielectric substrates using the co-evaporation technique, and were patterned into RF coils using designs developed for NMR at Conductus and Bruker. Two coils, one at 900 MHz and the other at 650 MHz, were then tested at the NHMFL. Tests were made both at zero field and in a resistive magnet. Coil temperature was maintained at 4.2 K during all tests. The 900-MHz coil had a matched quality factor (Q) of 25,800 at zero field, which dropped to 22,900 at 21.1 T (900-MHz proton frequency) and 19,900 at 25 T. The 650-MHz coil yielded a Q of 23,900 at fields up to 25 T. The 900-MHz coil carried over 12 amperes of RF current at 21.1 T (sufficient for 90-degree pulses shorter than 10 microseconds), while the 650-MHz coil carried more than 15 amperes at 25 T.

Based on these tests, we conclude that HTS materials are suitable for use in ultra-high-sensitivity NMR probes at fields beyond 1 GHz.

This work sponsored by the National Science Foundation, Grant No. DMI-9761221. The National High Magnetic Field Laboratory is supported by NSF Cooperative Agreement No. DMR-9527035 and by the State of Florida.

Scanning Evanescent Microwave Probe (SEMP)

X.-D. Xiang
Lawrecne Berkeley National Laboratory
2-300, One Cyclotron Rd. Berkeley, CA 94720
Phone: 510-486-4864, Fax: 510-486-8640
e-mail:xdxiang@lbl.gov

ABSTRACT

Electrical impedance is perhaps the most important and referred property of a semiconductor material. Although most inspection tools employ light as probing signal, the material's electrical impedance (i.e. the index of refraction) at frequencies of light has almost no direct correlation to that of at working frequencies of microelectronics. To electronic applications, lower range microwave frequencies (i.e. a few GHz) are most relevant and best suited to characterize electrical impedance. Evanescent microwaves are electromagnetic waves (in GHz range) with spatial frequencies higher than $2\pi/\lambda$ (where λ is the wavelength). Evanescent microwaves can be generated on a sharp conducting tip (with tip radius much less than λ) connected to the microwave source. They are sometimes called near-field microwaves. They differ from normal far-field microwaves (as in Radar) in that they do not radiate or propagate in space, but stay only on or near the surface of the conducting tip. Evanescent microwaves have much higher spatial resolving power than normal propagating microwaves ($\sim \lambda$). However, it is very difficult to isolate the evanescent microwaves from the normal propagating microwaves, whose presence can severely lower the resolution and sensitivity, and more importantly interfere with the subsequent quantitative analysis. There are several techniques that have been used for evanescent microwave imaging (see details below in the Review Section). One is using an open-ended coaxial cable with a sharpened center conductor protruding from the end and scans the samples. This technique was first described in details by Steven Chu at el.[10]. The main problem with this technique is that the open-ended cross-section still leaks out significant amount of normal propagating microwaves, which limit the resolution and ability to perform subsequent quantitative analysis. Another technique involves with a micro-strip resonator with a tip attached to the strip conductor [16]. The same problem also limits the capability of this technique. Another main disadvantage of both techniques is their low sensitivity due to the low quality factor (Q) of microwave sensors. The core of SEMP technology, developed and patented by LBNL and licensed to Ariel Technologies, inc., is its proprietary design in obtaining relatively pure evanescent microwaves near the tip and at the same time maintaining very high Q of the microwave sensor (i.e. resonator).

SEMP sends evanescent microwaves and detects their interaction with the sample through a conducting tip (Fig. 1). Since the tip is an integral part of a very sensitive detector (microwave resonator with Q of a few thousands), the sensitivity of the instrument is extremely high. This can be best demonstrated by the capability of measuring $\tan\delta$ (a ratio of dissipated and stored energies in a dielectric materials) of a good insulator (currently limited to $\tan\delta > 10^{-3}$). When the tip scans over a sample in a close range, evanescent microwaves interact with the sample. This interaction depends on the complex electrical impedance (including both the real

part and the imaginary part) of the sample and causes changes in the resonant frequency and quality factor of the resonator. By measuring these changes, together with a proprietary theoretical analysis methods, the new instrument has the capability of complex electrical impedance mapping of any materials ranging from dielectric insulator (as complex dielectric constant, $\varepsilon > 1$, $\tan\delta > 10^{-3}$), semiconductor (dopant level from 10^{13} to 10^{21} cm^{-3}), metal to superconductor ($\rho < 10^{-7}\Omega$-cm). With the proprietary methods, the instrument also has the capability to maintain tip-sample distance via feedback control from Å to tens of microns, therefore simultaneously obtain the topographic and electrical impedance (and its derivatives with respect to bias voltage or optical & magnetic modulations) images. By adjusting the radius of the tip and/or tip-sample distance, the evanescent microwave on the probe can penetrate different depth of the sample surface. This feature may be used to perform 3-D dopant profiling and detecting void via contacts in interconnect layers. Previously, we have demonstrated better than 100nm resolution on dielectric samples using a tip radius of 10 micron. We expect to improve the spatial resolution to be better than 5nm. Our analysis methods provide quantitative and analytical relationship between instrument signals and local electrical impedance as a function of tip radius and tip-sample distance. This will allow us to obtain real time images of quantitative mapping of electrical impedance. SEMP has been used in low temperature to study high T_c superconducting thin films.

In addition to the above-mentioned fundamental advantages of SEMP, this technology has several other attractive features. First, the SEMP (including all sensor, coarse approach and fine scanning parts) is compact in size (~1"x 1"x 2") so that it can be easily integrated into other systems. Second, it allows easy integration of conventional optical, STM, shear force microscope or NSOM with the microwave probe. Since the tip of the SEMP can also be the shear force tip or NSOM tip (sharpened optical fiber with metal coating), dual or multiple images representing different physical and topological information can be obtained. Therefore, the instrument may fulfill many different requirements by combining the capabilities of other microscopes with SEMP. Finally, the ability of SEMP to scan large area in a short amount of time ("zoom out" feature) and to scan small area with high resolution ("zoom in" feature) is critical for wafer inspection and/or defect review and classification. In most other scanning probe microscopes, such as STM, AFM and NOSM, signal can only be obtained in the range of tens of Å, "zoom out" feature is impossible to achieve. This has limited the use of most scanning probe microscopes in the semiconductor industry because of their low throughput. However, since the signal exists in the range from Å to tens of microns, SEMP can work with continuous tip-sample feedback control. This feature makes SEMP a much better practical tool in industrial applications. One class of potential applications is high throughput screening/imaging tool for materials discoveries and studies include:

1) high dielectric constant and low loss dielectrics used in capacitance devices/components,
2) ferroelectrics used in memory devices,
3) low-k dielectrics in interconnects,
4) magnetoresistive materials in recording head,
5) zero-magnetostrictive and high magnetization metal alloys in magnetic recording applications,
6) Superconding materials.

And many other applications where materials electrical properties need to be characterized as function of electric field, magnetic field, optical illumination and variation in temperatures. If successful, this project will provide industrial users a powerful tool to conduct combinatorial materials research.

Another class of applications is as thin film metrology, wafer inspection and diagnosis demands for semiconductor industry include:

1) Metal film conductivity mapping, or thickness/sheet resistance mapping,
2) Semi-conducting film dopant level profiling
3) Metal particle defects identification and classification,
4) Microwave microelectronic circuitry inspection
5) In situ processing monitoring

Potential applications may also include ferroelectric media storage and biomedical studies.

Chip Cooling by Normal metal - Insulator - Superconductor Peltier Effect

J.P. Pekola, A.J. Manninen, M.M. Leivo, K. Arutyunov, J.K. Suoknuuti, and T.I. Suppula
Department of Physics, University of Jyväskylä, PO Box 35, 40351 Jyväskylä, Finland

B. Collaudin
Thermal Control and Heat Rejection Section of the European Space Agency,
ESTEC, PO Box 299, 2200 AG Noordwijk ZH, The Netherlands

Abstract— The normal metal - insulator - superconductor (NIS) cooling method by tunnelling has been utilised in experiment for about five years now. We are developing this method into a device capable of refrigerating detectors like hot electron micro-bolometers and superconducting tunnel junction detectors. We are able to reduce the electronic temperature to 0.1 K starting from 0.3 K, the best result in this field so far. Experiments are in progress to obtain the same reduction of lattice temperature by indirect cooling of the platform consisting of a thin silicon nitride membrane thermally decoupled from the surrounding heat bath. The nitride film can house the detector to be cooled.

I. Introduction

If a normal metal / insulator / superconductor (NIS) tunnel junction is biased slightly below the superconducting energy gap Δ, only "hot" electrons can tunnel from the normal electrode into the superconductor. Thus, heat is removed from the normal metal. Because the conduction electrons are only very weakly coupled to the lattice at low temperatures, electrons of the normal metal can cool below the lattice temperature by NIS tunnelling [1], [2].

In the experiments of Refs. [1], [2] the bath temperature, i.e., the temperature of the lattice, remains constant. However, NIS tunnelling can be applied to refrigerate the surrounding lattice as well, if the normal electrode is thermally isolated from its environment. We have achieved this by fabricating the electrode on a thin dielectric membrane [3]. Thermal isolation can be further improved by a self-supporting bridge structure of the membrane [4].

II. Operational Principle

The cooling effect in NIS tunnel junctions is based on the existence of forbidden energy states within the energy gap, Δ, in the superconductor: Only electrons with energy E higher than the Fermi energy, E_F, can tunnel through an insulating barrier from the normal metal into the superconductor when bias voltage $V < \Delta/e$ is applied across the junction. With opposite polarity, the electrons that tunnel from the superconductor to the normal metal have $E < E_F$. In both cases, the energy distribution of the electrons in the normal metal tends to sharpen, and the electrons thermalize to a lower equilibrium temperature. Therefore it is possible to connect two NIS junctions back-to-back and form a SINIS structure for efficient cooling and isolation of the normal electrode.

The cooling power of a NIS refrigerator at temperatures well below the transition temperature, T_c, of the superconductor is approximately proportional to $T^{3/2}$ [2], [3]. More explicitely, the maximum cooling power of a single NIS junction at $T << T_c$ is achieved when $|V|$ is slightly below Δ/e, and it is

$$\dot{Q}_{\max} \approx 0.6 \frac{\Delta^{1/2}}{e^2 R_T} \left(k_B T_e\right)^{3/2}. \qquad (1)$$

Here R_T is the normal-state resistance of the junction and T_e is the temperature of the electrons in the normal metal.

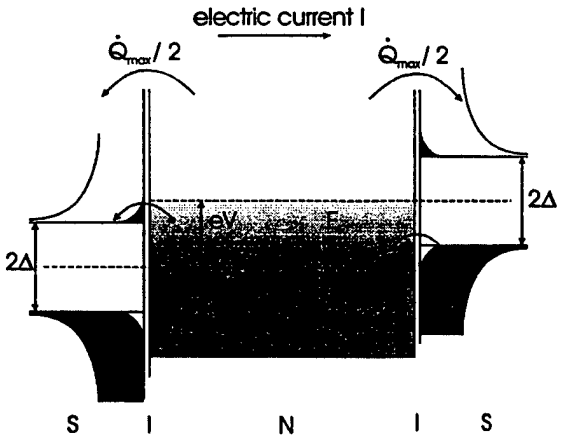

Fig. 1. Principle of operation of a SINIS refrigerator.

Electron-phonon coupling gives rise to heat flow

$$\dot{Q}_{e-p} = \Sigma U \left(T_p^5 - T_e^5\right), \qquad (2)$$

between phonons at temperature T_p and electrons at temperature T_e. Here Σ is a material-dependent constant of order 10^9 W/K^{5}m^3 and U is the volume of the normal electrode. At low temperatures this coupling is very weak, and there can be a large temperature difference between the conduction electrons and the lattice. NIS tunnelling decreases the temperature of the electrons in the normal metal. The lattice cools down also if the electron-phonon coupling is strong enough, and the direct heat load to the phonon system to be cooled is low.

III. Refrigeration of the Lattice

Up to now we have achieved a decrease of about 40 mK in lattice temperature starting at 0.15 K. By optimal design we will improve this result significantly. The main issues in doing this are the improvement of the quality of the

junctions, when they are made highly transparent for efficient cooling, thermal isolation by the dielectric micro-supports of the platform, and geometrical optimisation of the cooler. The critical aspects for space applications are higher cooling power, tolerance to radiation, operation in moderate magnetic fields, and the overall stability of the device. The results on lattice cooling will be presented elsewhere; here we review some of the critical issues for a high cooling power SINIS refrigerator.

A. Thermal conductance of the lattice

A preferable configuration for the SINIS refrigerator is to connect it with a cold finger on a thin dielectric membrane [4]. Silicon nitride is suitable for this purpose because it can form thin self standing membranes even with narrow bridges (see Fig. 2). The central membrane, of 200 nm thickness in our case, supported by these bridges provides a substrate which is thermally isolated from the surrounding heat bath.

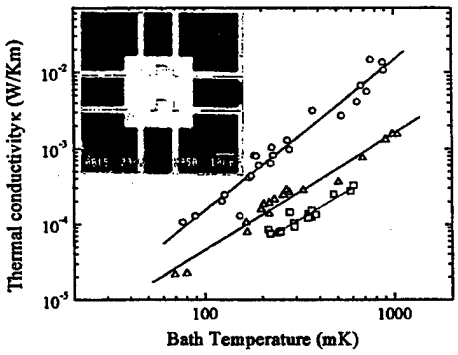

Fig. 2. Thermal conductance of silicon nitride membranes of about 250 nm thickness. The top set of data is for a plain membrane, the middle one is for a sample with 25 μm wide bridges, and the lowest set of data is for 4 μm wide bridges. Inset shows a SEM image of the sample with these narrow bridges.

A fairly striking observation in Fig. 2 is that the thermal conductance depends on the width of the bridges: the narrow bridges efficiently block the phonons outside the membrane.

B. Refrigerator design and experiments

To achieve high cooling power it is obviously necessary to increase the total area of the junctions in the tunnel refrigerator. R_T is inversely proportional to the area, and Eq. (1) therefore yields cooling power which is proportional to the total area of the junction(s). There are two conceivable ways to achieve the goal of high cooling power. The first one is to increase the number of cooling junctions connected in parallel with essentially not changing the size of the individual junctions. This is a method which works in practice in a satisfactory way.

A much simpler and more integrated design is to fabricate individual junctions of larger area. The small NIS junctions are typically made of copper and aluminium by electron beam lithography. Larger junctions (>> 1 μm^2) are not easy to fabricate this way. We have developed a method with lithographically fabricated mechanical mask, which allows us to make larger junctions with same materials and similar shadow mask evaporation as in electron beam lithography.

Figure 3 shows a somewhat arbitrary comparison of results where the temperature drop is shown for (a) a large SINIS pair of 3 x 3 μm^2 junctions (R_T = 800 Ω for the pair) cooling a large copper bar (40 μm x 3 μm x 40 nm), and in (b) a typical parallel configuration of a structure with 20 small SINIS junctions cooling a cold finger extending on a silicon nitride membrane (electronic temperature shown). It is obvious that some cooling can be achieved also with the large junctions but the effect at least in this first experiment in (a) is weak and tends to level off at low temperatures.

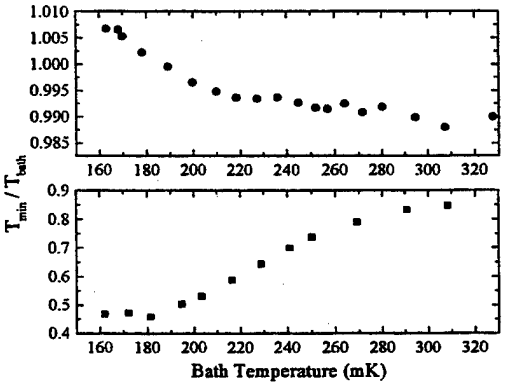

Fig. 3. Electron cooling experiments. Scaled electronic temperature as a function of bath temperature for (a) large (3 x 3 μm^2) and (b) small (0.3 x 0.3 μm^2) area junctions.

It is not obvious whether large junctions can be used at all in a practical refrigerator. A central problem there is the heating of the superconductor in the very vicinity of the refrigerating junctions due to the recombination of quasiparticles in the superconductor.

A. Thermal conductance of the cold fingers

In a membrane (lattice) refrigerator heat must be effectively removed from the isolated substrate along the cold fingers. In our case the cold fingers will be of evaporated (deposited in 10^{-9} mbar vacuum, electron gun evaporation) copper, or possibly a strip of another pure metal. The dimensions of this conductor have to be optimized. What is very important is the high thermal conductance along the cold finger. This is because we cannot increase the cross sectional area of the strip excessively, since this would lead to strong thermal contact to the phonon system because of large volume (see Eq. (2)). High electronic thermal conductance translates into high electrical RRR, residual resistivity ratio, which turns out to be surface limited in typical copper films that we

use. This is demonstrated by Table I, where experimental RRR values are given for three different thicknesses and two widths of copper strips. It is obvious that relatively thick cold fingers are preferable.

TABLE I

MEASURED RRR OF EVAPORATED COPPER STRIPS

thickness (nm)	RRR 0.2 μm wide strip	RRR 10 μm wide strip
20	1.91	2.21
50	2.69	3.75
200	5.33	10.28

IV. Discussion

Based on our experimental off-line tests we have discussed how a large cooling power SINIS refrigerator could possibly be designed.

V. Acknowledgment

This project is supported by the European Space Agency.

References

[1] M. Nahum, T. M. Eiles, and J. M. Martinis, *Appl. Phys. Lett.* **65**, 3123 (1994).
[2] M. M. Leivo, J. P. Pekola, and D. V. Averin, *Appl. Phys. Lett.* **68**, 1996 (1996).
[3] A. J. Manninen, M. M. Leivo, and J. P. Pekola, *Appl. Phys. Lett.* **70**, 1885 (1997).
[4] M. M. Leivo and J. P. Pekola, *Appl. Phys. Lett.* **72**, 1305 (1998).

Cooling by S_1IS_2 tunnel junctions

Antti J. Manninen, Janne K. Suoknuuti, Mikko M. Leivo, and Jukka P. Pekola
Department of Physics, University of Jyväskylä, P.O. Box 35 (Y5), FIN-40351 Jyväskylä, Finland

Abstract—Cryogenic Peltier cooling based on tunnelling between a superconductor and another metal has earlier been applied to cool a normal metal by NIS (normal metal - insulator - superconductor) tunnelling. We have extended the method to the S_1IS_2 case in which both metals S_1 and S_2 are superconducting but their energy gaps are different. The electron system of a titanium strip (S_2) with the superconducting transition temperature $T_{c2} = 0.51$ K was cooled from above T_{c2} to below 0.7 T_{c2} by this method, using aluminium as the superconductor S_1. If temperature is not too low compared to T_{c2}, the cooling power of an S_1IS_2 junction is comparable to and can be even larger than that of a similar NIS junction.

I. Introduction

A new cryogenic refrigeration method based on normal metal - insulator - superconductor (NIS) tunnelling has been developed during recent years. After the first demonstration of the operation principle [1], the electrons in a small normal metal island have been cooled from 300 mK down to 100 mK using this technique [2]. Refrigeration of a dielectric membrane has been demonstrated, too [3],[4]. Here we show that the tunnelling method can be applied to cool down electrons in a superconductor, as well. Our results are published in [5].

II. Theoretical Aspects

Let us consider tunnelling between two different superconductors, S_1 and S_2, with energy gaps Δ_1 and Δ_2, respectively. We assume that $\Delta_2 < \Delta_1$. As in the NIS case [1]-[4], which corresponds to $\Delta_2 = 0$, there is a heat flow

$$\dot{Q} = \frac{1}{e^2 R_T} \int_{-\infty}^{\infty} \left[f(\varepsilon, T_{e2}) - f(\varepsilon - eV, T_{e1}) \right] \times N_2(\varepsilon) N_1(\varepsilon - eV) \varepsilon d\varepsilon \qquad (1)$$

from S_2 through the S_2IS_1 junction which is biased at voltage V. Here $N_i(\varepsilon) = \Theta(\varepsilon^2 - \Delta_i^2)|\varepsilon|(\varepsilon^2 - \Delta_i^2)^{-1/2}$ is the normalised BCS density of states in the superconductor S_i, R_T is the normal-state tunnelling resistance of the junction, $f(\varepsilon,T)$ is the Fermi distribution function, and T_{ei} is the temperature of electrons in S_i. Figure 1 shows the calculated cooling power $\dot{Q}$ as a function of V for different values of Δ_2 at a constant temperature. When $eV < \Delta_1 + \Delta_2$, $\dot{Q} > 0$ and S_2 cools down: only the "hot" quasiparticle excitations from above the energy gap Δ_2 can tunnel from S_2 to S_1, which has free quasiparticle states only above the gap when $k_B T_{e1} << \Delta_1$. $\dot{Q}$ is symmetric with respect to V, allowing connection of two junctions in series as in the NIS case [2].

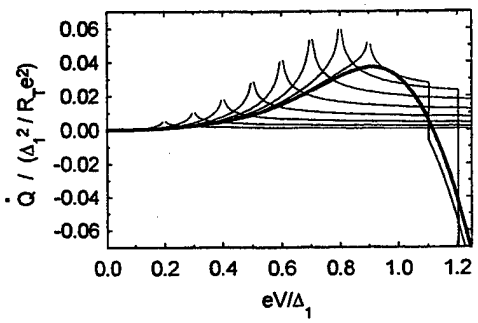

Fig. 1. Calculated heat flow $\dot{Q}$ from S_2 through an ideal S_2IS_1 junction which is biased at voltage V at a constant temperature $T_{e1} = T_{e2} = 0.15\ \Delta_1/k_B$, which corresponds to 0.37 K for our sample. Different lines have been calculated for $\Delta_2/\Delta_1 = 0$ (NIS structure; thick line), 0.1, 0.2, 0.3, 0.4, 0.5, 0.6, 0.7, and 0.8, respectively. The cooling power diverges when $|eV| = \Delta_1 - \Delta_2$. For our sample $\Delta_2/\Delta_1 \approx 0.29$ at $T = 0.37$ K.

Figure 1 also includes the cooling power of an NIS junction. Its maximum at $T_{e1} << \Delta_1/k_B$ is approximately $\dot{Q}_{max}^{NIS} \approx 0.6 e^{-2} R_T^{-1} \Delta_1^{1/2} (k_B T_{e2})^{3/2}$, which is reached when $|V|$ is slightly below Δ_1/e [2]. As Fig. 1 shows, the cooling power of an S_2IS_1 junction can be even larger than that of the NIS junction, if Δ_2 is small enough compared to Δ_1 and temperature is not too much lower than Δ_2/k_B (such that there is a finite density of quasiparticle excitations in S_2). For ideal BCS superconductors, cooling power should actually diverge logarithmically at $eV = \Delta_1 - \Delta_2$, as was found earlier in [6]. This corresponds to the well known "$\Delta_1 - \Delta_2$ singularity matching peak" in electric current between two different superconductors at $T > 0$ [7].

III. Samples

In the experiments we used aluminium as S_1 and titanium as S_2. The transition temperatures of our Al and Ti films were $T_{c1} \approx 1.4$ K and $T_{c2} = 0.51$ K, respectively, which are somewhat above the tabulated bulk values. Four samples with slightly different structures were studied, each of which showed cooling of Ti below T_{c2}. Here we concentrate on the experiments performed with the sample in which the cooling effect was strongest. Its SEM micrograph is presented in Fig. 2, together with a scheme of the electrical connections. The sample was fabricated onto a nitridised silicon substrate using electron beam lithography and three-angle evaporation. Two 15-nm thin Al layers were first evaporated at large angles of

Manuscript received April 30, 1999.
This work was financially supported by the European Space Agency (ESA), the Technology Development Centre of Finland (TEKES), and the Academy of Finland.

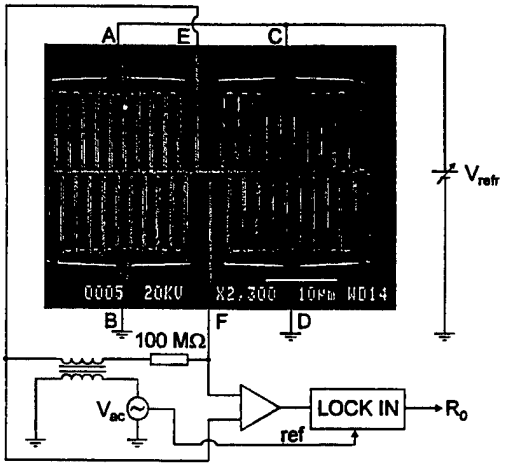

Fig. 2. A scanning electron micrograph of the Al/AlO$_x$/Ti cooler, and a scheme of the electrical connections. In the SEM micrograph only the titanium parts can be seen; the contrast of the aluminium lines is not good enough for a printed picture. However, each vertical line includes an Al layer which extends across the cooled horizontal Ti line in the middle and makes an Al/AlO$_x$/Ti tunnel contact with it.

±60 degrees with respect to the normal of the substrate in the direction of vertical lines of the structure. In this way the vertical lines were deposited on the substrate, but the narrow horizontal line in the middle was deposited on the walls of the resist in both Al evaporations, and was removed in the liftoff. Al was oxidised in pure O_2 at p = 10 mbar for 10 minutes. Finally a 30-nm Ti layer was evaporated directly perpendicular to the substrate. In this way, altogether 42 Al/AlO$_x$/Ti tunnel junctions were formed between the vertical lines and the 300-nm wide horizontal Ti line in the middle. The 40 junctions which were used for cooling (the comb-like structures A-D in Fig. 2) had an area of about 300 × 550 nm^2 and normal-state resistance $R_T \approx 1.9$ kΩ each. The junctions corresponding to E and F, which were used for thermometry, both had an area of about 300 × 350 nm^2 and $R_T \approx 3$ kΩ.

IV. Experiments

A. Thermometry

We determined the electron temperature of the Ti line, T_{e2}, from the zero-bias resistance, R_0, of the two Al/AlO$_x$/Ti tunnel junctions E and F connected in series. The inset of Fig. 3 shows current-voltage (IV) curves of EF at three different temperatures when Al is superconducting; the IV curves of the pairs AB and CD were qualitatively similar. When Ti is in normal state, EF forms an SINIS structure and has smooth but strongly temperature-dependent IV characteristics below the tunnelling threshold, $|V| = 2\,\Delta_1/e \approx 0.42$ meV (where the factor of 2 comes from the two tunnel junctions in series): I decreases and R_0 increases with decreasing temperature. When Ti gets superconducting at T_{c2} = 510 mK, new features develop in the IV curves at low voltages; this is typical for superconducting double-junction structures with submicron dimensions, in which single charge effects are important [8].

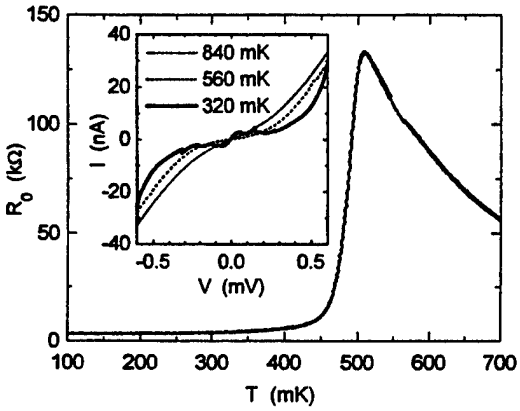

Fig. 3. Temperature dependence of the zero-bias resistance, R_0, of the Al/AlO$_x$/Ti junction pair EF of Fig. 2. Titanium becomes superconducting at T_{c2} = 510 mK. Inset: current-voltage curves of EF at three temperatures.

Some of the features had a hysteretic character, with jumps to different branches in our voltage biased measuring scheme. Most importantly for our thermometry, "supercurrent" appears near zero bias, and R_0 decreases rapidly when temperature decreases below T_{c2}; note that in submicron junctions the so-called supercurrent is not actual zero-voltage Josephson current but has a maximum at a finite voltage, in the case of Fig. 3 at $|V| \approx 40$ µV. The resistance of the Ti strip itself starts decreasing towards zero at the same temperature; this was checked by a 4-wire measurement, feeding current from A to C and measuring voltage across B and D.

The main frame of Fig. 3 shows the temperature dependence of R_0 for EF with $V_{refr} = 0$ (see Fig. 2). The temperature on the horizontal axis was determined by a carbon resistor which was thermally anchored to our sample chamber and calibrated against the primary CBT nanothermometer [9]. The floating measurement of R_0 was performed by the circuit shown in Fig. 2: using an isolation transformer, a constant ac current of about 0.15 nA was fed from E to F, and the voltage across the junctions was measured with a lock-in amplifier.

B. Cooling of Titanium

In Fig. 4 we present our main result: cooling of Ti to and in the superconducting state by quasiparticle tunnelling. The junction pair EF was used for thermometry as explained above. Cooling was achieved by applying a voltage V_{refr} across the "comb-pairs" AB and CD, which were connected in parallel as shown in Fig. 2. In such a structure the ohmic losses in the Ti strip due to the cooling current are negligible in spite of the large normal-state resistivity of Ti. When the substrate temperature $T_0 \equiv T(V_{refr} = 0) > 625$ mK, the system is an SINIS cooler and behaves as in the earlier experiments [2] (see the dashed curves in Fig. 4a): temperature T_{e2} of the electron system of Ti decreases (i.e., R_0 increases) when V_{refr} is applied, reaches a minimum when $|V_{refr}|$ is slightly below $2\,\Delta_1/e \approx 0.42$ meV, and starts increasing at higher voltages.

When $T_0 < 625$ mK, R_0 has a deep minimum when V_{refr} is near the value corresponding to the maximum cooling power

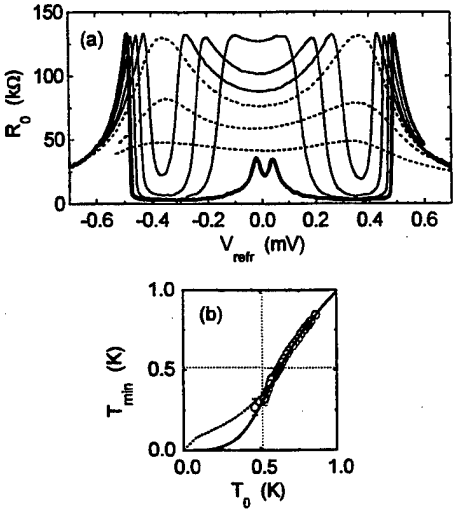

Fig. 4. (a) Zero-bias resistance, R_0, of the junction pair EF as a function of the voltage, V_{refr}, applied across the "comb-pairs" AB and CD, at different substrate temperatures T_0. R_0 is related to the temperature of the Ti electrons, T_{e2}, according to Fig. 3. Dashed lines: Ti is in normal state. Thin solid lines: Ti is cooled from normal to superconducting state. Thick solid line: Ti is superconducting already when $V_{refr} = 0$. (b) Open circles: measured minimum temperature of Ti, T_{min}, as a function of T_0. Solid line: T_0 dependence of T_{min} calculated for an SINIS structure. Thick dotted line: T_0 dependence of T_{e2} calculated at $V_{refr} = 1.9\ (\Delta_1 - \Delta_2)/e$ for our sample when Ti is superconducting. Thin dotted lines: transition temperature of Ti, $T_{c2} = 0.51$ K.

(see the solid lines in Fig. 4a): Ti cools to superconducting state. For example, when $T_0 = 520$ mK $\approx 1.02\ T_{c2}$, corresponding to $R_0(V_{refr}=0) = 127$ kΩ, the minimum temperature reached at $V_{refr} \approx 0.35$ mV is $T_{min} \approx (320 \pm 40)$ mK $\approx (0.63 \pm 0.08)\ T_{c2}$. At substrate temperatures below T_{c2} (thick line in Fig. 4a), the Ti strip, interestingly, heats up at very low voltages corresponding to the "supercurrent peak" and then cools down to temperatures below 300 mK; we cannot measure accurately so low temperatures, because R_0 looses its sensitivity to temperature at $T_{e2} \approx 300$ mK (see Fig. 3). The Ti strip is heated up to normal state when $V_{refr} > 0.5$ mV.

V. Discussion

In these experiments only the electrons in Ti cool down, and the lattice temperature T_{p2} stays near T_0 due to the very weak electron-phonon coupling at low temperatures. The minimum temperature, T_{min}, of the Ti electrons is determined by the competition between the cooling power (1) and the electron-phonon heat flow,

$$\dot{Q}_{e-p} = \Sigma U (T_{p2}^5 - T_{e2}^5) \qquad (2)$$

where U is the volume of the Ti electrode and Σ is a material-dependent constant of order 10^9 WK^{-5}m^{-3}. Figure 4b shows the measured T_{min} as a function of T_0. For comparison we have included the expectations based on (1) and (2) both for an SINIS structure and an $S_2IS_1IS_2$ structure with our geometry and materials. In calculations we used $\Delta_1(0) = 210\ \mu$eV, $\Delta_2(0) = 77\ \mu$eV in the $S_2IS_1IS_2$ case, $\Sigma = 1.3 \cdot 10^9$ WK^{-5}m^{-3} which is of the expected size, and the measured values for R_T and U. We applied the BCS temperature dependence for Δ_1 and Δ_2, and assumed that $T_{p2} = T_{e1} = T_0$, i.e., that the lattice in Ti and the electrons in Al stay at substrate temperature. In the $S_2IS_1IS_2$ case we used $\dot{Q}$ calculated at voltage $V = 0.95\ (\Delta_1 - \Delta_2)/e$ across each junction as an estimate of the "real" maximum cooling power. The experiments and calculations show that in superconducting Ti the cooling effect is as strong as in a corresponding SINIS structure when $T_{e2} > 0.7\ T_{c2}$. On the other hand, no clear improvement in the measured cooling power is observed when Ti gets superconducting. When $T_{e2} << T_{c2}$, maximal cooling is not observed at $V_{refr} = 2(\Delta_1 - \Delta_2)/e \approx 0.27$ mV, at which (1) predicts a diverging $\dot{Q}$ for two junctions in series, but at $V_{refr} \approx 0.33$ mV. No clear "singularity matching peak" in electric current was observed, either; it was buried under the other features of the IV curves.

VI. Conclusions

We have demonstrated that the cooling method based on tunnelling between a superconductor and another metal works even when both metals are superconducting, if the energy gaps are unequal. We have cooled the electron system of a titanium strip with transition temperature $T_{c2} = 0.51$ K from $1.02\ T_{c2}$ to below $0.7\ T_{c2}$ by Al/AlO$_x$/Ti tunnelling. This method can be applied for example in bolometric detectors based on the transition edge of superconductivity; their performance improves strongly with decreasing temperature.

Acknowledgment

We thank K. Arutyunov and B. Collaudin for discussions.

References

[1] M. Nahum, T.M. Eiles, and J.M. Martinis, "Electronic microrefrigerator based on a normal-insulator-superconductor tunnel junction", *Appl. Phys. Lett.*, vol. **65**, pp. 3123-3125, December 1994.

[2] M.M. Leivo, J.P. Pekola, and D.V. Averin, "Efficient Peltier refrigeration by a pair of normal metal / insulator / superconductor junctions", *Appl. Phys. Lett.*, vol. **68**, pp. 1996-1998, April 1996.

[3] A.J. Manninen, M.M. Leivo, and J.P. Pekola, "Refrigeration of a dielectric membrane by superconductor/insulator/normal-metal/insulator/superconductor tunneling", *Appl. Phys. Lett.*, vol. **70**, pp. 1885-1887, April 1997.

[4] M.M. Leivo, A.J. Manninen, and J.P. Pekola, "Microrefrigeration by normal-metal / insulator / superconductor tunnel junctions", *Appl. Supercond.*, vol. **5**, pp. 227-233, 1998.

[5] A.J. Manninen, J.K. Suoknuuti, M.M. Leivo, and J.P. Pekola, "Cooling of a superconductor by quasiparticle tunneling", *Appl. Phys. Lett.*, in press.

[6] B. Frank and W. Krech, "Electronic cooling in superconducting tunnel junctions", *Phys. Lett.*, vol. **A 235**, pp. 281-284, November 1997.

[7] M. Tinkham, *Introduction to Superconductivity*, 2nd ed. New York: McCraw-Hill, 1996.

[8] L.J. Geerligs, V.F. Anderegg, J. Romijn, and J.E. Mooij, "Single Cooper-pair tunneling in small-capacitance junctions", *Phys. Rev. Lett.*, vol. **65**, pp. 377-380, July 1990.

[9] J.P. Pekola, K.P. Hirvi, J.P. Kauppinen, and M.A. Paalanen, "Thermometry by arrays of tunnel junctions", *Phys. Rev. Lett.*, vol. **73**, pp. 2903-2906, November 1994; J.P. Kauppinen, K.T. Loberg, A.J. Manninen, J.P. Pekola, and R.A. Voutilainen, "Coulomb blockade thermometer: tests and instrumentation", *Rev. Sci. Instrum.*, vol. **69**, pp. 4166-4175, December 1998.

Workshops

SQUIDs

Cryogenic Calorimeter Based On Superconducting Phase Transition Thermometer With Thermal Feedback and SQUID Read Out Circuit For It

Oliver Meier[1], Franz Pröbst[1], Wolfgang Seidel[1], Monica Sisti[1], and Sergey V. Uchaikin[1,2]
[1]Max Planck Institut für Physik, Munich, 80805, Germany
[2]Joint Institute for Nuclear Research, Dubna, 141980, Russia

Abstract—Cryogenic calorimeters with superconducting phase transition (SPT) thermometers are extremely sensitive particle detectors. Some characteristics of SPT calorimeters such as linearity and dynamic range often suffer from the superconducting transition shape. The common way to improve the performances is to use the voltage bias to operate the SPT calorimeter in strong electrothermal feedback mode. This method does not allow to optimise the noise, linearity and dynamic properties simultaneously. We have developed a novel SQUID circuit with thermal feedback which allows to improve the linearity, dynamic range and speed of the SPT calorimeter. Results obtained with a cryogenic calorimeter based on a tungsten thermometer are presented.

I. Introduction

Cryogenic detectors based on superconducting phase transition thermometers are nowadays the most sensitive particle detectors. They consist of an absorber where the particle interaction takes place and a strip of a metal film serving as a superconducting phase transition thermometer (SPT). The SPT is coupled thermally to the bath. The detector is kept in the temperature range of the superconducting phase transition of the strip. The particle interaction in the absorber creates high frequency phonons which are collected by the SPT. For small signals, the temperature rise of ΔT of the SPT is proportional to the resistance rise ΔR. SQUID amplifiers are used for resistance measurements.

The output signal of the SQUID corresponding of the temperature change of the thermometer has a form of a pulse composed from exponential components [1]. A typical pulse shape is shown on Fig. 1. The decay time of the pulse consists of two components. The fast components is caused by the absorption of non-thermal phonons created by the particle interaction in the thermometer and the slow component is the thermal signal, which reflects the temperature rise of the absorber. The thermal signal results from the transmitting of a part of the energy thermalized in the thermometer into the absorber [2]. The thermal signal is much slower than the non-thermal one and may limit the tolerable count rate of the detector. The dynamic range and linearity of the detector is limited by the dynamic range and linearity of the phase transition curve.

Manuscript received April 20, 1999

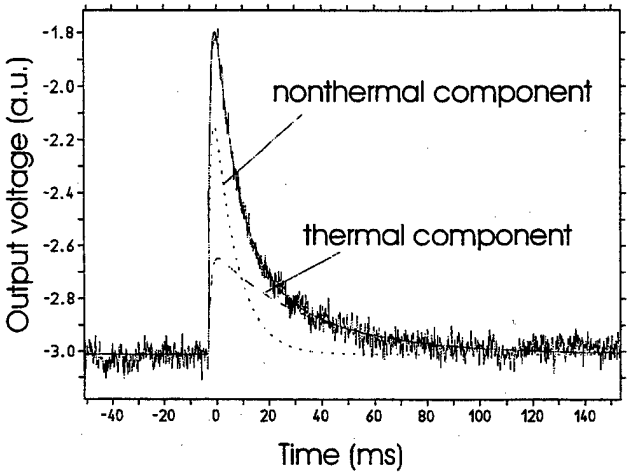

Fig. 1. A typical pulse resulting from the absorption of a 6 keV x-ray with a 262 g sapphire detector.

II. Electrothermal Feedback Technique

To improve the detector characteristics the operation in the voltage bias mode is often proposed [3,4] (Fig. 2). In this mode a selfheating effect appears which allows to stabilize the operating point. In steady state the temperature is determined by the balance of the heat flow from the detector to the bath and the Joule heating of the thermometer. If the heating from the particle interaction rises the resistance of the film the Joule heating decreases. This technique allows to decrease the slow component of the pulse and to shorten the decay time of the resistance signal. To increase the linearity one has to measure the integral of the pulse which represents the energy in this method. Because an integration is not a very good shaping it degrades the signal-to-noise ratio. One has to balance between requirements of linearity and signal-to-noise ratio in the ETF technique.

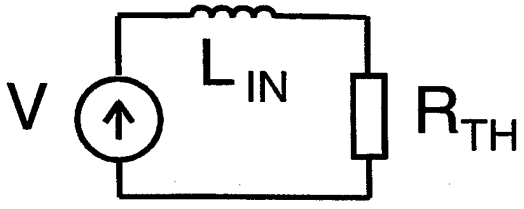

Fig. 2. The ETF read-out circuit. V is the bias voltage supply, L_{IN} - SQUID input coil.

III. SPT with Thermal Feedback

Recently a new type of the feedback for SPT was proposed, so-called thermal feedback (TF) [5]. In this method a

After this measurement the thermal feedback circuit was connected to the SQUID output. The thermal feedback coefficient was set to about 10 dB. The SQUID output signal obtained from a 6 keV phonon is shown on the Fig. 5, curve (b). At this value the thermal component in the output signal was suppressed but an oscillation part in the output occurred. A x-ray spectrum of the detector with thermal feedback is shown in Fig. 6.

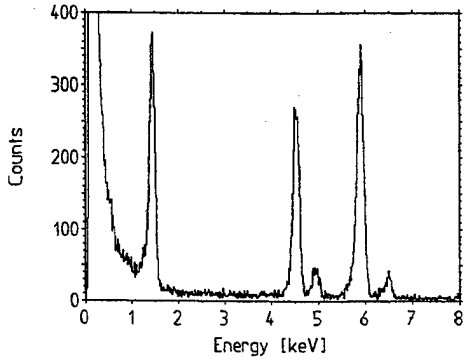

Fig.6. Pulse height spectrum of a 262 gram detector operated with thermal feedback [7]. X-ray fluorescence source provides Al (1.5 keV), Ti (4.5 keV), α-Mn (5.9 keV) and β-Mn (6.5 keV) lines. For the Al line a energy resolution of 133 eV PWH was obtained.

The parameters of the detector, the read-out, and feedback circuits were used to calculate the signal *V(t)* in the feedback mode. The result of the calculation of the system response to a 6-keV X-ray photon quantum is shown in Fig. 7 compared together with the measured output signal of the SQUID magnetometer. Both lines have a good qualitative compliance show that the model is adequate.

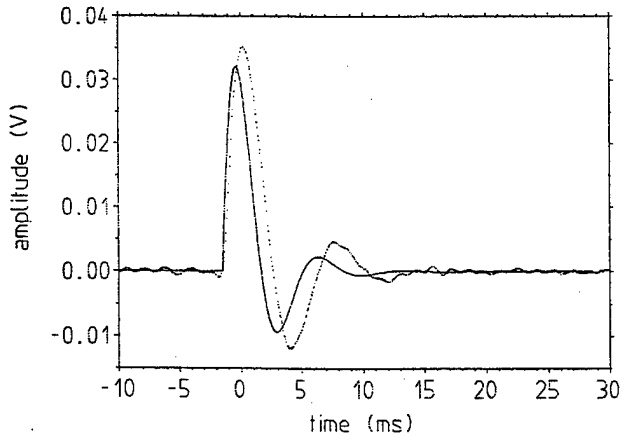

Fig.7. Comparison of the theoretical (solid line) and experimental forms of the 6 keV pulse.

VII. Conclusion

We have operated a cryogenic particle detector based on superconducting phase transition thermometer with thermal feedback technique. The thermal feedback technique suppresses the thermal signal component. The detailed model was developed which describes the detector behavior with good precision. A decrease of the heater time constant will further improve the dynamic characteristics of the detector.

References

[1] P. Ferger, P. Colling, S. Cooper, D. Dummer, M. Frank, U. Nagel, A. Nucciotti, F. Pröbst and W. Seidel, "A massive cryogenic particle detectors with good energy resolution," *Phys. Lett. B,* vol. 323, p. 95, 1994.

[2] F. Pröbst, M. Frank, S. Cooper, P. Colling, D. Dummer, P. Ferger, et al. "Model for Cryogenic Particle Detectors with Superconducting Phase Transition Thermometers," *J. Low Temp. Phys.,* vol. 100, pp. 69-104, July 1995.

[3l M. Frank, D. Dummer, S. Cooper, J. Igalson, F. Pröbst, W. Seidel, "A calorimetric particle detector using an iridium superconducting phase transition thermometer," *Nuclear. Instruments & Methods in Physics Research A,* vol. 345, pp. 367-368, 1994.

[4] K. D. Irwin, "An application of electrothermal feedback for high resolution cryogenic particle detector," *Appl. Phys. Lett.* vol. 66, pp. 1998-2000, 1995.

[5] O. Meier, F. Pröbst, W. Seidel and S. Uchaikin. "Cryogenic Particle Detector Based on Superconducting Phase Transition Thermometer using Thermal Feedback." *Was presented on ISEC'97,* Berlin, June 26-28, 1997.

[6] O. Meier, S. Uchaikin, F. Pröbst and W. Seidel. "SQUID-Amplifier for Cryogenics Particle Detector Based on Superconducting Phase Transition Thermometer. *Inst.Phys.Conf.Ser. No. 158. Paper presented on Applied Superconductivity (EUCAS'97).* The Netherland, Eindhoven, 30 June-3 July, 1997.

[7] S. Cooper et al. "GRESST Dark Matter Search." *Proceedings of the 2nd International Workshop on the Identification of Dark Matter,* Buxton, England, 7-11 Sept. 1998.

disturbances are required. The $YBa_2Cu_3O_{7-x}$ SQUID magnetometer sensors we developed for this purpose are fabricated in flip chip configuration [4]. SQUIDs with a small washer loop, prepared on 30° bicrystall substrates, are flipped to a coupling loop with 15 windings which is connected to pickup loop with a geometrical area of 8mm×8mm. This results in an effective area of $0.7mm^2$ of the complete sensor, which corresponds to a field to flux conversion factor of $3nT/\Phi_0$. The flipped SQUIDs show a voltage swing of typically 50μV.

To make the sensor robust against mechanical and chemical influences, the flip chip is encapsulated in fiber glass. To expel trapped flux, which can occur after movement of the system in the earth magnetic field, a heater is integrated. The short heating above the critical temperature of the superconductor resets the noise level of the SQUID magnetometer.

B. Read-out electronics

The large voltage swing of our SQUID magnetometers allows the use of a directly coupled SQUID electronics without any modulation, using the concept developed by Drung [5]. Our system has a bandwidth of > 1MHz. We are working without ac bias to achieve a maximum slew rate of $1\times10^6\ \Phi_0/s$ and to minimize power consumption. This results in a higher low-frequency noise level in shielded environment, but does not seem to affect the performance in the field.

C. System aspects

For TEM measurements it is very important to avoid metal parts near the SQUID, because the large primary field would also induce eddy currents there. This influences the shape of the measured transient (secondary field) at early times – causing difficulties during interpretation of the data by the geophysicist. On the other hand, it is strongly recommended to shield the sensor very good against rf signals to obtain a stable system under all circumstances. We solved this problem using a 30μm thick aluminum foil.

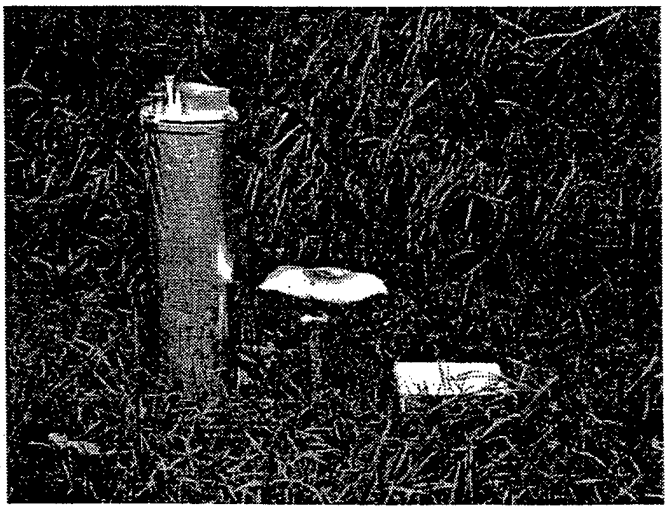

Fig. 3: The complete system in the field. For measurements, it has to be buried in the ground to reduce noise, generated by movements of the system in the wind.

TABLE I
SYSTEM PARAMETERS

Parameter	dc SQUID TEM system
Bandwidth	dc to 10kHz (limited by rf shielding)
White noise	30fT/√Hz @ 1kHz
Low frequency noise	1pT/√Hz @ 1Hz
Slew rate	3mT/s
Power consumption	< 1W
Liquid nitrogen hold time	> 3 days
Weight	6.5kg

Special attention was paid to the system design, in order to make it handy *and* robust (Fig. 3). A small cryostat with a liquid nitrogen volume of about 3 liters allows an operating time of at least 3 days. The electronics is located directly on top of the cryostat. The SQUID on the bottom of the dewar is connected to the electronics with 3 thin wire pairs (voltage, flux, heater), without affecting the hold time of the cryostat. The parameters of the system are listed in Table I.

III. TEM MEASUREMENTS

It is not possible to simulate a TEM measurement in the lab. Therefore, many tests were performed in field experiments in the last two years. To obtain experience in the real geophysicist working day, field trials with geophysical partners and companies in Australia and China above known targets were performed successfully in fall 1998.

Fig. 4 shows results of a typical TEM measurement in a rural place in North China, where the resistivity of the top layer is quite small (about 40Ωm). Here, a conventional cylindrical induction coil with an effective area of about $10{,}000m^2$ was used for comparison. Coil and SQUID system were located in the center of a 100m×100m transmitter loop. The TEM transmitter and receiver unit was developed by the chinese Institute of Geophysical & Geochemical Exploration (IGGE).

It is obvious, that the SQUID signal is smooth up to 50ms, while coil data are already scattering after 10ms. The investigation depth can roughly be estimated by the calculation of the skin depth. Thus, a 5 times longer useable transient recording corresponds to a $\sqrt{5}\approx2.2$ deeper detectable structure.

On the other hand, the coil would need a 25fold longer averaging time to achieve the same data quality as the SQUID – assuming, that the noise source is stochastic. Because a shorter averaging time decreases the probability of disturbances from single magnetic events, such as passing cars or sferics, with the SQUID qualitatively better signals can be achieved in significant shorter measuring times.

The deviation of the SQUID data from the coil data below 1ms is caused by the foil for the rf shield which in these experiments had a thickness of 80μm. A thinner foil of 30μm avoids this effect.

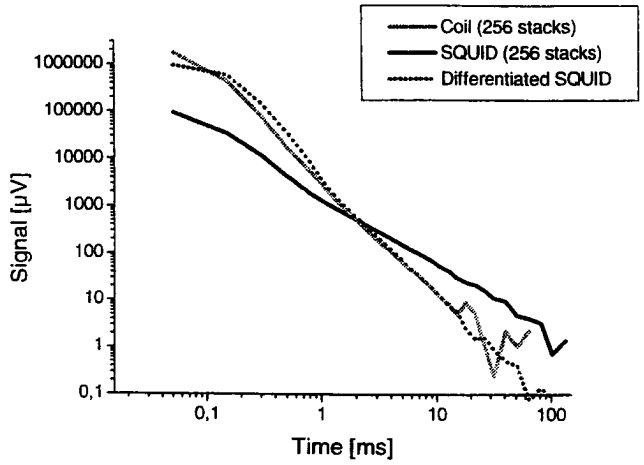

Fig. 4: Coil and SQUID transients, taken in identical manner. For comparison also the differentiated SQUID signal is shown, since coil measures dB/dt.

Recent experiments with a larger transmitter loop showed the advantages of the SQUID even more significant; reproducible transient data were taken up to 1.5s with the SQUID, while the coil data became noisy above 100ms. These results will be presented in the near future.

In Australia a profile with 18 points was measured in production mode, using two SQUID systems (our system and the rf SQUID system from FZ Jülich [6]), conventional air coil in center loop and PROTEM transmitter and receiver. We obtained very smooth transients, but compared to our measurements in Germany and China we observed a strange effect: for late times the transient goes to negative values as shown in Fig. 5. This phenomenon seems only to be visible on low conductive overburden, where the transient is decaying very fast. Both SQUID systems, which are constructed very different, show this effect and the coil does not. To clarify this effect what seems to be dependent on the different physical measurement principles of SQUIDs and coils, further investigations have to be made.

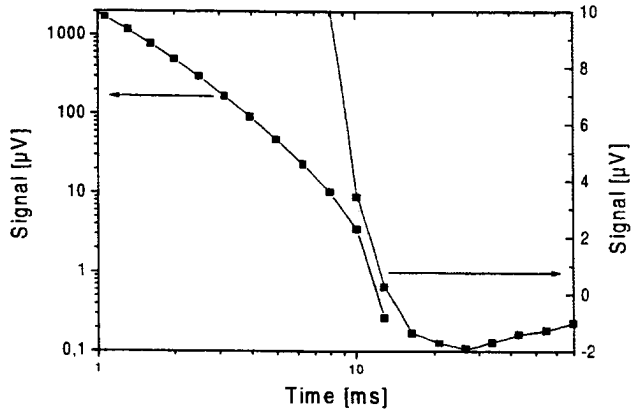

Fig. 5: Transient of our SQUID-TEM system. The late time values are plotted in linear scale, because it is not possible to show negative values in logarithmic scale.

IV. Conclusions

It could be shown, that dc SQUID magnetometers have a significant better performance compared to conventional coils for TEM measurements, what either allows an increased investigation depth of a factor of about 2 or a significant reduction of the measurement time for the same data quality. This has at least two reasons:

While coils measure the time derivative of the B-field; SQUIDs are B-field sensors. The decay of the B-field transient is slower than the voltage decay across a receiving coil ($t^{-3/2}$ against $t^{-5/2}$) [7].

Lower noise of the SQUID in the low-frequency range, which corresponds to a lower noise in the late-time region for TEM measurements.

Acknowledgment

We thank Uli Kalberkamp for introducing us in the TEM measurements. Andreas Chwala likes to thank Marcel Bick, Gregor Panaitov, and Yi Zhang from FZ Jülich for the good cooperation, especially in Australia and China; as well as Ray Lockwood (Geoterrex), Goran Panjkovic (BHP), and all chinese friends from IGGE and PKU.

Special thanks to Frank Bauer, who solves all problems with electronics.

References

[1] G.E. Montgomery, „Geophysical activitiy in 1986," *The Leading Edge*, vol. 6, no. 8, pp. 25-49, 1987.,

[2] B.R. Spies, „Depth of investigation in electromagnetic sounding methods," *Geophysics*, vol. 54, pp. 872-888, 1989.

[3] J. Clarke, „Geophysical Application of SQUIDs," *IEEE Trans. Magn.*, vol. 19, pp. 288-291, 1983.

[4] J. Ramos, R. IJsselsteijn, R. Stolz, V. Zakosarenko, V. Schultze, A. Chwala, H.G.Meyer, and H.E. Hoenig, „Key components for the fabrication of YBaCuO flip-chip SQUID magnetometers and current sensors," *Supercond. Science & Technol.*, vol. 11, pp. 887-890, 1998.

[5] D. Drung, "Advanced SQUID read-out electronics," in: SQUID Sensors: Fundamentals, Fabrication and Applications, NATO ASI Series, H. Weinstock, Ed., , Kluwer Academic Publishers, 1996, pp. 63-116.

[6] M.Bick, G.Panaitov, N.Wolters, Y. Zhang, H.Bousack, U.Kalberkamp, H.Burkhardt, U. Matzander, and A.I.Braginski, "A HTS rf SQUID Vector Magnetometer for Geophysical Exploration," *Applied Superconductivity Conference 1998, paper EMB-01*, to be published in *IEEE Trans. Appl. Supercond.*.

[7] U. Kalberkamp, U. Matzander, K-D. Husemann, G. Panaitow, E. Zimmermann, and Y. Zhang, "HTS rf-SQUID applications to geophysical exploration methods, " *Appl. Supercond.*, vol. 5, pp. 205-211, 1998.

High Tc SQUID microscope head for room temperature sample

Tatsuoki Nagaishi and Hideo Itozaki
Itami Research Laboratories, Sumitomo Electric Industries, Ltd.
1-1, Koya-kita, 1-Chome, Itami, 664-0016, Japan

Abstract—We designed and constructed a new type of a high Tc SQUID microscope head. The sapphire rod is directly cooled with the liquid nitrogen which passes through a liquid nitrogen tank made of glass fiber reinforced plastic. A bellows free simple structure is realized with mutually screwed inner and outer enclosures for separation adjustment between a SQUID and a window. A sample can be close to the SQUID by less than 1mm. We demonstrated the performance of this SQUID microscope by the measurement of a magnetic field from a 70μm diameter magnetized iron particle comparing with the result of a lift off distance of 5mm. The measured magnetic field was increased by 50 times and the detection ability was enhanced drastically.

I. Introduction

Recent progress of SQUID technology especially in the field of a high Tc SQUID broadens the area of magnetic sensing applications. In considering the biomedical application, non-destructive evaluation and geophysical exploration which have been studied from the early stage of low Tc SQUID, it can be seen that the SQUID clearly demonstrated its ability as a new evaluation technique in the field of advanced technology such as bioengineering and semiconductor world. Matz et al. firstly investigated antigen-antibody reactions in fluid samples with the SQUID using magnetic nanoparticles [1]. This technique is anticipated because of the possibility of superiority of the SQUID against a conventional fluorescent method. Immunoassays are widely used in biology and medicine these days and the human health care industry can make progress with this technology. In the semiconductor field, Neocera Inc. developed the MAGNA-C1 prototype system which can image current flow and make failure analysis in integrated circuits [2]. In these applications high magnetic field sensitivity with high spatial resolution is required as a feature of the SQUID. In case of a low Tc SQUID, a lift off distance which corresponds to the distance between the SQUID and the sample, is inevitably widened because of a cooling system with helium. On the other hand, a high Tc SQUID has an advantage of higher cooling temperature and it can work even under the black body radiation through a thin window. Therefore, several tens of microns of short order lift off distance can be achieved and high spatial resolution becomes realized. For instance, Black et al. who are pioneered the high Tc SQUID microscope made the lift off distance of 60μm [3] and since then several groups made this order of lift off distance. However, designs of these high Tc SQUID microscopes are very complex because of a precise separation adjustment system. In this article, we propose and introduce our new design of a high Tc SQUID microscope head which is simple with all glass fiber reinforced plastic (GFRP) except a sapphire thermal transfer rod and a sapphire window. We measured the magnetic field from a small iron particle with the SQUID microscope and compared our previous results using a capped SQUID in the liquid nitrogen dewer.

II. Design and Construction

A. Design

Fig. 1 shows a structure of a new design SQUID microscope head. The main feature of this structure is the effective heat transfer to the SQUID with direct cooling of the sapphire thermal transfer rod which is partially dipped in the liquid nitrogen. It has a simple structure with two mutually screwed different size enclosures without bellows and can adjust a separation between a SQUID and a window. The SQUID is placed in the vacuum thermal insulation layer between an inner enclosure and an outer enclosure. Since the inner and outer enclosures are screwed each other, the separation between the SQUID and the window can be adjusted by changing the screwed depth. This design leads the structure of the SQUID microscope head to be compact and simple with all GFRP made.

B. Construction

The vacuum layer between the inner (A) and outer (B) enclosure is sealed with a greased O-ring (E) to adjust the screwed depth and is pumped through a seal off valve (F). In a vacuum region, activated charcoal (I) and ten super insulation films (H) are wound around the inner enclosure. The inner enclosure has a hole at the bottom and the sapphire thermal transfer rod (J) passes through it. The sapphire rod and the inner enclosure are glued with an epoxy resin. The SQUID chip (L) is placed at the tip of the sapphire rod with silver paste. The modulation coil is wound around the sapphire rod and four other terminal wires are also glued on it. The terminal wires are electrically connected with the SQUID at its side end. The outer enclosure also has an 11mm diameter hole and a 200μm thick sapphire window is attached with an O-ring or is fixed with the epoxy resin. The separation between the SQUID and the sapphire window is adjusted with the screwed depth of the inner and outer enclosures. Because of this structure the wiring (K) passes through the inner enclosure from atmosphere to vacuum to avoid the break during the insertion and the adjustment of the inner enclosure to the outer enclosure. The picture of the

Manuscript received April 30, 1999.

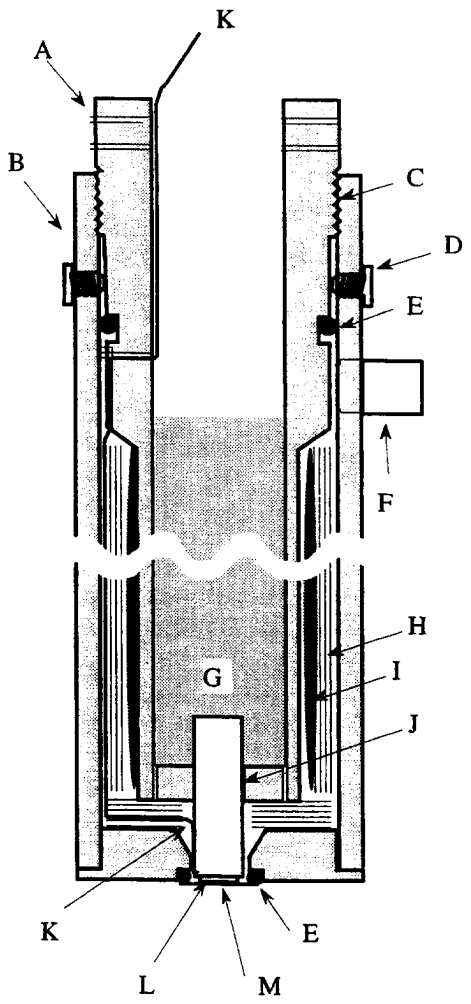

Fig. 1 Structure of a SQUID microscope. (A) inner enclosure, (B) outer enclosure, (C) screwed part, (D) stopper, (E) O-ring, (F) seal off valve, (G) liquid nitrogen, (H) super insulation, (I) activated charcoal, (J) sapphire rod, (K) wirings, (L) SQUID, (M) sapphire window

SQUID microscope head is shown in Fig. 2. The outer diameter of the head is 55mm and the total length is 221 mm.

C. SQUID and Electronics

A dc SQUID with two step-edge Josephson junctions is used. It is a 5mm square large washer type with a laser deposited $HoBa_2Cu_3O_{7-x}$ high Tc superconducting thin film on a 1mm thick $SrTiO_3$ substrate. The effective capture area of the magnetic field is $0.08mm^2$. The SQUID chip can be seen in Fig.2 through the sapphire window. A flux modulation type flux locked loop circuit with dc current bias was used for the SQUID driving. In this experiment, we used our conventional SQUID rather than a small SQUID chip to demonstrate the effectiveness of short lift off distance to detect a tiny magnetic field.

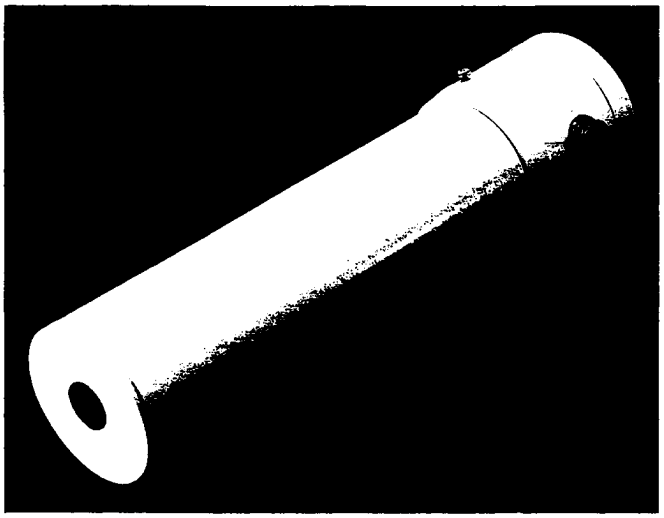

Fig. 2 Picture of SQUID microscope head The diameter of the head is 55mm and the total length is 221 mm.

III. PERFORMANCE AND DEMONSTRTION

A. Performance

The enclosure is pumped down to 10^{-4} Torr and then the liquid nitrogen is poured into the inner enclosure. The full volume of liquid nitrogen is $50cm^3$ and the SQUID measurement lasts 2 hours with this amount of coolant. The separation between the SQUID surface and the sapphire window is adjusted after pumping under the optical microscope utilizing focusing depth difference and it is set at about $110\mu m$.

The SQUID goes into superconducting state in about 5 minutes after the liquid nitrogen filling. The performance of the SQUID is described in Table 1. The critical current (Ic) decreased with the SQUID microscope head comparing with the one in the liquid nitrogen. This may be caused by the thermal loss at the interface of the SQUID chip and the sapphire rod, SQUID chip itself and the radiation through the sapphire window to the SQUID surface.

B. Demonstration

To clarify the advantage of the SQUID microscope with a short lift off distance, we demonstrated the detection of the

TABLE I

COMPARISON OF SQUID PERFORMANCE IN THE LIQUID NITROGEN AND AT THE MICROSCOPE HEAD

Cooling	$I_c(\mu A)$	$V_{pp}(\mu V)$	$S_B^{1/2}$ (10Hz) ($pT/Hz^{1/2}$)
in LN_2	100	7.5	1.2
at microscope head	60	7.5	0.9

magnetic field of a magnetized iron particle. The SQUID microscope head is placed inside the magnetic shield which has holes at the side wall to insert a sample. An iron particle with a diameter of 70μm was used as a sample for this demonstration. It was magnetized under the magnetic field of 1.3Tesla. The result is shown in Fig.3 with our earlier experiment with the same size iron particle. The lift off

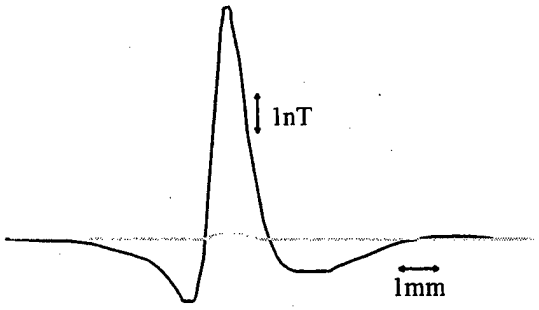

Fig. 3 Date acquired from the magnetized iron particle of diameter of 70μm. Dark line shows the data using the SQUID microscope (lift off distance : 1mm). Light line shows the data with the lift off distance of 5mm.

distance was 5mm. The signal was enlarged about 50 times with the SQUID microscope head. The lift off distance was calculated to be 1.3mm from the formula that the magnetic field is inversely proportional to the third power of distance. Since in this experiment, the sapphire window was attached to the outer enclosure with the O-ring of the free edge, the large dent of which the depth is unknown was made. In addition an inevitable space between the sample and the edge of the sapphire window made an extra 1mm lift off distance. The present result is plotted in our earlier result of the correlation between the iron particle size and the magnetic field with different lift off distance in Fig. 4 [4]. This indicates the detection of less than 20μm diameter can be easily detectable. When the window is glued directly on the outer enclosure, the dent of the window becomes shallow and the separation between the SQUID and the window can also be much closer than 110μm in this experiment. Further improvement will be possible.

IV. Conclusion

We developed a newly designed high Tc SQUID microscope head. The sapphire thermal transfer rod is directly cooled with liquid nitrogen for the effective heat transfer to the SQUID. The bellows free simple structure of a separation adjustment system with mutually screwed inner and outer enclosures was also designed. This design makes the high Tc SQUID microscope to be compact and simple. We measured the magnetic field of a 70μm diameter magnetized iron particle and a clear improvement of signal intensity of 50 times compared with the result of a lift off distance of 5mm.

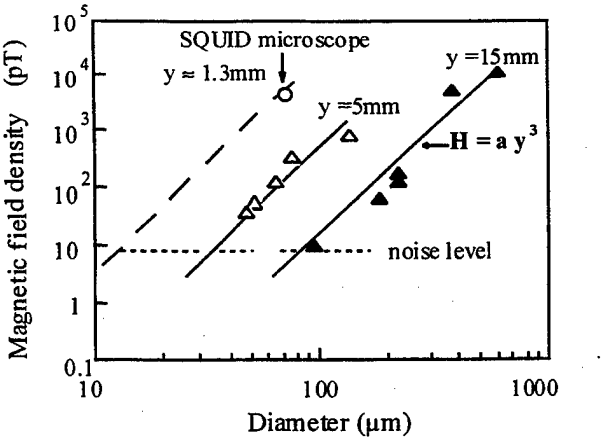

Fig. 4 The data acquired with the SQUID microscope is plotted in the earlier data of correlation between the iron particle size and the magnetic field with different lift off distance. An iron particle less than 20μm will be detected with the SQUID microscope.

The lift off distance of the SQUID microscope was calculated to be 1.3mm. Further development with a small SQUID chip will enable high spatial resolution for applications which need spatial resolution such as failure analysis of integrated circuits, etc.

References

[1] H. Matz, D. Drung , S. Hartwig, H. Grob, R. Kotitz, W. Muller, A. Vass and L. Trahms, "A SQUID Measurement System for Immunoassays", Extended abstracts of 6th Int. Superconductive Electronics Conference June 25-28, 1997, Berlin, Germany, vol. 3 A19, pp. 379-382.

[2] Web information from Neocera Inc. (http: www.neocera.com)

[3] R. C. Black, A. Mathai, F. C. Wellstood, E. Dantsker, A. H. Miklich, D. T. Nemeth, J. J. Kingston and J. Clarke, "Magnetic microscopy using a liquid nitrogen cooled Yba2Cu3O7 superconducting quantum interference device", Appl. Phys. Lett. vol. 62, pp. 2128-2130, April 1993

[4] T. Nagaishi H. Toyoda and H. Itozaki, "Detection of Magnetic Fine Particles in Motion by High Tc SQUID", Extended abstracts of 6th Int. Superconductive Electronics Conference June 25-28, 1997, Berlin, Germany, vol. 3 A14, pp. 364-366.

Author Index

Author Index

Abelson, Lynn A. PI-5.18
Adam, Roman PI-4.3, Or7.4, PII-1.4
Akaike, H. PI-5.5
Akazaki, Tatsushi PI-5.17
Akoh, H. PII-4.6, PII-4.5
Akoh, Hiroshi PII-1.1, PII-5.13
Alff, L. PII-5.10, PII-5.16
Allen, George I. Or9.4
Almasri, Mahmoud Or7.4
Alvarez, G. A. PII-5.6
Andre, Mark-Olivier Or8.1
Aono, M. Or8.7
Aoyagi, M. PII-4.5, PII-4.6
Aoyagi, Masahiro PII-1.1
Aoyama, T. PI-5.5
Arie, Hiroyuki PII-5.12
Aruga, Y. PII-5.4
Arutyunov, K. Or10.4
Arzumanov, Alexy V. PII-3.8
Asmann, C. Or8.3
Atencio, L. PII-2.2
Atencio, Leroy PI-2.16
Atkin, I. L. Or5.1
Balashov, D. PI-5.4
Barbosa, C. H. PII-2.10
Barner, Jeff PI-4.5
Barthel, K. Or9.1
Barthel, Knut Or8.6
Barthelmess, H. -J. PI-2.5
Baryshev, A. M. PII-3.2
Baryshev, Andrey M. Or4.8
Bauch, T. PII-5.10, PII-3.3
Beall, J. A. Or4.6
Bechstein, Sylke Or9.2
Behr, Ralf PI-1.18
Bennett, A. J. PI-5.7
Benson, Robert G. Or8.5
Benz, Georg PII-2.16
Benz, S. PII-5.1
Benz, S. P. Or5.7, PI-1.13
Berggren, Karl K. Or2.5
Bergren, N. F. Or7.1
Berkowitz, S. Or4.4
Berninger, Michael Or5.2
Beyer, Jorn Or9.2
Bhat, Anupama PI-5.3, PII-5.18
Biedermann, K. PI-3.1
Bier, A. PI-4.2
Billon-Pierron, D. PII-4.4
Blamire, M. G. PI-3.2, PI-5.7
Blamire, Mark G. PII-5.8
Blondel, J. PI-4.10, PII-4.4
Bocko, Mark F. PI-1.12
Bono, John T. Or9.4
Booij, W. E. PI-3.2, PI-5.7
Booij, Wilfred E. PII-5.8
Booth, J. C. PII-5.1, PI-3.7
Booth, James C. Or4.6, Or4.5
Borgmann, J. Or9.5
Boronin, S. G. PII-3.6
Borovitskii, Solomon I. Or2.8
Borzenets, V. PII-3.10, Or4.4
Braginski, A. I. Or8.6
Brey, William Or10.2
Brinkman, A. PI-5.15
Brock, D. Or2.1
Brock, Darren K. PI-1.16
Broussard, P. R. Or6.6
Bruno, A. C. PII-2.10, PII-2.11
Buchholz, F. -Im. PI-5.4
Buhrman, Robert A. Or5.2
Bulzacchelli, John F. Or2.2
Bunyk, Paul Or3.2
Burns, Deborah A. Or8.5
Burroughs, C. J. PI-1.13
Butler, Donald P. Or7.4
Cai, C. PII-5.11
Cai, Q. Y. PII-1.6
Cai, Qi Yu PI-1.17, PI-1.3
Cantor, R. PII-2.2
Cantor, Robin PI-2.17, PI-2.16
Carillo, F. PII-5.5
Carr, C. Or9.6
Celik-Butler, Zeynep Or7.4
Chen, J. PII-5.4
Chen, Jian PII-4.7, PI-4.8
Chen, T. C. PI-4.2
Chen, W. PI-5.1, Or6.4
Cherednichenko, Sergey PI-4.6
Chesca, Boris Or8.6
Chiba, K. PI-5.14
Choi, S. S. PI-1.1
Chong, Yonuk Or2.7
Chouvaev, Denis PII-4.1
Chwala, A. W-2.-1
Claassen, J. H. Or4.5, Or4.6

Clarke, John Or10.1, Or1.2, Or8.1, Or9.5
Clem, Ted R. Or9.4
Clinton, T. W. Or6.6
Collaudin, B. Or10.4
Corey, Alan M. Or8.5
Darula, Marian PII-1.4, PI-4.4
Davidson, B. A. PII-3.5
Dean, E. J. Or2.3
Dean, Eric J. Or3.5, Or3.7
Develos, Katherine D. PI-5.13
Dew-Hughes, D. PI-3.3
Dew-Hughes, David Or4.7
DiCamillo, B. PI-4.2
Diehl, Dirk PI-4.4
Dittmann, Regina Or6.1, Or2.7
Dmitriev, P. PI-4.10
Dmitriev, P. N. Or6.3, PII-3.2
Donaldson, G. B. Or9.6
Dorojevets, Mikhail Or3.2
Dörrer, L. Or9.7, PII-2.4
Dresselhaus, Paul D. Or3.7, Or3.5
Drozdov, Y. N. PI-5.19
Drung, D. Or8.3
Drung, Dietmar Or9.2, PII-2.16
Du, J. PII-5.17
Eaton, L. R. Or3.4
Eaton, Larry PII-1.15
Elsner, H. PI-5.10
Engelhardt, Achim Or2.7
Enomoto, Y. PII-5.6
Enomoto, Youichi PII-1.16
Enpuku, K. PI-2.1
Esposito, E. PI-3.6
Espy, M. A. PII-2.2
Espy, Michelle PI-2.16
Espy, Michelle A. PII-2.3, PI-2.17, PII-2.1
Eulenburg, A. Or9.6
Exon, Nick J. Or9.3
Fan, Y. PI-2.17
Fang, L. PII-5.14
Feld, David A. Or2.5
Feng, Y. J. PI-5.11
Ferro, F. Or6.3
Filippenko, L. V. PII-3.2, PII-3.1
Filippenko, Lyudmila V. Or4.8
Filippov, T. Or2.1
Filippov, Timur PI-1.5
Finkbeiner, F. M. PI-4.2
Fischer, M. Or9.1
Flees, Daniel J. Or6.4
Flynn, Christopher S. Or8.5
Foley, C. P. PII-5.17, PI-2.11
Foord, David T. PII-5.8
Forrester, M. G. Or2.6, Or2.3
Friedman, Barry Or6.5
Friedman, Jonathan R. Or6.4
Fritzsch, L. PI-2.8, PI-5.10
Fujimaki, A. PI-1.11, Or5.5, PI-5.5
Fujimaki, Akira PII-5.9, Or3.1, PI-3.9
Fujimoto, S. PII-2.14
Fukazawa, T. PII-5.2
Furuta, F. PI-1.11
Furutani, Toshiki PII-5.9
Gail, Jost Or8.1
Gao, Erzhen Or4.2
Gao, J. R. Or6.3
Gaponov, S. V. PI-5.19
Gershenson, Michael E. Or7.2
Gershenzon, E. Or7.3
Gia, Q. X. PI-2.17
Gim, Y. PI-2.17
Gohng, J. H. PII-2.8
Gol'tsman, G. Or7.3
Gol'tsman, G. N. Or7.5
Gol'tsman, Gregory N. PI-4.6
Golubov, A. A. PI-5.15
Granata, C. PI-3.6
Granozio, F. Miletto PII-5.5
Groot, P. de PI-2.14
Gross, R. PII-3.3, PII-5.10, PII-5.16, Or8.6, Or9.1
Gundlachs, K. H. PII-4.4
Guo, J. PII-1.6
Gupta, Deepnarayan PI-1.2
Gusev, S. A. PI-5.19
Hadfield, Robert Or6.1
Hagmann, Christian Or8.1
Hahn, T. S. PI-1.1
Halbritter, J. Or5.3, PI-5.12
Haller, A. PII-2.13
Hamilton, C. A. PI-1.13
Han, S. G. PII-2.8
Han, Siyuan PII-5.14
Hansen, J. Bindslev PI-2.6, PI-2.7
Hansen, Jørn Bindslev PI-3.5
Harada, N. PI-1.15
Harding, G. L. PII-5.17
Harnack, Oliver PI-4.5, PI-4.4, PII-1.4
Hartwig, S. PII-2.13
Hasegawa, H. PI-1.11
Hasegawa, Haruhiro PII-1.16
Hashimoto, Tatsunori PII-1.16
Hashimoto, Yoshihito Or1.1

Hattori, W. PII-1.5
Hayakawa, H. Or5.5, PI-5.5, PI-1.11
Hayakawa, Hisao Or3.1, PII-5.9
Hayashi, N. Or5.5
Heiden, Christoph Or8.1
Heinsohn, Jan-Klaas PI-4.4, Or6.1
Herr, Quentin PII-1.15
Herr, Quentin P. PI-5.18
Hilton, G. C. Or7.1
Hirano, Tetsuya Or8.4
Hirst, P. J. Or5.1
Hoenig, H. E. PI-2.4
Höfener, C. PII-5.16
Hohkawa, Kohji PII-5.13
Holst, T. PII-2.9, PI-2.6, PI-2.7
Hontsu, Shigeki PI-3.9
Horibe, M. Or5.5
Horibe, Masahiro PII-5.9
Horton, Tom Or9.3
Hoshino, K. Or8.7
Hosoki, T. PI-1.4
Hu, R. PII-5.15
Huang, Kao-Cheng Or4.7
Huber, Martin E. Or8.5
Hübers, H. -W. Or7.3
Hübers, Heinz-Wilhelm PII-4.2
Huebener, R. P. Or9.1
Humphreys, R. G. Or5.1
Humphreys, Richard G. Or9.3
Hunt, B. D. Or2.3, Or2.6
Hur, Jung PI-3.8
Hwang, Yunseok PII-2.5
IJsselsteijn, R. P. J. PI-2.4
Iguchi, Ienari PII-4.8, PII-5.12, Or6.5
Ikeda, T. PII-4.6, PII-4.5
Il'ichev, E. PI-2.4
Il'in, K. S. Or7.5
Inagaki, Y. Or5.5
Iosad, N. N. Or6.3
Irwin, K. D. Or7.1
Ishibashi, K. PII-4.5
Ishibashi, Takayuki Or6.5
Ishii, Junya PI-3.9
Itozaki, Hideo Or8.4, W-3.-1
Iwai, T. PI-5.5
Jackson, B. D. Or6.3
Jeffery, M. Or3.3, Or3.6
Jeffery, Mark Or3.8
Jenkins, A. PI-3.3
Jenkins, Alan Or4.7
Jeon, Duk Young PII-3.11
Jiang, J. F. PII-1.6
Jiang, Jian Fei PI-1.3, PI-1.17
Jin, B. B. PI-3.4
Johnson, Mark Or6.6
Jung, K. R. PI-1.1
Jung, Ku-Rak PII-3.11
Jutzi, Wilhelm PII-2.16
Kahlmann, F. PI-3.2
Kalabukhov, Alexey S. Or8.2
Kamekawa, Y. Or8.7
Kamijo, K. Or8.7
Kanaya, Haruichi PII-3.9
Kaneko, Atsushi PII-5.13
Kang, J. H. PII-2.8, PI-1.1
Kang, L. PI-5.11
Kang, Y. M. PII-2.14
Kaplunenko, Vsevolod K. PI-1.8, PII-1.13
Karasik, Boris PI-4.5
Karasik, Boris S. Or7.2
Karpov, A. PII-4.4, PI-4.10
Katayama, Masaaki Or3.1
Kato, H. PII-4.5, PII-4.6
Kato, Koichi PI-2.3
Kato, Yohsuke PII-1.7
Kawabe, U. PII-5.6
Kawai, K. Or5.5, PII-4.6, PII-4.5
Kawai, Tomoji PI-3.9
Kawakami, Akira PII-4.3, PI-5.6
Kawamura, Mitsuo PII-3.7
Kaya, Nobuyuki PII-4.3
Keane, Mark N. Or9.3
Keefe, George A. Or9.4
Keil, S. Or9.1
Kerber, George L. PI-5.18
Kessel, W. PI-5.4
Ketchen, Mark B. Or2.2
Ketterson, J. B. PI-5.2
Khabipov, M. I. PI-5.4
Kim, C. H. PI-1.1
Kim, In-Seon PII-2.15
Kim, J. Y. PII-2.8
Kim, Jin Kook PI-3.8
Kim, Jin-Mok PII-2.7, PII-2.15
Kim, Jin-Tae PII-2.5
Kim, Jin-Young PII-3.11
Kim, Sang-Jae Or5.6
Kim, Y. H. PI-1.1
Kimpara, T. Or4.3
Kinnunen, K. PI-4.1
Kirichenko, A. Or2.1
Kirichenko, Alex F. PII-1.12, PI-1.16

Kitagawa, M. PII-1.9, PI-1.4
Kitagawa, Yoshihiro PI-5.16
Kiviranta, Mikko PI-2.10, PI-2.9
Klapwijk, T. M. Or6.3
Klein, J. PII-5.16
Kleinsasser, Alan PI-4.5
Kluenkov, E. B. PI-5.19
Klushin, A. M. PII-5.1
Klushin, Alexander M. PII-5.3, Or2.8
Knappe, S. Or8.3
Kobayashi, Akira PII-3.7
Kobayashi, Eeisuke PI-4.8
Kobayashi, Hirokazu PII-5.12
Kobayashi, K. Or8.7
Kobayashi, T. PII-5.11
Koch, M. PI-5.8
Koch, R. H. Or9.5
Koch, Roger H. Or9.4
Kodaka, H. PI-1.4
Koelle, D. PII-3.3, Or9.1
Koelle, Dieter Or8.6
Koh, K. Hohkawa nad K. PII-1.10
Kohlmann, Johannes PI-1.18
Kohlstedt, H. PII-5.1
Koike, Koike Or8.7
Kollberg, Erik PII-4.2
Kornev, Victor K. PII-3.8
Koshelets, V. P. PII-3.2
Koshelets, Valery P. Or4.8
Koshiyama, J. Or3.3
Koshiyama, Junichi PI-1.7
Kosholets, V. PI-4.10
Kotaka, H. Or8.7
Kötitz, R. PII-2.12, PII-2.13
Kouznetsov, K. A. Or9.5
Koyabu, Y. Or8.7
Koyama, Satoshi Or5.4
Krasnopolin, Igor Y. PI-1.18
Krasnosvobodtsev, Sergey I. Or8.2
Krasnov, Vladimir PII-5.8
Kraus, R. H., Jr. PII-2.2
Kraus, Robert H., Jr. PI-2.16, PII-2.1, PI-2.17
Krauss, Robert H., Jr. PII-2.3
Kresin, Vladimir Z. PII-5.3
Kretzschmar, D. W-2.-1
Krey, S. PI-2.5
Kroug, Matthias PII-4.2
Kume, Eiji PII-4.8
Kupriyanov, M. Yu. PI-5.15
Kupriyanov, Mikhail Yu. Or2.8
Kuriki, Shinya PI-2.3
Kurin, V. V. PII-3.2
Kusunoki, M. PI-5.14, Or4.3
Kusunoki, Masanobu PI-5.13
Kutchinsky, J. PI-3.5
Kuzmin, Leonid PII-4.1
Kwak, Junesik PII-3.11
Kwon, H. J. PI-3.8
Kwon, Hyukchan PII-2.7, PII-2.15
Larsen, B. H. PI-2.7
Latyshev, Yu. I. Or5.6
LeDuc, Henry G. Or7.2
Lee, E. H. PII-2.8
Lee, Eun-Hong PI-2.2, PII-3.11
Lee, Hae-Seung Or2.2
Lee, J. H. PI-3.8
Lee, J. M. PI-1.1
Lee, Jeong-Soon PII-3.11
Lee, Kiejin Or6.5
Lee, Sang Young PI-3.8
Lee, Soon-Gul PII-2.5
Lee, W. H. PI-3.8
Lee, Yong-Ho PII-2.7, PII-2.15
Leivo, M. M. Or10.4
Leivo, Mikko M. Or10.5
Leslie, K. E. PII-5.17
Leung, M. Or3.4
Leung, Michael PI-5.18
Li, W. Or2.1
Li, Yijie Or6.2
Liang, J. -F. Or4.4
Likharev, Konstantin Or3.2
Lima, E. Andrade PII-2.11
Lindelof, Poul Erik PI-3.5
Linzen, S. Or9.7
Litskevitch, Peter Or3.2
Liu, L. PI-5.11
Liu, Q. G. PI-5.11
Lombardi, F. PII-5.5
Ludwig, Frank Or9.2
Luine, Jerome A. PII-5.3
Luinge, William Or4.8
Lukens, J. E. Or6.4, PI-5.1
Lumley, John M. PI-2.15
Luukanen, A. PI-4.1
Ma, Q. Y. Or4.2
Macmillan, G. PI-2.14
Maehata, K. PII-4.5
Mancini, Cesar A. PI-1.12
Mannik, J. Or6.4
Manninen, A. PI-4.1
Manninen, A. J. Or10.4

Manninen, Antti J. Or10.5
Manscher, M. H. PII-3.1
Martinis, John M. Or7.1
Maruyama, M. Or5.5
Maruyama, Michitaka PII-5.9
Marx, A. PII-5.10
Matijasevic, V. Or9.5
Matlashov, A. PII-2.2
Matlashov, Andrei A. PI-2.17
Matlashov, Andrei N. PI-2.16, PII-2.3, PII-2.1
Matsuda, G. Or5.5
Matsuda, Mizushi PI-2.3
Matsui, T. Or8.7
Matsui, Toshiaki PI-4.9
Matsuyama, T. PI-3.1, PI-5.8
Matz, H. PII-2.13
McBrien, P. F. PI-3.2
McDermott, R. Or9.5
McDermott, Robert Or10.1
McDonald, D. G. PI-4.7
McGrath, William PI-4.5
McGrath, William R. Or7.2
Meng, Xiaofan PII-5.18, PI-1.10, PI-5.3
Merkel, Harald PII-4.2
Merkt, U. PI-5.8, PI-3.1
Meyer, H. -G. PI-5.10, PI-2.8, W-2.-1, PI-2.4
Miki, Shigehito PII-4.3
Millar, A. J. Or9.6
Miller, D. L. Or2.6, Or2.3
Minotani, T. PI-2.1
Mironov, V. L. PI-5.19
Misewich, James A. Or2.2
Miteva, S. PI-3.3
Miyahara, Kazunori PII-1.16
Miyahara, S. PII-2.14
Miyasaka, H. PII-4.5, PII-4.6
Mizugaki, Y. PII-5.4
Mizugaki, Yoshinao PII-4.7
Moeckly, B. H. Or6.7
Moeckly, Brian H. Or5.2
Morishita, T. PII-5.6
Moriya, T. PI-5.14
Moseley, R. W. PI-5.7
Mros, Niklas PII-5.8
Muck, Michael Or8.1
Mukaida, M. PI-5.14, Or4.3
Mukaida, Masashi PI-5.13
Mukhanov, O. Or2.1
Mukhanov, Oleg A. PI-1.16, PII-1.12
Müller, Franz PI-1.18
Murduck, J. M. PII-5.15
Mygind, J. PII-3.1
Mygind, Jesper Or4.8
Nagaishi, Tatsuoki W-3.-1, Or8.4
Nagasawa, Shuichi PII-1.16
Nagawasa, Shuichi Or1.1
Nakagawa, H. PII-4.6, PII-4.5
Nakagawa, Hiroshi PII-1.1
Nakai, Harutaka PI-3.9
Nakajima, K. PII-5.4
Nakajima, Kensuke PII-4.7, PI-4.8
Nakamori, Masaya PI-3.9
Nakamura, Takuhiro PII-3.9
Nakayama, K. Or8.7
Narasaki, K. Or8.7
Neil, Patricia A. Or8.5
Netesova, N. P. PII-3.4
Nevirkovets, I. P. PI-5.2
Niemeyer, J. PI-5.4
Niemeyer, Jürgen PI-1.18
Ninomiya, Y. PI-5.5
Nisenoff, M. Or4.1, PII-1.11
Nishikawa, Hiroaki PI-3.9
Nitta, Junsaku PI-5.17
Noguchi, Yasumasa PI-3.9
Nordahn, M. A. PII-3.1, PII-2.9
Nowak, H. PII-2.6
Numata, Hideaki Or1.1, PI-5.16
Nuottajärvi, A. PI-4.1
Nurgaliev, T. PI-3.3
Ogawa, Akira Or3.1
Ohshima, S. PI-5.14, Or4.3
Ohshima, Shigetoshi PI-5.13
Ohta, H. Or8.7
Ohta, Hiroshi PI-4.9
Ohta, S. PI-2.1
Okabe, Y. PI-1.4, PII-1.9
Oke, R. PI-5.5
Oku, T. PII-4.6, PII-4.5
Ong, C. K. PI-3.4
Ono, R. PII-5.1
Ono, R. H. Or5.7, PI-3.7, Or4.5, Or4.6, PI-4.7
Ono, Syotaro PI-2.3
Ootani, W. PII-4.6, PII-4.5
Ornelas, P. H. PII-2.10
Otani, C. PII-4.6, PII-4.5
Overway, David J. Or9.4
Oya, E. PI-1.11
Oyama, Hiroshi PI-2.3
Pagano, S. PII-3.5
Park, Gwangseo PI-2.2
Park, J. H. PI-1.1

Park, Jong-Chul PII-2.7, PII-2.15
Park, Sang-Jin PII-3.11
Park, Yong Ki PII-2.5
Park, Yong-Ki PII-2.7
Park, Yonk-Ki PII-2.15
Pasturel, P PII-4.4
Patel, Vijay Or6.4, PI-5.1
Pegrum, C. M. Or9.6, PI-3.2
Pekola, J. PI-4.1
Pekola, J. P. Or10.4
Pekola, Jukka P. Or10.5
Perold, Willem J. Or3.8
Peschka, M. Or9.1
Peters, M. Or8.3
Petersen, P. R. E. PI-2.6, PI-2.7
Pettiette-Hall, C. L. PII-5.15
Phelan, R. J. PI-4.7
Pines, Alexander Or10.1
Platov, Konstatin Yu. Or2.8
Platzek, D. PII-2.6
Polonsky, Stas V. Or3.5, Or3.7
Polyakov, S. N. Or6.3
Polyakov, Yu. Or2.1
Polyakov, Yu. A. PII-1.3
Pöyhönen, S. PI-4.1
Przybysz, J. X. Or2.3
Przybysz, John X. Or3.7, Or3.5
Purpura, John W. Or9.4
Ramos, J. W-2.-1
Ramsden, J. PII-3.10
Rao, X. S. PI-3.4
Rassi, D. PI-2.14
Regalla, H. PI-5.15
Rheinländer, Th. PII-2.13
Richter, A. PI-5.8
Romans, E. J. Or9.6, PI-3.2
Rönnung, Fredrik PI-4.6
Rozen, James R. Or9.4
Ruck, Bernhard Or2.7
Rudman, D. A. Or7.1, Or4.6
Ruggiero, B. PI-3.6
Ruminer, P. PII-2.2
Russo, M. PI-3.6
Rylov, S. Or2.1
Sage, Jay P. Or2.5
Sager, M. PI-2.6
Sager, Y. Q. Shen. M. P. PI-2.7
Sahba, Shapur Or4.2
Saito, Yusuke PI-2.13
Saitoh, K. PI-1.6
Salmi, J. PI-4.1
Sandell, R. D. Or3.4
Sankrithyan, B. PII-5.17
Sarnelli, E. PII-5.5, PII-3.5
Sashiyama, Kazumi PII-3.9
Sata, K. PII-2.14
Satchell, J. S. Or5.1
Satchell, Julian S. Or9.3
Sato, H. PII-4.5, PII-4.6
Sato, Hiroshi PII-1.1, PII-5.13
Sato, Katsuaki Or6.5
Sato, M. PII-5.6
Schambach, J. PII-2.12
Scharnweber, R. PI-2.15
Scherbel, Jens PI-4.4
Schilling, M. PI-2.5
Schlenga, Klaus Or10.1
Schmidl, F. Or9.7, PII-2.4
Schonecke, M. PII-5.10
Schoop, U. PII-5.10
Schubert, J. Or7.3
Schubert, Josef PII-4.2
Schubert, M. PI-5.10
Schuler, J. PII-3.3
Schultze, V. PI-2.4, W-2.-1
Schulze, Holger PI-1.18
Schurig, Th. Or8.3
Schurig, Thomas Or9.2
Schwaab, G. Or7.3
Schymon, S. PII-5.10
Seidel, P. Or9.7, PII-2.4
Semenov, A. Or7.3
Semenov, V. Or2.1
Semenov, V. K. PII-1.3
Semenov, Vasili Or2.4
Semerad, R. PII-5.1
Semerad, Robert Or2.8
Seppa, Heikke PI-2.10
Seppa, Heikki PI-2.9
Shcherbakov, Nikita A. PII-3.8
Shen, Y. Q. PII-2.9, PI-2.6
Shimakage, H. PI-3.7, PII-5.14
Shimakage, Hisashi PII-3.9
Shimizu, H. M. PII-4.5, PII-4.6
Shimizu, Ryoji PI-2.13
Shimizu, T. Or8.7
Shinada, K. Or8.7
Shiraishi, F. PI-2.1
Shitov, S. V. PII-3.2
Shitov, Sergey V. Or4.8
Shoji, Akira PI-5.9
Siddiqui, Aleem Or2.5

Siegel, M. PI-2.4
Siegel, Michael Or2.7, Or2.8, PI-4.4
Silvestrini, P. PI-3.6
Simon, R. W. PII-3.10
Simon, Randy Or1.3
Sipilä, H. PI-4.1
Snigirev, Oleg V. Or8.2
Soble, C. Or9.5
Soble, Clifford Or10.2
Sobolewski, R. Or7.5
Sobolewski, Roman PII-1.4, Or7.4, PI-4.3
Sodtke, Erik Or2.7
Soghomonian, Victoria Or10.2
Sok, Junghyun PII-3.11
Song, I-Hun PII-3.11, PI-2.2
Song, I. H. PII-2.8
Sørensen, Claus B. PI-3.5
Soutome, Y. PI-1.6, PII-5.2
Souza, Ricardo E. de Or10.1
Spargo, J. W. Or3.4
Spooner, A. Or3.4
Starodubrovskii, Ruslan K. Or2.8
Stepantsov, Evgueni S. Or8.2
Stolz, R. W-2.-1, PI-2.8, PI-2.4
Straub, R. Or9.1
Sudoh, E. Or8.7
Suni, I. PI-4.1
Suoknuuti, J. K. Or10.4
Suoknuuti, Janne K. Or10.5
Suppula, T. I. Or10.4
Suzuki, Hideo PII-1.16
Suzuki, Y. PI-1.11
Sydow, Jason P. Or5.2
Szczupak, J. PII-2.11
Tabata, Hitoshi PI-3.9
Taboryski, Rafael PI-3.5
Tachiki, M. PII-5.11
Tachiki, T. PII-5.4
Tafuri, F. PII-5.5
Tahara, S. PII-1.5
Tahara, Shuichi PII-1.14, PI-5.16, Or1.1, PI-1.14
Taino, T. PII-4.5
Taino, Toru PII-1.1
Takagi, K. PII-5.2, PI-1.6
Takahara, H. Or8.7
Takahashi, Hirokazu PII-4.8
Takahata, M. Or8.7
Takano, Y. PI-5.14
Takayanagi, Hideaki PI-5.17
Takeuchi, S. Or8.7
Takizawa, H. PII-4.5
Takizawa, Y. PII-4.6
Talanov, V. V. PI-5.19
Talvacchio, J. Or2.6
Tanabe, K. Or6.2, Or8.7, PII-5.6
Tanabe, Keiichi Or5.4
Tanaka, Michi PI-5.16
Tanaka, Saburo PI-2.13
Tarasov, Michael PII-4.1
Tarasov, Michael A. Or8.2
Tarte, E. J. PI-3.2, PI-5.7
Tarte, Edward J. PII-5.8
Tarutani, Y. PII-5.2, PI-1.6
Teh, C. K. PII-1.9
Terai, Hirotaka PI-5.6, PI-1.9
Testa, G. PII-5.5
Tighe, Thomas S. PI-5.18
Tilbrook, D. L. PI-2.11, PII-5.17
Tinchev, S. S. PII-5.7
Tolpygo, Sergey K. PI-5.1
Toma, K. PII-5.6
Tomiyama, T. Or4.3
Tong, Ming Xhao PI-1.17, PI-1.3
Trahms, L. PII-2.13
Tsukamoto, A. PII-5.2
Tsunematsu, S. Or8.7
Uccio, U. Scotti di PII-5.5
Uchaikin, Sergey V. PI-2.12, W-1.-1
Uchikawa, Y. Or8.7
Uchiyama, Tetsuji PII-3.9
Usagawa, Toshiyuki Or5.4
Utagawa, T. PII-5.6, Or6.2
Utagawa, Tadashi Or5.4
Uzawa, Yoshinori PI-5.6, PII-4.3
V.Granata, V.Granata PII-3.5
Vaks, Vladimir L. Or4.8
Vale, L. PII-5.1
Vale, L. R. PI-4.7, PI-3.7, Or4.6, Or4.5
Van Duzer, T. Or3.6, Or3.3
Van Duzer, Theodore PII-5.18, PI-1.10, PI-5.3
Van Tendeloo, G. PII-5.5
Verbist, K. PII-5.5
Verevkin, A. A. Or7.5
Vogt, J. Or2.1
Vogt, Johannes M. PII-1.12
Vogt, T. Or9.7
Vorobiev, A. K. PI-5.19
Voronov, B. Or7.3
Voss, M. PII-4.4
Vostokov, N. V. PI-5.19
Waller, W. V. PI-2.11
Wang, H. B. PII-5.4

Wang, Wan Or6.5
Wang, Zeng PI-1.9
Wang, Zhen PII-3.9, PI-5.6, PII-4.3, PII-5.14
Warzemann, L. PII-2.12
Watanabe, H. PII-4.5
Watenabe, H. PII-4.6
Weber, C. PII-5.1
Weber, Clemens Or2.8
Weber, P. PII-2.12
Weidl, R. Or9.7
Weir, Terry Or2.5
Weiss, S. PII-3.3
Weiss, Stefan Or8.6
Weitschies, W. PII-2.12, PII-2.13
Wen, Jianguo Or5.4
Wenzel, K. Or8.3
Whiteley, S. R. Or3.6
Whiteley, Steve PI-1.10
Whyborn, Nick Or4.8
Wiedenhorst, B. PII-5.10
Wilaon, Y. M. PI-2.11
Wildt, Morten PI-3.5
Williams, Carlo PI-4.3, PII-1.4
Winkler, Dag PI-4.6, PII-5.8
Withers, Richard Or10.2
Wittie, Larry Or3.2
Wollman, D. A. Or7.1
Wong, A. PII-5.18
Wong, Andre PI-5.3
Wong-Foy, Annjoe Or10.1
Wooliscroft, M. J. Or5.1
Worsham, A. H. Or2.3
Worsham, A. Hodge Or3.5, Or3.7
Wu, J. Z. PII-5.14
Wu, P. H. PI-5.11, PII-5.4
Wunderlich, S. PII-2.4, Or9.7
Xiang, X. -D. Or10.3
Xie, Y. Y. PII-5.14
Xu, Hui Or4.2
Yagoubov, Pavel PII-4.2
Yamada, Y. Or8.7
Yamaguchi, Hiroshi PI-5.17
Yamamori, Hirotake PI-5.9
Yamashita, T. PII-5.4
Yamashita, Tsutomu PII-4.7, Or5.6, PI-4.8
Yamazaki, Osamu PI-2.13
Yan, S. L. PII-5.14
Yang, W. I. PI-3.8
Yasuda, Kyounei PII-5.12
Yokosawa, Koichi PI-2.3
Yokoyama, N. PI-1.15
Yoneyama, Kaolu PII-1.8
Yoon, Seok-Yeol PII-3.11, PI-2.2
Yorozu, Shinichi Or1.1, PI-1.14, PII-1.14
Yoshida, A. PI-1.15
Yoshida, Kazuhiro PII-5.9
Yoshida, Keiji PII-3.9
Yoshida, T. PII-2.14
Yoshida, Y. Or8.7
Yoshikawa, N. Or3.3
Yoshikawa, Nobuyuki PI-1.7, PII-1.7, PII-1.8
Yoshimori, Shigeru PII-3.7
You, L. X. PI-5.11
Young, R. M. Or2.6
Yu, Yang PII-5.14
Yulin, A. V. PII-3.2
Yurgens, August PII-5.8
Zakosarenko, V. PI-2.4
Zhang, Y. N. Or6.7
Zhang, Yongming PI-1.8, PI-1.2
Zheng, L. Or3.6, Or3.3
Zheng, Lizhen PI-1.10, PI-5.3
Zhilyaev, I. N. PII-3.6
Zhuravlev, Y. PI-2.14
Zimmermann, Peter PI-4.4
Zinoviev, Dmitry PI-1.14
Zinoviev, Dmitry Y. Or3.2, PII-1.2